

NASA Contractor Report 185158

Experimental Performance and Acoustic Investigation of Modern, Counterrotating Blade Concepts

Final Report

G.E. Hoff, et al.
GE Aircraft Engines
Advanced Technology Operations
Cincinnati, Ohio 45215

January 1990

Prepared for
Lewis Research Center
Under Contract NAS3-24080



(NASA-CR-185158) EXPERIMENTAL PERFORMANCE
AND ACOUSTIC INVESTIGATION OF MODERN,
COUNTERROTATING BLADE CONCEPTS Final Report
(GE) 185158-1

NP01-23591

CRCL 010

Unclass

03/05 0267646

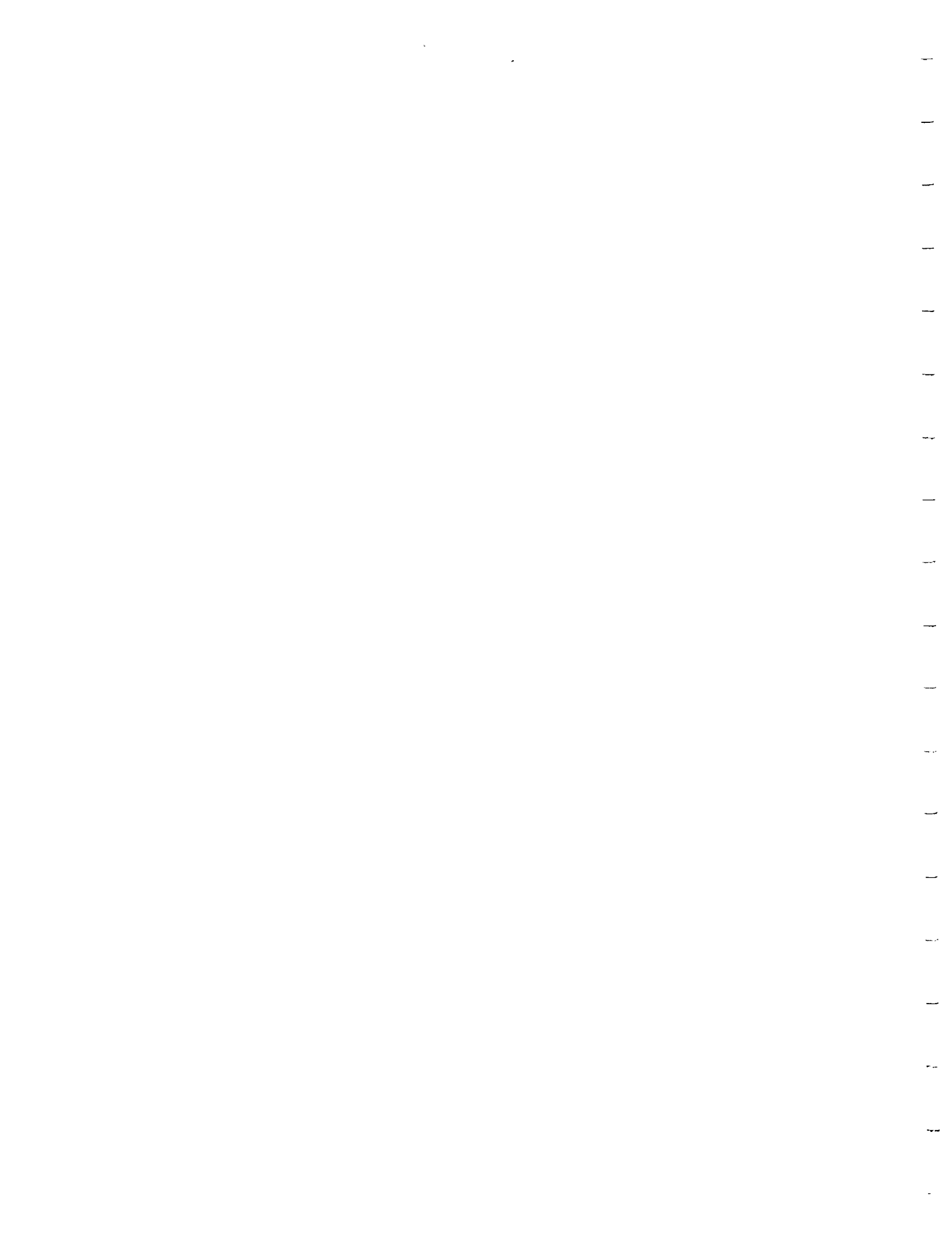


TABLE OF CONTENTS

Section	Page
1.0 SUMMARY	1
2.0 INTRODUCTION	2
3.0 ANALYTICAL METHODS DEVELOPMENT AND DESIGN	5
3.1 Aerodynamic Methods Development	5
3.1.1 Lifting Surface Model	5
3.1.2 Design Analysis and Code Validation	5
3.2 Aeroacoustics Methods Development	17
3.2.1 Scaling Procedures Development and Evaluation	17
3.3 Aerodynamic Design	43
3.3.1 General Aero Design Approach	43
3.3.2 Blade Configurations	46
3.3.3 Axisymmetric Design Flow Analysis	47
3.3.4 Blade Planform Selection and Euler 3D Analysis	55
3.4 Aeroacoustics Design and Design Evaluation	60
3.4.1 The Acoustic Model	60
3.4.2 Aeroacoustic Evaluation of Candidate MPS Blade Designs	66
3.4.3 Tip Vortex Interaction Investigation for Counterrotating Propellers	76
3.5 Aeromechanical Analysis and Design Evaluation	112
3.5.1 Aeroelastic Analyses	113
3.5.2 Stability Analyses	120
3.5.3 F-7/A-7 Forced Response Analysis	130
4.0 MECHANICAL DESIGN AND FABRICATION	133
4.1 Blade Mechanical Design	135
4.2 Blade Fabrication and Quality Control	157
4.3 Blade Instrumentation and Bench Testing	159
4.3.1 Blade Strain Distributions	159
4.3.2 Blade Frequency Testing	162
4.3.3 Blade Pull Testing	162
4.3.4 Blade Fatigue Testing	162
4.3.5 MPS Blade Instrumentation for Operational Testing	165
4.4 Specialized Support Hardware Design and Fabrication	168
4.4.1 Nine-Blade Hub	168

TABLE OF CONTENTS (Continued)

Section	Page
4.4.2 Aeromechanical Hub	178
4.4.3 F-7/A-7 Torque Blades	182
4.4.4 Simulated Ground Plane (Rig 2)	182
4.4.5 Wake Rake (Rig 3)	183
4.4.6 Pylon (Rig 2)	183
4.4.7 Simulated Fuselage (Rig 2)	183
5.0 ACOUSTIC AND PERFORMANCE TESTING	187
5.1 Rig 2/Cell 41 (GE Anechoic Chamber)	187
5.1.1 Facility Description	187
5.1.2 Vehicle Description and Instrumentation	190
5.1.3 Test Matrix Summary	223
5.1.4 Test Procedures	223
5.2 Rig 3/NASA 8x6 Supersonic Wind Tunnel	234
5.2.1 Facility Description	234
5.2.2 Vehicle Description and Instrumentation	238
5.2.3 Test Matrix Summary	269
5.2.4 Test Procedures	269
5.3 Rig 3/NASA 9x15 Low Speed Wind Tunnel	275
5.3.1 Facility Description	275
5.3.2 Vehicle Description and Instrumentation	276
5.3.3 Test Matrix Summary	283
5.3.4 Test Procedures	283
6.0 DATA ACQUISITION REDUCTION AND ANALYSIS	290
6.1 Anechoic Freejet Facility (Cell 41 With MPS Rig 2)	290
6.1.1 Acoustics	290
6.1.2 Aerodynamic	300
6.1.3 Aeromechanical	300
6.2 Rig 3/NASA 8x6 Supersonic Wind Tunnel	300
6.2.1 Aerodynamic	300
6.2.2 Aeromechanical	310
6.2.3 Acoustic	310

TABLE OF CONTENTS (Concluded)

Section	Page
6.3 Rig 3/NASA 9x15 Low Speed Wind Tunnel	320
6.3.1 Acoustics	320
6.3.2 Aerodynamics	325
6.3.3 Aeromechanics	325
7.0 DISCUSSION OF RESULTS	327
7.1 Rig 2/Cell 41 (GE Anechoic Chamber)	327
7.1.1 Acoustic	327
7.1.2 Aerodynamic	546
7.1.3 Aeromechanics	548
7.2 Rig 3/NASA 8x6 Supersonic Wind Tunnel	551
7.2.1 Aerodynamic Performance	551
7.2.2 Aeromechanics	585
7.2.3 Discussion of Acoustic Results	588
7.3 Rig 3/NASA 9x15 Low Speed Wind Tunnel	609
7.3.1 Discussion of Acoustic Results at the NASA Lewis 9x15 Wind Tunnel	609
7.3.2 Aerodynamics	627
7.3.3 Aeromechanics	627
8.0 LOW-RADIUS-RATIO MODULE AND DYNAMIC CALIBRATION LOADING FIXTURE SYSTEM	630
8.1 Low Module	630
8.2 Dynamic Calibration Rig Loading Fixture Subsystem	630
9.0 CONCLUSIONS	631
9.1 Acoustic	631
9.1.1 GE Anechoic Freejet Facility (Cell 41)	631
9.1.2 NASA Lewis 8x6 Wind Tunnel	633
9.1.3 NASA Lewis 9x15 Wind Tunnel	633
9.2 Aerodynamics	633
9.3 Aeromechanics	634
10.0 REFERENCES	635

LIST OF ILLUSTRATIONS

Figure	Page
1. GE Study of Bypass Ratio Spectrum.	3
2. SR-3 Data Match Results from Axisymmetric Flow Analysis.	7
3. Radial Distribution of Aero Parameters at Design Data Match, SR-3 at Mach = 0.80.	9
4. SR-3 Euler and Data Match Swirl Distribution.	10
5. SR-3 GE Euler Results.	11
6. Spanwise Mach Number Contours for Pressure Surface.	13
7. Spanwise Mach Number Contours for Suction Surface.	14
8. SR-1 Axisymmetric Flow Calculation Results.	16
9. SR-1 Meridional Mach Number Distribution – Hub Surface (Mach 0.80 Test Point).	18
10. Comparison of SR-1 Test Data and Data Match Calculations.	19
11. SR-1 Euler Results.	20
12. SR-1 Design Point Data Match Results.	21
13. Relative Mach Number Contours for SR-1, Suction Surface.	23
14. Relative Mach Number Contours for SR-1, Pressure Surface.	24
15. Definition of Rotor Coordinates and Rotor Angular Velocities.	27
16. Comparison of Tone Directivities of Flight Test Data and Scaled-Up Cell 41 Data.	31
17. Comparison of Tone Directivities of Cell 41 Data; Scaling Law Estimation, and Analytical Model Prediction.	33
18. Comparison of Tone Directivities of Cell 41 Data; Scaling Law Estimation, and Analytical Model Prediction.	38
19. F-7 Blade Geometry Change (Cold-to-Hot).	45
20. Radial Distribution of Solidity and Lift Coefficient for the F-4/A-4, F-5/A-5, and F-7/A-7 Blades.	48
21. Radial Distribution of Solidity and Lift Coefficient for the F-11/A-11 and F-21/A-21 Blades.	49
22. Radial Distribution of Blade Loading at Design.	50
23. Unducted Fan Blade Aerodynamic Sweep Distribution.	50
24. F-4/A-4 (8+8) Meridional Mach Number Contours.	51
25. F-5/A-5 (8+8) Meridional Mach Number Contours.	52
26. F-7/A-7 (8+8) Meridional Mach Number Contours.	53
27. Meridional Mach Number Contours for F-11/A-11 (11+9).	54
28. Meridional Mach Number Contours for F-21/A-21 (11+10).	55
29. F-4 Euler Results.	56
30. F-11 Euler Results.	58
31. F-21 Euler Results.	61
32. A-11 Euler Results.	63
33. A-21 Euler Results at Mach = 0.80.	64

LIST OF ILLUSTRATIONS (Continued)

Figure	Page
34. Low Speed Data/Theory Acoustic Comparison of Steady-Loading Tones.	67
35. Low Speed Data/Theory Acoustic Comparison of Interaction Tones.	68
36. High Speed Data/Theory Comparison.	69
37. MPS Blade Planforms Used in Blade Acoustic Evaluation Study.	70
38. MPS Blade Acoustic Evaluation Summary.	73
39a. Combined Forced and Free Vortex Model for the Tip Vortex.	81
39b. Nature of the Tip Vortex Flow Model for a Ducted Rotor	81
40. Comparison of Harmonic Gust Spectra at Three Spanwise Locations for Increasing Values of Tip Clearance and for No-Tip-Vortex Case.	82
41. Correlation and Data for the Streamwise Variation of Normalized $(V\theta)_{\max}$ of the Tip Vortex.	84
42. Correlation and Data for the Streamwise Variation of Normalized Radius of the Tip-Vortex Core.	84
43. Representative Correlation and Data for the Streamwise Variation of Normalized $(V\theta)_{\max}$ Radius, and Circulation of the Tip Vortex.	85
44. Streamwise Variation of Normalized Circulation of the Tip Vortex for Three Different Power-Law Decay Rates.	87
45. Correlation and Data for the Trajectory of the Tip Vortex.	87
46. Planform of the F-7/A-7 Unducted Fan Blade Design, Showing the Extent of Clipping on the Aft Rotor.	89
47. Narrowband Acoustic Spectrum of a 9x8 Blade Number Configuration.	91
48. Predicted Influence of the Tip Vortex Trajectory on Gust Harmonic Spectra at Three Streamlines in the Tip Region	92
49. Predicted Influence of the Tip Vortex Trajectory on Each Interaction Tone at Observer Angle of 91°.	93
50. Predicted Influence of the Tip Vortex Trajectory on Interaction Noise Tone SPL Sum.	93
51. Predicted Gust Harmonic Spectra at Two Rotor-to-Rotor Spacings for the Tip Vortex at Different Decaying Rates and for the Case of No Tip Vortex at Two Streamline Locations.	95
52. Assumed Performance of the Progressively Clipped Aft Rotor.	96
53. Predicted Effect of Progressive Clipping of the Aft Rotor on the Steady Loading and Thickness Noise.	96
54. Predicted Effect of Progressive Clipping of the Aft Rotor on the Wake/Tip Interaction Noise.	97
55. The Predicted Effect of Progressive Clipping of the Aft Rotor on the OASPL Directivity.	98
56a. Comparison of Measured and Predicted Effect of Clipping of the Aft Rotor on Steady Loading and Thickness Noise.	100
56b. Comparison of Measured and Predicted Steady Loading and Thickness Tones for Standard and Clipped Aft Rotor at 105° Observer Angle.	100
57a. Comparison of the Measured and Predicted Effect of Clipping of the Aft Rotor. on Interaction Tone SPL Sum With and Without the Tip Vortex Model.	102

LIST OF ILLUSTRATIONS (Continued)

Figure	Page
57b. Comparison of the Effect (Measured and Predicted) of the Aft Rotor. on Interaction Tone SPL Sum With and Without the Tip Vortex Model.	103
57c. A Measured and Predicted Effect Comparison of Clipping of the Aft Rotor. on Interaction Tone Sum With and Without the Tip Vortex Model.	104
58. Comparison of the Measured and Predicted Effect of Clipping of the Aft Rotor on Individual Interaction Tones, With and Without the Tip Vortex Model.	105
59. Predicted Spanwise Variation of Normalized Streamwise Distance, Wake Centerline Defect, and Semiwake Width.	107
60. Comparison of the Measured and Predicted Effect of Clipping of the Aft Rotor on Steady Loading and Thickness Noise for 80% rpm.	108
61. Measured and Predicted Effect of Clipping the Aft Rotor on Interaction Tone SPL Sum With and Without the Tip Vortex Model.	109
62. Comparison of Measured and Predicted Effect of Clipping the Aft Rotor on Individual Interaction Tones With and Without the Tip Vortex Model.	110
63. Flow Chart of the GAP (General Aeroelastic Program).	114
64. Schematic of Pressure Distortions.	118
65. Schematic of Incidence Variation Due to Pressure Distortion.	118
66. Turboprop Blade First Flexural Stability Estimate.	122
67. Turboprop Blade First Torsion Stability Estimate.	122
68. Stability Estimates for MPS F-4/A-4 Blades.	123
69. Stability Estimates for MPS F-5/A-5 Blades.	124
70. Stability Estimates for MPS F-7/A-7 Blades.	126
71. Stability Estimate for MPS F-11 Blade.	127
72. Stability Estimate for Clipped MPS F-11 Blade.	127
73. Stability Estimate for MPS A-11 Blade.	128
74. Stability Estimate for Clipped MPS F-21 Blade.	128
75. Stability Estimate for Clipped MPS F-21 Blade at 100% Speed.	129
76. Stability Estimate for Clipped MPS F-21 Blade at 90% Speed.	129
77. Stability Estimate for Clipped MPS A-21 Blades.	130
78. Comparison of the 1/rev Stress Variation at the Blade Critical Point due to AOA (Angle-of-Attack) for the F-7/A-7 MPS Blades at Mach 0.72.	132
79. Selected Counterrotating Blade Planform Shapes.	134
80. MPS Blade Mechanical Design Procedures Flow Chart.	136
81. F-4 Spar/Shell Design.	137
82. F-11 and A-11 MPS Blades.	137
83. Blade Ply Layup.	139
84. Typical Three-Element Sections of Finite Element Model Thickness Mesh.	140
85. Finite Element Mesh for MPS Blade Design.	143

LIST OF ILLUSTRATIONS (Continued)

Figure	Page
86. Typical Chordwise Slice Through Finite Element Mesh.	143
87. "Quick-Look" Stability Comparison, First-Flex Mode.	144
88. Quick-Look Stability Comparison of the F-11/A-11 in the First-Flex Mode.	145
89. Quick-Look Stability Comparison of the F-21/A-21 in the First-Flex Mode.	146
90. Quick-Look Stability Comparison, First-Torsion Mode.	147
91. Quick-Look Stability Comparison of the F-11/A-11 in the First-Torsion Mode.	148
92. Quick-Look Stability Comparison of the F-21/A-21 in the First-Torsion Mode.	149
93. Stability Estimate for the A-11 MPS Blade.	150
94. Stability Estimate for MPS F-4/A-4 Blades.	152
95. Stability Estimate for MPS F-5/A-5 Blades.	153
96. Stability Estimate for MPS F-7/A-7 Blades.	154
97. Stability Estimate for MPS F-11/A-11 Blades.	155
98. Stability Estimate for MPS F-21/A-21 Blades.	156
99. Hot-to-Cold Shape MPS Blade Determination.	157
100. Basic MPS Blade Manufacturing Process.	100
101. F-7 Blade Strain Distribution Instrumentation.	160
102. A-7 Blade Strain Distribution Instrumentation.	161
103. Pull Test Schematic.	162
104. F-5 No. 10 Fatigue Test Gauge Locations, Pressure Side.	167
105. F-5 No. 10 Fatigue Test Gauge Locations, Suction Side.	167
106. F-4 MPS Blade Gauge Locations.	169
107. A-4 MPS Blade Gauge Locations.	169
108. F-5 MPS Blade Gauge Locations.	170
109. A-5 MPS Blade Gauge Locations.	170
110. F-7 MPS Blade Gauge Locations.	171
111. A-7 MPS Blade Gauge Locations.	171
112. F-11 MPS Blade Gauge Locations.	172
113. A-11 MPS Blade Gauge Locations.	172
114. F-21 MPS Blade Gauge Locations.	173
115. A-21 MPS Blade Gauge Locations.	173
116. Aeromechanical Hub and Rigid Hub Configurations.	179
117. Aeromechanical Hub Structure.	180
118. Ground Plane Installation in Cell 41.	184
119. Ground Plane Installation Details.	185
120. Cell 41 Installation with Fuselage Body-of-Revolution.	185
121. Simulated Fuselage Calculated Mach Number Distribution Comparison.	186

LIST OF ILLUSTRATIONS (Continued)

Figure	Page
122. An Overall Schematic of the GE Anechoic Freejet Noise Facility.	188
123. The Anechoic Chamber (Schematic).	189
124. Schematic of the Test Vehicle Installation in the GE Anechoic Chamber Freejet Facility (Overall).	191
125. Close-Up of Test Vehicle Installation in GE's Anechoic Chamber Freejet Facility.	192
126. The Assembled MPS SN002 in Cell 41.	193
127. MPS SN002 Installation in Cell 41.	194
128. Schematic of MPS SN002 Lube System.	199
129. Schematic of MPS SN002 Control Console Panel Layout.	200
130. Schematic of MPS SN002 Control Console and Support Hardware Hook-Up Arrangement.	205
131. MPS SN002 Outer Turbine Instrumentation.	215
132. MPS SN002 Inner Turbine Instrumentation.	216
133. MPS SN002 Balance Cavity Instrumentation.	217
134. MPS SN002 Telemetry Instrumentation.	219
135. Blade Strain Gauge Monitor Set-Up Schematic for MPS SN002.	220
136. MPS SN002 Health and Control Instrumentation.	222
137. Schematic of Near- and Far-Field Microphone Arrangement in Cell 41 for MPS SN002 Testing.	225
138. NASA Lewis 8x6 Wind Tunnel Schematic.	237
139. The MPS SN003 in the NASA Lewis 8x6 Supersonic Wind Tunnel.	239
140. Schematic of MPS SN003 Installation in 8x6 Wind Tunnel.	240
141. The MPS SN003 Hub Shaft Module.	241
142. The MPS Turbine Drive Module.	244
143. Turbine Drive Air System for MPS SN003 Test in NASA 8x6 Wind Tunnel.	245
144. Schematic of the MPS SN003 Lube System.	248
145. MPS SN003 Outer Turbine Instrumentation.	259
146. MPS SN003 Inner Turbine Instrumentation.	260
147. Balance Cavity Instrumentation of the MPS SN003.	261
148. Telemetry Instrumentation for the MPS SN003.	263
149. Blade Strain Gauge Monitor Set-Up Schematic for MPS SN003.	264
150. The MPS SN003 Health and Control Instrumentation.	265
151. NASA Lewis 8x6 Supersonic Wind Tunnel Translating Acoustic Ceiling Plate Installation.	267
152. Translating Acoustic Ceiling Plate Transducer Locations.	267
153. Schematic of the NASA Lewis 9x15 Wind Tunnel.	276
154. MPS Installation in 9x15 Wind Tunnel.	278
155. The MPS in 9x15 Wind Tunnel, with Pylon, Fuselage, and Polar Microphone.	279

LIST OF ILLUSTRATIONS (Continued)

Figure	Page
156. Schematic of MPS Installation in the 9x15 Tunnel.	280
157. Schematic of Modified MPS SN003 Lube System.	281
158. The NASA Lewis 9x15 Low Speed Wind Tunnel Fixed Microphone Installation.	282
159. Schematic of Traversing Microphone Installation in NASA Lewis 9x15 Low Speed Wind Tunnel.	284
160. The NASA Lewis 9x15 Low Speed Wind Tunnel Polar Microphone Installation Schematic.	285
161. Locations of Fixed Microphones in the Anechoic Chamber, Cell 41.	291
162. Acoustic Data Acquisition and Reduction Procedure at Cell 41.	292
163. Typical Narrow-Band Spectra Measured at the Anechoic Facility.	294
164. Comparison of Steady and Interaction Tones SPL Sums for Various Selected Tones of 11+9 Configuration.	296
165. Comparison of Steady and Interaction Tones SPL Sums for Various Selected Tones of 8+8 Blade Configuration at Unequal rpm's.	297
166. Nomenclature for Cell 41 Performance Parameters.	301
167. Blade-Surface-Mounted Strain Gauge Effects on Net Efficiency (Eight Strain Gauges).	303
168. Typical Campbell Diagram from Engine Gauge No. 1 for F-5 Blade at Mach 0.33.	304
169. Engine Gauge No. 1 Campbell Diagram for A-5 Blade at Mach 0.33.	305
170. Engine Gauge No. 1 Campbell Diagram for Clipped F-11 Blade at Mach 0.34.	306
171. Flutter Response of Gauge No. 3 of MPS A-7 Blade with 35°-Ply Reference Angle on Aeromechanical Hub.	307
172. Response of Gauge No. 3 of MPS A-7 Blade on Aeromechanical Hub with Damper of Full Damping Force (8.5 lb) Showing no Flutter.	308
173. Gauge Response After Installing the Platform Adaptor Seals on the A-7 Aero-mechanical Hub; Flutter Response at 380 Hz Eliminated.	309
174. Flutter Response of MPS A-7 Blade on Rigid Hub at Design Point.	311
175. Flutter Response of MPS A-7 Blade on Rigid Hub.	312
176. Flutter Response for Original F-11 Blade at Mach 0.72.	313
177. Flutter Response for Clipped F-11 Blade at Mach 0.9.	314
178. Flutter Response for Original F-21 Blade at Mach 0.8.	315
179. Flutter Response for Clipped F-21 Blade at Mach 0.8.	316
180. Stress Response for Blade A-7 Aeromechanical Hub.	317
181. Translating Acoustic Plate and MPS in the 8x6 Wind Tunnel.	318
182. Transducer Positions on Translating Acoustic Plate, Standing Inside NASA 8x6 Tunnel Looking Up.	318
183. Transducer Locations at the Four Acoustic Plate Positions.	319
184. Typical Narrow-Band Spectrum from NASA's On-Line System.	321
185. The MPS SN003 and Acoustic Instrumentation Installed in the NASA 9x15 Wind Tunnel.	323

LIST OF ILLUSTRATIONS (Continued)

Figure	Page
186. Effect of the Number of Averages on Narrow-Band Data of 9x15 Wind Tunnel.	324
187. Dependence on the Number of Data Averages of Model-Scale Tones Measured at 9x15 Wind Tunnel.	325
188. Typical F-7/A-7 (11+9) Narrow-Band Data Measured at 9x15 Tunnel with the Traverse Microphone.	326
189. Noise-Source Mechanisms with Counterrotating Fan Engines.	327
190. Repeatability of Aero Performance Data of Baseline F-7/A-7 (8+8) Configuration at Cell 41.	329
191. Repeatability of Acoustic Data of Baseline F-7/A-7 Over a Range of Tip Speeds.	330
192. The Repeatability of PNL and dBA Directivities of Baseline F-7/A-7.	330
193. Repeatability of Baseline F-7/A-7 Spectra at 260 mps (854 fps) Tip Speed.	331
194. Comparison of Test Blade Configurations.	332
195. Aero Performance Data of F-7/A-7, F-1/A-1, and F-5/A-5 (8+8) Configurations.	334
196. Acoustic Data of F-7/A-7, F-1/A-1, and F-5/A-5 (8+8) Configurations.	335
197. OASPL and PNL Directivities of F-7/A-7, F-1/A-1, and F-5/A-5.	336
198. Selected Spectra of F-7/A-7, F-1/A-1, and F-5/A-5.	337
199. OASPL and PNL Directivities of F-7/A-7, F-1/A-1, and F-5/A-5.	338
200. Selected Spectra of F-7/A-7, F-1/A-1, and F-5/A-5.	339
201. Model-Scale Spectra of F-5/A-5, F-7/A-7, and F-1/A-1.	340
202. Model-Scale Tone Level Directivities of F-7/A-7, F-1/A-1, and F-5/A-5.	342
203. Model-Scale Tone Sum Levels of F-7/A-7, F-5/A-5, and F-1/A-1 as a Function of Total Thrust.	344
204. EPNL Comparison of F-7/A-7, F-1/A-1, and F-5/A-5 (8+8) Blade Configurations.	346
205. Comparison of Test Blade Configurations F-7/A-7 and F-11/A-11.	347
206. Aero Performance Data of F-7/A-7 and F-11/A-11.	348
207. Acoustic Data of F-7/A-7 and F-11/A-11.	349
208. OASPL and PNL Directivities of F-7/A-7 and F-11/A-11.	351
209. Selected Spectra of the F-7/A-7 and F-11/A-11.	352
210. The OASPL and PNL Directivities of F-7/A-7 and F-11/A-11.	353
211. Selected Spectra of the F-7/A-7 and F-11/A-11.	354
212. Model-Scale Spectra of F-7/A-7 and F-11/A-11.	355
213. Model-Scale Spectra of F-7/A-7 and F-11/A-11.	356
214. Model-Scale Tone Sum Directivities of F-7/A-7 and F-11/A-11 at 232 mps (760 fps) Tip Speed.	357
215. Model -Scale Tone Sum Directivities of F-7/A-7 and F-11/A-11 at 192 mps (630 fps) Tip Speed.	358
216. Model -Scale Tone Sum Levels of F-7/A-7 and F-11/A-11 as a Function of Total Thrust.	359

LIST OF ILLUSTRATIONS (Continued)

Figure	Page
217. EPNL Comparison of F-7/A-7 and F-11/A-11 (11+9) Blade Configurations.	360
218. Aero Performance Data of F-7/A-7 with Different Blade Numbers.	362
219. Acoustic Data of F-7/A-7 with Different Blade Numbers as a Function of Thrust.	363
220. Acoustic Data of F-7/A-7 (Nominal Rotor Spacing) with Different Blade Numbers as a Function of Tip Speed.	365
221. Acoustic Data of F-7/A-7 (Nominal Rotor Spacing) with Different Blade Numbers as a Function of Thrust per Blade.	366
222. Acoustic Data of F-7/A-7 (Nominal Rotor Spacing) with Different Blade Numbers as a Function of Power per Blade.	367
223. OASPL and PNL Directivities of F-7/A-7 (Nominal Rotor Spacing) with Different Blade Numbers at Typical Takeoff Thrust.	368
224. Spectra of F-7/A-7 (Nominal Rotor Spacing) with Different Blade Numbers at Typical Takeoff Thrust.	369
225. OASPL and PNL Directivities of F-7/A-7 (Nominal Rotor Spacing) with Different Blade Numbers at Typical Cutback Thrust.	370
226. Spectra of F-7/A-7 (Nominal Rotor Spacing) with Different Blade Numbers at Typical Cutback Thrust.	371
227. Selected Narrow-Band Data of F-7/A-7 with Different Blade Numbers at Equal Thrust.	373
228. Selected Narrow-Band Data of F-7/A-7 with Different Blade Numbers at Equal Tip Speed of 247 mps (810 fps).	374
229. Model-Scale Tone Directivities of F-7/A-7 with Different Blade Numbers at Matching Takeoff Thrust.	375
230. Model-Scale Tone Directivities of F-7/A-7 with Different Blade Numbers at Matching Cutback Thrust.	376
231. Model-Scale Tone Sum Levels of F-7/A-7 with Different Blade Numbers as a Function of Total Thrust.	377
232. Aero Performance of F-7/A-7 with Different Blade Numbers.	378
233. Acoustic Data of F-7/A-7 with Different Blade Numbers as a Function of Thrust.	379
234. Acoustic Data of F-7/A-7 with Different Blade Numbers as a Function of Tip Speed.	381
235. Acoustic Data of F-7/A-7 with Different Blade Numbers as a Function of Thrust per Blade.	382
236. Acoustic Data of F-7/A-7 with Different Blade Numbers as a Function of Power per Blade.	383
237. The OASPL and PNL Directivities of F-7/A-7 with Different Blade Numbers at Typical Takeoff Thrust.	384
238. Spectra of F-7/A-7 with Different Blade Numbers at Typical Takeoff Thrust.	385
239. OASPL and PNL Directivities of F-7/A-7 With Different Blade Numbers at Typical Cutback Thrust.	386
240. Spectra of F-7/A-7 with Different Blade Numbers at Typical Cutback Thrust.	387
241. Selected Narrow-Band Data of F-7/A-7 with Different Blade Numbers at Equal Tip Speed of 247 mps (810 fps).	388

LIST OF ILLUSTRATIONS (Continued)

Figure	Page
242. Selected Narrow-Band Data of F-7/A-7 with Different Blade Numbers at Approximately Equal Thrust.	389
243. Model-Scale Tone Sum Directivities of the F-7/A-7 with Different Numbers of Blades at Matching Takeoff Thrust.	390
244. Model-Scale Tone Sum Directivities of the F-7/A-7 with Different Numbers of Blades at Matching Cutback Thrust.	391
245. Model-Scale Tone Sum Levels of F-7/A-7 with Different Numbers of Blades as a Function of Total Thrust.	392
246. Model-Scale Tone Sum Levels in the Plane-of-Rotation of the Rotors as a Function of Total Blade Numbers.	393
247. Effect of Blade Numbers for the EPNL.	395
248. Schematic of MPS Cell 41 Setup of Rotor Installation Spacings.	396
249. Nominal and Maximum Rotor-to-Rotor Spacing Comparison for the F-7/A-7 Blades.	397
250. Typical Narrow-Band Data Comparison of F-7/A-7 at Tip Speed of 232 mps (760 fps).	398
251. SPL Directivity of BPF and Higher Harmonics for F-7/A-7 (8+8; 37.9o/37.4o).	399
252. Model-Scale Tone Sum Levels for F-7/A-7 (8+8) as a Function of Total Thrust.	400
253. Comparison of Spectra of F-7/A-7 (8+8; 37.9o/37.4o) with Nominal and Maximum Rotor Spacings at Tip Speeds of 220, 232, 810, and 855 mps.	401
254. PNL Directivity Comparison of F-7/A-7 (8+8; 37.9o/37.4o) with Nominal and Maximum Rotor Spacings.	402
255. Effect of Rotor-to-Rotor Spacing on the Maximum PNL and dBA of F-7/A-7.	404
256. Spectral Comparison of F-7/A-7 (8+8, 43.3o/40.4o) with Nominal and Maximum Rotor Spacings.	405
257. PNL and dBA Directivity Comparisons of F-7/A-7 (8+8; 43.3o/40.4o).	406
258. F-7/A-7 Effect of Spacing on the Maximum PNL and dBA.	407
259. Typical Narrow-Band Data Comparison of the F-7/A-7 at Nominal and Maximum Rotor Spacings and at a Tip Speed of 247 mps (810 fps).	408
260. Directivity of Steady-Loading and Rotor-to-Rotor Interaction Noise for F-7/A-7 (9+8; 38.4°/37.4°).	409
261. Directivity of Steady-Loading and Rotor-to-Rotor Interaction Noise for F-7/A-7 (9+8; 38.4°/37.4°).	410
262. Model-Scale Tone Sum Levels of F-7/A-7 (9+8) as a Function of Total Thrust.	411
263. Comparison of Spectra of F-7/A-7 (9+8; 38.4°/37.4°) with Nominal and Maximum Rotor Spacings at Tip Speeds of 247 mps (810 fps).	413
264. A PNL and dBA Directivity Comparison of the F-7/A-7 (9+8; 38.4°/37.4°) at Tip Speed of 247 mps (810 fps).	414
265. Effect of Rotor-to-Rotor Spacing on the Maximum PNL and dBA of the F-7/A-7.	415
266. Schematic Comparison of Planform and Blade Spacing of F-7/A-7 with Clipped Aft Blade.	416
267. Typical Narrow-Band Data Comparison of F-7/A-7 (Clipped) at a Tip Speed of 247 mps (810 fps).	417

LIST OF ILLUSTRATIONS (Continued)

Figure		Page
268.	Directivity of Steady-Loading and Rotor-to-Rotor Interaction Noise for F-7/A-7c (9+8; 36.3°/42.7°).	418
269.	Directivity of Steady-Loading and Rotor-to-Rotor Interaction Noise for F-7/A-7c (9+8; 36.3°/42.7°).	419
270.	Model-Scale Tone Sum Levels of F-7/A-7c (9+8) as a Function of Total Thrust.	421
271.	A Comparison of Spectra of the F-7/A-7c at a Tip Speed of 247 mps (810 fps).	422
272.	PNL and dBA Directivity Comparison of F-7/A-7 Clipped at a Tip Speed of 247 mps (810 fps).	423
273.	Effect of Rotor-to-Rotor Spacing on the Maximum PNL and dBA of the F-7/A-7 Clipped.	424
274.	Rotor-to-Rotor Spacing Comparison for F-11/A-11 Blades.	425
275.	Typical Narrow-Band Comparison of F-11/A-11 for Maximum and Supermaximum Spacing at a Microphone Angle of 97°.	426
276.	Comparison of Spectra of F-11/A-11 (11+9; 48.7°/45.3°) with Maximum and Supermaximum Rotor Spacings at a Tip Speed of 220 mps (720 fps).	428
277.	PNL and dBA Directivity Comparison of F-11/A-11 (11+9; 48.7°/45.3°) at Tip Speed of 220 mps (720 fps).	429
278.	PNL and dBA Directivity Comparisons of F-11/A-11 (11+9; 48.7°/45.3°) with Maximum and Supermaximum Spacings at Tip Speed of 192 mps (630 fps).	430
279.	Effect of Rotor-to-Rotor Spacing on the Maximum PNL and dBA of F-11/A-11 (11+9).	431
280.	Effect of Rotor-to-Rotor Pitch-Change-Axes Spacing on EPNL Data for F-7/A-7 and F-11/A-11 Configurations.	433
281.	Variation in Blade Spacing as a Function of Radii for the F-7/A-7 at Different Test Pitch Angles.	434
282.	Aero Performance of the F-7/A-7 at Different Blade-Pitch Angles.	435
283.	Acoustic Data of the F-7/A-7 at Different Blade-Pitch Angles.	436
284.	The OASPL and PNL Directivities of F-7/A-7 for Different Tip Speeds at a Typical Cutback.	439
285.	The OASPL and PNL Directivities of F-7/A-7 for Different Tip Speeds at Typical Takeoff.	440
286.	Spectra at a 96° Emission Angle for Different Tip Speeds of the F-7/A-7 (8+8) with Nominal Rotor Spacing.	441
287.	Selected Model-Scale Narrow-Band Spectra for Different Tip Speeds at Typical Cutback.	442
288.	Selected Model-Scale Narrowband Spectra for Different Tip Speeds at Typical Takeoff.	443
289.	Model-Scale Tone Level Directivities of F-7/A-7 (8+8, Nominal Rotor Spacing) for Different Tip Speeds at Typical Cutback.	444
290.	Model-Scale Tone Level Directivities of F-7/A-7 (8+8, Nominal Rotor Spacing) for Different Tip Speeds at Typical Takeoff.	445
291.	Effect of Tip Speed on the Steady-Loading Noise of the F-7/A-7 (8+8).	446
292.	Aero Performance of F-7/A-7 at Different Blade-Pitch Angles.	447
293.	Acoustic Data of F-7/A-7 at Different Blade-Pitch Angles.	448

LIST OF ILLUSTRATIONS (Continued)

Figure	Page
294. OASPL and PNL Directivities of F-7/A-7 (8+8, Maximum Rotor Spacing) for Different Tip Speeds at a Typical Cutback.	449
295. OASPL and PNL Directivities of F-7/A-7 (8+8, Maximum Rotor Spacing) for Different Tip Speeds at Typical Takeoff.	450
296. Spectra at an Emission Angle of 91° for the F-7/A-7 (8+8, Maximum Rotor Spacing) at Different Tip Speeds.	451
297. F-7/A-7 Aero Performance at Different Blade-Pitch Angles.	452
298. F-7/A-7 Acoustic Data at Different Blade-Pitch Angles.	454
299. OASPL and PNL Directivities of F-7/A-7 (9+8, Maximum Rotor Spacing) at Different Tip Speeds for a Typical Cutback.	455
300. OASPL and PNL Directivities of F-7/A-7 (9+8, Maximum Rotor Spacing) at Different Tip Speeds at Takeoff.	456
301. Spectra at an Emission Angle of 91o for the F-7/A-7 (9+8, Maximum Rotor Spacing) at Different Tip Speeds.	457
302. Selected Typical Model-Scale Narrow-Band Spectra of F-7/A-7 for Different Tip Speeds.	458
303. Model-Scale Typical Tone Sum Level Directivities of F-7/A-7 (9+8, Maximum Rotor Spacing) for Different Tip Speeds.	460
304. Model-Scale Tone Sum Levels for Different Tip Speeds as a Function of Thrust.	462
305. Benefit of Reduced Tip Speed on EPNL of F-7/A-7 (9+8, Maximum Rotor Spacing).	463
306. Aero Performance of the F-7/A-7c (Clipped) at Different Blade-Pitch Angles.	464
307. Acoustic Data at Different Blade-Pitch Angles.	465
308. OASPL and PNL Directivities for Different Tip Speeds at a Typical Cutback.	466
309. Spectra (Emission Angle, 91o) for Different Tip Speeds at Typical Cutback.	467
310. Selected Typical Model-Scale Narrow-Band Spectra of F-7/A-7c (Clipped) for Different Tip Speeds.	469
311. Model-Scale Tone Sum Level Directivities of Clipped F-7/A-7 for Different Tip Speeds.	471
312. Model-Scale Tone Sum Levels for Different Tip Speeds as a Function of Thrust.	473
313. Variation in Blade Spacing as a Function of Radii for F-11/A-11 for Different Test Pitch Angles.	474
314. F-11/A-11 Aero Performance at Different Blade-Pitch Angles.	475
315. F-11/A-11 Acoustic Data at Different Blade-Pitch Angles.	476
316. PNL Directivity and a Spectra of F-11/A-11 (11+9, Maximum Rotor Spacing) for Different Tip Speeds at a Typical Takeoff.	477
317. Selected Model-Scale Narrow-Band Spectra of F-11/A-11 for Different Tip Speeds.	478
318. F-11/A-11 Aero Performance at Different Blade-Pitch Angles.	481
319. Acoustic Data for F-11/A-11 (11+9 Supermaximum Spacing) at Different Pitch Angles.	482
320. PNL Directivity and a Spectra of F-11/A-11 (11+9, Supermaximum Spacing) for Different Tip Speeds at Typical Takeoff.	483

LIST OF ILLUSTRATIONS (Continued)

Figure	Page
321. Selected Model-Scale Narrow-Band Spectra of F-11/A-11 for Different Tip Speeds at Typical Takeoff.	484
322. Model-Scale Tone Sum Level Directivities of F-11/A-11 (11+9 Supermaximum Spacing) for Different Tip Speeds at Typical Takeoff.	485
323. Model-Scale Tone Sum Levels for Different Tip Speeds as a Function of Thrust.	486
324. Effect of Clipped Aft Blade on the Maximum OASPL, PNL, and dBA of F-7/A-7 (9-8), Nominal Pitch.	488
325. OASPL and PNL Directivity Comparison of F-7/A-7 (9+8; Nominal Pitch) at Cutback.	490
326. Selected Spectra of Aft Unclipped and Clipped F-7/A-7 (9+8) at Cutback.	491
327. Narrow-Band Spectra of the Unclipped and Clipped F-7/A-7 (Nominal Pitch) at Cutback.	492
328. Directivity of Rotor-to-Rotor Interaction Noise of the Unclipped and Clipped F-7/A-7 (9+8; Nominal Pitch) at Cutback.	493
329. Model-Scale Tone Sum Levels of F-7/A-7 and F-7/A-7c (9+8; Nominal Pitch) as a Function of Total Thrust.	494
330. Effect of Clipped Aft Blade on Maximum OASPL, PNL, and dBA of F-7/A-7 (9+8), Open Pitch.	495
331. OASPL and PNL Directivity of the F-7/A-7 (9+8; Open Pitch) Configurations at Cutback.	498
332. Selected Spectra of the F-7/A-7 (9+8, Open Pitch) Configurations at Cutback.	499
333. OASPL and PNL Directivity of the F-7/A-7 (9+8; Open Pitch) Configurations at Typical Takeoff.	500
334. Selected Spectra of the F-7/A-7 (9+8 Open Pitch) Configurations at a Typical Takeoff.	501
335. Narrow-Band Spectra of Aft Unclipped and Clipped F-7/A-7, Open Pitch.	502
336. Model-Scale Tone Sum Levels as a Function of Total Thrust.	504
337. OASPL and PNL Directivity of F-7/A-7c (9+8) Compared to Baseline F-7/A-7 (8+8).	505
338. Aero Performance of F-7/A-7 (9+8) for Various Community Mach Numbers.	507
339. The Acoustic Data of F-7/A-7 (9+8) at a Pitch Angle of 38.4/37.4 at Various Community Mach Numbers.	508
340. Aero Performance of F-7/A-7 (11+9) for Various Community Mach Numbers.	511
341. Acoustic Data of F-7/A-7 (11+9) at a Pitch Angle of 38.4/37.4 for Various Community Mach Numbers.	512
342. PNL Directivity and Selected Spectra for F-7/A-7 (11+9), with Pitch Angle of 38.3/38.6.	515
343. Model-Scale Tone Sum Directivities of F-7/A-7 (11+9, 38.3/38.6) at Flight Mach Numbers 0.25 and 0.20 for Cutback and High Thrust.	517
344. Model-Scale Tone Sum Levels at Mach Numbers 0.25 and 0.20 for F-7/A-7 as a Function of Thrust.	518
345. Schematic of MPS Cell 41 Setup Detailing the Nominal and Close Pylon Positions.	520
346. Effects of Pylon on Maximum Noise Data of F-7/A-7 with 8+8 and 9+8 Blades.	521

LIST OF ILLUSTRATIONS (Continued)

Figure	Page
347. A Comparison of OASPL and PNL Directivities of F-7/A-7 (8+8) With and Without Nominal Pylon.	522
348. Spectral Comparison of F-7/A-7 (8+8) With and Without Nominal Pylon.	523
349. OASPL and PNL Directivities of F-7/A-7 (9+8) Without any Pylon and With Nominal and Close Pylons at Typical Takeoff.	525
350. Spectral Comparison of F-7/A-7 (9+8) With No Pylon and With Nominal and Close Pylons at Typical Takeoff.	526
351. OASPL and PNL Directivities Without Pylon and With Nominal and Close Pylons at Typical Cutback.	527
352. Spectral Comparison Without Pylon and With Nominal and Close Pylons at Typical Cutback.	528
353. Comparison of Forward Rotor, Aft Rotor, and Rotor-to-Rotor Interaction Tone Sum Results of F-7/A-7 (9+8) With No Pylon, and With Nominal and Close Pylons.	529
354. Directivity of Pylon/Rotor Interaction Noise with Nominal and Close Pylons at Typical Takeoff and Cutback.	531
355. Steady-Loading, Rotor-to-Rotor, and Pylon-to-Rotor Interaction Noise Components as a Function of Total Thrust.	532
356. Effect of a Mounting Pylon on the EPNL of F-7/A-7 Configuration with 8+8 and 9+8 Blades.	533
357. Effects of Pylon on Maximum Noise Data of F-7/A-7c at Maximum Rotor Spacing.	535
358. A Comparison of OASPL and PNL Directivities of F-7/A-7c (9+8) With and Without Nominal Pylon at Typical Cutback.	536
359. A Spectral Comparison of the F-7/A-7c (9+8) With and Without Nominal Pylon at Typical Cutback.	538
360. Comparison of OASPL and PNL Directivities With and Without Nominal Pylon.	540
361. Spectral Comparison of F-11/A-11 (11+9) With and Without Nominal Pylon.	541
362. Noise Power Distance Curves as a Function of Corrected Thrust.	543
363. Cell 41 Acoustic Highlights.	547
364. Effect of Rotor-to-Rotor Spacing Variation on F-7/A-7 (8+8) Low Speed Performance (Cell 41).	549
365. Effect of Rotor-to-Rotor Spacing Variations on the F-11/A-11 (11+9) Cell 41 Low Speed Performance at Mach 0.25.	549
366. Effect of Blade Number Variation on F-11/A-11 (Supermaximum Spacing) Low Speed Performance in Cell 41 at Mach 0.25.	550
367. F-7/A-7 (8+8) Overall Performance in 8 **6 Tunnel at Mach 0.67.	552
368. F-7/A-7 (8+8) Overall Performance in the NASA 8x6 Wind Tunnel at Mach 0.72.	554
369. F-7/A-7 (8+8) Overall Performance in NASA 8x6 Wind Tunnel at Mach 0.76.	556
370. F-7/A-7 (8+8) Overall Performance in NASA's 8x6 Tunnel at Mach 0.8.	558
371. Overall Performance for F-7/A-7 (8+8) at Mach 0.85.	560

LIST OF ILLUSTRATIONS (Continued)

Figure	Page
372. Mach Number Effect on F-7/A-7 (8+8) Nominal Spacing Overall Performance.	563
373. Disk Loading Effect on F-7/A-7 (8+8) Nominal Spacing Overall Performance.	564
374. Spacing Effect on F-7/A7 Power Absorption at Mach 0.72.	565
375. Rotor Spacing Effect on F-7/A-7 Net Efficiency at Mach 0.72.	566
376. Rotor Spacing Effect on F-7/A-7 Net Efficiency at Mach Numbers 0.67 and 0.80.	567
377. Spacing Effects on Baseline F-7/A-7 Torque Ratio at Mach 0.72.	568
378. Effect of Angle-of-Attack on F-7/A-7 (8+8), at Mach 0.70 with No Pylon (in BTWT).	569
379. Effect of Angle-of-Attack on F-7/A-7 (8+8), at Mach 0.70 with Pylon On (in BTWT).	571
380. Effect of Angle-of-Attack on Baseline F-7/A-7 at Mach 0.24 with Pylon On (in BTWT).	572
381. Effect of Mismatched rpm's on F-7/A-7 (8+8) Nominal Spacing Performance at Mach 0.72 (ENET Versus PQA/J3).	573
382. Effect of Mismatched Speed on the F-7/A-7 (8+8) Nominal Spacing Performance at Mach 0.72.	575
383. Effect of F-11 Clipping (for Stability) on F-11/A-11 Performance Measured in 8x6 Tunnel.	576
384. Disk Loading Effect on F-11c/A-11 Performance at Mach 0.80.	577
385. Comparison of Standard and Modified Forebodies and Aftbodies for F-21/A-21.	579
386. F-21c/A-21 Performance Comparison Between Standard and New forebody Configurations in 8x6 Tunnel.	580
387. Effects of Aftbody Configuration and Blade Strain Gauges on F-21c/A-21 Performance in 8x6 Tunnel (ENET Versus PQA/J3).	582
388. Effects of Aftbody Configuration and Blade Strain Gauges on F-21c/A-21 Performance in the 8x6 Tunnel (PQA Versus J1C).	583
389. Performance Summary for F-21c/A-21 in 8x6 Tunnel.	584
390. F-4/A-4 Performance Map.	586
391. The F-5/A-5 Performance Map.	587
392. MPS Blade Planforms Tested in the 8x6 Wind Tunnel.	589
393. Comparison of Data and Theory for the BPF Tone at Different Plate Positions.	590
394. Comparison of Data and Theory for the 2xBPF Tone at Different Plate Positions.	591
395. Comparison of Data and Theory for the 3xBPF Tone at Different Plate Positions.	592
396. Collapse of Data (from Different Plate Positions) at Plate Position 2, Using the Inverse-Square Law (Readings 2047 through 2050).	593
397. Comparison of 8x6 Data with Theory and Data from BTWT for the F-7/A-7, at Plate Position 2.	594
398. Spanwise Variation of Axial Blade-to-Blade Spacing, Normalized by Rotor 1 Axial Chord, Under Cruise Conditions.	598
399. The Effect of Rotor Spacing on Tone Noise at Cruise for the F-7/A-7, at 100% rpmc.	599
400. Tone Sum Comparison of F-7/A-7 and F-21/A-21 (Mach 0.8, 100% rpmc, at Maximum Spacing).	602

LIST OF ILLUSTRATIONS (Concluded)

Figure	Page
401. Components of BPF Tones for F-21/A-21, Reading 5300, 100% rpmc, Mach 0.80.	603
402. F-7/A-7 Data/Theory Comparison for Reading 4377, at 100% rpmc, Mach 0.80.	604
403. F-21/A-21 Tone Sum Data/Theory Comparison for Reading 5300, at 100% rpmc, Mach 0.80.	605
404. F-21/A-21 BPF Tone Data/Theory Comparison for Reading 5300.	606
405. F-21/A-21 2xBPF Tone Data/Theory Comparison (Reading 5300).	607
406. A Comparison of F-21/A-21 3xBPF Tone Data/Theory for Reading 5300.	608
407. Comparison of Predicted Steady-Loading and Thickness Components of BPF for the F-7/A-7 (Reading 4377) and the F-21/A-21 (Reading 5300).	610
408. Predicted Steady-Loading and Thickness Contributions to BPF Tones for F-21/A-21 (Reading 5300).	611
409. Predicted Steady-Loading and Thickness Contributions to BPF Tones for the F-7/A-7 (Reading 4377).	612
410. Comparison of F-11/A-11 and F-21/A-21 (Readings 2839 and 5186, respectively) BPF Tones at Mach Number 0.80.	613
411. Components of BPF Tones for F-11/A-11 (Reading 2839) and F-21/A-21 (Reading 5186) at Mach Number 0.80.	614
412. Comparison of Acoustic Data from the Traversing Microphones.	616
413. Comparison of Measured Aerodynamic Performance.	617
414. A Comparison of Acoustic Narrow-Band Data Measurements.	618
415. Comparison of Measured Steady-Loading and Rotor-to-Rotor Interaction Noise Data.	619
416. Selected Model-Scale Spectral and Overall Sound Pressure Level Directivity Comparison of Data Measured at Tip Speed of 247 mps (810 fps).	620
417. Comparison of Cell 41 and NASA 9x15 Measured Model-Scale Acoustic Data.	621
418. A Comparison of SPL Results Using Cell 41 and NASA 9x15 Measured Model-Scale Data.	622
419. Comparison of Axial Projections and Spacing for Pitch-Change-Axes Spacing Tests with F-7/A-7 Blades at the NASA Lewis 9x15 Wind Tunnel.	624
420. Performance Comparison at Three Spacings Between Pitch-Change Axes of Forward and Aft Blades.	625
421. Model-Scale Tone Sum Directivities of F-7/A-7 for Different Axial Spacings at 260 mps (850 fps).	626
422. Model-Scale Peak Steady-Loading and Interaction Tone Sum Levels from Three Spacing Tests.	628

LIST OF TABLES

Table	Page
1. Comparison of SR-3 and F-7/A-7 Blade Aero Design Parameters.	6
2. Comparison of SR-3 and SR-1 Blade Aero Design Parameters.	15
3. Comparison of SR-1 Test and GE Data Match Analysis Results.	15
4. Nomenclature for Scaling Procedures Development and Evaluation Equations.	26
5. Aerodesign Parameters of the Unducted Fan Blade Configurations.	46
6. MPS Blade Design Parameters.	72
7. MPS Blade Acoustic Evaluation Conditions.	72
8. Nomenclature for Tip/Vortex Model Equations.	78
9. The Normalized Acoustic Frequencies and Spinning Modes Associated with Wake/Tip Vortex Interaction.	91
10. MPS Test/Prediction Stability Correlation.	131
11. Unducted Fan Aerodynamic Design Parameters.	134
12. Scale Model Counterrotating Blade Dimensions.	134
13. AS (Graphite)/PR288 (Epoxy) Ply Properties.	142
14. AS (Graphite) – S (Glass)/PR288 (Epoxy) Ply Properties.	142
15. F-7 Bench Test Frequencies (Hz).	163
16. Comparison of F-7 Analytical and Bench Test Frequencies (Hz).	163
17. A-7 Bench Test Frequencies (Hz).	164
18. Comparison of A-7 Analytical and Bench Test Frequencies (Hz).	164
19. F-5 (No. 4) Fatigue Test Results.	165
20. F-5 (No. 1A) Fatigue Test Results.	166
21. F-5 (No. 10) Fatigue Test Results, Concave Side.	166
22. F-5 (No. 10) Fatigue Test Results, Convex Side.	166
23. F-4 MPS Blade Scope Limits.	168
24. A-4 MPS Blade Scope Limits.	174
25. F-5 MPS Blade Scope Limits.	174
26. A-5 MPS Blade Scope Limits.	175
27. F-7 MPS Blade Scope Limits.	175
28. A-7 MPS Blade Scope Limits.	176
29. F-11 MPS Blade Scope Limits.	176
30. A-11 MPS Blade Scope Limits.	177
31. F-21 MPS Blade Scope Limits.	177
32. A-21 MPS Blade Scope Limits.	177
33. MPS Aeromechanical Hub Design Frequency Comparison.	181
34. MPS Aeromechanical Hub Design Test Versus Analysis and MPS Versus Demo Frequency Comparison.	182

LIST OF TABLES (Concluded)

Table	Page
35. Numerical Code Nomenclature for the MPS Control Console First-Fault Detector.	202
36. MPS SN003 Instrumentation.	206
37. MPS SN003 Telemetry Instrumentation Summary.	218
38. Health/Blade Magnetic Tape Channel Assignments for MPS SN002.	221
39. MPS SN002 Instrumentation for Control Console Input Signals.	224
40. Acoustic Magnetic Tape Channel Assignments for MPS SN002.	226
41. Console Parameters for MPS SN002 Test (Cell 41).	227
42. Cell 41 Acoustic and Performance Test Matrix Summary.	228
43. MPS SN002 Aero Hub Test Summary.	232
44. MPS SN002 Operational Procedures for Cell 41.	235
45. MPS Control Console – Indicator and Shutdown Limits, Cell 41.	236
46. MPS SN003 Instrumentation.	249
47. MPS SN003 Telemetry Instrumentation Summary.	262
48. MPS SN003 Instrumentation Used for Control Console Input Signals.	266
49. Transducer Angular Positions (Ceiling Plate).	268
50. Transducer Angular Positions (Sidewall).	268
51. Summary of 8x6 MPS Test Configurations.	269
52. NASA Lewis 8x6 MPS Test Matrix Summary.	270
53. MPS SN003 Operational Procedures for 8x6 Tunnel.	275
54. Summary of 9x15 MPS Test Configurations.	285
55. NASA Lewis 9x15 Test Matrix Summary.	286
56. Configuration Summary of Acoustic Tests Conducted at Cell 41.	298
57. Cell 41 Test Configuration Summary for Aerodynamic DataAnalysis.	302
58. Translating Acoustic Plate Transducer Locations.	320
59. NASA 8x6 Wind Tunnel Acoustic Test Summary.	322
60. Summary of Cell 41 Rotor Spacing Tests.	396
61. Summary of Cell 41 Tip Speed Variation Tests.	432
62. Cell 41 Pylon Test Summary.	519
63. Aircraft/Engine Information for FAR, Part 36, Stage 3 Noise Assessment.	542
64. Noise Status Projection, EPNdB.	544
65. Summary of F-7/A-7 Flutter Events at the NASA 8x6 Wind Tunnel, with a Hub Configuration of 8+8.	588
66. MPS Blade Design Parameters.	595
67. Performance Parameters of Acoustic Test Points (8x6 Wind Tunnel).	596
68. Axial Spacing Comparison for the F-7/A-7 (11+11) MPS Tests in NASA's 9x15 Tunnel.	627

1.0 SUMMARY

This report describes the work performed by GEAE (GE Aircraft Engines) on NASA Contract NAS3-24080 to theoretically and experimentally evaluate the aerodynamic, acoustic, and aeromechanical performance of GE-defined counterrotating blade concepts. The analytical methods development and design are addressed in this document. Utilizing the analytical methods which evolved during the conduct of this work, aerodynamic and aeroacoustic predictions were first developed and then compared to NASA and GE wind tunnel test results.

This report also presents detailed mechanical design and fabrication descriptions for five different composite shell/titanium spar counterrotating blade set configurations. Further, design philosophy, analysis methods, and material geometry are addressed, as well as the aerodynamic, aeromechanical, and aeroacoustic influences on the design procedures. Blade fabrication and quality control procedures are detailed, bench-testing procedures and results to verify blade integrity are presented, and instrumentation associated with bench-testing is identified. The additional hardware to support specialized testing is also described as are operating blade instrumentation and associated stress limits.

Five GE-designed counterrotating blade concepts were scaled to a 2-foot tip diameter so they could be incorporated into the MPS (model propulsion simulators). Aerodynamic and aeroacoustic performance testing was conducted in the NASA Lewis 8x6 supersonic and 9x15 V/STOL (vertical or short takeoff and landing) wind tunnels and the GE freejet anechoic test chamber (Cell 41) in order to generate an experimental data base for these counterrotating blade designs. Facility and MPS vehicle descriptions are provided, along with descriptions of the test instrumentation. Complete test matrices are provided, detailing test procedures. Effects on performance of rotor-to-rotor spacing, blade number, angle-of-attack, pylon proximity, mismatched rotor speeds, and reduced diameter aft blades are also addressed. In addition, counterrotating blade and specialized aeromechanical hub stability test results are furnished.

2.0 INTRODUCTION

Over the past several years, GE has been engaged in internal as well as government-sponsored studies to evaluate advanced technology, energy efficient propulsion systems for potential use both in commercial and military subsonic aircraft. These studies have covered a wide spectrum of engines, from pure turbojets to helicopters, in terms of size and performance as a function of effective bypass ratio. These studies have included modern turbofans, such as the direct-drive NASA/GE E³ (Energy Efficient Engine), and the geared fan for very high bypass ratio, such as the NASA/GE QCSEE (Quiet, Clean, Short-haul Experimental Engine); conventional turboprops; and the more modern, NASA single-rotation propfans.

Figure 1 illustrates the spectrum of bypass ratios considered. Between the bypass ratio spectrum bounded by the turbofan and turboprop engines lies a region of counterrotation propulsors, unique and unconventional engines. This region is identified as the "unused range" of engines. Included in this class of propulsion concepts are engines which can combine the advantages of turbofans and turboprops.

The GE studies identified particular aerodynamic and acoustic performance advantages for unconventional propulsors that utilized a modern counterrotation blading system, particularly for "pusher type" propulsor designs incorporating a blading concept of high hub-to-tip radius ratio and high disk loading ($shp/D \approx 60$). The work described in this report involves an investigation of these modern, GE-conceived, counterrotation blade concepts; such as, those utilized by the GE UDF®* (unducted fan) engine.

GE began a major, in-house, full-scale UDF development program in 1983. At the outset it was recognized that an adequate data base on counterrotating blade concepts was needed and that the CR/PTR (counterrotating propulsor test rigs) would be required to generate the data. A test rig scale of 0.622 m (24.5-inch) blade-tip diameter was chosen, to match the existing test rig utilized in the NASA Lewis Single-Rotation Propfan Program. These rigs were designated as the 2-foot MPS (model propulsion simulators) and are designed to investigate propulsion-system-installed-performance interactions, as well as to evaluate the mechanical and aerodynamic performance of the counterrotating blades.

In January 1983, GE initiated an in-house, intensive preliminary design study to determine the mechanical design and functional use requirements for the MPS rigs. Both NASA Lewis and GE requirements were reviewed. GE subsequently solicited the Boeing Commercial Airplane Company of Seattle, WA, in April 1983 to finalize the design, fabricate, conduct check-out tests, and deliver three MPS rigs. GE's decision to utilize Boeing was based primarily on Boeing's expertise in the design and fabrication of precision thrust/torque measurement balances and their existing drive module components.

Of three test rigs fabricated (outside of this contracted program), the first rig (No. 1) was utilized in wind tunnel testing at Boeing under a joint GE/Boeing effort to provide precontractual check-out of the test rig systems and preliminary screening of some blade concepts. The second rig (No. 2) was

*Registered trademark of the General Electric Company, USA.

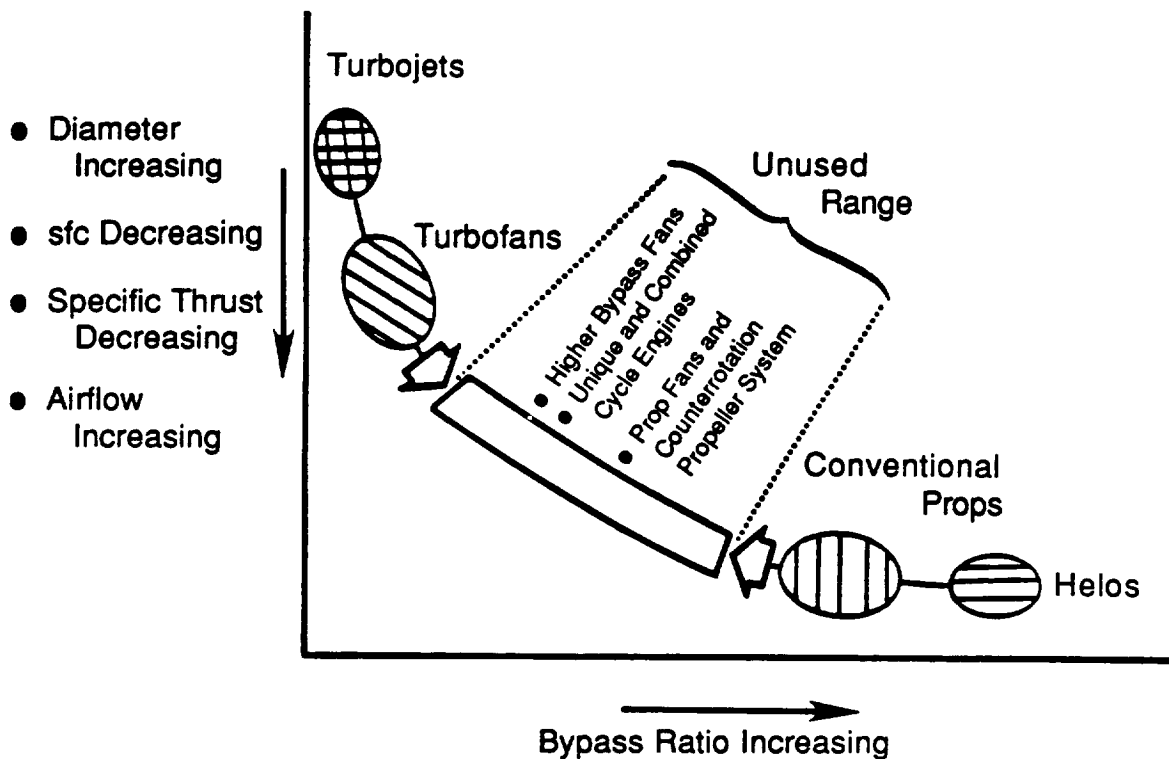


Figure 1. GE Study of Bypass Ratios Spectrum.

used by GE in its anechoic chamber freejet facility to generate data under this program. In compliance with the terms and conditions of this contracted program, the third test rig (No. 3) was provided to NASA Lewis by GE and was used by NASA Lewis in their wind tunnel facilities at Cleveland, OH. GE also provided test support services (personnel) to assist NASA in conducting their own experimental test investigations.

The overall objective of the program associated with this document was to investigate, both theoretically and experimentally, unique GE counterrotation blade concepts. (The experimental investigations were conducted using scale model blading.) The aerodynamic, acoustic, and aeromechanical performances of these concepts were defined, evaluated, and documented for application to future advanced technology (IOC 1990–1995) propulsion systems. In order to accomplish this, the work was segmented into the six tasks listed below:

- Task I – Technical Program Plan and Management
- Task II – Analytical Methods Development and Design
- Task III – Blade Mechanical Design and Fabrication
- Task IV – Simulated Takeoff Flight Acoustic and Performance Experiments
- Task V – NASA Wind Tunnel Performance Test Support
- Task VI – Data Reduction and Analysis.

This report will address subject matter related to these tasks performed under NASA Contract NAS3-24080.

While the intent of this Contractor Report is to mainly present test results obtained under NASA Contract NAS3-24080, the results obtained under separate additional testing conducted at NASA-Lewis by NASA-Lewis personnel are also included to provide a complete documentation of all testing of the five blade designs described in this report.

Separate informal reports compiled for Tasks II, III, and V and the Comprehensive Data Report (CDR) contain more detailed coverage of the work under each of these tasks. Such informal reports are not publicly distributed and thus are referred to in the text only by the contract task number for reference purposes.

The data compiled and discussed in this report are a combination of that required under the terms of the GE contract with NASA and additional data obtained by NASA-Lewis engineers in support of the common industry/government research priorities. Specifically, the low speed data in NASA's 9x15 foot wind tunnel were essentially government furnished supplemental data for comparison to and enhancement of the GE contract data. Acknowledgment of the joint research efforts are appropriate to clarify and distinguish the source of data, hardware, and report figures. Minor issues regarding data accuracy interpretations are still pending as of the publication of these data. However, final resolution of any differences are not expected to substantially affect the overall report quality.

3.0 ANALYTICAL METHODS DEVELOPMENT AND DESIGN

The work effort for this portion of the program involved aerodynamic, aeroacoustic, and aeromechanical design of GE counterrotation blade concepts. It also involved the development of analytical methods needed to support this design effort. Aerodynamic and aeroacoustic predictions were also developed using these analytical methods for comparison with wind tunnel test results from acoustic and performance testing conducted under this program.

3.1 Aerodynamic Methods Development

The approach for aerodynamic methods development was to divide the effort into two main thrusts: the development of a lifting surface model, and design analysis and code validation. The following sections discuss the technical approach used in accomplishing this.

3.1.1 Lifting Surface Model

The principal goal of this activity was to provide a method for shaping the camber line of a swept blade near the tip; to meet this goal, the approach selected was to build on previously established work performed by Professor John Sullivan of the Purdue Research Foundation. Specifically, to modify the Purdue Vortex Lattice Model to include compressibility corrections, optional analytic chordwise loading distributions, blade taper, solidity, sweep, and relative Mach number to provide a measure of the departure angle perturbations due to end effects alone. Results of this activity are contained in Reference 1, which provides a model description, discussion of general theory, software description, and sensitivity study.

3.1.2 Design Analysis and Code Validation

Repeated adjustments and iterations to the GE-CRDC (Corporate Research and Development Center) Euler 3D computer program model were made during the design analysis and code validation investigations involving the SR-3 blade. These studies evaluated the effects of wall boundary conditions, grid density, smoothing parameters, and the distance of the grid boundaries from the blade edges. Three consistency checks were made to determine the optimum method for utilizing Euler 3D to verify design guidelines being employed in counterrotating propulsor blade design. These consistency checks were on: conservation of circulation, torque, and plots of relative total pressure.

The final recommendations for using Euler 3D as a tool in propeller flow field analysis were:

- To use as fine a grid as possible
- To use first-order boundary conditions
- If the blade Mach number distribution is of primary concern, the upstream and downstream boundaries can be fairly close to the edge of the blade
- Second- and fourth-order smoothing should be reduced until any further reduction causes shock overshoots and oscillations in the solution.

The justification for the preceding conclusions is provided in an internal GE report, (GE TM No. 85-515 by R.D. Caney), documenting the Euler 3D work.

3.1.2.1 SR-3 Data Match

Prior to the aerodynamic design of the full-scale F-7/A-7 counterrotating blades, an analytical study was performed to assess the performance of the single-rotation propfan, SR-3, which was designed by Hamilton-Standard under NASA Contract NAS3-20769. The propfan model has 8 blades with a 0.25 inlet-radius ratio and a 45° tip sweep (as defined by Hamilton Standard). It was designed in scale model size (62.2-cm diameter) at a cruise flight condition of Mach 0.80, 10,667-meter (35,000-foot) altitude. The summarized aerodynamic design point parameters are compared in Table 1 to the design parameters of the F-7/A-7 blades.

Table 1. Comparison of SR-3 and F-7/A-7 Blade Aero Design Parameters.

	SR-3	SR-3 Data Match	F-7/A-7
Design Point, Mach/Alt.	0.80/10,667 m	0.80/10,667 m	0.72/10,667 m
Advance Ratio, J	3.06	3.002	2.80
Power Coefficient, Cp	1.70	1.385	2.68
Disk Loading, shp/D ² , kw/m ² (HP/ft ²)	300(37.5)	262(32.6)	444(55.5)
Tip Speed, m/s (ft/s)	243.8(800)	249(816)	237.7(780)
Number of Blades	8	8	8+8
Aero Tip Sweep, degrees	45	45	33/29
Blade Activity Factor	235	235	147/152

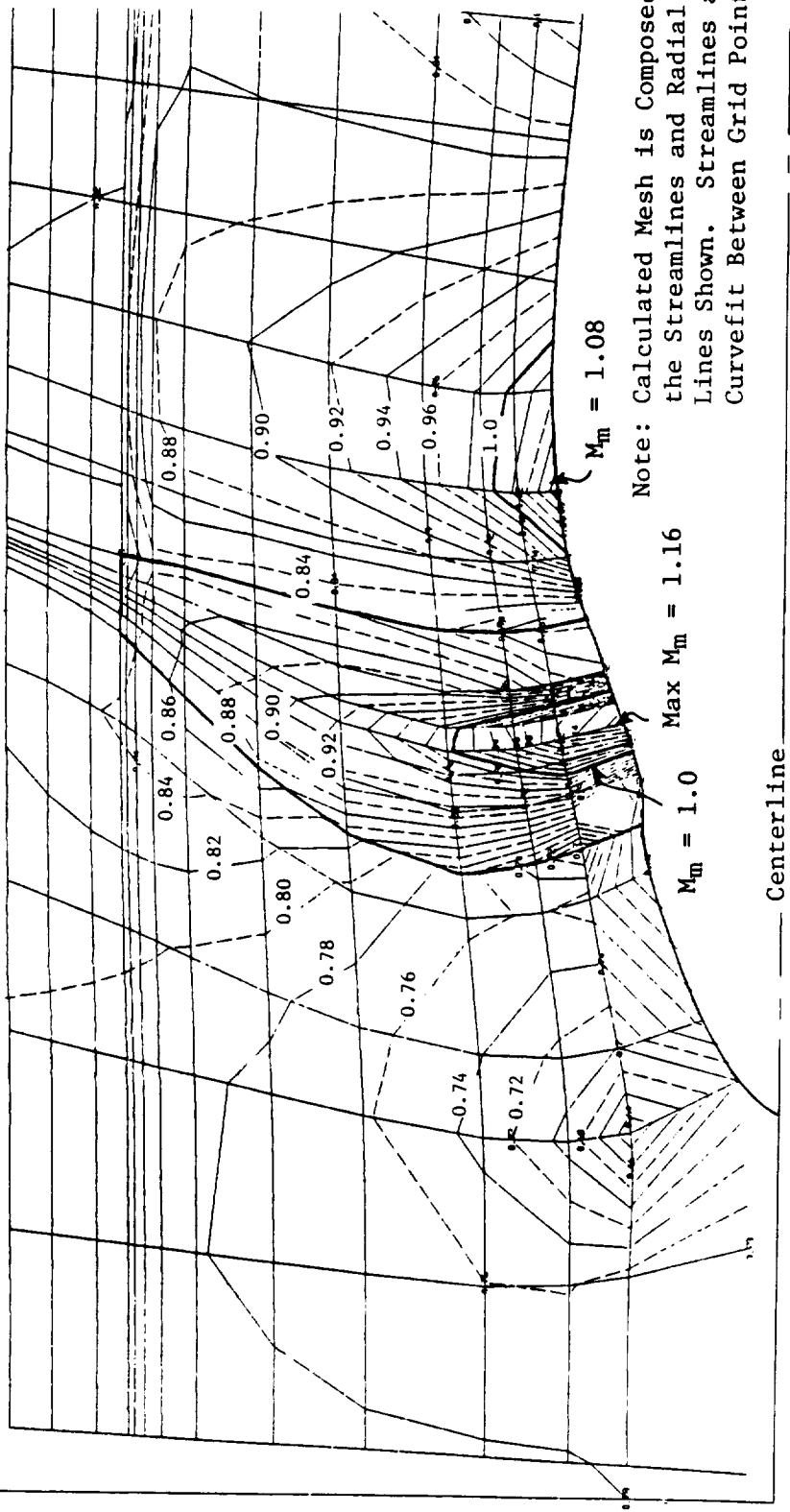
In order to evaluate the S2-3 design and calibrate the GE dedesign procedure, an axisymmetric flow analysis was set up using the SR-3 model flowpath, blade geometry, and test data taken close to the design point as reported by Hamilton-Standard (Reference 2). This procedure is termed a data match. It requires the input of measured data and gives meridional Mach numbers and other circumferentially averaged data throughout the flow field. Figure 2 illustrates the results of this flow analysis. Flow streamlines and calculation stations are depicted with contours of meridional Mach numbers superimposed on the plot. In the blade passage, Mach numbers peak at 1.16, where the blade root thickness tends to choke the local hub flow. Downstream of the blade TE (trailing edge), the large hub accelerating curvature raises the Mach number to 1.08. The axisymmetric flow analysis results compares well with the results described in Reference 3.

The data match was performed using wind tunnel test data at Mach 0.80 near the design advance ratio at a lower-than-design power coefficient. Wake survey probe measurements of total pressure and total temperature were input to the GE axisymmetric flow analysis at a number of radial

- $M_0 = 0.80$
- $U_r = 243.8 \text{ m/s}$

Meridional Mach No. Contours

Radial Direction



Note: Calculated Mesh is Composed of the Streamlines and Radial Grid Lines Shown. Streamlines are Curved Between Grid Points.

Axial Direction

Centerline

Figure 2. SR-3 Data Match Results from Axisymmetric Flow Analysis.

immersions; output results are demonstrated in Figure 3. The blade relative flow angles, lift coefficients, and adiabatic efficiency are plotted from flow calculations. The normalized loading distribution, as calculated from the input temperature rise, is also indicated. Euler 3D analyses were also performed on the SR-3 blade using the GE Euler code. The blade-to-blade 3D (three-dimensional) flow field was analyzed at the Mach 0.8 data match point to obtain surface Mach number and loading distributions. The Euler calculation of exit flow angle (Figure 4) indicates a greater loading level than the test data match over the entire blade span; this suggests that the blade is more open than the hot-intended airfoil coordinates used in the data match. Figure 5 identifies the surface Mach numbers for streamline sections near the tip, pitchline, and hub.

For the airfoil section near the tip, surface Mach numbers reveal a large loading over the entire chord length and a strong normal shock at the TE. The shock is less strong for the midspan or pitchline section, but is concentrated at the TE, expanding from a Mach of 1.15 down to approximately 0.85. Near the hub, the surface Mach number distributions are strongly influenced by the thick airfoil sections. The LE (leading edge) thickness and incidence angle causes the Mach number to spike near the edge, decelerate, and then accelerate to midchord. The Mach numbers along both surfaces peak near the maximum thickness location before diffusing to the trailing edge at a 1.75 velocity ratio. Spanwise Mach number contours are shown in Figures 6 and 7 along the pressure and suction surfaces of the blade. These plots show the strong shock at the tip trailing edge, diminishing down the blade span toward the hub. The surface Mach number distributions resulting from this 3D analysis of the SR-3 blade suggest that the thick airfoil sections near the hub, plus the accelerating curvatures of streamlines in the hub, adversely affect the overall aerodynamic performance at Mach 0.80 cruise. Improvements in hub area-ruling and airfoil mean-line shaping could lead to better aerodynamic performance.

3.1.2.2 SR-1 Data Match

The SR-1 single-rotation propfan, designed by Hamilton-Standard under NASA Contract NAS3-20219, was analyzed using the GE data match calculation procedure. The SR-1 model is similar to the SR-3 having 8 blades with a 0.25-inlet-radius ratio. The principal difference in the two designs is the planform shape. The SR-3 has a 45°-aero tip sweep, while that of the SR-1 is only 30°; the SR-1 is also straighter in the inner portion of the blade, having no forward sweep. Another difference occurs in the flowpath shape; the SR-1 hub flowpath is more conical through the blade, not employing the area-ruling of the later SR-3 design. Both configurations were designed for the same flight condition as indicated in Table 2. The lower efficiency of the SR-1 can be attributed to less sweep and poorer hub performance.

Test data taken in the wind tunnel near the aero design point were used to perform the data match analysis. Table 3 identifies the test data as well as the GE data match values.

The GE axisymmetric flow calculation code was run using the SR-1 scale model flowpath coordinates, blade geometry, and design point test data. The results of this calculation are presented in Figure 8. The flow streamlines and calculation stations are shown, with contours of meridional Mach numbers superimposed on the plots. The Mach numbers inside the blade row indicate a large region of supersonic flow near the hub; the peak Mach number calculated is 1.21, at the hub, where maximum blade thickness occurs. Downstream of the blade another region of supersonic flow occurs where the curvature of the hub flowpath causes local flow to accelerate over Mach 1. Both of these regions of high Mach number flow are verified by the Hamilton-Standard final report (Reference 3).

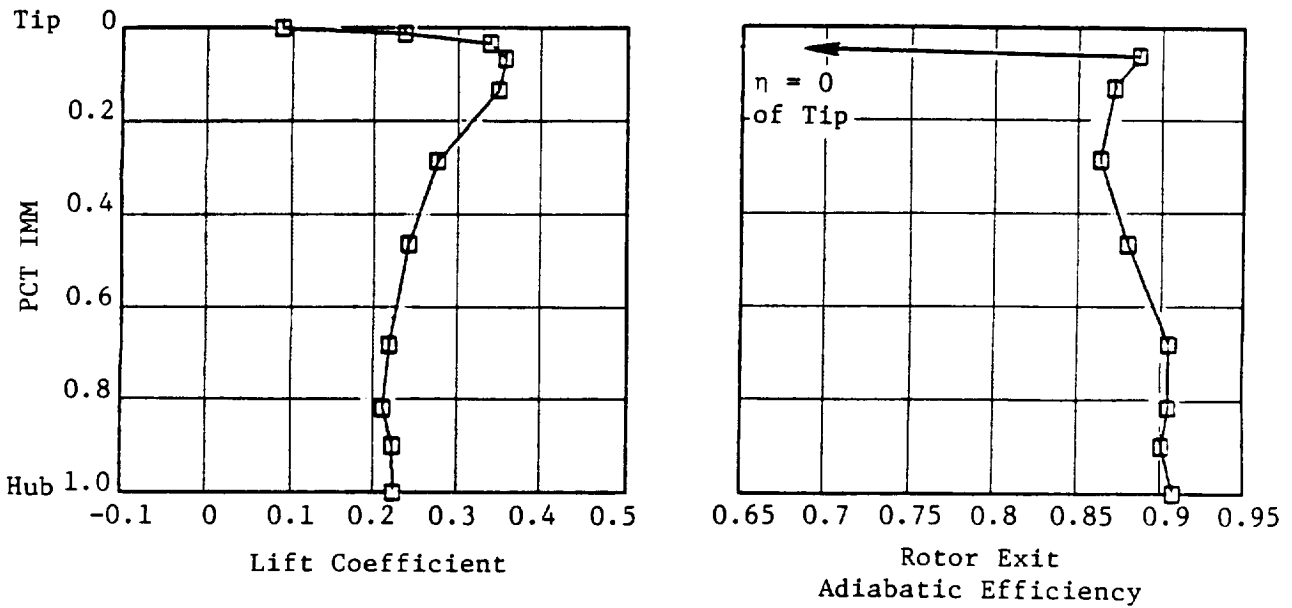
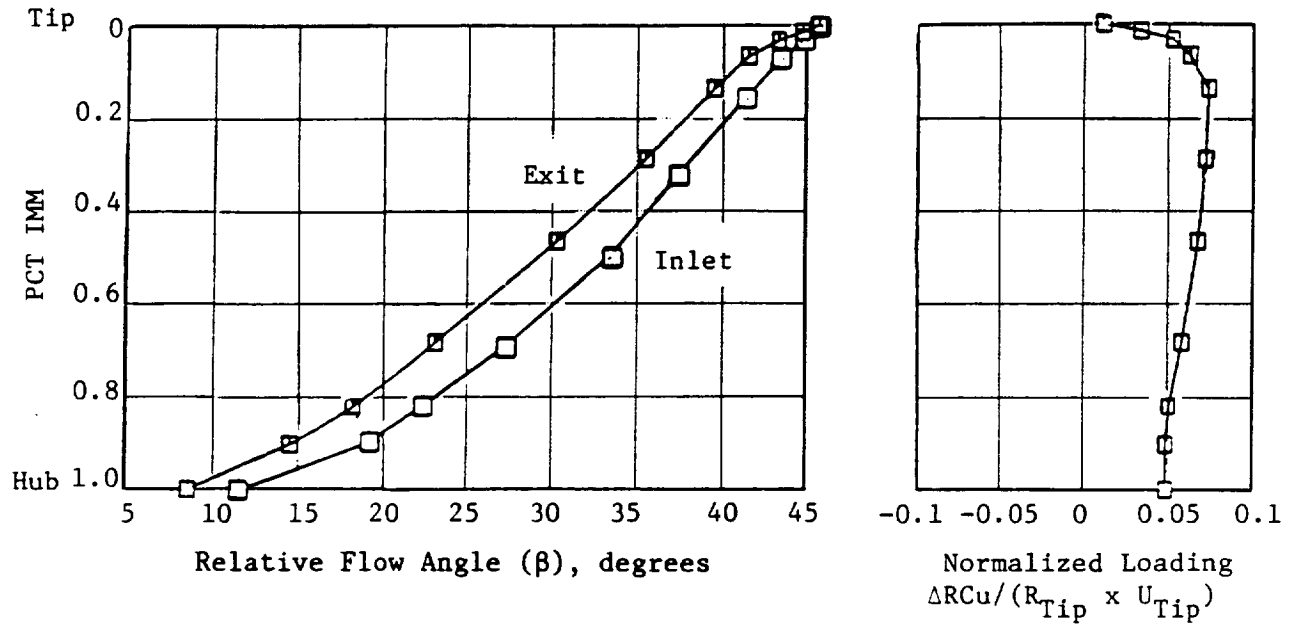


Figure 3. Radial Distribution of Aero Parameters at Design Data Match, SR-3 at Mach = 0.80. (As Calculated with Axisymmetric Throughflow Code)

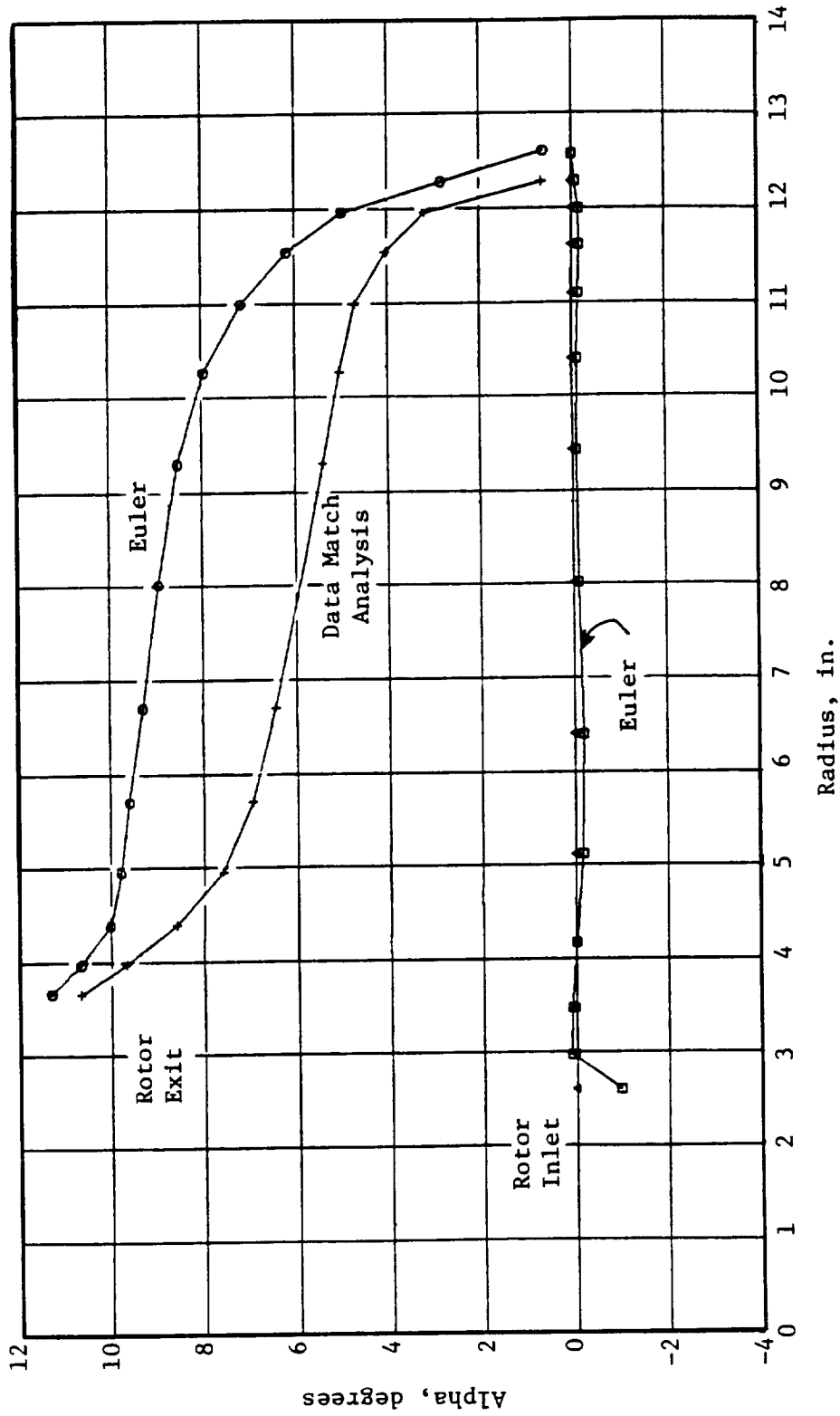


Figure 4. SR-3 Euler and Data Match Swirl Distribution.

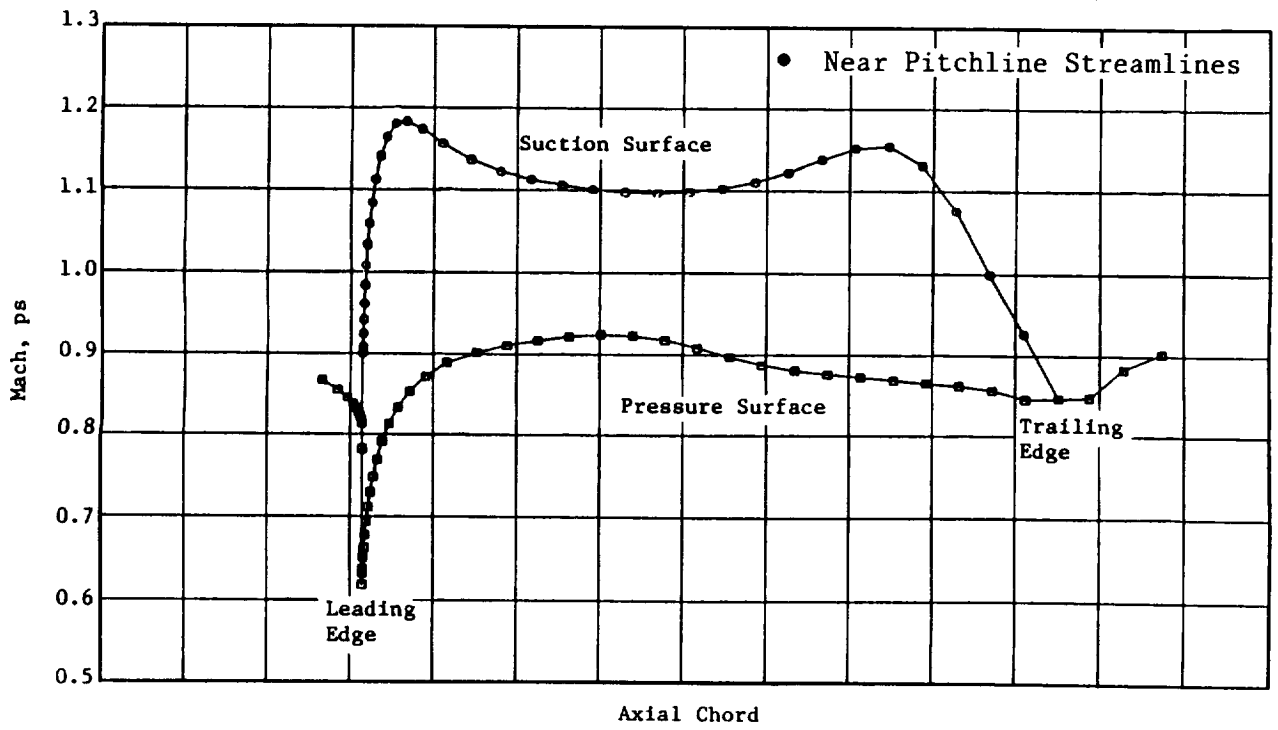
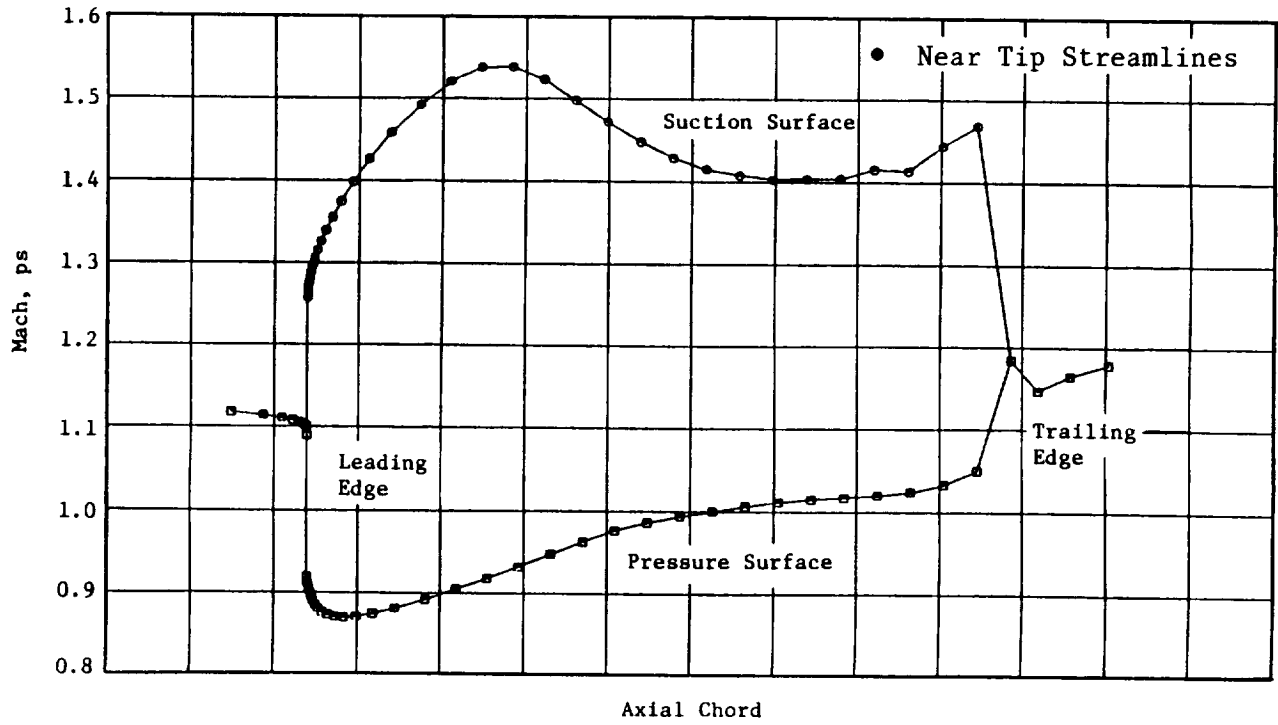


Figure 5. SR-3 GE Euler Results.

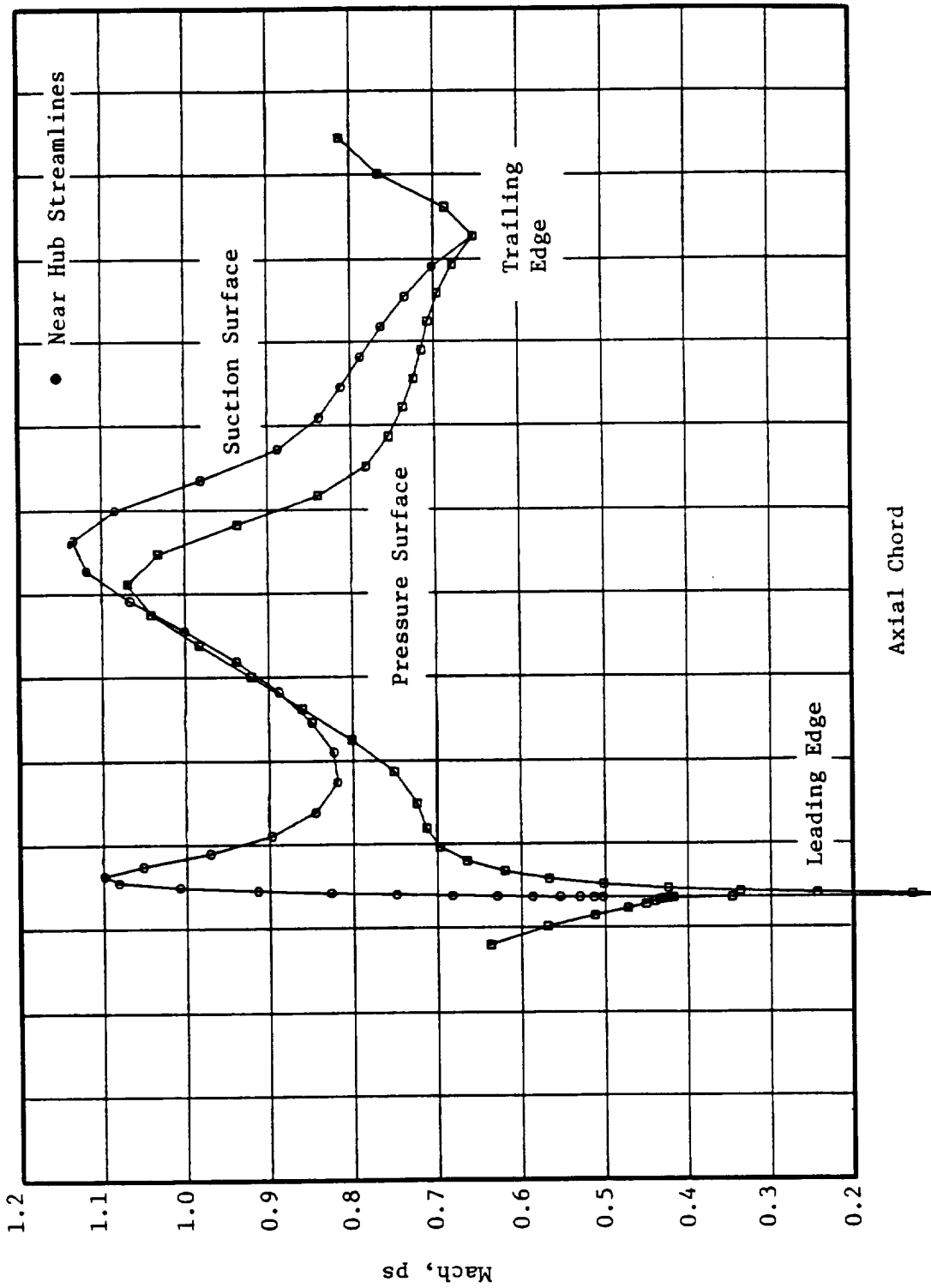


Figure 5. SR-3 GE Euler Results (Concluded).

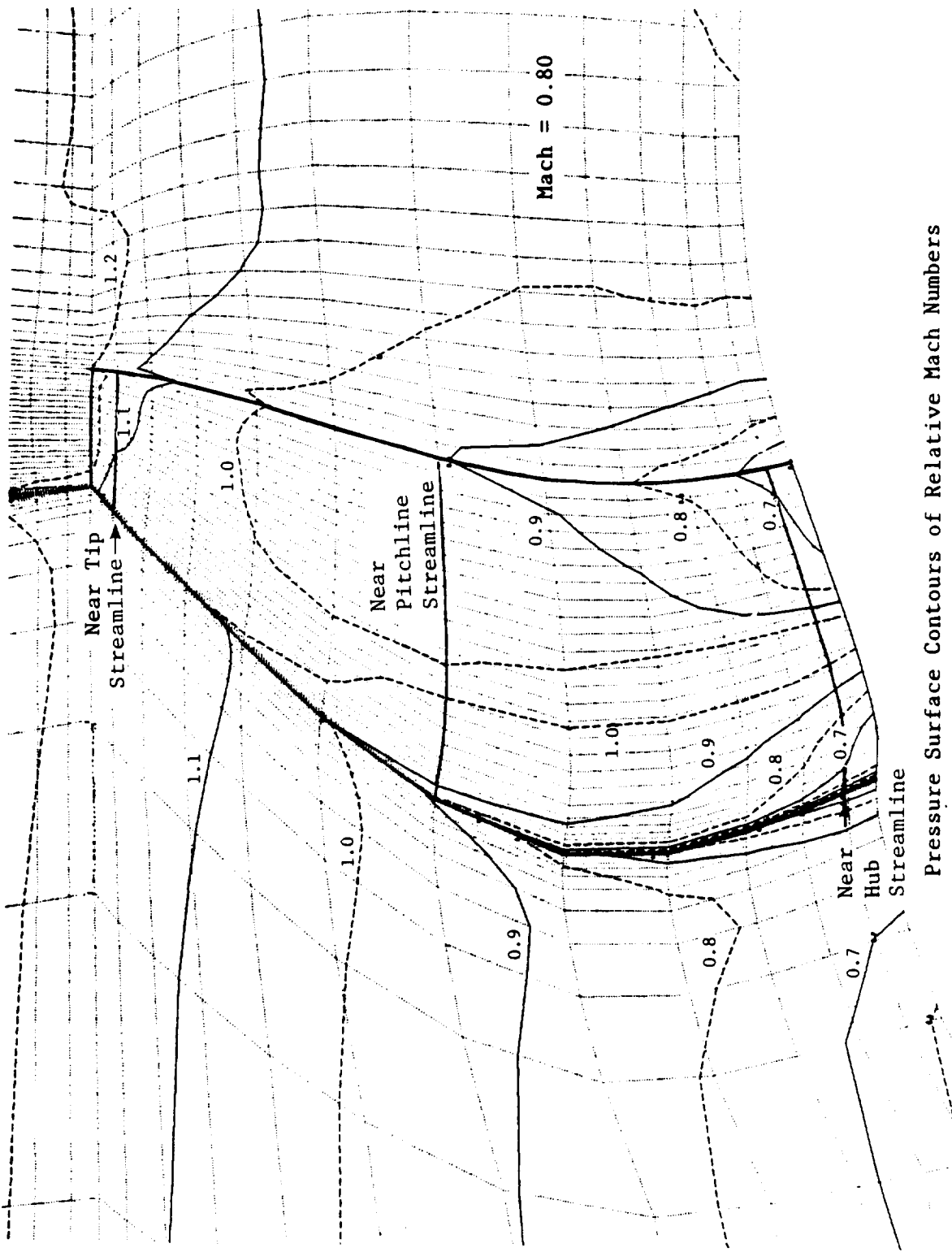
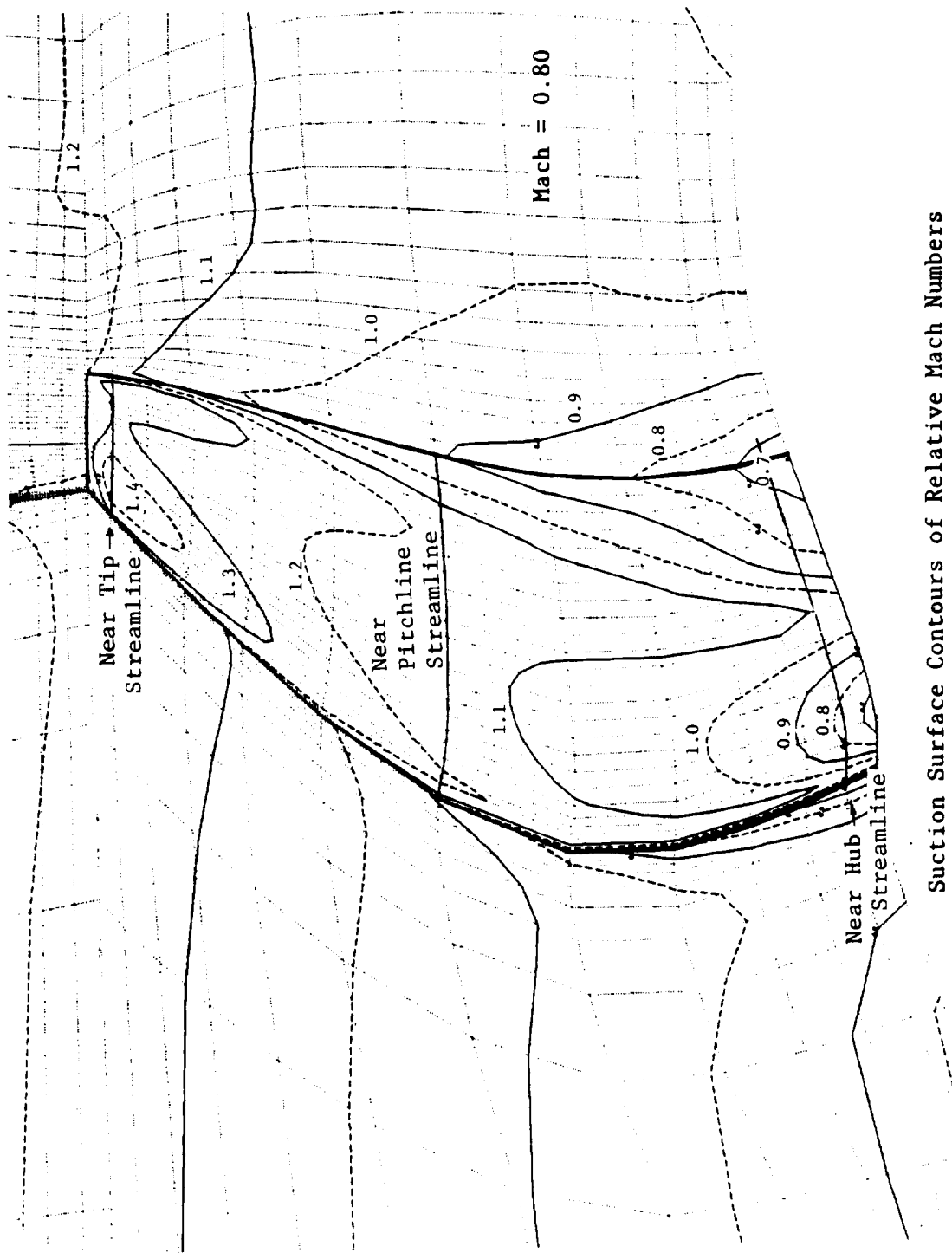


Figure 6. Spanwise Mach Number Contours for Pressure Surface.



Suction Surface Contours of Relative Mach Numbers

Figure 7. Spanwise Mach Number Contours for Suction Surface.

Table 2. Comparison of SR-3 and SR-1 Blade Aero Design Parameters.

	SR-3	SR-1
Design Point Mach No./Alt.	0.80/10,667 m.	0.80/10,667 m.
Advance Ratio, J	3.06	3.12
Power Coefficient, Cp	1.70	1.73
Disk Loading, Shaft Power/D ² kw/m ² (HP/ft ²)	300(37.5)	300(37.5)
Tip Speed, m/s (ft/s)	243.8(800)	243.8(800)
Aero Tip Sweep	45°	30°
Blade Activity Factor	235	203
Number of Blades	8	8

Table 3. Comparison of SR-1 Test and GE Data Match Analysis Results.

	SR-1 Test Point	GE Data Match
Mach Number	0.80	0.80
Advance Ratio, J	3.12	3.118
Tip Speed, U _T , m/s (ft/s)	243.8(800)	243.8(800)
Power Coefficient, CP	1.73	1.702
Disk Loading, Shaft Power/D ² kw/m ² (HP/ft ²)	300(37.5)	283(35.4)
Net Efficiency	0.773	0.787

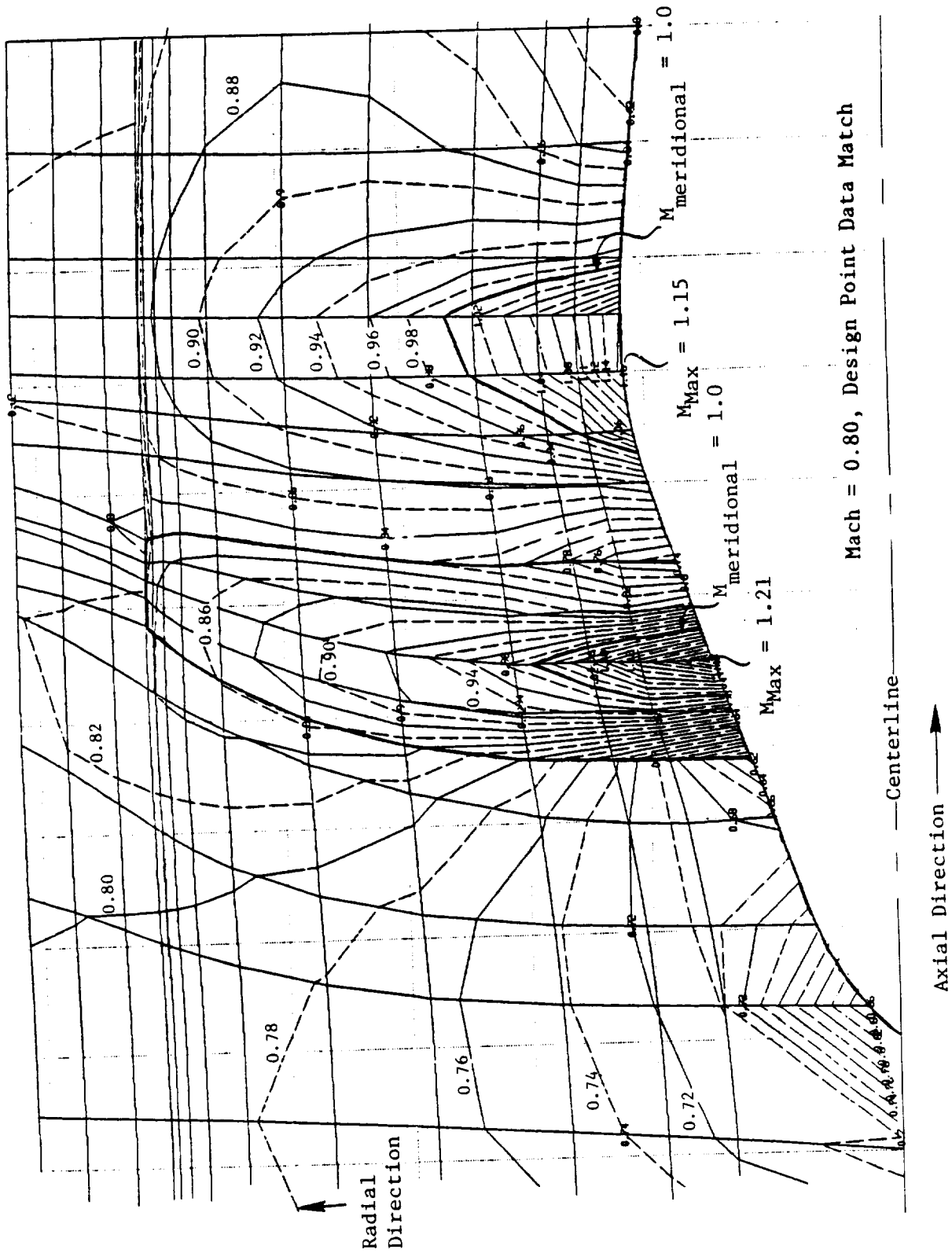


Figure 8. SR-1 Axisymmetric Flow Calculation Results.

ORIGINAL PAGE IS
OF POOR QUALITY

As shown in Figure 9, the meridional Mach number distribution along the hub surface compares well with the test values reported. The GE axisymmetric flow calculation also matches well with the total pressure ratio and swirl angles measured with rakes downstream of the rotor. Figure 10 illustrates the comparison of test measurements to the calculation. The measured total pressure ratio was initially input, and the losses were adjusted to obtain a reasonable adiabatic efficiency profile while matching the exit swirl as closely as possible. The losses and pressures were adjusted slightly from the initial inputs to obtain the best data match. The resulting radial profiles of adiabatic efficiency and loading also are presented in Figure 10.

Utilizing the GE Euler code, blade-to-blade 3D flow analyses were also performed for the SR-1. The 3D flowfield was analyzed at the Mach 0.80 data match point to obtain surface Mach number distributions. Radial distributions of exit swirl and angular momentum (ΔRCU) are also calculated by Euler code and compared with the axisymmetric values in Figures 11 and 12. The Euler-calculated swirl is within 1° of the axisymmetric calculation in the outer span of the blade but does not fall off in the hub region like the test data and the axisymmetric calculation show.

The change in angular momentum across the blade as calculated by Euler 3D is significantly higher across the span, particularly in the hub region. In general, the Euler code overpredicts the amount of loading carried by the SR-1 blade, but not as great an overprediction as achieved by the SR-3 calculation. Accounting for the viscous effects and a blade running more closed than predicted would bring the Euler-calculated loading level closer to matching the experimental data.

Figure 12 identifies the surface Mach number distributions from the Euler calculation for representative airfoil sections near the tip, pitchline, and hub. Blade surface Mach number contours for suction and pressure sides of the SR-1 blade (Figures 13 and 14) indicate a very strong trailing shock (stronger than the SR-3 Euler results) over the outer two-thirds of the blade span; this is consistent with the fact that the SR-1 has a lower activity factor and less aerodynamic sweep. Even though loading is not large in the hub region, blade thickness and solidity causes the shock to occur near mid-passage, creating a surface Mach number distribution such as that depicted in View C of Figure 12. Area-ruling of the hub surface would alleviate this problem. The surface Mach number distributions of the SR-1, as compared to that of the SR-3, reveal a lighter leading edge loading with a smaller incidence angle but a much greater trailing edge shock.

3.2 Aeroacoustic Methods Development

3.2.1 Scaling Procedures Development and Evaluation

Scaling procedures are required to relate aeroacoustic results from model test rigs to full-scale engine flight conditions. In this report, a formal procedure has been developed for scaling the measured scale model tones to those of full-scale engines; however, due to flow-similarity consideration, this procedure does not include broadband noise scaling.

In order to establish scaling procedures, one has to first retain the geometric similarity between model tests and the desired full-scale operating conditions. When aerodynamic performance similarities need to be maintained, control is required, during the test, over the following three parameters: tip Mach number, Reynolds number, and the advance ratio; that is, a ratio of flight speed to tip speed (Reference 4).

Gutin's equation (References 5 and 6) demonstrated that aerodynamic tone noise generated by propfans depends directly on such associated performance variables as thrust, shp (shaft

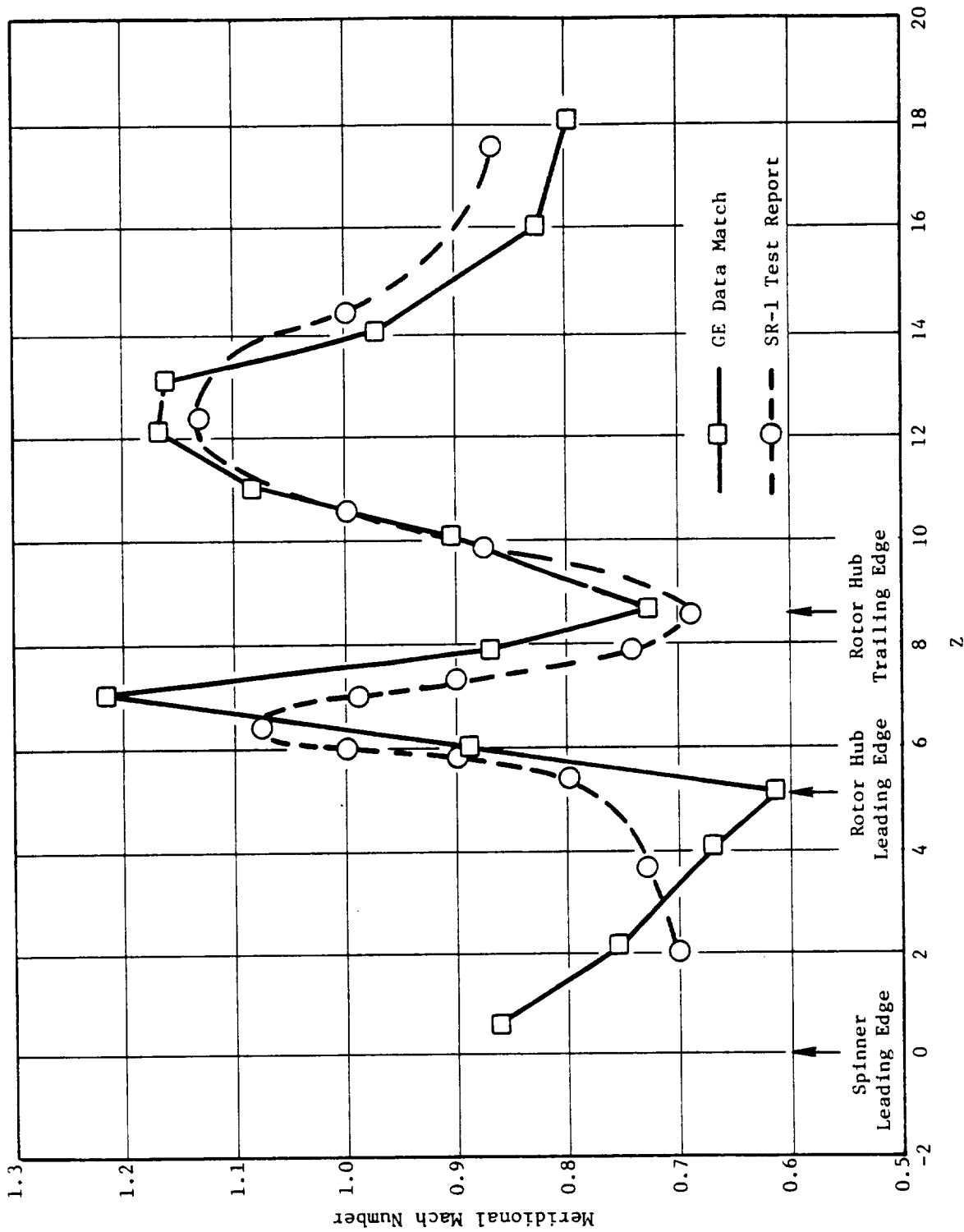


Figure 9. SR-1 Meridional Mach Number Distribution - Hub Surface (Mach 0.80 Test Point).

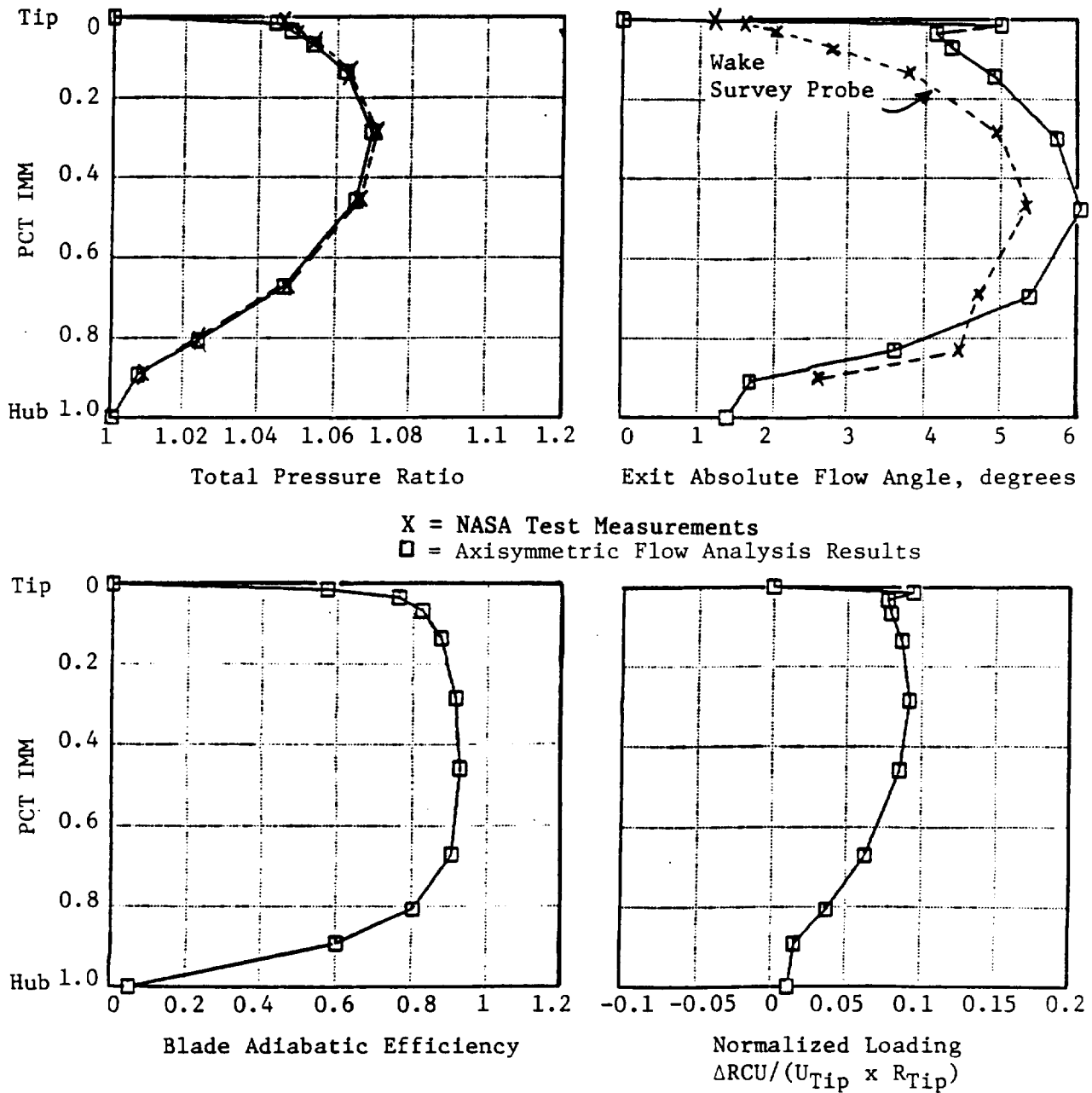


Figure 10. Comparison of SR-1 Test Data and Data Match Calculations.

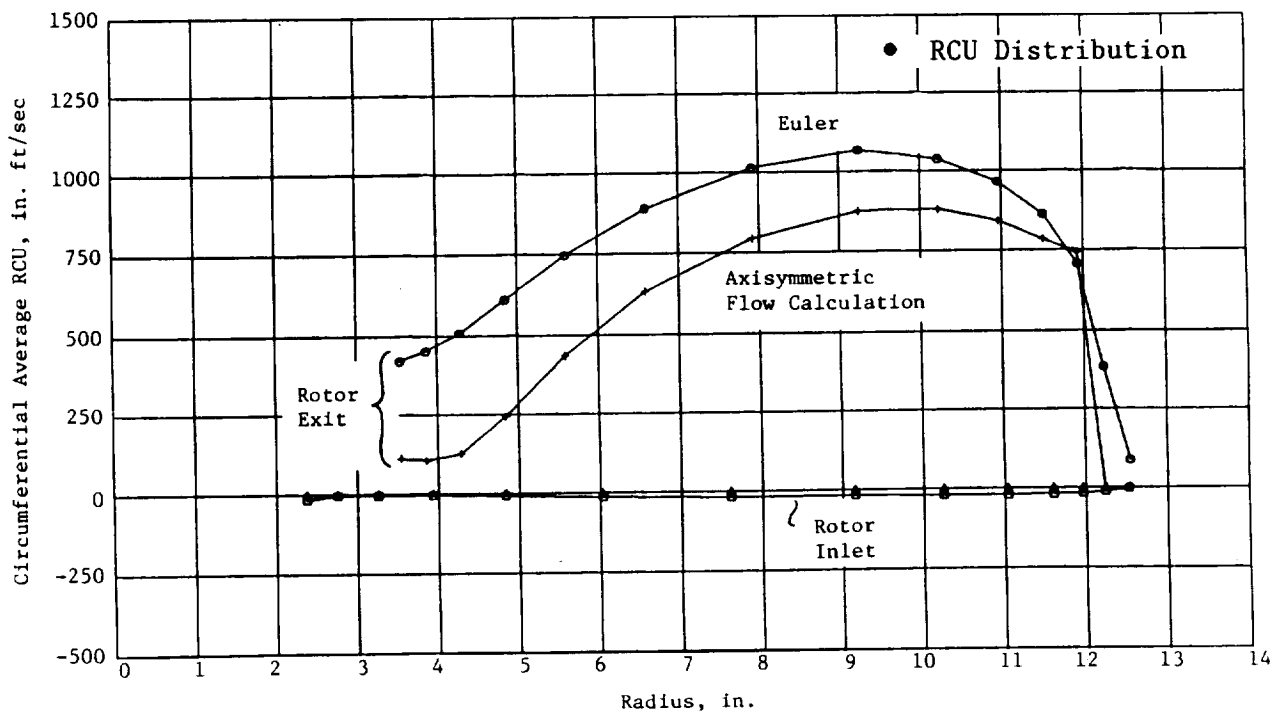
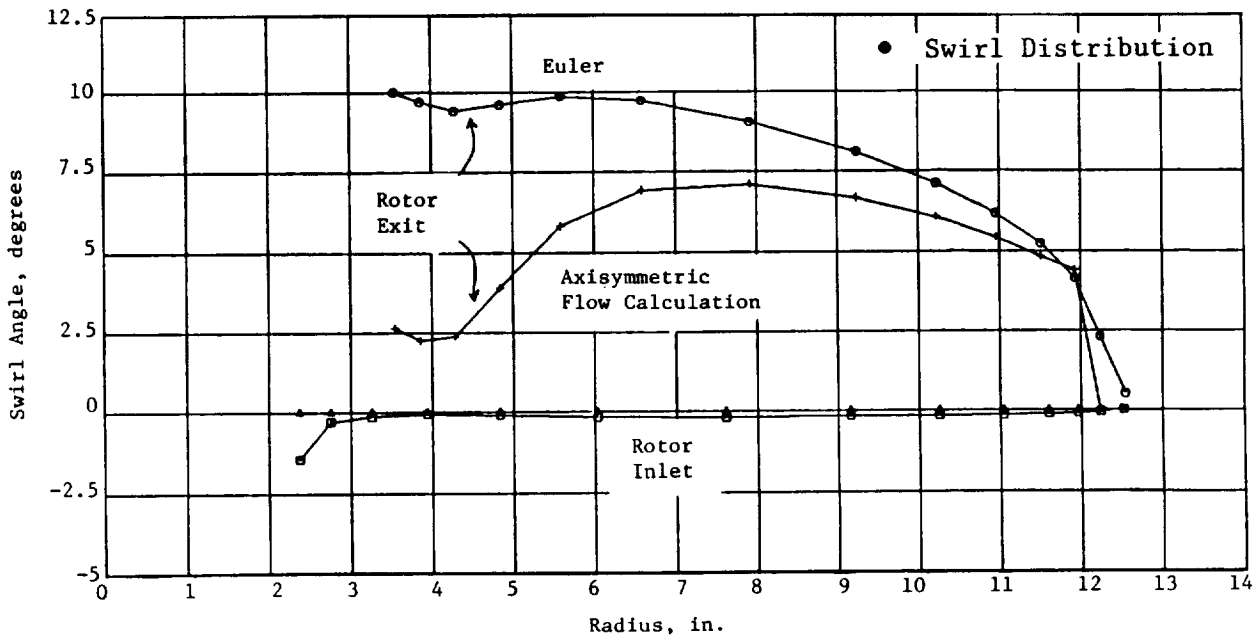


Figure 11. SR-1 Euler Results.

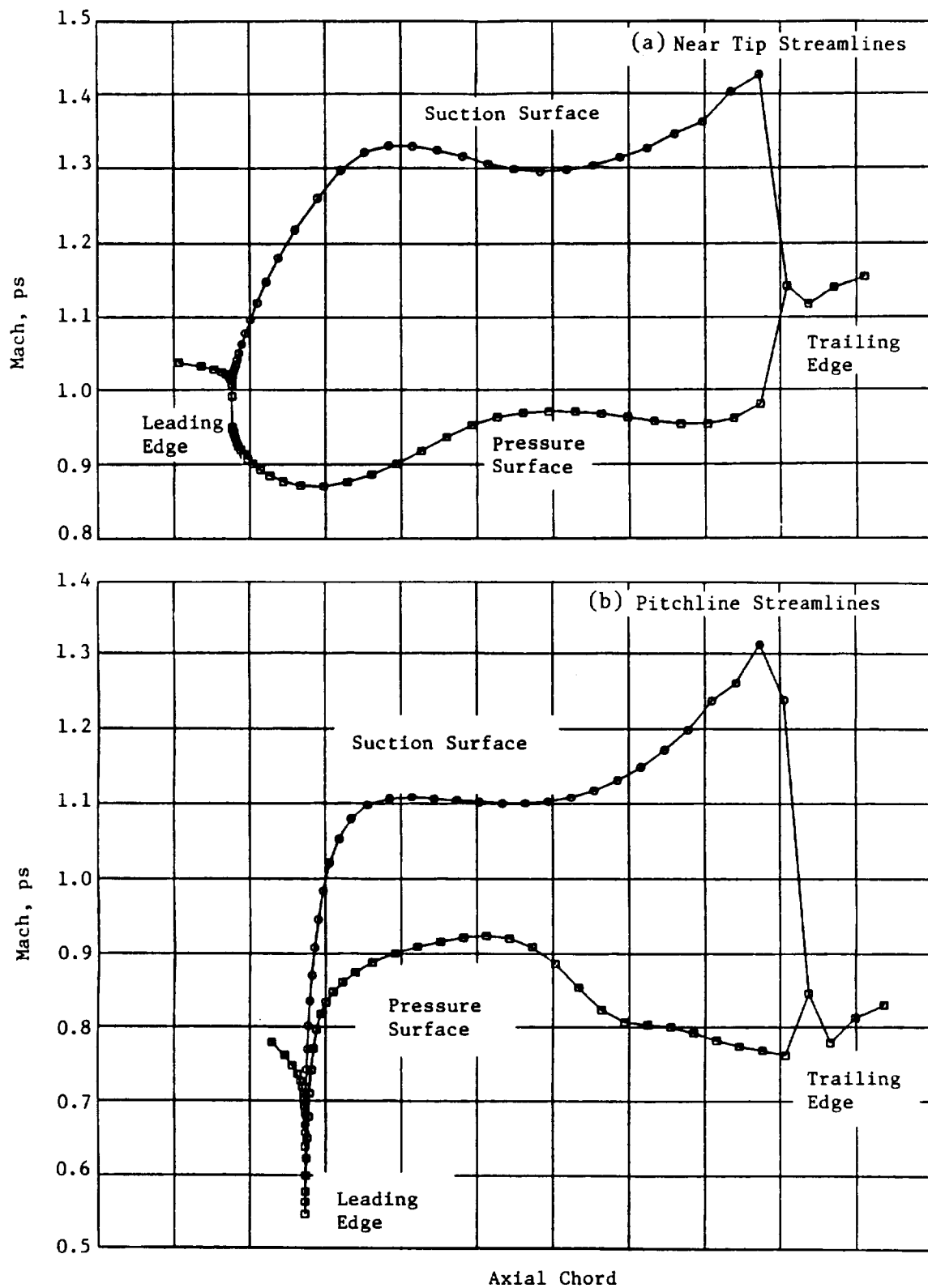


Figure 12. SR-1 Design Point Data Match Results.

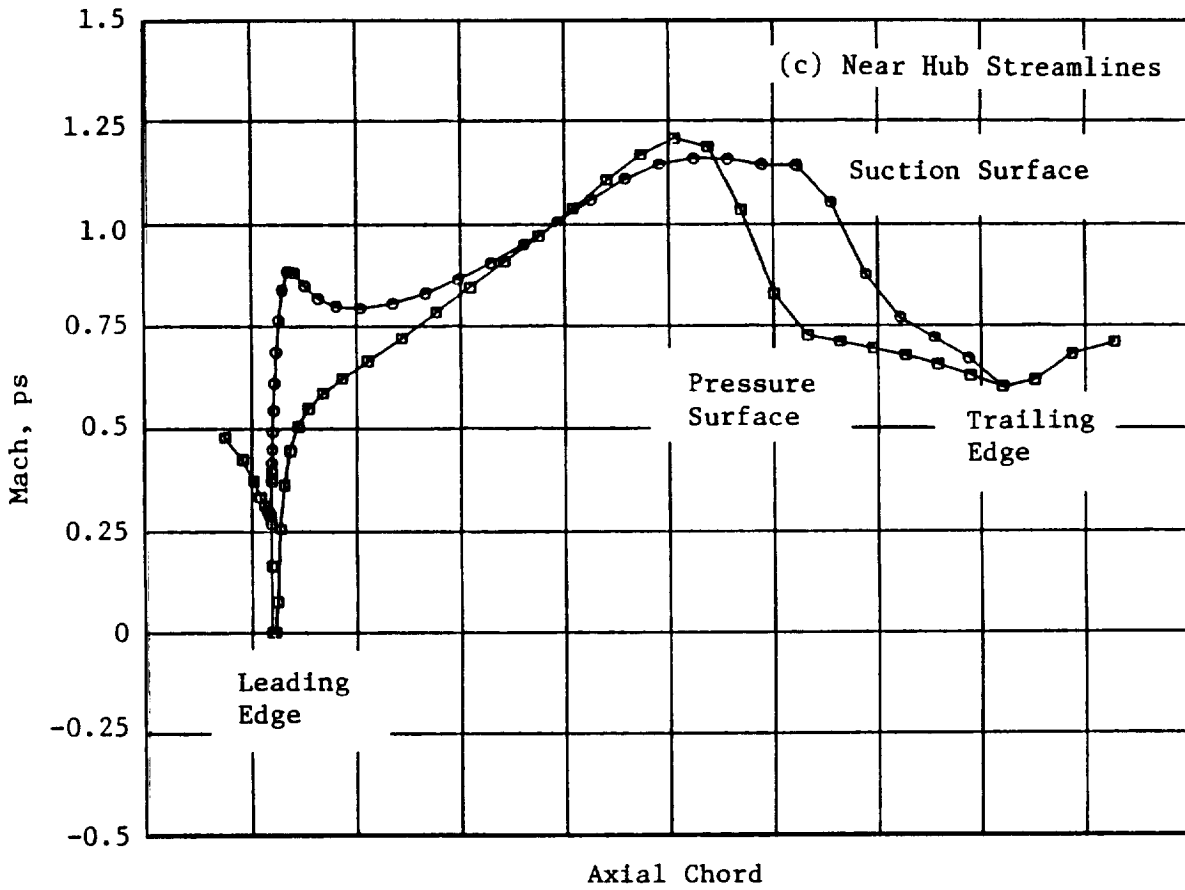
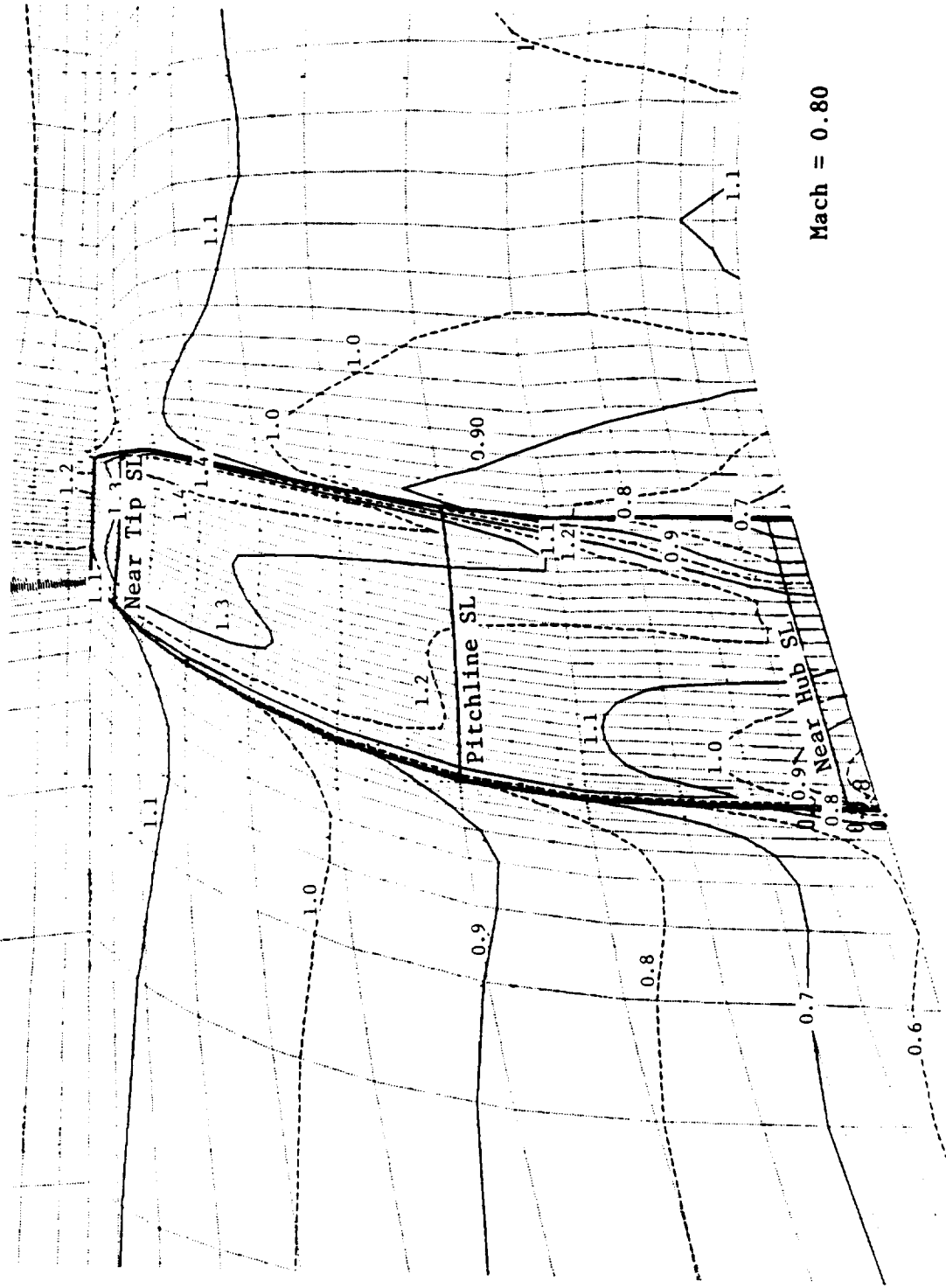


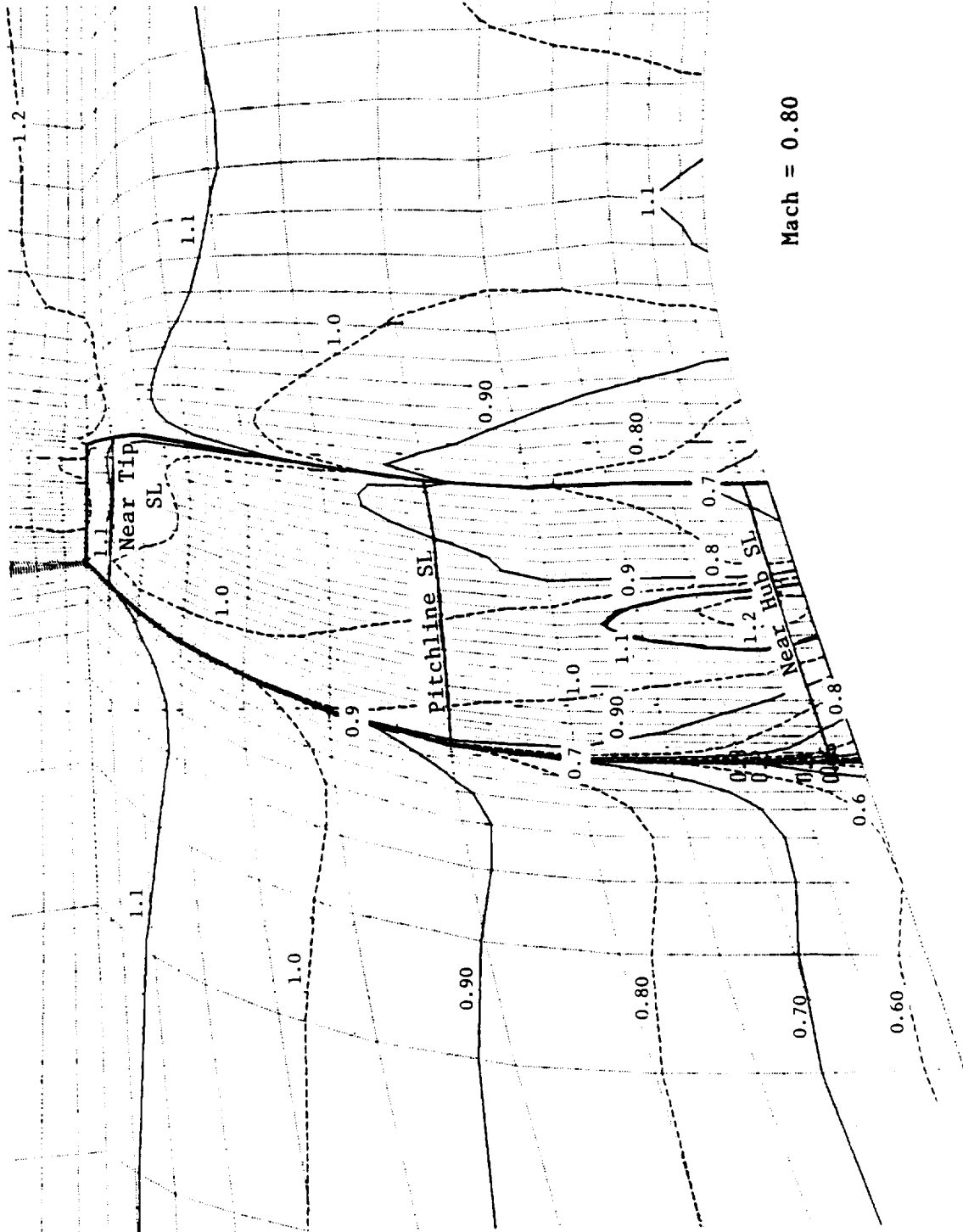
Figure 12. SR-1 Design Point Data Match Results (Concluded).



Mach = 0.80

Figure 13. Relative Mach Number Contours for SR-1, Suction Surface.

ORIGINAL PAGE IS
OF POOR QUALITY



Mach = 0.80

Figure 14. Relative Mach Number Contours for SR-1, Pressure Surface.

ORIGINAL PAGE IS
OF POOR QUALITY

horsepower), flight Mach number, and tip Mach number. Consequently, the same set of dimensionless parameters governing the performance similarity is assumed in this report to also govern aeroacoustic similarity.

In a typical model test, not all of the above similarities can be maintained; for example, geometric deformation of the model blades at off-design conditions may be different than that of full-scale blades. As a result, both the geometric and the performance similarities are not kept; correction in the scale-up procedure may be needed. Also, having decided the tip Mach number and the advance ratio for a test point, there is no freedom left to choose a desired Reynolds number of the simulated flight condition.

On the assumption that the viscosity of the air is constant, the Reynolds number of the associated full-scale condition is less than that of the model test by a factor equal to the ratio of the diameter of the model blades to the diameter of the full-scale blades. The effect of the difference in Reynolds number on propfan performance has been found to be small and, thus, is ignored in the performance scaling procedure. However, flows of different Reynolds numbers have different turbulent structures. Broadband noise has been shown to be related to inflow turbulence and turbulent boundary layers passing the blade trailing edge (Reference 7); there is no simple equation relating broadband noise of propfans measured from cases of different Reynolds numbers.

In contrast, there is Gutin's equation describing tone noise generated by a single-rotor propeller (Reference 5) which is expressed in simple terms of aeroperformance variables. Tone frequencies predicted by the equation have been verified by all of the test measurements. In addition, the extension of Gutin's equation for nonuniform inflow to rotors has been derived in the text of Morse and Ingard (Reference 6). In Section 3.2.1.1, Gutin's equation is further generalized to deal with the case of nonuniform inflow to rotors with time-dependence. Interaction tones, which are generated by the forward-rotor wake flow impinging on aft-rotor blades, can then be described by the same equation as the steady-loading tones.

Section 3.2.1.2 identifies and discusses the two empirical constants in the generalized Gutin equation. Scaling law based on the equation is used to scale the tone noise for cases of different sizes, as well as for cases under different operating conditions. The scaling procedure is different from predictions by analytical models which do not rely on empirical coefficients for each set of rotor/blade angles. Results presented in Section 3.2.1.3 are shown to have reasonable agreement between scaled and measured data, in reference to the prediction of our existing analytical model. Discrepancies between the scaled results and these data are discussed in Section 3.2.1.4. The significance of improving the scaling law is emphasized, in that it leads to important information on the lump characteristics of forward rotor wakes for the study of interaction noise.

Table 4 lists and defines the various nomenclature used in the equations appearing in the above-named subsections.

3.2.1.1 The Generalized Equation of Gutin

The acoustic pressure of discrete tones, as produced by a single-rotor propeller in uniform flow, can be described by Gutin's equation:

$$p_m = \frac{\alpha_m B}{4\pi r_o C_o} \cdot \frac{550 \text{ shp}}{R_e} \cdot \left(\frac{M_e}{M_o} \cdot \eta \cdot \cos \theta - \frac{1}{M_e} \right) \cdot J_{mB}(mB M_e \sin \theta). \quad (1)$$

Table 4. Nomenclature for Scaling Procedures Development and Evaluation Equations.

Subscript F:	Quantities Associated with the Forward Rotor
Subscript A:	Quantities Associated with the Aft Rotor
Subscript e:	Quantities Derived Using the Effective Radius, R_e
B:	Number of Blades
C_0 :	Speed of Sound
D, E:	Collective Terms of Gutin's Equation, Useful for Scaling Purposes
f_x :	Amplitude Related to the Total Thrust of a Rotor
f_g :	Amplitude Related to the Total Drag Force of a Rotor
F_x :	Thrust at a Point of the Rotor Disk
F_g :	Drag Force at a Point of the Rotor Disk
g:	An Arbitrary Function
i:	-1
J:	Bessel Functions of Integer Orders
m:	Harmonic Numbers of the Forward Rotor
n:	Harmonic Numbers of the Aft Rotor
M_0 :	Flight Mach Number
M_e :	Effective Tip Mach Number
p:	Sound Pressure
r_o :	Distance from a Sound Source to an Observer
R_T :	Tip Diameter
R_e :	Effective Radius (0.7 to 0.8 R_T)
shp:	Shaft Horsepower
x:	Direction of Flight (Reference Figure 15)
X, Y:	Empirical Constants in Gutin's Equation
α :	Fourier Coefficient from the -space of the Rotor Tone Pressure Level
β :	Fourier Coefficient from the -space of the Rotor Thrust (Reference 6, p. 741)
δ :	Fourier Coefficient from the -space of the Rotor Drag Force (Reference 6, p. 741)
ϑ :	Azimuthal Angle About the Axis of Rotor Rotation (Reference Figure 15)
Ω :	Absolute Values of the Angular Velocity of Rotors
θ :	Emission Angle
η :	Propulsion Efficiency

This equation does not include interaction tones which are generated by the wake flow of a forward rotor impinging on aft-rotor blades. The inflow to the aft rotor is not only nonuniform, but also time-dependent; the case of nonuniform inflow to the rotor has been presented in the text of Morse and Ingard (Reference 6). In this section, time-dependence is included in the analysis using notation similar to those of Reference 6, pp. 739-744. Note that in Equation 1, the expression on the left-hand side has no radial r -dependence of the rotor (Reference Figure 15). The dependence has been averaged over r and written in terms of both effective radius, R_e , and effective tip Mach number, M_e . Similar results are to be derived for interaction tones; thus, the radial dependence is also ignored in the present analysis.

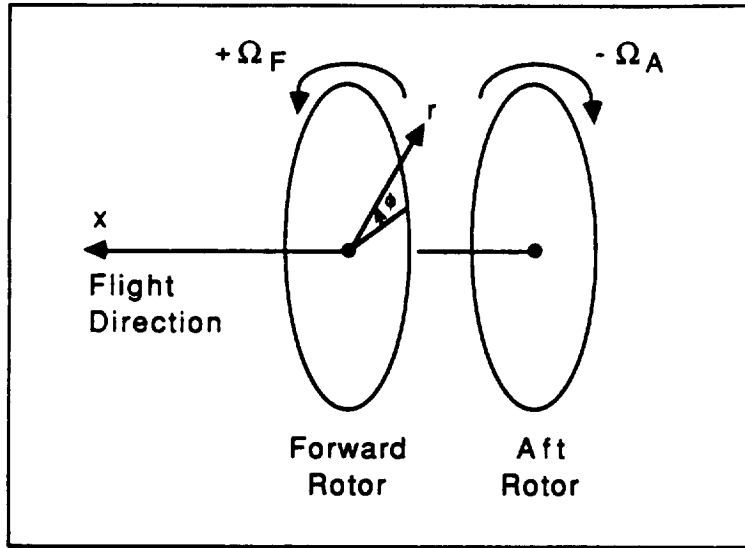


Figure 15. Definition of Rotor Coordinates and Rotor Angular Velocities.

Referring to Figure 15, the axial force exerted on the fluid by the aft rotor is expressed in Fourier series as Equation 11.3.2 of Reference 6:

$$F_x(\vartheta, t) = f_x \cdot g(\vartheta, t) \cdot \sum_{\eta=-\infty}^{\infty} \alpha_{\eta} \cdot e^{-i(n \Omega_A B_A)} \cdot \left(t + \frac{\vartheta}{\Omega_A} \right); \quad (2)$$

assuming the angular velocity of the aft rotor is $-\Omega_A$. The function $g(\vartheta, t)$ in the above equation accounts for the wake effect on the aft-rotor loading. If one defines a coordinate,

$$\bar{\vartheta} = \vartheta - \Omega_F t, \quad (3)$$

which is stationary in reference to the blades of the front rotor, the time-dependence of $g(\vartheta, t)$ can be absorbed into $\bar{\vartheta}$. The function of the wake effect has only $\bar{\vartheta}$ -dependence:

$$g(\vartheta, t) = \sum_{m=-\infty}^{\infty} \beta_m \cdot e^{i(mB_F \bar{\vartheta})} \quad (4)$$

or,

$$g(\vartheta, t) = \sum_{m=-\infty}^{\infty} \beta_m \cdot e^{i(mB_F \bar{\vartheta})} \cdot e^{-i m(B_F \cdot \Omega_F) t}.$$

The substitution of Equation 4 into Equation 2 yields:

$$F_x(\vartheta, t) = f_x \sum_m \sum_n \beta_m \alpha_n e^{i(mB_F - nB_A)\vartheta} e^{-i(mB_F \Omega_F + nB_A \Omega_A)t}. \quad (5)$$

Similarly the Fourier series expansion for the drag force can be expressed as:

$$F_g(\vartheta, t) = f_x \sum_m \sum_n \delta_m \alpha_n e^{i(mB_F - nB_A)\vartheta} e^{-i(mB_F \Omega_F + nB_A \Omega_A)t}. \quad (6)$$

It should be noted that the predicted angular frequency $mB_F \Omega_F + nB_A \Omega_A$ is associated with the mode $mB_F - nB_A$ in the ϑ -space.

The derivation from this point to the result of the total sound pressure generated by the aft rotor is identical to that of Reference 6 (Equations 11.3.14 through 11.3.18). The only difference is that Ω_F is identically zero for the case dealt in the text. The derivation starts with obtaining the far-field approximation of the monopole sources, in terms of Bessel functions, and then, the same approximation for dipole sources. Dipole sources of strength, F_x and F_g , are integrated separately over the rotor disk. Discrete tones fall out from the integration over the variable ϑ (Figure 15). Variables having radial dependence in all of the integrands are replaced by proper mean values. The total sound pressure is the sum of p calculated from the thrust, F_x , and that from the drag force, F_g . The derived pressure amplitude:

$$p_{mn} = \frac{\alpha_n \beta_m (mB_F - nB_A)}{4\pi r_o C_o} \cdot \frac{550 \text{ shp}}{R_e} \cdot J_{(mB_F - nB_A)}(mB_A M_e \sin \theta) \quad (7)$$

$$\cdot \left[\frac{-nB_A}{mB_F - nB_A} \cdot \frac{(M_e)_A}{M_o} \cdot \eta_A \cdot \cos \theta - \frac{1}{(M_e)_A} \frac{\delta_m}{\beta_m} \right]$$

is valid for steady- as well as unsteady-loading tones generated by the aft rotors.

3.2.1.2 Scaling Law Based on Gutin's Equation

Scaling laws are empirical relationships intended for the interpolation or extrapolation of existing acoustical data to that of similar rotor geometry under similar operating conditions. In contrast, an analytical model can, in principle, make the same prediction without referring to test

data. The scope of predictions by scaling is more limited than those achieved by analytical models. Another major difference between these two prediction methods is that scaling laws rely on empiricism and ignore many physical principles employed in the analytical models.

There has been good agreement on tone frequencies between those predicted by the generalized equation of Gutin (Equation 7) and those measured in all of the test data. According to Equation 7, propfan tones associated with the integer pair (m,n) exist for all possible combinations of m and n. The integers m and n can be of the same signs for modes of orders $|m|B_F + |n|B_A$, or of opposite signs for modes of orders $|m|B_F - |n|B_A$.

However, Morse and Ingard (Reference 6, p. 746) pointed out that the tones associated with $|m|B_F + |n|B_A$ are negligible compared with the tones associated with $|m|B_F - |n|B_A$. Clearly, predicted angular frequencies (Equations 5 and 6) for the dominating modes of $|m|B_F - |n|B_A$ are: $|m|B_F \Omega_F + |n|B_A \Omega_A$ (Ω_F and $\Omega_A > 0$).

Test data have consistently verified the fact that dominating tones do occur at the frequencies predicted by the theory. To write Equation 7 in the form convenient for tone-scaling purpose:

$$P_{mn} = X (D + E Y), \quad (8)$$

where

$$X = \alpha_n \beta_m, \quad (9)$$

$$Y = \frac{\delta_m}{\beta_m}, \quad (10)$$

$$D = \frac{mB_F - nB_A}{4\pi r_o C_o} \cdot \frac{550 \text{ shp}}{(R_e)_A} \cdot J_{(mB_F - nB_A)}(nB_A M_e \sin \theta) \cdot \left[\frac{-nB_A}{mB_F - nB_A} \cdot \frac{(M_e)_A}{M_o} \cdot \eta_A \cdot \cos \theta \right], \quad (11)$$

and

$$E = \frac{mB_F - nB_A}{4\pi r_o C_o} \cdot \frac{550 \text{ shp}}{(R_e)_A} \cdot J_{(mB_F - nB_A)}(nB_A M_e \sin \theta) \cdot \left[\frac{1}{(M_e)_A} \right]. \quad (12)$$

The terms D and E in Equation 8 are variables that depend on mode numbers of a tone, numbers of rotor blades, and aerodynamic performance of a given propfan test; (for a specified tone, D and E can be calculated without knowing its pressure). The terms X and Y (combinations of β_m , δ_m , or α_n) are regarded as empirical constants for the scaling procedure and must be solved from the given tone pressure. As was previously discussed (Equations 2 and 4), β_m is the Fourier coefficient of the axial unsteady loading of the aft rotor, which depends on forward-rotor wakes. Similarly, δ_m depends on the same wake, but for the tangential component of the loading. The Fourier coefficient α_n is a function of chordwise distribution of the steady loading on aft-rotor blades.

In general, the two constants (X and Y) defined in Equations 9 and 10 are expected to vary both with different rotor geometry and with factors affecting forward-rotor wakes. Once these are determined from the scaled-model data, Equation 8 can be used to scale the tone pressures for propfans of different sizes and for those operating under different, but similar, conditions. In Equation 8, there are only two unknowns (X and Y) for each given tone measured from a test. There are more than two microphone locations where the tone pressures are measured. Since each tone pressure at one microphone location corresponds to one equation for the unknowns, there are more equations than unknowns for a tone. A method based on the criterion of least-square-errors has been adopted in this report to solve for X and Y. Having obtained the X and Y from model test data of a desired case, Equation 8 can be immediately utilized for scaling purposes. A measured tone pressure can be projected to that of a full-size propfan.

As explained in Section 3.2.1, the validity of the scaling procedure is based on assumed similarities of both geometry and aerodynamic performance. The geometric similarity implies that:

$$(R_e)_{\text{Full-Scale}} = \frac{(R_T)_{\text{Full-Scale}}}{(R_T)_{\text{Model}}} \cdot (R_e)_{\text{Model}}. \quad (13)$$

The performance similarity gives the following relationship:

$$(\text{shp})_{\text{Full-Scale}} = \left[\frac{(R_T)_{\text{Full-Scale}}}{(R_T)_{\text{Model}}} \right]^2 \cdot (\text{shp})_{\text{Model}}. \quad (14)$$

The preceding two relationships are used to scale tone pressure for propfans of different sizes but of the same geometric and aerodynamic similarity conditions. In predictions for propfans of different configurations and operating conditions, the desired numbers of blades and rotor efficiency are substituted into Equations 11 and 12 to arrive at the corresponding values of D and E. It should be noted that the region of validity for a given set of X and Y may be limited; consequently, the prediction may not be valid, if the full-scale condition is not comparable to the model test condition from which X and Y are derived.

In this report, a scaled tone of propfans is referred to all tones which are indexed by the same values of the two integers, m and n, in Equation 8. However, tone frequencies change as the tone pressure is scaled for various conditions. The scaled tone frequencies of a full-size propfan can be written in terms of the associate model tone frequencies as:

$$(\text{Tone Freq})_{\text{Full-Scale}} = \frac{(M_e \cdot C_o \cdot R_e)_{\text{Full-Scale}}}{(M_e \cdot C_o \cdot R_e)_{\text{Model}}} \cdot (\text{Tone Freq})_{\text{Model}}. \quad (15)$$

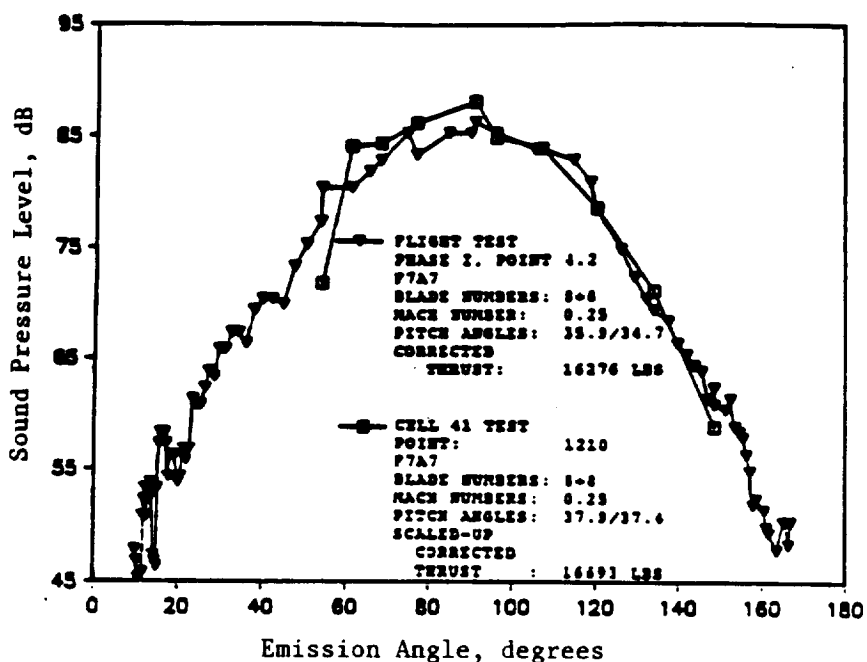
3.2.1.3 Results of Applying the Scaling Law

Three examples are given for evaluating the scaling law discussed in the preceding section. The first example, Figure 16 (Views A through C), which involves comparison of Cell 41 data and flight test data, demonstrates acoustic tone noise of a propfan being scaled up for size difference. The second example, Figure 17 (Views A through I), evaluates the scaling law of Equation 8 for propfan cases of the same geometric configuration which are operated under different conditions. In the third

example, Figure 18 (Views A through I), the scaling formula of the second example is evaluated against cases of different pitch-angle settings of the same propfan. In Figure 16, the data of Cell 41 (Test Point 1210) have been scaled up for a full-size engine. The difference between the test operating condition and that of the selected case of flight tests has been ignored. Both cases have F-7/A-7 design 8+8 blades. Because the forward and aft rotors have the same number of blades and the same rotational speed, the steady-loading tones of each rotor and the interaction tones cannot be distinguished at multiples of the BPF's (blade passing frequencies).

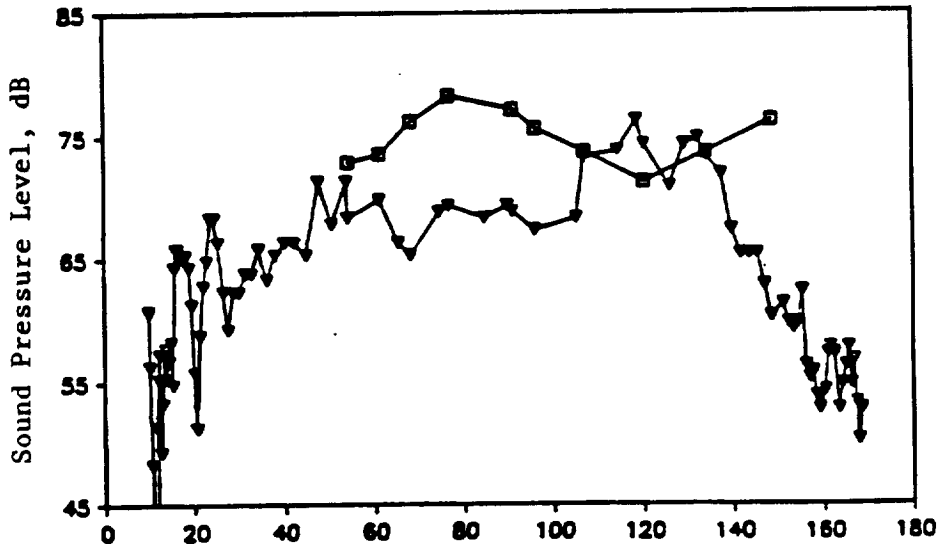
Figure 16 (Views A and C) indicates good agreement between the scaled-up Cell 41 data and the flight test data both of the tones at primary and at 3x the BPF. However, the difference of the tone at 2xBPF between these two sets of data is significant; View B demonstrates an almost 10-dB difference in the emission angle range from 70o to 100°. However, within that range, the dip in the directivity pattern of flight test data is unusual to known patterns of steady-loading tones of a propfan, and the peak SPL (sound pressure level) of the tone at 2xBPF is lower than that of the other two tones. Effects of this difference is not significant to the total SPL of all three tones.

As another example, Test Points 5605 and 5606 of Cell 41 are selected to evaluate the scaling law of Equation 8, which is applied to cases of different operating conditions. The two empirical constants (X and Y) of Equation 8 are determined from Point 5606. Acoustic data of Point 5605 are measured under different operating conditions than that of Point 5606. Estimations from the scaling law are compared with measured data in Figure 17 (Views A through I) for Point 5605. In addition to the comparison in each figure, predictions of the GE analytical model for propfan noise are included as references.

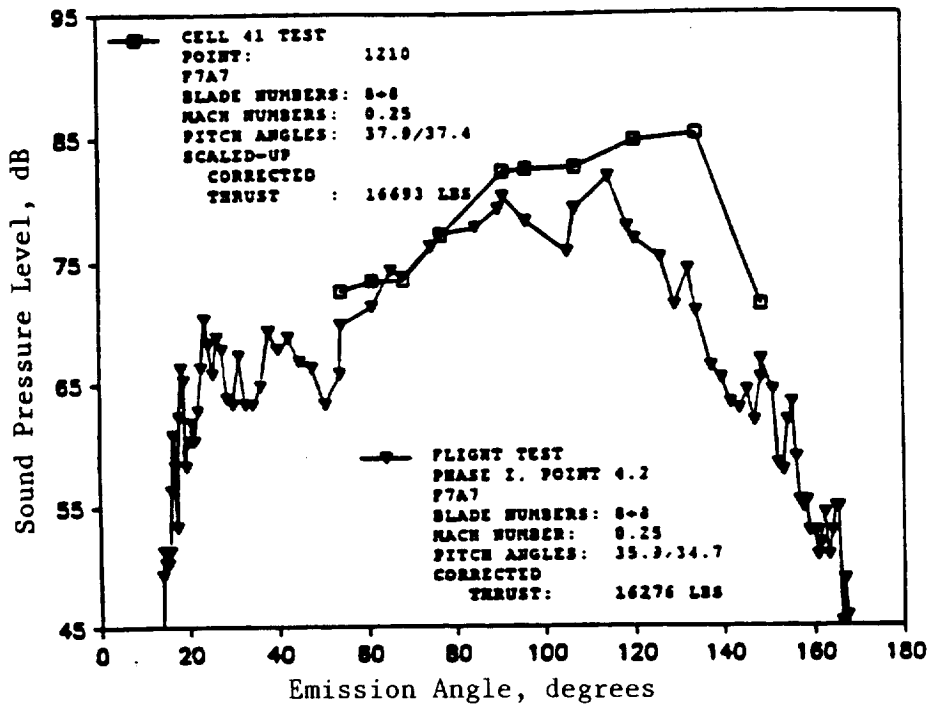


(a) Tones at Primary Blade Passing Frequency

Figure 16. Comparison of Tone Directivities of Flight Test Data and Scaled-Up Cell 41 Data.

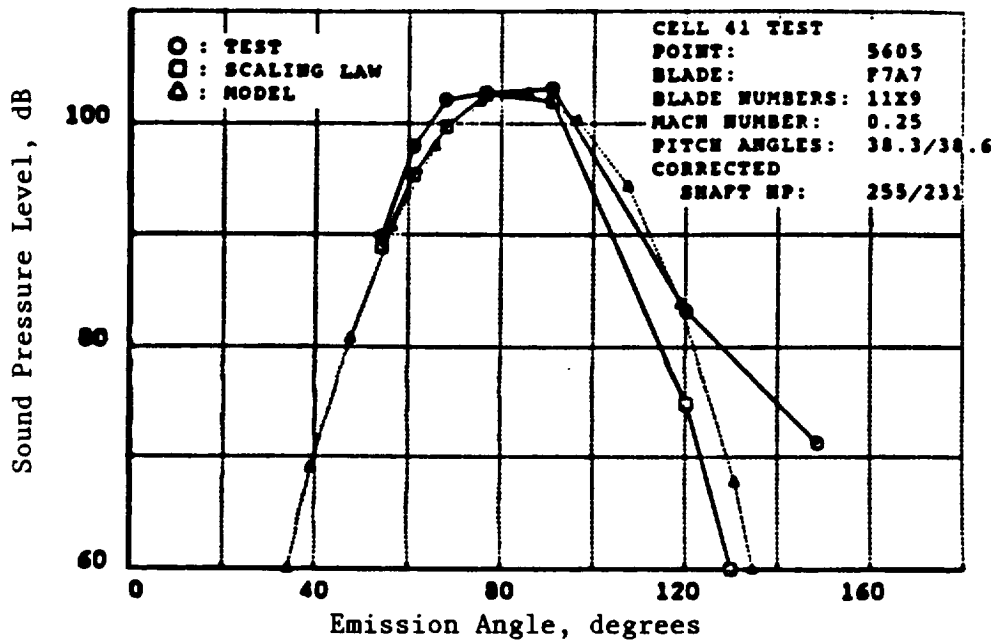


(b) Tones at $2\times$ Blade Passing Frequency

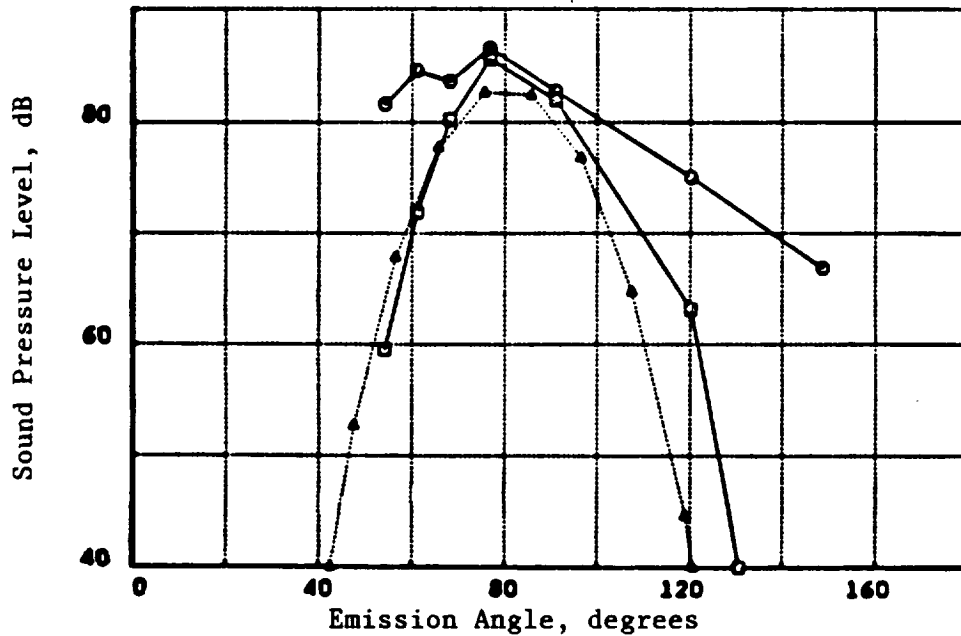


(c) Tones at $3\times$ Blade Passing Frequency

Figure 16. Comparison of Tone Directivities of Flight Test Data and Scaled-Up Cell 41 Data (Concluded).



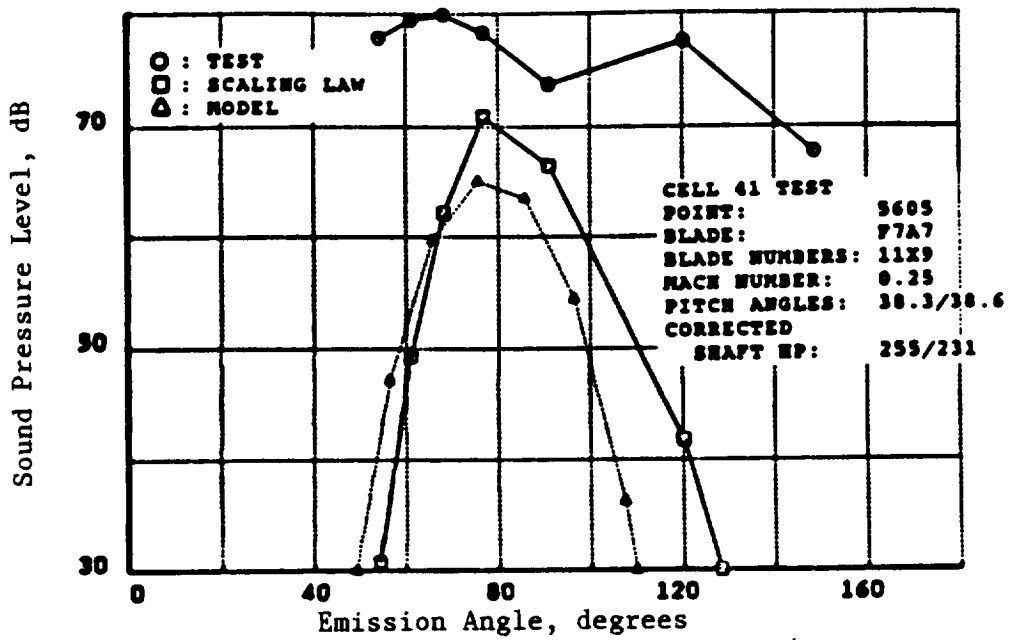
(a) Tone at Primary Blade Passing Frequency of the Forward Rotor ($F1+A0$)



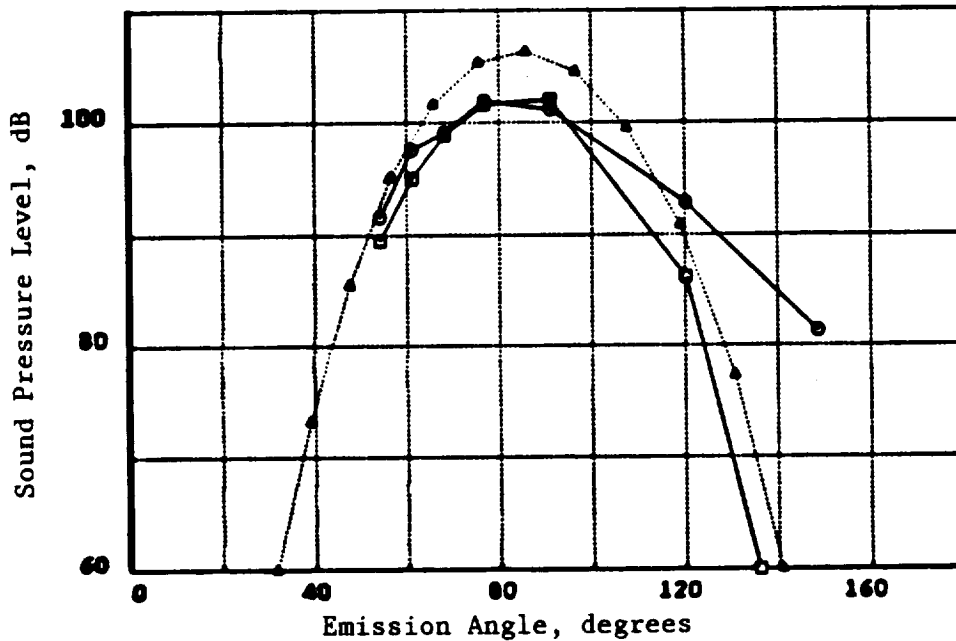
(b) Tone at $2\times$ Blade Passing Frequency of the Forward Rotor ($F2+A0$)

Figure 17. Comparison of Tone Directivities of Cell 41 Data; Scaling Law Estimation, and Analytical Model Prediction.

ORIGINAL PAGE IS
 OF POOR QUALITY

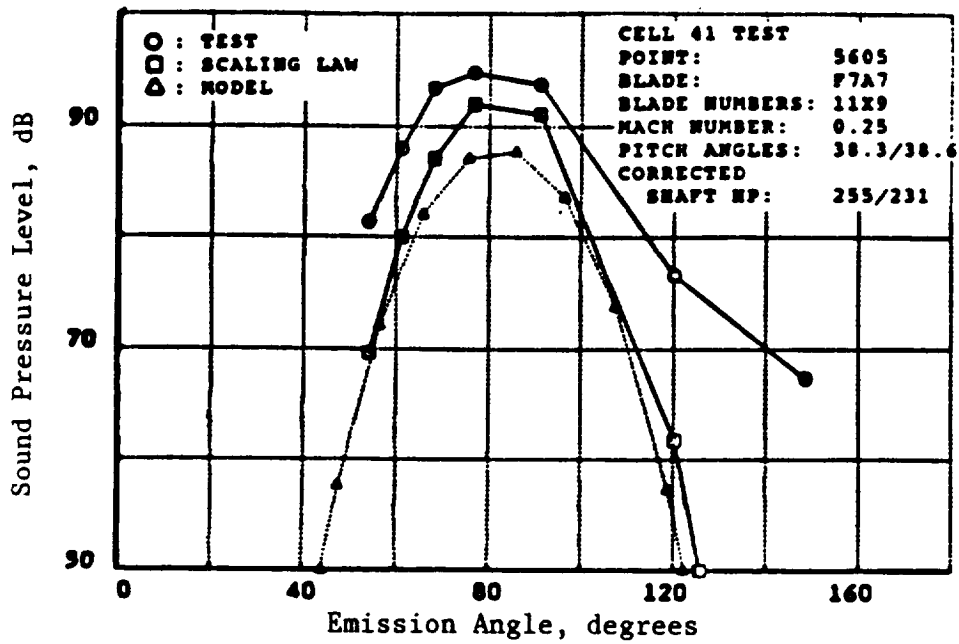


(c) Tone at $3 \times$ Blade Passing Frequency of the Forward Rotor ($F3+A0$)

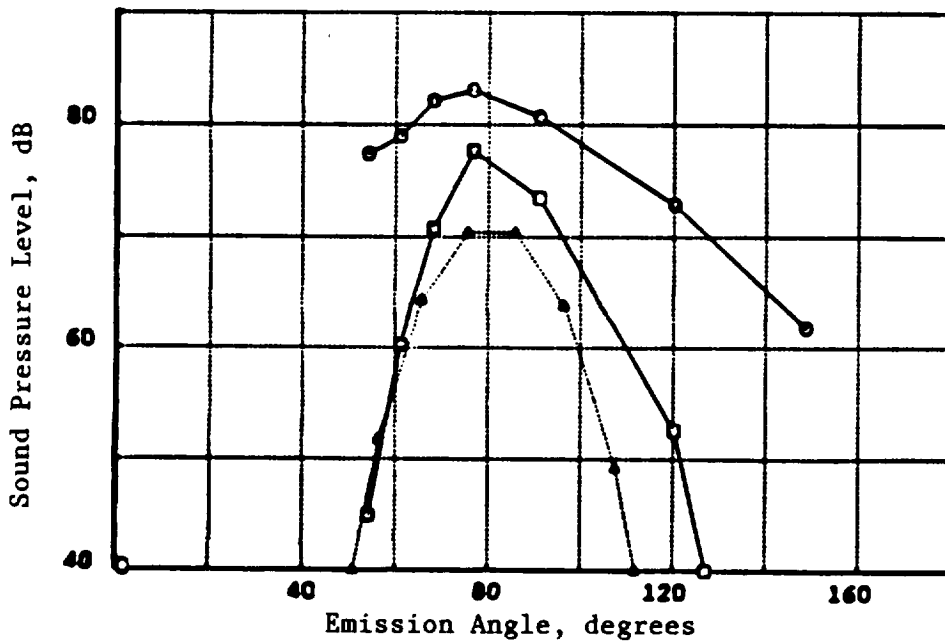


(d) Tone at Primary Blade Passing Frequency of the Aft Rotor ($F0+A1$)

Figure 17. Comparison of Tone Directivities of Cell 41 Data; Scaling Law Estimation, and Analytical Model Prediction (Continued).

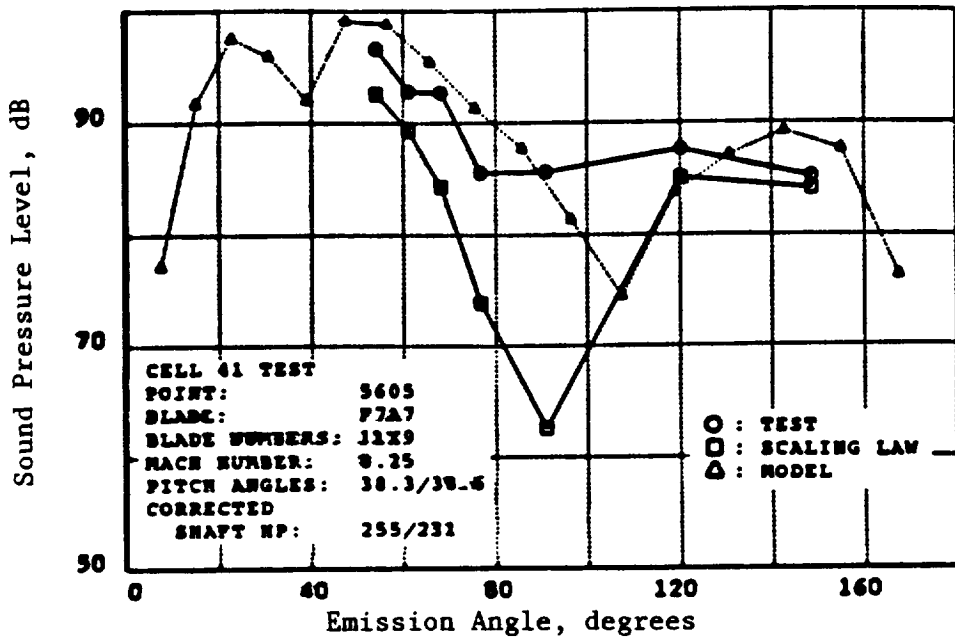


(e) Tone at 2x Blade Passing Frequency of the Aft Rotor (F0+A2)

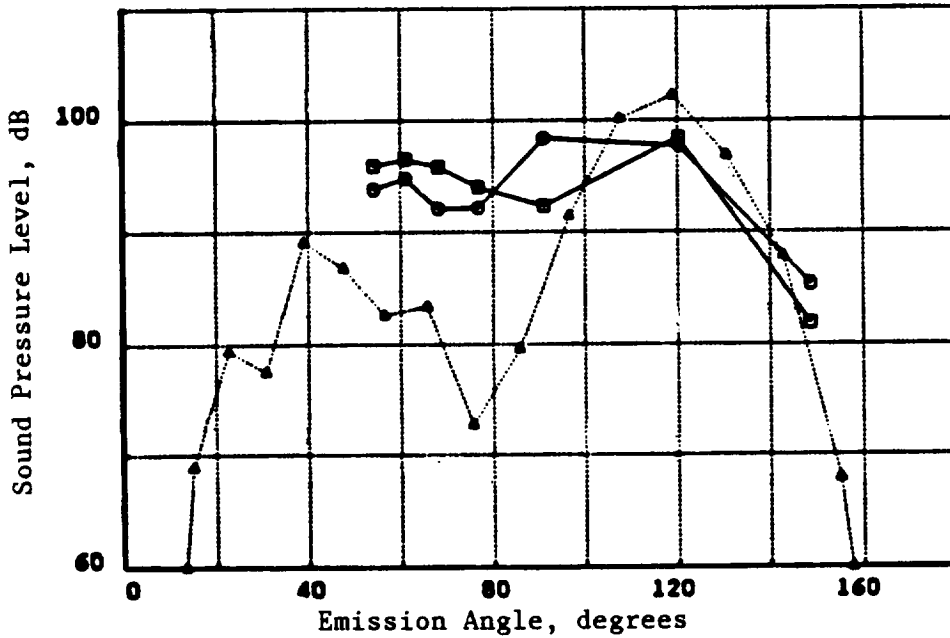


(f) Tone at 3x Blade Passing Frequency of the Aft Rotor (F0+A3)

Figure 17. Comparison of Tone Directivities of Cell 41 Data; Scaling Law Estimation, and Analytical Model Prediction (Continued).

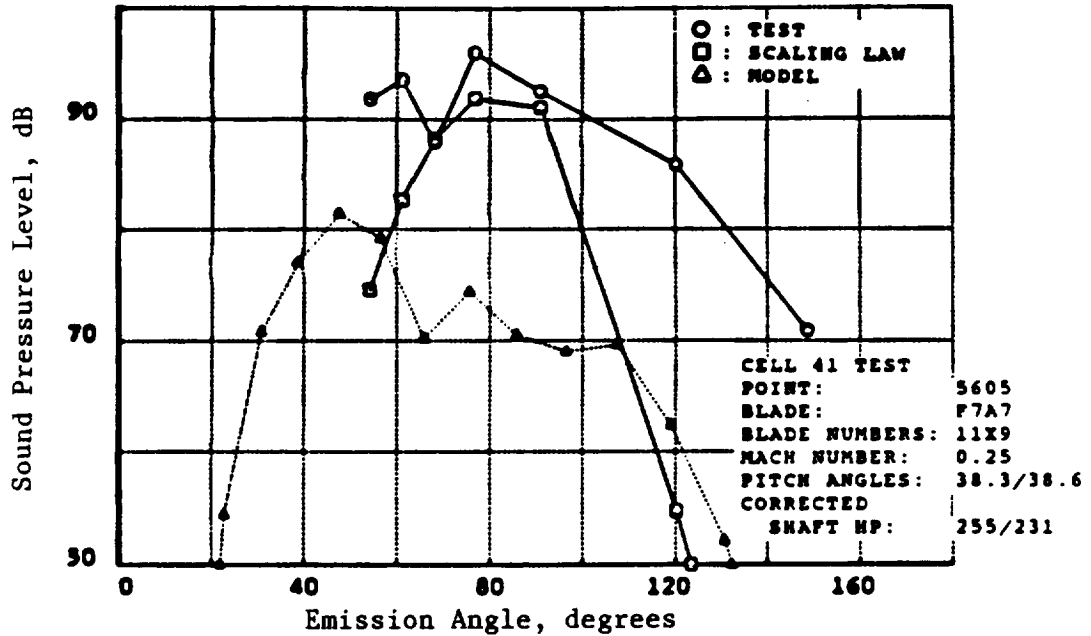


(g) First Interaction Tone at Forward-Rotor Blade Passing Frequency Plus Aft-Rotor Blade Passing Frequency ($F1+A1$)



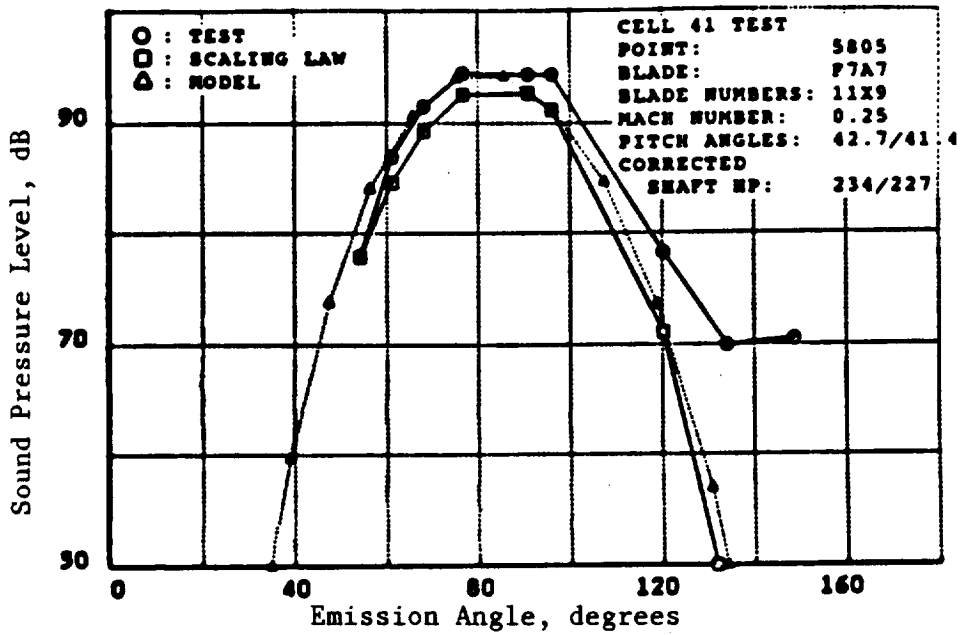
(h) Second Interaction Tone at Forward-Rotor Blade Passing Frequency Plus $2 \times$ Aft-Rotor Blade Passing Frequency ($F1+A2$)

Figure 17. Comparison of Tone Directivities of Cell 41 Data; Scaling Law Estimation, and Analytical Model Prediction (Continued).

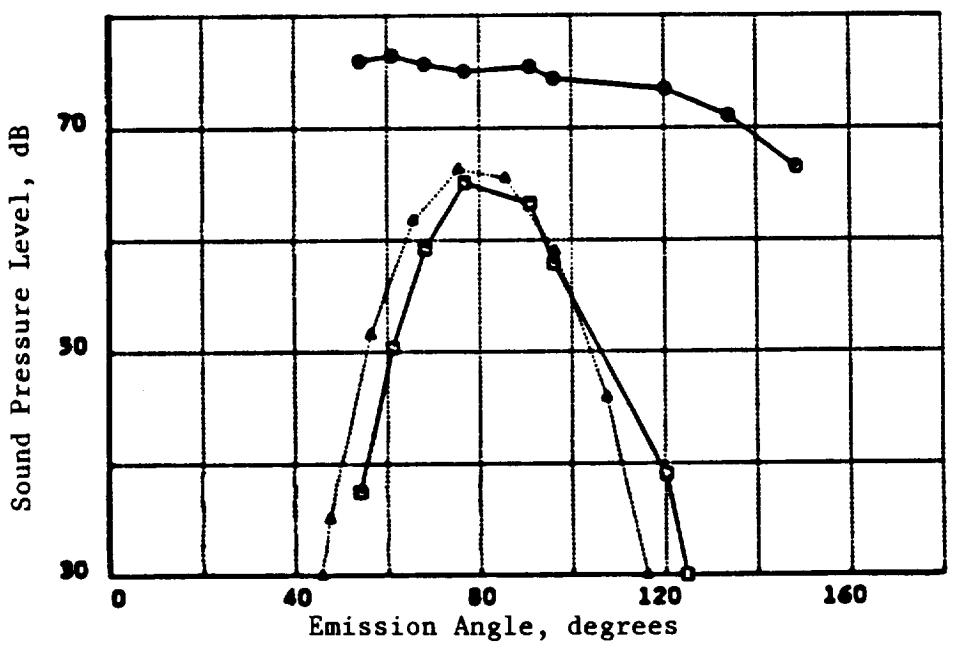


(i) Third Interaction Tone at $2 \times$ Forward-Rotor Blade Passing Frequency Plus Aft-Rotor Blade Passing Frequency ($F_2 + A_1$)

Figure 17. Comparison of Tone Directivities of Cell 41 Data; Scaling Law Estimation, and Analytical Model Prediction (Concluded).

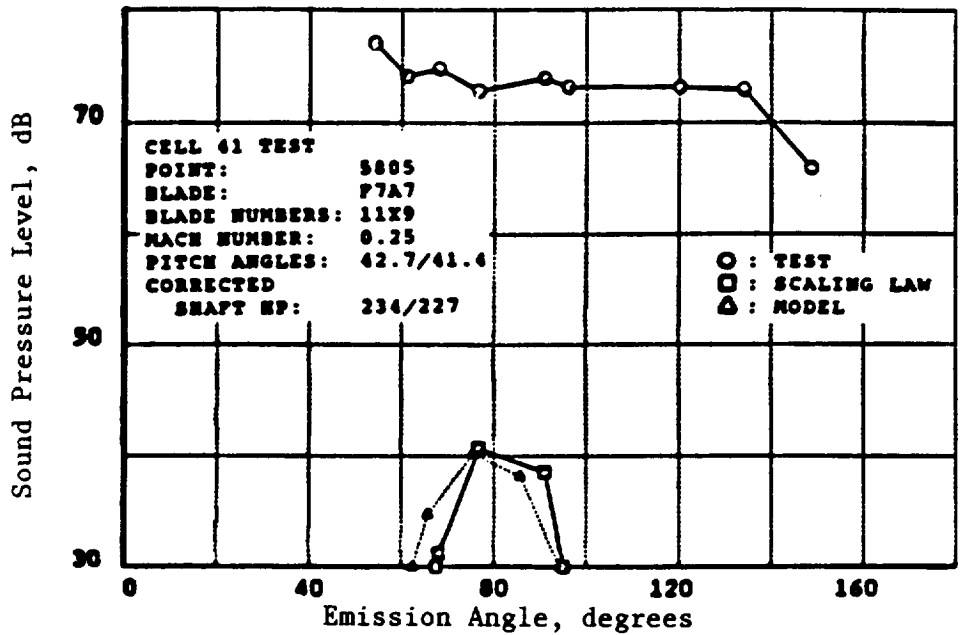


(a) Tone at Primary Blade Passing Frequency of the Forward Rotor ($F1+A0$)

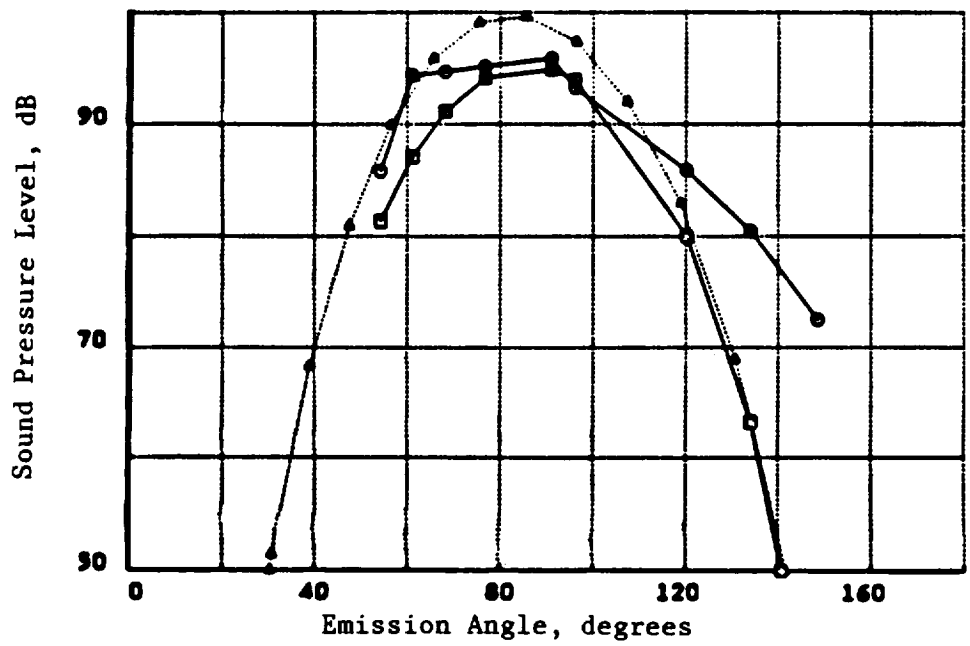


(b) Tone at $2\times$ Blade Passing Frequency of the Forward Rotor ($F2+A0$)

Figure 18. Comparison of Tone Directivities of Cell 41 Data; Scaling Law Estimation, and Analytical Model Prediction.

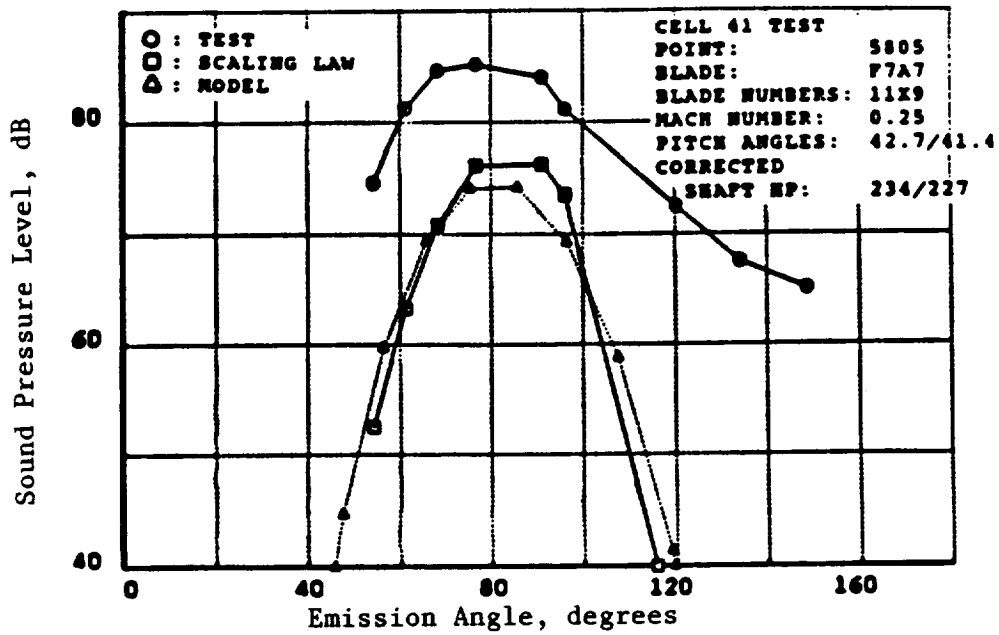


(c) Tone at 3x Blade Passing Frequency of the Forward Rotor (F3+A0)

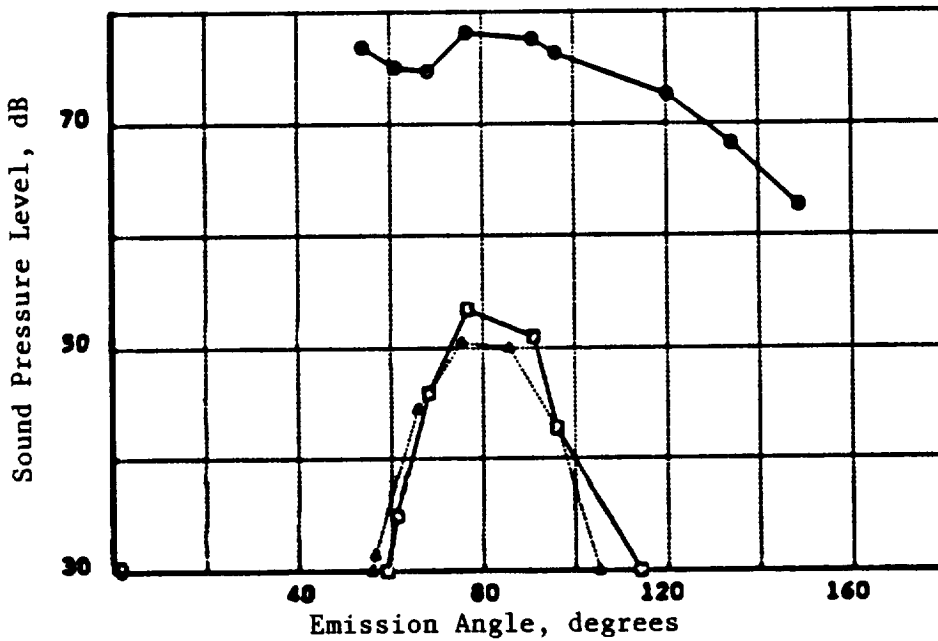


(d) Tone at Primary Blade Passing Frequency of the Aft Rotor (F0+A1)

Figure 18. Comparison of Tone Directivities of Cell 41 Data; Scaling Law Estimation, and Analytical Model Prediction (Continued).

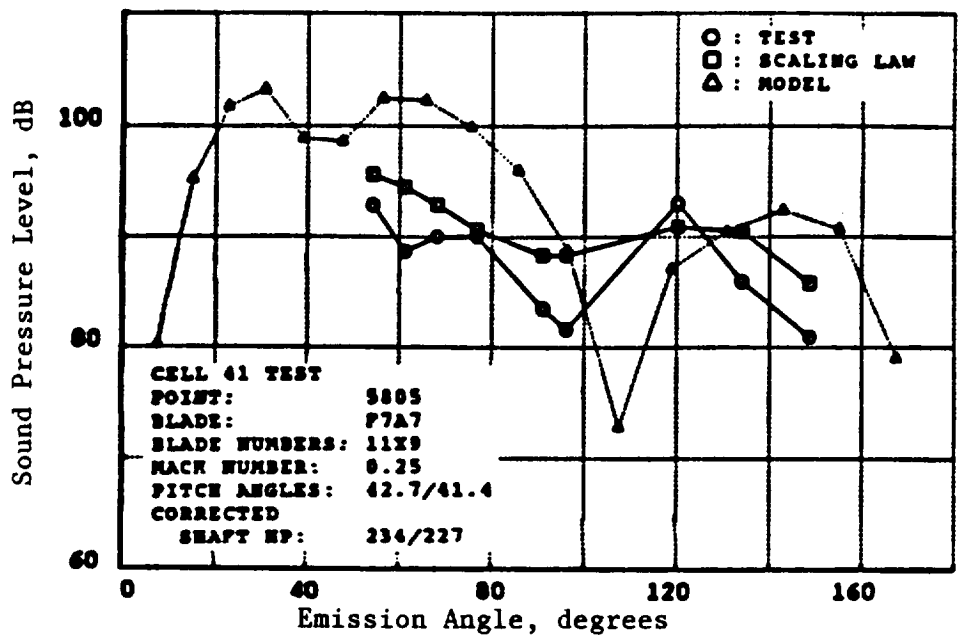


(e) Tone at 2x Blade Passing Frequency of the Aft Rotor (F0+A2)

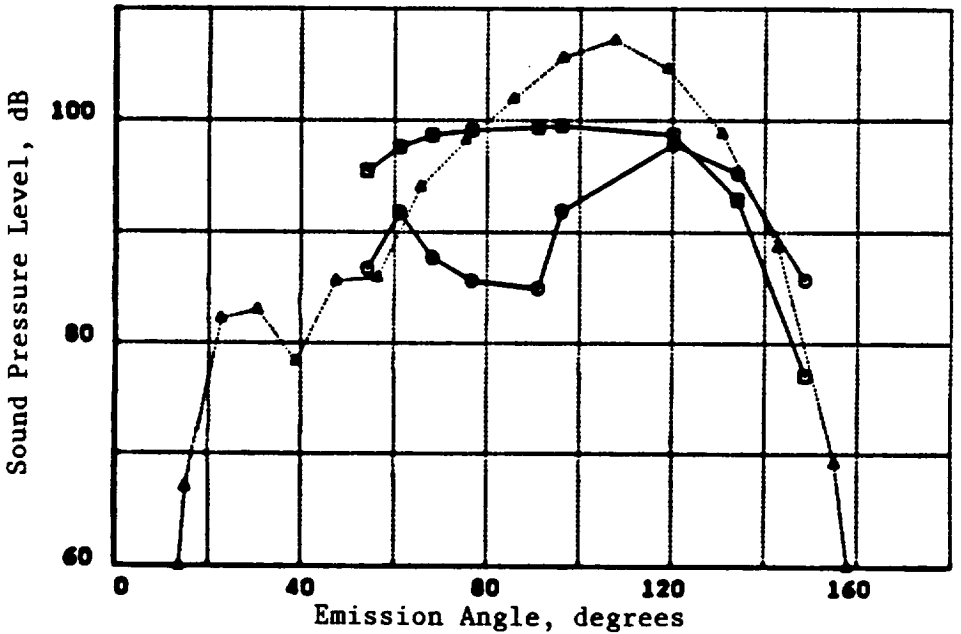


(f) Tone at 3x Blade Passing Frequency of the Aft Rotor (F0+A3)

Figure 18. Comparison of Tone Directivities of Cell 41 Data; Scaling Law Estimation, and Analytical Model Prediction (Continued).

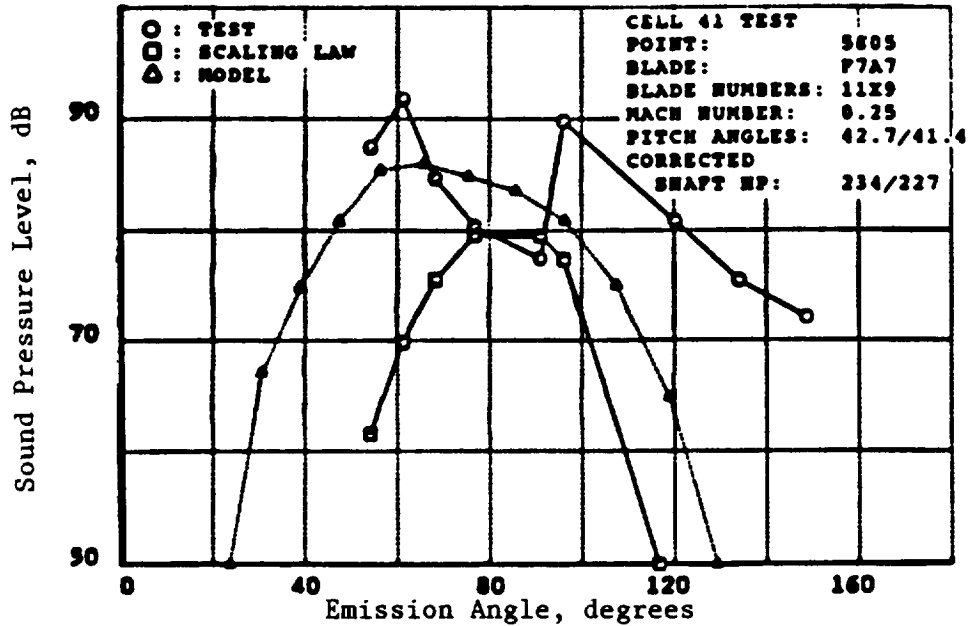


(g) First Interaction Tone at Forward-Rotor Blade Passing Frequency Plus Aft-Rotor Blade Passing Frequency ($F1+A1$)



(h) Second Interaction Tone at Forward-Rotor Blade Passing Frequency Plus $2\times$ Aft-Rotor Blade Passing Frequency ($F1+A2$)

Figure 18. Comparison of Tone Directivities of Cell 41 Data; Scaling Law Estimation, and Analytical Model Prediction (Continued).



(i) Third Interaction Tone at $2 \times$ Forward-Rotor Blade Passing Frequency Plus Aft-Rotor Blade Passing Frequency (F_2+A_1)

Figure 18. Comparison of Tone Directivities of Cell 41 Data, Scaling Law Estimation, and Analytical Model Prediction (Concluded).

The comparisons between the data and estimations by scaling law show good agreement for all tones at primary blade-passing frequencies of forward and aft rotors (F_1+A_0 and F_0+A_1 tones). In regard to other tone comparisons, the disagreements are especially prominent for the higher frequency steady-loading tones as depicted in Figure 17 (Views B, C, E, and F). However, it has been found that when a significant difference between the test data and scaling law estimations exists, the estimations are always close to the analytical model predictions.

Pitch angles for Series 56 tests are set at 38.3° for the forward-rotor blades and 38.6° for the aft. The third example (Figure 18) is intended to evaluate the extension of the scaling formula derived from a test of Series 56 to Test Point 5805 of Series 58, for which the blade-pitch angles were set at 42.7° and 41.4° . Because blade-pitch angles in the third example were reset, most of the tone directivity comparisons indicate that the differences between test data and estimations by Equation 8 are larger than the differences of the corresponding tone comparisons of the second example. However, comparisons of tones at primary blade passing frequencies still show good agreement. In addition, when significant differences exist between estimations and data for tone directivities, it is observed again (as in the previously cited example) that the scaling law estimations generally approximate the predictions of the analytical model.

3.2.1.4 Discussion of Scaling Law Application Results

In all three examples presented in the preceding section, the data and scaling law estimations agree very well for F_1+A_0 tone and F_0+A_1 tone. This implies that Gutin's equation can be effectively applied to scale F_1+A_0 and F_0+A_1 tones, not only for propfan size difference, but also for differences of operating conditions. In the third example, it is demonstrated that an empirical

scaling formula can be borrowed and applied successfully, even for a case with different pitch angles of propfan blades.

Unfortunately, disagreements between test data and estimations by scaling law are significant for all tones except the F1+A0 and F0+A1. Either the tone pressure levels do not agree, or the directivity patterns are different. One possible explanation for these discrepancies is that the generalized equation of Gutin derived in this report has accounted only for steady- and unsteady-loading noise; whereas, actual tone pressure measured in a test may include thickness noise, unexpected installation noise, and noise from other unknown sources.

It was mentioned in the discussion of the second and third examples, that the directivity patterns of F2+A0, F0+A2, F3+A0, and F0+A3 tones estimated by the scaling law have prominent peaks and are similar to those predicted by the analytical model; nonetheless, they are quite different from the flat patterns of the measured data. As a matter of fact, this discrepancy does not arise in the (first example) comparison study of Cell 41 data and flight test data; all measured data seems to agree on the flat patterns of the tone directivities. This raises the question of whether, in the theoretical formulation, all of the possible noise sources have been included for the steady-loading tones of 2x or 3x the blade-passing frequencies. For example, quadrupole sources are not included in Gutin's equation nor in the analytical model utilized in this report (References 8 and 9).

In the immediate future, to resolve the discrepancies and to afford an enhanced understanding of the noise generation mechanisms of the propfans, there are two roles that scaling laws can play. First, empirical scaling laws should be refined. Because they are by nature empirical formulas, these scaling laws are ideal tools enabling the use of available data to identify and quantify the missing pieces of noise sources that have not been included in the existing theoretical formulation.

Second, a refined scaling law has the potential to provide information of installation and wake effects on propfan noise. According to the formal derivation of the scaling law (Equation 8), the two empirical constants depend on the lump characteristics of wake effect on noise. When solved from a set of test data, these constants can be further analyzed and provide important and needed information to the study of interaction tone noise of propfans.

In summary, Gutin's equation is cast in a general form, which can be used to estimate tone pressure for both steady- and unsteady-loading noise generated by the counterrotation propfans. The equation is used as a scaling law to scale tone pressure measured from tests to that of propfans with different sizes, as well as those operated under different conditions. Results indicate agreements and discrepancies between the estimations and test data. In order to resolve these discrepancies, future improvement of the scaling law has been proposed.

3.3 Aerodynamic Design

3.3.1 General Aerodynamic Design Approach

The approach selected for aerodynamic design of the UDF (unducted fan) blade is the same quasi-three dimensional approach utilized for a conventional ducted fan. Much of the technology used in the aerodynamic design of these highly loaded, counterrotating blade rows is the same as that established for engines with high bypass-ratio transonic fans. Principal design challenges in the UDF® design are eliminating the choking of flow in the blade hub region, where the blade thickness is the greatest, and minimizing passage shock losses due to the high through-flow velocities. Another critical design challenge is the correct modeling and prediction of the 3D flow field in the open tip region of the blades.

Two effects identified as very important in the design of high performance unducted fan blades, in contrast to ducted fans, are: large secondary flows that are generated at the tips of the blades, and the use of aerodynamic sweep to reduce the effective Mach number. Both of these effects were investigated during the design phase; accordingly, the blade airfoil shapes were specifically tailored.

The circumferential-average-flow solution is calculated for the UDF® configuration using the optimum-loading distribution developed by Theodorsen for counterrotating propellers. When executing the aero design, primary attention is focused on the top-of-climb design point. This is where the blading Mach numbers are the highest and, therefore, where the greatest need for design precision exists. The open tip condition is simulated in the flow calculation by employing a wall boundary far removed from the blade flow field, such that only 10% of the total flow passes through the blades. A calculation is also made with only 1% of total flow passing through the blades to further assure that the boundary is not influencing the flow field in the blade region. The flow calculation models the nacelle/nozzle flowpaths and the circumferential-average-flowpath through the blade hub region.

Flow properties are calculated along 11 streamlines through the blades as well as 7 streamlines above the bladetips. Numerous calculation stations are utilized, ranging from far upstream (of the blades) to far downstream. Eight internal blade stations are also implemented in the calculation to accurately represent the blade presence in the flow field. The lean and blade blockage terms are incorporated in the radial equilibrium equation which is solved at each of these stations and streamline grid locations. The resulting vector diagrams representing the Mach 0.72 aerodynamic design point are utilized for setting the blade mean-line angles.

Airfoils are designed on the design stream surfaces using blade-to-blade analyses or cascade concepts. In general, the airfoil designs need to recognize changes in lamina thickness and change in radius of the stream surfaces from leading edge to trailing edge as well as the effects of blade sweep and secondary flows.

The blade planform shape is chosen to afford optimum aeroacoustic sweep distribution and still meet aeromechanical stability requirements. Initially, the blade axis is defined for each blade row by radial distributions of sweep and tangential lean. A chord distribution consistent with the spanwise loading distribution is specified. The airfoil sections are then defined along stream surfaces from the blade tip to hub. Radial and chordwise thickness distributions are defined to satisfy the aeromechanical stress and stability constraints; this, together with the blade mean-line angle distribution, specifies an airfoil shape along each streamline.

The fully 3D blade is then analyzed using the GE Euler code to determine surface velocity distributions. Several iterations on blade mean-line angle are made to improve the velocity distributions and to reduce the passage shock strengths. Airfoil coordinates are defined at the hot running condition (aero design point), but the cold manufacturing airfoil shape is defined by applying appropriate deflections calculated from both air loads and centrifugal loads. Figure 19 depicts an example of the change in blade stagger and camber angles from static to running condition.

Airfoils designed by this process are stacked to generate blades for manufacturing. It is generally necessary to iterate the blade design with the circumferential-average analysis to assure that the latter contains the proper blade force and blockage distributions.

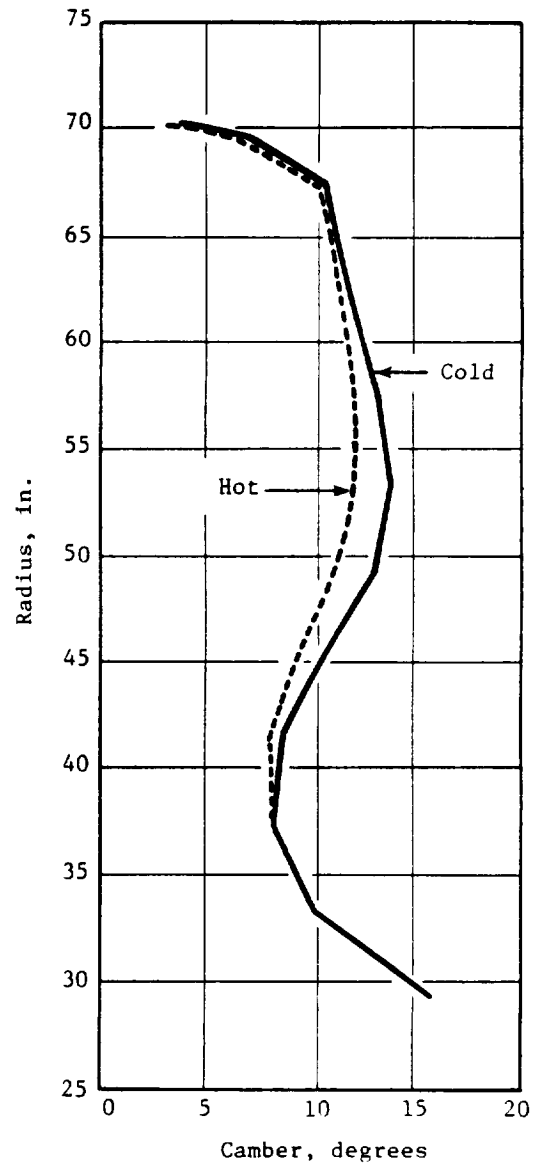
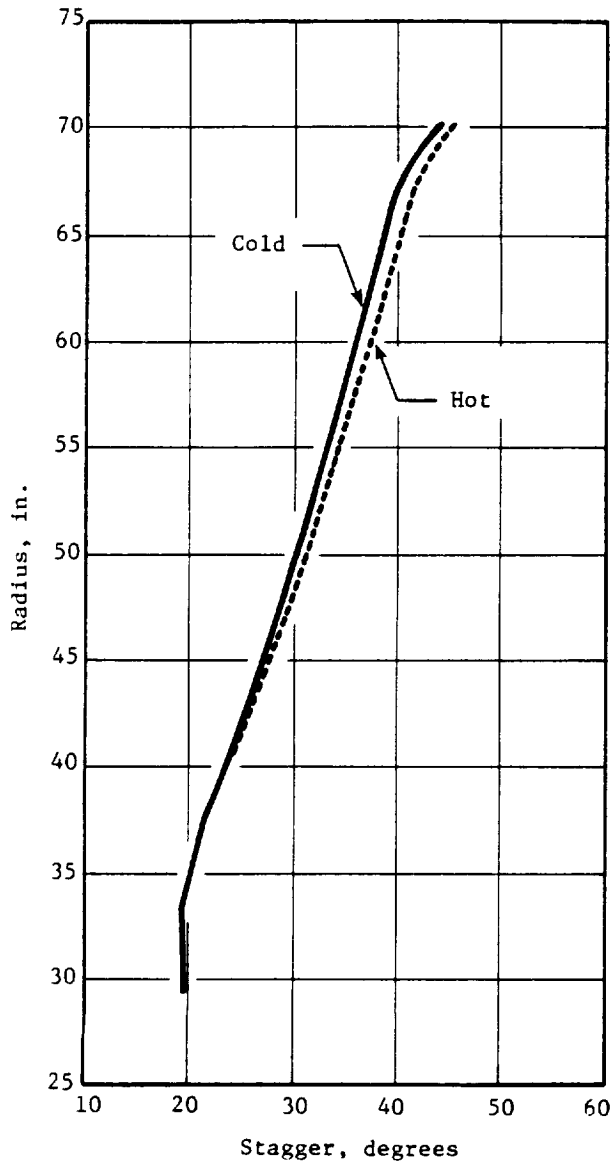


Figure 19. F-7 Blade Geometry Change (Cold-to-Hot).

3.3.2 Blade Configuration

Three unducted fan blade configurations (F-4/A-4, F-5/A-5, and F-7/A-7) were designed in scale model size at the maximum-climb flight condition of Mach 0.72; 10,668-m (35,000-ft) altitude. Two others, the F-11/A-11 and F-21/A-21, were designed at Mach 0.80 maximum-climb. All five blade designs were manufactured for scale model testing using the 0.62-m (24.5-in.) diameter MPS rig. Table 5 summarizes the pertinent aerodynamic design parameters.

Mach 0.72 configurations were the earliest designs completed, each having 8+8 counterrotating blades and a moderately high annulus loading (shaft power/Aa) of 86 HP/ft² at the aerodesign point. The F-4/A-4 and F-5/A-5 were designed to study effects of blade-activity factors, while maintaining the aero tip sweep and other parameters nearly the same. The F-4/A-4 blades had 25% more chord than the F-5/A-5 blades; both designs employed planforms with no hub sweep and radially straight trailing edges. F-7/A-7 blades were designed with more aerodynamic sweep over the entire blade span and with chord lengths similar to the F-4/A-4 blades. The planform shape of the F-7/A-7 blades also differed from that of the F-4/A-4 and F-5/A-5, using forward sweep at the hub and backward sweep at the tip. All Mach 0.72 configurations were designed for the nominal rotor-to-rotor spacing of 10.57 cm (4.16 in.).

Table 5. Aerodesign Parameters of the Unducted Fan Configurations.

	F-4/A-4	F-5/A-5	F-7/A-7	F-11/A-11	F-21/A-21
Design Flight Mach No.	0.72	0.72	0.72	0.80	0.80
Advance Ratio, J	2.80	2.80	2.80	3.12	3.12
Power Coefficient, PQA	4.15	4.15	4.15	4.63	5.58
Annulus Loading, Shaft Power/Aa, kw/m ² (HP/ft ²)	682 (85)	682 (85)	682 (85)	771 (85)	947 (118)
Number of Blades	8+8	8+8	8+8	11+9	11+10
Total Activity Factor	2456	1968	2392	3780	3713
Tip Speed (R1), m/s (fps)	237.7 (780)	237.7 (780)	237.7 (780)	237.7 (780)	243.8* (800)
Aero Tip Sweep, Degrees (Forward/Aft)	19/20	15/18	34/31	37/34	45/25
Inlet-Radius Ratio	0.425	0.425	0.425	0.425	0.431
* Standard Day + 18° F Conditions					

Figure 20 compares the radial distributions of the lift coefficients and solidities of the Mach 0.72 forward and aft blade rows. The lower solidity (F-5/A-5) blades have lift coefficients that are approximately 25% larger.

The F-7/A-7 configuration was designed to scale of the full-scale demo engine UDF® design, except that the model-scale blades were fabricated with a different composite-ply stiffness than design intent. This affected the cold-to-hot transformation, resulting in airfoils with 2° to 4° more camber than intended over most of the blade span at the high speed running condition.

The F-11/A-11 and F-21/A-21 configurations were designed at the Mach 0.80 maximum-climb condition, with different numbers of blades in the forward and aft rotors. The F-11/A-11 has 11 forward and 9 aft blades; whereas, the F-21/A-21 uses 11 forward and 10 aft. Due to a higher design Mach number (0.80), disk loading of the F-11/A-11 was higher than the earlier Mach 0.72 designs. The disk loading at Mach 0.72 remained the same as the F-4/A-4, F-5/A-5, and F-7/A-7 configurations. Larger chords and more blades (compared to earlier designs) were employed to both increase the total activity factor and lower the blade-lift coefficients. The radial distributions of the F-11/A-11 and F-21/A-21 blade solidities and lift coefficients are illustrated in Figure 21.

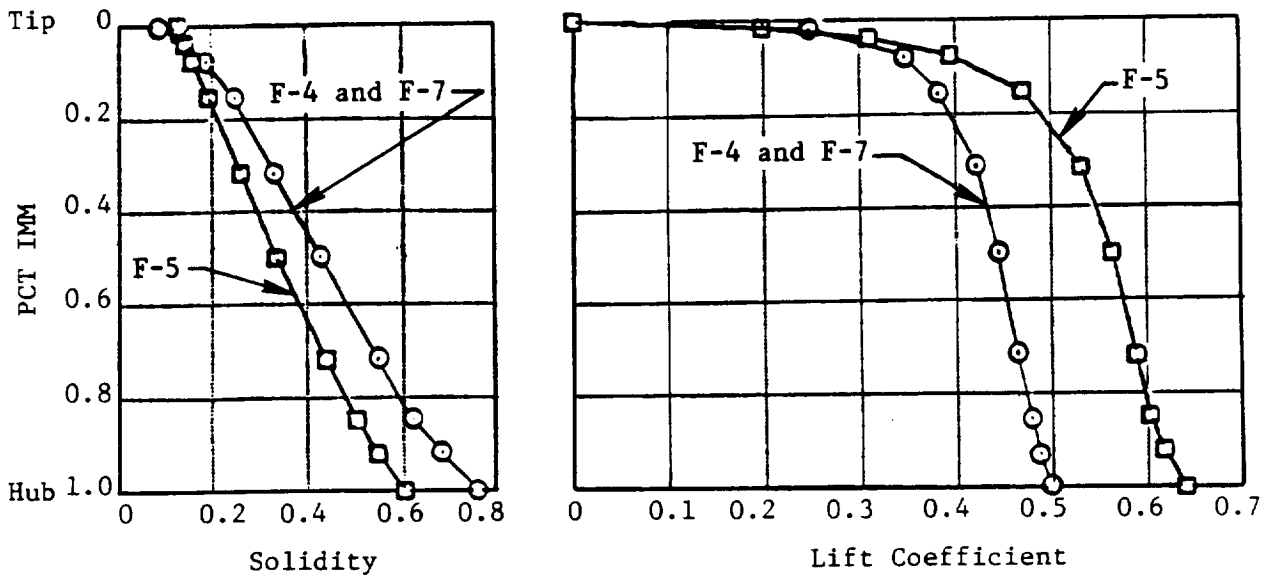
The F-21/A-21 configuration was designed for a 25% higher disk loading than the other configurations at the Mach 0.80 maximum-climb condition; Figure 22 compares the radial load distribution of the F-21/A-21 to the nominal load distribution of the other blade configurations. The full-size blade diameter was reduced from 3.56 m (11 ft, 8 in.) to 3.05 m (10 ft), with the same total horsepower. All of the designs employed Theodorsen's optimum-loading distribution, which concentrates the loading over the inner portion of the blade, out to approximately 60% span, then falls off rapidly to 0% at the tip. The F-21/A-21 design also employed a higher tip sweep (45°) on the forward blades. Figure 23 presents the radial distributions of aero sweep for each of these blade configurations.

3.3.3 Axisymmetric Design Flow Analysis

The axisymmetric flow analysis was performed at the maximum-climb aerodynamic design point for each configuration. Figures 24 through 28 depict the meridional view of the UDF® configurations with the streamlines, calculation stations, and meridional Mach number contours superimposed. Flow streamlines are calculated after the blade row work addition and losses are input, along with the blade speed and freestream Mach number. The meridional Mach number contours indicate the regions of the flow field where the highest through-flow velocities occur, generally inside the blade rows where the thickness blockage reduces the effective flow area.

Higher flight Mach number designs, such as the F-11/A-11 and F-21/A-21, have local regions inside and downstream of the aft rotor where the flow is at or very near a choked condition. These designs were specified to have larger rotor-to-rotor spacings to reduce the effects of acoustical interaction. Some area-ruling of the hub flowpath in the region of the blades was employed to alleviate the choked conditions as much as possible. Upstream of the blades, the nacelle was shaped to provide a gentle diffusion ahead of the forward-rotor leading edge. Downstream of the rotors, the hub contour was designed to follow the direction of the exhaust plume for the demo engine. Calculations for four of the configurations were performed for the full-scale (3.56-m diameter) UDF demo engine, and then the blade coordinates were scaled to the MPS size, 0.62-m (24.5-in.) diameter. The F-11/A-11 configuration was designed and analyzed in the scale model size, since it was considered only for scale model testing.

Forward Rotors - F-4, F-5, and F-7



Aft Rotors - A-4, A-5, and A-7

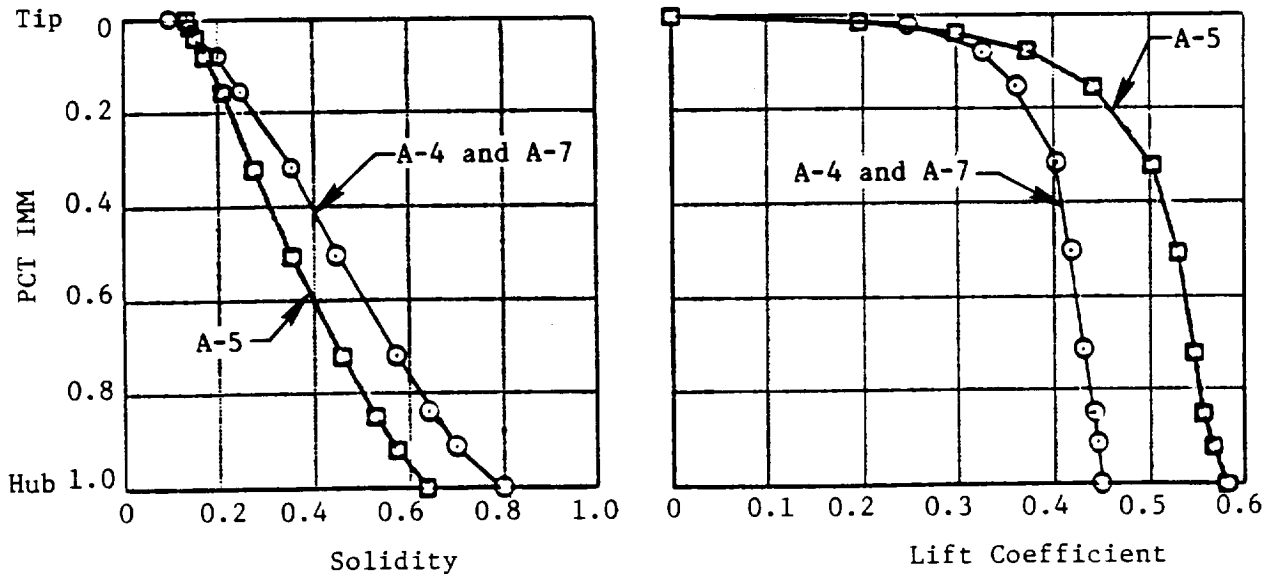
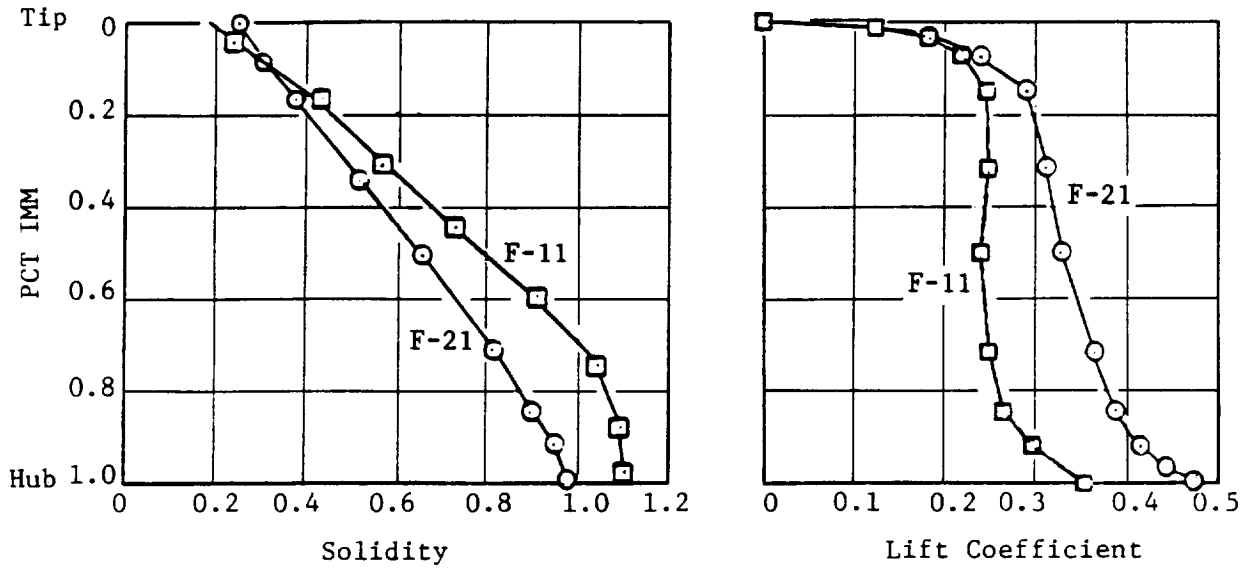


Figure 20. Radial Distribution of Solidity and Lift Coefficient for the F-4/A-4, F-5/A-5, and F-7/A-7 Blades.

Forward Rotors - F-11 and F-21



Aft Rotors - A-11 and A-21

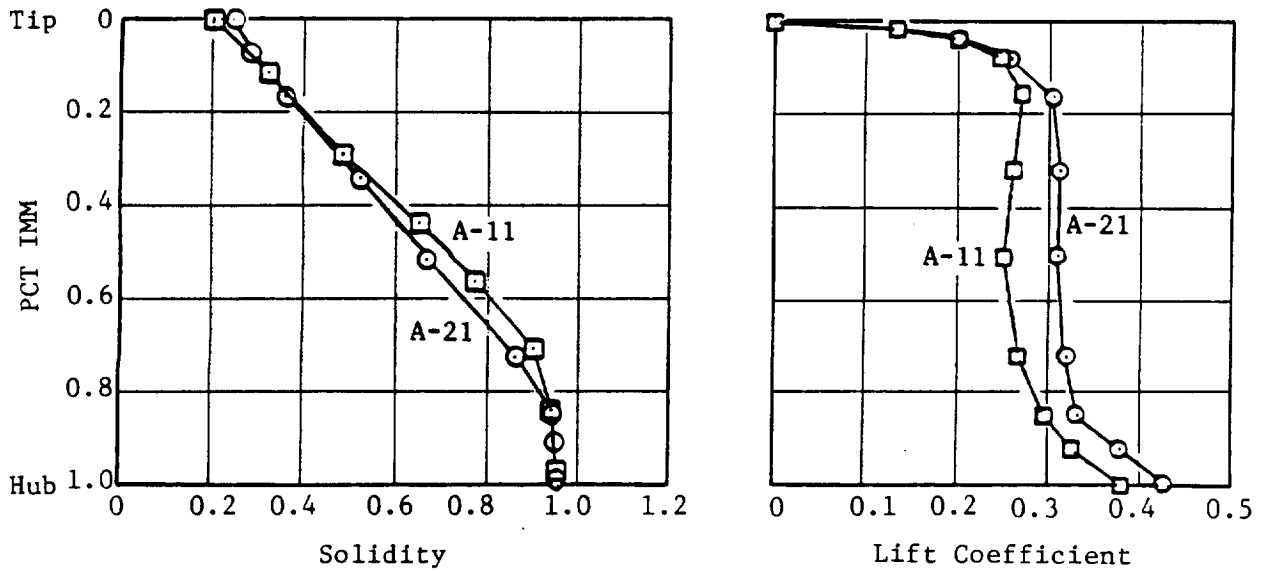


Figure 21. Radial Distribution of Solidity and Lift Coefficient for the F-11/A-11 and F-21/A-21 Blades.

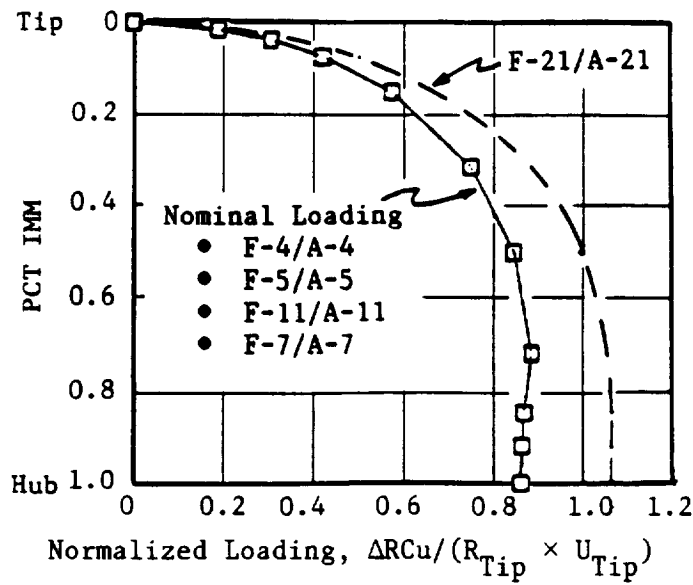


Figure 22. Radial Distribution of Blade Loading at Design.

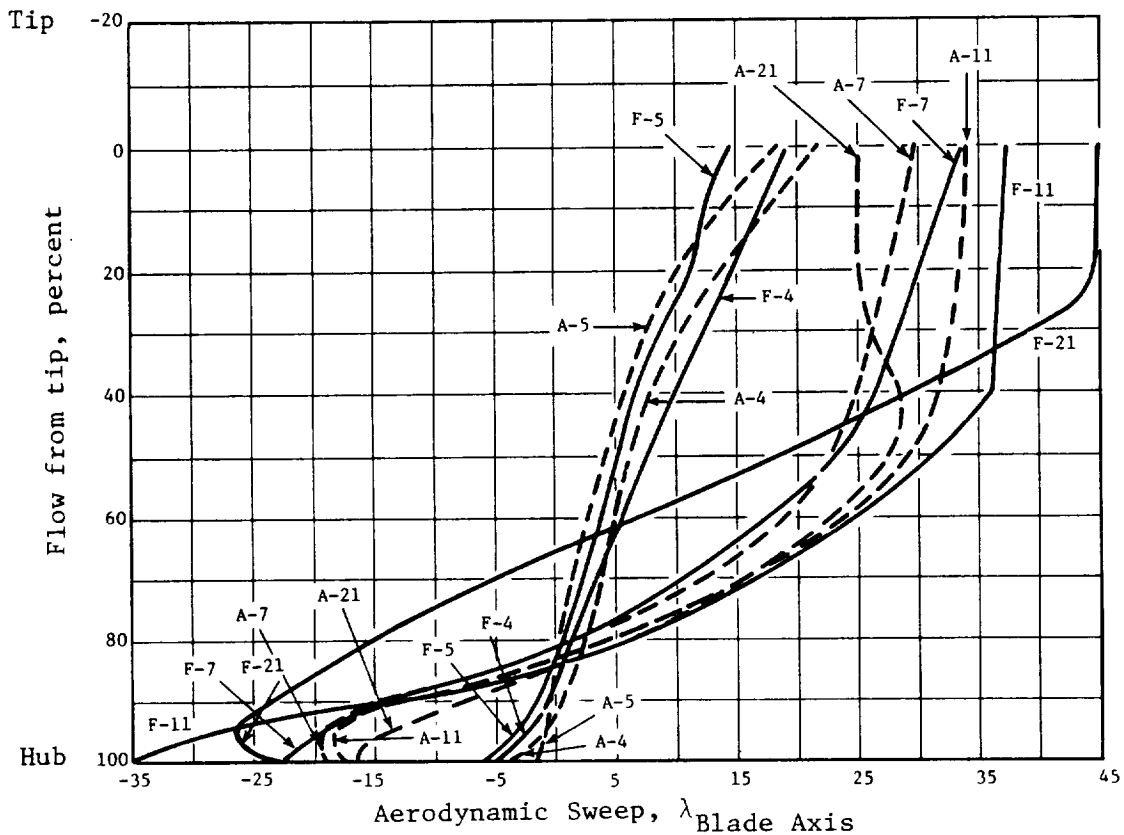


Figure 23. Unducted Fan Aerodynamic Sweep Distribution.

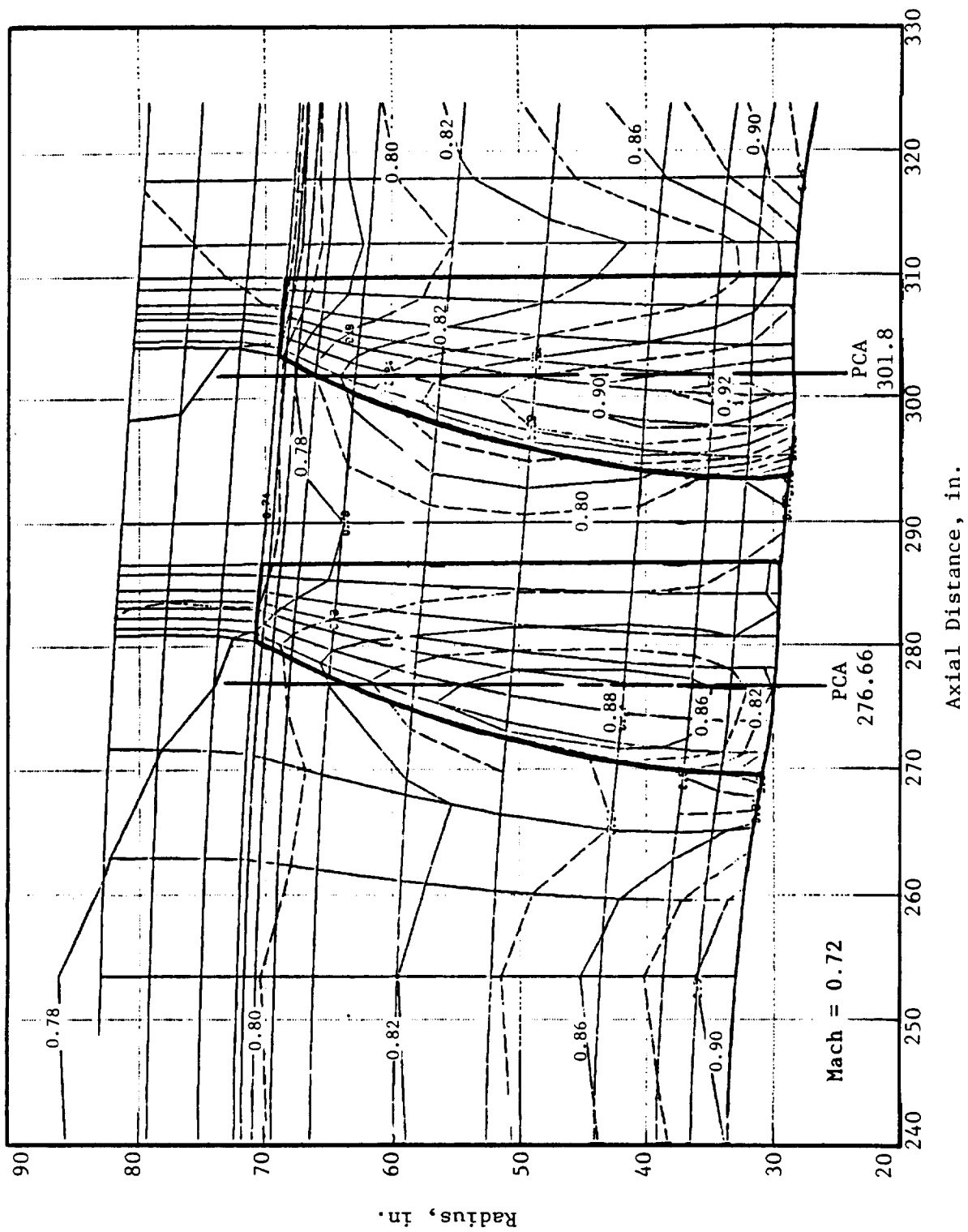


Figure 24. F-4/A-4 (8+8) Meridional Mach Number Contours.

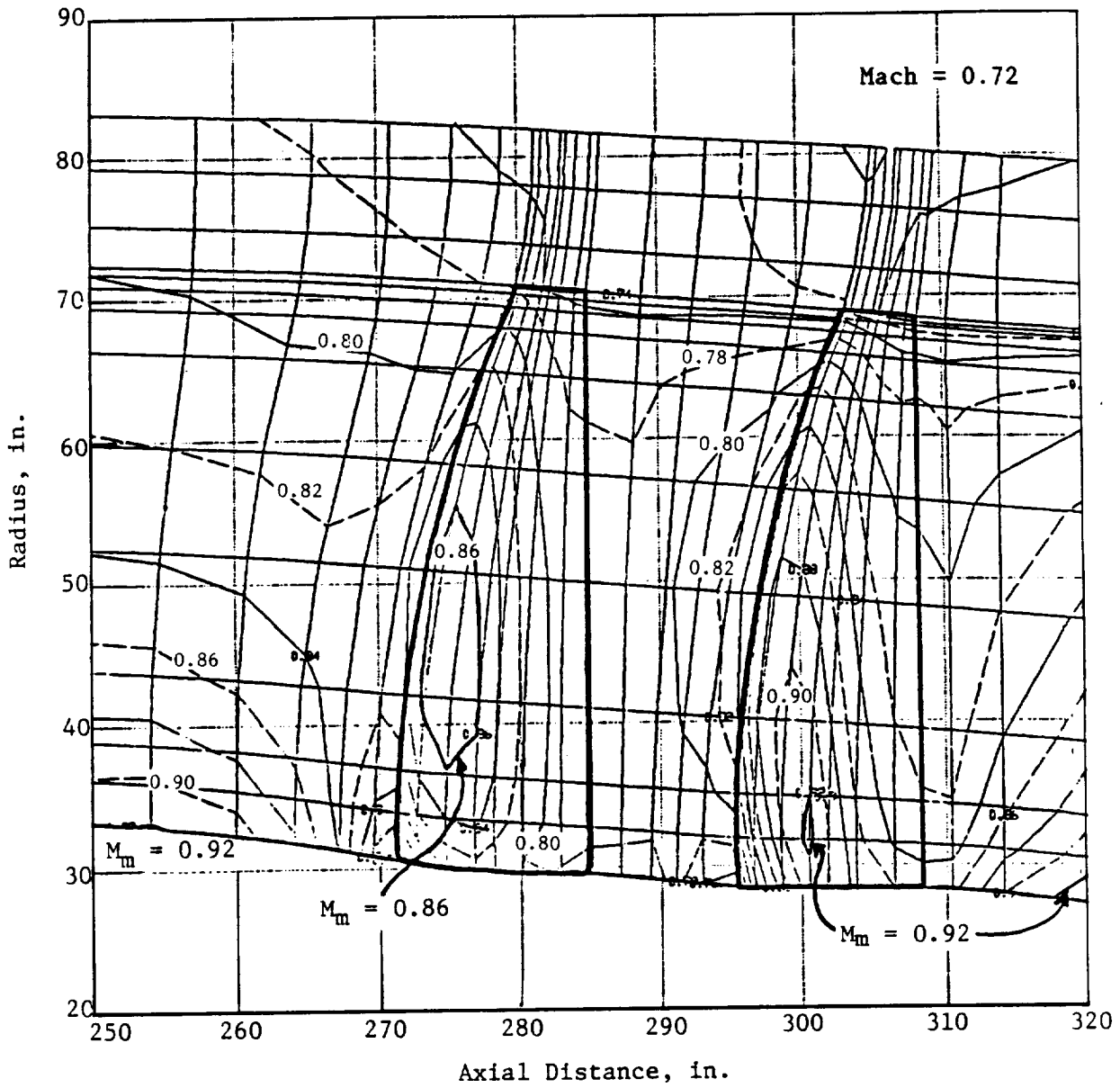


Figure 25. F-5/A-5 (8+8) Meridional Mach Number Contours.

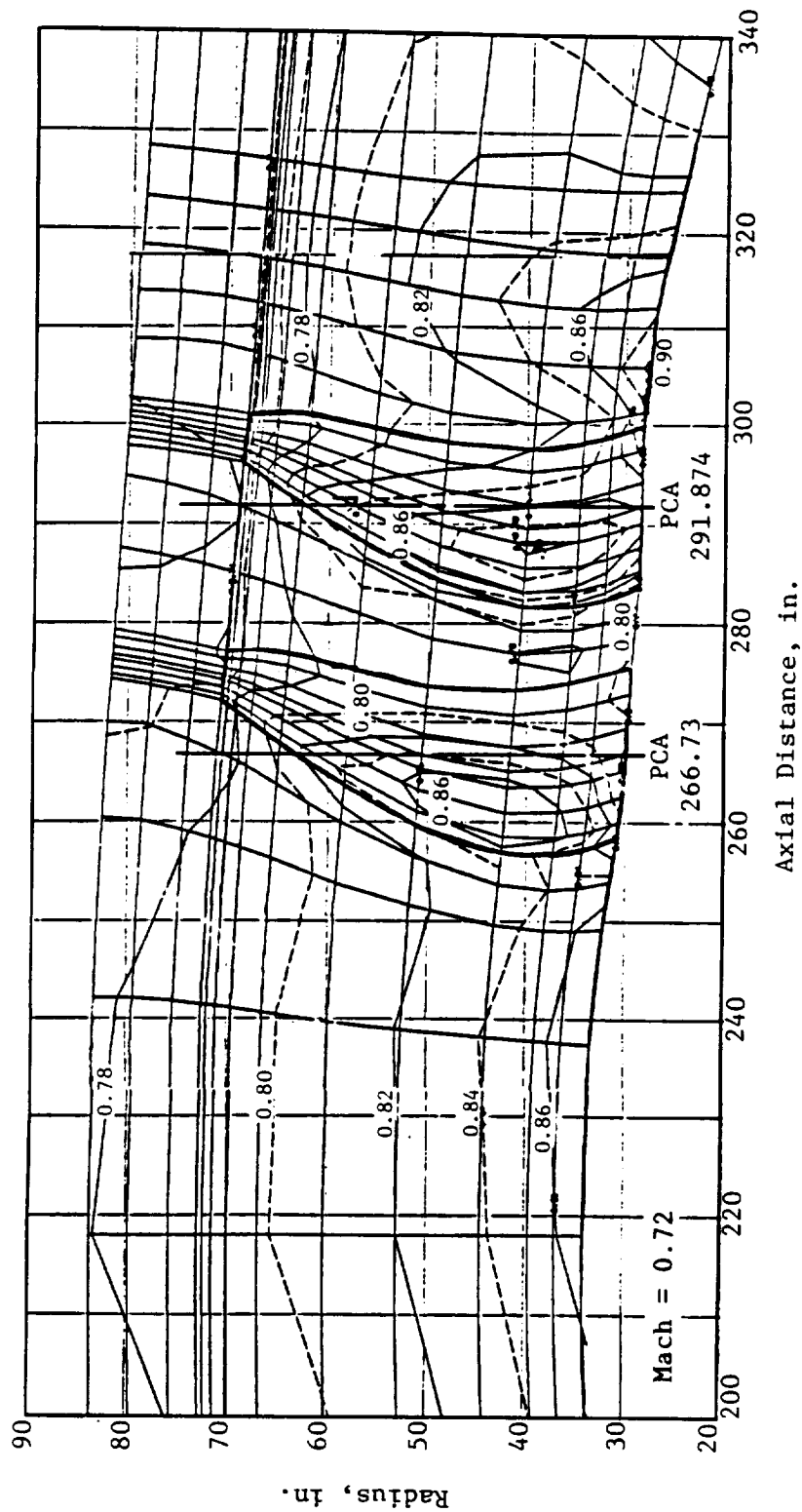


Figure 26. F-7/A-7 (8+8) Meridional Mach Number Contours.

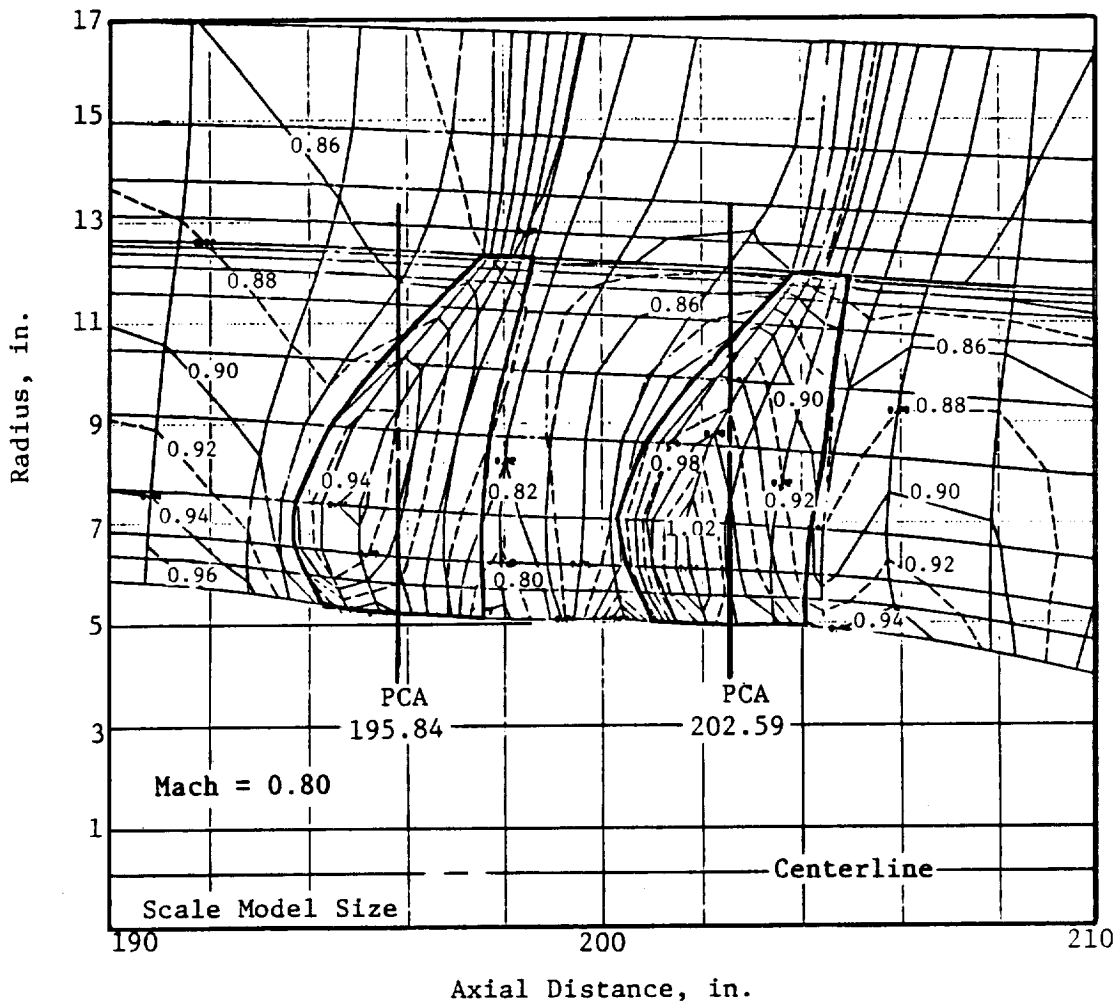


Figure 27. Meridional Mach Number Contours for F-11/A-11 (11+9).

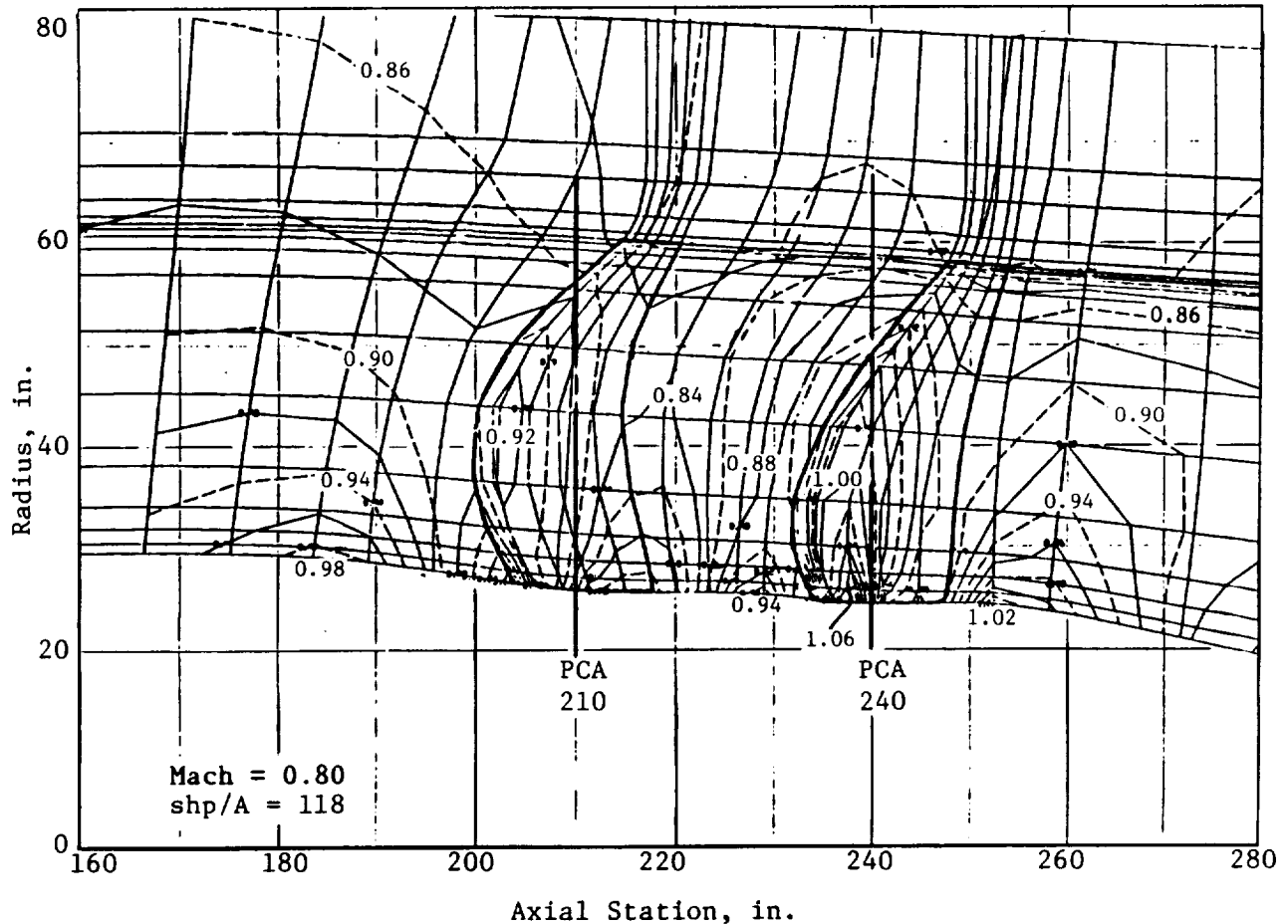


Figure 28. Meridional Mach Number Contours for F-21/A-21 (11+10).

3.3.4 Blade Planform Selection and Euler 3D Analysis

The blade planform shapes were defined early in the design phase to allow time for the detailed aerodynamic cascade flow and aeromechanical stability analyses. The planform was shaped by stacking custom-tailored airfoil sections along the swept and leaned blade axis. The airfoil mean-line shapes were then finely tuned at all streamlines with several iterations, using GE's three-dimensional Euler code (Reference 10), commonly referred to as Euler 3D.

The airfoil shapes for each blade configuration were selected using the standard blade generator code, making allowances for the sweep-end effects and secondary flow vorticity as described by Smith in Reference 3. Single-rotor methods test cases of the axisymmetric flow field were set up in order to process the 3D calculation obtained with the GE Euler code.

At the time these blade configurations were being designed, Euler 3D was in the early development stage and was only capable of performing calculations for single-rotor cases. Since then, the code has been modified to handle two-rotor cases, where one of the blade rows is represented by flow-field source terms while the calculation is performed on the other. Euler 3D calculation results for the forward rotors (F-4, F-11, and F-21) are presented in Figures 29 through 31. Aft-rotor methods test cases were run for the A-11 and A-21 blades and are shown in Figures

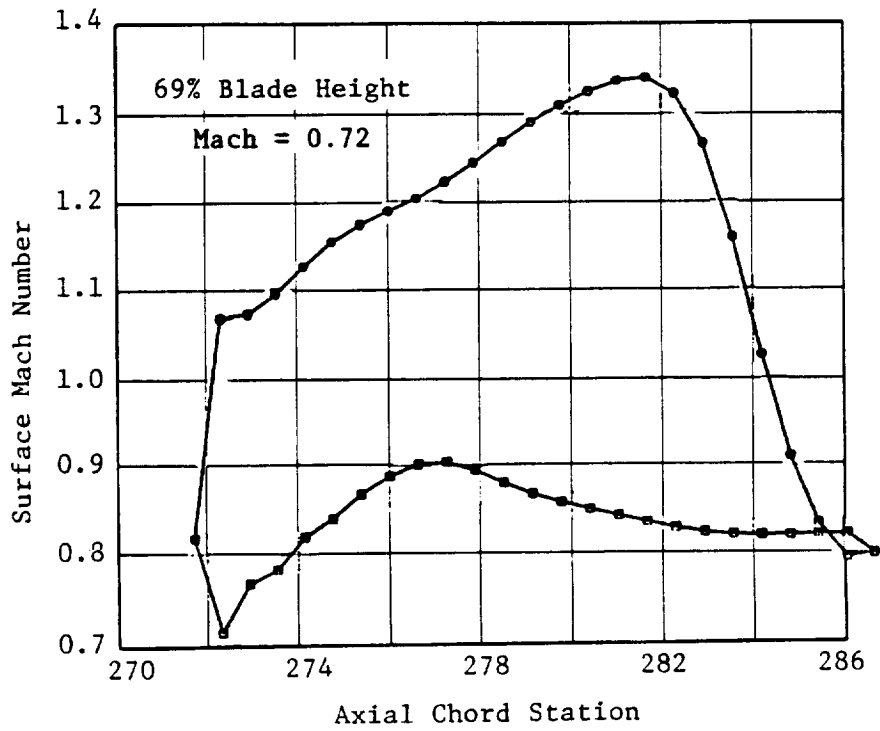
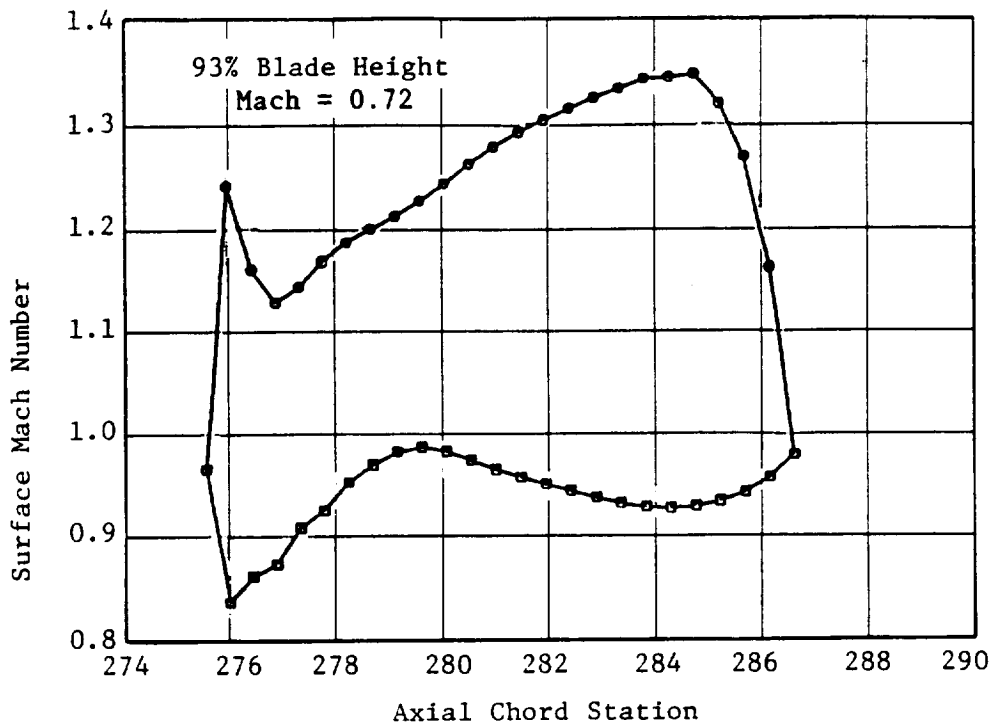


Figure 29. F-4 Euler Results.

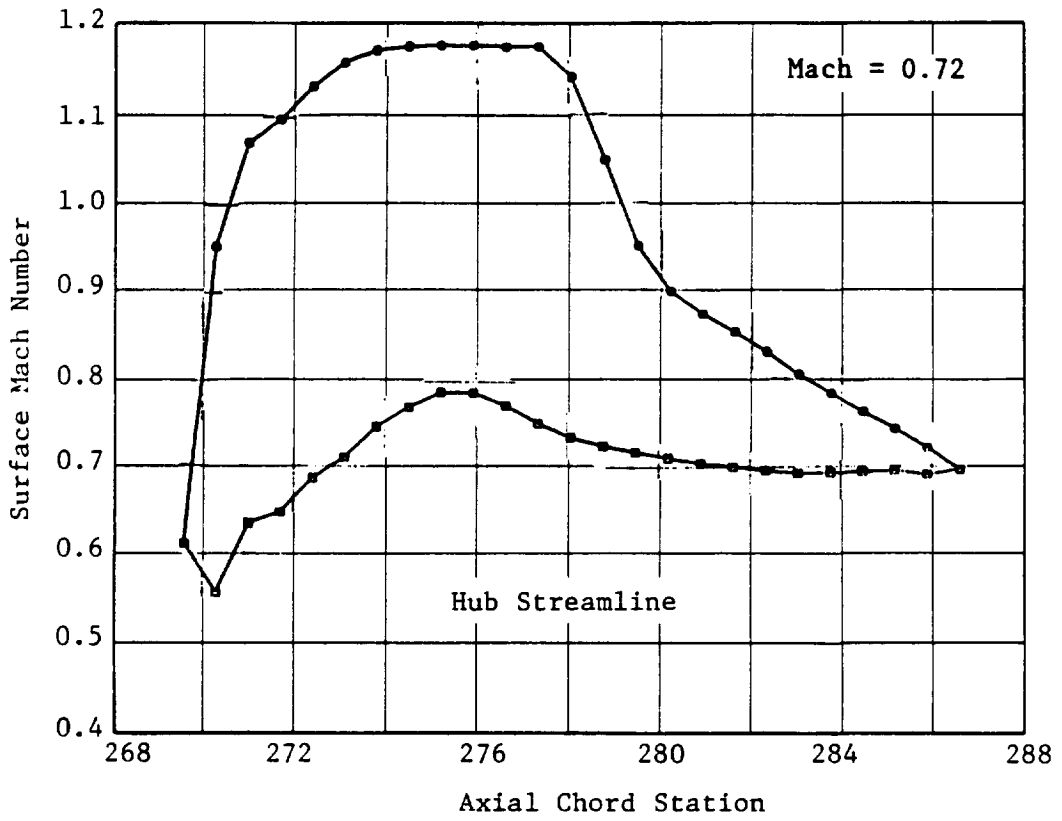


Figure 29. F-4 Euler Results (Concluded).

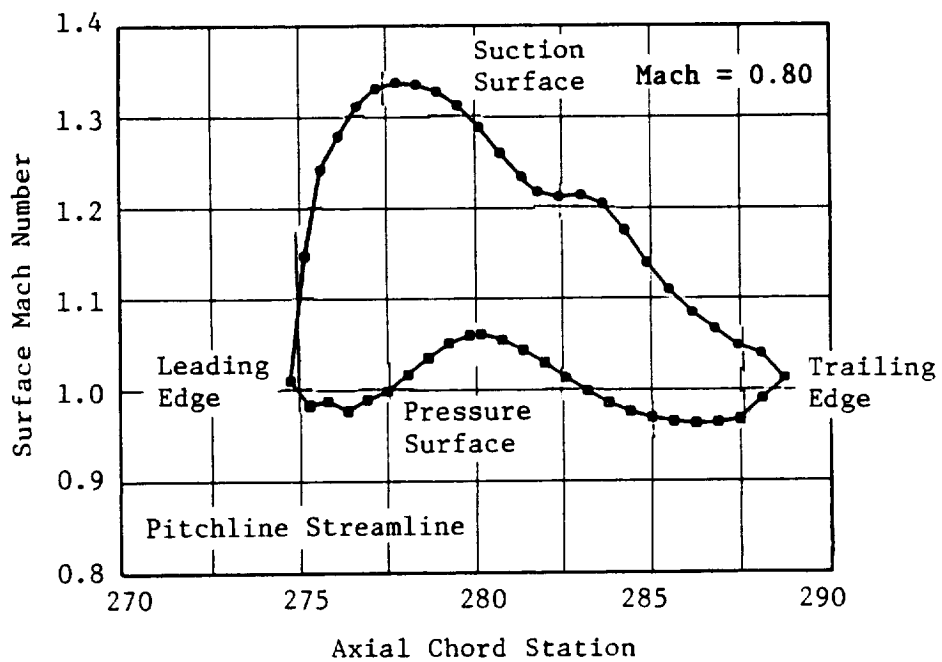
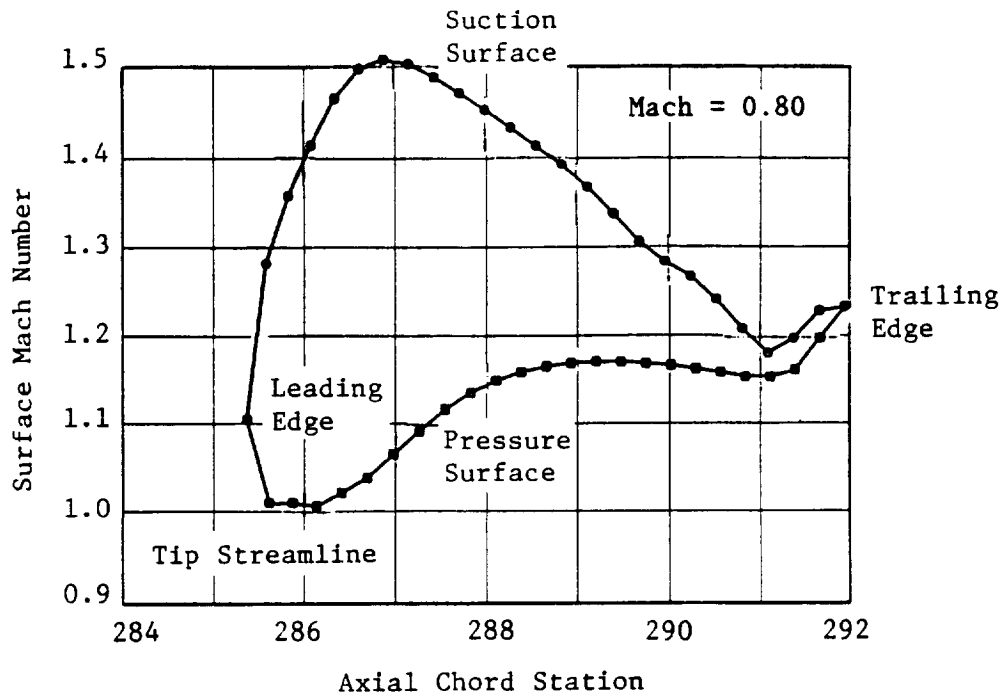


Figure 30. F-11 Euler Results.

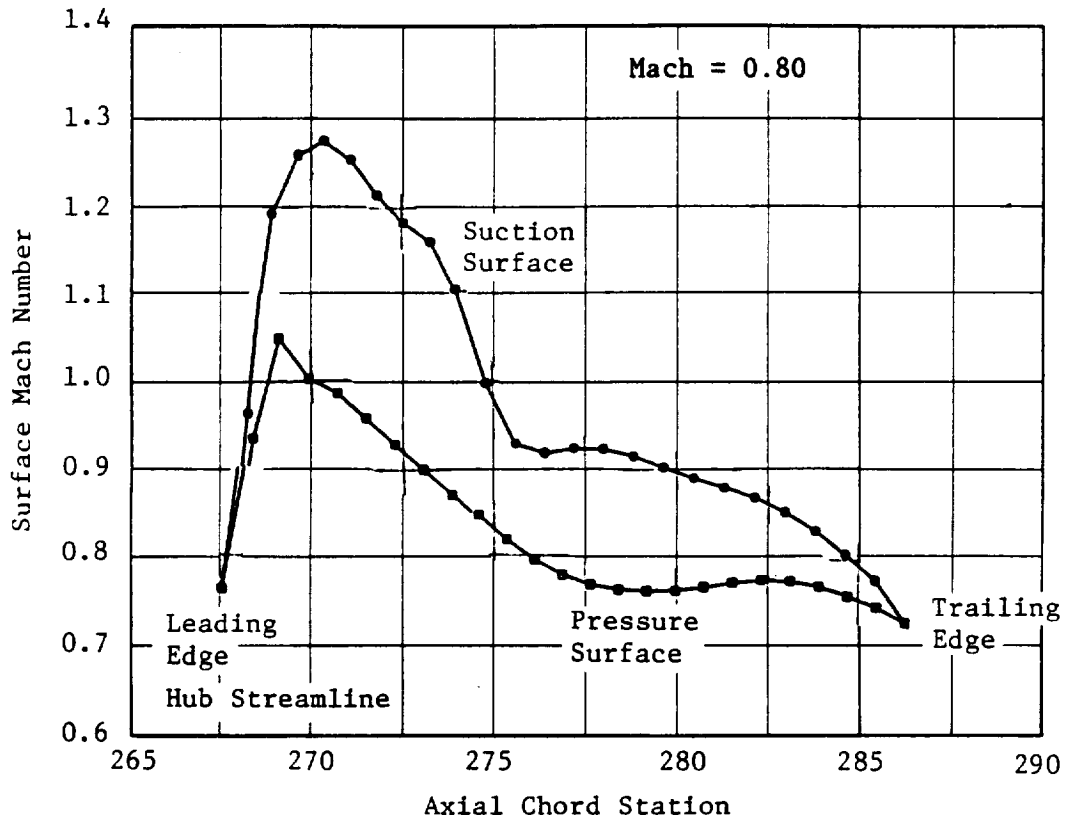


Figure 30. F-11 Euler Results (Concluded).

32 and 33. Surface Mach number distributions for representative streamline sections also are portrayed. Several iterations on blade mean-line shapes were performed in order to obtain the best possible surface Mach number distributions.

The early F-4 design indicated a strong trailing edge shock near the tip; this was reduced significantly in the shaping of the later F-11 blade design. Even though the freestream Mach number was higher, the F-11 surface Mach number distributions were generally more favorable because of the larger chord and tip sweep. The F-21 blades also had more favorable surface Mach number distributions, but the additional loading and increased blade hub thickness adversely affected the A-21 distributions (Figure 33).

3.4 Aeroacoustic Design and Design Evaluation

3.4.1 The Acoustic Model

Noise from counterrotating blade rows can be considered as a result of:

- Steady-loading and thickness noise of the forward rotor
- Steady-loading and thickness noise of the aft rotor
- Unsteady-loading noise resulting from the aft rotor interaction with the wakes shed from the forward blades
- Unsteady-loading noise as a result of the interaction of the aft rotor with vortices shed from the forward blade tips.

In addition to these, the installation environment also will affect the noise perceived, and broadband noise cannot be ignored. The tool used to evaluate candidate counterrotating blade designs from an acoustic standpoint is built upon experience gained by GE both in the analysis of single-rotation propeller noise and in the modeling of compressor rotor wakes. References 11 and 12 provide a detailed description of this work. Extension of the single-rotation model to counterrotation was conducted in two parts; the inclusion of tip-vortex effects was performed under this contract, but the major portion of work was done "in-house," under an IR&D (independent research and development) project. The tip-vortex model is described in detail in Reference 13.

3.4.1.1 Steady Loading and Thickness

The steady-loading and thickness model used for both rotors resembles the formulation of Hanson (Reference 14) and is described in detail in Reference 11. The model employs a source description that is noncompact in both the chordwise and the spanwise directions. The input required for each blade row includes blade geometry, flight Mach number, and details of the blade aerodynamic loads. The BPF harmonic noise for each rotor is calculated separately, and the axial separation between rotors is taken into account when computing the observed sound.

3.4.1.2 Rotor-to-Rotor Interaction Noise

Two models are employed in the prediction of unsteady-loading noise as a result of aft-rotor blades passing through flow disturbances generated by the forward rotor. The tip-vortex noise model (which calculates noise resulting from the interaction of the second rotor with vortices shed from the tips of the forward-rotor blades) was developed under this contract and is described in detail in Reference 13. The rotor-wake noise model (which calculates noise resulting from interaction of the second rotor with viscous wakes shed from the forward rotor) was developed under

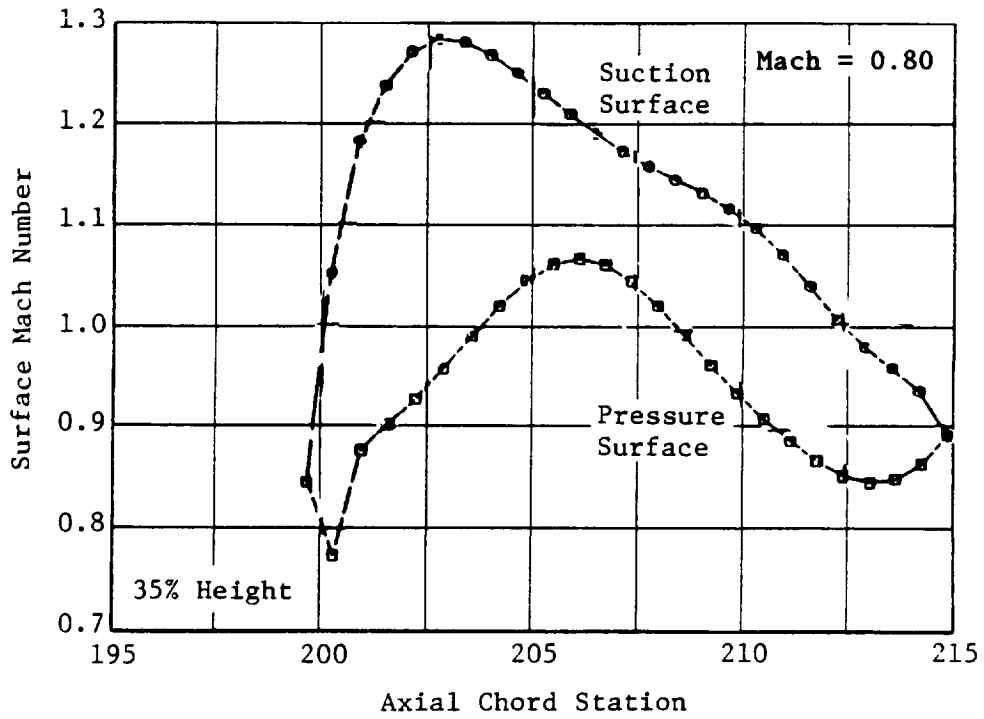
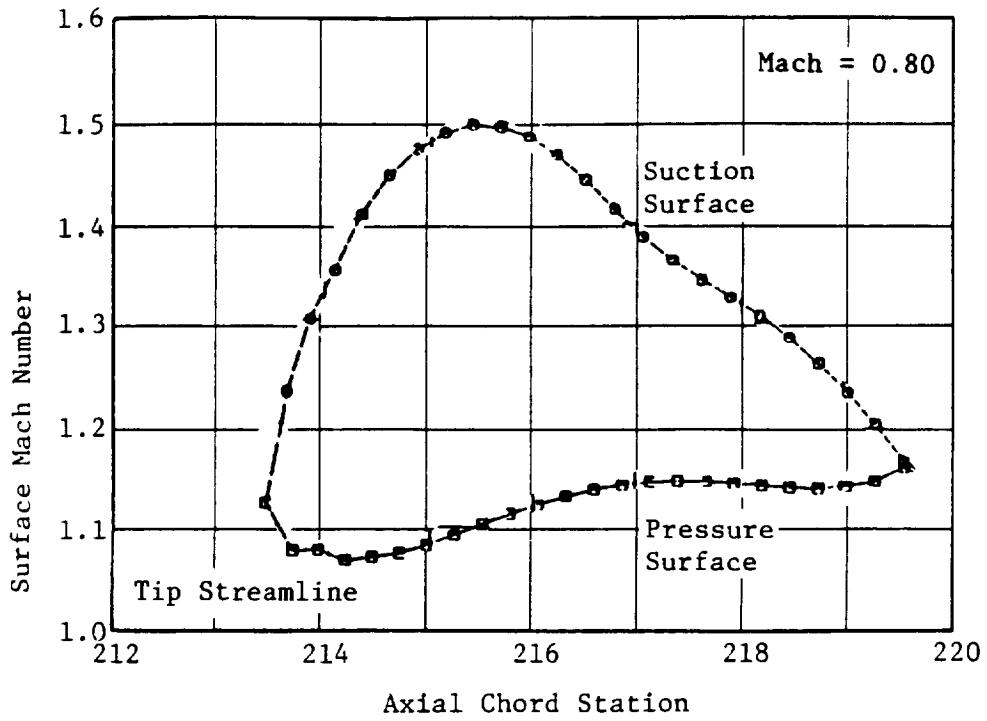


Figure 31. F-21 Euler Results.

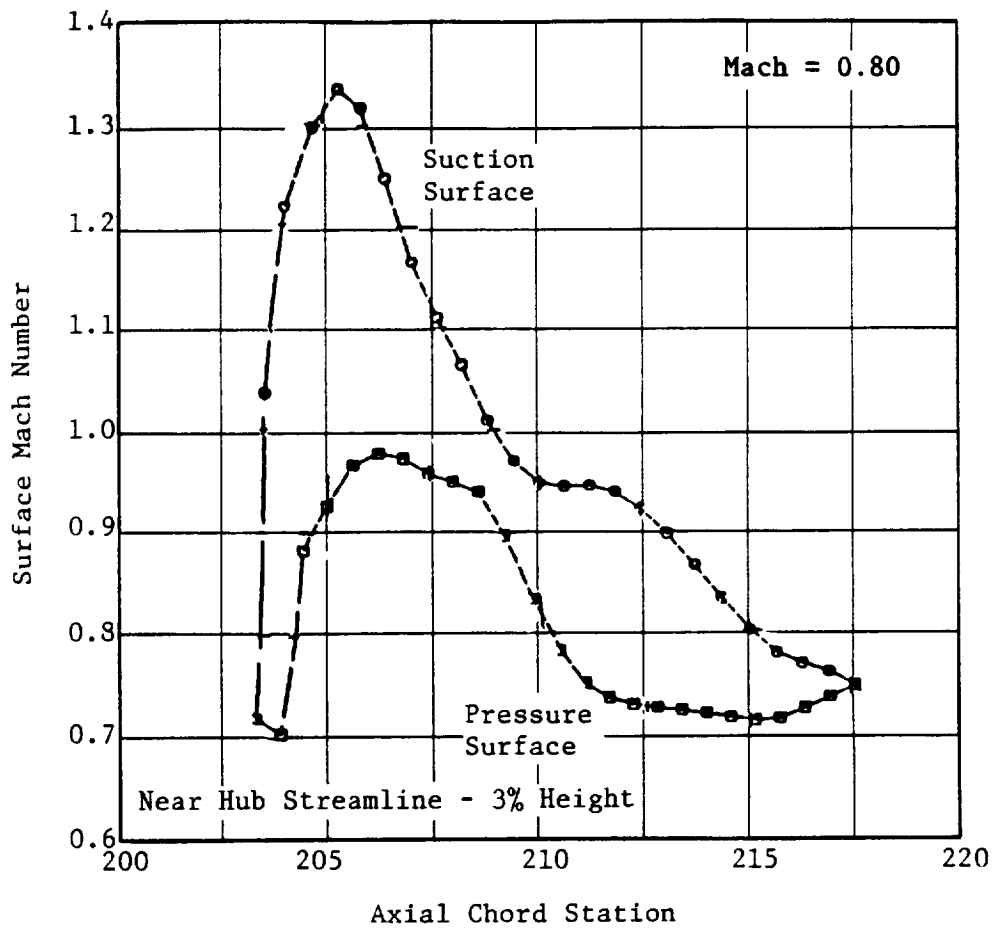


Figure 31. F-21 Euler Results (Concluded).

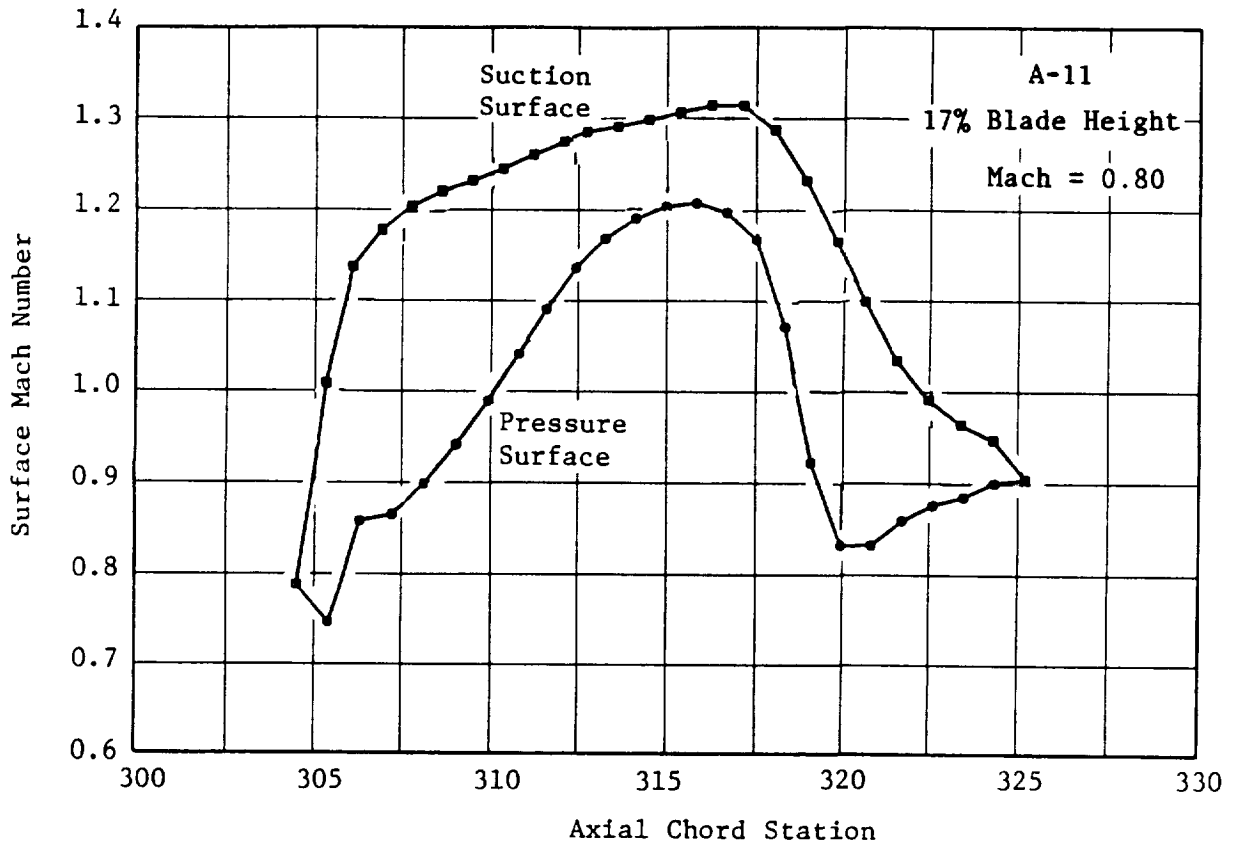


Figure 32. A-11 Euler Results.

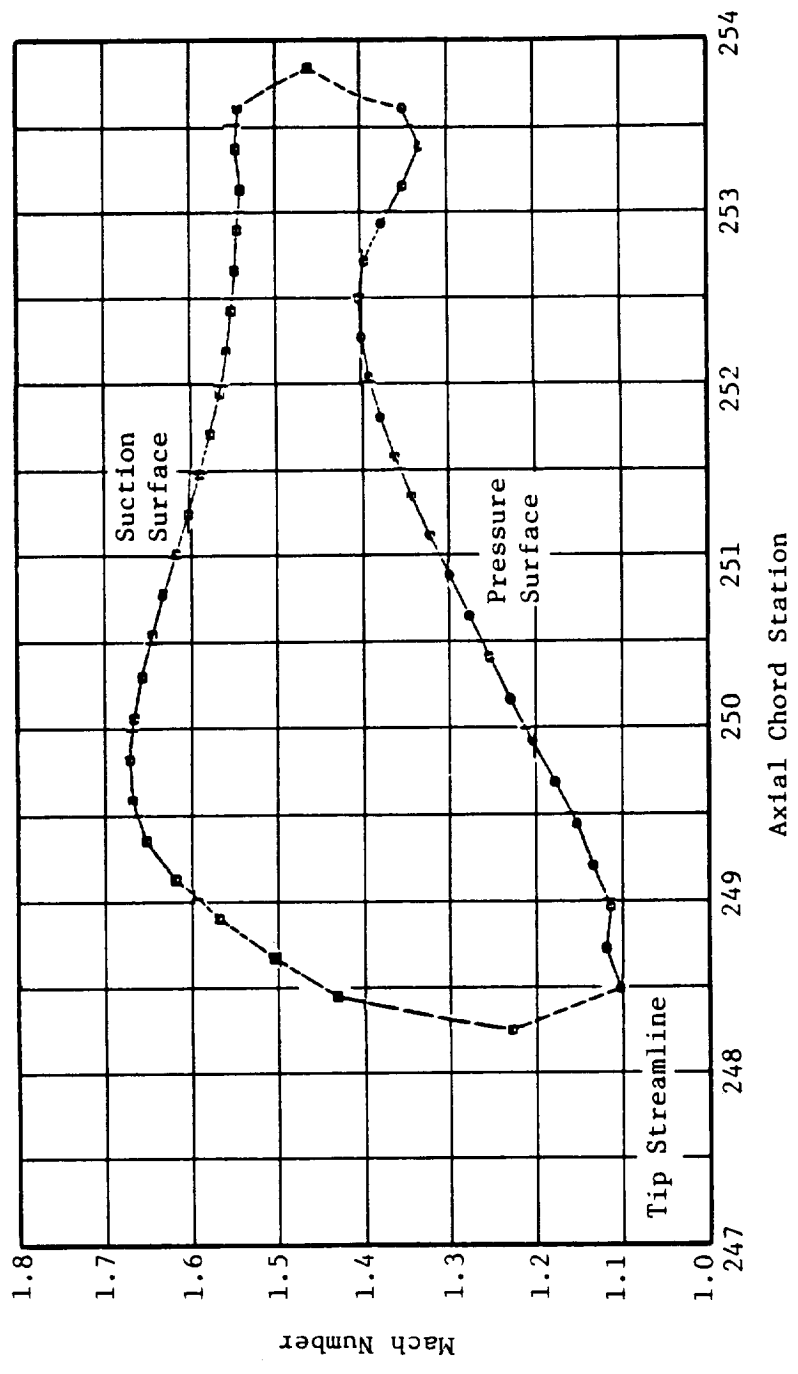


Figure 33. A-21 Euler Results at Mach = 0.80.

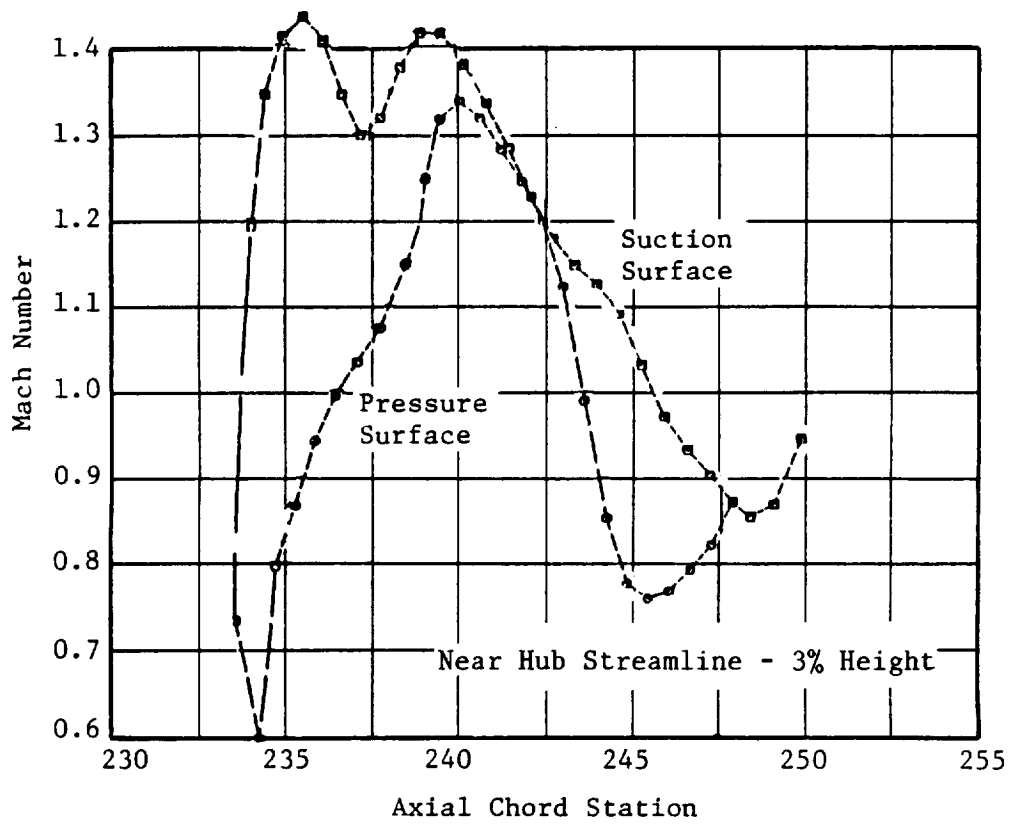
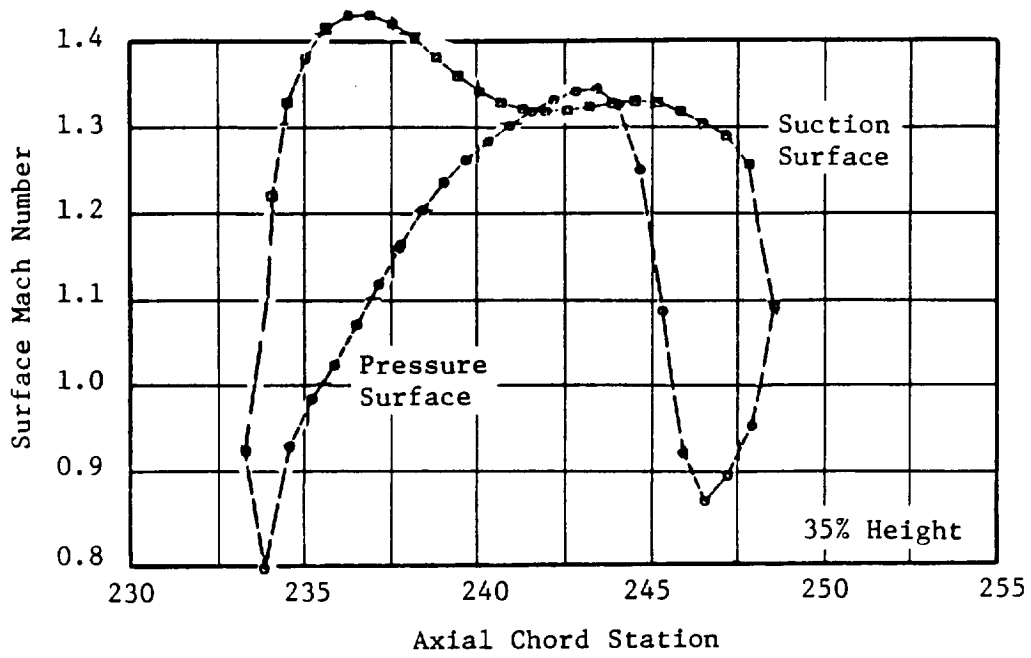


Figure 33. A-21 Euler Results at Mach = 0.80 (Concluded).

an in-house IR&D technology program, building on previous GE experience in the modeling of compressor rotor wakes. In both of these models, the blades are assumed to be acoustically noncompact in the spanwise direction only. The blade geometry (in terms of sweep, lean, blade chord, blade-pitch angle, and pitch-change-axis spacing) is taken into account in the modeling.

3.4.1.3 Near-Field Cabin Noise Considerations

A semiempirical near-field model, developed for single-rotation propfans and described in detail in Reference 11, is included in the noise model. Additional factors involved in the calculation of cabin noise include: noise generated by the airplane-fuselage boundary layer; cabin-wall reflection and refraction effects, and transmission losses through the cabin wall. These factors are included in the model in the following manner:

- **Fuselage Boundary Layer Noise**
 - The noise spectrum is calculated as a function of boundary layer thickness (Reference 15). One-third-octave levels obtained thusly are added to the previously calculated one-third-octave tone spectrum levels (including effects of cabin-wall reflection and refraction) to determine the resultant level on the cabin wall.
- **Reflection and Refraction**
 - These effects rely on user input; possibly as a result of exercising a model such as that described in Reference 11. A default value of +6 dB, which corresponds to in-phase reflection, is present in the program.
- **Transmission Losses**
 - Data on cabin-wall insulating materials tend to be viewed as proprietary by aircraft manufacturers. The information used in the model is taken from Reference 16 and, again, can be overwritten by the user.

3.4.1.4 Data/Theory Comparisons

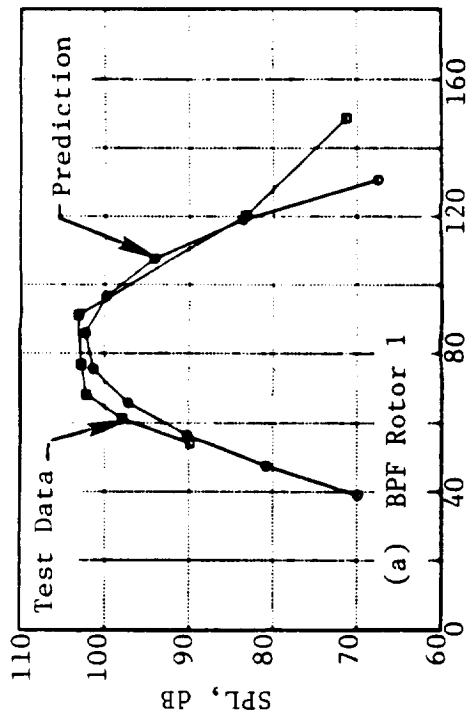
Figures 34 through 36 show tone comparisons between data and theoretical predictions for both low speed, flight Mach No. 0.25, and high speed, flight Mach 0.72, conditions. In both instances, the blades under consideration are those designated as F-7 (forward rotor) and A-7 (aft rotor). Low speed data are taken from an 11-forward plus 9-aft (11+9) blade configuration tested in the GE Cell 41 anechoic facility. High speed data are taken from an 8-forward plus 8-aft (8+8) blade configuration tested in the 8x6 wind tunnel at the NASA Lewis Research Center, and in the BTWT (Boeing Transonic Wind Tunnel). The degree of agreement between measurement and prediction for both low- and high-speed cases is considered sufficient to justify the use of this model in the evaluation of candidate blade designs.

3.4.2 Aeroacoustic Evaluation of Candidate MPS Blade Designs

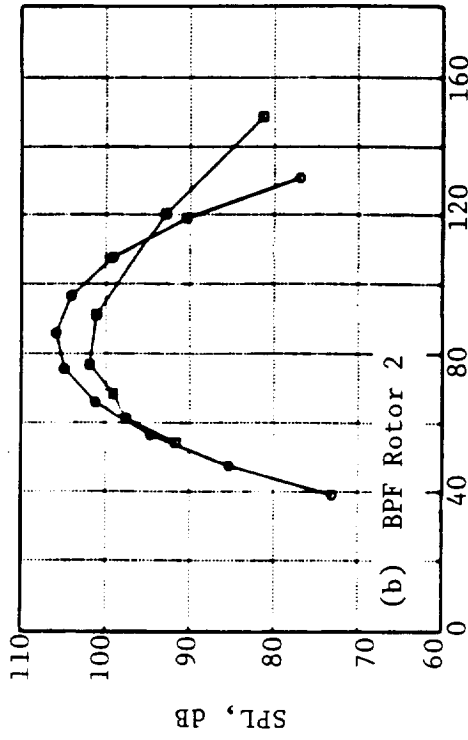
3.4.2.1 Basis of Comparison

The candidate blade design parameters used in this study are tabulated in Table 6, and planform shapes are presented in Figure 37. They fall into two main categories; those designed to operate at a flight Mach No. of 0.72, and those designed to cruise at a higher speed, namely Mach 0.8.

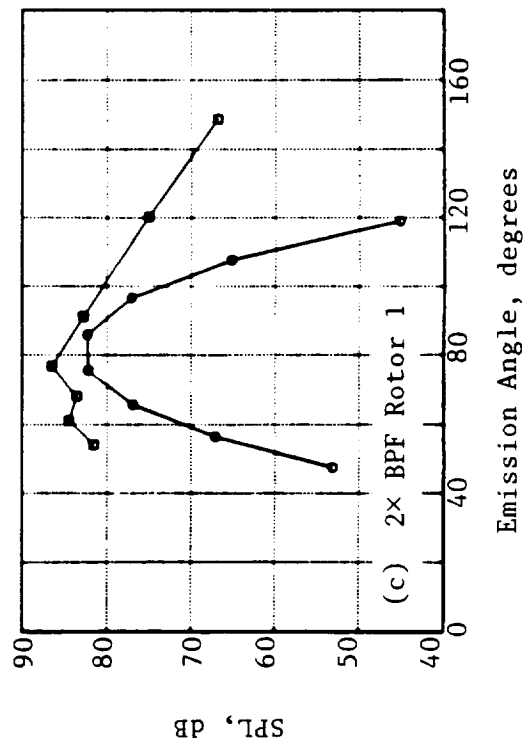
Because these blades were designed for different missions, in Table 6 two options are given for disk loading (in terms of thrust per unit annulus area); and two different blade diameters are used.



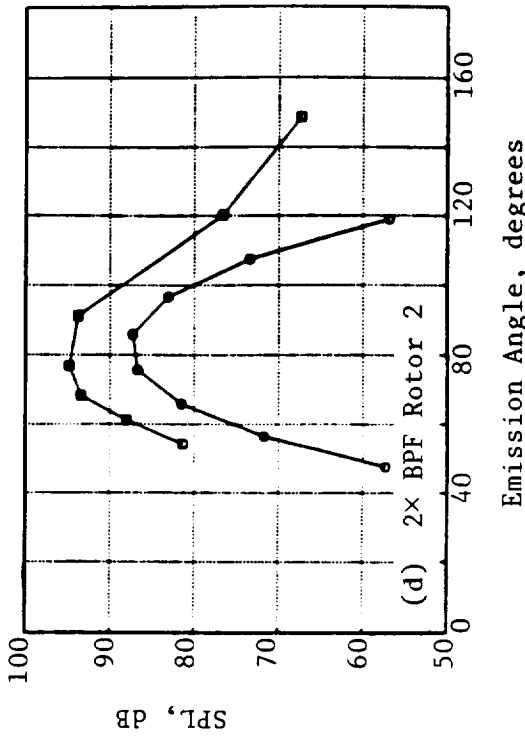
(a) BPF Rotor 1



(b) BPF Rotor 2

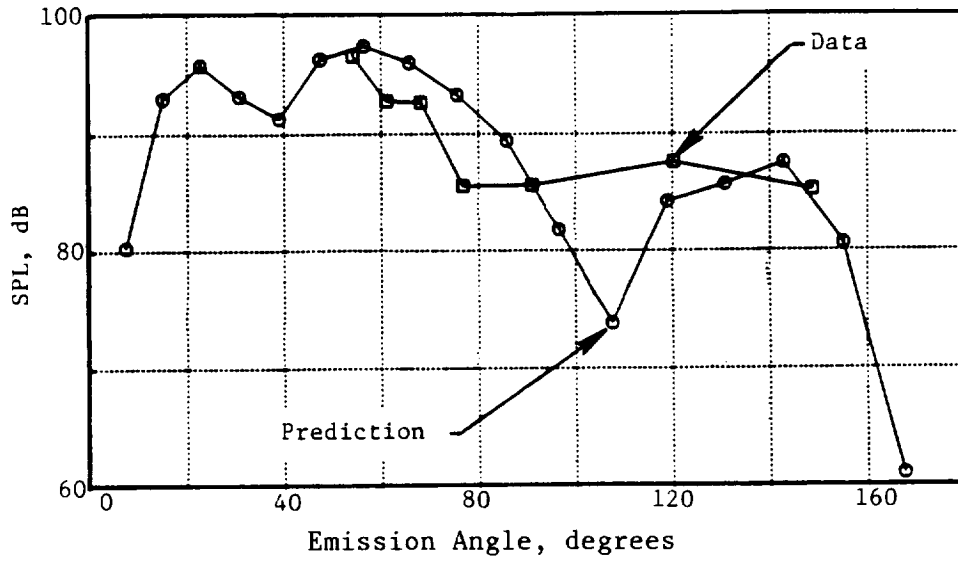


Emission Angle, degrees

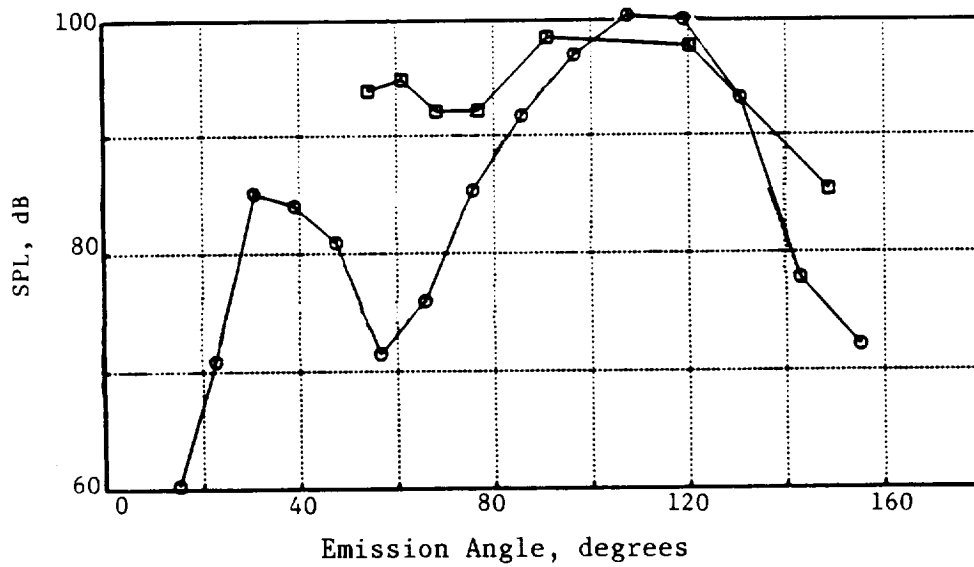


Emission Angle, degrees

Figure 34. Low Speed Data/Theory Acoustic Comparison of Steady-Loading Tones.



(a) F1/A1



(b) F1/A1

Figure 35. Low Speed Data/Theory Acoustic Comparison of Interaction Tones.

Configuration/Conditions

- F-7/A-7 (8+8)
- Mach No. 0.72
- BTWT
- NASA (8x6)
- Run 2049

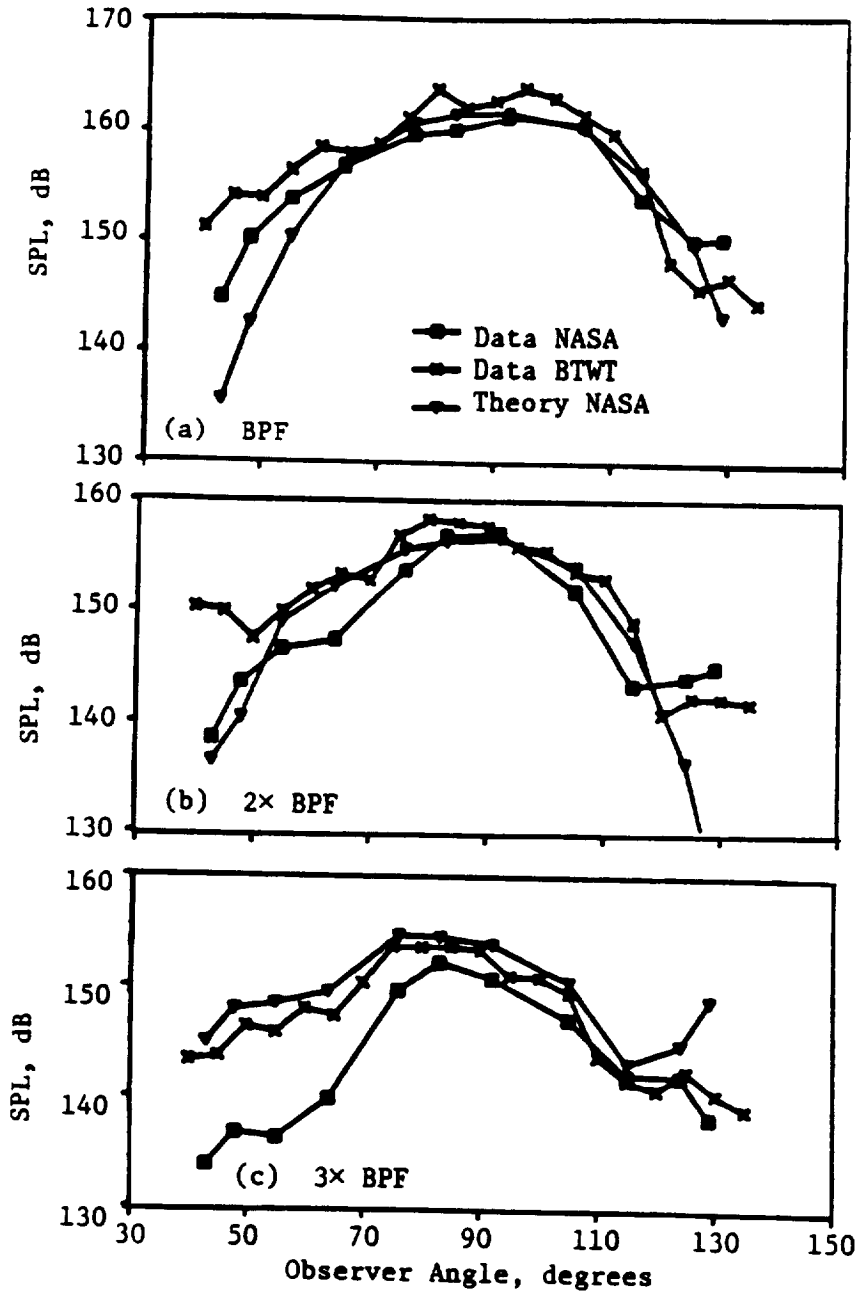
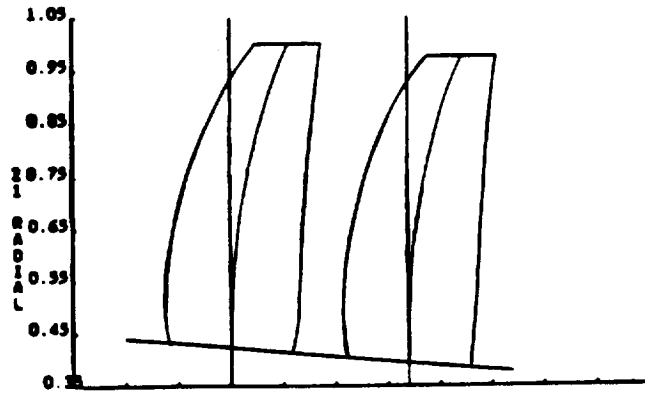
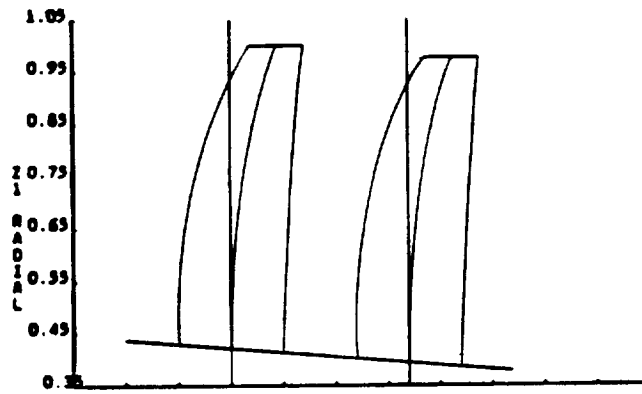


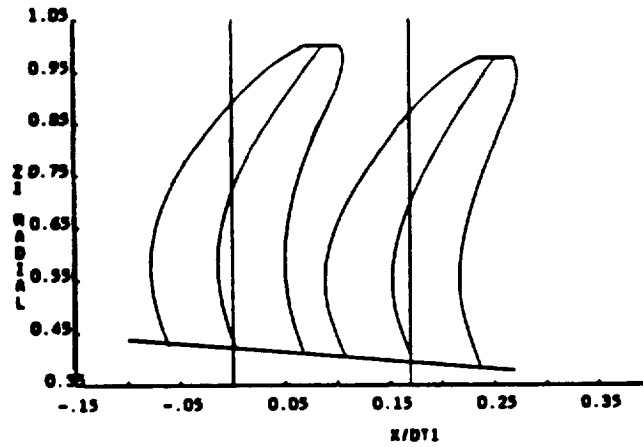
Figure 36. High Speed Data/Theory Comparison.



(a) F-4/A-4

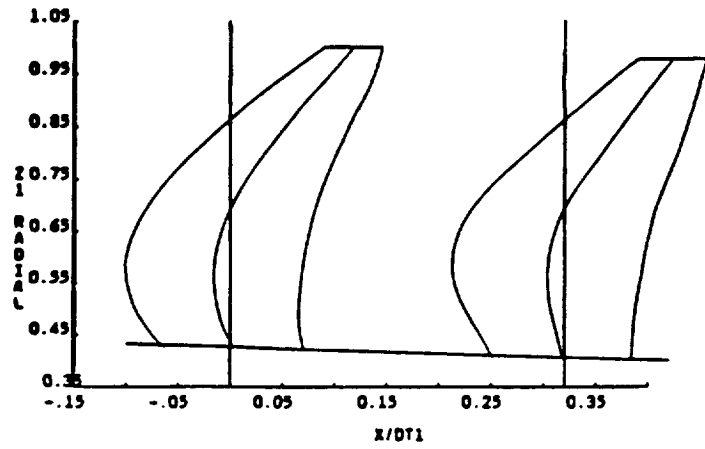


(b) F-5/A-5

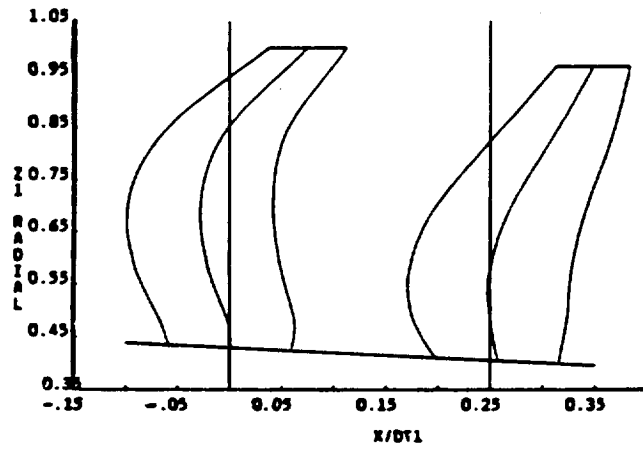


(c) F-7/A-7

Figure 37. MPS Blade Planforms Used in Blade Acoustic Evaluation Study.



(d) F-11/A-11



(e) F-21/A-21

Figure 37. MPS Blade Planforms Used in Blade Acoustic Evaluation Study (Concluded).

Table 6. MPS Blade Design Parameters.

Configuration	F-4/A-4	F-5/A-5	F-7/A-7	F-11/A-11	F-21/A-21
Design M_o	0.72	0.72	0.72	0.8	0.8
Number of Blades	8+8	8+8	8+8	11+9	11+10
Tip Sweep, degrees (1)	19	15	34	37	45
Tip Sweep, degrees (2)	21	18	31	34	25
Activity Factor (1)	150	120	147	180	173
Activity Factor (2)	157	126	152	200	121
PCA $\Delta z/D_{tl}$	0.17	0.17	0.17	0.32	0.25
Annular Loading, ($F_n/\Delta A_{ann}$)	Demo	Demo	Demo	Demo	Product
D_{tl} Used (m)	3.4	3.4	3.4	3.4	3.05

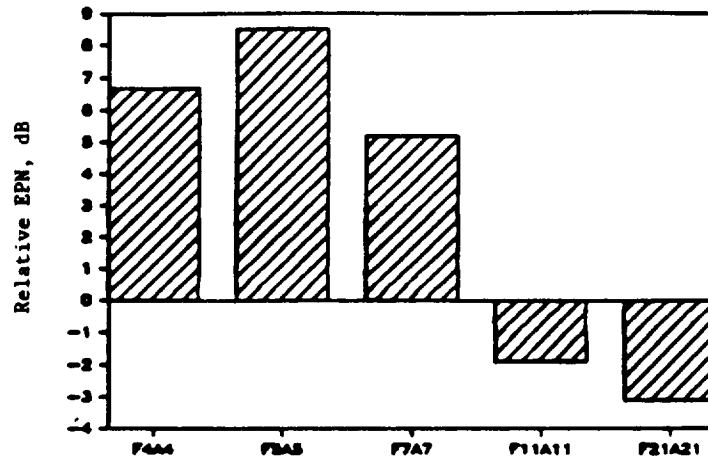
It was felt that the only valid comparison for evaluation purposes was to predict the noise from each set of blades, since they generated the same thrust, but to adjust the diameter of the rotors to maintain the differences in design blade loading. The operating conditions at which the MPS blades were evaluated are listed in Table 7.

3.4.2.2 Results of Comparison

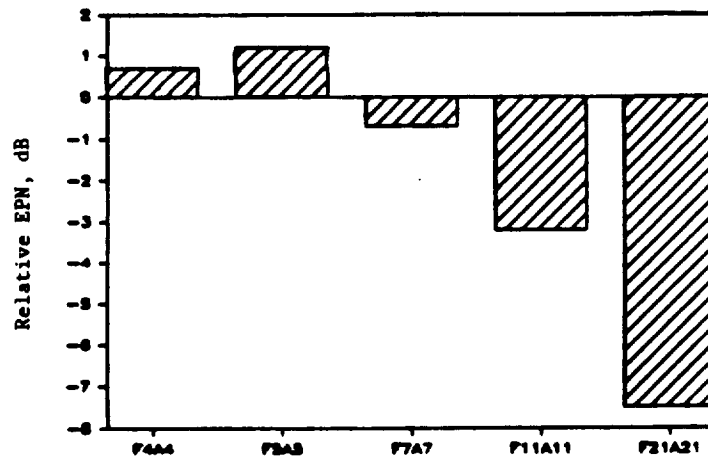
Figure 38 provides a "bottom line" comparison of the five blade designs. Further details are presented in the Task II report.

Table 7. MPS Blade Acoustic Evaluation Conditions.

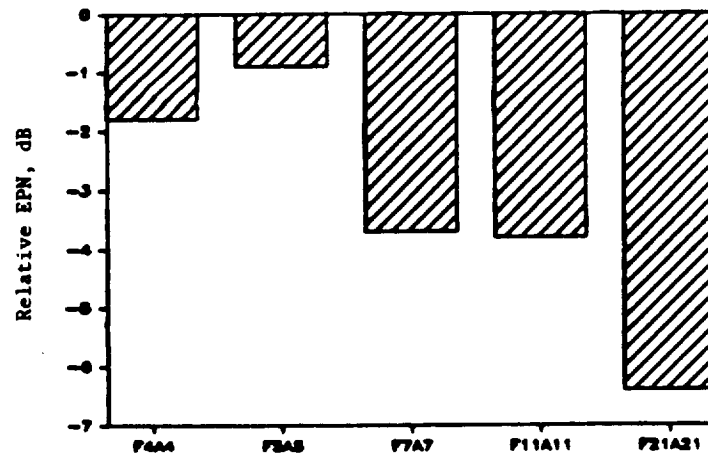
Condition	R1 Tip			
	Thrust (N)	Speed (m/s)	Range (m)	M_o
Sideline	73,392	253	512	0.25
Cutback	43,146	229	732	0.25
Approach	15,234	183	122	0.22
Cruise	19,611	238	2	*
* 0.72 or 0.80 Depending on the Blade Design Point				



(a) Sideline EPNL

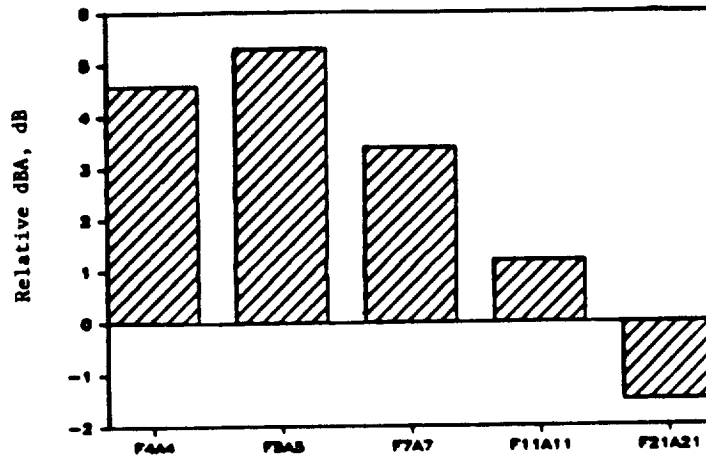


(b) Cutback EPNL

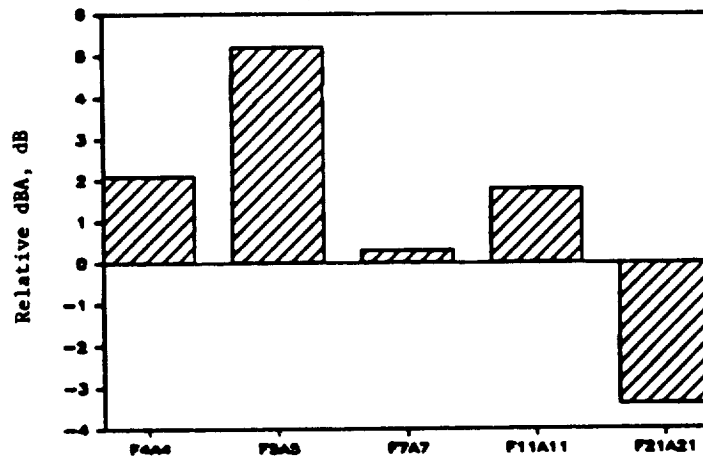


(c) Approach EPNL

Figure 38. MPS Blade Acoustic Evaluation Summary.

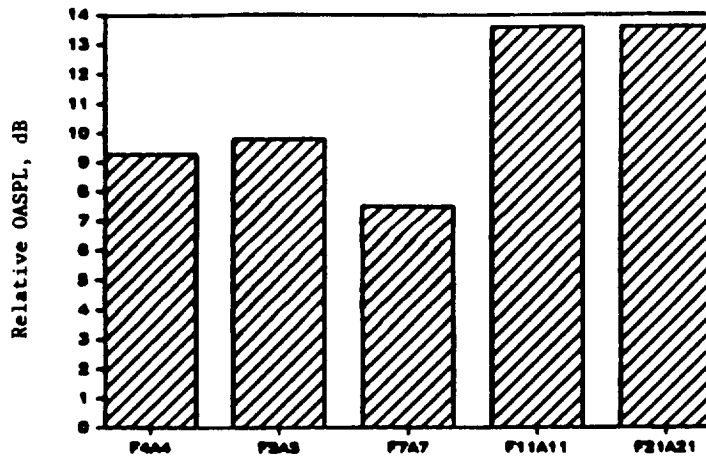


(d) Cutback dBA Max

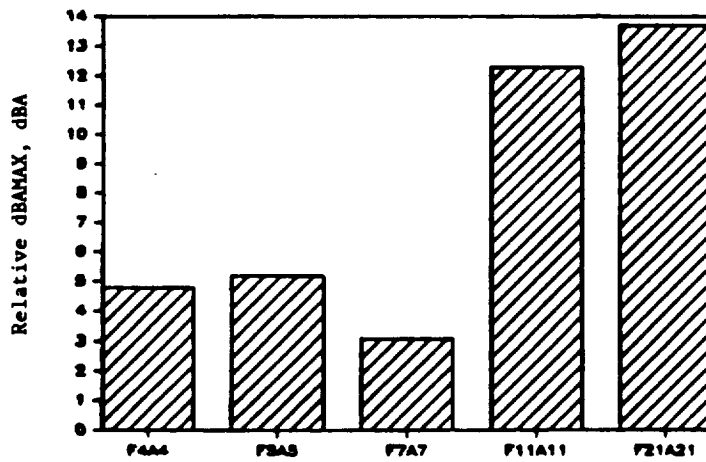


(e) Approach dBA Max

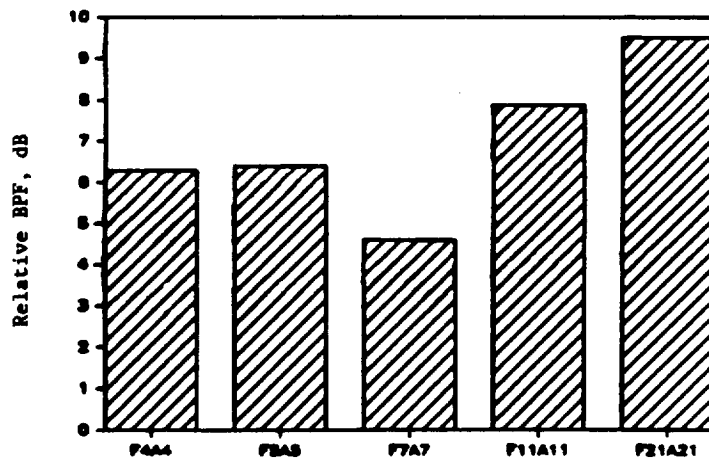
Figure 38. MPS Blade Acoustic Evaluation Summary (Continued).



(f) Cruise OASPL



(g) Cruise dBA Max



(h) Cruise BPF Max

Figure 38. MPS Blade Acoustic Evaluation Summary (Concluded).

For the low speed designs, the levels calculated for the F-5/A-5 blading are consistently higher than those for the F-4/A-4 and F-7/A-7. Table 6 and Figure 37 show that these blades have both lower sweep and reduced blade chord (leading to increased blade loading) relative to the other two designs. These factors adversely affect the noise. On the other hand, F-4/A-4 blades have similar chords to the F-7/A-7 but, again, reduced sweep. In all cases, their noise is predicted to be higher than that of the F-7/A-7.

The high speed designs, F-11/A-11, indicate that benefits of increases in blade number, spacing, and blade area (as shown by the large activity factors for F-11/A-11) are manifest under the community noise conditions of sideline, cutback, and approach. The cruise case reflects the result of the increase in flight speed (and, hence, helical tip Mach number), together with the effect of the increase in blade number. The predicted increase in noise under these conditions is due, in part, to the increase in thickness (volume displacement) noise resulting from those very changes in chord and blade number that were of benefit under community conditions. Conclusions to be drawn from this study are that:

- Of the $M_0 = 0.72$ designs, the F-7/A-7 – with its higher sweep and “nominal” chord – is predicted to be quieter than both the F-4/A-4 and F-5/A-5 designs.
- The $M_0 = 0.80$ designs are predicted to be quieter under community noise conditions, owing to the increases in blade number, blade row spacing, and blade area. However, when combined with the higher cruise Mach number, these increases lead to higher noise levels under high speed conditions.

3.4.3 Tip-Vortex-Interaction Investigation for Counterrotating Propellers

The acoustic signature of a counterrotating propeller is rich in tonal content which can be ascribed to various noise-generating mechanisms at work. The analytical modeling of these mechanisms will provide a better physical understanding which, in turn, will assist in evolving a methodology for low noise designs. Principal noise mechanisms associated with the tonal spectrum of the counterrotating propeller are:

- Steady-loading and thickness noise of each rotor
- Unsteady-loading noise generated by the aft rotor as a result of interaction with the wake shed by the forward rotor
- Unsteady-loading noise generated by the aft rotor due to an interaction with the tip vortex of the forward rotor
- Unsteady-loading noise generated by either rotor due to the presence of a rotating potential field of the other rotor.

This section documents the work accomplished on analytically modeling the unsteady-loading noise due to tip-vortex interaction. The physical process involved in the generation of the tip vortex of these propulsors is similar to that of fixed wings; that is, a static pressure differential between the pressure and suction sides of the airfoil in the tip region of the wing results in a flow from the pressure to the suction side which, ultimately, rolls up into a tip vortex. This process can be explained using finite-wing theory; that is, the effect of a reduction in the span of a wing from infinity to a finite length may be viewed as the effect of a removal of tip vortices extending indefinitely in the direction of the span and a replacement of these vortices by trailing vortices connected at their downstream ends by starting vortices (Reference 17).

Analytical modeling of the upwash field (gust) created by the tip vortex of the forward propulsor at the aft propulsor LE (or 1/4 chord) is based on an approach previously taken for fan-tone noise (Reference 12). This approach consists of modeling the tip vortex as a free vortex (that is, $\Gamma = \text{constant}$, $V_\theta \propto 1/r$) with a forced vortex core (within the core, $V_\theta \propto r$); the strength, size, and streamwise development of which are empirically modeled. The gust field of the tip vortex at the aft rotor determines the unsteady-lift response of the aft rotor blade and, hence, the additional unsteady-loading noise due to the tip vortex.

3.4.3.1 Counterrotating Blade Tip Vortex Model

This section briefly describes the aerodynamic model developed for predicting the gust field at the aft rotor due to the tip vortex of the forward rotor. This data is used to evaluate the fluctuating lift and the associated unsteady loading or interaction noise of the counterrotating propellers. The quasi-3D (quasi-three-dimensional) aerodynamic model of the forward rotor exit flow field employs a streamline-by-streamline approach (Reference 3 provides a detailed description). The velocity field induced by the tip vortex of the forward rotor at the aft rotor is computed first for a coordinate system rotating with the forward rotor. A coordinate transformation of this velocity field relative to the aft rotor is performed; this yields the upwash velocity perturbations from the freestream value for the aft rotor. The upwash velocity perturbations exhibit a periodicity coinciding with that of the forward rotor. Fourier analysis of the upwash waveform yields the upwash gust harmonics distribution. The twist of the forward rotor blade from hub to tip causes a time/phase lag between the flow field from the hub and tip regions impinging on the aft rotor blade. This spanwise distortion and clocking of the rotor wake/vortex "sheet" as it convects downstream results in a spanwise phase variation of the wake/vortex field. The analysis for predicting this phase lag due to the twist of the rotor blades was developed under a previous GE IR&D (Independent Research and Development) project and is described in Reference 3. The spanwise distribution of the gust harmonics, along with the above-described aerodynamic phase, gives a complete description of the gust field impinging on the aft rotor.

Computation of the fluctuating lift force on the aft rotor due to the upwash gust is performed next by using the classical (incompressible) unsteady lift response theory of Sears (Reference 18), modified to take compressibility effects into account according to a procedure developed by Amiet (Reference 19). The fluctuating lift force forms the right-hand side of the wave equation, whose formulation and method of solution are described briefly in Section 3.4.1 of this report.

The following paragraphs briefly describe the tip-vortex model development and the procedures followed in establishing certain empirical relationships associated with the tip-vortex model. Nomenclature for the equations presented in these paragraphs is defined in Table 8.

The tip vortex model has evolved from a similar model for computing secondary flow vortices (in and behind a ducted rotor blade passage) which are dominated by the tip clearance leakage flow (References 20 and 21). The tip vortex model assumes the existence of a core that contains all of the shed vorticity, so that the motion outside is irrotational. Figure 39a is a sketch of the radial variation of tangential velocity (V_θ) induced by the tip vortex and the associated circulation of the vortex. Obviously, even at large distances from the vortex center, sufficiently large swirl velocities exist, in terms of $V_\theta/(V_\theta)_{\text{max}}$. It should be noted that the current tip vortex model does not include an effect of an axial velocity component of the tip vortex; however, this will be included in future work, as detailed data become available.

Table 8. Nomenclature for Tip Vortex Model Equations.

a	Radius of the core of the tip vortex
AR	Aspect ratio (span/chord)
b_r	Radial distance of the center of the tip vortex from rotor tip
b_t	Tangential location of the center of the tip vortex in the interblade passage relative to wake centerline
B1	Number of blades in the forward rotor
B2	Number of blades in the aft rotor
c	Chord
c_a	Axial Chord
C_D	Local section drag coefficient
C_i	Circulation index (Equation 13.1)
C_L	Local section lift coefficient
dBA	A-weighted dB level
d_{tip}	Tip diameter
D_{T1}	Tip diameter of forward rotor
D_{T2}	Tip diameter of aft rotor
f_{s1q}	qth harmonic of steady loading and thickness noise of forward rotor (see Equation 26)
f_{s2q}	rth harmonic of steady loading and thickness noise of aft rotor (see Equation 27)
f_{wqr}	rth harmonic of aft rotor unsteady noise due to qth gust harmonic
HTR	Hub/tip ratio
K_{vtx}	Empirical constant for tip vortex trajectory (see Equation 25)
M_g	Aircraft Mach number
$mwqr$	Spinning mode number of rth harmonic of aft rotor unsteady noise due to qth gust harmonic of forward rotor
η	Exponent for decay of circulation of tip vortex (see Equation 22)
OASPL	Overall sound pressure level
PNL	Perceived noise level
q	Gust harmonic
R	Radius

Table 8. Nomenclature for Tip Vortex Model Equations.

r	Radial distance from center of vortex core
R_{hub}	Hub radius
R_{tip}	Tip radius
R_{vtx}	Radial location of tip vortex
R_{T1}	Tip radius of forward rotor
rpm1	RPM of forward rotor
rpm2	RPM of aft rotor
S	Blade-to-blade tangential spacing
s	Streamwise distance
SPL	Sound pressure level
S_{tip}	Blade-to-blade tangential spacing at the tip
UDF	Unducted fan
$V_{a/c}$	Aircraft flight velocity
V_{tip}	Tip speed
V_q	Tangential velocity created by tip vortex
$(V_q)_{\text{max}}$	Maximum value of tangential velocity created by tip vortex
V_g	Freestream velocity
W_{dc}	Wake centerline defect (relative to forward rotor)
W_{FS}	Freestream velocity (relative to forward rotor)
x,y	Coordinates of the unwrapped annulus (see Figure 39b)
X_f	Axial distance from pitch change axis of forward rotor
XPCA	Axial distance between pitch change axis
Z_{vtx}	Axial location of tip vortex
Greek Symbols	
Γ	Circulation
$(\Gamma)_{\text{vtx}}$	Circulation of the tip vortex
δ	Semiwake width
τ	Tip clearance
ω	Angular velocity of the tip vortex

In the case of the ducted fan rotor, the tip vortex model superimposes a row of combined forced/free vortices and an image row on the opposite side of the annulus wall to enforce the zero normal velocity at the wall. Figure 39b depicts a sketch of unwrapped annulus with both the tip vortices and the image vortices. The vortices are located at a periodic tangential spacing that is equal to the blade spacing. The spanwise and the tangential (+y and +x directions, respectively) velocities outside the tip vortex core were determined by using an extension of Lamb's solution (Reference 22) for the induced flow field about two infinite rows of vortices of finite radius, as modeled (Figure 39b). Reference 13 provides the detailed formulation.

For the unducted fan, the annulus wall does not exist. This is mathematically modeled by increasing the value of the tip clearance to a large value, so that the effect of the image vortex is made negligible. Figure 40 compares the gust spectra at three spanwise locations for increasing values of tip clearance. The nondimensional tip clearance shown in Figure 39b is tip clearance divided by the forward rotor chord at the tip. Typical values of τ for ducted fan rotors are 0.01. It is seen that when τ is increased by a factor of 1000, the solution has converged so that even an increase in τ does not alter the results. For the sake of completeness, gust harmonic spectra for the case of no tip vortex (that is, wake alone) are also presented (Figure 40).

Although the tip vortex is seen to have considerable influence on the gust harmonic spectra at the tip streamline and at the streamline which is 89% of the span from hub, the gust harmonic spectra at the hub are not affected by the tip vortex. Also note that the gust spectral levels without the tip vortex (that is, wake alone) in the tip region are much lower in amplitude, compared to the hub region. This is because the smaller spacing and larger chord at the hub yield smaller values of streamwise distance/chord ratio which, in turn, makes the wakes stronger at the hub (compared to the tip).

The gust spectra (with the tip vortex) at the tip streamline and the streamline 89% of the span from hub demonstrate a different character. Based on the tip vortex trajectory model, the 89% streamline is very close to the region of impact of tip vortex on the aft rotor. The gust spectral levels at the 89% streamline are seen to be higher than for the tip streamline. The gust harmonic falloff for increasing values of the gust harmonic "q" is also lower for the 89% streamline (compared to the tip streamline), indicating a sharp profile for the gust waveform near the point of impact of the tip vortex.

Computation of the flow field created due to the tip vortex can be performed if one knows both the:

- Circulation of tip vortex at the axial station of interest (Γ_{vtx})
- Radial and tangential coordinates of the tip vortex (b_r and b_t).

The experimental data reported in Reference 23 contained information on the variation of $(VF_\theta)_{\text{max}}$ and radius of the vortex core of a uniform NACA-0012 airfoil (with an aspect ratio of 6), set at an angle-of-attack of 7.5° , at two freestream velocities (70 and 100 fps). Vortex measurements were made with a yawhead pressure probe from 10 to 30 chord lengths downstream of the trailing edge. The experimental data chosen from Reference 24 were obtained on a NACA-0012 airfoil of an aspect ratio of 6 at a freestream velocity of 110 fps. The variation of tip vortex radius with angle-of-attack was measured at approximately six chord lengths downstream of the trailing edge using a vorticity meter. The applicability of the data (based on the wing configuration) to the

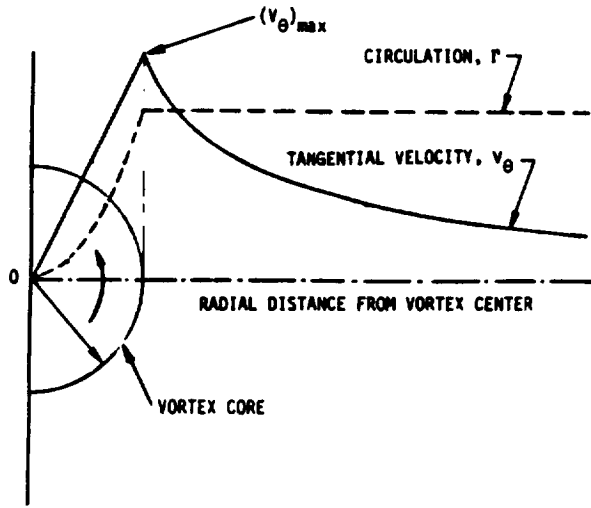


Figure 39a. The Combined Forced (Within the Core) and Free (Outside the Core) Vortex Model for the Tip Vortex.

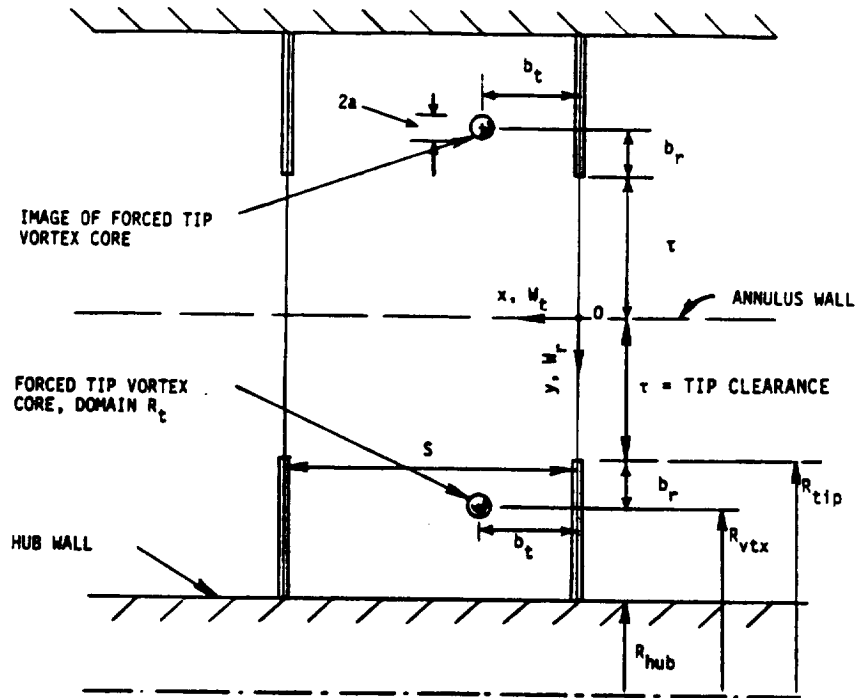


Figure 39b. Nature of the Tip Vortex Flow Model for a Ducted Rotor.

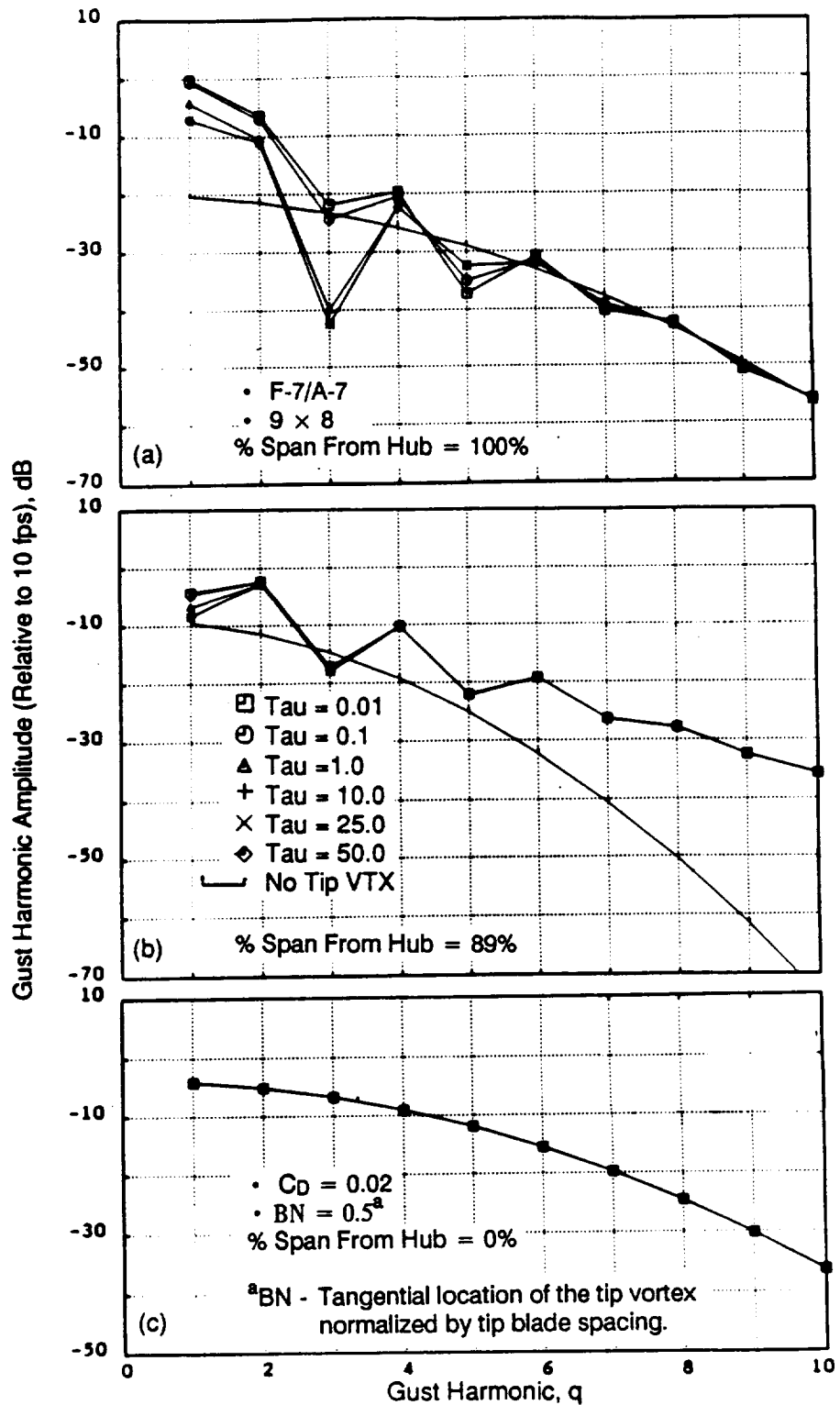


Figure 40. Comparison of Gust Harmonic Spectra at Three Spanwise Locations for Increasing Values of Tip Clearance and for No Tip Vortex Case.

significantly swept UDF® blade geometry should be verified once experimental tip vortex data can be obtained from these UDF® blade configurations.

Empirical corrections for $(V\theta)_{\max}/(V_{\infty}\sqrt{C_L}$ and $a/(c\sqrt{C_L})$ were developed by employing a linear rational function of the type (Reference 12):

$$y = \frac{dx + e}{fx + 1} \quad (16)$$

where d, e, and f are empirically determined constants, and y could be $(V\theta)_{\max}/(V_{\infty}\sqrt{C_L})$ or $a/(c\sqrt{C_L})$, and $x = s/c$.

$$\frac{(V\theta)_{\max}}{V_{\infty}\sqrt{C_L}} = \frac{0.024 (s/c) + 0.5586}{0.0504 (s/c) + 1.0} = Y(s/c) \quad (17)$$

Constants d, e, and f in Equation 16 were determined through an iteration scheme aimed at minimizing the standard deviation (Reference 12 provides more details). The following correlations yielded minimum standard deviation:

where:

- $(V\theta)_{\max}$ = maximum tangential velocity of the tip vortex
- V_{∞} = freestream velocity
- C_L = local section lift coefficient
- s = streamwise distance
- c = chord

and

$$\frac{a}{c\sqrt{C_L}} = \frac{0.01584 (s/c) + 0.0014}{0.184 (s/c) + 1.0} = Z(s/c) \quad (18)$$

Figures 41 and 42 demonstrate these correlations, along with the data for:

$$\frac{(V\theta)_{\max}}{V_{\infty}\sqrt{C_L}} \text{ and } \frac{a}{c\sqrt{C_L}},$$

respectively. The empirical corrections provided in Equations 17 and 18 can be improved by adjusting the constants d, e, and f when more detailed experimental data for the UDF® blades become available.

By definition, the circulation of the tip vortex is:

$$\begin{aligned} (\Gamma)_{\text{vtx}} &= \int_{\theta=0}^{2\pi} (V\theta)_{\max} a \, d\theta \quad (19) \\ &= \int_{\theta=0}^{2\pi} V_{\infty}\sqrt{C_L} Y(s/c) c\sqrt{C_L} Z(s/c) \, d\theta \\ &= 2\pi (V\theta)_{\max} a \end{aligned}$$

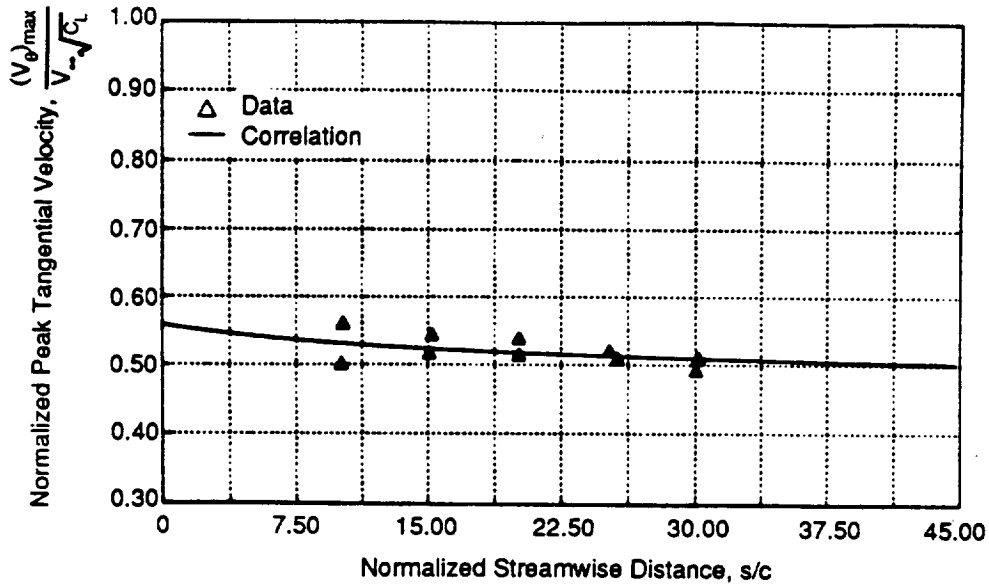


Figure 41. Correlation and Data for the Streamwise Variation of Normalized $(V_\theta)_{\max}$ of the Tip Vortex.

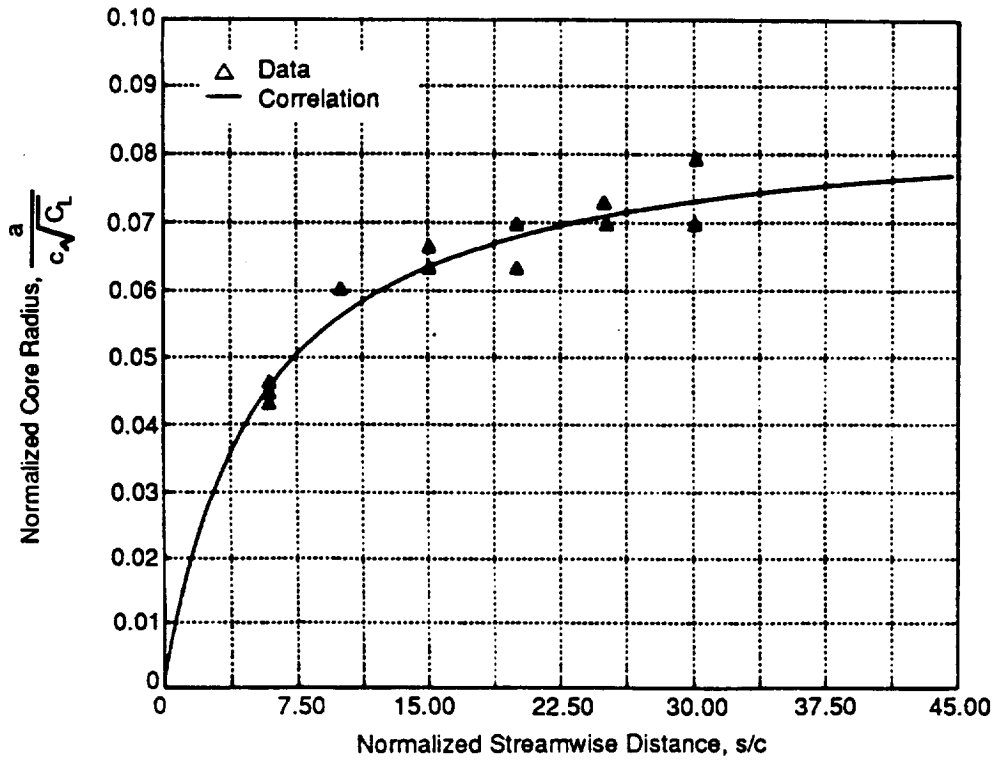


Figure 42. Correlation and Data for the Streamwise Variation of Normalized Radius of the Tip Vortex Core.

Figure 43 shows the correlations given by Equations 17 and 18 and the computed circulation (Equation 19), along with the data. It is seen that the maximum tangential velocity decreases with s/c ; whereas, the radius of the vortex core increases with s/c , and the tip vortex circulation initially rises and then shows almost no decay over 10 to 30 chord lengths. The absence of a decay in the circulation of the tip vortex noted in the above set of data has been confirmed on full-scale aircraft tip vortex measurements for up to 1,000 chord lengths downstream of the aircraft (Reference 25).

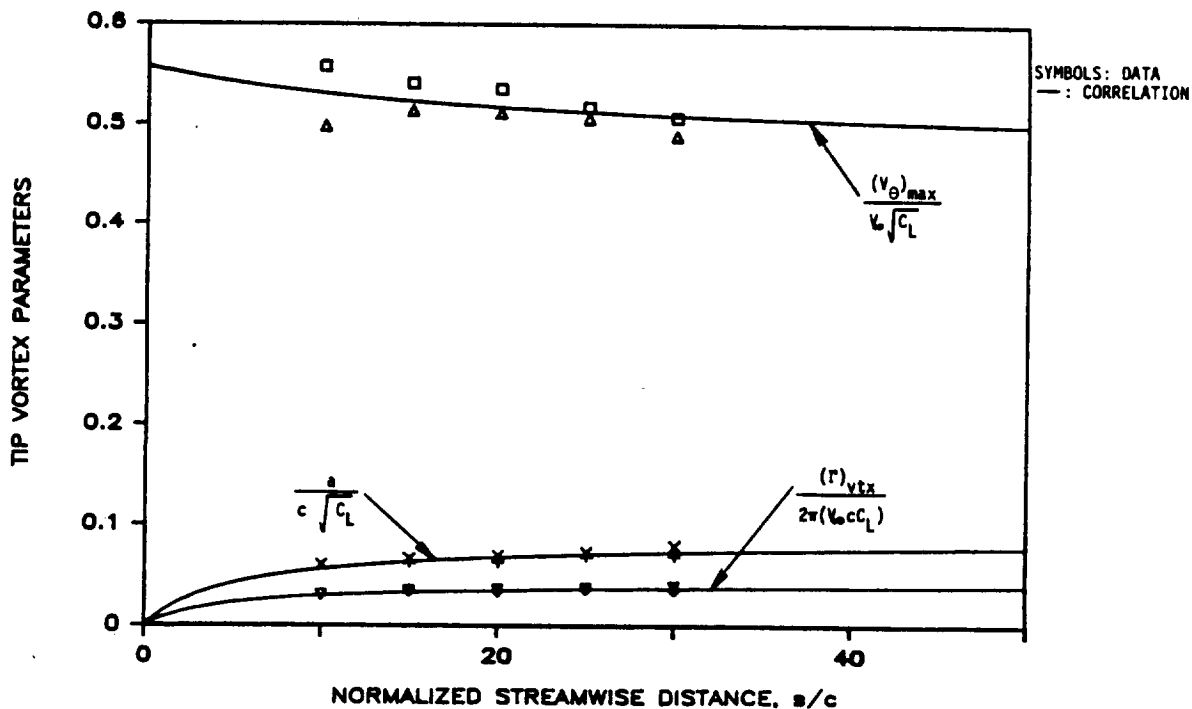


Figure 43. Representative Correlation and Data for the Streamwise Variation of Normalized $(V\theta)_{max}$, Radius, and Circulation of the Tip Vortex.

The linear-rational-function correlations employed for $(V\theta)_{max}$ and radius of the vortex core simulate this behavior of the tip vortex very well. Certain limiting forms of $(\Gamma)_{vtx}$ are examined next. For example:

$$\text{At } (s/c) = 0 \quad (\Gamma)_{vtx} = 2\pi V_{\infty} c C_L (0.5586 \times 0.0014) \quad (20)$$

or

$$\frac{(\Gamma)_{vtx}}{2\pi V_{\infty} c} = 0.000782$$

For large values of s/c :

$$\lim_{(s/c) \rightarrow \infty} \left[\frac{(\Gamma)_{vtx}}{2\pi V_{\infty} c C_L} \right] = \left(\frac{0.024}{0.0504} \right) \left(\frac{0.01584}{0.184} \right) = 0.040994 \quad (21)$$

Hence, for large values of s/c , the circulation of the vortex reaches an asymptotic value which is higher than the value at the trailing edge. The initial rise in tip vortex circulation (as indicated by these correlations) may be viewed as a result of the initial roll-up of the shed spanwise vorticity into

a well-defined tip vortex. Thus, the correlations seem to represent some of the physical features exhibited by the wing tip vortices. Unfortunately however, for the UDF® configurations, the range of the s/c value (that is, spacing between the forward and aft rotors) is less than 5.0; within this range, there is a lack of data, as evidenced by Figures 41 through 43.

Flow-field visualization studies conducted on helicopter rotors (Reference 26) show that the shed tip vortices for rotating blade rows diffuse within one to two revolutions, and the distinction of the tip vortices is lost. However, no quantitative information exists regarding the circulation of $(V\theta)_{\max}$ or radius of such rotating tip vortices for use in modeling the decay of rotating tip vortices. The more rapid decay of rotating tip vortices (compared to translating tip vortices) may be due to the relatively larger turbulence and more efficient mixing processes prevalent in the near field of a rotating blade row, compared to a wing in translation wherein the decay could be due predominantly to viscous dissipation. In the absence of applicable information regarding the decay of the tip vortex for an unducted rotor, different power law decay rates are proposed for the current model:

$$(\Gamma)_{\text{vtx}} \propto \frac{1}{(1 + s/c)^\eta} \quad (22)$$

Figure 44 demonstrates streamwise variations of normalized tip vortex circulation for three decay rates (that is, $\eta = 0, 1/4,$ and $1/2$); the exponential value that was used for tip vortices of the ducted fan rotor was $1/2$ (Reference 12). The presence of the annulus wall and the large number of blades of a ducted fan rotor would cause a faster diffusion of tip vortex, compared to the unducted fan rotor; hence, $\eta = 1/4$ is proposed as the exponent for the tip vortex decay rate of an unducted fan. The influence of the decay rate on the acoustic predictions of unducted rotors will be examined through parametric studies in Section 3.4.3.2.2.

Next, an empirical relationship is developed for the trajectory of the tip vortices employing the flow visualization data (Reference 26) which were obtained for helicopter blades in a typical hover mode. All of these data indicated that tip vortices move radially inward for increasing axial distance, which is ascribable to the stream tube contraction (Figure 45).

Linear-rational-function correlation methods (Reference 12) were used again to develop an empirical relation for the trajectory of the tip vortex. Linear-rational functions are applicable if the dependent variable shows a monotonic trend with the independent variable. Since the radial movement of the tip vortex with axial distance is monotonic, approaching an asymptotic value, linear-rational function was chosen. The empirical relationship which yielded minimum standard deviation is:

$$\frac{R_{\text{vtx}}}{R_{\text{tip}}} = \frac{12 (Z_{\text{vtx}})/R_{\text{tip}} + 1.0}{16 (Z_{\text{vtx}})/R_{\text{tip}} + 1.0} \quad (23)$$

where

R_{vtx} : radial location of core of tip vortex

Z_{vtx} : axial location of core of tip vortex.

Since the formulation for tip vortex (see Figure 39b) uses $b_r = R_{\text{tip}} - R_{\text{vtx}}$, Equation 23 is written in terms of b_r :

$$\frac{b_r}{R_{\text{tip}}} = 1 - \frac{R_{\text{vtx}}}{R_{\text{tip}}} = \frac{4 (Z_{\text{vtx}})/R_{\text{tip}}}{16 (Z_{\text{vtx}})/R_{\text{tip}} + 1.0} \quad (24)$$

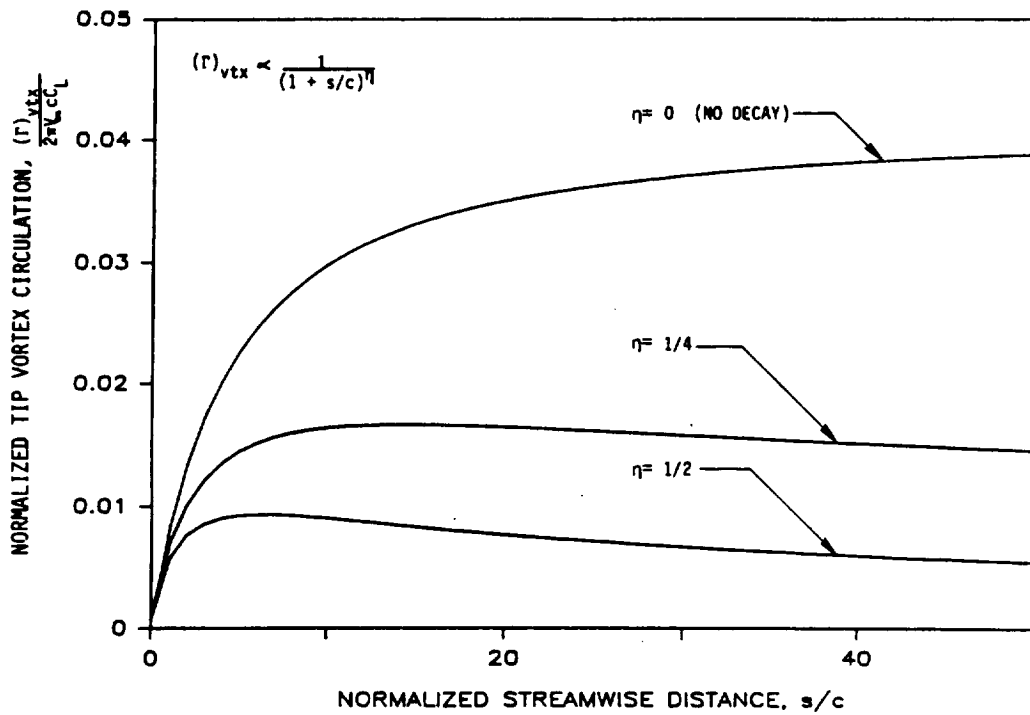


Figure 44. Streamwise Variation of Normalized Circulation of the Tip Vortex for Three Different Power Law Decay Rates.

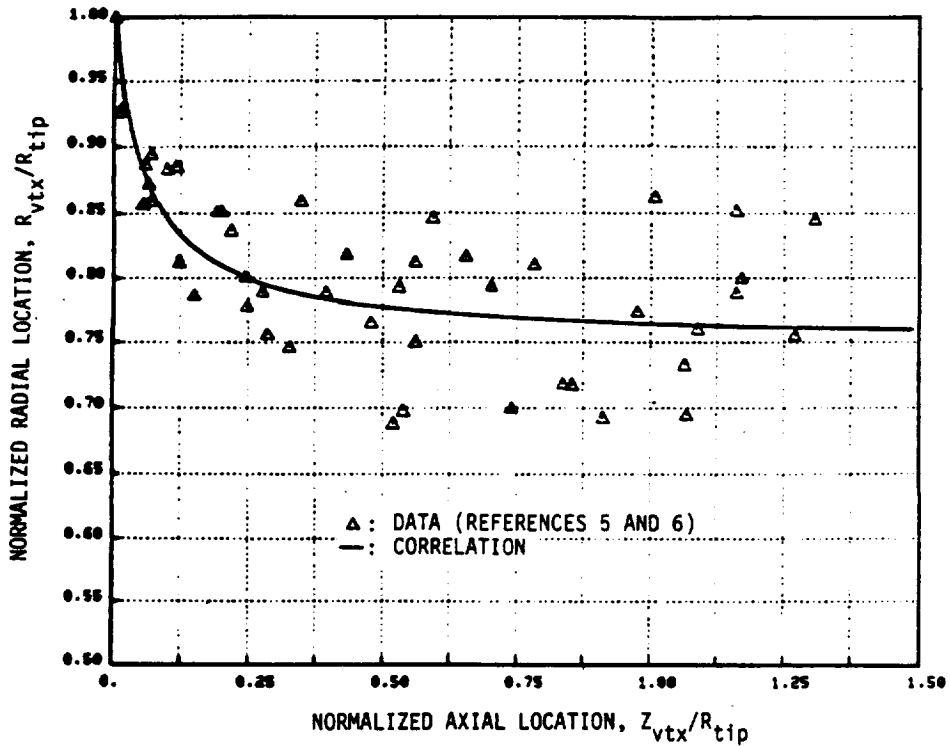


Figure 45. Correlation and Data for the Trajectory of the Tip Vortex.

There is a lot of scatter in the data for large values of Z/R_{tip} ; this, mainly, is a result of the uncertainty in defining the tip vortex at large values of Z/R_{tip} due to the diffusion of the tip vortex.

The development of Equation 24 is based on the data base for helicopter rotors. The HTR for helicopter rotors is approximately less than 0.1; however, the HTR for the UDF® blades is approximately 0.4. This introduces some amount of uncertainty regarding the applicability of the tip vortex trajectory correlation of Equation 24 to the UDF® configuration. Due to the lack of a data base for the higher values of HTR, the general form of the tip vortex trajectory for UDF® blades is assumed from Equation 24 as follows:

$$\frac{b_r}{R_{tip}} = \frac{K_{vtx} (Z_{vtx})/R_{tip}}{16 (Z_{vtx})/R_{tip} + 1.0} \quad (25)$$

where K_{vtx} is an adjustable constant.

For a given HTR, the tip vortex trajectory can be expressed in terms of a blade span percent of the tip by: $(b_r/R_{tip})/(1-HTR)$. For example, the value of $b_r/R_{tip} = 0.1$ translates to about a 17% span from the tip, with $HTR = 0.4$. On the other hand, the value of $b_r/R_{tip} = 0.1$ approximates K_{vtx} to be 2 for $Z_{vtx}/R_{tip} = 0.3$. Thus, the value of K_{vtx} for the UDF® blades should be chosen with consideration of blade geometries, forward and aft rotor spacing, aero performance, etc., which would affect the tip vortex trajectories. The value of K_{vtx} was assumed to be between 0.5 and 2.0, based on a flow-field computation performed using GE's in-house codes. The parametric evaluation of the tip vortex trajectory on the unsteady noise due to the tip vortex is reported in Section 3.4.3.2.2. Again, a detailed experimental data base will be required to obtain the proper value of K_{vtx} for the UDF® blade configurations.

3.4.3.2 Model Evaluation

The aerodynamic model for the tip vortex of counterrotating propulsors (described in Section 3.4.3.1) is evaluated in this section by:

1. Parametrically evaluating the effect certain key parameters (such as: tip vortex trajectory, decay rate, and extent of clipping of the aft rotor) have on the acoustic characteristics of the counterrotating UDF® propulsors.
2. Comparing selective acoustic data and predictions of the counterrotating UDF® propulsors, aimed at evaluating the tip vortex model.

Additional data/theory comparisons and parametric studies are discussed in Reference 13.

Due to the relatively low values of solidity over most of the span, UDF® propulsors may be viewed as isolated airfoils in computing the gust harmonic spectra resulting from impingement of the forward rotor wake and the tip vortex on the aft rotor. Hence, the unsteady gust model developed by Kemp and Sears (Reference 27) was selected for predicting the gust harmonic spectra of unsteady loadings induced by the tip vortex and the rotor wakes.

3.4.3.2.1 Parametric Studies

The studies described in this section parametrically evaluate the effect of certain geometric and aerodynamic parameters of the tip vortex on the acoustic characteristics of a counterrotating propeller. The principal objective of these studies was to develop an understanding of the sensitivity of the acoustic characteristics to certain key geometric and aerodynamic parameters of the tip vortex. The parametric studies described herein are:

- Influence of tip vortex trajectory (K_{vtx} sensitivity)
- Influence of decay rate of tip vortex (η sensitivity)
- Influence of progressive clipping of the aft rotor.

For the parametric studies, standard F-7/A-7 blade design parameters are used to calculate the gust harmonic spectra and unsteady loading noise through the present model; Figure 46 portrays a planform of these blades. The parametric studies are performed based on the aeroperformance data of TP (test point) 3706 of a 90% rpm case with 9x8 F-7/A-7 blades at a take-off Mach number, obtained from GE Cell 41. For an unequal blade number configuration (such as, 9x8) but equal rpm, the steady loading and thickness noise and the noise due to wake/tip vortex interaction occur at distinctly different frequencies (Reference 14), as listed below:

- Steady loading and thickness noise of forward rotor

$$f_{s1q} = q * \frac{\text{rpm1}}{60} * B1 \quad q = 1, 2, 3, \dots \quad (26)$$

where f_{s1q} is the qth harmonic of steady loading and thickness noise of the forward rotor, and B1 is the number of blades in the forward rotor, and $q = 1$ corresponds to BPF (blade passing frequency), $q = 2$ corresponds to 2xBPF of forward rotor, etc.

- Steady loading and thickness noise of aft rotor

$$f_{s2r} = r * \frac{\text{rpm2}}{60} * B2 \quad r = 1, 2, 3 \dots \quad (27)$$

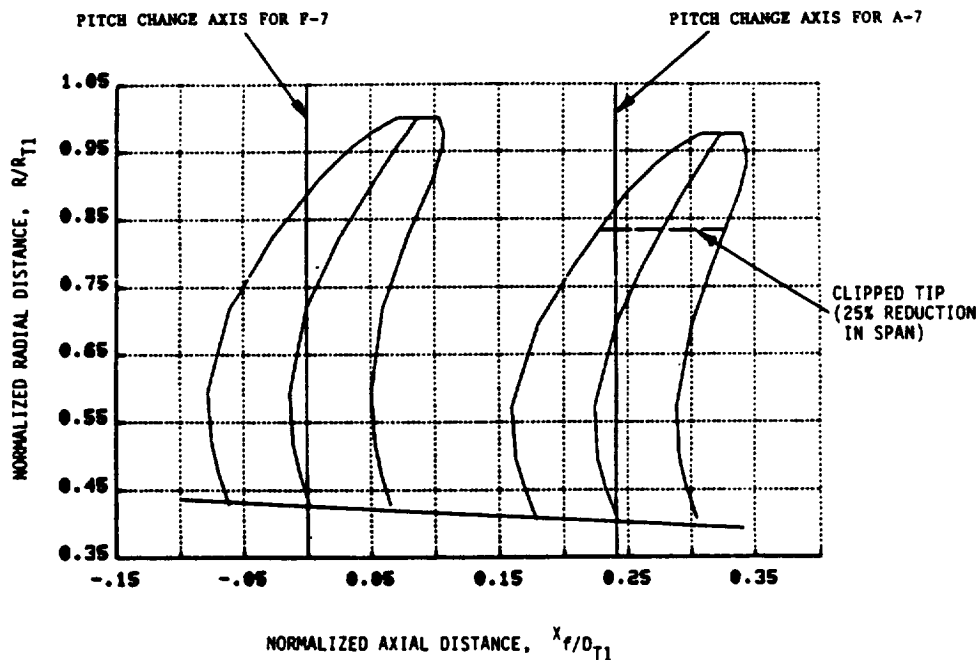


Figure 46. Planform of the F-7/A-7 Unducted Fan Blade Design, Showing the Extent of Clipping on the Aft Rotor.

where f_{s2r} is the r th harmonic of steady loading and thickness noise of the aft rotor; $B2$ is the number of blades in the aft rotor; and $r = 1$ corresponds to BPF; $r = 2$ corresponds to $2 \times$ BPF of the aft rotor, and so on.

- Noise due to wake/tip vortex interaction

$$f_{wqr} = f_{s1q} + f_{s2r}, \quad \begin{matrix} q = 1, 2, 3 \dots \\ r = 1, 2, 3 \dots \end{matrix} \quad (28)$$

For equal rpm's (say, $\text{rpm1} = \text{rpm2} = \text{rpm}$), normalized frequencies are defined as:

$$\bar{f}_{s1q} = \frac{f_{s1q}}{(\text{rpm}/60)} = qB1, \quad q = 1, 2, 3 \dots \quad (29)$$

$$\bar{f} = \frac{f_{2sr}}{(\text{rpm}/60)} = rB2, \quad r = 1, 2, 3 \dots \quad (30)$$

and

$$\bar{f}_{wqr} = \frac{f_{wqr}}{(\text{rpm}/60)} = qB1 + rB2, \quad \begin{matrix} q = 1, 2, 3, \dots \\ r = 1, 2, 3, \dots \end{matrix} \quad (31)$$

The spinning mode numbers associated with steady loading and thickness noise of forward and aft rotors are $qB1$ and $rB2$, respectively. The spinning mode number associated with the noise due to wake/tip vortex interaction is given by:

$$m_{wqr} = rB2 - qB1 \quad (32)$$

where m_{wqr} is the spinning mode number of the r th harmonic or aft rotor unsteady noise, due to q th gust harmonic of forward rotor.

Table 9 lists the tone designation, f_{wqr} , m_{wqr} , q , and r for increasing frequencies for a 9×8 blade configuration. Figure 47 is a schematic of the steady loading and unsteady loading noise spectra for the 9×8 blade number configuration.

In the following parametric studies, the sensitivity of each parameter was examined individually by varying the particular parameters from the basic stage of each. The value of each parameter at the basic stage is given as $C_i = 2.0$, $K_{vtx} = 2.0$, $bt/S = 0.5$, and $\eta = 1/4$.

Influence of Tip Vortex Trajectory

The influence of the tip vortex trajectory on gust spectra and its consequent influence on the interaction noise were studied by parametrically varying the K_{vtx} (see Equation 25).

Figure 48 indicates the predicted influence of the tip vortex trajectory on the gust harmonic spectra at three streamlines in the tip region. As K_{vtx} increases, the tip vortex moves radially inward. At the tip streamline, the gust harmonic spectrum for $K_{vtx} = 0.5$ has the highest levels (compared to $K_{vtx} = 1$ and 2), since the tip vortex for $K_{vtx} = 0.5$ is closest to the tip streamline. For the 89.1% streamline, the gust harmonic spectrum for $K_{vtx} = 1$ has the highest levels compared to $K_{vtx} = 0.5$ and 2 , since the 89.1% streamline is closer to the tip vortex point of impact when $K_{vtx} = 1$. However, for the 70.1% streamline, gust spectrum levels for $K_{vtx} = 0.5$ and 1 are about same. This indicates the tip vortex effects induced by $K_{vtx} = 0.5$ and 1 are minor at this streamline location. The gust spectrum levels for $K_{vtx} = 2$ are quite different from others. The noted relative dominance of even-numbered gust harmonics over odd-numbered gust harmonics is due to the fact that the tangential location of the tip vortex is at the midpassage.

Table 9. Normalized Acoustic Frequencies and Spinning Modes Associated with Wake/Tip Vortex Interaction for a 9 x 8 Blade Number Configuration.

Tone Designation	\bar{f}_{wqr}	m_{wqr}	q	r
(A+F)	17	-1	1	1
(2A+F)	25	7	1	2
(A+2F)	26	-10	2	1
(3A+F)	33	15	1	3
(2A+2F)	34	-2	2	2
(A+3F)	35	-19	3	1
(4A+F)	41	23	1	4
(3A+2F)	42	6	2	3
(2A+3F)	43	-11	3	2
(A+4F)	44	-28	4	1
(5A+F)	49	31	1	5
(4A+2F)	50	14	2	4
(3A+3F)	51	-3	3	3
(2A+4F)	52	-20	4	2
(A+5F)	53	-37	5	1

\bar{f}_{wqr} - Normalized acoustic frequency

m_{wqr} - Spinning mode

q - Forward rotor gust harmonic

r - Aft rotor acoustic harmonic

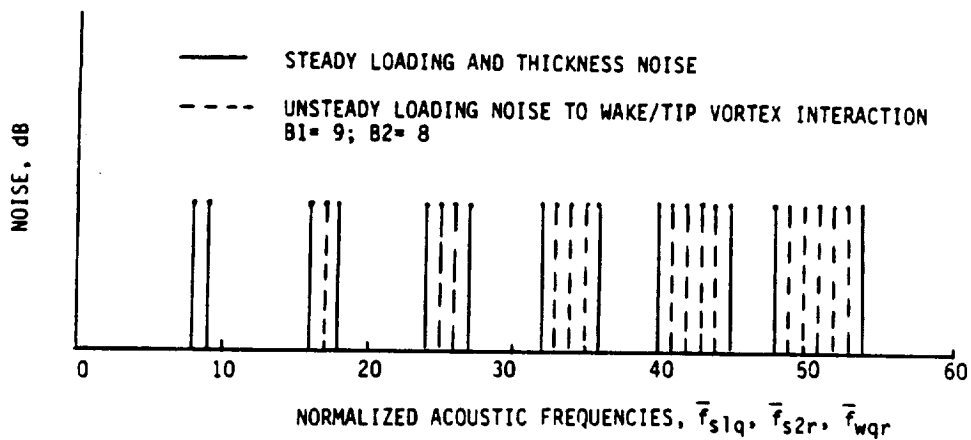


Figure 47. Schematic of a Narrowband Acoustic Spectrum of a 9 x 8 Blade Number Configuration.

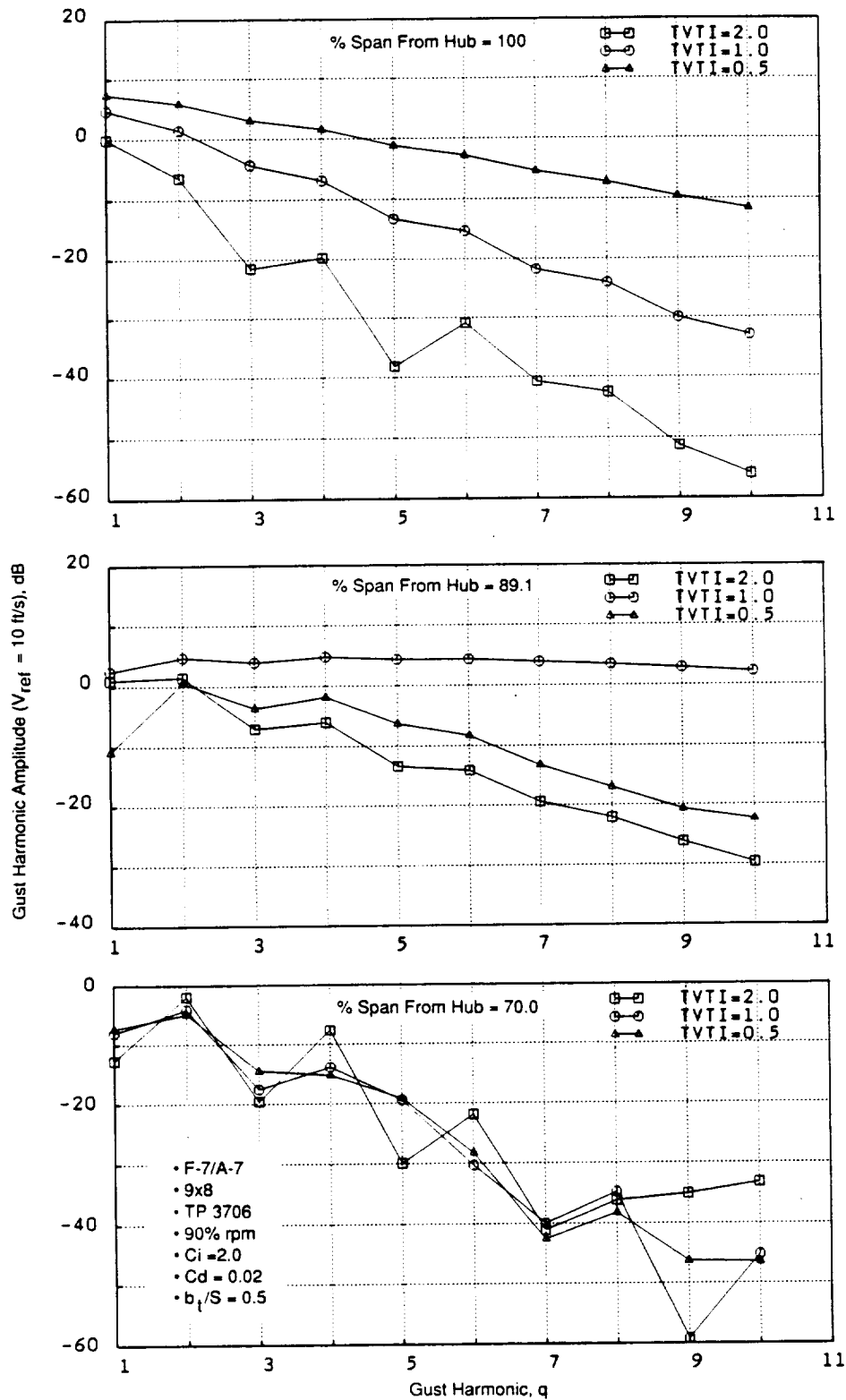


Figure 48. Predicted Influence of the Tip Vortex Trajectory on Gust Harmonic Spectra at Three Streamlines in the Tip Region.

Figure 49 shows the influence of the tip vortex trajectory on each individual interaction tone at an observer angle of 91° along with the data. Apparently, the sensitivity of K_{VTX} on the acoustic predictions is insignificant. This probably happens because the gust spectra at different radial locations are enhanced for different values of K_{VTX} . The comparisons between data and predictions indicate that the K_{VTX} values do not improve the accuracy of the model. The differences between the predictions and data (up to 10 dB) are noted in Figure 49.

Figure 50 shows the influence of tip vortex trajectory on the directivity of tone SPL sum of interaction noise. Variations in the tip vortex trajectory do not significantly alter the interaction tone SPL sum; however, the trajectory parameter does significantly affect the interaction noise prediction for the clipped aft rotor blades configuration, as shown in the subsequent parametric studies.

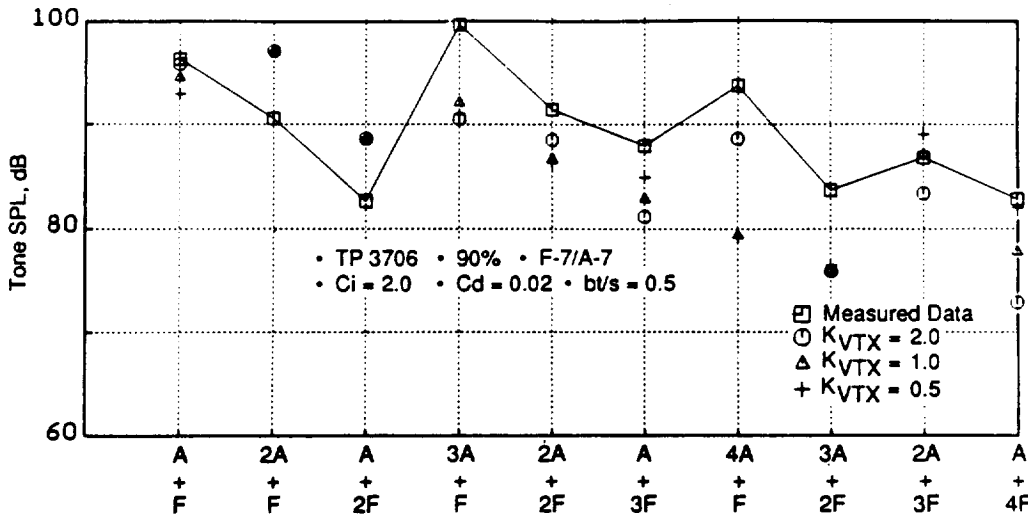


Figure 49. Predicted Influence of Tip Vortex Trajectory on Each Interaction Tone at Observer Angle of 91°.

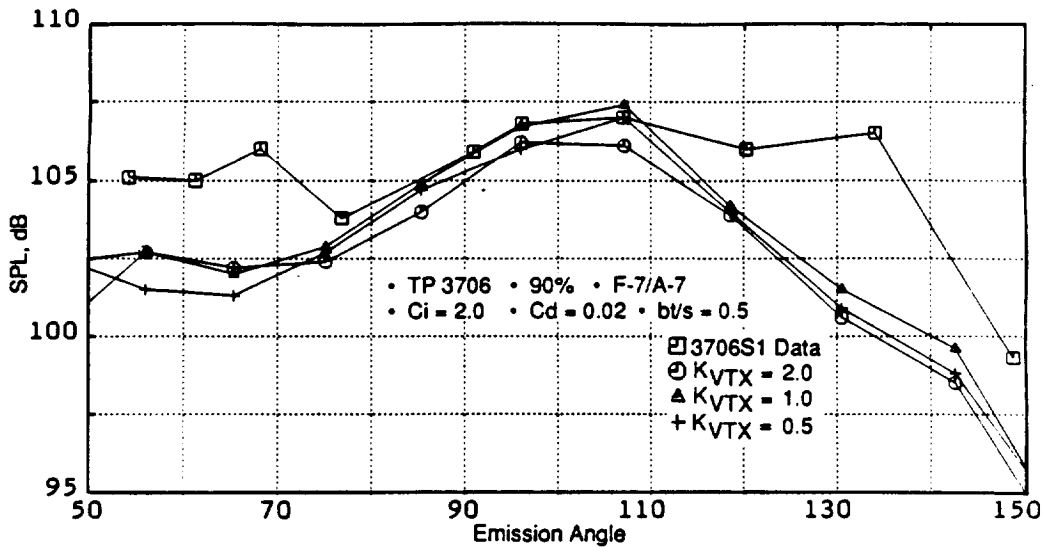


Figure 50. Predicted Influence of Tip Vortex Trajectory on Interaction Noise Tone SPL Sum.

Influence of Decay Rate of Tip Vortex

Also investigated was the influence of the decay rate of the tip vortex on gust harmonics. As discussed in Section 3.4.3.1, a power law decay rate was proposed for the circulation of the tip vortex:

$$(\Gamma)_{\text{vtx}} \propto \frac{1}{(1 + s/c)^\eta} \quad (33)$$

The cycle corresponds to a typical cutback. Figure 51 demonstrates the predicted gust harmonic spectra for tip vortex decaying with different rates at the streamlines of the tip and 70.7% span from the hub. The case of no tip vortices also was included for the sake of comparison. For this study, $K_{\text{vtx}} = 2.0$ and $bt/S = 0.5$ are used.

The gust spectral levels for the nondecaying tip vortex are the highest. As the rate of decay increases from 0 to 1/4, to 1/2, the gust spectral levels decrease monotonically.

Influence of Progressive Clipping of Aft Rotor

The tip vortex is a noise-generating mechanism. By clipping the aft rotor to minimize interactions between the tip vortex and the aft rotor blades, the interaction noise is reduced. This phenomenon has also been verified from the GE in-house UDF® acoustic data base. The thrust loss due to clipping and the associated required reduction in shp (shaft horsepower) can be made up either by increasing the rpm, or loading of the aft rotor; however in this parametric study, no attempt has been made to recover thrust loss resulting from clipping. This study was conducted with the objective of discovering the sensitivity (relating to the percent clipping of the aft rotor) on noise reductions. Consequently, this study considered four values of percent span clipping (5%, 10%, 15%, and 20%), in addition to 0% and 25% span clippings. Figure 46 presented the planforms of the standard F-7/A-7 and the F-7/A-7 with 25% clipping of span on the aft rotor.

Thrust and shp data are available only at 0% and 25% clippings for $M_\infty = 0.25$. Figure 52 shows the assumed interpolation of the thrust and shp of the aft rotor with the end points (0% and 25% clipping) coinciding with data for the 90% rpm case.

The steady loading and thickness noise and the wake/tip vortex interaction noise occur at distinctly different frequencies for unequal blade number configurations (Figure 47). As illustrated in Figure 12, tones associated with the steady loading and thickness noise were summed on a mean-squared pressure basis; this is also true for the tones associated with the wake/tip vortex interaction noise. Figure 53 demonstrates the predicted effect of progressive clipping of the aft rotor on the sum of steady loading and thickness noise. It is evident that the steady loading and thickness noise reduces uniformly as the percent clipping increases, a reflection of the assumed performance of clipped aft rotor (Figure 52). Predicted effect of the clipping sensitivity on the interaction tones is portrayed in Figure 54; whereas, the predicted effect on the OASPL (overall sound pressure level) is presented in Figure 55.

As discussed previously, unsteady loading interaction tone predictions depend on many empirical correction parameters. To predict the clipping effect on the interaction noise, the tip vortex strength (C_i) and the tip vortex tangential location (bt/S) were fixed at 2.0 and 0.5, respectively. Figure 54 (View A) shows the predicted effect of progressive clipping of the aft rotor on wake/tip vortex interaction noise by using $C_d = 0.02$ and $K_{\text{vtx}} = 2.0$. A value of $C_d = 0.02$ induces the strong rotor viscous wakes which control the interaction noise generation and reduces the influence of the

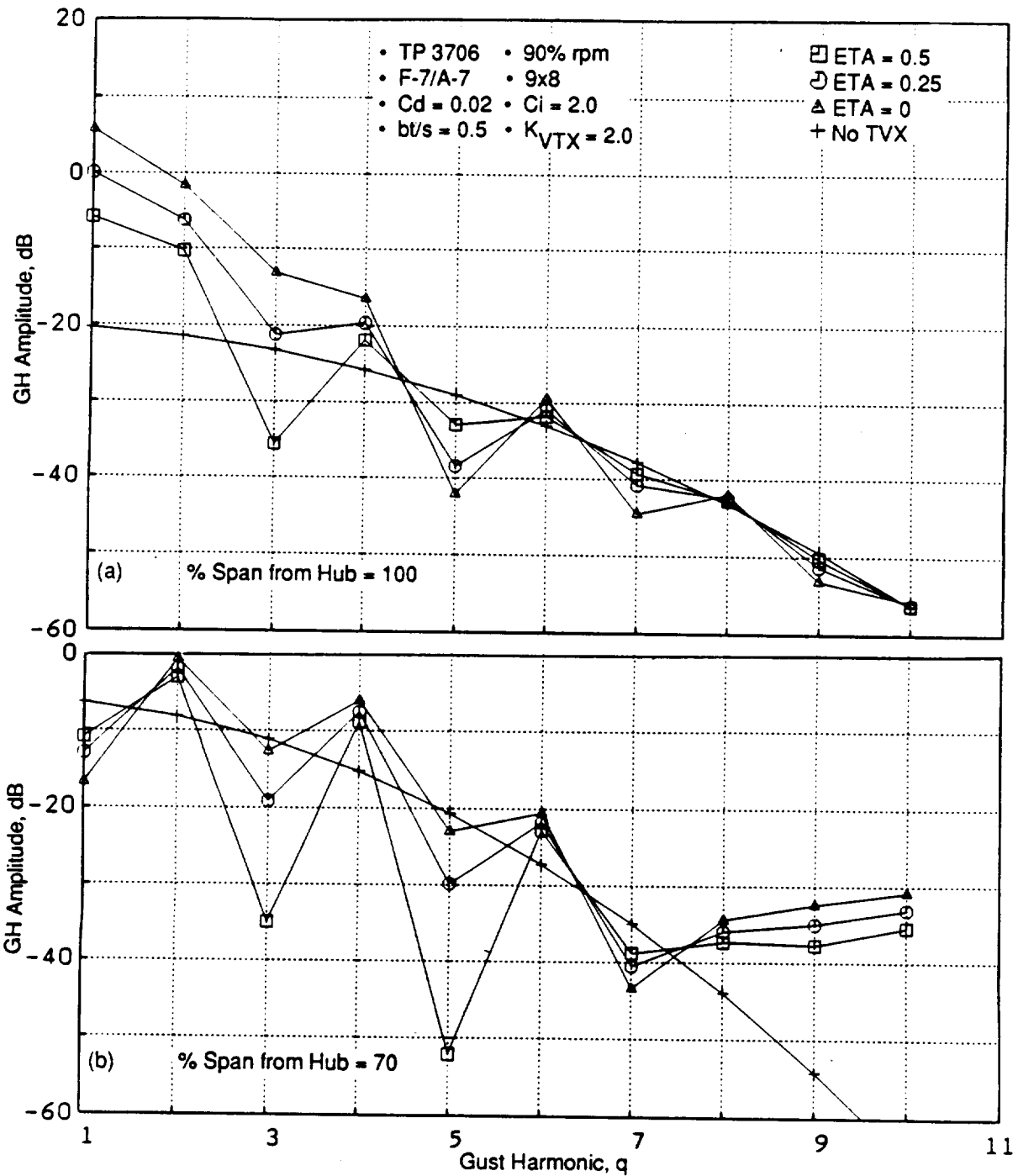


Figure 51. Predicted Gust Harmonic Spectra at Two Rotor-to-Rotor Spacings for the Tip Vortex at Different Decaying Rates and for the Case of No Tip Vortex at Two Streamline Locations.

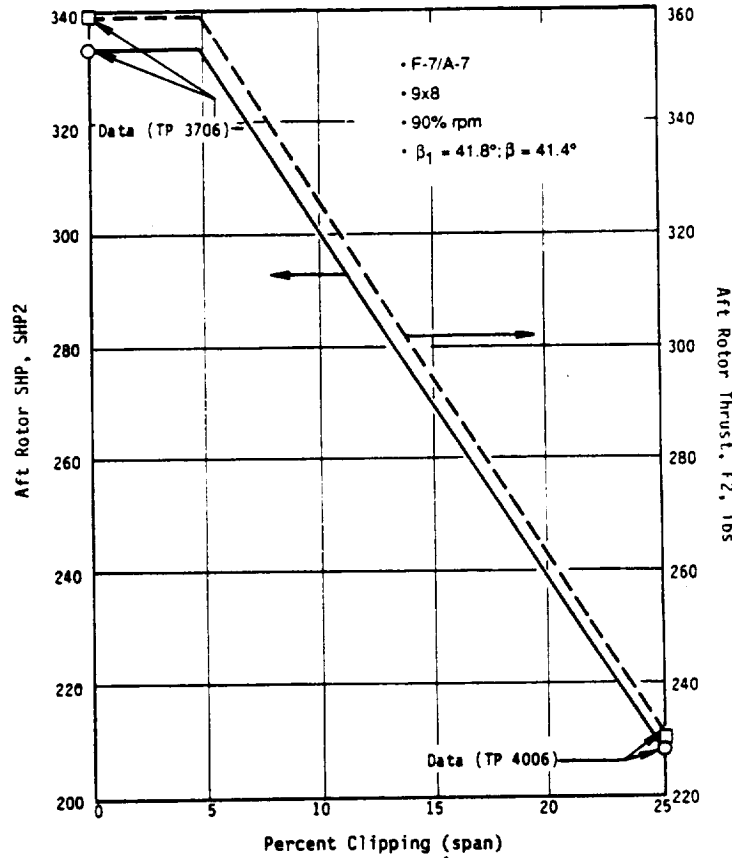


Figure 52. Assumed Performance of the Progressively Clipped Aft Rotor.

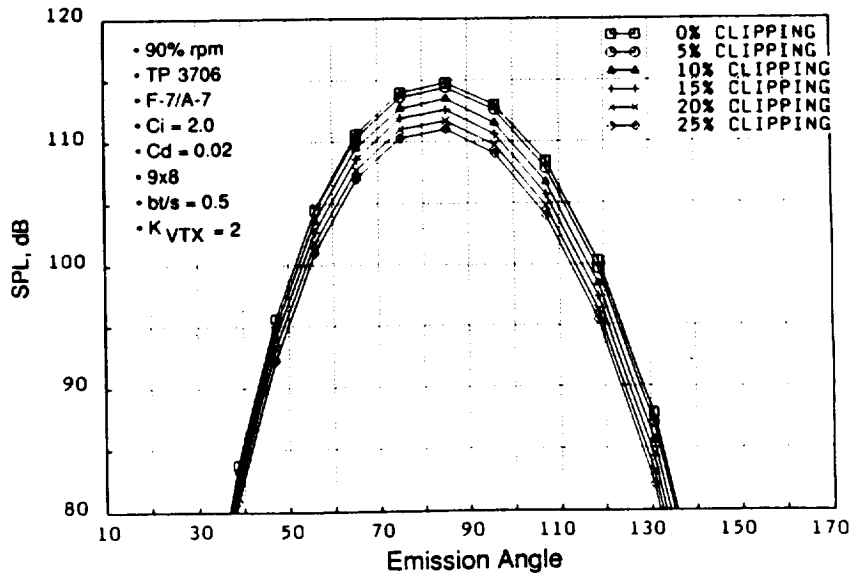


Figure 53. Predicted Effect of Progressive Clipping of the Aft Rotor on the Steady Loading and Thickness Noise.

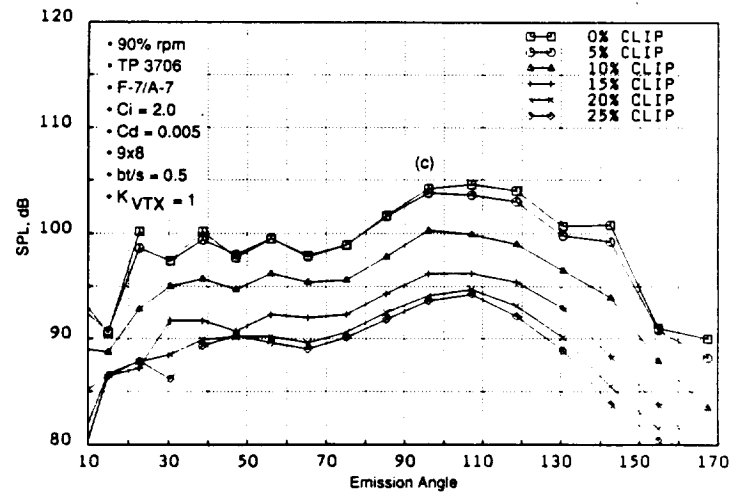
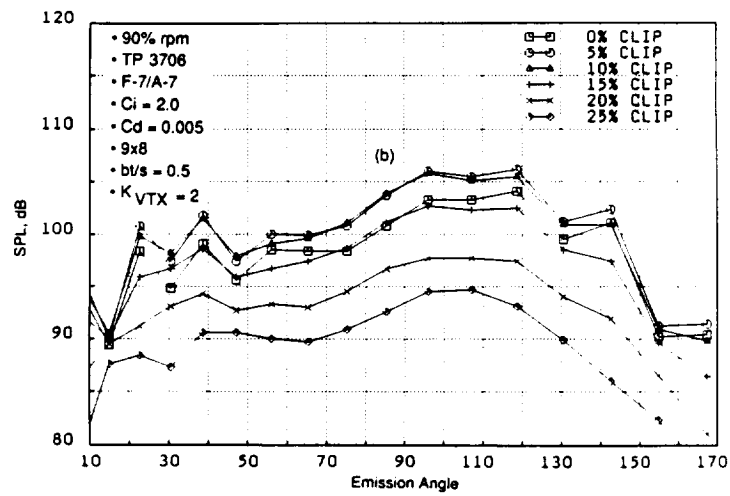
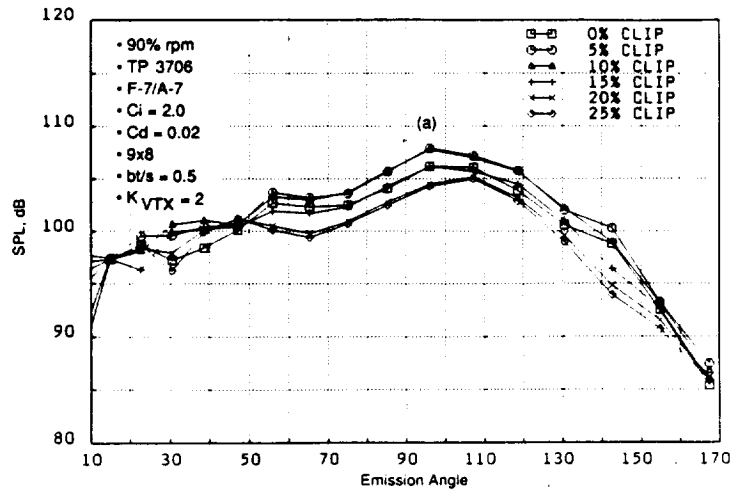


Figure 54. Predicted Effect of Progressive Clipping of the Aft Rotor on the Wake/Tip Vortex Interaction Noise.

ORIGINAL PAGE IS
OF POOR QUALITY

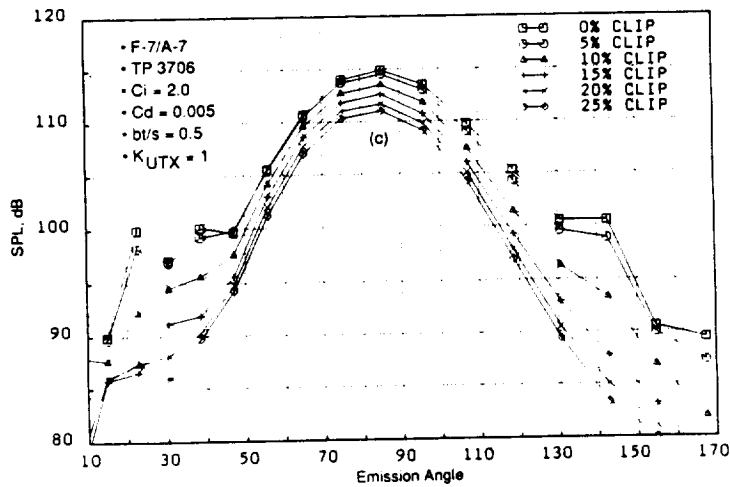
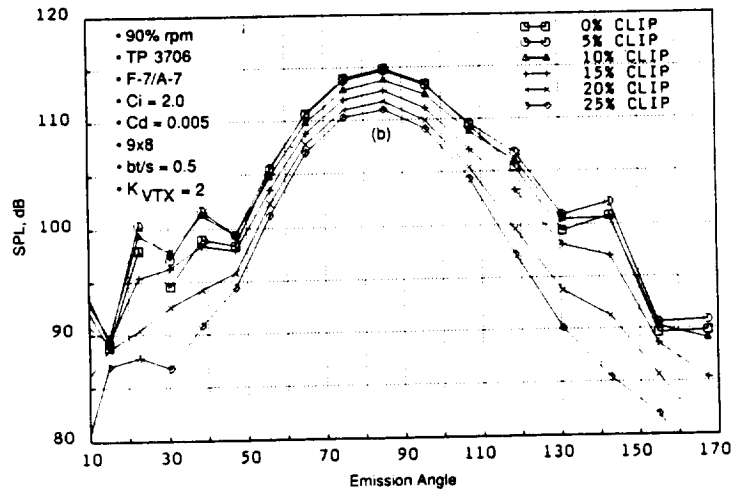
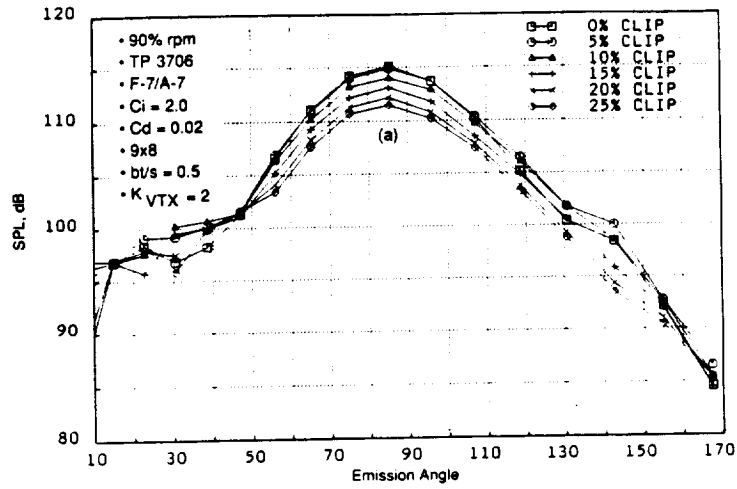


Figure 55. The Predicted Effect of Progressive Clipping of the Aft Rotor on the OASPL Directivity.

ORIGINAL PAGE IS
OF POOR QUALITY

tip vortex. Since the tip vortex effect is small with a combination of these C_d and K_{vtx} , the clipping effect is also shown as small ($C_d = 0.02$).

On the other hand, View B of Figure 54 shows the significant clipping effect when the drag coefficient is reduced to 0.005 to amplify the effect of the tip vortex. With the value of $K_{vtx} = 2.0$, the tip vortex is located approximately at 17% span from the tip of the aft rotor; thus, a large reduction in interaction noise is obtained by going from 15% to 20% clipping, and there are no reductions for percent clippings less than 15% span, as evidenced in Figure 54, View B.

The predicted clipping effect with $C_d = 0.005$ and $K_{vtx} = 1.0$ is depicted in Figure 54 (View C), where the only difference between Views B and C is the reduction of K_{vtx} (from 2.0 to 1.0). With $K_{vtx} = 1.0$, the tip vortex center is located at about 8% span; thus, a significant noise reduction is observed with the 10% and 15% clippings. Hardly any noise reduction is noted for clippings less than 5% or greater than 20%, since the influence of the tip vortex is concentrated at approximately 8% span.

Figure 55 (Views A through C) reveals predicted OASPL directivities for the various percent clippings with values of C_d and K_{vtx} corresponding to those used in Figure 54 (Views A through C, respectively). The OASPL reduction due to the aft rotor clipping is clearly shown, but the magnitudes of reduction are not as significant as those of the interaction noise. This is primarily due to the relatively high levels of the aft rotor steady loading and thickness noise.

This study has demonstrated that the current tip vortex model can be used to predict the interaction noise reduction that can be attained by the clipping of the aft rotor. However, to determine the optimum value for percent clipping of the aft rotor, in terms of noise reductions at a nominal thrust loss, the empirical correction parameters of the current model need more refinements. This effort is currently in progress as part of a GE IR&D project.

3.4.3.2.2 Data – Predictions Evaluation

Systematic data/theory comparisons are performed to evaluate the applicability and limitations of the current tip vortex model. Figure 46 provided a planform of the standard F-7/A-7 blade design, along with the clipped aft rotor. Narrowband acoustic data, measured at Cell 41 for the F-7/A-7 (standard and clipped) blade geometries at a freejet Mach number of 0.25 and an axial distance of 0.2408 between pitch-change axes angle, were used to perform the following comparisons of data and theory. The acoustic data have been transformed from the freejet situation to an equivalent flight situation by accounting for the refraction effect of the freejet shear layer using ray theory, in order that a one-to-one comparison of data and theory can be performed. These comparisons, as discussed below, refer to a 90% rpm case (Test Points 3706 and 4110). Test Point 3706 is for the standard A-7 blade, and Test Point 4110 is for the clipped A-7 blade. For Test Point 4110, the aft pitch angle was opened to recover the thrust loss due to clipping, but the rpm was maintained to be the same for both standard and clipped configurations. Figure 56a identifies the shp and pitch angle data. The narrowband data employed has a bandwidth from 6 Hz to 5 kHz. Since the BPF is at about 1 kHz, the narrowband data contains tones up to about 5 harmonics of BPF.

Figure 56a compares measured and predicted directivities of the tone SPL sum of all of the steady loading and thickness noise for standard and clipped aft rotor blades. The tone SPL sum was obtained by adding only the tones associated with the steady loading and thickness noise of the forward and aft rotors on a mean-squared pressure basis. The measured reduction in steady loading noise due to the clipping of the aft rotor is well predicted; the directivities also are in relatively good

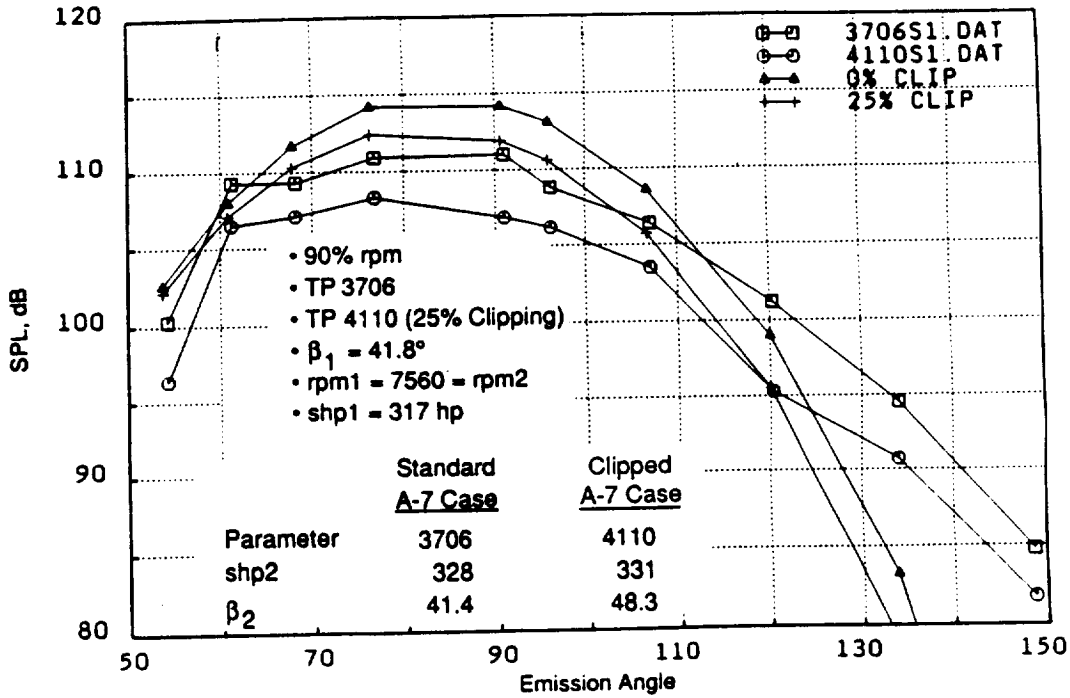


Figure 56a. Comparison of the Measured and Predicted Effect of Clipping of the Aft Rotor on Steady Loading and Thickness Noise.

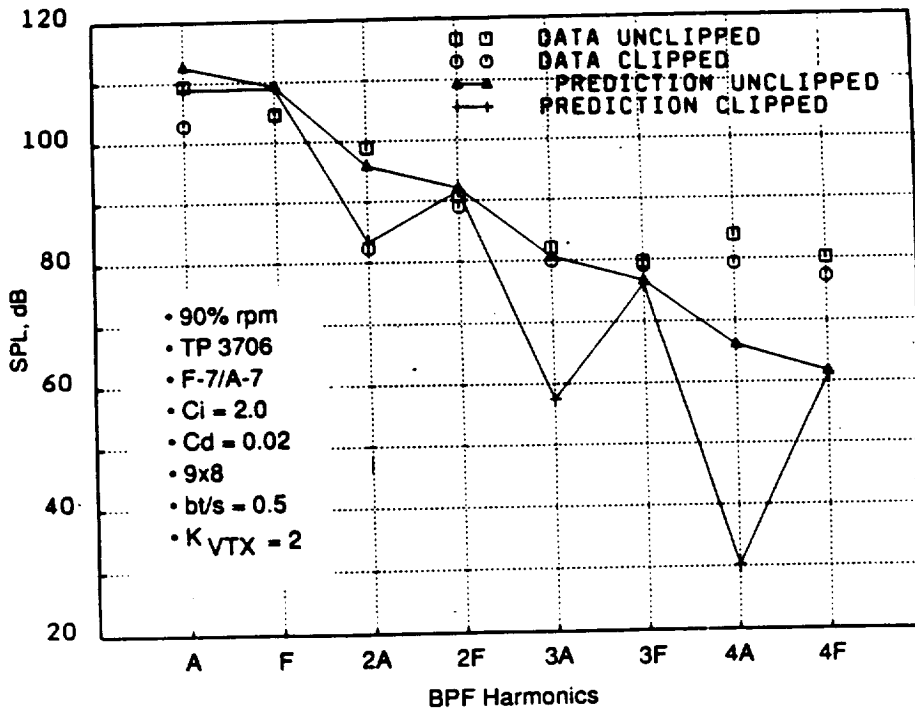


Figure 56b. Comparison of the Measured and Predicted Steady Loading and Thickness Tones for Standard and Clipped Aft Rotor at 105° Observer Angle.

agreement. Figure 56b compares the measured and predicted steady loading and thickness tones for standard and clipped aft rotor at an observer angle of 105° . The measured and predicted reductions in tone levels of the aft rotor BPF and its harmonics, indicated by 1A and 2A, due to clipping are in good agreement. The measured and predicted tone levels of the forward rotor BPF and its harmonics (denoted by 1F, 2F, and 3F) are also in good agreement. Actual tone data reveal a slower falloff with an increase in harmonics, as compared to the predictions; this may indicate the presence of some inflow distortion into the rotors.

Figure 57 compares the predicted and measured tone SPL sum for wake/tip vortex interaction noise for unclipped and clipped aft rotor cases. As previously discussed, the interaction tone predictions are sensitive to the empirical constants utilized in the tip vortex model. Therefore, several sets of the empirical constants are tested in the following data/theory comparisons and are specified in each figure. The term “no tip vortex” in the figures indicates that the tip vortex model was turned off for the specific predictions and that, these interaction tones are induced only by the forward rotor viscous wakes. The tone SPL sum was obtained (as in the case of steady loading and thickness noise) by adding all of the interaction noise tones on a mean-squared pressure basis.

The predictions presented in Figure 57a were performed using the empirical constants of $C_d = 0.02$, $C_i = 2$, $K_{vtx} = 2.0$, and $bt/S = 0.5$ for the tip vortex model. As discussed, the value of $C_d = 0.02$ produces such strong viscous wakes that the tip vortex effect is masked. However, the predictions with no tip vortex indicate that the clipping blade increases the interaction tone sum, which contradicts the data. The predictions in Figure 57b are performed with a C_d of 0.005; results indicate the accurate predictions of the clipping effect, but with the underpredictions of the SPL. Without the tip vortex model, Figure 57b shows that predictions for both the standard and clipped blades are underpredicted and that, the interaction tone noise is still higher for the clipped case than for the standard case. Figure 57c presents the predictions made with the same empirical constants used in Figure 57b, except C_i , the strength parameter of the vortex, is increased to 3.0. With this set of parameters, the data/theory comparisons show good predictions for the standard aft blade configuration; however, the inaccurate prediction of the clipped blades was still present. Since predictions with no tip vortex are not affected by the K_{vtx} and C_i values, the no tip vortex comparisons in Figures 57b and 57c are identical to each other.

Next, data and theory comparisons of the individual interaction tone directivity contained within the interaction tone sum of Figure 57c are examined utilizing the empirical constants of $C_d = 0.005$, $C_i = 3$, $K_{vtx} = 1$ and $bt/S = 0.5$. Figure 58 compares predicted and actual data for 1A+1F, 2A+1F, 1A+3F, 2A+2F and 3A+1F interaction tones (Table 9 identifies these interaction tones), both with and without the tip vortex model. For each interaction tone, the predicted Δ dB between standard and clipped aft rotors is in better agreement with the data for cases with tip vortex influence, as compared to those without tip vortex. Note that predictions for the clipped aft rotor (with or without the tip vortex model) have altered only slightly. However for most individual interaction tones, the predictions for the standard aft rotor with the tip vortex model have increased, relative to those without the tip vortex model. In general, it is obvious that the current acoustic prediction model including viscous wake/tip vortex model can not predict accurate individual interaction tones, even though (as demonstrated in Figure 57) the interaction tone sum can be well-predicted.

To examine the effect of the rotor viscous wake alone, Figure 59 demonstrates the predicted spanwise variation of the streamwise distance per chord, normalized wake centerline defect, and the semiwake width for Test Point 3706, with the C_d values of 0.02 and 0.005. This figure does not

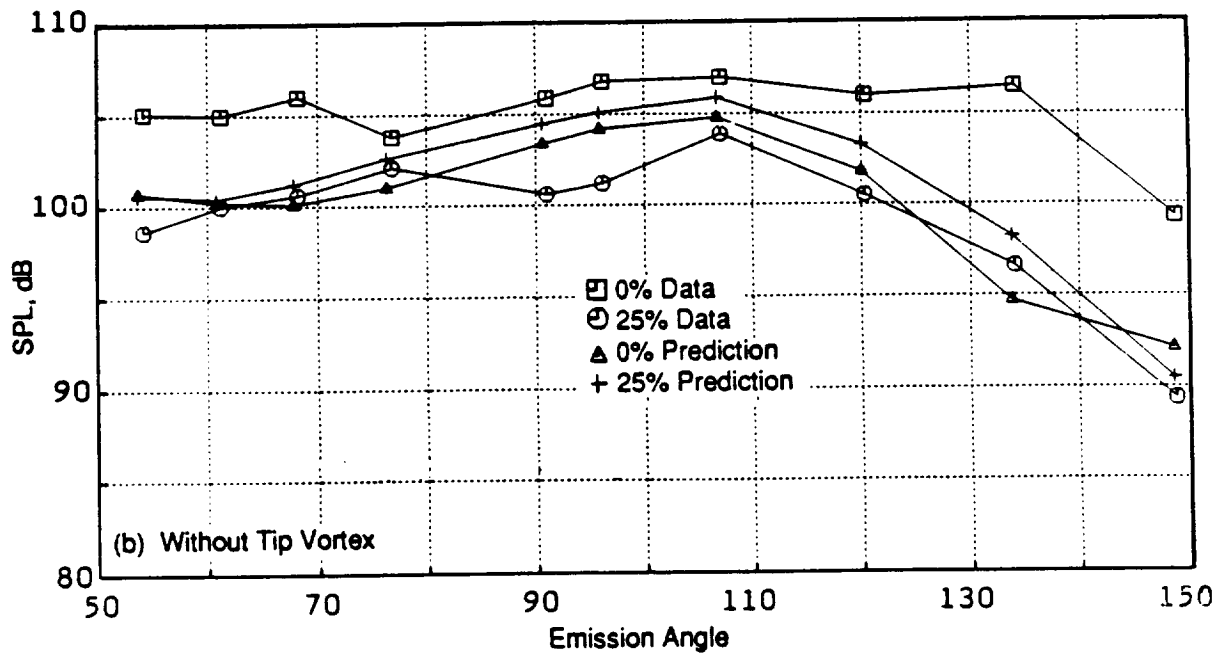
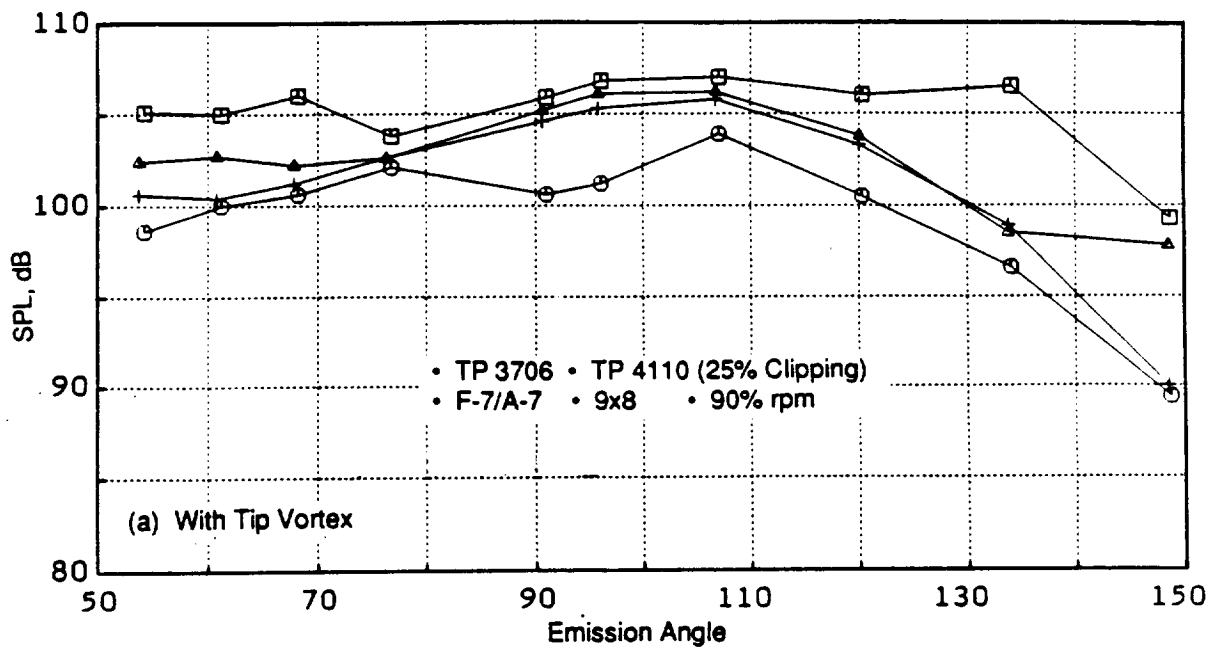


Figure 57a. Comparison of the Measured and Predicted Effect of Clipping of the Aft Rotor on Interaction Tone SPL Sum With and Without the Tip Vortex Model ($C_d = 0.02$, $C_l = 2$, $K_{vtx} = 2.0$, $bt/S = 0.5$).

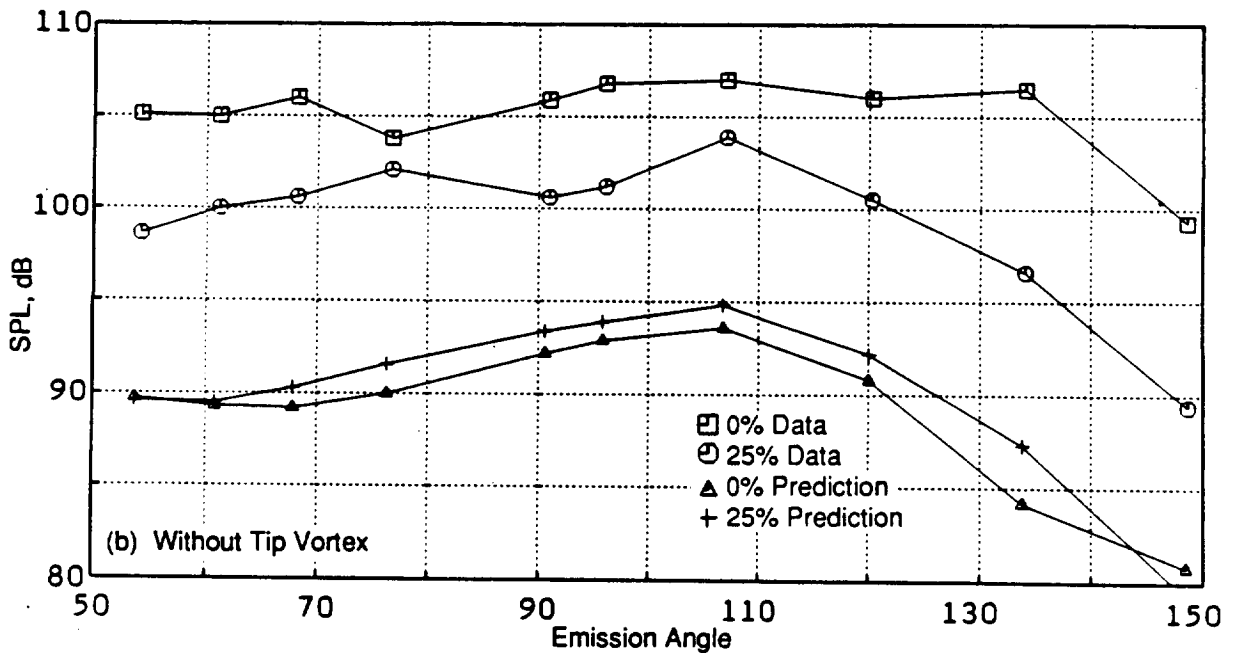
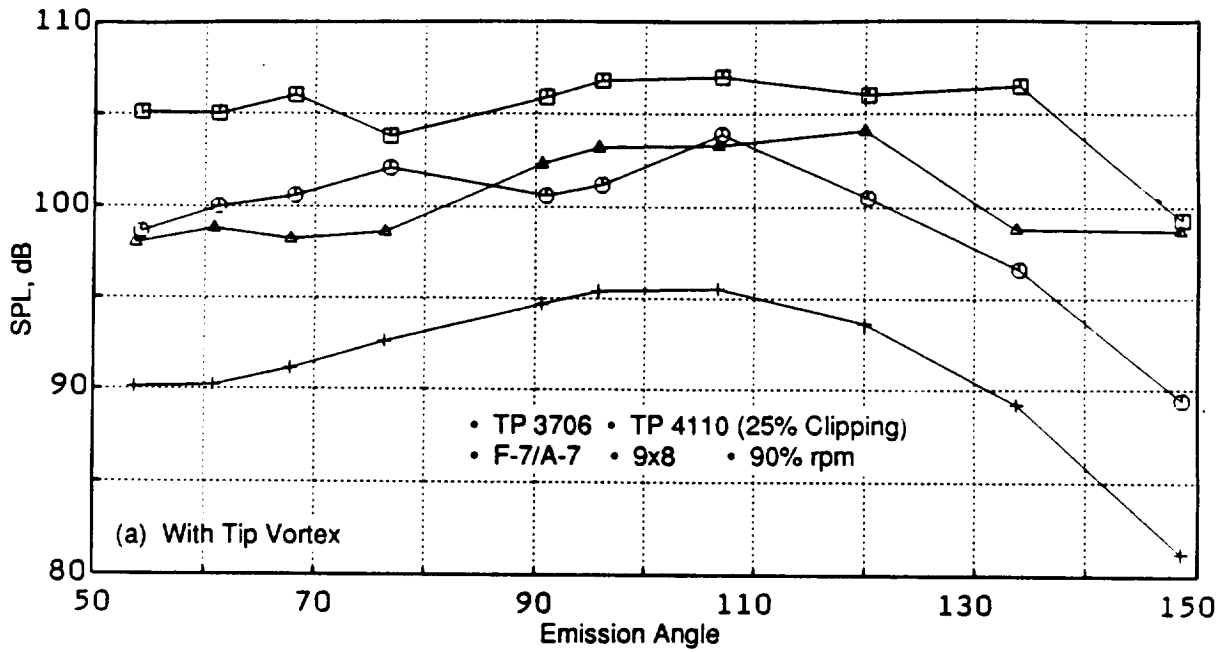


Figure 57b. Comparison of the Effect (Measured and Predicted) of Clipping of the Aft Rotor on Interaction Tone SPL Sum With and Without the Tip Vortex Model ($C_d = 0.005$, $C_l = 2$, $K_{vtx} = 2.0$, $bt/S = 0.5$).

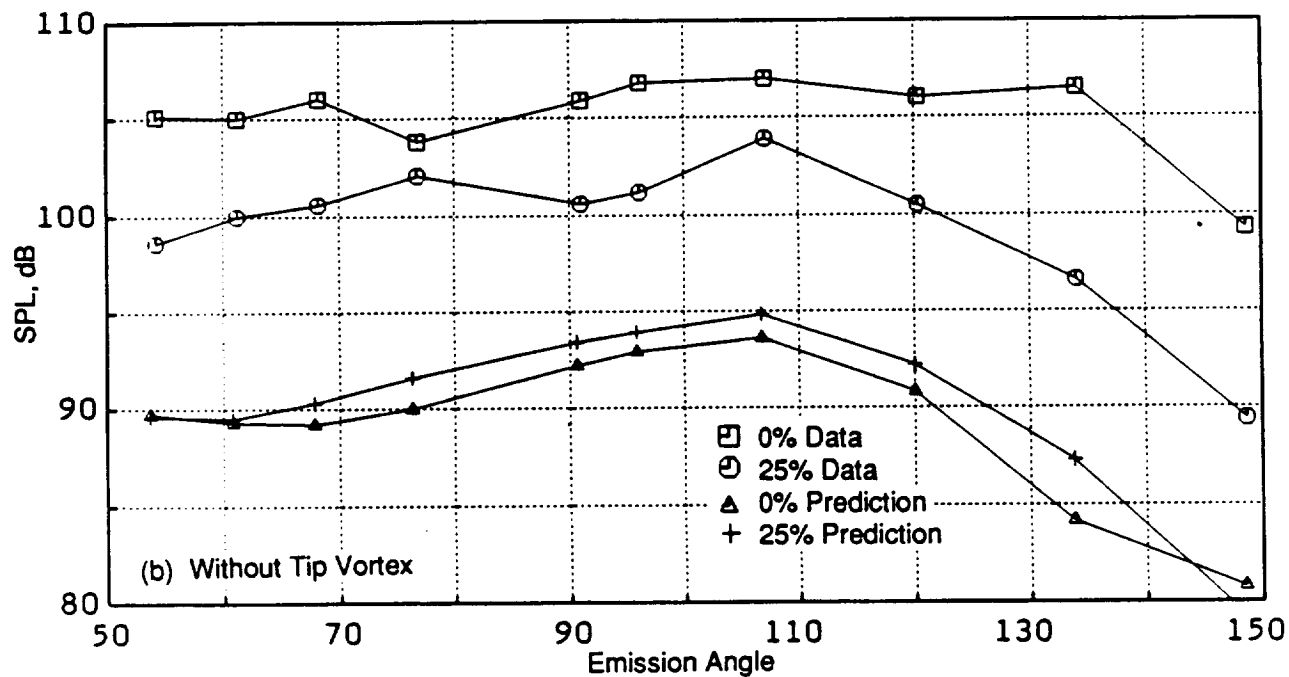
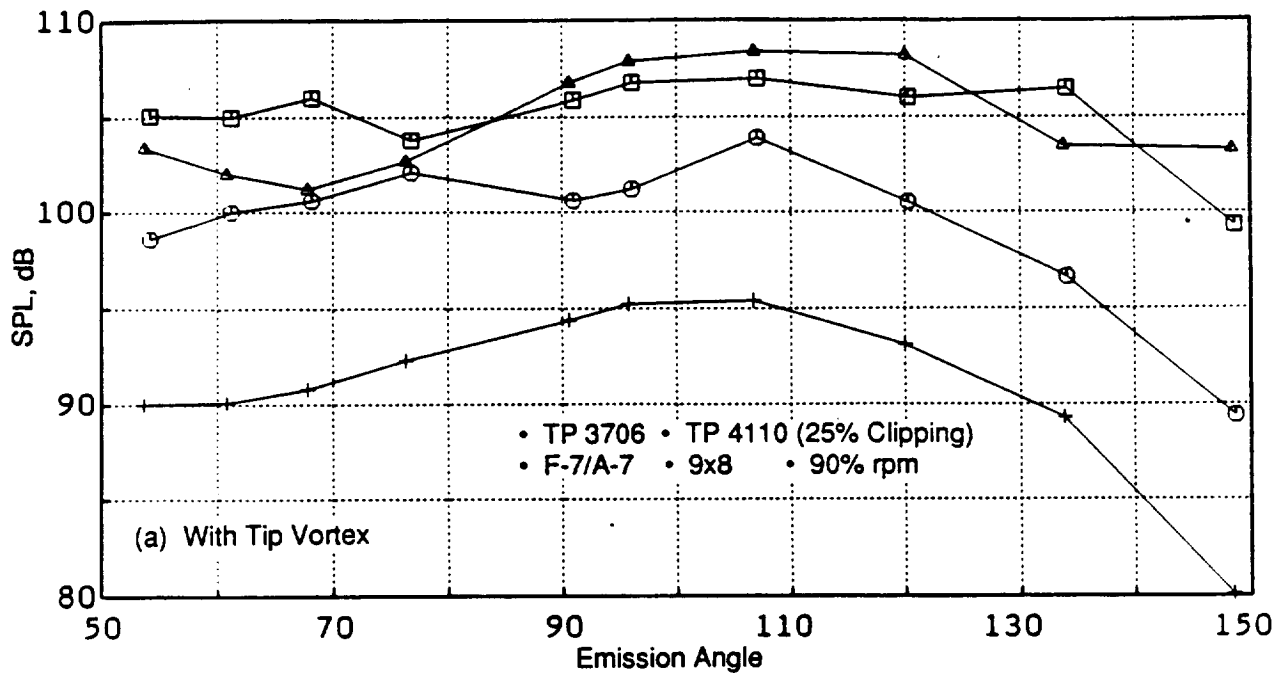


Figure 57c. A Measured and Predicted Effect Comparison of Clipping of the Aft Rotor on Interaction Tone Sum With and Without the Tip Vortex Model ($C_d = 0.005$, $C_i = 3$, $K_{vtx} = 2.0$, $bt/S = 0.5$).

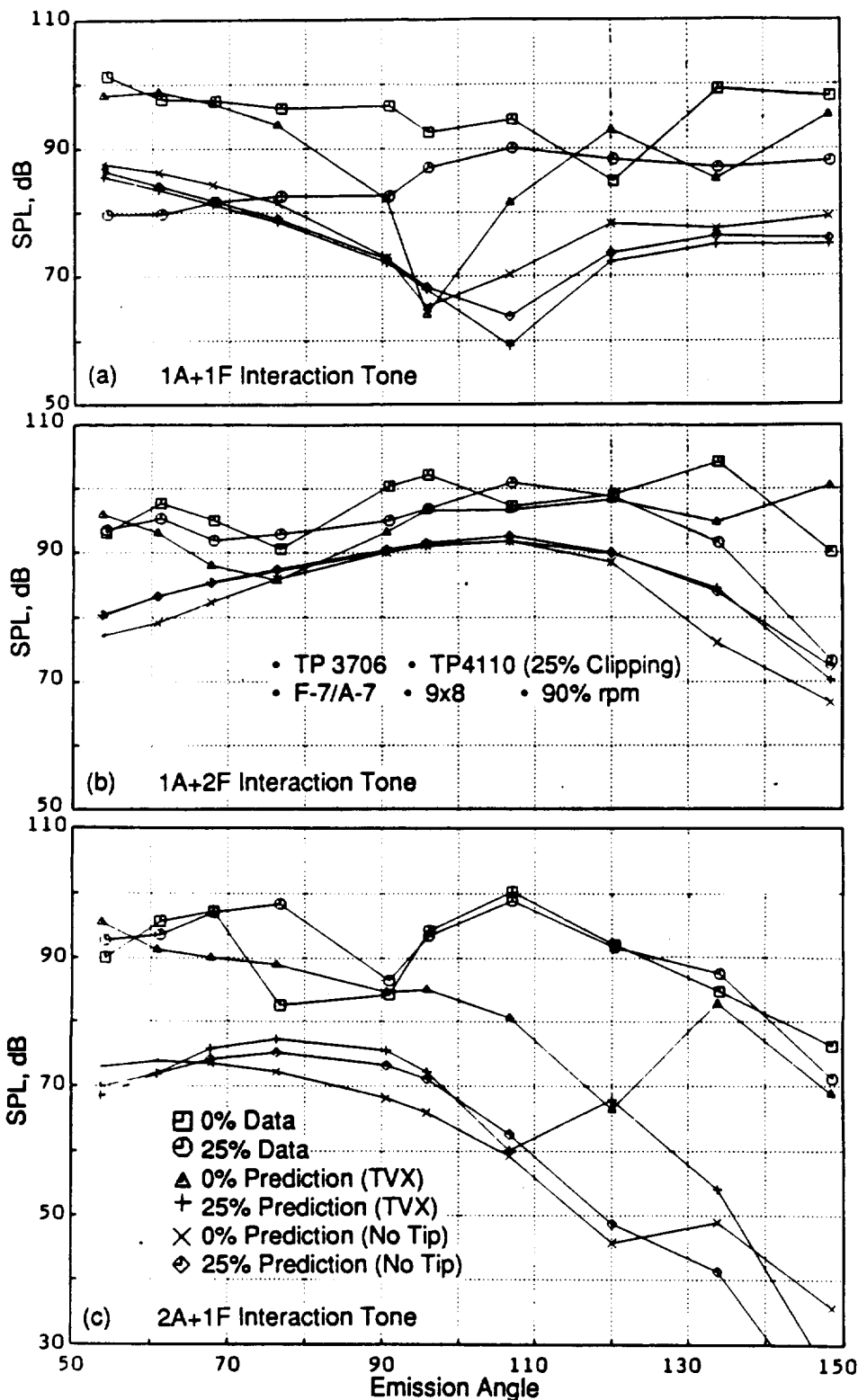


Figure 58. Comparison of the Measured and Predicted Effect of Clipping of the Aft Rotor on Individual Interaction Tones, With and Without the Tip Vortex Model ($C_d = 0.005$, $C_l = 3$, $K_{vtx} = 1.0$, $bt/S = 0.5$).

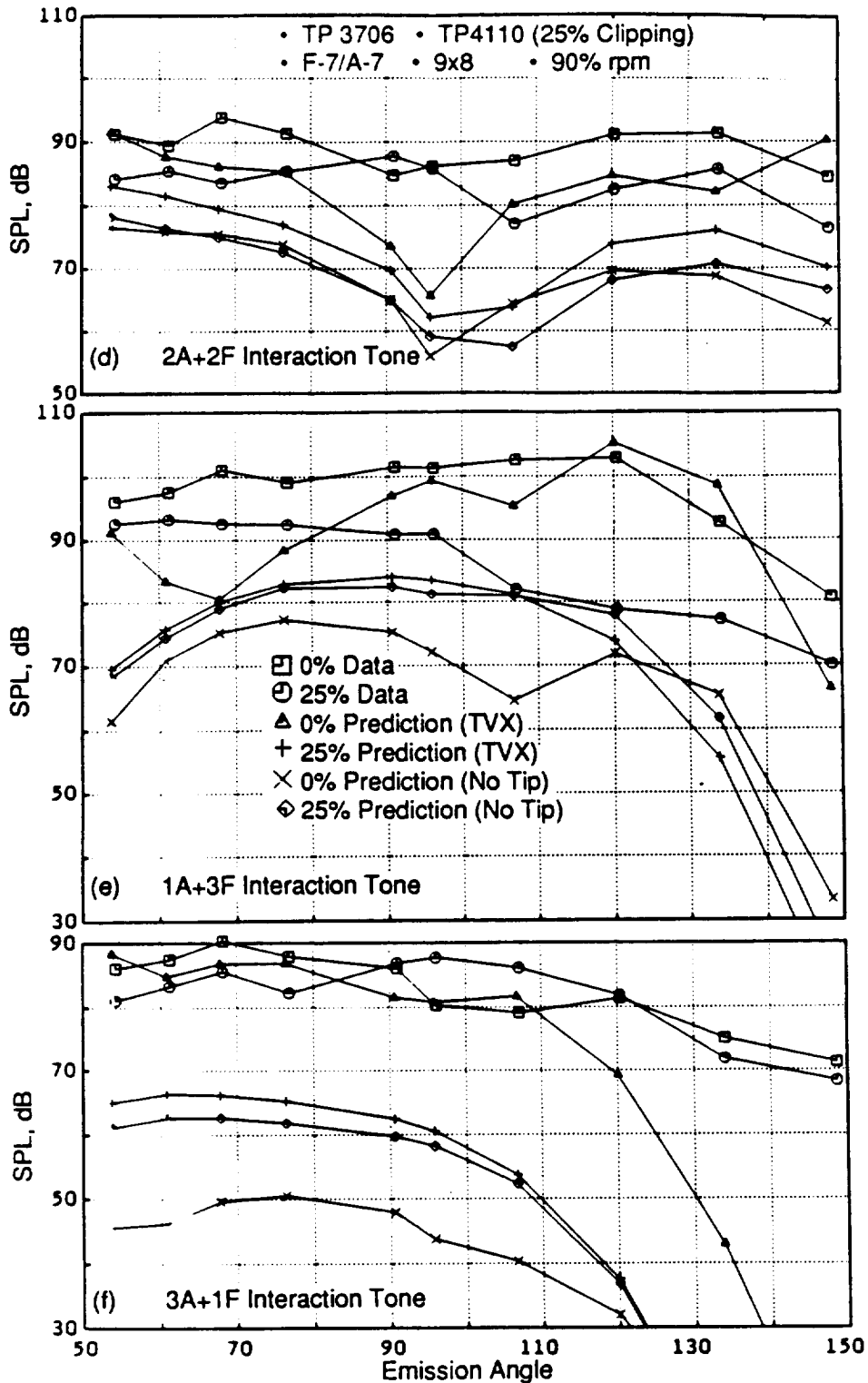


Figure 58. Comparison of the Measured and Predicted Effect of Clipping of the Aft Rotor on Individual Interaction Tones, With and Without the Tip Vortex Model ($C_d = 0.005$, $C_l = 3$, $K_{vtx} = 1.0$, $bt/S = 0.5$) Concluded.

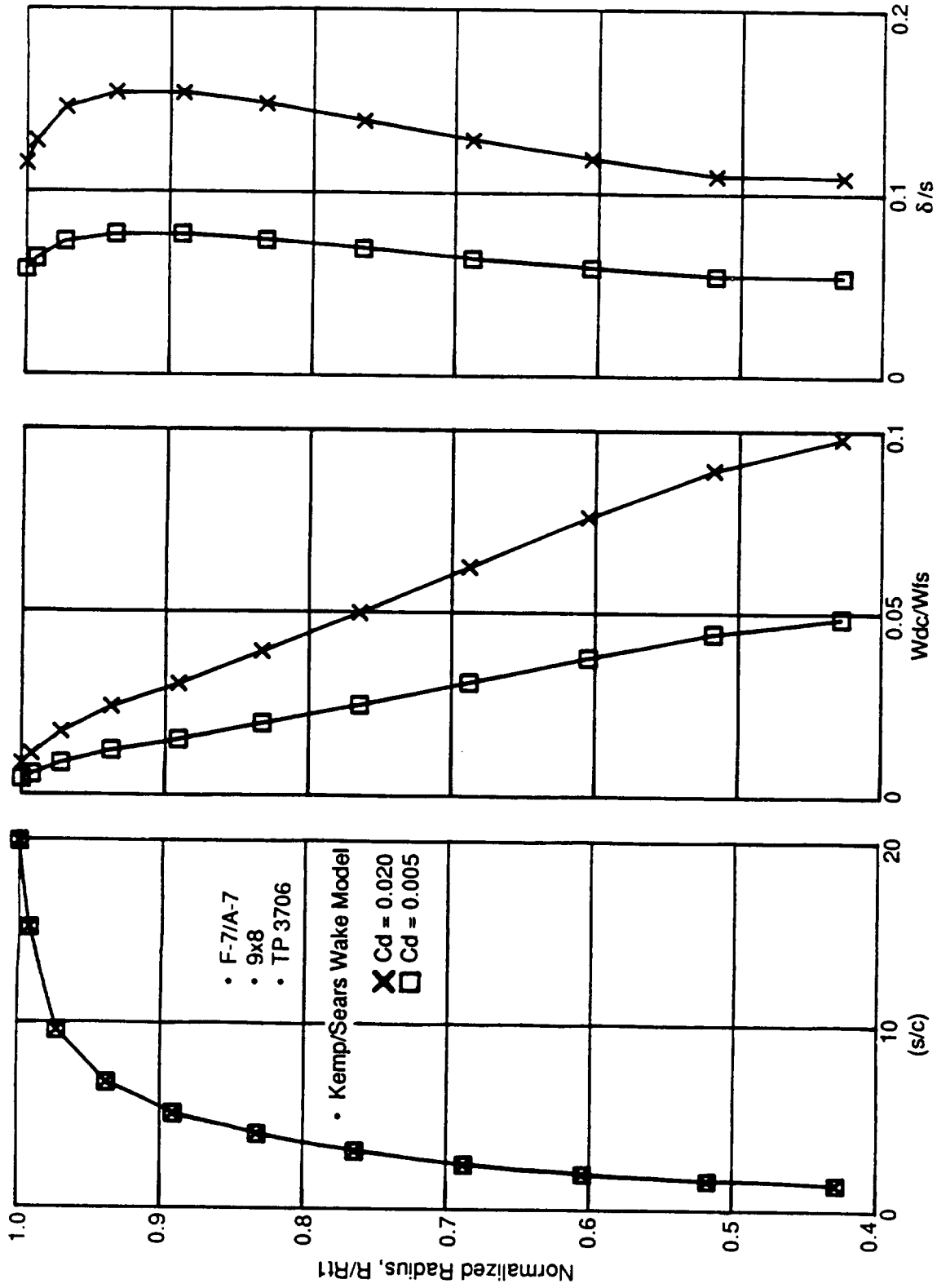


Figure 59. The Predicted Spanwise Variation of Normalized Streamwise Distance, Wake Centerline Defect, and Semiwake Width.

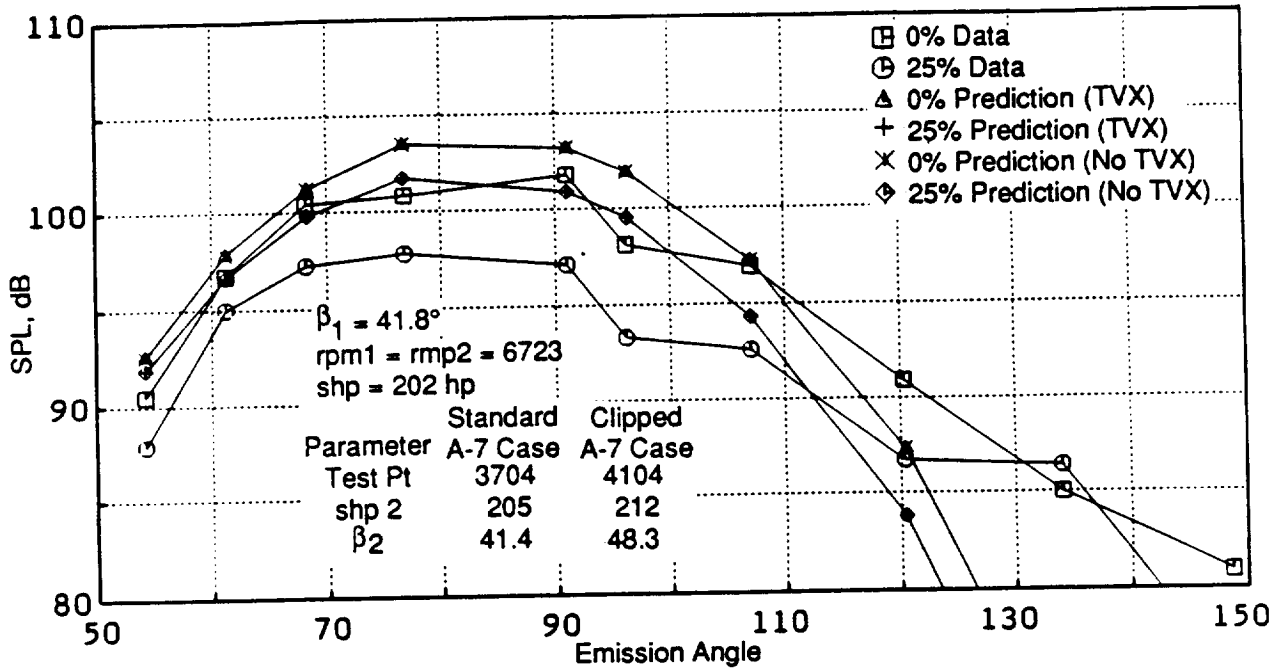


Figure 60. Comparison of the Measured and Predicted Effect of Clipping of the Aft Rotor on Steady Loading and Thickness Noise for 80% rpm.

contain the tip vortex effect. It is seen that due to relatively large s/c values in the tip region, the wake has decayed much more (compared to the hub region). The semiwake width determines the shape of the gust harmonic spectra, and the wake centerline defect determines the amplitude of the gust spectra (Reference 12). The harmonic falloff rate increases as the semiwake width increases. The amplitude of the gust spectra increases with a corresponding increase in the wake centerline defect. Due to the deeper (larger values of the wake centerline defect) and the narrower (smaller values of semiwake width) wakes in the hub region, compared to the tip region, the gust harmonic levels that are due to wake alone are much higher in the hub region than in the tip region. Therefore, the contribution of the wakes from the outer 25% span in the tip region probably is not a significant contribution to the total interaction noise. Accordingly, the outer 25% span of the aft rotor was clipped; the total interaction noise is not predicted to be much different from the standard blade case (for the wake alone model).

A set of data and theory comparisons also were generated for 80% rpm for standard (Test Point 3704) and clipped (Test Point 4104) aft rotor blades. Aeroperformance data for these two test points are contained in Figure 60, where the pitch angle of the clipped aft rotor is opened more (than that of the standard aft rotor) to recover performance loss caused by the clipping. Figure 60 compares the measured and predicted directivities of the tone SPL sum of steady loading and thickness noise for standard and clipped aft rotor configurations. As in the case of 90% rpm (Figure 56a), the predicted reduction in steady loading and thickness noise due to clipping of the aft rotor is in relatively good agreement with the data.

Figure 61 compares measured and predicted effects of clipping of the aft rotor on interaction tone SPL sum, with and without tip vortex model. The predictions are performed with the empirical

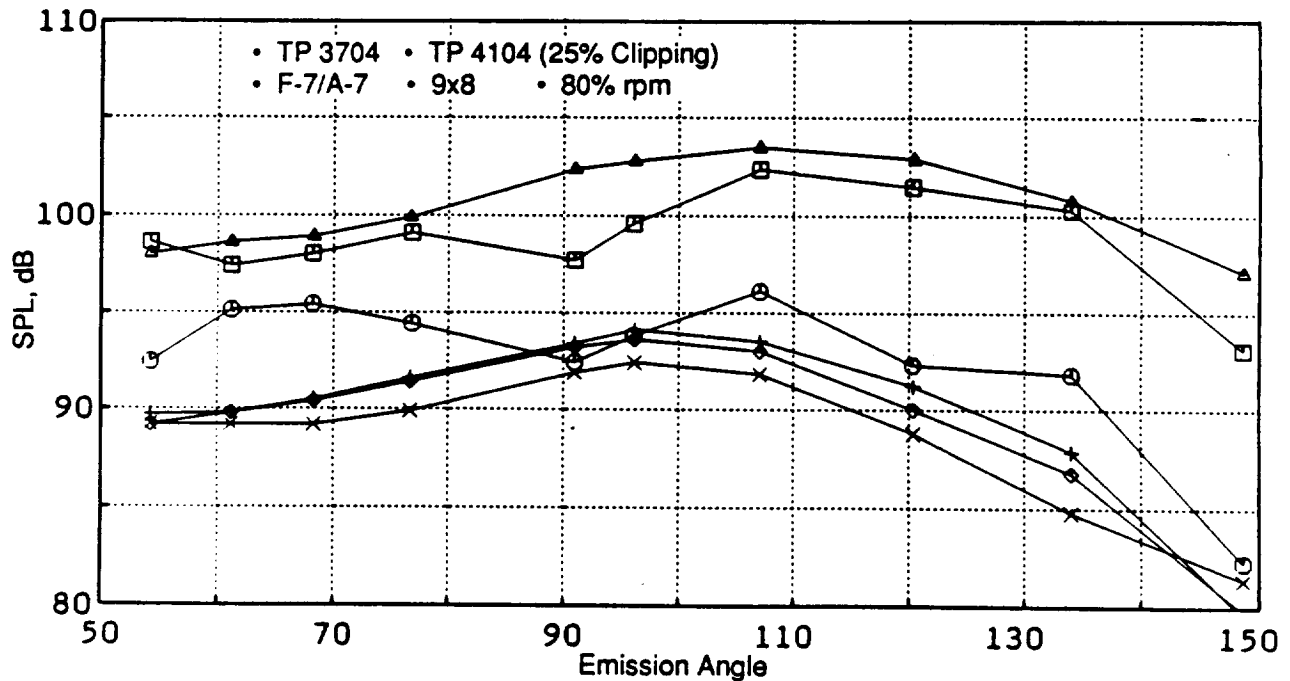


Figure 61. Measured and Predicted Effect of Clipping of the Aft Rotor on Interaction Tone SPL Sum With and Without the Tip Vortex Model ($C_d = 0.005$, $C_l = 3$, $K_{vtx} = 1.0$, $bt/S = 0.5$).

constants of $C_d = 0.005$, $C_l = 3$, $K_{vtx} = 1$, $bt/S = 0.5$, as in Figure 36 of the 90% rpm case. As in the case of 90% rpm (Figure 57), when the tip vortex model is included in the predictions, the predicted Δ dB between standard and clipped aft rotor is in better agreement with the data, as compared to those where the tip vortex model is not included. The predicted Δ dB with the tip vortex model between standard and clipped aft rotor, however, is greater than the measured Δ dB. Since the C_l (or strength) of the tip vortex is computed based on the average lift coefficient over the outboard 30% of the span in the current model (Reference 13), the strength of the tip vortex is reduced at lower rpm; hence, the prediction at 80% rpm (due to clipping) is seen as lower than that predicted at 90% rpm. The measured Δ dB due to clipping at 80% rpm is seen as greater than that at 90% rpm (Figures 57c and 61). Hence, the predicted change (with the tip vortex model) of the effect of clipping with rpm contradicts other data with this particular set of empirical constants.

Figure 62 summarizes the comparisons for the measured and predicted effect of clipping of the aft rotor on 1A+1F, 2A+1F, 1A+2F, 3A+1F, 2A+2F, and 1A+3F interaction tones at 80% rpm, with and without tip vortex. Figure 62 indicates that predictions for the standard aft blade are in relatively good agreement with the data using the tip vortex model, although data/theory comparisons for the clipped blade need improvement. In general, the predicted Δ dB (due to clipping of the aft rotor) when the tip vortex model is included is still in better agreement with the data, as compared to those predictions not including the tip vortex model.

These comparisons of data and theory show that the current model can be utilized to investigate the noise characteristics of the UDF® blade configuration and can, eventually, become a useful design tool when the empirical constants used in the present model will be determined accurately from well-controlled experimental studies.

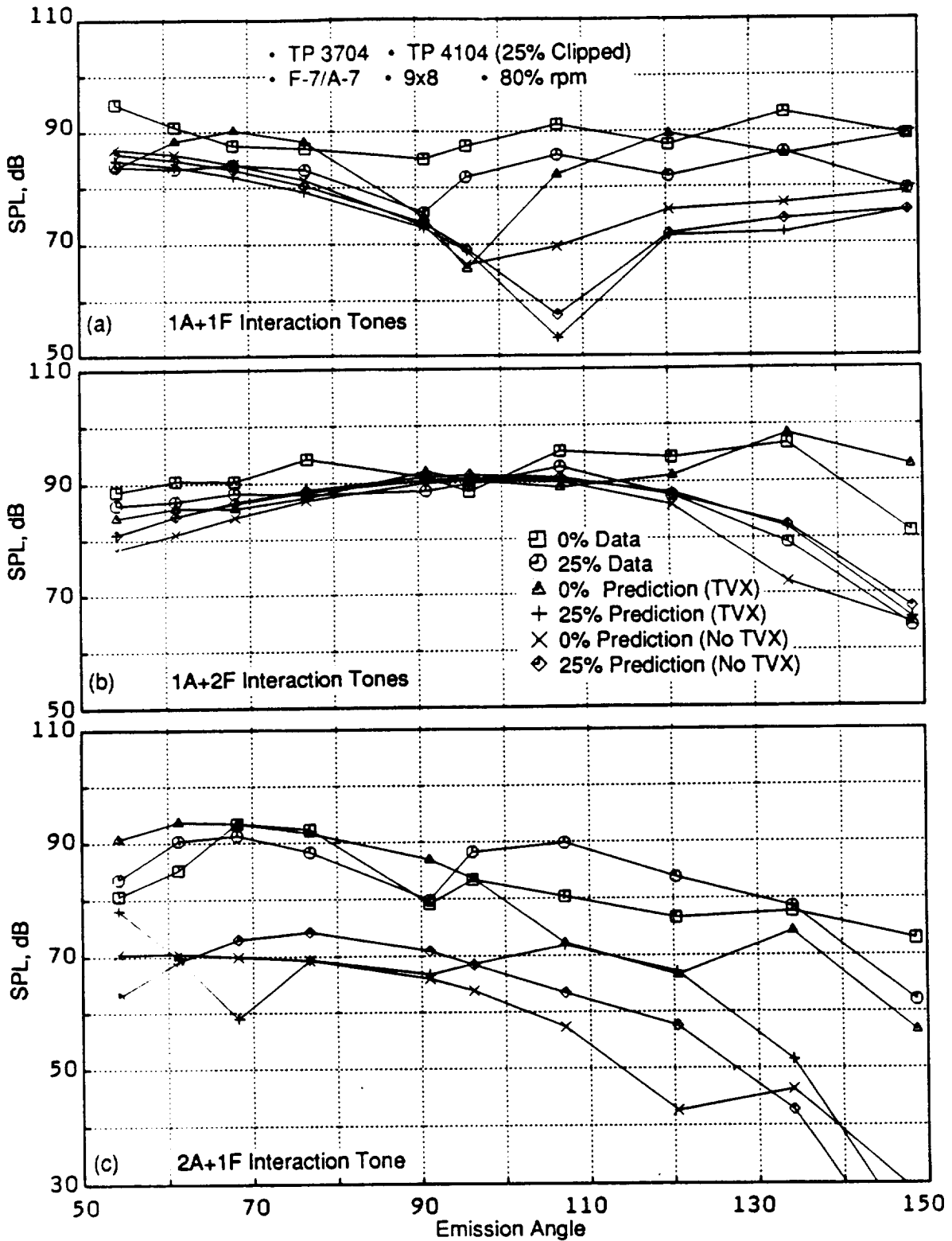


Figure 62. Comparison of the Measured and Predicted Effect of Clipping of the Aft Rotor on Individual Interaction Tones, With and Without the Tip Vortex Model ($C_d = 0.005$, $C_l = 3$, $K_{vtx} = 1$, $bt/S = 0.5$).

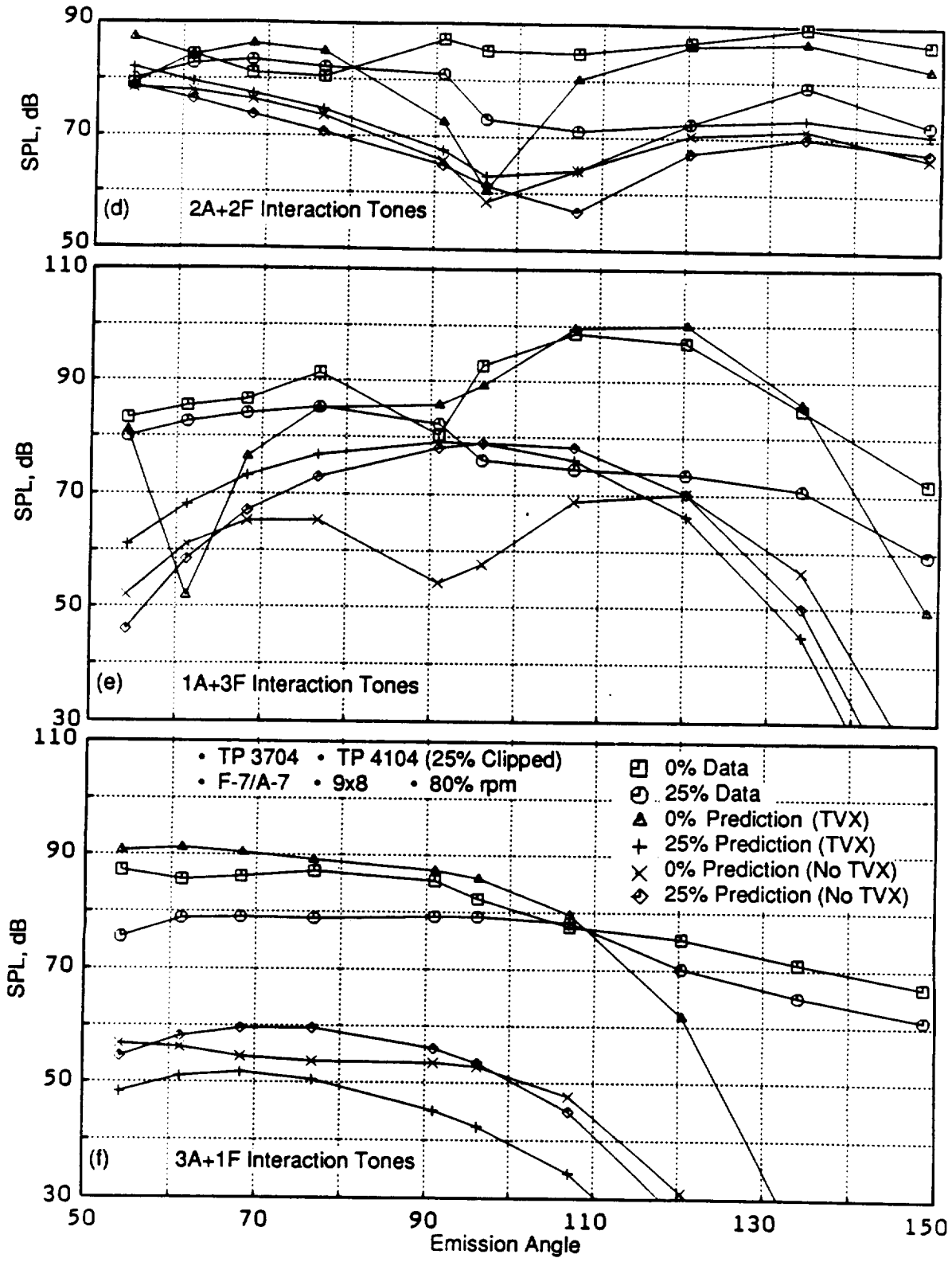


Figure 62. Comparison of the Measured and Predicted Effect of Clipping of the Aft Rotor on Individual Interaction Tones, With and Without the Tip Vortex Model ($C_d = 0.005$, $C_l = 3$, $K_{vtx} = 1$, $bt/S = 0.5$), Concluded.

3.4.3.3 Conclusions and Recommendations Related to the Tip Vortex Needed

This report has documented the analytical modeling, limited data and prediction comparisons, and certain key parametric studies pertaining to the tip vortex as a part of the noise–source mechanism for unsteady loading noise of counterrotating propellers. The viscous rotor wake effect is also modeled in order to compute the unsteady loading noise. The upwash field created by the combined tip vortex and the viscous rotor wake was analytically modeled employing an approach previously taken for fan tone noise. The strength, size, and streamwise development of the tip vortex are empirically modeled, based on fixed wing and helicopter rotor data. The present work should be considered as a basic frame model containing a number of empirical constants. These constants cannot be defined accurately at the present time, due to insufficient aerodynamics data for the UDF® blades configurations. However, the model had been structured in such a manner that it can be improved and refined with minor modifications when detailed UDF® aerodynamics data become available. Some of the significant conclusions and recommendations for future work are presented in the following sections.

The following significant conclusions are a product of the above–described analyses:

- The measured reduction in interaction noise due to clipping the aft rotor is very well predicted by the tip vortex model; however, the wake alone model (that is, without the tip vortex) could not predict the measured reduction in interaction noise due to clipping.
- Tip vortex trajectory does not have a noticeable impact on the interaction noise for the standard aft blade configuration; however, it controls the effectiveness of the clipping on interaction noise levels for the clipped aft blade configuration.
- The decay rate of the tip vortex has a significant effect on the noise reduction achievable due to an increase in rotor–to–rotor spacing.

Various physical parameters of the tip vortex, such as the tangential location and strength of the tip vortex, had to be extracted from the measured acoustic data. An improved aerodynamic model of the tip vortex would reduce the amount of empiricism in the model. These improvements can be attained either through experimental measurements of flow fields or through flow–field computations.

An axisymmetric model is recommended for the tip vortex (rather than an unwrapped annulus model), because of the significant geometric and aerodynamic radial variations of the blades. Such an approach may require a numerical solution rather than the analytical (closed form) solution that has been possible with the unwrapped annulus or rectilinear array of vortices adopted in the existing model.

In the current tip vortex model, an axial velocity component of the tip vortex has not been considered, which may affect the upwash perturbation velocity as much as the tangential component of the tip vortex.

3.5 Aeromechanical Analysis and Design Evaluation

Like any other device that operates in air, counterrotating blades could experience aeromechanical or aeroelastic vibration problems, which in turn, could lead to mechanical failure. This

is caused by the physical interaction of an elastic structure with the air. Examples of aeromechanical problems may be gleaned from aircraft wing, turbine engine airfoil, helicopter blade, and single-stage propeller technologies. The role of aeromechanics in propeller and fan blade development is twofold. First, it assures the mechanical safety of the propulsion system during the development phase and durability (long life) of the production design. Second, it provides understanding through analyses of aeromechanical problems so that such problems can be predicted and, thus, avoided during the design phase of a propulsion system. The helicopter rotor blade, single-stage propeller, and fan in a turbine engine are the closest relatives of counterrotating blades. Aeromechanical problems associated with these propulsive devices are expected to be pertinent to the aeromechanical design of counterrotating propulsion devices. Rotation of propellers/blades introduces centrifugal forces and an inherent periodic or cyclic loading on the blades and supporting structures which, due to their proximity, experience dynamic interactions that are mechanical or elastic and aerodynamic. Therefore, in the planned work it was important to review and identify the potential aeromechanical problems that could be encountered by counterrotating blades and to evaluate and analyze the selected designs for these phenomena.

Some of these phenomena, particularly those unique to counterrotating blades, have not been fully studied, and the implications are only marginally understood. For this reason, the aeromechanical efforts in this program were divided into the following three areas:

- Identify and define potential aeromechanical problems of unique counter-rotating blade concepts developed for this program
- Survey and review the criteria and analytical methods for the most pertinent problems
- Implement these criteria and analyses to evaluate prospective designs and assist in the identification of optimal aeromechanical design configurations consistent with desired aeroacoustic performance.

3.5.1 Aeroelastic Analyses

The linearized boundary-value problem for cascades both in steady- and unsteady-compressible flow is formulated in the GE GAP (General Aeroelastic Program), Figure 63, in terms of potential acceleration (or pressure), instead of velocity, for load evaluation of the blades. This acceleration potential is used for all three flow regimes (subsonic, transonic, and supersonic) for convenience, consistency, and other intrinsic advantages. One of these advantages is that the integral equation which relates the known downwash on the blade surface to the unknown pressure differential distribution over the blade need only be extended over the blade area, since the pressure jump across the wake is zero. Another advantage is that the known downwash distribution due to blade motion, which is explicitly defined, is not part of the integration; this is demonstrated by Equation 33. The 2D (two-dimensional) integral equation relating pressure and downwash distributions is given by the following general form, which is applicable to all pertinent flow regimes:

$$\frac{w(x)}{V_R} = \frac{\beta}{8\pi} \int_{-1}^1 \Delta C_p(\xi) K(x-\xi) d\xi \quad (33)$$

where

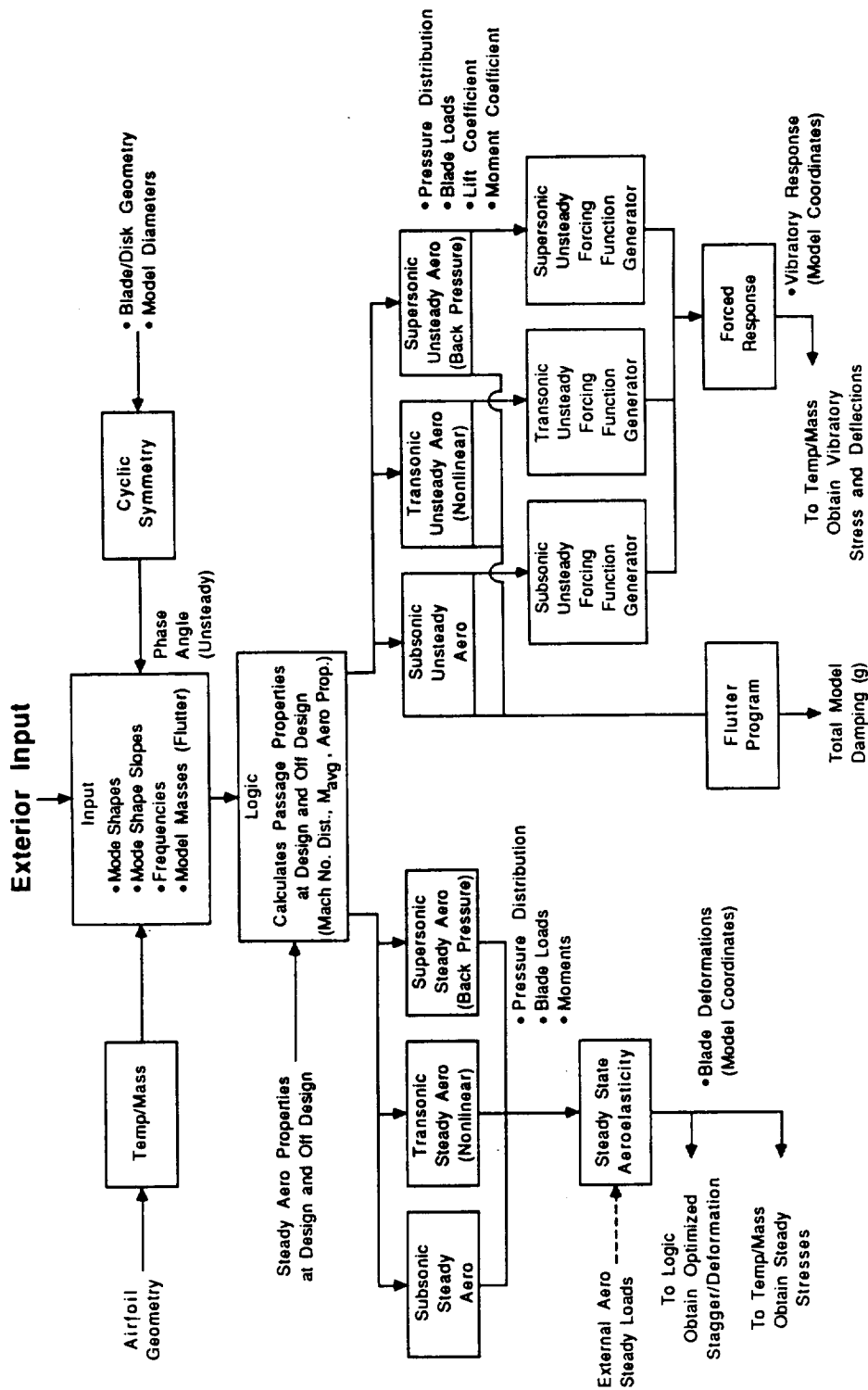


Figure 63. Flow Chart of the GAP (General Aeroelastic Program).

$w(x)$ = velocity amplitude normal to the blade surface (downwash) at any chordwise station x

β = $\sqrt{1-M^2}$ in subsonic flow,
 = $\sqrt{M^2-1}$ in supersonic flow, and M is the relative Mach number

V_R = the relative velocity

$\Delta C_p(\xi) = \frac{\Delta p(\xi)}{\frac{1}{2}\rho V_R^2}$ is the chordwise pressure differential distribution

$\Delta p(\xi)$ = the pressure difference along the blade chord

ρ = the fluid density

$K(x-\xi)$ = the 2D kernel function which physically represents the contribution to the airfoil surface velocity at a point x , due to a pulsating pressure doublet of unit strength which located at ξ on the airfoil surface.

Equation 33 is the integral equation to be solved for the unknown chordwise pressure differential coefficient distribution, $\Delta C_p(\xi)$, since both the kernel function, $K(x-\xi)$, and the downwash, $w(x)$, are known quantities. The general expression for the downwash (required on the left-hand side of Equation 33) is given by:

$$\frac{w(x)}{V_R} = \left(j \frac{k}{b} + \frac{\partial}{\partial x} \right) z(x) \quad (34)$$

where $k = wb/V_R$ is the reduced frequency, based on the semichord, and $z(x)$ is the instantaneous small displacement of the chordline. When $z(x)$ is expressed in terms of modal displacements, Equation 34 becomes:

$$\frac{w(x)}{V_R} = \sum_{r=1} \left(\frac{jk}{b} + \frac{\partial}{\partial x} \right) A^r(x) q_r \quad (35)$$

for modal steady ($k = 0$) and unsteady aero load evaluation. This approach is employed in the GAP for evaluation of both steady- and unsteady-pressure and for steady aeroelastic, flutter, and forced vibratory response applications.

3.5.1.1 Steady Aerodynamic Load Evaluation

The steady modal aerodynamic loads required for steady-state aeroelastic response evaluation, including chordwise mode shapes, are represented by the following:

$$\{Q_r\}_A = \begin{bmatrix} A_{x_m}^{r+} & A_{z_m}^{r+} & \theta_{y_m}^{r+} \end{bmatrix} \begin{Bmatrix} \{Q_{x\alpha}\}_m \\ \{Q_{z\alpha}\}_m \\ \{Q_{\alpha\alpha}\}_m \end{Bmatrix} \quad (36)$$

and

$$\{Q_{rk}\}_A = \begin{bmatrix} A_{x_m}^{r+} & A_{z_m}^{r+} & \theta_{y_m}^{r+} \end{bmatrix} \begin{Bmatrix} \{F_{1r}\}_m \\ \{F_{2r}\}_m \\ \{F_{3r}\}_m \end{Bmatrix} \quad (37)$$

where

$$\begin{aligned} \{Q_{x\alpha}\}_m &= [\sin \bar{\theta}_{y_m}] \{L_m\} \\ \{Q_{z\alpha}\}_m &= [\cos \bar{\theta}_{y_m}] \{L_m\} \\ \{Q_{\alpha\alpha}\}_m &= \{M'_m\} \end{aligned} \quad (38)$$

and

$$\begin{aligned} \{F_{1r}\}_m &= [\sin \bar{\theta}_{y_m}] \{L_m^r\} \\ \{F_{2r}\}_m &= [\cos \bar{\theta}_{y_m}] \{L_m^r\} \\ \{F_{3r}\}_m &= \{M'_m{}^r\} \end{aligned} \quad (39)$$

and

$$\begin{aligned} A_{x_m}^{r+}, A_{z_m}^{r+} &= \text{the } r\text{th nondimensionalized mode shapes in the } x\text{+ axis, respectively,} \\ &\quad \text{at the } x\text{+ chordwise stations} \\ \theta_{y_m}^{r+} &= \text{the } r\text{th slope of the mode shape about the } y\text{+ axis at the } x_m \text{ chordwise} \\ &\quad \text{stations} \\ \bar{\theta}_{y_m} &= \text{the difference between the camber slope and the stagger at the } x_m \\ &\quad \text{chordwise stations.} \end{aligned}$$

Chordwise distribution of elemental flexible modal loads L_r and moments M'^r are evaluated from the steady-state chordwise pressure distributions by substituting Equation 35 with $k = 0$ in the downwash on the left side of Equation 33, which becomes:

$$\frac{w(x)}{V_R} = \sum_{r=1} \theta_y^r(x) q_r = \frac{\beta}{8\pi} \int_{-1}^1 \Delta C_p(\xi) K(x-\xi) d\xi. \quad (40)$$

The modal elemental loads and moments are evaluated for each mode shape and will be of the form:

$$L_m^1, L_m^2, L_m^3, \dots, L_m^r \text{ with } q_r = 1$$

$$M_m^1, M_m^2, M_m^3, \dots, M_m^r \text{ with } q_r = 1$$

for $r = 1, 2, \dots$, number of modes to be analyzed.

3.5.1.2 Flutter Analysis

The chordwise pressure differential coefficient distribution $\Delta C_p(\xi)$ is now complex and a function of reduced frequency.

Unsteady modal aerodynamic loads required for flutter analysis, including chordwise mode shapes, are obtained with Equations 37 and 39; an evaluation of blade flutter (instability) is determined from the solution of the dynamically coupled modal equations given by:

$$[M_{rk}] \{\ddot{q}_k\} + [(1+jg_r)M_r \omega_r^2] \{q_r\} = [Q_{rk}]_A \{Q_k\} + \{Q_r\}_G \quad (41)$$

with

$$\{Q_r\}_G = 0$$

where

$[M_{rk}]$ = the modal mass matrix

g_r = the r th modal structural damping at speed

ω_r = the r th blade frequency at speed

$[Q_{rk}]_A$ = the unsteady generalized aerodynamic force matrix, where Q_{rk} is the r th mode force induced by the k th deformation made at speed

$Q_r G$ = the r th mode unsteady gust loading

q_r = the r th generalized coordinate

$k = r$ = the number of modes in the analysis, = 1,2,3,...

Simple harmonic motion is assumed throughout this analysis, which states that:

$$\ddot{q}_k = -(\omega)^2 q_k.$$

Flutter is obtained from the solution of Equation 41 when the total damping, aero plus structural, becomes zero.

3.5.1.3 Forced Response Analysis

Inflow distortion patterns are usually presented in the form of absolute total pressure or absolute velocity distributions as the combination of superposed radial and circumferential components. For compatibility with forced vibratory response prediction methods in the GAP, either of these distributions is transformed into radial and circumferential components of downwashes. A given arbitrary inlet pressure or velocity distortion pattern will first be transformed into an inlet distortion pattern of velocity downwashes prior to being decomposed into its Fourier harmonics. For instance, Figure 64 presents an arbitrary circumferential absolute total pressure pattern for two spanwise

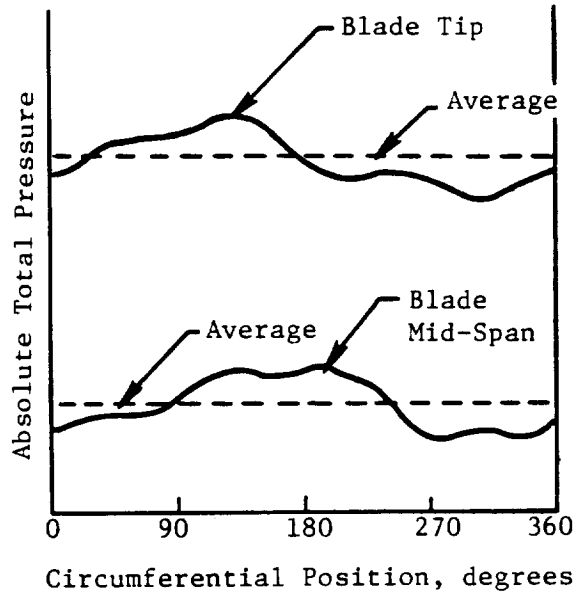


Figure 64. Schematic of Pressure Distortions.

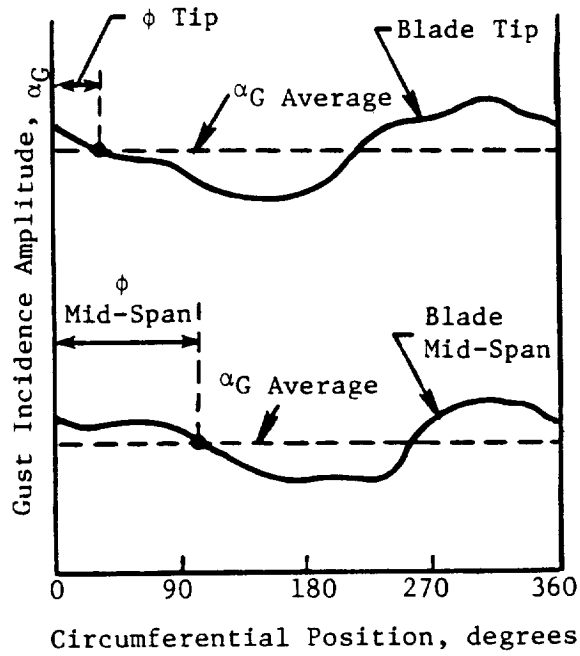


Figure 65. Schematic of Incidence Variation Due to Pressure Distortion.

point-by-point to a circumferential gust incidence amplitude distortion pattern (Figure 65). The resulting circumferential gust incidence pattern is then decomposed into its Fourier components to yield:

$$\alpha_G = \alpha_{G_{avg}} + \sum_{n=1}^{\infty} \alpha_{G_n} \sin n\omega t \quad (42)$$

where

$\alpha_{G_{avg}}$ = the average circumferential gust incidence amplitude to distortion

α_{G_n} = the nth harmonic gust incidence amplitude.

The average circumferential gust incidence amplitude for the clean inlet reference pressure or velocity characteristics is merely the steady-state spanwise blade LE incidence distribution. To obtain baseline gust incidences, clean inlet or reference harmonic gust incidence amplitudes are also evaluated since these may also produce significant resonant vibration stresses.

Unsteady loads (due to unit sinusoidal gust downwash) are generated from the unsteady subsonic, transonic, and supersonic programs presently available in the GAP as is shown in Figure 63. Evaluation of gust amplitude and phase variation along the blade span due to arbitrary inlet distortion patterns is presented below.

The sinusoidal gust incidence amplitude is shown in Reference 28 to be of the form:

$$\frac{w_G}{V_R} = \alpha_G \exp \left[j\omega(t - xb/V_R) \right] \quad (43)$$

where α_G contains the n-harmonic-incidence amplitudes given by Equation 42 for any arbitrary inlet distortion pattern at any spanwise blade station. The sinusoidal gust amplitude for the nth harmonic at the blade tip, for instance, can be written as:

$$\left(\frac{w_G}{V_R} \right)_n = \alpha_{G_n} \exp \left[j(n\omega t - nk_n x - \phi_{tip}) \right]. \quad (44)$$

Since periodicity is assumed, the circumferential position of the n-harmonics in the above equation is immaterial as long as all blade spanwise phase angles are referred to a common, or reference, circumferential position as depicted in Figure 65. Equation 44 can be rewritten as:

$$\left(\frac{w_G}{V_R} \right)_n = \alpha_{G_n} e^{-j\phi} (\cos k_n x - j \sin k_n x) e^{jn\omega t} \quad (45)$$

where

$n\omega$ = $n\Omega$ (at resonance)

k_n = $\omega_r b/V_r$ is the reduced frequency of the rth vibration mode

ω_r = $\Omega (N/\text{rev})/60$ (at resonance).

$N/\text{rev} = n$ denotes the engine order integers; also the number of blade passages per revolution.

From Equation 45, the unsteady sinusoidal gust amplitude to be introduced into the loads calculation is:

$$\text{Unsteady gust amplitude} = \alpha_{G_n} e^{-j\phi}, \quad (46)$$

and the unsteady loading for a unit sinusoidal gust downwash is:

$$\left(\frac{W_G}{V_R} \right)_n = (\cos k_n x - j \sin k_n x) e^{jn\omega t}. \quad (47)$$

At resonance, the reduced frequency corresponds to $k_n = (n\Omega)b/V_r$ at a given spanwise blade station since the semichord b and the relative inlet velocity V_r vary along the blade span. The phase angle is obtained from the harmonic decomposition of the distortion pattern at all spanwise blade stations for each harmonic n . Thus, both the phase angle ϕ as well as the amplitude α_{G_n} at any spanwise blade station will vary for each harmonic n .

The unsteady pressure distributions $C_p(\xi)$, due to sinusoidal gusts, are evaluated by substituting Equation 45 into the kernel function, Equation 33. The dynamically coupled modal equation for forced response evaluation is shown in Equation 41 where, for forced response, $\{Q_r\}_G = 0$. Also, the harmonic motion assumption is now of the form:

$$\ddot{q}_k = -(n\omega)^2 q_k \equiv -(n\Omega)^2 q_k, \quad (48)$$

following Equation 45.

Substituting Equation 48 into 41 and solving this latter equation for the complex generalized response q_k for each harmonic n by direct inversion yields the following:

$$\{q_k\}_n = \left[-(n\Omega)^2 [M_{rk}] + \left\{ (1+jg_r) M_r W_r^2 \right\} - [Q_{rk}]_A \right]^{-1} \{Q_r\}_G. \quad (49)$$

The unsteady modal generalized aerodynamic loads $[Q_{rk}]_A$ and gust loads $\{Q_r\}_G$ are functions of the reduced frequencies $k_n = (n\Omega)b/V_r$, as defined in Equation 45.

It should be noted that Equation 49 has a full “ $r \times r$ ” matrix, as utilized in this program, and not a series of “ r ” uncoupled matrices since the unsteady generalized aerodynamic matrix $[Q_{rk}]_A$ is not a diagonal matrix. Without this aerodynamic matrix, only the structural damping g_r would provide the vibratory deflection amplitude at resonance for vibratory stress evaluation.

3.5.2 Stability Analyses

An evaluation of the stability of the UDF®/MPS blades was conducted by utilizing GE’s GAP (Figure 63); the GAP code was verified by comparing its predictions against experimental data from several turboprop blade designs.

The CDR provides a detailed description of the correlations with the NASA SR–3 and SR–5 blade stability predictions obtained from using the code with test data. This comments on the effects of cascading (number of blades in a given stage) and chordwise deformations on the stability characteristics of swept turboprop blades.

Analysis of the turboprop blades indicated that chordwise variation of the mode shape (referred to as “mode–shape slope”) is a key parameter in influencing the stability of a given aero design.

Since the mode–shape slope and its spanwise variation can be controlled by judiciously selecting the ply definitions (material properties, orientations, and stackup) on composite blading, such as that of the MPS blades; the mode–shape slopes have become one of the main design parameters.

Aeromechanical design of these blades is accomplished in two phases. In the preliminary design phase, the designer evaluates candidate ply definitions for a selected aero profile of the blade. This evaluation is accomplished by checking mode–shape slopes against preliminary design rules (Figures 66 and 67), obtained through compilation of test/analysis data from numerous turboprop blade designs. These rules identify stable and unstable combinations of mode–shape slopes and reduced frequencies for the fundamental modes, 1F (first flex) and 1T (first torsion). If one of the candidate ply definitions satisfies the preliminary design guidelines comfortably, it is adopted in the design release for blade fabrication. Using the GAP code for quantitative design records, final aeromechanical evaluation of a design release is conducted.

Most of the candidate designs usually fall in the “gray” boundary zone which separates the stable and unstable regions. The reason for this is that every new design selected represents an incremental venture in extending the known state–of–the–art design technology. A full stability audit, utilizing the GAP code, is conducted on those designs which do fall in the gray area. This audit identifies the following if the blade is unstable:

- Modal diameter of the potential flutter response
- Instability frequency (which could be significantly different from the normal mode frequency)
- The dominant vibratory pattern
- Behavior of aerodynamic damping versus interblade phase angles in normal modes
 - oThe effects of cascading, density variation, changes in mode–shape slopes, and increases in relative Mach number in the blade channels.

This information provides the designer with insights for design tradeoffs. Each subsequent, improved design is again judged on the basis of mode–shape slope versus reduced frequency, against the background of the detailed flutter analysis previously performed. A comprehensive flutter analysis is then conducted on the final design before the blade is released for fabrication.

Stability analyses were performed for several UDF® blade configurations as part of this contract. These configurations are identified as: F–4/A–4, F–5/A–5, F–7/A–7, F–11/A–11, and F–21/A–21.

Stability estimates for the F–4/A–4 and F–5/A–5 are shown in Figures 68 and 69, respectively. These stability plots are in terms of the aerodynamic damping coefficient, g_{aero} , versus the interblade phase angle, γ . In other more familiar terminology, the damping (g_{aero}) corresponds to the loss factor, η , or to δ/π where δ is the logarithmic decrement, or to $1/Q$ where Q is the synchronous amplification or quality factor. The interblade phase angle (γ) is related to the response nodal diameter through $\gamma = 360^\circ n/N_B$ where n is the nodal diameter, and N_B is the number of blades in the stage. Thus, for the MPS 8+8 configurations, $\gamma = 45^\circ n$. Note that $\gamma = 0 - 180^\circ$ corresponds to FTW (forward traveling waves), and that $\gamma = 180^\circ - 360^\circ$ corresponds to BTW (backward traveling waves).

There were two ply layups for the F–4/A–4 and F–5/A–5 blades; they are discussed in greater detail in Section 4.1. The first set of these blades had 5–mil, 80%/20% graphite/glass plies; the

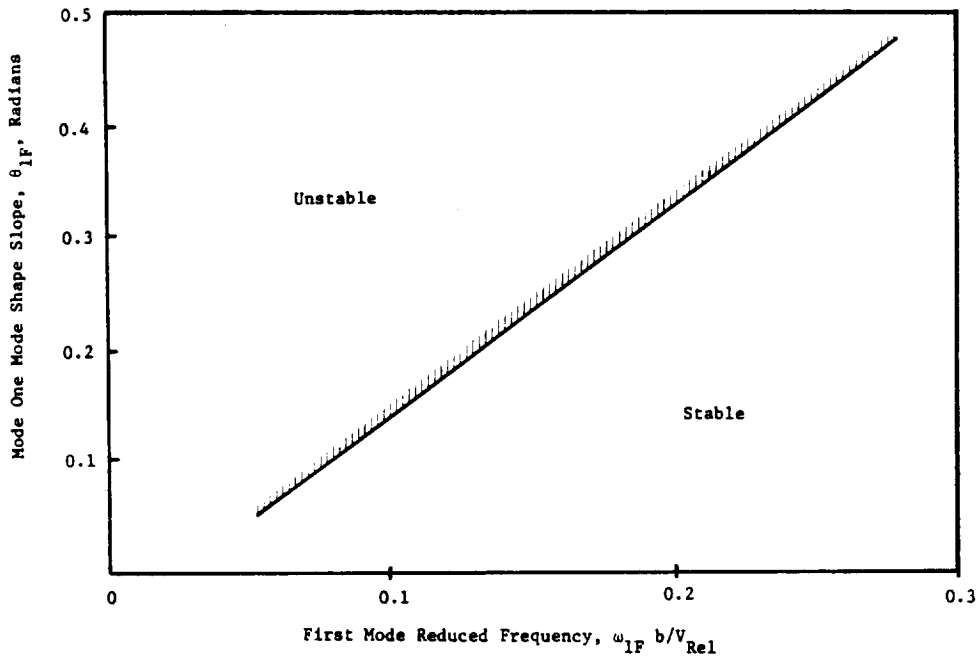


Figure 66. Turboprop Blade First Flexural Stability Estimate.

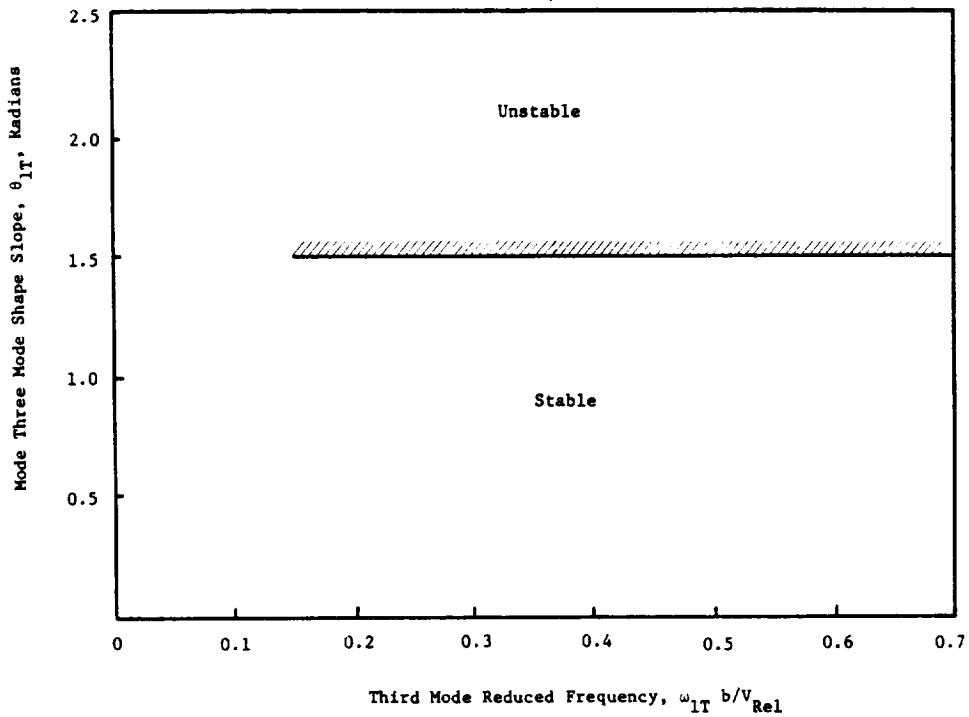


Figure 67. Turboprop Blade First Torsion Stability Estimate.

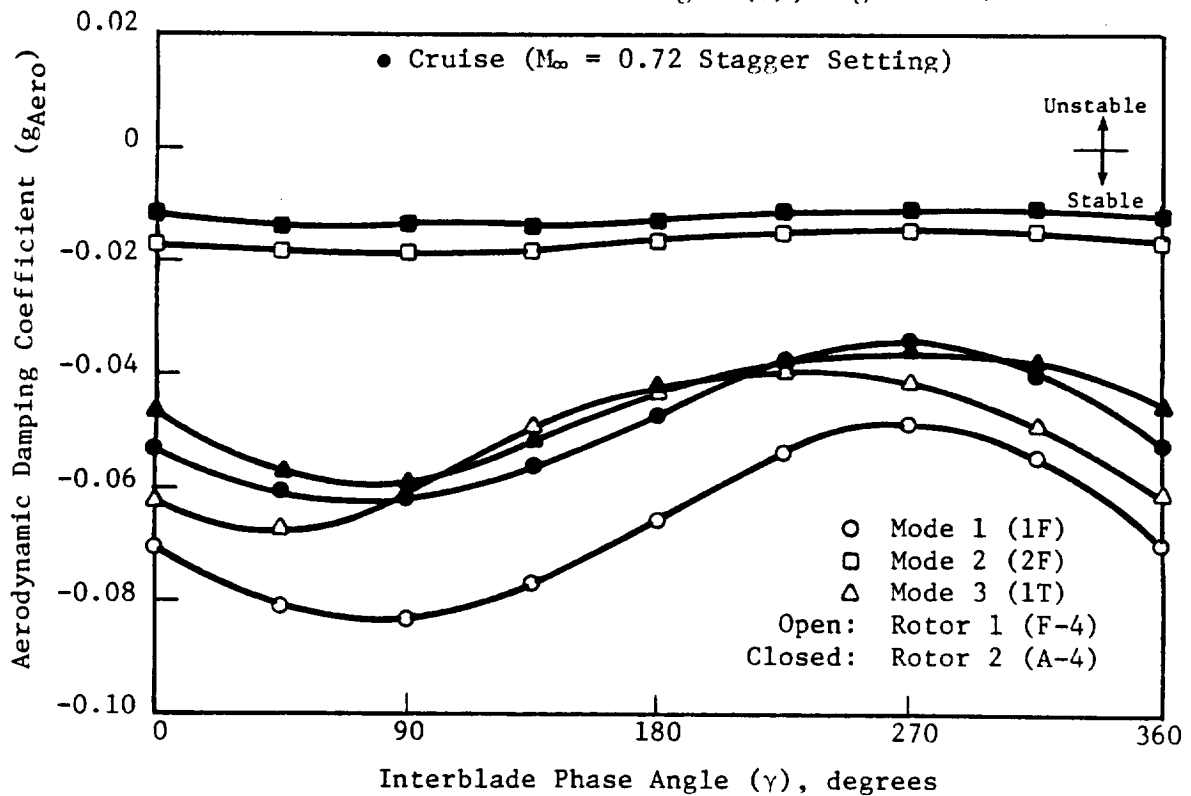
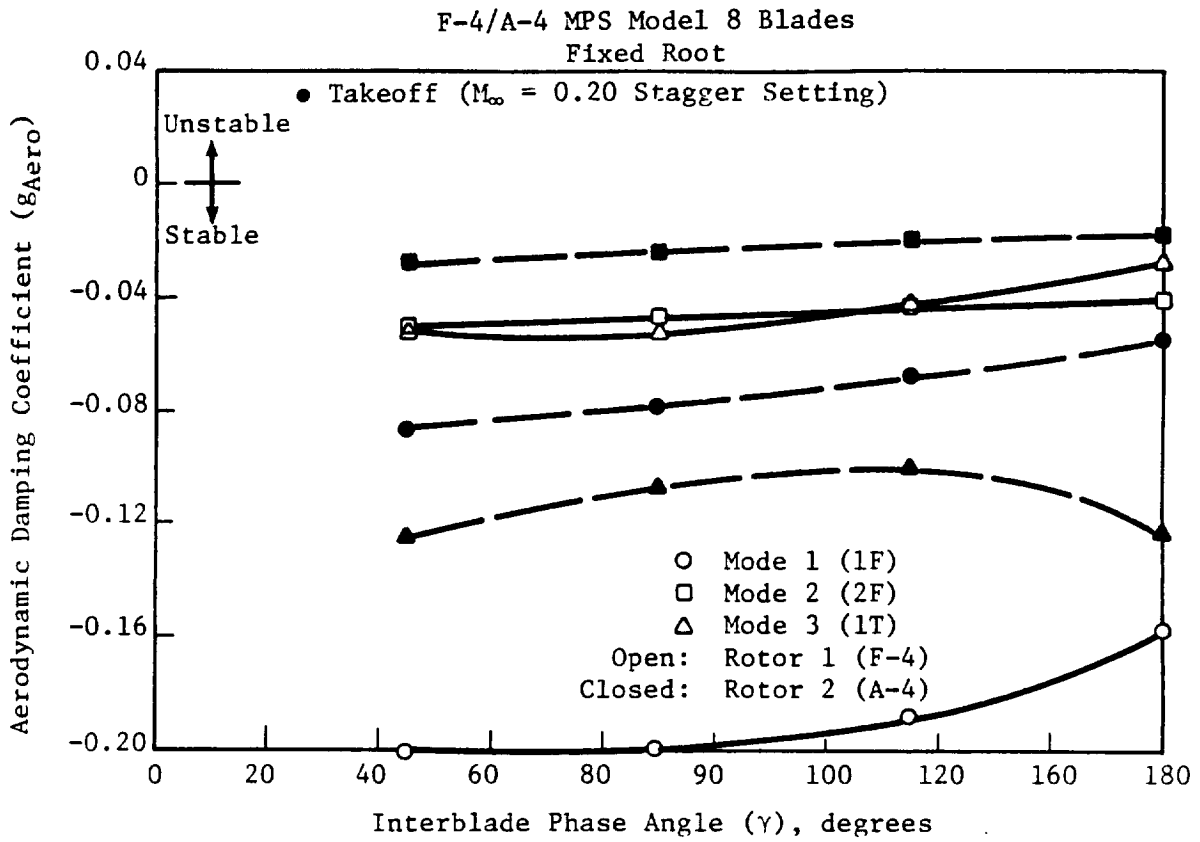


Figure 68. Stability Estimates for MPS F-4/A-4 Blades.

F-5/A-5 MPS Model 8 Blades
Fixed Root

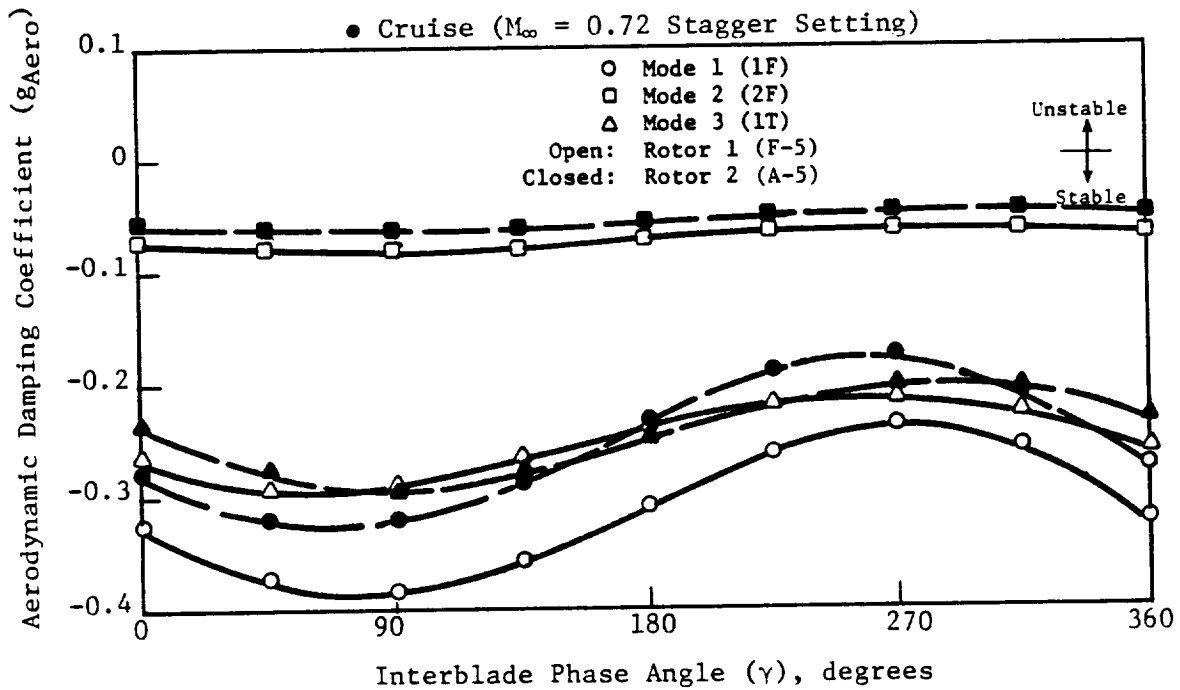
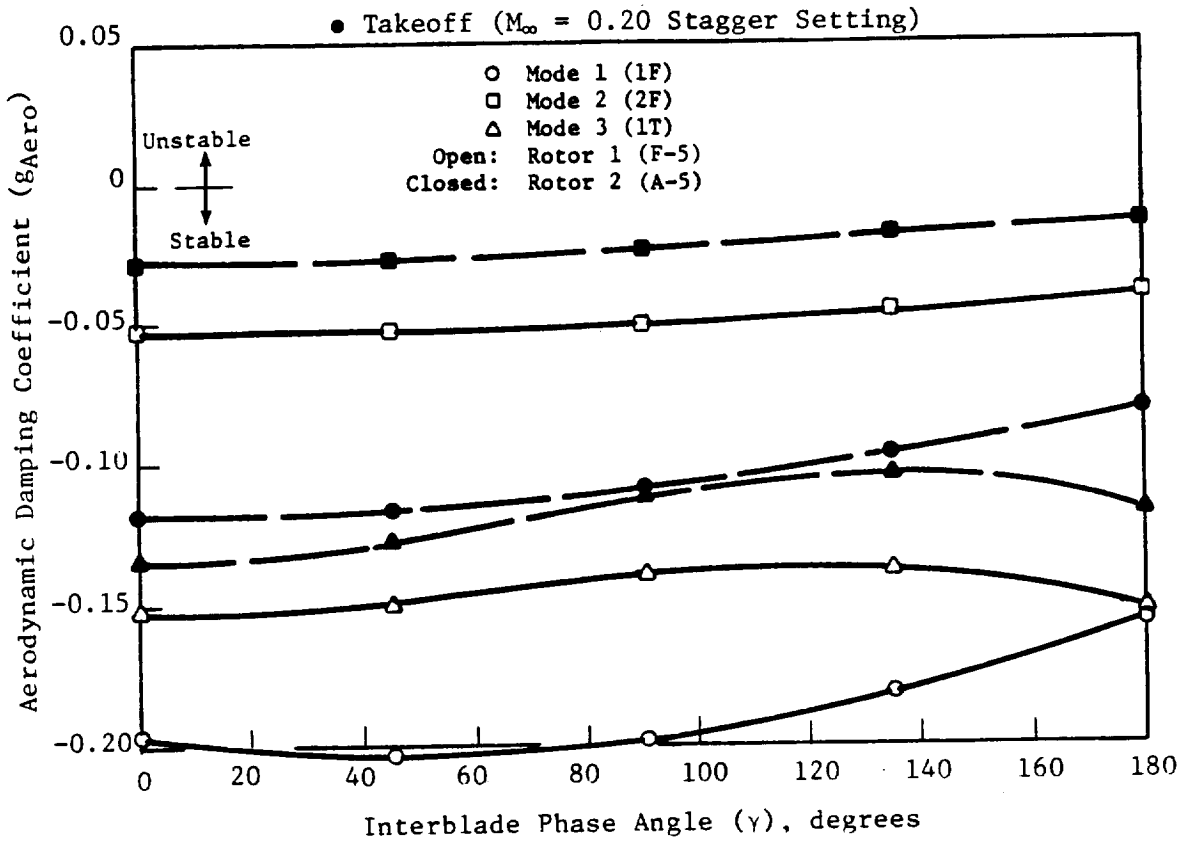


Figure 69. Stability Estimates for MPS F-5/A-5 Blades.

second set had outer plies of 2.5-mil 100% graphite, which is the new ply layup referred to in Figures 68 and 69 (Views B, each). From these analyses, both the F-4/A-4 and the F-5/A-5 blades were adjudged to be stable for both the takeoff and cruise conditions.

Figure 70 presents results of the stability analyses for F-7/A-7 blades with the 13°-ply orientation and rigid hub for takeoff and cruise conditions. As shown, the F-7 blades were predicted to be stable at both operating conditions, but the A-7 blades were predicted to be marginally unstable at takeoff (only about 3% structural damping is required for stability) and unstable in a three-nodal-diameter BTW at cruise.

As illustrated in Figures 71 through 73, F-11/A-11 blades were analyzed for the 11+9 configuration at the cruise condition only. Figure 71 shows the original F-11 blade to be marginally unstable for the 1T mode in a one-nodal-diameter BTW. Another analysis was made for the F-11 blade with 10% trailing edge clipped (Figure 72) which demonstrated the clipped blade to be stable. A stability assessment of the A-11 blade (Figure 73) proved this blade to be stable at cruise.

Preliminary analysis of the F-21 blade indicated that it was less stable than the F-11 blade. Consequently, the detailed stability analyses of the F-21 blade concentrated on a 10% TE clipped blade (designated F-21c), as shown in Figures 74 through 76; once again, only the cruise condition was analyzed. It can be seen in Figure 74 that the F-21c may be unstable in the 1T mode in a one-nodal-diameter BTW.

Further analyses were performed by varying the response frequency at the least stable interblade phase angle, $\gamma = 327.3^\circ$; (this type of analysis serves to determine the response frequency and damping of the complete aeroelastic system). The results, illustrated in Figure 75, prove the F-21c blade to be unstable in the 1T mode responding at about the 2F frequency; that is, the 2S (second system) frequency. It should be noted here that the MPS stability analyses were made with full-scale UDF® finite element models with the ply thicknesses scaled appropriately. Thus, the flutter frequency of about 96 Hz in Figure 75 scales to 474 Hz for the MPS F-21c. Another F-21c analysis was made at 90% speed for the cruise condition (Figure 76); this reveals the F-21c to be marginally unstable (only about 3% structural damping is needed for stability) at this reduced speed condition. Figure 77 demonstrates the results of the stability analysis for a 10% TE clipped A-21 blade at the cruise condition. This shows the potential for a 1F instability in a three-nodal-diameter BTW. (The A-21 blade was manufactured thicker than the design intent so that it was stable throughout the testing.)

As demonstrated by the above, the various stability analyses have been expanded throughout the MPS experience. Early analyses were naturally influenced by past experience with ducted turbo-blading. Thus, the investigations were conducted in the $\gamma = 0 - 180^\circ$ regime (Figures 68 and 69) where FTW have been observed in ducted turbomachinery instabilities. Once it was learned that unducted fan instabilities are manifested through BTW, the analysis was extended to $\gamma = 360^\circ$.

Another deviation from ducted turbomachine aeromechanical experience was the mixed-mode instabilities which occurred in the MPS testing (Figure 75). As opposed to single-blade-mode instabilities, observed even in NASA SR-3 and SR-5 series testing, mixed-mode instability occurs when one of the blade modes (mode shapes) responds near the frequency of another mode. This was first observed during F-7/A-7 testing where the A-7 blades experienced instability in the 2F (second flex) mode at the 1A (first axial) frequency. Thus, the stability analyses were expanded again.

F-7/A-7 MPS Model 8 Blades
Fixed Root

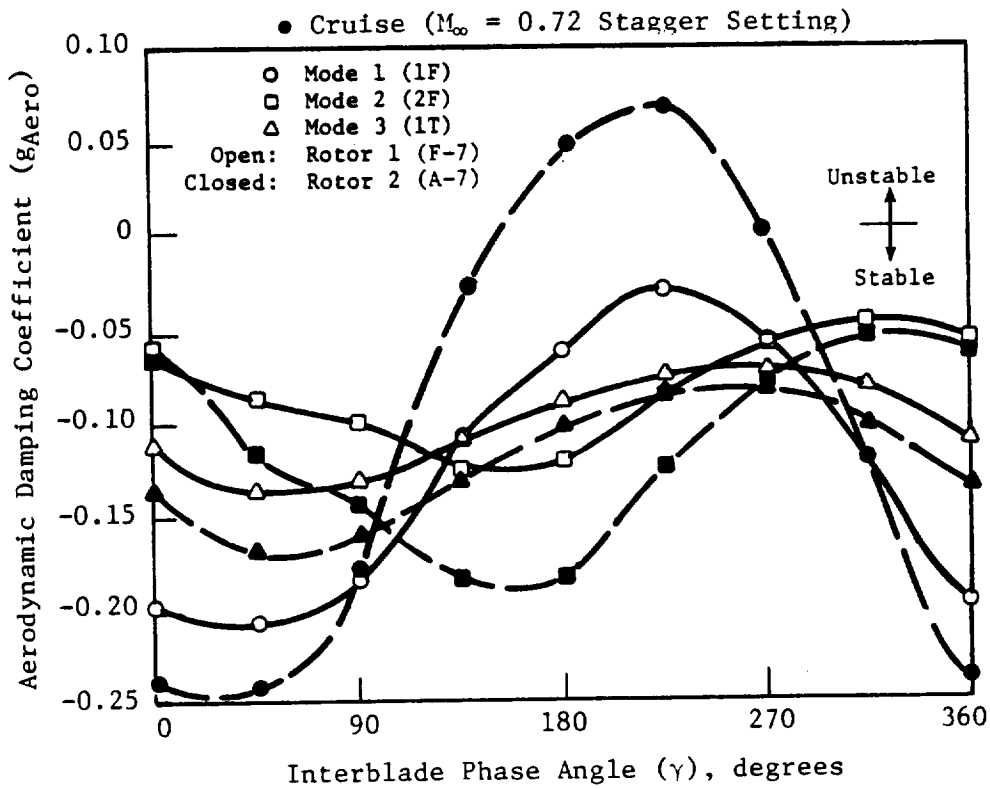
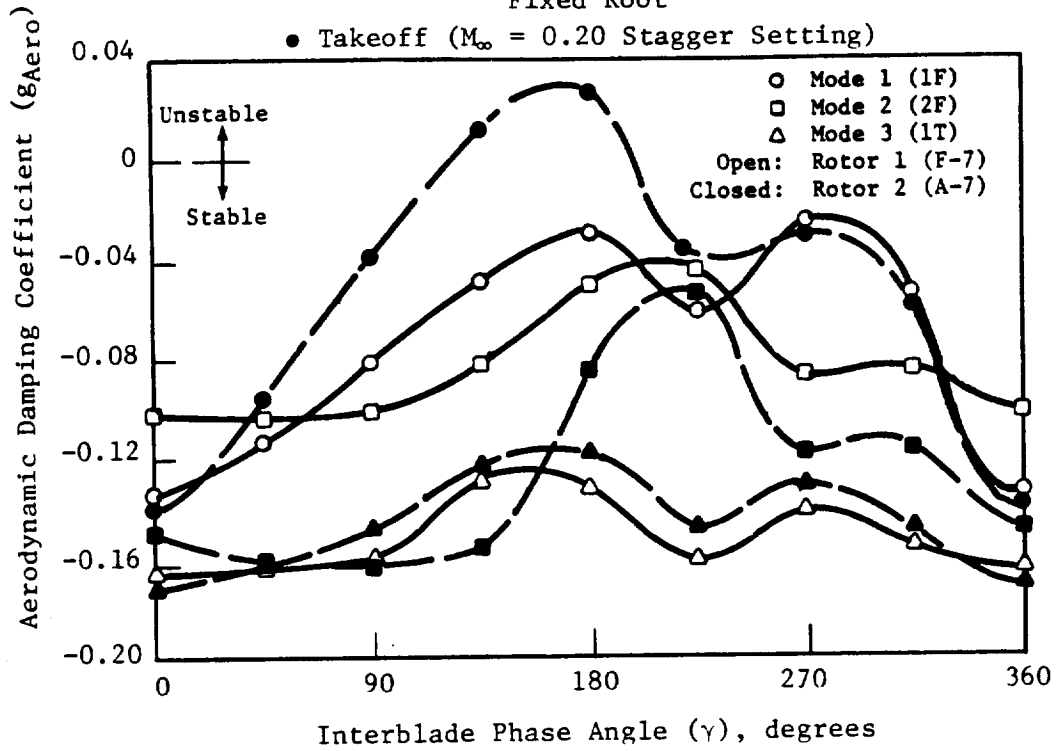


Figure 70. Stability Estimates for MPS F-7/A-7 Blades.

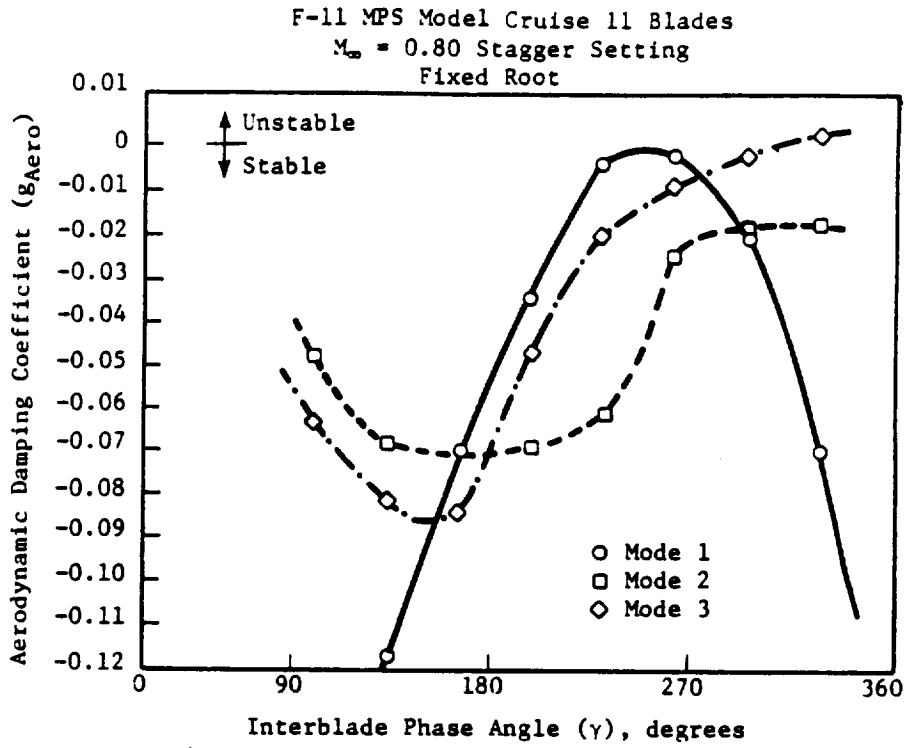


Figure 71. Stability Estimate for MPS F-11 Blade.

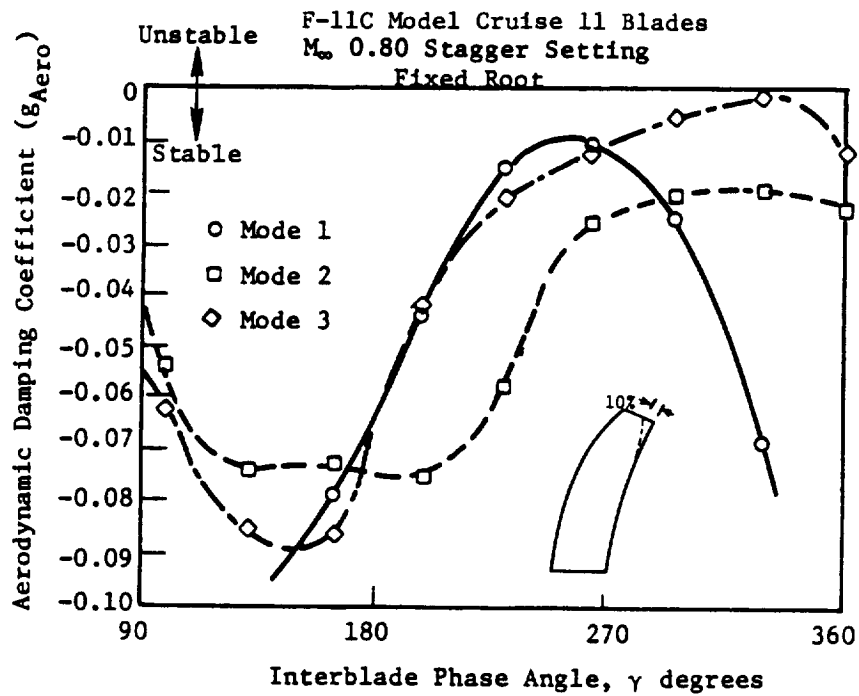


Figure 72. Stability Estimate for Clipped MPS F-11 Blade.

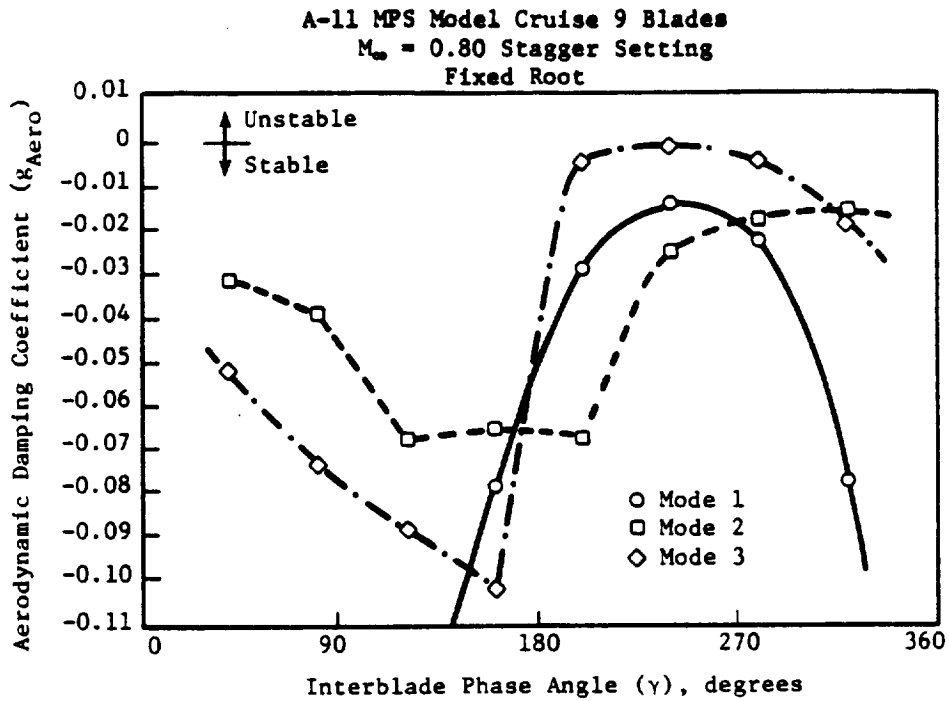


Figure 73. Stability Estimate for MPS A-11 Blade.

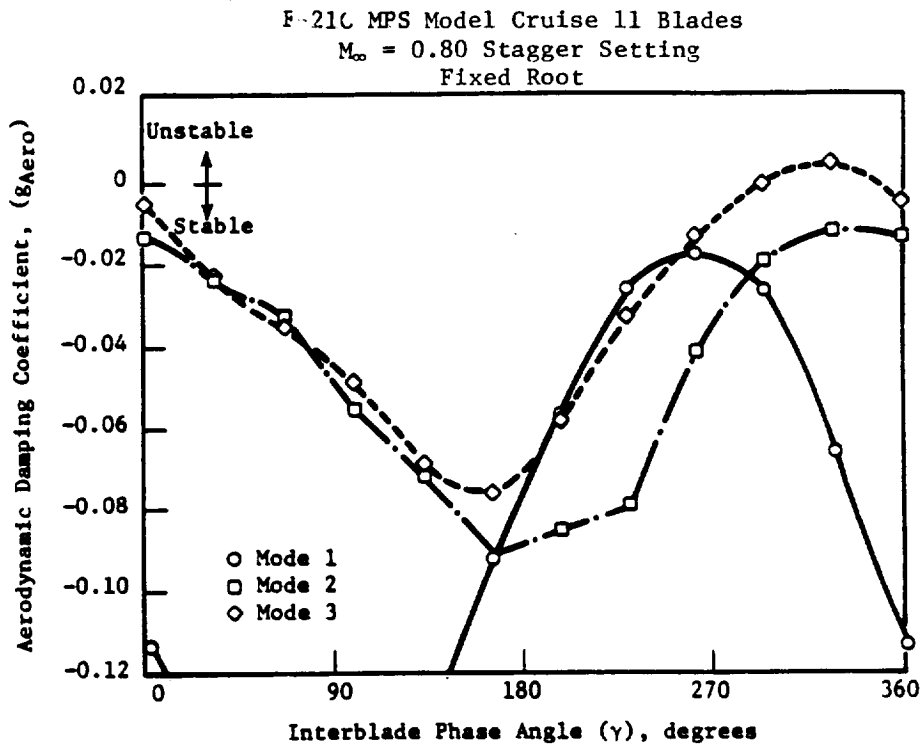


Figure 74. Stability Estimate for Clipped MPS F-21 Blade.

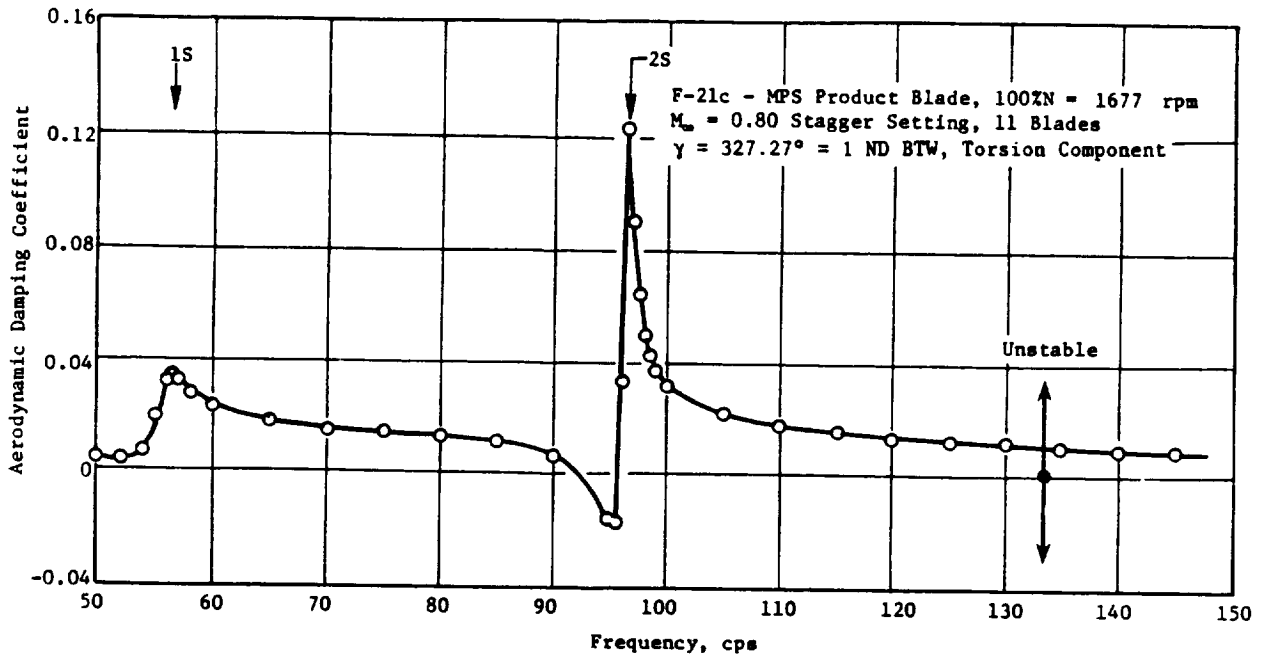


Figure 75. Stability Estimate for Clipped MPS F-21 Blade at 100% Speed.

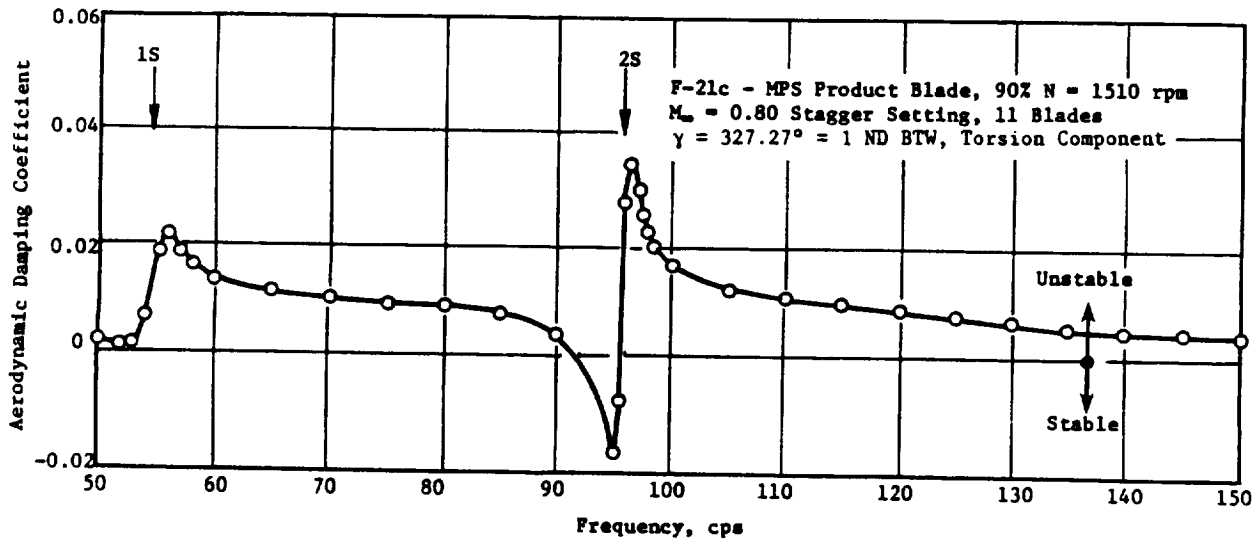


Figure 76. Stability Estimate for Clipped MPS F-21 Blade at 90% Speed.

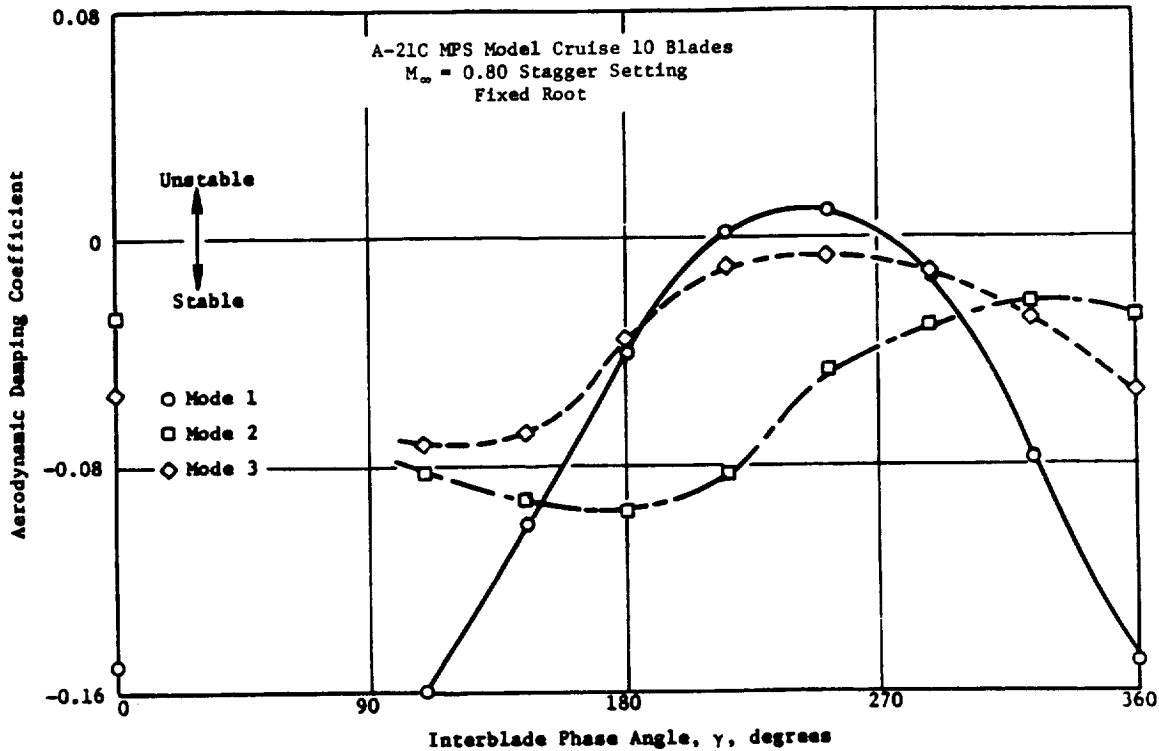


Figure 77. Stability Estimate for Clipped MPS A-21 Blades.

Once the particular γ was determined to be critical (least stable in the usual g_{aero} versus γ plots), the third dimension of the stability analysis was examined using a “frequency sweep” at the least stable interblade phase angle (Figures 75 and 76). In this part of the analysis, the reduced frequencies used to calculate the unsteady aerodynamic coefficients are varied about the nominal values which correspond to the blade hot shape.

For the composite material used in the construction of the blades, the relatively low structure/fluid mass ratio can result in significant modification of the blade structural dynamics. These changes in blade frequencies and mode shapes arise from the effects of the homogeneous, unsteady aerodynamics in the form of “virtual mass” and “virtual stiffness” terms, as well as mode cross-coupling effects. The magnitude and sign of the frequency modification depends on blade mode and flight condition. The frequency sweep then serves to determine the frequency and damping of the complete aeroelastic system. The GAP frequency sweep stability analyses for mixed-mode instabilities has correlated well with MPS test data, as demonstrated in Table 10.

3.5.3 F-7/A-7 Forced Response Analyses

Using the analytical methods described in Section 3.5.1.3, forced response analyses were made for the F-7/A-7 blades and compared with the MPS AOA (angle-of-attack) test data at the following conditions.

Tunnel Mach, MPS	MPS AOA, degrees
0.72	2, 8
0.40	5, 14
0.25	5, 16

Blade response was predominantly at 1/rev and 2/rev engine orders. The 1/rev response at M = 0.72 was analyzed with the GAP utilizing the procedures listed below:

- Evaluate the vibratory stresses for each blade mode (1F, 2F, 1T, etc.)
- Evaluate the 1/rev incidence and phasing due to angle-of-attack along the blade span, and introduce this distribution into the GAP unsteady-gust program
- Evaluate the modal deflections utilizing the distortion portion of the GAP
- Calculate the physical vibratory stresses by superposition of the modal deflections.

Results of this analysis are shown in Figure 78 to be in good agreement with the test data herein presented for comparison.

Table 10. MPS Test/Prediction Stability Correlation.

Prediction		Test Data
A-7, 13° Ply (A/M Hub)	2F Mode at 1A fn = 351 Hz	2F Mode at 1A fn = 380 Hz (Cell 41, M 0.25)
A-7, 35° Ply (A/M Hub)	2F Mode at 1A fn = 351 Hz	2F Mode at 1A fn = 380 Hz (Cell 41, M 0.25)
A-7, 13° Ply (Fixed)	1T Mode at 2F fn = 336 Hz	1T Mode at 2F fn = 354 Hz (Boeing, M 0.6)
F-11 (Fixed)	1T Mode at 2F fn = 530 Hz (2n) = 510 Hz (1n)	1T Mode at 2F fn = 540 Hz (NASA, M 0.8)
F-21 (Fixed)	1T Mode at 2F fn = 474 Hz	1T Mode at 2F fn = 480 Hz (NASA, M 0.8)
Note: fn denotes blade natural frequency		

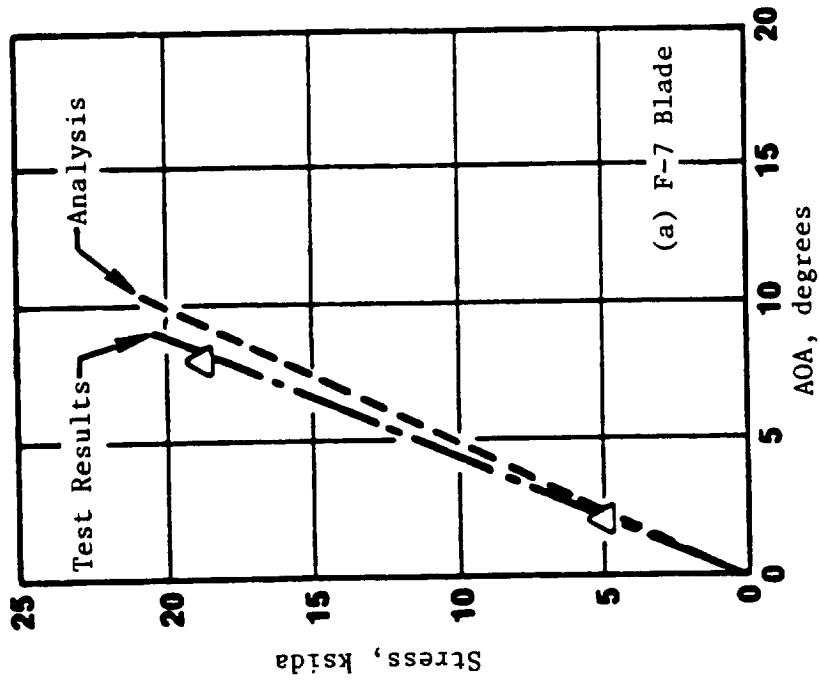
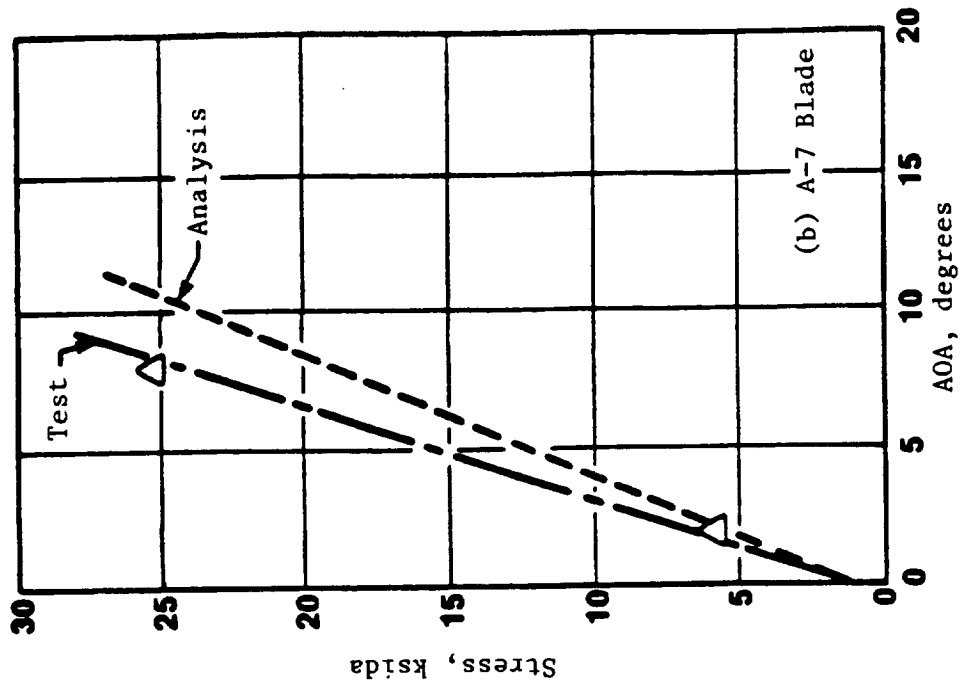


Figure 78. Comparison of the 1/rev Stress Variation at the Blade Critical Point due to AOA (Angle-of-Attack) for the F-7/A-7 MPS Blades at Mach 0.72.

4.0 MECHANICAL DESIGN AND FABRICATION

Under this contract, candidate counterrotating UDF blade configurations were identified.

Selection of a high fan radius ratio (nominally 0.42) facilitated the desired higher disk loading design by permitting an increased total activity factor without problems with hub crowding. Blade hub solidity determines the extent to which blades may be moved into reverse pitch and, together with hub thickness/chord ratio, largely determines the onset of hub choking.

In addition, the high radius ratio was used advantageously to lower the blade aspect ratio (nominally 2.4) while also adopting a low (by propfan standards) per blade activity factor of 150. This was expected to result in a stiffer, more rugged blade with lower tip losses.

With these considerations in mind, theoretical studies led to adoption of a baseline design configuration of 0.425 radius ratio and 8+8 blades of 150 activity factor. Engine performance for this configuration was estimated by scaling the results of advanced propeller prediction techniques and was subsequently verified by comparison with SR-3 blade test data.

This baseline configuration, designed for Mach 0.72 flight, analytically exhibited good propulsive efficiency at that condition. Follow-on aerodynamic studies, however, indicated that careful selection of the nacelle shape would enable this configuration to be flown at Mach 0.8 without hub choke.

Having identified a baseline counterrotating blade configuration, a program was defined to generate a data base for this baseline design and to investigate significant perturbations from it; specifically, variations in the following design parameters:

- Number of Blades
- Radius Ratio
- Tip Speed
- Activity Factor
- Blade Sweep
- Disk Loading

Consequently, five blade configurations, represented by the forward blade planform shapes illustrated in Figure 79 and the aerodesign parameters listed in Table 11, were selected to be aerodynamically and acoustically evaluated in scale model high- and low-speed wind tunnel tests, defined in Tasks IV and V of NASA Contract NAS3-24080. The blades were designed for evaluation in the MPS rigs. Table 12 summarizes corresponding hub and tip radii for the model blades F-4/A-4, F-5/A-5, F-7/A-7, F-11/A-11, and F-21/A-21 ("F" and "A" denote "forward" and "aft," respectively, for each of the five blade designs).

Sections 4.0 through 4.2 describe the design and fabrication of the five composite-shell/titanium-spar blade sets of Figure 79. Details of mechanical design philosophy, analysis methods, and material properties are presented. Aerodynamic, aeromechanical, and aeroacoustic influences on the design process are also addressed, along with blade fabrication and quality control procedures. Bench testing to verify blade mechanical integrity is described, the results of which are presented, and instrumentation is identified. MPS blade instrumentation and measured stress limits are also reported. Finally, fabrication of several items of hardware to support the specialized investigations into acoustic, aerodynamic, and aeromechanical phenomena experienced during Tasks IV and V testing is described.

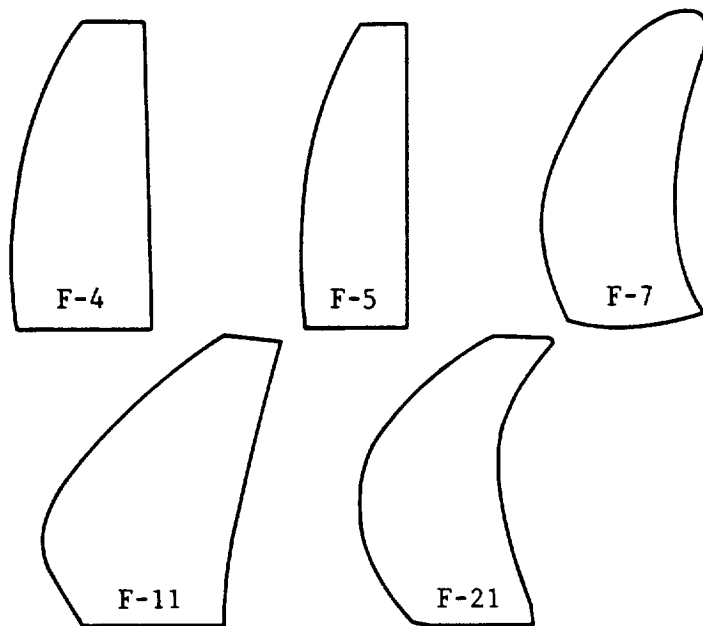


Figure 79. Selected Counterrotating Blade Planform Shapes.

Table 11. Unducted Fan Aerodynamic Design Parameters.

Parameter	F/A-4	F/A-5	F/A-7	F/A-11	F/A-21	SR-3
Design Flight Mach No.	0.72	0.72	0.72	0.80	0.80	0.80
Advance Ratio (J)	2.80	2.80	2.80	3.12	3.12	3.10
Power Coefficient (PQA)	4.15	4.15	4.15	4.63	5.58	2.30
Thrust Coefficient (TQA)	1.26	1.26	1.26	1.27	1.50	0.60
Disk Loading (shp/Aa)	86	86	86	96	118	50
Number of Blades	8+8	8+8	8+8	11+9	11+10	8
Total Activity Factor	2456	1968	2392	3780	3713	1880
Tip Speed (R1), ft/s	787	788	785	784	801*	800
Aero Tip Sweep, degrees	19-20	15-18	34-31	37-34	45-25	45
Inlet Radius Ratio	0.424	0.423	0.425	0.425	0.431	0.240
Net Efficiency Goal	0.850	0.850	0.850	0.856	0.840	0.812

* Standard Day + 18° F Conditions

Table 12. Scale Model Counterrotating Blade Dimensions.

Blade	Hub Radius, in.	Tip Radius, in.
F-4	5.22	12.36
A-4	4.96	12.02
F-5	5.22	12.37
A-5	4.96	12.02
F-7	5.21	12.32
A-7	4.96	11.97
F-11	5.24	12.31
A-11	4.96	11.94
F-21	5.24	12.17
A-21	4.96	11.75

4.1 Blade Mechanical Design

Mechanical design of the F-4/A-4, F-5/A-5, F-7/A-7, F-11/A-11, and F-21/A-21 blades was performed by GE under Contract NAS3-24080. Detailed design procedures identified in Figure 80 are described in this section.

After detailed aerodynamic design, the candidate blade shapes at design point operating conditions (hot shape) underwent mechanical design. For the MPS blades, a graphite/glass composite shell with a Ti6-4 airfoil-shaped spar which extends to approximately 50% of the blade height was chosen. The platform and trunnion sections which allow the blade to be installed in the MPS rotating hub assemblies were machined in one piece, integral with the spar.

Figure 81 is a sketch of an F-4 blade. The size and shape of the spar, the composite layup, and the trunnion size vary with each design. The 8- and 9-blade MPS hubs accept only large-trunnion blades (F-4/A-4, F-5/A-5, and F-7/A-7); whereas, the 10- and 11-blade MPS hubs accept only small-trunnion blades (F-21 and A-21). Because the F-11 and A-11 blades have threaded shanks, a removable trunnion of either size can be installed, allowing these blades to be tested in any of the MPS hubs. Figure 82 shows the F-11 and A-11 blades.

Due to the strength-to-weight ratio of the composite material and the presence of the spar, steady-state operating stresses were expected to be low; however, natural blade frequencies were of particular concern. AOA (angle-of-attack) and simulated-pylon testing would produce disturbances of 1/rev and 2/rev. Due to the counterrotation, each blade row would create n/rev and 2n/rev excitations for the other blade row, where n is the number of blades in each row. Vibration modes that could be potentially damaging had to be tuned; for example, the fundamental flex (F) modes, torsion (T) modes, and the chordwise bending or stripe (S) modes. These modes could not cross the per revs mentioned above during simulator operation or must do so at low speeds where the excitation energy was lower. Tuning was accomplished using ply orientation, overall blade thickness, spar thickness, and chord-length changes based on guidelines established from experience with composite structures relating to stability and stress.

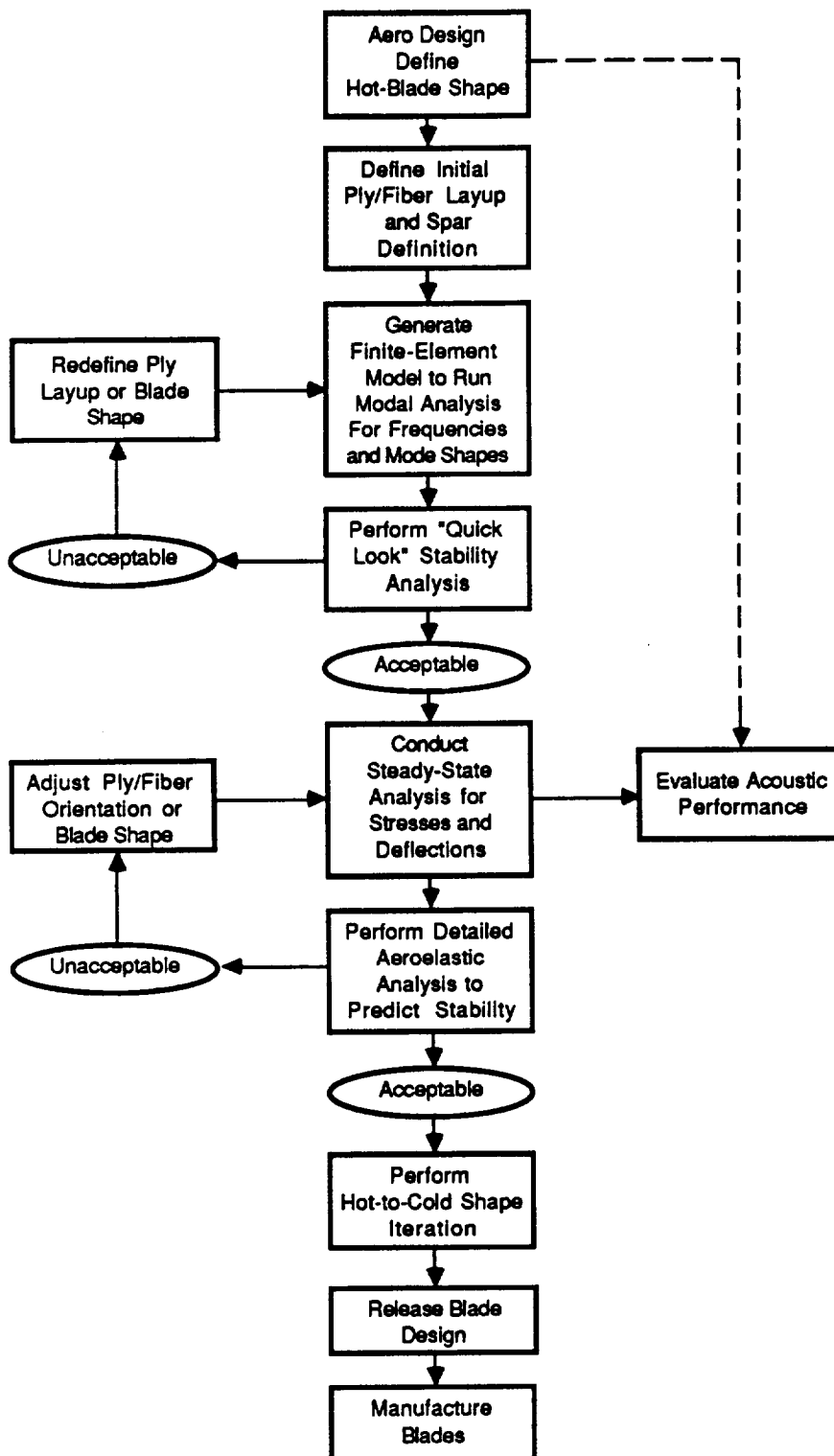


Figure 80. MPS Blade Mechanical Design Procedures Flow Chart.

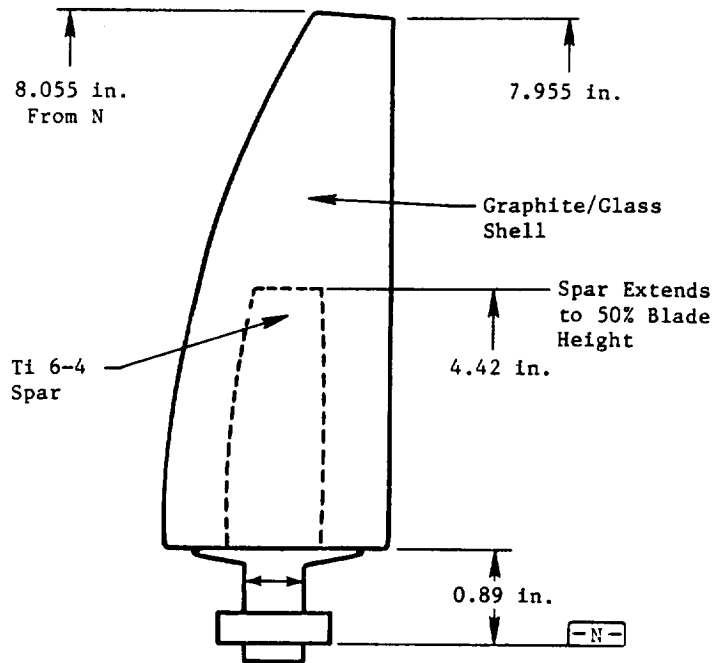


Figure 81. F-4 Spar/Shell Design.

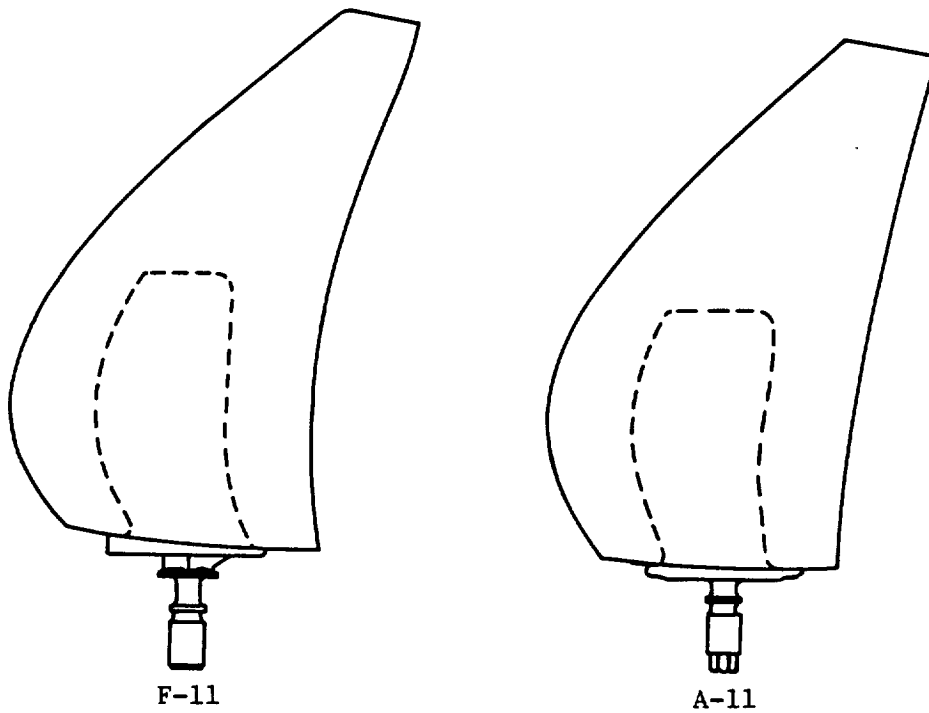


Figure 82. F-11 and A-11 MPS Blades.

The initial shell ply-layup pattern for each blade was chosen separately in order to provide blades anticipated to be stable, at the design point, with stresses lower than the capability of the material.

Chordwise mode-shape slopes of the 1F (first flex) and 1T (first torsion) modes were discovered to play a big role in stability; minimizing these slopes tends to stabilize the blades. The material reference axis can be varied to minimize the slopes. (The material reference axis is the direction in which a 0°-fiber would lie, relative to the radial direction with a positive angle being in the direction of positive blade sweep.) The F-4/A-4 and F-5/A-5 blades, both of which are straight, were given 0°-reference axes. The F-7/A-7 blades had a 13°-reference axis (A-7 blades tested in an aeromechanical hub had a 35°-reference axis). The F-11/A-11 blades had a 45°-reference axis. The F-21 blades had a 40°-reference axis, and the A-21 blades had a 50°-reference axis; the F-21 and A-21 designs had different reference axes for stability reasons.

Because MPS blades were to be constructed of the same material as that used on a full-scale design, the original F-4/A-4 and F-5/A-5 designs utilized 5-mil, 80%/20% graphite/glass plies. The layup was [0/20/0/-20/] relative to the blade-stacking axis. However, initial testing of these blades revealed the shortcomings of this layup. Since the blades were so thin at the leading and trailing edges, only the two outer 0° plies made up these regions. This caused cracks to develop along the fibers in these regions. Additionally, the F-5/A-5 blade failure was caused by a 2S mode, 16/rev crossing resonance, as the 0/20/0/-20 plies did not provide enough chordwise strength.

To obviate these problems, a new material/layup combination was needed; extensive analysis determined the best possible layup for each design. The introduction of 2.5-mil 100% graphite plies allowed four plies to be fit into the thinnest 10-mil region, instead of two. Placing 0/90 plies on the blade surface provided the needed crossbracing.

The final plies chosen for the MPS blades had a [0/90/45/90/0/-45] 2.5-mil and [0/20/0/-20/...] 5-mil layup orientation. As depicted in Figure 83, only the top three plies were changed from the original layup: six 2.5-mil plies were substituted for the three 5-mil plies. On the F-11/A-11 and F-21/A-21 designs, 45°-plies were substituted for the 20°-plies; this provided more torsional stiffness. The 90°-plies provided the stiffness needed to drive the 2S mode out of the 16/rev range; on swept blades where stability is a problem, the 90° and 45° plies helped stabilize the blade.

The orthotropic material properties of the graphite elements depended on the number of plies in the element which, in turn, depended on the thickness of the element. A preprocessor was used to calculate these thicknesses and to assign the corresponding material properties. Each element was comprised of many plies, having unidirectional material properties. Laminate plate theory was used to convert the individual ply properties into bulk element properties through the thickness for use in the finite element model. Figure 84 details typical three-element sections for three different airfoil regions.

In the six-ply-thick section, outer elements were assigned bulk material properties of a 0/90 layup; whereas, the center element had the properties of a single 45°-ply. The eight-ply section does not divide into three equally spaced elements, so fractions of plies were used for material property calculations. Since skin thickness in the spar region is constant, all the outer elements over the spar had the same properties. Material direction cosines were used to relate the material layup axis to the global coordinate axis.

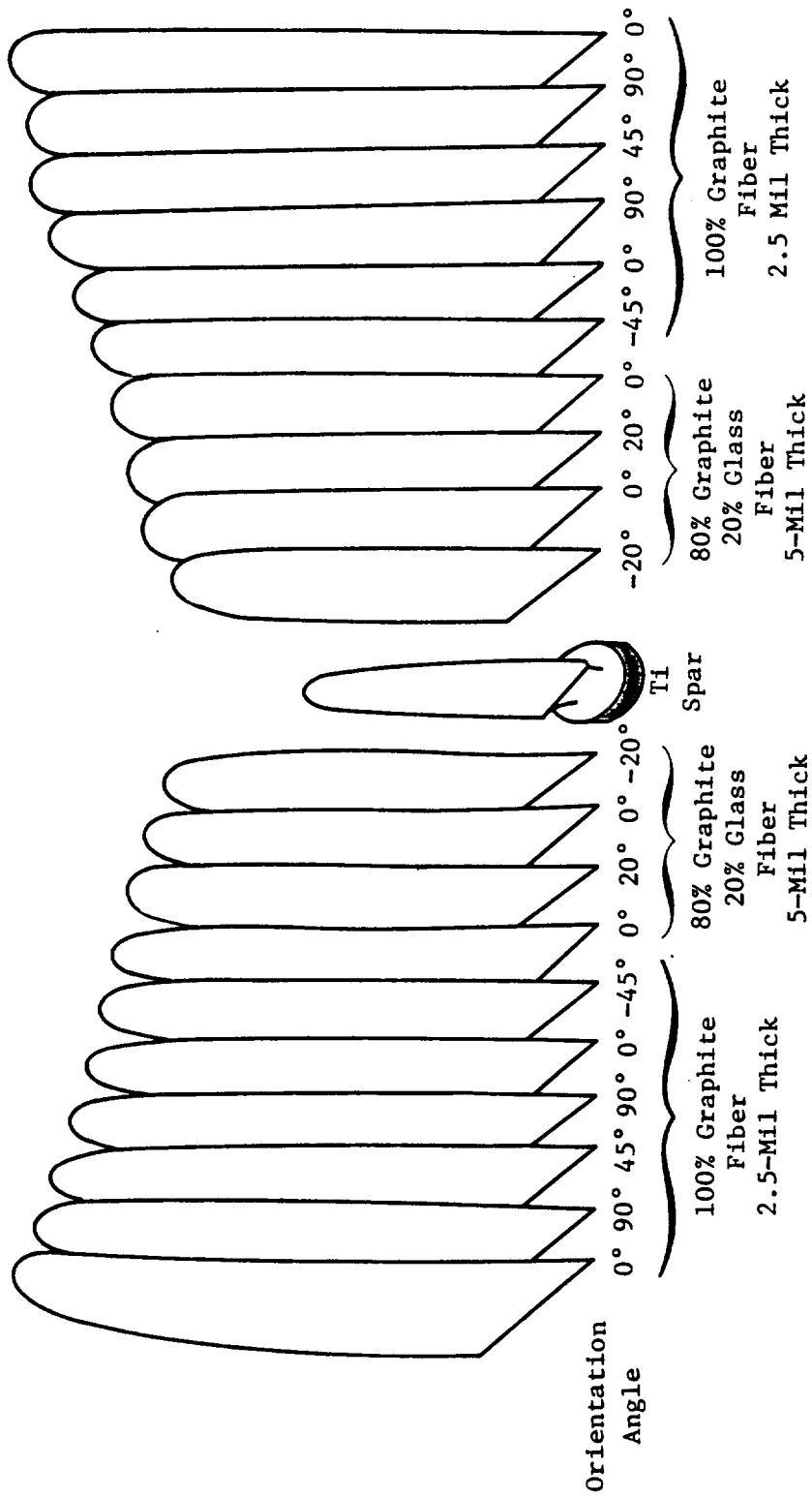


Figure 83. Blade Ply Layout.

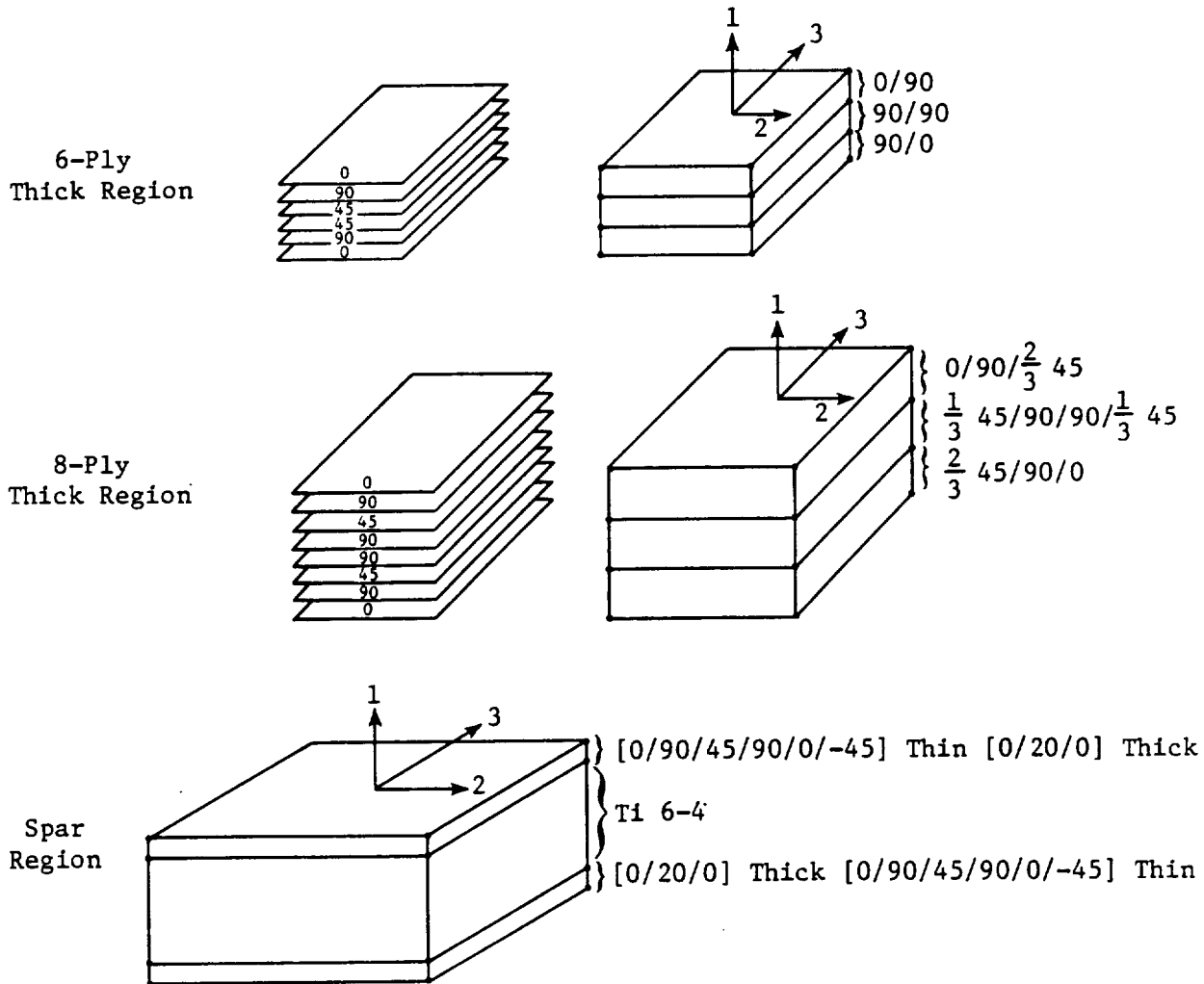


Figure 84. Typical Three-Element Sections of Finite Element Model Thickness Mesh.

Table 13 shows the 100% graphite properties, and Table 14 lists the 80%/20% graphite/glass properties.

To ensure safe operation over the full range of testing desired, stress and vibration characteristics of each blade configuration were predicted using a finite element computer program (GE TAMP/MASS) that takes into account the anisotropic nature of the composite material.

A finite element model of each blade design was set up using GE's TAMP/MASS program. The elements are eight-noded bricks that handle orthotropic material properties. A 3x8x20 mesh was used; 3 elements through the thickness, 8 across the chord, and 20 along the span. A mesh plot of each forward blade design is provided in Figure 85; a slice through the chord of a typical design would resemble Figure 86.

To represent fixed/free boundary conditions of the blade designs, models were fixed at the base of the spar. This caused the predicted frequencies to be higher than actual because hub and trunnion stiffnesses were not taken into account. Experience indicates the effect of rigid hubs is not very large. A spring stiffness matrix was used at the base of the blade for aeromechanical hub analysis. Trunnion stress analysis was performed by utilizing root reaction loads from blade finite element analyses to calculate tensile and bending stresses. This method has been shown to give accurate results when compared to actual bench test frequencies.

A modal analysis of the finite-element models was then run to assess the frequencies and mode shapes. The Task III report presents the individual frequencies and mode shapes for the F-4, A-4, F-5, A-5, F-7, A-7, F-11, A-11, F-21, and A-21 blades. This information was utilized to conduct a preliminary ("quick look") stability analysis which checks mode-shape slopes against preliminary design rules. These rules identify stable and unstable combinations of modal slopes and reduced frequencies for the fundamental modes (first flex and first torsion). The 1F- and 1T-mode quick look stability plots from this analysis for the contract blades are illustrated in Figures 87 through 92. All blade designs passed the quick look stability analysis, except the A-11 (Figure 91). In that instance, the blade design fell into the "gray" boundary zone separating the stable and the unstable regions. The reason for this is that every new aerodynamic design selected represents an incremental venture in pushing the then-known state-of-the-art technology. For such a case, a full stability audit is conducted, using the GE GAP code. Figure 93 plots the results of the stability audit for this blade.

If the blade is unstable, the audit will reveal the following:

- Modal Diameter of Potential Flutter Response
- Instability Frequency (which could be significantly different from the normal mode frequency)
- The Dominant Vibratory Pattern
- The Expected Loss of Aerodynamic Damping
- Behavior of Aerodynamic Damping Versus Interblade Phase Angles in Normal Modes
- Effects of Cascading, Density Variation, Changes in Mode-Shape Slopes, and Increased Relative Mach Number in Blade Channels.

This information provides the designer with insights for design tradeoffs (based on parametric studies conducted in the past), with respect to each of the above parameters and pertinent

Table 13. AS (Graphite)/PR288 (Epoxy) Ply Properties.

Property	Mean Value	
	74° F	200° F
Axial Elastic Modulus (Tensile), x 10 ⁶ psi	18.56	17.25
Transverse Elastic Modulus (Tensile), x 10 ⁶ psi	1.27	0.97
Shear Strength, x 10 ⁶ psi	0.671	0.452
Poisson's Ratio, in./in.	0.32	0.31
Axial Ultimate Tensile Strength, ksi	185.1	179.8
Axial Ultimate Strain (Tensile), % in./in.	1.03	1.07
Transverse Ultimate Tensile Strength, ksi	9.27	7.80
First-Ply Failure Transverse Tensile Strength, ksi	5.21	2.99
Transverse Ultimate Strain (Tensile), % in./in.	0.80	1.11
Transverse Ultimate Shear Strength, ksi	17.49	11.59
HCF (High Cycle Fatigue) Axial Endurance Limit, ksi	55.0	55.0
HCF Transverse Endurance Limit, ksi	1.9	1.1 *
HCF Shear Endurance Limit, ksi	3.0	1.8 *
(HCF at Minimum/Maximum Load = -1.0, 30 Hz)		
* Estimated from RT (Room Temperature) Data		

Table 14. AS (Graphite) - S (Glass)/PR288 (Epoxy) Ply Properties.

Property	Mean Value	
	74° F	200° F
Axial Elastic Modulus (Tensile), x 10 ⁶ psi	16.19	16.08
Transverse Elastic Modulus (Tensile), x 10 ⁶ psi	1.45	1.17
Shear Strength, x 10 ⁶ psi	0.771	0.530
Poisson's Ratio, in./in.	0.31	0.32
Axial Ultimate Tensile Strength, ksi	178.6	194.9
Axial Ultimate Strain (Tensile), % in./in.	1.12	1.24
Transverse Ultimate Tensile Strength, ksi	7.63	7.58
First-Ply Failure Transverse Tensile Strength, ksi	4.22	3.11
Transverse Ultimate Strain (Tensile), % in./in.	0.58	0.83
Transverse Ultimate Shear Strength, ksi	13.78	9.53
HCF (High Cycle Fatigue) Axial Endurance Limit, ksi	50.0	50.0 *
HCF Transverse Endurance Limit, ksi	1.4	1.0 *
HCF Shear Endurance Limit, ksi	3.3	1.9 *
LCF (Low Cycle Fatigue) Axial Strength, ksi	130.0	130.0 *
(HCF at Minimum/Maximum Load = -1.0, 30 Hz; LCF at Minimum/Maximum Load = 0.1, 1.0 Hz)		
* Estimated from RT (Room Temperature) Data		

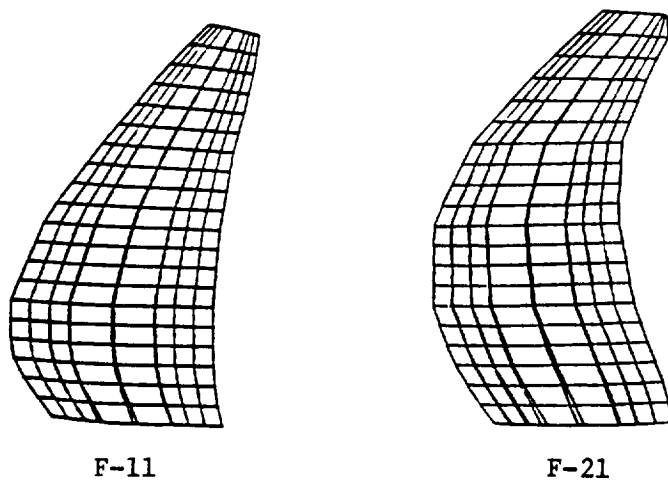
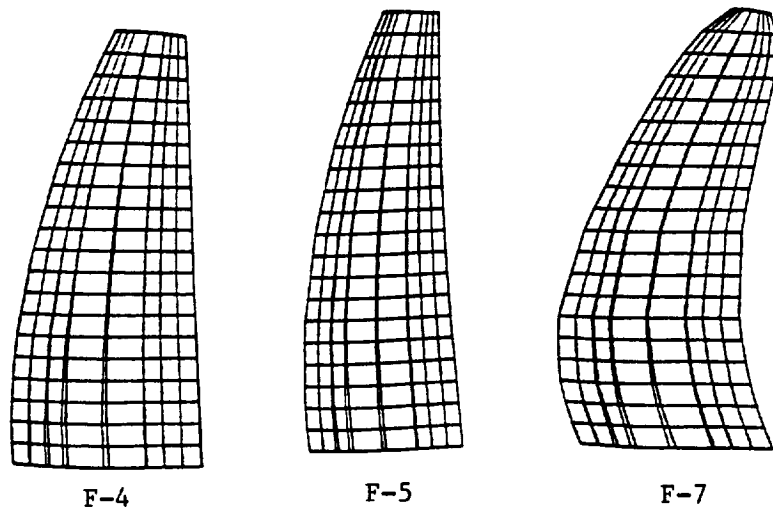


Figure 85. Finite Element Mesh for MPS Blade Design.

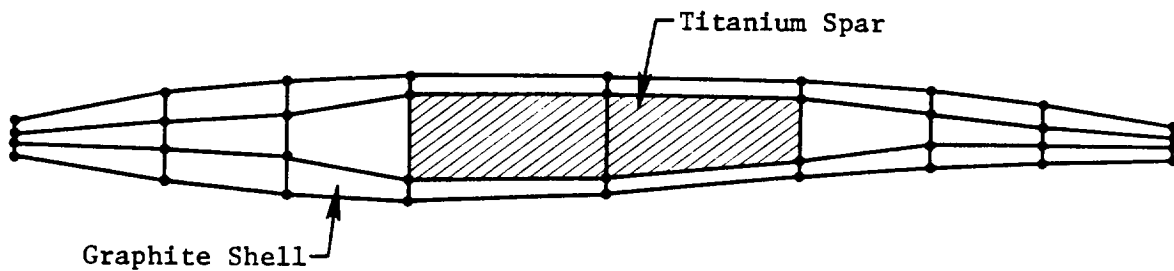


Figure 86. Typical Chordwise Slice Through Finite Element Mesh.

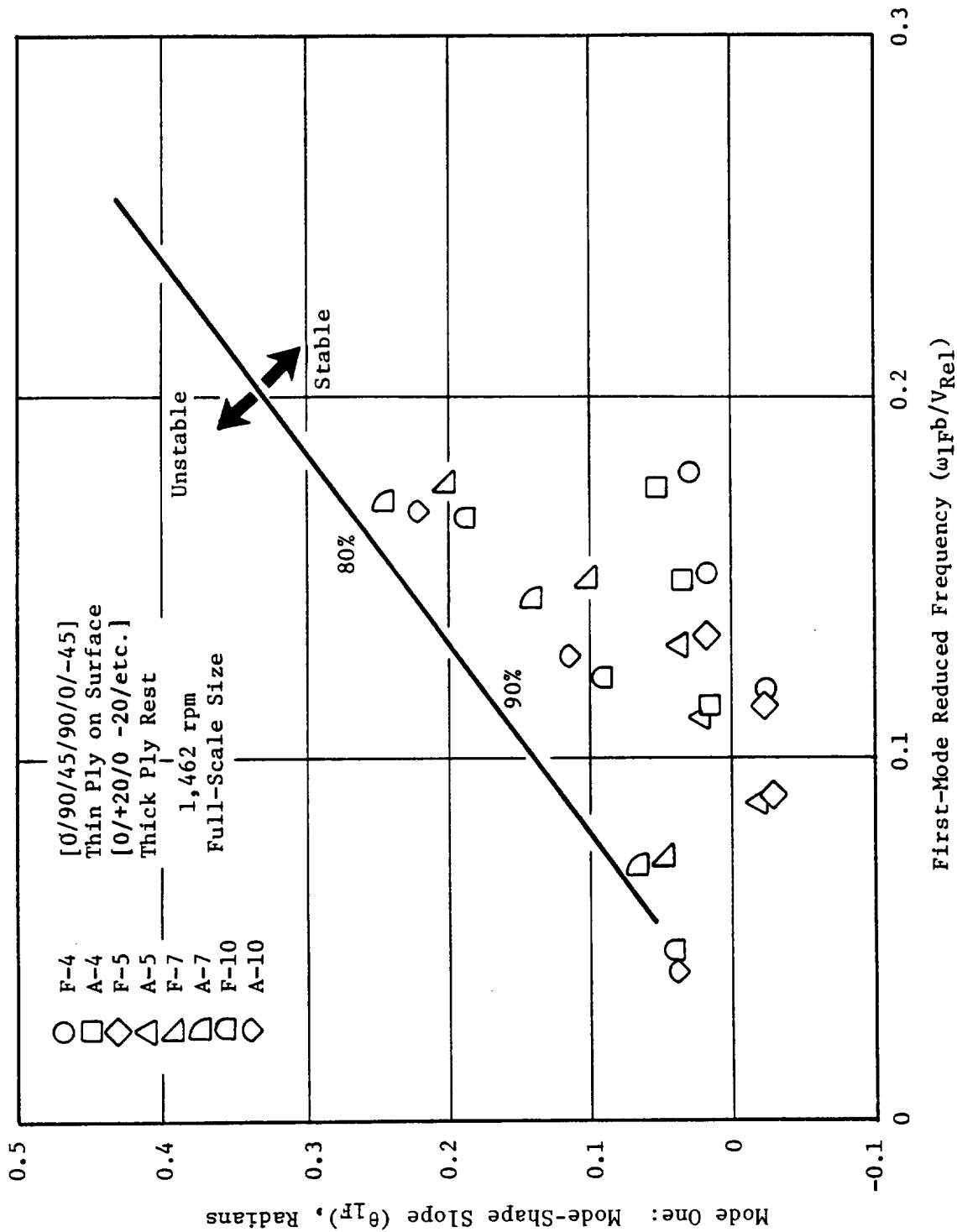


Figure 87. "Quick-Look" Stability Comparison, First-Flex Mode.

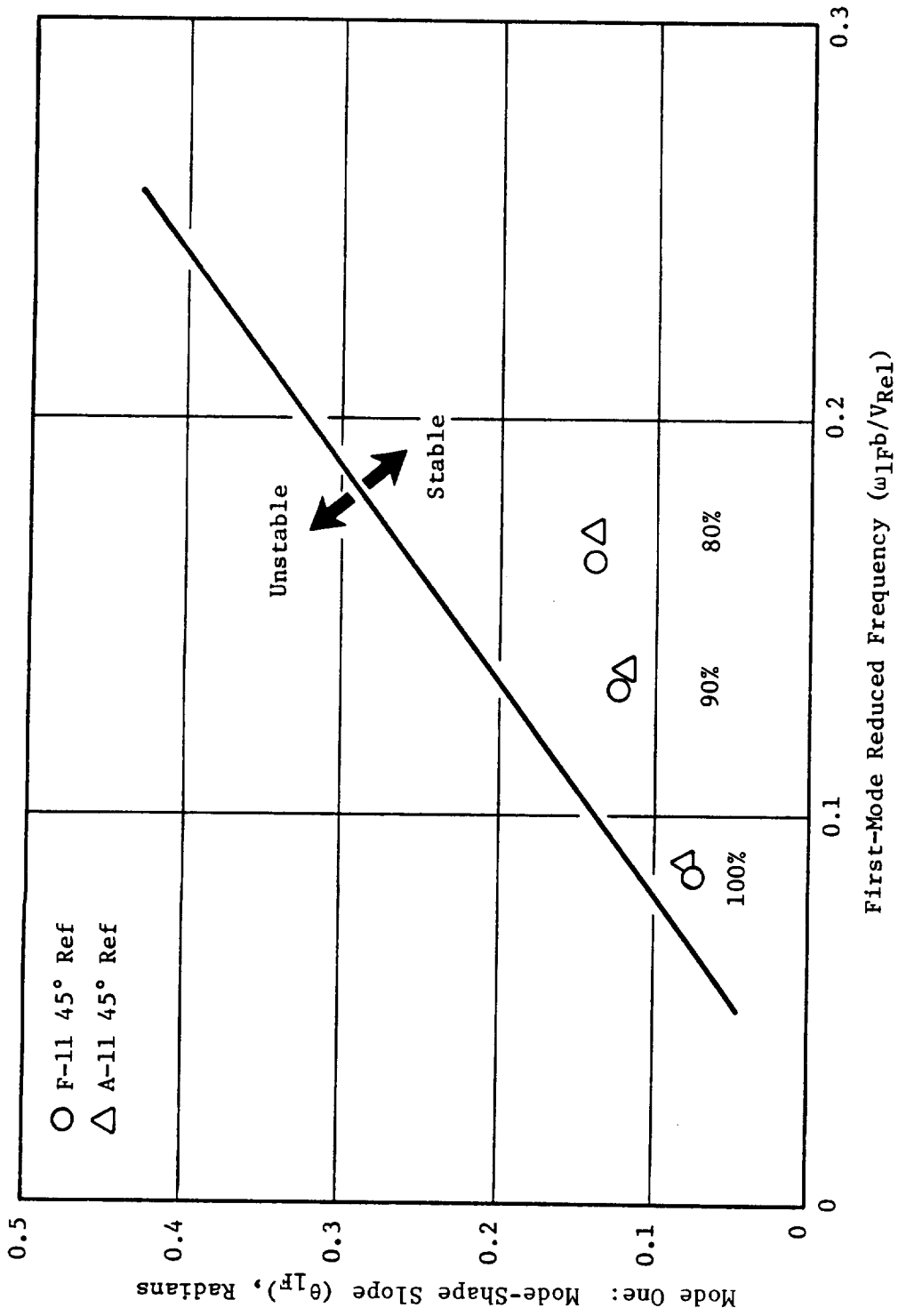


Figure 88. Quick-Look Stability Comparison of the F-11/A-11 in the First-Flex Mode.

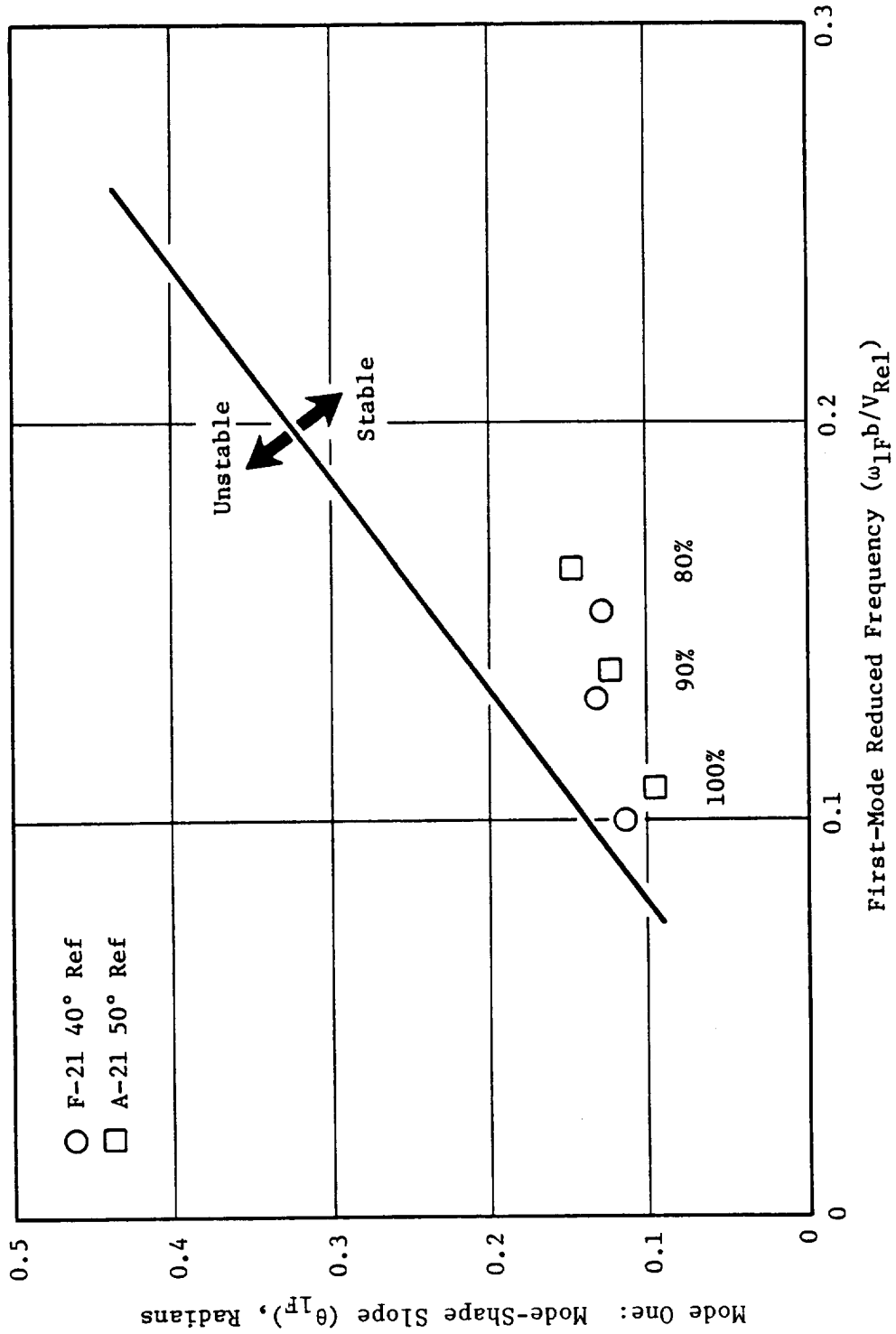


Figure 89. Quick-Look Stability Comparison of the F-21/A-21 in the First-Flex Mode.

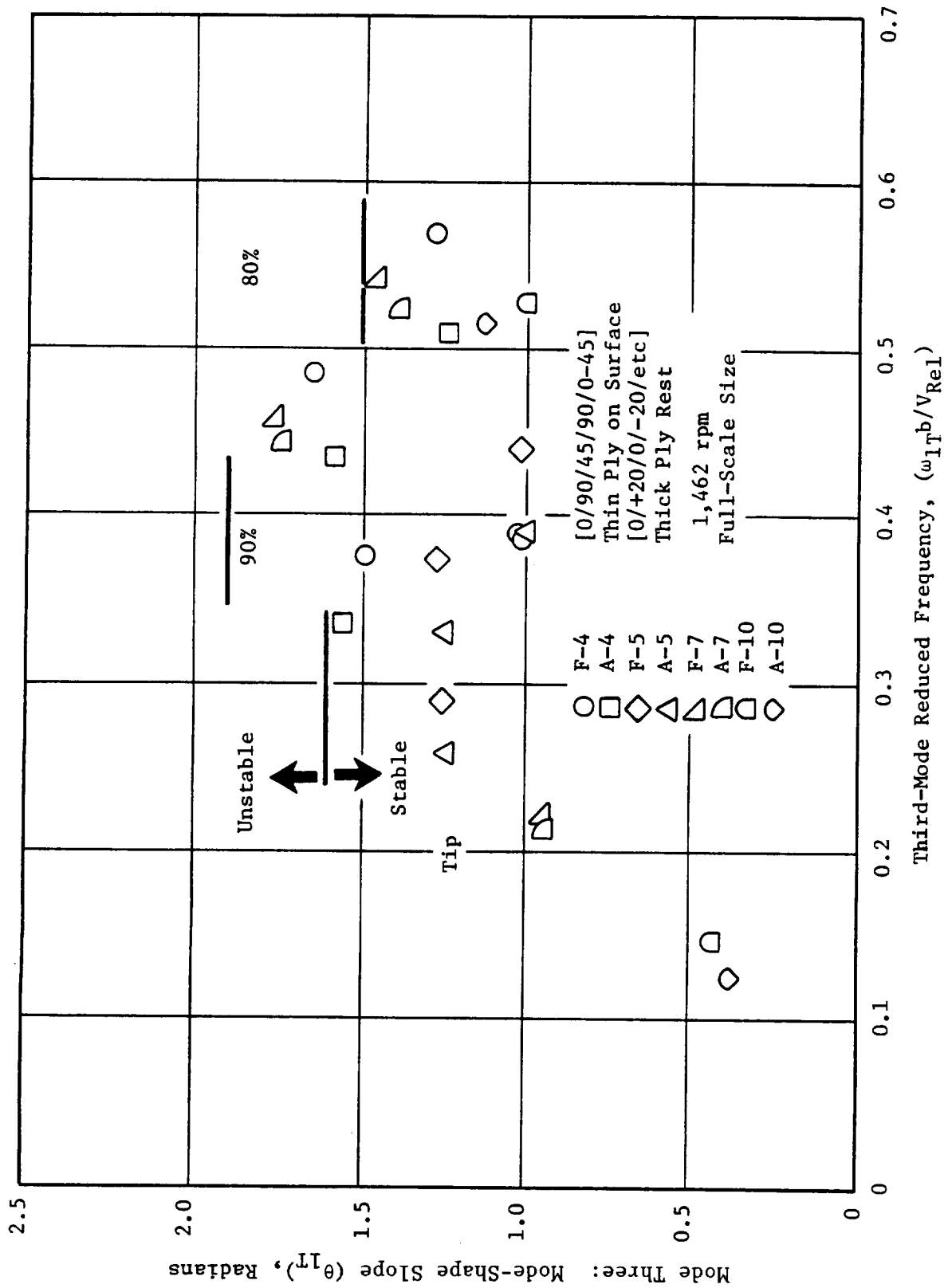


Figure 90. Quick-Look Stability Comparison, First-Torsion Mode.

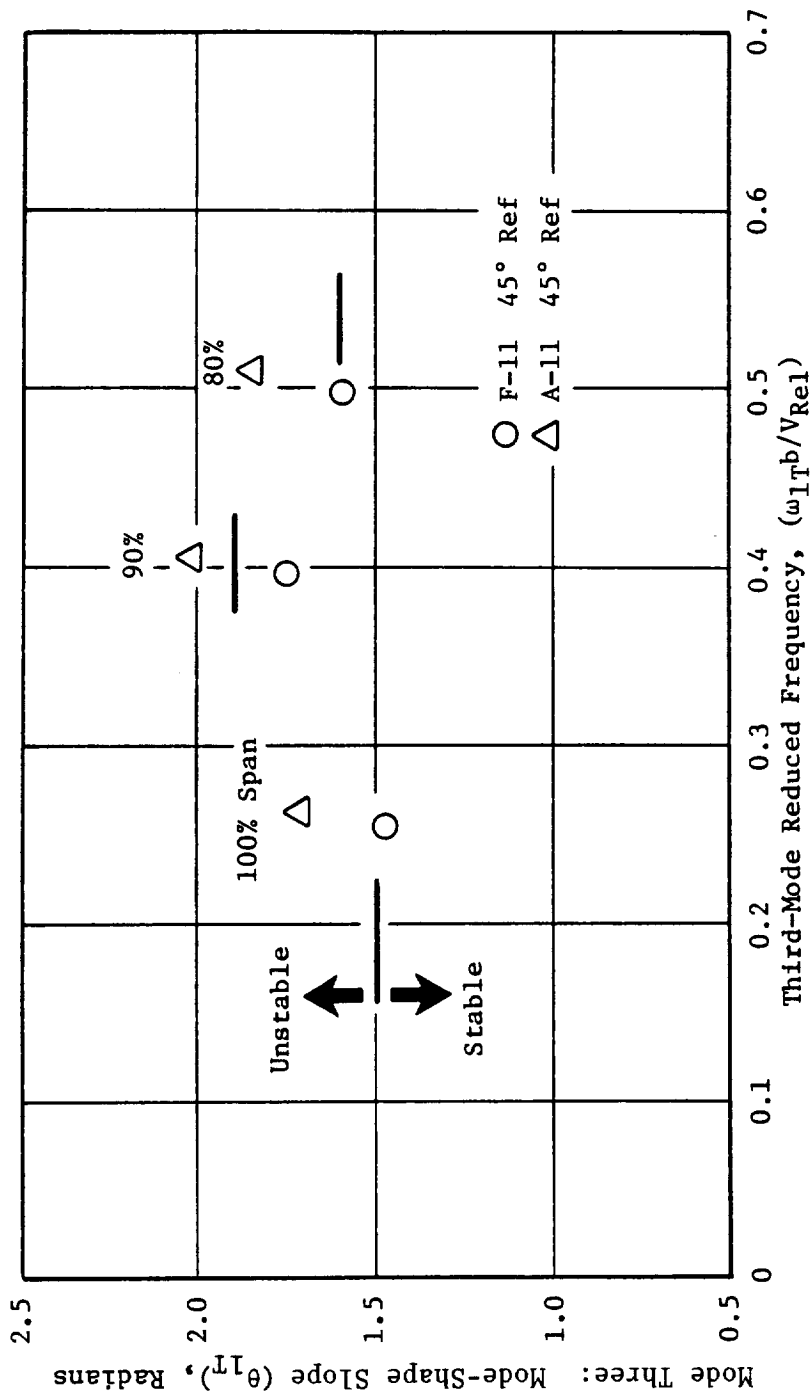


Figure 91. Quick-Look Stability Comparison of the F-11/A-11 in the First-Torsion Mode.

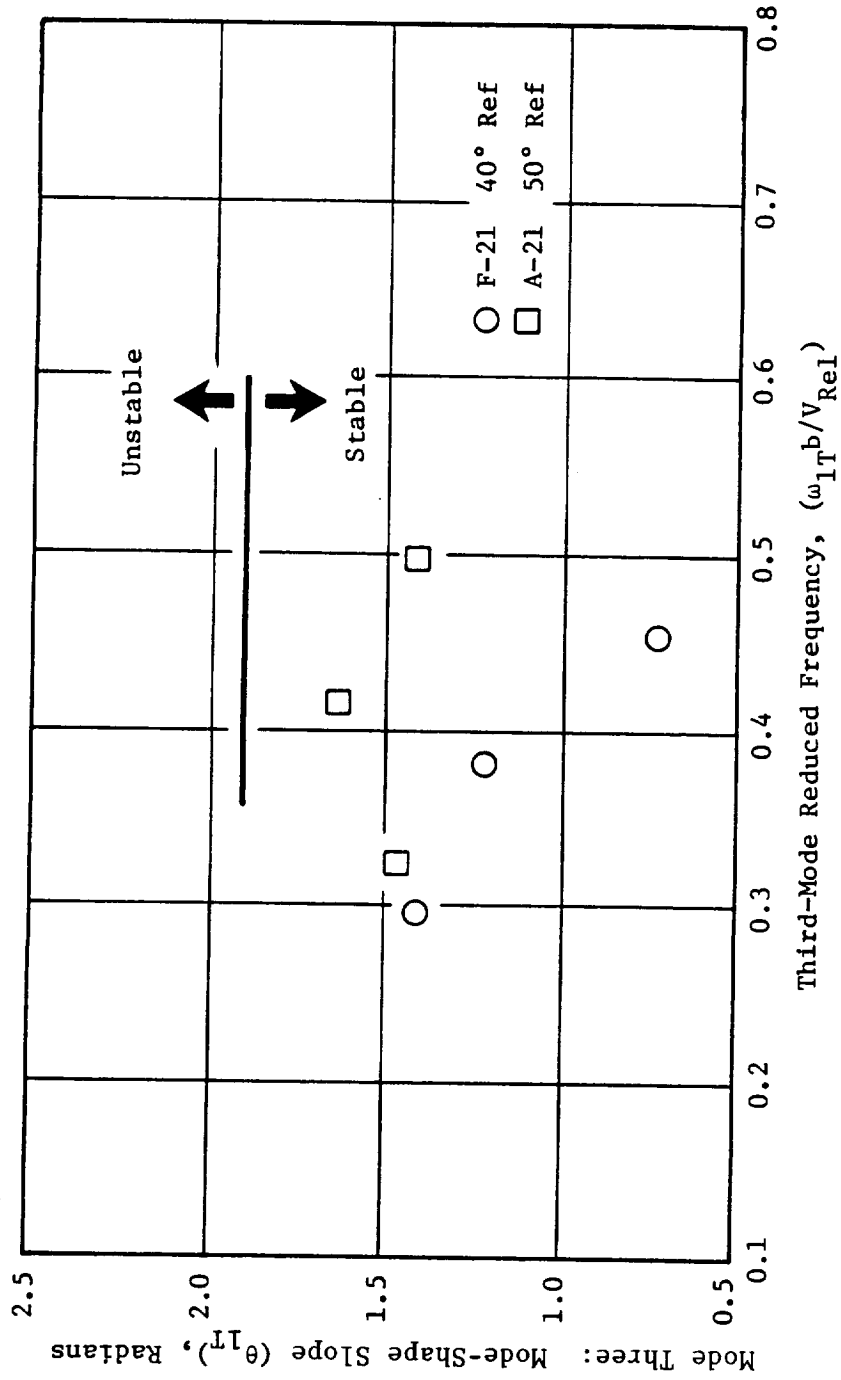


Figure 92. Quick-Look Stability Comparison of the F-21/A-21 in the First-Torsion Mode.

A-11 MPS Model Cruise 9 Blades
 $M_\infty = 0.80$ Stagger Setting
 Fixed Root

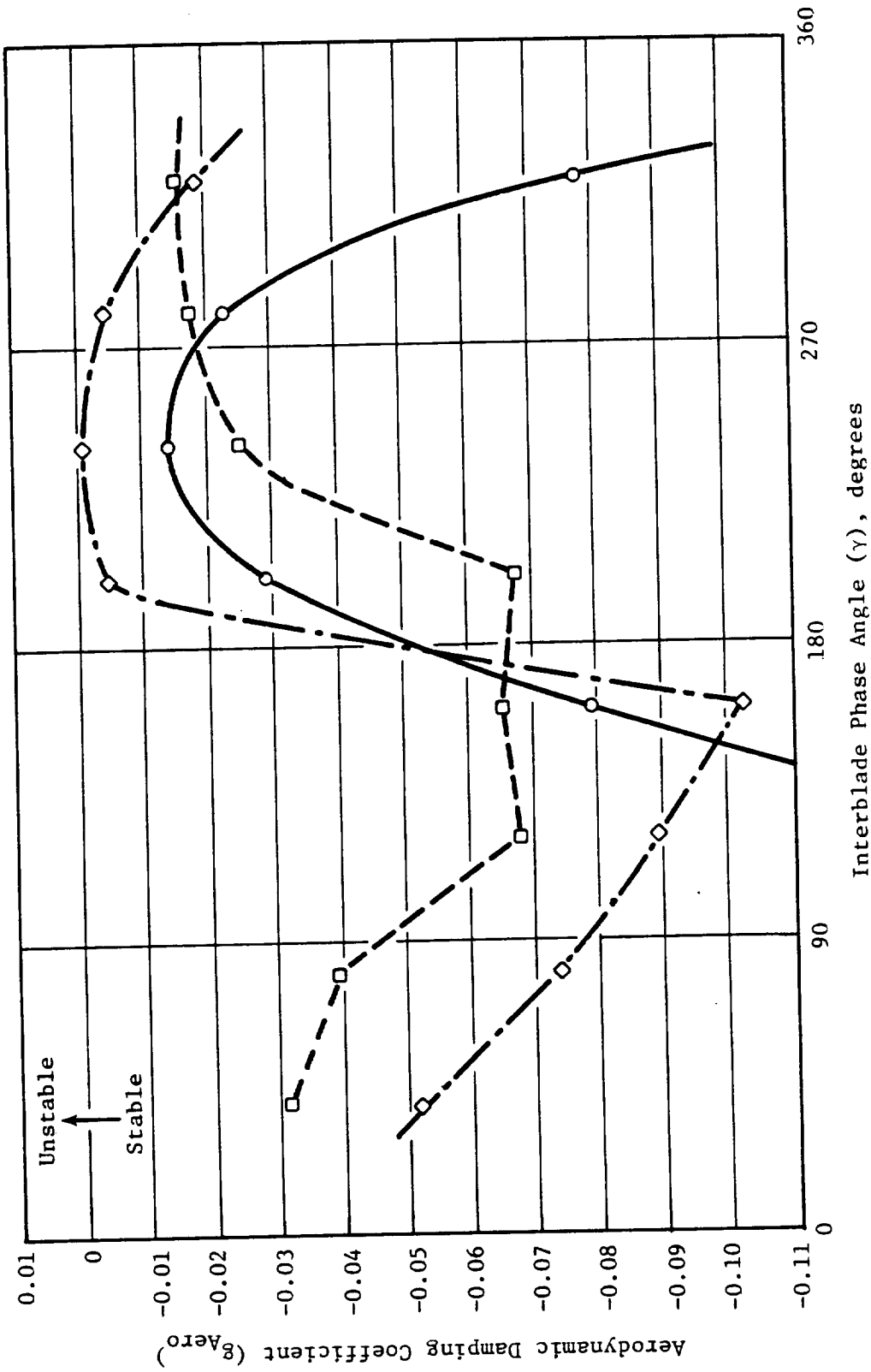


Figure 93. Stability Estimate for the A-11 MPS Blade.

combinations thereof, to guide the tradeoffs and arrive at acceptable candidate blade designs efficiently should an iterative process be necessary to obtain a stable blade. As demonstrated in Figure 93, the A-11 blade passed the audit. Meanwhile, an assessment of the blades was made to evaluate the acoustic performance of the designs.

Next, a steady-state analysis was conducted at design loadings to obtain the calculated stresses and deflections contained in the Task III report; whereupon, the stresses, frequencies, and stability were found to be in the desired range for the blades with the material ply layups chosen for the composite shells. Thus, it was not necessary to recycle the design process to alter ply layup or modify airfoil shapes to refine the aerodynamic design.

Having identified acceptable blade designs, detailed aeroelastic analyses were performed to predict stability. The results are presented in Figures 94 through 98. Blade stability was acceptable and so design proceeded to define the cold (static) shapes so MPS blades could be fabricated.

When determining the cold shape of blades, an iterative procedure is used which recognizes that deflections are usually large and nonlinear. The hot-shape model was run first in GE's CLASS/MASS computer program, and resultant deflections were then subtracted from the original hot shape to obtain the first cold shape. The cold-shape model was then run through CLASS/MASS again, and the resultant hot shape was compared to the original hot shape. If the two were not within an acceptable tolerance, the cold-shape coordinates were adjusted, and the process repeated until a final cold shape was defined which would deflect to the desired hot shape. The accuracy of CLASS/MASS deflection predictions are largely dependent on the gas loadings input from aerodynamic design. Preliminary results of actual blade deflections measured with lasers indicate good agreement with analysis. Figure 99 illustrates the hot-to-cold-shape determination process.

In summary, the MPS blade design process followed the steps listed below:

1. Initial hot aerodynamic shape is defined.
2. Initial ply layup is chosen based on experience.
3. A finite element model is set up using geometry and gas loads from aerodynamic design and the initial ply layup definition.
4. A modal analysis is run to obtain frequencies and mode shapes.
5. Modal analysis is used to conduct quick look stability assessment; if stability is unacceptable, the ply layup is redefined, the correspondingly altered finite element analysis repeated, and the quick look stability analysis reiterated until stability is acceptable. If the redefinition of ply layup does not produce acceptable stability, the airfoil aerodynamic shape is modified and the ply layup cycle repeated until blade stability is acceptable.
6. A steady-state analysis is run at design loadings and stresses to investigate deflections.
7. Detailed aeroelastic analysis is used to predict stability. If stability is unacceptable, the procedures from Step 5 involving ply/fiber adjustments and/or blade shape changes are reiterated until a stable blade is produced.
8. The cold airfoil shape is then obtained through an iterative process.

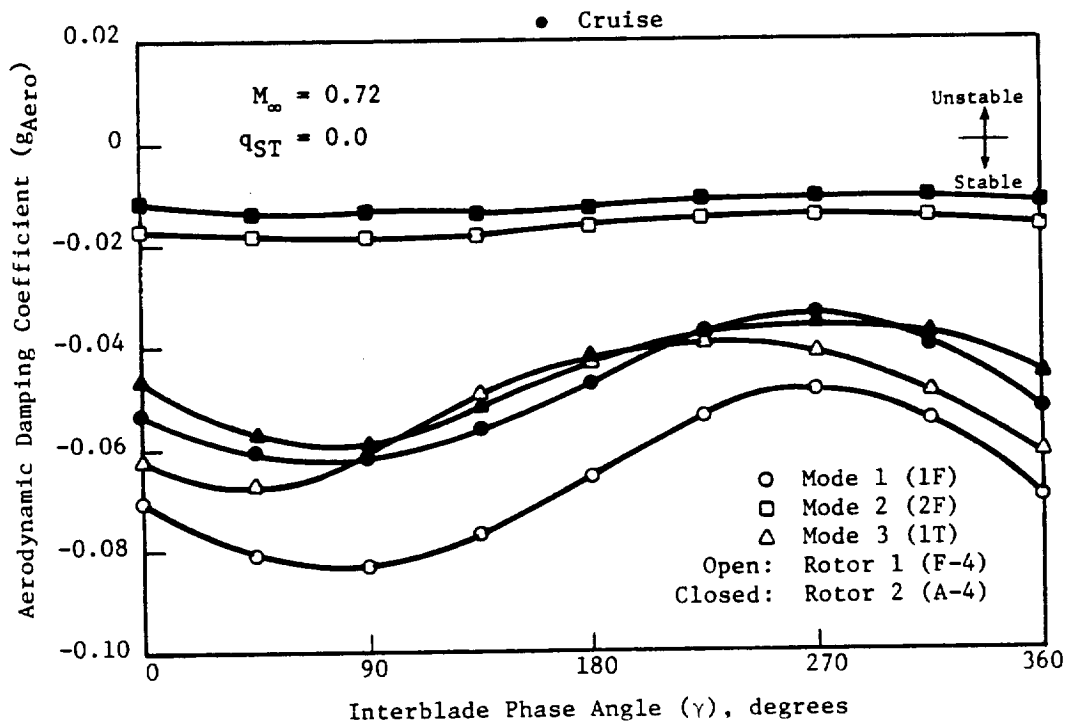
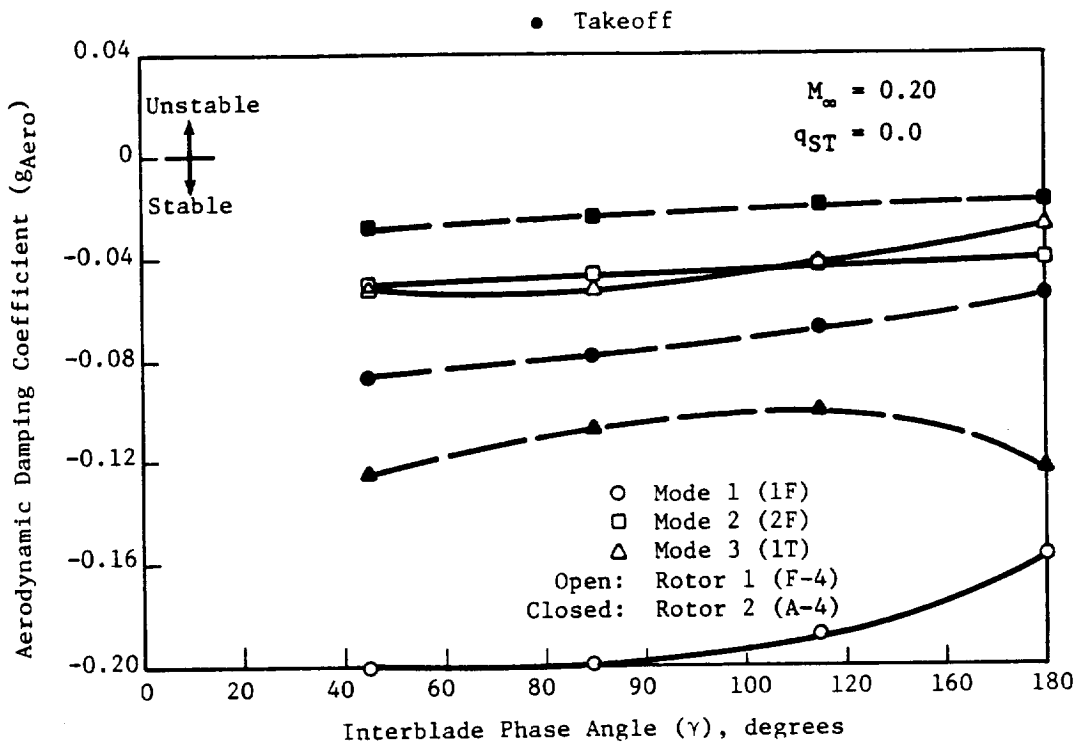


Figure 94. Stability Estimate for MPS F-4/A-4 Blades.

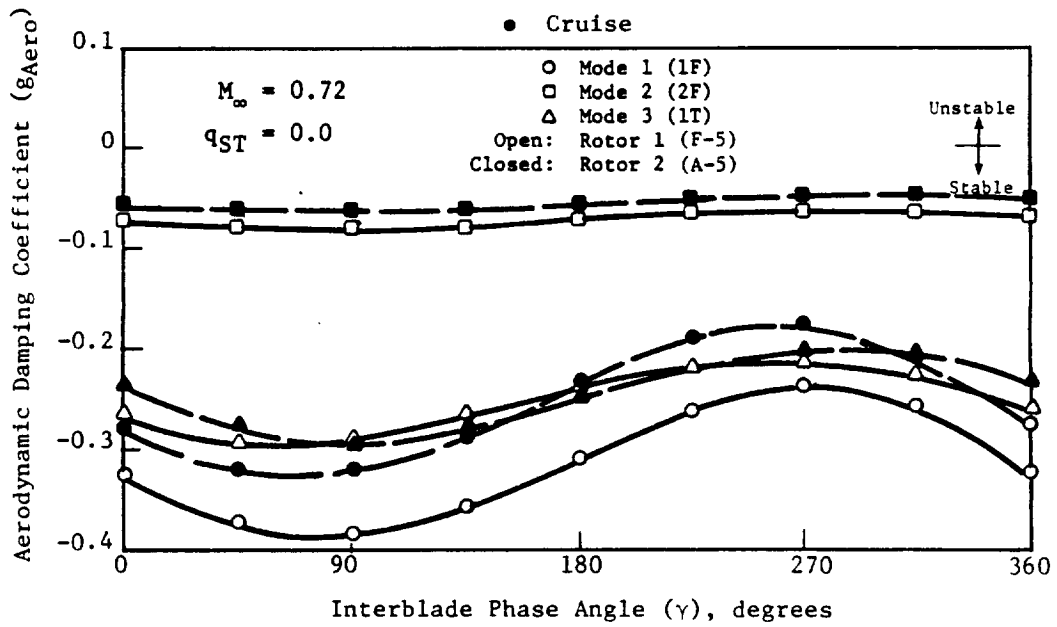
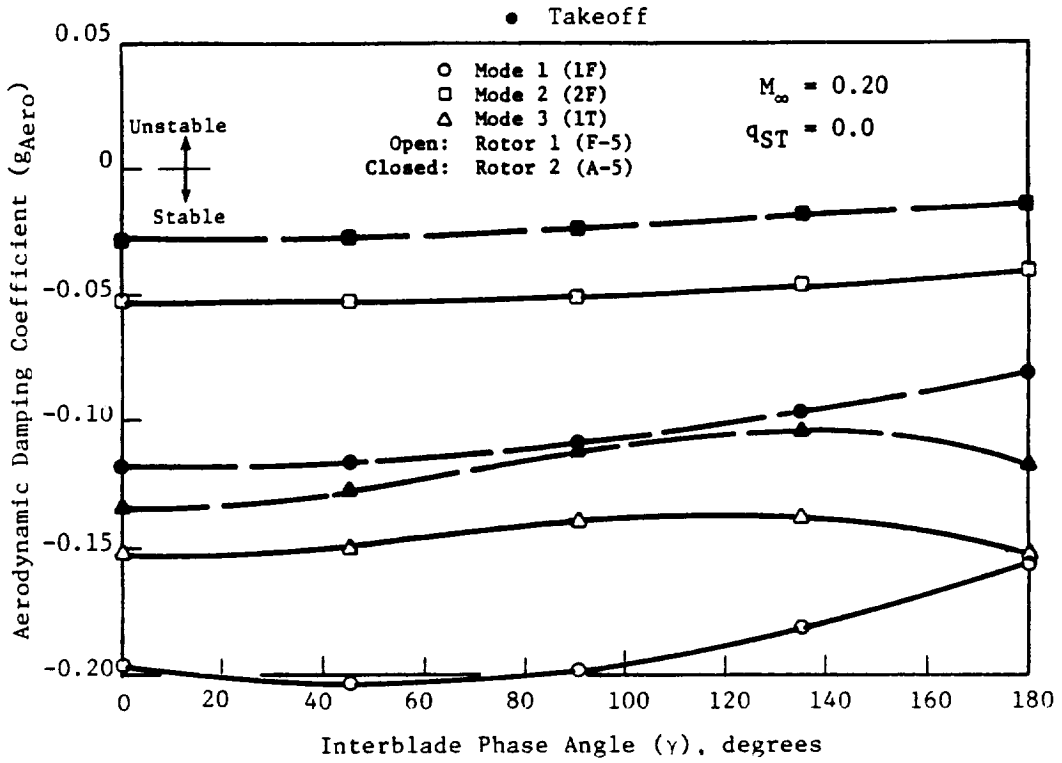


Figure 95. Stability Estimate for MPS F-5/A-5 Blades.

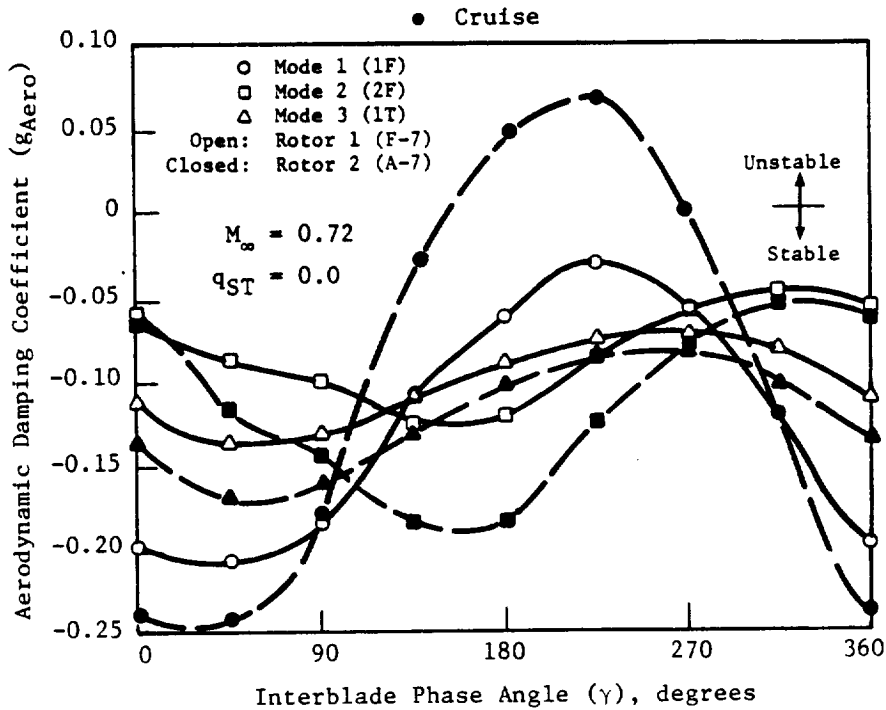
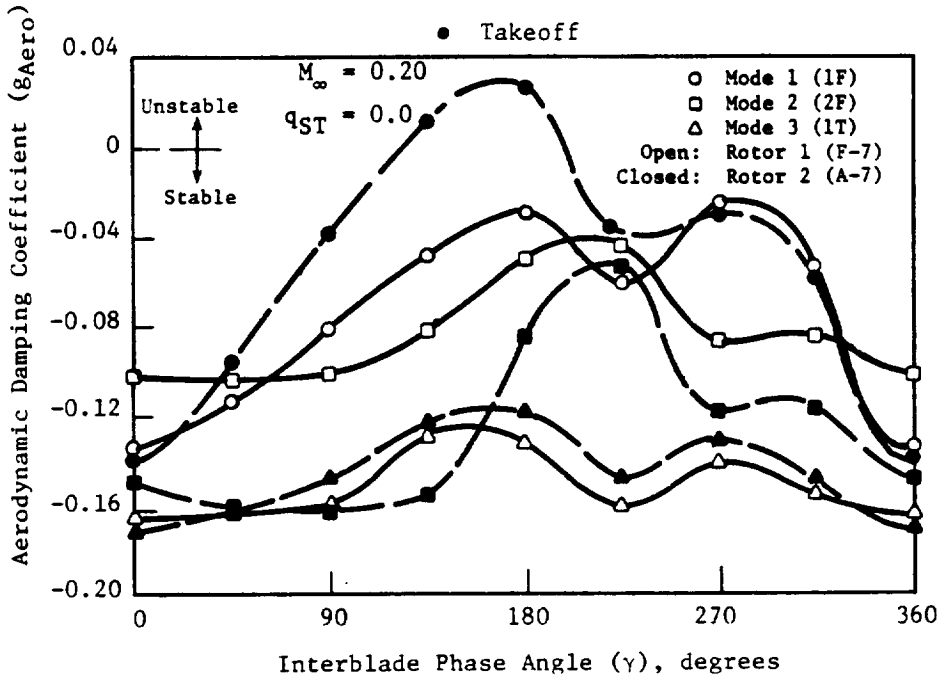


Figure 96. Stability Estimate for MPS F-7/A-7 Blades.

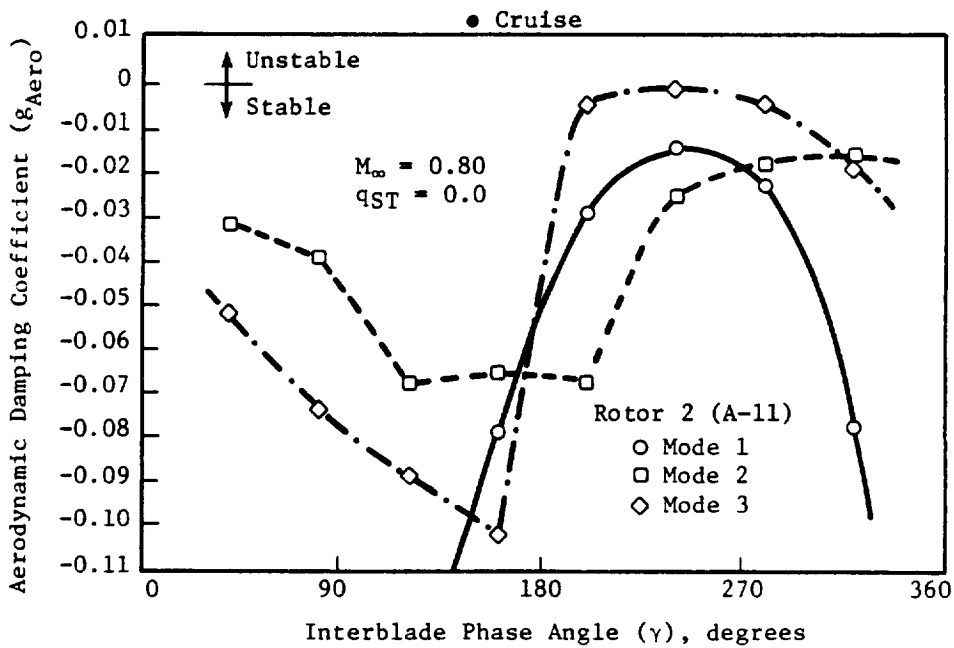
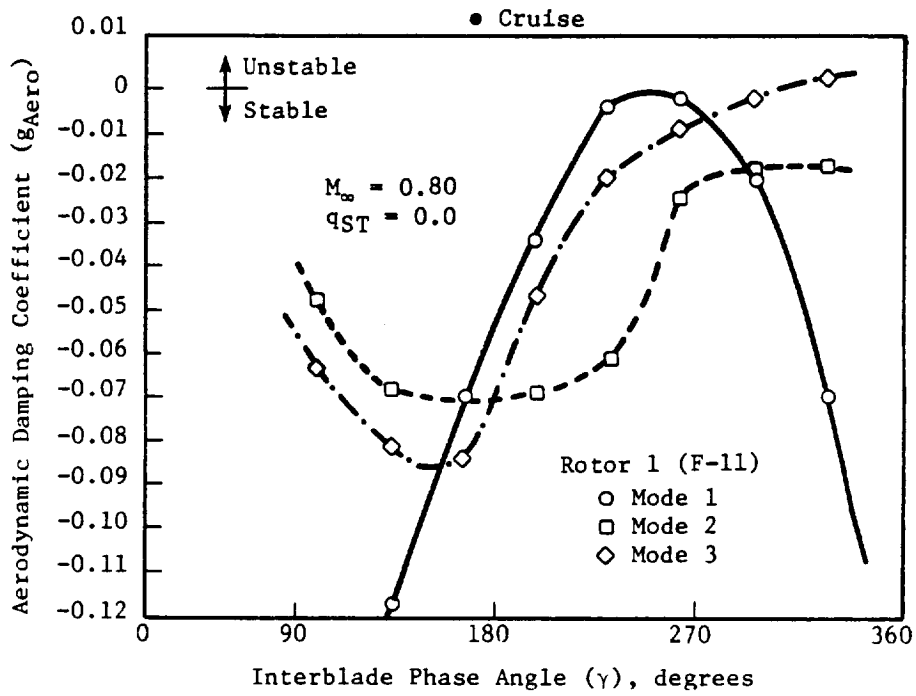


Figure 97. Stability Estimate for MPS F-11/A-11 Blades.

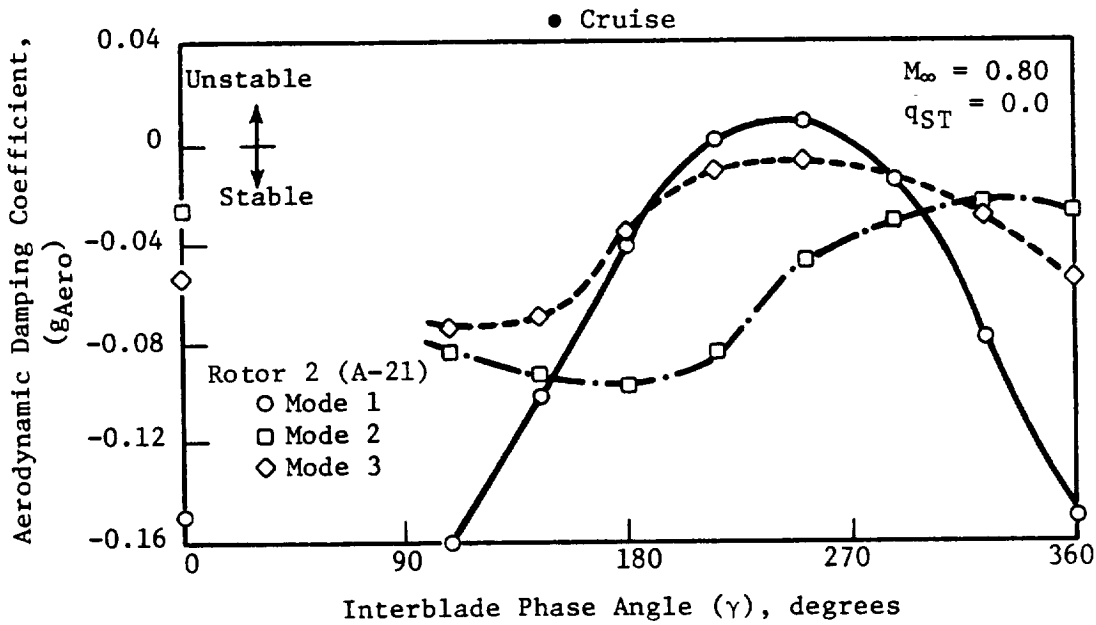
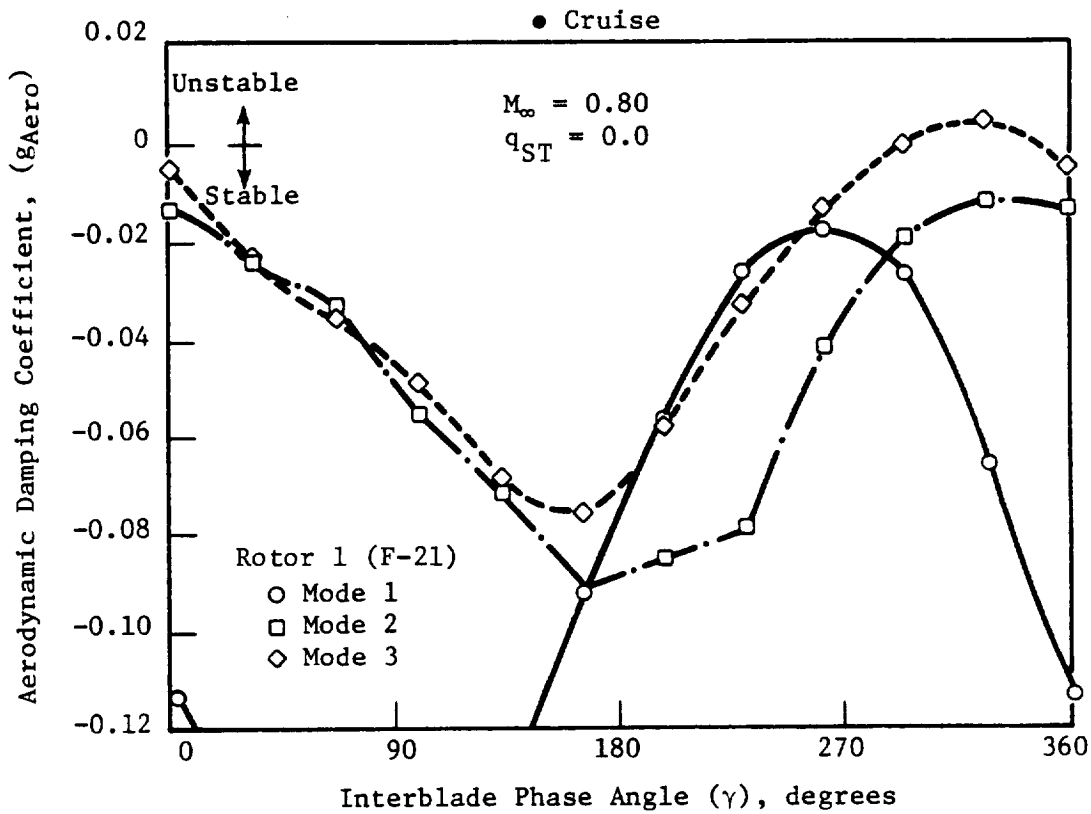


Figure 98. Stability Estimate for MPS F-21/A-21 Blades.

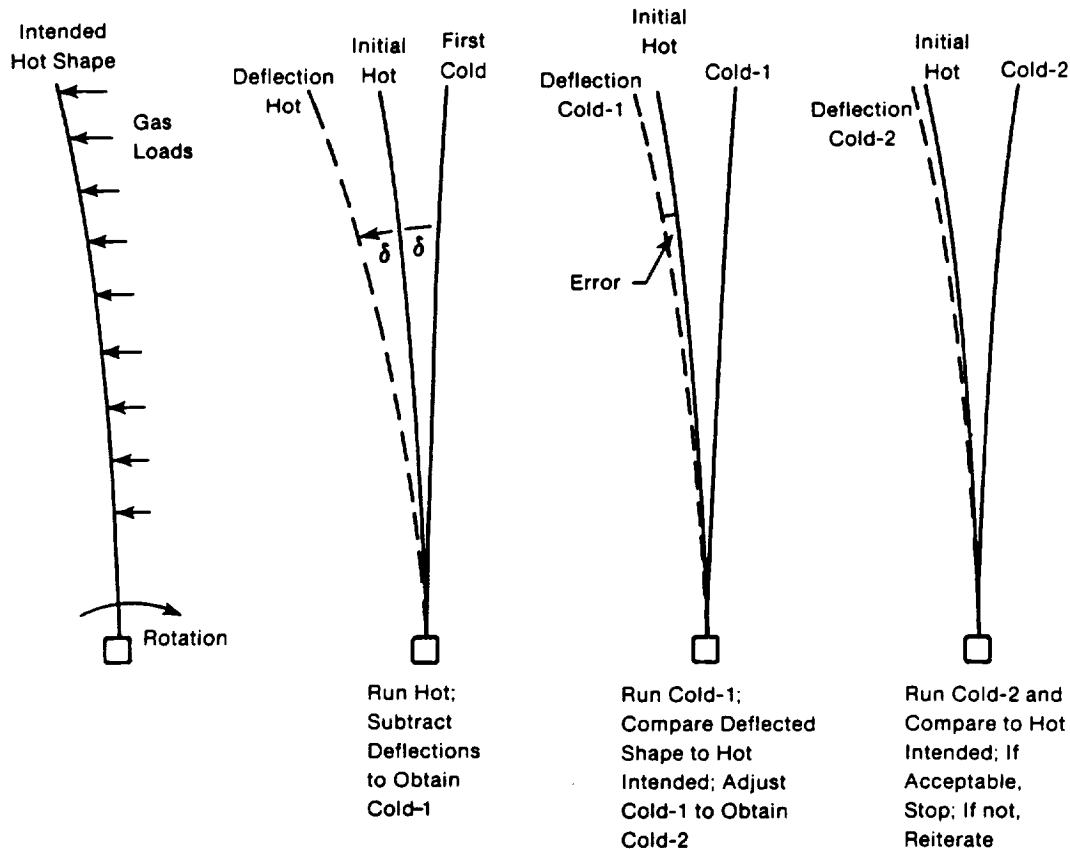


Figure 99. Hot-to-Cold Shape MPS Blade Determination.

9. The cold shape is released to Drafting, where the appropriate manufacturing drawings are made.
10. A titanium master model, spars, and blades are fabricated.

4.2 Blade Fabrication and Quality Control

Blade fabrication was achieved by utilizing outside vendors to machine the Ti6-4 master model and spars, and then using existing GE facilities and personnel to apply the composite shells to the spars. Adequate quantities were procured for the bench testing required and to ensure that spars were available to run the planned MPS rig tests.

For each airfoil configuration, a metal master tool was machined to exact airfoil coordinates, by an outside vendor. To assure conformance to design drawings, the model was inspected at each airfoil section; a die was then cast from the master blade. Utilizing the dies, the composite shell was applied over the spar and formed to final blade shape. This method of fabrication produced very small variance from blade to blade. All blades were weighed, ultrasonically scanned, and inspected (visually and dimensionally).

The basic compression molding process developed by GE for composite airfoils as applied to MPS blades is diagrammed in Figure 100 and includes the following:

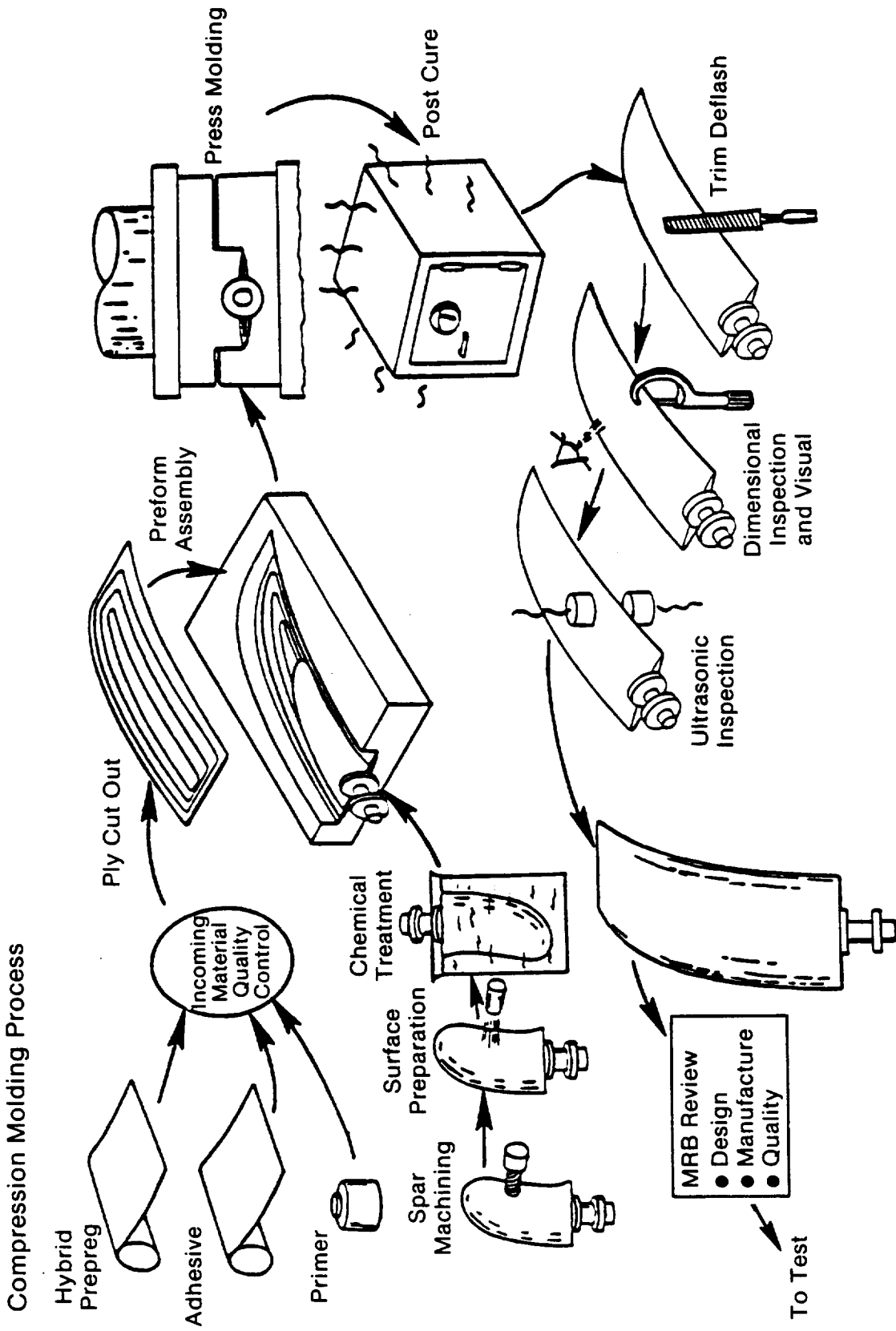


Figure 100. Basic MPS Blade Manufacturing Process.

- **Ply Pattern Generation** – The requisite number and geometry of laminae that would uniformly fill the mold and/or the volume between the metallic spar and the die cavity were determined by scribing the metallic master model blade topographically.
- **Ply Assembly** – Fixtures were manufactured for assembling the blade laminae in the correct sequence and relative location.
- **Spar Preparation** – Fully NC (numerically controlled), machined spars were chemically and mechanically etched and primed to prepare the surface for bonding to the composite airfoil during the co-curing process.
- **Molding** – Using a metallic, fully machined and approved master model blade, epoxy mold tools were fabricated. The critical molding process was accurately controlled to ensure good consolidation of the composite, void-free laminates, and molding uniformity. Precise die-closure programs were developed to produce blades of consistent quality.
- **Finishing Operations** – The minor finishing operations to the molded airfoils included deflashing and finishing of leading and trailing edges.

The detailed process used by GE to fabricate the MPS blades is outlined more thoroughly in the itemized procedures presented in a separate informal report covering Task III of this contract (GE TM No. 87-528).

Manufacturing and quality-control specifications, plans, and procedures were implemented to ensure the use of the highest quality materials and to control the blade fabrication processes. The plans covered every operation of the blade manufacturing processes from the time the raw materials were procured until the part was delivered to test. Process control records were maintained in individual files and included such information as routing cards, molding cycle charts, temperature recording charts, dimensional inspections, material properties, and chemical analyses. All blades were nondestructively inspected by ultrasonic through-transmission with a C-scan print-out record that also formed part of the individual blade documentation.

Before any blade was released to test, a Material Review Board Committee (consisting of a cognizant design engineer, a manufacturing engineer, and a quality representative) reviewed it visually, together with the dimensional-inspection records, process records, and C-scans to ensure acceptable quality.

4.3 Blade Instrumentation and Bench Testing

Each blade configuration underwent bench testing prior to operation on the MPS; the following subsections provide details and results of the bench testing.

4.3.1 Blade Strain Distributions

One blade from each stage of each configuration was heavily instrumented with strain gauges, and the strain distributions for the relevant modes were measured. The gauge locations for the F-7 and A-7 blades are shown in Figures 101 and 102, and results of the strain distribution bench tests are provided in the Task III informal report (GE TM 87-528), along with gauge locations and strain distributions for the remaining blade configurations tested.

All Gages are 1/16 Inch, Except as Noted
 Gages are Equally Spaced
 Leads are 5-Foot Long, 36-Gage, with Copper Splice

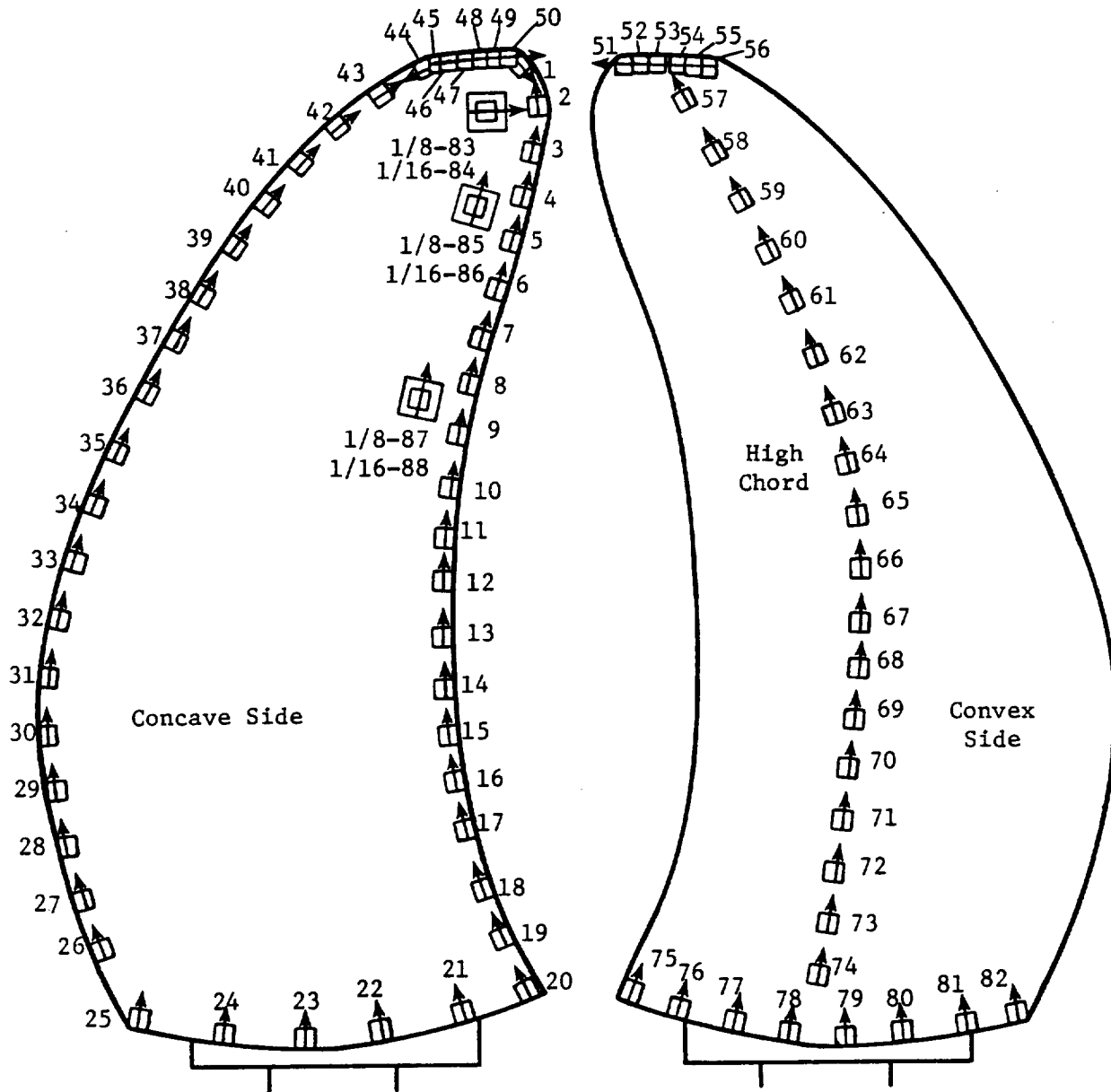


Figure 101. F-7 Blade Strain Distribution Instrumentation.

All Gages are 1/16 Inch, Except as Noted
 Gages are Equally Spaced
 Leads are 5-Foot Long, 36-Gage, with Copper Splice

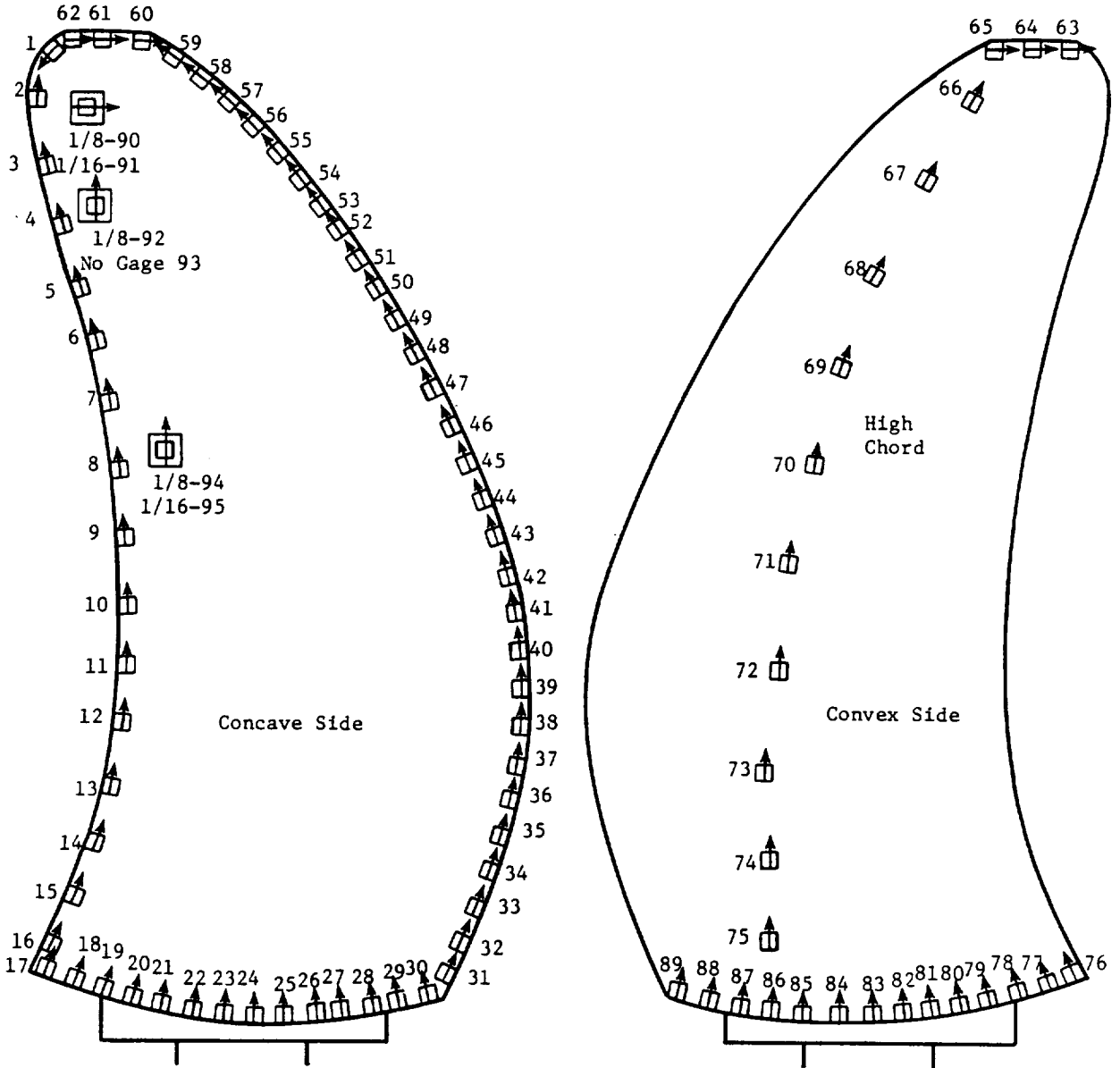


Figure 102. A-7 Blade Strain Distribution Instrumentation.

4.3.2 Blade Frequency Testing

Blade designs were frequency checked, and the mode shapes of the natural frequencies were determined. Bench test frequencies and comparisons with analytical frequencies for the F-7 and A-7 blades are tabulated in Tables 15 through 18. Mode shapes from bench testing are compiled in the Task III informal report (GE TM 87-528), as well as the frequency information for the remaining blade configurations.

4.3.3 Blade Pull Testing

A pull test was performed on the F-1/A-1 type MPS blades to determine the bond strength of the spar/shell interface. A radial load, oriented at the composite shell center of gravity, was applied until the spar separated from the shell. The blade shell was molded into a Devcon block (Figure 103) to which the load was uniformly applied. The load was increased at a slow rate until failure occurred. The spar separated from the shell at slightly over 15,000 lb; this is well above the operating load on the blade. At cruise conditions, the load is estimated to be 1,100 lb. It was concluded that the bond between the spar and shell had excellent strength characteristics, and it was assumed that all blades with similar-size spars would produce similar results.

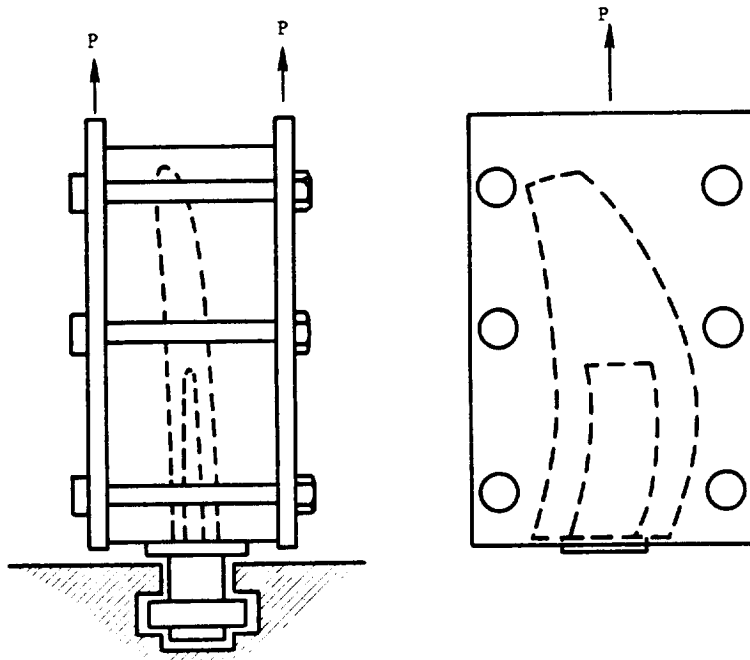


Figure 103. Pull Test Schematic.

4.3.4 Blade Fatigue Testing

Blade-tip damage occurred during MPS testing of the F-4/A-4 and F-5/A-5 blades with the original (0/20/0/-20/...) 5-mil ply layup. It was determined that the F-5/A-5 blades had failed in

Table 15. F-7 Bench Test Frequencies (Hz).

Mode	Test-Blade Number									
	2	3	4	5	6	7	8	9	10	11
1 1F	198	188	188	194	195	190	192	192	194	193
2 2F	516	512	510	514	510	510	512	506	508	500
3 1T	706	675	681	730	708	670	700	716	722	690
4 3F	988	989	992	1006	982	993	994	988	984	970
5 3F'	1128	1106	1100	1104	1116	1095	1122	1120	1124	1138
6 2T	1310	1285	1283	1350	1374	1292	1306	1332	1314	1270
7 4F	1624	1660	1661	1698	1650	1677	1666	1676	1654	1600
8 3T	1874	1841	1853	1954	1878	1856	1854	1822	1868	1800
9 5F	2434	2434	2496	2436	2474	2476	2470	2388	2480	2372
10 4T	2646	2778		2608	2790	2800	2760	2528		2648

	12	13	14	15	16	17	18	19	Mean	σ
1 1F	186	197	196	198	194	194	192	195	193	3.4
2 2F	504	510	502	508	510	502	505	510	508	4.3
3 1T	675	706	720	728	738	704	687	700	703	20.0
4 3F	985	990	996	996	986	972	984	986	988	8.4
5 3F'	1089	1122	1120	1134	1106	1124	1091	1122	1114	14.5
6 2T	1277	1304	1310	1324	1342	1284	1307	1308	1307	22.0
7 4F	1661	1654	1608	1616	1660	1618	1661	1654	1650	26.2
8 3T	1853	1868	1844	1874	1934	1848	1905	1850	1868	34.9
9 5F	2500	2474	2410	2444	2564	2420	2358	2448	2449	49.9
10 4T			2734	2768		2670	2560	2774	2697	92.7

Table 16. Comparison of F-7 Analytical and Bench Test Frequencies (Hz).

Mode	Analytic, 0% Speed	Analytic, 100% Speed	Average Bench
1 1F	196	293	193
2 2F	468	558	508
3 1T	773	906	703
4 3F	901	1037	988
5 3F'	1115	1136	1114
6 2T	1373	1528	1307
7 4F	1522	1643	1650
8 3T	2000	2231	1868
9 5F	2279	2402	2449
10 4T	2778	3095	2697

Table 17. A-7 Bench Test Frequencies (Hz).

Mode	Test-Blade Number									
	1	2 *	3 †	4 *	5	6	7	8	9	10 *
1 1F	205	200	202	192	201	201	201	201	178	194
2 2F	530	534	516	517	524	528	532	522	522	519
3 1T	664	636	688	629	666	652	656	654	636	630
4 3F	1000	1014	976	982	982	994	1008	984	996	989
5 A	1214	1208	1240	1205	1248	1228	1234	1230	1212	1200
6 2T	1256	1248		1247	1292	1286	1292		1277	1240
7 4F	1612	1636	1570	1578	1584	1600	1622	1590	1608	1600
8 3T	1870	1884	1974	1874	1910	1872	1871	1852	1848	1876
9 5F	2304	2342	2258	2294	2278	2300	2318	2276	2296	2284
10 4T	2592	2606	2628	2584	2618	2564	2584	2528	2560	2628
11	2806	2800	2894	2864	2898	2800	2862	2814	2824	2844

	12 *	13 *	14	15	16	17	18	Mean	σ	
1 1F	198	198	200	202	200	204	205	199	6.4	
2 2F	531	529	530	526	526	530	536	527	5.8	
3 1T	634	638	648	648	640	660	664	650	15.8	
4 3F	1024	1012	990	998	1000	998	1004	997	13.1	
5 A	1207	1210	1234	1220	1214	1244	1250	1223	16.2	
6 2T	1249	1253	1292	1292	1286	1290	1296	1273	21.1	
7 4F	1634	1628	1590	1628	1608	1618	1616	1607	19.9	
8 3T	1906	1881	1874	1866	1850	1902	1896	1880	21.7	
9 5F	2333	2314	2272	2322	2790	2334	2328	2302	24.6	
10 4T	2632	2594	2560	2576	2562	2600	2592	2589	28.7	
11	2838	2778	2792	2760	2840	2870	2800	2828	39.9	

* Blade Frequencies Checked After Application of Engine Gauges

† Strain-Distribution and Mode-Shape Blade

Table 18. Comparison of A-7 Analytical and Bench Test Frequencies (Hz).

Mode	Analytic, 0% Speed	Analytic, 100% Speed	Average Bench
1 1F	198	291	199
2 2F	489	565	527
3 1T	705	893	650
4 3F	932	1039	997
5 A	1112	1130	1223
6 2T	1323	1536	1273
7 4F	1548	1654	1607
8 3T	1973	2167	1880
9 5F	2325	2443	2302
10 4T	2751	3138	2589

a 2S mode; to verify this, bench fatigue testing was conducted driving the F-5 (-1 design) in the 2S mode at approximately 2000 z. Three blades (F-5, No. 4; F-5, No. 1A; and F-5, No. 6) were driven in this mode acoustically by a siren. Failure occurred at the tip of these blades in a manner similar to that experienced during MPS testing. Test results are summarized in Tables 19 and 20 for F-5 (No. 4) and F-5 (No. 1A) blades, respectively.

A fatigue test was also performed on the new ply layup F-5 (-2 design) blade. This new ply layup was (0/90/45/90/0-45) for thin (0.0025-in.) plies and (0/20/0/-20/ ...) for thick (0.005-in.) plies. This blade did not have a 2S mode in the operating regime on the Campbell diagram; instead, it was driven in 2F, the mode determined most likely to be excited during operation by instability or separated-flow vibration. No failure occurred while the blade was driven in this mode. The instrumentation for the F-5 (No. 10) blade utilized in this evaluation is illustrated in Figures 104 and 105, and test results are presented in Tables 21 and 22.

4.3.5 MPS Blade Instrumentation for Operational Testing

As previously mentioned, all of the blade configurations were tested to identify strain distribution and vibration characteristics. During MPS operation, strain gauges were applied to four blades on each rotor stage for monitoring the aeromechanical activity of the MPS blades. Gauge locations were based on analytical mode-shape data. There were usually two radially oriented gauges to pick up flex modes and one chordwise gauge near the tip to pick up chordwise-bending

Table 19. F-5 (No. 4) Fatigue Test Results.

Strain on Gauge 4, $\mu\text{in/in. DA}$	Cycles	Frequency, Hz
500	10^7	1960
600	10^7	↓
700	10^7	↓
800	10^7	↓
900	10^7	↓
1000	10^7	↓
1100	10^6	↓
1200	10^6	↓
1300	10^6	↓
1500	10^6	↓
1700	10^6	↓
1900	10^6	↓
2100	10^6	↓
2300	10^6	↓
2500	10^6	↓
2700	10^6	↓
2900	10^6	↓
3100	10^6	↓
3300	10^6	↓
3500	10^6	↓
3700	10^6	↓
3900	10^6	1957
4100	2×10^5 (Failed)	1957

Table 20. F-5 (No. 1A) Fatigue Test Results.

Strain on Gauge 4, $\mu\text{in/in. DA}$	Cycles	Frequency, Hz
2900	10^6	1953
3100	10^6	1953
3300	10^6	1961
3500	10^6	1961
3700	10^6	1960
3900	10^6	1957
4100	10^6	↓
4300	10^6	↓
4500	10^6	↓
4600	10^6	↓
4800	<100 (Failed)	\approx 1957

Table 21. F-5 (No. 10) Fatigue Test Results, Concave Side.

Element	Radial		Chordwise	
	% Max. Stress	Stress, ksi	% Max. Stress	Stress, ksi
1	2	0.4	2	0.4
4	3	0.6	2	0.4
7	3	0.6	4	0.8
10	4	0.8	5	1.0
13	2	0.4	6	1.2
16	7	1.4	1	0.2
19	12	2.4	0	0
22	14	2.8	0	0

Table 22. F-5 (No. 10) Fatigue Test Results, Convex Side.

Element	Radial		Chordwise	
	% Max. Stress	Stress, ksi	% Max. Stress	Stress, ksi
3	0	0	3	0.6
6	1	0.2	2	0.4
9	0	0	4	0.8
12	4	0.8	8	1.6
15	9	1.8	12	2.4
18	8	1.6	7	1.4
21	6	1.2	2	0.4
24	2	0.4	0	0

Not to Scale. Dimensions are Inches (± 0.02). One-Eighth-Inch Gages.

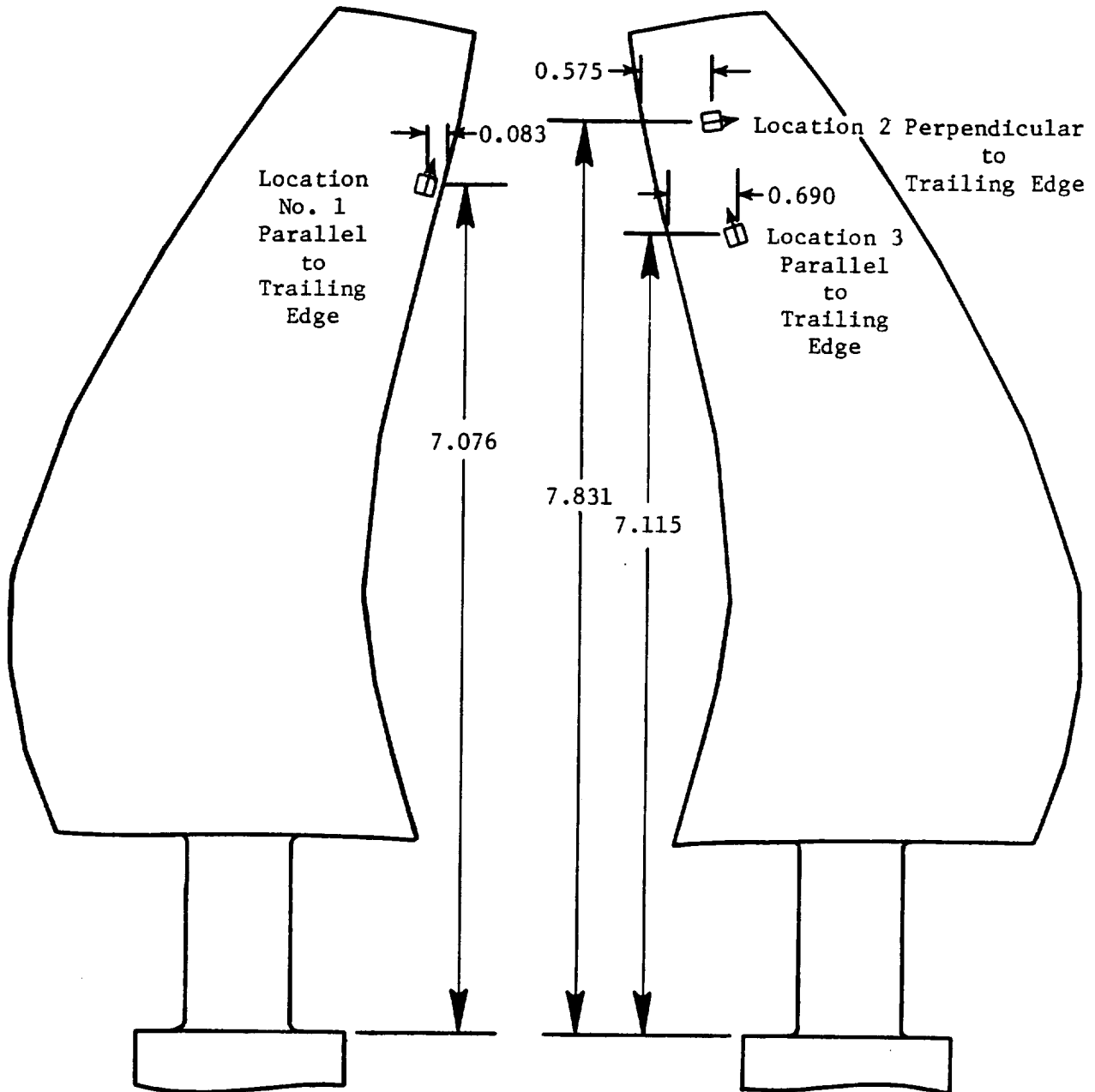


Figure 104. F-5 No. 10 Fatigue Test Gauge Locations, Pressure Side.

Figure 105. F-5 No. 10 Fatigue Test Gauge Locations, Suction Side.

Table 23. F-4 MPS Blade Scope Limits.

Mode	Stress Limit, ksi		
	Gauge 1	Gauge 2	Gauge 3
1 1F	0.4	23.6	29.7
2 2F	1.3	25.2	22.5
3 1T	9.0	14.5	10.4
4 3F	8.8	12.4	6.4
5 3F'	7.3	12.2	1.3
6 2T	6.9	10.6	2.9
7 4F	12.0	5.9	10.2
8 3T	1.6	7.3	6.2
9 4T	20.0	18.8	1.9
10 2S	2.2	9.8	7.9
11	9.6	2.4	2.1
12	2.8	8.4	1.4
13	0.7	1.1	0.9
14	1.4	1.3	1.3
15	11.4	7.4	2.0
16	4.4	3.3	0.8

modes. Gauges were positioned to record as many vibration modes as possible within the engine operating range. Gauge locations for the F-4, A-4, F-5, A-5, F-7, A-7, F-11, A-11, F-21, and A-21 blades as run on the MPS are identified in Figures 106 through 115.

Stress scope limits for gauge monitoring were based on bench test strain-distribution data. Material strengths for the blade layups were calculated using laminate-plate theory with a first-ply failure criterion. The endurance limit for vibratory stresses was assumed to be 30% of the steady-state limit. Goodman diagrams drawn from these two points had an assumed shape based on experience. A computer program was utilized to calculate the limits for each gauge at each mode; inputs were: strain distribution data, analytical steady-state stress distributions, and Goodman diagrams. The resultant scope limits for all MPS blade designs are tabulated in Tables 23 through 32.

4.4 Specialized Support Hardware Design and Fabrication

Several items of hardware were fabricated to support test activities directed toward specialized investigations of acoustic, aerodynamic, and/or aeromechanical phenomena in the GE anechoic chamber and the NASA Lewis 8x6 and 9x15 wind tunnels. This section presents descriptive material related to this specialized support hardware equipment.

4.4.1 The Nine-Blade Hub

The nine-blade hub was designed to be utilized on either the forward or the aft rotor of any of the three MPS rigs. Aluminum nine-blade hub forward and aft fairings were also fabricated to complete the hub assembly. The blade retention and pitch-angle adjustment schemes for the nine-blade hub are identical to those designed into the eight-blade hubs. Complete details of the

Not to Scale. Dimensions are Inches (± 0.02). One-Eighth-Inch Gages.

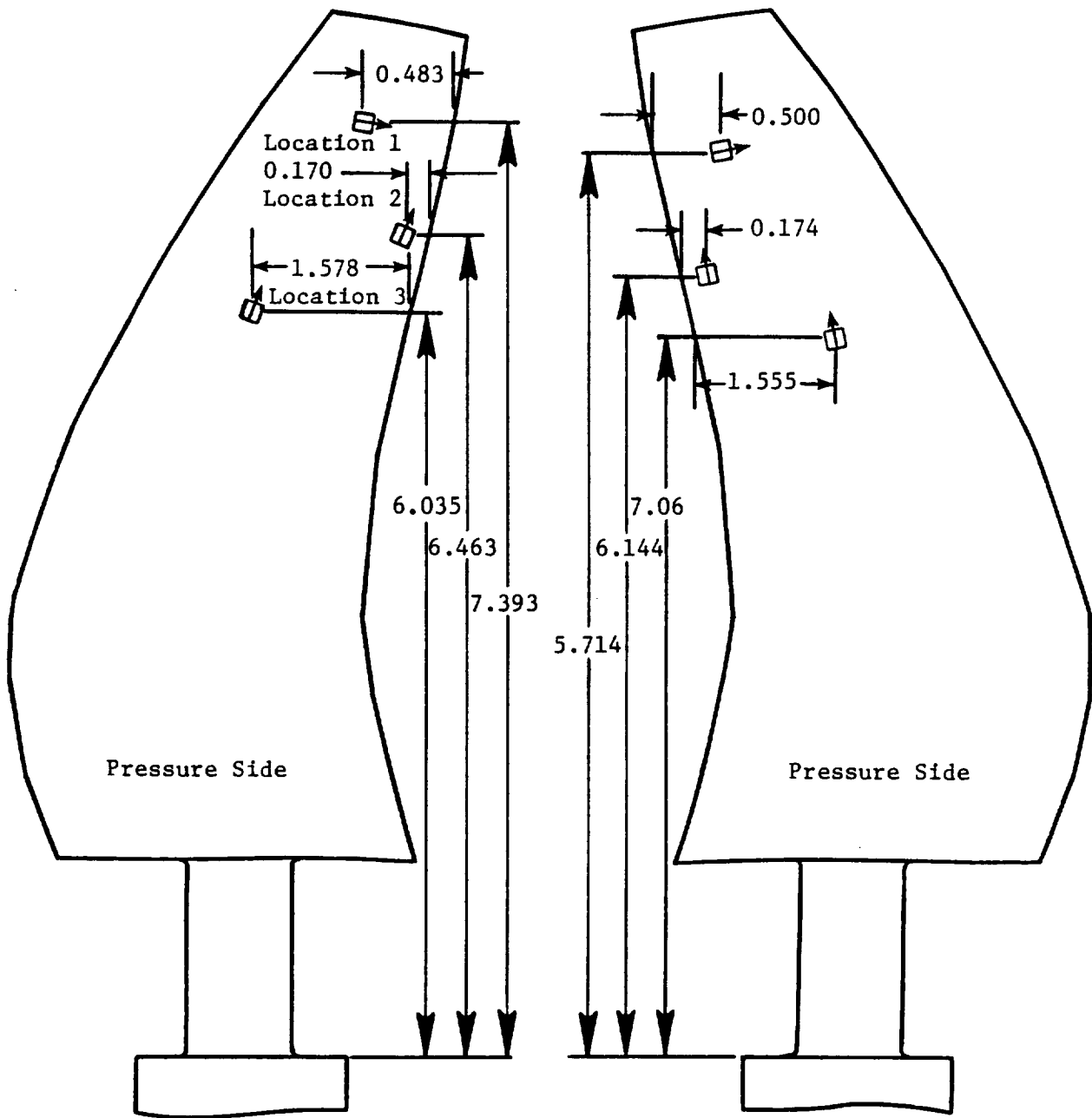


Figure 106. F-4 MPS Blade Gauge Locations.

Figure 107. A-4 MPS Blade Gauge Locations.

Not to Scale. Dimensions are Inches (± 0.02). One-Eighth-Inch Gages.

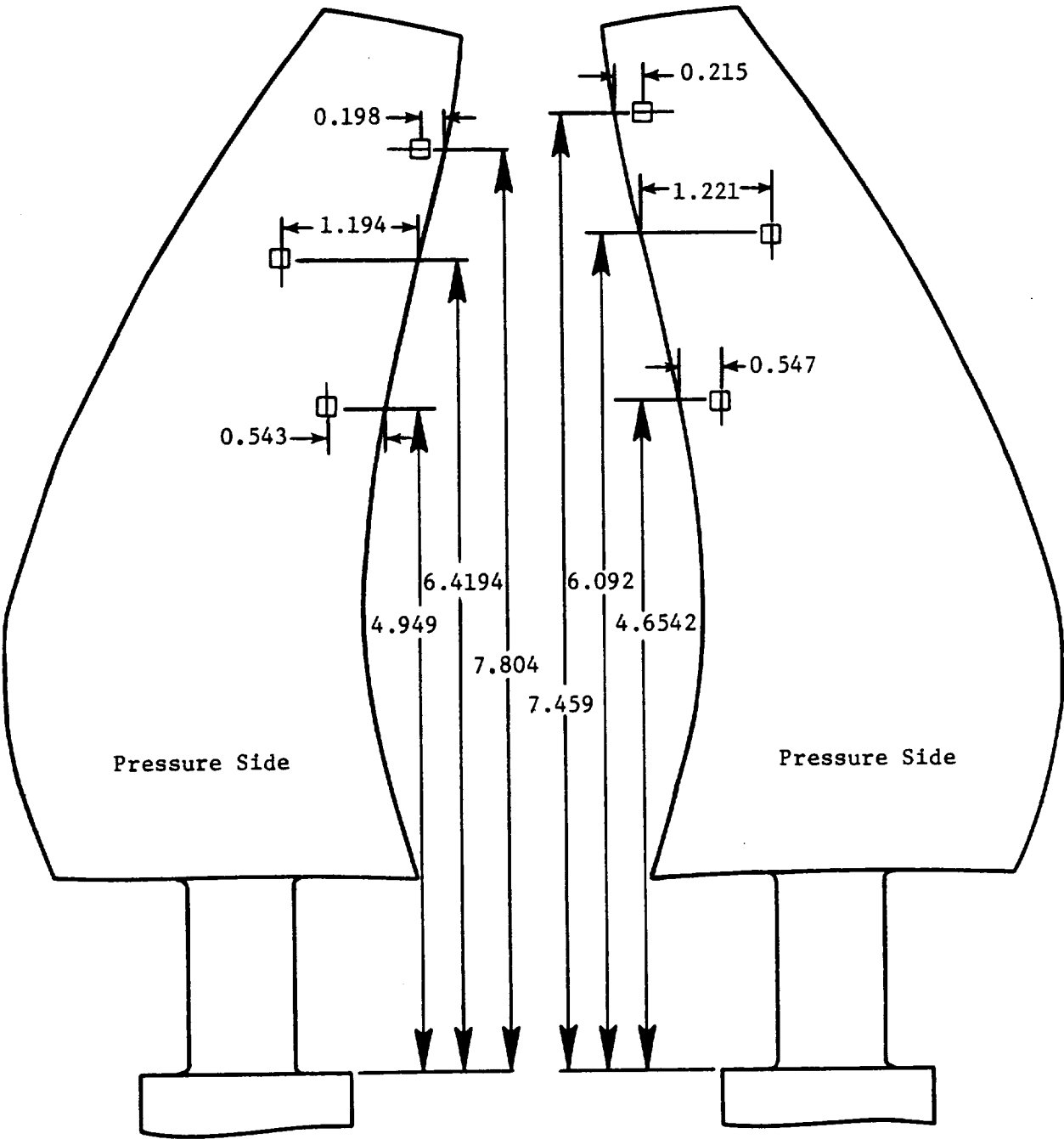


Figure 108. F-5 MPS Blade Gauge Locations.

Figure 109. A-5 MPS Blade Gauge Locations.

Not to Scale. Dimensions are Inches (± 0.02). One-Eighth-Inch Gages.

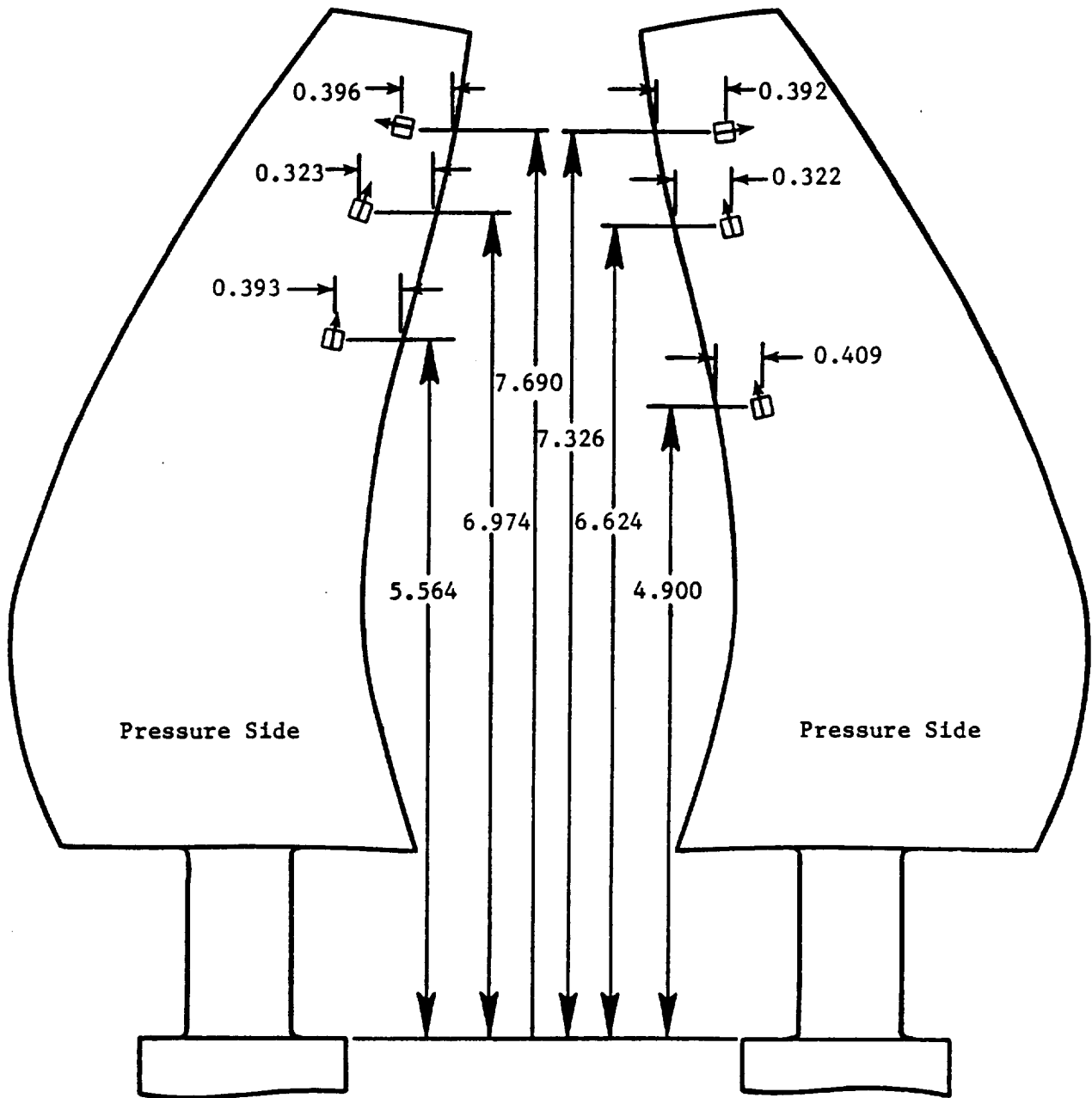


Figure 110. F-7 MPS Blade Gauge Locations.

Figure 111. A-7 MPS Blade Gauge Locations.

Not to Scale. Dimensions are Inches (± 0.02). One-Eighth-Inch Gages.

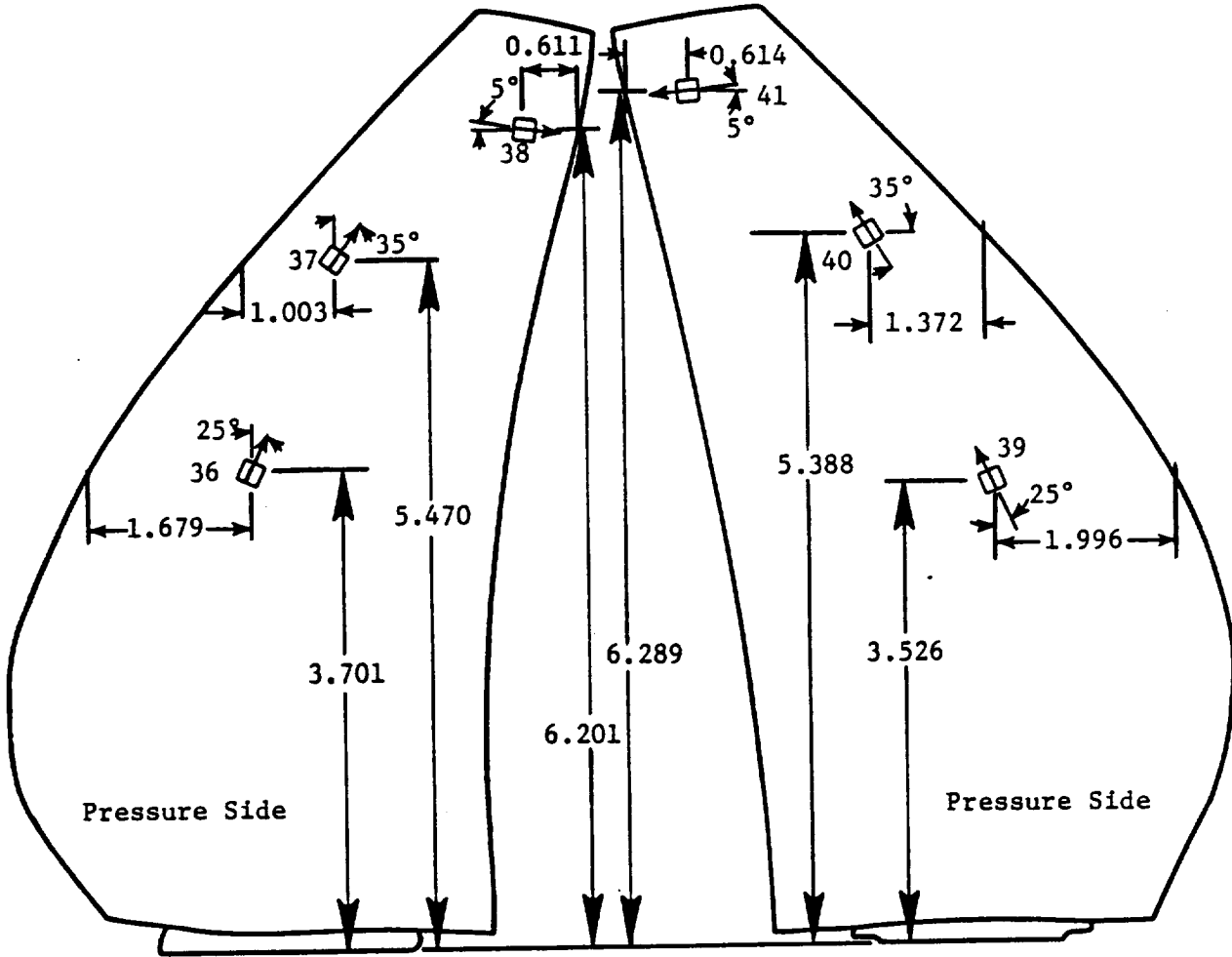


Figure 112. F-11 MPS Blade Gauge Locations.

Figure 113. A-11 MPS Blade Gauge Locations.

Not to Scale. Dimensions are Inches (± 0.02). One-Eighth-Inch Gages.

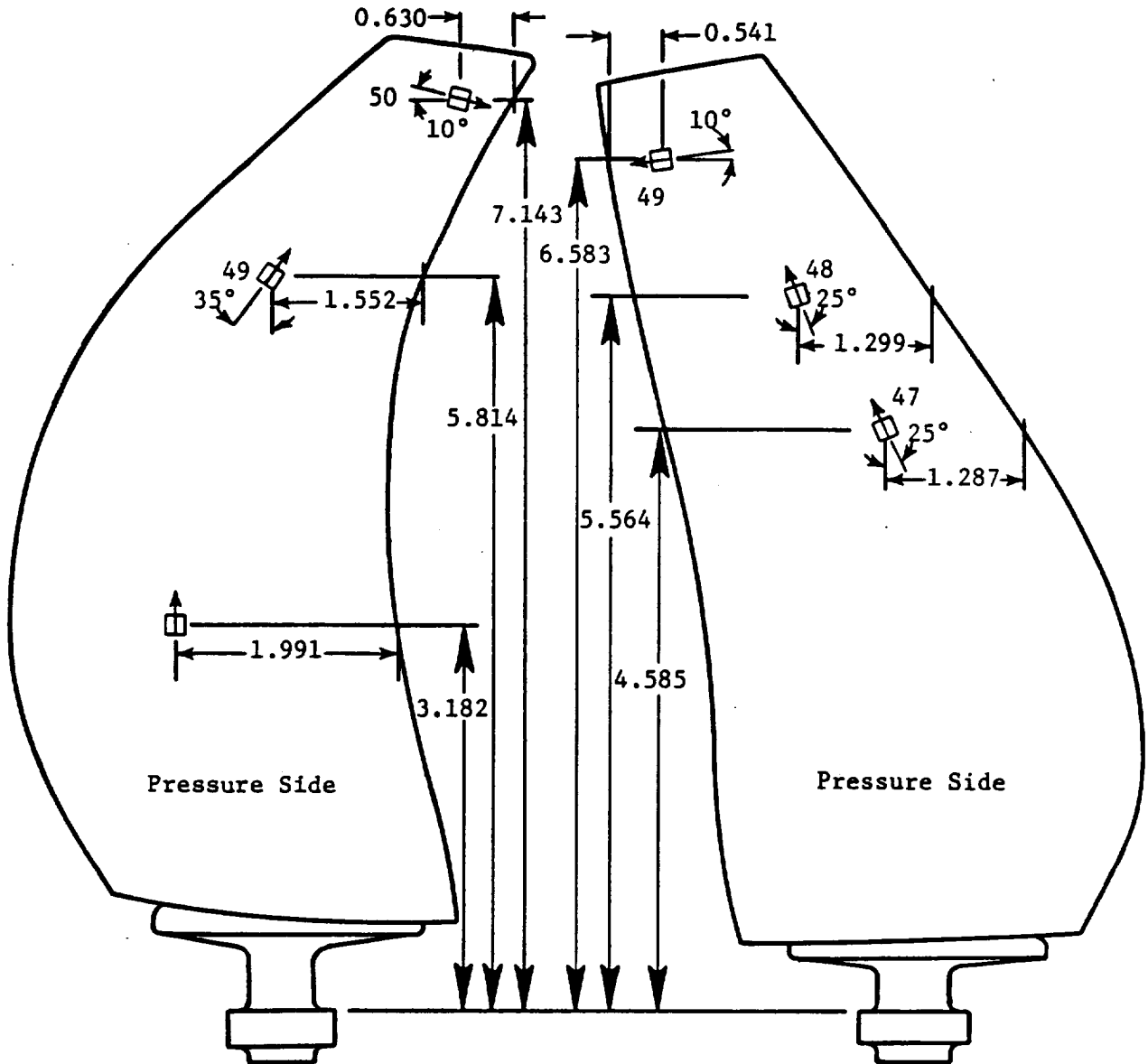


Figure 114. F-21 MPS Blade Gauge Locations.

Figure 115. A-21 MPS Blade Gauge Locations.

Table 24. A-4 MPS Blade Scope Limits.

Mode	Stress Limit, ksi		
	Gauge 1	Gauge 2	Gauge 3
1 1F	2.2	21.0	23.7
2 2F	2.2	30.2	22.6
3 1T	11.8	13.6	14.7
4 3F	0.5	18.1	4.8
5 3F'	1.1	14.8	0.9
6 2T	15.0	16.4	8.7
7 4F	1.2	3.6	1.9
8 3T	15.3	18.3	13.4
9 4T	4.8	3.8	2.6
10 5F	8.2	24.0	12.7
11 2S	23.6	5.4	5.0
12 2S'	5.7	2.6	0.9
13	23.5	10.3	0.7
14	5.8	13.8	0.9
15	7.4	2.6	2.8
16	5.0	6.2	0.9

Table 25. F-5 MPS Blade Scope Limits.

Mode	Stress Limit, ksi		
	Gauge 1	Gauge 2	Gauge 3
1 1F	0	29.1	20.5
2 2F	0.4	25.5	3.3
3 1T	4.7	6.3	3.3
4 3F	5.1	16.5	12.1
5 A	3.6	4.0	0.2
6 2T	8.3	3.3	0.5
7 4F	2.5	11.3	1.8
8 3T	9.4	2.9	3.5
9 5F	4.5	10.3	6.3
10 4T	4.7	5.9	0
11 2S+F	9.3	0.9	0.5
12 6F	6.9	0.6	0.8
13 5T	3.0	1.0	0.7
14 2S'	9.0	2.1	2.4
15 ?T	2.8	0.2	0.4
16 2S''	8.9	1.5	0.5

03

Table 26. A-5 MPS Blade Scope Limits.

Mode	Stress Limit, ksi		
	Gauge 1	Gauge 2	Gauge 3
1 1F	0.3	26.5	17.4
2 2F	0	34.4	5.0
3 1T	5.0	10.8	1.8
4 3F	3.7	17.5	11.0
5 2T	6.1	8.1	2.0
6 A	8.6	1.8	0.8
7 4F	6.5	12.6	1.4
8 3T	7.9	0	5.4
9 5F	8.9	10.9	6.5
10 4T	4.0	5.4	2.0
11 5T	6.9	2.6	1.4
12 ?	8.9	1.0	1.4
13 2S	8.7	0.8	0.6
14 ?	8.7	2.4	2.3
15 ?	8.6	2.2	0.1

Table 27. F-7 MPS Blade Scope Limits.

Mode	Stress Limit, ksi					
	Uncorrected			Corrected*		
	Gauge 1	Gauge 2	Gauge 3	Gauge 1	Gauge 2	Gauge 3
1 1F	0.3	10.1	17.7	1.4	4.9	9.7
2 2F	1.9	17.2	13.8	2.4	9.4	9.4
3 1T	4.7	0.5	0	4.2	2.0	0
4 3F	1.2	20.7	0	3.0	13.4	0
5 A	0.9	15.2	0.3	1.0	11.3	0.4
6 2T	10.0	0	3.8	7.0	0	3.0
7 4F	0.4	16.9	8.8	0.6	14.0	7.0
8 3T	12.5	0	4.8	8.5	0	1.9
9 5F	2.5	13.7	6.5			
10 4T	11.5	0	2.0			

* This Correction was Necessary Due to the Deviation of Calibration Data from Strain-Distribution Data

Table 28. A-7 MPS Blade Scope Limits.

Mode	Stress Limit, ksi					
	Uncorrected			Corrected*		
	Gauge 1	Gauge 2	Gauge 3	Gauge 1	Gauge 2	Gauge 3
1 1F	1.2	9.4	13.7	1.6	7.3	15.6
2 2F	4.6	18.3	11.9	3.2	11.1	11.2
3 1T	8.1	6.6	1.1	5.3	9.2	1.2
4 3F	8.4	29.4	0	5.3	19.2	0
5 A	14.2	4.9	8.2	8.4	5.6	9.8
6 2T	14.4	4.8	3.2	11.8	10.8	9.5
7 4F	5.8	24.9	13.6	5.7	19.4	11.3
8 3T	22.3	7.8	2.3	11.5	4.9	1.0
9 5F	2.7	19.6	5.4	4.0	18.2	5.3
10 4T	22.6	4.5	7.0			

* This Correction was Necessary Due to the Deviation of Calibration Data from Strain-Distribution Data

Table 29. F-11 MPS Blade Scope Limits.

Mode	Stress Limit, ksi		
	Gauge 1	Gauge 2	Gauge 3
1 1F	0.2	15.2	14.2
2 2F	4.2	13.0	2.0
3 1T	24.9	5.7	3.5
4 3F	1.7	4.7	6.5
5 A	8.7	3.7	7.7
6 2T	19.4	2.5	1.5
7 4F	3.2	6.2	1.0
8 3T	12.0	3.2	0.2
9 5F	1.5	3.2	4.7
10 4T	2.7	6.5	2.0

Table 30. A-11 MPS Blade Scope Limits.

Mode	Stress Limit, ksi		
	Gauge 1	Gauge 2	Gauge 3
1 1F	0.7	14.7	17.4
2 2F	4.0	19.9	2.5
3 1T	18.4	7.7	2.0
4 3F	8.5	10.2	6.7
5 A	14.9	12.2	1.7
6 2T	19.2	6.7	2.7
7 4F	9.7	1.0	0.5
8 3T	18.7	0.2	0.5
9 5F	7.0	2.5	2.5
10 2S+T	10.5	6.7	0.2

Table 31. F-21 MPS Blade Scope Limits.

Mode	Stress Limit, ksi		
	Gauge 1	Gauge 2	Gauge 3
1 1F	8.0	22.7	19.2
2 2F	11.0	6.7	7.0
3 1T	13.2	5.5	0.3
4 3F	7.0	3.7	1.2
5 3F'	5.2	5.5	1.0
6 2T	10.7	2.5	2.0
7 2T'	2.7	0.5	0.7
8 4F	12.0	4.2	5.0
9 4T	0	0	0.3
10 5F	12.0	9.0	3.2

Table 32. A-21 MPS Blade Scope Limits.

Mode	Stress Limit, ksi		
	Gauge 1	Gauge 2	Gauge 3
1 1F	1.2	24.9	21.4
2 2F	2.7	24.9	7.0
3 1T	16.4	17.7	5.5
4 1A	14.4	17.9	7.7
5 3F	1.7	11.7	11.9
6 2T	17.9	5.5	3.7
7 3T	2.5	2.5	4.2
8 4F	16.4	3.7	6.5
9 4T	0.2	4.2	4.0
10 5F	11.5	9.2	3.5

nine-blade hub and fairings are available in Boeing Drawing Nos. 5802-608 and 5802-612, respectively, which have been supplied to NASA. This hardware was utilized to investigate acoustic-phasing effects during Cell 41 and NASA Lewis 8x6 and 9x15 wind tunnel tests.

4.4.2 Aeromechanical Hub

Hub flexibility was studied using a specially configured aeromechanical hub. The intent was to acquire design data to aid in assessing flexibility effects in the fan blade attachment ring used on the full-scale engine. Data were acquired during testing in the anechoic chamber, Cell 41, at GE and in the NASA Lewis 8x6 wind tunnel.

The aeromechanical hub was designed to simulate hub flexibility of the full-scale UDF® Demonstrator blade support structures which include a rotating polygonal ring and turbine frame. The design requirements included matching Demonstrator 2 and 4 nodal frequencies while maintaining a 2x stress margin at maximum speed. The frequency match was based on a full-scale ANSYS beam model of the Demonstrator configuration with the F1E9 blade, polygonal ring, brackets, and turbine frame, because no test data were available during the design phase. However, the design task was quite difficult since the heavier MPS blade was not usable with scaled-down versions of the Demonstrator support structures with 2x margin.

The initial concepts utilized the MPS blade with the standard trunnion; however, these early studies showed that even a reasonable frequency match on first flex and axial modes was impossible with the polygonal-ring-type structure. As a result, the threaded (turned-down) trunnion concept was envisioned and approved. With this modification to the MPS blade, design proceeded in two basic phases. The first phase involved free/free mode frequency analysis of the blade and polygonal ring to match first flex and axial frequencies. In this analysis, the MPS model had the same blade beam representation as the Demonstrator model, except lumped masses of the heavier trunnion were used. Various polygonal-ring materials were examined, but the most successful was the same material (Ti6-4) as the Demonstrator. The final ring configuration had a rail cross section and spacing similar to the Demonstrator but was not an exact scaled-down version. In addition, the final shape was very close to an ideal ring to minimize cyclic-fatigue-induced bending.

With the ring structure defined, the final task (encompassing the second phase) was to design a bracket simulating the Demonstrator bracket and turbine frame. Initial bracket concepts were simply two radial legs with a flange interface at the ring; these simple bracket concepts were unsuitable due to high stress induced by centrifugal ring displacement. The key was to then design a two-piece bracket in which the upper portion simulated the radially flexible Demonstrator bracket (for ring/frame radial decouple) and the lower portion simulated the stiff turbine frame. As in the Demonstrator bracket, a "V-configuration" with tapering thicknesses was used. The lower legs of the MPS bracket were subsequently designed to tune in the first axial frequencies. With this design, target frequencies were matched within 2% (full-scale) as evidenced by Table 33.

The final aeromechanical hub design, diagrammed in Figures 116 and 117, consisted of MPS blades with threaded stems passed through a hole in the hub of the polygonal ring and attached to the ring with self-locking nuts. The ring had eight flanges (one at each hub) which bolted to the upper flange of the eight V-brackets. The lower ends of the V-brackets were integral with the lower legs of the one-piece MPS bracket. These lower ends were connected to a large flange bolted to the octagonal hub ring that replaced the original balance ring. Both of the bracket flanges used two

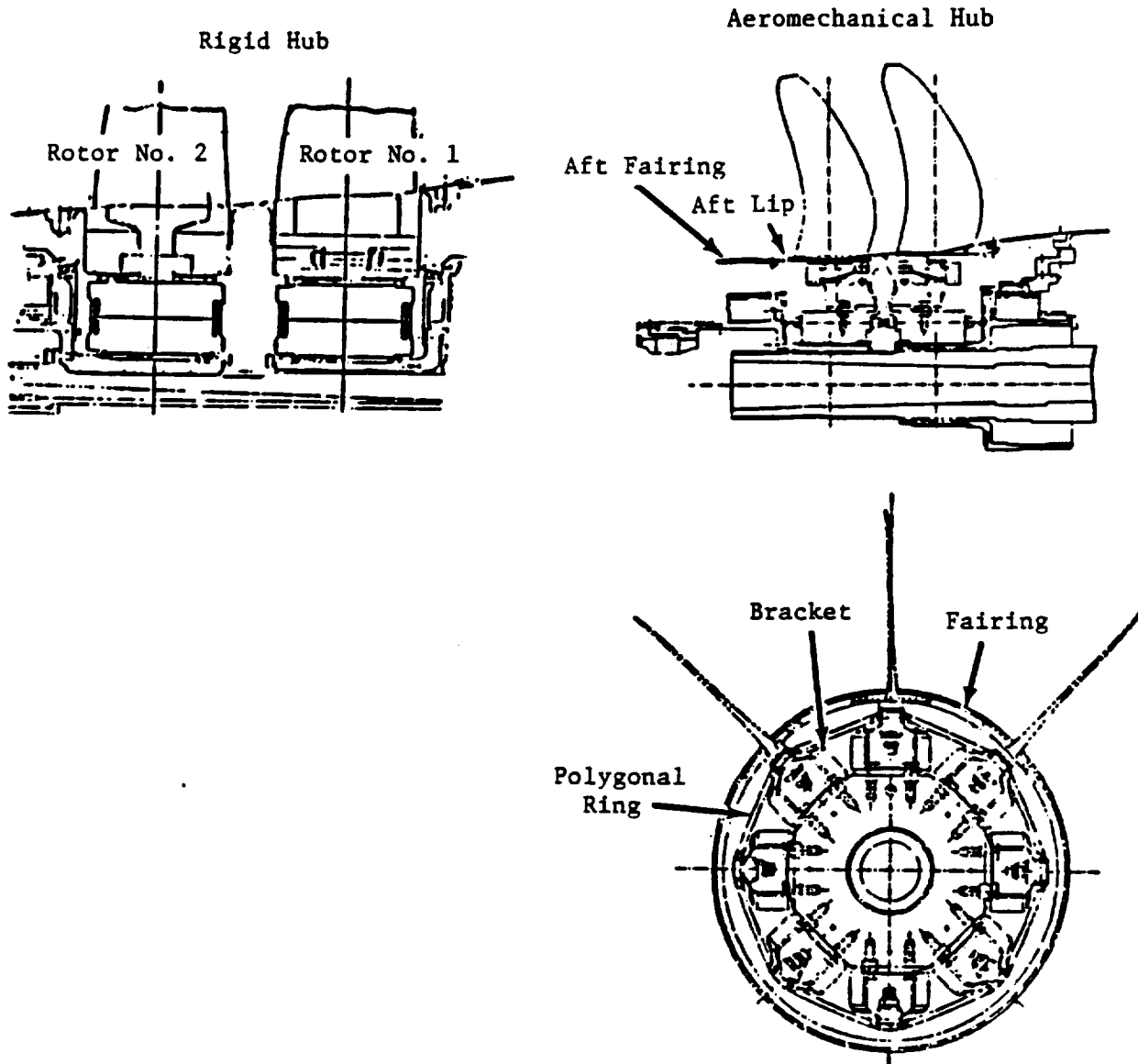


Figure 116. Aeromechanical Hub and Rigid Hub Configurations.

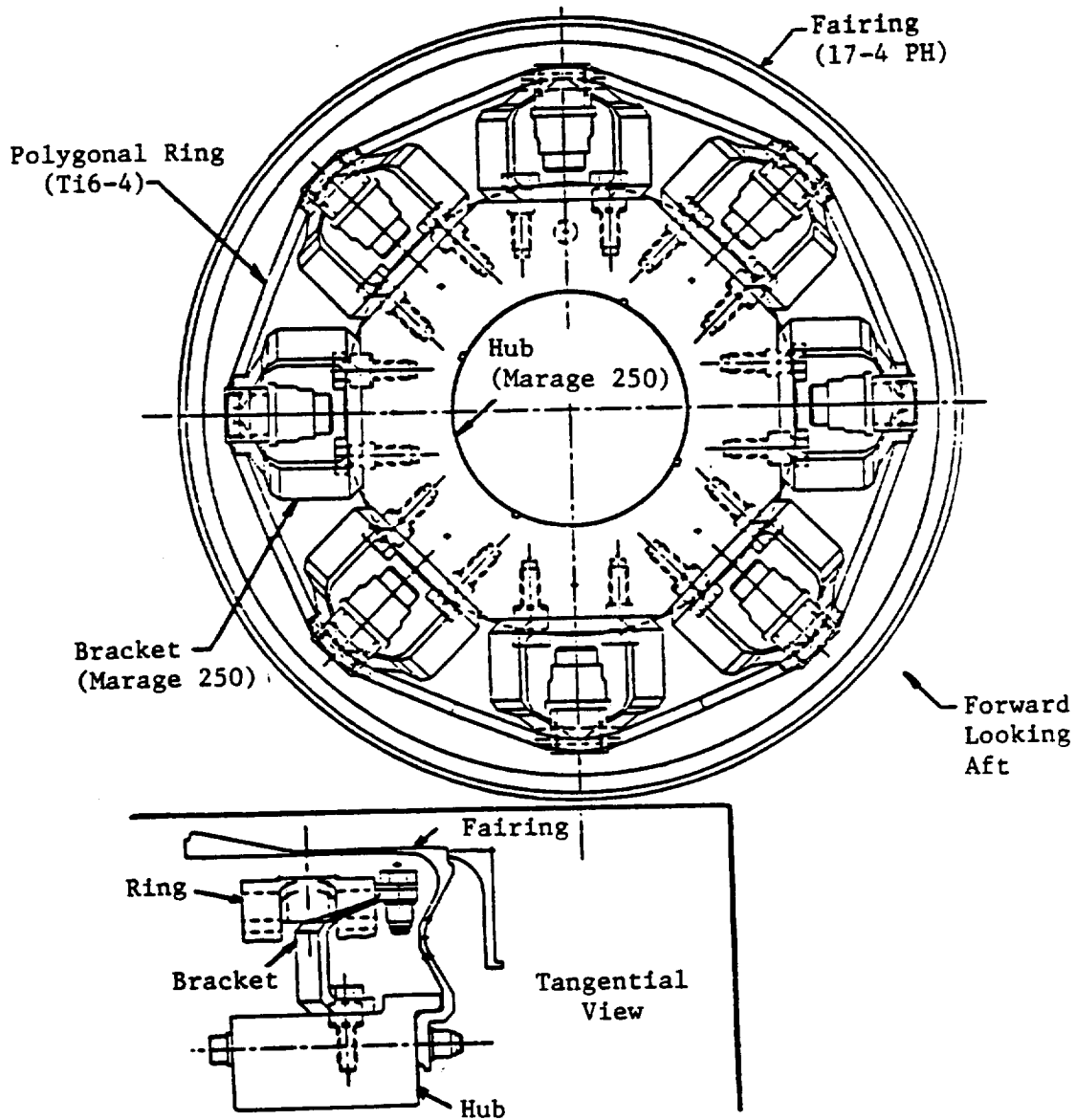


Figure 117. Aeromechanical Hub Structure.

ORIGINAL PAGE IS
OF POOR QUALITY

Table 33. MPS Aeromechanical Hub Design Frequency Comparison.

Model	rpm	Frequency, Hertz (Full-Scale)					
		2N-1F	3N-1F	4N-1F	2N-1A	3N-1A	4N-1A
Demo	0	31.4	32.7	32.6	42.0	53.0	57.8
MPS	0	31.5	32.3	32.7	40.4	51.5	56.4
Demo	1537	51.0	52.6	52.5	62.8	73.6	75.8
MPS	1537	51.7	53.1	53.2	63.3	74.4	77.1

1/4-inch-diameter bolts, and the lower flange had a dowel pin to help center the brackets and ring. The entire bracket was made of the same material (Inco 718) as the Demonstrator bracket and frame.

Initially, only the first stage was to be designed, but studies revealed that both stages had similar dynamic characteristics. Furthermore, the Demo polygonal rings were identical, which supported the decision to utilize the same MPS aeromechanical hardware for both stages. The differences between the two stages were in the assembly. The Stage 1 polygonal ring flange was located on the aft side; whereas, the Stage 2 flange was on the forward side. This arrangement facilitated access to the blade self-locking nuts for pitch change. Additional differences were manifested in the threaded trunnion of the Stages 1 and 2 blades.

The clamping arrangements were slightly different due to shorter Stage 2 stems which resulted from the decreasing flowpath radius. Although both stems had the same thread diameter and pitch (0.4375-20 UNJF), Stage 1 had a right-hand thread, and Stage 2 had a left-hand thread. This arrangement enhanced self-locking, as the blade steady-state twist moment tended to tighten the nut for most pitch angles. Both of the stems had approximately the same thread length, but Stage 1 had a large-wrench feature (5/8-in. hex) just below the blade platform, compared to that of Stage 2 (5/16-in. hex) at the end of the stem. Further, both stems had a 1/16-in. long pilot feature (same diameter as thread) just above the threaded portion; this provided proper alignment during installation and tightening. Also, both stems had a neck diameter (5/16-in.) between the pilot and blade platform to provide a feature for the stem strain during tightening. Stage 1 had a longer neck than Stage 2; however, both were tightened with about the same preload, set to prevent joint separation for maximum F-7/A-7 steady-state and alternating loads. The proper preload was achieved by precise rotation (35° from seating) of the nut.

Although the aeromechanical hub was designed employing the F1E9 blade, testing was conducted with the F7B4 and A7B4 blades. An ANSYS analysis of the aeromechanical hub with the A7B4 blade was performed; a comparison with the MPS Stage 1 vibration test results indicated that the Stage 1 frequencies were significantly lower for all first flex and axial modes. However, a similar comparison with results from a Demonstrator Stage 2 vibration test showed that the two- and three-nodal first axial frequencies were with 1 z (Demonstrator scale). The vibration test 4N-1A frequency of the Demonstrator was about 8 z higher, but first flex frequencies were about 4 z lower than MPS analysis.

Furthermore, bench (fixed base) vibration testing of both Demonstrator and MPS blades demonstrated Stage 1 first flex and axial frequencies which were significantly lower than Stage 2.

This might explain the differences (Table 34) between Stages 1 and 2 MPS vibration test and analysis results.

4.4.3 F-7/A-7 Torque Blades

The F-7 and A-7 torque blades were identical to the standard F-7 and A-7 blades, with the exception of the stem. Here, flats were machined 180° from each other so that four strain gauges could be applied in a bridge arrangement to provide the capability of measuring torque on the stem. The output of these gauges used the existing balance and telemetry ring wiring previously dedicated for blade stress measurement with one modification: the output connection was made to a static strain transmitter rather than a dynamic strain transmitter so the signal could be picked up on a discrete frequency at the telemetry ground station. The intent was to have two F-7 and two A-7 torque blades tested simultaneously. The resultant data would be input for full-scale engine actuator system design. More definitive torque blade details are available in Boeing Drawing No. 5806-14.

4.4.4 Simulated Ground Plane (Rig 2)

Full-scale UDF® proof-of-concept testing was conducted in proximity to a ground plane; this may have affected performance and acoustic measurements. Testing at GE's outdoor crosswind facility at Peebles, Ohio was similar to the tests conducted in GE's anechoic chamber (Cell 41) in the presence of a freejet in order to simulate flight speed.

It was necessary and practical to assess ground-plane effects in back-to-back, ground-plane versus no-ground-plane tests which could only be performed in the anechoic chamber. These scale model tests were run with the F-7/A-7 blades, modeled after the first full-scale engine blades. The ground plane designed for use in the anechoic chamber was a 5x5-foot flat surface, attached to a

Table 34. MPS Aeromechanical Hub Design Test Versus Analysis and MPS Versus Demo Frequency Comparison.

Flexible-Base Condition	Blade	Mode					
		2N-1F	3N-1F	4N-1F	2N-1A	3N-1A	4N-1A
MPS Stage 2 ANSYS Model	A7B4	29.5	30.2	30.5	49.9	60.0	64.0
MPS Stage 1 Vib Test	F7B4	27.6	N/A	N/A	42.9	48.0	51.6
Demo Stage 2 ANSYS Model	A7D3	24.6	25.3	25.5	51.7	63.9	65.4
Demo Stage 2 Vib Test	A7D3	25.9	27.5	N/A	49.3	59.0	72.0

Fixed-Base (Blade Only)	Blade	Mode					
		1F	2F	1T	3F	1A	2T
Demo ANSYS Beam Model	A7D3	26.8	78.3	97.9	N/A	N/A	N/A
Demo Bench Test	A7D3	26.9	77.4	92.8	N/A	N/A	N/A
Demo Bench Test	F7D3	21.9	70.2	97.9	N/A	N/A	N/A
MPS Bench Test	A7B4	35.0	91.9	113.8	174.1	214.4	223.1
MPS Bench Test	F7B4	33.3	88.4	122.5	172.4	194.3	228.4

mount on the external side of the freejet nozzle structure, designed to be installed at a distance of 4.9 in. to 5.2 in. (28.0 in. to 29.7 in., full-scale) from the MPS blade tips. Figure 118 shows the ground plane installed in Cell 41; Figure 119 illustrates design and installation details.

4.4.5 Wake Rake (Rig 3)

The autotraversing wake rake was used in the Boeing 8x12 transonic wind tunnel to study the discharge flow field from the fan blades. It was designed to be adaptable for use in the NASA Lewis 8x6 wind tunnel but was not employed during the 1985 or 1986 test entries in that facility. This rake mounted on the MPS nacelle support assembly to position 15 (each) total pressure, total temperature, and flow-angle probes at MPS Station 205. The range of circumferential travel for this rake is $\pm 30^\circ$. The design details of this rake are provided in Boeing Drawing No. LO-062884 (previously supplied to NASA).

4.4.6 Pylon (Rig 2)

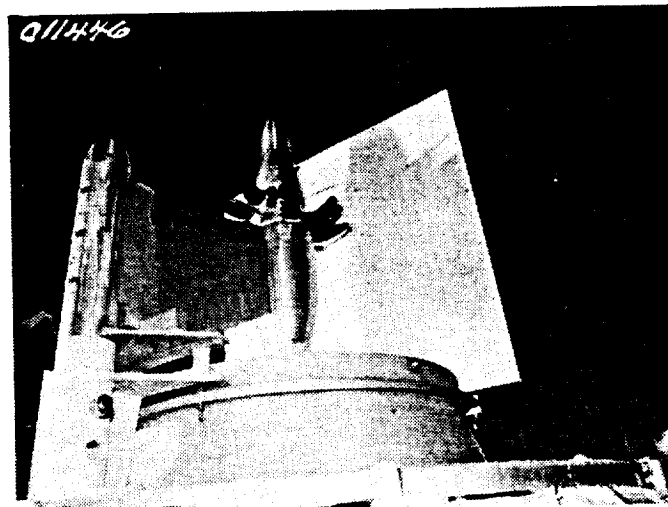
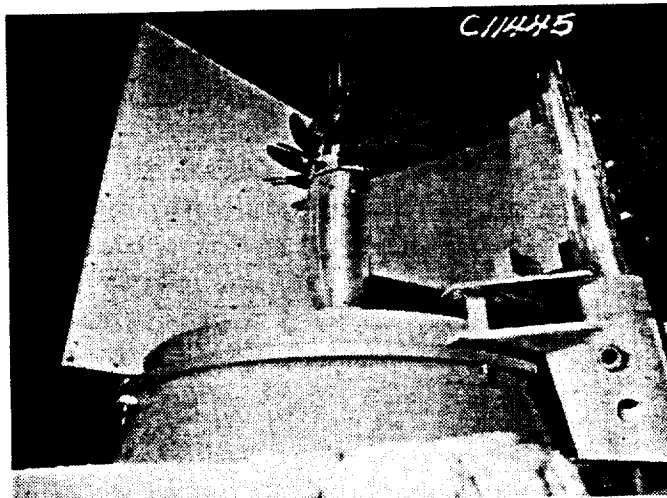
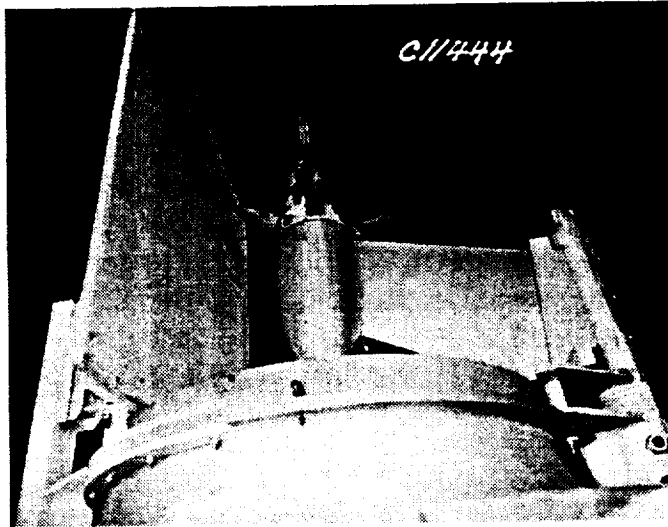
A pylon with an airfoil section based on Boeing Drawing Nos. 5809-215, -216, and -217 was designed to be installed in Cell 41 and tested with the MPS Rig 2. It was attached to a mount that bolted to the anechoic chamber freejet nozzle external flange structure. Slots in the mount facilitated vertical movement of the pylon to permit a range of axial distances to be set from the plane-of-rotation of the forward blade row. Bolt-on tip fairings were available to account for contour differences at the pylon/nacelle interface when this was done. Axial location could be set 1.84 in. (minimum), 2.936 in. (nominal), and 5.2 in. (maximum) from the forward blade row plane-of-rotation. Also, the pylon could be positioned at six different circumferential locations on the freejet nozzle. North and south locations placed the pylon relative to the anechoic chamber microphone arrangement to simulate port and starboard engine installations, respectively. GE Drawing Nos. 4013339-598 (Sheets 1, 2, and 3) and 4013339-600 show the details of the pylon.

4.4.7 Simulated Fuselage (Rig 2)

A simulated fuselage section was designed based on the Boeing 727 contour information for installation at the freejet nozzle exit in Cell 41. Figure 120 illustrates the resultant body-of-revolution schematically in relation to the freejet nozzle and MPS Rig 2.

Instrumentation proposed for the simulated fuselage is summarized in the Task III report. Figure 121 compares calculated Mach number distributions for both the body-of-revolution and the Boeing 727 fuselage shape. Design details of the simulated fuselage are contained in the GE Drawing Nos. 4013339-754 and 4013339-755, Sheets 1 and 2. Although design work was complete, the simulated fuselage was not fabricated.

ORIGINAL PAGE
BLACK AND WHITE PHOTOGRAPH



ORIGINAL PAGE IS
OF POOR QUALITY

Figure 118. Ground Plane Installation in Cell 41.

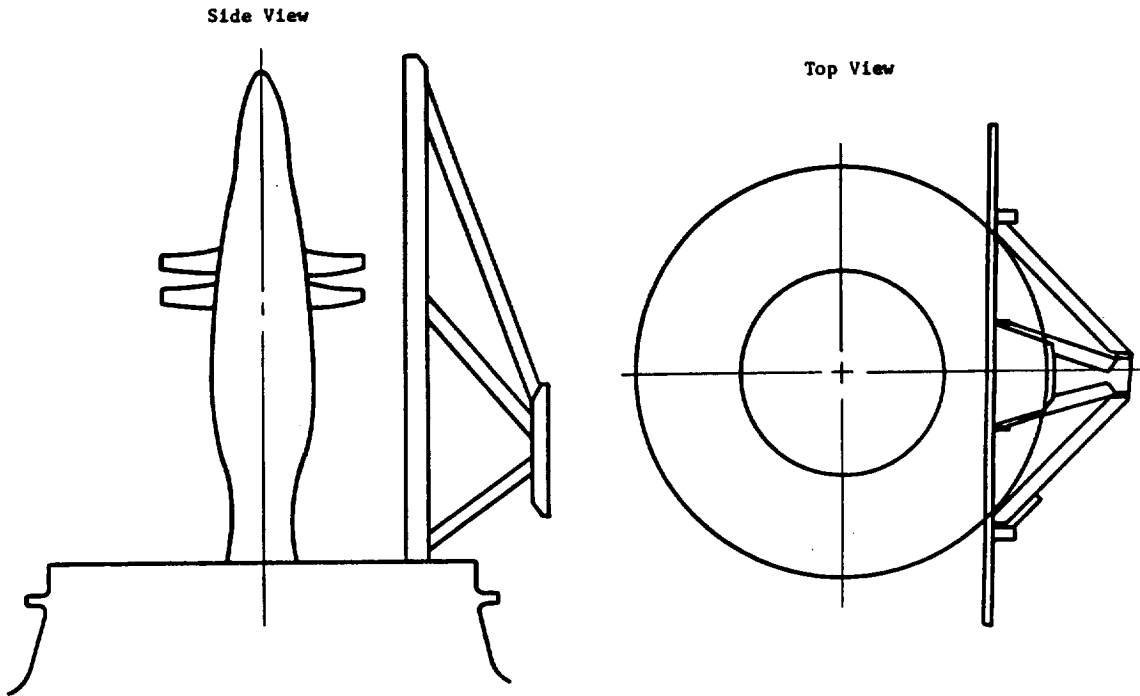


Figure 119. Ground Plane Installation Details.

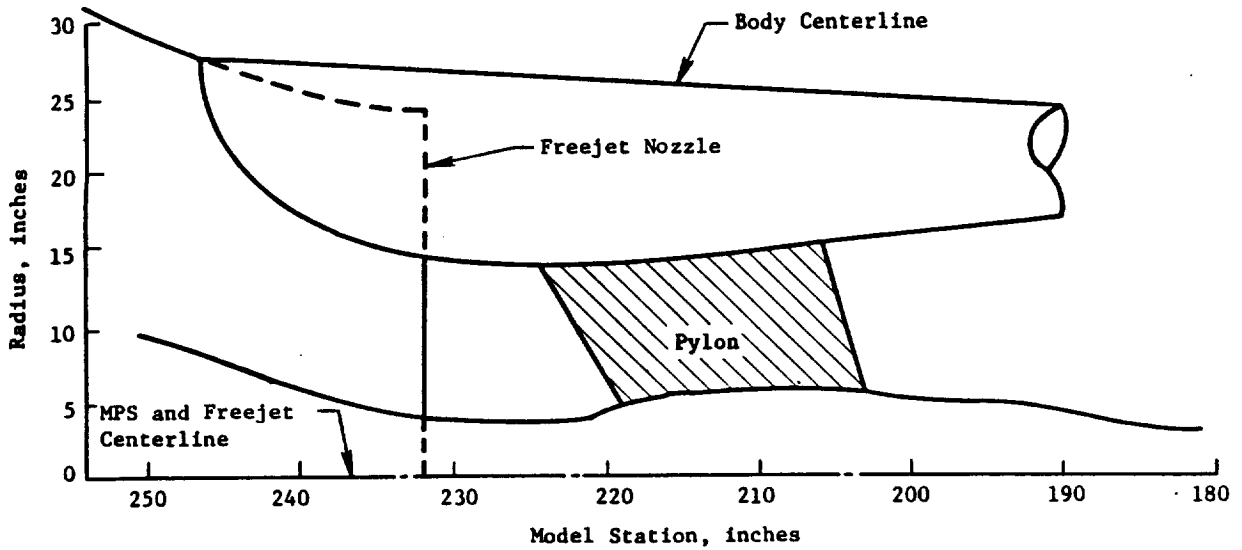


Figure 120. Cell 41 Installation with Fuselage Body-of-Revolution.

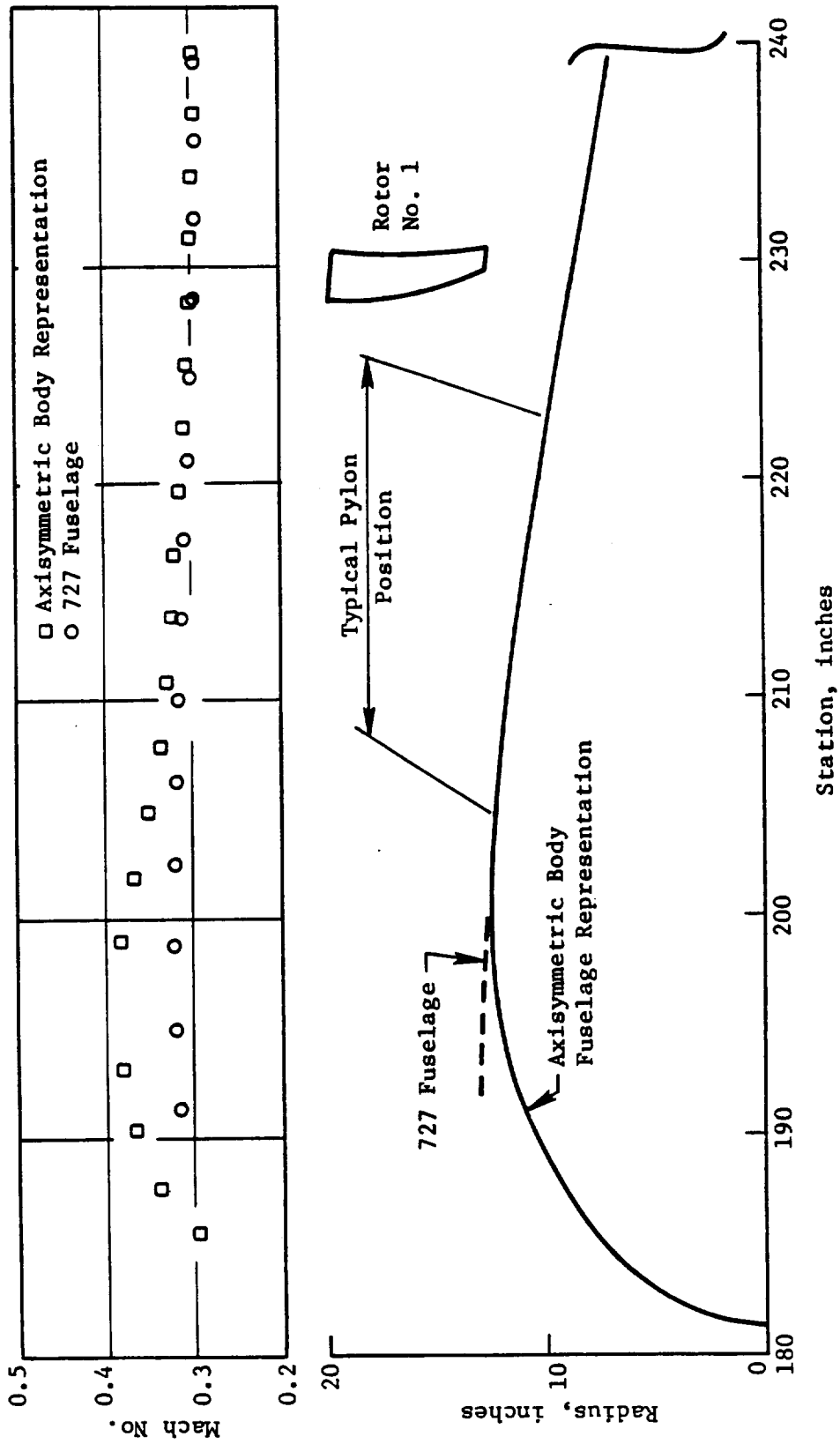


Figure 121. Simulated Fuselage Calculated Mach Number Distribution Comparison.

5.0 ACOUSTIC AND PERFORMANCE TESTING

5.1 Rig 2/Cell 41 (GE Anechoic Chamber)

MPS SN002 testing in GE's anechoic freejet facility (Cell 41), involving contract blading (but not necessarily contract configurations) was conducted during the time period of October 1984 through July 1986, inclusive.

The objective of the test program was to investigate the acoustic, aerodynamic, and aeromechanical performance of unique GE counterrotation blade concepts at low speed for application to future advanced technology propulsion systems. This was accomplished using scale model blading on the MPS SN002 in GE's anechoic chamber, Cell 41. Blade design variables included: tip sweep, activity factor, pitch angle, and blade row axial spacing. Mach numbers up to 0.35 at an angle-of-attack of 0° were set with the MPS on an isolated nacelle-type wind tunnel installation arrangement. The effects of pylon interaction were also evaluated during the test program.

5.1.1 Facility Description

All of the planned experimental measurements within Task IV of this program were conducted in the GE anechoic freejet facility located at Evendale, Ohio, and herein identified as Cell 41. Depicted schematically in Figures 122 and 123, Cell 41 is a cylindrical chamber 45-ft in diameter and 72-ft high; the inner surfaces of which are lined with anechoic wedges made of fiberglass wool to yield a low frequency cutoff below 220 Hz and an absorption coefficient of 0.99 above 220 Hz. Descriptions and results of the tests conducted in order to determine the acoustic characteristics of the anechoic chamber (such as, inverse-square-law tests), and mean velocity and turbulence intensity distributions in the freejet were reported in internal GE reports (R81AEG212 and TM 84-597 by P.G. Vogt and B.A. Janardan, respectively).

The primary air supply for the simulator rig is a freejet air system that consists of a 250,000 cfm (50 in.), water-column static pressure facility fan driven by a 3,500-hp (horsepower) electric motor. Air to the facility fan is pulled through the existing buildup area inlet silencer. A transition duct and silencer route air discharged from the facility fan to a silencer plenum chamber which reduces the noise level by 30 dB to 50 dB, and the air is then discharged through the 1.2 m freejet exhaust. Freejet flow at maximum permits simulation up to Mach 0.35. This Mach number variation at the counterrotating blades is obtained by varying the facility airflow rate. The combined freejet and entrained airflow, finally, is exhausted through a "T-stack" directly over the simulator rig in the ceiling of the chamber.

The facility operating parameters were monitored during testing at the control console to ensure that prescribed facility limits were not exceeded and to set the test-point conditions.

Measured on rakes at the metering station, freejet discharge pressures were used for setting the desired freejet Mach numbers. These parameters were also routed through the dynamic scanning system and recorded by the ADH (aerodynamic data handling) system.

Facility temperatures were monitored at the control console using a Doric multichannel temperature indicator. The unit had a 24-channel capability and was designed for use with Type K thermocouples (chromel-alumel).

The basic Rig 2 Test System, supplied by Boeing under a joint GE/Boeing effort prior to use in this contracted program, included the fully assembled and instrumented rig mounted in a three-strut,

• Freestream Mach Number Capability up to $M_0 = 0.35$

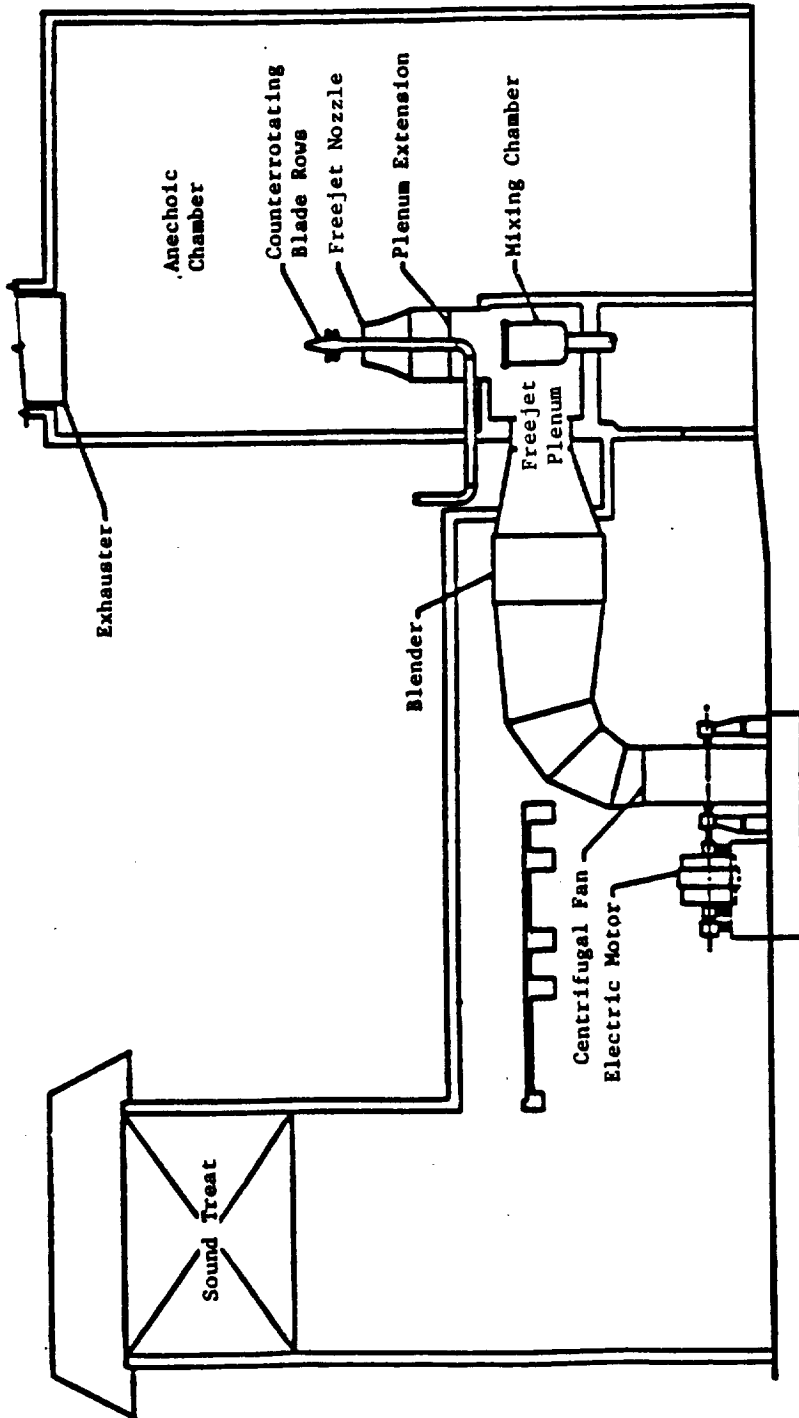


Figure 122. An Overall Schematic of the GE Anechoic Freejet Noise Facility.

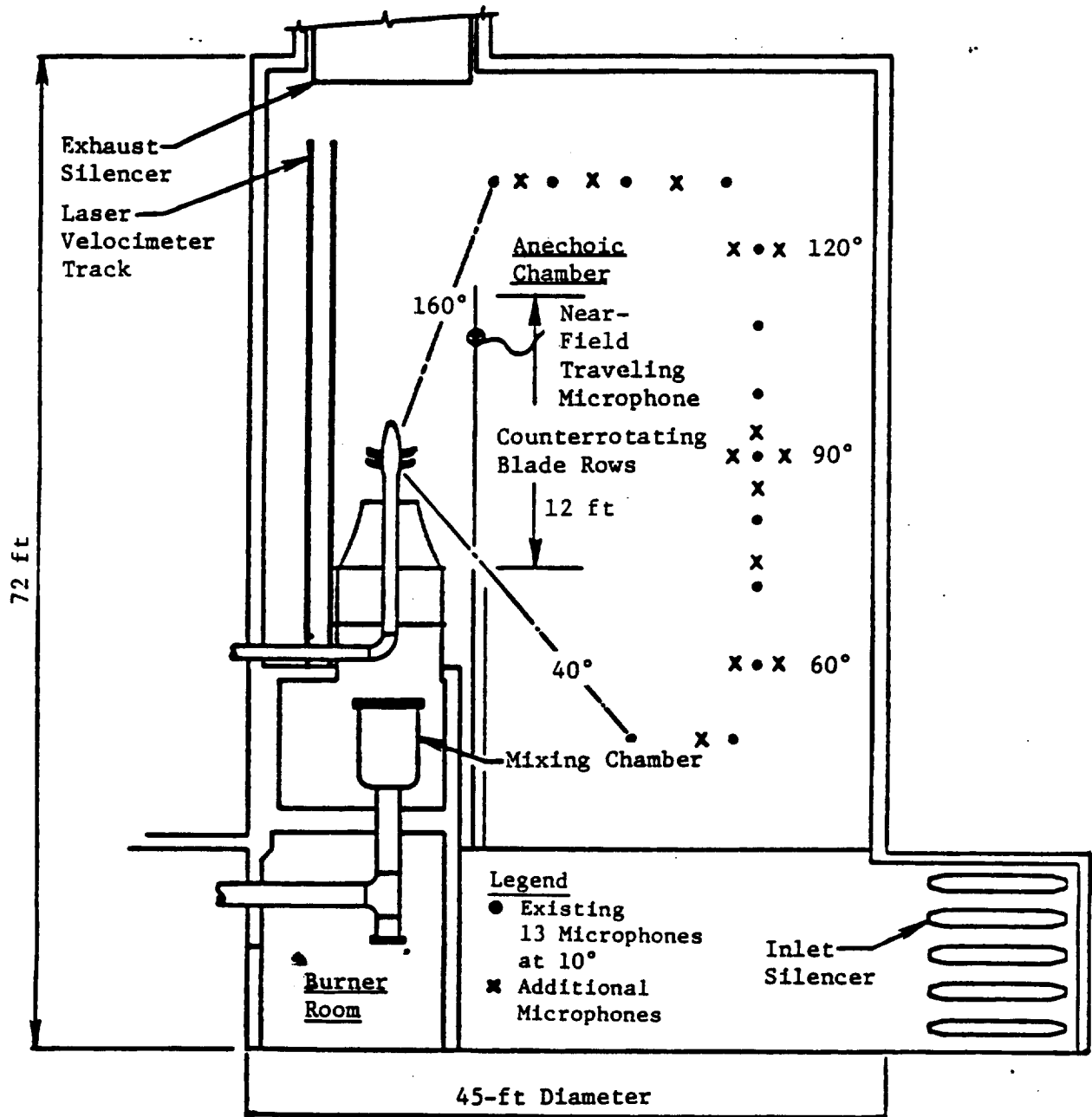


Figure 123. The Anechoic Chamber (Schematic).

vertical "rig frame" as shown in Figure 124. Boeing conducted a mechanical and instrumentation check-out of this system before shipping to GE. This system was mounted and installed on the "service frame" in the Cell 41 facility, as described above and depicted in Figure 124. During the installation of the system, services required to operate the rig (such as lubrication supply and scavenge, turbine air supply, and slave air supplies to vehicle sumps) were connected.

A complete check-out of all rig service systems was performed prior to the implementation of planned testing. Insofar as possible, rig configuration changes were performed in the test facility without removal from Cell 41. These model changes included changes to the: blade configuration, blade row spacing, pitch angle, pylon, ground plane, and hub configuration.

A simulated fuselage section was designed, but not fabricated. A nacelle support pylon was designed and fabricated for installation at the exit of the freejet nozzle, as illustrated in Figure 125. The mounting was designed for locating the pylon at six azimuthal positions, relative to the wall-mounted far-field microphones.

5.1.2 Vehicle Description and Instrumentation

5.1.2.1 General Description

The MPS is a pneumatically powered counterrotating unducted fan engine model propulsion system which is designed for testing fan blade configurations in either subsonic or transonic wind tunnels. A photograph of the assembled MPS SN002 in Cell 41, in the vertical mode, is presented as Figure 126. The tunnel airflow direction is from the bottom to the top. The overall length is 117 inches (Model Station 173.00 to Model Station 290.00) and the nominal propulsor diameter is 24.5 inches. The MPS components are discussed briefly in the following sections of this document. However, a more thorough description of these component parts and their function is available in an internal Boeing report (D6-52523 by R.M. Swanson).

5.1.2.2 Mounting and Installation

For this test, the MPS SN002 unit was mounted in the center of the Cell 41 freejet nozzle (Figure 127). The MPS centerline coincided with the freejet nozzle centerline section.

5.1.2.3 Hub Shaft Module

GE defines the section of the MPS consisting of the blades, hubs, center shaft, rotating shafts, nacelle, and nacelle support hardware as the hub shaft module.

5.1.2.3.1 Inner (Aft) Hub

The inner hub is the aft hub on MPS SN002; it rotates CWALF (clockwise, aft looking forward) and provides the attachment and locking mechanisms for the aft blades. The eight-blade hub is constructed of a titanium inner diameter ring with a microballoon outer diameter covering on the external surface shaped to the nacelle contour with eight cutout areas for the blade shanks.

A portion of the hub near the blade platform is dished, as is the blade platform. This is done to area-rule the hub/blade at the blade root to reduce Mach numbers through the blades in the maximum blade thickness regions. This inner hub attaches to the metric side of a rotating force balance which, in turn, attaches to the inner rotating shaft. An 11-blade hub was fabricated for the F-11 blades; its construction is similar to the 8-blade hub, but an aluminum fairing replaces the microballoon for external surface shaping.

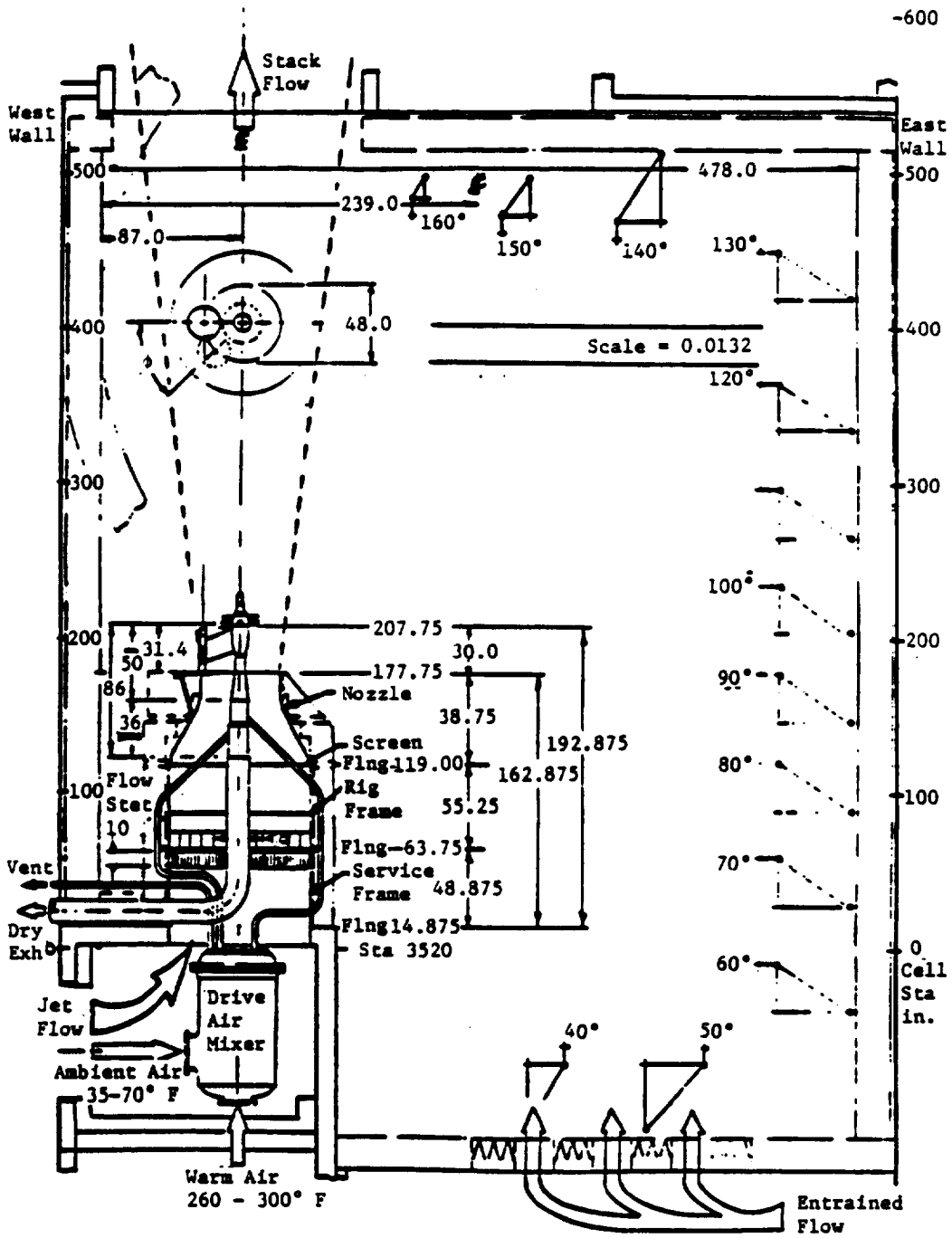


Figure 124. Schematic of the Test Vehicle Installation in the GE Anechoic Chamber Freejet Facility (Overall).

ORIGINAL PAGE IS
OF POOR QUALITY

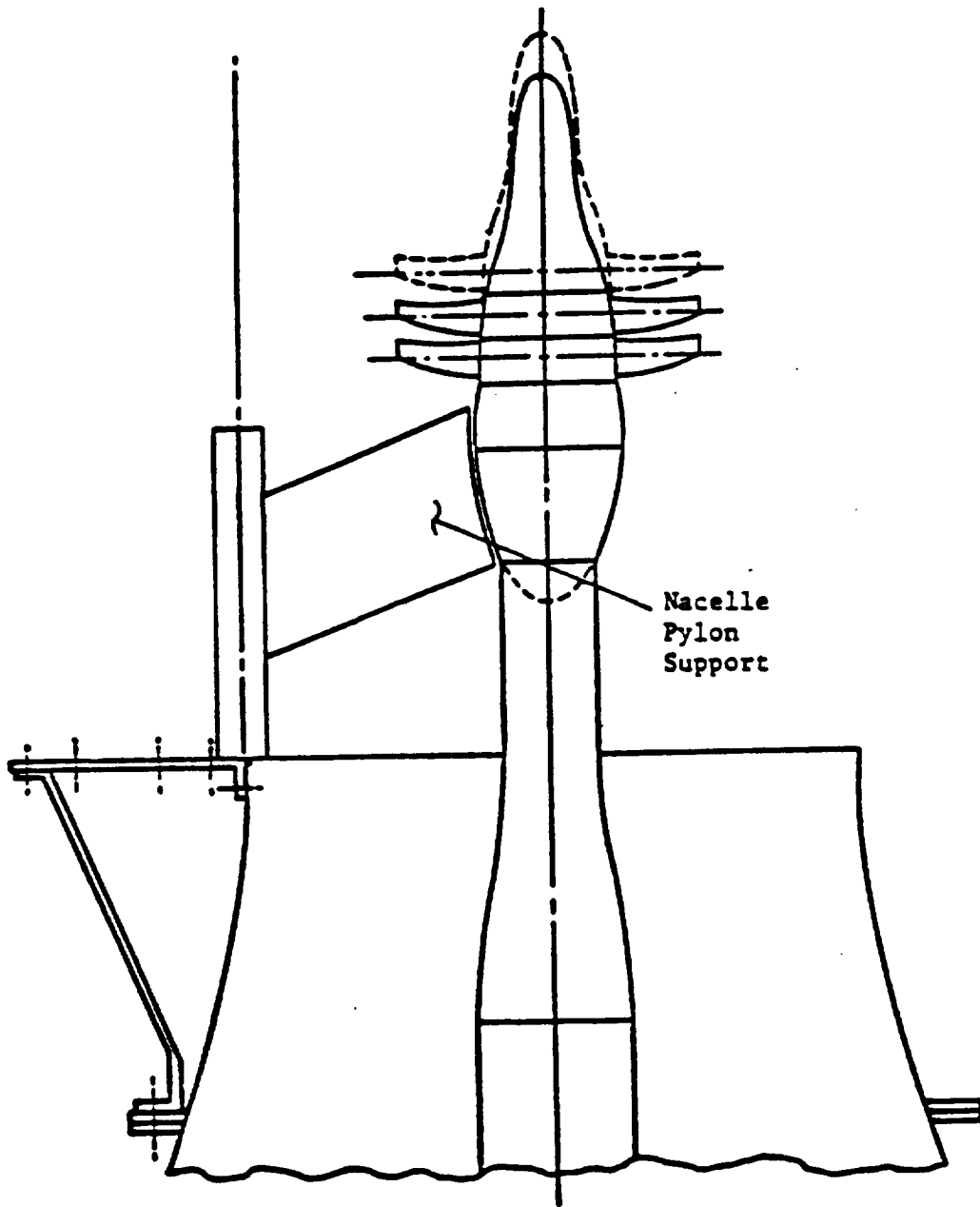


Figure 125. Close-Up of Test Vehicle Installation in GE's Anechoic Chamber Freejet Facility.

MODEL PROPULSION SIMULATOR INSTALLED IN GE ANECHOIC FACILITY (CELL-41)



Figure 126. The Assembled MPS SN002 in Cell 41.

5.1.2.3.2 Outer (Forward) Hub

The outer hub is the forward hub on MPS SN002. It rotates CCWALF (counterclockwise, aft looking forward), and the eight blade hub is constructed in the same manner as the aft eight blade hub, providing the retainment function on the forward blades. The outer hub attaches to a second rotating force balance which, in turn, is affixed to the outer rotating shaft. A 9-blade hub was fabricated for the A-11 blades; its construction and associated fairing is similar to that of the 11-blade hub.

5.1.2.3.3 Inner Rotating Shaft

The inner rotating shaft is concentric (inside) with the outer rotating shaft. It is supported on the id (inside diameter) by bearings Nos. 1 and 4, and on the od (outside diameter) by the Nos. 2 and 5 bearings, and provides support on the aft end, for the aft blade telemetry module and incorporates the attach point for the nonmetric side of the rotating force balance associated with the inner hub and aft blades. The inner rotating shaft also incorporates different removable spacers which allow a variation in axial location of the aft blade row, relative to the forward blade row. The forward end is mechanically connected to the inner turbine drive shaft by means of a coaxial, flexible diaphragm (Bendix-type) coupling which allows compensation for minor shaft misalignments and thermal expansion differentials. It also mechanically decouples the turbines and hub shafts. This coupling arrangement takes place between MPS Stations 238.275 and 245.6.

5.1.2.3.4 Outer Rotating Shaft

The outer rotating shaft is supported on the id by bearings Nos. 2 and 5, and on the od by bearings Nos. 3 and 6; of these, Nos. 2 and 3 are considered thrust bearings. The aft end of this shaft provides a surface for supporting the telemetry module associated with the forward blades and also provides the attach point for the nonmetric side of the rotating force balance which is connected to the outer hub holding the forward blades. The forward end of the outer rotating shaft mechanically connects to the outer turbine drive shaft by means of a second Bendix coupling. This takes place between the MPS Stations 240.41 and 245.425.

5.1.2.3.5 Nonrotating Center Shaft

Inside the rotating inner shaft, the nonrotating center shaft provides a seat for the Nos. 1 and 4 bearings. The nacelle aftbody is supported from the aft end of the center shaft which extends through almost the entire length of the MPS and serves as a conduit for instrumentation and lubrication service lines which must be routed out of the simulator.

5.1.2.3.6 Nacelle and Nacelle Support Housing

The nacelle consists of two sections, identified as the forebody and aftbody. The forebody is an ellipsoid-shaped shell from MPS Stations 201.63 to 221.0 (approximately), and is supported from the nacelle support housing. It represents the nacelle of an unducted fan engine. It also provides a mounting surface for the forward blade telemetry antenna and power source and the other instrumentation-related equipment. The aftbody is a shell from MPS Stations 194.12 to (approximately) 173.00 which resembles the aftbody section of an unducted fan engine nacelle. It provides a mounting surface for the aft blade telemetry antenna and power source, as well as for additional instrumentation- and service-related equipment.

The nacelle support housing is comprised of a support structure which is cantilevered from the turbine drive module. It houses the concentric drive shafts, nonrotating center shaft, and Bendix

couplings. The housing also provides a seat for the No. 6 bearing. At the aft end of the housing is a damper section which acts as a shock absorber to minimize vibrations on the hub shaft module. This damper also provides a seat for the No. 4 bearing and a mounting surface for designated instrumentation. An assembly drawing of the entire hub shaft module and Bendix couplings is provided in Boeing drawing No. 5802-2 and in an internal GE report (MPS 84-02 by G.E. Hoff).

5.1.2.4 Turbine Drive Module

GE defines the forward section of MPS SN002, which consists of the drive turbines, drive shaft, high pressure air passageways, and section support structure, as the turbine drive module.

5.1.2.4.1 Inner Turbine and Drive Shaft

The inner turbine is the forward turbine in the MPS SN002; a two-stage turbine, it is connected to the inner turbine drive shaft which is supported by the Nos. 9 and 10 bearings. On the forward end of the inner drive shaft is a 60-tooth disk installed for use with a magnetic-speed pickup instrumentation device. Operating limits at the inner turbine inlet are 300 psi for pressure and 250° F for temperature. Inlet temperature is set at 160°F in order to eliminate the possibility of ice formation.

5.1.2.4.2 Outer Turbine and Drive Shaft

The outer turbine is the aft turbine on MPS SN002; it also is a two-stage turbine and is connected to the outer turbine drive shaft which is supported by bearings Nos. 7 and 8. On the aft end of the outer turbine drive shaft, just forward of the Bendix coupling, is a 60-tooth disk installed for use with a magnetic-speed pickup instrumentation device. Operating limits at the outer turbine inlet are the same as those for the inner turbine. The inner and outer turbines are interchangeable, and this interchangeability affords the flexibility of reversing the direction of rotation of the drive shafts.

5.1.2.4.3 Turbine Drive System

These two turbines are mounted, as previously described, in tandem on the counterrotating concentric inner and outer turbine drive shafts and are driven by dual air supplies. In Cell 41, both hot air and ambient air travel through facility piping to a mixing chamber beneath the freejet nozzle. The drive air to both turbines then advances from the chamber location to the MPS turbine drive module housing by means of piping through the MPS support struts which extend from the freejet nozzle wall.

From there, the air for the outer turbine enters the drive module housing through a 3-in. diameter hole which is lined up with one of six 3.06-in. diameter holes in the outer turbine plenum inlet. Six holes are available, allowing some degree of flexibility from an installation standpoint. Once through this hole, the air is in the outer turbine plenum. From there, air travels from the MPS by means of an outer duct in the turbine drive module.

Air for the inner turbine enters the turbine drive module housing through a second 3-in. diameter hole (4.8-in. forward of the first hole) into a cavity which serves as a manifold to six air passageways through struts within the outer turbine exhaust ducting. These six strut air passageways bring drive air to the inner turbine air plenum; from which the air traverses through the inner turbine and then exits from the MPS by means of an inner duct in the turbine drive module. The turbine section support structure provides seats for the Nos. 7, 8, 9, and 10 bearings and contains passageways for

routing the instrumentation and lubrication lines out of the MPS. A detailed assembly drawing (including parts list) of the turbine drive module is provided in the Boeing drawing No. 5801-2, and in an internal GE report (MPS 84-02 by G.E. Hoff).

5.1.2.5 Rotating Force Balance

The rotating force balance incorporates strain-gauge-instrumented flexure beams for load measurement. These beams provide a means to measure reactions due to thrust and torque loads, as well as various reactions and moments due to components of loading which are not of primary interest, such as centrifugal force, but which are used to make interaction corrections. Balances are installed between the rotating inner shaft and aft hub, and the rotating outer shaft and forward hub. These balances are completely interchangeable.

5.1.2.6 Lubrication System

The MPS lubrication system utilizes a tank which contains MIL-L-7808 oil heated to approximately 150°F. Normal MPS operation requires seven to eight gallons; if the tank level should fall too low, perhaps due to a leak, a level indicator switch will illuminate a warning lamp on the control console. Oil is pumped from the tank through two lines by means of two Nichols-Zenith 1-gpm (gallon per minute) pumps designated as the lube pump and the damper pump.

In the first line, after encountering the lube pump and passing a check valve, a portion of the oil is cooled by circulating water running through a cooler at 0.45- to 0.50-gpm and 50- to 60-psig water pressure. A trim valve in the water line provides adjustment capability, and a pressure sensor causes a yellow light on the control console to illuminate if the water pressure drops below 20 psig. The portion of oil remaining in the first line bypasses the cooler and then enters a three-way thermostat, along with the cooled oil. The thermostat balances these two oil flows to yield an output flow at approximately 140°F. This oil then passes through a 5- μ m filter to pressure and temperature sensors in the line. Linked to the control console, these sensors display the status of the oil. If the oil pressure is less than 150 psig, the console will shut down the MPS; if the temperature is greater than 250°F, a red light located on the console panel will illuminate.

Next, the oil line progresses to a point where it merges with a line that carries excess oil from the damper pump, forming a single line. (All hardware discussed thus far is housed within the lube cabinet.) This single lube line then exits from the cabinet and confronts the warmup solenoid. This solenoid is closed, and the oil directed to a relief bypass valve and then back to the tank, if the pressure exceeds 250 psig when the MPS is rotating at less than 150 rpm.

During this phase of MPS operation, whatever oil remains in the simulator bearings and supply lines downstream of the warmup solenoid is then siphoned through the purge solenoid to the evacuated deoiler. This is done to avoid oil temperature transients, especially when the MPS has been inactive and at ambient temperature for an extended time period (for example, the beginning of a test period). Once the MPS is operating above 150 rpm, the purge solenoid closes, and the warmup solenoid opens. The ensuing oil line branches into two sections. One section has the manifolded oil supply lines from the Nos. 1, 2, 4, 5, and 10 bearings connected to it; the other section has manifolded oil supply lines from the Nos. 3, 6, and the combined Nos. 7, 8, and 9 bearings connected to it. Each of the eight bearing supply lines has its own individually adjustable needle valve to provide for oil flow balance capability. Oil then enters the MPS through the bearing supply lines.

In the second line from the tank, the damper pump in the lube cabinet channels oil through a check valve and 5- μ m filter. Upon exiting the filter, the oil line branches into two sections, with one leading to the damper bypass relief valve and the other connecting with the oil line segment from the thermostat discussed in the preceding paragraphs.

The oil does not flow through the relief valve until the pressure exceeds 175 psid, after which the valve maintains a 175 psi differential. When this occurs, the oil is heated to approximately 160°F and then flows to pressure and temperature sensors in the line. These sensors are connected to the control console where the MPS running status of the damper oil is displayed. If the pressure here is less than 20 psig, the console will shut down the MPS; if the temperature is less than 130°F, a yellow light is illuminated on the control console. All of the damper line components discussed to this point are housed within the lube cabinet. When the damper line exits from the cabinet, it is directed to the damper unit in the nacelle support housing.

Bearing sump oil is removed from the MPS through eight scavenge lines. The scavenge lines from the Nos. 1, 7, 8, 9, and 10 bearings; and the combined Nos. 2 and 3; combined Nos. 3 and 4; and combined Nos. 5 and 6 bearings exit the MPS and then are routed to the lube cabinet. These eight lines connect to eight separate scavenge pumps. The exit lines from the scavenge pumps drain into the oil supply tank.

An air and oil mixture is removed from the MPS by means of two lines that are eventually connected to a vacuum pump. One of these lines exits the MPS in the Bendix cavity region (Bendix vent line) and the other line leaves the MPS through the turbine section structure (aft vent line). Both lines lead to the lube cabinet, where they terminate at the top of the deoiler tank. In the deoiler, gravity forces the oil to the bottom of the tank. From there, a line with a 1.55- μ m filter and a ball valve transports the oil from the deoiler to the supply tank through the transfer pump. The parasitic air from the MPS is sucked from the deoiler through a line to a vacuum pump outside the cabinet.

A vacuum trim valve is provided within the cabinet; also, instrumentation in the vacuum line inside the cabinet is connected to the control console to illuminate warning lights on the MPS control panel when the vacuum does not remain between 4 and 9 psia. Oil supply and scavenge line sizes range from 0.33 to 1.5 in., and the pumps are Nichols-Zenith 1-gpm pumps. A schematic of the lube system for MPS SN002 is provided (Figure 128). All lubrication system limits pertinent to MPS control console warning and shutdown displays are adjustable.

Facility requirements for the lubrication system are: a 110-V/ac and 16-amp (starting) power supply for each pump (pumps will be ripple started), a continuous 4-psia vacuum for scavenging, and a standard tap water source for cooling flow. The lube cabinet measures approximately 19x36x60 inches; an internal Boeing report (D6-52523 by R.M. Swanson) presents additional information regarding the MPS lube system.

5.1.2.7 MPS Control System and Support Equipment

The control console was designed to control the speed of the two counterrotating shafts in the MPS unit. This is done through the operation of valves in the high pressure air supply system, the movement of which is regulated by the console. The simulator operating conditions can be set either manually or automatically through the proper use of controls on the appropriate console panel, and the speed of both rotors can be controlled simultaneously or independently to the same or different speed values.

In the automatic mode, rates of acceleration are variable up to 400 rpm per second. The console also displays such primary-operating and condition-monitoring parameters as: the bearing temperatures, vibrations, and balance forces, on four separate panels (Figure 129) which will be discussed in more detail later. It also has protective circuits which activate yellow and red warning lights when preset low- or high-threshold limits are exceeded. In some instances, these circuits also shut the MPS down. These limits are set by making adjustments to the individual monitoring meters.

AC Power Circuit Breakers	First Fault Detector	Air Management	Vibration Monitors
Hydraulic Supply Status	Bearing Temperature Displays	Torque Indicators	Vibration Monitors
Inner Rotor Servocontroller		Pressure and Speed Indicators	Vibration Monitors and Balance Analyzer
Outer Rotor Servocontroller	Lube System Status	Setpoint Controller	

Figure 129. Schematic of MPS SN002 Control Console Panel Layout.

The left outboard panel, the first of four console panels, contains the ac (alternating current) power control circuit breakers, the hydraulic supply control switch and status indicators, and the servocontrollers for the two air control valve assemblies. The four circuit breakers at the top of this panel allow power to be transmitted to the instruments and controls in the console and the MPS telemetry equipment. Below the circuit breakers and to the right is a switch to activate power to the hydraulic bench. Here, a pump provides the necessary hydraulic pressure and flow to control air valves which regulate air flow to the MPS turbine drive module. Lights to the left of this switch indicate whether the bench is functioning normally or has been turned off by the console due to low hydraulic pressure, low fluid level, or excessive oil temperature. If the hydraulic system is not performing properly, the console will not permit the air management controls to become operational. Finally, two servocontrollers are located at the bottom of the first console panel; for each rotor, the air pressure signal sensed by a strain-gauge transducer and the rpm signal sensed by a magnetic-speed pickup are conditioned and combined in the servocontrollers to manipulate rotor speed by means of a nested, double closed-loop-feedback method.

The second panel (left inboard) accommodates the first-fault detector, bearing temperature displays, and the MPS lubrication system control circuitry and status indicators. The first-fault detector (located at the top of this panel) contains circuitry which will warn the console operator, even shutting down the MPS if necessary, in the event that abnormal operating conditions are

encountered. There are 40-warning and 40-trip circuits available. Of the 40-trip circuits, 6 will initiate a 50-ms emergency MPS shutdown, while the other 34 will prompt a 400-ms automatic shutdown by interrupting airflow to the MPS turbines. When any of the 40-warning circuits are activated, a yellow light (to the right of the first-fault detector) is illuminated, and an audio alarm is sounded (provided the switch below the light is turned on).

This system is capable of detecting multiple warning signals, provided the circuitry is rearmed after each incident. When a shutdown occurs, red lights (at the left of the first-fault detector) indicate whether it was an automatic or emergency shutdown, and a digital display at the center indicates the numerical code associated with the most probable cause for the event. The nomenclature for the fault numerical code associated with an MPS shutdown is listed and defined in Table 35. After a shutdown, MPS operation cannot resume until the situation causing the abnormal condition is rectified and the fault-clear button (below the digital display) is depressed.

The 10 MPS bearing temperatures are shown on 10 separate digital meters at the center of the second console panel; of these displays, 8 receive their signals directly from the bearing thermocouples. No. 2 and 5 bearing temperature signals are conditioned and buffered by telemetry equipment before they are displayed on the console.

Low- and high-temperature limits are set by adjustments made directly to screws on the meter face. Normal bearing operating temperatures are generally a function of the tunnel test section pressure and temperature and the lube temperature. The design temperature limit for the Nos. 3 and 5 bearings is 300°F; the remaining bearings have a temperature limit of 225°F.

The bottom of the left inboard console panel is occupied by lubrication system control status indicators. To function properly, the MPS depends on a steady flow of heated oil to lubricate and cool the bearings and to dampen shaft vibrations. The operation of the lube system was discussed in earlier paragraphs. The lube system control functions are automatically directed by the console, and the running status of the various lube system components is displayed by console indicators. The lube and damper systems have pressure and temperature status indicators, and the supply tank level status is also displayed. In addition, the vacuum level produced by the facility vacuum pump is indicated, as is the operation of the oil temperature control heater and cooler. Located at the left of the indicator lights is a switch to activate the lube system. Special procedures (discussed in a later section of this report) are required for the lube system control at the start of testing to avoid transitory situations which will not permit MPS operation.

The third console panel is the right inboard panel and contains the air management controls, torque indicators for both rotors, pressure and speed indicators, and the setpoint controllers. Located at the top of this panel, the air management controls actuate the valving which permits facility air to flow to the servos; supply line pressure level and air control valve positions are monitored at this station. The console ignition switch and emergency stop button are also located in this section of the third panel.

Propulsor loads are measured by rotating force balances gauged to measure the thrust, torque, and centrifugal force. These parameters are conditioned by and routed through telemetry to the dual digital displays in the middle of the third console panel. The WOZ (wind-off zero) button between the torque displays allows for a wind-off zero to be accounted for in the displayed force balance data readout on the console.

Table 35. Numerical Code Nomenclature for the MPS Control Console First-Fault Detector.

Code	Reason	Explanation
00	Emergency Stop Button (Console Panel)	Console Operator Shuts Down MPS (Manually)
01	Outer Rotor Overspeed	Outer Rotor Speed Limit is Exceeded
02	Inner Rotor Overspeed	Inner Rotor Speed Limit is Exceeded
03	Emergency Stop Button (Blade Monitor Station)	Blade Stress Monitor Shuts Down MPS
04	Tunnel Shutdown	Tunnel Shutdown Triggers MPS Shutdown
11	Hydraulic Pressure	Pressure Level in Air Valve Hydraulic System Below Minimum Limit
12	Outer Rotor Torque	Outer Rotor Force Balance Torque Limit Exceeded
13	Inner Rotor Torque	Inner Rotor Force Balance Torque Limit Exceeded
14	Outer Rotor Servo Error	Outer Rotor Supply Pressure Difference Between Command and Feedback Exceeds Limit
15	Inner Rotor Servo Error	Inner Rotor Supply Pressure Difference Between Command and Feedback Exceeds Limit
16	Outer Rotor Servo Limit	Outer Rotor Speed Difference Between Command and Feedback Exceeds Limit
17	Inner Rotor Servo Limit	Inner Rotor Speed Difference Between Command and Feedback Exceeds Limit
18	Lube Pressure	Pressure in Lubrication System Below Minimum
19	Damper Pressure	Pressure in MPS Damper Section Below Minimum
20	Vibration 1	Vibrations Exceed Limit at Inner Shaft Tracking Filter Frequency (No. 1 Bearing, Vertical)
21	Vibration 2	Vibrations Exceed Limit at Inner Shaft Tracking Filter Frequency (No. 3 Bearing, Vertical)
22	Vibration 3	Vibrations Exceed Limit at Inner Shaft Tracking Filter Frequency (No. 3 Bearing, Horizontal)
23	Vibration 4	Vibrations Exceed Limit at Inner Shaft Tracking Filter Frequency (No. 1 Bearing, Horizontal)
24	Vibration 5	Vibrations Exceed Limit at Outer Shaft Tracking Filter Frequency (No. 1 Bearing, Vertical)
25	Vibration 6	Vibrations Exceed Limit at Outer Shaft Tracking Filter Frequency (No. 3 Bearing, Vertical)
26	Vibration 7	Vibrations Exceed Limit at Outer Shaft Tracking Filter Frequency (No. 6 Bearing, Vertical)

Table 35. Numerical Code Nomenclature for the MPS Control Console First-Fault Detector (Concluded).

Code	Reason	Explanation
27	Vibration 8	Vibrations Exceed Limit at Outer Shaft Tracking Filter Frequency (No. 6 Bearing, Horizontal)
28	Vibration 9	Vibrations Exceed Limit at Broad-Band Tracking Filter Frequency (No. 7 Bearing, Vertical)
29	Vibration 10	Vibrations Exceed Limit at Broad-Band Tracking Filter Frequency (No. 10 Bearing, Horizontal)
30	Bearing No. 1 Overtemperature	Temperature at No. 1 Bearing Exceeds Limit
31	Bearing No. 2 Overtemperature	Temperature at No. 2 Bearing Exceeds Limit
32	Bearing No. 3 Overtemperature	Temperature at No. 3 Bearing Exceeds Limit
33	Bearing No. 4 Overtemperature	Temperature at No. 4 Bearing Exceeds Limit
34	Bearing No. 5 Overtemperature	Temperature at No. 5 Bearing Exceeds Limit
35	Bearing No. 6 Overtemperature	Temperature at No. 6 Bearing Exceeds Limit
36	Bearing No. 7 Overtemperature	Temperature at No. 7 Bearing Exceeds Limit
37	Bearing No. 8 Overtemperature	Temperature at No. 8 Bearing Exceeds Limit
38	Bearing No. 9 Overtemperature	Temperature at No. 9 Bearing Exceeds Limit
39	Bearing No. 10 Overtemperature	Temperature at No. 10 Bearing Exceeds Limit

Rotational speed (in rpm) of the MPS inner and outer rotors is displayed, along with the MPS inlet turbine pressures (psig) at the lower half of the third control console panel. To establish MPS operating setpoint conditions, controls located at the bottom of this console are utilized to allow either a manual adjustment of rotor speeds by means of dials at the panel sides, or an automatic acceleration to a target value at a given rate. Target values for the rotors are selected using thumbwheel dials below the displayed setpoint rpm's; these setpoint rotor speeds can be different, and one rotor can be accelerating while the other is decelerating.

A fourth console panel (right outboard) contains MPS vibration monitoring equipment, consisting of 2 four-channel tracking filters, 10 vibration amplifiers, and 10 amplifier meters. Two additional tracking filters (lower left corner of this console) are used for rig trim balance.

The electrical power for the MPS control console must be supplied from 30-amp, 120-V/ac, 60 Hz, single-phase circuits. Grounding must be rigorous to ensure clean power as free from electronic noise as possible. The support hardware to supplement the MPS control console includes the hydraulic bench, MPS lubrication system, and the facility vacuum pump. All of these items have been discussed briefly in preceding sections of this report. Electrical power to the hydraulic bench must be supplied by a 60-amp, 120-V/ac, 60 Hz, single-phase circuit; electrical power to the lube cabinet must be supplied by three 30-amp, 120-V/ac, 60 Hz, single-phase circuits. The power to the MPS control console support hardware is independent of the power source to the console and, therefore, need not be of equivalent quality. A schematic of the hookup of the MPS control console, together with its support hardware, is illustrated in Figure 130; an internal Boeing report (D6-52523 by R.M. Swanson) provides a complete description of this equipment.

5.1.2.8 Instrumentation

Table 36 contains a complete listing of the pressure, temperature, force and moment, speed, vibration, and acoustic instrumentation utilized during the MPS SN002 testing in Cell 41. It also provides a description of the instrumentation and its location, purpose, recommended label designation, expected measurement ranges, and indicators to signify which instrumentation items are to be used for input signals to the control console, the health/blade magnetic tape, the acoustic magnetic tape, the GE facility control console, the vibration monitoring station, and which are tele-metered measurements. A pictorial representation of all MPS instrumentation is presented in an internal GE report (MPS 84-02 by G.E. Hoff) and as GE drawing No. 4013338-571. For convenience, Figures 131 through 133 present instrumentation schematics of the outer turbine, the inner turbine, and the balance cavity, respectively.

5.1.2.8.1 Aeromechanical Instrumentation and Telemetry

Four of the blades on each hub were instrumented with three strain gauges each. Signals from these strain gauges were routed by telemetry to a blade/health magnetic tape and monitoring equipment in the IDR (instrumentation data room). A summary of the telemetry instrumentation is provided in Table 37 and Figure 134. The monitoring and recording equipment required in the IDR for the blade strain gauges consisted of 14 oscilloscopes, a spectrum analyzer, amplifiers (signal conditioners), and a magnetic tape recorder. The hookup for the strain gauge output to the scopes is illustrated in Figure 135. Table 38 outlines the arrangement of blade parameters on the magnetic tape which was running continuously when the MPS was operating.

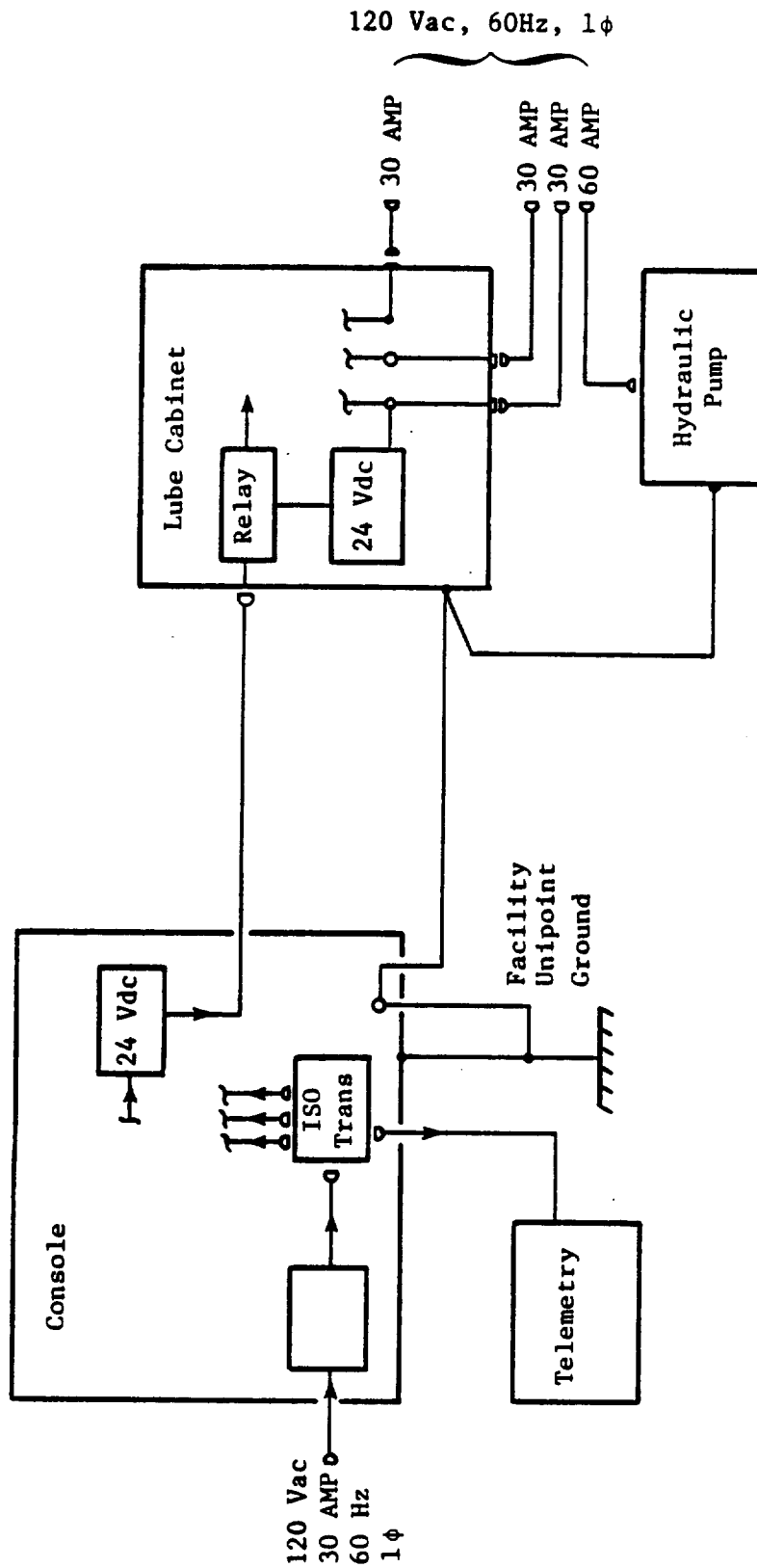


Figure 130. Schematic of MPS SN002 Control Console and Support Hardware Hook-Up Arrangement.

Table 36. MPS SN003 Instrumentation.

Parameter	GE No.	θ, ° CCW/ALF	MPS Station Rotor Spacing			Range	Routing Code ¹	Location or Description	Purpose
			Maximum	Nominal	Minimum				
ZVR110	1	0	184.76	186.50	187.32	0-20 mils	C, H, V	Aftbody Int. Support Structure	Vibration (No. 1 Bearing Vert.)
ZHR100	2	270	184.76	186.50	187.32			Aftbody Int. Support Structure	Vibration (No. 1 Bearing Hor.)
ZVR810	3	0	205.10	205.10	205.10			Damper Area	Vibration (No. 3 Bearing Vert.)
ZHR300	4	90	205.10	205.10	205.10			Damper Area	Vibration (No. 3 Bearing Hor.)
ZVR610	5	180	241.25	241.25	241.25		C, V	Macelle Support Housing	Vibration (No. 6 Bearing Vert.)
ZHR600	6	180	241.25	241.25	241.25			Macelle Support Housing	Vibration (No. 6 Bearing Hor.)
ZYB710	7	0	249.00	249.00	249.00			Near No. 7 Bearing	Vibration (No. 7 Bearing Vert.)
ZHB000	8	90	271.70	271.70	271.70			Forward End of Center Shaft	Vibration (No. 10 Bearing Hor.)
PW2180	55	0	218.83	218.83	218.83	6-17 psia	S	Macelle Forebody	Static Pressure for Macelle Force Calculations
PW2150	57		215.15	215.15	215.15				
PW2090	59		209.11	209.11	209.11				
PW2040	61		204.91	204.91	204.91				
PW2020	63		202.29	202.29	202.29				
PW1930	64	0	191.80	193.54	194.36				
PW1920	66		190.40	191.14	192.96				
PW1900	68		188.38	190.12	190.94				
PW1880	70		186.37	188.11	188.93				
PW1850	72		184.11	185.95	186.67				
PW1820	74		181.10	182.84	183.66				
PW2280	199	0	228.00	228.00	228.00				
PS1940	201	0	192.35	194.09	194.91	6-17 psia	S	Macelle Housing Fairing	Static Pressure for Force Balance Tare
PS1941	202	90						IR (Inner Rotor) Balance, Aft Cavity at r = 4.61	Spare for GE No. 201
PS1942	203	180							Spare for GE No. 202
PS1943	204	270	192.35	194.09	194.91				Static Pressure for Force Balance Tare
PS1944	205	0						IR Balance, Aft Cavity at r = 3.81	Spare for GE No. 205
PS1945	206	90							Spare for GE No. 206
PS1946	207	180							
PS1947	208	270							
PS1970	209	---	195.76	197.50	198.32	6-17 psia	S, T	Int. Bal. Cav. at r = 4.71 (Forward Side of Aft Hub)	Static Pressure for Force Balance Tare
PS1980	210	---	195.40	195.40	198.40	4-17 psia		Int. Bal. Cav. at r = 4.71 (Aft Side of Forward Hub)	
PS1971	211	---	195.66	197.40	198.22	6-17 psia		Int. Bal. Cav. at r = 1.77 (Forward Side of Aft Hub)	
PS1981	212	---	198.50	198.50	198.50	4-17 psia		Int. Bal. Cav. at r = 1.77 (Aft Side of Forward Hub)	
PS2010	213	0	201.70	201.70	201.70	6-17 psia	S	OR (Outer Rotor) Balance, Forward Cavity at r = 5.21	Spare for GE No. 213
PS2011	214	90							Spare for GE No. 214
PS2012	215	180							Static Pressure for Force Balance Tare
PS2013	216	270	201.75	201.75	201.75		S	OR Balance Forward Cavity at r = 3.81	Spare for GE No. 217
PS2014	217	0							Spare for GE No. 218
PS2015	218	90							
PS2016	219	180							
PS2017	220	270							

Table 36. MPS SN003 Instrumentation (Continued).

Parameter	GE No.	θ, ° CCVALF	MPS Station Rotor Spacing		Range	Routing Code ¹	Location or Description	Purpose
			Maximum	Nominal Minimum				
PT2600	226	105	260.00	260.00	15-200 psia	C	Outer Turb. Air Supply Pipe	Outer Turb. Air Supply Pressure
PT2601	227	105	260.00	260.00	↓	S	Outer Turb. Air Supply Pipe	Spare for GE No. 226
PT2510	228	0	251.20	251.20	↓	S	Outer Turb. Air Plenum	Outer Turb. Inlet Air Pressure
PT2511	229	90	251.20	251.20	5-60 psia	B	Outer Turb. Air Plenum	Spare for GE No. 228
PS2550	230	0	255.20	255.20	↓	S	Outer Turb. Stage 1 Tip Region	Turbine Diagnostics
PS2551	231	30	255.10	255.10	↓	S	Outer Turb. Stage 1 Hub Region	Turbine Diagnostics
PS2552	232	150	↓	↓	↓	B	↓	Spare for GE No. 231
PS2553	233	270	↓	↓	↓	B	↓	Spare for GE No. 231
PS2582	234	30	258.10	258.10	5-40 psia	M	Outer Turb. Exit, Tip Region	Turbine Diagnostics
PS2583	235	210	↓	↓	↓	M	Outer Turb. Exit, Tip Region	Turbine Diagnostics
PS2580	236	30	↓	↓	↓	S	Outer Turb. Exit, Hub Region	Turbine Diagnostics
PS2581	237	210	↓	↓	↓	B	Outer Turb. Exit, Hub Region	Spare for GE No. 236
PS2760	238	45	276.90	276.90	5-40 psia	S	Outer Turb. Exit Duct, Wall	Outer Turb. Exit Duct Wall Ps
PS2761	239	135	↓	↓	↓	B	↓	Spare for GE No. 238
PS2762	240	225	↓	↓	↓	B	↓	Spare for GE No. 241
PT18DA	241	45	↓	↓	5-50 psia	S	Outer Turb. Exit Duct, r = 4.926	Outer Turb. Exit Duct Pt
PT18KA	242	135	↓	↓	↓	B	↓	Spare for GE No. 241
PT18RA	243	225	↓	↓	↓	B	↓	Spare for GE No. 241
PT18DB	244	45	286.90	286.90	↓	S	Outer Turb. Exit Duct, r = 4.473	Outer Turb. Exit Duct Pt
PT18KB	245	135	↓	↓	↓	B	↓	Spare for GE No. 244
PT18RB	246	225	↓	↓	↓	B	↓	Spare for GE No. 244
PS2763	247	45	276.90	276.90	5-40 psia	S	Inner Turb. Exit Duct, Wall	Inner Turb. Exit Duct Ps
PS2764	248	135	↓	↓	↓	B	↓	Spare for GE No. 247
PS2765	249	225	↓	↓	↓	B	↓	Spare for GE No. 247
PT2650	250	345	265.00	265.00	15-200 psia	C	Inner Turb. Air Supply Pipe	Inner Turb. Air Supply Pressure
PT2651	251	345	265.00	265.00	↓	S	Inner Turb. Air Supply Pipe	Spare for GE No. 250
PS2630	252	0	263.70	263.70	↓	B	Inner Turb. Air Plenum	Inner Turb. Inlet Air Pressure
PS2631	253	120	263.70	263.70	↓	S	Inner Turb. Air Plenum	Spare for GE No. 252
---	254	0	265.20	265.20	5-60 psia	M	Inner Turb. Stage 1 Tip Region	Turbine Diagnostics
---	255	0	267.15	267.15	5-40 psia	M	Inner Turb. Interstage	Turbine Diagnostics
PS2680	256	0	268.30	268.30	5-40 psia	M	Inner Turb. Exit Tip Region	Turbine Diagnostics
PS2681	257	180	268.30	268.30	5-40 psia	M	Inner Turb. Exit Tip Region	Turbine Diagnostics
PT27DA	258	45	278.10	278.10	5-50 psia	S	Inner Turb. Exit Duct, r = 3.576	Inner Turb. Exit Duct Pt
PT27KA	259	135	↓	↓	↓	B	↓	Spare for GE No. 258
PT27RA	260	225	↓	↓	↓	S	↓	Spare for GE No. 261
PT27DB	261	45	↓	↓	↓	B	↓	Spare for GE No. 261
PT27KB	262	135	↓	↓	↓	B	↓	Spare for GE No. 261
PT27RB	263	225	↓	↓	↓	B	↓	Spare for GE No. 261
PS2850	264	0	285.00	285.00	5-40 psia	S	MPS Exit Shroud Int. Wall	Mixed Flow Exit Static Pressure
PS1900	276	---	180.56	191.12	4-17 psia ²	↓	No. 1 Bearing, Forward Cavity	No. 1 Bearing Cavity Pressure
PS1870	277	---	185.86	188.42	↓	↓	No. 1 Bearing, Aft Cavity	↓
PS1918	278	---	190.06	192.62	↓	↓	Cav. Aft of IR Tel. Mod.	↓
PS2310	279	---	231.50	231.50	↓	↓	No. 6 Bearing, Aft Cavity	No. 6 Bearing Cavity Pressure
PS2350	280	---	235.00	235.00	↓	↓	No. 6 Bearing, Forward Cavity	↓

Table 36. MPS SN003 Instrumentation (Continued).

Parameter	GE No.	θ , ° CCW/ALF	MPS Station Rotor Spacing			Range	Routing Code ¹	Location or Description	Purpose
			Maximum	Nominal	Minimum				
PS2440	281	---	244.00	244.00	244.00	4-17 psia ²	S	Bendix Coupling Cavity Pres.	
PS2540	282	60	254.50	254.50	254.50	4-60 psia ²	N	Cavity Pressure	
PS2541	283	0	254.00	254.00	254.00	4-17 psia ²	S		
PS2590	284	0	259.20	259.20	259.20	4-17 psia ²	S		
PS2640	285	60	264.70	264.70	264.70	4-60 psia ²	N		
PS2641	286	0	264.50	264.50	264.50	4-17 psia ²	S		
PS2710	287	0	271.00	271.00	271.00	4-17 psia ²	S		
PS2050	288	---	205.50	205.50	205.50	4-25 psia ²	↓		
PS2030	289	---	203.90	203.90	203.90	4-25 psia ²	↓		
TA1940	302	45	192.35	194.09	194.91	40-150° F	S	Cavity Temperature	
TA1941	302	225	↓	↓	↓	↓	↓		
TA1942	303	45	↓	↓	↓	↓	↓		
TA1943	304	225	↓	↓	↓	↓	↓		
TA1970	305	---	195.76	197.50	198.32	30-200° F	S, T		
TA1980	306	---	198.40	198.40	198.40	30-200° F	S, T		
TA2010	307	45	201.70	201.70	201.70	40-150° F	S		
TA2011	308	225	201.70	201.70	201.70	↓	↓		
TA2012	309	40	201.75	201.75	201.75	↓	↓		
TA2013	310	225	201.75	201.75	201.75	↓	↓		
TM2510	326	97	251.20	251.20	251.20	160-200° F	S	Outer Turb. Inlet Air Temp.	
TM2511	327	263	↓	↓	↓	↓	↓		
TM2512	328	353	↓	↓	↓	↓	↓		
TM28DC	329	45	276.90	276.90	276.90	0-200° F	S	Outer Turb. Exit Duct Tt Spare for GE No. 329	
TM28K	330	135	↓	↓	↓	↓	↓		
TM28RC	331	225	↓	↓	↓	↓	↓		
TM28DB	332	45	↓	↓	↓	↓	↓		
TM28KB	333	135	↓	↓	↓	↓	↓		
TM28RB	334	225	↓	↓	↓	↓	↓		
TM28DA	335	45	↓	↓	↓	↓	↓		
TM28KA	336	135	↓	↓	↓	↓	↓		
TM28RA	337	225	↓	↓	↓	↓	↓		
TM2630	338	0	263.20	263.20	263.20	160-200° F	S	Inner Turb. Inlet Air Temp.	
TM2631	339	120	↓	↓	↓	↓	↓		
TM2632	340	240	↓	↓	↓	↓	↓		
TM27DA	341	45	278.10	278.10	278.10	0-200° F	S	Inner Turb. Exit Duct Tt Spare for GE No. 341	
TM27KA	342	135	↓	↓	↓	↓	↓		
TM27RA	343	235	↓	↓	↓	↓	↓		
TM27DB	344	45	↓	↓	↓	↓	↓		
TM27KB	345	135	↓	↓	↓	↓	↓		
TM27RB	346	225	↓	↓	↓	↓	↓		
TM27DC	347	45	↓	↓	↓	↓	↓		
TM27KC	348	135	↓	↓	↓	↓	↓		
TM27RC	349	225	↓	↓	↓	↓	↓		

Table 36. MPS SN003 Instrumentation (Continued).

Parameter	GE No.	θ, ° CCW/ALF	MPS Station Rotor Spacing			Range	Routing Code ¹	Location or Description	Purpose
			Maximum	Nominal	Minimum				
TKB100	351	90	187.56	189.30	190.12	0-225° F	C,H	No. 1 Bearing	No. 1 Bearing Metal Temp.
TKB101	352	270	187.56	189.30	190.12	↓	B	No. 1 Bearing	Spare for GE No. 351
TKB200	353	15	203.20	203.20	203.20	↓	C,H,T	No. 2 Bearing	No. 2 Bearing Metal Temp.
TKB201	354	195	203.20	203.20	203.20	↓	B,T	No. 2 Bearing	No. 2 Bearing Metal Temp.
TKB300	357	0	206.75	206.75	206.75	0-300° F	C,H	No. 3 Bearing	No. 3 Bearing Metal Temp.
TKB301	358	90	206.75	206.75	206.75	0-300° F	B	No. 3 Bearing	Spare for GE No. 357
TKB400	359	0	209.10	209.10	209.10	0-225° F	C,H	No. 4 Bearing	No. 4 Bearing Metal Temp.
TKB401	360	180	209.10	209.10	209.10	0-225° F	B	No. 4 Bearing	Spare for GE No. 359
TKB500	361	90	228.60	228.60	228.60	0-300° F	C,H,T	No. 5 Bearing	No. 5 Bearing Metal Temp.
TKB501	362	270	228.60	228.60	228.60	0-300° F	B,T	No. 5 Bearing	No. 5 Bearing Metal Temp.
TKB600	363	0	234.00	234.00	234.00	0-225° F	C,H	No. 6 Bearing	No. 6 Bearing Metal Temp.
TKB601	366	90	234.00	234.00	234.00	0-225° F	B	No. 6 Bearing	Spare for GE No. 365
TKB700	367	90	248.90	248.90	248.90	0-225° F	C,H	No. 7 Bearing	No. 7 Bearing Metal Temp.
TKB701	368	270	248.90	248.90	248.90	↓	B	No. 7 Bearing	Spare for GE No. 367
TKB800	369	97	253.50	253.50	253.50	↓	C,H	No. 8 Bearing	No. 8 Bearing Metal Temp.
TKB801	370	263	253.50	253.50	253.50	↓	B	No. 8 Bearing	Spare for GE No. 369
TKB900	371	120	259.70	259.70	259.70	↓	C,H	No. 9 Bearing	No. 9 Bearing Metal Temp.
TKB901	372	240	259.70	259.70	259.70	↓	B	No. 9 Bearing	Spare for GE No. 371
TKB000	373	90	269.70	269.70	269.70	↓	C,H	No. 10 Bearing	No. 10 Bearing Metal Temp.
TKB001	374	270	269.70	269.70	269.70	↓	B	No. 10 Bearing	Spare for GE No. 373
TKAM01	376	---	190.98	192.72	293.54	40-250° F	N,T	IR Tel. Mod. No. 16	Inner Rotor Tel. Mod No. 1 Temp.
TKAM06	377	---	↓	↓	↓	↓	↓	IR Tel. Mod. No. 17	Inner Rotor Tel. Mod No. 6 Temp.
TKAM07	378	---	---	---	---	30-200° F	S,T	IR Tel. Mod. No. 17	Inner Rotor Tel. Mod No. 7 Temp.
TKBLA0	380	---	---	---	---	↓	↓	IR Balance	Inner Rotor Balance Temp.
TKBLA1	381	---	---	---	---	↓	↓	↓	↓
TKBLA2	382	---	---	---	---	↓	↓	OR Balance	Outer Rotor Balance Temp.
TKBLA3	383	---	---	---	---	↓	↓	↓	↓
TKBLF0	384	---	---	---	---	30-200° F	S,T	↓	↓
TKBLF1	385	---	---	---	---	↓	↓	↓	↓
TKBLF2	386	---	---	---	---	↓	↓	↓	↓
TKBLF3	387	---	---	---	---	↓	↓	↓	↓
TKFH01	388	---	203.90	203.90	203.90	40-250° F	N,T	OR Tel. Mod. No. 3	Outer Rotor Tel. Mod. No. 1 Temp.
TKFH03	389	---	---	---	---	↓	↓	↓	Outer Rotor Tel. Mod. No. 3 Temp.
TKFH06	390	---	---	---	---	↓	↓	↓	Outer Rotor Tel. Mod. No. 6 Temp.
TKFH10	391	---	---	---	---	↓	↓	↓	Outer Rotor Tel. Mod. No. 10 Temp.
TKFH12	392	---	---	---	---	↓	↓	↓	Outer Rotor Tel. Mod. No. 12 Temp.
TKFH15	393	---	---	---	---	↓	↓	↓	Outer Rotor Tel. Mod. No. 15 Temp.
TKFH00	394	0	217.00	217.00	217.00	40-500° F	S	Support Housing	Support Housing Metal Temp.
TKFH01	395	90	217.00	217.00	217.00	40-500° F	B	Support Housing	Spare for GE No. 394
TKAA00	396	15	191.56	193.30	191.56	40-250° F	S	IR Tel. Antenna	Inner Rotor Tel. Ant. Temp.
TKAA01	398	150	191.56	193.30	191.56	↓	↓	IR Tel. Antenna	Inner Rotor Tel. Ant. Temp.
TKFA00	398	210	202.70	202.70	202.70	↓	↓	OR Tel. Antenna	Outer Rotor Tel. Ant. Temp.
TKFA01	399	345	202.70	202.70	202.70	↓	↓	OR Tel. Antenna	Outer Rotor Tel. Ant. Temp.
TKFH02	400	0	234.00	234.00	234.00	0-500° F	C	Nacelle Support Housing	Support Housing Metal Temp.

Table 36. MPS SN003 Instrumentation (Continued).

Parameter	GE No.	$\theta, ^\circ$ CCW/ALF	MPS Station Rotor Spacing			Range	Routing Code ¹	Location or Description	Purpose
			Maximum	Nominal	Minimum				
PT19GA	401	---	189.10	190.84	191.66	14-25 psia	S	Prop. Wake Trav. Rake, $r = 12.55$	Propeller Wake, Total Pressure Profile
PT19GB	403	---	---	---	---	---	---	$r = 11.80$	
PT19GC	405	---	---	---	---	---	---	$r = 10.80$	
PT19GD	407	---	---	---	---	---	---	$r = 9.30$	
PT19GE	409	---	---	---	---	---	---	$r = 8.00$	
PT19GF	411	---	---	---	---	---	---	$r = 6.80$	
PT19GG	413	---	---	---	---	---	---	$r = 5.60$	
PT19GH	415	---	---	---	---	---	---	$r = 4.75$	
KSBLA0	501	---	---	---	-630 to + 4730 in./#	C, H, T	Inner Rotor Balance	Inner Rotor Balance Torque	
KSBLA1	502	---	---	---	-300 to + 600 #	---	---	Inner Rotor Balance Thrust	
KSBLA2	503	---	---	---	0 to 5-V	N	---	IR Bal. Forward Cent. Force	
KSBLA3	504	---	---	---	---	---	---	IR Bal. Aft Centrifugal Force	
KSBLA4	505	---	---	---	---	---	---	Dynamic Strain, Balance Flex. 2 Aft	
KSBLA5	506	---	---	---	---	---	---	Dynamic Strain, Balance Flex. 3 Aft	
KSBLA6	507	---	---	---	---	---	---	Outer Rotor Balance Torque	
KSBLA7	508	---	---	---	---	---	---	Outer Rotor Balance Thrust	
KSBLF0	511	---	---	---	-630 to + 4730 in./#	C, S, T	Outer Rotor Balance	OR Bal. Forward Cent. Force	
KSBLF1	512	---	---	---	-300 to + 600 #	---	---	OR Balance Aft Cent. Force	
KSBLF2	513	---	---	---	0 to 5-V	N	---	Dynamic Strain, Balance Flex. 2 Aft	
KSBLF3	514	---	---	---	0 to 5-V	---	---	Dynamic Strain, Balance Flex. 3 Aft	
KSBLF4	515	---	---	---	---	---	---	Rotor Thrust (Outer Rotor)	
KSBLF5	516	---	---	---	---	---	---	Prop. Blade Dynamic Strain	
KSBLF6	517	---	---	---	---	---	---	---	
KSBLF7	518	---	---	---	---	---	---	---	
KSBLF0	550	---	249.30	249.30	249.30	---	Forward of No. 7 Bearing	---	
KDAB10	601	---	---	---	0-40 ksi	M, T	Inner Rotor, No. 1 Blade	---	
KDAB11	602	---	---	---	---	---	Inner Rotor, No. 3 Blade	---	
KDAB12	603	---	---	---	---	---	Inner Rotor, No. 5 Blade	---	
KDAB30	611	---	---	---	---	---	Outer Rotor, No. 1 Blade	---	
KDAB31	612	---	---	---	---	---	---	---	
KDAB32	613	---	---	---	---	---	---	---	
KDAB50	621	---	---	---	---	---	---	---	
KDAB51	622	---	---	---	---	---	---	---	
KDAB52	623	---	---	---	---	---	---	---	
KDAB70	631	---	---	---	---	---	---	---	
KDAB71	632	---	---	---	---	---	---	---	
KDAB72	633	---	---	---	---	---	---	---	
KDFB10	651	---	---	---	---	---	---	---	
KDFB11	652	---	---	---	---	---	---	---	
KDFB12	653	---	---	---	---	---	---	---	

Table 36. MPS SN003 Instrumentation (Continued).

Parameter	GE No.	θ, ° CCW/ALF	MPS Station Rotor Spacing			Range	Routing Code ¹	Location or Description	Purpose
			Maximum	Nominal	Minimum				
KDFB30	661	---	---	---	0-40 ksi	H, J	Outer Rotor, No. 3 Blade	Prop. Blade Dynamic Strain	
KDFB31	662	---	---	---	---	---	Outer Rotor, No. 5 Blade		
KDFB32	663	---	---	---	---	---	Outer Rotor, No. 7 Blade		
KDFB50	671	---	---	---	0-10,000 rpm	A, C, H	Between Bendix Coupling and OR Air Plenum Aft of No. 10 Bearing	Outer Turb. Rotor Speed, 1/rev Outer Turb. Rotor Speed, 60/rev Inner Turb. Rotor Speed, 1/rev Inner Turb. Rotor Speed, 60/rev	
KDFB51	672	---	---	---	0-10,000 rpm	C, S			
KDFB52	673	---	---	---	0-10,000 rpm	A, C, H			
KDFB70	681	---	---	---	0-10,000 rpm	C, S			
KDFB71	682	---	---	---	12-16 psia	S	Fwd. of Freejet Noz. Screen Nacelle Support Housing (Freejet Nozzle Inner Wall)	For Screen AP Calculation Freejet Nozzle Discharge Ps	
KDFB72	683	---	---	---	12-17 psia	S			
XNR101	901	0	247.10	247.10	12-17 psia	S	Freejet Nozzle Outer Wall	Freejet Total Pressure	
XNR160	902	90	247.10	247.10	12-17 psia	S			
XNR201	903	0	271.20	271.20	14-17 psia	S, S	Aft of Freejet Noz. Screen	Freejet Total Pressure	
XNR260	904	90	271.20	271.20	14-17 psia	S, S			
PW2940	1000	195	294.43	294.43	---	---	---	---	
PW23SB	1005	15	232.43	232.43	---	---	---	---	
PW23SF	1006	75	232.43	232.43	---	---	---	---	
PW23SP	1007	195	---	---	---	---	---	---	
PW23ST	1008	255	---	---	---	---	---	---	
PW23LB	1009	15	232.43	232.43	---	---	---	---	
PW23LF	1010	75	---	---	---	---	---	---	
PW23LP	1011	195	---	---	---	---	---	---	
PW23LT	1012	255	---	---	---	---	---	---	
PT28DA	1013	45	282.46	282.46	---	---	---	---	
PT28DB	1014	---	---	---	---	---	---	---	
PT28DC	1015	---	---	---	---	---	---	---	
PT28DD	1016	---	---	---	---	---	---	---	
PT28DE	1017	---	---	---	---	---	---	---	
PT28DF	1018	---	---	---	---	---	---	---	
PT28DG	1019	---	---	---	---	---	---	---	
PT28DH	1020	---	---	---	---	---	---	---	
PT28DJ	1021	---	---	---	---	---	---	---	
PT28DK	1022	---	---	---	---	---	---	---	
PT28MA	1023	165	---	---	---	---	---	---	
PT28MB	1024	---	---	---	---	---	---	---	
PT28MC	1025	---	---	---	---	---	---	---	
PT28MD	1026	---	---	---	---	---	---	---	
PT28ME	1027	---	---	---	---	---	---	---	
PT28MF	1028	---	---	---	---	---	---	---	
PT28MG	1029	---	---	---	---	---	---	---	
PT28MH	1030	---	---	---	---	---	---	---	
PT28HJ	1031	---	---	---	---	---	---	---	
PT28MK	1032	---	---	---	---	---	---	---	

Table 36. MPS SN003 Instrumentation (Continued).

Parameter	GE No.	θ, ° CCWALF	MPS Station Rotor Spacing			Range	Routing Code ¹	Location or Description	Purpose
			Maximum	Nominal	Minimum				
PW28LB	1033	15	282.46	282.46	282.46	12-17 psia	S	Outer Wall, Aft of Freejet Nozzle Screen	Screen AP Calc. and Freejet Ps
PW28LF	1034	75	→	→	→	→	→	→	→
PW28LP	1035	195	→	→	→	→	→	→	→
PW28LT	1036	255	282.46	282.46	282.46	12-17 psia	M	Inner Wall, Aft of Freejet Nozzle Screen	Freejet Static Pressure
PW28SB	1037	15	→	→	→	→	→	→	→
PW28SF	1038	75	→	→	→	→	→	→	→
PW28SP	1039	195	→	→	→	→	→	→	→
PW28ST	1040	255	340.93	340.93	343.93	0-100° F	S	Upstream of Honeycomb Grid	Freejet Temperatures
TH340A	1041	---	→	→	→	→	→	→	→
TH340B	1042	→	→	→	→	→	→	→	→
TH340C	1043	→	→	→	→	→	→	→	→
TH340D	1044	→	→	→	→	→	→	→	→
TH340E	1045	→	→	→	→	→	→	→	→
TH340F	1046	→	→	→	→	→	→	→	→
TH340G	1047	→	→	→	→	→	→	→	→
TH340H	1048	→	→	→	→	→	→	→	→
TH340J	1049	→	→	→	→	→	→	→	→
TH340K	1050	→	→	→	→	→	→	→	→
PL0ILD	1051	---	---	---	---	0-300 psia ²	C	In Damper Oil Line	Pressure in Damper Line
PDJETA	1052	→	→	→	→	0-0.2 psid	G	Freejet Nozzle Entrance	Set Inlet Guide Vanes
PSR1VU	1053	→	→	→	→	0-250 psig	→	Outer Turb. Drive Flow Venturi Inlet	Ps for Outer Turbine Drive Flow
PDR1VD	1054	→	→	→	→	0-25 psid	→	Outer Turb. Drive Flow Vent. Inlet	AP for Outer Turb. Dr. Flow
PSR2VU	1055	→	→	→	→	0-250 psig	G	Inner Turb. Dr. Flow Vent. Inlet	Ps for Inner Turb. Dr. Flow
PSN02Z	1057	---	---	---	---	0-250 psig	→	Mixer Chamber Vent Pipe	Bleed Flow Static Pressure
PLCRFH	1058	---	---	---	---	0-1500 psig	→	Burner	Set Fuel/Air Ratio
PSDRIV	1059	0	285.00	285.00	285.00	5-40 psia	→	Same as GE No. 264	Turb. Disch. Duct Stat. Pres.
PSSTRH	1060	→	→	→	→	14-200 psia	→	Steam Header	Steam Header Pressure
PSSEVO	1061	→	→	→	→	2-15 psia	→	Steam Ejector	Steam Ejector Vacuum
PSSEV1	1062	→	→	→	→	2-15 psia	→	Steam Ejector	Steam Ejector Vacuum
PTJETA	1063	45	282.46	282.46	282.46	14-17 psia	G	Same as GE No. 1014	Freejet Total Pressure
PDR1FR	1064	---	---	---	---	0-25 psia	→	Aft of Outer Turbine Drive Flow Venturi	Drive Flow Filter AP
PDR2FR	1065	→	→	→	→	0-25 psia	→	Aft of Inner Turbine Drive Flow Venturi	→
PDSCRN	1066	→	→	→	→	0-0.5 psid	→	Freejet Noz. Inlet Screen	Screen AP
PDRVLV	1067	→	→	→	→	0-50 psid	→	Facility Water Relief Valve	Water Relief Valve Pressure
THR1VU	1068	---	---	---	---	160-250° F	G,S	Outer Turbine Drive Flow Venturi Temperature	Temp. for Outer Turbine Drive Flow
THR2VU	1069	→	→	→	→	160-250° F	→	Inner Turbine Drive Flow Venturi Temperature	Temp. for Inner Turbine Drive Flow
TAN0ZZ	1070	→	→	→	→	0-300° F	→	Mixer Chamber Vent Pipe	Bleed Flow Temperature
TAOILD	1071	→	→	→	→	50-250° F	C	In Damper Oil Supply Line	Temp. in Damper Line

Table 36. MPS SN003 Instrumentation (Continued).

Parameter	GE No.	θ, ° CCWALF	MPS Station Rotor Spacing			Range	Routing Code ¹	Location or Description	Purpose
			Maximum	Nominal	Minimum				
PSLURE	1072	---	---	---	0-150 psig ²	C	Upstream of Warm-Up Solenoid	Pressure in Lube Line	
TALURE	1073	---	---	---	0-300° F	C	In Oil Supply Line	Temperature in Lube Line	
PSVACU	1074	---	---	---	4-25 psia ²	C	In Line From Deoiler to Vacuum Pump	Deoiler Vacuum Pressure	
PSWATR	1075	---	---	---	0-150 psig ²	C	In Cooling Water Line	Cooling Water Pressure	
QVPOS1	1076	---	---	---	0-100% (Open)	C	On Outer Drive Valve	Valve Position	
QVPOS2	1077	---	---	---	0-100% (Open)	C	In Inner Drive Valve	Valve Position	
PSFNSD	1078	---	---	---	14-250 psig	C,G	Bypass Duct	Mixing Chamber Pressure	
PSHEAD	1081	---	---	---	0-300 psia	G,S	Supply Air Line	Supply Air Header Pressure	
UPCORE	1082	---	---	---	14-250 psig	→	Upstream of Core Flow Orifice	Upstream Pressure	
DELCOR	1083	---	---	---	0-5 psid	→	Core Flow Orifice	AP for Core Flow	
UPFANP	1084	---	---	---	14-250 psig	→	Upstream of Fan Flow Orifice	Upstream Pressure	
DELFAN	1085	---	---	---	0-5 psid	→	Fan Flow Orifice	AP for Fan Flow	
DEWPNT	1086	---	---	---	0-100° F	→	Anechoic Chamber	Despoint	
PT20A1	1096	---	---	---	14-17 psia	S	Pressure Scanner E	Cell 41 Ambient Pressure	
PT20A2	1092	---	---	---	→	→	Pressure Scanner G	→	
PT20A3	1093	---	---	---	→	→	Pressure Scanner H	→	
PT20A4	1094	---	---	---	→	→	Pressure Scanner F	→	
PT20A5	1095	---	---	---	→	→	Pressure Scanner C	→	
PT20A6	1096	---	---	---	→	→	Pressure Scanner A	→	
PT20A7	1097	---	---	---	→	→	Pressure Scanner D	→	
PSFS01	2001	---	200.00	220.00	6-17 psia	S	Fuselage Egg	Fuselage Static Pressure	
PSFS02	2002	---	210.50	210.50	→	→	→	→	
PSFS03	2003	---	204.25	204.25	→	→	→	→	
PSFS04	2004	---	201.50	201.50	→	→	→	→	
PSFS05	2005	---	199.00	199.00	→	→	→	→	
PSFS06	2006	---	197.00	197.00	→	→	→	→	
PSFS07	2007	---	195.00	195.00	→	→	→	→	
PSFS08	2008	---	193.00	193.00	→	→	→	→	
PSFS09	2009	---	188.00	188.00	→	→	→	→	
PSFS10	2010	---	180.00	180.00	→	→	→	→	
TT20A1	3000	---	---	---	0-100° F	S	Anechoic Chamber	Cell 41 Ambient Temperature	
TFANUP	3001	---	---	---	→	G,S	Upstream of Fan Flow Orifice	Upstream Temperature	
TCORUP	3002	---	---	---	→	G,S	Upstream of Core Flow Orifice	Upstream Temperature	
TT90A1	3003	---	---	---	→	S	Mixing Chamber Ext. Wall	Mixing Chamber Skin Temp.	
TT90A2	3004	---	---	---	→	S	Mixing Chamber Ext. Wall	Mixing Chamber Skin Temp.	
TFMTOH	3005	---	---	---	→	G,S	Fan Duct Flowpath	Mixing Chamber Temperature	
TELSKN	3006	---	---	---	0-100° F	S	Fan Duct Ext. Surface	Fan Duct Skin Temperature	
TCMB5	3007	---	---	---	0-800° F	→	Downstream of Burner	Set Fuel/Air Ratio	
TBRN5	3008	---	---	---	0-800° F	→	Downstream of Burner	Set Fuel/Air Ratio	
TBRN0	3009	---	---	---	0-100° F	G	Burner Room	Burner Room Ambient Temp.	
TT90A3	3010	---	---	---	0-100° F	S	Mixing Chamber Ext. Wall	Mixing Chamber Skin Temp.	

Table 36. MPS SN003 Instrumentation (Concluded).

Parameter	GE No.	θ, ° CCW/ALF	MPS Station Rotor Spacing			Range	Routing Code ¹	Location or Description	Purpose
			Maximum	Nominal	Minimum				
FHIC01	4001	0	456.37	456.37	456.37	50-100 dB	A	Fixed Microphone (r; Angle) r = 29.26'; 43.1°	Far-Field Noise Measurement
FHIC02	4002		456.43	456.43	456.43			r = 32.01'; 48.12°	
FHIC03	4003		403.53	403.53	403.53			r = 31.89'; 51.87° M	
FHIC04	4004							r = 31.89'; 57.87°	
FHIC05	4005		334.34	334.34	334.34			r = 31.89'; 57.87° S	
FHIC06	4006		303.28	303.28	303.28			r = 29.23'; 67.48°	
FHIC07	4007		273.56	273.56	273.56			r = 28.34'; 72.32°	
FHIC08	4008		244.77	244.77	244.77			r = 27.49'; 77.21°	
FHIC09	4009		216.41	216.41	216.41			r = 27.25'; 82.13°	
FHIC10	4010							r = 27.03'; 87.10° M	
FHIC11	4011							r = 27.03'; 87.10°	
FHIC12	4012		188.06	188.06	188.06			r = 27.03'; 87.10° S	
FHIC13	4013		159.29	159.29	159.29			r = 27.02'; 92.11°	
FHIC14	4014		98.54	98.54	98.54			r = 27.22'; 97.16°	
FHIC15	4015		29.36	29.36	29.36			r = 28.29'; 107.39°	
FHIC16	4016							r = 30.52'; 117.77° M	
FHIC17	4017							r = 30.52'; 117.77°	
FHIC18	4018		-55.49	-55.49	-55.49			r = 30.52'; 117.77° S	
FHIC19	4019		-58.25	-58.25	-58.25			r = 34.39'; 128.25°	
FHIC20	4020		-60.51	-60.51	-60.51			r = 31.42'; 133.23°	
FHIC21	4021		-60.58	-60.58	-60.58			r = 29.09'; 138.27°	
FHIC22	4022		-60.49	-60.49	-60.49			r = 27.07'; 143.34°	
FHIC23	4023		-105.42	-105.42	-105.42			r = 25.47'; 148.46°	
FHIC24	4024							r = 28.40'; 153.66°	
THIC01	4101	---	---	---	---	50-100 dB	A	Traverse Microphone	Near-Field Noise Measurement Traverse Microphone Position Cabin Noise Measurement
MICP05	4200		224.20	224.20	224.20	0-4 ft		Traverse Microphone Boom	
FKUL30	4530		217.15	217.15	217.15	0-1 psid		Fuselage Egg	
FKUL40	4540		212.40	212.40	212.40				
FKUL50	4550		208.75	208.75	208.75				
FKUL60	4560		205.70	205.70	205.70				
FKUL70	4570		202.80	202.80	202.80				
FKUL80	4580		200.00	200.00	200.00				
FKUL90	4590		197.92	197.92	197.92				
FKLMA	4592		195.84	195.84	195.84				
FKLMB	4593		194.10	194.10	194.10				
FKLMA	4594								
FKLMB	4595								
FKLMA	4599								

¹ Routing Code Explanation:

- A - Acoustic magnetic tape in IDR
- C - Boeing control console
- H - Health/blade magnetic tape in IDR
- S - Steady-state data system (DMS)
- V - Vibration spectrum
- M - Missing instrumentation (will be hooked up if found)

- B - Back-up instrumentation to be used only as spare
- G - GE Cell 41 control console
- M - Not used during Cell 41 testing
- T - Telemetry
- C No. - DVM (digital volt meter) near Boeing control console

² Special transducer required (liquid environment involved)

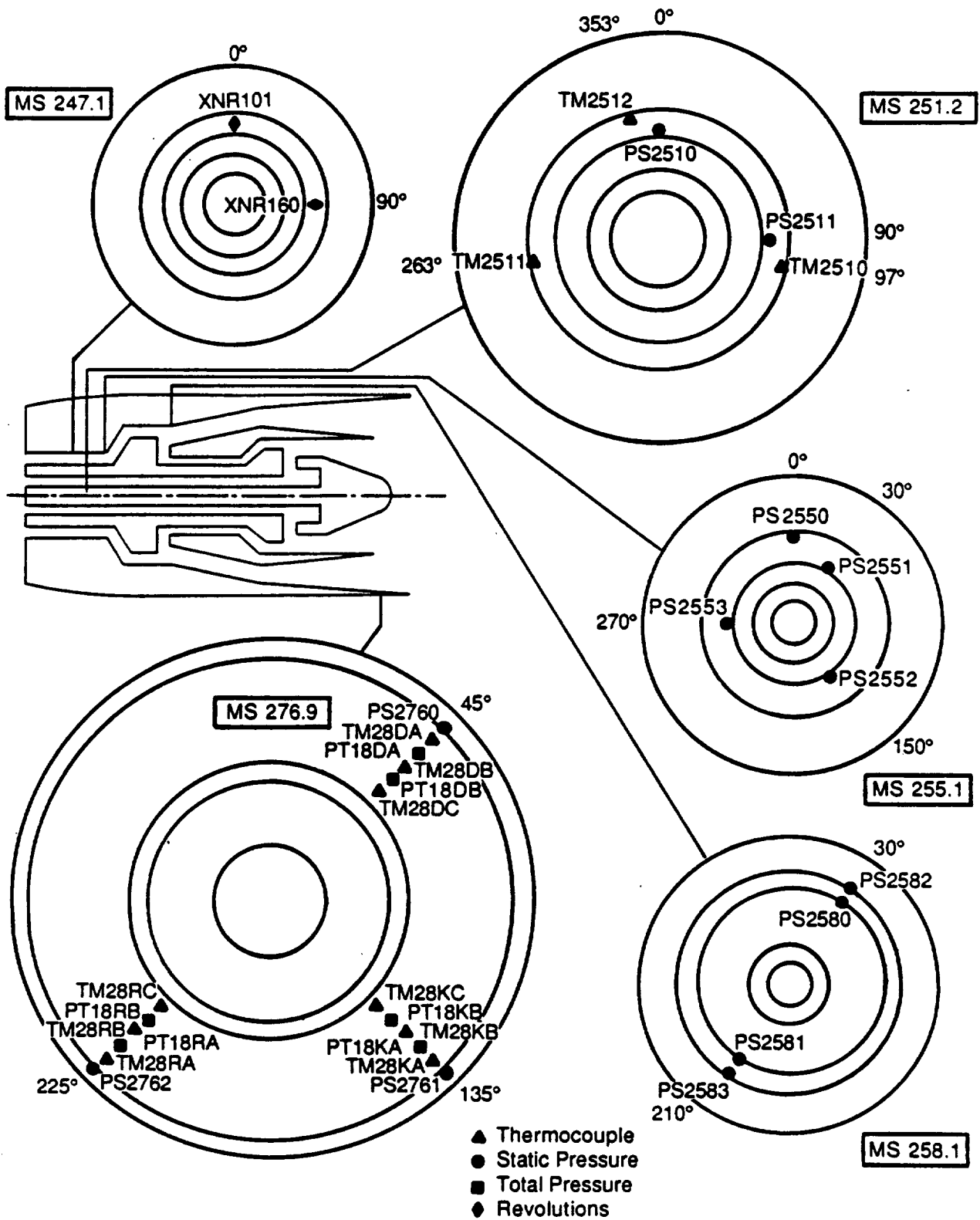


Figure 131. MPS SN002 Outer Turbine Instrumentation.

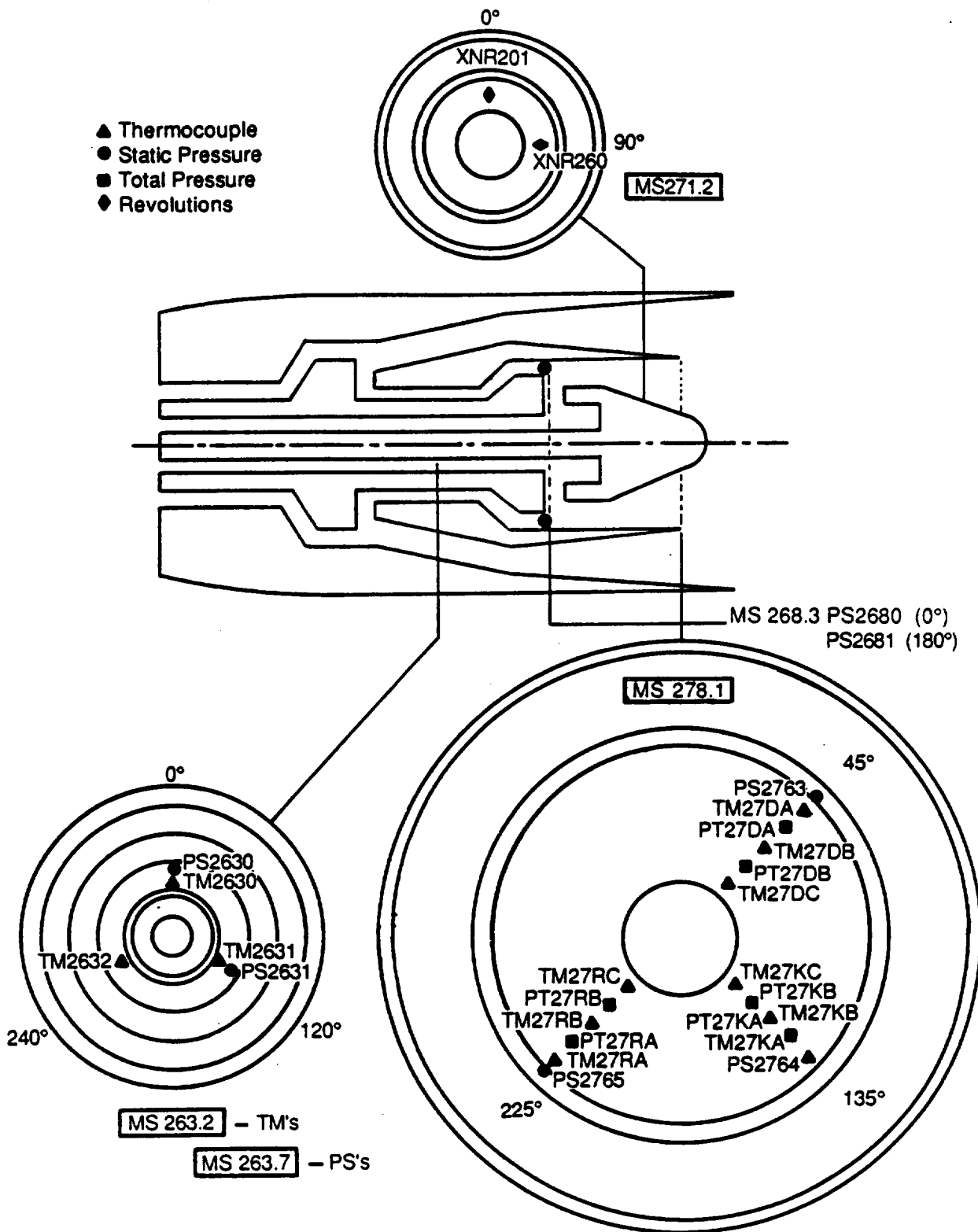


Figure 132. MPS SN002 Inner Turbine Instrumentation.

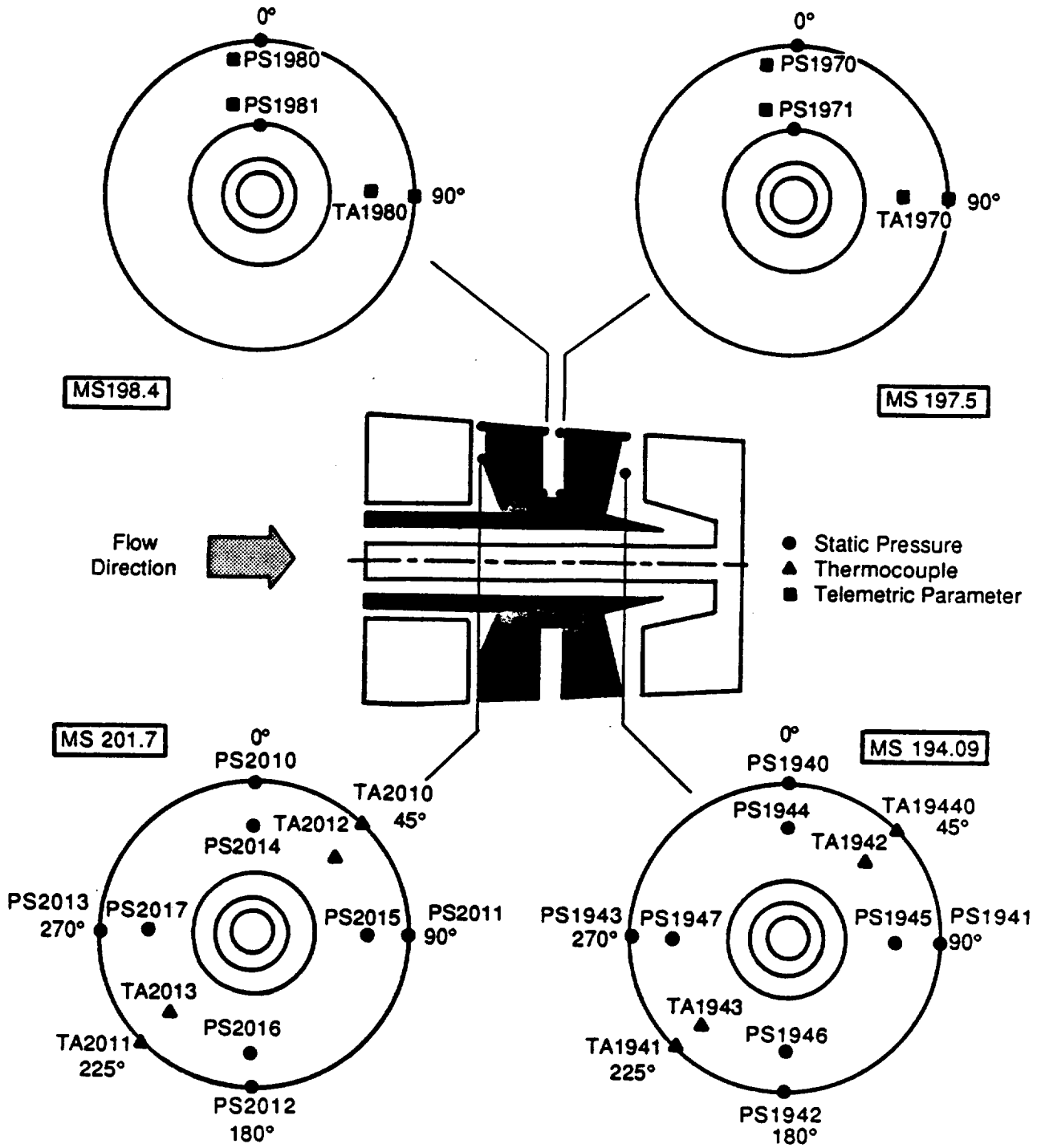


Figure 133. MPS SN002 Balance Cavity Instrumentation.

Table 37. MPS SN003 Telemetry Instrumentation Summary.

Inner Rotor				Outer Rotor					
Parameter	GE No.	Module	Description	Routed To	Parameter	GE No.	Module	Description	Routed To
KSBLA1	502	1	Thrust	DMS, BCO	KSBLF1	512	1	Thrust	DMS, BCO
KDAB11	602	2	Blade No. 1 Dynamic Strain	TAP	KDFB11	652	2	Blade No. 1 Dynamic Strain	TAP
KDAB31	612	5	Blade No. 3 Dynamic Strain	TAP	TKBLF3	384	3	Balance Temperature	DMS
KDAB30	611	5	Blade No. 3 Dynamic Strain	TAP	TKBLF0	306	3	Balance Temperature	DMS
KDAB32	613	5	Blade No. 3 Dynamic Strain	TAP	TA1980	390	3	Cavity Temperature	DMS
KSBLA0	501	6	Torque	DMS, BCO	TKFH06	388	6	Module 1 Temperature	DMS
TKBLA2	382	7	Balance Temperature	DMS	TKFH01	389	7	Module 3 Temperature	DMS
TKAM07	378	7	Module 7 Temperature	DMS	TKFH03	212	5	Balance Cavity Pressure	DMS, BCO
TKBLA1	381	7	Balance Temperature	DMS	PS1981	514	6	Aft Centrifugal Force	TAP
TKAM06	377	7	Module 6 Temperature	DMS	KSBLF3	514	6	Blade No. 5 Dynamic Strain	TAP
TKB500	361	9	No. 5 Bearing Temperature	BCO, TAP	KDFB51	672	8	Blade No. 5 Dynamic Strain	TAP
TKB200	353	9	No. 2 Bearing Temperature	BCO, TAP	KDFB50	671	8	Blade No. 5 Dynamic Strain	TAP
PS1970	209	9	Balance Cavity Pressure	DMS	KDFB72	683	9	Blade No. 7 Dynamic Strain	TAP
KSBLA2	503	10	Forward Centrifugal Force	DMS, BCO	KDFB71	682	9	Blade No. 7 Dynamic Strain	TAP
KDAB52	623	11	Blade No. 5 Dynamic Strain	TAP	KDFB70	681	9	Balance Cavity Pressure	DMS
KDAB72	633	13	Blade No. 7 Dynamic Strain	TAP	PS1980	210	10	Forward Centrifugal Force	DMS, BCO
KDAB71	632	13	Blade No. 7 Dynamic Strain	TAP	KSBLF2	513	10	Blade No. 5 Dynamic Strain	TAP
KDAB70	631	13	Blade No. 7 Dynamic Strain	TAP	KDFB52	673	11	Module 15 Temperature	DMS
KDAB51	622	14	Blade No. 5 Dynamic Strain	TAP	TKFH15	393	12	Module 10 Temperature	DMS
KDAB50	621	14	Blade No. 5 Dynamic Strain	TAP	TKFH10	391	12	Module 12 Temperature	DMS
PS1971	211	14	Balance Cavity Pressure	DMS, BCO	TKFH12	392	12	Module 12 Temperature	DMS
KSBLA3	504	15	Aft Centrifugal Force	DMS	TKBLF2	386	14	Balance Temperature	DMS
TKBLA3	383	16	Balance Temperature	DMS	TKBLF1	385	14	Blade No. 3 Dynamic Strain	DMS
TKAH01	376	16	Module 1 Temperature	DMS	KDFB32	663	14	Blade No. 3 Dynamic Strain	DMS
TKB201	354	16	No. 2 Bearing Temperature	DMS	KDFB31	662	14	Blade No. 3 Dynamic Strain	DMS
TKB501	362	16	Balance Temperature	DMS	KDFB30	661	14	Blade No. 3 Dynamic Strain	DMS
TKBLA0	380	18	Balance Temperature	DMS	KSBLF0	511	15	Torque	DMS, BCO
TA1970	305	18	Cavity Temperature	DMS	KDFB10	651	18	Blade No. 1 Dynamic Strain	TAP
KDAB10	601	18	Blade No. 1 Dynamic Strain	TAP	KDFB12	653	18	Blade No. 1 Dynamic Strain	TAP
KDAB12	603	18	Blade No. 1 Dynamic Strain	TAP					

Note: DMS = Steady-State Data System
 BCO = Boeing Control Console
 TAP = Health/Blade Magnetic Tape in IDR

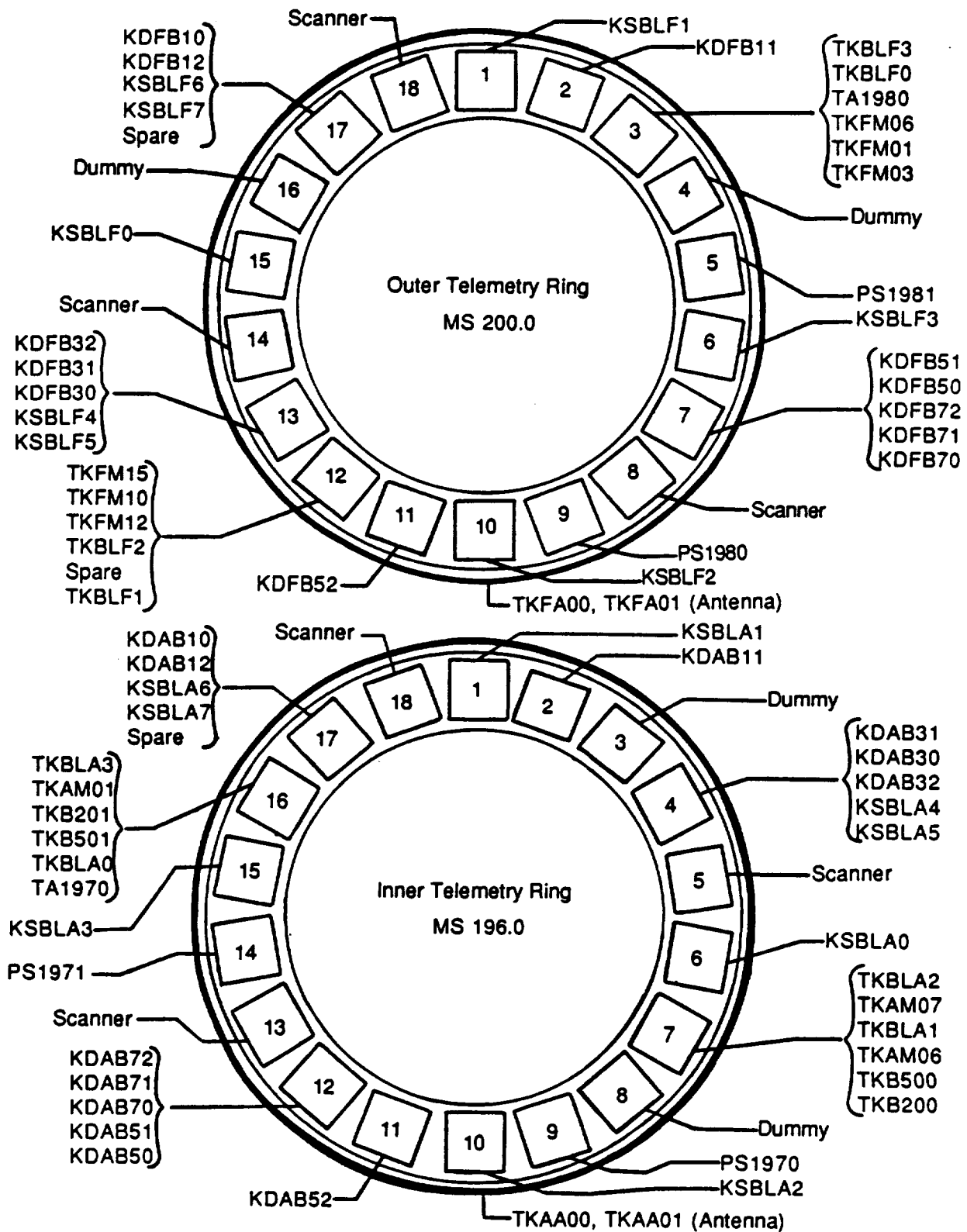
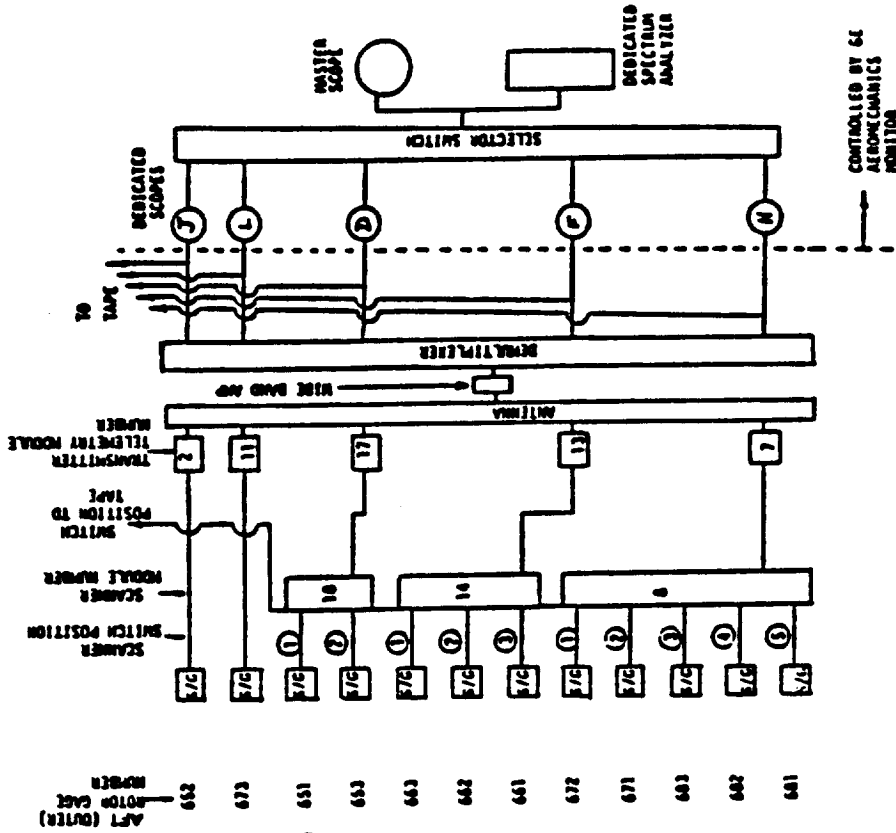


Figure 134. MPS SN002 Telemetry Instrumentation.

Outer Rotor

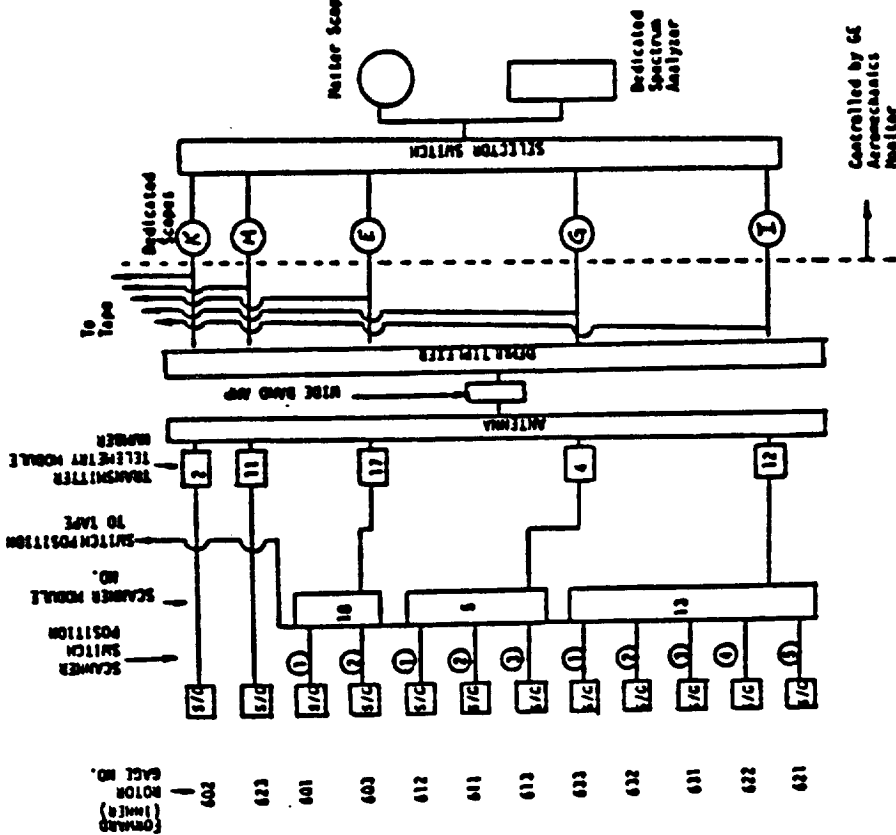
Note: For torque blade testing, scanner switch must be in ① position.



Scopes are to be calibrated to 40 dSI peak-to-peak (±20 dSI) with ability to be set at 20 dSI peak-to-peak. Being to supply internal square wave signal (PS 1000 Hz) for phasing each channel. For calibration, use method supplied by Bill Curtis (GE) or equivalent. Both calibration and phasing signals are to be put on tape.

Inner Rotor

Note: For torque blade testing, scanner switch must be in ② position.



Scopes are to be calibrated to 40 dSI peak-to-peak (±20 dSI) with ability to set at 20 dSI peak-to-peak. Being to supply internal square wave signal (PS 1000 Hz) for phasing each channel. For calibration, use method supplied by Bill Curtis (GE) or equivalent. Both calibration and phasing signals are to be put on tape.

Figure 135. Blade Strain Gauge Monitor Set-Up Schematic for MPS SN002.

Table 38. Health/Blade Magnetic-Tape¹ Channel Assignments for MPS SN002.

Channel	Scope	Switch Pos.	GE No.	Parameter	Description
1	A	---	---	Voice	Voice Transmission
2	B	---	901	XNR101	Outer Rotor Speed (1/rev)
3	C	---	903	XNR201	Inner Rotor Speed (1/rev)
4	D	1	651	KDFB10	Outer Hub Blade No. 1 Strain
4	D	2	653	KDFB12	Outer Hub Blade No. 1 Strain
5	E	1	601	KDAB10	Inner Hub Blade No. 1 Strain
5	E	2	603	KDAB12	Inner Hub Blade No. 1 Strain
6	F	1	663	KDFB32	Outer Hub Blade No. 3 Strain
↓	↓	2	662	KDFB31	↓
↓	↓	3	661	KDFB30	↓
7	G	1	612	KDAB31	Inner Hub Blade No. 3 Strain
↓	↓	2	611	KDAB30	↓
↓	↓	3	613	KDAB32	↓
8	H	1	672	KDFB51	Outer Hub Blade No. 5 Strain
↓	↓	2	671	KDFB50	Outer Hub Blade No. 5 Strain
↓	↓	3	683	KDFB72	Outer Hub Blade No. 7 Strain
↓	↓	4	682	KDFB71	↓
↓	↓	5	681	KDFB70	↓
9	I	1	633	KDAB72	Inner Hub Blade No. 7 Strain
↓	↓	2	632	KDAB71	↓
↓	↓	3	631	KDAB70	↓
↓	↓	4	622	KDAB51	Inner Hub Blade No. 5 Strain
↓	↓	5	621	KDAB50	Inner Hub Blade No. 5 Strain
10	J	---	652 ²	KDFB11	Outer Hub Blade No. 1 Strain
11	K	---	601 ²	KDAB11	Inner Hub Blade No. 1 Strain
12	L	---	673 ²	KDFB52	Outer Hub Blade No. 5 Strain
13	M	---	623 ²	KDAB52	Inner Hub Blade No. 5 Strain
14	N	---	1	ZVB110	Vibration
15	O	---	2	ZHB100	↓
16	P	---	3	ZVB310	↓
17	Q	---	4	ZHB300	↓
18	R	---	351	TKB100	No. 1 Bearing Temperature
19	S	---	353	TKB200	No. 2 Bearing Temperature
20	T	---	357	TKB300	No. 3 Bearing Temperature
21	U	---	359	TKB400	No. 4 Bearing Temperature
22	V	---	361	TKB500	No. 5 Bearing Temperature
23	W	---	365	TKB600	No. 6 Bearing Temperature
24	X	---	367	TKB700	No. 7 Bearing Temperature
25	Y	---	369	TKB800	No. 8 Bearing Temperature
26	Z	---	371	TKB900	No. 9 Bearing Temperature
27	AA	---	373	TKB000	No. 10 Bearing Temperature
28	BB	---	---	IRIG Time	Time Code

¹ Tape Speed Should be 15 ips (Minimum)

² Continuous

5.1.2.8.2 Health Monitoring and Control Instrumentation

The MPS health parameters were routed to: the Boeing control console, a magnetic tape blade/health monitoring station, and a vibration monitoring station. The locations for the bearing and vibration health parameters are depicted in Figure 136.

The control console has been discussed in a previous section; Table 39 lists the instrumentation parameters used as input signals. The health monitoring station, also in the IDR, consists of 14 oscilloscopes, amplifiers (signal conditioners), and a magnetic tape recorder. Table 38 outlines the arrangement of the health parameter signals on the scopes and magnetic tape; this tape was running continuously when the MPS was operating. The vibration monitor station received the accelerometer signals and, through a switching arrangement, was capable of displaying these signals one at a time on a spectrum analyzer.

5.1.2.8.3 Acoustic Instrumentation

The acoustic instrumentation employed for this test consisted of 24 fixed microphones and 1 traversing microphone. Figure 137 illustrates the location of these microphones, relative to the MPS. Signals from this instrumentation were routed to a 28-track, magnetic tape recorder. Only 22 fixed microphones could be assigned to this recorder at a given time, due to other instrumentation demands. During the course of testing, the chosen 22 varied. The format for the 28-channel acoustic magnetic tape is listed in Table 40.

5.1.2.8.4 Aerodynamic Instrumentation

All instrumentation on the MPS nacelle surface is identified in Table 36. This instrumentation consists of five static pressure taps on the forebody and six static pressure taps on the aftbody.

5.1.2.8.5 Facility Instrumentation

The MPS-related facility instrumentation is listed and described herein (Table 36). The instrumentation associated with the GE control console is summarized in Table 41.

5.1.3 Test Matrix Summary

Table 42 presents the acoustic and performance testing conducted on Rig 2 in Cell 41 and summarizes the results of these acoustic and performance tests, regardless of whether the individual tests were contract-related, or not.

Also, during the time period of July 8, 1985 through September 26, 1985 the Rig 2/Cell 41 testing was devoted to aeromechanical hub evaluations. This activity is not included in Table 42; however, Table 43 defines the myriad of configurations investigated, incorporating one or both of the aeromechanical hubs. Aeromechanical hub testing was directly charged to the contract, but only involved the testing activity associated with the first two test runs. During the first run (July 11, 1985) A-7 blade flutter activity was detected that was considered significant enough to have the A-7 blades relaid to a 35°-ply arrangement, rather than the original 13°-ply layup. The A-7 blades were retested on July 17, 1985. During this second run, blade/hub system instability resulted in the loss of an A-7 blade from the second stage hub. Following this, separate noncontract funding was provided to conduct a failure investigation and to continue aeromechanical hub testing to evaluate potential design solutions for the phenomenon exhibited on July 17, 1985.

5.1.4 Test Procedures

Prior to operation of the MPS each test period, instructions outlined in a prerun check list were followed to activate the facility air system used for the MPS turbine drive air supply and the MPS

Table 40. Acoustic Magnetic Tape Channel Assignments for MPS SN002.

Channel	GE No.	Parameter	Description
1	---	Voice	Voice Transmission
2	901	XNR101	Outer Rotor Speed, 1/rev
3	903	XNR201	Inner Rotor Speed, 1/rev
4	4001	FMIC01	Fixed Microphone
5	4002	FMIC02	
6	4003	FMIC03	
7	4004	FMIC04	
8	4005	FMIC05	
9	4006	FMIC06	
10	4007	FMIC07	
11	4008	FMIC08	
12	4009	FMIC09	
13	4010	FMIC10	
14	4011	FMIC11	Fixed Microphone
15	4012	FMIC12	
16	4013	FMIC13	
17	4014	FMIC14	
18	4015	FMIC15	
19	4017	FMIC17	
20	4019	FMIC19	
21	4020	FMIC20	
22	4021	FMIC21	
23	4022	FMIC22	
24	4023	FMIC23	
25	4024	FMIC24	
26	4101	TMIC01	Traverse Microphone
27	4200	MICPOS	Traverse Microphone Position
28	---	IRIG Time	Time Code

Table 41. Console Parameters for MPS SN002 Test (Cell 41).

Parameter	GE No.	Description
PT28DB ¹	1014	Freejet Total Pressure
PDJETA	1052	Freejet Nozzle ΔP
PSR1VU	1053	Outer Turbine Drive Flow Venturi Inlet Pressure
PSR1VD	1054	Outer Turbine Drive Flow Venturi ΔP
PSR2VU	1055	Inner Turbine Drive Flow Venturi Inlet Pressure
PSR2VD	1056	Inner Turbine Drive Flow Venturi ΔP
PSNOZZ	1057	Mixing Chamber Bleed Flow Pressure
PLCRFM	1058	Burner Pressure
PSDRIV	1059	Turbine Discharge Duct Pressure
PSSTMH	1060	Steam Header Pressure
PSSEVO	1061	Steam Ejector Vacuum Pressure
PSSEV1	1062	Steam Ejector Vacuum Pressure
PTJETA	1063	Freejet Total Pressure
PDR1FR	1064	Drive Flow Filter ΔP (Outer Rotor)
PDR2FR	1065	Drive Flow Filter ΔP (Inner Rotor)
PDSCRN	1066	Screen ΔP
PDRVLN	1067	Water Relief Valve Pressure
TMR1VU ²	1068	Outer Turbine Drive Flow Venturi Temperature
TMR2VU ²	1069	Inner Turbine Drive Flow Venturi Temperature
TANOZZ ²	1070	Bleed Flow Temperature
PSFNSD ³	1078	Mixing Chamber Pressure
PSHEAD ²	1081	Supply Air Header Pressure
UPCORE ²	1082	Core Flow Orifice Upstream Pressure
DELCOR ²	1083	Core Flow Orifice ΔP
UPFANP ²	1084	Fan Flow Orifice Upstream Pressure
DELFAN ²	1085	Fan Flow Orifice ΔP
DEWPNT ²	1086	Dewpoint
TFANUP ²	3001	Fan Flow Orifice Upstream Temperature
TCORUP ²	3002	Core Flow Orifice Upstream Temperature
TFNTOM ²	3005	Mixing Chamber Temperature
TBRNRO	3009	Burner Room Ambient Temperature

¹ Pneumatic Split, to Scannivalve for DMS and to Trans. for GE Console
² Also Routed to DMS
³ Also Routed to Boeing Control Console (Pneumatic Split)

Table 42. Cell 41 Acoustic and Performance Test Matrix Summary.

Date	Blade Design	Blade Configuration	Spacing	Pylon Position	Pitch Angle, degrees		Mach Number
					Forward	Aft	
10/27/84	F-5/A-5	8+8	Nominal	Off	38.4	37.6	0.25
10/30/84					38.4	37.6	0.26
10/31/84					38.4	37.6	0.25
11/3/84	F-7/A-7	8+4	Nominal	Close	37.9	37.4	0.25
12/15/84					37.9	37.4	0.25, 0.30, 0.20
12/17/84					43.3	40.4	0.25, 0.30, 0.20
12/17/84					36.0	35.2	0.25, 0.10, 0.20
12/18/84					40.0	38.0	0.25
12/20/84					53.9	40.4	0.25, 0.11
1/4/85					53.9	34.0	0.25
1/4/85	34.5	51.4	0.25, 0.30, 0.35				
1/7/85	37.9	37.4	0.25				
1/14/85	37.9	37.4	0.30, 0.20				
1/16/85	8+4	Close	0.29, 0.25				
1/22/85	4+4	Off	0.30, 0.25				
1/23/85	9+4	Close	0.30, 0.25, 0.21				
1/24/85	9+4	Close	0.28, 0.25				
1/30/85	9+4	Close	0.25				
2/1/85	9+8	Maximum	0.25, 0.30, 0.20				
2/11/85	8+8	Maximum	0.25, 0.30, 0.20				
2/12/85	8+8	Maximum	0.25, 0.30, 0.20				
2/15/85	9+8	Maximum	0				
2/19/85	9+8	Maximum	0.21, 0.11				
2/20/85	9+8	Maximum	0.25, 0.20, 0.30, 0.22				
2/28/85	9+8	Maximum	0.25, 0.20, 0.30				
3/1/85	F-7/A-7C	8+8	Nominal	Close	36.3	37.4	0.25, 0.20, 0.30
3/12/85					36.3	37.4	0.25, 0.20, 0.30
3/14/85					41.8	41.4	0.25, 0.20, 0.30
3/15/87					41.8	41.4	0.25, 0.20
3/15/85					41.8	41.4	0.25, 0.20, 0.30
3/21/85					41.8	41.4	0.25, 0.20, 0.30
3/22/85					41.8	48.3	0.25, 0.20, 0.30
3/25/85					37.4	37.4	0.25
3/27/85					36.3	42.7	0.25
3/27/85					36.3	42.7	0.25
4/10/85	F-7/A-7C	8+8	Nominal	Off	36.3	42.7	0.25, 0.20
4/10/85					36.3	42.7	0.25, 0.20

Table 42. Cell 41 Acoustic and Performance Test Matrix Summary (Continued).

Date	Blade Design	Blade Configuration	Spacing	Pylon Position	Ground Plane Position, Inches	Pitch Angle, degrees		Mach Number
						Forward	Aft	
2/24/86	F-7/A-7T	8+8	Nominal	Nominal ²	In (4.9)	37.9 (38.2)	37.4 (38.0)	0.25
2/26/86	F-11/A-11	11+9	Maximum	Off	Out	44.8	43.3	0.25, 0.35
3/21/86	F-7/A-7T	8+8	Nominal	Off	Out	37.9	37.4	0.25, 0.20, 0.35
3/21/86				Nominal ²	Out	37.9	37.4	0.25, 0.20, 0.35
3/26/86					In (5.2)	37.9	37.4	0.25, 0.2, 0.35, 0.1
3/26/86						32.5	32.4	0
3/27/86					Out	33.8	32.4	0, 0.1, 0.35
3/27/86						33.8	32.4	0
3/31/86						33.8	32.4	0
3/31/86						-17.6	-17.6	0
4/2/86						-17.6	-17.6	0.2, 0.1
4/2/86						20	20	0.1, 0.2, Maximum
4/2/86						5	5	0.1, 0.2, Maximum
4/3/86						50	47	0.25, 0.2, 0.1
4/3/86						84.4	84.1	0.1, 0.2, Maximum
4/4/86					N/A	52	44	0.25, 0.30, 0.20, 0.10, Maximum
4/4/86						12.5	12.5	0.11, 0.20
4/21/86	F-11/A-11	11+9	Maximum	Off		38.2	38.9	0.25
4/22/86						38.7	38.9	0.25
4/23/86						48.7	45.3	0.25
4/25/86						52.6	47.5	0.25
4/25/86						54.2	47.5	0.25
4/25/86						54.2	47.5	0.25
5/7/86	F-21/A-21	12+10	Maximum	Off		41.0	44.7	0.25
5/8/86						44.0	44.7	0.25
5/9/86						50.5	49.0	0.25
5/12/86						52.0	49.0	0.25
5/12/86						44.0	44.7	0.25
5/12/86	F-21/A-21 (5% A-21 Clip)					44.0	44.7	0.25
5/13/86	F-21/A-21 (10% A-21 Clip)					44.0	44.7	0.25
5/14/86	F-21/A-21 (10% A-21 Clip)					44.0	46.3	0.25
5/14/86	F-21/A-21 (15% A-21 Clip)					44.0	44.7	0.25

¹ Nominal, North

² Nominal, South

Table 42. Cell 41 Acoustic and Performance Test Matrix Summary (Concluded).

Date	Blade Design	Blade Configuration	Spacing	Pylon Position	Pitch Angle, degrees		Mach Number
					Forward	Aft	
5/15/86	F-21/A-21 (15% A-21 Clip)	12+10	Maximum	Off	44.0	46.6	0.25
5/15/86	F-21/A-21 (20% A-21 Clip)	↓	↓	↓	44.0	44.7	0.25
5/16/86	F-21/A-21 (20% A-21 Clip)	↓	↓	↓	44.0	47.7	0.25
5/16/86	F-21/A-21 (25% A-21 Clip)	↓	↓	↓	44.0	47.7	0.25
5/19/86	F-21/A-21 (25% A-21 Clip)	↓	↓	↓	44.0	49.1	0.25
5/23/86	F-7/A-7	10+8	Nominal	Douglas ²	36.4	37.4	0.25, 0.20
5/27/86	↓	↓	↓	Boeing ²	36.4	37.4	0.25, 0.20
5/28/86	↓	↓	↓	Boeing ¹	36.4	37.4	0.25
6/2/86	↓	↓	↓	Douglas ¹	36.4	37.4	0.25
6/2/86	↓	↓	↓	↓	41.6	40.4	0.25
6/3/86	↓	↓	↓	↓	46.4	43.7	0.25
6/3/86	↓	↓	↓	↓	57.0	57.0	0.20, 0.10, 0
6/9/86	↓	↓	↓	↓	85.0	85.0	0.20, 0.10, 0
6/10/86	F-7/A-3	11+9	↓	↓	36.4	42.5	0.25, 0.20
6/19/86	F-7/A-3	↓	↓	↓	41.6	45.8	0.25, 0.20
6/26/86	↓	↓	↓	↓	48.7	45.3	0.25, 0.20
7/10/86	F-11/A-11	11+9	Supermax	Off	44.8	43.3	0.25, 0.20
7/11/86	↓	13+11	↓	↓	47.4	44.1	0.25, 0.20
7/22/86	↓	↓	↓	↓	44.2	42.1	0.25, 0.20
7/28/86	↓	↓	↓	↓			

¹ Nominal, North

² Nominal, South

Table 43. MPS SN002 Aero Hub Test Summary (Concluded).

Date	Configuration		Blade				A-7 Blades			Platform Adaptors	Platform Adaptor Seals		Hub Face	Aft Panel Lip Flap	Aft Cavity	Aft Cavity	Aft Cavity	Ground Plane	Tylon Block	Mach Number	
	Hub	Damper	Pitch Angle, degrees	Ply Layup, degrees		Strain Gages	Tip	Mid	Clip, Percent		1	2									
				1	2																
9/5	Rigid	Aero	M/A	8.5# Clamp	32.0	33.0	13	35	Off	Off	0	M/A	On	On	Off	On	Open	Mo	Out	On	0.1
9/12	Aero	Rigid	8.5# Clamp	M/A	32.0	33.0	13	35	Off	Off	0	On	M/A	Off	On	Open	Mo	Im	Off	Off	0, 0.1
9/23	Aero	Aero	8.5# Clamp	None	32.0	33.0	13	35	Off	Off	3	On	Off	Off	Open	Mo	Out	Off	Off	Off	0, 0.1
	Aero	Aero	8.5# Clamp	None	32.0	33.0	13	35	Off	Off	6	On	Off	Off	Open	Mo	Out	Off	Off	Off	0
	Aero	Aero	8.5# Clamp	None	32.0	33.0	13	35	Off	Off	6	On	On	Off	Open	Mo	Out	Off	Off	Off	0
9/25	Aero	Aero	8.5# Clamp	None	32.0	33.0	13	35	Off	Off	10	On	On	Off	Open	Mo	Out	Off	Off	Off	0, 0.1
	Aero	Aero	8.5# Clamp	None	32.0	33.0	13	35	Off	Off	10	On	On	Off	Open	Mo	Out	Off	Off	Off	0, 0.1
	Aero	Aero	8.5# Clamp	None	32.0	33.0	13	35	Off	Off	15	On	On	Off	Open	Mo	Out	Off	Off	Off	0
	Aero	Aero	8.5# Clamp	None	32.0	33.0	13	35	Off	Off	20	On	On	Off	Open	Mo	Out	Off	Off	Off	0, 0.1

1 Forward
2 Aft

hydraulic and lube support equipment; having completed that, the MPS prestart check list was addressed. Once these tasks were accomplished, procedures outlined in the MPS start check list were followed to achieve MPS start up.

When the MPS was up and operating, and the tunnel conditions were established, the MPS setpoints corresponding to values outlined in the test matrix were loaded and engaged to accomplish the desired test objectives. During the course of testing, two types of speed points were requested. The first was an equal rpm speed point where the inner and outer rotor speeds were matched; the second type of MPS setpoint reflected conditions where equal torques on the inner and outer rotor were desired.

To do this, the forward and aft rotor speeds were ramped to the requested speed setpoint. When conditions stabilized, the speed of the inner rotor was adjusted to obtain the torque value of the outer rotor. When console torque displays indicated readings that were within approximately 10-inches per pound of the goal, the control mode was switched to "track," and the inner rotor speed was manually fine-tuned to produce the desired torque value. To assure safe MPS operation in the anechoic chamber, specific considerations were adhered to during testing in Cell 41; these safeguards are outlined in Table 44. Procedures to enact a normal MPS shutdown at the end of a test period were available, as was a postrun check list. Control console limits set for MPS SN002 testing in Cell 41 are specified in Table 45.

A more detailed accounting of the procedures in the check lists discussed in the preceding paragraphs is available in an internal GE report (MPS 84-02 by G.E. Hoff).

5.2 The Rig 3/8x6 Supersonic Wind Tunnel

Under Task V of NASA Contract NAS3-24080, during the time period of July 1985 through April 1986, the MPS SN003 was tested in the NASA Lewis 8x6 supersonic wind tunnel. The objective of the test program was to evaluate the high speed aerodynamic, acoustic, and aeromechanical performance of GE's counterrotating blade concepts for application in future advanced-technology propulsion systems. Blade design variables tested included tip sweep, activity factor, and pitch angle. Other model variables included rotor-to-rotor axial spacing and the number of blades per rotor stage. A specially designed aeromechanical hub, which simulated the hub flexibility of the full-scale blade support structure of the UDF® engine, was also tested. Data were acquired over a Mach number range of 0.36 through 0.9 for various angles-of-attack between $\pm 4^\circ$.

5.2.1 Facility Description

Reference 29 contains a detailed description of the 8x6 supersonic wind tunnel. However, to summarize, the 8x6 supersonic wind tunnel is capable of attaining isolated test section flow in the Mach number range of 0.36 to 2.0. Because of the blockage associated with the MPS however, the test section was calibrated with the MPS installed. Results showed that the presence of the MPS reduced the tunnel test section measured Mach number by 0.5 to 1.0%. Change in Mach number is continuous up to 1.3, and in increments of 0.1 between 1.3 and 2.0. The tunnel can be operated in either of two mode cycles; aerodynamic or propulsion.

The major wind tunnel components are the air dryer, compressor, flexible wall nozzle, test section, acoustic muffler, and the cooler. A floor plan of the wind tunnel layout is depicted in Figure 138.

The test section is 8-foot high by 6-foot wide, with parallel side walls, for a total length of 23-ft, 6-in. Downstream (for a distance of 2-ft, 3-in.) the walls diverge to a width of 6-ft, 4-in. to

Table 44. MPS SN002 Operational Procedures for Cell 41.

Item No.	Description
1.	MPS Start Up Should Always Occur from a Windmill Condition, (except at Mach = 0)
2.	A Facility Shutdown Should Always Activate an MPS Shutdown
3.	MPS Should be at Corrected Speed \leq 60% for any Mach Number Change
4.	Always Check Console Thrust and Torque Displays After a Telemetry Override to Determine if Retuning is Required
5.	If Necessary, Set Shutdown Limits on Nos. 2 and 5 Bearings Temperatures to High Level if Telemetry is "Noisy"
6.	Avoid Prolonged Operation at a Given Condition; Telemetry Noise Seems to Affect Nos. 2 and 5 Bearings Temperatures More as Time on Point Progresses
7.	Avoid Steady-State Operation with a Combined Thrust Loading Between 165 and 195; this Operating Condition Lies in the Regime of a Load Reversal on the No. 2 Bearing
8.	Operation with Equal Speeds on Both Rotors may Result in a High Vibration Situation at Certain Speeds; be Watchful for this, and if it Occurs, it Should be Possible to Relieve the Condition by Mismatching the Rotor Speeds by a Difference of 100- to 400-rpm's
9.	For Reverse Thrust Testing, to Avoid Hub Rotation in the Wrong Direction Since Blade-Pitch Angles are Negative, the Rotors are to be Driven to a Predetermined Speed Prior to Freejet Nozzle Operation

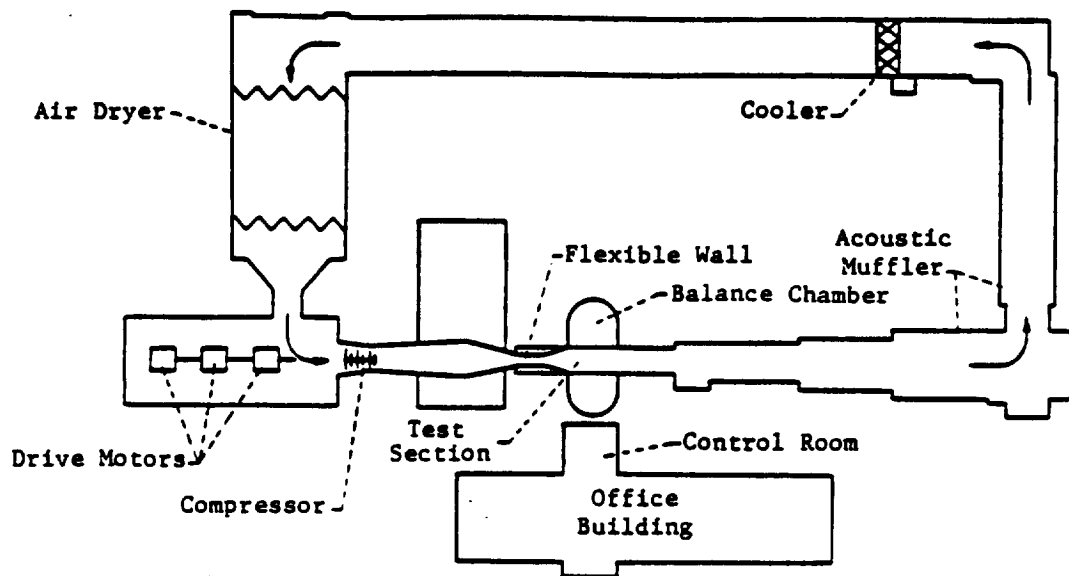
Table 45. MPS Control Console - Indicator and Shutdown Limits, Cell 41.

Parameter	Units	Display	Indicator Light Limits			Over Limit Response	Fault No.
			Green	Amber	Red		
Rotor Speed/No.	rpm	DPM & LTS	---	---	N<150	Emergency, Automatic Shutdown	1 - Outer
Vibration 1	rpm	DPM & LTS	↓	---	M210K	Auto Shutdown	2 - Inner
Vibration 3	ips	APH & LTS	↓	1.0<1.5	>1.5		↓
Torque	↓	SPH	↓	↓	↓		↓
	in./lb		↓	---	>4730		12 - Outer
Bearing No./Temp.	° F	DPM & LTS					
1	↓	↓	---	200<210	>210	Auto Shutdown	30
2	↓	↓	↓	210<225	>225	↓	31
3	↓	↓	↓	235<250	>250	↓	32
4	↓	↓	↓	190<200	>200	↓	33
5	↓	↓	↓	235<250	>250	↓	34
6	↓	↓	↓	210<225	>225	↓	35
7	↓	↓	↓	190<200	>200	↓	36
8	↓	↓	↓	210<220	>220	↓	37
9	↓	↓	↓	190<200	>200	↓	38
10	↓	↓	↓	190<200	>200	↓	39
Lube Pressure	psig	LTS	P>180	150<P<180	<150	Auto Shutdown	18
Lube Temperature	° F	↓	100°<T<180°	180°<T<250°	T>250°	Warning Heater Shutdown	---
Lube Level	gal	↓	L>1.5	L<1.5	---	↓	---
Damper Pressure	psig	↓	P>20	20<P<10	P<10	Auto Shutdown	19
Damper Temperature	° F	↓	T>130°	T<130°	---	Warning	↓
Vacuum Pressure	psia	↓	4<P<9	P<4	P>9	↓	↓
Lube Filter Power	---	↓	On	Off	---	↓	↓
Lube Coolant Pressure	psig	↓	P>20	P<20	---	↓	↓
Hydraulic Pressure	psig	LTS	>1K	---	<1K	Auto Shutdown	11
Hydraulic Temperature	° F	LT	---	↓	>180°	↓	↓
Hydraulic Level	gal	↓	↓	↓	<18	↓	16 - Outer
Servo Limit	---	↓	↓	↓	---	↓	17 - Inner
Servo Error	↓	LTS	↓	↓	↓	↓	14 - Outer
Servo Error	↓	LTS	↓	↓	↓	↓	15 - Inner
Panic Button	↓	---	↓	↓	↓	Manual Emergency S/D	00
Remote Panic/"Pickle System"	↓	---	↓	↓	↓	Manual Emergency S/D	03
Facility Power	lb	All LTS	↓	↓	↓	Auto Shutdown	11
Thrust	lb	---	↓	↓	↓	Yellow ¹	---

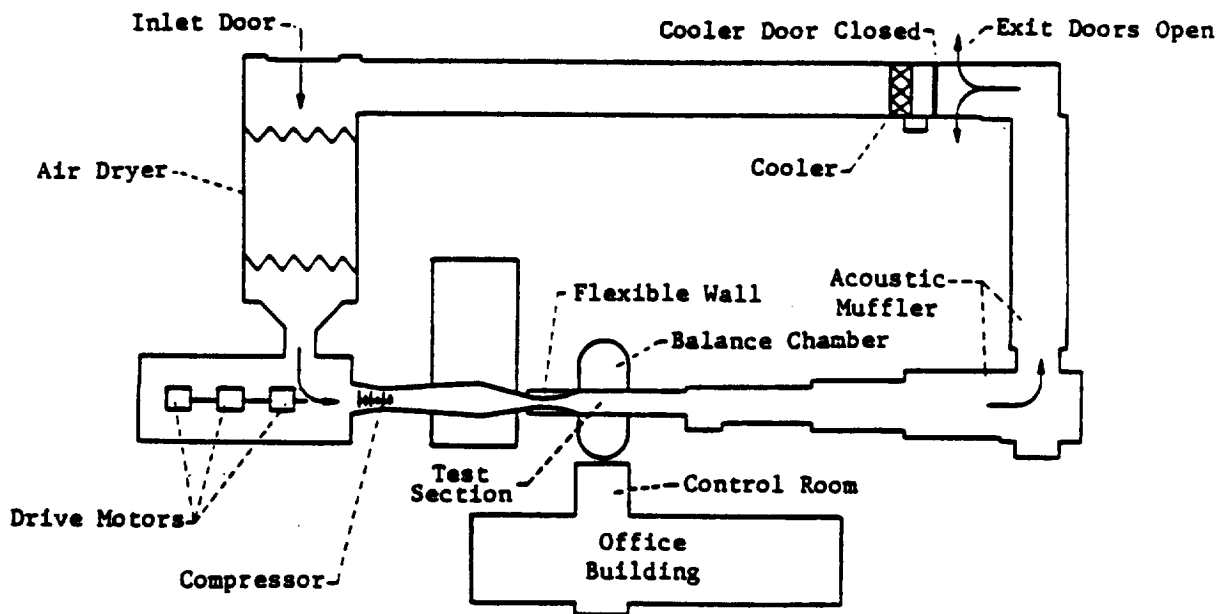
¹ Yellow: Limit - 400; Action - Backoff to Last Point

Key to Display Codes:

- DPM - Digital Panel Meter
- APH - Analog Panel Meter
- LT(S) - Panel Light (2)
- S/D - Shutdown
- SPH - Smart Panel Meter



(a) Aerodynamic Cycle



(b) Propulsion Cycle

Figure 138. NASA Lewis 8x6 Wind Tunnel Schematic.

compensate for the blockage of the transonic strut. All of the walls are made of 1-in. thick stainless steel plates; the test section is perforated on all four sides. One-inch-diameter perforations start at 9-ft, 1-in. from the upstream end of the test section and extend 14-ft, 5-in. downstream. These perforations provide approximately 6% porosity; however, this can be reduced or varied along the length of the test section by selectively using inserts in the perforations.

5.2.2 Vehicle (MPS) Description and Instrumentation

5.2.2.1 General Description

The MPS is a pneumatically powered, counterrotating unducted fan engine model propulsion system that is designed for testing fan blade configurations in either subsonic or transonic wind tunnels. A photograph of the assembled SN003 MPS in the 8x6 wind tunnel is shown in Figure 139. Measured from model Station 170.62 to model Station 290.00, the overall length is 119.38 inches, and the propulsor diameter is 24.5 inches.

Although the MPS components are discussed briefly within the following sections, a more thorough account of these component parts and their function is available in an internal GE report (MPS 84-02 by G.E. Hoff).

5.2.2.2 Mounting and Installation

For this test, the MPS SN003 unit was mounted on a strut extending from the floor of the NASA Lewis 8x6 supersonic wind tunnel test section, as shown in Figure 140. The MPS centerline coincided with that of the wind tunnel test section. NASA provided the necessary air lines from the test facility air supply system to the MPS drive valves and from the valves to the MPS, modifying the air supply system as necessary to accommodate the MPS. NASA also made modifications to the existing facility strut to mount the MPS, and to provide passageways for instrumentation, lube, and air lines.

5.2.2.3 Hub Shaft Module

GE defines the section of the MPS consisting of the blades, hubs, center shaft, rotating shafts, nacelle, and nacelle support hardware as the hub shaft module. A cross section of the MPS SN003 hub shaft module is diagrammed in Figure 141.

5.2.2.3.1 Inner (Forward) Hub

The inner/forward hub (Figure 141, Item 1) on MPS SN003 rotates CCWALF (counter-clockwise, aft looking forward) and provides attachment and locking mechanisms for the forward blades. The eight-blade hub is constructed of a titanium inner diameter ring with a microballoon outer diameter covering. The microballoon surface is shaped to the nacelle contour with eight cutout areas for the blade shanks. However, the 9-, 11-, and 13-blade hubs have aluminum fairings instead of the microballoon.

A portion of the hub near the blade platform is dished, as is the blade platform, in order to area-rule the hub/blade at the blade root and, also, to reduce Mach numbers through the blades in the region of maximum blade thickness. This inner hub attaches to the metric side of a rotating force balance which, in turn, attaches to the inner rotating shaft.

5.2.2.3.2 Outer (Aft) Hub

The outer, or aft, hub (Figure 141, Item 2) on MPS SN003; rotates CWALF (clockwise, aft looking forward) and is constructed in the same manner as the forward hub, providing the retainment

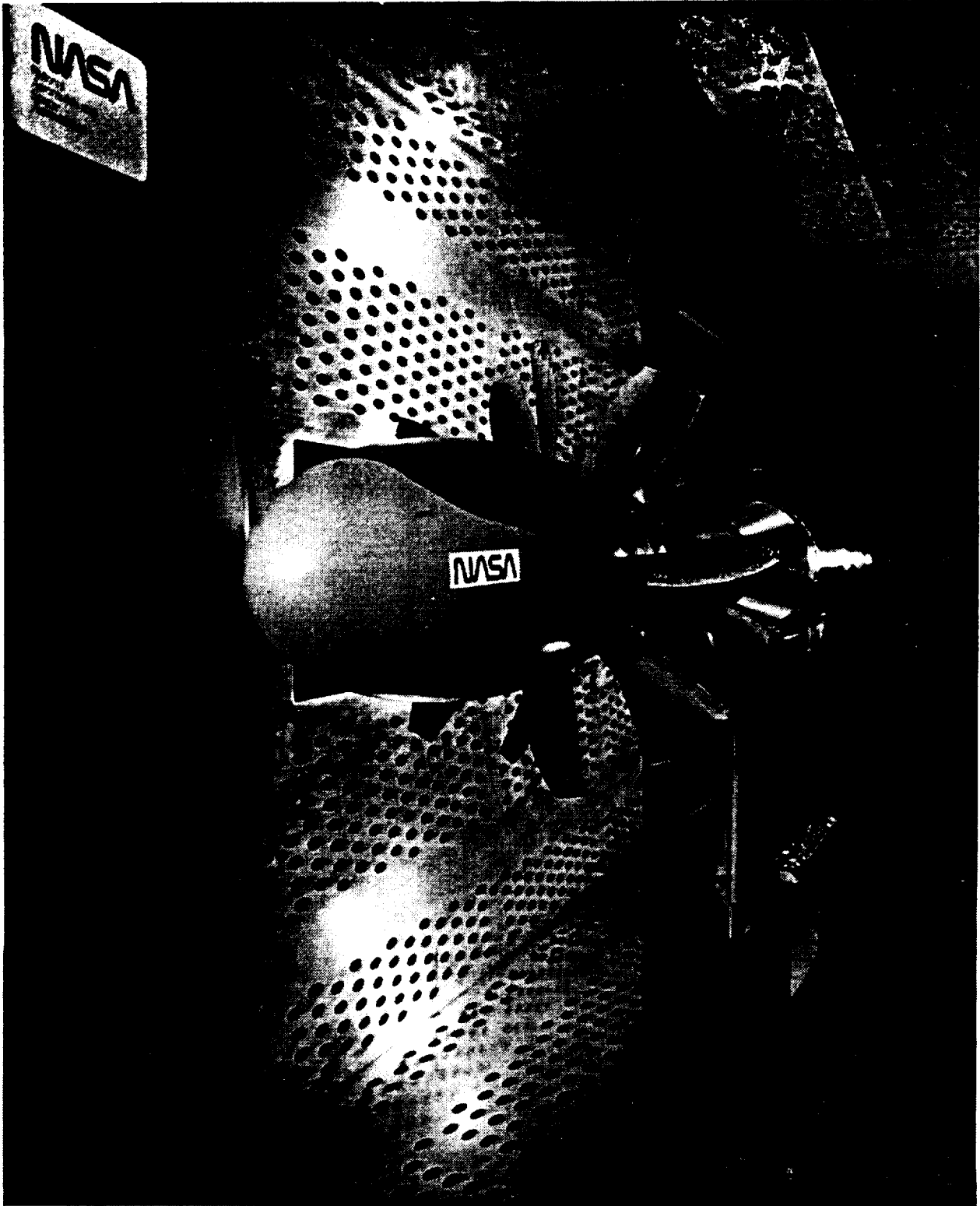


Figure 139. The MPS SN003 in the NASA Lewis 8x6 Supersonic Wind Tunnel.

T.S. 151

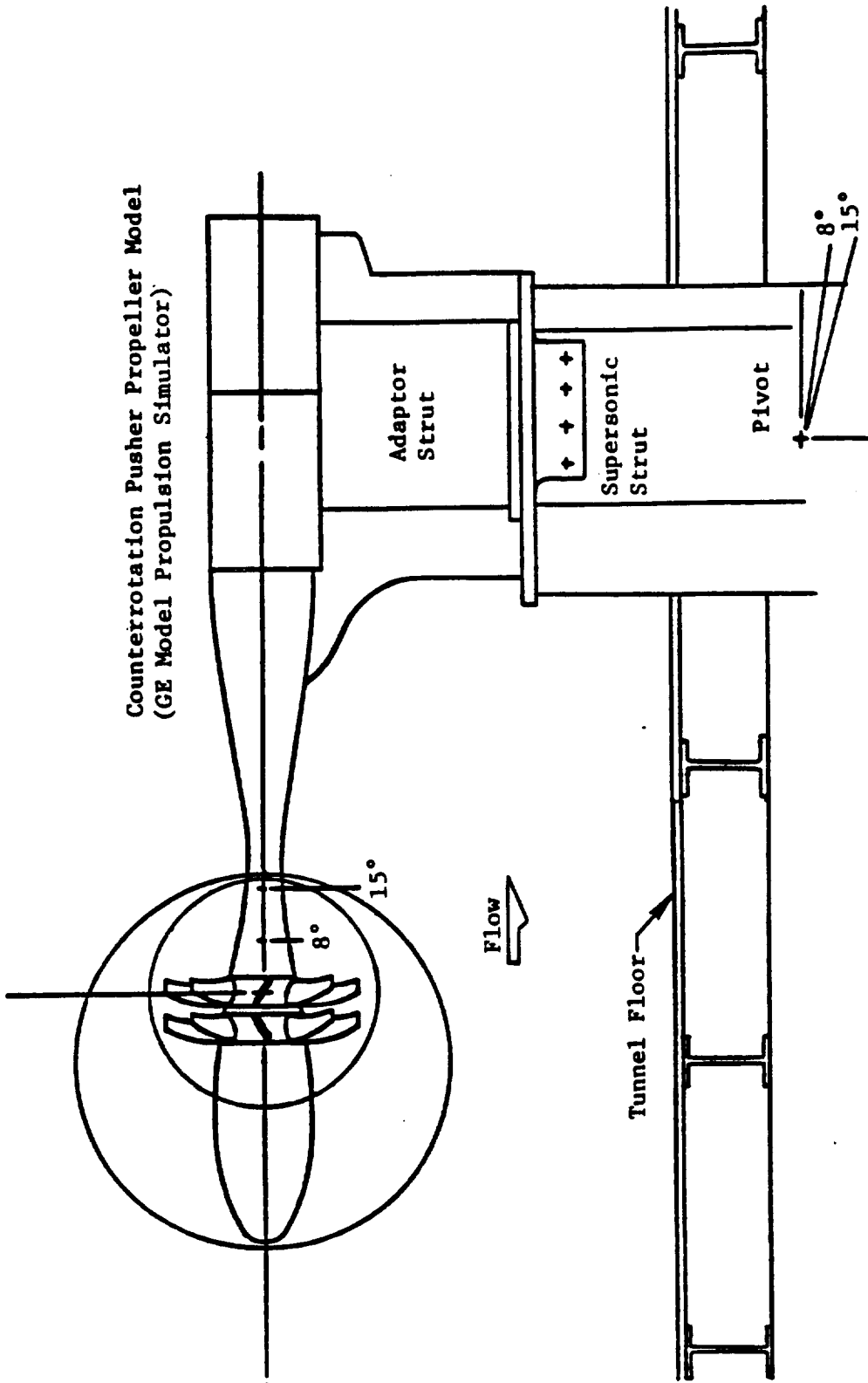


Figure 140. Schematic of MPS SN003 Installation in 8x6 Wind Tunnel.

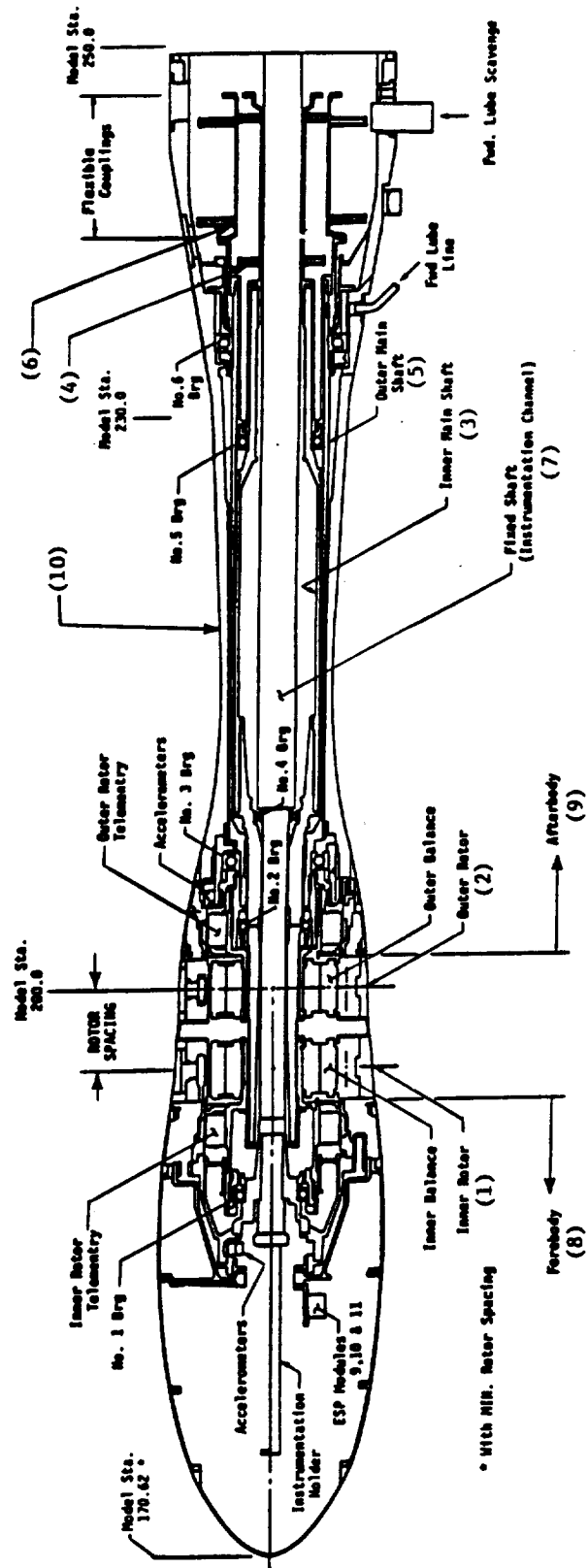


Figure 141. The MPS SN003 Hub Shaft Module.

function on the aft blades. The outer hub attaches to a second rotating force balance which, in turn, is affixed to the outer rotating shaft.

5.2.2.3.3 Inner Rotating Shaft

The inner rotating shaft (Figure 141, Item 3) is concentric with (inside of) the outer rotating shaft. It is supported on the id (inside diameter) by the Nos. 1 and 4 bearings, and on the od (outside diameter) by the Nos. 2 and 5 bearings. On the forward end, it provides support for the forward blade telemetry module and incorporates the “attach” point for the nonmetric side of the rotating force balance associated with the inner hub and forward blades. It also incorporates different removable spacers, which allow a variation in axial location of the forward blade row relative to the aft blade row.

The aft end of the inner rotating shaft is mechanically connected to the inner turbine drive shaft by means of a coaxial, flexible diaphragm (Bendix-type) coupling (Figure 141, Item 4), which allows compensation for minor shaft misalignments and thermal expansion differentials. It mechanically decouples the turbines and hub shafts; this coupling arrangement takes place between MPS Stations 238.275 and 245.6.

5.2.2.3.4 Outer Rotating Shaft

The outer rotating shaft (Figure 141, Item 5) is supported, on the id, by the Nos. 2 and 5 bearings, and on the od, by the Nos. 3 and 6 bearings (Nos. 2 and 3 are considered thrust bearings). The forward end of this shaft provides a surface for supporting the telemetry module associated with the aft blades and, also, provides the attach point for the nonmetric side of the rotating force balance which is connected to the outer hub holding the aft blades. The aft end of the outer rotating shaft mechanically connects to the outer turbine drive shaft by means of a second Bendix coupling (Figure 141, Item 6); taking place between MPS Stations 240.41 and 245.425.

5.2.2.3.5 Nonrotating Center Shaft

The nonrotating center shaft (Figure 141, Item 7) is inside the rotating inner shaft and provides a seat for the Nos. 1 and 4 bearings. The nacelle forebody is supported from the forward end of the center shaft, which extends through almost the entire length of the MPS and serves as a conduit for the instrumentation and lubrication service lines which need to be routed out of the simulator.

5.2.2.3.6 Nacelle and Nacelle Support Housing

The nacelle is comprised of two sections: the forebody and aftbody. An ellipsoid-shaped shell from MPS Stations 170.622 to 194.12, the forebody is supported from the nonrotating center shaft and represents the faired-over inlet and nacelle of an unducted fan engine (Figure 141, Item 8). The forebody also provides a mounting surface for the forward blade telemetry antenna and power source, ESP units, and other instrumentation-related equipment. The aftbody is a conical-shaped shell, from MPS Stations 201.63 to approximately 205.98, which resembles the aftbody section of an unducted fan engine nacelle as is represented by Item 9 in Figure 141. It provides a mounting surface for the aft blade telemetry antenna and power source.

The nacelle support housing (Figure 141, Item 10) consists of a support structure cantilevered from the turbine drive module. It houses the concentric drive shafts, nonrotating center shaft, and Bendix couplings, in addition to providing a seat for the No. 6 bearing. The external contour shape from the nacelle aftbody TE (trailing edge) to approximately MPS Station 218 represents a simulated jet exhaust plume shape. At the forward end of the housing is a damper section, which

acts as a shock absorber to minimize vibrations on the hub shaft module and which provides a seat for the No. 3 bearing and a mounting surface for designated instrumentation. An assembly drawing of the entire hub shaft module and Bendix couplings is provided in Boeing drawing No. 5802-1.

5.2.2.4 Turbine Drive Module

GE defines the aft section of the MPS, consisting of the drive turbines, drive shaft, high pressure air passageways, and section support structure, as the turbine drive module. Figure 142 provides a detailed cross section of the turbine drive module.

5.2.2.4.1 Inner Turbine and Drive Shaft

The inner turbine (Figure 142, Item 11) is the aft turbine in the MPS; a two-stage turbine, it is connected to the inner turbine drive shaft, which is supported by bearings Nos. 9 and 10. On the aft end of the inner drive shaft is a 60-tooth disk, installed for use with a magnetic-speed pickup instrumentation device. Operating limits at the inner turbine inlet are 300 psi for pressure and 250°F for temperature. The inlet temperature is set at 160°F to eliminate the possibility of ice formation.

5.2.2.4.2 Outer Turbine and Drive Shaft

The outer, or forward, turbine (Figure 142, Item 12) on the MPS is a two-stage turbine connected to the outer turbine drive shaft, which is supported by the Nos. 7 and 8 bearings. On the forward end of the outer turbine drive shaft, just aft of the Bendix coupling, is a 60-tooth disk installed for use with a magnetic-speed pickup instrumentation device. Operating limits are the same at the outer turbine inlet as those for the inner turbine. The inner and outer turbines are interchangeable, thus affording the flexibility of reversing the direction of rotation of the drive shafts.

5.2.2.4.3 Turbine Drive System

The above-described turbines are mounted in tandem on the counterrotating concentric inner and outer turbine drive shafts and are driven by dual air supplies.

In the 8x6 tunnel, drive air, to both turbines, travels through facility piping and control valves outside the tunnel to the base of the support strut (Figure 143). The drive air then advances from the tunnel floor location to the MPS turbine-drive-module housing through bored holes in the support strut. From there, the air from the forward bored air passageway in the support strut enters the drive-module housing through a hole which is lined up with one of six 3.06-inch-diameter holes in the forward plenum inlet (six holes are available to afford some degree of flexibility, from an installation standpoint). Once through this hole, the air is in the forward plenum. From there, the air travels from the MPS by means of an outer duct in the turbine drive module.

Air from the aft bored air passageway in the support strut enters the turbine-drive-module housing through a second hole (aft of the first hole) into a cavity which serves as a manifold to six air passageways through struts within the outer turbine exhaust ducting. These six strut air passageways bring drive air to the inner turbine air plenum. From there the air traverses through the inner turbine and then exits the MPS by means of an inner duct in the turbine drive module.

The turbine section support structure provides seats for the Nos. 7, 8, 9, and 10 bearings and passageways for routing instrumentation and lubrication lines out of the MPS. A detailed assembly drawing (including parts list) of the turbine drive module is provided in Boeing drawing No. 5801-1 (Sheets 1 and 2).

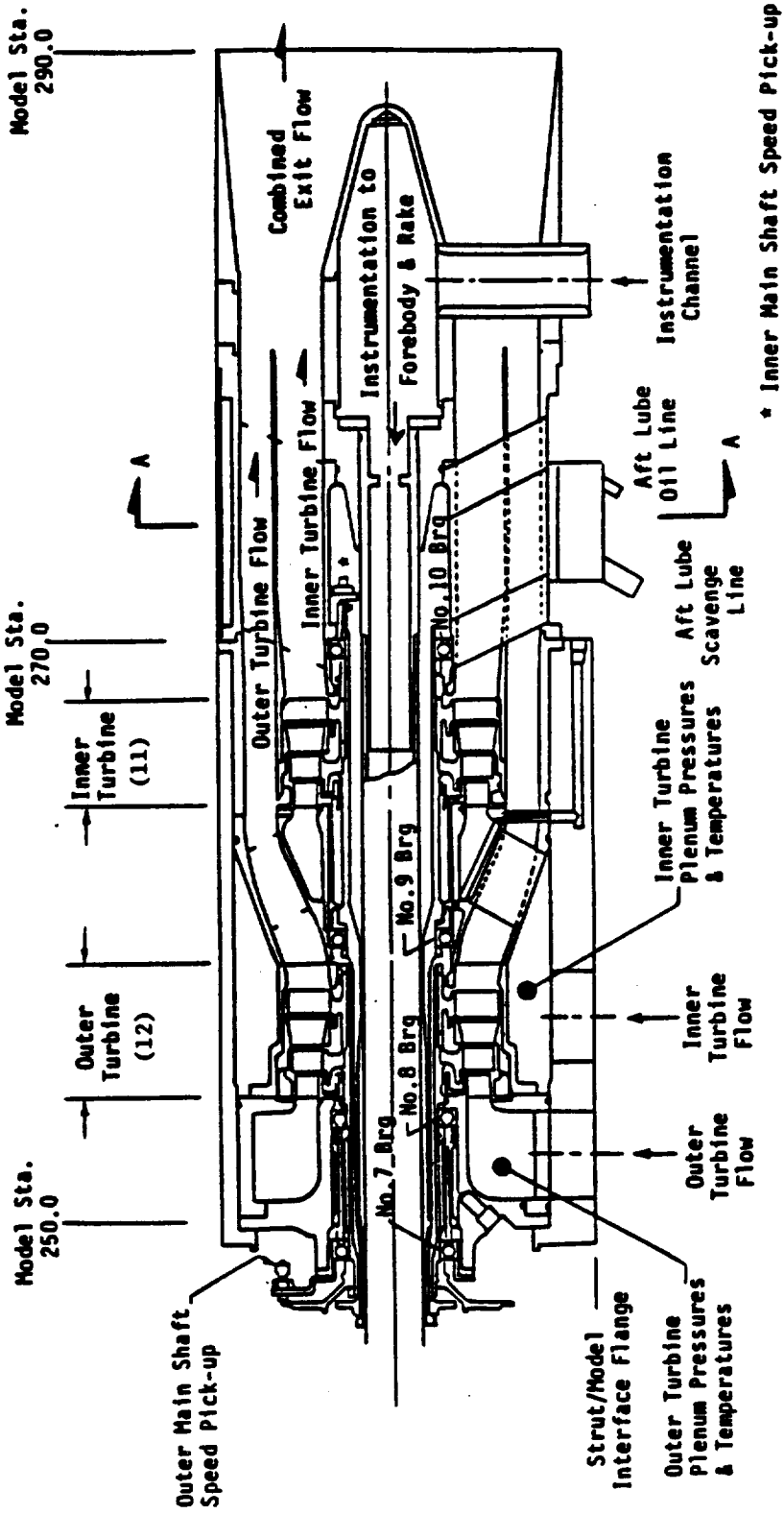


Figure 142. The MPS Turbine Drive Module.

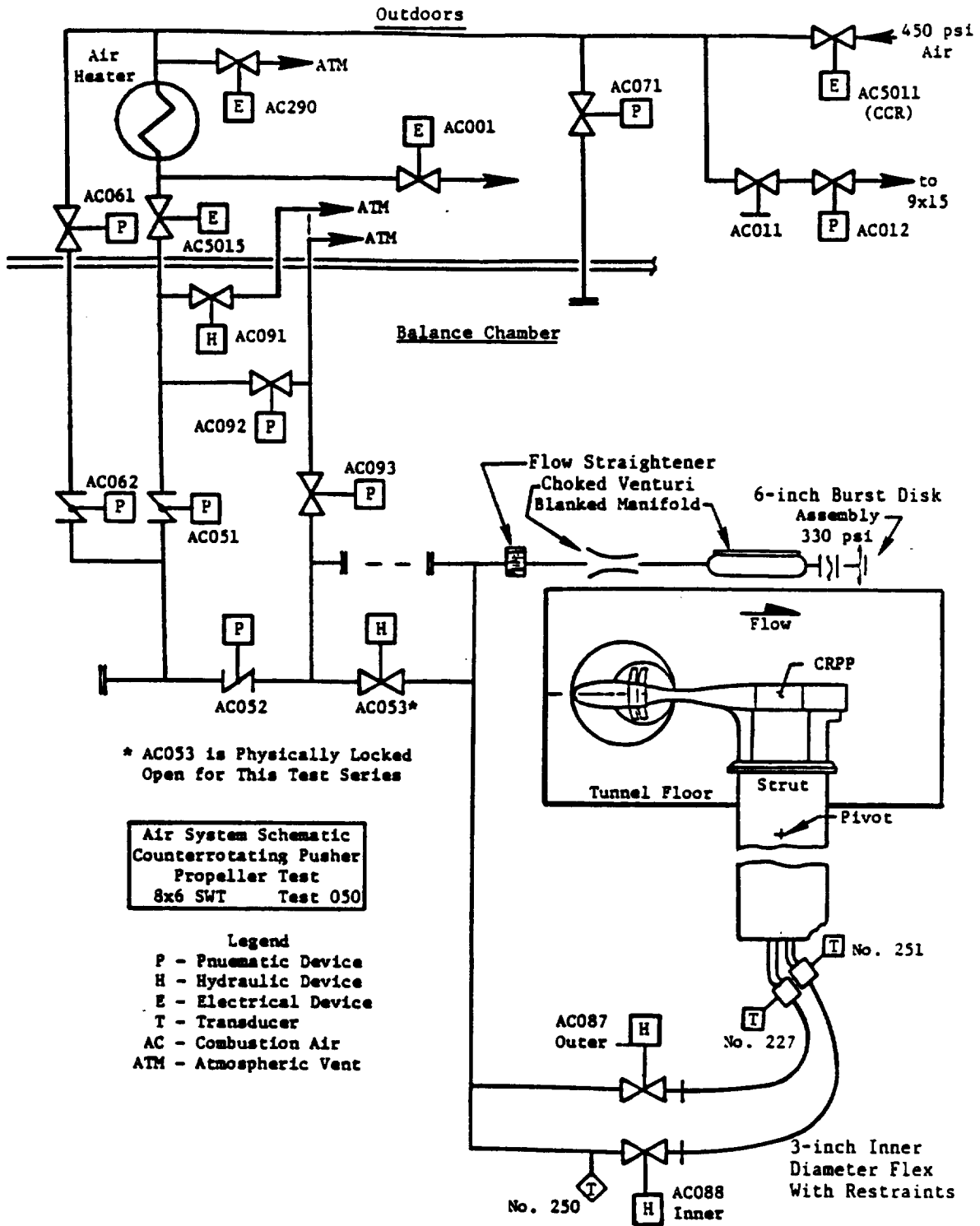


Figure 143. Turbine Drive Air System for MPS SN003 Test in NASA 8x6 Wind Tunnel.

5.2.2.5 Rotating Force Balance

The rotating force balances incorporate strain-gauge instrumented flexure beams for load measurement. These beams provide a means to measure reactions due to thrust and torque loads as well as various reactions and moments due to components of loading which are not of primary interest; such as, centrifugal force, but which are used to make interaction corrections. These balances are installed between the rotating inner shaft and forward hub, and the rotating outer shaft and aft hub.

Isolated static calibration data for MPS SN003 rotating force balances were provided to NASA Lewis. Although, these data were not obtained through the telemetry instrumentation which was utilized during testing; the installed static calibration data, corresponding to dead weight check loading through the telemetry, was incorporated into the matrix for each balance. In addition, an analytical adjustment for the effects of centrifugal force on both thrust and torque was supplied for these rotating force balances. This analytical adjustment is described in more detail in Section 5.3 of this report.

5.2.2.6 Lubrication System

The MPS lubrication system uses a tank containing MIL-L-7808 oil heated to approximately 150°F. Seven to eight gallons are required for normal MPS operation. If the tank level should fall too low, perhaps caused by a leak, a level indicator switch will illuminate a warning lamp on the control console. Oil is pumped from the tank through two lines by two Nichols-Zenith pumps (capability, 1-gpm), designated the lube and damper pumps. In the first line, after encountering the lube pump and passing a check valve, a portion of the oil is cooled by water circulating through a cooler at 0.45- to 0.50-gpm and 50- to 60-psig water pressure.

A trim valve in the water line provides adjustment capability, and a pressure sensor trips a yellow light on the control console if the water pressure drops below 20 psig. The remaining portion of the oil in the first line bypasses the cooler and then enters a three-way thermostat (along with the cooled oil), which balances the two oil flows to yield an output oil flow at approximately 140°F.

This oil then passes through a 5- μ m filter to the pressure and temperature sensors in the line which are linked to the control console, and which display the status of the oil. If the oil pressure is less than 150 psig, the console will shut down the MPS. If the temperature is greater than 250°F, a red light illuminates on the console panel. The oil line then progresses to a point where it combines with a line carrying excess oil from the damper pump to form a single line. (All hardware discussed thus far is housed within the lube cabinet.) The lube line then exits from the cabinet and confronts the warmup solenoid. If pressure exceeds 250 psig when the MPS is rotating at less than 150 rpm, the warmup solenoid is closed, and the oil is directed to a relief bypass valve and then back to the tank.

During this phase of MPS operation, oil remaining in the simulator bearings and supply lines downstream of the warmup solenoid is siphoned through the purge solenoid to the evacuated deoiler. This is necessary to avoid oil temperature transients, especially when the MPS has been inactive and at ambient temperature for an extended period of time; for example, at the beginning of the test period.

Once the MPS is operating above 150 rpm, the purge solenoid closes, and the warmup solenoid opens. The ensuing oil line then enters the MPS support strut, branching into two sections. One

section has the manifold oil supply lines from bearings Nos. 1, 2, 4, 5, and 10 connected to it; the other section has the manifold oil supply lines from bearings Nos. 3 and 6, and the combined bearing Nos. 7, 8, and 9 connected to it. Each bearing supply line has its own individually adjustable needle valve to provide capability for oil-flow balance. Oil then enters the MPS through the bearing supply lines.

In the second oil line from the tank, the damper pump in the lube cabinet channels oil through a check valve and 5- μ m filter. Upon exiting the filter, the line branches into two sections, with one leading to the damper bypass relief valve, and the other connecting with the oil line segment from the previously mentioned three-way thermostat. Oil does not flow through the relief valve until the pressure exceeds 175 psid, after which the valve maintains a 175-psi differential. When this occurs, the oil is heated to approximately 160°F and then flows to pressure and temperature sensors in the line. These sensors are connected to the control console, where the MPS running status of the damper oil is displayed. If the pressure here is less than 20 psig, the console will shut down the MPS, and if the temperature is less than 130°F, a yellow light will illuminate on the console panel. All damper line components discussed to this point are housed within the lube cabinet. When the damper line exits from the cabinet, it extends to, and then through, the MPS support strut; after which, it is directed to the damper unit in the nacelle support housing.

Bearing sump oil is scavenged from the MPS through eight scavenge lines, which connect to eight separate scavenge pumps. The scavenge lines from the Nos. 1, 7, 8, 9, and 10; the combined Nos. 2 and 3; combined Nos. 3 and 4; and combined Nos. 5 and 6 bearings exit the MPS, travel through the support strut, and then enter the lube cabinet. The exit lines from the scavenge pumps drain into the oil supply tank.

An air/oil mixture is removed from the MPS through two lines which are eventually connected to a vacuum pump; one line exits the MPS in the Bendix cavity region (Bendix vent line), and the other departs through the turbine section structure (aft vent line). Both lines pass through the MPS support strut and into the lube cabinet where they terminate at the top of the deoiler tank. In the deoiler, gravity forces the oil to the bottom of the tank. A line with a 1.55- μ m filter and a ball valve carries the oil from the deoiler to the supply tank through the transfer pump. Parasitic air from the MPS is sucked from the deoiler through a line to a vacuum pump outside the cabinet. A vacuum trim valve is provided within the cabinet, and instrumentation in the vacuum line inside the cabinet is connected to the control console to activate warning lights on the MPS control panel when the vacuum deviates from between 4- and 9-psia.

Oil supply and scavenge line sizes range from 0.33-inch to 1.5-inches in diameter, and the pumps are Nichols-Zenith 1-gpm pumps. The MPS SN003 lube system is diagrammed in Figure 144. All lubrication system limits pertinent to MPS control console warning and shutdown displays are adjustable. Facility requirements for the lube system consist of a 110-V/ac and 16-amp (starting) power supply for each pump (pumps will be ripple started), a continuous 4-psia vacuum for scavenging, and a standard tap water source for cooling flow. The lube cabinet measures approximately 19-in. by 36-in. by 60-in. An internal Boeing report (D6-52523 by R.M. Swanson) provides additional information regarding the MPS SN003 lube system.

5.2.2.7 MPS Control System and Support Equipment

The information provided in Section 5.1.2.7 pertaining to the control system of the MPS SN002 also applies to the MPS SN003 control system.

Table 46. MPS SN003 Instrumentation.

Parameter	GE No.	θ, °, ALF	MPS Station Rotor Spacing		Range	Routing Code*	Location or Description	Purpose
			Maximum	Nominal Minimum				
A1	1	0	184.76	186.5	0-10 ips	C,M,V	Forward Macelle Int. Support Structure	Vibration
A2	2	270	184.76	186.5			Support Structure	
A3	3	0	205.1	205.1			Damper Area	
A4	4	90	205.1	205.1			Aft Macelle Support Housing	
A5	5	180	241.25	241.25			Aft Macelle Support Housing	
A6	6	180	241.25	241.25			Forward Side of Turbine Drive Mod.	
A7	7	0	249.0	249.0			Aft End of Center Shaft	
A8	8	90	271.7	271.7			Macelle Forebody Surface	
VPBD 1,2,3,4,5	51	0	168.88	170.62	3-15 psia	S	Macelle Forebody Surface	Static Pressure for Macelle Force Calculations.
VPBD6	52		170.38	172.12				
VPBD11	53		171.87	173.61				
VPBD16	54		173.52	175.26				
VPBD21	55		175.27	177.01				
VPBD26	56		176.98	178.72				
VPBD31	57		178.95	180.69				
VPBD36	58		181.31	183.05				
VPBD41	59		184.99	186.73				
VPBD46	60		187.44	189.18				
VPBD51	61		189.19	190.93				
VPBD56	62		190.94	192.68				
VPBD61	63		191.81	193.55				
VPBD66	64		202.30	202.30			Macelle Afterbody Surface	
VPBD70	65		203.00	203.00				
VPBD74	66		203.70	203.70				
VPBD78	67		204.71	204.71				
VPBD82	68	0	205.72	205.72	3-15 psia	S	Macelle Afterbody Surface	Static Pressure for Macelle Force Calculations.
VPBD86	69		206.72	206.72				
VPBD90	70		207.73	207.73				
VPBD94	71		208.74	208.74				
VPBD98	72		209.99	209.99				
VPBD102	73		211.50	211.50				
VPBD106	74		213.00	213.00				
VPBD110	75		216.50	216.50				
VPBD7	76		170.38	172.12			Macelle Forebody Surface	
VPBD12	77	90	171.87	173.61				
VPBD17	78		173.52	175.26				
VPBD22	79		175.27	177.01				
VPBD27	80		176.98	178.72				
VPBD32	81		178.95	180.69				
VPBD37	82		181.31	183.05				
VPBD42	83		184.99	186.73				
VPBD47	84		187.44	189.18				

Table 46. MPS SN003 Instrumentation (Continued).

Parameter	GE No.	θ , °, ALF	MPS Station Rotor Spacing		Range	Routing Code ^a	Location or Description	Purpose
			Maximum	Nominal Minimum				
VPRD52	85	90	189.19	190.93	3-15 psia	S	Nacelle Forebody Surface	Static Pressure for Macelle Force Calculations
VPRD57	86		190.94	192.68				
VPRD62	87		191.81	193.55				
VPRD67	88		202.30	202.30				
VPRD71	89		203.00	203.00				
VPRD75	90		203.70	203.70				
VPRD79	91		204.71	204.71				
VPRD83	92		205.72	205.72				
VPRD87	93		206.72	206.72				
VPRD91	94		207.73	207.73				
VPRD95	95	208.74	208.74					
VPRD99	96	209.99	209.99					
VPRD103	97	211.50	211.50					
VPRD107	98	213.00	213.00					
VPRD111	99	216.50	216.50					
VPRD115	100	170.38	172.12	3-15 psia	S	Nacelle Forebody Surface	Static Pressure for Macelle Force Calculations	
VPRD119	101	171.87	173.61					
VPRD123	102	173.52	175.26					
VPRD127	103	175.27	177.01					
VPRD131	104	176.98	178.72					
VPRD135	105	178.95	180.69					
VPRD139	106	181.31	183.05					
VPRD143	107	184.99	186.73					
VPRD147	108	187.44	189.18					
VPRD151	109	189.19	190.93					
VPRD155	110	190.94	192.68					
VPRD159	111	191.81	193.55					
VPRD163	112	170.38	172.12	3-15 psia	S	Nacelle Forebody Surface	Static Pressure for Macelle Force Calculations	
VPRD167	113	171.87	173.61					
VPRD171	114	173.52	175.26					
VPRD175	115	175.27	177.01					
VPRD179	116	176.98	178.72					
VPRD183	117	178.95	180.69					
VPRD187	118	181.31	183.05					
VPRD191	119	184.99	186.73					
VPRD195	120	187.44	189.18					
VPRD199	121	189.19	190.93					
VPRD203	122	190.94	192.68					
VPRD207	123	191.81	193.55					
VPRD211	124	202.30	202.30	180		Nacelle Afterbody Surface	Static Pressure for Macelle Force Calculations	
VPRD215	125	203.00	203.00					
VPRD219	126	203.70	203.70					

Table 46. MPS SN003 Instrumentation (Continued).

Parameter	GE No.	θ , °, ALF	MPS Station Rotor Spacing		Range	Routing Code ^a	Location or Description	Purpose
			Maximum	Nominal Minimum				
VPBD80	127	180	204.71	204.71	3-15 psia	S	Macelle Afterbody Surface	Static Pressure for Macelle Force Calculations
VPBD84	128		205.72	205.72				
VPBD88	129		206.72	206.72				
VPBD92	130		207.73	207.73				
VPBD96	131		208.74	208.74				
VPBD100	132	209.99	209.99	3-15 psia	S	Macelle Forebody Surface	Static Pressure for Macelle Force Calculations	
VPBD104	133	211.50	211.50					
VPBD108	134	213.00	213.00					
VPBD112	135	216.50	216.50					
VPBD110	136	170.38	172.94					
VPBD115	137	171.87	173.61	3-15 psia	S	Macelle Afterbody Surface	Static Pressure for Macelle Force Calculations	
VPBD120	138	173.52	175.26					
VPBD25	139	175.27	177.01					
VPBD30	140	176.98	178.72					
VPBD35	141	178.95	180.69					
VPBD40	142	181.31	183.05	3-15 psia	S	Macelle Afterbody Surface	Static Pressure for Macelle Force Calculations	
VPBD45	143	183.05	184.79					
VPBD50	144	184.99	186.73					
VPBD55	145	187.44	189.18					
VPBD60	146	189.19	190.93					
VPBD65	147	190.94	192.68	3-15 psia	S	Macelle Afterbody Surface	Static Pressure for Macelle Force Calculations	
VPBD69	148	191.81	193.55					
VPBD73	149	192.68	194.37					
VPBD77	150	202.30	202.30					
VPBD81	151	203.00	203.00					
VPBD85	152	203.70	203.70	3-15 psia	S	IR (Inner Rotor) Balance Forward Cavity ($r = 5.17$)	Static Pressure for Force Balance Tests	
VPBD89	153	204.71	204.71					
VPBD93	154	205.72	205.72					
VPBD97	155	206.72	206.72					
VPBD101	156	207.73	207.73					
VPBD105	157	208.74	208.74	3-15 psia	S	IR Balance Forward Cavity ($r = 3.80$)	Static Pressure for Force Balance Tests	
VPBD109	158	209.99	209.99					
VPBD113	159	211.50	211.50					
VPBD113	159	213.00	213.00					
VPBD113	159	216.50	216.50					
VPRC1	201	0	194.09	3-15 psia	S	IR (Inner Rotor) Balance Forward Cavity ($r = 5.17$)	Static Pressure for Force Balance Tests	
VPRC2	202	90	194.91					
VPRC3	203	180						
VPRC4	204	270						
VPRC5	205	0						
VPRC6	206	90						
VPRC7	207	180						
VPRC8	208	270						

Table 46. MPS SN003 Instrumentation (Continued).

Parameter	GE Mn.	θ , ° ALF	MPS Station Rotor Spacing		Range	Routing Code ^a	Location or Description	Purpose
			Maximum	Nominal Minimum				
VPRC11	209	---	195.76	197.50	3-15 psia	S, T	Intermediate Balance Cavity (r = 4.71)	Static Pressure for Force Balance Tests
VPRC12	210	---	198.40	198.40			Intermediate Balance Cavity (r = 1.73)	
VPRC13	211	---	195.66	197.40		S	OR (Outer Rotor) Balance Aft Cavity (r = 4.58)	
VPRC14	212	---	198.50	201.70				
VPRC9	213	0	201.70	201.70				
VPRC10	214	90						
VPRC11	215	180						
VPRC12	216	270	201.75	201.75				
VPRC13	217	0						
VPRC14	218	90						
VPRC15	219	180						
VPRC16	220	270						
POI1	226	---	---	---	15-200 psia	M, C	Upstream of Outer Turb. Cont. Valve	Outer Turb. Supply Pressure
PCV4	227	---	---	---		S, C	Downstream of Outer Turb. Cont. Valve	
VPT413	228	0	251.20	251.20		S	Outer Turbine Air Plenum	Outer Turb. Supply Pressure Outer Turb. Inlet Pressure
VPT414	229	90	251.20	251.20	5-60 psia		Outer Turbine Stage 1 Tip Region	
PTRB15	230	0	255.20	255.20			Outer Turbine Stage 1 Hub Region	Outer Turb. Inlet Pressure Turbine Diagnostics
PTRB16	231	30	255.10	255.10				
POIH2	232	150						
POIH3	233	270						
PTRB17	234	30	258.10	258.10	5-40 psia	M, N, S	Outer Turbine Exit, Tip Region	Outer Turbine Exit Duct Wall Static Pressure
PTRB18	235	210					Outer Turbine Exit, Tip Region	
PTRB19	236	30					Outer Turbine Exit, Hub Region	Outer Turbine Exit Duct Total Pressure
PTRB110	237	210					Outer Turbine Exit, Hub Region	
VP714	238	45	276.90	276.90	5-50 psia		Outer Turbine, Exit Duct (r = 4.926)	Outer Turbine Exit Duct Wall Static Pressure
VP715	239	135					Outer Turbine, Exit Duct (r = 4.673)	
VP716	240	225						
VPT717	241	45						
VPT718	242	135						
VPT719	243	225						
VPT7110	244	45						
VPT7111	245	135						
VPT7112	246	225						
VP711	247	45	278.10	278.10	5-40 psia	S	Inner Turbine Exit Duct, Wall	Inner Turbine Exit Duct Wall Static Pressure
VP712	248	135						
VP713	249	225						
PCV1	250	---	---	---	15-200 psia	S, C	Upstream of Inner Turb. Cont. Valve	Inner Turb. Supply Pressure
PCV2	251	---	---	---		S	Downstream of Inner Turb. Cont. Valve	
VPT411	252	0	263.70	263.70			Inner Turbine Air Plenum	Inner Turb. Supply Pressure Inner Turb. Inlet Pressure
VPT412	253	120	263.70	263.70	5-60 psia		Inner Turbine Air Plenum	
PTRB11	254	0	265.20	265.20			Inner Turbine Stage 1 Tip Region	Inner Turb. Inlet Pressure Turbine Diagnostics

Table 46. MPS SN003 Instrumentation (Continued).

Parameter	GE No.	θ, °, ALF	MPS Station Rotor Spacing		Range	Routing Code*	Location or Description	Purpose
			Maximum	Nominal				
PTRR12	255	0	267.15	267.15	5-40 psia	S	Inner Turbine Interstage	Turbine Diagnostics
PTRR13	256	0	268.30	268.30	5-50 psia		Inner Turbine Exit, Tip Region	Inner Turb. Exit Duct Total Pressure
PTRR14	257	180	268.30	268.30			Inner Turbine Exit, Tip Region	
VPT711	258	45	278.10	278.10			Inner Turbine Exit Duct (r = 3.576)	
VPT712	259	135						
VPT713	260	225					Inner Turbine Exit Duct (r = 2.916)	
VPT714	261	45						
VPT715	262	135						
VPT716	263	225						
PE	264	0	288.00	288.00	5-40 psia		MPS Exit Shroud Int. Wall	Mixed Flow Exit Static Pres.
VPCAV1	276	---	188.56	190.30	3-15 psia		No. 1 Bearing, Aft Cavity	No. 1 Bearing Cavity Pressure
VPCAV2	277	---	185.86	187.60			No. 1 Bearing, Forward Cavity	
VPCAV3	278	---	190.06	191.80			Cavity Forward of IR Telem. Mod.	
VPCAV4	279	---	231.50	231.50			No. 6 Bearing, Forward Cavity	No. 6 Bearing Cavity Pressure
VPCAV5	280	---	235.00	235.00			No. 6 Bearing, Aft Cavity	No. 6 Bearing Cavity Pressure
VPCAV6	281	---	244.00	244.00			Bendix Coupling Cavity	Bendix Coupling Cavity Pressure
VPCAV7	282	60	254.50	254.50			Forward of OR Stage 1 Labyrinth	
VPCAV8	283	0	255.00	255.00			No. 8 Bearing, Aft Cavity	
VPCAV9	284	0	259.20	259.20			No. 9 Bearing, Forward Cavity	
VPCAV10	285	60	264.70	264.70			Forward of IR Stage 1 Labyrinth	
VPCAV11	286	0	264.50	264.50			No. 9 Bearing, Aft Cavity	
VPCAV12	287	0	272.00	272.00			No. 10 Bearing, Aft Cavity	
VPCAVR2	288	---	205.50	205.50			No. 3 Bearing, Forward Cavity	
VPCAVX1	289	---	203.90	203.90			OR Aft Telemetry Cavity	
VTRCA1	301	45	192.35	194.09	40-150° F	S	Forward Side of Inner Hub (r = 5.17)	Cavity Temperature
TCF02	302	225				N		
VTRCA2	303	45				S	Forward Side of Inner Hub (r = 3.80)	
TCF12	304	225				N		
TRC11	305	---	195.76	197.50	30-200° F	S,T	Aft Side of Inner Hub (r = 4.71)	
TRC12	306	---	198.40	198.40	30-200° F	S,T	Fwd. Side of Outer Hub (r = 4.71)	
VTRCA3	307	45	201.70	201.70	40-150° F	S	Aft Balance Cavity (r = 4.58)	
TCN02	308	225	201.70	201.70		N		
VTRCA4	309	40	201.75	201.75		S	Aft Balance Cavity (r = 3.80)	
TCN12	310	225	201.75	201.75		N		
ESPTF	---	---	181.56	183.30	40-250° F	S	Forebody Cavity	Forebody ESP Temperature
VTT411	326	97	251.20	251.20	160-250° F		Outer Turbine Air Plenum	Outer Turb. Inlet Temp.
VTT412	327	263						
TOP13	328	353						
VTT711	329	45	276.90	276.90	0-200° F	N	Outer Turbine Exit Duct (r = 4.228)	Outer Turbine Exit Duct, Total Temperature
TTDF4	330	135				N		
TTDF7	331	225				N		

Table 46. MPS SN003 Instrumentation (Continued).

Parameter	GE No.	θ, °, AIF	MPS Station Rotor Spacing		Range	Routing Code	Location or Description	Purpose
			Maximum	Nominal				
TTDE2	332	45	276.90	276.90	0-200° F	N	Outer Turbine Exit Duct (r = 4.705)	Outer Turbine Exit Duct, Total Temperature
VT7712	333	135	276.90	276.90	↓	S	↓	↓
TTDE8	334	225	276.90	276.90	↓	N	↓	↓
TTDE3	335	45	276.90	276.90	↓	↓	↓	↓
TTDE6	336	135	276.90	276.90	↓	↓	↓	↓
TTDE9	337	225	276.90	276.90	↓	↓	↓	↓
VT7413	338	0	263.20	263.20	160-250° F	S	Inner Turbine Air Plenum	Inner Turbine Inlet Temp.
VT7414	339	120	263.20	263.20	↓	S	↓	↓
TTPL3	340	240	263.20	263.20	↓	S	↓	↓
VT7713	341	45	278.10	278.10	0-200° F	M	Inner Turb. Exit Duct (r = 3.864)	Inner Turbine Exit Duct, Total Temperature
TTIE4	342	135	278.10	278.10	↓	S	↓	↓
TTIE7	343	225	278.10	278.10	↓	↓	↓	↓
TTIE2	344	45	278.10	278.10	↓	↓	↓	↓
VT7714	345	135	278.10	278.10	↓	S	↓	↓
TTIE8	346	225	278.10	278.10	↓	↓	↓	↓
TTIE3	347	45	278.10	278.10	↓	↓	↓	↓
TTIE6	348	135	278.10	278.10	↓	↓	↓	↓
TTIE9	349	225	278.10	278.10	↓	↓	↓	↓
TBRG1	351	90	187.56	189.30	0-225° F	C, H, S	No. 1 Bearing	No. 1 Brg. Metal Temperature
TBRG2	352	270	187.56	189.30	↓	N	↓	↓
TBRG3	353	15	203.20	203.20	↓	C, M, S, T	No. 2 Bearing	No. 2 Brg. Metal Temperature
TBRG4	354	195	203.20	203.20	↓	M, T	↓	↓
TBRG5	355	0	206.75	206.75	0-300° F	C, H, S	No. 3 Bearing	No. 3 Brg. Metal Temperature
TBRG6	356	90	206.75	206.75	↓	N	↓	↓
TBRG7	357	270	206.75	206.75	↓	C, H, S, T	No. 4 Bearing	No. 4 Brg. Metal Temperature
TBRG8	358	0	209.10	209.10	↓	N	↓	↓
TBRG9	359	160	209.10	209.10	↓	C, H, S	No. 5 Bearing	No. 5 Brg. Metal Temperature
TBRG10	360	90	228.60	228.60	↓	N	↓	↓
TBRG11	361	270	228.60	228.60	↓	C, H, S, T	No. 6 Bearing	No. 6 Brg. Metal Temperature
TBRG12	362	0	234.00	234.00	↓	N	↓	↓
TBRG13	363	90	234.00	234.00	↓	C, H, S	No. 7 Bearing	No. 7 Brg. Metal Temperature
TBRG14	364	270	234.00	234.00	↓	N	↓	↓
TBRG15	365	0	248.90	248.90	↓	C, H, S	No. 8 Bearing	No. 8 Brg. Metal Temperature
TBRG16	366	90	248.90	248.90	↓	N	↓	↓
TBRG17	367	270	248.90	248.90	↓	C, H, S	No. 9 Bearing	No. 9 Brg. Metal Temperature
TBRG18	368	0	253.50	253.50	↓	N	↓	↓
TBRG19	369	90	253.50	253.50	↓	C, H, S	No. 10 Bearing	No. 10 Brg. Metal Temperature
TBRG20	370	270	253.50	253.50	↓	N	↓	↓
TBRG21	371	0	259.70	259.70	↓	C, H, S	No. 11 Bearing	No. 11 Brg. Metal Temperature
TBRG22	372	120	259.70	259.70	↓	N	↓	↓
TBRG23	373	240	259.70	259.70	↓	C, H, S	No. 12 Bearing	No. 12 Brg. Metal Temperature
TBRG24	374	90	269.70	269.70	↓	N	↓	↓
TBRG25	375	270	269.70	269.70	↓	C, H, S	No. 13 Bearing	No. 13 Brg. Metal Temperature
TBRG26	376	---	190.98	192.72	40-250° F	S, T	IR (Inner Rotor) Telem. Mod. 16	IR Telem. Mod. 1 Temperature
TTEL1	377	---	↓	↓	↓	↓	IR Telem. Mod. 7	IR Telem. Mod. 3 Temperature
TTEL3	378	---	↓	↓	↓	↓	IR Telem. Mod. 7	IR Telem. Mod. 7 Temperature

Table 46. MPS SN003 Instrumentation (Continued).

Parameter	CF No.	θ, ° ALF	MPS Station Rotor Spacing		Range	Routing Code ^a	Location or Description	Purpose	
			Maximum	Nominal					
VTRBL11	380	---	---	---	30-200° F	S, T	Inner Rotor Balance	IR Balance Temperature	
VTRBL12	381	---	---	---	→	→	Outer Rotor Balance	OR Balance Temperature	
VTRBL13	382	---	---	---	→	→	OR Telem. Mod. 4	OR Telem. Mod. 1 Temperature	
VTRBL14	383	---	---	---	→	→	OR Telem. Mod. 12	OR Telem. Mod. 3 Temperature	
VTRBL15	384	---	---	---	→	→	Support Housing	OR Telem. Mod. 6 Temperature	
VTRBL16	385	---	---	---	→	→	Support Housing Metal Temp.	OR Telem. Mod. 10 Temperature	
VTRBL17	386	---	---	---	→	→	IR Telemetry Antenna	OR Telem. Mod. 12 Temperature	
VTRBL18	387	---	---	---	→	→	OR Telemetry Antenna	OR Telem. Mod. 15 Temperature	
TTEL4	388	---	203.90	203.90	→	→	IR Telemetry Antenna	Support Housing Metal Temp.	
TTEL5	389	---	→	→	→	→	OR Balance Torque	OR Balance Torque	
TTEL6	390	---	→	→	→	→	OR Balance Thrust	OR Balance Thrust	
TTEL7	391	---	→	→	→	→	OR Balance Aft Cent. Force	OR Balance Aft Cent. Force	
TTEL8	392	---	→	→	→	→	IR Balance Torque	IR Balance Torque	
TTEL9	393	---	→	→	→	→	IR Balance Thrust	IR Balance Thrust	
TSK1	394	0	217.00	217.00	→	→	OR Torq. Blade (No. 1)	IR Balance Forward Cent. Force	
TSK2	395	90	217.00	217.00	→	→	OR Torq. Blade (No. 7)	IR Balance Aft Cent. Force	
TAMT1	396	15	191.56	193.30	→	→	IR Torq. Blade (No. 3)	Blade Stem Torque Measurement	
TAT2	397	150	191.56	193.30	→	→	IR Torq. Blade (No. 5)	→	
TAMT2	398	210	202.70	202.70	→	→	Aft of No. 7 Bearing	→	
TAD2	399	345	202.70	202.70	→	→	Inner Rotor, No. 1 Blade	Outer Rotor, Thrust	
STQ2	511	---	---	---	-630 - 4730 in./#	C, S, T	OR Balance	Prop. Blade Dynamic Strain	
STH2	512	---	---	---	-300 - 600 #	→	→	→	→
SCFU2	513	---	---	---	0-5 Volts	→	→	→	→
SCFD2	514	---	---	---	0-5 Volts	→	→	→	→
STQ1	501	---	---	---	-630 - +4730 in./#	→	→	→	→
STH1	502	---	---	---	-300 - +600 #	→	→	→	→
SCFU1	503	---	---	---	0-5 Volts	→	→	→	→
SCFD1	504	---	---	---	→	→	→	→	→
TQBLD1	---	---	---	---	→	→	→	→	→
TQBLD7	---	---	---	---	→	→	→	→	→
TQBLD3	---	---	---	---	→	→	→	→	→
TQBLD5	---	---	---	---	→	→	→	→	→
FTV	550	---	249.30	249.30	-100 - 600 #	→	→	→	→
SPI1	601	---	---	---	0-40 ksi	B, T	Inner Rotor, No. 1 Blade	→	
SPI2	602	---	---	---	→	→	→	→	
SPI3	603	---	---	---	→	→	No. 3 Blade	→	
SPI4	611	---	---	---	→	→	→	→	
SPI5	612	---	---	---	→	→	→	→	
SPI6	613	---	---	---	→	→	No. 5 Blade	→	
SPI7	621	---	---	---	→	→	→	→	
SPI8	622	---	---	---	→	→	→	→	
SPI9	623	---	---	---	→	→	→	→	

Table 46. MPS SN003 Instrumentation (Continued).

Parameter	CE No.	θ, °, ALF	MPS Station Rotor Spacing		Range	Routing Code*	Location or Description	Purpose
			Maximum	Nominal				
SP110	631	---	---	---	0-40 ksi	B, T	Inner Rotor, No. 7 Blade	Prop. Blade Dynamic Strain
SP111	632	---	---	---	0-10,000 rpm	A, B, C, H, V C, S	Outer Rotor, No. 1 Blade	
SP112	633	---	---	---			Mo. 3 Blade	
SP01	651	---	---	---			Mo. 5 Blade	
SP03	652	---	---	---			Mo. 7 Blade	
SP04	661	---	---	---			Forward of Outer Rotor	
SP05	662	---	---	---			Air Plenum	
SP06	663	---	---	---			Aft of No. 10 Bearing	
SP07	671	---	---	---			Macelle Supt. Housing (r = 4.26)	
SP08	672	---	---	---			Macelle Supt. Housing (r = 4.21)	
SP09	673	---	---	---			Outer Turbine Drive Flow	
SP010	681	---	---	---			Venturi Inlet	
SP011	682	---	---	---			Outer Turbine Drive Flow	
SP012	683	---	---	---	Venturi			
NO	901	0	247.10	247.10	0-300° F	N	Outer Turbine Drive Flow	Motor Speed of Outer Turbine Inner Turbine
SRPH2	902	90	247.10	247.10	0-300° F		Outer Turbine Drive Flow	
NI	903	0	271.20	271.20	15-200 psia		Inner Turbine Drive Flow	
SRPH1	904	90	271.20	271.20	0-30 psid		Inner Turbine Drive Flow	
THB6	---	180	234.00	234.00	160°-250° F		Inner Turbine Drive Flow	
THB8	---	0	234.00	234.00	0-150 psig		Inner Turbine Drive Flow	
PHO	---	---	---	---	0-100% (Open)		Inner Turbine Drive Flow	
DPNO	---	---	---	---	0-100% (Open)		Upstream of W/U Solenoid in Oil Supply Line	
TTNO	---	---	---	---	0°-300° F		In Damper Oil Supply Line	
PNI	---	---	---	---	0-2.5 gpm		In Damper Oil Supply Line	
DPWI	---	---	---	---	0-250 psig		In Line from Deceler to Vac. Pump	
TTNI	---	---	---	---	50°-250° F		In Cooling Water Line	
PLUB	---	---	---	---	4-15 psia	On Outer Drive Valve		
TLUB	---	---	---	---	0-100% (Open)	On Inner Drive Valve		
VLUB	---	---	---	---	0-100% (Open)	On Inner Drive Valve		
PDAM	---	---	---	---	0-100% (Open)	On Inner Drive Valve		
TDAM	---	---	---	---	0-100% (Open)	On Inner Drive Valve		
PVAC	---	---	---	---	0-100% (Open)	On Inner Drive Valve		
PMAT	---	---	---	---	0-100% (Open)	On Inner Drive Valve		
VPOS1	---	---	---	---	0-100% (Open)	On Inner Drive Valve		
VPOS1	---	---	---	---	0-100% (Open)	On Inner Drive Valve		

Table 46. MPS SN003 Instrumentation (Concluded).

Parameter	GE No.	θ, °, ALF	MPS Station Rotor Spacing		Range	Routing Code*	Location or Description	Purpose
			Maximum	Nominal				
PTPROB	---	180	---	---	14-20 psia	S	Traversing Wake, Survey Probe	Prop. Wake Total Pressure
TTPROB	---	0	---	---	50°-200° F	A		
HAPROB	---		---	---	-20° - +20°		Translating Ceiling Plate	Prop. Wake Horiz. Flow Angle
VAPROB	---		---	---	-20° - +20°			
ACPO1	---		---	---	30-20,000 Hz		Right Sidevall Plate	Sideline Noise
ACPO2	---		---	---				
ACPO3	---		---	---				
ACPO4	---		---	---				
ACPO5	---		---	---				
ACPO6	---		---	---				
ACPO7	---		---	---				
ACPO8	---		---	---				
ACPO9	---		---	---				
ACP10	---		---	---				
ACP11	---		---	---				
ACP12	---		---	---				
ACP13	---		---	---				
ACP14	---		---	---				
ACP15	---		---	---				
ACP16	---		---	---				
ACP17	---		---	---				
ARSP01	---	90	---	---	30-20,000 Hz	A		
ARSP02	---		---	---				
ARSP03	---		---	---				
ARSP04	---		---	---				
ARSP05	---		---	---				

* Routing Codes

A = Acoustic Tape
R = Blade Tape

C = Control Console
H = Health Tape

N = Not Being Read Out
S = Steady-State Data

T = Telemetry
V = Vibe Monitor Station

5.2.2.8 Instrumentation

Table 46 itemizes the complete pressure, temperature, force and moment, speed, vibration, and acoustic instrumentation used during MPS SN003 testing in the 8x6 tunnel. Table 46 also includes instrumentation location, purpose, description, recommended label designation, expected measurement ranges, and indicators to signify which instrumentation items were used for input signals to the control console, the 14-track blade magnetic tape, the two 14-track acoustic magnetic tapes, the two 14-track health magnetic tapes, the vibration monitoring station, and identifies which are telemetered measurements. A pictorial representation of all MPS instrumentation is provided in GE drawing No. 4013312-548. For convenience, Figures 145, 146, and 147 provide schematics of the outer turbine instrumentation, the inner turbine instrumentation, and the balance cavity instrumentation, respectively.

5.2.2.8.1 Aeromechanical Instrumentation and Telemetry

Four of the blades on each hub were instrumented with three strain gauges each. Signals from these strain gauges were routed by means of telemetry to a 14-track magnetic tape and monitoring equipment in the control room. Table 47 and Figure 148 summarizes this telemetry instrumentation. The monitoring and recording equipment in the control room for the blade strain gauges consisted of 14 oscilloscopes, a spectrum analyzer, amplifiers (signal conditioners), channel switches, and a 14-track magnetic tape recorder. The hookup for the strain gauge output to the scopes is illustrated in Figure 149.

During the aeromechanical hub testing, two of the blade dynamic strain gauges on each rotor were replaced by strain gauges mounted on the brackets connecting the polygonal ring to the hub. Laser measurements and strobe techniques were also utilized to investigate blade tip deflections.

5.2.2.8.2 Health Monitoring and Control Instrumentation

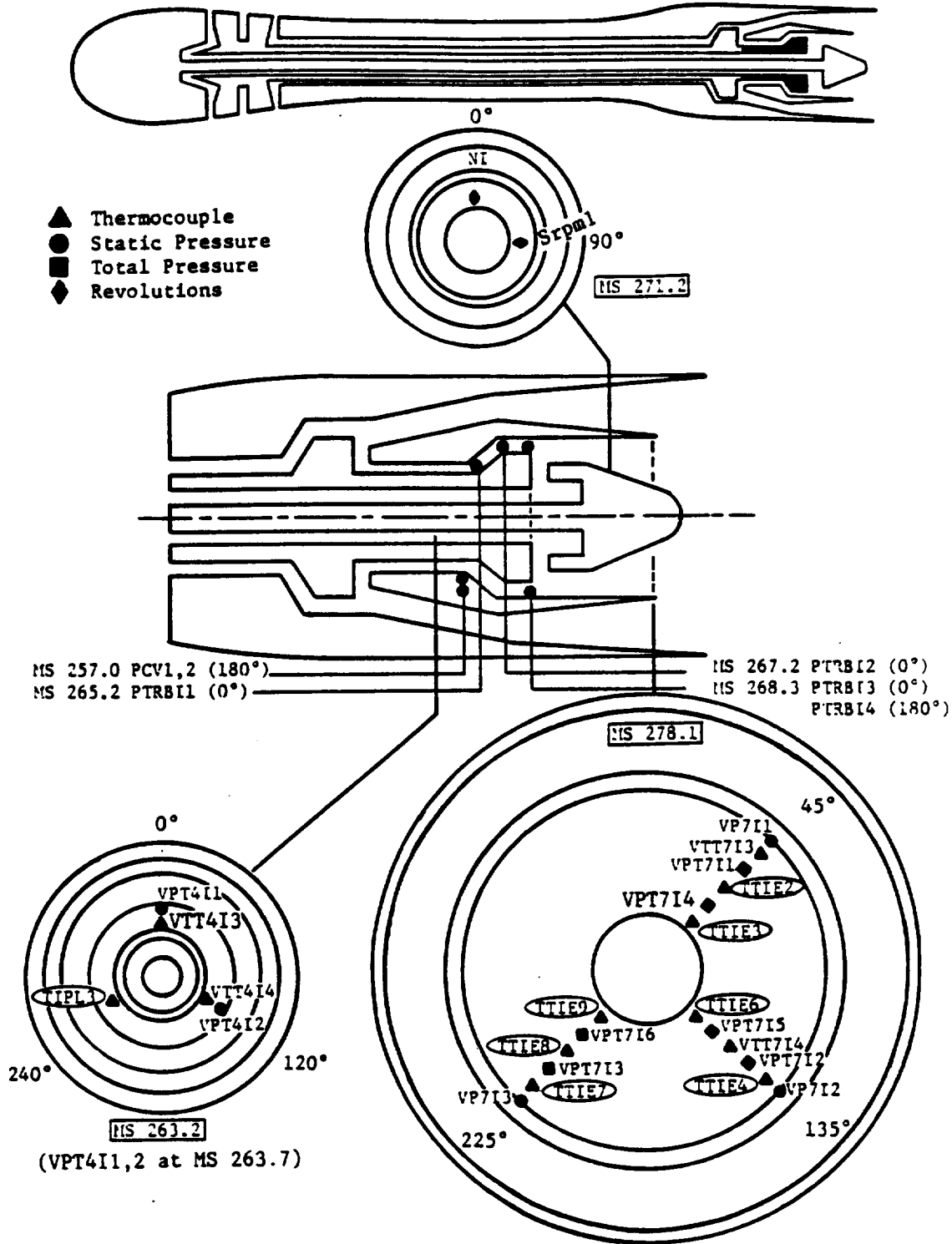
MPS health parameters were routed to the control console (discussed in an earlier section of this report), magnetic-tape health monitoring station, and a vibration monitoring station. Locations for bearing and vibration health parameters are depicted in Figure 150. The instrumentation parameters used as input signals to the console are itemized in Table 48.

The control room health monitoring station consisted of 28 oscilloscopes, amplifiers (signal conditioners), and two 14-track magnetic tape recorders. The vibration monitor station received the accelerometer signals and, through a switching arrangement, was capable of displaying them one at a time on a spectrum analyzer.

5.2.2.8.3 Acoustic Instrumentation

Acoustic instrumentation for this test consisted of pressure transducers mounted on a special plate attached to the ceiling and transducers located on the tunnel wall. A schematic of the ceiling plate is provided as Figure 151; the transducer location on the ceiling plate is defined in Figure 152. The angular positions are identified, relative to the propeller inlet axis, for ceiling-plate-mounted pressure transducers (Table 49) and for the side wall transducers (Table 50). When acoustic measurements were taken with the MPS at angle-of-attack, only five of the ceiling plate transducers were used. Their corresponding angular positions changed from that designated at zero angle-of-attack since the reference location was fixed on the MPS and the MPS rotated (pitched up) as angle-of-attack changed. The resulting angular positions for these transducers are included in Table 50.

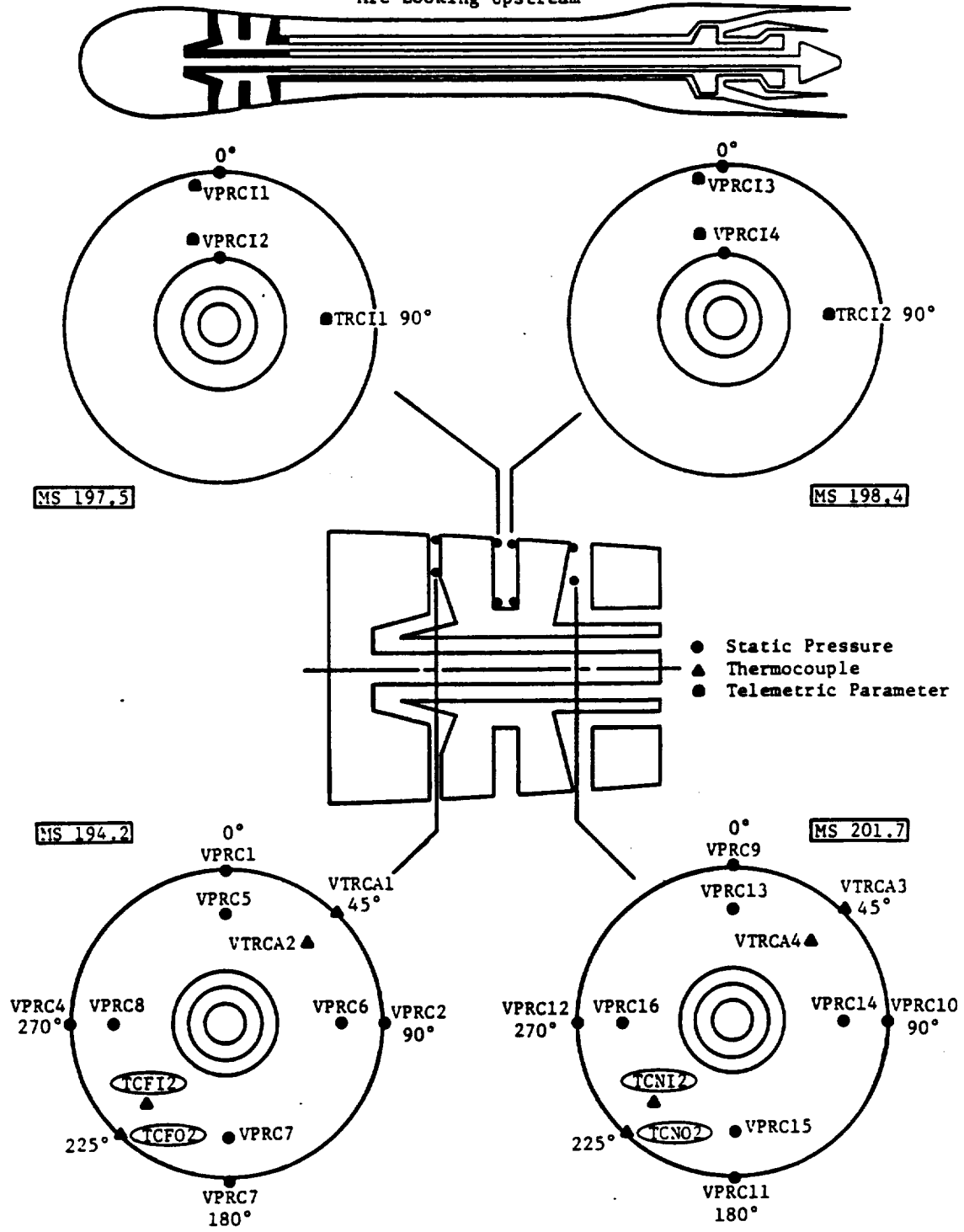
Cross-Sectional Views
Are Looking Upstream



Note: Circled Instrumentation Not Being Read Out

Figure 146. MPS SN003 Inner Turbine Instrumentation.

Cross-Sectional Views
Are Looking Upstream

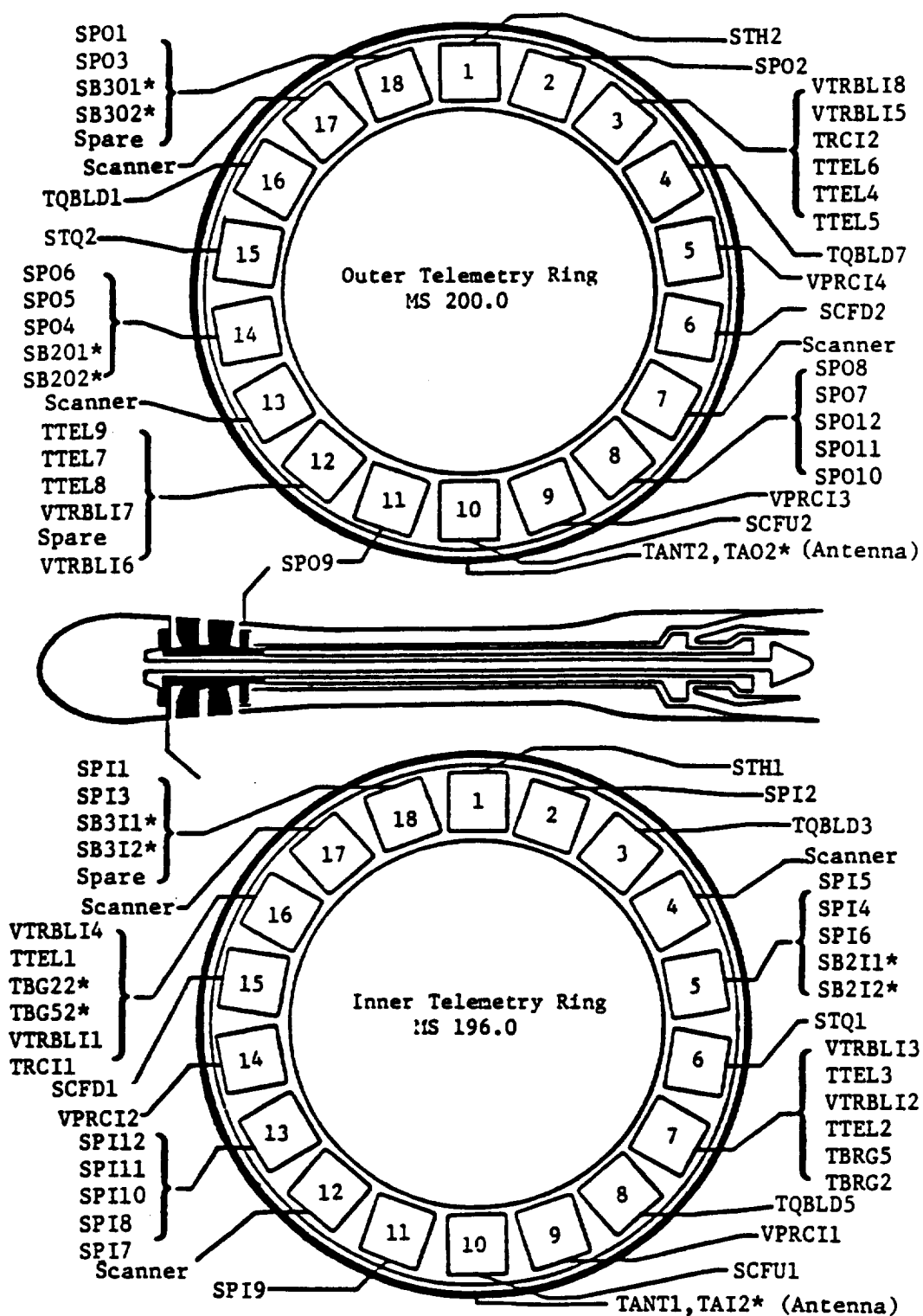


Note: Circled Instrumentation Not Being Read Out

Figure 147. Balance Cavity Instrumentation of the MPS SN003.

Table 47. MPS SN003 Telemetry Instrumentation Summary.

Inner Rotor				Outer Rotor			
Parameter	GE No.	Module	Description	Parameter	GE No.	Module	Description
STH1	502	1	Thrust	STH2	512	1	Thrust
SPI2	602	2	Blade No. 1 Dynamic Strain	SPO2	652	2	Blade No. 1 Dynamic Strain
SPI5	612	5	Blade No. 3 Dynamic Strain	VTRBL18	387	3	Balance Temperature
SPI4	611			VTRBL15	384		Balance Temperature
SPI6	613			TRC12	306		Cavity Temperature
STQ1	501	6	Torque	TTEL6	386		Module 6 Temperature
VTRBL13	382	7	Balance Temperature	TTEL4	388		Module 1 Temperature
TTEL3	378		Module 7 Temperature	TTEL5	389		Module 3 Temperature
VTRBL12	381		Balance Temperature	VPRC14	212	5	Balance Cavity Pressure
TTEL2	377		Module 3 Temperature	SCFD2	514	6	Aft Centrifugal Force
TBRG5	361		No. 5 Bearing Temperature	SPO8	672	8	Blade No. 5 Dynamic Strain
TBRG2	353		No. 2 Bearing Temperature	SPO7	671		Blade No. 5 Dynamic Strain
VPRC11	209	9	Balance Cavity Pressure	SPO12	683		Blade No. 7 Dynamic Strain
SCFU1	503	10	Forward Centrifugal Force	SPO11	682		
SPI9	623	11	Blade No. 5 Dynamic Strain	SPO10	681		
SPI12	633	13	Blade No. 7 Dynamic Strain	VPRC13	210	9	Balance Cavity Pressure
SP111	632			SCFU2	513	10	Forward Centrifugal Force
SP110	631			SP09	673	11	Blade No. 5 Dynamic Strain
SP18	622			TTEL9	393	12	Module 15 Temperature
SP17	621			TTEL7	391		Module 10 Temperature
VPRC12	211	14	Blade No. 5 Dynamic Strain	TTEL8	392		Module 12 Temperature
SCFD1	504	15	Balance Cavity Pressure	VTRBL17	390		Balance Temperature
VTRBL14	383	16	Aft Centrifugal Force	VTRBL16	385	14	Balance Temperature
TTEL1	376		Balance Temperature	SPO6	663		Blade No. 3 Dynamic Strain
TBRG22	354		Module 1 Temperature	SPO5	662		
TBRG52	362		No. 2 Bearing Temperature	SPO4	661	15	Torque
VTRBL11	380		No. 5 Bearing Temperature	STQ2	511	18	Blade No. 1 Dynamic Strain
TRC11	305		Balance Temperature	SPO1	651	18	Blade No. 1 Dynamic Strain
SP11	601	18	Cavity Temperature	SPO3	653	16	Blade No. 1 Stem Torque
SP13	603	18	Blade No. 1 Dynamic Strain	TQBLD1	---	4	Blade No. 7 Stem Torque
TQBLD3	---	3	Blade No. 3 Stem Torque	TQBLD7	---		
TQBLD5	---	8	Blade No. 5 Stem Torque				

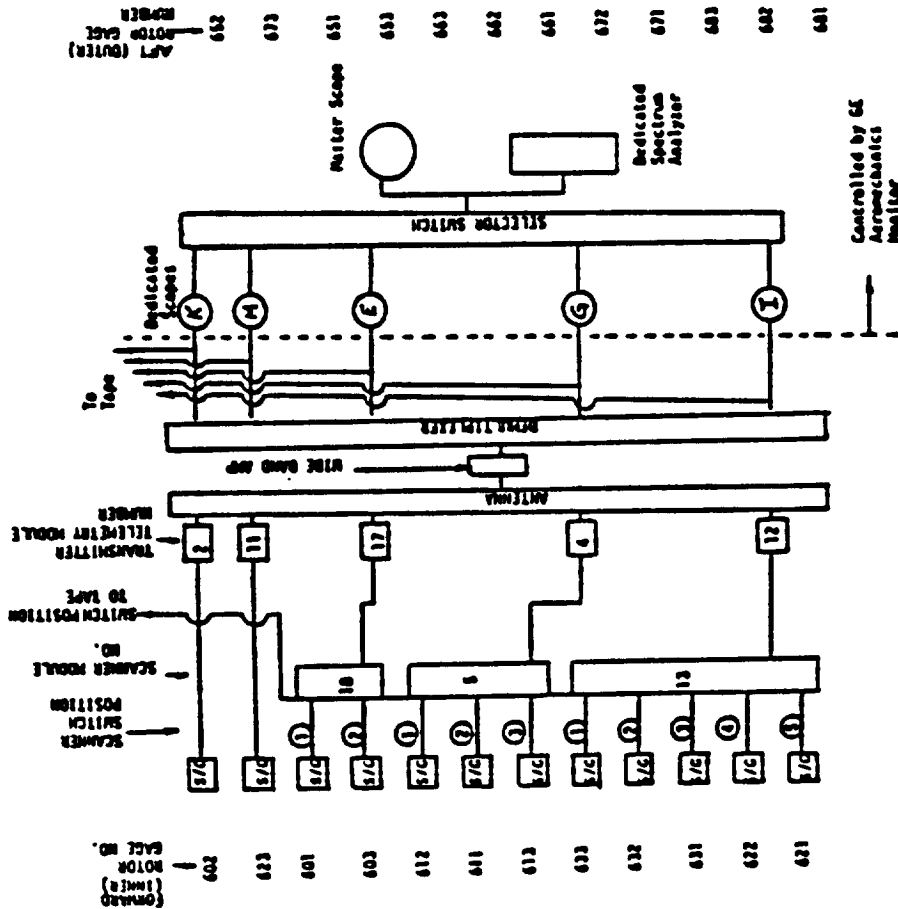


* Not Being Read Out

Figure 148. Telemetry Instrumentation for the MPS SN003.

Inner Rotor

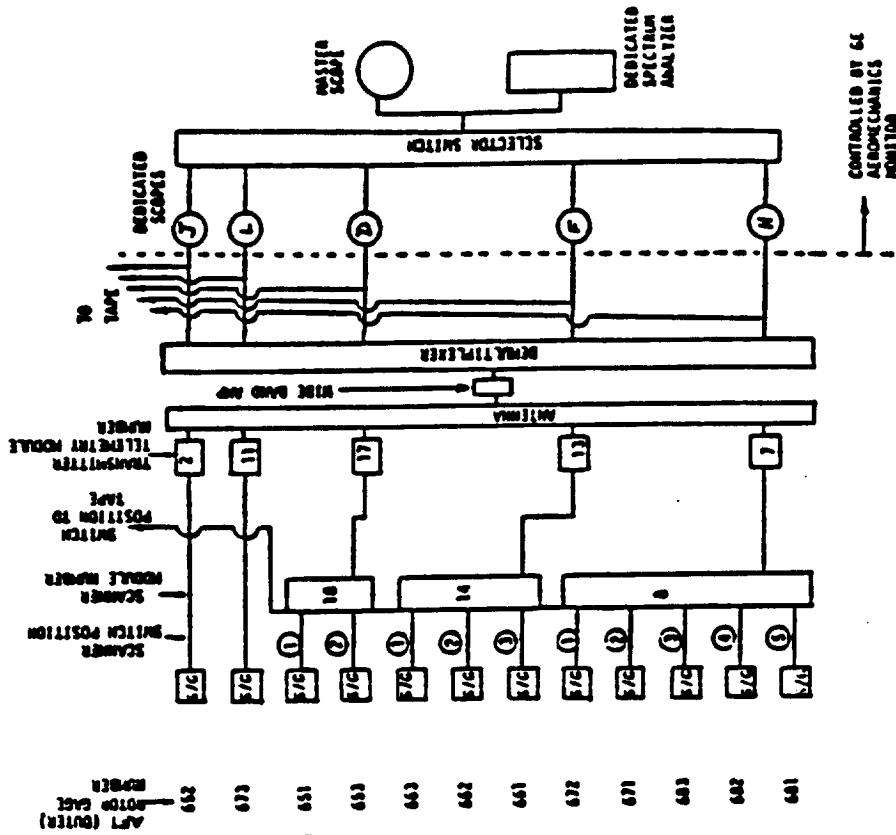
Note: For torque blade testing, scanner switch must be in ② position.



Scopes are to be calibrated to 40 dB peak-to-peak (±20 dB) with ability to set at 20 dB peak-to-peak. Being to supply internal square wave signal (25 1000 Hz) for phasing each channel. For calibrations, use method supplied by 8111 Curtis (GE) or equivalent. Both calibration and phasing signals are to be put on tape.

Outer Rotor

Note: For torque blade testing, scanner switch must be in ① position.



Scopes are to be calibrated to 40 dB peak-to-peak (±20 dB) with ability to be set at 20 dB peak-to-peak. Being to supply internal square wave signal (25 1000 Hz) for phasing each channel. For calibrations, use method supplied by 8111 Curtis (GE) or equivalent. Both calibration and phasing signals are to be put on tape.

Figure 149. Blade Strain Gauge Monitor Set-Up Schematic for MPS SN003.

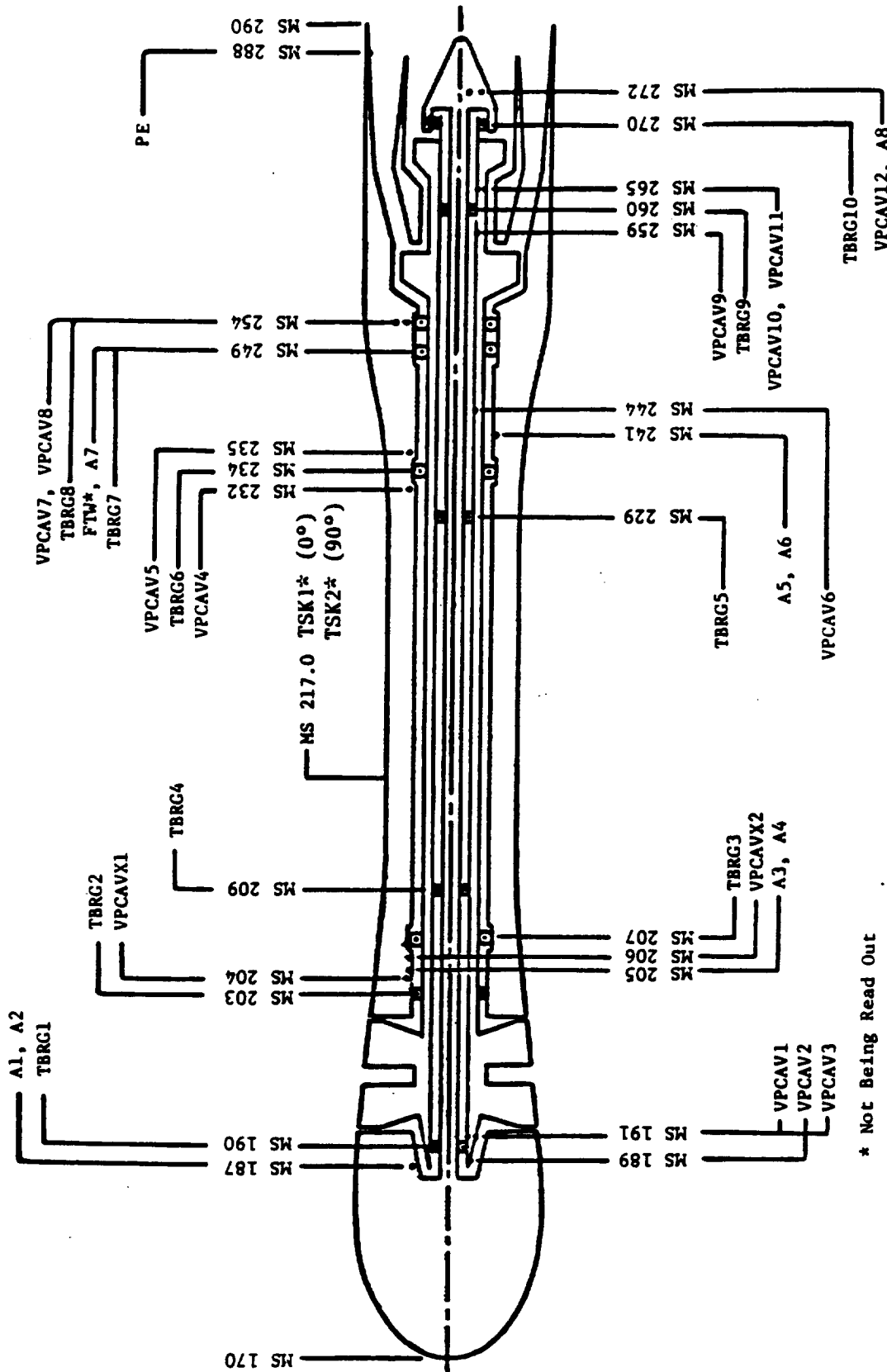




Figure 150. The MPS SN003 Health and Control Instrumentation.

Table 48. MPS SN003 Instrumentation Used for Control Console Input Signals.

Parameter	GE No.	Description
A1	1	Vibration 
A2	2	
A3	3	
A4	4	
A5	5	
A6	6	
A7	7	
A8	8	
PCV4	227	Outer Rotor Supply Pressure Inner Rotor Supply Pressure Bearing Temperature 
PCV2	251	
TBRG1	351	
TBRG2	353	Inner Rotor Torque Inner Rotor Thrust Inner Rotor Forward Centrifugal Force Inner Rotor Aft Centrifugal Force Outer Rotor Torque Outer Rotor Thrust Outer Rotor Forward Centrifugal Force Outer Rotor Aft Centrifugal Force Outer Rotor Speed (1/rev) Inner Rotor Speed (1/rev) Lube Line Pressure Lube Line Temperature Damper Line Pressure Damper Line Temperature De-Oiler Vacuum Pressure Lube System Cooling Water Pressure Outer Rotor Drive Valve Position Inner Rotor Drive Valve Position Outer Rotor Speed (60/rev) Inner Rotor Speed (60/rev)
TBRG3	357	
TBRG4	359	
TBRG5	361	
TBRG6	365	
TBRG7	367	
TBRG8	369	
TBRG9	371	
TBRG10	373	
STQ1	501	
STH1	502	
SCFU1	503	
SCFD1	504	
STQ2	511	
STH2	512	
SCFU2	513	
SCFD2	514	
NO	901	
NI	903	
PLUB	-	
TLUB	-	
PDAM	-	
TDAM	-	
PVAC	-	
PWAT	-	
VPOS1	-	
VPOS2	-	
SRPM2	902	
SRPM1	904	

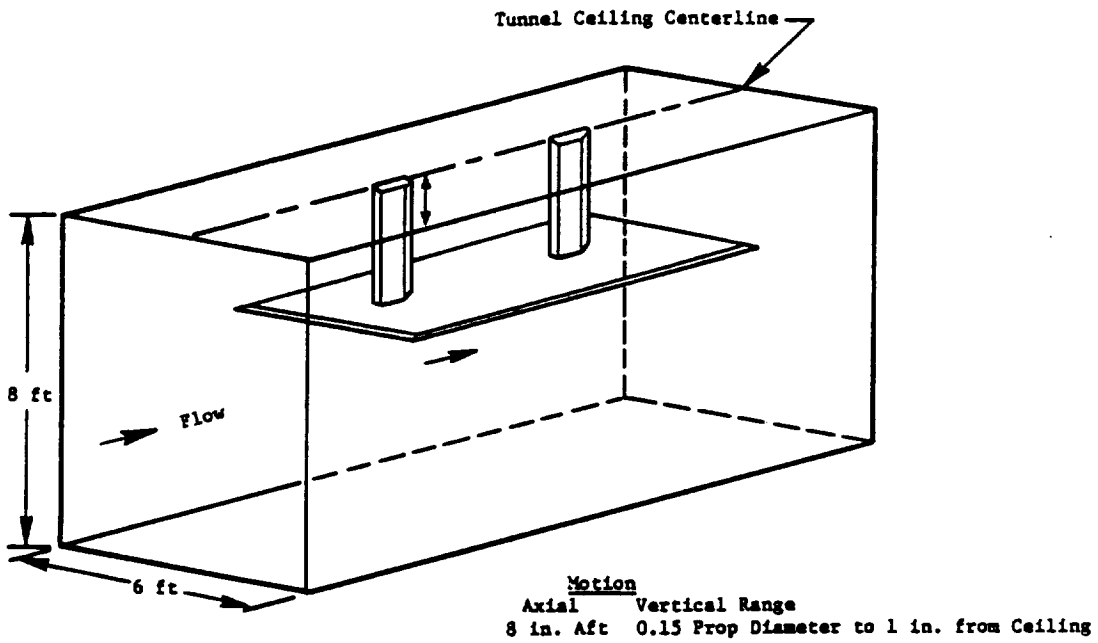


Figure 151. NASA Lewis 8×6 Supersonic Wind Tunnel Translating Acoustic Ceiling Plate Installation.

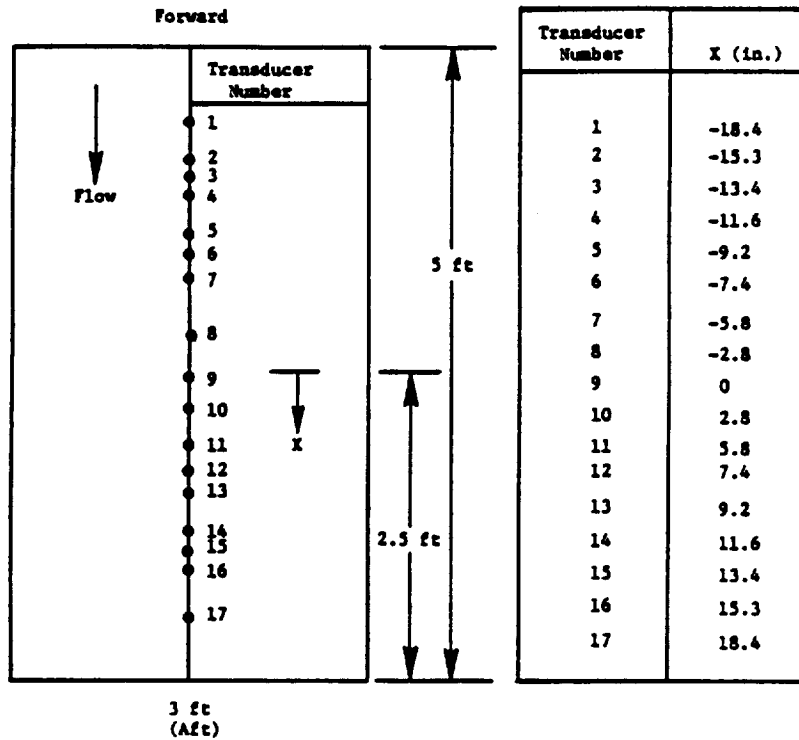


Figure 152. Translating Acoustic Ceiling Plate Transducer Locations.

Table 49. Transducer Angular Positions¹ (Ceiling Plate).

Transducer	Angle ² , degrees	Angle ³ , degrees			Angle ⁴ , degrees		
		Close	Nominal	Far	Close	Nominal	Far
1	46.8	49.6	50.3	51.7	44.3	43.7	42.6
2	52.0	55.2	56.0	57.7	49.1	48.4	47.1
4	59.4	63.2	64.1	66.1	55.8	55.0	53.5
6	69.3	73.8	74.9	77.1	65.1	64.1	62.3
8	81.8	86.8	88.0	90.3	77.1	76.0	73.8
9	90.0	95.0	96.1	98.4	85.0	83.9	81.6
10	98.2	102.9	104.0	106.2	93.2	92.0	89.7
12	110.7	114.9	115.9	117.7	106.2	105.1	102.9
14	120.6	124.2	125.0	126.5	116.8	115.9	113.9
16	128.0	130.9	131.6	132.9	124.8	124.0	122.3
17	133.2	135.7	136.3	137.4	130.4	129.7	128.3

¹ All Angles are for Plate Position 0.3D from Propeller Tip
² Measured from Point Halfway Between Propellers (all Spacings)
³ Measured from Forward Propeller at Spacing
⁴ Measured from Aft Propeller at Spacing

Table 50. Transducer Angular Positions.

Transducer ^a	Propeller Angle-of-Attack, α , deg				
	0	2	4	-2	-4
	Angle from Propeller Test Rig Centerline Axis, deg				
1P	63	58	53	68	73
2P	72	67	62	78	83
3P	90	84	79	95	101
4P	99	94	88	105	110
5P	110	105	99	115	120
1W	63	60	57	66	69
2W	72	69	66	76	79
3W	89	85	82	92	96
4W	99	96	92	103	106
5W	110	107	103	113	116

^a P denotes plate transducers; W denotes side-wall transducers.

One 14-channel tape recorder was utilized, which received the forward rotor 1/rev, aft rotor 1/rev, and time code; the remaining 11 channels were used to record the acoustic signals.

5.2.2.8.4 Aerodynamic Instrumentation

In addition to the nacelle surface static pressure instrumentation listed in Table 46, the aerodynamic instrumentation included a single-element survey probe to measure propulsor discharge total pressure, temperature, and flow angle. The survey probe was mounted from the tunnel floor and was remotely actuated to travel radially through the propulsor wake. NASA Lewis supplied both the survey probe and the actuator mechanism.

5.2.3 Test Matrix Summary

The 8x6 wind tunnel tests were carried out using F-4/A-4, F-7/A-7, the F-7/A-7/aero-mechanical hub, F-8/A-8, F-11/A-11, F-10/A-10, F-1/A-1, F-1/A-3, and F-21/A-21 blade configurations. Both the F-11/A-11 and F-21/A-21 blades exhibited high stresses during the initial part of the testing in their design configuration; subsequent testing utilized clipped blades designated as F-11c/A-11 and F-21c/A-21 configurations.

Systematic attempts were made to vary the test configuration parameters in order to evaluate their influence. Table 51 summarizes the major test configurations and their objectives. A summary of the performance and acoustic testing carried out in the 8x6 wind tunnel is presented in Table 52.

5.2.4 Test Procedures

Prior to the operation of the MPS during each test period, instructions outlined in a prerun check list were followed to activate the facility air system used for the MPS turbine drive air supply and

Table 51. Summary of 8x6 MPS Test Configurations.

No.	Blade Type	Hub Config.	Spacing	Objectives
1	F-4/A-4	8+8	Nominal	Effect of Tip Sweep and Activity Factor on Performance and Acoustics
2	F-7/A-7	8+8	↓	
3	F-8/A-8	8+8	↓	
4	F-10/A-10	8+8	↓	
5	F-1/A-1	8+8	↓	
6	F-1/A-3	8+8	Nominal	Effect of Reduced Diameter Aft Rotor on Acoustic and Performance
7	F-1/A-3	9+8	↓	
8	F-1/A-3	9+8	↓	Effect of Differential Blade Number
9	F-7/A-7	8+8	Maximum	
10	F-7/A-7	8+8	Minimum	Combined with Item No. 2, Effect of Spacing
11	F-8/A-8	4+4	Nominal	Effect of Number of Blades
12	F-11/A-11	11+9	Maximum	
13	F-21/A-21	11+10	↓	Effect of Wide Chord Blades Design Configuration
14	F-21/A-21	11+10	↓	
15	F-7/A-7	8+8	Nominal	Effect of Loading Design Configuration
				Effect of Slender Nacelle Aeromechanical Hub

Table 52. NASA Lewis 8x6 MPS Test Matrix Summary.

Date	Blades	Hub Config.	Spacing	Pitch Angle, degrees		March No.	Angle of Attack, degrees	Speed Range, Percent	Data		Trav. Probe	Remarks
				Fwd	Aft				Perf.	Acous.		
8/8/85	F-4/A-4	8+8 (Rigid)	Nominal	58.4	54.6	0.76	0	W/M - 90	Yes	No	No	None
8/10/85				42.8	41.0	0.36		W/M - 102				
						0.40		W/M - 105				
						0.50		W/M - 105				
10/2/85	F-7/A-7	8+8 (Rigid)	Nominal	31.8	30.8	0	0	0 - 110	Yes	No	No	C/O Run (Acoustic Plate In)
10/3/85				56.9	54.4	0.67		W/M - 105				Acoustic Plate In
10/3/85				56.9	54.4	0.72		W/M - 105				Acoustic Plate In
10/4/85				60.2	56.8	0.80		W/M - 100				Acoustic Plate In and No Forward Thrust
10/5/85						0.72		W/M - 110				
10/6/85						0.67		W/M - 110				
						0.85		W/M - 110				
						0.85		W/M - 110				
						0.80		W/M - 105				
						0.72		W/M - 105				
						0.67		W/M - 100				
						0.67		W/M - 100				
						0.72		W/M - 110				
						0.72		W/M - 110				
12/6/85	F-7/A-7	8+8 (Acro)	Nominal	56.9	54.4	0.76	0	W/M - 64	No	No	No	Loose Forward Hub Retainer Nut
						0.40		W/M - 72				
						0.50		W/M - 75				
						0.60		W/M - 93				
						0.67		W/M - 97				
						0.72		W/M - 99				
						0.80		W/M - 99				
						0.72		W/M - 98				
12/10/85				60.2	56.8	0.40	0	W/M - 64.5				
						0.50		W/M - 74				
						0.60		W/M - 74				
						0.72		W/M - 96				
						0.80		W/M - 98				
						0.85		W/M - 99				
						0.8		W/M - 95				
						0.8		W/M - 105				
						0.72		W/M - 95				
						0.76		W/M - 100				
						0.80		W/M - 105				
						0.85		W/M - 110				
12/11/85												
12/19/85	F-8/A-8	8+8 (Rigid)	Nominal	62.2	61.6	0.40	-1	W/M - 64.5	Yes	Yes		Hub Brackets (Both Rotor) and Flange Broken
				60.0	58.8	0.50	1	W/M - 74				
				60.9	59.4	0.60	2	W/M - 74				
						0.72	4	W/M - 96				
						0.80	0	W/M - 98				
						0.85		W/M - 99				
						0.8		W/M - 95				
						0.8		W/M - 105				
						0.72		W/M - 95				
						0.76		W/M - 100				
						0.80		W/M - 105				
						0.85		W/M - 110				

Table 52. NASA Lewis 8x6 MPS Test Matrix Summary (Continued).

Date	Blades	Hub Config.	Sparring	Pitch Angle, degrees		Mach No.	Angle-of-Attack, degrees	Speed Range, Percent	Data		Trav. Probe	Remarks
				Full	Aft				Perf.	Acous.		
1/7/86	F-8/A-8	4+4 (Rigid)	Nominal	59.0	59.4	0.8	0	W/M - 105	Yes	Yes	Yes	Make Investigation Blades Off Blade Instability Blade Instability Failed Forward Blade Forward Rotor Damage Blade Activity
	Dummy	0+0 (Rigid)				0.76		W/M - 100				
1/8/86		8+8 (Rigid)		N/A	N/A	0.72		W/M - 95		N/A		
1/9/86	F-8/A-8	8+8 (Rigid)		60.9	59.4	0.85		W/M - 105		Yes		
1/23/86	F-11/A-11	11+9 (Rigid)	Maximum	61.5	59.8	0.80		W/M - 87		Yes		
						0.76		W/M - 84				
1/24/86	F-11C/A-11					0.72		W/M - 81				
1/25/86	F-11C/A-11			60.3	58.2	0.80		W/M - 95				
1/29/86	F-10/A-10	8+8 (Rigid)	Nominal	59.9	57.3			W/M - 102				
								W/M - 105				
1/30/86				60.5	57.9	0.85		W/M - 103				
						0.72		W/M - 106				
1/31/86	F-1/A-1	8+8 (Rigid)				0.76		W/M - 92				
1/31/86	F-1/A-1					0.80		W/M - 98				
						0.67		W/M - 103				
2/1/86	F-1/A-1	8+8 (Rigid)	Nominal	59.5	56.5	0.72	0	W/M - 89				
				59.5	56.5	0.80		W/M - 97.5				
2/3/86	F-1/A-3			57.1	54.8	0.72		W/M - 105	Yes	Yes		
						0.76		W/M - 113				
2/4/86				57.6	58.3	0.67		W/M - 98				
						0.72		W/M - 105				
				60.7	60.9	0.76		W/M - 97		No		
						0.80		W/M - 105		Yes		
2/7/86	F-7/A-7		Minimum			0.76		W/M - 100				
2/7/86				58.5	55.7	0.72		W/M - 95				
2/8/86						0.67		W/M - 92.5				
						0.76		W/M - 106				
						0.80		W/M - 106				
						0.67		W/M - 110				
						0.60		W/M - 95		No		
2/14/86						0.72		W/M - 74		Yes		
2/14/86						0.60		W/M - 102		No		
						0.60		W/M - 74		No		

24

Table 52. NASA Lewis 8x6 MPS Test Matrix Summary (Continued).

Date	Blades	Hub Config.	Spacing	Pitch Angle, degrees		Mach No.	Angle-of-Attack, degrees	Speed Range, Percent	Data		Trav. Probe	Remarks
				Fwd	Aft				Perf.	Acous.		
2/15/86	F-7/A-7	8+8 (Rigid)	Maximum	58.5	55.7	0.72	0	W/M - 107	Yes	Yes	No	None
2/18/86			Nominal			0.76		W/M - 96	No	No		Data at Equal rpm and at ± 10% rpm
2/19/86						0.80		W/M - 105	Yes	Yes		Data at Equal Torque
2/20/86						0.72		W/M - 110	No	No		Blade Activity
2/21/86						0.80		W/M - 95	Yes	Yes		
2/22/86						0.76		W/M - 106	No	No		
						0.72		W/M - 105	Yes	Yes		
						0.80		W/M - 110	No	No		
						0.76		W/M - 105	Yes	Yes		
						0.67		W/M - 87	No	No		
						0.72		W/M - 106	Yes	Yes		
						0.80		W/M - 110	No	No		
						0.76		W/M - 110	Yes	Yes		
						0.67		W/M - 89	No	No		
						0.67		W/M - 105	Yes	Yes		
						0.72		W/M - 110	No	No		
						0.60		W/M - 110	Yes	Yes		
						0.85		W/M - 82	No	No		
						0.90		W/M - 110	Yes	Yes		
						0.80		W/M - 101	No	No		
						0.50		W/M - 83	Yes	Yes		
						0.50		W/M - 90	No	No		
						0.60		W/M - 90	Yes	Yes		
						0.80		W/M - 109	No	No		
						0.85		W/M - 114	Yes	Yes		
						0.90		W/M - 115	No	No		
						0.76		W/M - 75	Yes	Yes		
						0.80		W/M - 108	No	No		
						0.85		W/M - 115	Yes	Yes		
						0.90		W/M - 115	No	No		
3/1/86	F-7/A-7	8+8 (Rigid)	Nominal	58.5	55.7	0.72	0	W/M - 105	Yes	Yes	No	Matched rpm, Torque Runs
3/4/86							-2					
3/4/86							-4					
3/6/86							+4					
3/4/86	F-11C/A-11	11+9	Maximum	61.4	59.2	0.85	0	W/M - 101	Yes	Yes		Apparent Instability
3/4/86						0.90		W/M - 94	No	No		Possible Instability
3/6/86						0.72		83 - 93	Yes	Yes		High Stress (Forward Blades)

Table 52. NASA Lewis 8x6 MPS Test Matrix Summary (Continued).

Date	Blades	Hub Config.	Spacing	Pitch Angle, degrees		Mach No.	Angle-of-Attack, degrees	Speed Range, Percent	Data		Trav. Probe	Remarks
				Fwd	Aft				Perf.	Acous.		
3/6/86	F-11C/A-11	11+9	Maximum	57.8	55.9	0.76	0	90 - 95	Yes	Yes	No	High Stress (Aft Blades) High Stress (Aft Blades) Acoustic Plate Anomaly
3/6/86	F-11C/A-11	11+9	Maximum	60.3	58.2	0.80	0	86 - 95	No	No	New Afterbody ↓ Standard Body	
3/7/86	F-1/A-1	9+8	Nominal	57.2	54.3	0.72	0	W/M - 87	No	No		
3/8/86	F-1/A-3	0+0	Maximum	58.0	58.0	0.76	0	W/M - 105 W/M - 111	Yes	Yes		
3/10/86	Dummy	0+0	Maximum	N/A	N/A	0.67	0	W/M - 98 W/M - 103 W/M - 107 W/M - 98	No	No		
3/11/86						0.60		N/A				
3/12/86			Nominal			0.72						
3/13/86			Maximum			0.76						
3/14/86	F-21/A-21	11+10	Maximum	61.0	62.7	0.80		W/M - 90				New Forebody ↓ New Forebody
3/15/86	F-21/A-21	11+10	Maximum	61.8	61.2	0.80		W/M - 90 W/M - 88				
3/17/86	F-21C/A-21	11+10	Maximum	59.9	58.8	0.85		W/M - 88 W/M - 93				
3/19/86	F-21C/A-21	11+10	Maximum	59.9	58.8	0.80		W/M - 102 W/M - 97 W/M - 92 W/M - 98	Yes	Yes		
3/20/86						0.76		W/M - 102 W/M - 105				High Stresses (Forward Blades) High Stresses (Forward Blades)

Table 52. NASA Lewis 8x6 MPS Test Matrix Summary (Concluded).

Date	Blades	Hub Config.	Spacing	Pitch Angle, degrees		Mach No.	Angle-of-Attack, degrees	Speed Range, Percent	Data		Trav. Probe	Remarks
				Fwd	Aft				Perf.	Acous.		
3/20/86	F-21C/A-21	11+10	Maximum	60.2	61.6	0.80	0	W/H - 103	Yes	Yes	No	None
↓	↓	↓	↓	↓	↓	0.85	↓	W/H - 91	↓	No	↓	↓
3/21/86	↓	↓	↓	↓	↓	0.76	↓	W/H - 99	Yes	Yes	↓	↓
↓	↓	↓	↓	↓	↓	0.72	↓	W/H - 92	Yes	Yes	↓	↓
3/24/86	↓	↓	↓	↓	↓	0.80	↓	W/H - 94	No	No	↓	↓
↓	↓	↓	↓	↓	↓	0.76	↓	W/H - 100	Yes	Yes	↓	↓
↓	↓	↓	↓	↓	↓	0.72	↓	W/H - 91	Yes	Yes	↓	↓
↓	↓	↓	↓	↓	↓	0	↓	W/H - 91	No	No	↓	↓
3/25/86	Dummy	0+0	Nominal	↓	↓	0.50	↓	W/H - 100	↓	↓	↓	↓
↓	↓	↓	↓	↓	↓	0.80	↓	N/A	↓	↓	↓	↓
3/26/86	F-7/A-7	8+8 (Rigid)	↓	↓	↓	0.72	↓	↓	↓	↓	↓	↓
↓	↓	↓	↓	↓	↓	0.76	↓	↓	↓	↓	↓	↓
↓	↓	↓	↓	↓	↓	0.80	↓	↓	↓	↓	↓	↓
↓	↓	↓	↓	↓	↓	0	↓	W/H - 105	↓	↓	↓	↓
↓	↓	↓	↓	↓	↓	0.50	↓	W/H - 110	↓	↓	↓	↓
3/27/86	↓	↓	↓	↓	↓	0.80	↓	↓	↓	↓	↓	↓
↓	↓	↓	↓	↓	↓	0.85	↓	↓	↓	↓	↓	↓
↓	↓	↓	↓	↓	↓	0	↓	↓	↓	↓	↓	↓
↓	↓	↓	↓	↓	↓	0.50	↓	W/H	↓	↓	↓	↓
↓	↓	↓	↓	↓	↓	0.72	↓	W/H - 104	↓	↓	↓	↓
↓	↓	↓	↓	↓	↓	0.85	↓	W/H - 105	↓	↓	↓	↓
↓	↓	↓	↓	↓	↓	0	↓	↓	↓	↓	↓	↓
↓	↓	↓	↓	↓	↓	0.50	↓	↓	↓	↓	↓	↓
↓	↓	↓	↓	↓	↓	0.72	↓	↓	↓	↓	↓	↓
↓	↓	↓	↓	↓	↓	0.80	↓	W/H - 101	↓	↓	↓	↓
3/31/86	F-21C/A-21	11+10	Maximum	60.2	61.6	0.76	0	W/H - 92	Yes	Yes	No	Shutdown Anomaly Resulted in Damage to Blade
↓	↓	↓	↓	↓	↓	0.72	↓	W/H - 94	↓	↓	↓	New Afterbody
↓	↓	↓	↓	↓	↓	0	↓	W/H - 101	↓	↓	↓	↓
↓	↓	↓	↓	↓	↓	0.80	↓	W/H - 102	↓	↓	↓	↓
↓	↓	↓	↓	↓	↓	0.76	↓	W/H - 99	↓	↓	↓	↓
4/1/86	F-21C/A-21	11+10	Maximum	60.2	61.6	0.80	0	W/H - 102	Yes	No	No	New Afterbody; High Stresses
4/1/86	F-21C/A-21	11+10	Maximum	60.2	61.6	0.76	0	W/H - 99	Yes	No	No	New Afterbody and Blade Gages Removed

for the MPS hydraulic and lube support equipment. This was followed by a prestart check list and then a start up check list.

Various considerations regarding safe MPS operation in the wind tunnel facility led to the operational procedures outlined in Table 53, which were followed during testing. Check lists for normal shutdown procedures and postrun checks were also followed during the MPS testing in the NASA Lewis 8x6 high speed wind tunnel. More detailed information pertaining to all MPS SN003 check lists and procedures is available in the Task V report.

All aero performance data were acquired with the acoustic plate stowed near the ceiling of the test section. The acoustic data were obtained with the ceiling plate positioned at 0.3 blade diameter away from the rotor tips.

Table 53. MPS SN003 Operational Procedures for 8x6 Tunnel.

Item	Description
1	MPS Should be at Corrected Speed $\leq 60\%$ for any Angle-of-Attack Change
2	MPS Should be at Corrected Speed $\leq 60\%$ and at Angle-of-Attack = 0° for any Mach Number Change
3	A Facility Shutdown Should Always Activate an MPS Shutdown
4	MPS Start-Up Should Always Occur from a Windmill Condition
5	Always Check Console Thrust and Torque Displays After a Telemetry Override to Determine if Retuning is Required
6	If Telemetry is "Noisy," the Shutdown Limits may be set at High Level for Numbers 2 and 5 Bearings Temperatures, as Needed
7	Avoid Prolonged Operation at any Given Condition; Telemetry Noise seems to Affect Numbers 2 and 5 Bearings Temperatures more as Time-on-Point Progresses
8	Operation with Equal Speeds on both Rotors may Result in a High Vibe Situation at Certain Speeds; be Watchful for this, and if it Occurs, it Should be Possible to Relieve the Condition by Mismatching the Rotor Speeds by a Difference of 100 rpm to 400 rpm

5.3 The Rig 3/9x15 Low Speed Wind Tunnel

The MPS SN003 was tested in the NASA Lewis 9x15-ft low speed wind tunnel during the time period from October 1986 through March 1987, under Task V of NASA Contract NAS3-24080. The principal objective of the test program was to evaluate the low speed acoustic, aerodynamic, and aeromechanical performance of GE's counterrotating blade concepts. Effects of blade numbers, diameter, rotor-to-rotor spacing, and pitch angles on acoustic and aerodynamic performance were studied; installation effects (such as, pylon and simulated fuselage proximity) on performance were also investigated. Extensive acoustic measurements were made utilizing a specially designed polar traverse microphone. The majority of the testing was conducted at 0.2 Mach number for angles-of-attack between $\pm 16^\circ$.

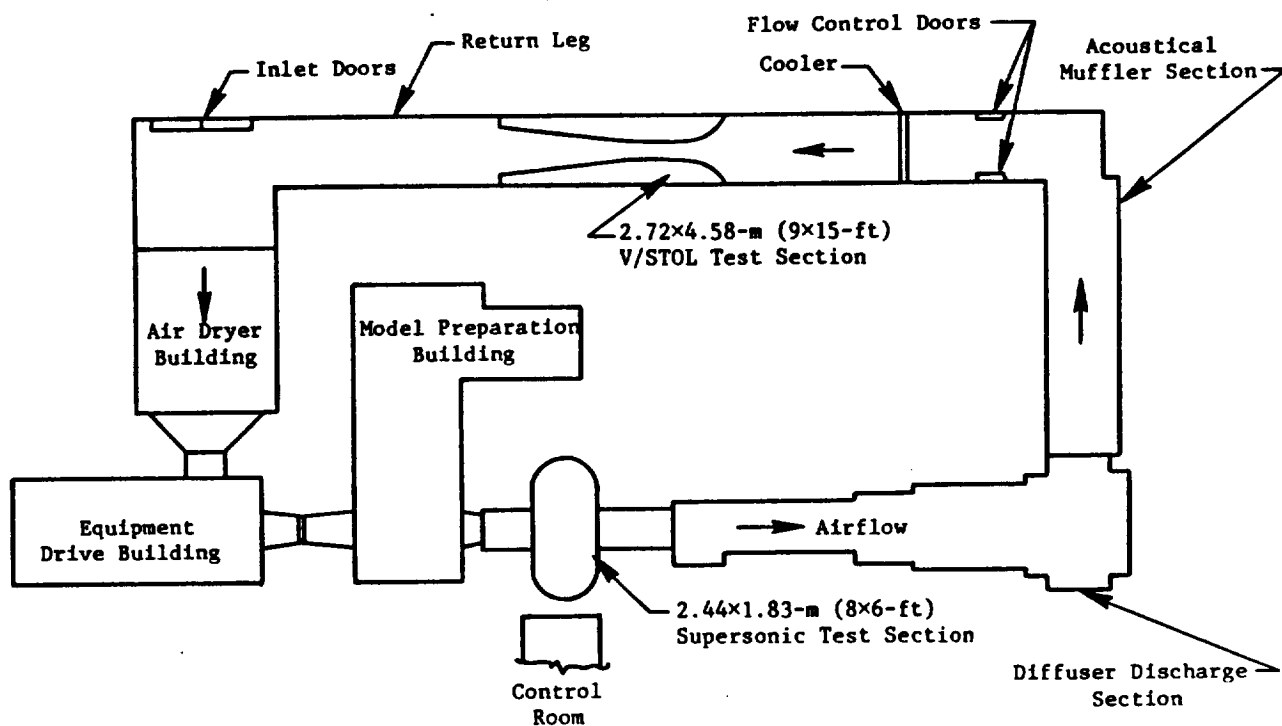


Figure 153. Schematic of the NASA Lewis 9×15 Wind Tunnel.

5.3.1 Facility Description

References 30 and 31 provides a detailed description of the NASA Lewis 9x15-foot low speed wind tunnel; however, in summary, the 9x15-foot low speed wind tunnel is located in the return leg of the 8x6-foot supersonic wind tunnel, as depicted in Figure 153. The area contraction ratio is 8:1, and the test section is 28.67-feet long. The test section wall diverges slightly to account for longitudinal boundary layer buildup. The cross-sectional dimensions are 9-foot high by 15-foot wide at Station 27.7, and 9-foot high by 15.25-foot wide at Station 56.3. The ceiling and floor are completely closed, but the side walls are 11% open, a result of four 4-in. slots which run the entire length of the test section. All four sides of the wind tunnel test section were treated acoustically to provide good quality acoustic data. The test section velocity (measured in feet per second) can be varied from a minimum of 50 ft/s to a maximum of 250 ft/s, which corresponds to a range of Mach numbers from 0.05 to 0.23.

5.3.2 Vehicle (MPS) Description and Instrumentation

A detailed description of MPS SN003 is given in Subsection 5.2.2 of this report. The major modifications to the test vehicle for utilization in the 9x15, however, consisted of changes in the support strut and the addition of a pylon and a fuselage to study the effect of their installation on the acoustic performance. Based on the experience gained in the 8x6 wind tunnel tests, significant changes were made to the lubrication system. These changes are addressed in the appropriate subsection that follow.

5.3.2.1 Mounting and Installation

The 9x15 wind tunnel support strut was essentially made of a circular pipe 8 inches in diameter, along with necessary fairings to give it an aerodynamic shape. The support strut was designed and fabricated by NASA Lewis and provided necessary attachment points to support the simulated fuselage and pylon, along with a specially designed polar traversing microphone. Turbine drive air supplies were routed through the inside of the pipe; the lube and instrumentation lines were routed on the outside of the support strut inside the aerodynamic fairings.

At the same height as the tunnel centerline (52 inches from the tunnel floor), the MPS centerline was offset by 2 feet from the centerline right, ALF (aft looking forward), of the tunnel toward one wall. The pivot point for angle-of-attack was located at model Station 254.60 (Tunnel Station 50.2).

A photograph of the isolated MPS installation in the 9x15 wind tunnel is presented (Figure 154); the MPS installation with the polar microphone, simulated fuselage, and pylon installed is shown in Figure 155. A schematic of the MPS installation in the 9x15 wind tunnel is also depicted in Figure 156.

5.3.2.2 Lubrication System Modifications

The lubrication fluid for the 9x15 testing was changed to MIL-L-23699. The scavenge pumps were removed from the lubrication cabinet, and all of the return lines from the model were connected to the deoiler. Scavenge was accomplished by vacuum. The number of transfer pumps from the deoiler to the supply tank was increased to three in order to accommodate all of the returning oil from the model flowing through the deoiler.

These modifications increased the reliability of the lube system, as the total number of pumps was reduced from nine to five. Scavenge efficiency also improved significantly, which reduced the leakage of oil into the wind tunnel. Figure 157 demonstrates, schematically, the modified lubrication system.

5.3.2.3 Instrumentation

Such performance instrumentation as: the pressures, temperatures, forces and moments, rotor speeds; and safety and health instrumentation such as, the vibration monitoring accelerometers and blade strain gauges were basically the same as for the 8x6 wind tunnel tests. A detailed description is contained in Section 5.2.2.8 of this report.

All significant changes to the instrumentation were related to acoustic parameters, since the major objective of the 9x15 testing placed emphasis on low speed acoustics.

5.3.2.3.1 Acoustic Instrumentation

Acoustic instrumentation for 9x15 MPS testing consisted of:

- Two Arrays of Fixed Microphones (five, each array)
- Two Linear-Traversing Microphones
- One Polar-Traverse Microphone.

The two arrays of fixed microphones, consisting of five microphones each, were mounted on the floor and the near wall. All microphones were staggered to avoid interference from the shed vortices of the leading microphones. The arrangement of the fixed microphones is shown in Figure 158. The

ORIGINAL PAGE
BLACK AND WHITE PHOTOGRAPH

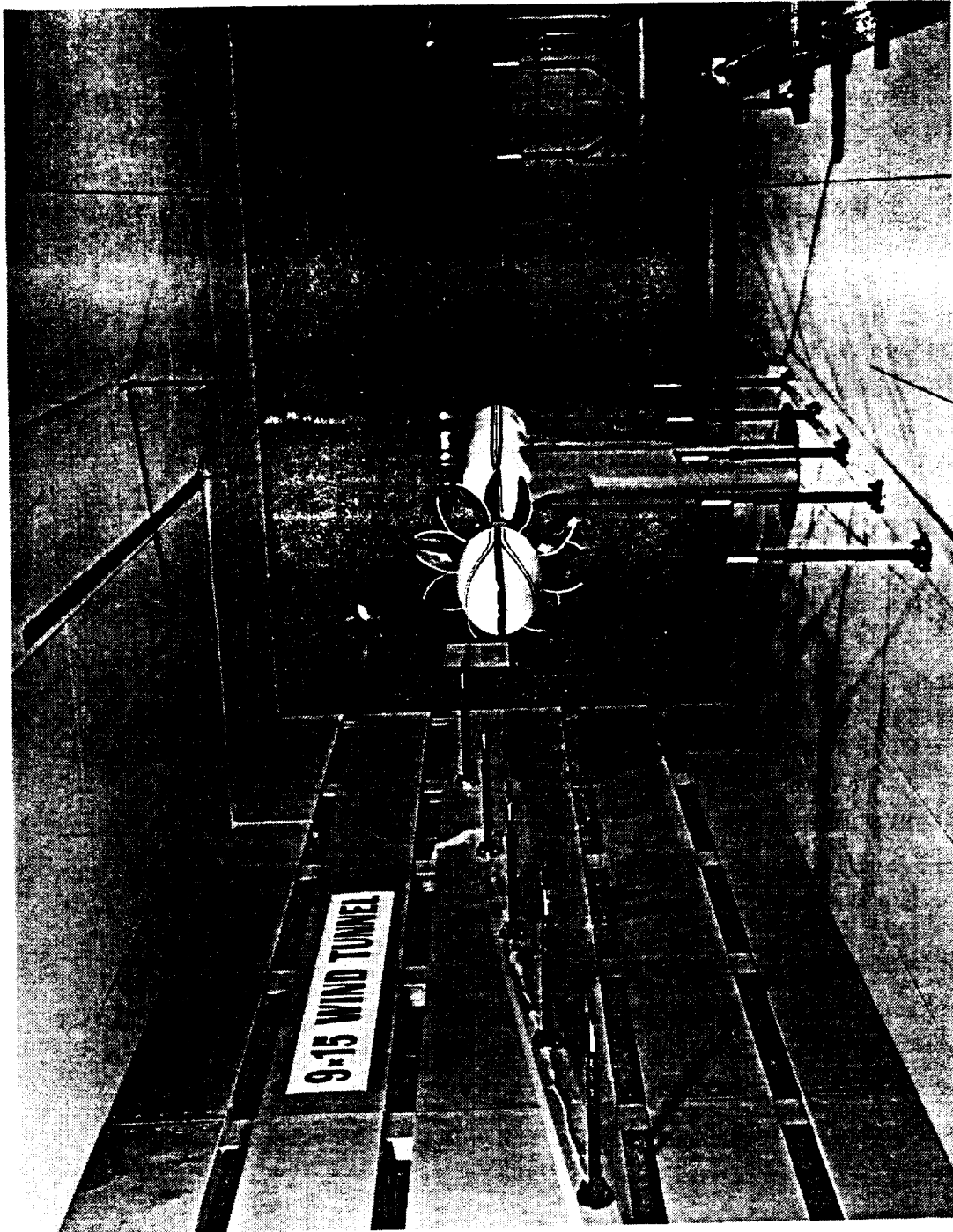


Figure 154. MPS Installation in 9x15 Wind Tunnel.

ORIGINAL PAGE IS
OF POOR QUALITY

ORIGINAL PAGE
BLACK AND WHITE PHOTOGRAPH

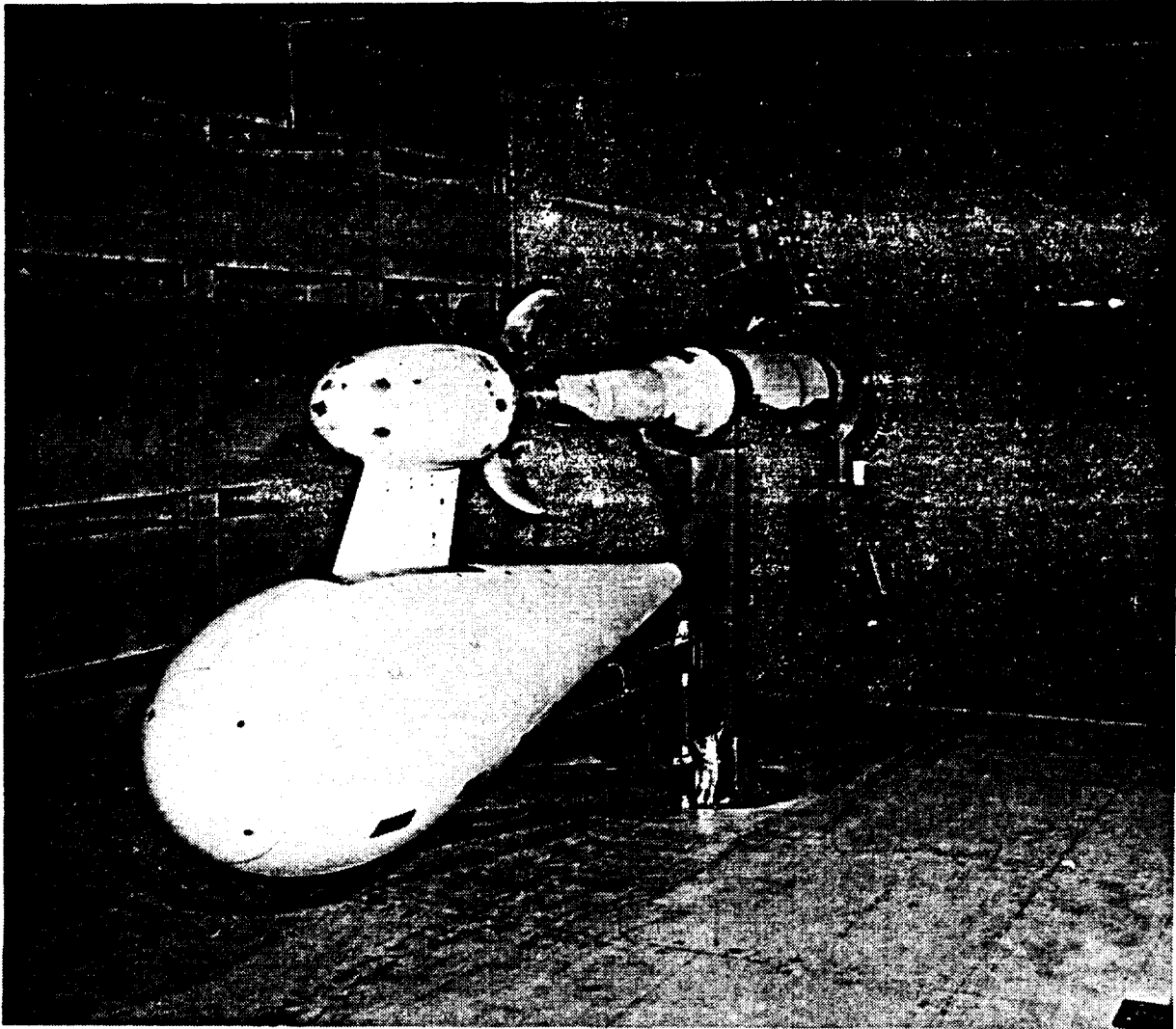


Figure 155. The MPS in 9×15 Wind Tunnel, with Pylon, Fuselage, and Polar Microphone.

ORIGINAL PAGE IS
OF POOR QUALITY

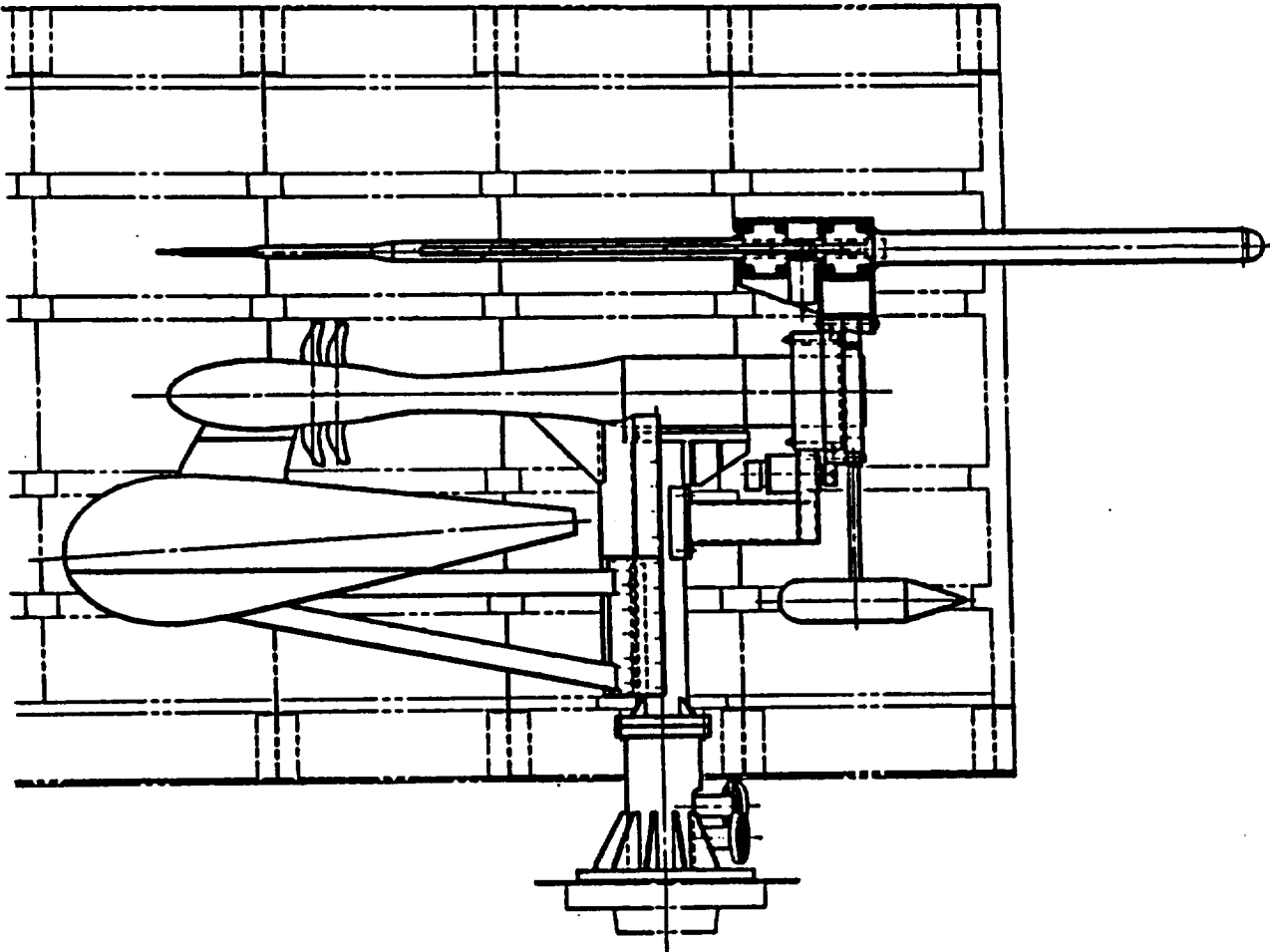


Figure 156. Schematic of MPS Installation in the 9x15 Tunnel.

o Side Wall

● Floor

All Dimensions Listed in Inches

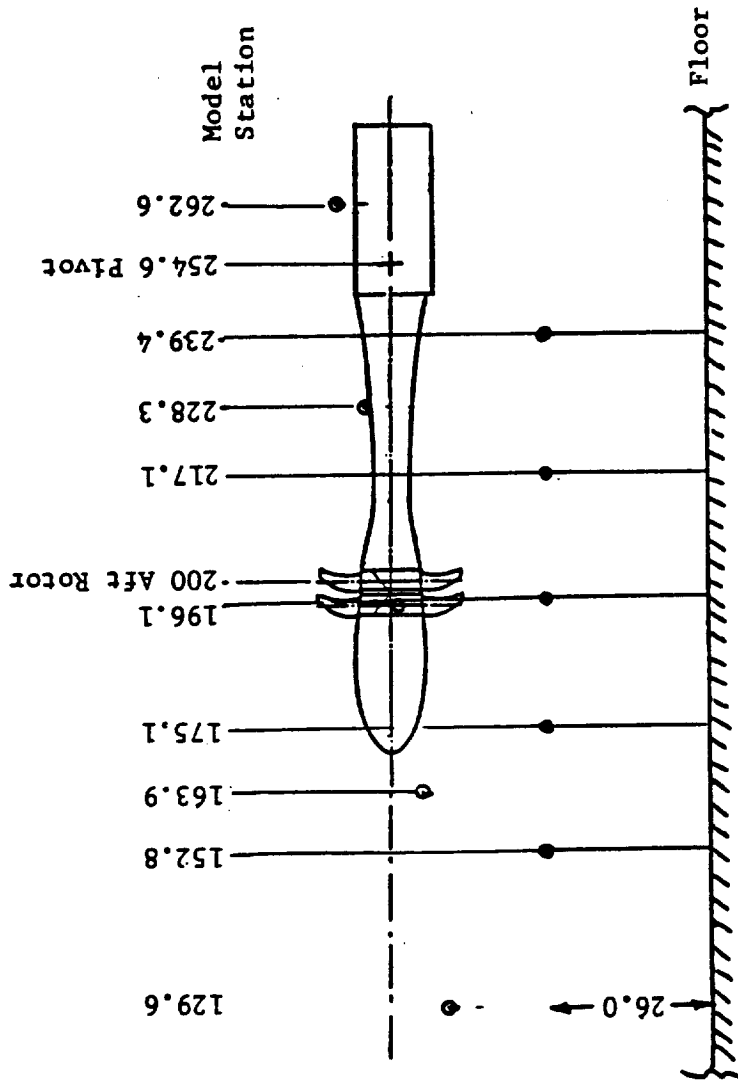
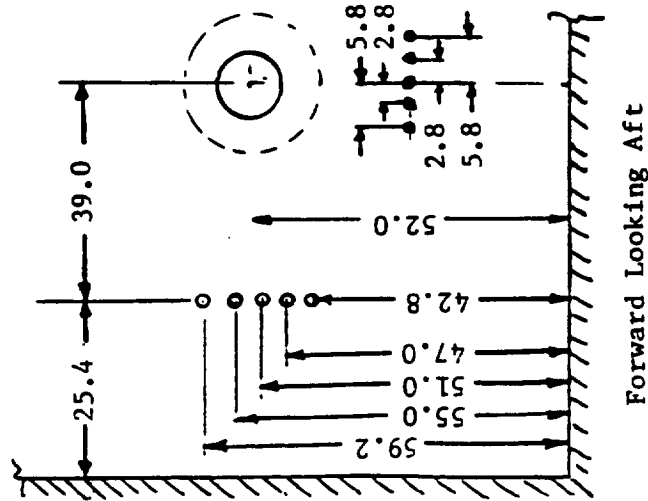


Figure 158. The NASA Lewis 9x15 Low Speed Wind Tunnel Fixed Microphone Installation.

near-wall microphones were removed after installation of the polar microphone, because the polar microphone boom interfered with the near-wall microphones at model angles-of-attack exceeding + 12°. The floor microphones were removed prior to testing with the simulated pylon and fuselage because these microphones interfered with the installation of this hardware.

The two linear-traversing microphones traveled along the length of the tunnel floor parallel to the MPS centerline at a 0° angle-of-attack. These microphones were located at a height of 1-inch below the model centerline. Both of the traversing microphones were mounted on the same traverse post and traversed at distances of 54 inches and 66 inches from the model centerline, between the model and the far wall. A schematic of the linear-traversing microphone installation is provided in Figure 159.

The polar-traverse microphone was mounted on the model and traversed at a fixed radius of 2 feet from the model centerline. Circumferential travel was limited to approximately 240°, and the axial position of the traverse varied. Axial traverse of the polar microphone was parallel to the model axis at all angles-of-attack and was limited to 51.2 inches (from model Station 174.4 to model Station 225.6). A schematic of the polar microphone installation is illustrated in Figure 160.

During the test program, limited data were acquired using blade-mounted kulites with specially instrumented blades. These blade-mounted kulite data were telemetered through the dynamic blade strain transmitters and replaced selected dynamic strain-gauge instrumentation.

5.3.3 Test Matrix Summary

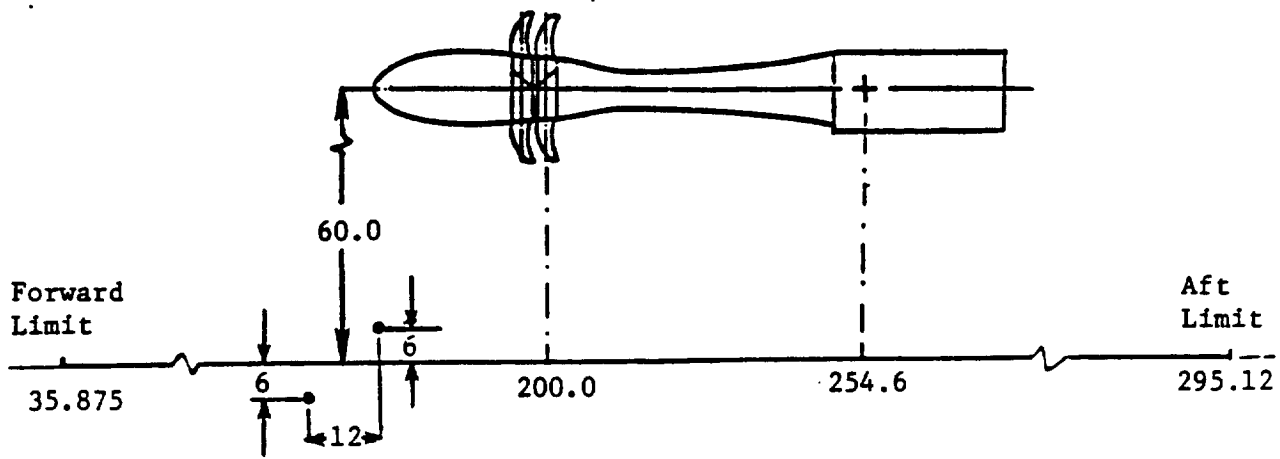
The 9x15 wind tunnel MPS test was performed using F-7/A-7, F-7/A-3, and F-11/A-11 blade configurations. All of the test coverage and data analysis associated with the F-7/A-3 testing were conducted using noncontract funding. Additional reverse-thrust testing was performed both on F-7/A-7 and F-1/A-7 blade configurations. All associated test coverage and data analysis for the F-1/A-7 were executed using noncontract funding.

Any data presented in this document related to testing covered by noncontract funding is provided for reference purposes only. Table 54 summarizes the major test configurations and their objectives. A detailed summary of the acoustic and performance testing conducted in the 9x15 wind tunnel is also presented (Table 55).

5.3.4 Test Procedures

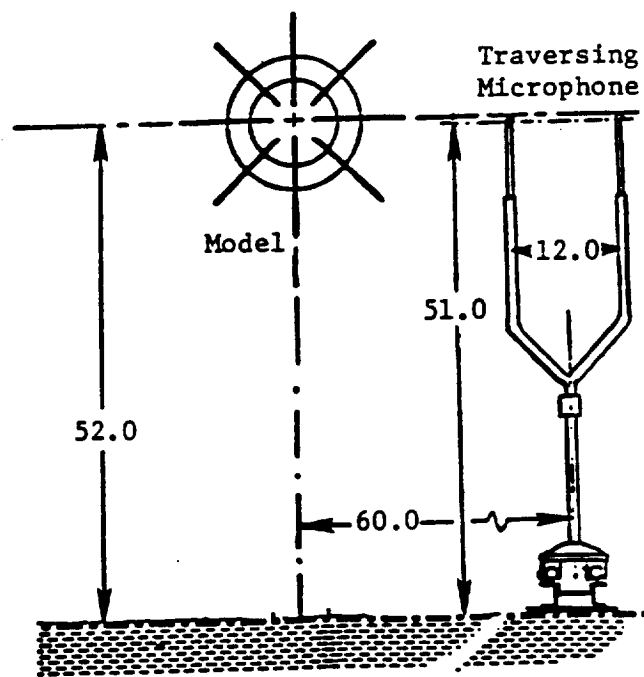
Test procedures for the 9x15 low speed wind tunnel tests were identical to the 8x6 high speed test procedures previously described (Section 5.2.4).

All of the aerodynamic performance data were acquired with the linear-traversing microphone stowed at the far downstream position of the test section. Similarly, the polar microphone was fully retracted, and the microphone was located at the bottom-most-position possible in the counter-clockwise direction (forward looking aft). This ensured that any effect of the polar and linear-traversing microphones remained the same for all of the aero performance data acquired.



Plan View

All Dimensions Listed in Inches



View, Forward Looking Aft

Figure 159. Schematic of Traversing Microphone Installation in NASA Lewis 9x15 Low Speed Wind Tunnel.

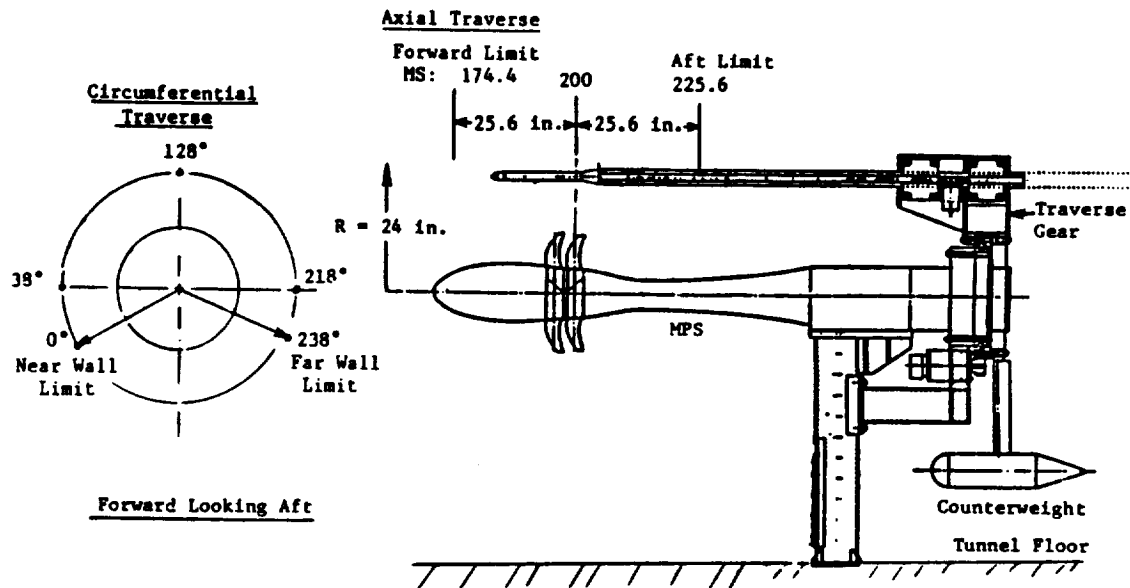


Figure 160. The NASA Lewis 9x15 Low Speed Wind Tunnel Polar Microphone Installation Schematic.

Table 54. Summary of 9x15 MPS Test Configurations.

No.	Blade Type	Hub Configuration	Spacing	Pylon + Fuselage	Objectives*
1	F-7/A-7	8+8	Nominal	No	Baseline Test Configuration
2	↓	↓	Maximum	No	Effect of Spacing
3	↓	↓	Maximum	Yes	Installation Effect
4	↓	11+9	Maximum	No	Effect of Spacing
5	↓	↓	Nominal		Plus Differential
6	↓	↓	Minimum		No. of Blades
7	F-7/A-3	11+9	Maximum	No	Effects of Spacing
8	↓	↓	Nominal		Plus Reduced Aft
9	↓	↓	Minimum		Rotor Diameter
10	F-11/A-11	11+9	Maximum	No	Effect of Wide Chord Blades
11	F-7/A-7	11+9	Maximum	Yes	Installation Effect
12	F-7/A-3	11+9	Maximum	Yes	Installation Effect

* All Blade Configurations were Investigated for Effect of Loading

Table 55. NASA Lewis 9x15 Test Matrix.

NASA Run No. Data Points	Date	Configuration/Spacing ¹	Blade Angle Degrees		Mach Number	Angle-of- Attack, Degrees	Data Points Corrected Speeds			Results
			Fwd	AR			Perf.	Polar	Traverse	
1-16-(28-373)	9/12/86	F-0/A-0/5.90 in.	—	—	0.2,0.15,0.1	0	X			Balance Calibration
16-18(390-468)	9/15/86	→	→	→	0.1,0.2	0	X			Blades Off Clean
19-22(472-570)	9/15/86	→	→	→	0.1,0.2	0	X			Reference Drag Runs
24(589-640)	9/17/86	→	→	→	0.1	0		X		Fixed Microphone Installed
25(652-699)	9/19/86	→	→	→	0.2	0			X	
26-43(711-1042)	11/7/86	F-17/A-7 8+8/4.2 in.	36.6	37.4	0.20	+8,+16.0 -8,-16	W/M-97		65,70,75,80 85,90,95	First Performance Runs
44(1077-1088)	11/13/86	→	→	→	0.10	0	W/M-88			Balance Calibration Runs
45(1095-1119)	11/17/86	→	→	→	0.20	0	W/M-80			High Vibration
46(1121-1131)	11/18/86	→	→	→	0.20	0	W/M-90		65,70,75,80 85,90,95	
47(1135-1198)	11/20/86	→	→	→	0.18	0	W/M-95			
48-54(1207-1407)	12/3/86	F-0/A-0/5.9 in.	36.2	35.4	0.20	+8,+16 -8,-16	W/M-88 W/M-80 W/M-90 W/M-95 W/M-96 W/M-79	X	65,75 85,95	Blades Off Reference Drag with Polar Microphone
55(1418-1482)	12/16/86	→	→	→	0.20	0,+8,-8	W/M-95	X		Nominal Loading 0.2 Mach
56(1437-1465)	12/17/86	→	→	→	0.20	0	W/M-95		65,70,75,80 85,90,95	
57(1467-1497)	12/18/86	→	→	→	0.20	+8	→	→	80,90 80,90 80,90 809,90	Higher Loading 0.2 Mach
58(1499-1512)	12/19/86	→	→	→	0.20	-8	→	→	80,90 80,90	Ref. Pitch Angles Call 41 Forward Thrust Signal Bad
			41.8	18.4	0.20	-16	W/M-90		70,75,80,85,90	
			41.8	18.4	0.20	-8,-16,+8	W/M-95		65,70,75,80 85,90,95	
			38.6	17.4	0.20	0	W/M-95			

¹Maximum = 5.90 inches; Nominal = 4.16 inches; Minimum = 3.14 inches

Table 55. NASA Lewis 9x15 Test Matrix (Continued).

NASA Run No. Data Points	Date	Configuration/Spacing ¹	Bleed Angle Degrees		Mach Number	Angle-of- Attack, Degrees	Data Points Corrected Speeds			Results
			Fwd	AR			Pert.	Polar	Traverse	
59(1529-1549)	1/7/87	F-11/A-11 11+9/5.9 in.	46.7	43.2	0.20	0,-8,-16	W/M-80	80	70,75,80	Lost Forward Thrust Signal
60(1553-1568)	1/8/87	F-11/A-11 11+9/5.9 in.	42.4	41.1	0.20	0,-16	W/M-88	80	70,75,80	Removed Near-Wall Fixed Mics; Lost Forward Thrust
61(1582-1599)	1/13/87	F-7/A-7 11+9/5.9 in.	41.1	39.4	0.20	0,-8,-16	W/M-85	80	75,80,85	Lost Forebody Pressure Module
62(1602-1626)	1/14/87					0,-8,-16	W/M-90	80	75,80,85	
63(1629-1634)	1/15/87					-16	W/M-85	80	75,80,85	
64(1637-1643)	1/16/87					+8	W/M-85	80	75,80,85	
65(1646-1662)	1/16/87					-8,+16	W/M-90	80	75,80,90	
66(1663-1678)	1/16/87		39.0	38.6		0	W/M-93			Reference Run (Cell 41), One Forward Blade Off By -4 Inch Pitch Setting
67-74(1680-1976)		F-0/A-0/5.9 in.			0	0	W/M-93			Balance Calibration Runs
75(1989-2004)	1/22/87	F-7/A-7 11+9/5.9 in.	39.0	38.6	0.20	0	W/M-93			Reference Run (Cell 41), Repeat Run
76(2005-2035)	1/22/87		36.4	36.5	0.20	-8,-16	W/M-95	80,90	70,80,90	Nominal Loading B's
77-78(2037-2065)	1/23/87	F-7/A-7 11+9/4.2 in.	36.4	36.5	0.20	0,+8,+16	W/M-95	80,90	70,80,90	Spacing Test
79-80(2068-2100)	1/24/87	F-7/A-7 11+9/3.3 in.	36.4	36.5	0.20	-16,-8,0,+8, +16	W/M-95	80,90	70,80,90	Spacing Test
81(2113-2124)	1/29/87	F-7/A-3 11+9/4.2 in.	36.4	40.3	0.20	0	W/M-95	80,90	70,80,90	Low FOA - Trial I
82(2126-2133)	1/30/87		36.4	41.7	0.20	0	W/M-90			Low FOA - Trial II
83(2134-2163)			36.4	43.5	0.20	0,-8,+8, -16,+16	W/M-95			Nominal Loading Final Pitch Angle
84(2166-2196)	1/31/87	F-7/A-3 11+9/3.34 in.	36.4	43.5	0.20	0,-8,-16, +8,+16	W/M-95	80,90	70,80,90	Spacing Test
85(2207-2232)	2/4/87	F-7/A-3 11+9/5.9 in.	36.4	43.5	0.20	0,-8,-16, +8,+16	W/M-95	80,90	70,80,90	Spacing Test
86(2234-2262)	2/5/87		41.1	46.4		0,-8,-16, +8,+16	W/M-90	80,90	70,80,90	Stress Limit at Ada = 16° and W/M; Removed Floor- Fixed Microphones
87(2265-2288)	2/6/87	Pylon On				0,-8,-12, +8,+12	W/M-90	80,85	70,80,85	
88(2291-2316)	2/9/87	Pylon and Fuselage On				0,-8,-12 +8,+12	W/M-90	80,85	70,80,85	
89(2321-2342)	2/10/87		42.5	45.4		0,-8,-12	W/M-90	80,85	70,80,85	-8° Torque Ratio Trial
89(2321-2342)	2/10/87		42.5	45.4		0,-8,-12	W/M-90	80,85	70,80,85	-85 Torque Ratio Trial
90(2343-2364)	2/10/87		43.8	44.4		0,-8,-12	W/M-90	80,85	70,80,85	-8° Torque Ratio
92(2379-2399)	2/11/87		39.9	48.0		0,+8,+12	W/M-90	80,85	70,80,85	+8° Torque Ratio

¹Minimum = 5.90 inches, Nominal = 4.16 inches, Maximum = 3.34 inch

Table 55. NASA Lewis 9x15 Test Matrix (Continued).

NASA Run No. Data Points	Date	Configuration/Spacing ¹ Pylon and Fuselage on	Blade Angle Degrees		Mech Number	Angle-of-Attack, Degrees	Data Points Corrected Speeds			Results
			Pwd	Aft			Perf.	Polar	Traverse	
93(2401-2423)	2/12/87	R-7/A-7 11+9/5.9 in. Pylon and Fuselage on	41.1	39.4	0.20	0, -8, -12, +8, +12	W/M-90	80,85	70,80,85	Effect of Pylon and Fuselage
94(2425-2447)	2/13/87		43.8	37.5	↓	0, -8, -12	W/M-90	80,85	70,80,85	-8° Torque Ratio
95(2455-2475)	2/17/87		39.9	41.3	↓	0, +8, +12	W/M-90	80,85	70,80,85	+8° Torque Ratio
96-102(2477-2676)	2/18/87	R-0/A-0/5.9 in. Pylon and Fuselage on	—	—	0.20	0, -8, -16, +8, +16	X	X	X	Reference Drag Pylon Plus Fuselage
103(2679-2695)	2/19/87		41.8	38.4	0.10	0	W/M-90	80,90	70,75,80, 85,90	
104(2697-2722)	2/20/87	R-7/A-7 8+8/5.9 in. Pylon and Fuselage on	43.0	37.1	↓	0, -8, -12	W/M-90	80,90	70,75,80, 85,90	-8° Torque Ratio
106(2726-2753)	2/20/87		40.4	39.9	↓	0, +8, +12	W/M-90	80,90	70,75,80, 85,90	+8° Torque Ratio
107(2757-2773)	2/23/87	R-7/A-7 8+8/5.9 in. Pylon and Fuselage Off	36.2	35.4	0.20	0, +16	W/M-95	80,90	70,75,80 85,90	Higher Loading Air Pitch Angles at Maximum Spacing
108(2774-2795)			38.4	38.4	↓	0	W/M-95	80,90	70,75,80, 85,90	Acoustic Comparison
109(2796-2813)			41.4	41.4	↓	0	W/M-90	80,90	70,75,80, 85,90	↓
110(2815-2824)	2/24/87		38.6	37.4	0.20	0	W/M-95	80,90	70,75,80 85,90	Acoustic Test Cell 41 Reference Pitch Angles at Maximum Spacing
2825-2842)					0.19	0	W/M-95			
2843-2859)					0.20	0	W/M-95			
2860-2876)					0.21	0	W/M-95			
110-115(2880-3032)	2/25/87	R-0/A-0/5.9 in.			0.20	0	X	X	X	Ref Drag with Polar Microphone
116-120(3033-3203)					0.20	0	X	X	X	Ref Drag Without Polar Microphone
121-124(3205-3276)					0	0	W/M-91			Air Balance Cal. Checks
125(3279-3292)	2/28/87	R-7/A-7 8+8/5.9 in.	38.6	37.4	0.20	0	W/M-91			Perf. Run - Cell 41 Ref.
3293-3305)					0.19	0	W/M-91			
3306-3317)					0.21	0	W/M-91			
126(3318-3353)			41.8	38.4	0.20	0, -8, -16 +8, +16	W/M-90		70,75,80 85,90	D/NW Comparison
127(3360-3369)	3/3/87	R-7/A-7 8+8/4.16 in.	37.1	36.5	0.22	0	W/M-95		70,75,80, 85,90	
3370-3378)			↓	↓	0.20	0	W/M-95			

¹Minimum = 5.90 inches; Nominal = 4.16 inches; Maximum = 3.34 inches

Table 55. NASA Lewis 9x15 Test Matrix (Concluded).

NASA Run No. Data Points	Date	Configuration/Speeding ¹	Blade Angle Degrees		Mach Number	Angle-of- Attack, Degrees	Data Points Corrected Speeds			Results	
			Fwd	Aft			Perf.	Polar	Traverse		
128(3382-3397)	3/3/87	F-7/A-7 8+8 4.16 in.	38.6	37.4	0.20	0	W/M-95			70,75,80, 85,90	Repeat Run - Cell 41 Ref.
(3399-3414)	↓		-21.8	-21.8	0	0	65-95			70,80,90	Begin Reverse Thrust Tests at Demo Lima Pitch Angles
130(3416-3430)	3/4/87		↓	↓	0.10	0	W/M-93			70,80,90	
131(3431-3449)	↓		↓	↓	0.20	0	W/M-95			70,80,90	
132(3451-3460)	↓		↓	-24.1	0.10	0	70-90			70,80,90	0.1 Mach Target Thrust Damaged 7 F-7 Blades
133(3463-3471)	3/5/87	F-7/A-7 8+8 4.16 in.	-8.4	-18.5	0.20	0	75-84			70,80	Trial Run F-7/A-7
134(3475-3488)	3/6/87		-21.8	-21.8	0	0	65-94			70,80,94	Reference to F-7/A-7
135(1489-3503)	↓		-15.0	↓	0.20	0	65-87			70,80,87	0.2 Mach Target Thrust
136(3504-3517)	↓		-13.5	↓	0.20	0	66-85			70,80,85	
137(3519-3529)	3/7/87		8.6	↓	0	0	65-90			80,90	Reverse Thrust Capabilities, Forward Rotor Feathered
(3530-3540)	↓		↓	↓	0.10	0	65-90			80,90	
(3541-3546)	↓		↓	↓	0.20	0	28-52				
138(3547-3555)	↓		-18.0	↓	0.10	0	70-90			70,80,90	
(3556-3561)	↓		-18.0	↓	0.20	0	24-54				
139(3562-3584)	↓		↓	-12.0	0.20	0	30-85			70,80	
140(3586-3599)	3/9/87		0	0	0.10	0	70-80				Flat Pitch to Eyebase, Reverse Thrust and Power- Absorbing Capabilities
(3600-3613)	↓		↓	↓	0.20	0	70,86				
(3614-3617)	↓		↓	↓	0.15	0	76				
141(3618-3626)	↓		-21.8	8.6	0.10	0	60-68			68	Reverse Thrust with Aft Rotor Feathered High Stress Encountered on Way to 0.2
142(3629-3646)	3/10/87		-21.8	-24.3	0.10	0	62-90			90	0.1 Mach Target Thrust Trial
143(3647-3671)	↓		-23.0	-23.0	0	0	59-86			80	Static Target Thrust Trial
144(3672-3687)	↓		-23.0	-26.5	0.10	0	65-85			80	Final - 0.1 Mach Target
145(3688-3711)	↓		-23.0	-24.5	0	0	65-90			80	Final - Static Target Matched Torques and Speed
146(3712-3732)	↓		166.5	138.2	0.20	0	28-60				Reverse Thrust Feather-Max Reverse Thrust Capabilities Exploratory Study
147(3735-3751)	3/11/87		↓	↓	0.10	0	31-56			56	
(3752-3763)	↓		↓	↓	0.20	0	41-63			58	
(3764-3776)	↓		↓	↓	0	0	25-60			60	
148(3777-3785)	↓		150.0	↓	0.20	0	36-46	48			
(3786-3790)	↓		↓	↓	0.10	0	31-38			36	
(3791-3802)	↓		↓	↓	0	0	36-62			60	Final Balance Calibration
149-153(3806-4347)	3/13/87	F-7/A-7 8+8 4.16 in.	↓	↓	0	0					

¹Minimum = 5.90 inches, Nominal = 4.16 inches, Maximum = 3.34 inches

6.0 DATA ACQUISITION, REDUCTION, AND ANALYSIS

6.1 Anechoic Freejet Facility (Cell 41 with MPS Rig 2)

6.1.1 Acoustics

As was previously discussed (Section 5.1), all experimental measurements pertaining to Task IV of this program were conducted in GE's anechoic freejet facility (Cell 41). Descriptions and results of the tests conducted in order to determine the acoustic characteristics of the anechoic chamber, as well as the mean velocity and turbulence intensity distributions in the freejet are presented in internal GE reports (R81AEG212 and TM 84-597 by P.G. Vogt and B.A. Janardan, respectively).

Figure 161 is a schematic of the fixed microphone locations within the anechoic chamber. The angular positions and radial distances of each of these microphones, relative to the axial midpoint between nominally spaced rotors, ($X/Dt = 0.169$) are also tabulated in this figure.

6.1.1.1 Acoustic Data Acquisition and Reduction

A flow chart (Figure 162) illustrates the acoustic data acquisition and reduction system which has been optimized for obtaining acoustic data up to 40-kHz, 1/3-octave-band center frequency. The microphones used to obtain the data are the B&K 4133, 12.5 cm (0.5 in.) condenser microphones with microphone grid caps. The cathode followers utilized in the chamber are transistorized B&K 2639 with B&K 2807 dual-channel power supply.

The primary system employed for recording acoustic data is a 28-track Honeywell-96 FM recorder. The system is set up for wide-band Group I (intermediate band, double extended) at 1.524 mps (meters per second), which translates to 60 ips (inches per second), tape speed. Operating at this tape speed provides adequate dynamic range for obtaining the high frequency, low amplitude portion of the acoustic signal. The tape recorder is set up for +40% carrier deviation, with a recording level of 8-V peak-to-peak; during recording, the signal gain is adjusted to maximum without exceeding this 8-V level. Individual monitor scopes are used for observing signal characteristics during operation.

Standard data reduction is conducted in the IDR (instrumentation and data room) at GE Aircraft Engines. Data tapes are played back on a CDC3700B tape deck with electronics capable of reproducing signal characteristics within the specifications indicated for wide-band Groups I and II. Automatic shuttling control is incorporated in the system.

In the normal operation, a tone is inserted on the recorder in the time slot designed for data analysis. The tape control automatically shuttles the tape, initiating an "integration start" signal to the analyzer at the tone as the tape moves in its forward motion. This motion continues until a signal, indicating "integration complete" is received from the analyzer; at which time the tape direction is reversed, and the tape restarts at the tone in a forward direction advancing to the next channel to be analyzed until all channels have been processed. A time code generator is also implemented to signal the tape position of the readings as directed by the computer program control; upon completion of one reading, the tape is advanced to the next reading.

All 1/3-octave analyses are performed on a General Radio 1921 1/3-octave analyzer. Normal integration time is set for 16 seconds to ensure good interaction for the low frequency content. The analyzer has 1/3-octave filter sets from 12.5 Hz to 100 kHz and has a rated accuracy of $\pm 1/4$ dB in each band. Each data channel passes through an interface to the interdata computer; these data

Mic. No.	Radial R, m	Distance R, ft.	Angular Location θ , degrees
1	8.96	29.4	42.9
2	9.78	32.1	47.9
3	9.75	32.0	57.6
4	8.93	29.3	67.2
5	8.66	28.4	72.0
6	8.44	27.7	76.9
7	8.32	27.3	81.8
8	8.23	27.0	86.7
9	8.23	27.0	91.7
10	8.29	27.2	96.8
11	8.60	28.2	107.1
12	9.27	30.4	117.5
13	10.46	34.3	128.0
14	9.54	31.3	133.0
15	8.84	29.0	138.0
16	8.20	26.9	143.1
17	7.71	25.3	148.3
18	7.50	24.6	153.5

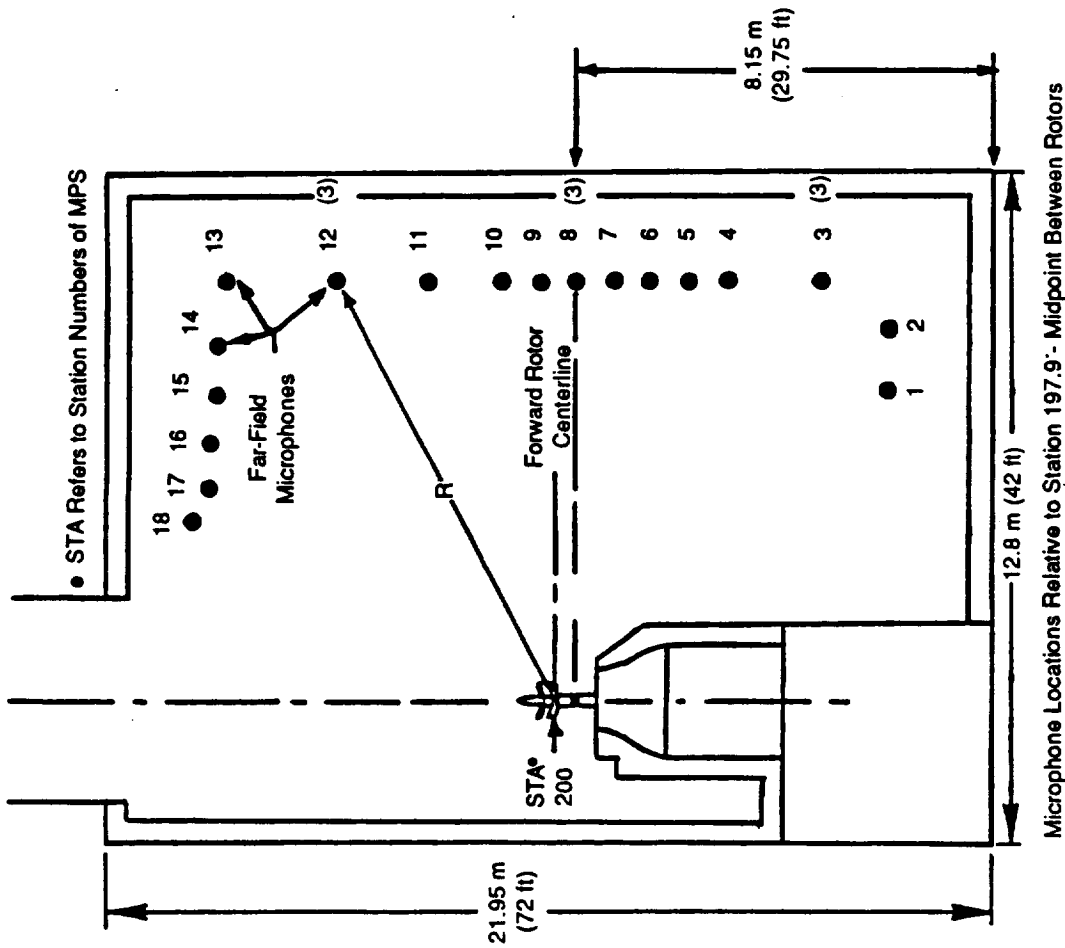


Figure 161. Locations of Fixed Microphones in the Anechoic Chamber, Cell 41.

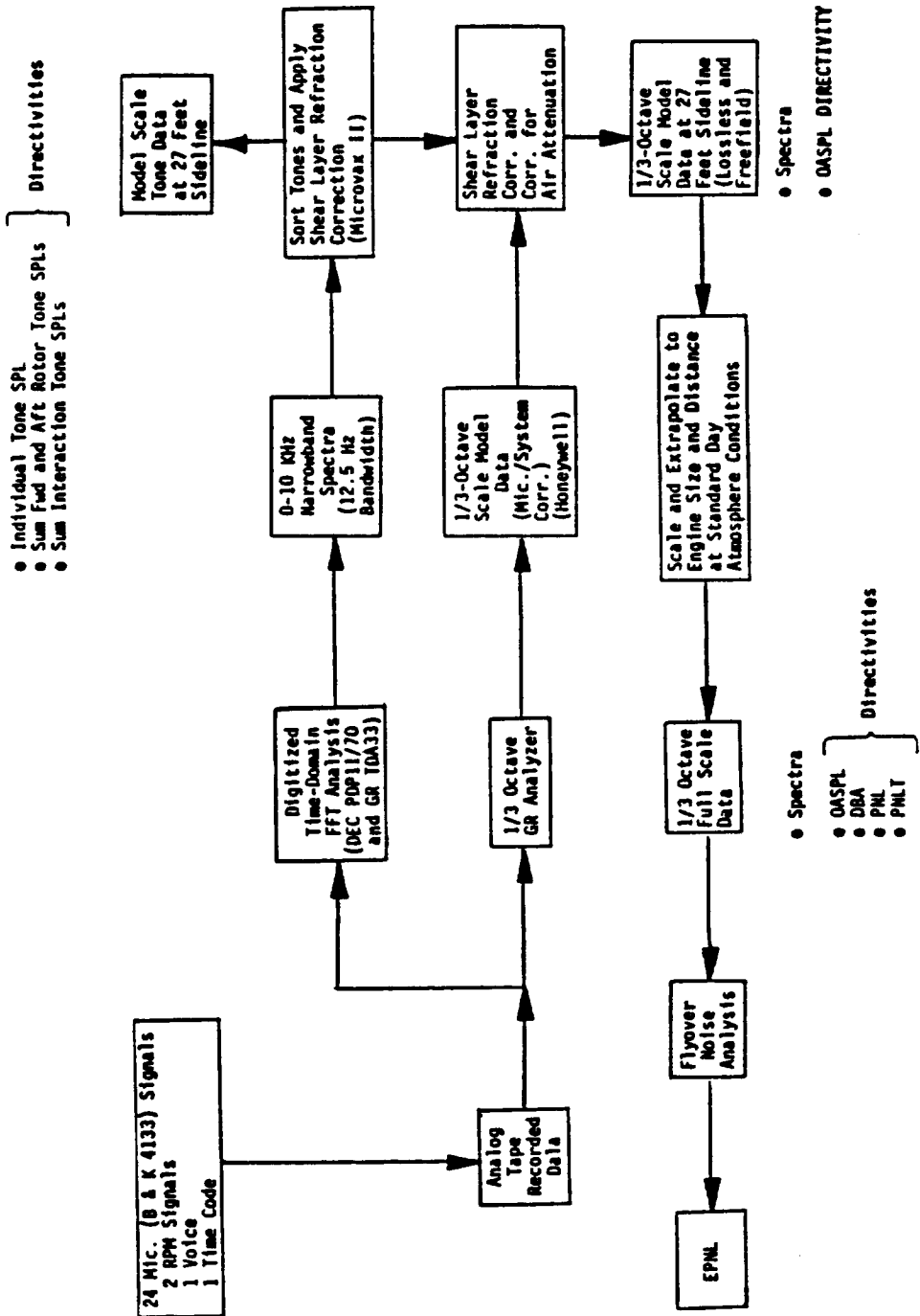


Figure 162. Acoustic Data Acquisition and Reduction Procedure at Cell 41.

are corrected for frequency responses of the microphones and recording and playback systems. The data then are sent to a Honeywell 6000 computer for further processing. This is accomplished by transmitting SPL (sound pressure level) data by means of a direct time-share link to the 6000 computer through a 1200-band modem. The Honeywell 6000 processes these data through the PANDA (Propulsion Aeroacoustic Noise Data Analysis) Program, and appropriate calculations are performed.

In the PANDA Program, scale model data are first corrected for background noise using the background noise spectra obtained with only the freejet at the required simulated flight velocity. Corrected scale model data are processed next through a transformation procedure to correct for shear-layer-refraction correction, using the shear-layer correction model of Reference 32 to obtain data representative of the noise produced in a wind tunnel. The Shields and Bass "pure tone method" (Reference 33) is used for all atmospheric attenuation corrections.

Next, the scale model data are scaled to the desired engine size using the scaling criteria evaluated in Section 3.2.1, and then these data are extrapolated to the required sideline distance. This procedure yields 1/3-octave band engine-scale spectra and OASPL, PNL, PNL_T, and dBA directivities at corresponding engine test conditions. A fly-over analysis of the engine-scale PNL_T-directivity results in providing the EPNL value.

For report purposes, the Cell 41-measured 1/3-octave band acoustic data were scaled to an engine size of 3.05 m (10 ft) and extrapolated to a fly-over sideline distance of 549 m (1800 ft).

6.1.1.2 Acoustic Narrow-Band Data

In addition, recorded analog acoustic data of selected test conditions at specified microphone locations are digitized through an FFT (Fast Fourier Transform) analyzer to obtain narrow-band spectra up to 10 kHz and with a bandwidth of 12.5 Hz. A demonstration of typical narrow-band spectra obtained with equal and unequal number of forward and aft rotor blades is presented as Figure 163.

Narrow-band spectral data next are processed in a MicroVax with an SST (sort and sum tones) program that sorts the sound pressure levels at the blade passing frequencies, and their harmonics of forward and aft rotors, and at the various interaction tones. Using the model of Reference 32, these sorted data are corrected for shear-layer-refraction correction to obtain representative tone data that would be measured in an anechoic wind tunnel. Corrected model-scale data are extrapolated to a reference 8.2-m (27-ft) sideline. Tone data then are available to obtain, for each of the processed points, model-scale directivities of:

1. Sound pressure levels of various individual tones (such as, F, A, 2F, F+A, 2A, 3F, 2F+A, F+2A, 3A,...).
2. The sum of the sound pressure levels at forward rotor blade passing frequency and harmonics (that is, F+2F+3F+4F...). This is the total steady-loading noise component associated with the forward rotor blades.
3. The sum of the sound pressure levels at aft rotor blade passing frequency and harmonics (for example, A+2A+3A+4A...). This is the total steady-loading noise component associated with aft rotor blades.
4. The sum of "b" and "c" (generally referred to herein as the sum of sound pressure levels corresponding to forward and aft rotor BPF's and harmonics); this is the total steady-loading noise.

5. Sum of sound pressure levels at all interaction tones; such as, $(A+F) + (2A+F) + (A+2F) + (\dots)$; herein referred to as aerodynamic rotor-to-rotor interaction noise or the unsteady-loading noise due to rotor-to-rotor interaction.

The above-described sums of various component noise levels can be obtained for test configurations when the frequencies of various tones are sufficiently separate in the narrow-band spectra. Such configurations are those having:

- An unequal number of blades rotating at equal rpm's
- An equal number of blades rotating at unequal rpm's.

Since significant numbers of tests were conducted with equal numbers of blades at equal rpm's, the following assumptions were made in obtaining their steady-loading noise and aerodynamic rotor-to-rotor interaction noise components:

- The SPL (sound pressure level) at the BPF's (blade passing frequencies) of equal blade number configuration is a measure of the steady-loading noise. This is generally true since, as was observed with data from unequal blade number configurations, the SPL's of the higher harmonics of the fundamental are lower than those of the fundamental by 6 dB to 15 dB or more over a range of emission angles ($60 < \theta_e < 120$).
- The summation of SPL's of all harmonics, excluding fundamental, for an equal blade number configuration at equal rpm's measures the total aerodynamic rotor-to-rotor interaction noise (herein referred to as rotor-to-rotor unsteady-loading noise). This is generally true since SPL's of steady-loading harmonics, as were observed from data with unequal blade number configurations, are much lower than those of the interaction tone levels.

To confirm the validity of these preceding assumptions, acoustic narrow-band data from test points of configurations with an unequal number of blades rotating at equal rpm's, and an equal number of blades rotating at unequal rpm's were processed using the SST program with and without these assumptions. Data for the two test cases are compared in Figures 164 and 165. A comparison for both the equal and unequal blade number configurations indicates that:

- The effect of neglecting the harmonics of BPF's of the forward and aft rotor on the steady-loading noise sum is within 0.5 dB
- The effect of including the SPL's of the harmonics of the BPF's of forward and aft rotors in the interaction noise sum level is also within 0.5 dB over most of the emission angles.

Based on these and other similar test cases, it was concluded that the assumptions made are qualitatively valid for the purpose of obtaining steady-loading and aerodynamic rotor-to-rotor interaction tone sum levels of equal blade number configurations at each rpm. Narrow-band data of such configurations were then processed to obtain steady-loading and aerodynamic rotor-to-rotor interaction (or unsteady) noise component levels.

6.1.1.3 Acoustic Test Results Analysis

The scale model tests conducted in Cell 41 with Rig 2 are summarized in Table 56; a total of 828 acoustic test points were performed, using four blade design configurations.

Model Scale; 8.2 m (27 ft); 0.25 M_0
 from 12.5 Hz Narrow-Band Data

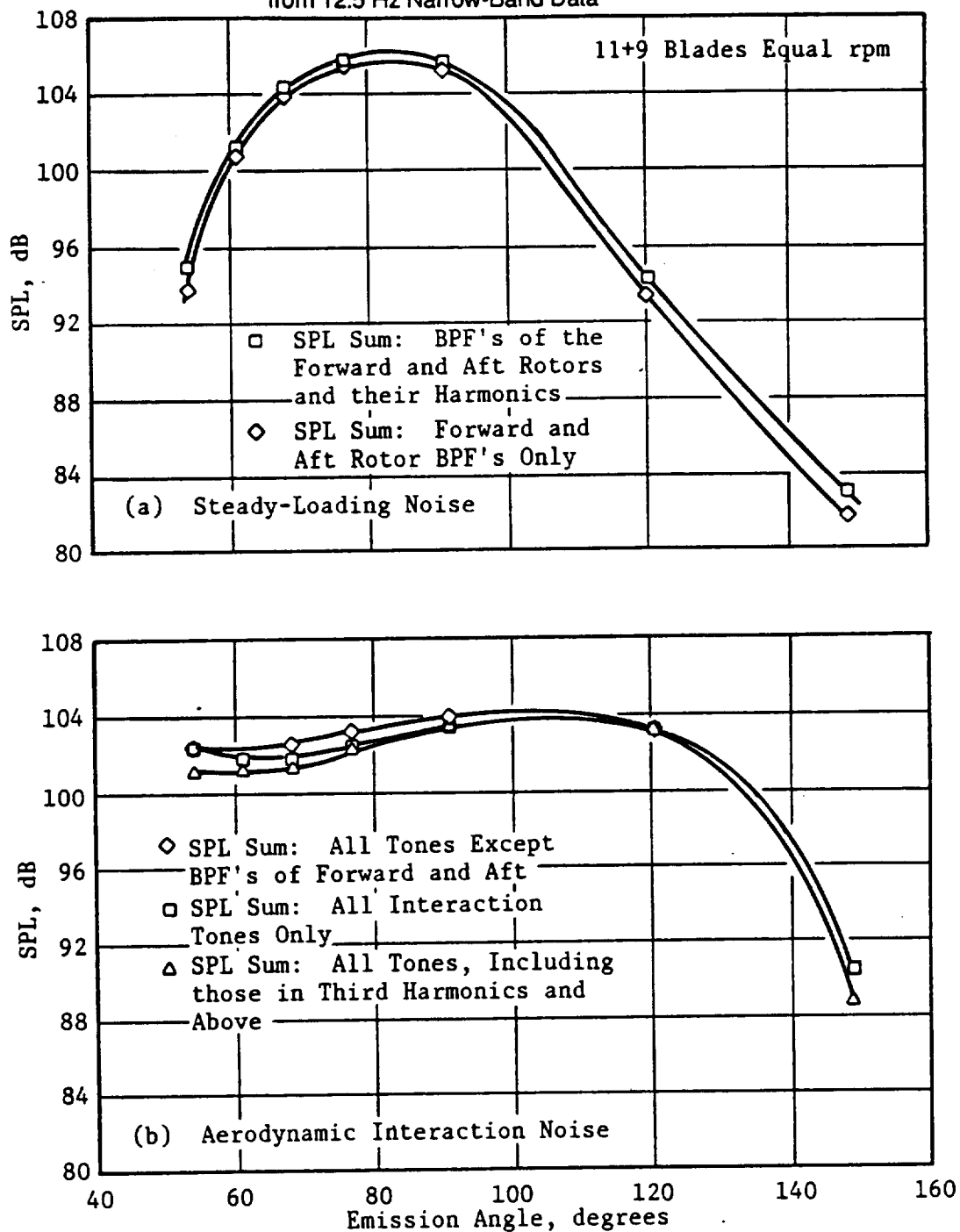


Figure 164. Comparison of Steady and Interaction Tones SPL Sums for Various Selected Tones of 11+9 Configuration.

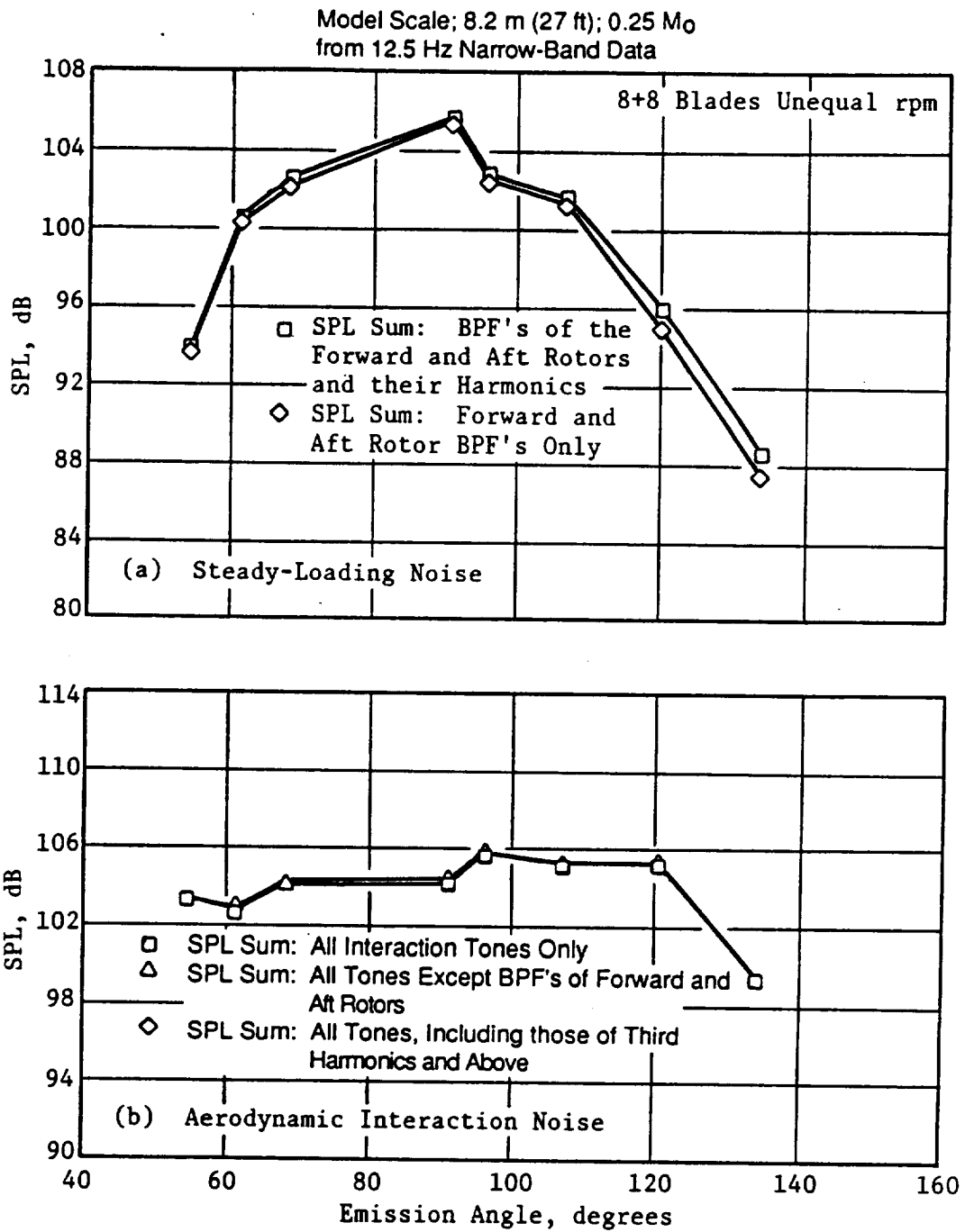


Figure 165. Comparison of Steady and Interaction Tones SPL Sums for Various Selected Tones of 8+8 Blade Configuration at Unequal rpm's.

Table 56. Configuration Summary of Acoustic Tests Conducted at Cell 41.

BLADE DESIGN	RUN NUMBER	BLADE NUMBER	AXIAL SPACING	PITCH ANGLE	PYLON SPACING	REMARKS	NO. TP
F5A5	4,5	8XB	NOM	38.4/37.6	NONE	EVALUATE BLADE	9
F7A7	11,12	8XB	NOM	37.9/37.4	NONE	EVALUATE BLADE LOADING, TIP SPEED, AND FLIGHT EFFECTS	23
	13			43.3/40.4			18
	14			36.0/35.2			11
	15			40.0/38.0			9
	16	8XB	NOM	53.9/40.4	NONE	FIXED FRONT ROTOR PITCH	11
	17			53.9/34.0			2
	18			34.5/51.4		FIXED AFT ROTOR PITCH	4
	19,20	8XB	NOM	37.9/37.4	CLOSE	EVALUATE PYLON EFFECT	23
	21	8X4	NOM	39.1/36.8	NONE	BLADE NUMBER AND DIFFERENTIAL BLADE NUMBER DIAGNOSTIC	23
	22	4X4	NOM	38.4/36.8			12
	23			37.9/37.4		AND PARAMETRIC STUDIES	22
	24			43.3/40.4			15
	25	9X4	NOM	39.5/37.2			
	26	9XB	NOM	38.4/37.4	NONE	DIFFERENTIAL BLADE NUMBER	7
	27	8XB	MAX	37.9/37.4	NONE	EVALUATE AXIAL SPACING	17
	28			43.3/40.4			28
	30	8XB	MAX	-16/-18	NONE	REVERSE THRUST	7
	31			-16/-16			8
	32	9XB	MAX	38.4/37.4	NONE	BLADE LOADING/TIP SPEED OPT.	26
	35			36.3/37.4			23
	37			41.8/41.4			26
	38	9XB	MAX	41.8/41.4	CLOSE	PYLON EFFECTS	15
	39			41.8/41.4	NOMINAL		15
	40	9XBC	MAX	41.8/41.4	NONE	CLIPPED AFT ROTOR STUDIES (TIP VORTEX)	25
	41			41.8/48.3			18
	42			36.3/37.4			11
	43			36.3/42.7		PYLON EFFECTS	8
	44			36.3/42.7	NOMINAL		
	45	9XBC	NOM	36.3/42.7	NONE	SPACING EFFECT ON TIP VRTX.	9
	46	9XBC	NOM	36.3/42.7	NOMINAL	PYLON EFFECTS	14

Table 56. Configuration Summary of Acoustic Tests Conducted at Cell 41 (Concluded).

BLADE DESIGN	RUN NUMBER	BLADE NUMBER	AXIAL SPACING	PITCH ANGLE	PYLON SPACING	REMARKS	NO. TP
F1A1	47	BXB	NOM	37.9/37.4	NONE	EVALUATE BLADE	26
	48			37.9/35.8			7
F7A7	95	BXB	NOM	37.9/37.4	NONE	REPEAT OF BASELINE RUN	12 20
TORQUE BLADES	96	BXB	NOM	37.9/37.4	NOM		18
	98			37.9/37.4		RUNS 01 AND 98 HAD	18
	101			33.8/32.4		GROUND PLANE AFFIXED	18
	102			33.8/32.4			6
	106			50.0/47.0			6
	108			52.0/44.0			11
	103,104			-17.6/-17.6		REVERSE THRUST	26
F11A11	94	11X9	MAX	44.8/43.3	NONE		13
	109			38.7/38.9		EVALUATE BLADE LOADING,	6
	110			48.7/45.3		TIP SPEED, AND FLIGHT	11
	111			52.6/47.5		EFFECTS	8
	112			54.2/47.5			8
	113	11X9	MAX	54.2/47.5	NOM SOUTH	PYLON EFFECTS	11
	139	11X9	SUPER MAX	48.7/45.3	NONE	DESIGN SPACING	18
	140			44.8/43.3			21
The following non-contract configurations are included here for reference only. Data from these tests are used in discussion of results in the contractor final report.							
F1A3	53	BXB	NOM	37.9/41.9	NONE	EVALUATE REDUCED	14
	54			43.3/45.3		DIAMETER AFT BLADE	14
F7A7	55	11X9	MAX	38.3/38.6	NOMINAL	INCREASED BLADE	14
	56			38.3/38.6	NONE	NUMBER EFFECT	9
	58			42.7/41.4	NONE		5
F7A3	60	11XB	MAX	36.4/42.5	NONE	EVALUATE REDUCED	10
	61,63			42.7/46.0	NONE	DIAMETER AFT BLADE	21
	62			42.7/46.0	NOMINAL		14

The majority of the tests were associated with the baseline F-7/A-7 blade design. However, in addition to conducting these tests with various F-7/A-7 blade number combinations to determine the effect of blade number on noise, a number of tests were performed using the baseline design to evaluate effects of rotor-to-rotor spacing, blade loading, tip speed, test Mach number, differential blade diameter, and the presence of a typical pylon at two spacings. The other blade designs that were tested under this program were the F-5/A-5, F-1/A-1, and F-11/A-11. Noncontract configurations of F-7/A-7 (11+9), F-7/A-3 (11+8) and F-1/A-3 (8+8) tested in Cell 41 are referenced later in this report during the discussion of test results.

6.1.2 Aerodynamic

The data reduction equations used to generate the aerodynamic performance parameters for Cell 41 are provided in an internal GE report (MPS 84-02 by G.E. Hoff). Nomenclature for the key performance parameters are listed and defined in Figure 166. Two corrections are applied for the calculation of net, ideal, and profile efficiencies, and for lift/drag. The first accounts for centrifugal force effects on balance thrust and torque output; the analytically developed corrections are presented as follows:

- $TORQUE_{correction} = 1/[1-0.000192(rpm/9000)^2]$
- $THRUST_{correction} = 1/[1-0.027(rpm/9000)^2]$.

The balance thrust and torque outputs are adjusted by multiplying them by the correction factors; these are then combined with the remaining components comprising the total thrust and torque for the efficiency determinations. The second adjustment compensates for the presence of strain gauge instrumentation on the propulsor blades during MPS testing. This correction is a scalar added directly to the net efficiency calculation; Figure 167 depicts the magnitude of this scalar which was determined during MPS SNO03 testing in the NASA Lewis 8x6 wind tunnel.

Table 57 lists the Cell 41 test configurations pertinent to data analysis for determining effects of disk loading, rotor-to-rotor spacing, blade design, blade clipping, number of blades per rotor, and pylon proximity on low speed aerodynamic performance.

6.1.3 Aeromechanics

MPS blades tested in Cell 41 were the 5, 7 (including the clipped version and torque blade), and 11 blade series. Except for the testing of the torque blades, which was uneventful, the reduced aeromechanical data from Cell 41 are presented in the CDR.

However, included herein are some typical Campbell diagrams (Figures 168 and 169) illustrating engine Gauge No. 1 for Blades F-5 and A-5, respectively, and from engine Gauge No. 1 for the clipped F-11 blade (Figure 170). Figures 171 through 173 are representative Campbell diagrams from engine Gauge No. 3 of the A-7 blade on the aeromechanical hub for a flutter and two nonflutter conditions. These figures (168 through 173) are intended to illustrate the typical format for reduced aeromechanical data. Discussions regarding the contents within the figures are presented in a later section of this report (Section 7.1.3).

6.2 Rig 3/NASA Lewis 8x6 Wind Tunnel

6.2.1 Aerodynamic

Rig 3 performance data acquired in the NASA Lewis 8x6 tunnel was for the F-7/A-7, F-11/A-11, and F-21/A-21 configurations. By comparing performance information for selectively

Parameter	Description	Units
BET1	Forward Rotor Pitch Angle	
BET2	Aft Rotor Pitch Angle	
ETAEF	MPS Scale Total Net Efficiency	
ETAFF1	MPS Scale Forward Rotor Net Efficiency	
ETAFF2	MPS Scale Aft Rotor Net Efficiency	
FEFCE	Engine-Scale Corrected Total Propeller Net Thrust	lb
FEFIC	MPS Scale Corrected Forward Rotor Propeller Net Thrust	lb
FEF2C	MPS Scale Corrected Aft Rotor Propeller Net Thrust	lb
J1	Forward Rotor Advance Ratio	lb
J2	Aft Rotor Advance Ratio	1/rev
M _o	Test Cell Freestream Mach Number	
PCNR1	Forward Rotor Percent Corrected Speed	
PCNR2	Aft Rotor Percent Corrected Speed	
PQA	Total Power Coefficient	
ShpCE	Engine-Scale Corrected Shaft Horsepower	hp
Shp1C	MPS Scale Corrected Forward Rotor Shaft Horsepower	hp
Shp2C	MPS Scale Corrected Aft Rotor Shaft Horsepower	hp
TRK2Q1	Torque Ratio (Aft/Forward)	
UTIC	MPS Forward Rotor Corrected Tip Speed	ft/second
Ideal Eff	MPS Scale, Total	
Profile Eff	MPS Scale, Total	
L/D	MPS Scale, Lift/Drag	
Net Eff	Full-Scale, Total	

No Centrifugal Straightening Corrections, Blade Surface-Mounted Strain Gauge Corrections, or Reynolds Number Scaling

Includes Centrifugal Straightening Corrections, Blade Surface-Mounted Strain Gauge Corrections; No Reynolds Number Scaling

Includes Centrifugal Straightening Corrections, Blade Surface-Mounted Strain Gauge Corrections, and Reynolds Number Scaling

Figure 166. Nomenclature for Cell 41 Performance Parameters.

Table 57. Cell 41 Test Configuration Summary for Aerodynamic Data Analysis.

Blades	Configuration	Beta 1	Beta 2	Spacing	Pylon
F-7/A-7	8+8	37.9	37.4	Maximum	Off
F-7/A-7	8+8	37.9	37.4	Nominal	
F-7/A-7	9+8	43.3	40.4	Maximum	
F-7/A-7	8+8	43.3	40.4	Nominal	
F-7/A-7	9+8	36.3	37.4	Maximum	
F-7/A-7	8+8	37.9	37.4	Maximum	
F-7/A-7	9+8	38.4	37.4	Nominal	Off
F-7/A-7	8+8	37.9	37.4	Nominal	
F-7/A-7	9+8	41.8	41.4	Maximum	
F-7/A-7	8+8	43.3	40.4		
F-7/A-7	11+9	38.3	38.6		
F-7/A-7	8+8	37.9	37.4		
F-7/A-7	11+9	42.7	41.4	Maximum	Off
F-7/A-7	8+8	43.3	40.4	Maximum	
F-1/A-1	8+8	37.9	37.4	Nominal	
F-7/A-7	8+8	37.9	37.4		
F-1/A-1	8+8	37.9	35.8		
F-7/A-7	8+8	37.9	37.4		
F-7/A-7c	9+8	36.3	42.7	Maximum	Off
F-7/A-7	9+8	36.3	37.4		
F-7/A-7c	9+8	41.8	48.3		
F-7/A-7	9+8	41.8	41.4		
F-7/A-3	11+8	36.4	42.5		
F-7/A-7	8+8	37.9	37.4	Nominal	Off
F-7/A-3	11+8	42.7	46.0	Maximum	Off
F-7/A-7	8+8	43.3	40.4	Maximum	
F-1/A-3	8+8	37.9	41.9	Nominal	Off
F-7/A-7	8+8	37.9	37.4		
F-1/A-3	8+8	43.3	45.3		
F-7/A-7	8+8	43.3	40.4		
F-7/A-7	9+8	41.8	41.4	Maximum	On
F-7/A-7	9+8	41.8	41.4		
F-7/A-7	11+9	38.3	38.6		
F-7/A-7	11+9	38.3	38.6		
F-7/A-7c	9+8	36.3	42.7		
F-7/A-7c	9+8	36.3	42.7		
F-7/A-3	11+8	42.7	46.0	Maximum	On
F-7/A-3	11+8	42.7	46.0	Maximum	On
F-7/A-7	8+8	36.0	35.2	Nominal	Off

Note: A-7c Indicates a 22% Span Clip

Table 57. Cell 41 Test Configuration Summary for Aerodynamic Data Analysis (Concluded).

Blades	Configuration	Beta 1	Beta 2	Spacing	Pylon
F-7/A-7	8+8	40.0	38.0	Nominal	Off
F-7/A-7	8+8	53.9	40.4		
F-7/A-7	8+8	53.9	34.0		
F-7/A-7	8+8	34.5	51.4		
F-7/A-7	8+8	50.0	47.0		
F-7/A-7	8+8	52.0	44.0		
F-7/A-7c	9+8	36.3	42.7	Nominal	Off
F-7/A-7c	9+8	36.3	42.7	Nominal	On
F-7/A-7c	9+8	41.8	41.4	Maximum	Off
F-7/A-7c	9+8	36.3	37.4		
F-11/A-11	11+9	38.7	38.9		
F-11/A-11	11+9	52.6	47.5		
F-11/A-11	11+9	54.2	47.5	Maximum	Off
F-11/A-11	11+9	54.2	47.5		On
F-11/A-11	11+9	44.8	43.3		Off
F-11/A-11	11+9	48.7	45.3		
F-11/A-11	11+9	44.8	43.3	Supermax	
F-11/A-11	11+9	48.7	45.3	Supermax	
F-5/A-5	8+8	38.4	37.6	Nominal	

Note: A-7c Indicates a 22% Span Clip

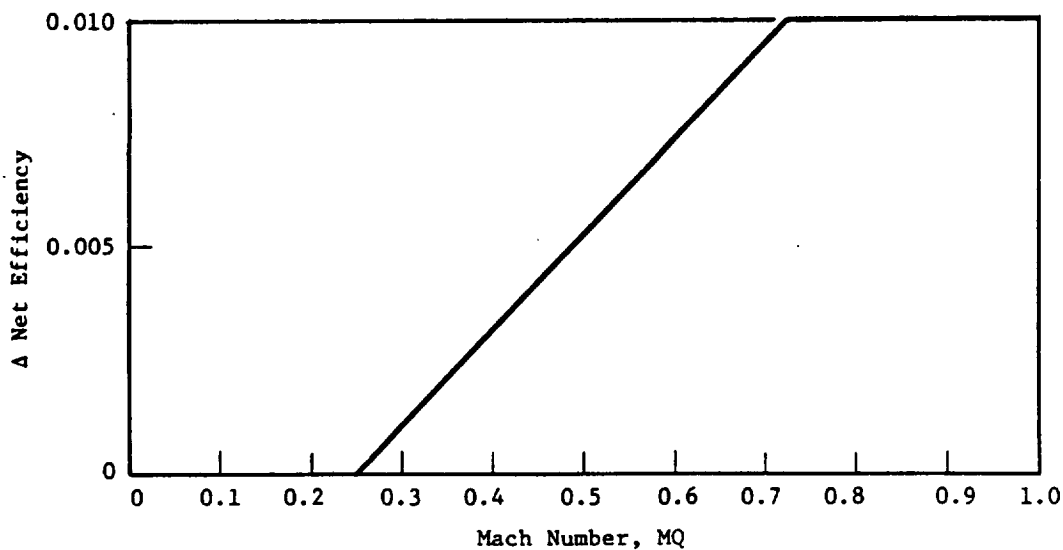


Figure 167. Blade-Surface-Mounted Strain Gauge Effects on Net Efficiency (Eight Strain Gauges).

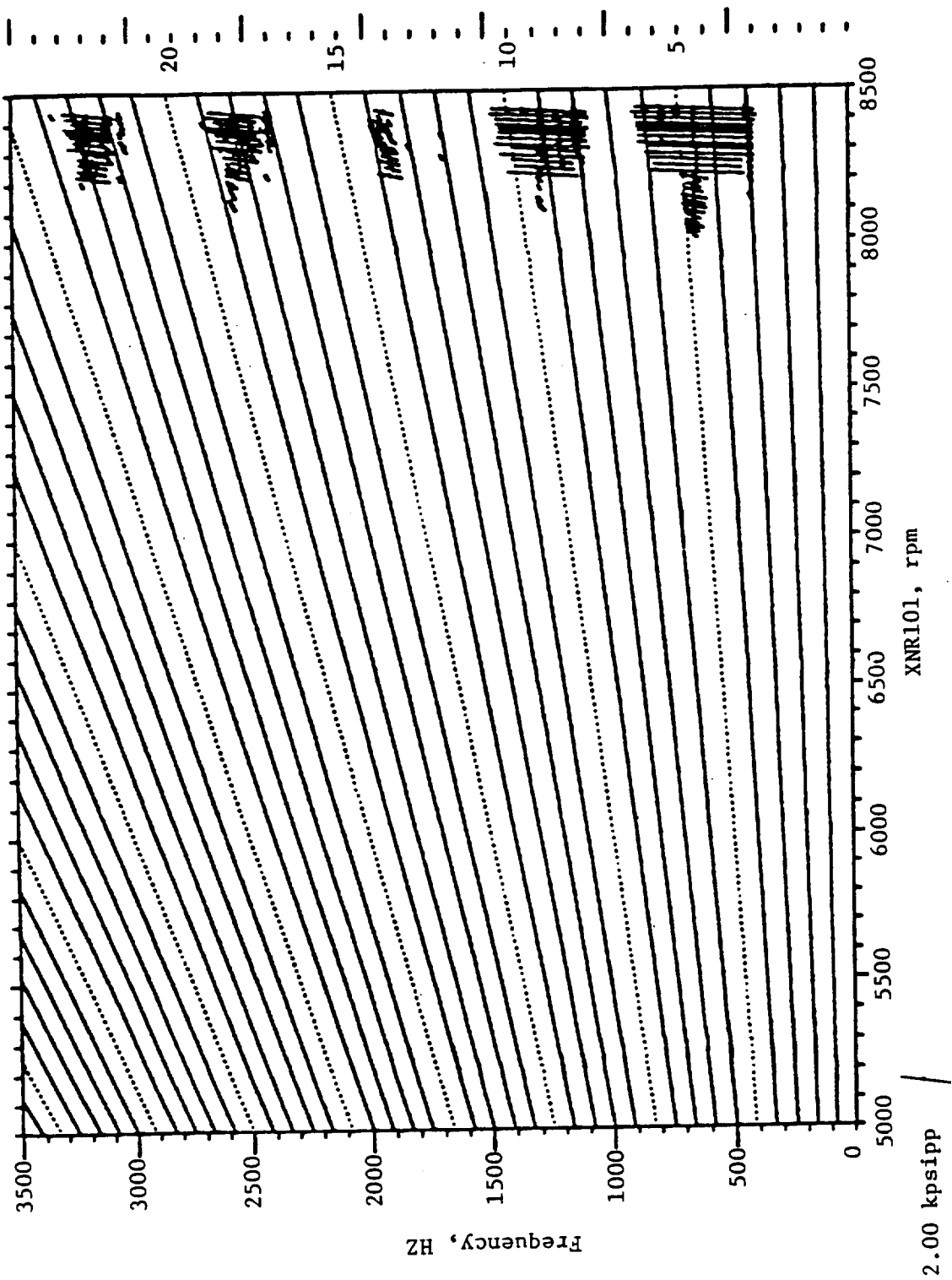


Figure 168. Typical Campbell Diagram from Engine Gauge No. 1 for F-5 Blade at Mach 0.33.

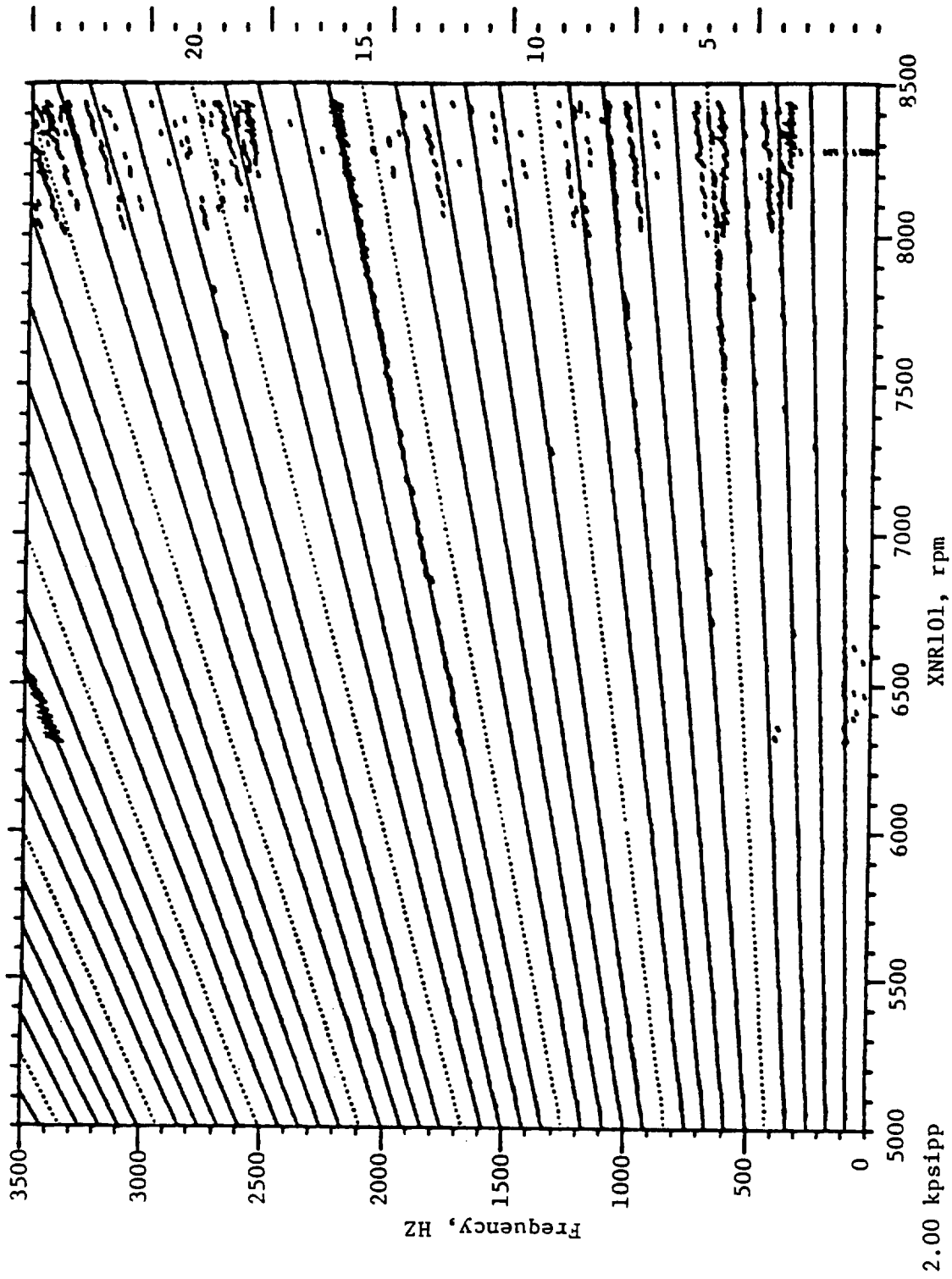


Figure 169. Engine Gauge No. 1 Campbell Diagram for A-5 Blade at Mach 0.33.

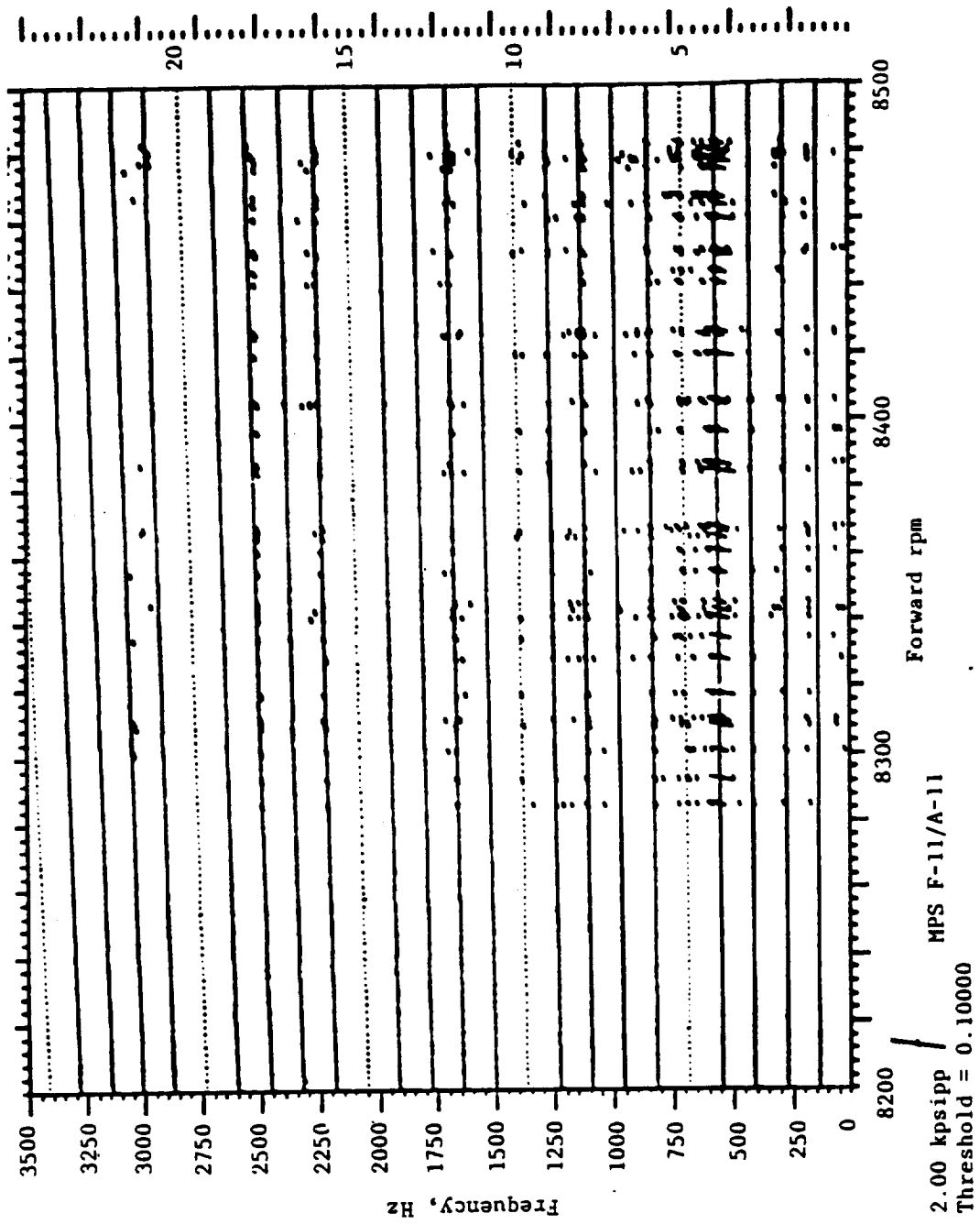


Figure 170. Engine Gauge No. 1 Campbell Diagram for Clipped F-11 Blade at Mach 0.34.

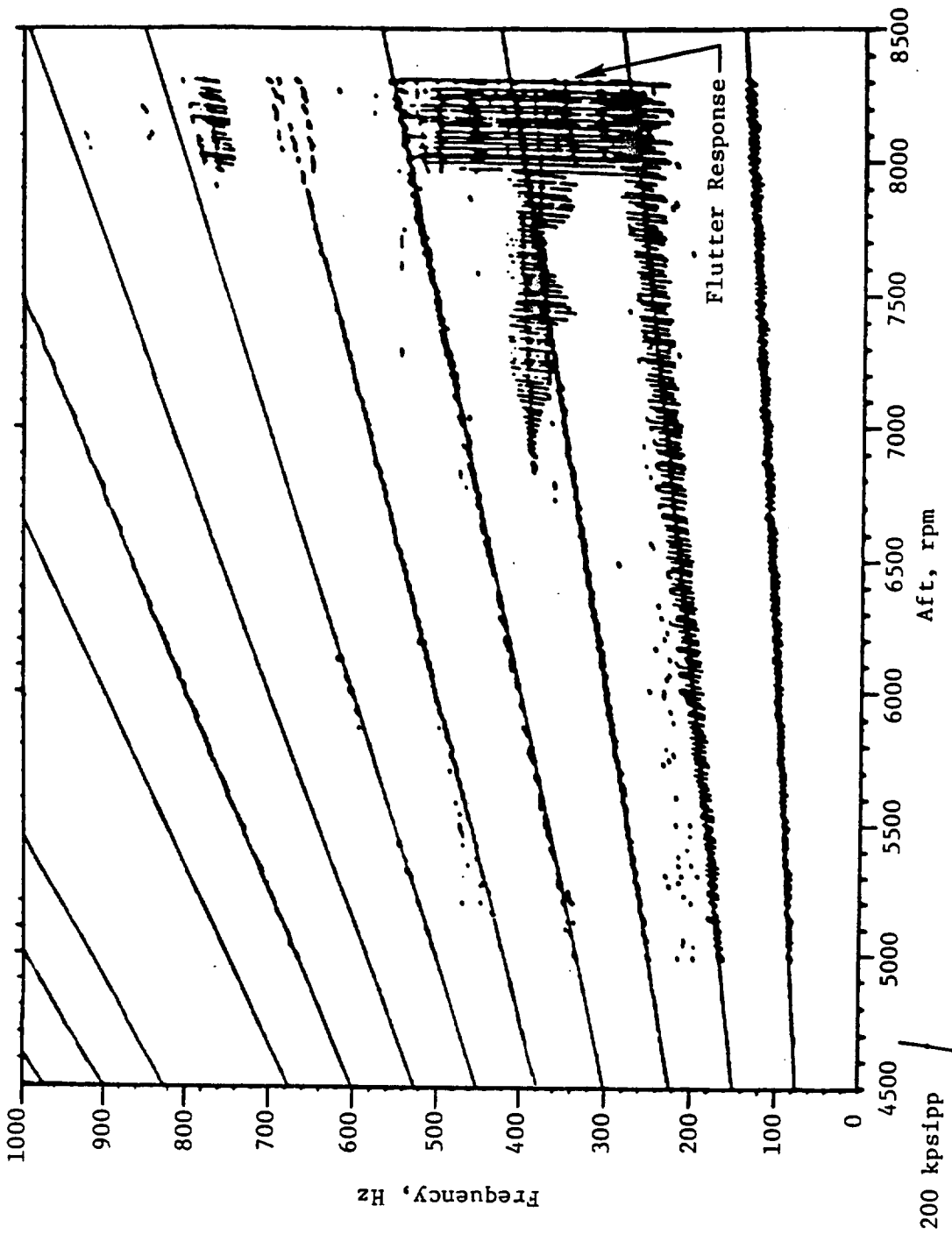


Figure 171. Flutter Response of Gauge No. 3 of MPS A-7 Blade with 35°-Ply Reference Angle on Aeromechanical Hub.

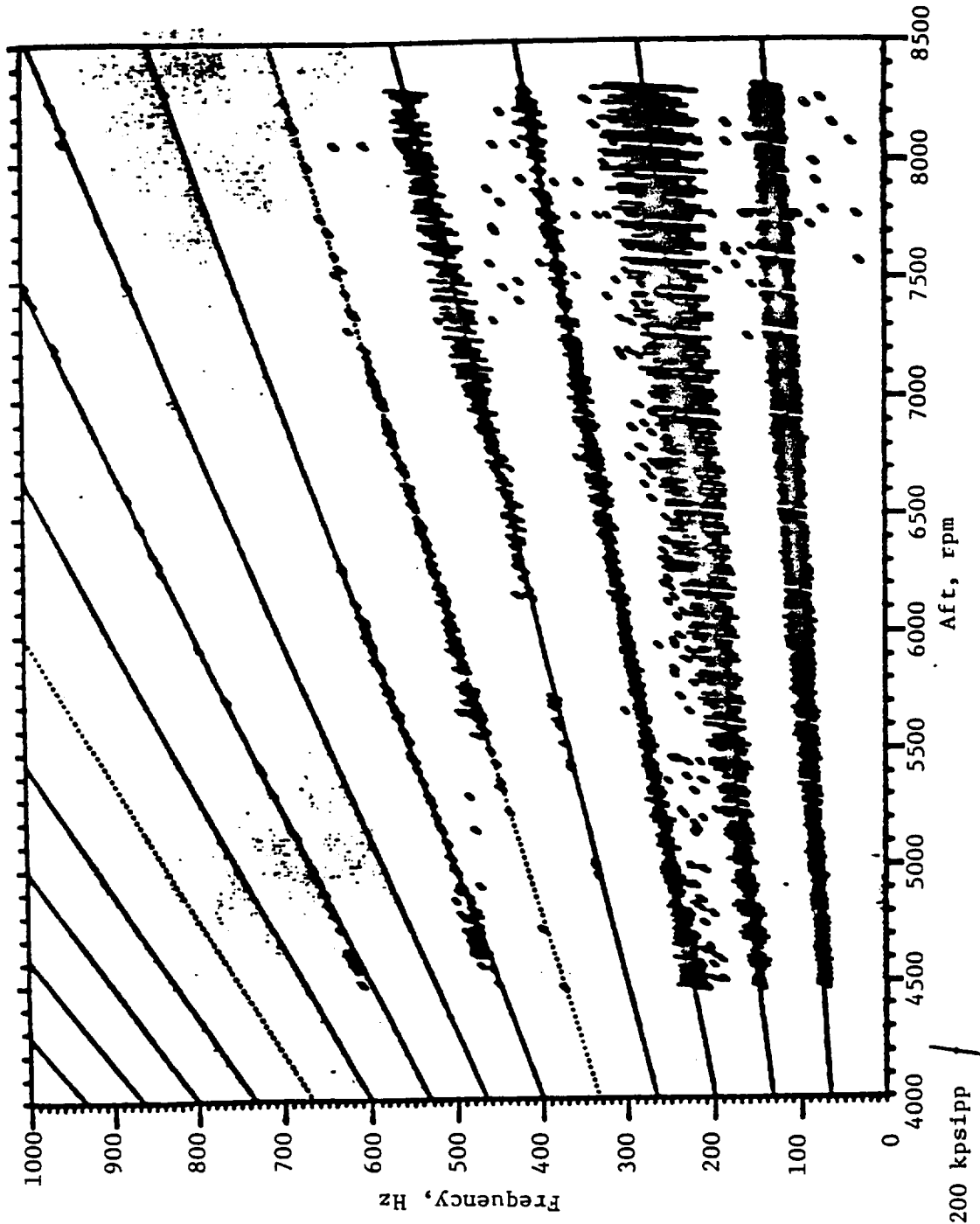


Figure 172. Response of Gauge No. 3 of MPS A-7 Blade on Aeromechanical Hub with Damper of Full Damping Force (8.5 lb) Showing no Flutter.

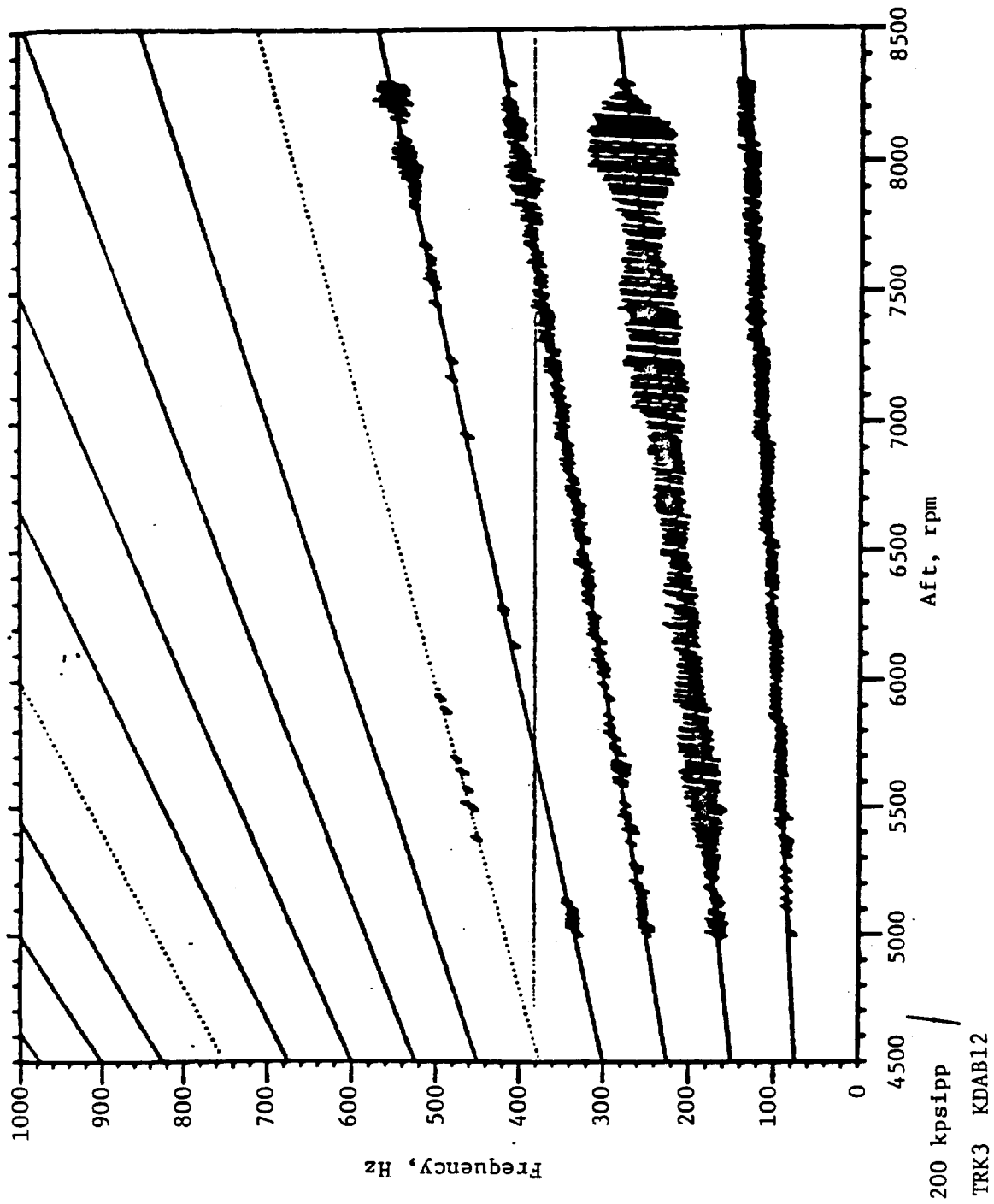


Figure 173. Gauge Response After Installing the Platform Adaptor Seals on the A-7 Aeromechanical Hub; Flutter Response at 380 Hz Eliminated.

chosen configurations from Table 52, the effects of disk loading, rotor-to-rotor spacing (for F-7/A-7 only), blade clipping for stability, blade design, and the forebody and aftbody contour (for F-21C/A-21 only) on high speed performance can be determined.

The data reduction equations used to generate the aerodynamic performance parameters for the 8x6 wind tunnel test are provided in an internal GE report (MPS 85-1 by C. Balan).

6.2.2 Aeromechanics

The blade series tested at the NASA 8x6 tunnel were the 4, 7, 11, 11c, 21, and 21c (c indicates clipped blade). Because the test for F-4/A-4 blades was uneventful, there was no attempt to reduce the data from this test. The data reduction/analysis for the MPS blade testing in the 8x6 wind tunnel are reported in the CDR.

Representative frequency amplitude time history diagrams presented herein, Figures 174 and 175, demonstrate the flutter response for Blade A-7 on the rigid hub. Typical preclipping and postclipping test results for the F-11 are presented (Figures 176 and 177), and for the F-21 (Figures 178 and 179). A typical Campbell diagram, Figure 180, indicates no flutter for the A-7 blade on the aeromechanical hub.

6.2.3 Acoustic

6.2.3.1 Data Acquisition

The acoustic data from the MPS SN003, operating under cruise conditions, were acquired by means of pressure transducers flush-mounted in a 1.5x0.9-m (5x3-foot) steel plate suspended from the ceiling of an otherwise unmodified perforated wall working section of the NASA Lewis Research Center's 2.4x1.8-m (8x6-foot) transonic wind tunnel. Having 17 transducers mounted along its centerline, this plate was suspended such that the line of transducers was directly above the centerline of the tunnel.

The plate could be moved in both the axial and vertical directions, with the motion being controlled remotely, and digital read-outs identifying the location at any moment in time. The range of movement from the extreme forward position was 0.2 m (8 in.) rearward; vertical traverse was from 0.04 m (1.5 in.) below the tunnel ceiling to 0.4 m (15.915 in.) above the tunnel centerline. The plate was positioned in the axial direction such that its midpoint was directly above the midpoint of a line joining the pitch-change axes of the two MPS rotors; and four vertical locations were employed to give sideline distances of 0.4 m (15.925 in.), 0.5 m (19.6 in.), 0.8 m (31.85 in.), and 1.1 m (42 in.), respectively. These sideline distances translate into tip clearance-to-diameter ratios of 0.15, 0.3, 0.8, and 1.21.

The 17 pressure transducers on the acoustic plate were connected parallel to a tape recorder and spectrum analyzer through a switching mechanism that selected which transducer(s), to a maximum of 11, would be recorded at any one plate position. Transducers were arranged on the plate such that, at the four plate positions, those activated lay approximately on ray lines emanating from the axis of the MPS at a point midway between rotor pitch-change axes.

The wind tunnel setup is described in References 34 through 36. Figures 181 through 183 depict the acoustic plate in the tunnel and the arrangement of the pressure transducers on its surface. Table 58 provides details of the angular location of the transducers, relative to the mid-pitch-change-axis origin.

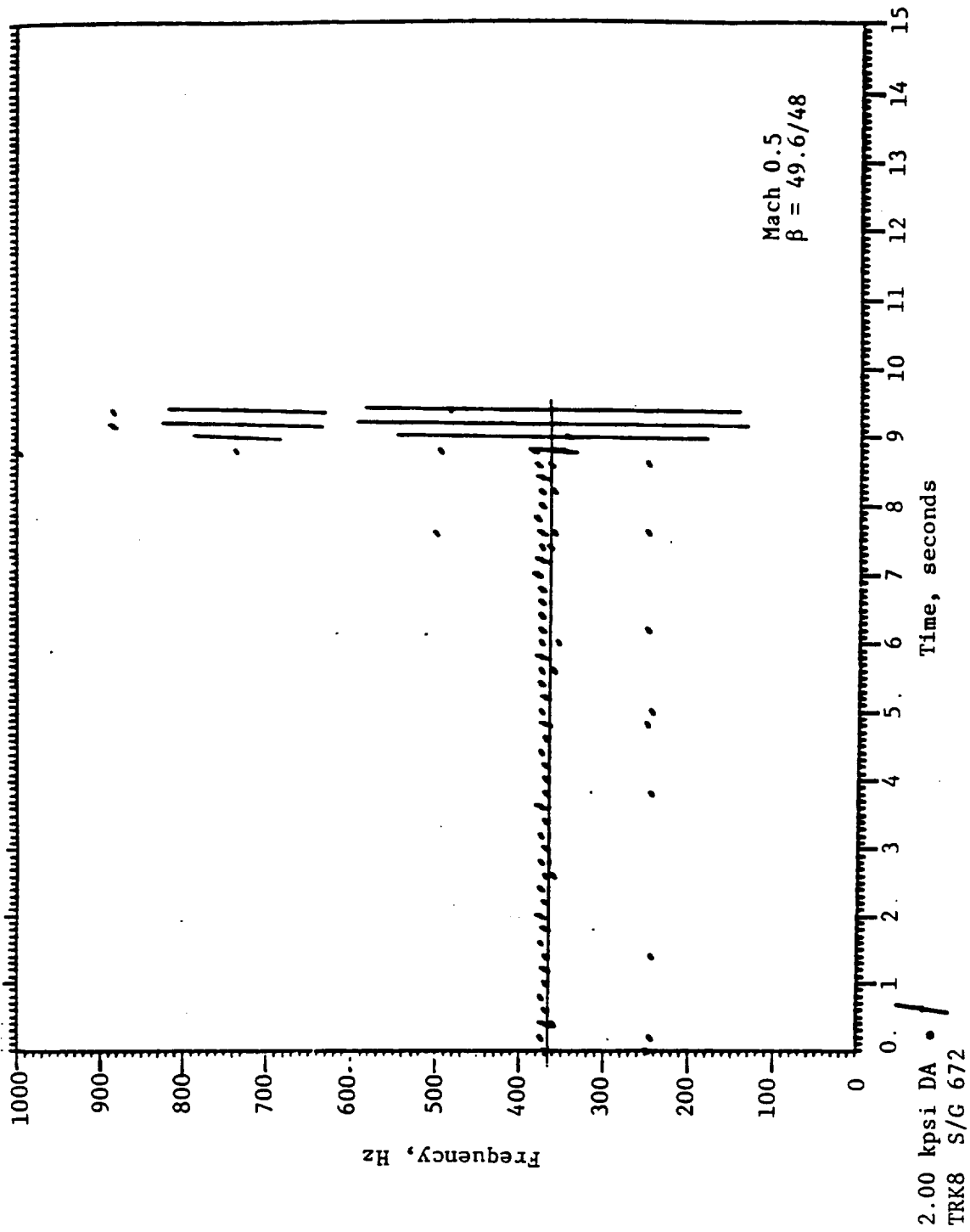


Figure 174. Flutter Response of MPS A-7 Blade on Rigid Hub at Design Point.

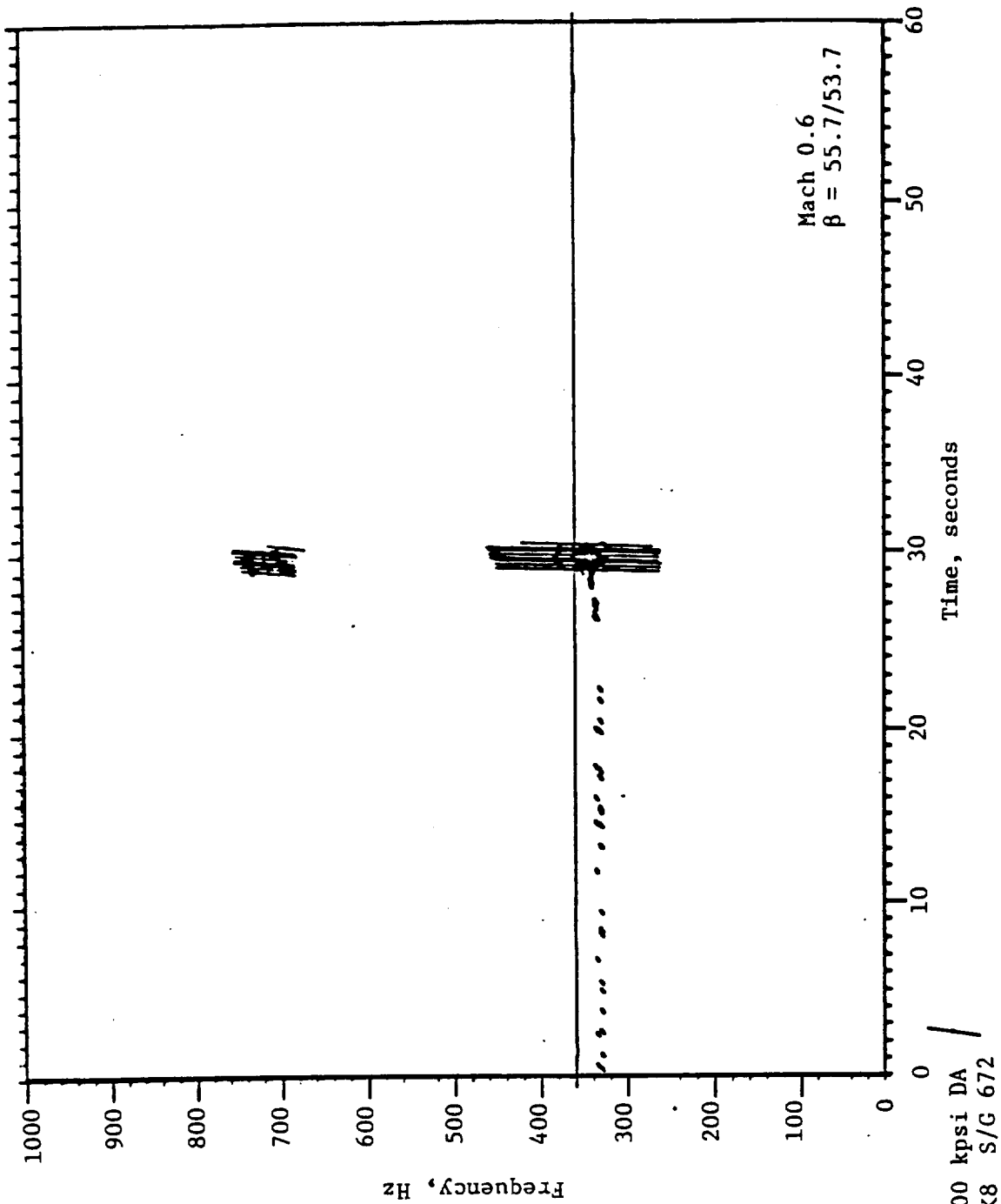


Figure 175. Flutter Response of MPS A-7 Blade on Rigid Hub.

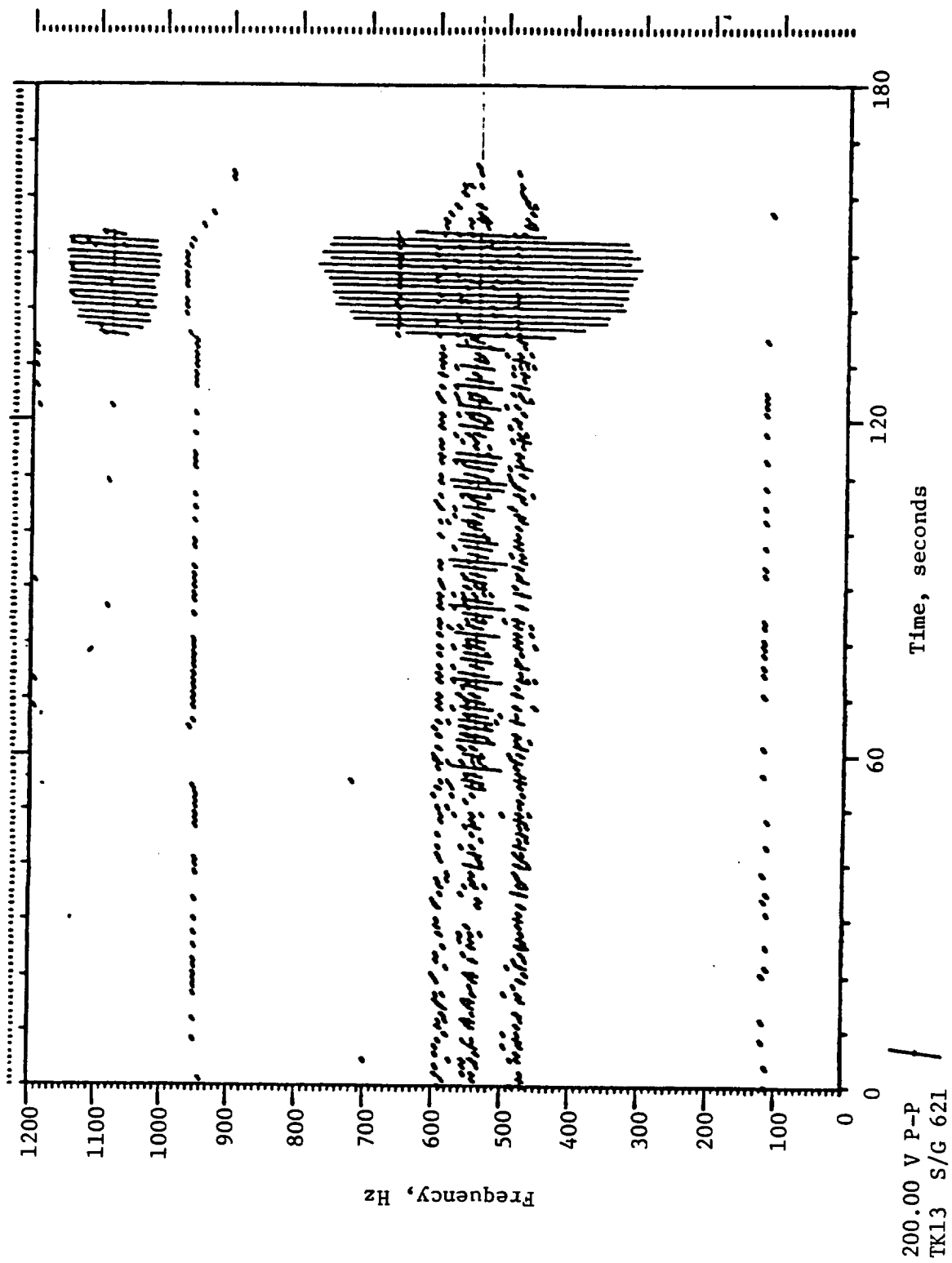


Figure 176. Flutter Response for Original F-11 Blade at Mach 0.72.

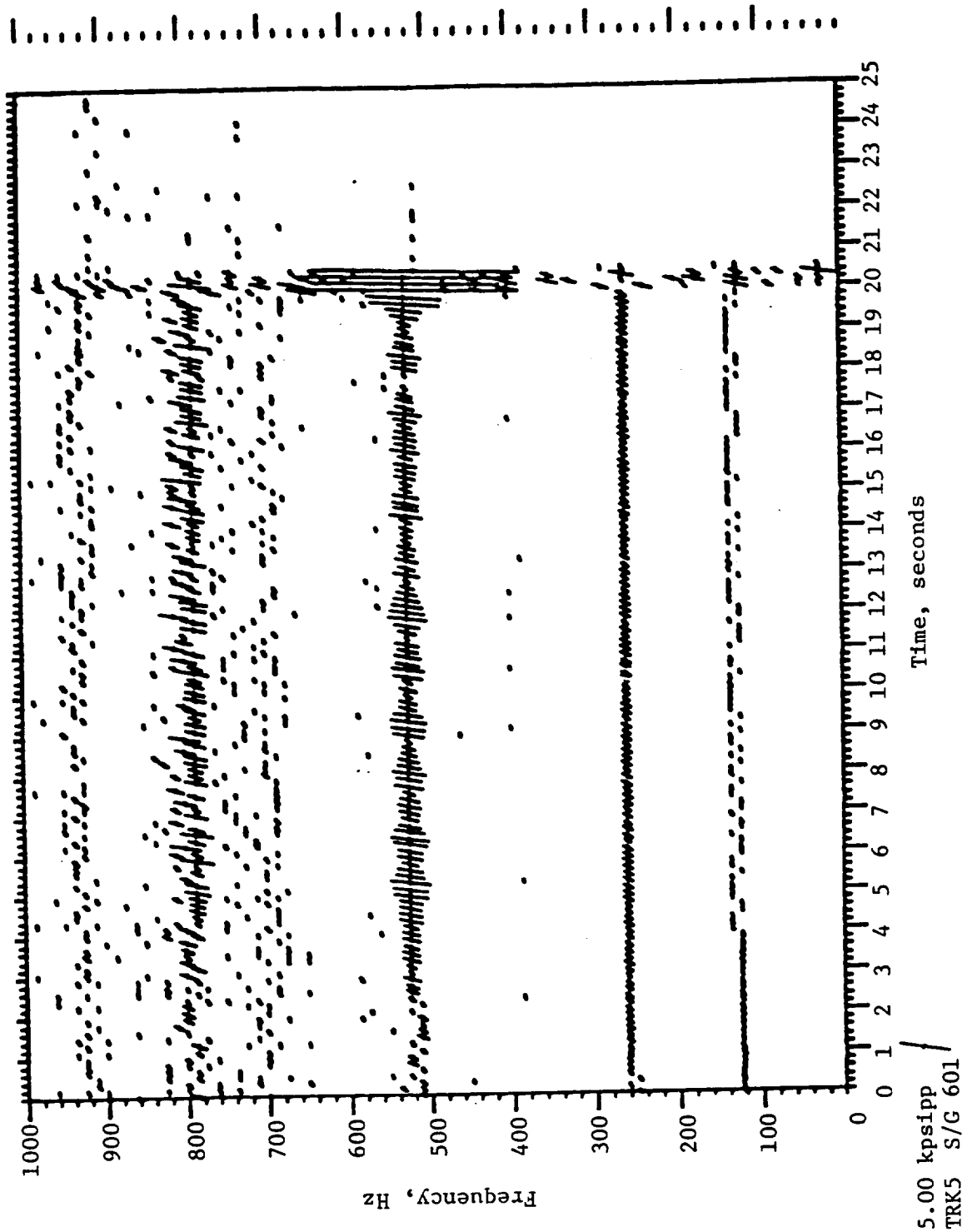


Figure 177. Flutter Response for Clipped F-11 Blade at Mach 0.9.

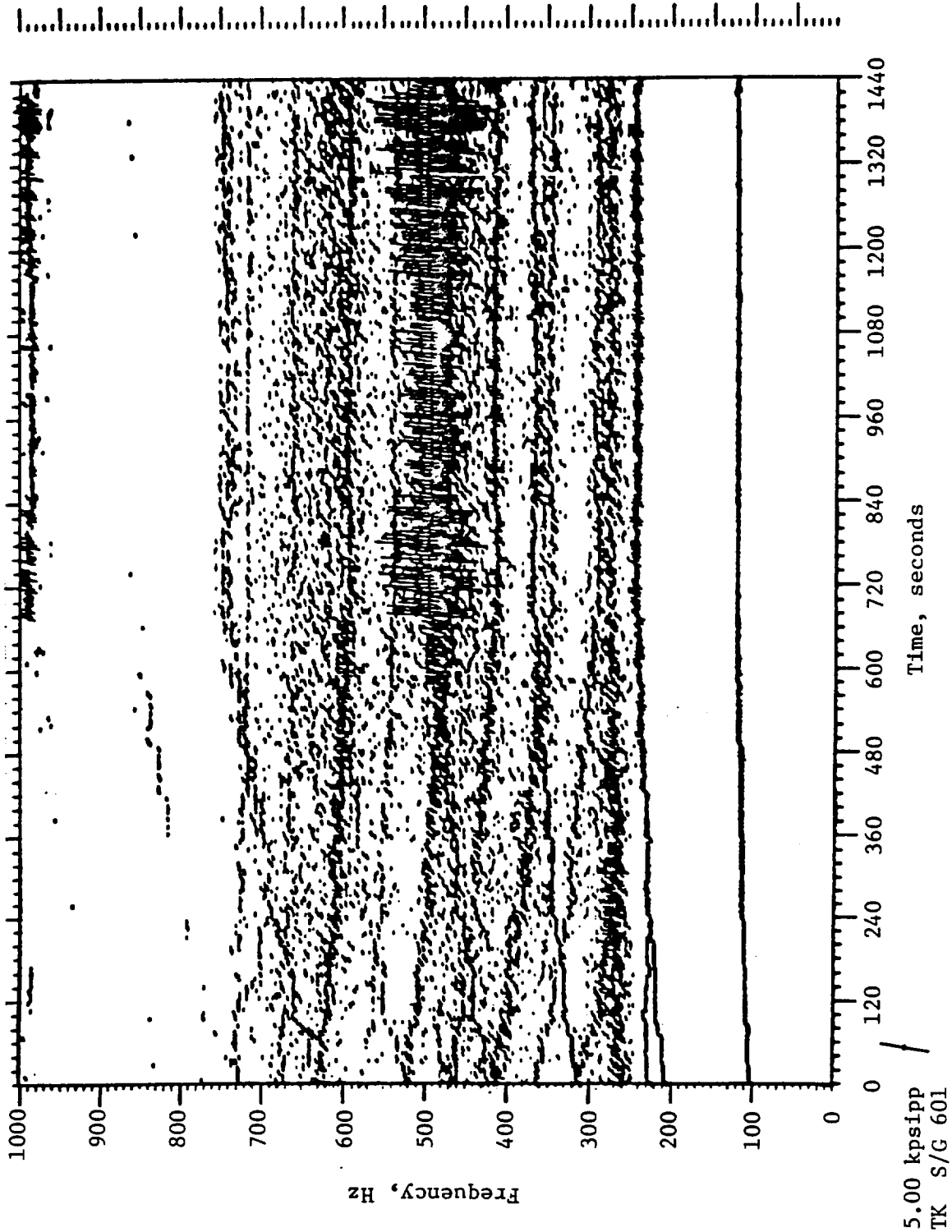


Figure 178. Flutter Response for Original F-21 Blade at Mach 0.8.

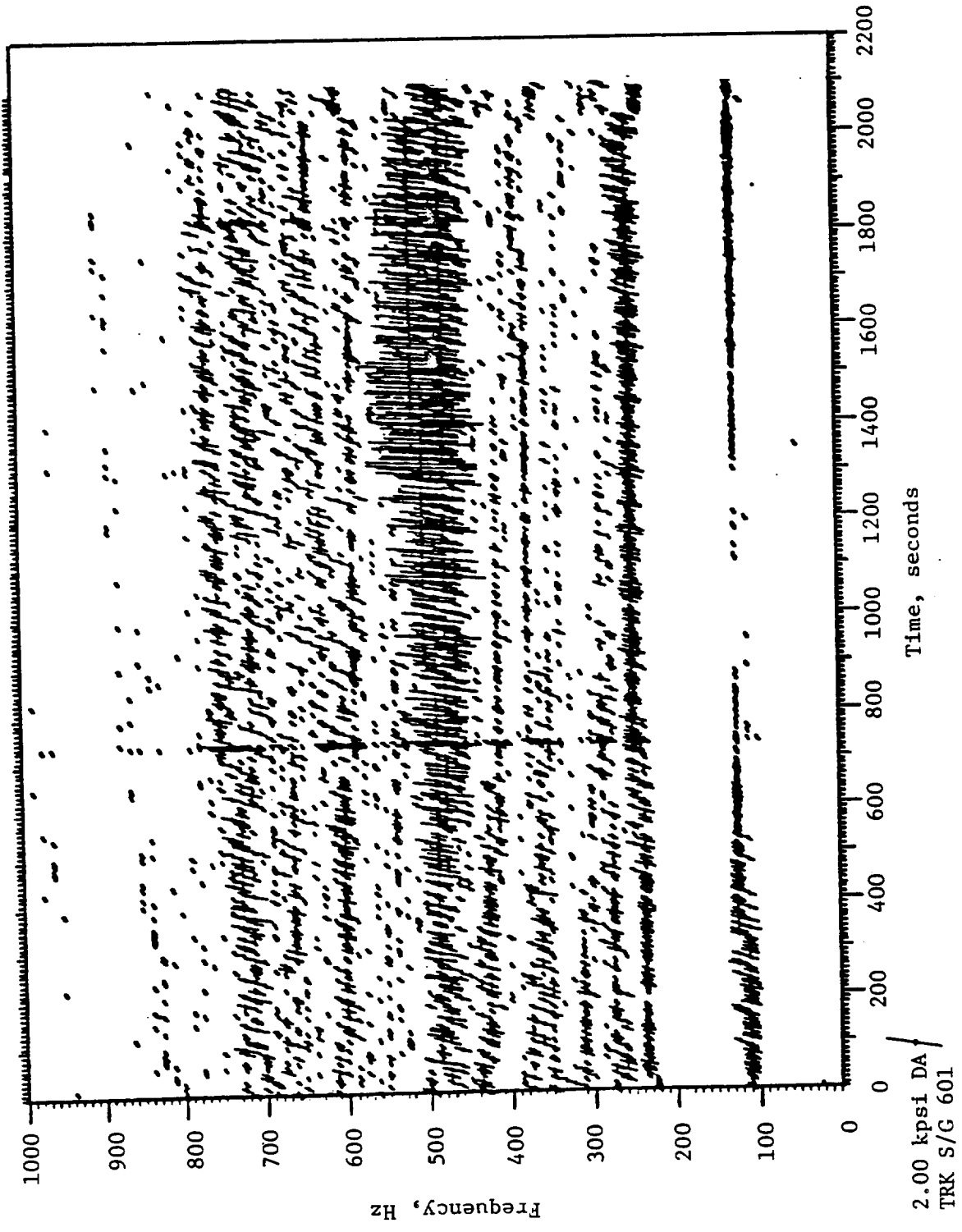


Figure 179. Flutter Response for Clipped F-21 Blade at Mach 0.8.

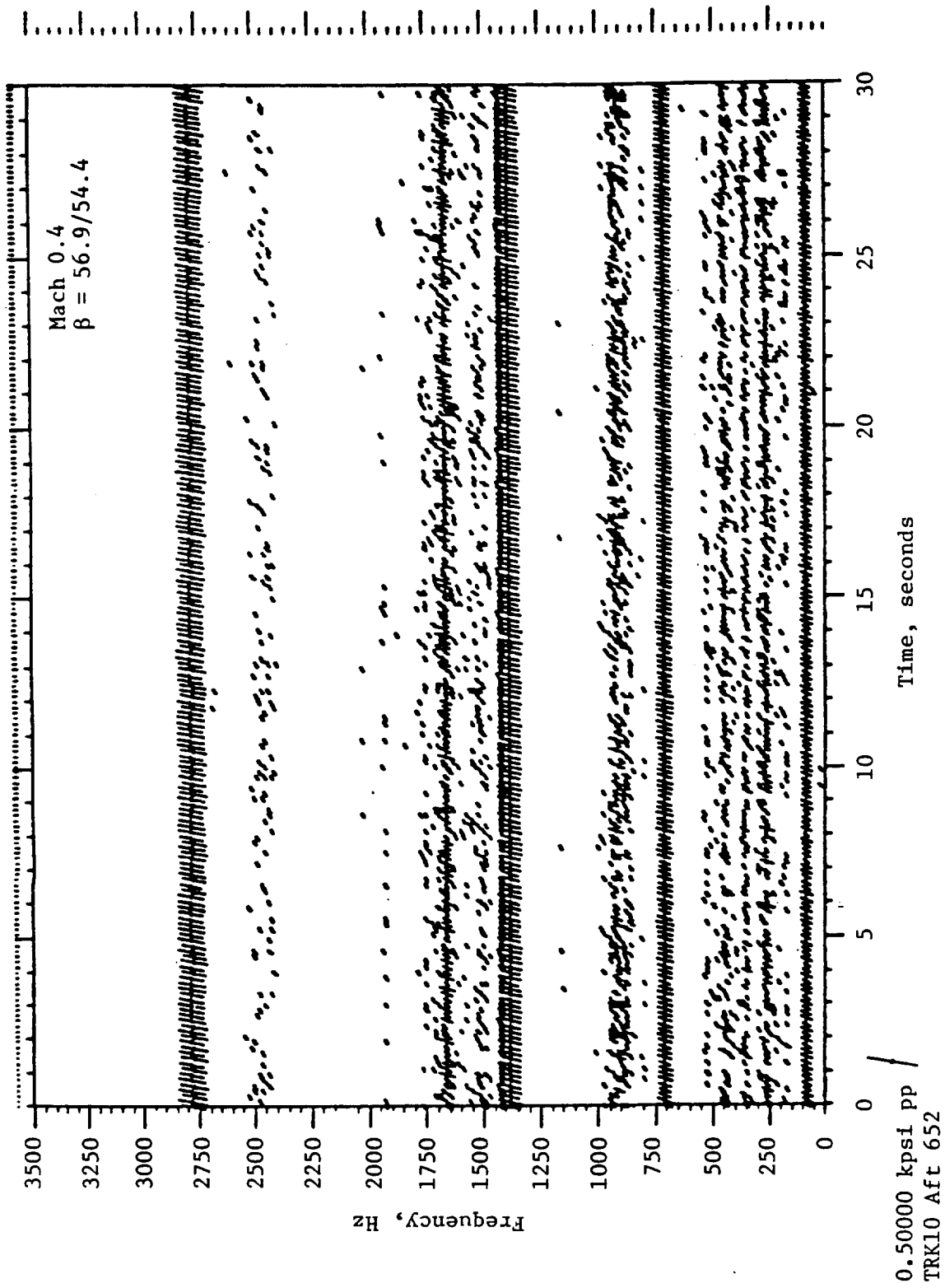


Figure 180. Stress Response for Blade A-7 Aeromechanical Hub.

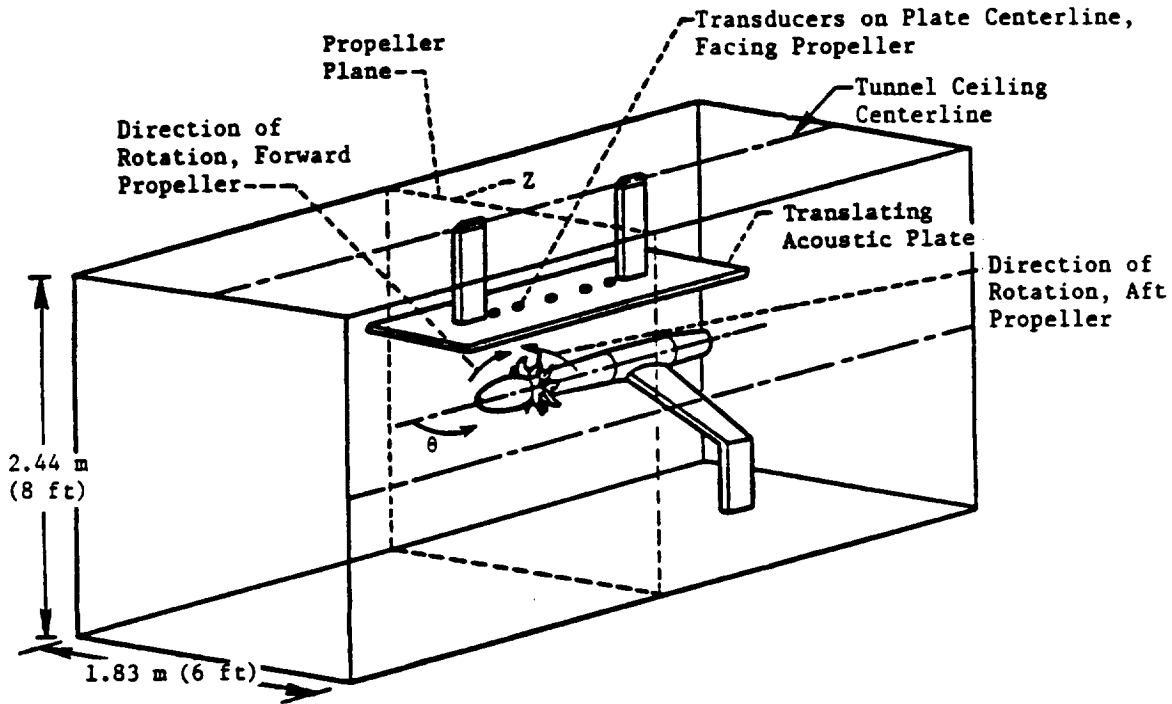


Figure 181. Translating Acoustic Plate and MPS in the 8x6 Wind Tunnel.

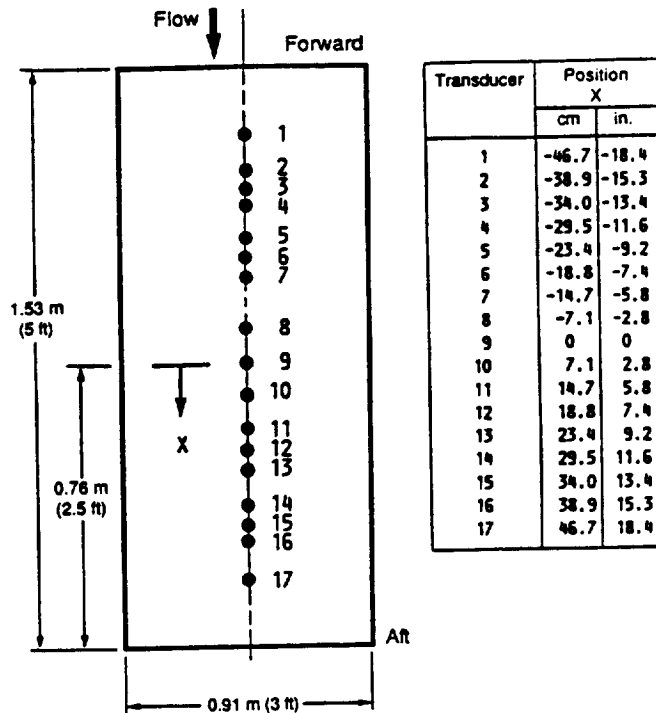


Figure 182. Transducer Positions on Translating Acoustic Plate, Standing Inside NASA 8x6 Tunnel Looking Up.

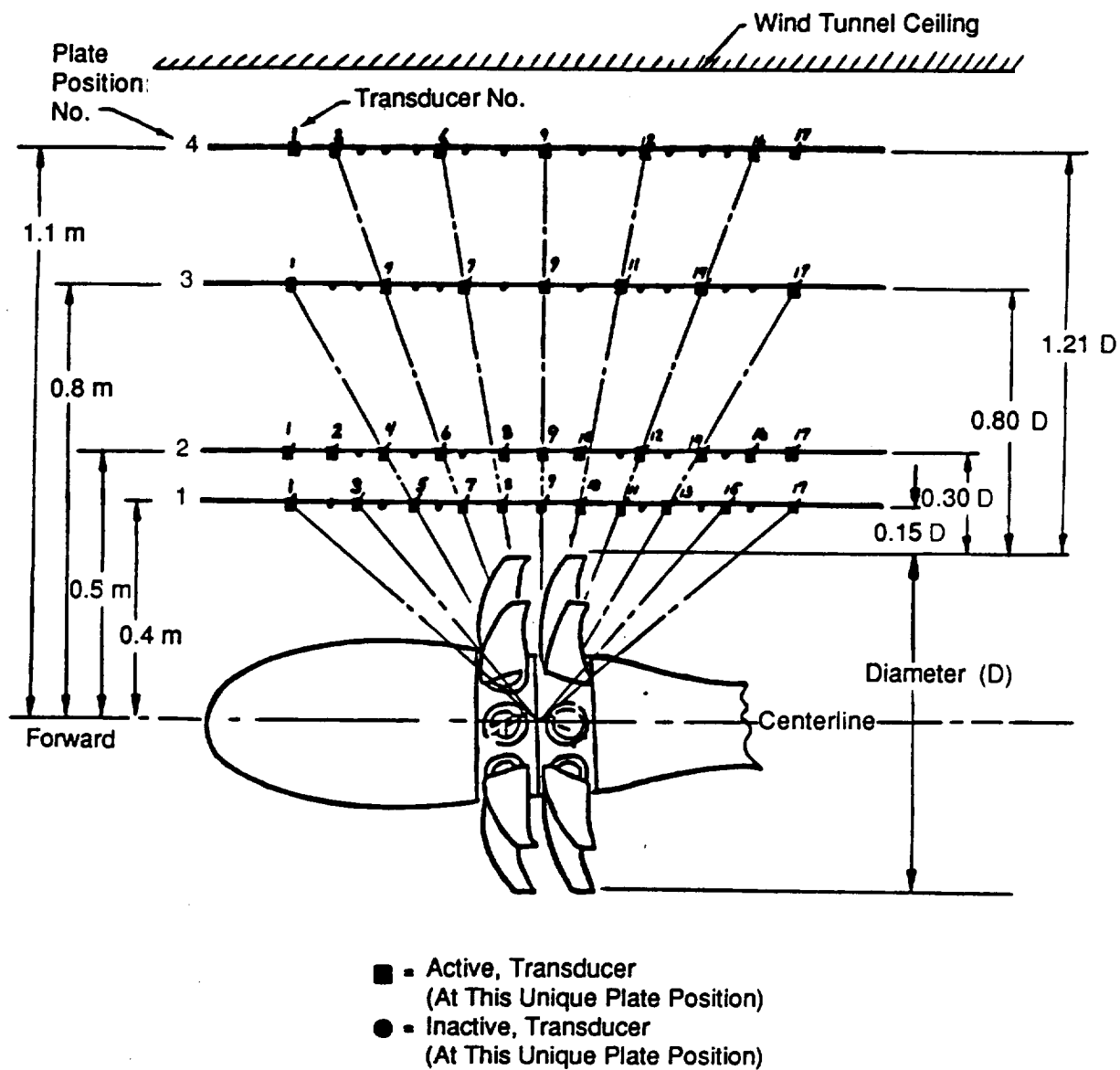


Figure 183. Transducer Locations at the Four Acoustic Plate Positions.

Table 58. Translating Acoustic Plate - Transducer Locations.

Transducer Number	Position ×		Approximate Angle from Inlet Axis with Plate, degrees			
			Plate Position			
			1	2	3	4
			Tip Clearance, Diameter			
cm	inch	0.15	0.3	0.8	1.21	
1	-46.7	-18.4	40.1*	46.8*	60.0*	66.4*
2	-38.9	-15.3	46.2	52.0*	64.4	70.0*
3	-34.0	-13.4	50.0*	55.7	67.2	72.4
4	-29.5	-11.6	54.0	59.4*	70.0*	74.6
5	-23.4	-9.2	60.0*	64.9	73.9	77.7
6	-18.8	-7.4	65.1	69.3*	76.9	80.0*
7	-14.7	-5.8	70.0*	73.5	79.7	82.1
8	-7.1	-2.8	80.0*	81.8*	85.0	86.2
9	---	---	90.0*	90.0*	90.0*	90.0*
10	7.1	2.8	100.0*	98.2*	95.0	93.8
11	14.7	5.8	110.0*	106.5	100.3*	97.9
12	18.8	7.4	114.9	110.7*	103.1	100.0*
13	23.4	9.2	120.0*	115.1	106.1	102.3
14	29.5	11.6	126.0	120.6*	110.0*	105.4
15	34.0	13.4	130.0*	124.3	112.8	107.6
16	38.9	15.3	133.8	128.0*	115.6	110.8*
17	46.7	18.4	139.9*	133.2*	120.0*	113.6*

* These are the transducers that are to be operational at this plate position

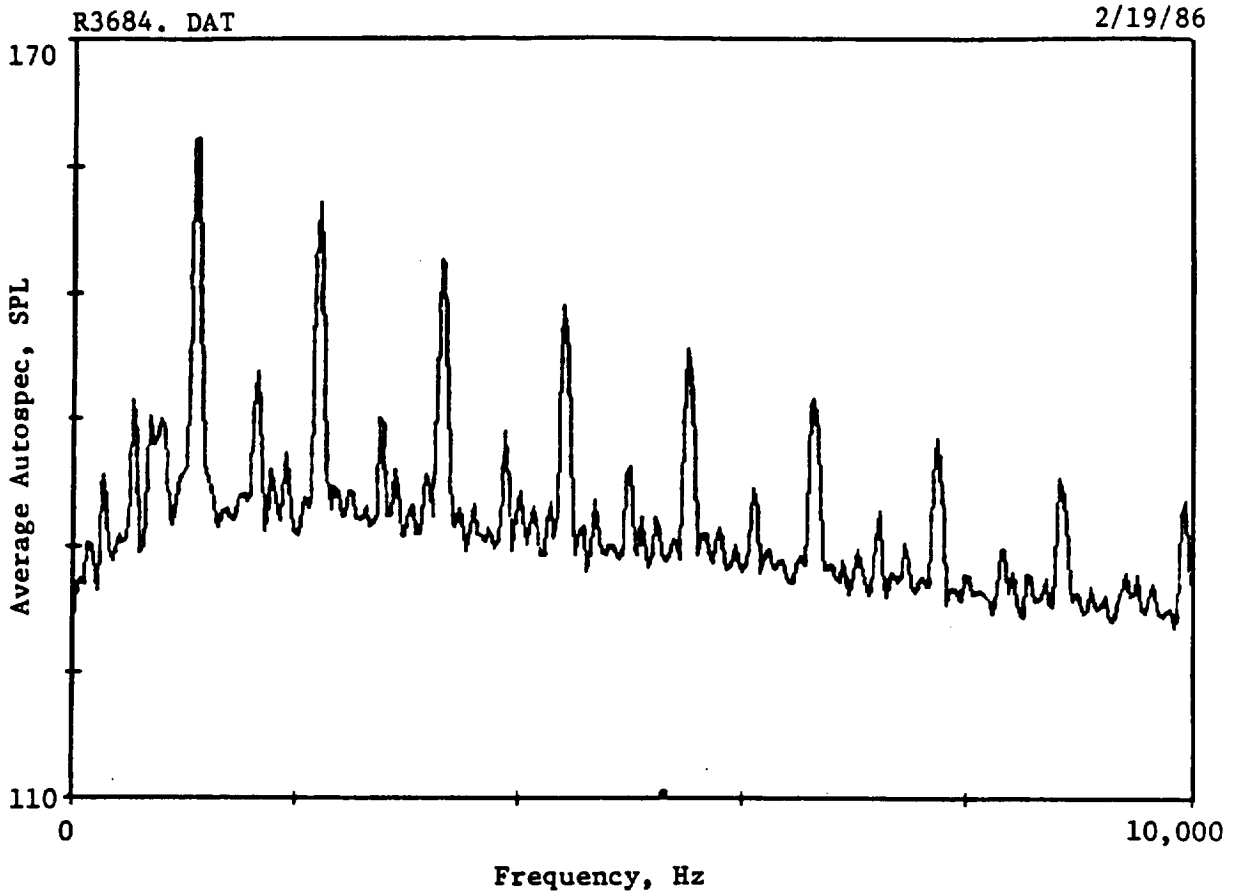
6.2.3.2 Data Reduction and Analysis

Experimental data obtained from the transducers on the acoustic plate was reduced by NASA and made available to GEAE in the form of narrow-band spectra generated by the NASA on-line system. These spectra were generated on line either at the time of the test or by replaying the tape-recorded information through the analyzer. A typical spectrum is illustrated in Figure 184, which also gives details of the number of averages (64) employed in the analysis and the resolution (bandwidth = 32 Hz). In general, the frequency range employed was 0 to 10 kHz; but some data were analyzed to 5 kHz, with a corresponding increase in resolution and reduction in bandwidth to 16 Hz. Tone levels were obtained from the spectra either directly by digitization or, in the case of some of the later tests, a digital readout was obtained from the analyzer by NASA-written software. Table 59 summarizes the acoustic analysis of the MPS 8x6 tests.

6.3 Rig 3/NASA 9x15 Low Speed Wind Tunnel

6.3.1 Acoustics

The acoustic instrumentation used in the 9X15 wind tunnel is described in Reference 37. Instrumentation consisted of an array of fixed microphones on the tunnel floor, a polar microphone probe that moved parallel to the axis of MPS at all angles-of-attack, and a translating microphone



CH 6 Resolution = 32 Hz
 64 Averages Hanning Window
 rpm = 8250, 8300
 F-7/A-7 Nominal Mach = 0.72 100%

Frequency (Hz)		Amplitude (SPL)
F1	1120	162.2
F2	2208	157.3
F3	3296	152.7
F4	4416	149.2
F5	5504	145.7
A1	1120	162.2
A2	2208	157.3
A3	3328	152.4
A4	4416	149.2
A5	5536	144.4

Figure 184. Typical Narrow-Band Spectrum from NASA's On-Line System.

Table 59. NASA 8x6 Wind Tunnel Acoustic Test Summary.

Blades	Mach Numbers	Blade No./ Spacing	Angles
F-7/A-7	0.72, 0.67	8+8/Nominal	56.9/54.4
F-7/A-7	0.8, 0.67, 0.72, 0.76	8+8/Minimal	58.5/55.7
F-7/A-7	0.67, 0.72, 0.76, 0.80	8+8/Maximum	58.5/55.7
F-7/A-7	0.72, 0.80, 0.76, 0.67	8+8/Nominal	58.5/55.7
F-7/A-7	0.72, 0.76, 0.67	8+8/Nominal	61.7/55.7
F-7/A-7	0.67, 0.72, 0.76	8+8/Nominal	55.7/53.7
F-7/A-7	0.8, 0.85, 0.9	8+8/Nominal	63.0/58.8
F-7/A-7	0.8, 0.85, 0.9	8+8/Maximum	61.2/57.9
F-7/A-7	0.8, 0.85, 0.9	8+8/Nominal	61.2/57.9
F-11/A-11	0.80, 0.76, 0.72	11+9/Maximum	61.5/59.8
F-11/A-11	0.80	11+9/Maximum	60.3/58.2
F-11/A-11	0.85, 0.90	11+9/Maximum	61.4/59.2
F-11/A-11	0.72, 0.76	11+9/Maximum	57.8/55.9
F-21/A-21	0.80, 0.85, 0.76	11+10/Maximum	61.8/61.2
F-21/A-21	0.72, 0.76, 0.80	11+10/Maximum	59.9/58.8
F-21/A-21	0.80, 0.76, 0.72	11+10/Maximum	60.2/61.1

probe on a track on the tunnel floor that traverses parallel to the axis of the MPS at a 0° angle-of-attack. The translating microphone probe had two microphones; the inner microphone on the probe was located 1.37 m (54 in.) from the MPS axis, and the outer microphone was located 1.68 m (66 in.) further from the axis of the MPS. A photograph of the MPS installed in the 9x15 wind tunnel with the acoustic instrumentation as discussed above is presented in Figure 185.

The analog acoustic data recorded with the translating microphone probes and selected fixed microphones were provided by NASA to GE on magnetic tape. Since the translating microphone traverses parallel to the axis of the MPS for a 0° angle-of-attack, only data with an angle-of-attack of 0° were selected for processing through an FFT analyzer. This processing is similar to the Cell 41 narrow-band processing previously described under Section 6.1.1.

In order to determine the quality of data processed from the traversing microphones, typical analog data from a fixed microphone were processed first with different numbers of averages. This set of data is presented in Figure 186, indicating that although a small number of averages is adequate to obtain reasonable values for the tone sound pressure levels, a sufficiently large number of averages is required to achieve good broadband definition. Tone definition rather than broadband definition, however, was the primary goal of the translating probes. Detailed broadband analysis at particular locations was possible from the fixed microphone data.

The data set, with different numbers of averages, was also processed by the SST program described in Section 6.1.1.2. Figure 187 illustrates the sound pressure sum levels with steady-loading tones (forward and aft rotor BPF's and harmonics) and rotor-to-rotor interaction tones, demonstrating that a minimum of five averages are required in order to attain reliable SPL's of the various tones.

ORIGINAL PAGE
BLACK AND WHITE PHOTOGRAPH

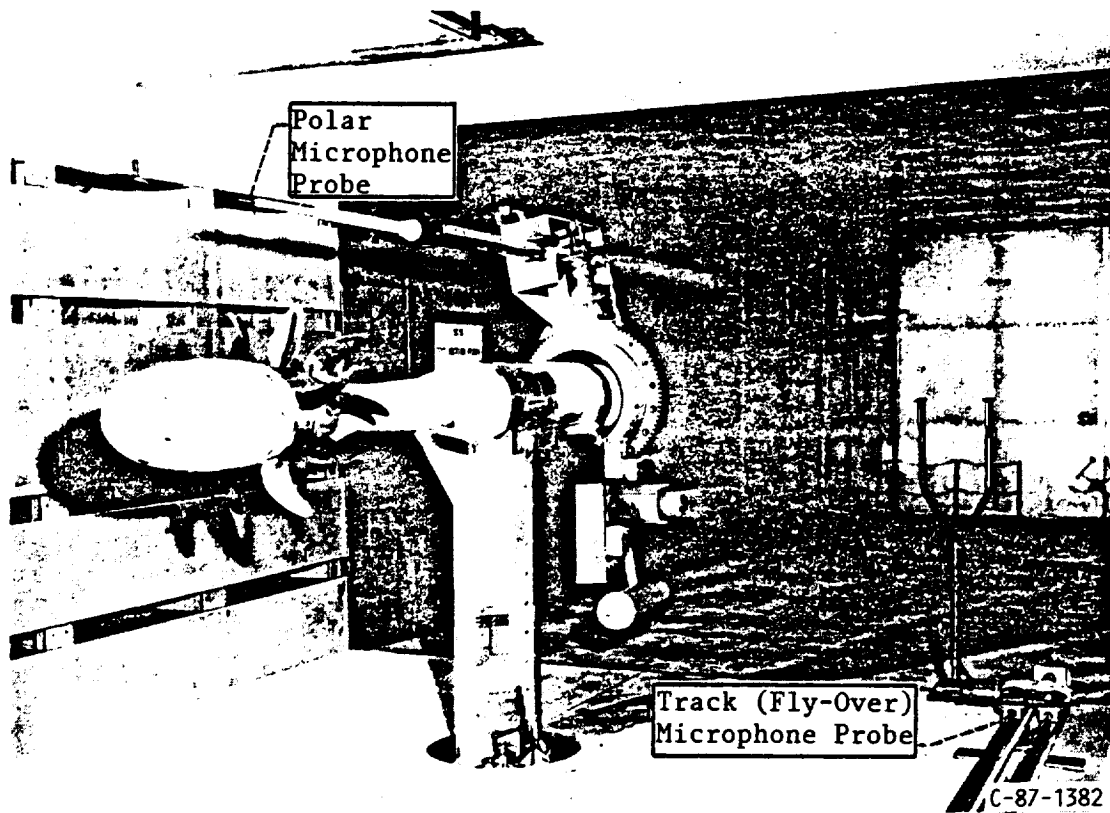


Figure 185. The MPS SN003 and Acoustic Instrumentation Installed in the NASA 9x15 Wind Tunnel.

ORIGINAL PAGE IS
OF POOR QUALITY

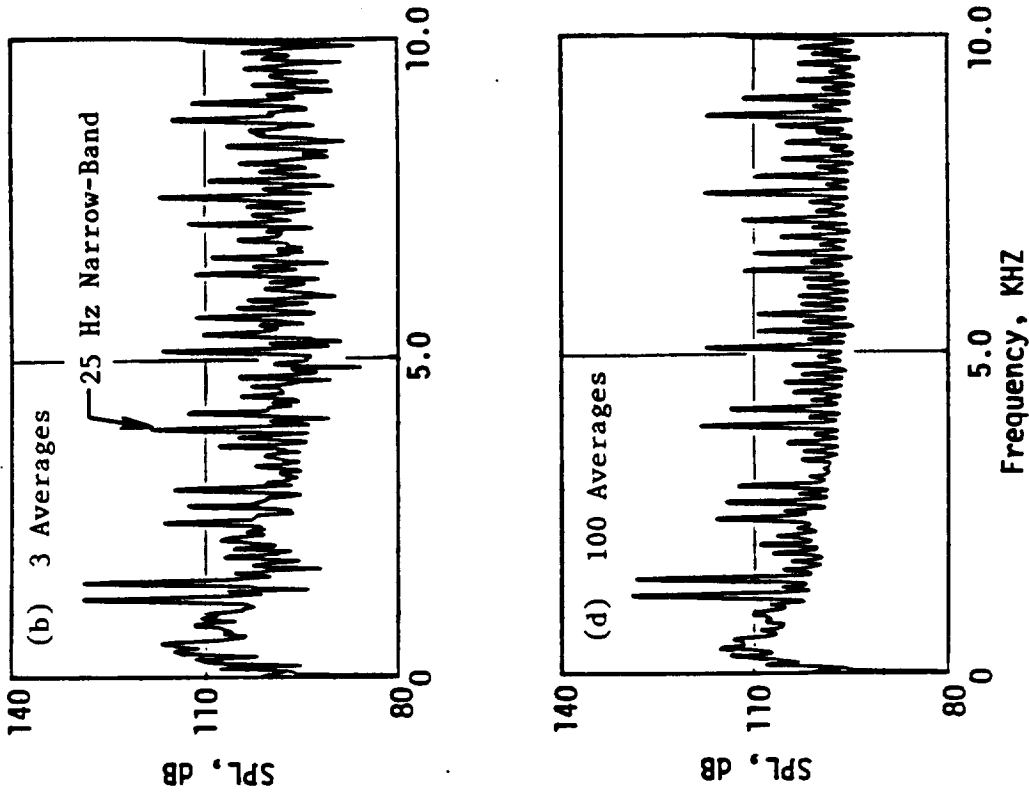


Figure 186. Effect of the Number of Averages on Narrow-Band Data of 9x15 Wind Tunnel.

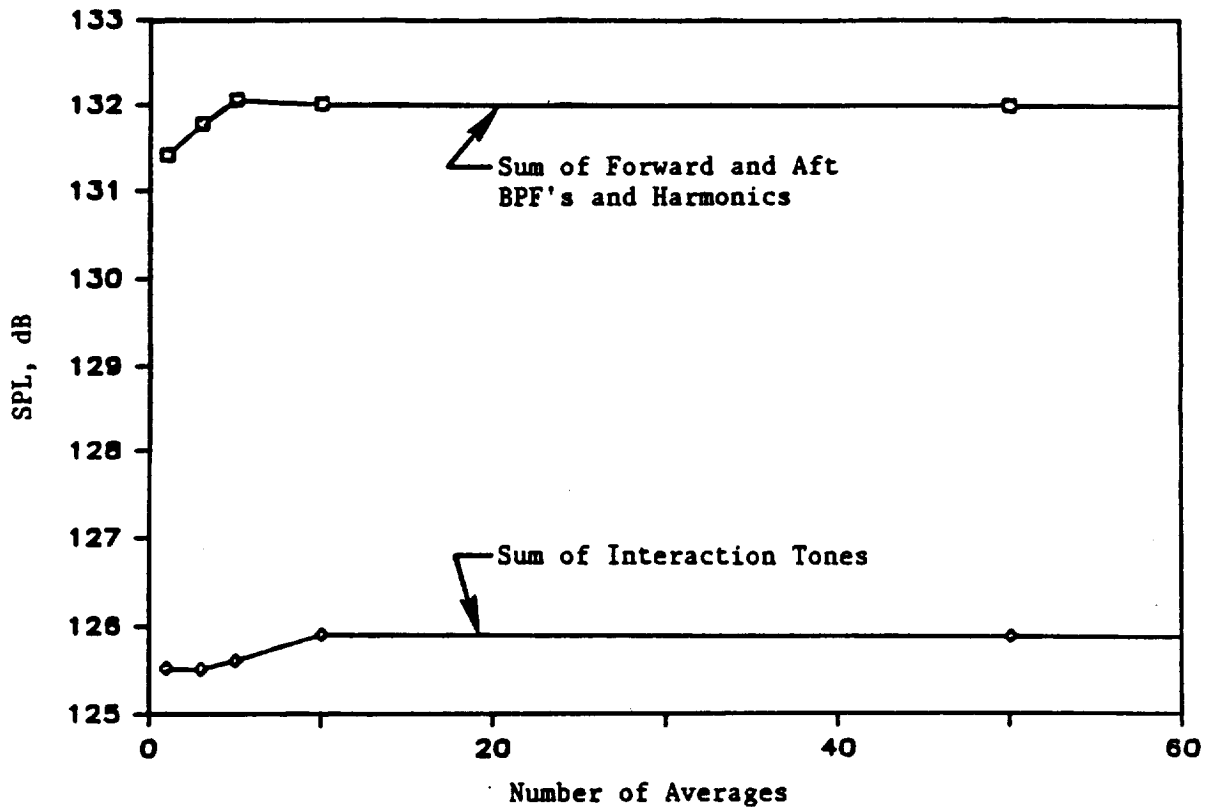


Figure 187. The Dependence on the Number of Data Averages of Model-Scale Tones Measured at 9x15 Wind Tunnel.

The analog acoustic data from traverse microphones for selected configurations, from the test series conducted at the 9x15 tunnel, were processed to obtain narrow-band data up to 10 kHz and with a bandwidth of 25. Figure 188 depicts a typical set of these data processed with the traversing microphone. Because the traverse microphone traveled at a constant linear rate of approximately 5 cm/s (1.95 in./s) the number of averages attainable in the plane-of-rotation of the rotors was limited to two or three. However, the uncertainty in the measured tone levels was less than 1 dB.

For the purpose of qualitative analysis related to the comparison of 9x15 wind tunnel and Cell 41 test results discussed later in this document (Section 7.3.1.1), this procedure proved to be adequate.

6.3.2 Aerodynamics

Performance data acquired in the 9x15 wind tunnel utilizing MPS Rig 3 was for the F-7/A-7, F-7/A-3, and F-11/A-11 configurations. The data for selectively chosen configurations from Table 55 can be compared to determine the effects of spacing and disk loading at Mach 0.2.

An internal GE report (MPS 86-2 by C. Balan) provides the data reduction equations used to generate the aerodynamic performance parameters for the NASA Lewis 9x15 wind tunnel test.

6.3.3 Aeromechanics

Because tests at the NASA 9x15 tunnel were aeromechanically uneventful, no data reduction was conducted.

Model Scale, 1.37m (54 inch) Sideline
36.4/36.5

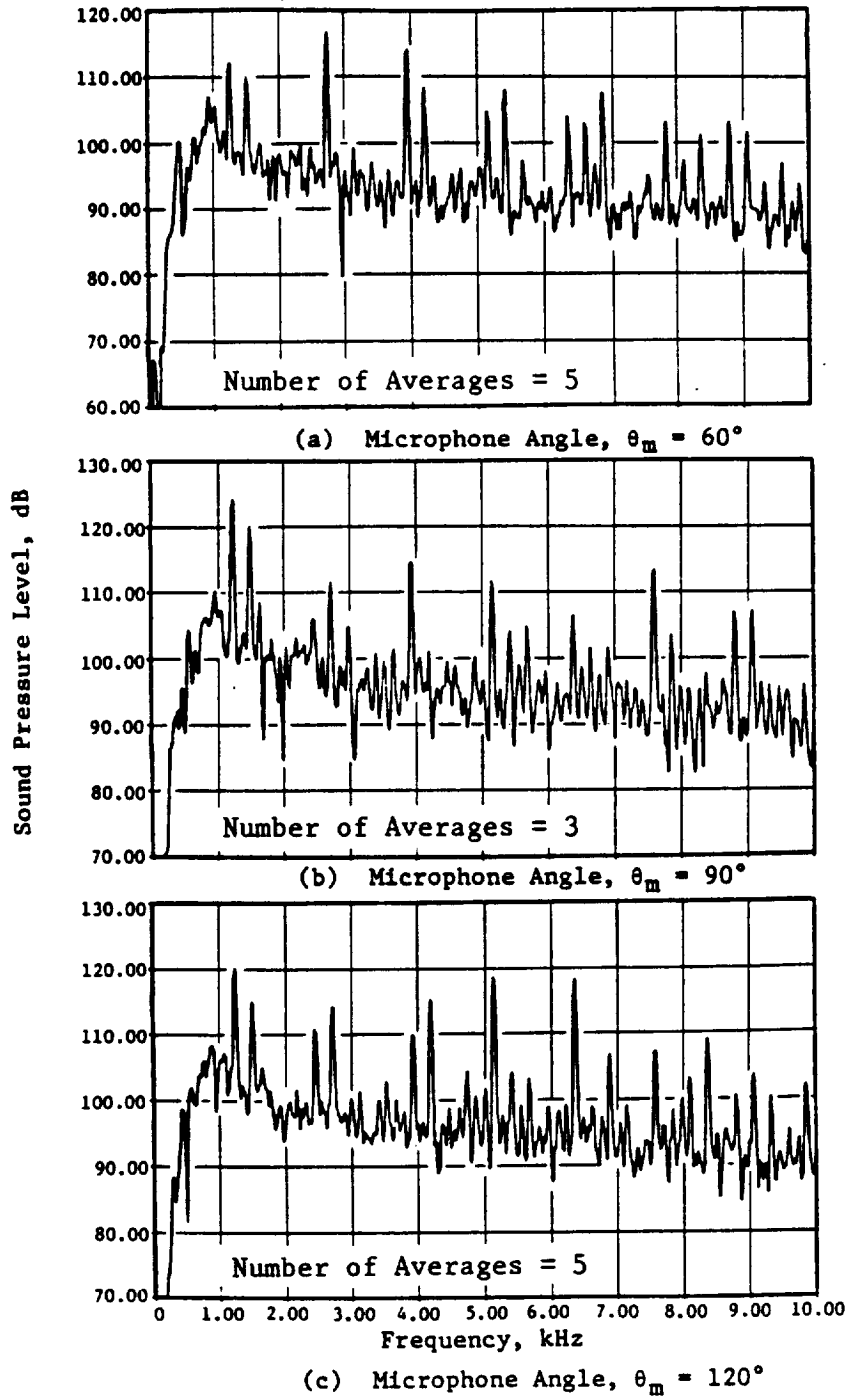


Figure 188. Typical F-7/A-7 (11+9) Narrow-Band Data Measured at 9x15 Tunnel with the Traverse Microphone.

7.0 DISCUSSION OF RESULTS

7.1 Rig 2/Cell 41 (Anechoic Chamber)

7.1.1 Acoustics

The acoustic data measured in Cell 41 with the model-scale configurations outlined in Table 56 are analyzed and presented in this section. In addition to an acoustic evaluation of the various blade design concepts, the objectives of some of the tests were to ascertain the impact of configurational changes on sound pressure levels, due to various acoustic sources for a given blade design. Figure 189 identifies, for easy reference, the various noise sources associated with a counterrotating fan engine. These components include:

- Forward rotor steady-loading and thickness noise
- Aft rotor steady-loading and thickness noise
- Noise due to interaction of the aft blades with the blade wakes of the forward rotor blades
- Noise due to interaction of the aft blades with tip vortices from the forward blade tip
- Noise due to the interaction of forward blades with the wakes from a mounting pylon
- Aerodynamic broadband noise.

The configurational changes considered for evaluation during the model-scale testing to assess their acoustic impact included the following:

- Variation of blade numbers, tip speed, blade spacing, and test Mach number
- Reduction in the diameter of the aft blades
- With and without a mounting pylon.

Results of these acoustic evaluations are presented in this section with a description and discussion of various analytical methods employed in this evaluation.

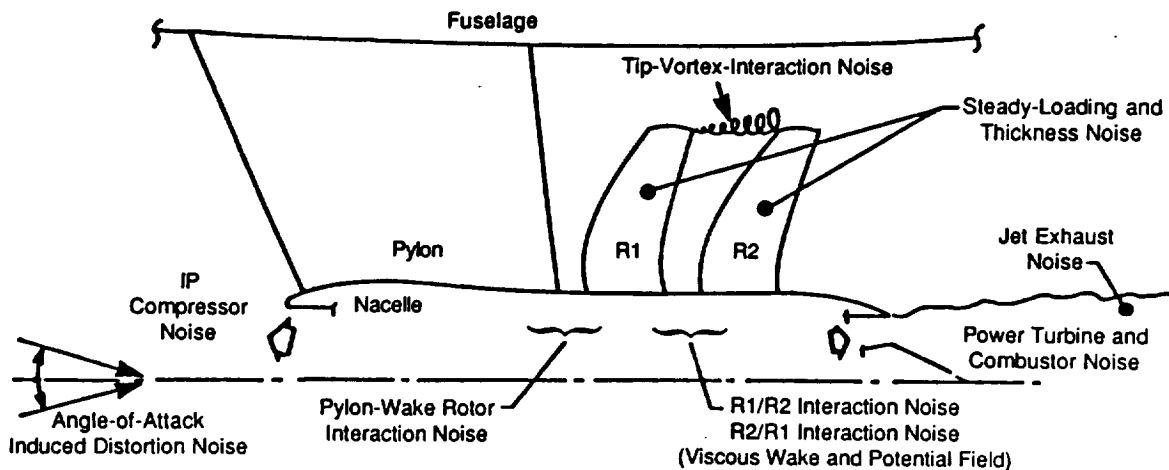


Figure 189. Noise-Source Mechanisms with Counterrotating Fan Engines.

7.1.1.1 Repeatability of Acoustic and Performance Data

To ascertain the repeatability of acoustic and aeroperformance data at Cell 41 and to broaden the data base of the F-7/A-7 baseline configuration, MPS tests with the F-7/A-7 blades (8+8, nominal rotor spacing $X/D_r=0.169$, no pylon, and pitch angle of $37.9^\circ/37.4^\circ$) were repeated during different periods of this contract over identical range of tip speeds. These two test runs are identified as Runs 12 and 95 in Table 56. The measured aeroperformance and typical acoustic data are summarized in Figures 190 through 193.

Figure 190 compares the aeroperformance data of forward rotor, aft rotor, and total corrected thrusts that were measured during these two test runs as a function of forward rotor tip speed and, also, compares these data in terms of the total power absorbed by the rotor as a function of total output thrust. An examination of this figure indicates a very good agreement between the data from the two tests.

The acoustic comparison, in terms of the scaled maximum PNL (peak noise levels) and dBA on an extrapolated sideline, as a function of the total thrust is shown in Figure 191, indicating that the results are within acceptable data scatter. Typical PNL and dBA directivities and selected spectral comparison at a tip speed of 260 mps (854 fps) and at typical takeoff thrust plotted in Figures 192 and 193, demonstrating a very good repeatability in measured and processed acoustic results between the two tests. The variation in the calculated values for EPNL for the two test conditions (Figure 192) was determined to be 0.5 dB.

7.1.1.2 Acoustic Evaluation of Different Blade Designs

Aerodynamic and acoustic characteristics of blade designs F-5/A-5, F-7/A-7, F-1/A-1 (designed for cruise Mach Number 0.72), and F-11/A-11 (designed for cruise Mach Number 0.80) were measured at Cell 41 to evaluate the effects of blade sweep and activity factor. Data from these analyses are presented in this section under two sets of comparisons, as follows:

- Series 1
 - F-5/A-5, F-7/A-7, and F-1/A-1, each with 8+8 (8 forward and 8 aft) blade configuration with nominal spacing between rotor pitch-change axes ($X/D_t = 0.169$) and at nominal pitch angles
- Series 2
 - F-7/A-7 and F-11/A-11, each with 11+9 (11 forward and 9 aft) blade configuration at open pitch angles and with comparable normalized rotor-to-rotor spacing.

These data results were measured at a simulated flight Mach number of 0.25 and were with no pylon installation.

7.1.1.2.1 F-5/A-5, F-7/A-7, and F-1/A-1 (8+8): Series 1

A comparison of the geometry of the test blades is provided (Figure 194) wherein the F-7/A-7 and F-1/A-1 are noted to have similar chord and sweep, but the F-5/A-5 has a shorter chord and a reduced sweep. The decrease in chord and, hence, the blade area of the F-5/A-5, relative to F-7/A-7 and F-1/A-1, is also reflected in the smaller activity factor associated with the F-5/A-5

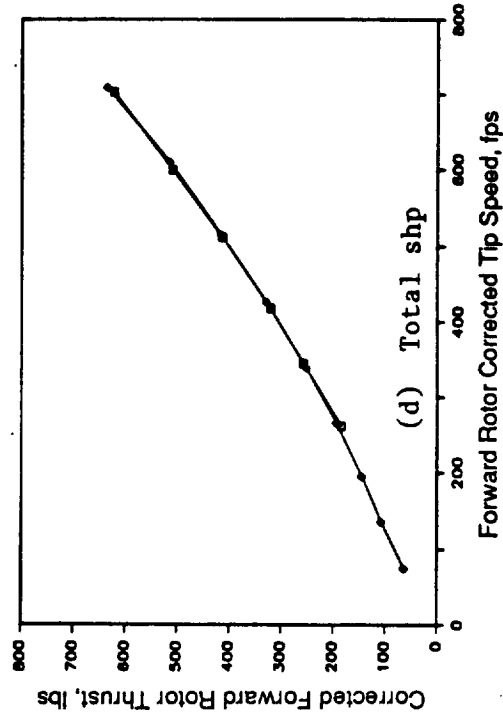
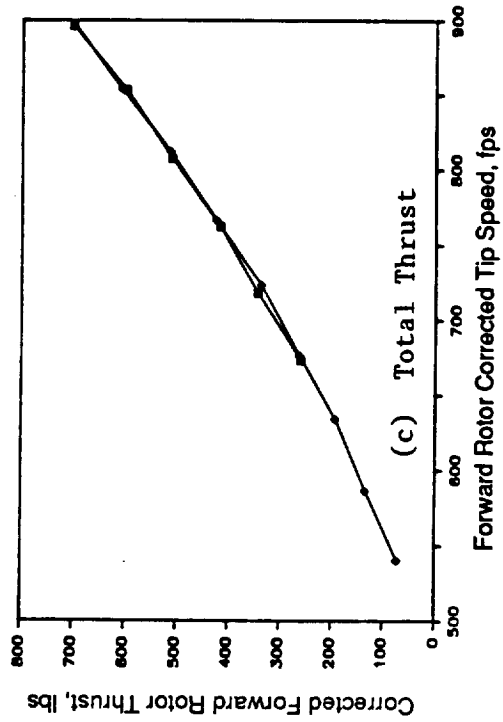
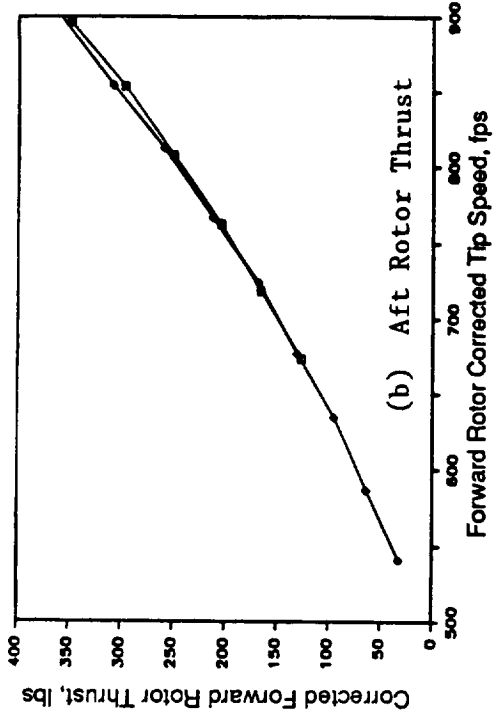
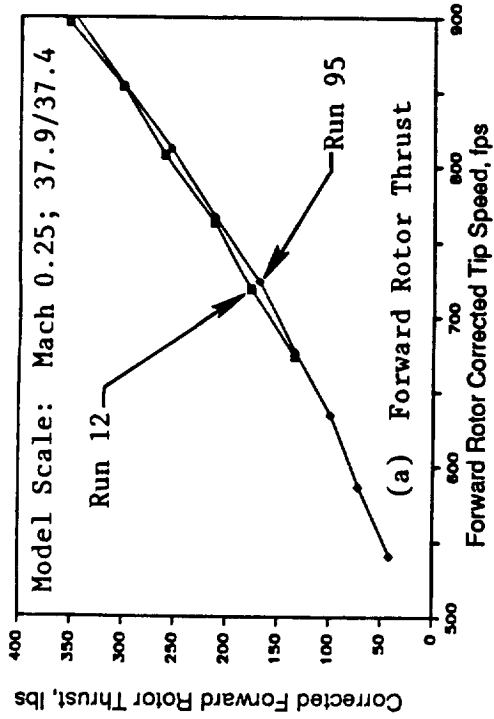


Figure 190. Repeatability of Aero Performance Data of Baseline F-7/A-7 (8+8) Configuration at Cell 41.

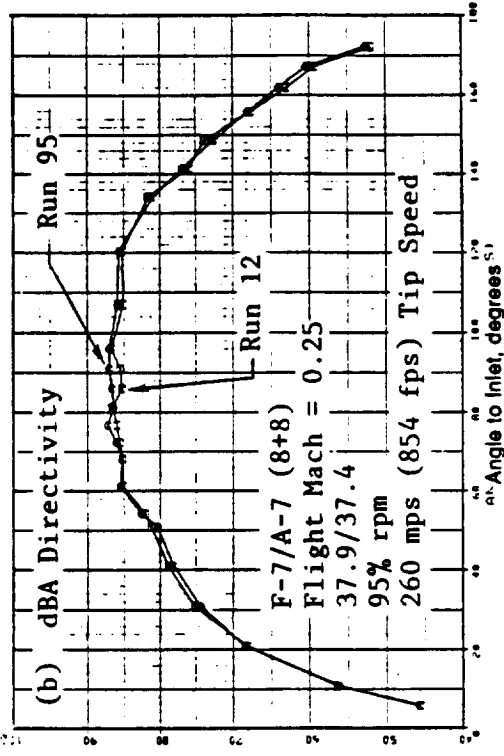
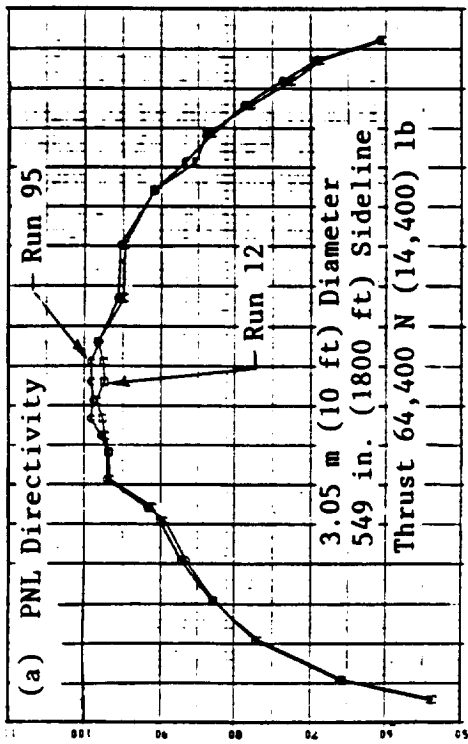


Figure 192. The Repeatability of PNL and dBA Directivities of Baseline F-7/A-7.

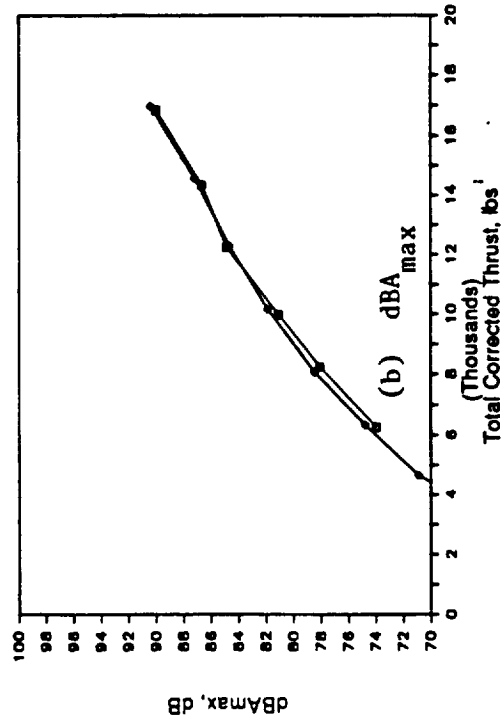
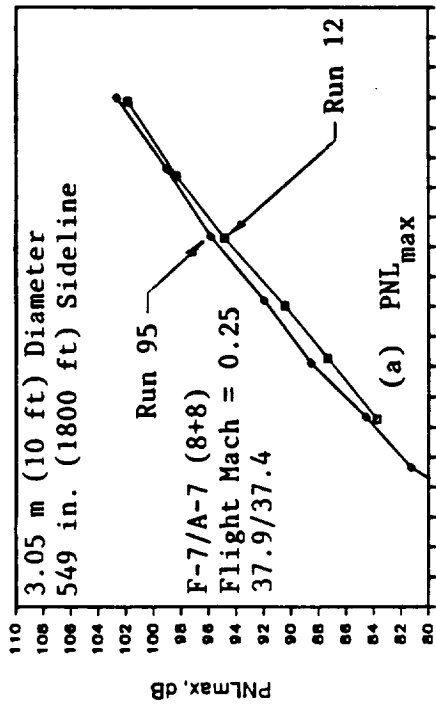


Figure 191. Repeatability of Acoustic Data of Baseline F-7/A-7 Over a Range of Tip Speeds.

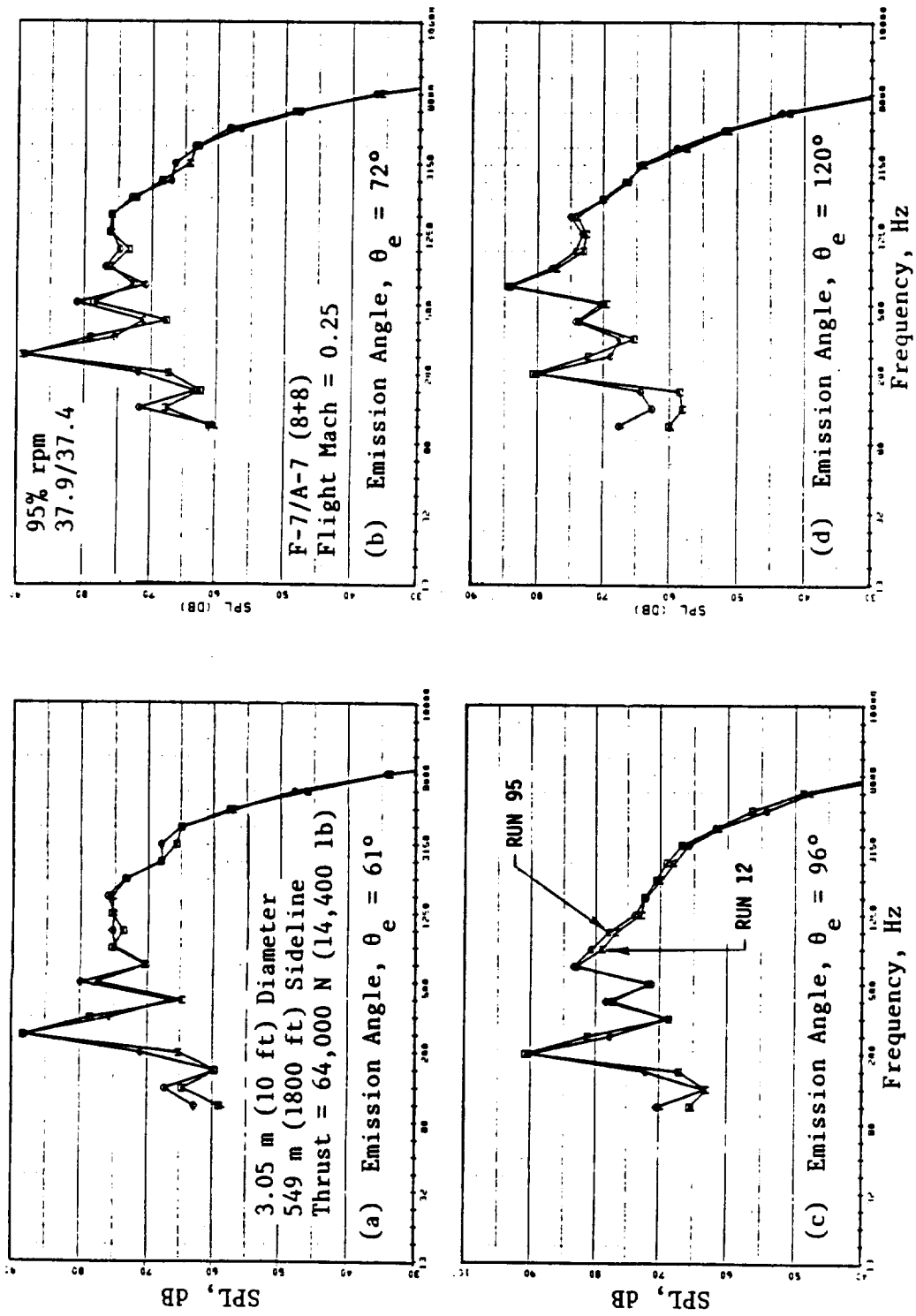
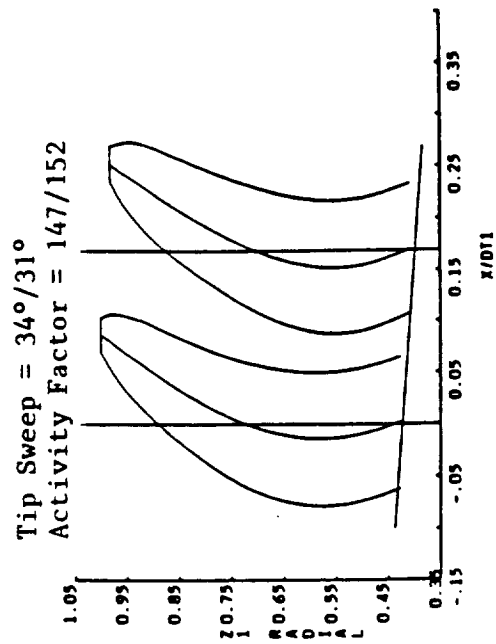
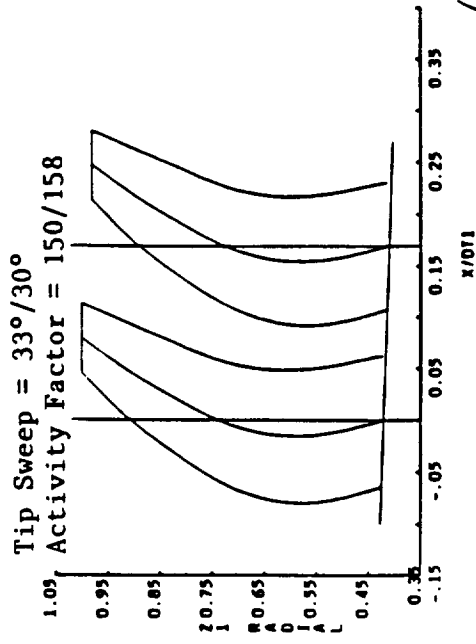


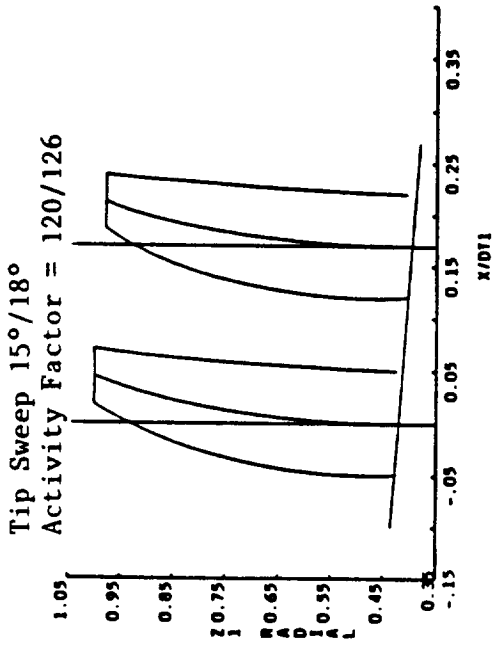
Figure 193. Repeatability of Baseline F-7/A-7 Spectra at 260 mps (854 fps) Tip Speed.



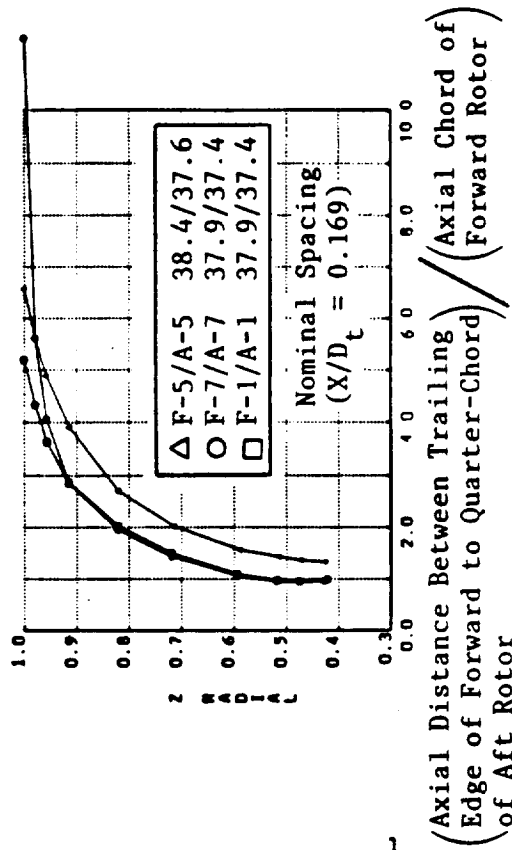
(a) F-7/A-7 Planform



(b) F-1/A-1 Planform



(c) F-5/A-5 Planform



(d) Blade Spacing

Figure 194. Comparison of Test Blade Configurations.

design. In addition, for the nominal spacing between rotor pitch-change axes ($Z/D_t = 0.169$) of this test series, the shorter chord of F-5/A-5 results in an increased axial spacing between the TE (trailing edge) of the forward rotor and the quarter-chord point of the aft rotor. This spacing comparison for the test pitch settings is provided in View D of Figure 194.

Measured thrust and power for the three blade configurations at the test pitch settings are compared in Figure 195. Examination of this figure reveals that for a given tip speed, F-1/A-1 results in slightly higher thrust relative to F-7/A-7 and F-5/A-5; for a given absorbed shaft power, the F-1/A-1 provides a slightly higher thrust than F-7/A-7, which in turn, provides a higher thrust than does the F-5/A-5 (low activity factor) design.

Figure 196 provides an acoustic data comparison, in terms of scaled and maximum OASPL (overall sound pressure levels), PNL, and dBA as a function of total thrust, demonstrating that the higher sweep and higher activity factor (F-7/A-7 and F-1/A-1) designs result in lower overall noise levels as compared to the lower sweep and lower activity factor (F-5/A-5) design. Since the F-1/A-1 produced a slightly higher thrust for a given tip speed and given absorbed power, it is noted to be slightly quieter than the F-7/A-7 for a given total thrust.

The OASPL and PNL directivities and selected spectra of the three blade designs are compared (Figures 197 through 200) for tip speeds of 247 mps (810 fps) and 232 mps (760 fps). The F-1/A-1 and F-7/A-7 designs resulted in identical overall noise characteristics for a given tip speed; the F-5/A-5 design exhibited substantial higher overall noise levels, particularly, at the higher tip speed. Spectral comparison at the higher tip speed also indicates significantly higher noise levels between BPF and 2xBPF, and also higher broadband noise at higher frequencies.

Figure 201 provides narrow-band model-scale spectral comparisons of the three blade designs at tip speeds of 247 mps (810 fps) and 232 mps (760 fps). These data confirm the increased broadband levels associated with the F-5/A-5 design, particularly at the higher tip speed. In addition, these plots reveal substantial numbers of multiple pure tones between the BPF and 3xBPF; this is probably due to separated flow. No significant differences are noted in the narrow-bands of F-7/A-7 and F-1/A-1. For the two selected cases, Figure 202 compares the individual tone level directivities of the F-7/A-7, F-1/A-1, and F-5/A-5. Comparing the directivities of F-5/A-5, F-7/A-7, and F-1/A-1 at the BPF indicates no significant differences in the levels of steady-loading noise of the three blade designs; however, some differences are noted in the SPL's at higher harmonics.

Sound pressure levels at the 2xBPF of F-1/A-1 are lower than those of F-7/A-7 and F-5/A-5. SPL's at the 4xBPF and 5xBPF of F-5/A-5 are significantly lower than those of F-1/A-1 and F-7/A-7, probably due to the increased spacing achieved as a result of the shorter chord design of F-5/A-5. However, no significant differences are noted in the sound pressure sum levels of the higher harmonic tones of F-5/A-5, F-7/A-7, and F-1/A-1 (as evidenced by Views F and L of Figure 202) that are a measure of the sum of the aerodynamic rotor-to-rotor interaction or unsteady-loading noise (as is described in Section 6.1.1.2).

Figure 203 depicts model-scale tone sum levels of the F-7/A-7, F-1/A-1, and F-5/A-5 configurations at selected emission angles as a function of model-size thrust. Again, due to the slightly improved performance of F-1/A-1, the steady-loading noise of F-1/A-1 is noted to be slightly smaller than that of the F-5/A-5 and F-7/A-7, for a given thrust. No significant differences

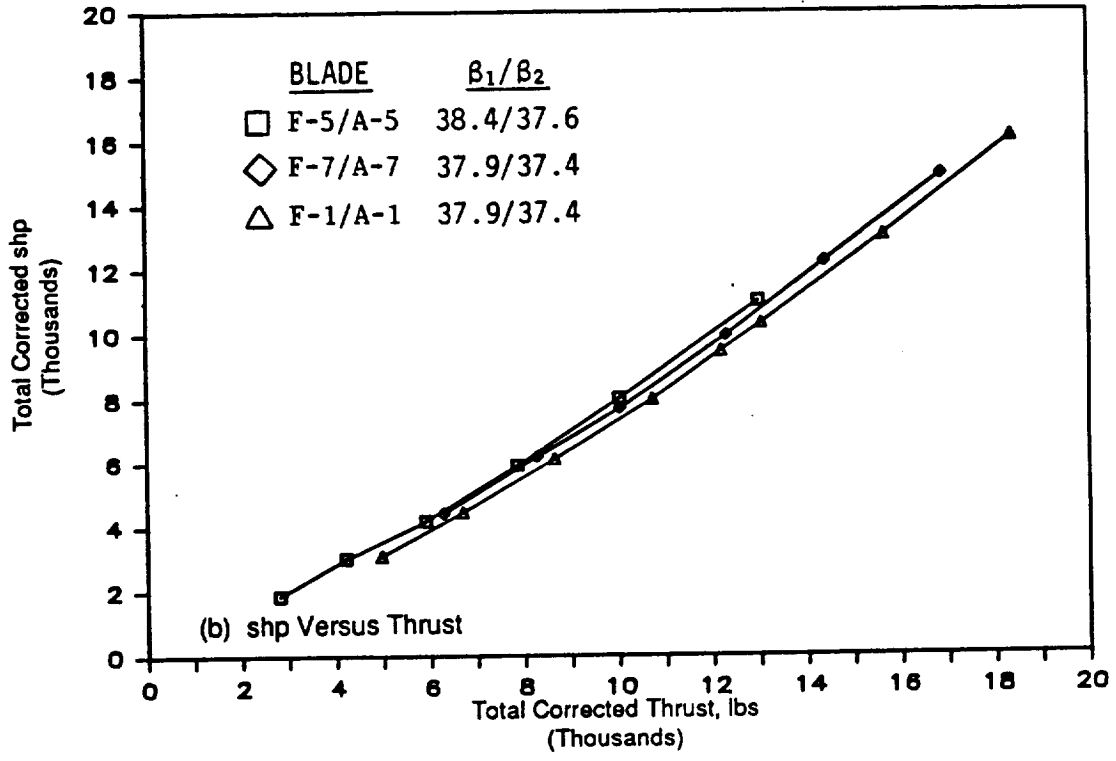
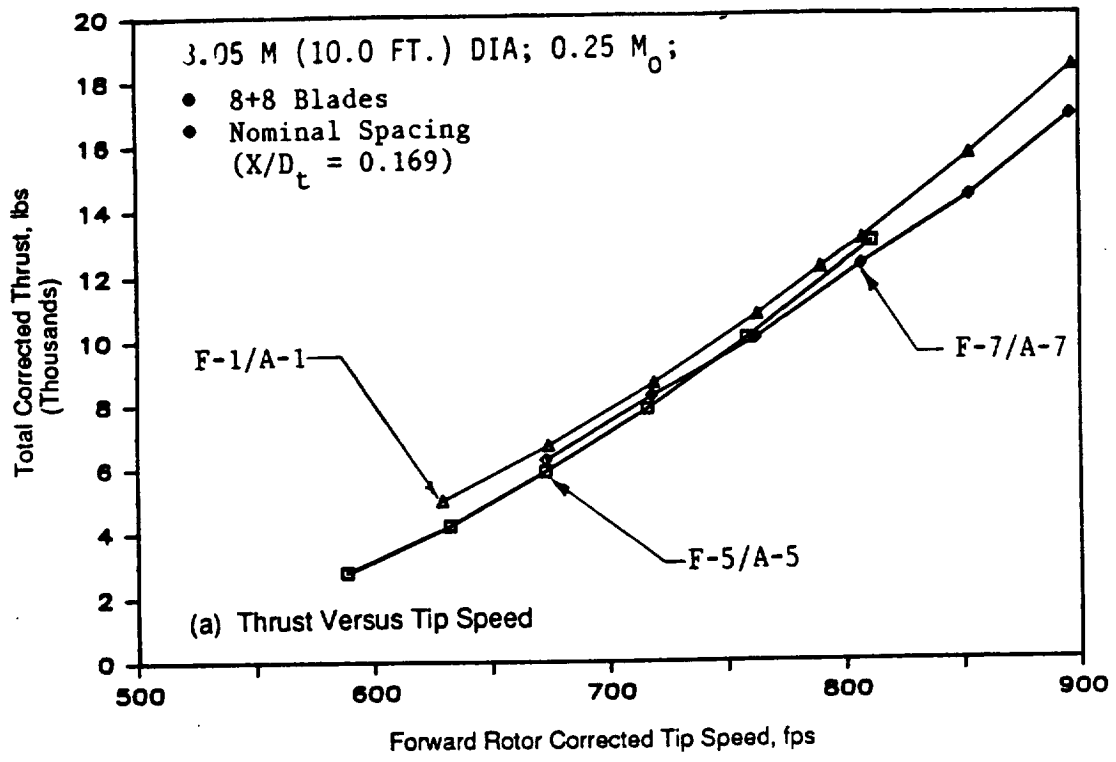


Figure 195. Aeroperformance Data of F-7/A-7, F-1/A-1, and F-5/A-5 (8+8) Configurations.

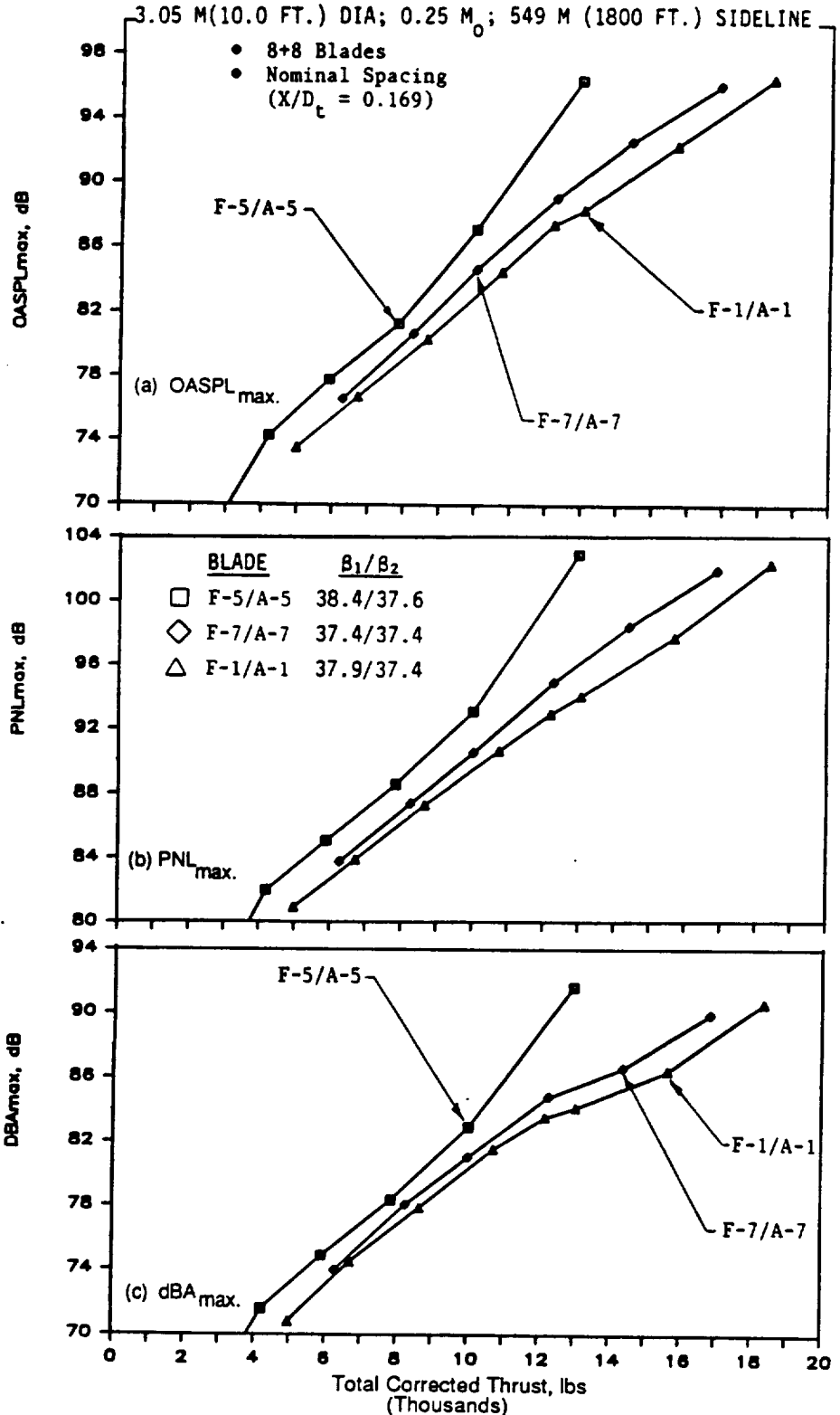


Figure 196. Acoustic Data of F-7/A-7, F-1/A-1, and F-5/A-5 (8+8) Configurations.

3.05 M (10.0 FT.) DIA; 0.25 M_0 ; 549 M (1800 FT.) SIDELINE

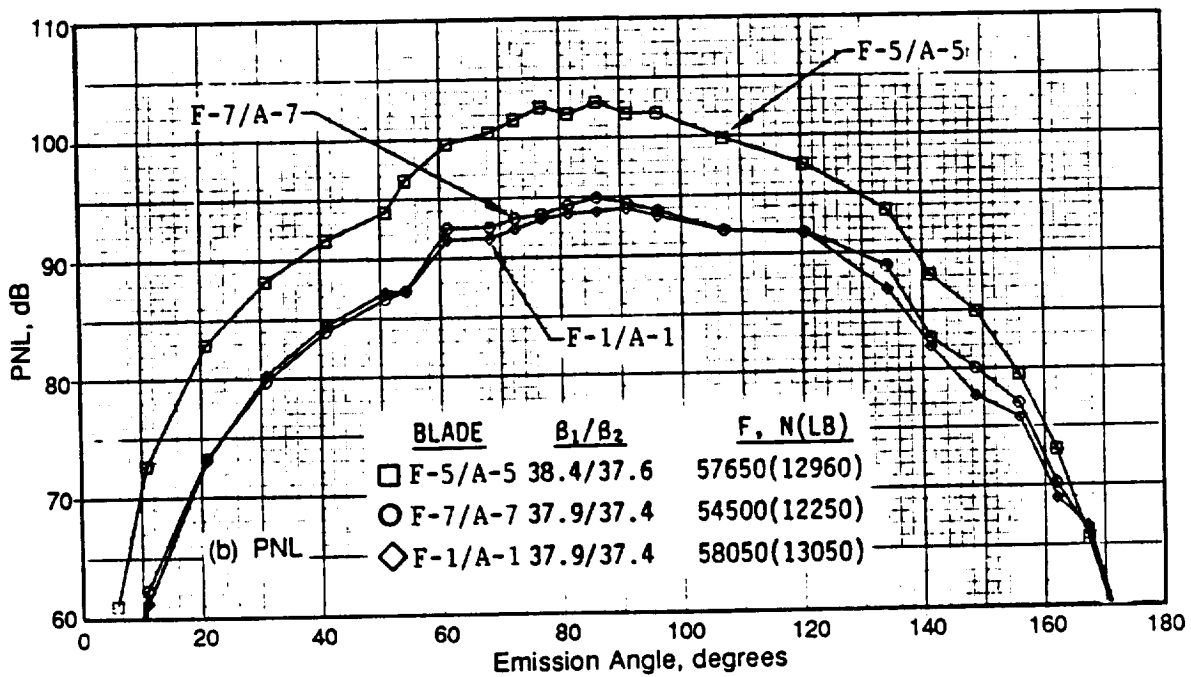
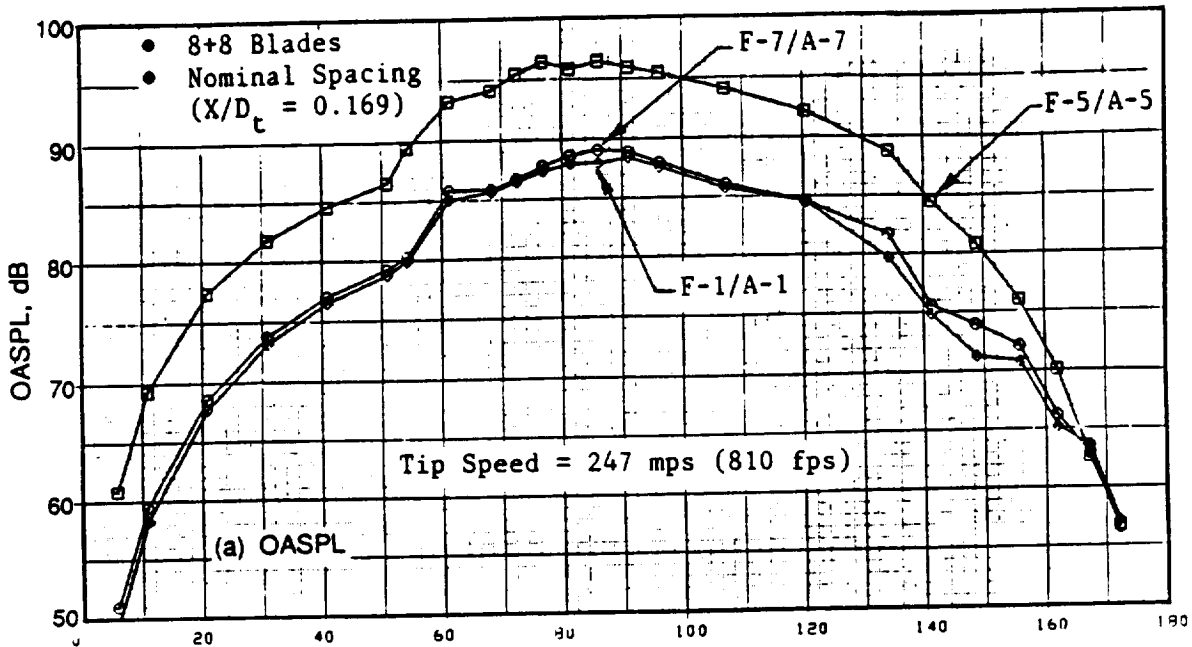


Figure 197. OASPL and PNL Directivities of F-7/A-7, F-1/A-1, and F-5/A-5.

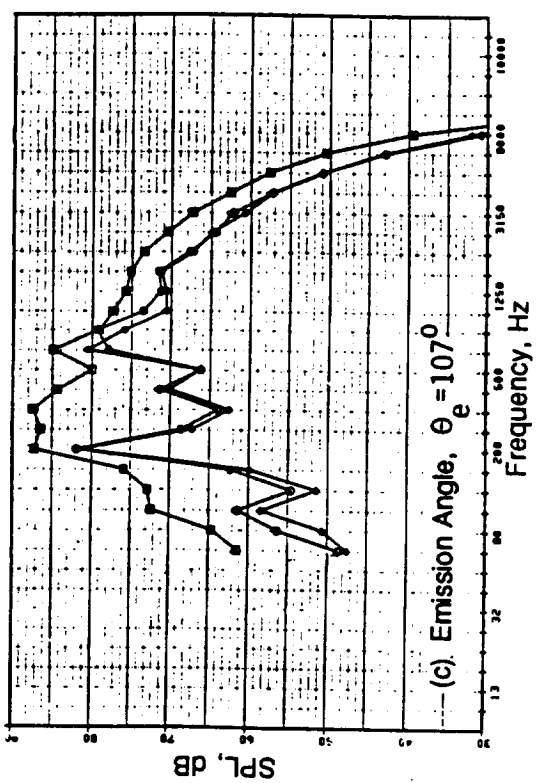
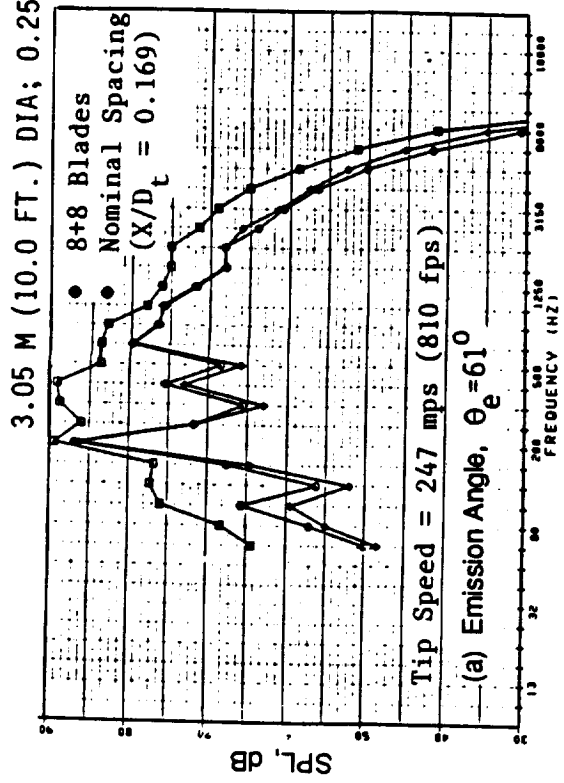
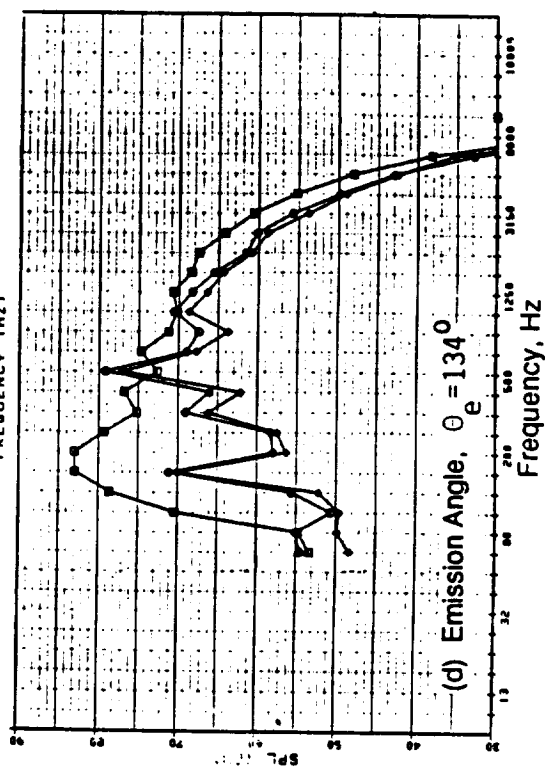
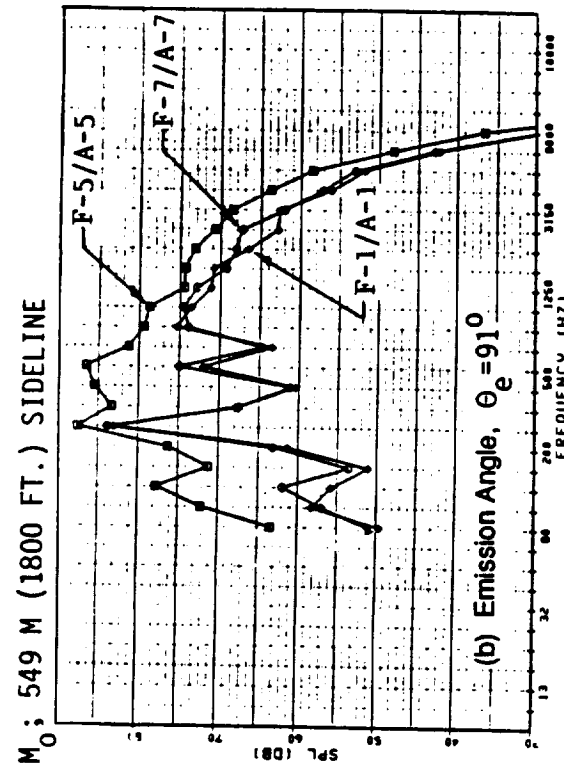


Figure 198. Selected Spectra of F-7/A-7, F-1/A-1, and F-5/A-5.

3.05 M (10.0 FT.) DIA; 0.25 M₀; 549 M (1800 FT.) SIDELINE

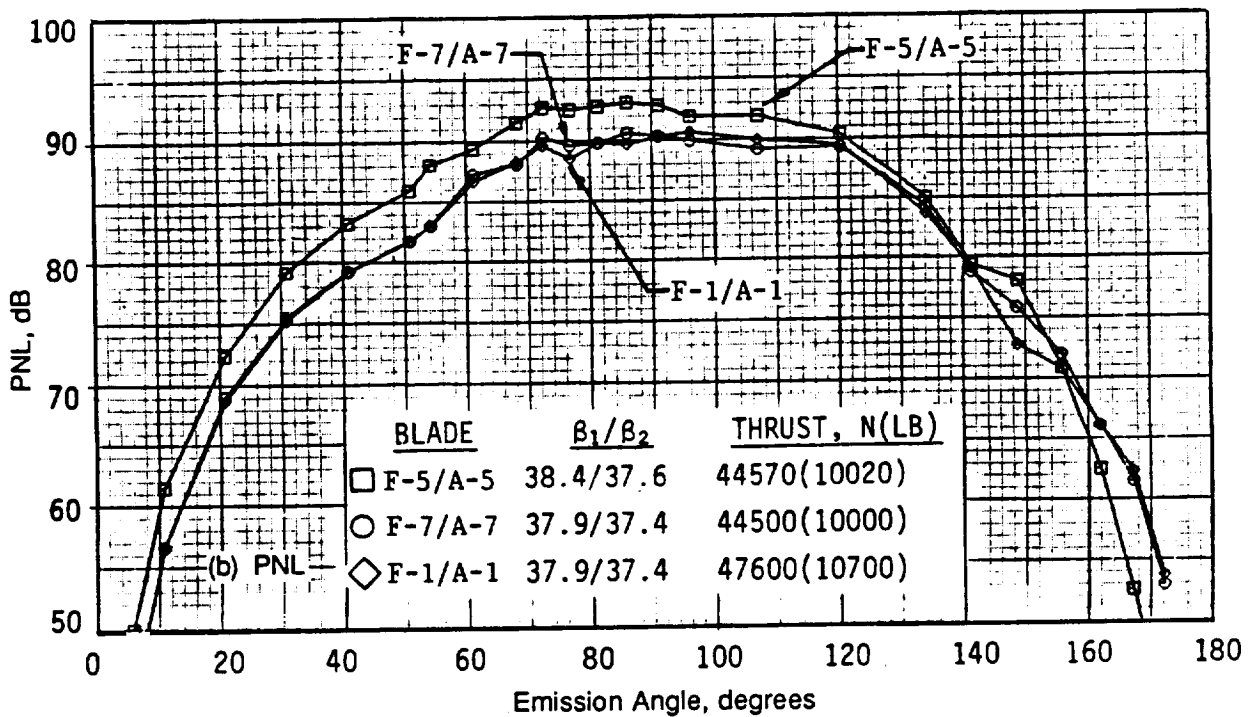
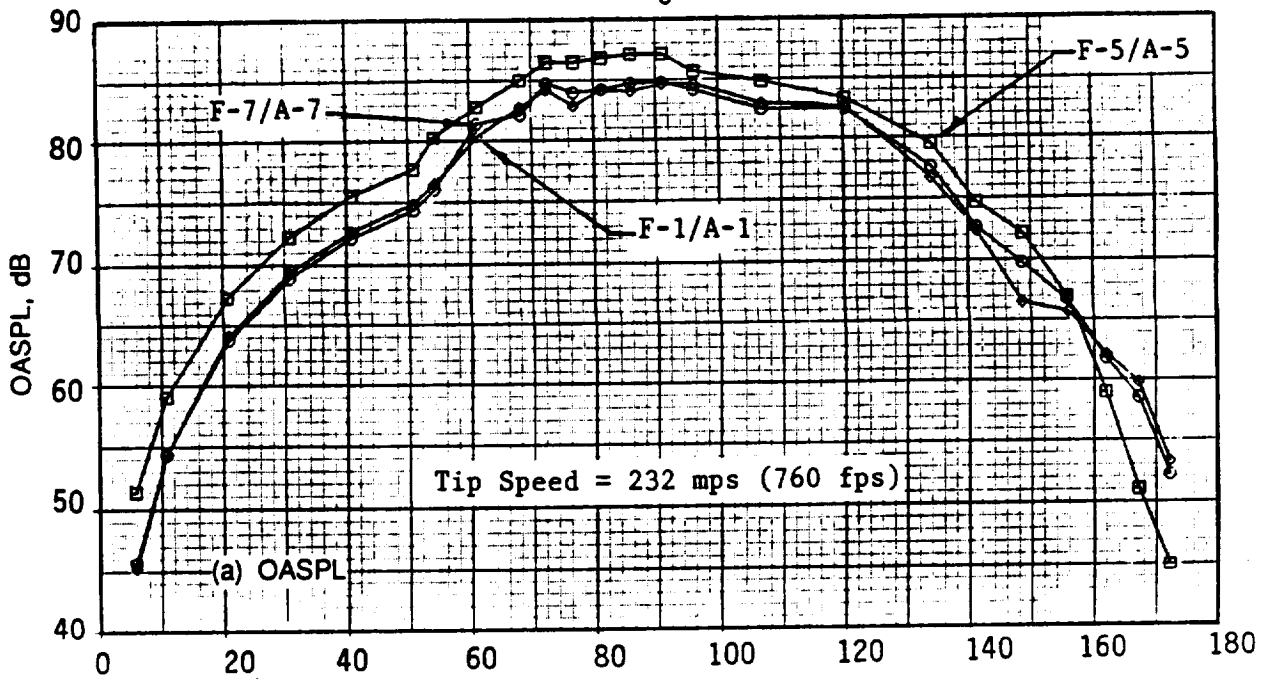


Figure 199. OASPL and PNL Directivities of F-7/A-7, F-1/A-1, and F-5/A-5.

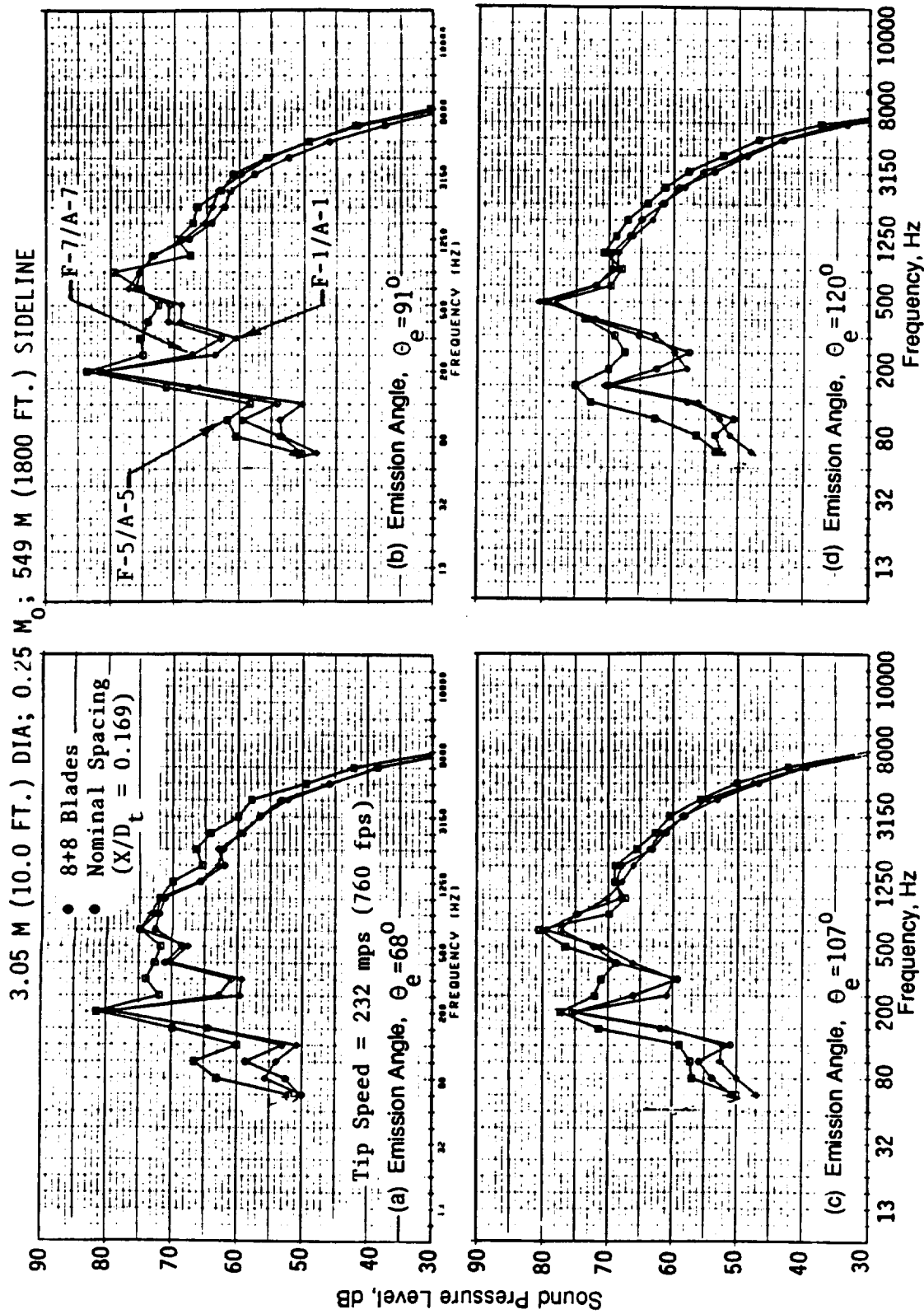


Figure 200. Selected Spectra of F-7/A-7, F-1/A-1, and F-5/A-5.

Model Scale: As-Measured Data; 8+8 Blades
 Nominal Rotor Spacing ($X/D_r = 0.169$); Tip Speed = 247 mps (810 fps)

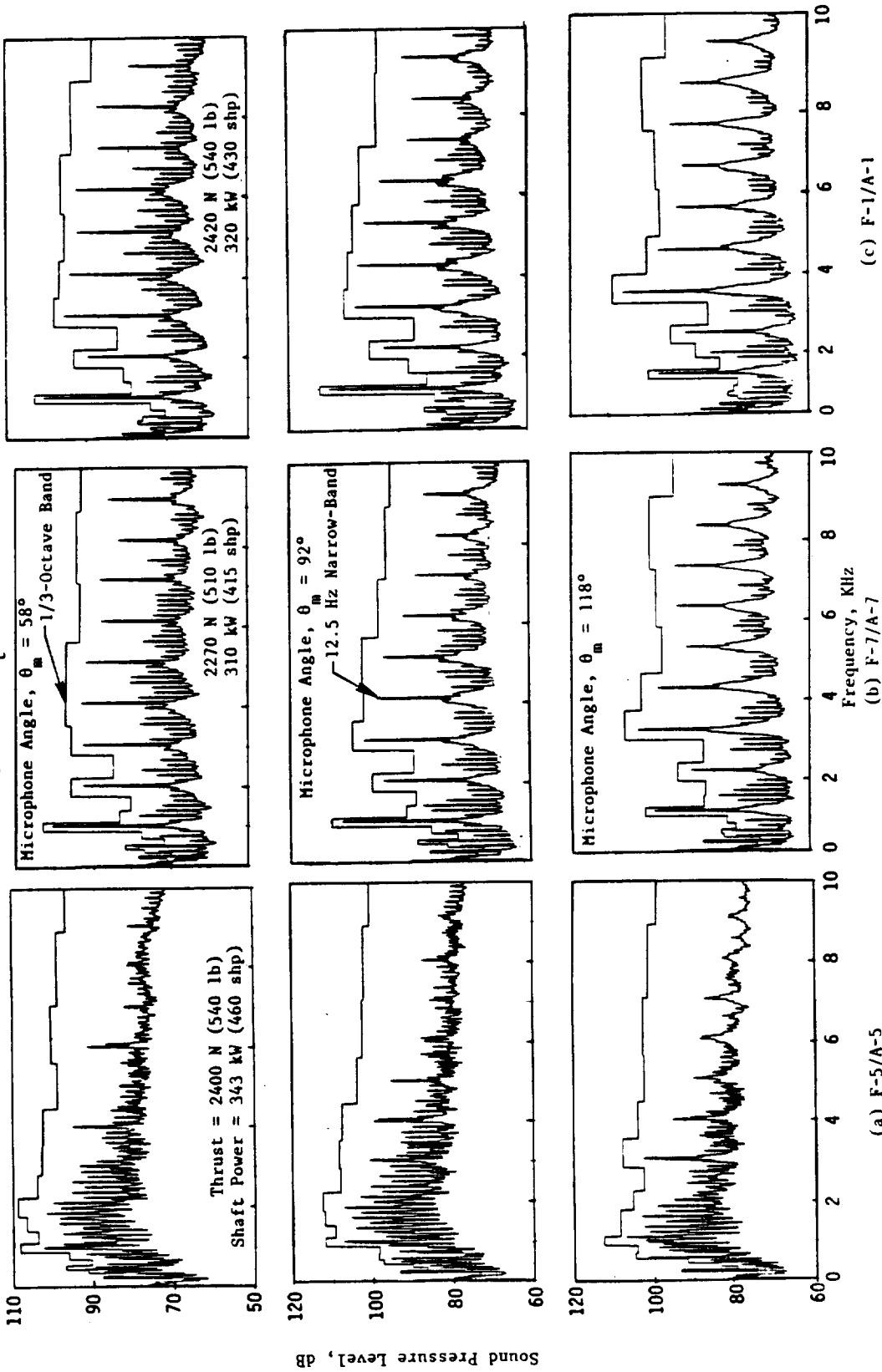


Figure 201. Model-Scale Spectra of F-5/A-5, F-7/A-7, and F-1/A-1.

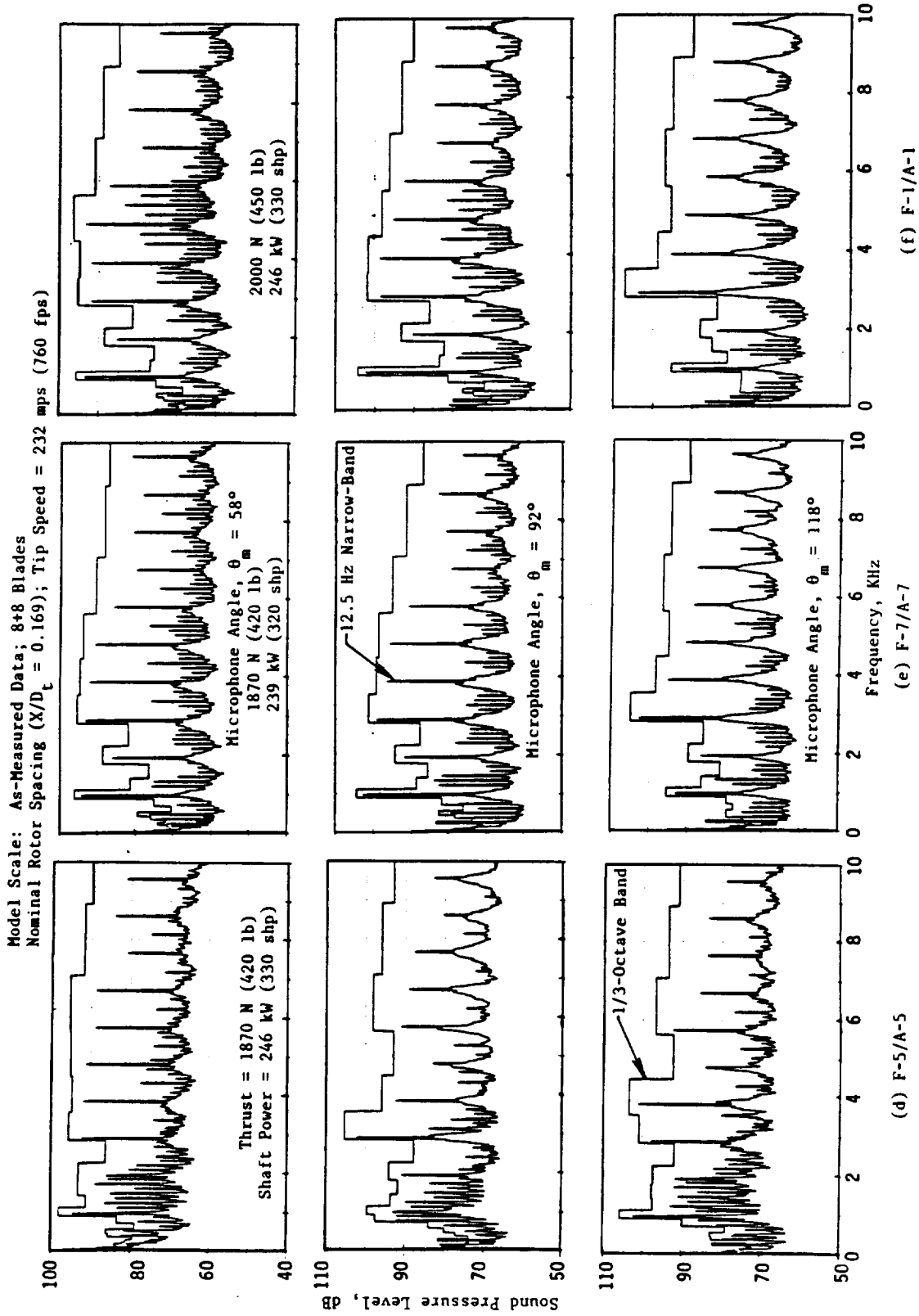


Figure 201. Model-Scale Spectra of F-5/A-5, F-7/A-7, and F-1/A-1 (Concluded).

- MODEL SCALE; 8.2 M(27 FT.) SIDELINE ; 0.25 M_0
- MODEL THRUST=2400 N(540 LB); TIP SPEED=247 MPS(810 FPS)
- 12.5 HZ NARROWBAND DATA

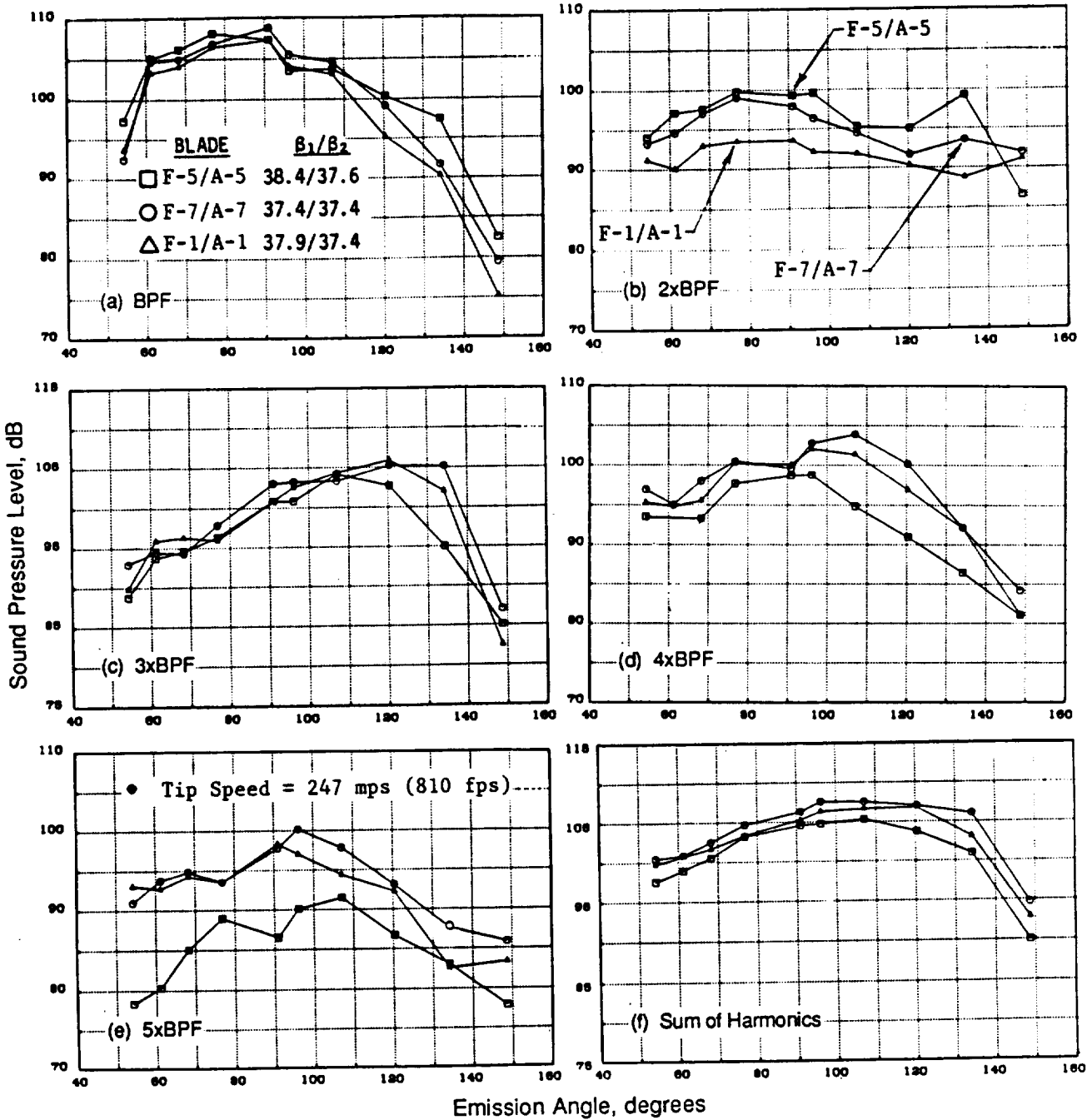


Figure 202. Model-Scale Tone Level Directivities of F-7/A-7, F-1/A-1, and F-5/A-5.

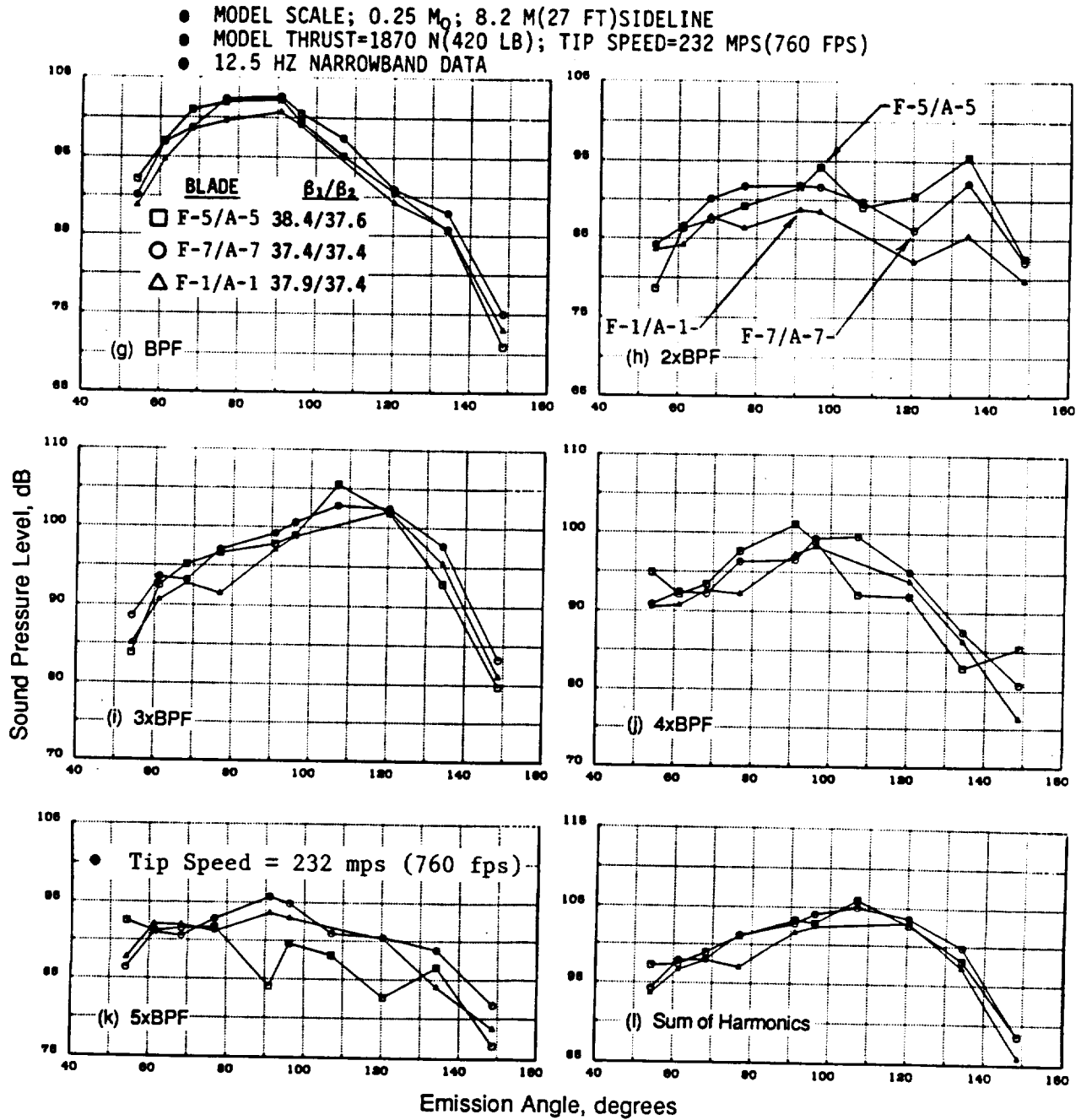
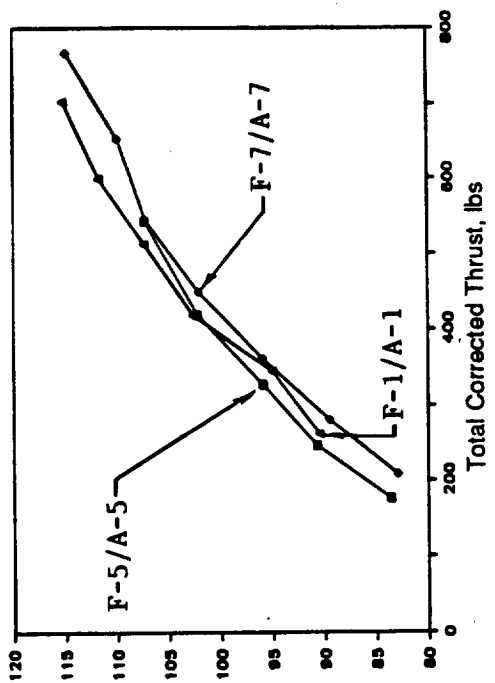


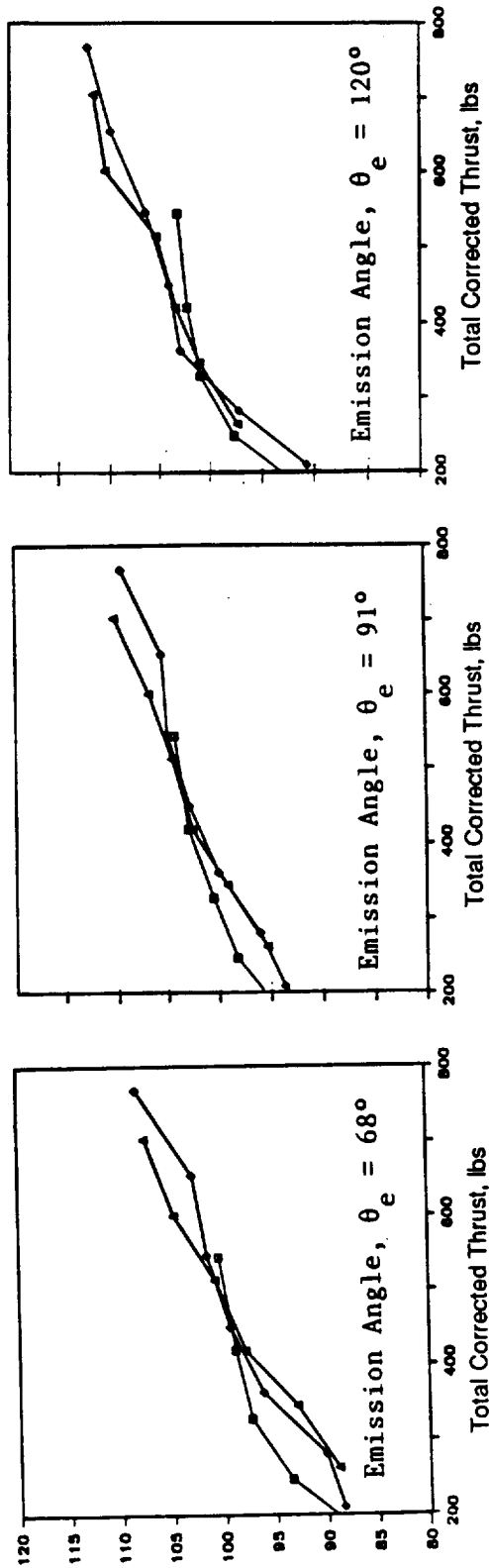
Figure 202. Model-Scale Tone Level Directivities of F-7/A-7, F-1/A-1, and F-5/A-5 (Concluded).



(a) BPF at Emission Angle, $\theta_e = 91^\circ$

- MODEL SCALE
- $M_0=0.25$
- 8.2 M(27 FT.) SIDELINE
- 8x8 BLADES
- NOMINAL ROTOR SPACING ($Z/D_t=0.17$)
- NOMINAL PITCH

BLADE	β_1/β_2
□ F-5/A-5	38.4/37.6
○ F-7/A-7	37.4/37.4
△ F-1/A-1	37.9/37.4



(b) Sum of Harmonics

Figure 203. Model-Scale Tone Sum Levels of F-7/A-7, F-5/A-5, and F-1/A-1 as a Function of Total Thrust.

are noted in the SPL sums of the higher harmonic tones that are a measure of the rotor-to-rotor interaction or unsteady-loading noise.

The acoustic evaluation of F-5/A-5, F-7/A-7, and F-1/A-1 blade designs is concluded by providing a comparison on the basis of EPNL (Figure 204) at two selected thrusts: 44,500 N (10,000 lb) and 57,800 N (13,000 lb). At these thrusts, the lower sweep and activity factor design (F-5/A-5) is noisier than the higher sweep and higher activity factor (F-7/A-7) design by 2.2 dB and 4.2 dB, respectively. Due to the slightly improved performance of the F-1/A-1, it is quieter, compared to the F-7/A-7, at these thrusts by 1.0 dB and 1.8 dB, respectively.

7.1.1.2.2 F-7/A-7 and F-11/A-11 (11+9): Series 2

Figure 205 provides a geometric comparison of the F-7/A-7 and F-11/A-11 blade designs. F-11/A-11 blades have a higher sweep, a significantly higher activity factor, and a higher chord than the F-7/A-7. An increased spacing (referred to as supermaximum, $X/D_t = 0.32$) between rotor pitch-change axes was used for the F-11/A-11 tests; the rotor pitch-change-axes spacing utilized for the F-7/A-7 test configuration was the maximum spacing with $X/D_t = 0.24$. The use of two different spacings for the rotor pitch-change axes during this test series, however, resulted in equivalent values for normalized axial distances between the trailing edge of the forward rotor and the aft rotor quarter-chord point. This equivalent spacing for the test configurations of this series is depicted in Figure 205, View B; both the F-7/A-7 and the F-11/A-11 were tested with 11 forward and 9 aft blades at an open pitch angle.

Measured thrust and power data (Figure 206) demonstrate that these data sets are comparable; with the F-11/A-11 yielding a slightly higher thrust for a given tip speed, and F-7/A-7 providing slightly higher thrust for a given absorbed power. In terms of the scaled and maximum OASPL, PNL, and dBA, the comparison of acoustic data as a function of total thrust (Figure 207) reveals that for thrusts greater than 53,400 N (12,000 lb), higher sweep and significantly higher activity factor blades (such as, F-11/A-11) result in slightly lower maximum PNL and dBA data and equal maximum OASPL data, as compared to an equivalent F-7/A-7 configuration.

Figures 208 through 211 compare OASPL and PNL directivities and selected spectra of test configurations for tip speeds of 229 mps (750 fps) and 204 mps (670 fps). The F-11/A-11 is slightly quieter at the higher tip speed than the F-7/A-7; at the lower tip speed, both blades result in the same overall noise levels. Spectral comparison at higher tip speeds shows some benefit with the F-11/A-11 at forward rotor BPF and at higher frequencies; however at lower tip speeds, some increase is noted in the noise levels of F-11/A-11 at some of the higher harmonic frequencies.

Selected model-scale narrow-band spectra are shown in Figures 212 and 213 at tip speeds of 232 mps (760 fps) and 192 mps (630 fps), respectively; model-scale tone sum directivities for these two cases are presented in Figures 214 and 215. These data indicate that at the higher tip speed, and hence, higher thrust condition, the F-11/A-11 resulted in a small reduction of the steady-loading noise as evidenced by a decrease in sound pressure sum level of the forward and aft rotor BPF's and harmonics and a reduction in unsteady-loading noise as shown by a decrease in the sound pressure sum level of the rotor-to-rotor interaction tones. At the lower tip speed and lower thrust condition, no such clear reductions are noted with F-11/A-11 blades.

Model-scale tone sum levels of test configurations at selected emission angles are illustrated in Figure 216 as a function of model-size thrust. The F-11/A-11 design yields a steady-loading noise

3.05 M(10.0 FT.) DIA.; 0.25 M₀; 549 M(1800 FT.) SIDELINE

Blade (β_1/β_2)	Δ EPNL, dB		
	F-7/A-7 (37.9/37.4)	F-1/A-1 (37.9/37.4)	F-5/A-5 (38.4/37.6)
Thrust, N(LB)↓			
44500(10000)	0	-1.0	+2.2
57800(13000)	0	-1.8	+4.2

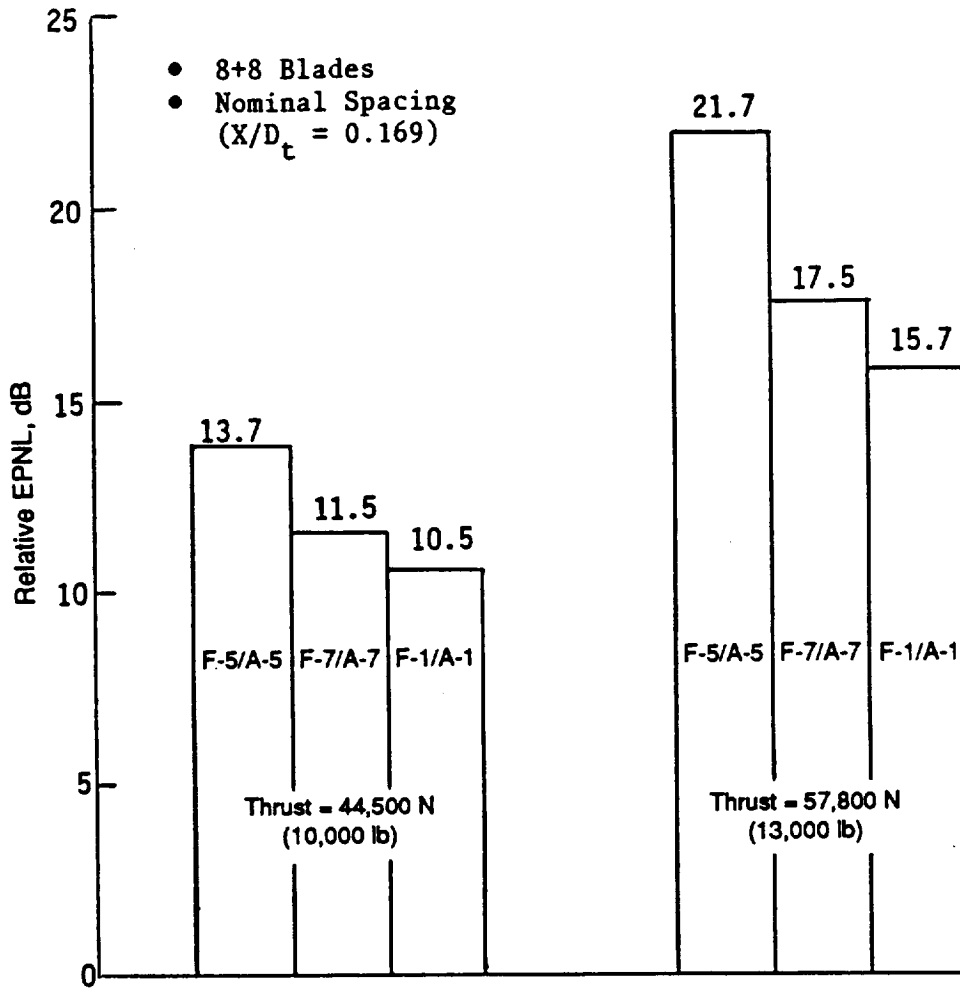
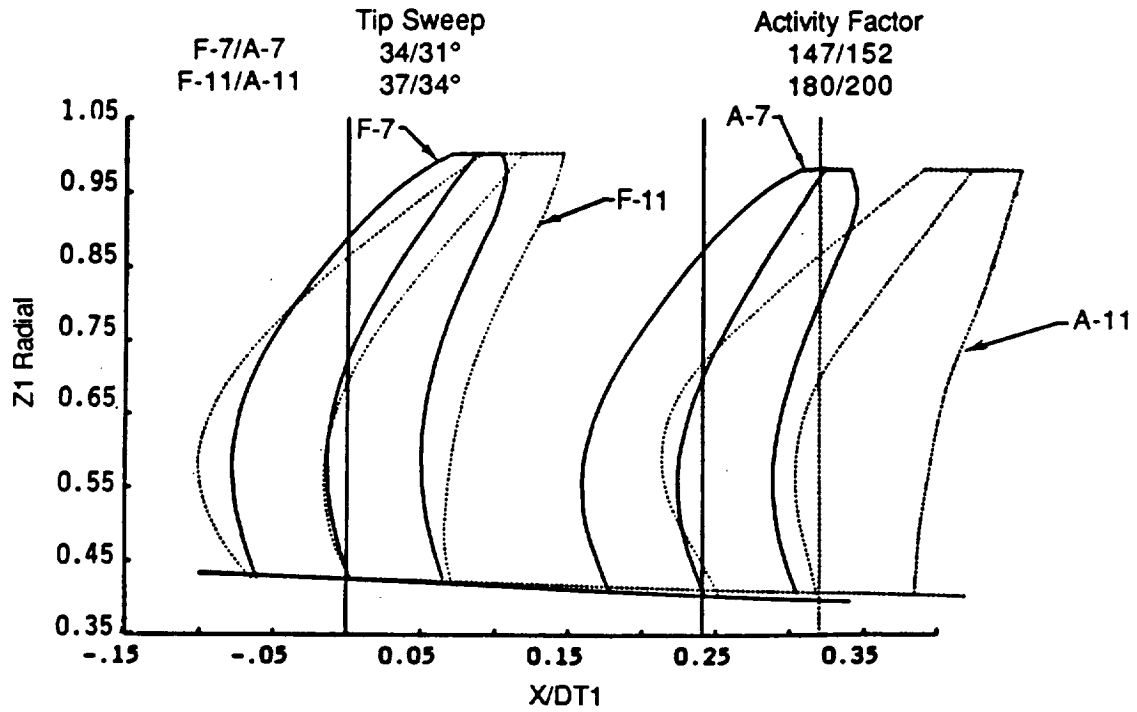
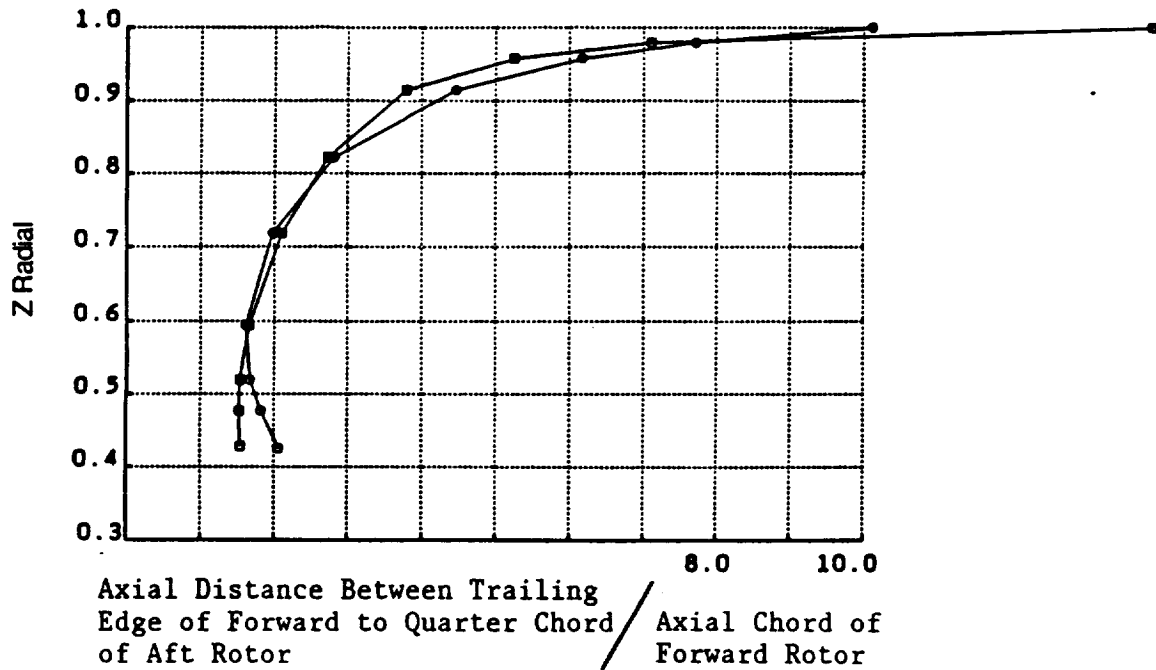


Figure 204. EPNL Comparison of F-7/A-7, F-1/A-1, and F-5/A-5 (8+8) Blade Configurations.

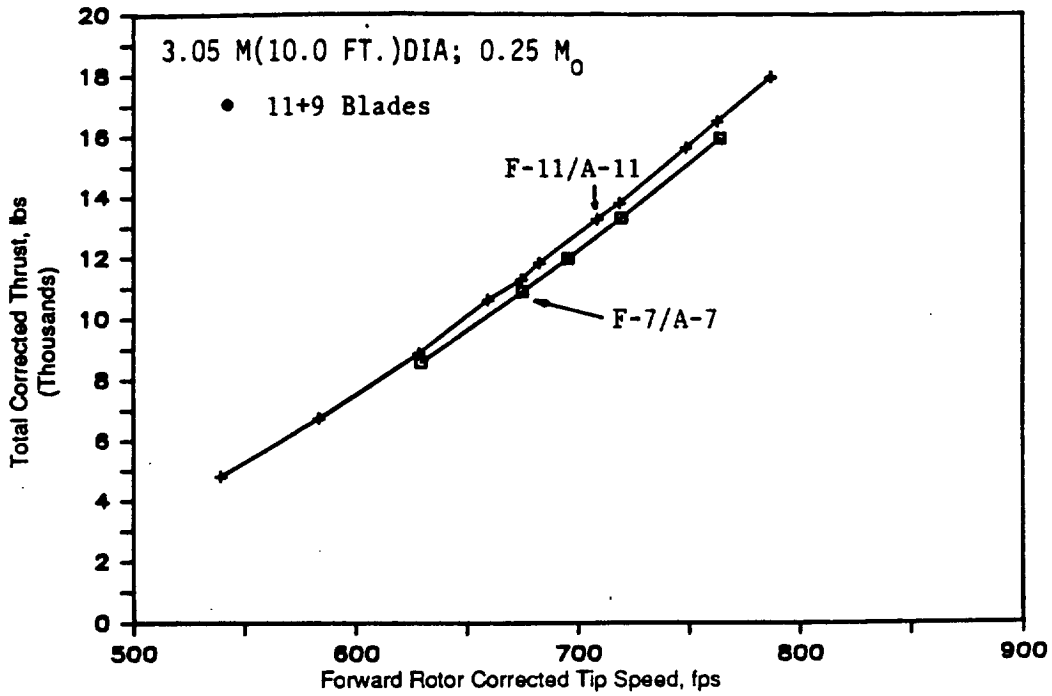


(a) Blade Planform

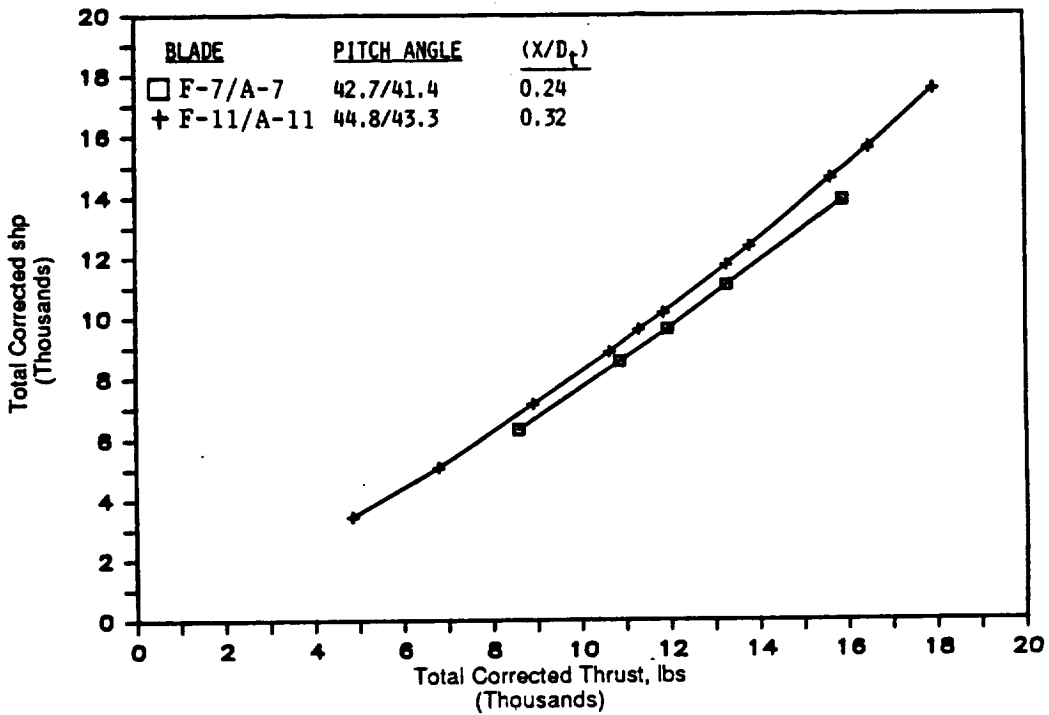


(b) Blade Spacing

Figure 205. Comparison of Test Blade Configurations F-7/A-7 and F-11/A-11.

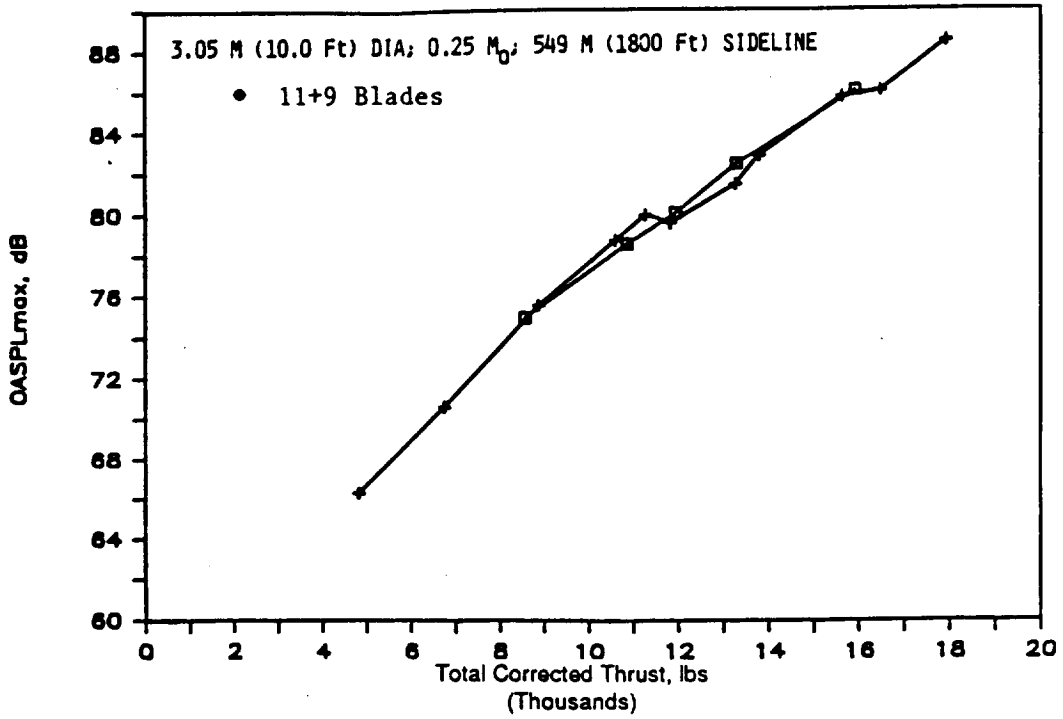


(a) Thrust Versus Tip Speed

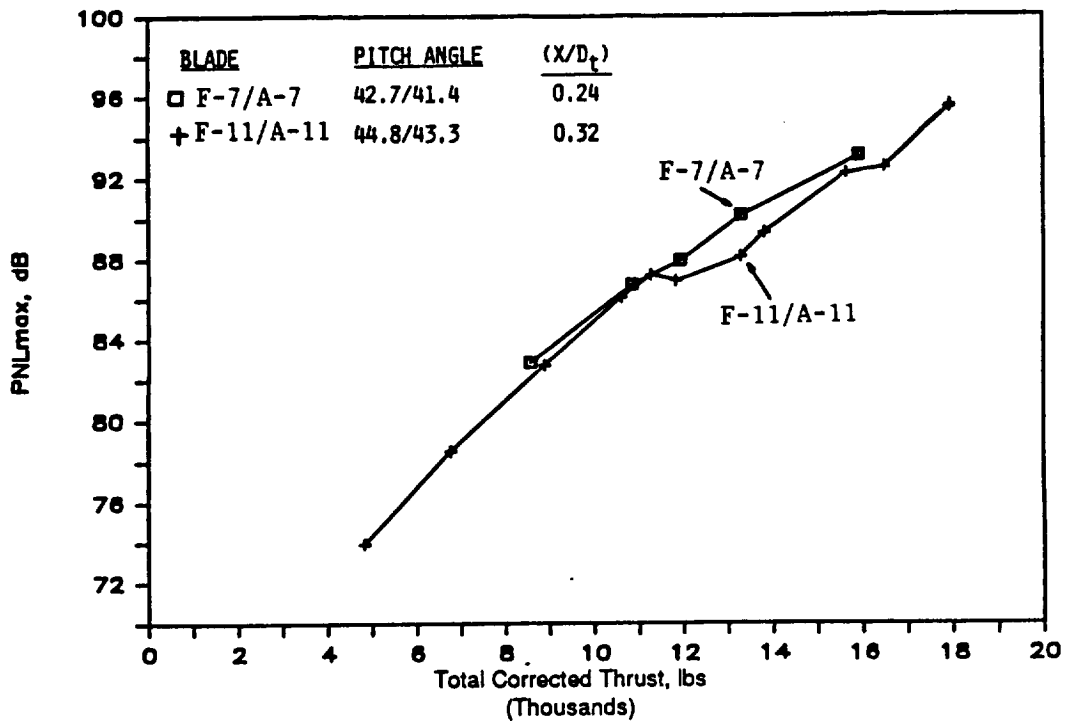


(b) Shaft Horsepower

Figure 206. Aeroperformance Data of F-7/A-7 and F-11/A-11.

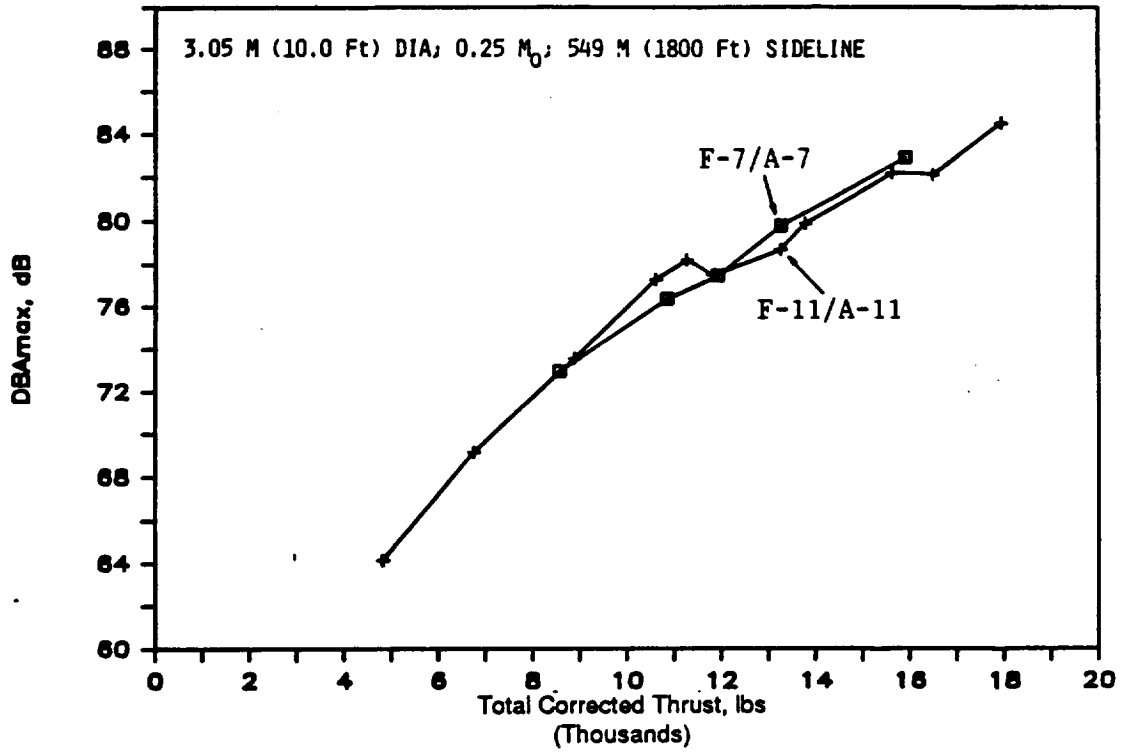


(a) OASPL_{max}.



(b) PNL_{max}

Figure 207. Acoustic Data of F-7/A-7 and F-11/A-11.



(c) dBA max.

Figure 207. Acoustic Data of F-7/A-7 and F-11/A-11 (Concluded).

3.05 M(10.0 FT.)DIA; 0.25 M₀; 549 M(1800 FT.)SIDELINE

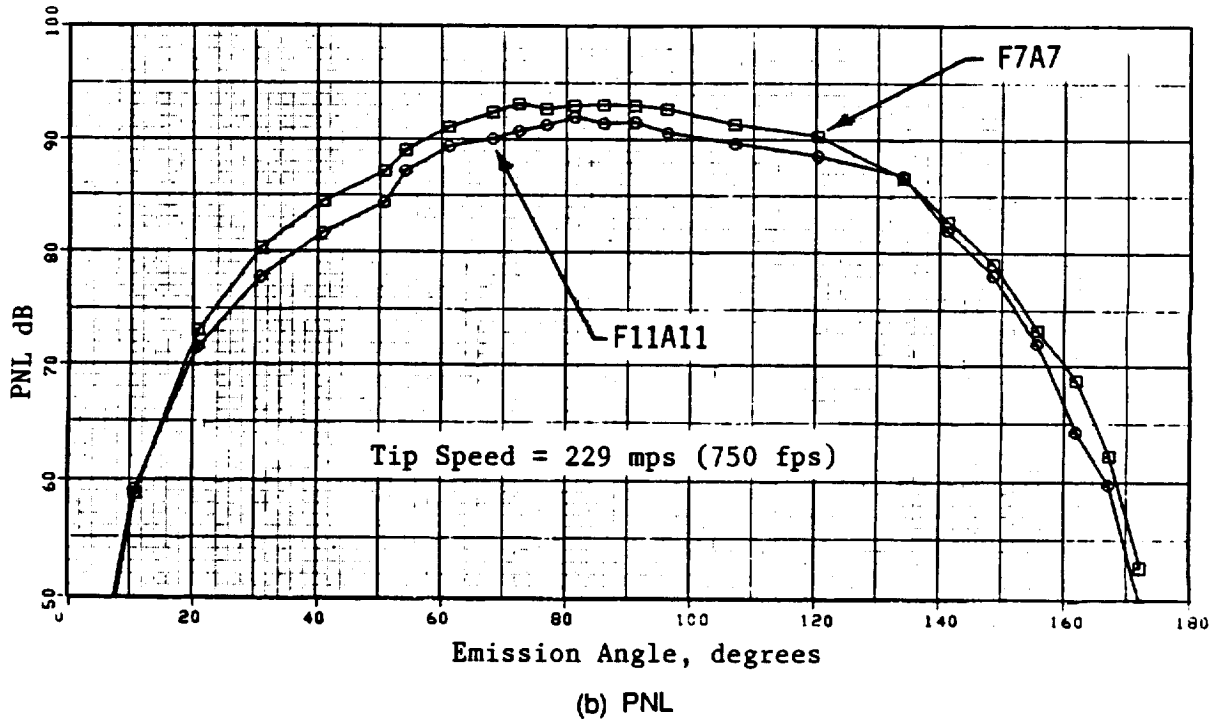
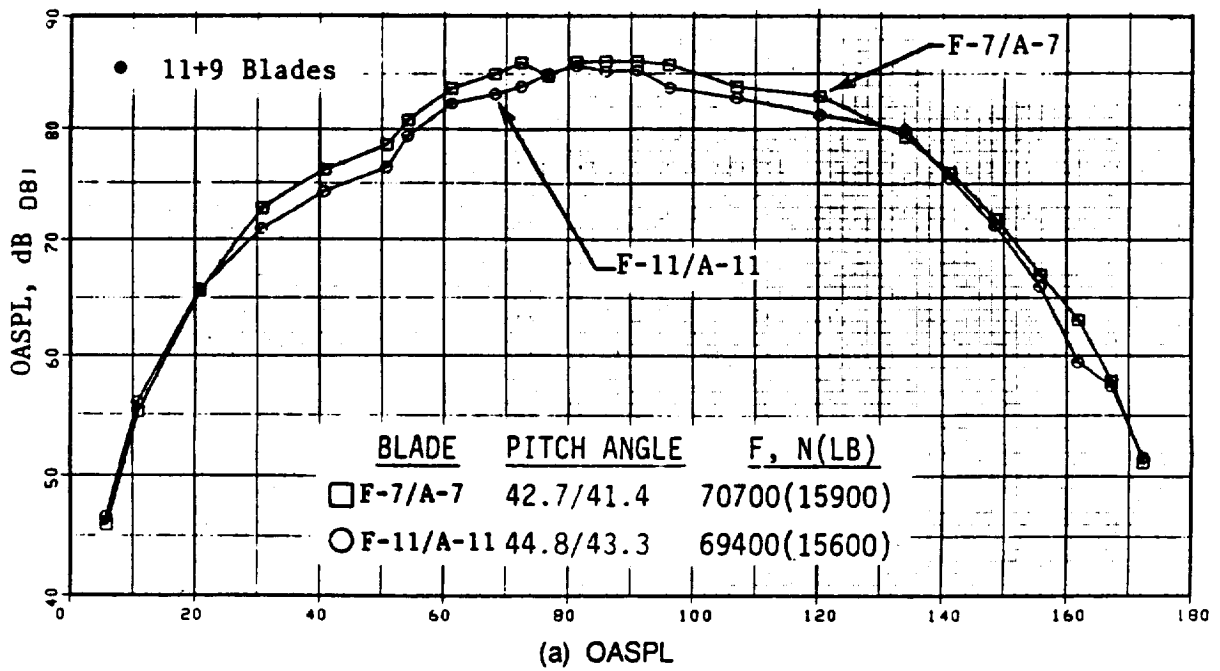
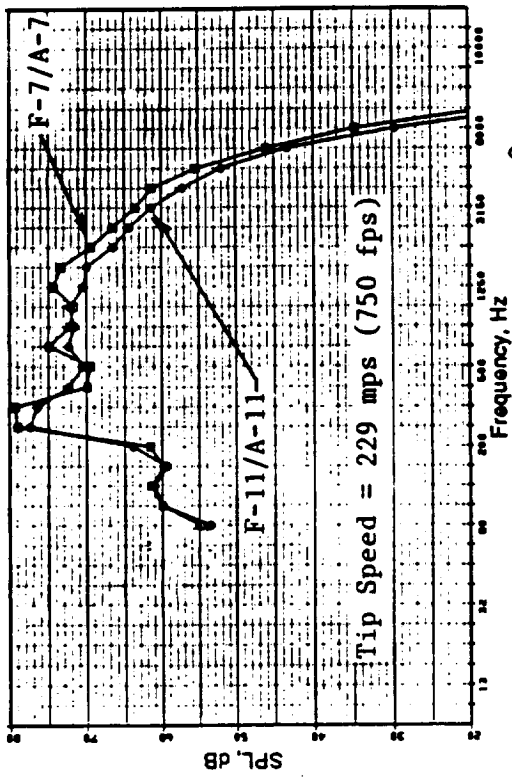
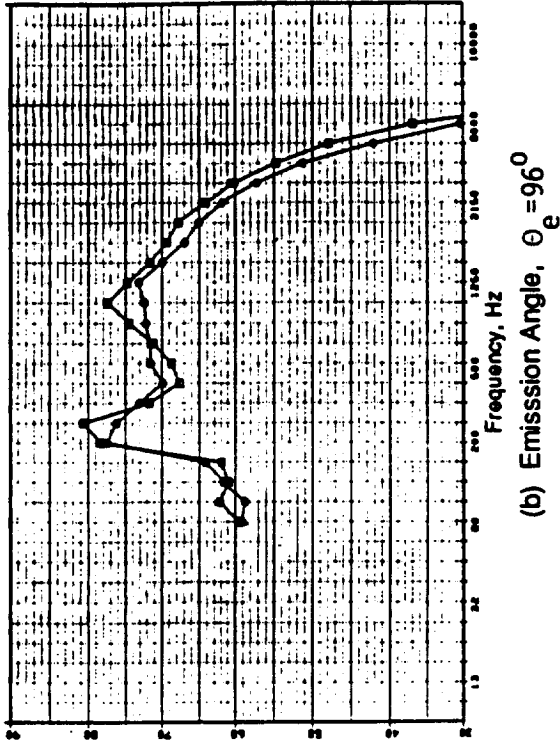


Figure 208. OASPL and PNL Directivities of F-7/A-7 and F-11/A-11.

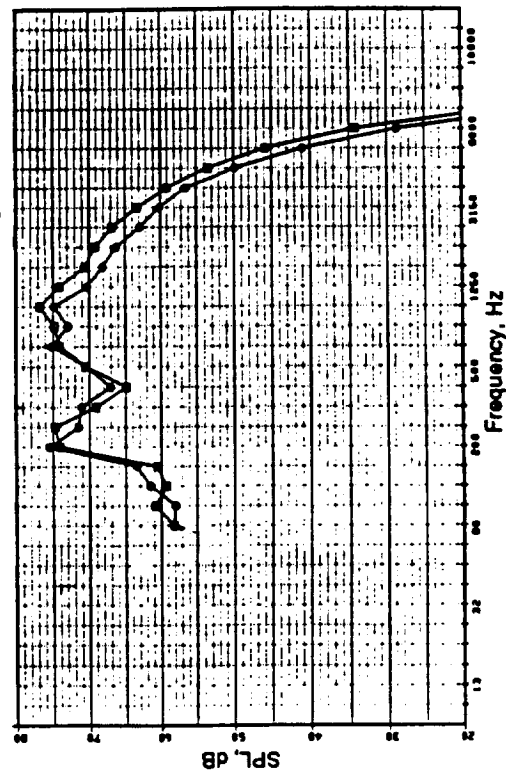
3.05 M(10.0 FT.)DIA; 0.25 M₀; 549 M(1800 FT.)SIDELINE



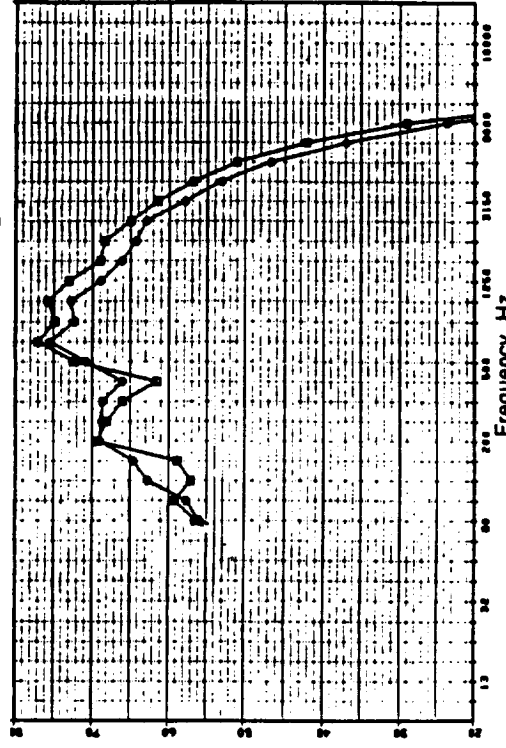
(a) Emission Angle, $\theta_e = 68^\circ$



(b) Emission Angle, $\theta_e = 96^\circ$



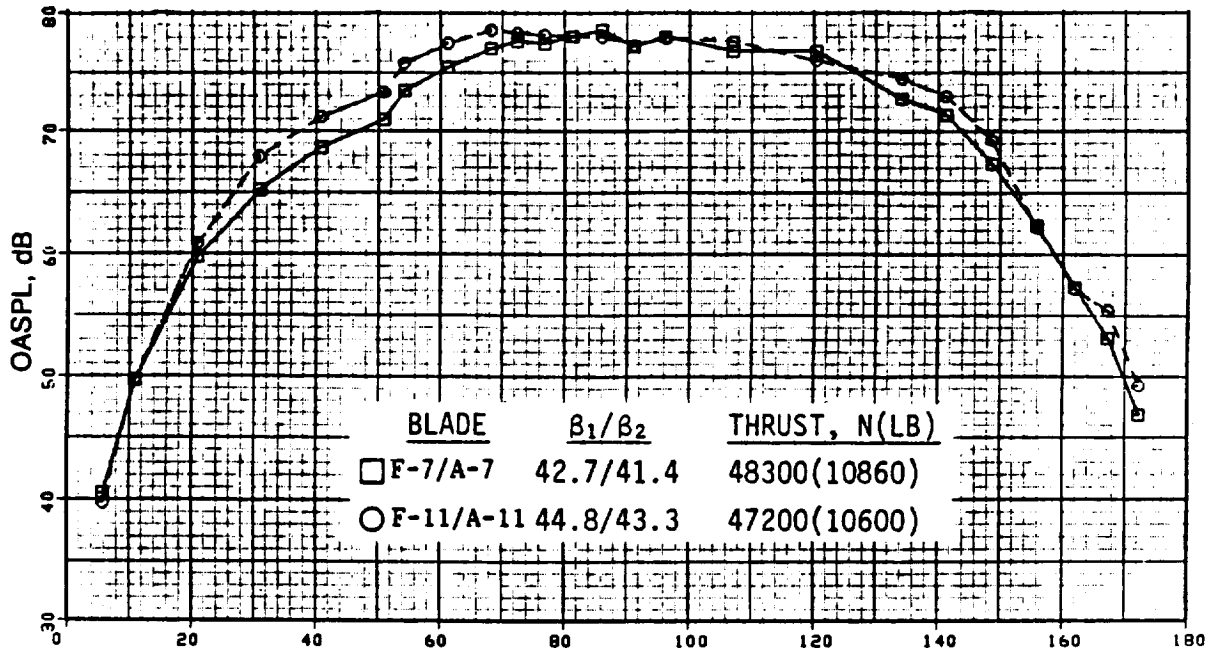
(c) Emission Angle, $\theta_e = 107^\circ$



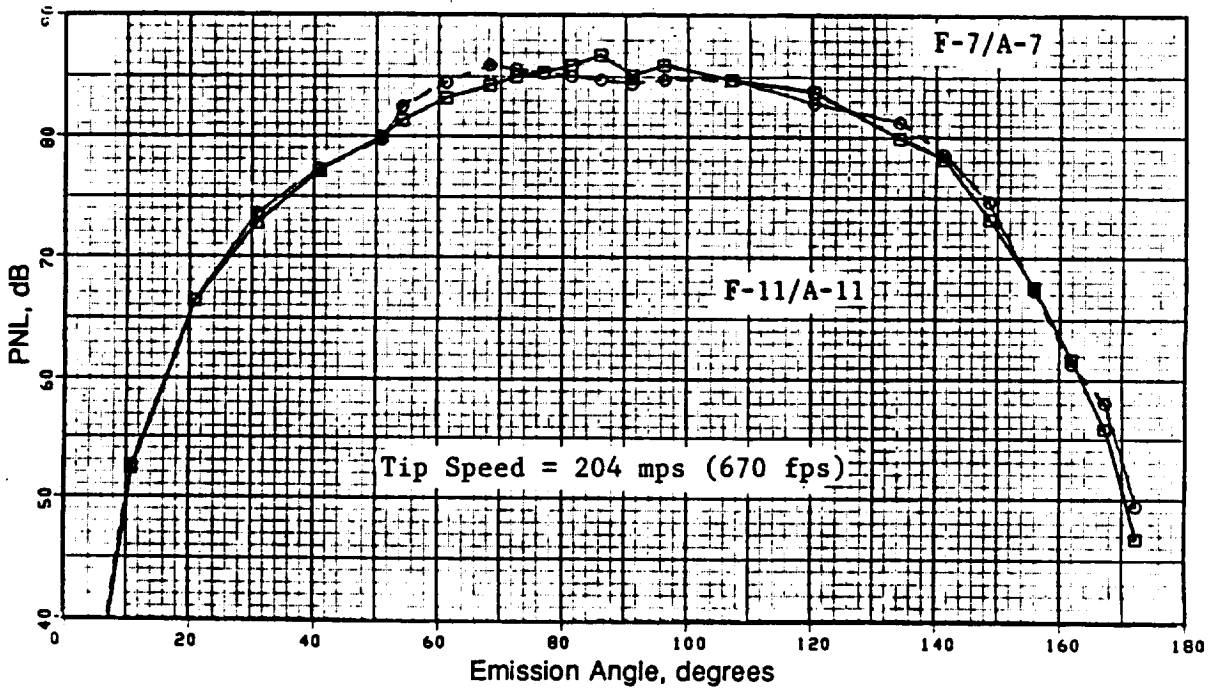
(d) Emission Angle, $\theta_e = 120^\circ$

Figure 209. Selected Spectra of the F-7/A-7 and F-11/A-11.

3.05 M(10.0 FT.)DIA; 0.25 M₀; 549 M(1800 FT.)SIDELINE



(a) OASPL



(b) PNL

Figure 210. The OASPL and PNL Directivities of F-7/A-7 and F-11/A-11.

3.05 M(10.0 FT.)DIA; 0.25 M₀; 549 M(1800 FT.)SIDELINE 11+9 BLADES;

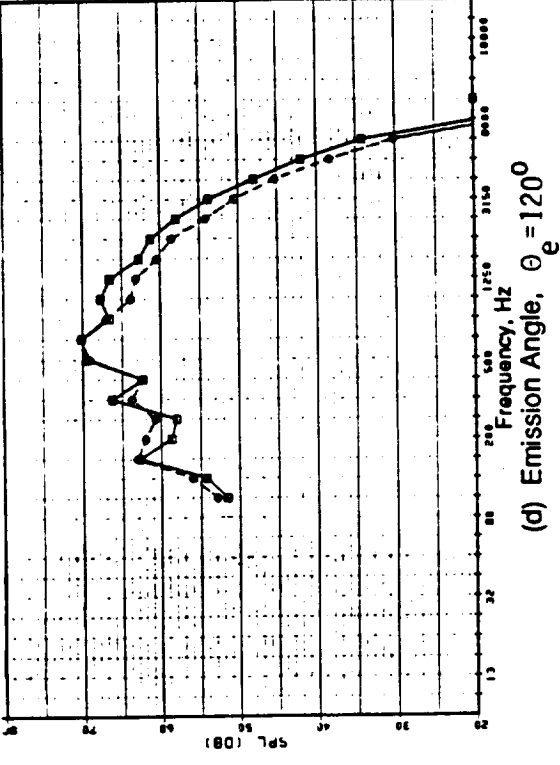
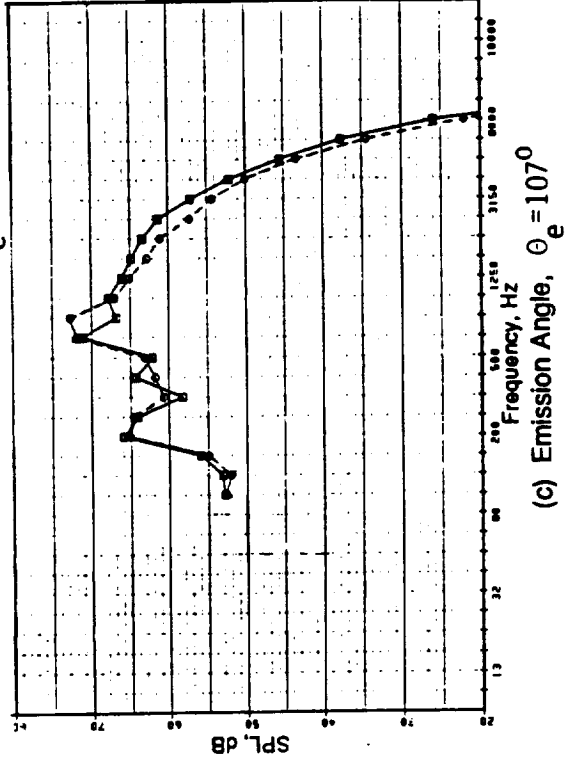
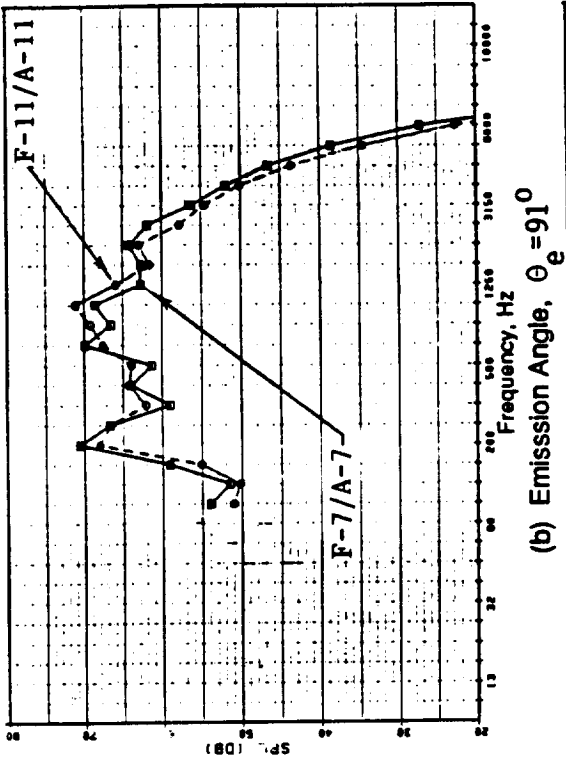
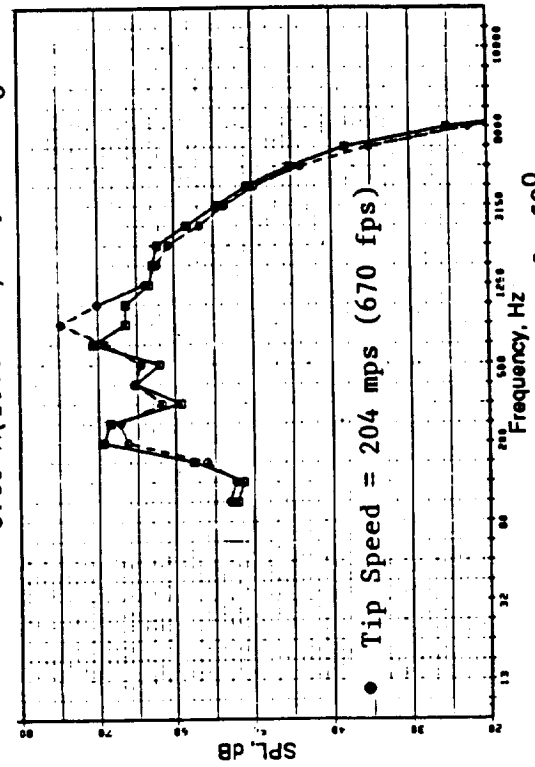


Figure 211. Selected Spectra of the F-7/A-7 and F-11/A-11.

Model Scale; As Measured Data 11+9 Blades

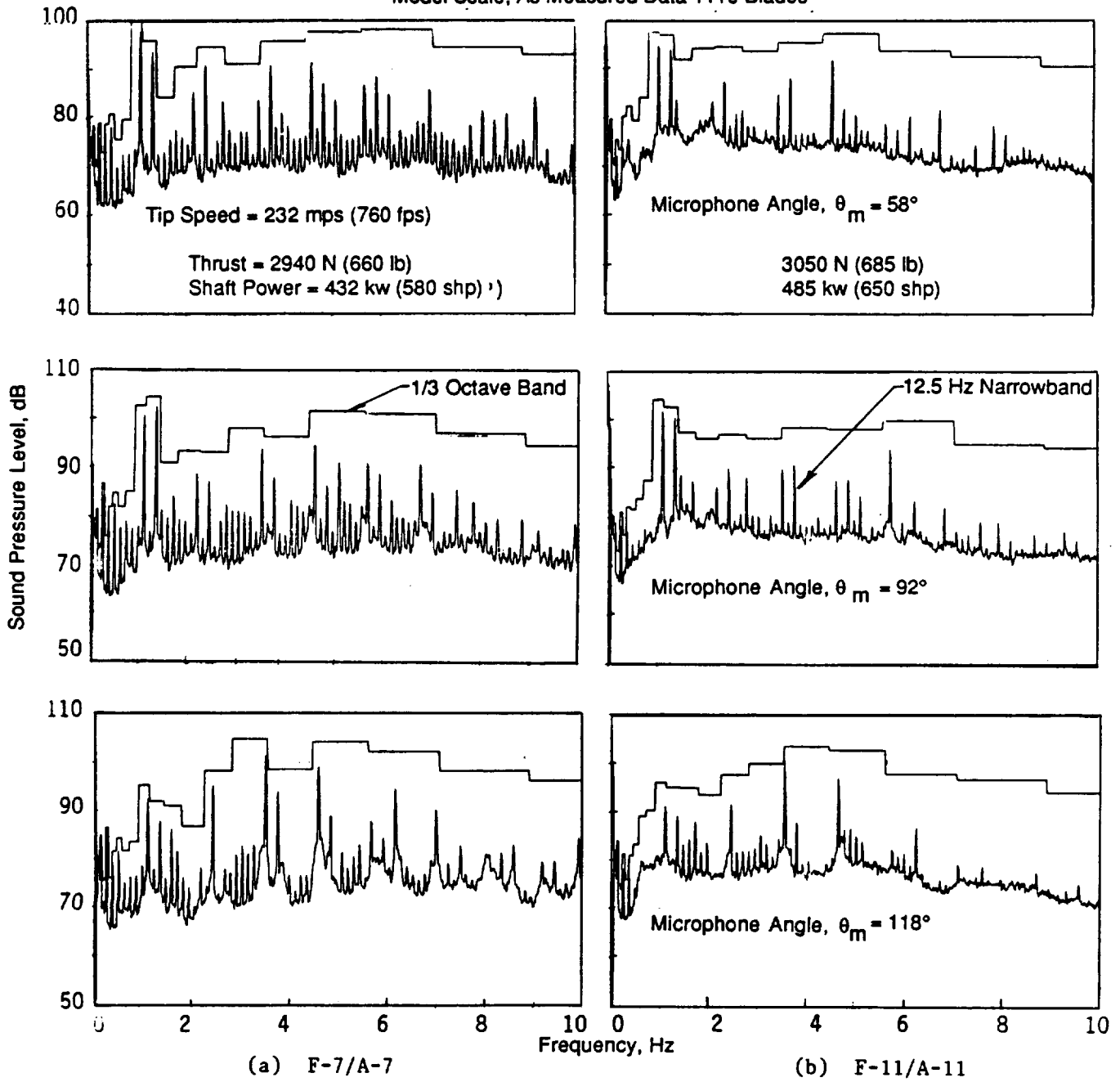


Figure 212. Model-Scale Spectra of F-7/A-7 and F-11/A-11.

Model Scale; As Measured Data 11+9 Blades

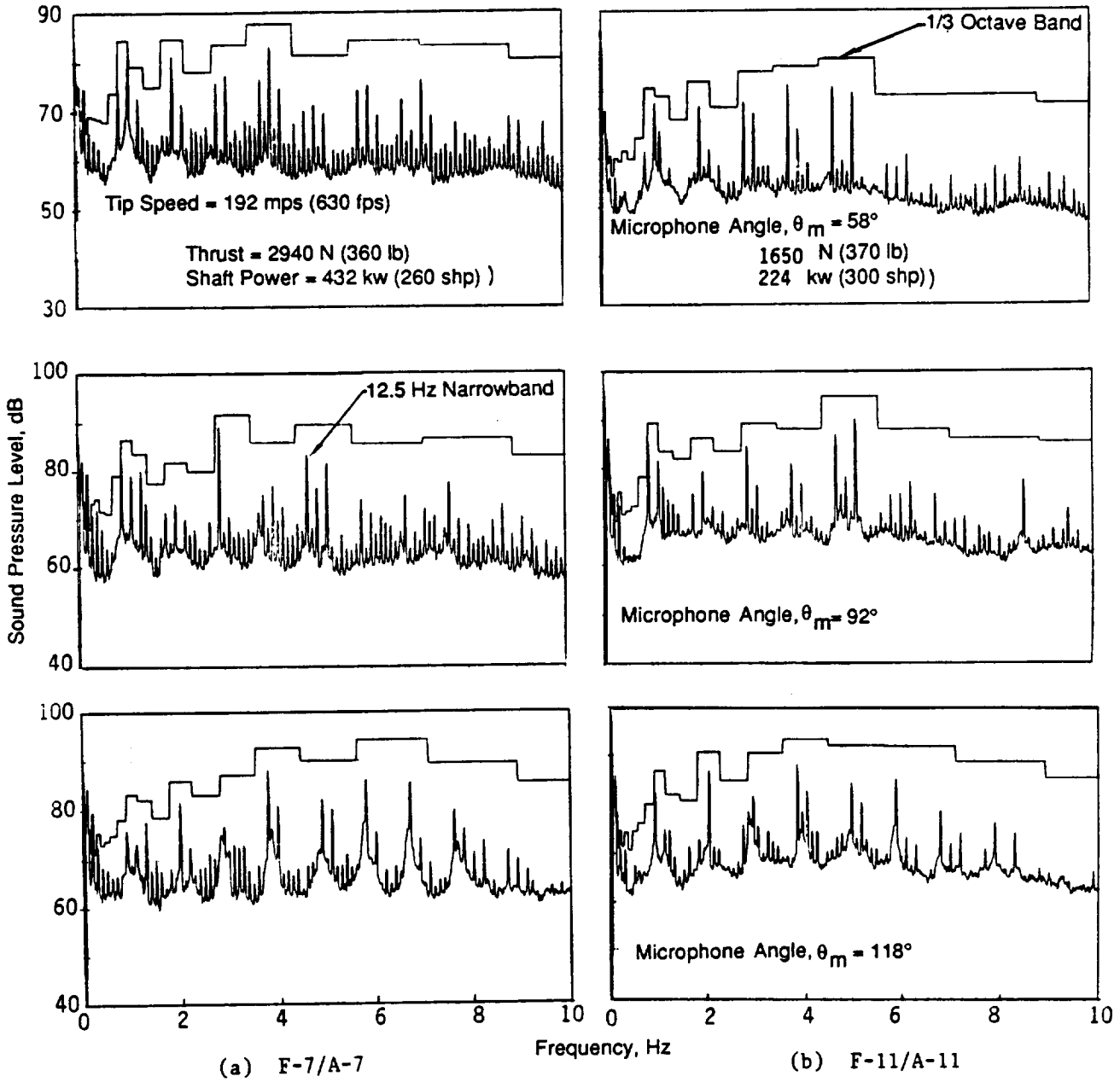
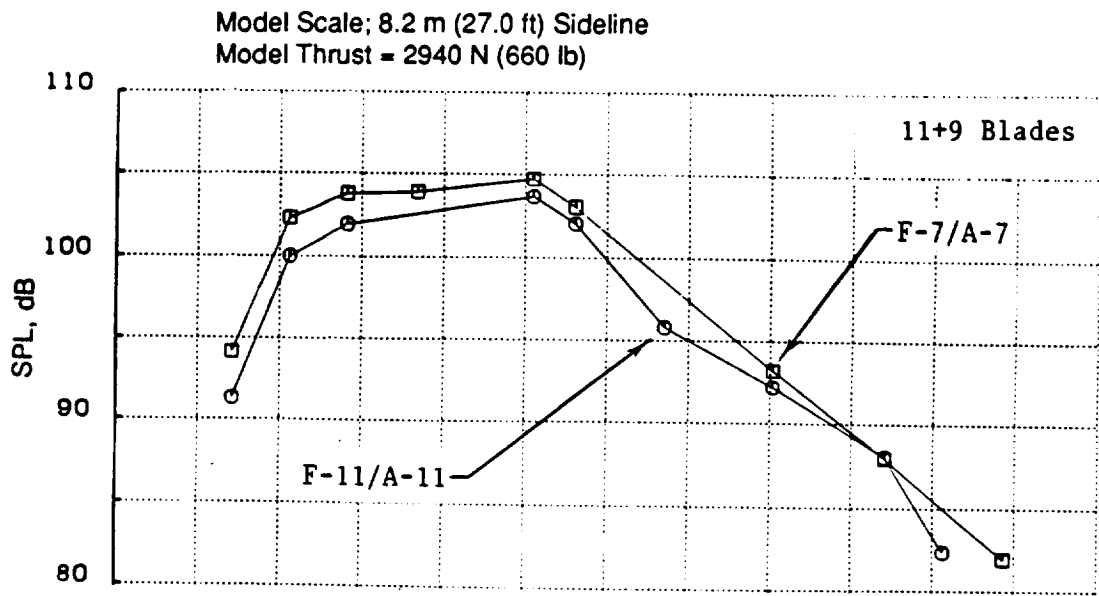
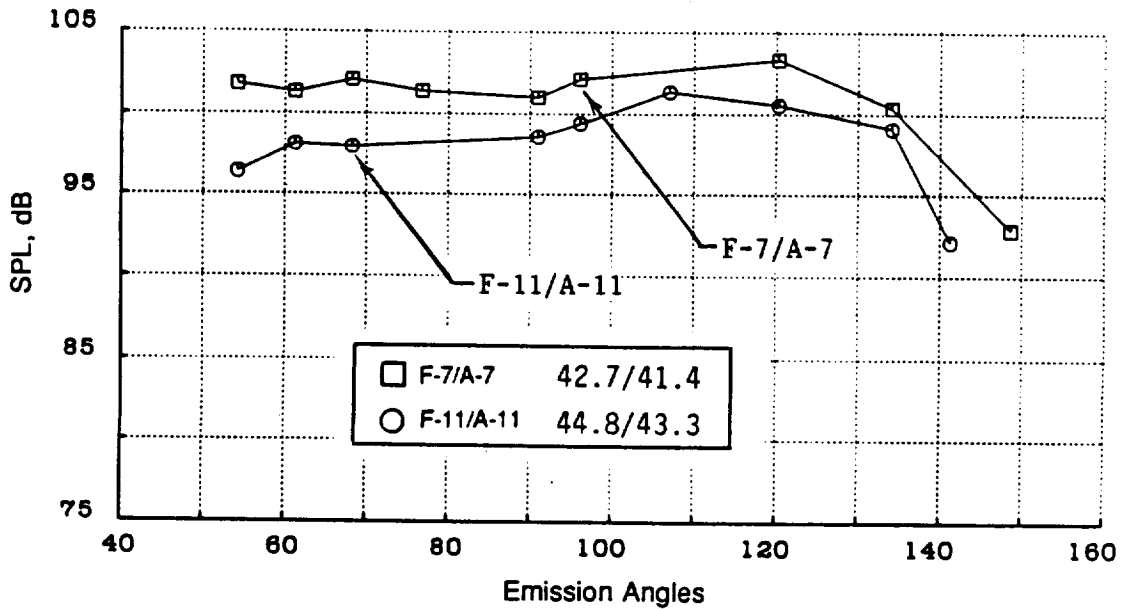


Figure 213. Model-Scale Spectra of F-7/A-7 and F-11/A-11.

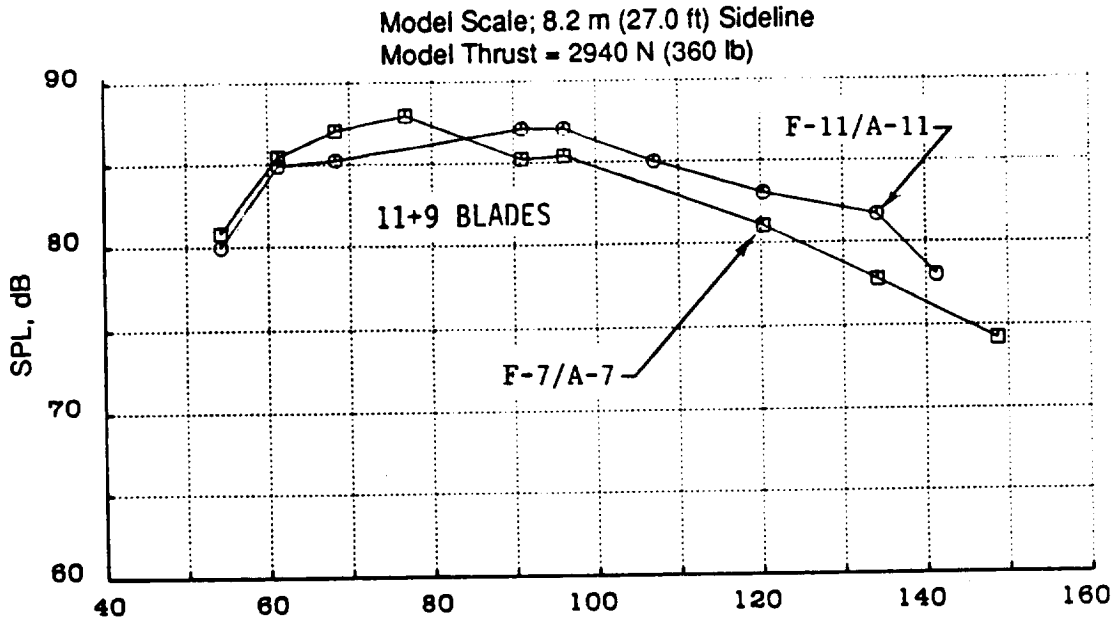


(a) Forward and Aft Rotor BPF's and Harmonics Sum

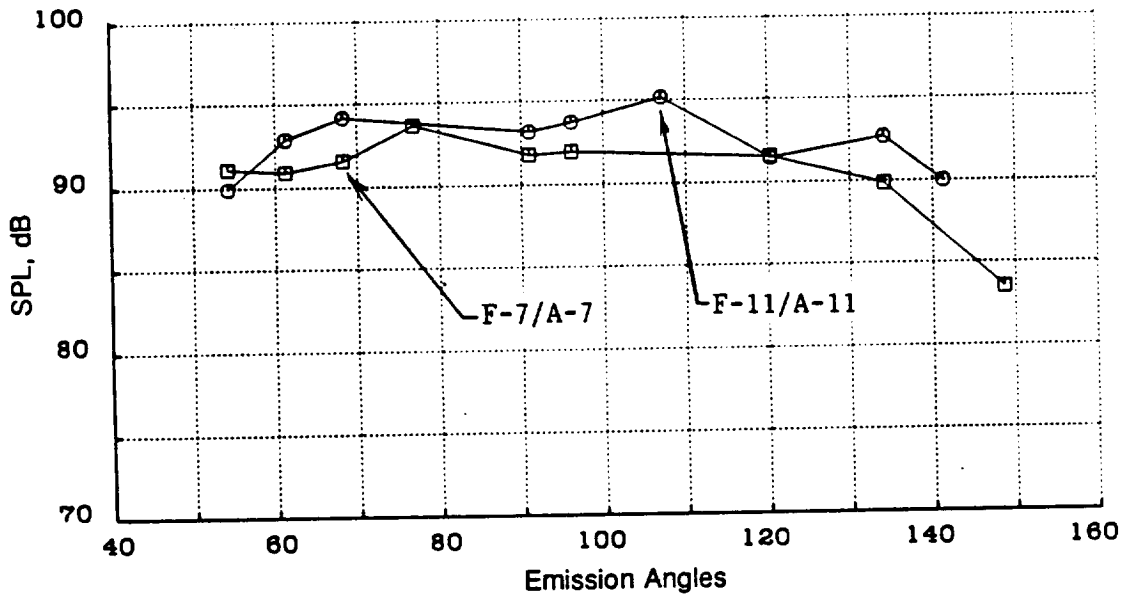


(b) Rotor-to-Rotor Interaction Tones Sum

Figure 214. Model-Scale Tone Sum Directivities of F-7/A-7 and F-11/A-11 at 232 mps (760 fps) Tip Speed.



(a) Fwd and Aft Rotor BPFs & Harmonics Sum

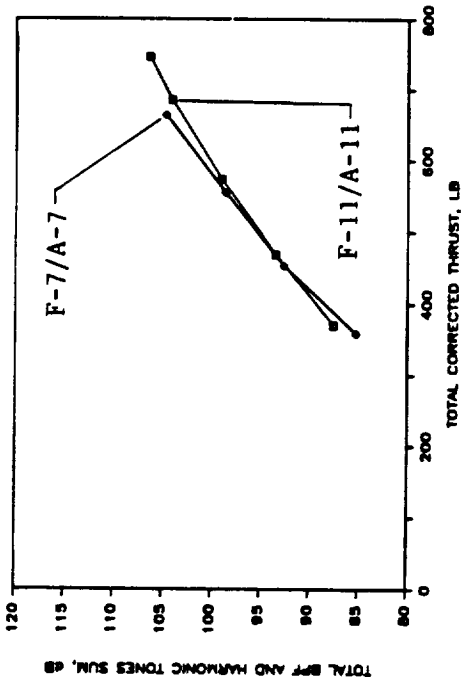


(b) Rotor-to-Rotor Interaction Tones Sum

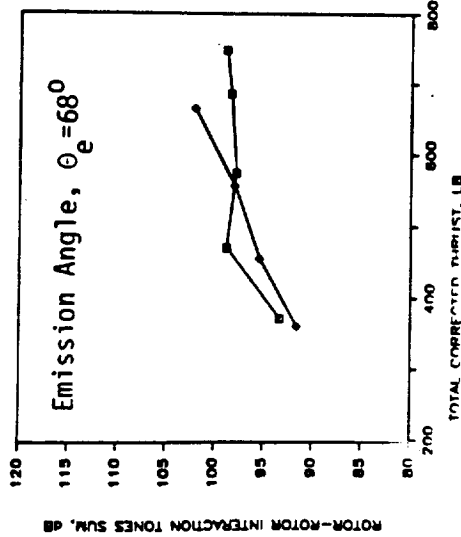
Figure 215. Model-Scale Tone Sum Directivities of F-7/A-7 and F-11/A-11 at 192 mps (630 fps) Tip Speed.

- MODEL SCALE
- $M_0 = 0.25$
- 8.2 M(27 FT.) SIDELINE
- 11x9 BLADES
- OPEN PITCH

SYMBOL	BLADE	β_1/β_2	X/D_t
□	F-7/A-7	42.7/41.4	0.24
◇	F-11/A-11	44.8/43.3	0.32



a) Fwd and Aft Rotor BPF & Harmonics Sum @ Emission Angle, $\theta_e = 91^\circ$



b) Rotor-to-Rotor Interaction Tones Sum

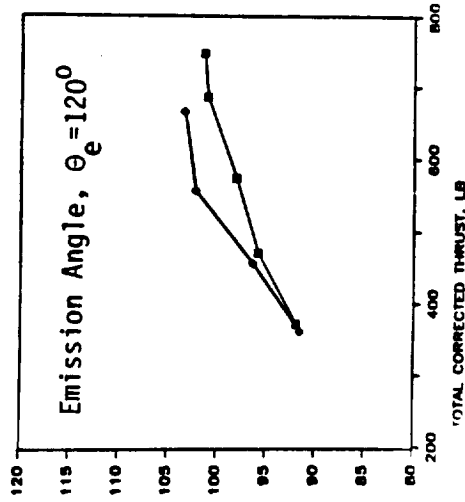


Figure 216. Model-Scale Tone Sum Levels of F-7/A-7 and F-11/A-11 as a Function of Total Thrust.

comparable to F-7/A-7 and a rotor-to-rotor interaction noise and unsteady-loading noise smaller than that of the F-7/A-7 at higher thrust conditions.

Acoustic evaluation of the F-11/A-11 blade design is concluded by providing a comparison with the F-7/A-7 design on the basis of EPNL (Figure 217) at selected thrusts of 44,500 N (10,000 lb), 57,800 N (13,000 lb) and 66,700 N (15,000 lb). The higher sweep and higher activity factor design (F-11/A-11) is quieter than the F-7/A-7 by 0.7 dB and 1.0 dB at higher thrusts; 57,800 N (13,000 lb) and 66,700 N (15,000 lb) respectively; and is noisier by 0.5 dB at the lower thrust of 44,500 N (10,000 lb).

Thrust, N (lb)	Δ EPNL, dB	
	F-7/A-7	F-11/A-11
	42.7/41.4 $X/D_t = 0.24$	44.8/43.3 $X/D_t = 0.32$
44,500 (10,000)	0	+0.5
57,800 (13,000)	0	-0.7
66,700 (15,000)	0	-1.0

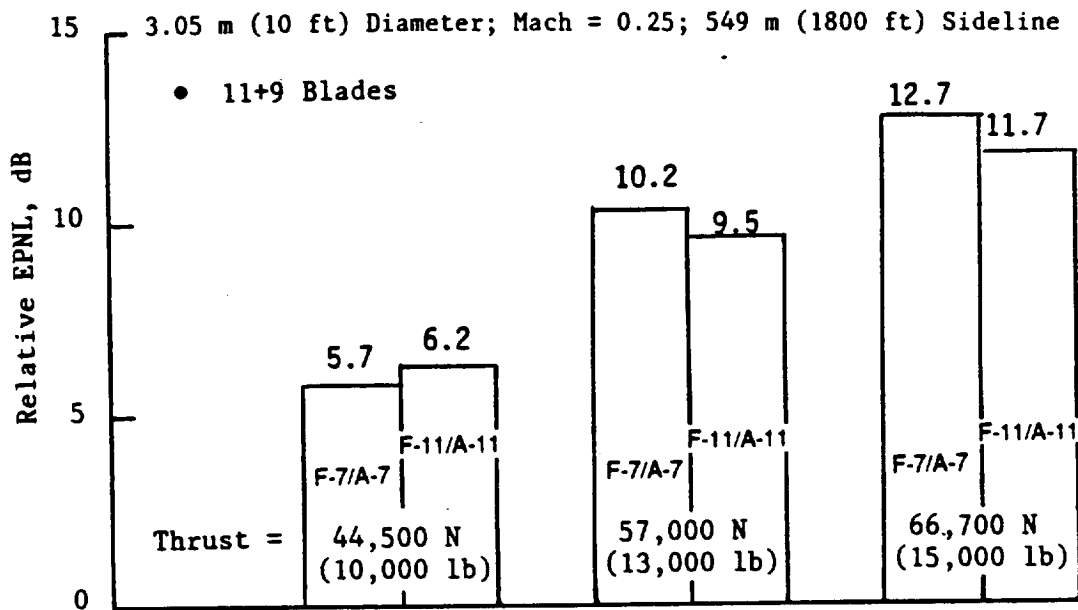


Figure 217. EPNL Comparison of F-7/A-7 and F-11/A-11 (11+9) Blade Configurations.

7.1.1.3 Acoustic Evaluation of Blade Numbers

In order to evaluate the effect of blade numbers on acoustic data, the baseline F-7/A-7 blades were tested with various blade number combinations/configurations. Results from this study are presented in this section under two sets of comparisons as follows:

- Series 1
 - The F-7/A-7 with nominal spacing between rotor pitch-change-axes ($X/D_t = 0.169$) and with blade number combinations of 4+4, 8+4, 8+8, 9+4, and 9+8
- Series 2
 - The F-7/A-7 with maximum spacing between rotor pitch-change-axes ($X/D_t = 0.24$) and with blade number combinations of 8+8, 9+8, and 11+9.

The tests in these series were conducted at nominal pitch settings that were selected to give equal lift per blade at takeoff power tip speed. The results presented herein were measured at a simulated flight Mach number of 0.25 and were measured without a pylon.

7.1.1.3.1 F-7/A-7 with 4+4, 8+4, 9+4, and 9+8 Blades: Series 1

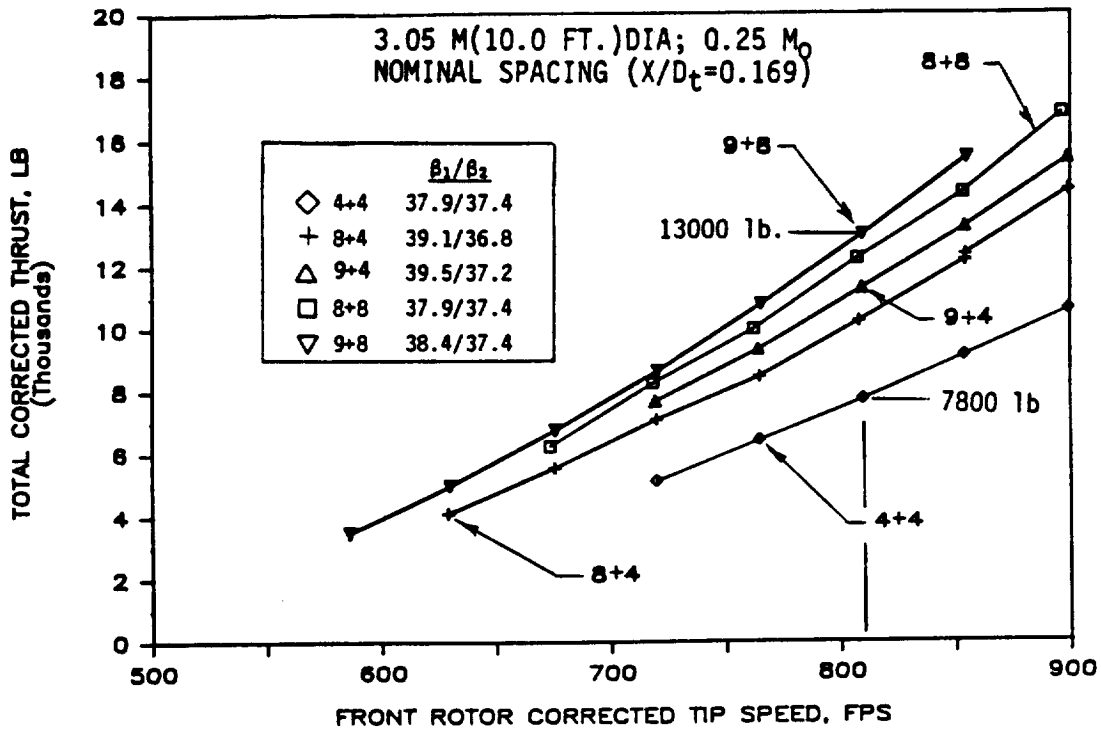
Figure 218 plots total thrust and power data for the five different blade number configurations for the F-7/A-7 at nominal rotor-to-rotor spacing. The data indicate that together with an increase in blade numbers at the low Mach number test conditions, the thrust output increases for a given power input at typical takeoff and cutback conditions. This indicates improved efficiency can be attained with an increase of blade numbers.

Acoustic data is compared for the various blade number configurations in terms of scaled and maximum OASPL, PNL, and dBA as a function of total thrust (Figure 219) and demonstrates a significant reduction in noise levels with an increase in blade number; from a 4+4 to a 9+8 combination for a whole range of thrust conditions. For example, at a thrust of 44,500 N (10000 lb), reductions to the extent of 15 dB, 11 dB, and 8 dB are measured in peak values of OASPL, PNL, and dBA of a 9+8 configuration relative to a 4+4 configuration.

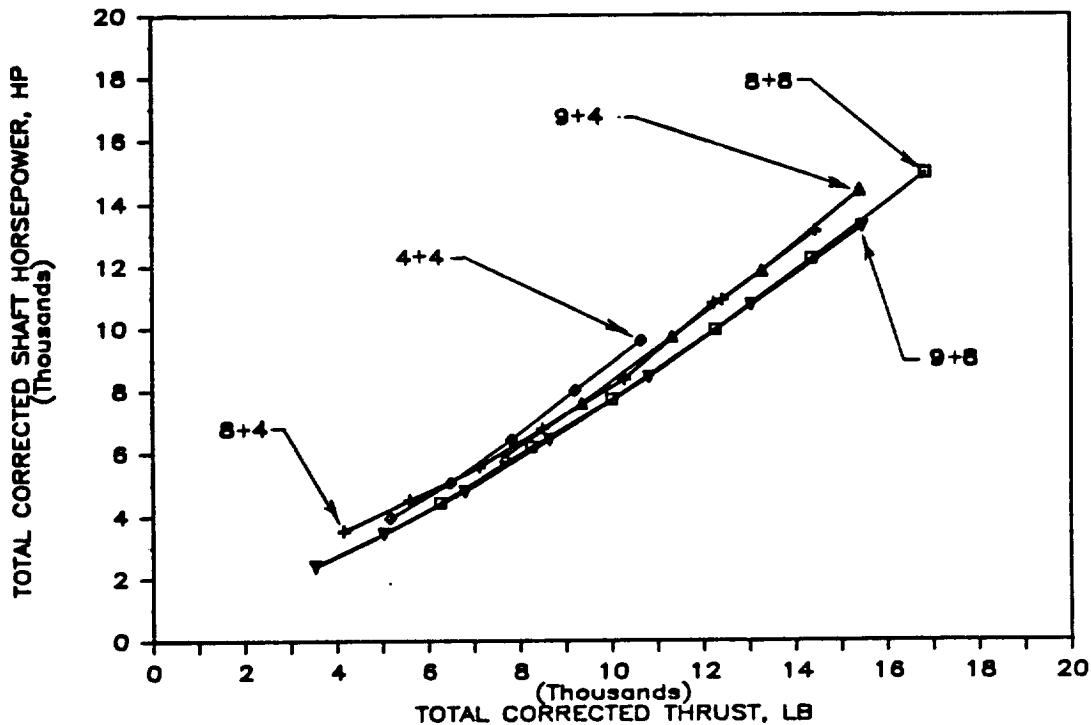
These OASPL and PNL data (Figure 219) are replotted in Figure 220 as a function of tip speed. Resultant data indicate that, for example, at a tip speed of 247 mps (810 fps) while thrust was increased by 66%, from 34,700 N (7,800 lb) to 57,800 N (13,000 lb), maximum OASPL and PNL increased by 5.6 dB and 4 dB over the blade number variations of this test series. However, for any one of these blade number combinations, this increase in thrust by only a tip speed increase would have caused the maximum OASPL and PNL to increase by approximately 10 dB and 9 dB, respectively (Figure 218).

Maximum OASPL and PNL data of Figure 219 are then replotted (Figures 221 and 222) as functions of thrust per blade and power per blade, respectively, indicating that the maximum OASPL of all blade number combinations and the maximum PNL of all of the blade number combinations (except that of the 4+4) correlate within a 2 dB band spread on the basis of thrust/power per blade. The PNL data for the 4+4 configuration does not correlate with the rest of the data due to the lesser weighting of the lower interaction frequencies of a 4+4 blade configuration, relative to higher weighting of the higher interaction frequencies of larger blade number configurations.

Figures 223 through 226 depict OASPL and PNL directivities and selected spectra at an emission angle of 86° for the various blade number combinations at two thrust settings that approximately

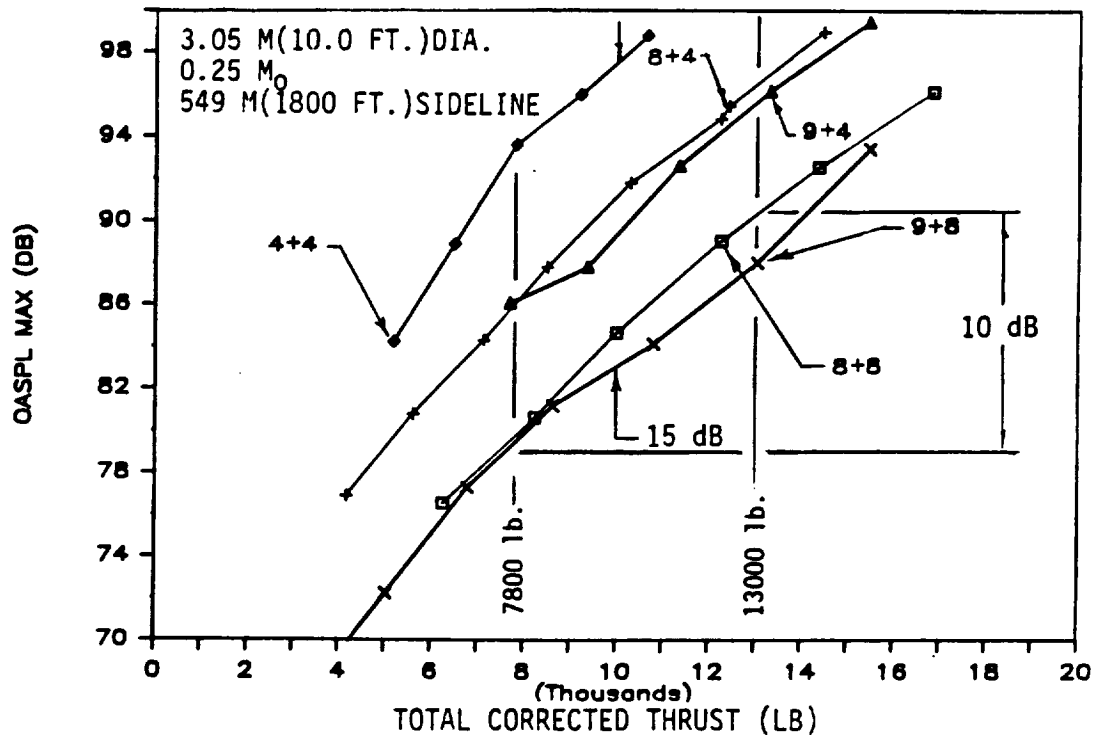


a) THRUST VS TIP SPEED

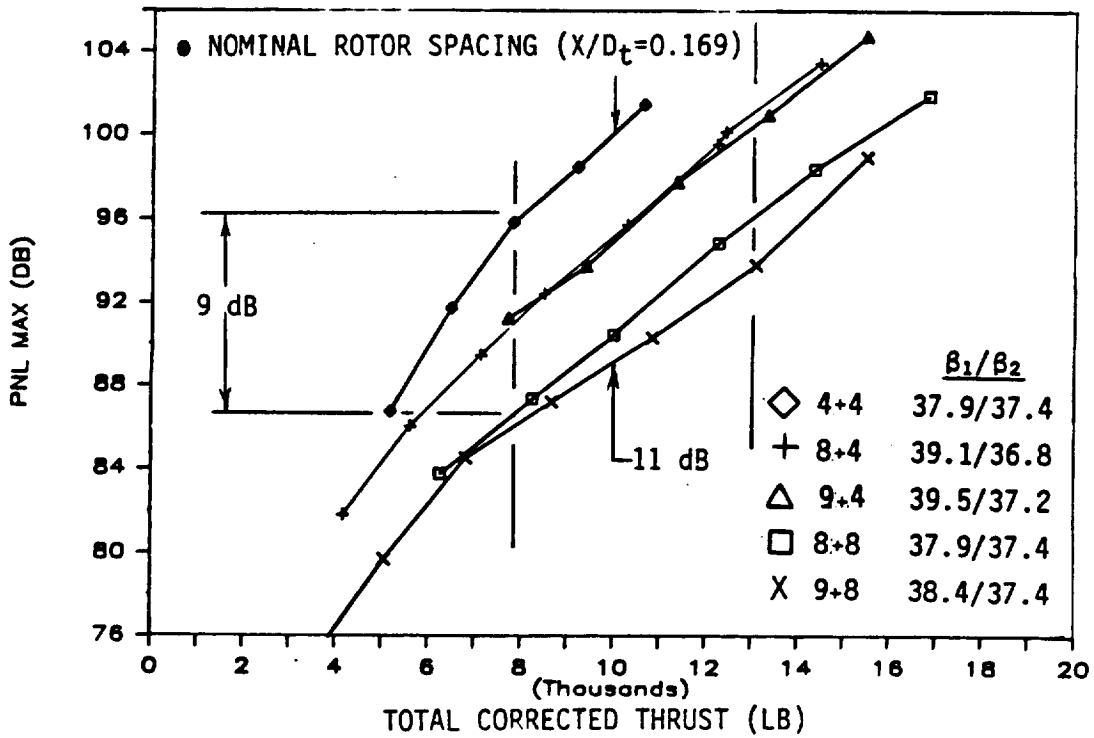


b) SHAFT POWER VS THRUST

Figure 218. Aero Performance Data of F-7/A-7 with Different Blade Numbers.

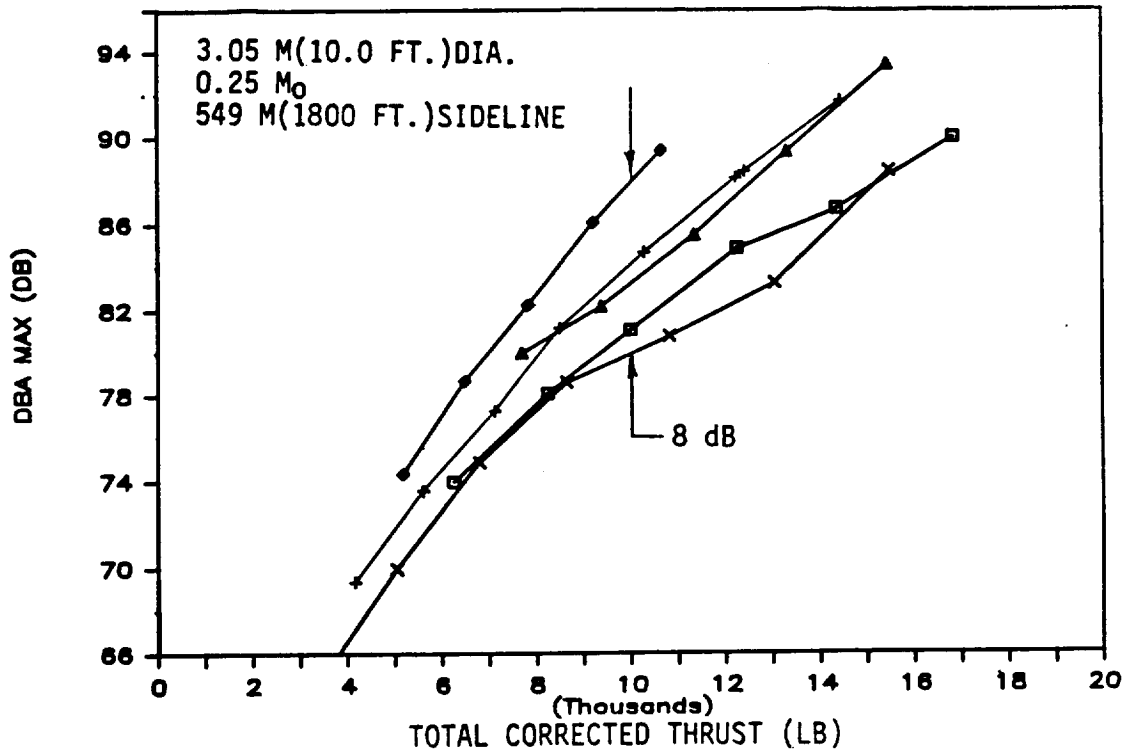


a) OASPL_{max}



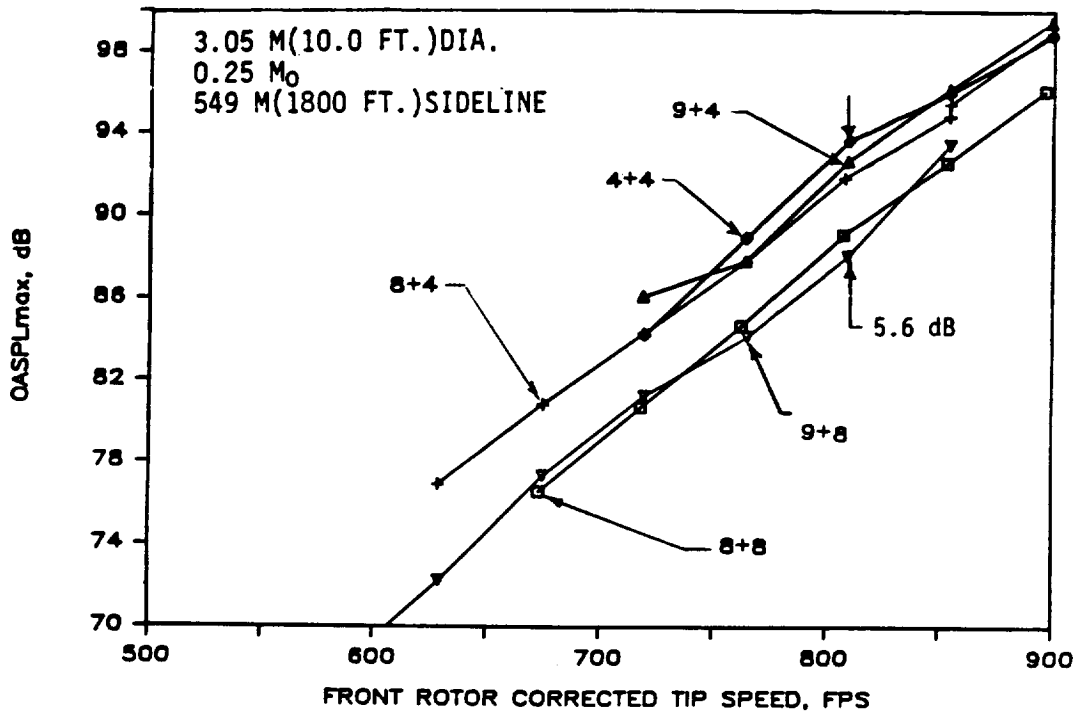
b) PNL_{max}

Figure 219. Acoustic Data of F-7/A-7 with Different Blade Numbers as a Function of Thrust.

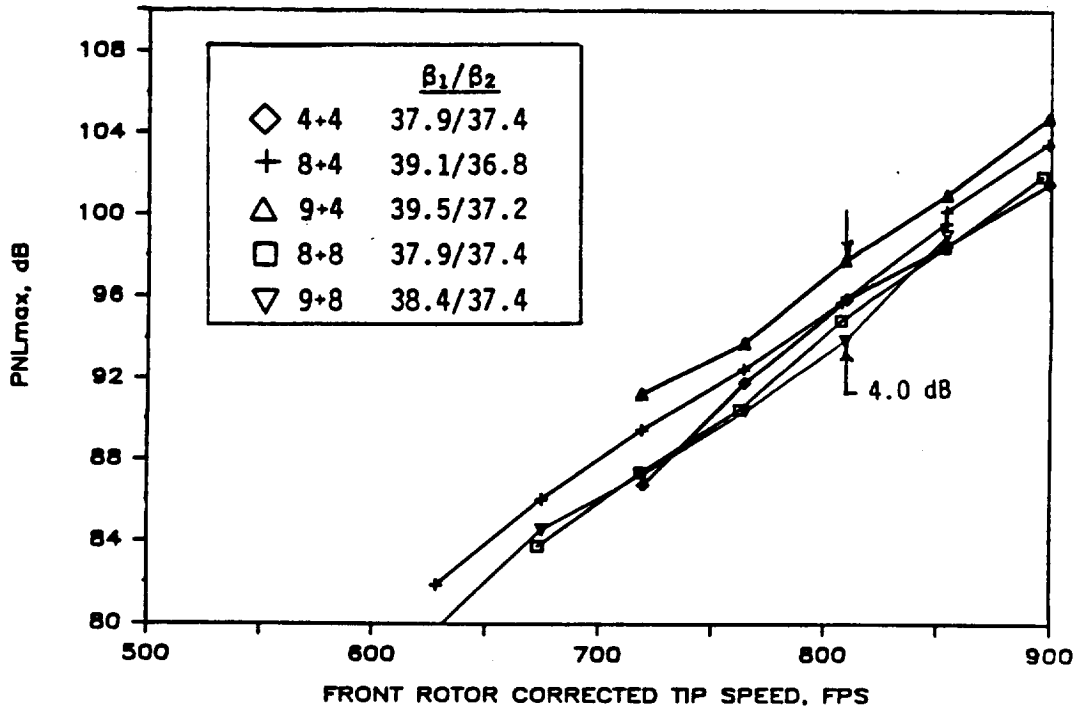


c) dB_{max}

Figure 219. Acoustic Data of F-7/A-7 with Different Blade Numbers as a Function of Thrust (Concluded).



a) OASPL_{max}



b) PNL_{max}

Figure 220. Acoustic Data of F-7/A-7 (Nominal Rotor Spacing) with Different Blade Numbers as a Function of Tip Speed.

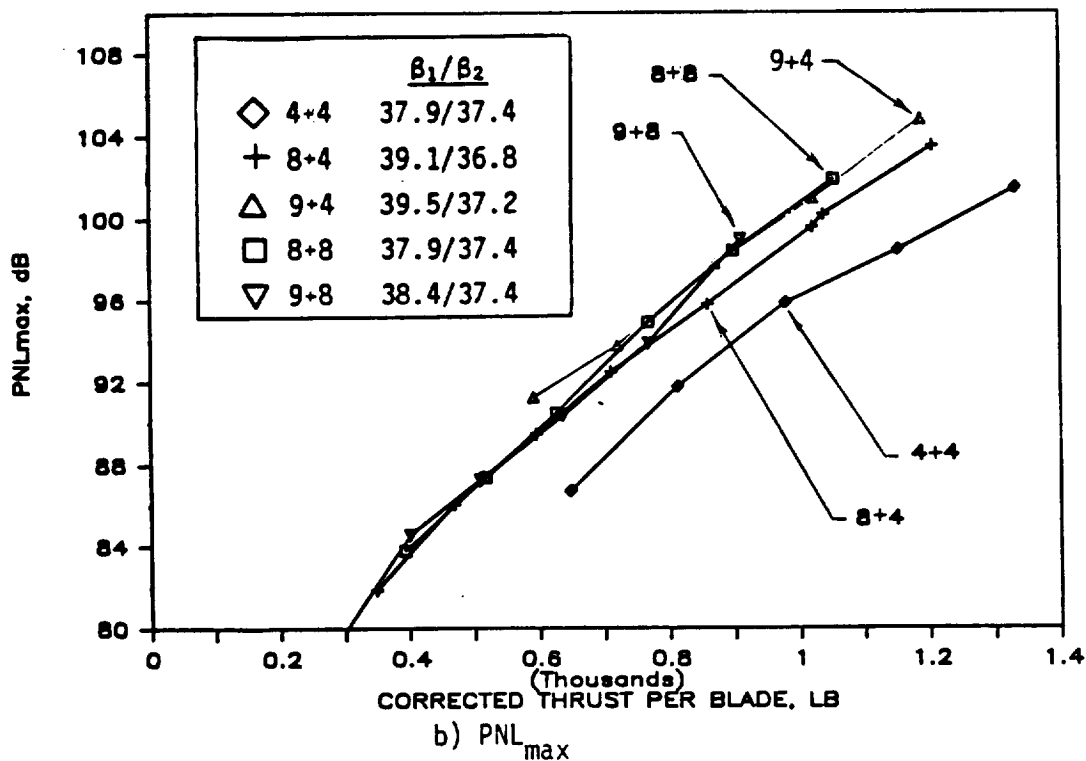
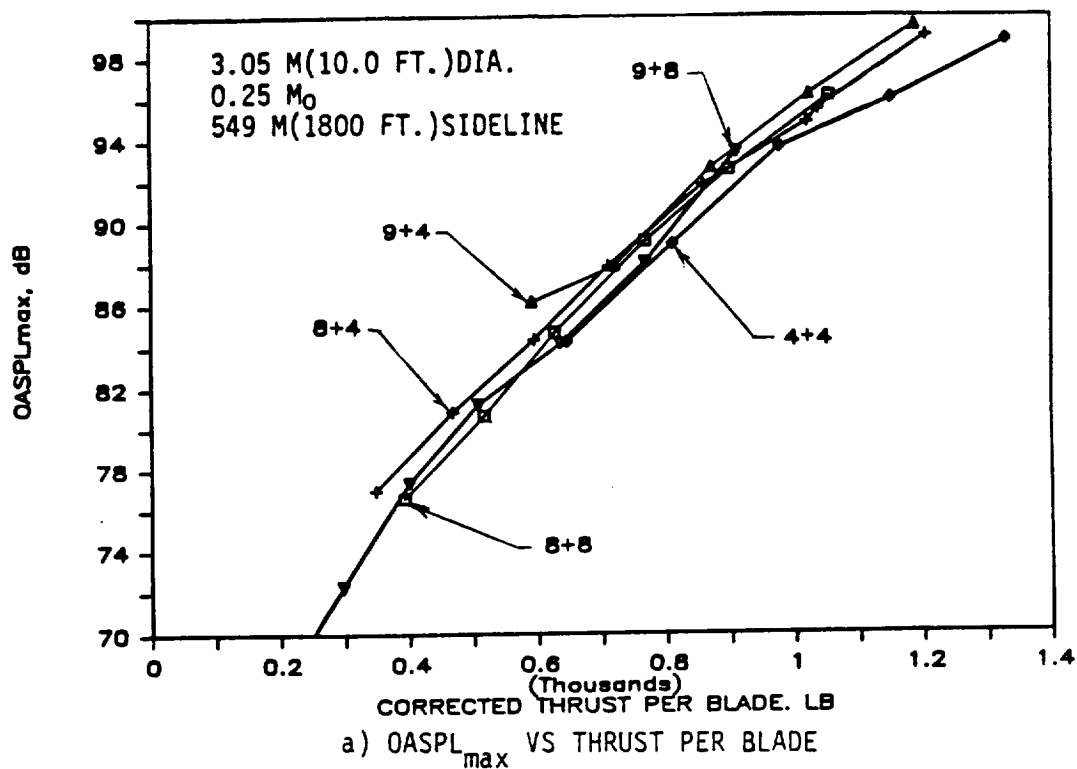


Figure 221. Acoustic Data of F-7/A-7 (Nominal Rotor Spacing) with Different Blade Numbers as a Function of Thrust per Blade.

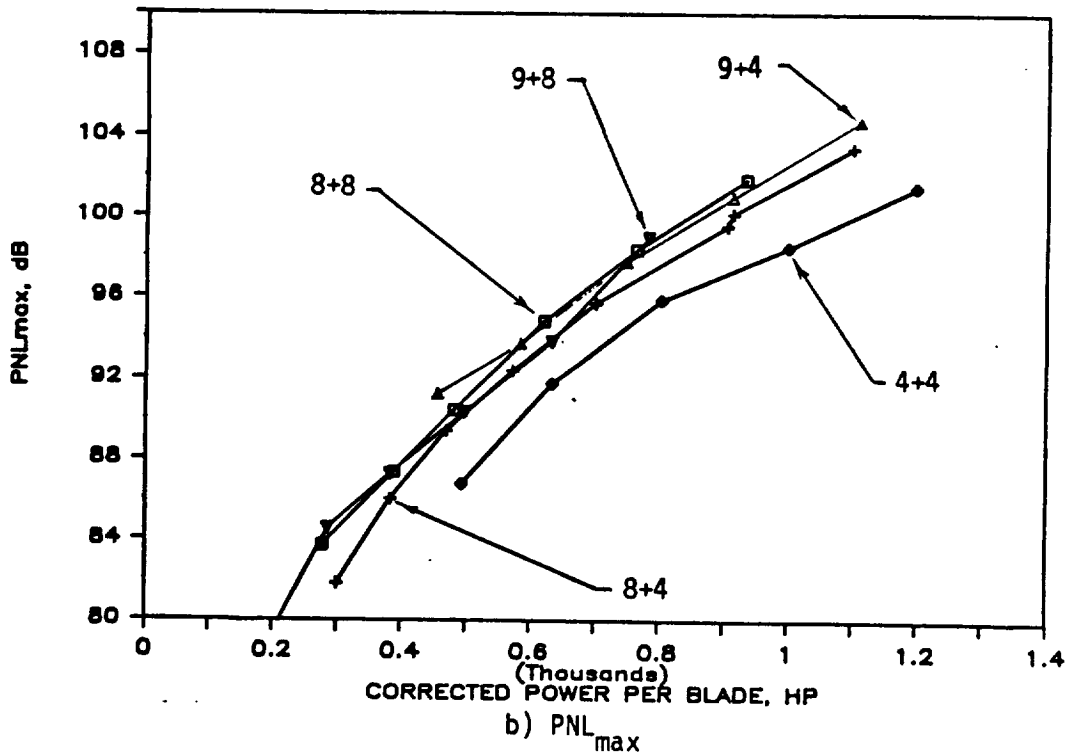
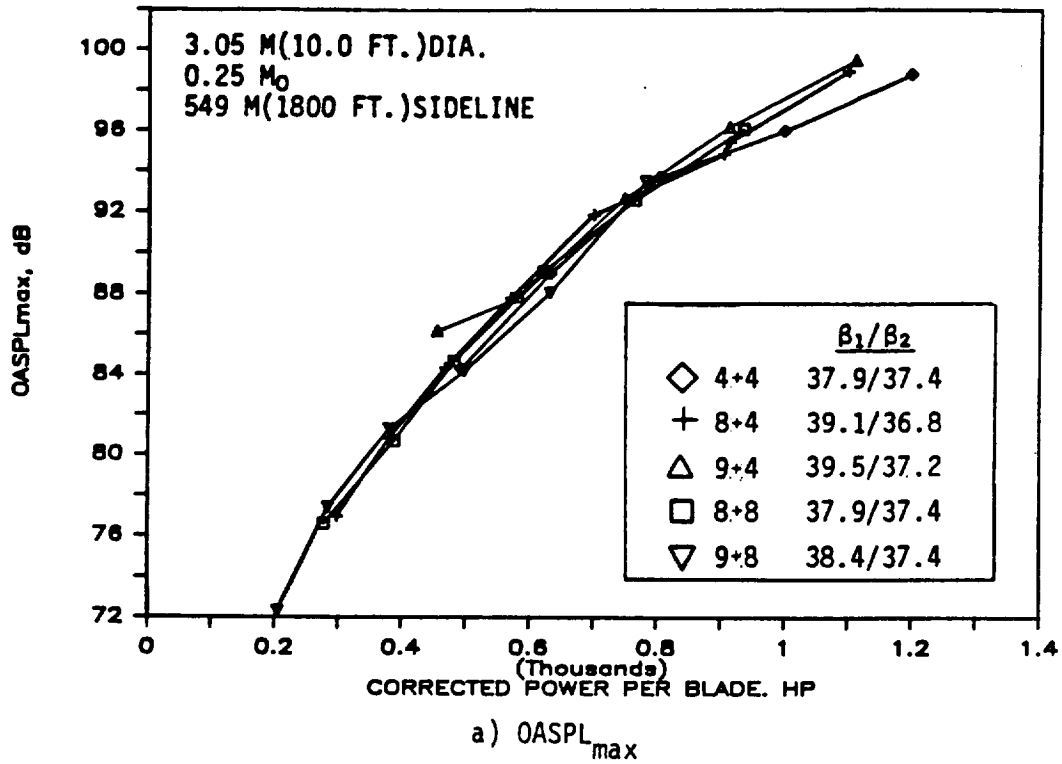
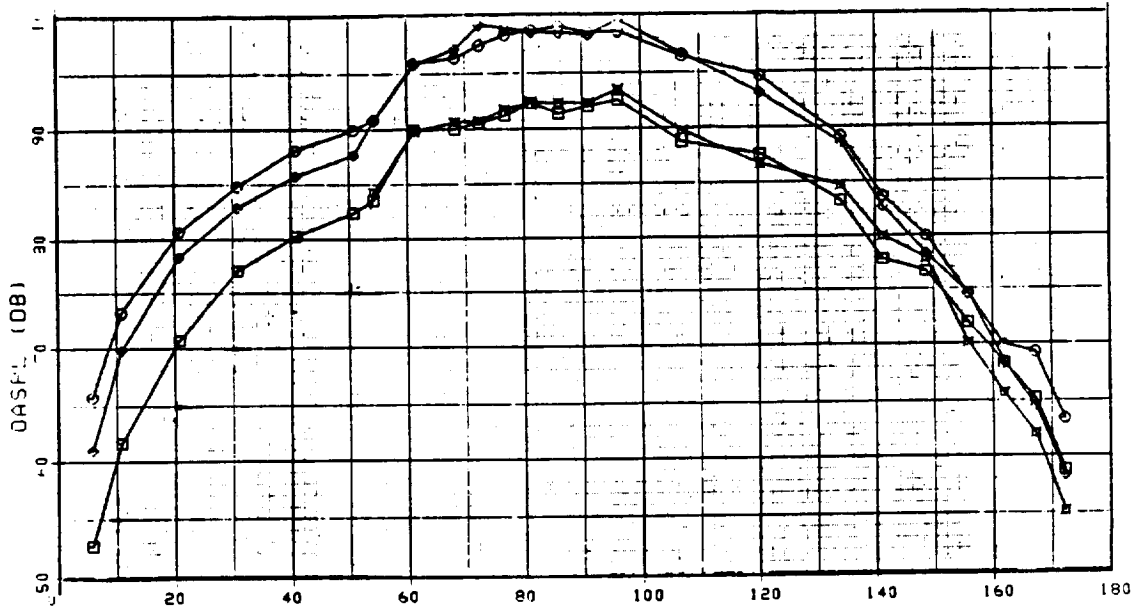
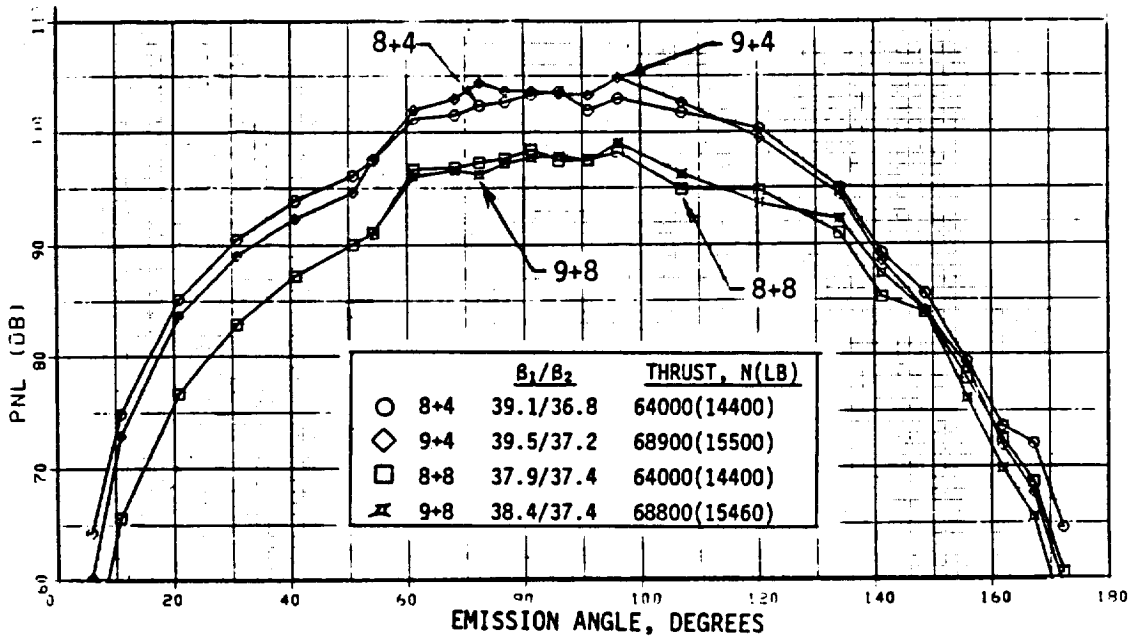


Figure 222. Acoustic Data of F-7/A-7 (Nominal Rotor Spacing) with Different Blade Numbers as a Function of Power per Blade.

3.05 M(10.0 FT.)DIA; 0.25 M₀; 549 M(1800 FT.)SIDELINE



a) OASPL



b) PNL

Figure 223. OASPL and PNL Directivities of F-7/A-7 (Nominal Rotor Spacing) with Different Blade Numbers at Typical Takeoff Thrust.

3.05 M(10.0 FT.)DIA; 0.25 M₀; 549 M(1800 FT.)SIDELINE

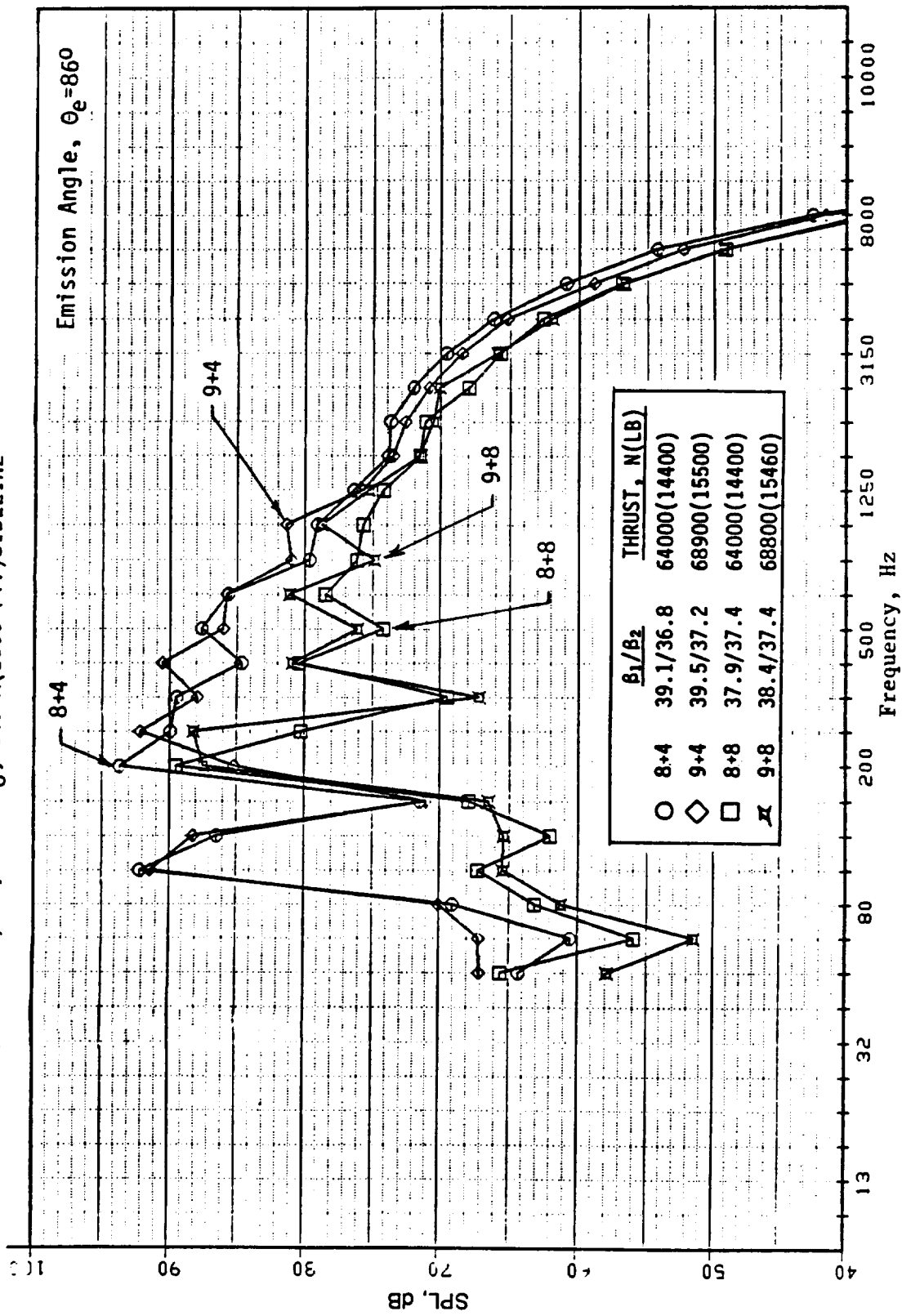
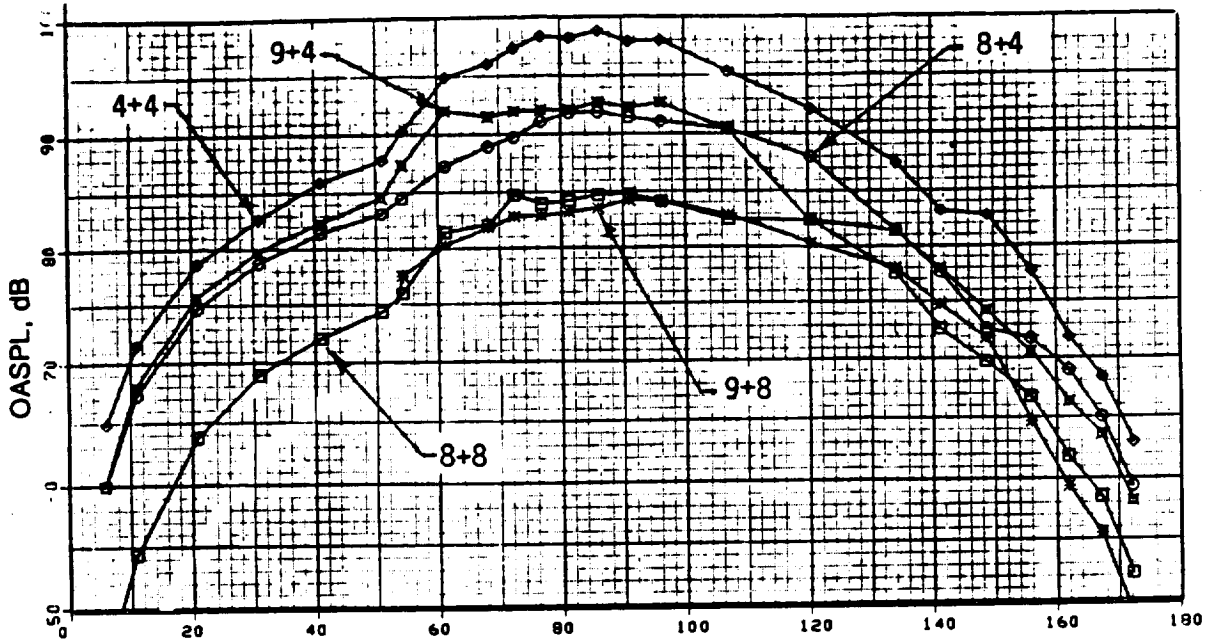
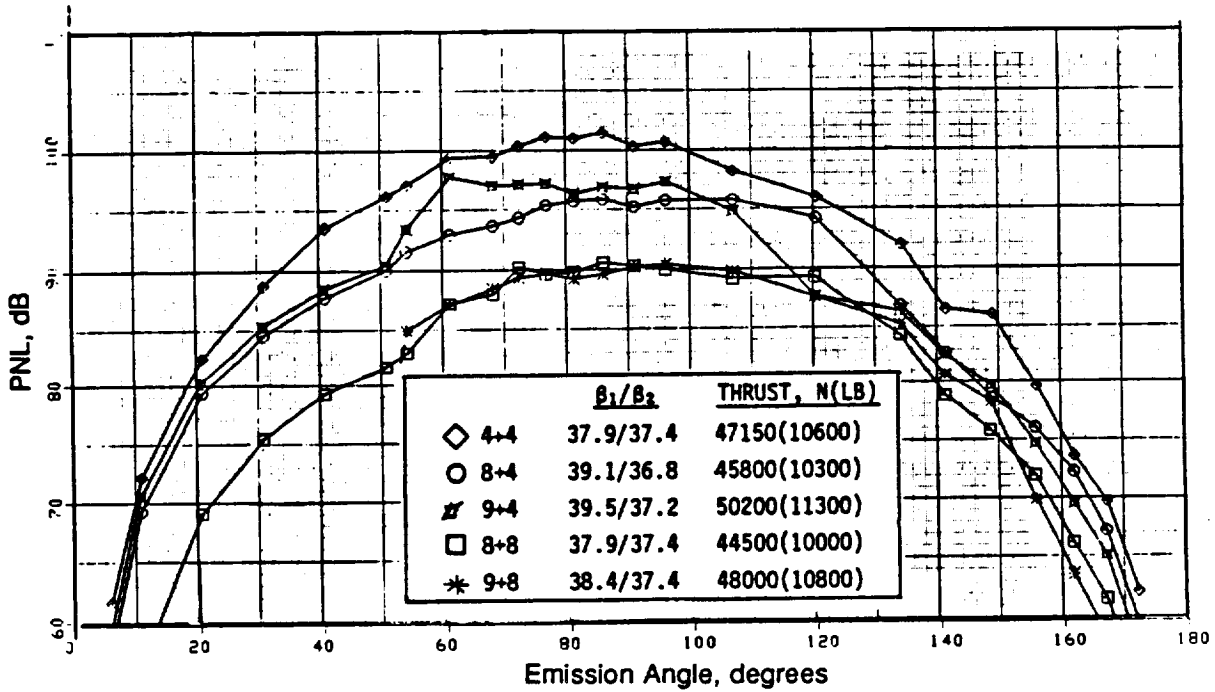


Figure 224. Spectra of F-7/A-7 (Nominal Rotor Spacing) with Different Blade Numbers at Typical Takeoff Thrust.

3.05 (10.0 FT.) DIA; 0.25 M₀; 549 M(1800 FT.) SIDELINE



a) OASPL



b) PNL

Figure 225. OASPL and PNL Directivities of F-7/A-7 (Nominal Rotor Spacing) with Different Blade Numbers at Typical Cutback Thrust.

3.05 M(10.0 FT.)DIA; 0.25 M₀; 549 M(1800 FT.)SIDELINE

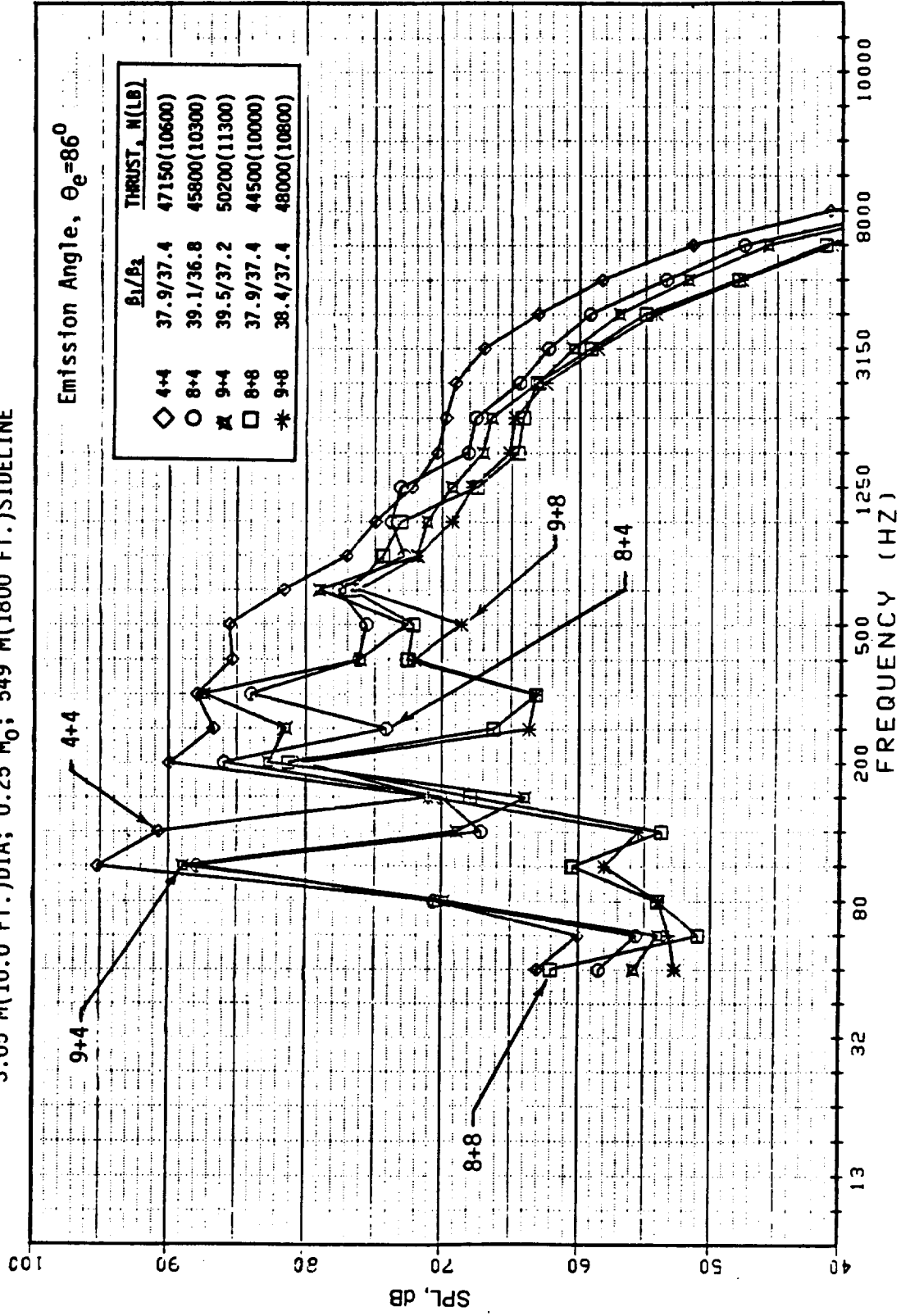


Figure 226. Spectra of F-7/A-7 (Nominal Rotor Spacing) with Different Blade Numbers at Typical Cutback Thrust.

angle range ($5 < \sigma_e < 167$) with significant benefit over angles in the range of $51^\circ < \sigma_e < 120^\circ$. Typical spectral data indicate reduced sound pressure levels at blade passing frequencies due to reduction in steady-loading noise and reduction in levels at higher harmonics due to reduction in rotor-to-rotor interaction noise with increased blade numbers. One of the reasons for this decrease in interaction noise is the wake strength reduction that results from decreased blade loading due to increased blade numbers.

Model-scale narrow-band comparisons with different blade numbers at equal thrust and different blade numbers at equal tip speed are presented in Figures 227 and 228, respectively. A reduction in each of the tone levels of the 4+4 configuration (with increase in forward and aft blade numbers) is noted for a given total thrust.

Model-scale SPL tones sum directivities, for typical takeoff and cutback thrust (Figures 223 through 226), are shown in Figures 229 and 230. Further, the model-scale tone sum levels, at selected emission angles and for various blade number configurations of the test series, are depicted (Figure 231) as a function of model-size total thrust. These figures demonstrate the following two benefits from the increased blade numbers. The first benefit, a significant decrease in steady-loading noise, is a result of the reduction in blade loading and tip speeds. The second benefit (a natural consequence of the first) is a decrease in the interaction noise due to aft rotor blades, at a lower tip speed, interacting with the weakened wakes and tip vortices from the forward rotor blades.

7.1.1.3.2 F-7/A-7 with 8+8, 9+8, and 11+9 Blades: Series 2

Data for the various F-7/A-7 blade combinations of Series 2 at maximum spacing between the rotor pitch-change axes are shown in Figures 232 through 236. These data are arranged in a manner similar to that previously presented for Series 1 at nominal rotor-to-rotor spacing.

Figure 232 shows the total thrust and power for the three different blade number combinations at maximum spacing. As before, these data indicate an improvement in the thrust delivered for a given power input; this corresponds with the increase in blade numbers.

The acoustic data are illustrated in terms of scaled and maximum OASPL, PNL and dBA as a function of thrust (Figure 233). Maximum OASPL and PNL data are replotted (Figures 234 through 236) as functions of tip speed, thrust per blade, and shaft power per blade, respectively. As before, this set of data demonstrates the significant reduction in noise levels with increase in blade numbers. For example, at a typical takeoff thrust level of 64,500 N (14,500 lb), reductions to the extent of 5.5 dB, 4.2 dB, and 3.0 dB are obtained in peak values of OASPL, PNL, and dBA for increase of blade numbers from an 8+8 to an 11+9 configuration, respectively. Also, the acoustic data of Series 2 correlated within a 2.0-dB band spread when plotted on the basis of thrust per blade and power per blade.

The OASPL and PNL directivities and selected spectra at emission angle $\sigma_e = 86^\circ$ for the three F7A7 blade number combinations are presented in Figures 237 through 240 for typical takeoff and cutback thrust conditions. The directivity data indicate a significant benefit due to the increased blade numbers over most of the test angle range. The spectral data denotes reduction, which corresponds with the increase in blade numbers, in the sound pressure levels at blade passing frequencies, due to a reduction in steady-loading noise and also a decrease in levels at higher harmonics, indicating lesser aerodynamic interaction noise.

MODEL SCALE AS MEASURED DATA
 NOMINAL ROTOR SPACING ($X/D_t=0.169$)
 MICROPHONE ANGLE, $\theta_m=92^\circ$
 12.5 HZ BANDWIDTH

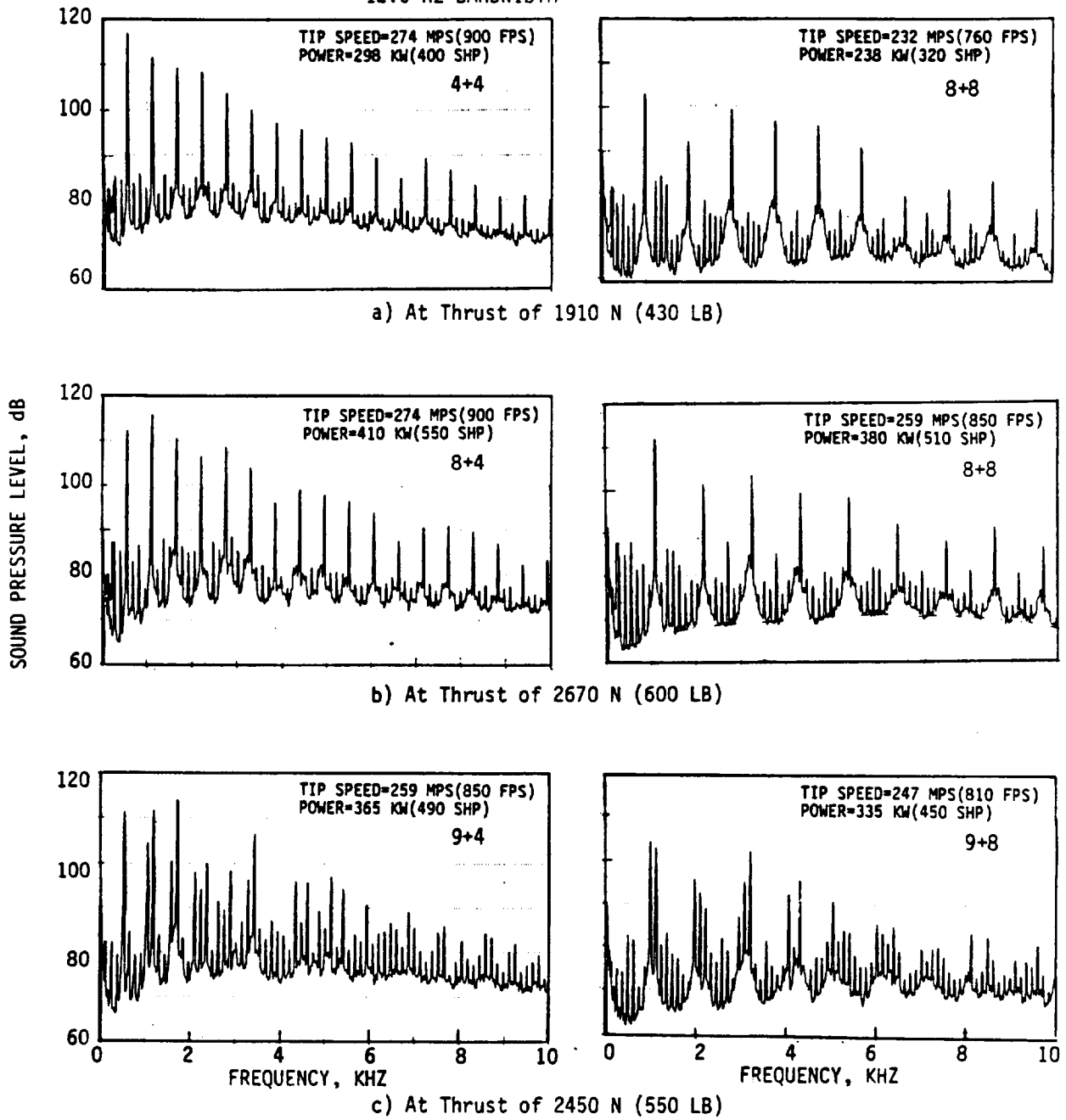


Figure 227. Selected Narrow-Band Data of F-7/A-7 with Different Blade Numbers at Equal Thrust.

MODEL SCALE AS MEASURED DATA
 NOMINAL ROTOR SPACING ($\lambda/D_t=0.169$)
 MICROPHONE ANGLE, $\Theta_m=92^\circ$
 12.5 HZ BANDWIDTH

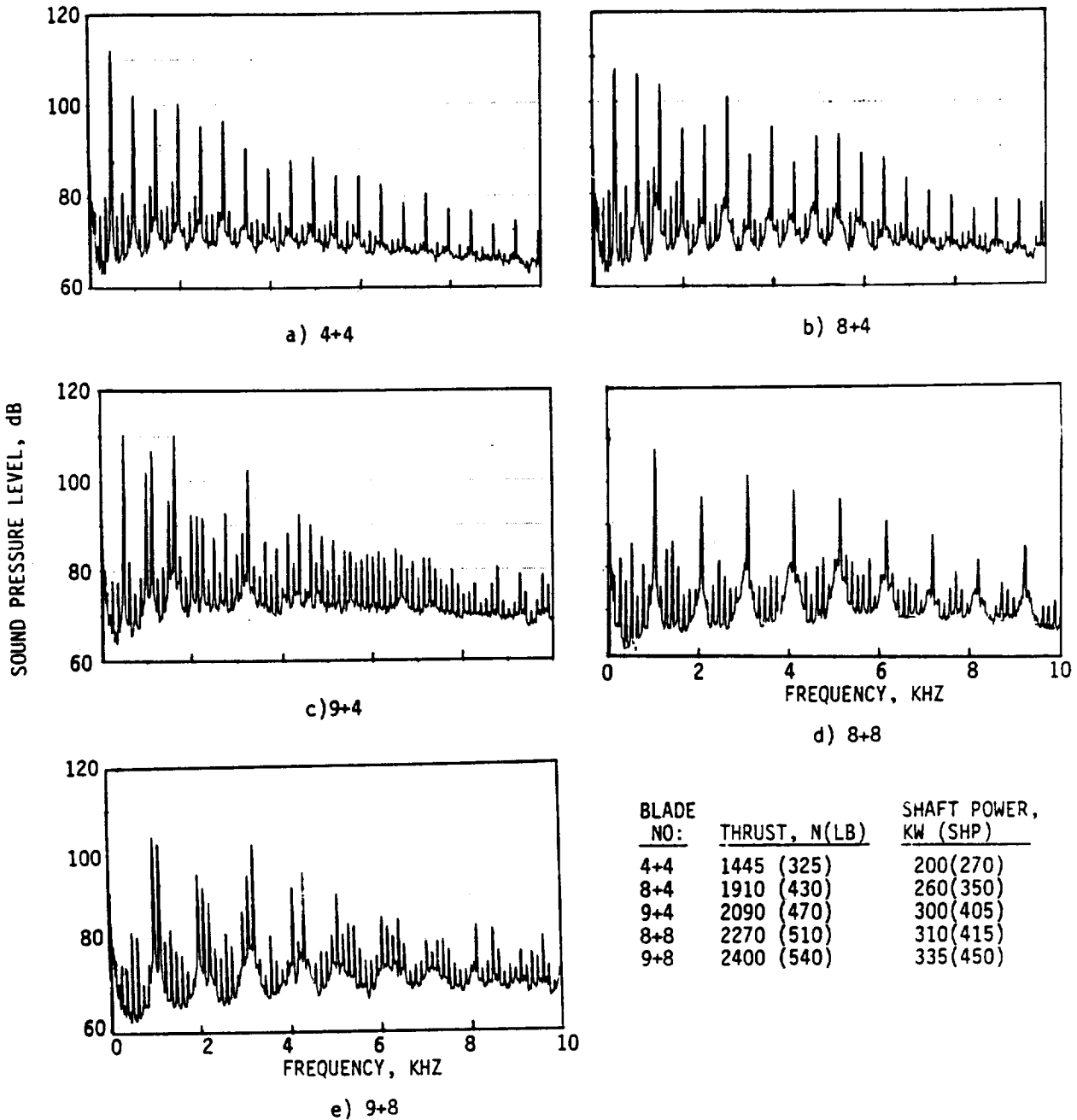


Figure 228. Selected Narrow-Band Data of F-7/A-7 with Different Blade Numbers at Equal Tip Speed of 247 mps (810 fps).

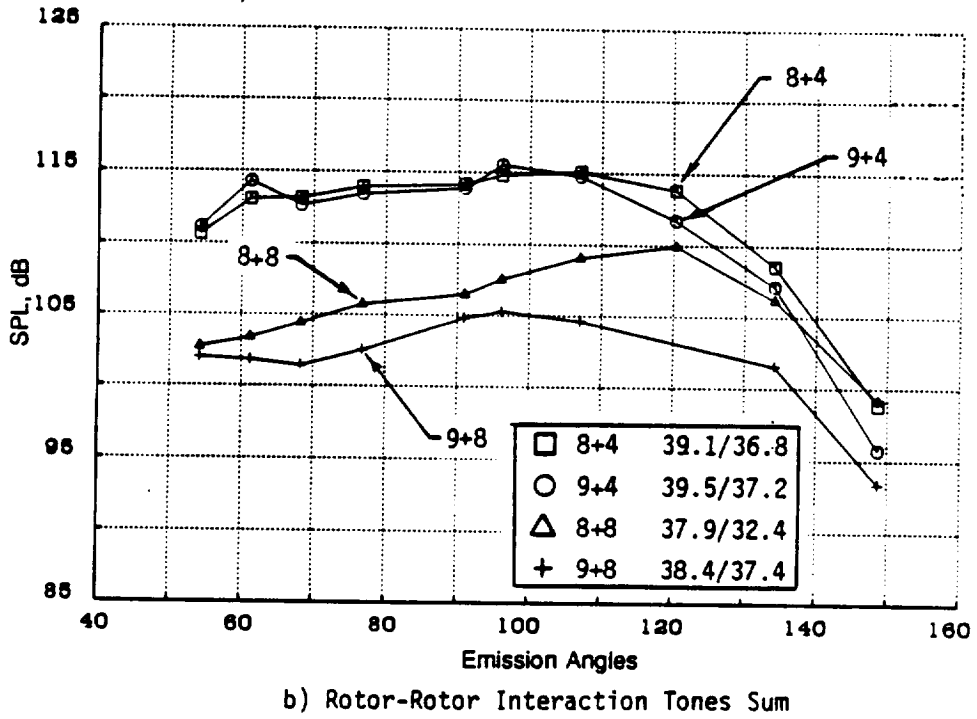
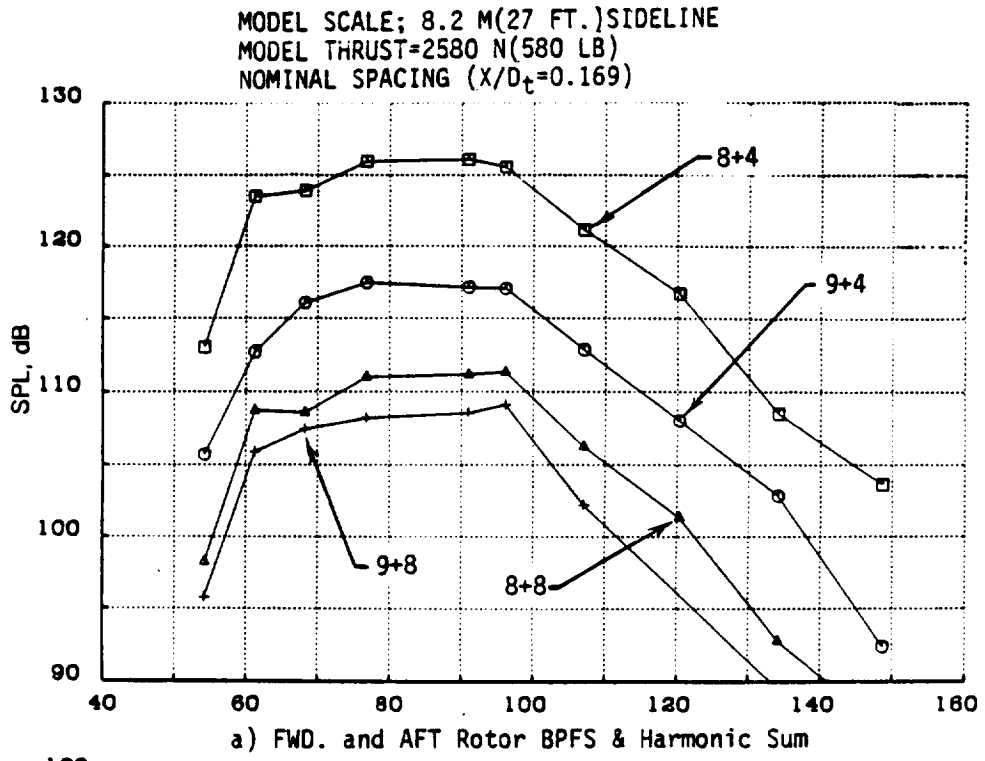
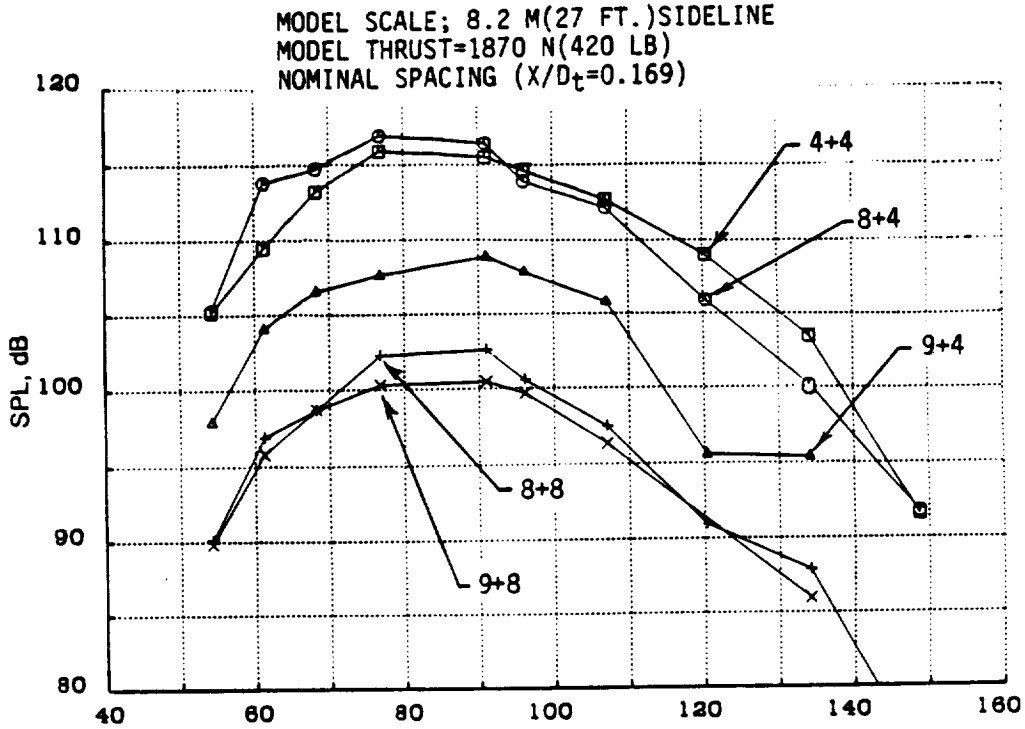
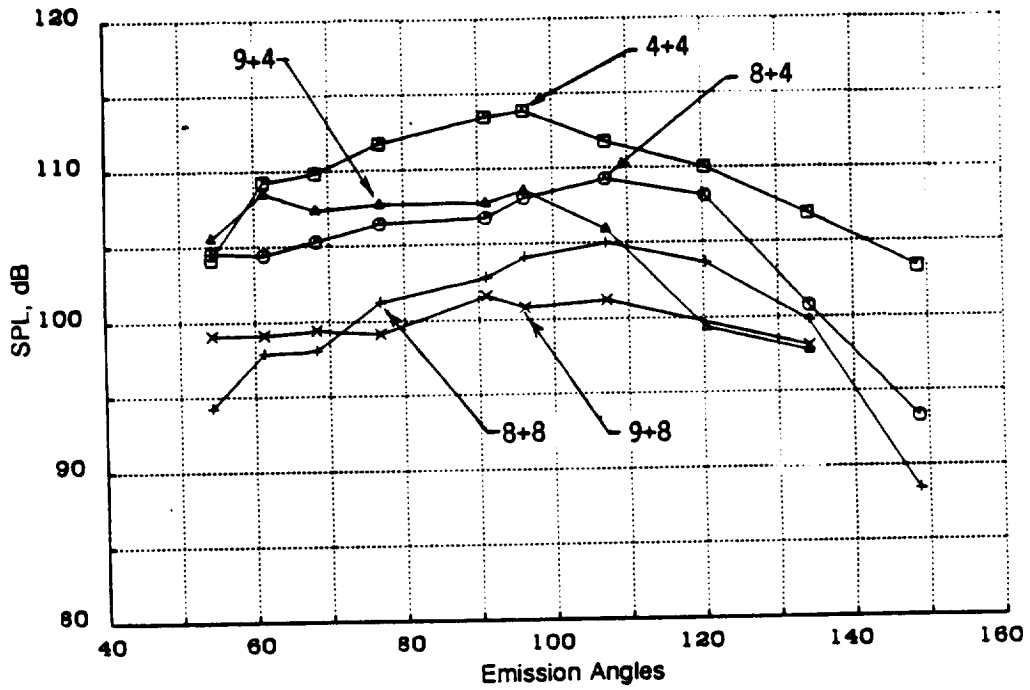


Figure 229. Model-Scale Tone Directivities of F-7/A-7 with Different Blade Numbers at Matching Takeoff Thrust.

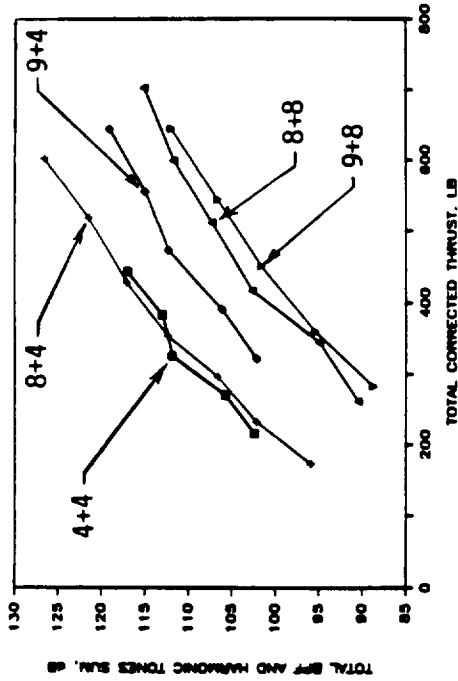


a) Fwd and Aft Rotor BPFs and Harmonics Sum

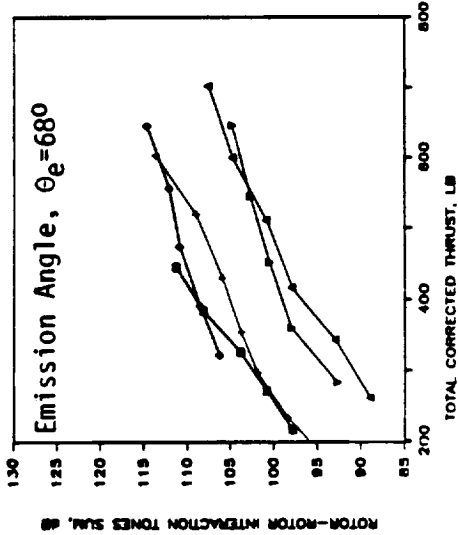


b) Rotor-to-Rotor Interaction Tones Sum

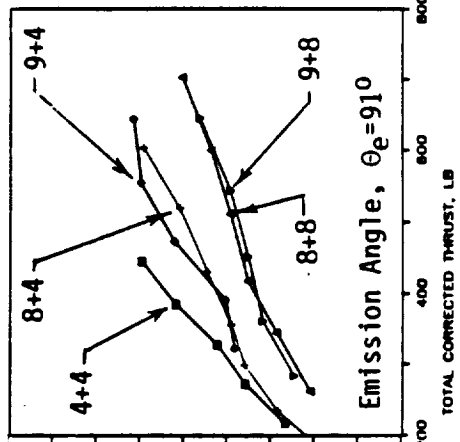
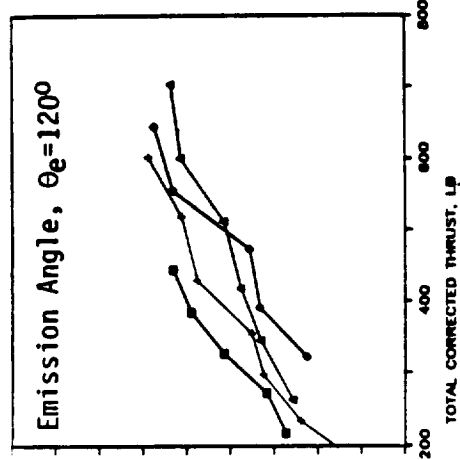
Figure 230. Model-Scale Tone Directivities of F-7/A-7 with Different Blade Numbers at Matching Cutback Thrust.



a) Fwd and Aft Rotor BPF & Harmonics Sum @ Emission Angle, $\theta_e=91^\circ$



b) Rotor-to-Rotor Interaction Tones Sum



BLADE NO.	β_1/β_2
□ 4+4	37.9/37.4
+ 8+4	39.1/36.8
◇ 9+4	39.5/37.2
△ 8+8	37.9/37.4
▽ 9+8	38.4/37.4

- MODEL SCALE
- $M_0=0.25$
- 8.2 M(27 FT.)SIDELINE
- F7A7 BLADES
- NOMINAL ROTOR SPACING ($X/D_t=0.17$)
- NOMINAL PITCH

Figure 231. Model-Scale Tone Sum Levels of F-7/A-7 with Different Blade Numbers as a Function of Total Thrust.

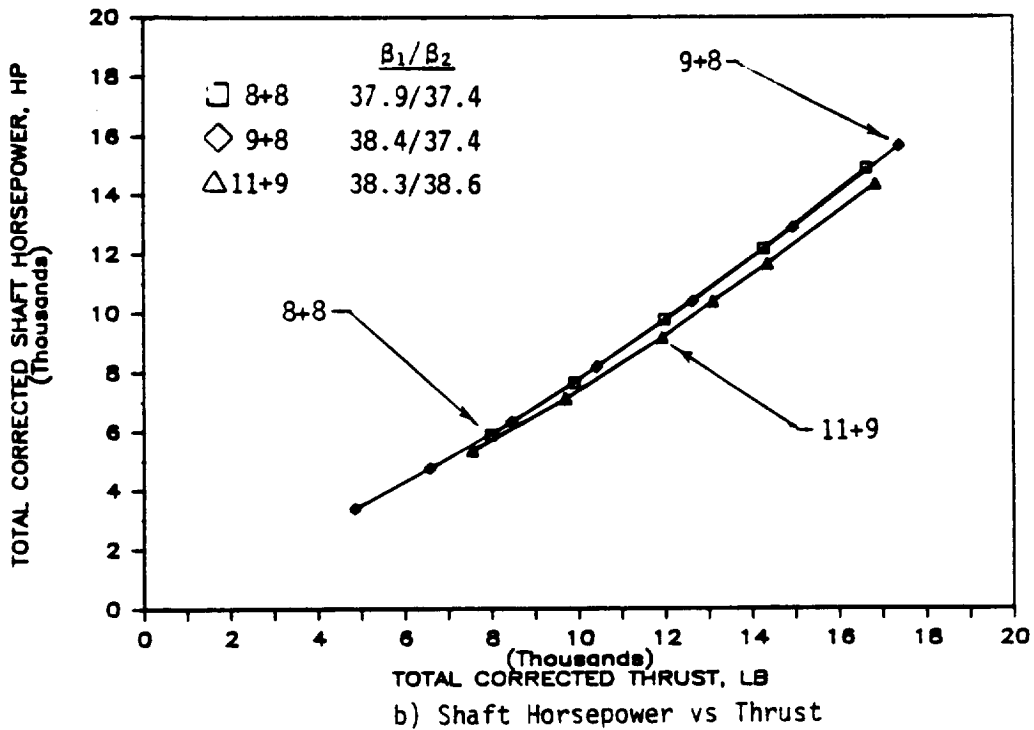
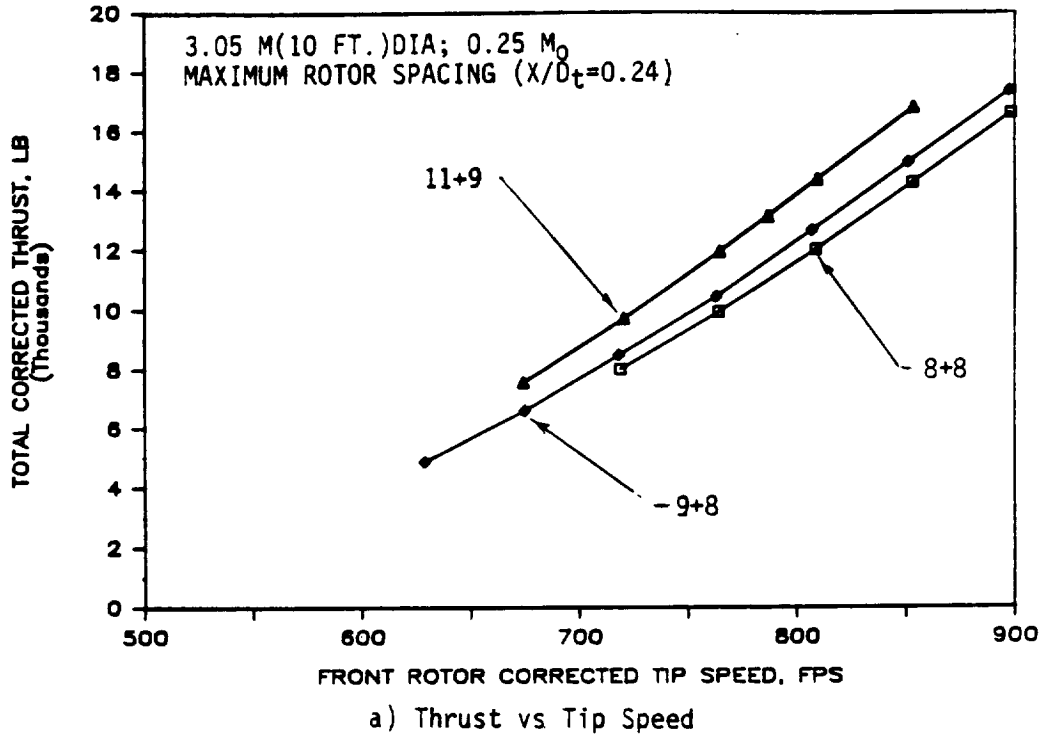


Figure 232. Aero Performance of F-7/A-7 with Different Blade Numbers.

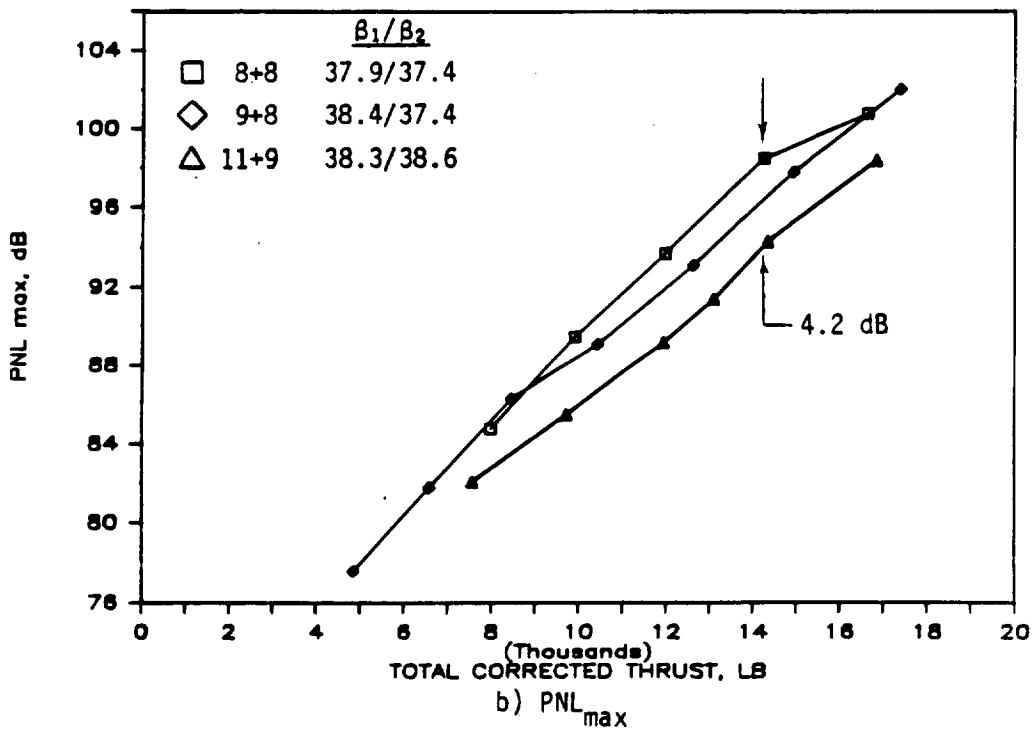
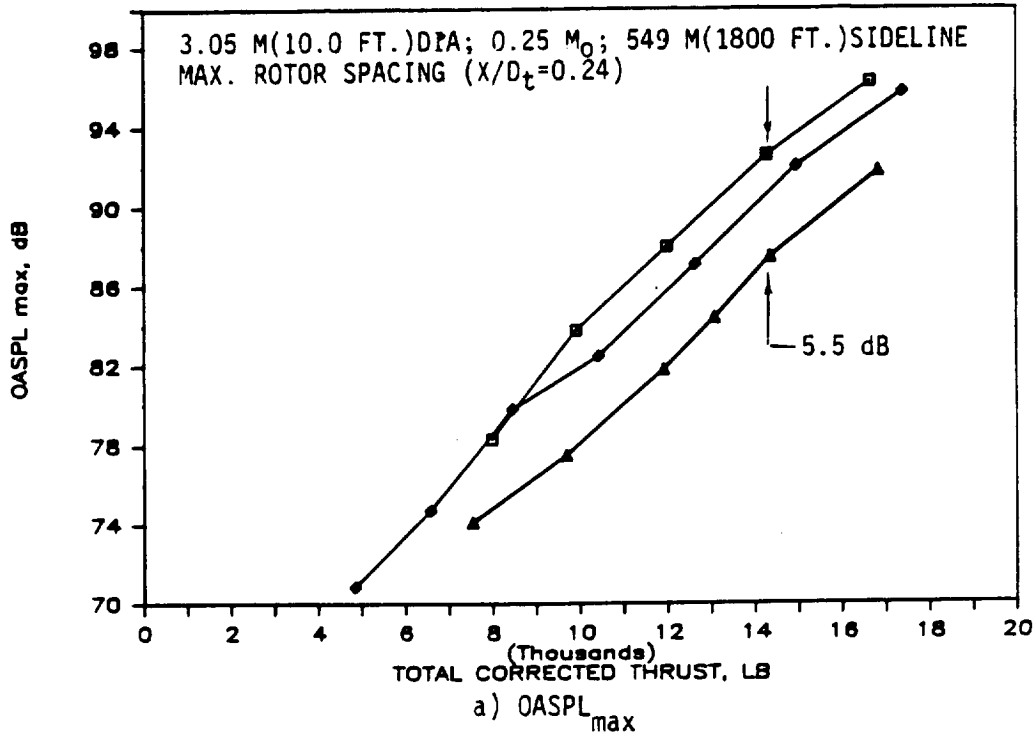
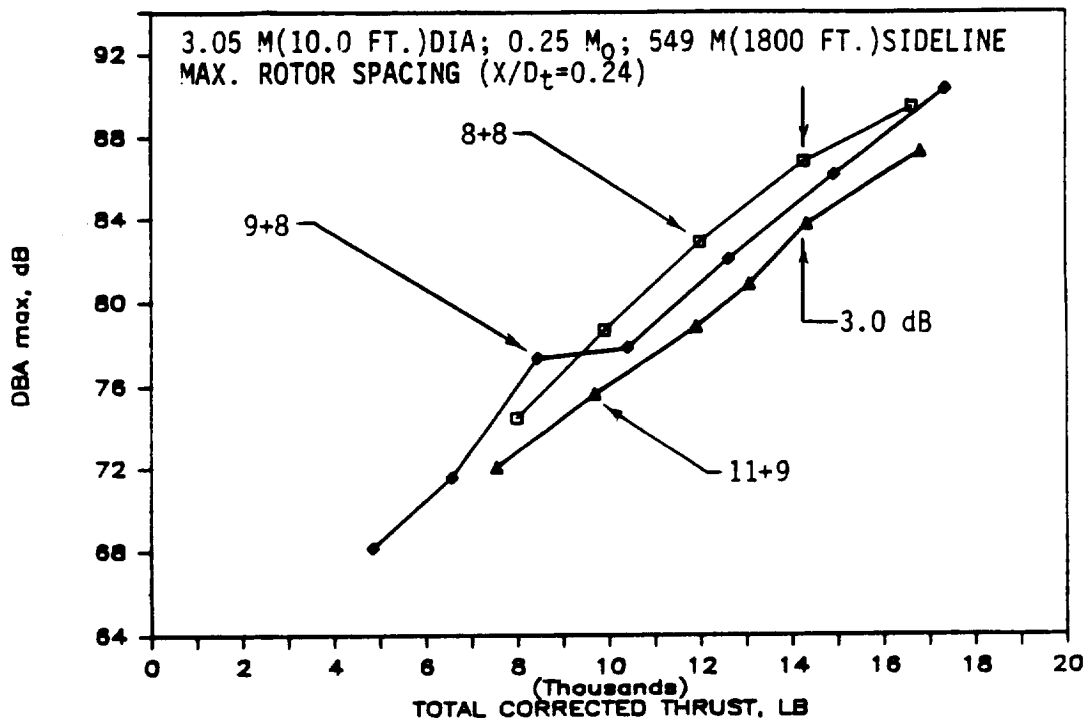


Figure 233. Acoustic Data of F-7/A-7 with Different Blade Numbers as a Function of Thrust.



c) dBA_{max}

Figure 233. Acoustic Data of F-7/A-7 with Different Blade Numbers as a Function of Thrust (Concluded).

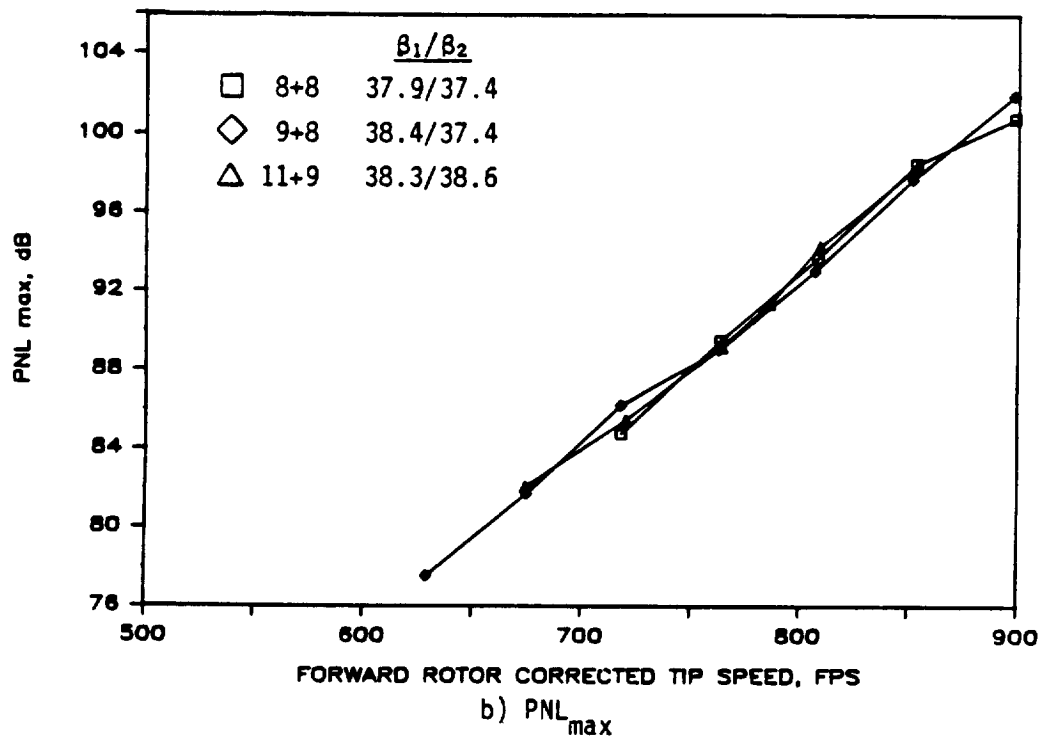
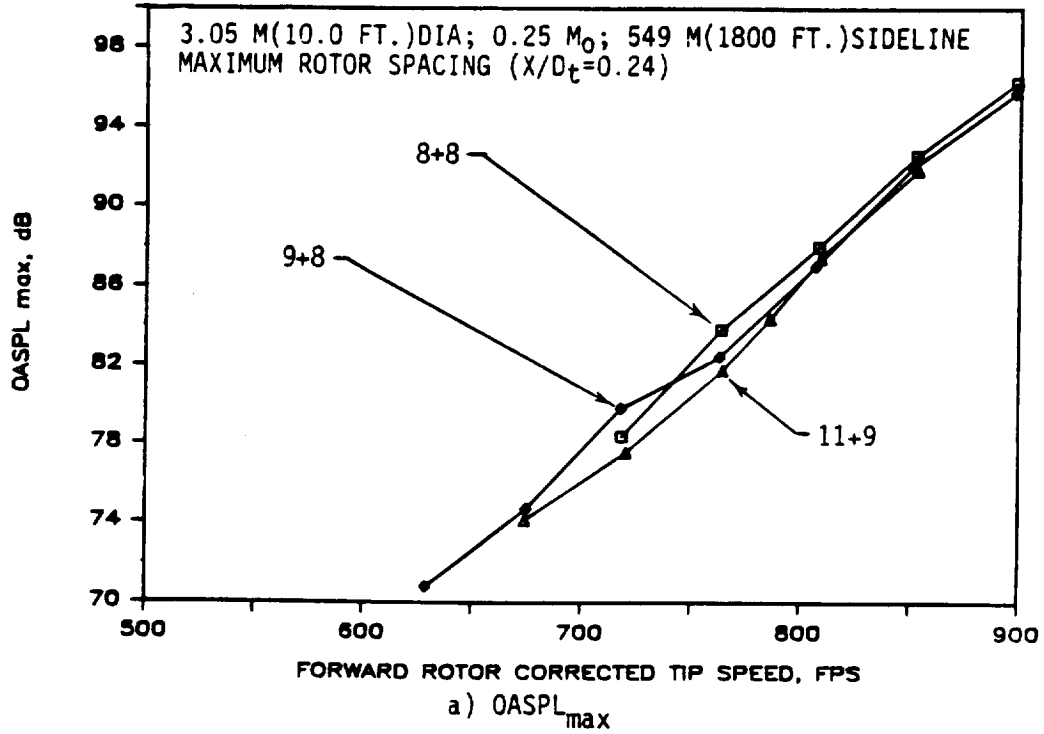


Figure 234. Acoustic Data of F-7/A-7 with Different Blade Numbers as a Function of Tip Speed.

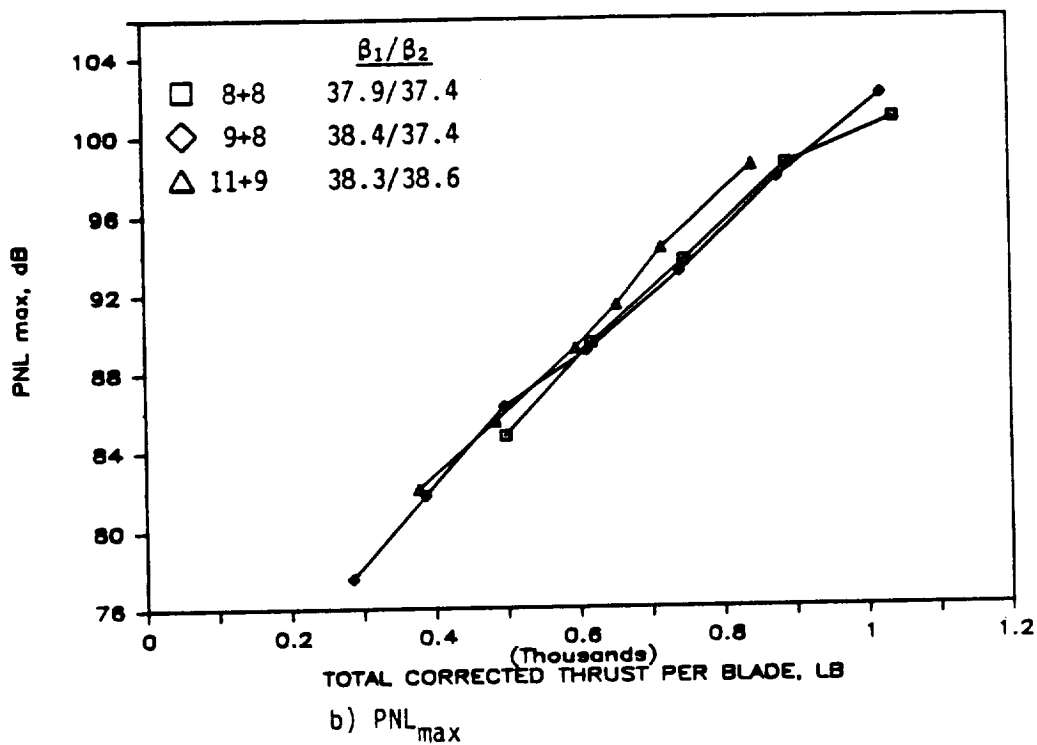
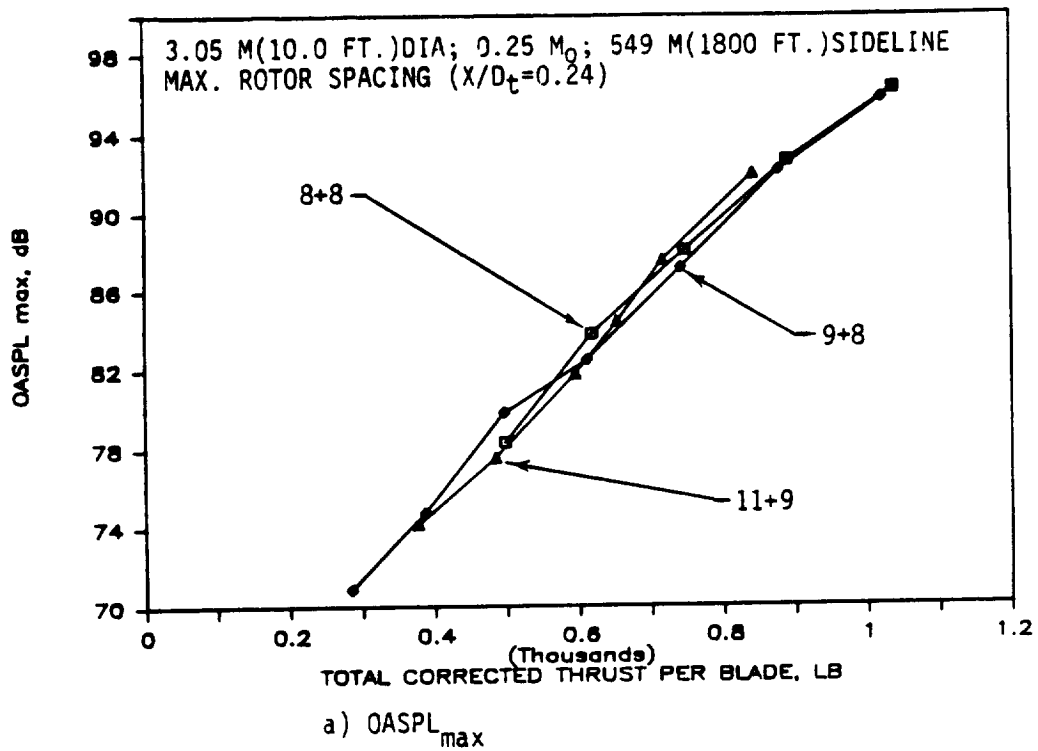
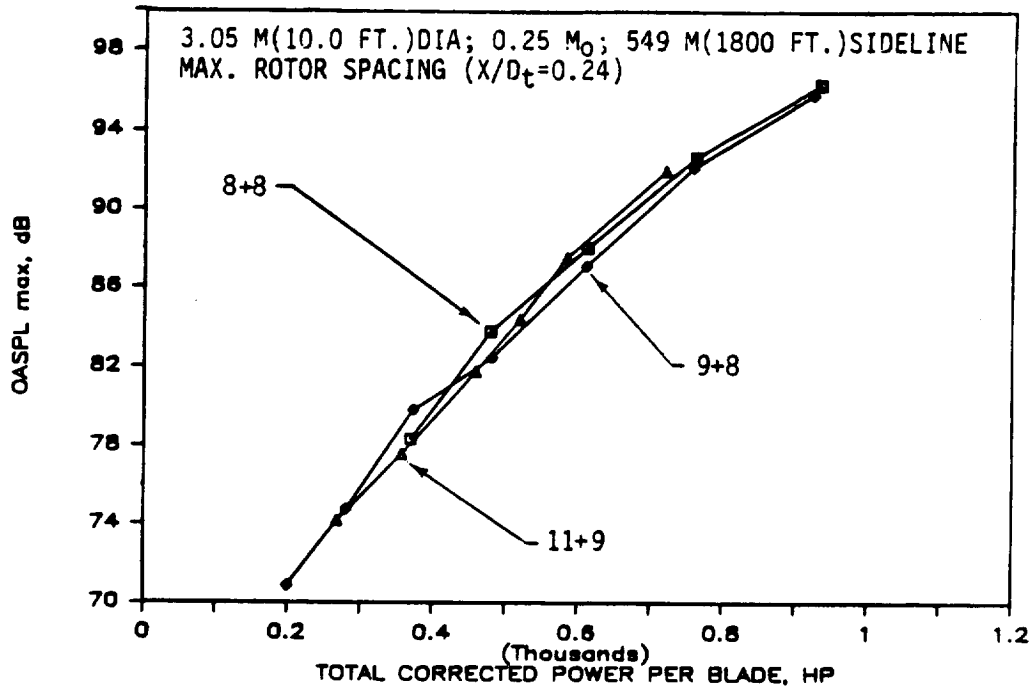
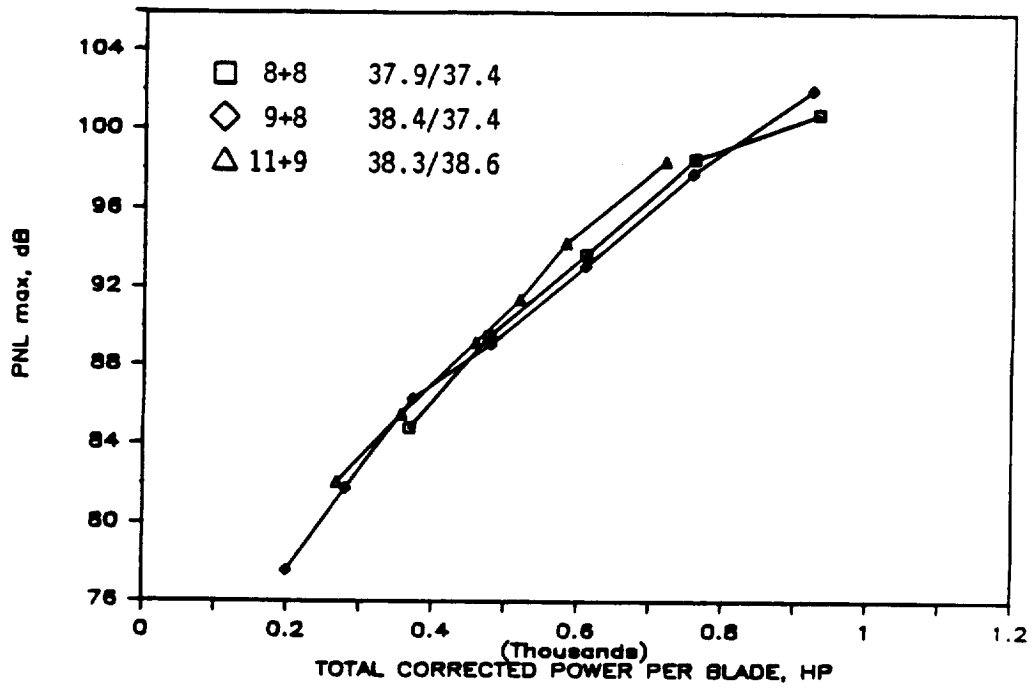


Figure 235. Acoustic Data of F-7/A-7 with Different Blade Numbers as a Function of Thrust per Blade.

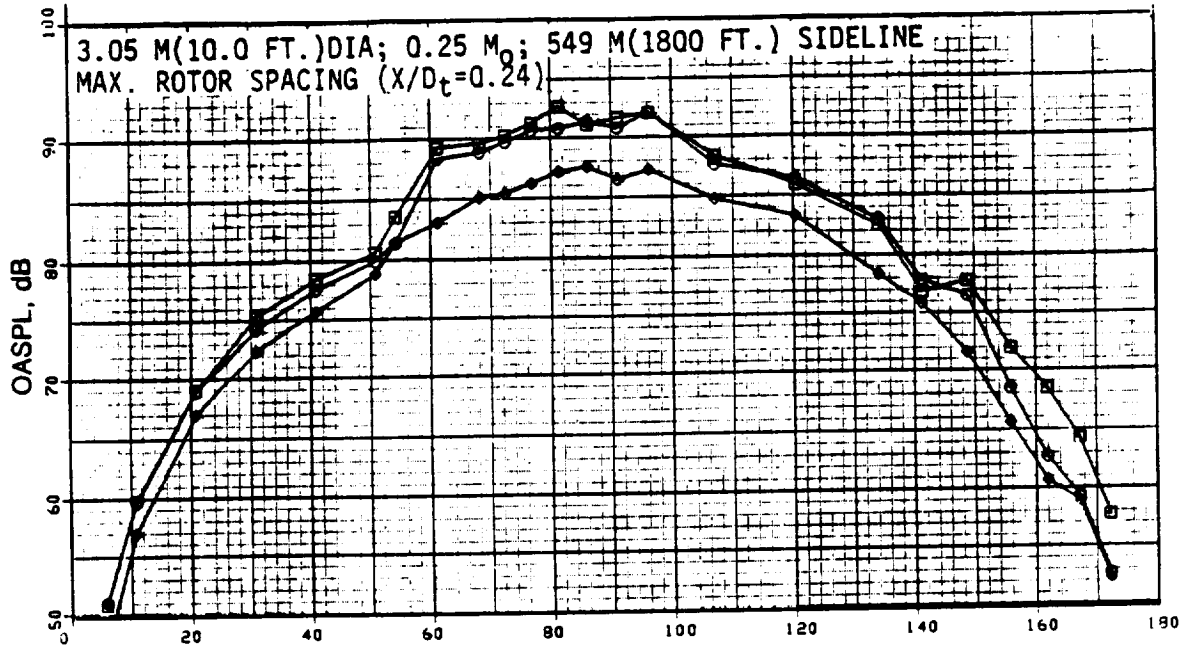


a) OASPL_{max}

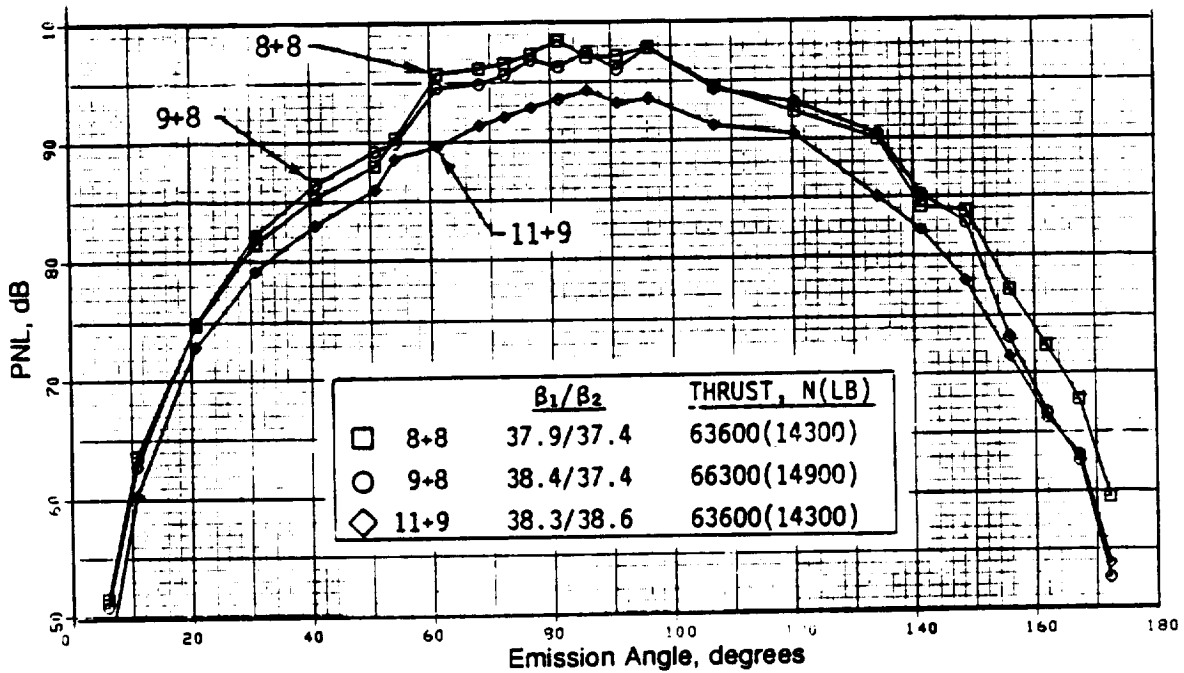


b) PNL_{max}

Figure 236. Acoustic Data of F-7/A-7 with Different Blade Numbers as a Function of Power per Blade.



a) OASPL



b) PNL

Figure 237. The OASPL and PNL Directivities of F-7/A-7 with Different Blade Numbers at Typical Takeoff Thrust.

3.05 M(10.0 FT.) DIA; 0.25 M_0 ; 549 M(1800 FT.) SIDELINE
 MAX. ROTOR SPACING ($X/D_t=0.24$)

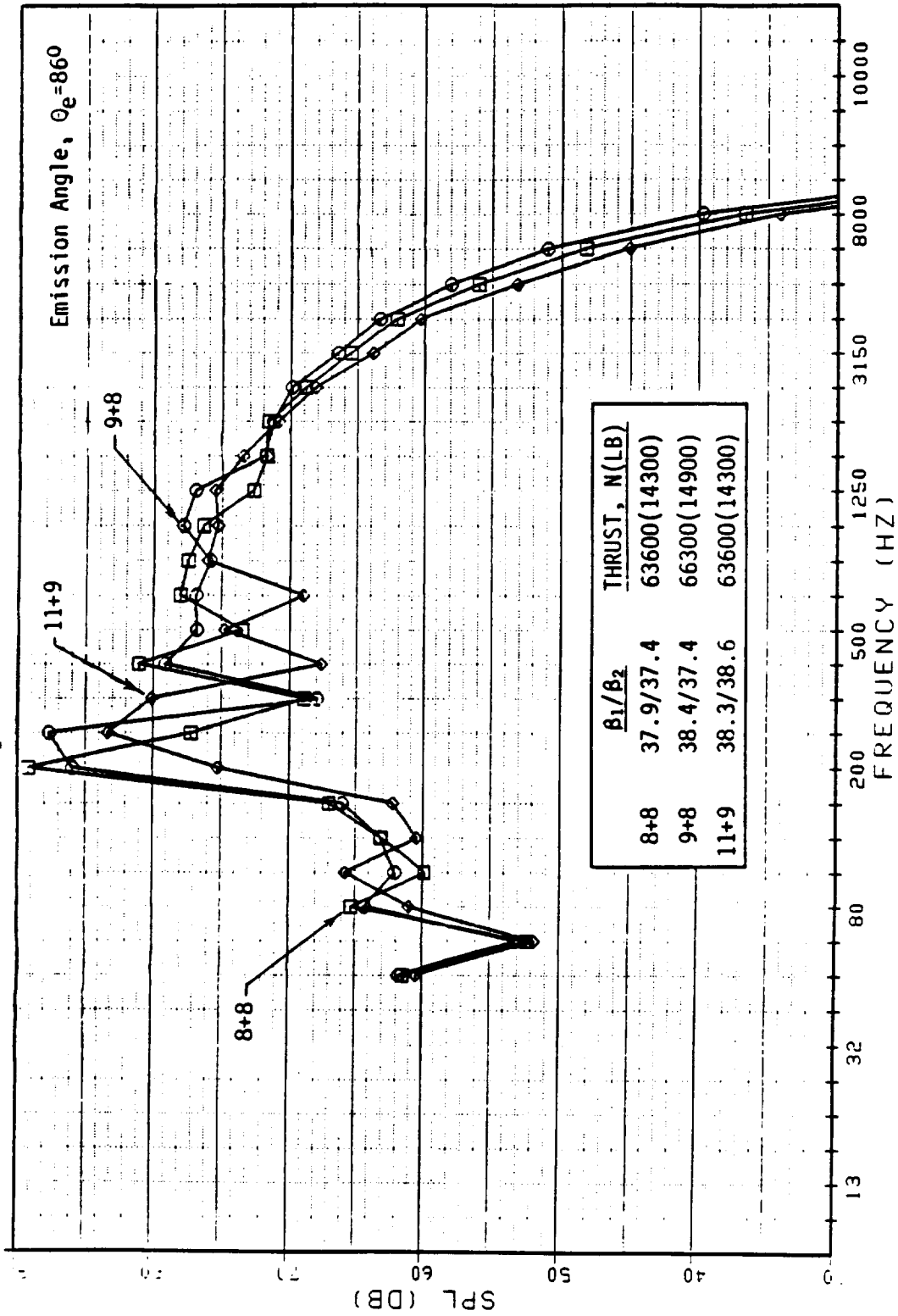
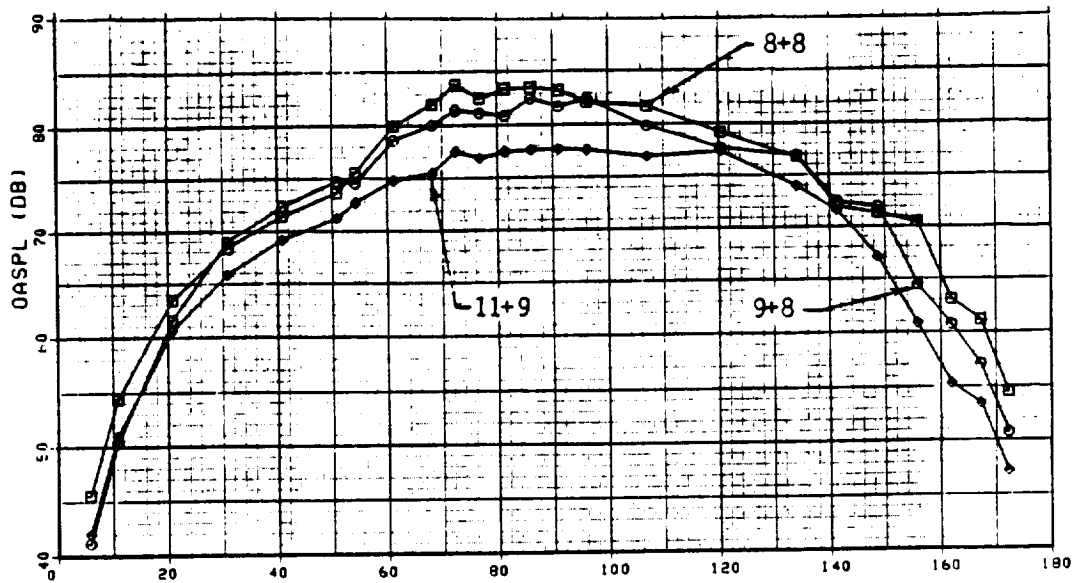
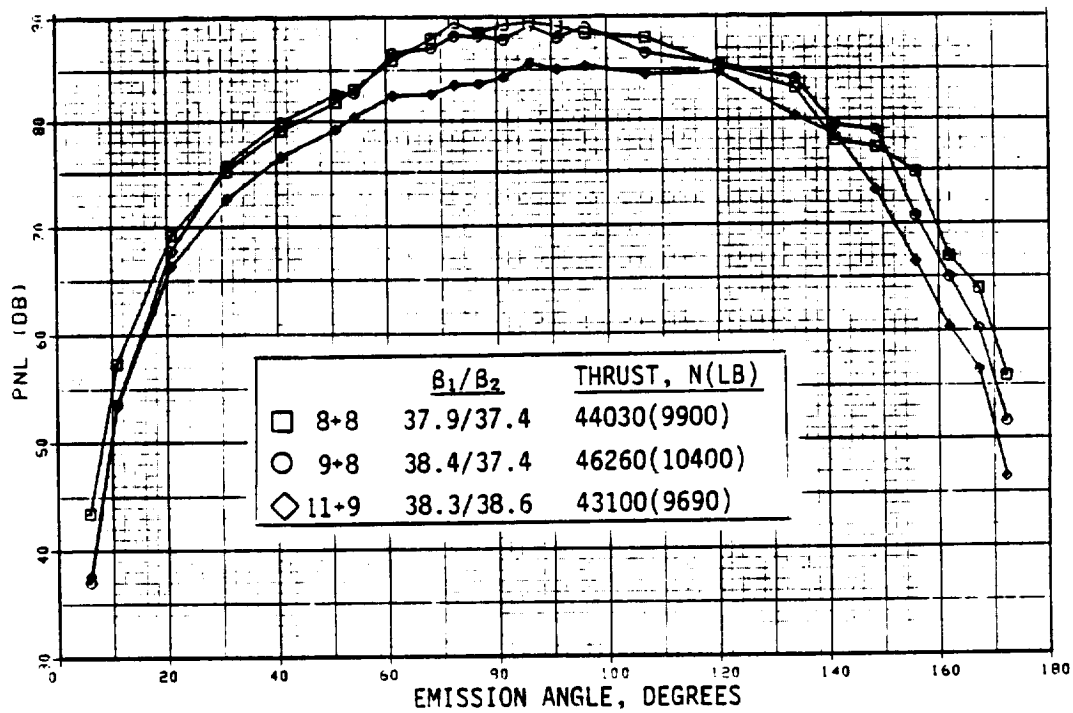


Figure 238. Spectra of F-7/A-7 with Different Blade Numbers at Typical Takeoff Thrust.

3.05 M(10.0 FT.)DIA; 0.25 M_0 ; 549 M(1800 FT.)SIDELINE
 MAX. ROTOR SPACING ($X/D_t=0.24$)



a) OASPL



b) PNL

Figure 239. OASPL and PNL Directivities of F-7/A-7 With Different Blade Numbers at Typical Cutback Thrust.

3.05 M(10.0 FT.)DIA; 0.25 M₀; 549 M(1800 FT.)SIDELINE
 MAX. ROTOR SPACING (X/D_t=0.24)

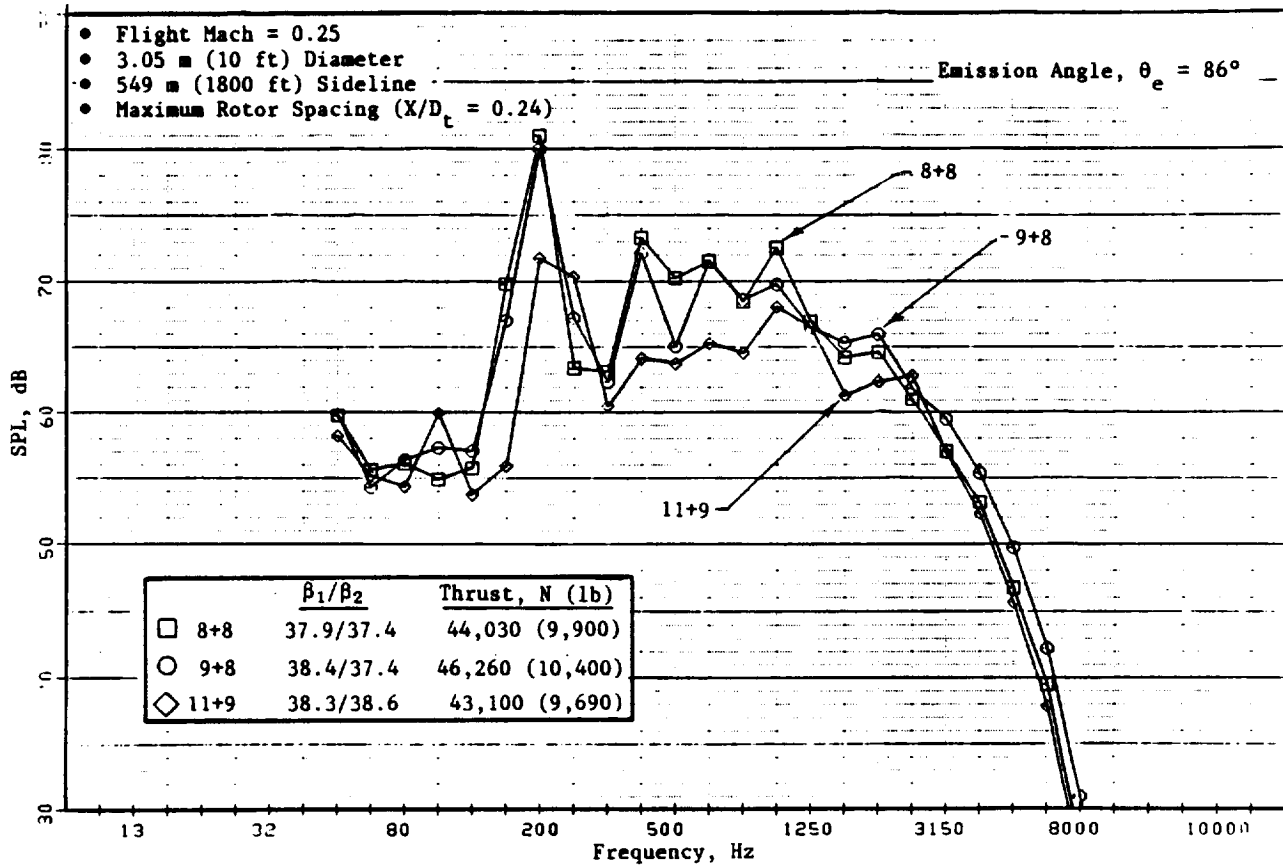


Figure 240. Spectra of F-7/A-7 with Different Blade Numbers at Typical Cutback Thrust.

Figures 241 and 242 show model-scale narrow-band spectra at equal thrust and equal tip speed for the different blade number combinations. For a given thrust, pressure level reductions in most of the tone levels are noted for increasing the blade count from a 9+8 to an 11+9 configuration.

Figures 243 and 244 depict the model-scale tone SPL (tones sum) directivities at model thrusts that match the typical takeoff and cutback conditions, respectively, of Figures 237 through 240. In addition, model-scale tone sum levels at selected emission angles are presented (Figure 245) as a function of model thrust. As with the test data of F-7/A-7 at nominal spacing between the rotor pitch-change axes, these results (with the maximum spacing) demonstrate a decrease in steady-loading and aerodynamic interaction noise components as a result of blade number increase. This is made clear by replotting model-scale tone sum data from Figure 246 as a function of total numbers of blades for a selected angle that is in the plane-of-rotation of the rotor (Figure 246).

3.05 M(10.0 FT.) DIA; 0.25 M_0 ; 549 M(1800 FT.) SIDELINE
 MAX. ROTOR SPACING ($X/D_t=0.24$)

THRUST=2220 N(500 LB)
 POWER=305 KW(410 SHP)

THRUST=2335 N(525 LB)
 POWER=320 KW(430 SHP)

THRUST=2670 N(600 LB)
 POWER=360 KW(485 SHP)

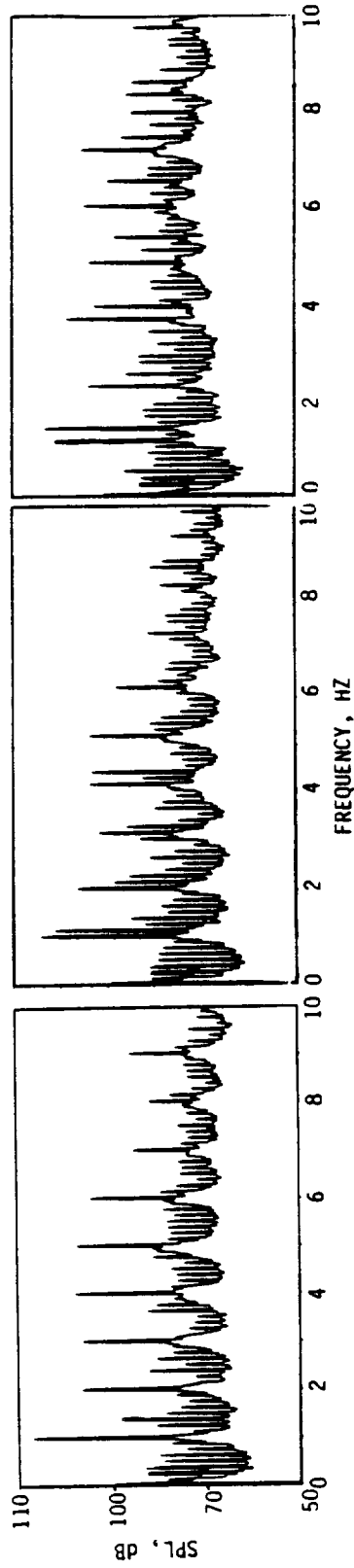


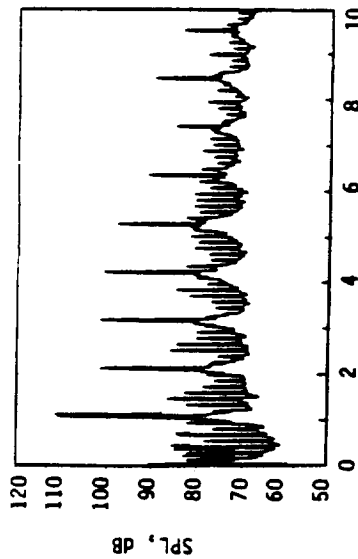
Figure 241. Selected Narrow-Band Data of F-7/A-7 with Different Blade Numbers
 at Equal Tip Speed of 247 mps (810 fps).

MODEL SCALE: AS MEASURED DATA
 MAXIMUM ROTOR SPACING ($X/D_t=0.24$)
 MICROPHONE ANGLE, $\theta_m=92^\circ$

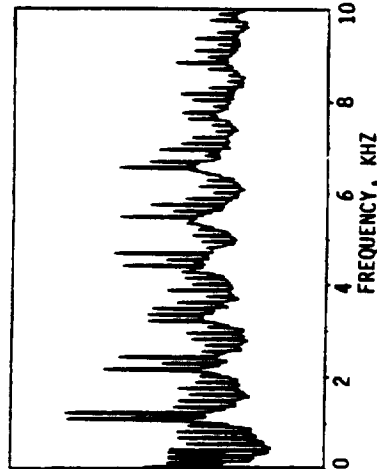
TIP SPEED=260 mps (850 fps)
 THRUST=2650 N (595 LB)
 POWER=375 KW (505 SHP)

TIP SPEED=260 mps (850 fps)
 THRUST=2760 N (620 LB)
 POWER=400 KW (535 SHP)

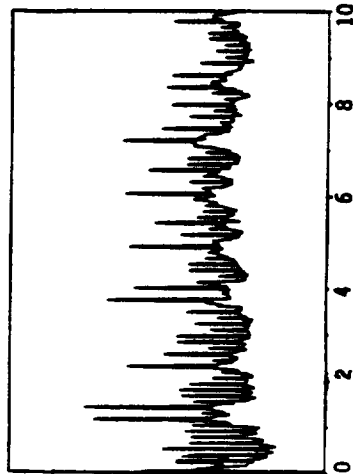
TIP SPEED=247 mps (810 fps)
 THRUST=2650 N (595 LB)
 POWER=360 KW (485 SHP)



a) 8+8



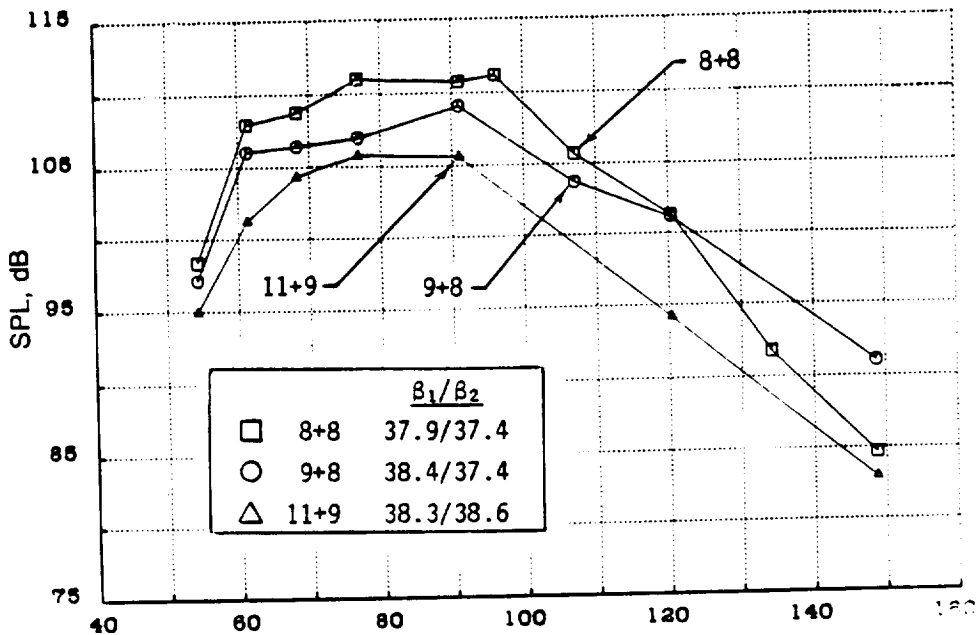
b) 9+8



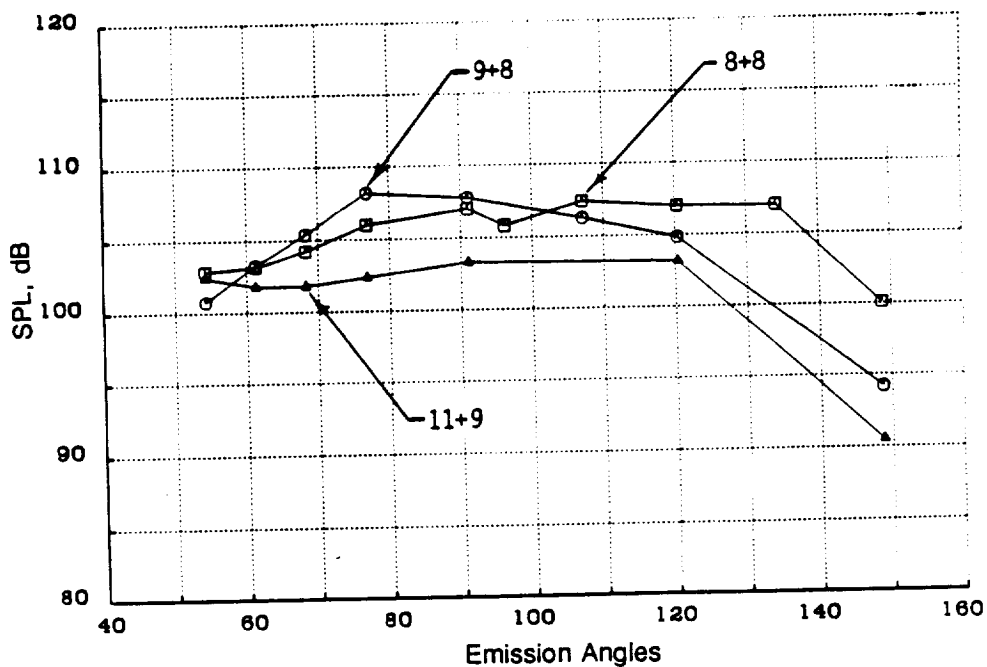
c) 11+9

Figure 242. Selected Narrow-Band Data of F-7/A-7 with Different Blade Numbers at Approximately Equal Thrust.

MODEL SCALE; 8.2 M(27 FT.)SIDELINE
 MODEL THRUST=2650 N(595 LB)
 MAXIMUM SPACING ($x/D_t=0.24$)

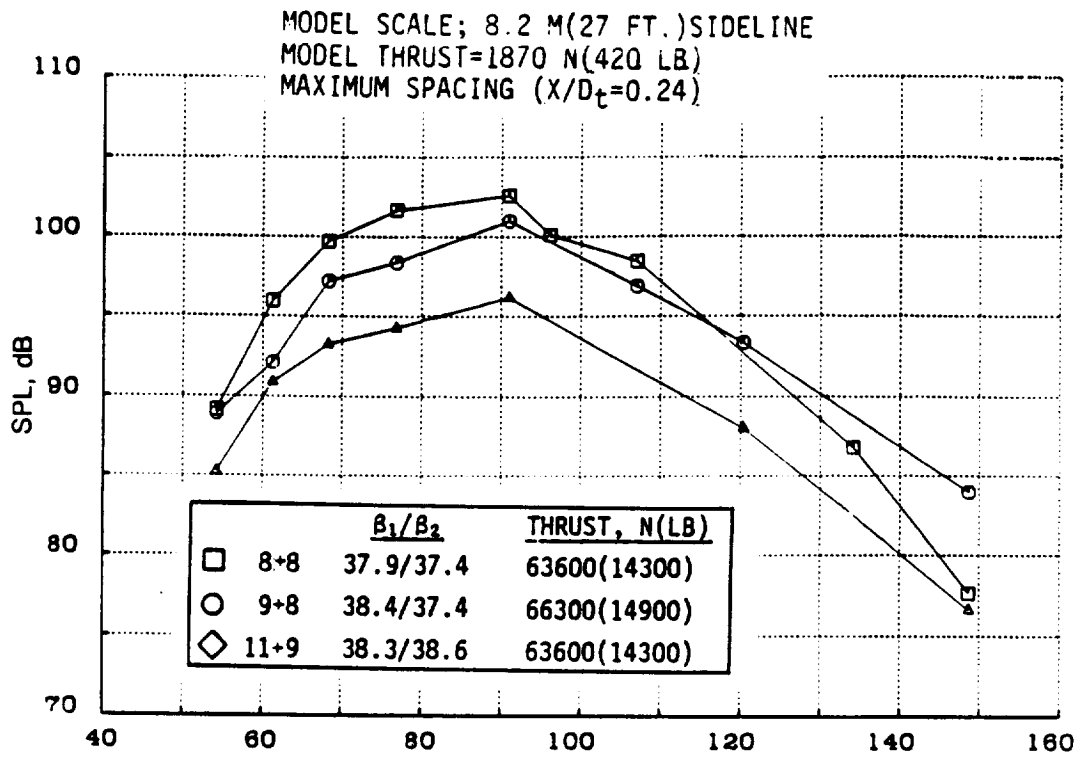


a) Fwd and Aft Rotor BPFs and Harmonics Sum

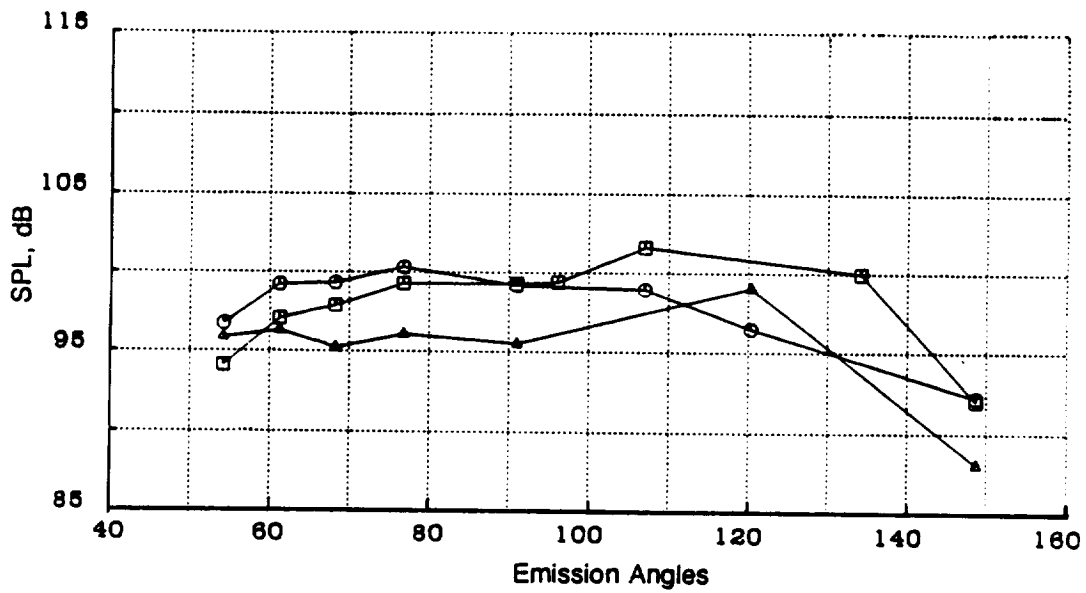


b) Rotor-to-Rotor Interaction Tones Sum

Figure 243. Model-Scale Tone Sum Directivities of the F-7/A-7 with Different Numbers of Blades at Matching Takeoff Thrust.

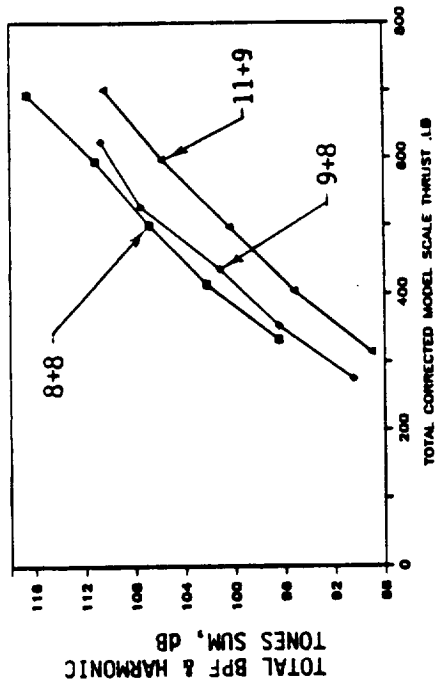


a) Fwd and Aft Rotor BPFs and Harmonics Sum



b) Rotor-to-Rotor Interaction Tones Sum

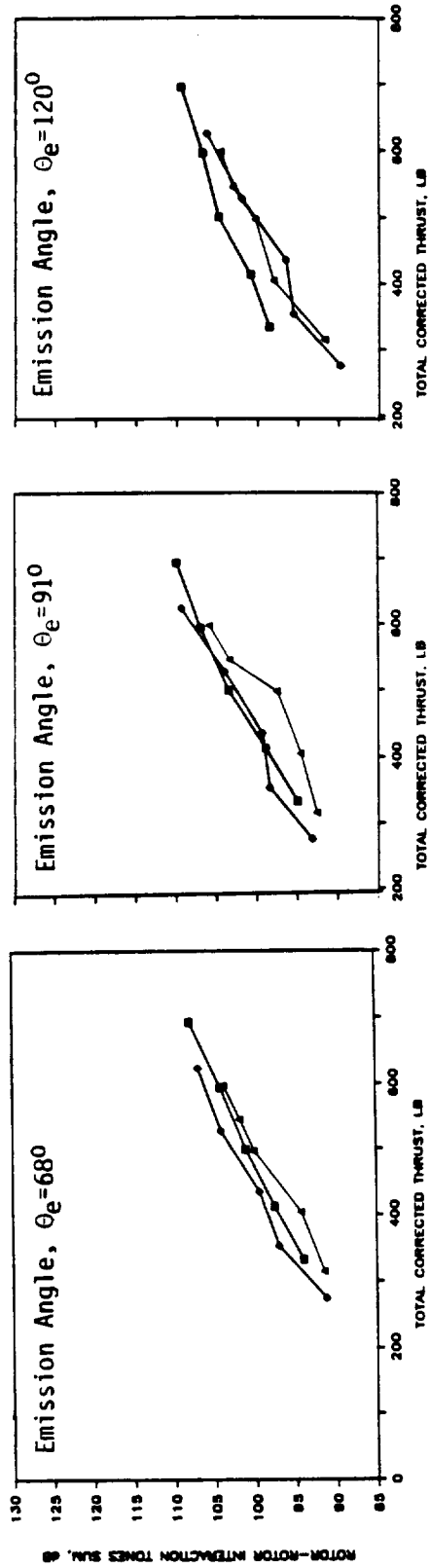
Figure 244. Model-Scale Tone Sum Directivities of the F-7/A-7 with Different Numbers of Blades at Matching Cutback Thrust.



	β_1/β_2
□	8+8 37.9/37.4
◇	9+8 38.4/37.4
△	11+9 38.3/38.6

- MODEL SCALE
- $M_0=0.25$
- 8.2 M(27 FT.) SIDELINE
- MAXIMUM ROTOR SPACING ($Z/D_t=0.24$)
- NOMINAL PITCH

a) Fwd and Aft Rotor BPF and Harmonics Sum @ Emission Angle, $\theta_e=91^\circ$



b) Rotor-to-Rotor Interaction Tones Sum

Figure 245. Model-Scale Tone Sum Levels of F-7/A-7 with Different Numbers of Blades as a Function of Total Thrust.

MODEL SCALE; 8.2 M(27 FT.) SIDELINE
 MAXIMUM ROTOR SPACING ($X/D_r=0.24$)
 EMISSION ANGLE, $\theta_e=91^\circ$

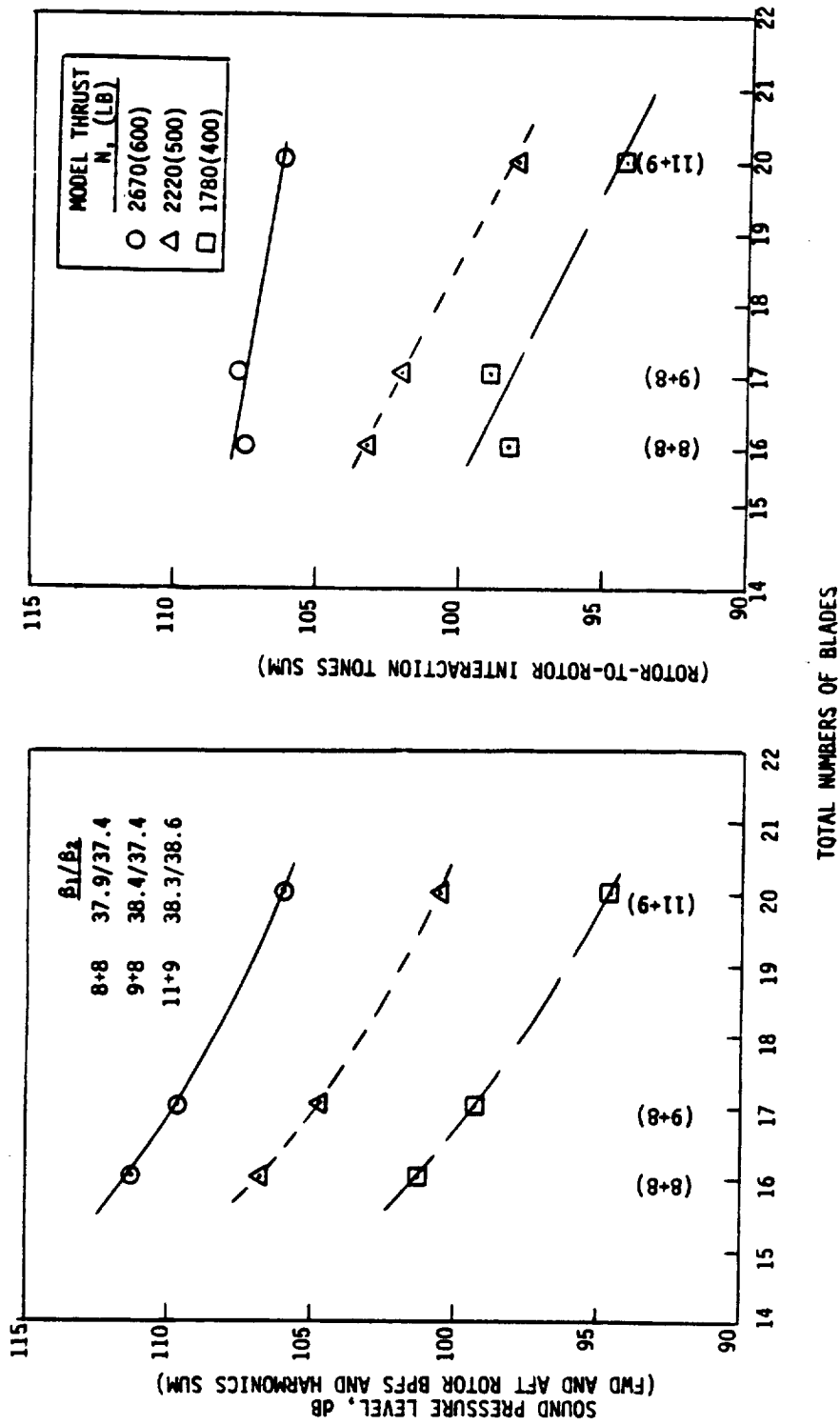


Figure 246. Model-Scale Tone Sum Levels in the Plane-of-Rotation of the Rotors as a Function of Total Blade Numbers.

The acoustic evaluation of the blade number effect on the F-7/A-7 configuration is concluded by comparing the processed EPNL values, measured with the various blade numbers, at both nominal and maximum spacings between the pitch-change axes. Figure 247 compares these EPNL data to the corresponding EPNL value of the F-7/A-7, with a blade count of 8 forward and 8 aft.

Examination of this figure verifies the significant acoustic benefit of increasing blade numbers. For example, the increase of blade numbers from a 4+4 configuration to an 8+8 blade, with both at nominal spacing, results in a benefit of 9.6 EPNdB at a thrust of 44,500 N (10,000 lb). A similar increase from an 8+8 configuration to an 11+9 blade count, with both at maximum rotor spacing, results in an additional benefit of 3.4 EPNdB at the above thrust; which, in turn, increases with thrust to yield a 5 EPNdB reduction at 62,300 N (14,000 lb) for increasing blade numbers from an 8+8 to an 11+9 configuration.

7.1.1.4 Effect of Spacing Between Forward and Aft Rotors

To determine what effect, if any, the axial spacing between the forward and aft rotors of counterrotating fan blades might have on their acoustic characteristics, tests were conducted with different spacings between rotor pitch-change axes utilizing the F-7/A-7 and F-11/A-11 model-scale blades. The test configurations for this study are summarized in Table 60. The rotor-to-rotor spacings (referred to as nominal, maximum, and supermaximum), defined by the axial distance between pitch-change axes of the forward and aft rotors, are equal to: 10.6 cm (4.16 in.), 15.0 cm (5.90 in.), and 19.9 cm (7.82 in.), respectively. These axial spacings result in a spacing-to-diameter ratio of 0.169, 0.24, and 0.32 for the test configurations. Figure 248 illustrates the various rotor spacing installations. All of the above tests were conducted without a pylon.

The acoustic data measured during the four series of tests (Table 60) are presented and discussed in this section. These data were measured at a simulated flight Mach number of 0.25.

7.1.1.4.1 F-7/A-7 (8+8) at Nominal and Open Pitch Angles: Series 1

The F-7/A-7 8+8 blade configuration was tested at the nominal and maximum rotor-to-rotor spacings with pitch angles of 37.9°/37.4° and 43.4°/40.4°. For these test conditions, the impact of the increased rotor-to-rotor spacings, in terms of a normalized axial distance between the TE of a forward blade and the quarter-chord point of an aft blade, is depicted in Figure 249.

A comparison of selected acoustic data obtained for this test series, using nominal and maximum rotor spacings, with pitch angles of 37.9°/37.4° is provided as follows:

- Figure 250 compares model-scale narrow-band data at microphone locations of 67°, 92°, and 107° at a tip speed of 232 mps (760 fps)
- Figure 251 portrays sound pressure level directivity of blade passing frequency and higher harmonics (narrow-band scale model data) at a tip speed of 232 mps (760 fps)
- Figure 252 presents model-scale tone sum levels as a function of total thrust
- Figure 253 compares scaled spectral data at the flight emission angle of 91° for tip speeds of 220 mps (720 fps), 232 mps (760 fps), 247 mps (810 fps), and 260 mps (855 fps)
- Figure 254 provides a PNL directivity comparison at tip speeds of 220 mps (720 fps) and 247 mps (810 fps)

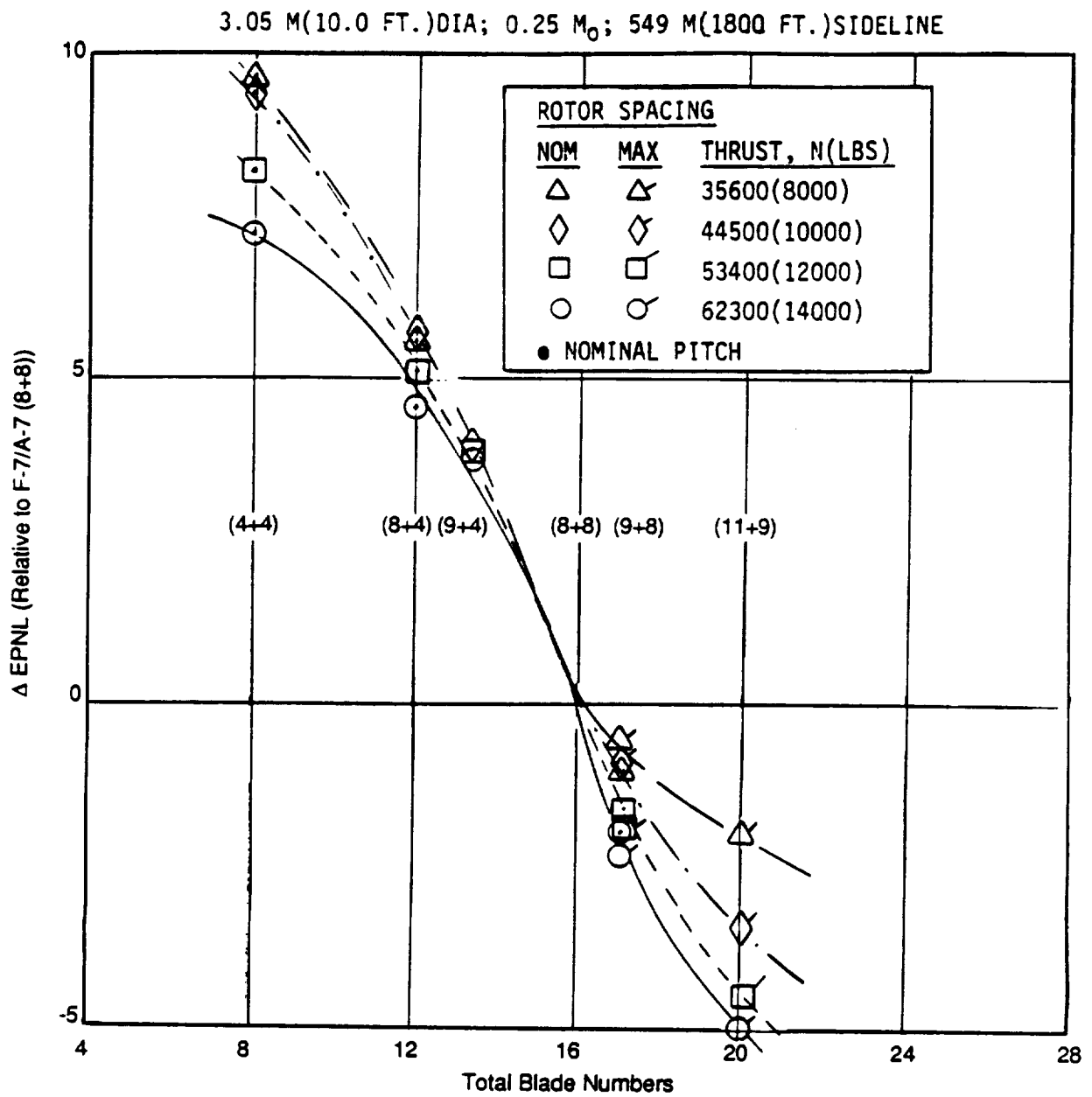


Figure 247. Effect of Blade Numbers for the EPNL.

Table 60. Summary of Cell 41 Rotor Spacing Tests.

Test Series	Configuration	Number of Blades	Pitch Angle, degrees	Rotor Spacing	Run No.
1	F-7/A-7	8+8	37.9/37.4 (Nominal)	Nominal	12
				Maximum	27
	F-7/A-7	8+8	43.4/40.4 (Open)	Nominal	13
				Maximum	28
2	F-7/A-7	9+8	38.4/37.4 (Nominal)	Nominal	26
				Maximum	32
3	F-7/A-7c	9+8	36.4/42.7 (Nominal)	Nominal	43
				Maximum	45
4	F-11/A-11	11+9	44.8/43.3 (Open)	Maximum	94
				Supermaximum	140
	F-11/A-11	11+9	48.7/45.3 (Open)	Maximum	110
			Supermaximum	139	

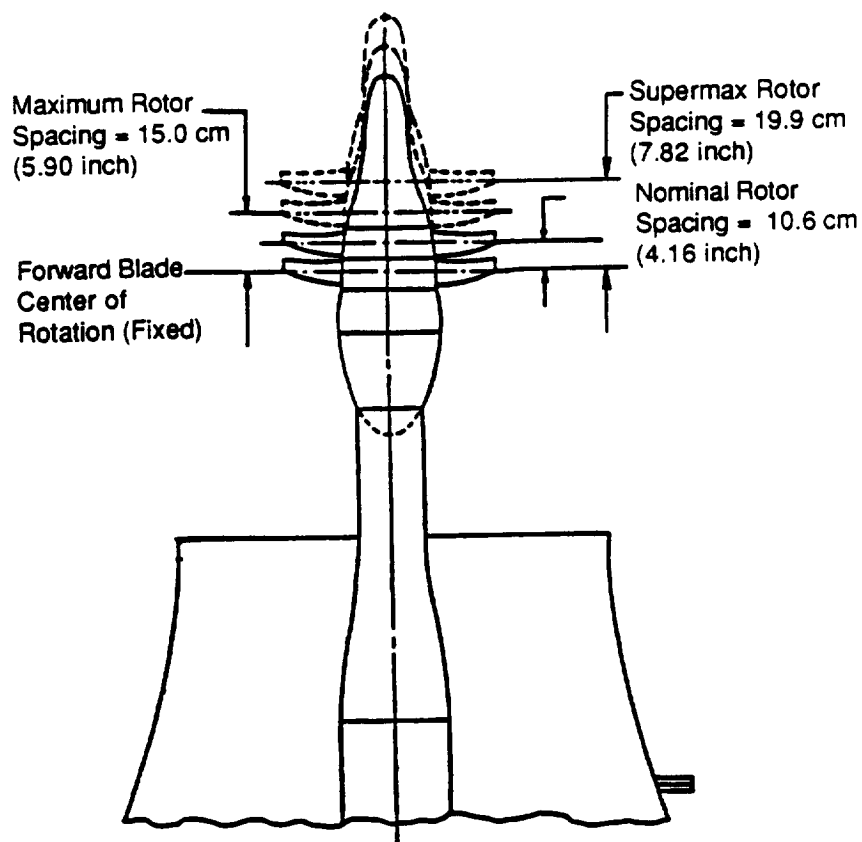


Figure 248. Schematic of MPS Cell 41 Setup of Rotor Installation Spacings.

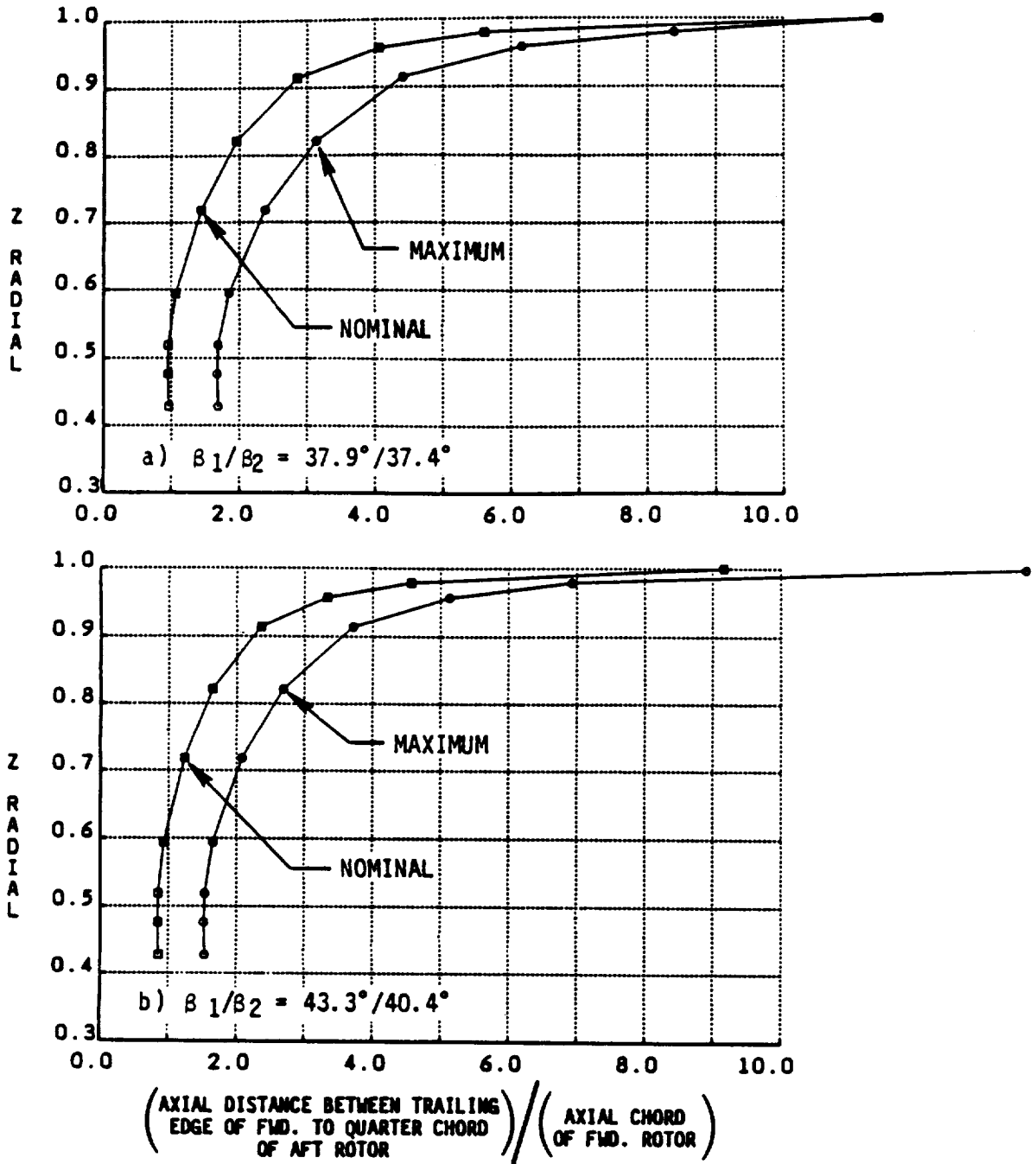


Figure 249. Nominal and Maximum Rotor-to-Rotor Spacing Comparison for the F-7/A-7 Blades.

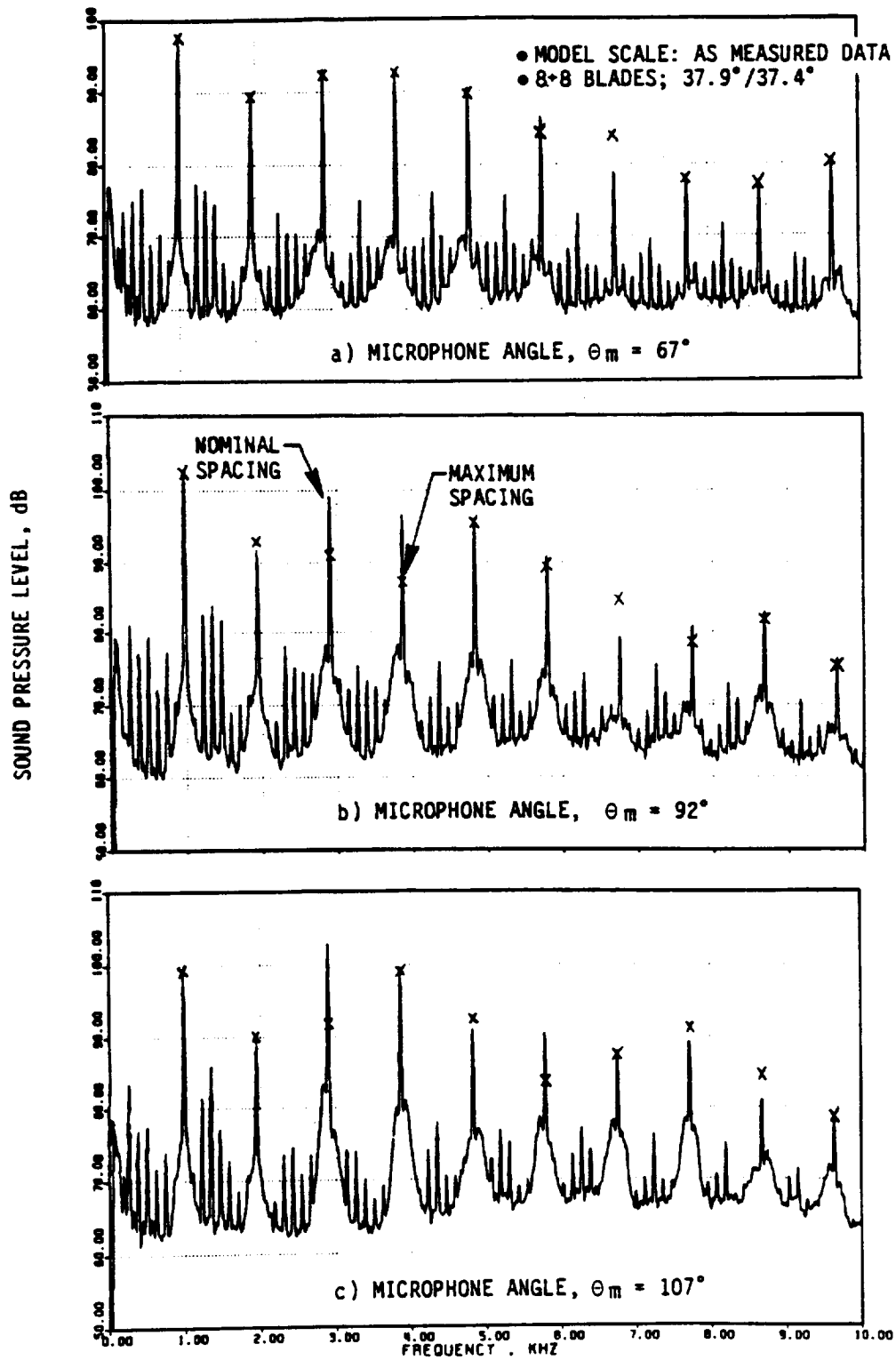


Figure 250. Typical Narrow-Band Data Comparison of F-7/A-7 at Tip Speed of 232 mps (760 fps).

• MODEL SCALE; 0.25 M_0 ; 8.2 M (27.0 FT) SIDELINE
 • MODEL THRUST = 1845 N (415 LB); TIP SPEED = 232 MPS (760 FPS)
 • 12.5 HZ NARROWBAND DATA

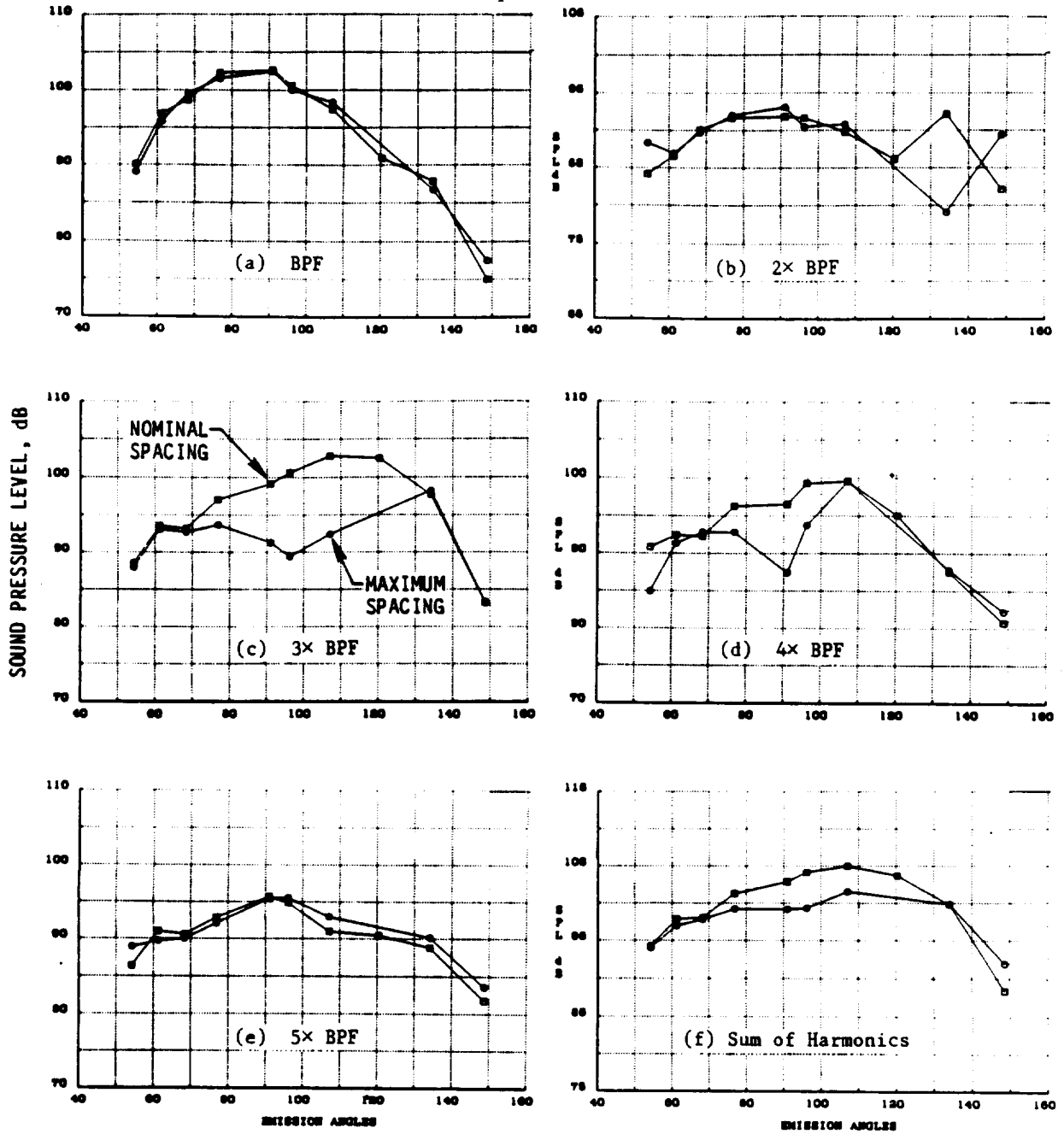
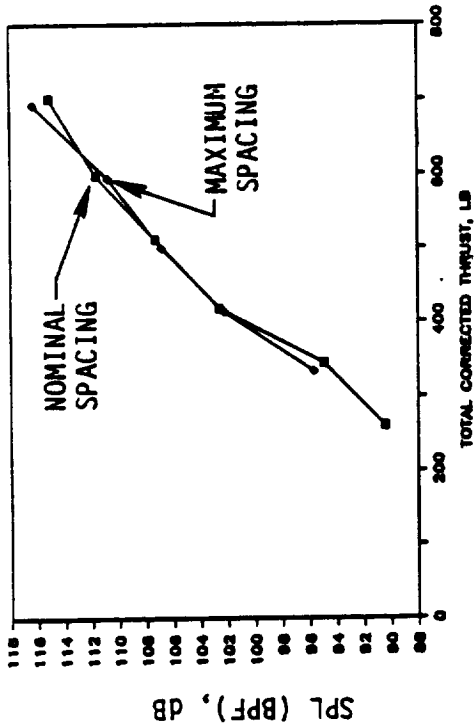
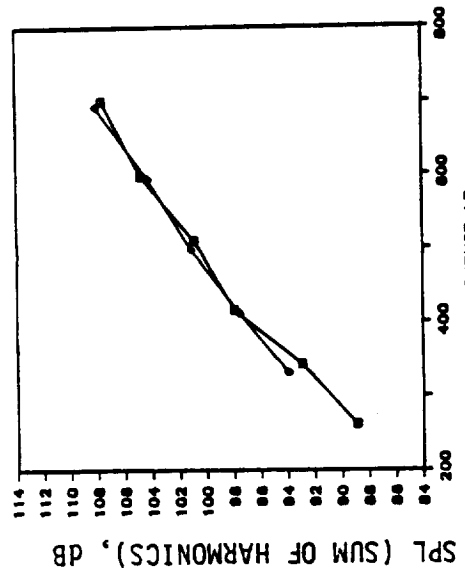


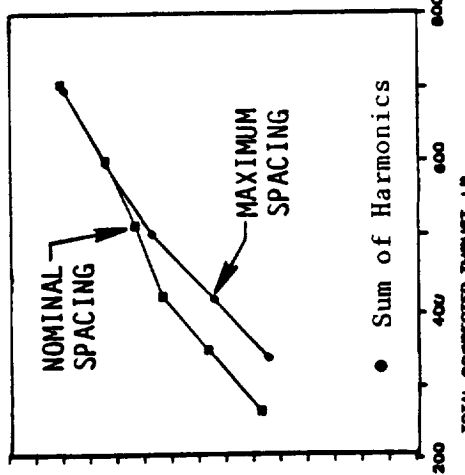
Figure 251. SPL Directivity of BPF and Higher Harmonics for F-7/A-7 (8+8; 37.9°/37.4°).



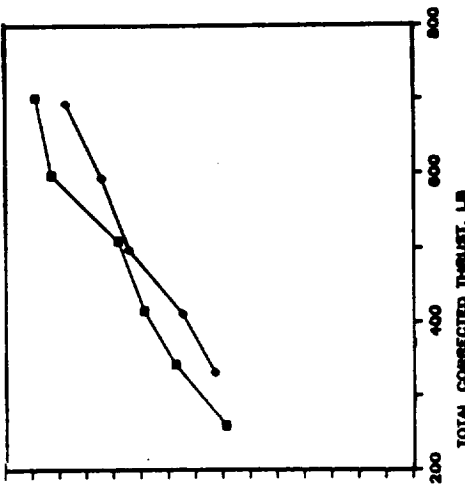
BPF AT EMISSION ANGLE, $\theta_e = 91^\circ$



EMISSION ANGLE, $\theta_e = 68^\circ$



EMISSION ANGLE, $\theta_e = 91^\circ$



EMISSION ANGLE, $\theta_e = 120^\circ$

Figure 252. Model-Scale Tone Sum Levels for F-7/A-7 (8+8) as a Function of Total Thrust.

● 3.05 M (10.0 FT) DIA; 0.25 M₀; 549 M (1800 FT) SIDELINE

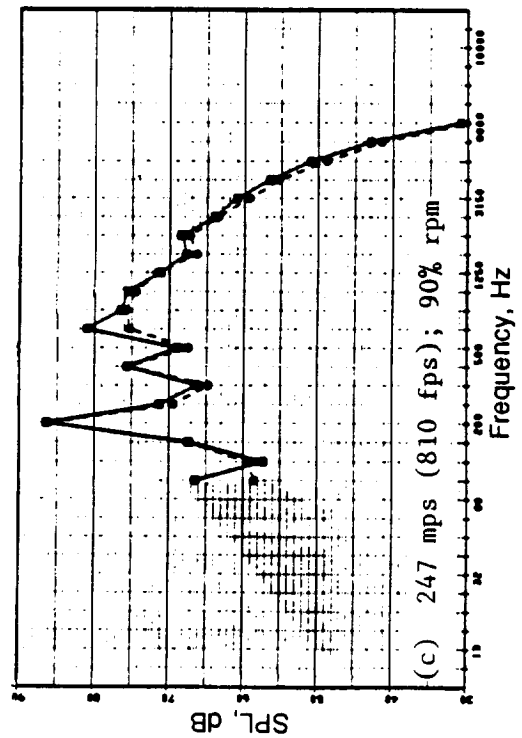
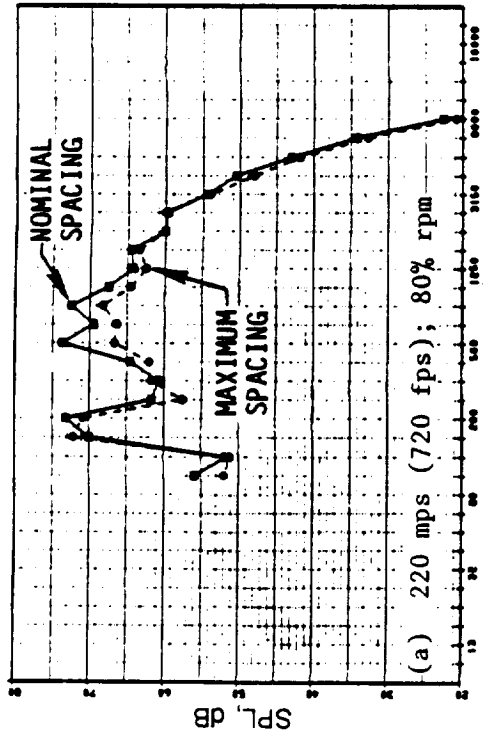
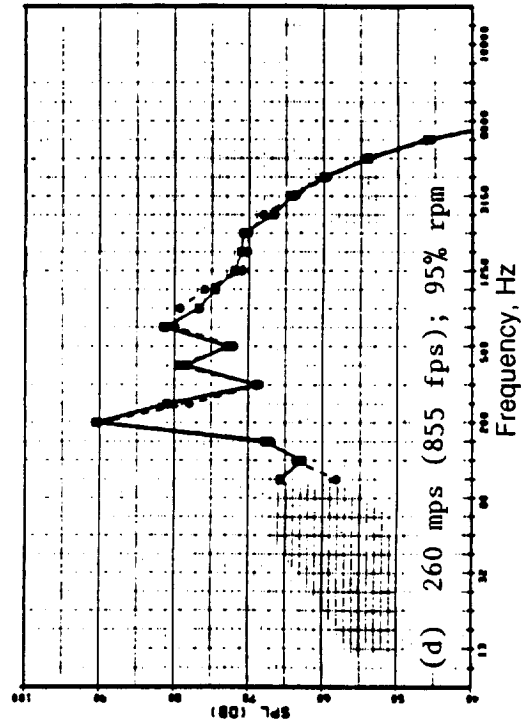
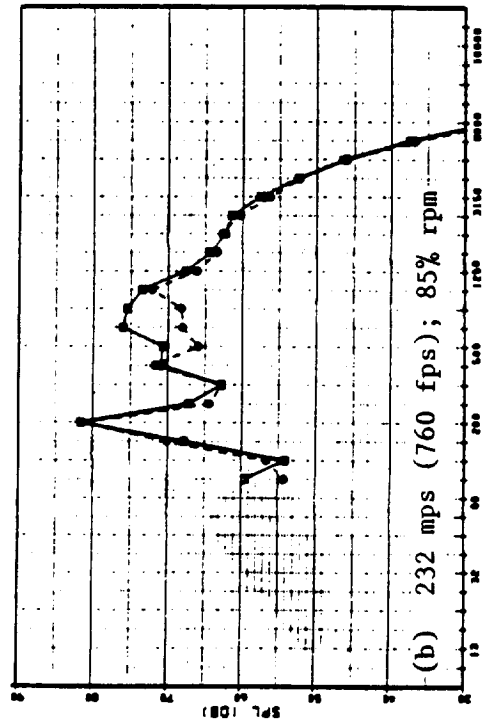


Figure 253. Comparison of Spectra of F-7/A-7 (8+8; 37.9°/37.4°) with Nominal and Maximum Rotor Spacings at Tip Speeds of 220, 232, 810, and 855 mps.

• 3.05 M (10.0 FT) DIA; 0.25 M₀; 549 M (1800 FT) SIDELINE

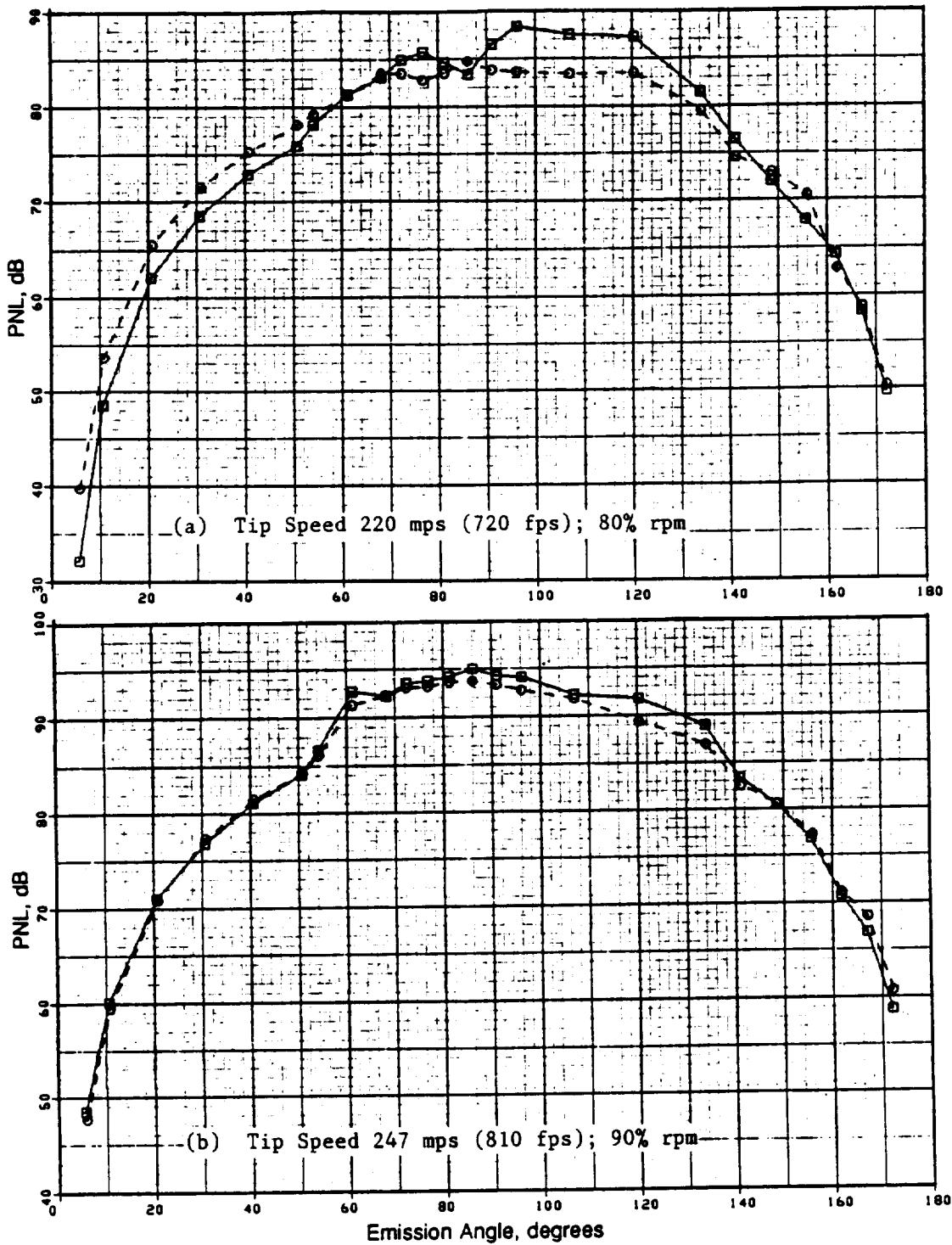


Figure 254. PNL Directivity Comparison of F-7/A-7 (8+8; 37.9°/37.4°) with Nominal and Maximum Rotor Spacings.

- Figure 255 depicts the maximum PNL and dBA data as a function of total thrust.

Also presented, as described below, are a limited number of acoustic data comparisons which were similarly measured with nominal and maximum rotor spacings with pitch angles of 43.3°/40°:

- Figure 256 demonstrates spectral data at tip speeds of 220 mps (720 fps) and 247 mps (810 fps)
- Figure 257 compares PNL and dBA directivities at tip speeds of 220 mps (720 fps) and 247 mps (810 fps)
- Figure 258 presents the maximum PNL and dBA data as a function of total thrust.

A closer examination of narrow-band and scaled 1/3-octave band spectral data reveals no change in SPL's at the BPF and 2xBPF over a range of angles ($60 < \theta_e < 120$); this indicates, as expected, that the rotor spacing has no effect on the steady-loading noise component. At both test pitch angles, significant SPL reductions are noted at the third harmonic over a range of angles; however, smaller reductions are noted in SPL's of some of the harmonics higher than the third. Since tip vortices are known to decay at a much slower rate, relative to blade wakes with increase in downstream distance, the observed SPL reductions are attributed to the increased decay of the front blade wakes with increase in rotor spacing. This benefit of increased spacing decreases with a corresponding increase in thrust.

The open pitch angle of the F-7/A-7 (8+8) was selected to give the same thrust as the Series 1 nominal pitch configuration, but at a 10% reduced tip speed. A comparison of the 91° spectra at a tip speed of 220 mps of the open pitch blades (View A of Figure 256) with the corresponding data tip speed of 947 mps (90% rpm) of the nominal pitch blades (Figure 253, View C) verifies this benefit, particularly at BPF, due to the decreased tip speed at a given thrust. Due to reduced BPF levels, SPL reductions at the third harmonic as a result of increased spacing have a greater impact on the total noise (PNL and dBA) of Figure 258, relative to that of Figure 255. Figure 258 indicates an approximate 1 dB to 2 dB reduction in peak PNL and dBA.

7.1.1.4.2 F-7/A-7 (9+8) at Nominal Pitch: Series 2

The F-7/A-7 design with 9+8 (9 forward and 8 aft) blades was tested at a nominal pitch angle of 38.4°/37.4°; because this pitch setting is almost equal to that used for the nominal pitch setting of the F-7/A-7 (8+8) configuration, Figure 249 (View A) can be used to determine the impact of spacing increase at various radii for this test series. Selected acoustic data measured at the two rotor spacings are compared as follows:

- Figure 259 provides model-scale narrow-band data at microphone locations of 67°, 92°, and 107° and at a tip speed of 247 mps (810 fps)
- Figure 260 plots the directivity of model-scale steady-loading and rotor-to-rotor interaction noise at a tip speed of 247 mps (810 fps)
- Figure 261 is similar to the data presented in Figure 260, but was measured at a tip speed of 220 mps (720 fps)
- Figure 262 compares the model-scale steady-loading and rotor-to-rotor interaction noises, as a function of total thrust

• F7A7; 8x8; 37.9°/37.4°
 3.05 M(10.0 FT) DIA; 0.25 M₀; 549 M(1800 FT) SIDELINE

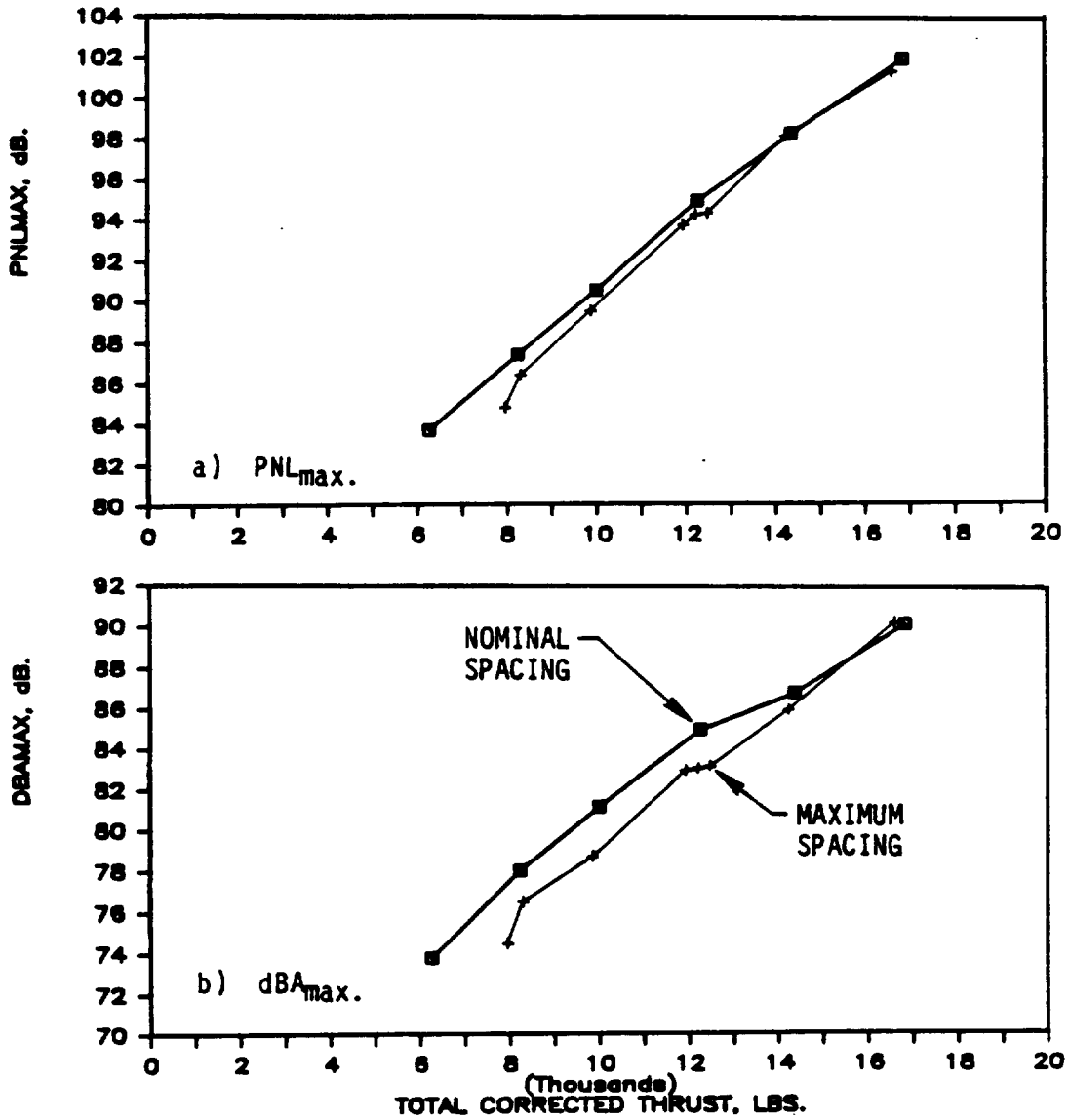
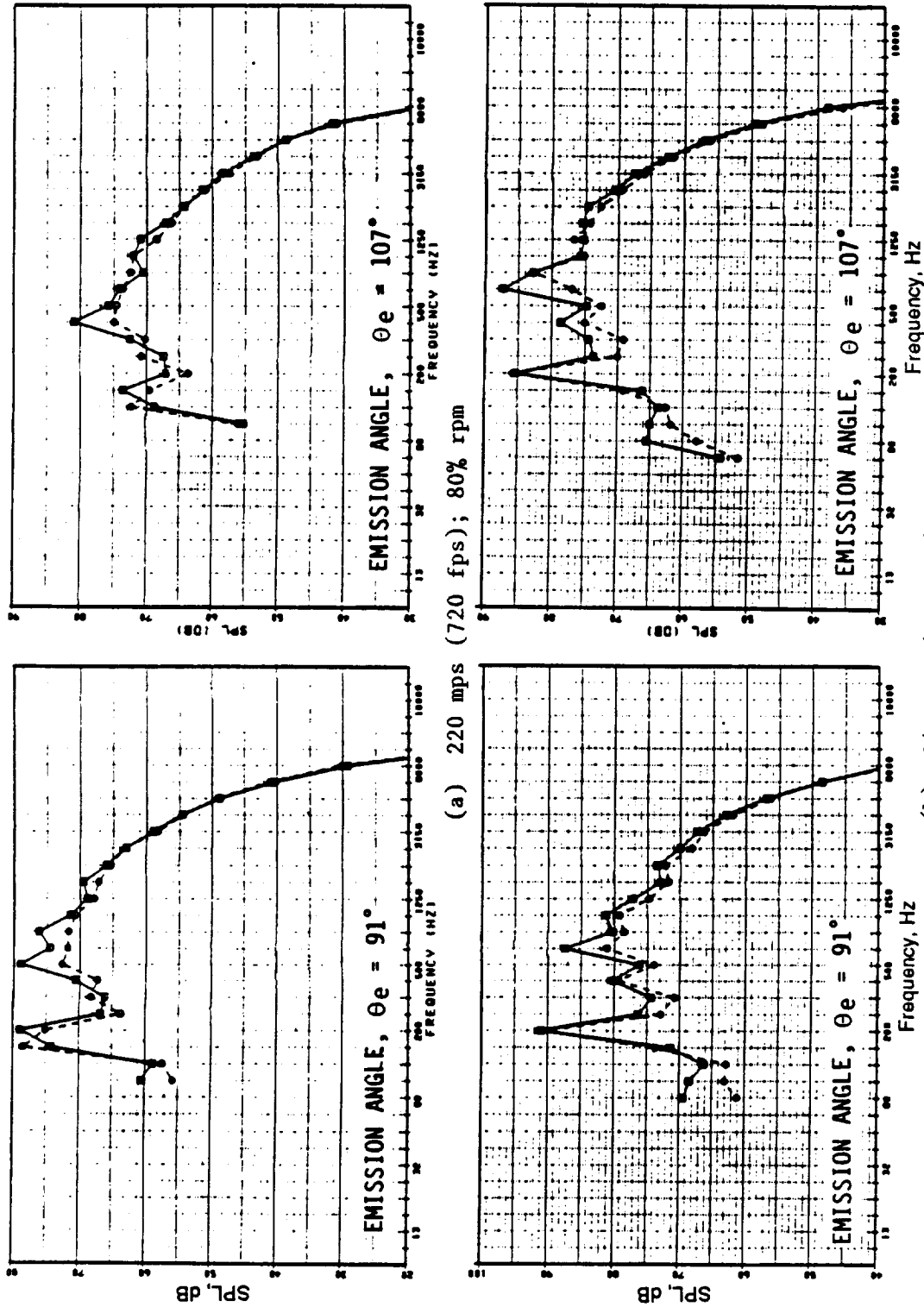


Figure 255. Effect of Rotor-to-Rotor Spacing on the Maximum PNL and DBA of F-7/A-7.

• 3.05 M (10.0 FT) DIA; 0.25 M₀; 549 M (1800 FT) SIDELINE

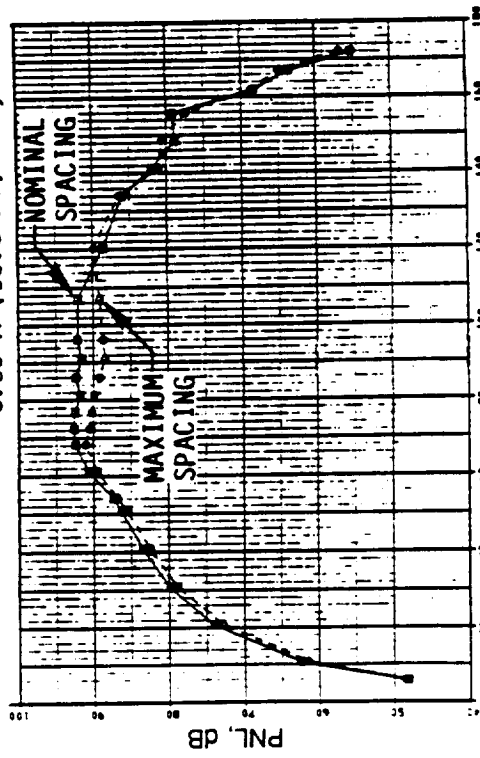


(a) 220 mps (720 fps); 80% rpm

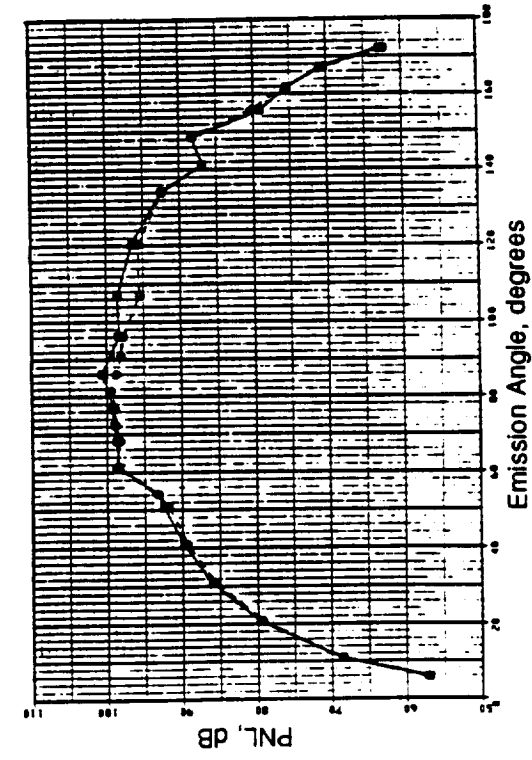
(b) 247 mps (810 fps); 90% rpm

Figure 256. Spectral Comparison of F-7/A-7 (8+8, 43.3°/40.4°) with Nominal and Maximum Rotor Spacings.

● 3.05 M (10.0 FT) DIA; 0.25 Mo:549 M (1800 FT) SIDELINE



a) 220 MPS (720 FPS); 80% RPM



b) 247 MPS (810 FPS); 90% RPM

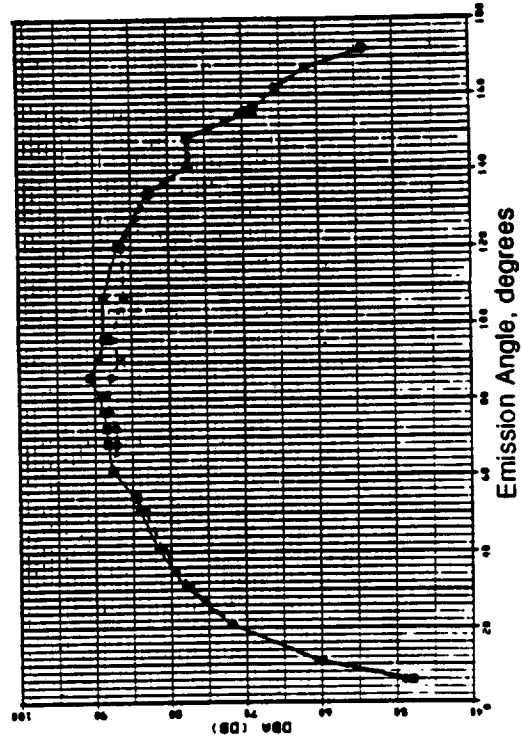
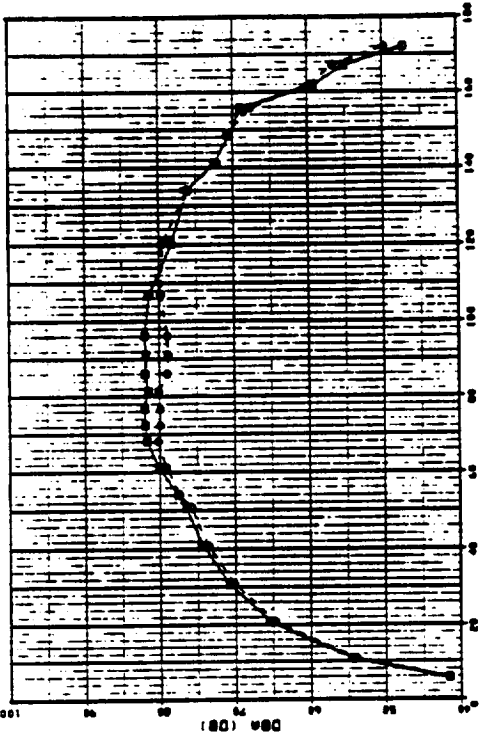


Figure 257. PNL and dBA Directivity Comparisons of F-7/A-7 (8+8; 43.3°/40.4°).

- F7A7; 8x8; 43.3°/40.4°
- 3.05 M (10.0 FT) DIA; 0.25 M₀; 549 (1800 FT) SIDELINE

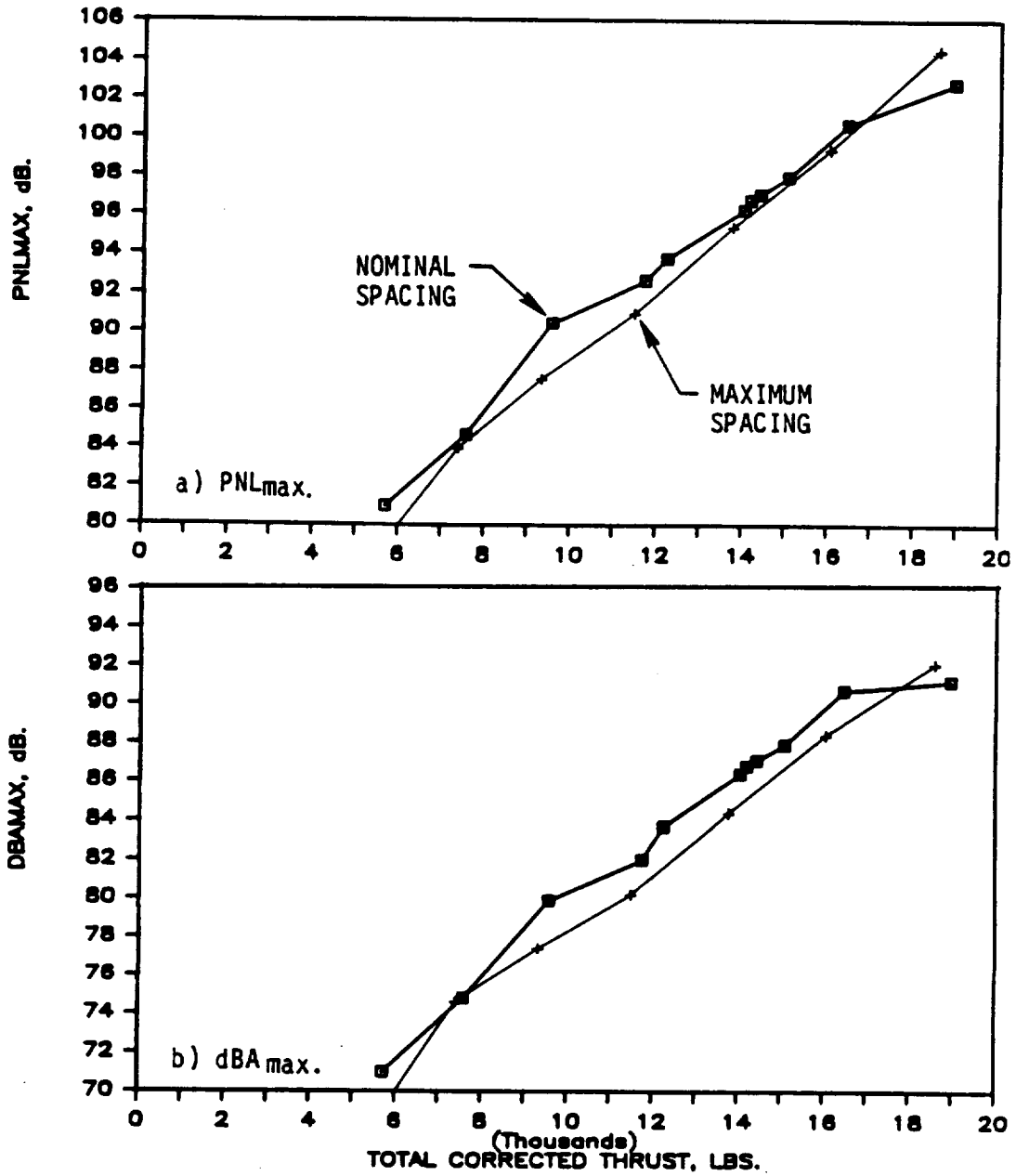


Figure 258. F-7/A-7 Effect of Spacing on the Maximum PNL and dBA.

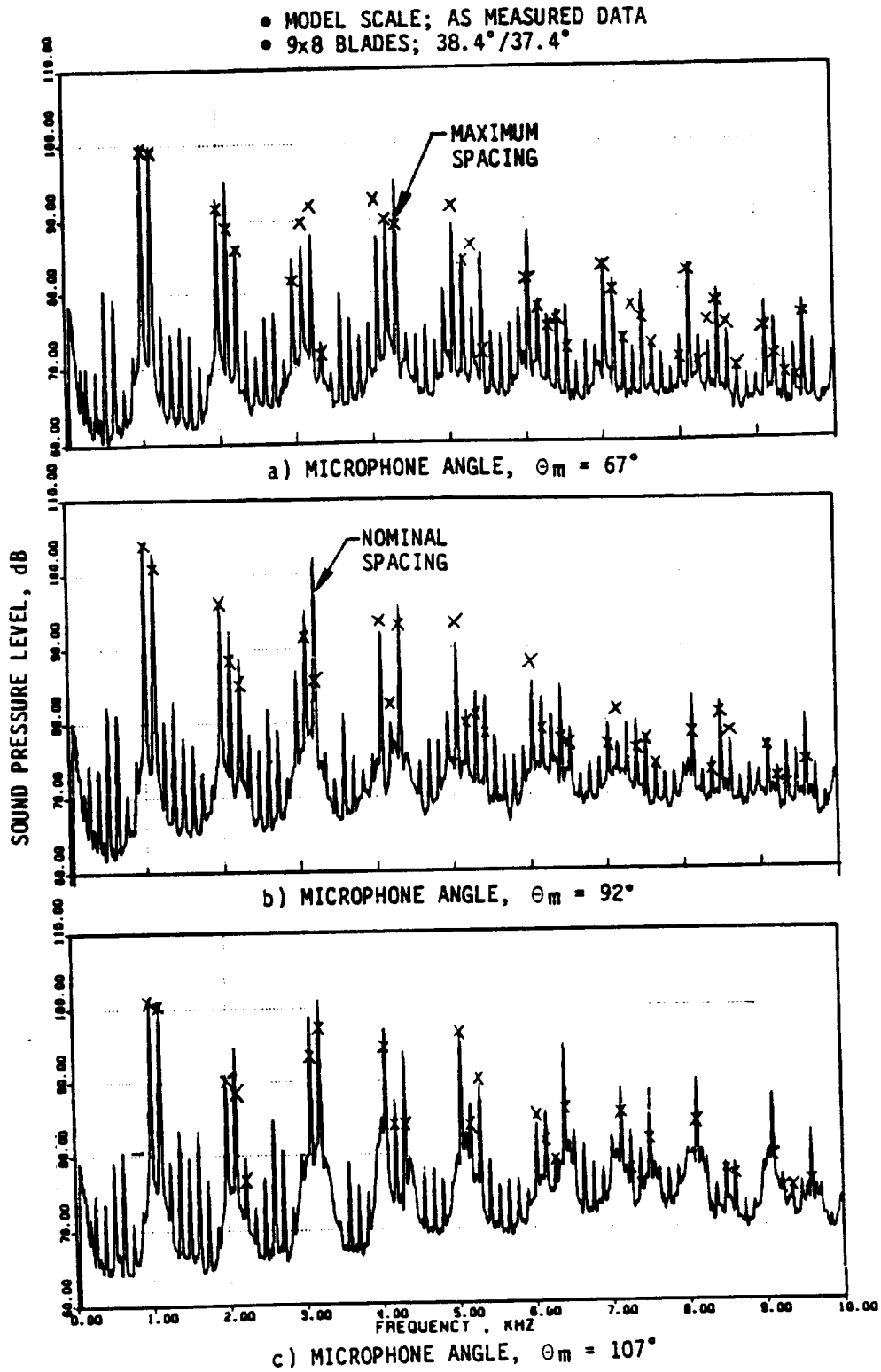


Figure 259. Typical Narrow-Band Data Comparison of the F-7/A-7 at Nominal and Maximum Rotor Spacings and at a Tip Speed of 247 mps (810 fps).

- MODEL SCALE; 0.25 M_0 ; 8.2 M (27.0 FT) SIDELINE
- MODEL THRUST = 2400 N (540 LB); Tip Speed = 247 MPS (810 FPS)
- 12.5 HZ NARROWBAND DATA

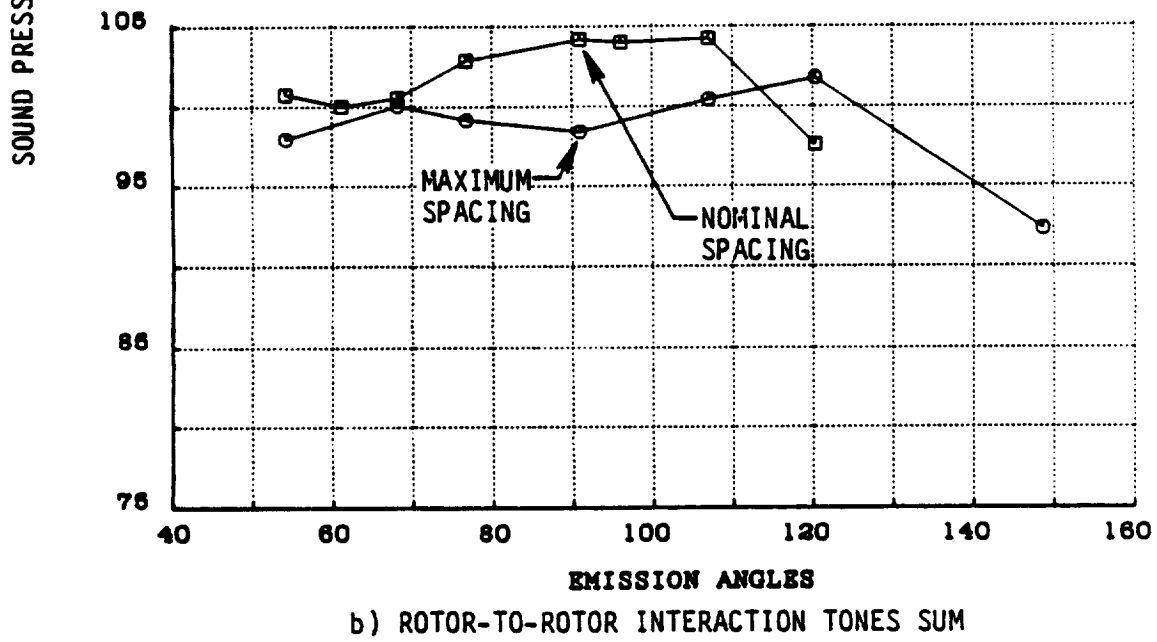
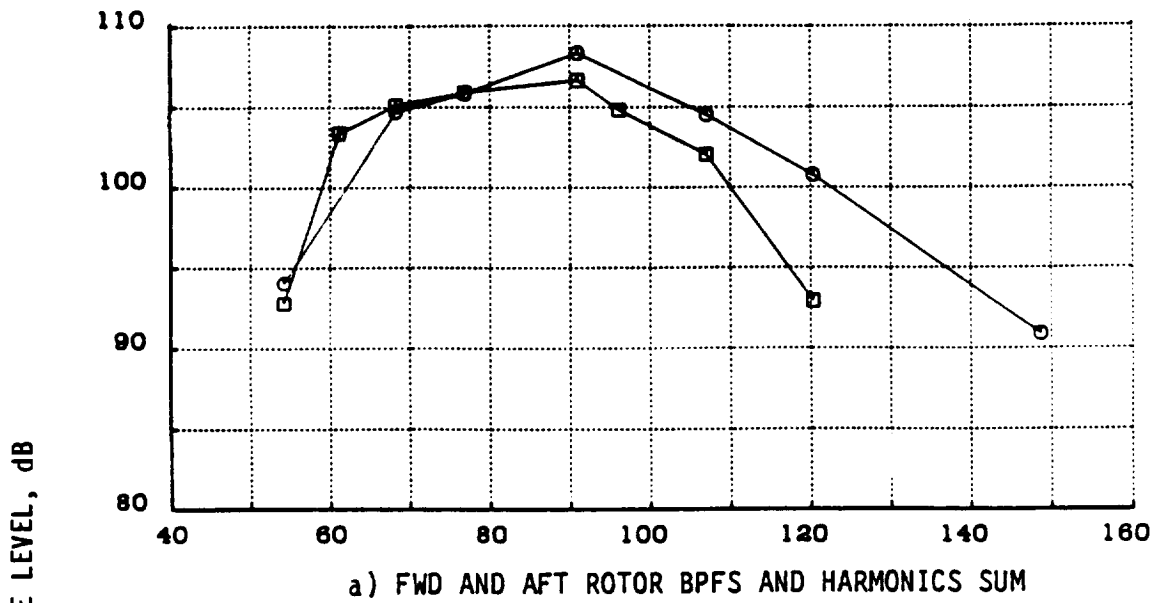


Figure 260. Directivity of Steady-Loading and Rotor-to-Rotor Interaction Noise for F-7/A-7 (9+8; 38.4°/37.4°).

- MODEL SCALE; 0.25 M_0 ; 8.2 M (27.0 FT) SIDELINE
- MODEL THRUST = 1550 N (350 LB); TIP SPEED 222 MPS (720 FPS)
- 12.5 HZ NARROWBAND DATA

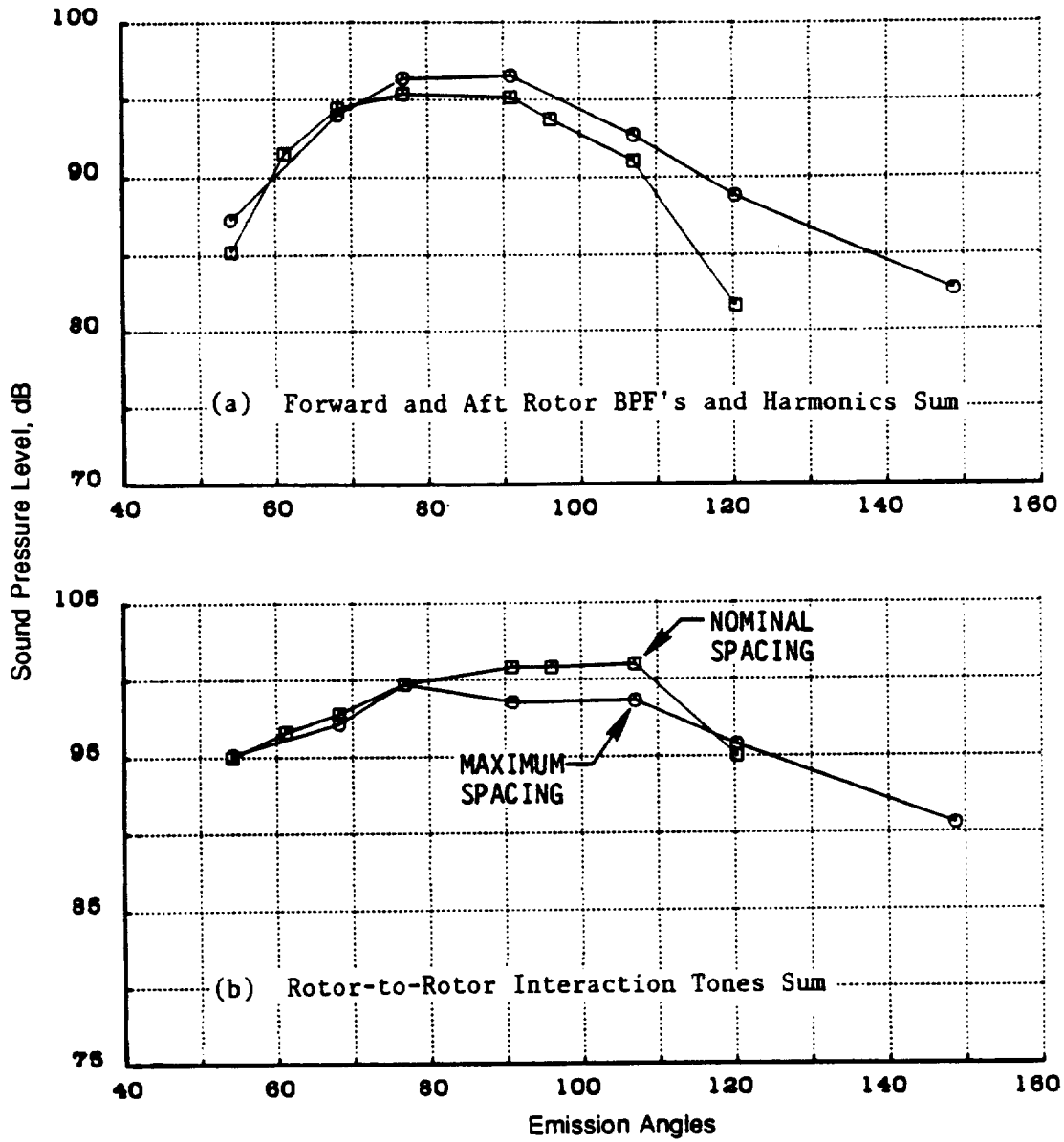
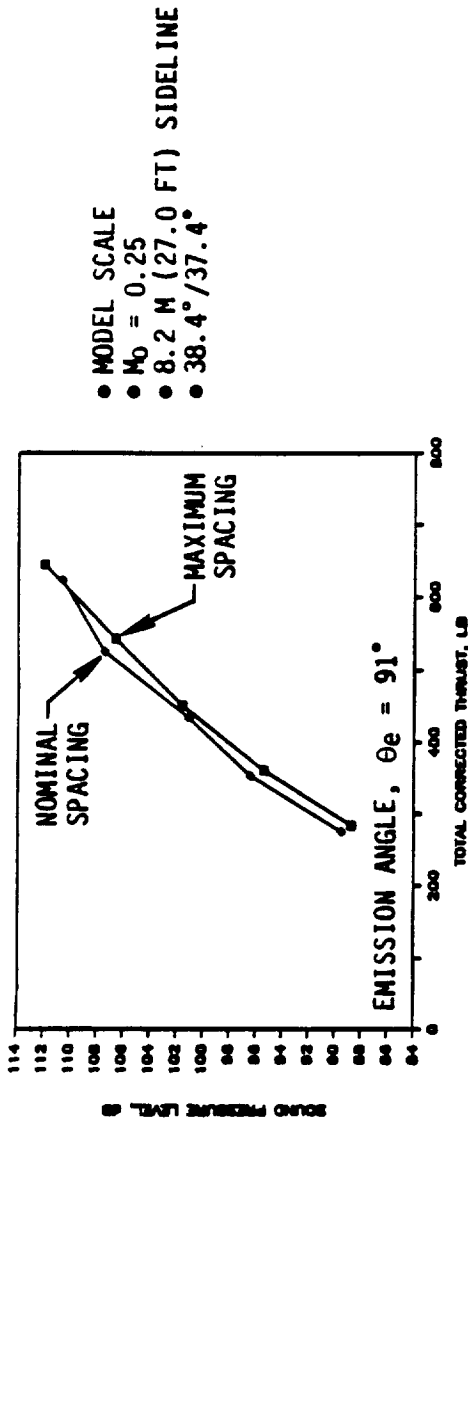
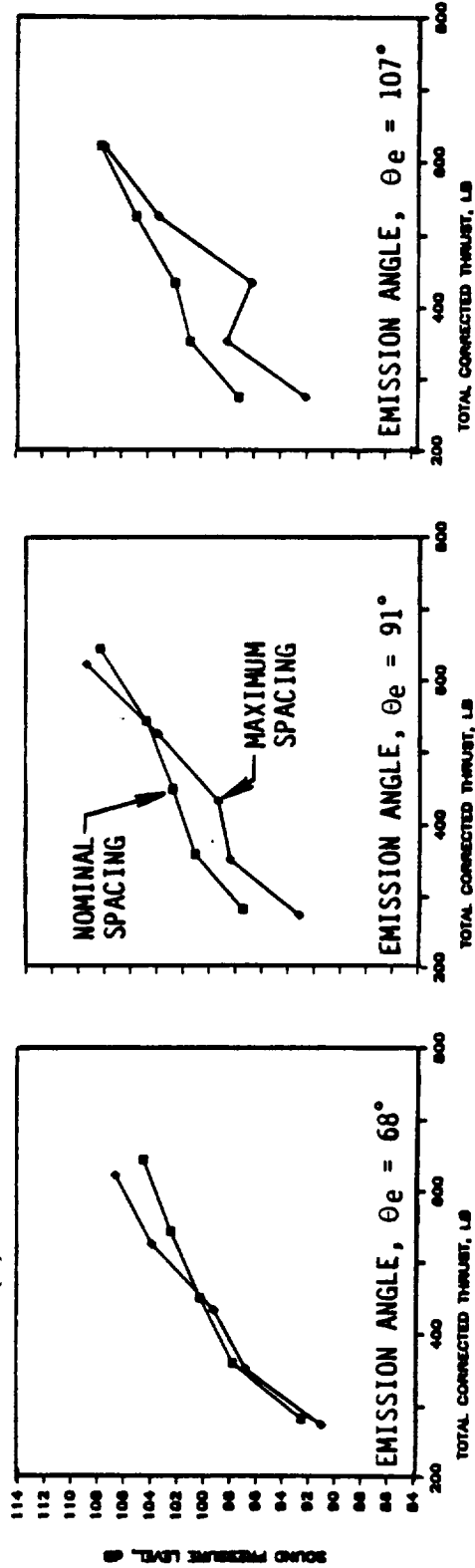


Figure 261. Directivity of Steady-Loading and Rotor-to-Rotor Interaction Noise for F-7/A-7 (9+8; 38.4°/37.4°).



(a) Forward and Aft Rotor BPF's and Harmonics Sum



(b) Rotor-to-Rotor Interaction Tones Sum

Figure 262. Model-Scale Tone Sum Levels of F-7/A-7 (9+8) as a Function of Total Thrust.

- Figure 263 shows scaled spectral data at flight emission angles of 61°, 91°, 108°, and 120° at a tip speed of 247 mps (810 fps)
- Figure 264 illustrates PNL and dBA directivities at a tip speed of 247 mps (810 fps)
- Figure 265 compares the maximum PNL and dBA data, as a function of total thrust.

As with the results of the F-7/A-7 8+8, test data for the 9+8 indicate no change in the SPL's at BPF and 2xBPF, nor in the total steady-loading noise component with change in spacing. The significant impact of spacing is the reduced A+2F tone level of the third harmonic.

Figure 259, for example, indicates a reduction of up to 15 dB in the A+2F tone level for increasing the spacing from nominal to maximum. Accordingly, the 1/3-octave-band spectral data presented in Figure 263 further indicates a reduction of 1/3-octave band with the third harmonic to extend over a range of angles in the plane-of-rotation and in the aft quadrant. A reduction in SPL's associated with the second harmonic are noted due to reductions in the first interaction (A+F) tone levels; smaller reductions are noted (mostly in the aft quadrant) at some of the higher frequency interaction tones. Because the tip vortices are known to decay at a much slower rate, with distance relative to blade wakes; the reduction noted for interaction tones is attributed mainly to the increased decay of forward blade wakes before they interact with the aft rotor blades.

Reductions in PNL and dBA are in the range of 1 dB to 3 dB over most of the thrust range; and for a given thrust, the spacing benefit is 1 dB to 2 dB over most of the angles. Like the F-7/A-7 with 8+8 blades at nominal pitch, significant SPL reductions noted in rotor-to-rotor interaction noise components are not fully reflected in total maximum noise levels because the SPL's at BPF are greater than those at 3xBPF over most of the peak noise angles.

7.1.1.4.3 F-7/A-7c (9+8) at Nominal Pitch: Series 3

The aft blades of the model-scale F-7/A-7 measure 17.8 cm (7 in.) from the hub to tip of the blade. The aft blades were clipped at 75% of their span to achieve the clipped aft blades (F-7/A-7c) utilized in this series of tests. Figure 266 (View A) compares the difference between the unclipped and clipped aft blades.

To compensate for the loss in thrust at a given rpm due to clipping, the aft blade was set at a more open pitch angle than that used in Series 2. The impact of the spacing increase at various radii for this clipped configuration at the set pitch angle of 36.3°/42.7° is demonstrated in View B of Figure 266. Comparing this with the unclipped spacing increase data (Figure 249, View A) reveals very similar increases in the normalized value of the axial distance between the trailing edge of a forward blade and quarter-chord point of the aft blade over the remaining span of the clipped configuration.

Selected acoustic data measured at the nominal and maximum spacings are compared as follows:

- Figure 267 presents model-scale narrow-band data at microphone locations of 67°, 92°, and 118° and at a tip speed of 247 mps (810 fps)
- Figure 268 plots the directivity of model-scale steady-loading and rotor-to-rotor interaction noise at a tip speed of 247 mps (820 fps)
- Figure 269 contains data similar to that of Figure 268, but at the tip speed of 220 mps (720 fps)

• 3.05 M (10.0 FT) DIA; 0.25 M₀; 549 M (1800 FT) SIDELINE

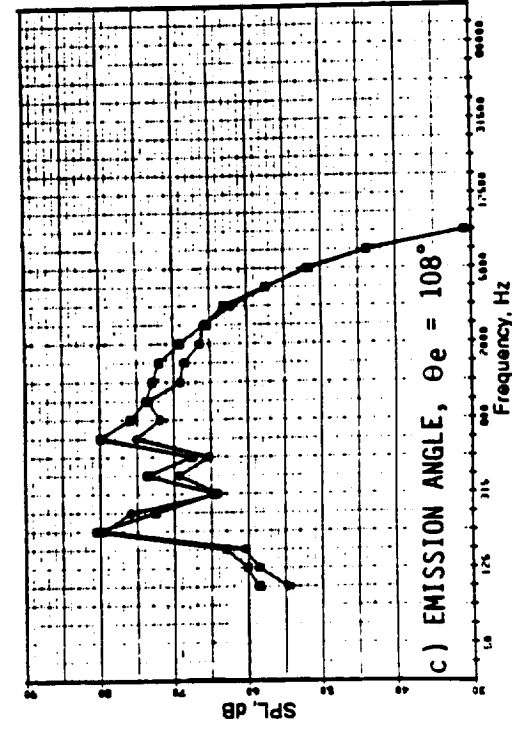
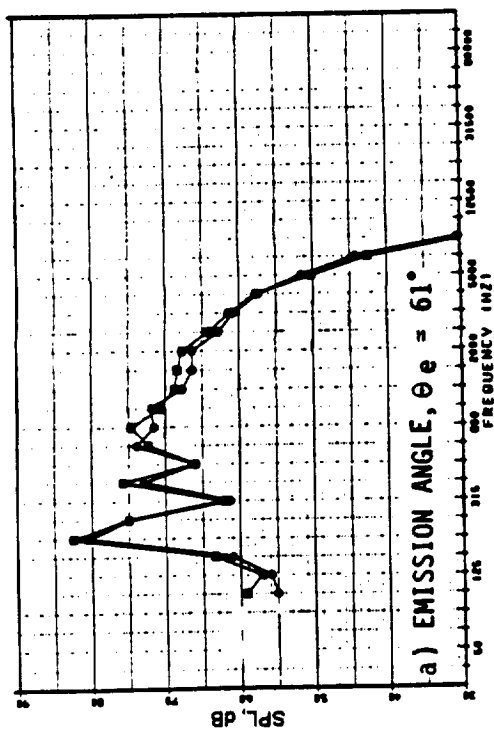
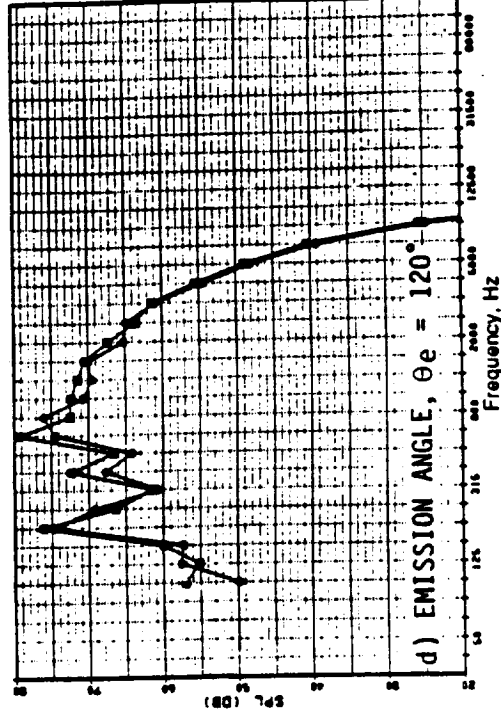
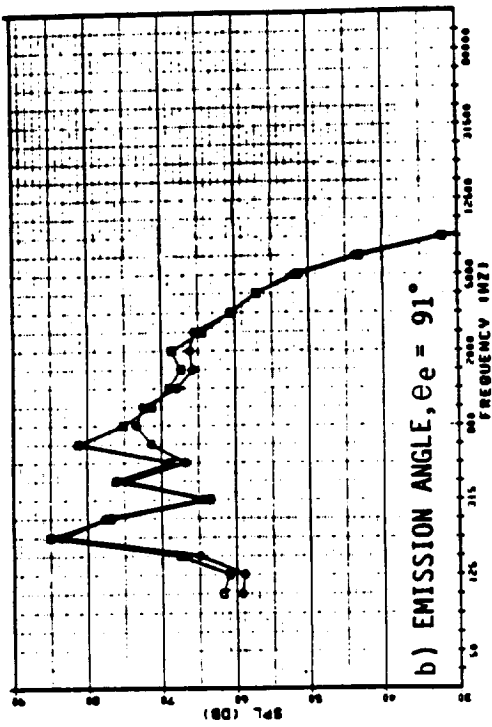


Figure 263. Comparison of Spectra of F-7/A-7 (9+8; 38.4°/37.4°) with Nominal and Maximum Rotor Spacings at Tip Speeds of 247 mps (810 fps).

• 3.05 M (10.0 FT) DIA; 0.25 M_0 ; 549 M (1800 FT) SIDELINE

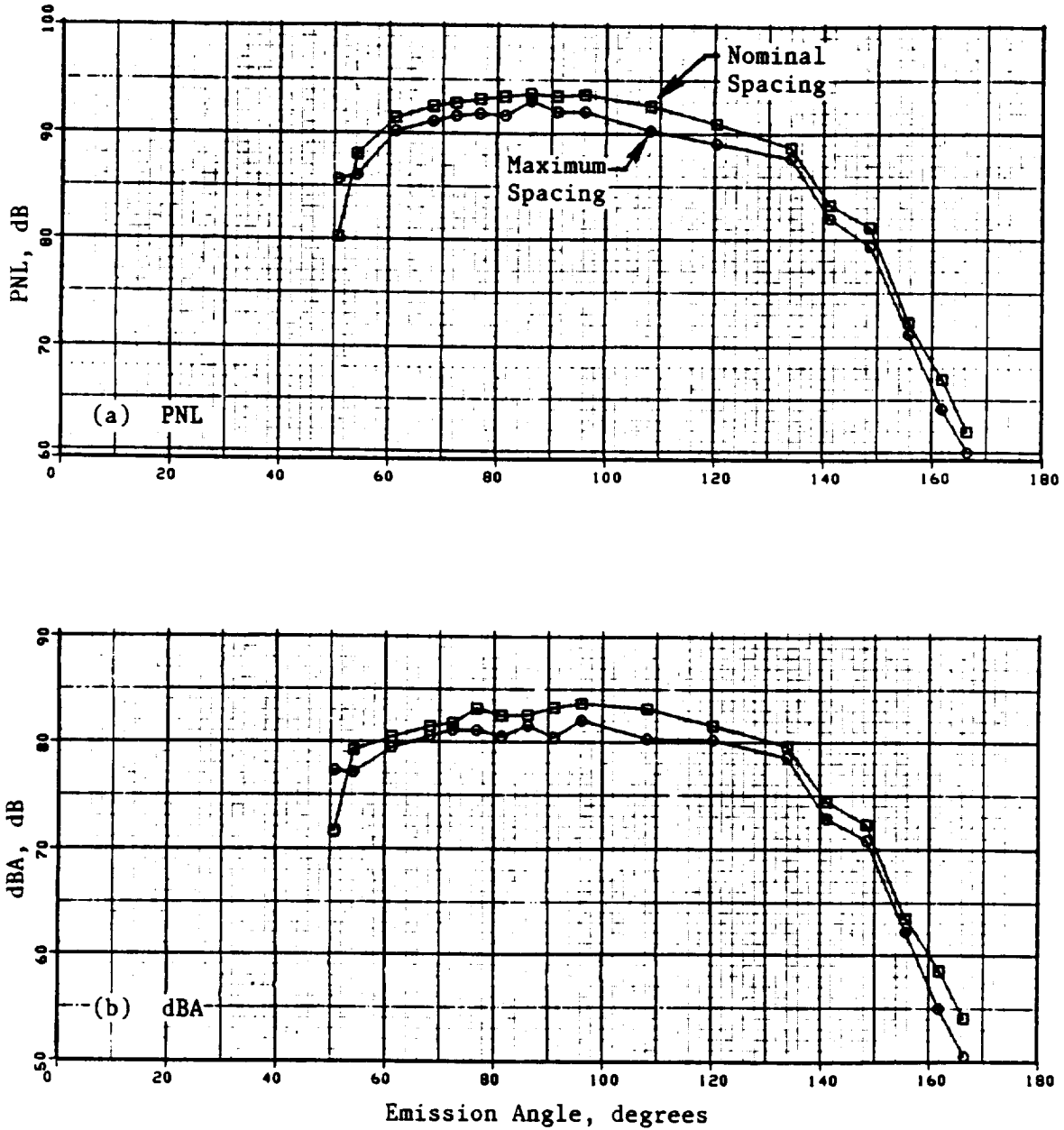


Figure 264. A PNL and dBA Directivity Comparison of the F-7/A-7 (9+8; 38.4/37.4°) at Tip Speed of 247 mps (810 fps).

• F7A7; 9x8; 38.4°/37.4°
 • 3.05 M (10.0 FT) DIA; 0.25 M₀; 549 M (1800 FT) SIDELINE

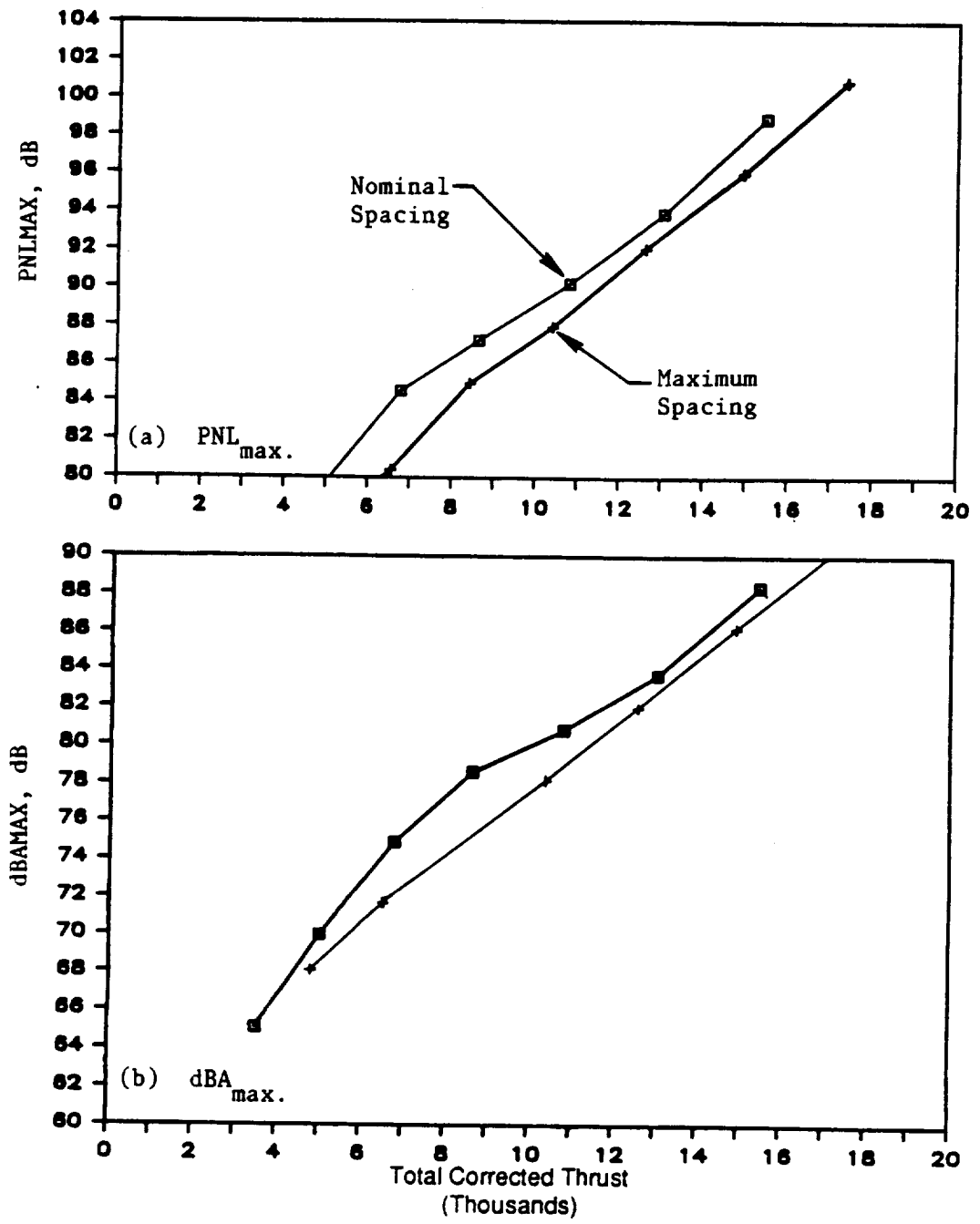
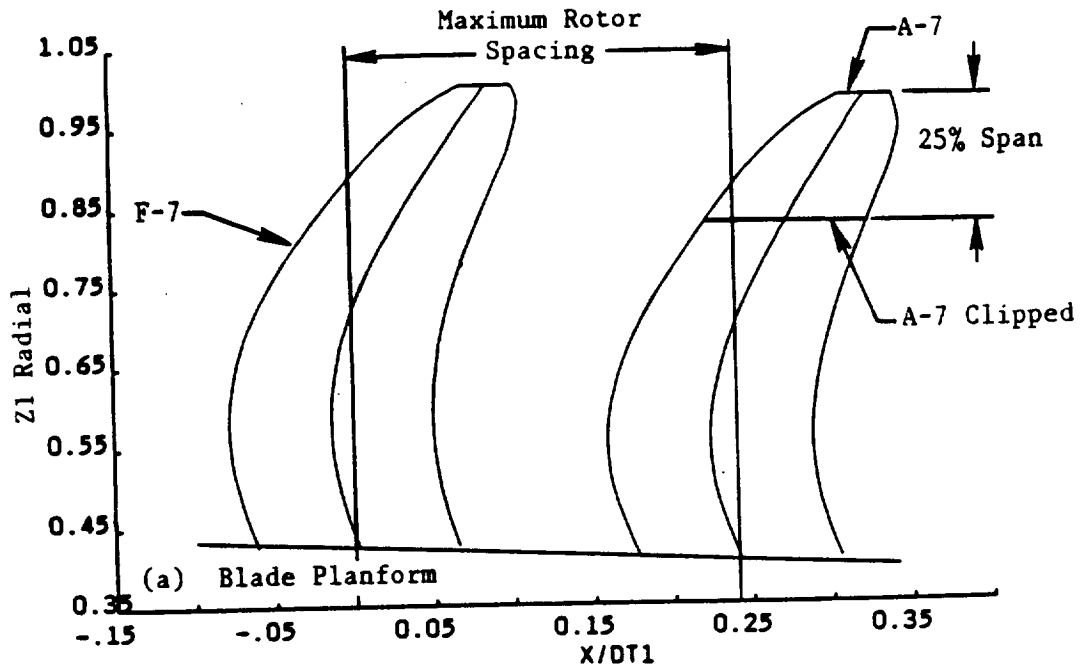


Figure 265. Effect of Rotor-to-Rotor Spacing on the Maximum PNL and dBA of the F-7/A-7.



$$\frac{\left(\text{AXIAL DISTANCE BETWEEN TRAILING EDGE OF FWD. TO QUARTER CHORD OF AFT ROTOR} \right)}{\left(\text{AXIAL CHORD OF FWD. ROTOR} \right)}$$

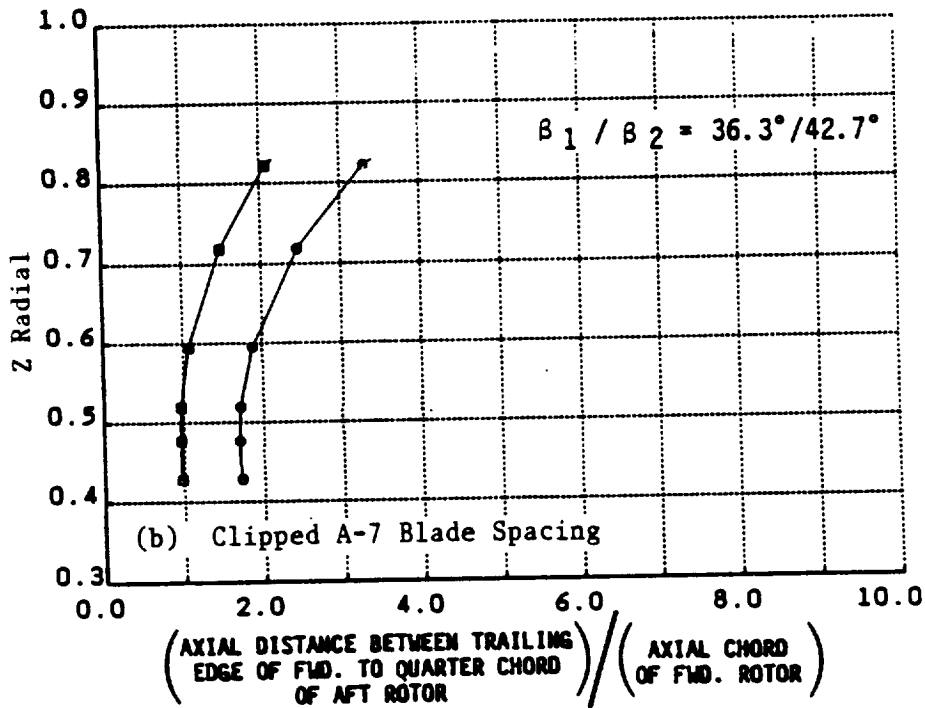


Figure 266. Schematic Comparison of Planform and Blade Spacing of F-7/A-7 with Clipped Aft Blade.

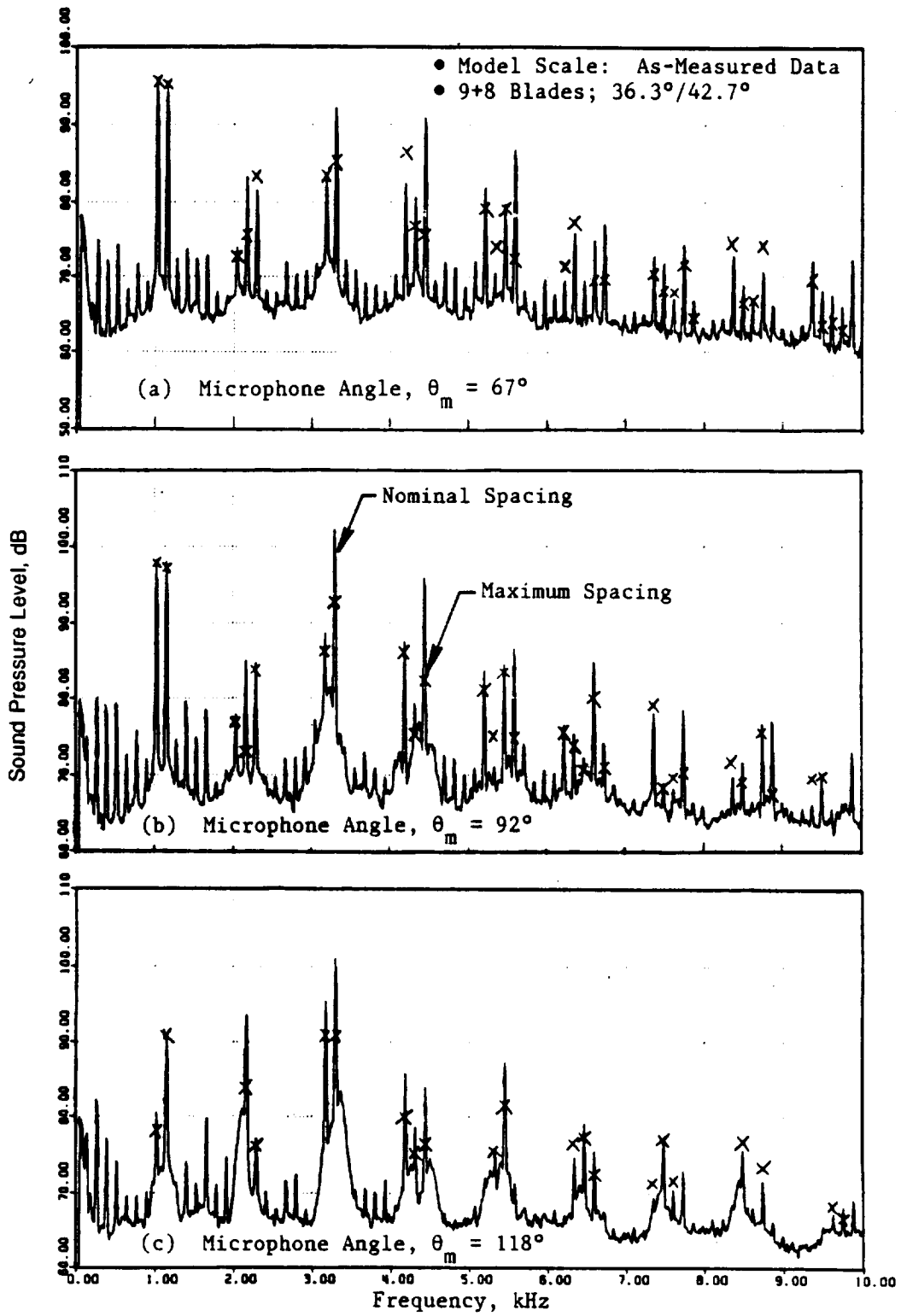


Figure 267. Typical Narrow-Band Data Comparison of F-7/A-7 (Clipped) at Tip Speed of 247 mps (810 fps).

- MODEL SCALE; 0.25 M_0 ; 8.2 M (27 FT) SIDELINE
- MODEL THRUST = 2000 N (450 LB); TIP SPEED = 247 MPS (820 FPS)
- 12.5 Hz NARROWBAND DATA

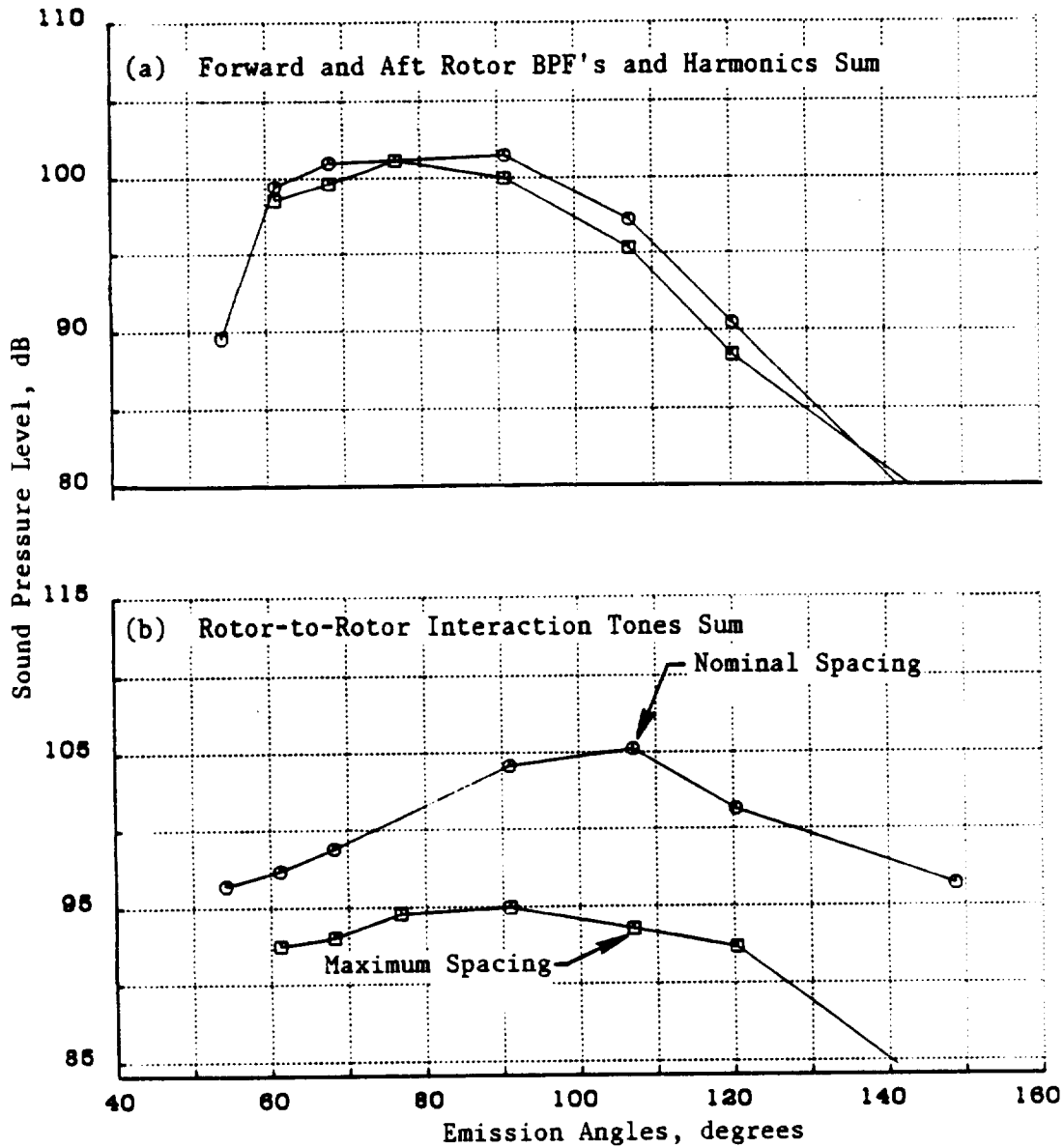


Figure 268. Directivity of Steady-Loading and Rotor-to-Rotor Interaction Noise for F-7/A-7c (9+8; 36.3°/42.7°).

- MODEL SCALE; 0.25 M_0 ; 8.2 M (27.0 FT) SIDELINE
- MODEL THRUST = 1375 N (310 LB); TIP SPEED = 220 MPS (720 FPS)
- 12.5 Hz NARROWBAND DATA

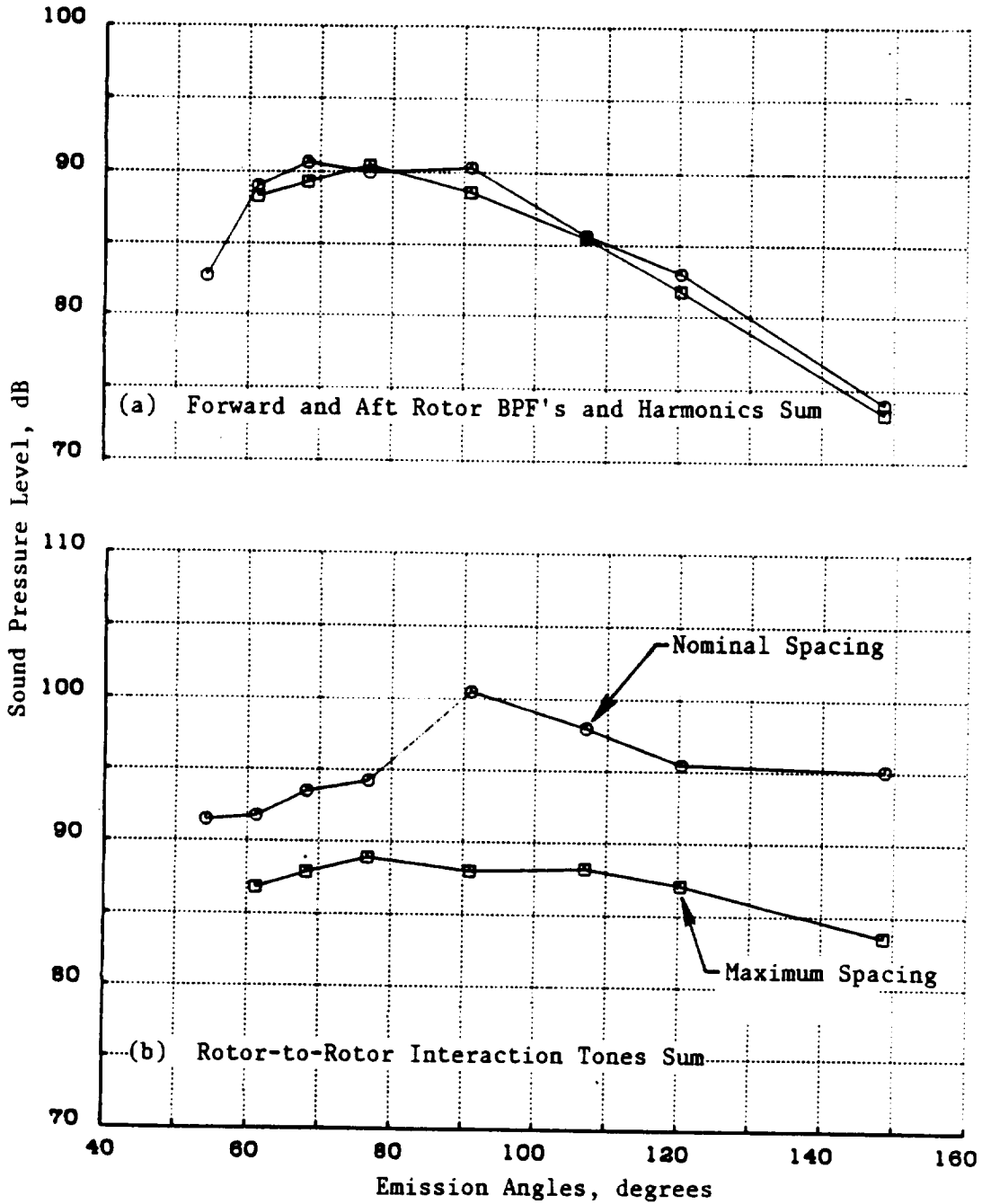


Figure 269. Directivity of Steady-Loading and Rotor-to-Rotor Interaction Noise for F-7/A-7c (9+8; 36.3°/42.7°).

- Figure 270 compares the model-scale steady-loading and rotor-to-rotor interaction noises as a function of total thrust
- Figure 271 shows scaled spectral data at flight emission angles of 61°, 91°, 120°, and 134° at a tip speed of 247 mps (810 fps)
- Figure 272 depicts the PNL and dBA directivities at a tip speed of 247 mps (810 fps)
- Figure 273 presents maximum PNL and dBA data, as a function of total thrust.

As with the unclipped F-7/A-7 configurations of this study, no effect of spacing is observed on the steady-loading noise components. This is substantiated by the absence of change in the SPL's at BPF and 2xBPF, as evidenced in Figures 267 and 271, and by a lack of any significant change in the steady-loading sums (Figures 268 through 270). However, significant reductions to the sound pressure levels are noted, not unlike the Series 2 unclipped blades, over all of the measured angles at the third harmonic and, in particular, in the level of the A+2F tone.

Unlike unclipped blades, however, reductions of 5 dB to 10 dB are noted in some interaction tones of the fourth and fifth harmonics in the levels of A+3F and A+4F tones. Reduced SPL's associated with the second harmonic are noted, due to the significantly reduced levels of A+F tone; smaller reductions also are noted in some higher frequency tones beyond the fifth harmonic. The combined effect of individual tone reductions in total rotor-to-rotor interaction noise is illustrated in Figures 268 through 270; wherein these reductions are noted as significantly higher than those previously measured (Figures 260 through 262) for the unclipped blades.

For this clipped configuration (F-7/A-7c), it can be assumed that the tip vortices of the forward rotor do not interact with the clipped aft blades and, hence, produce no unsteady vortex/rotor interaction tones for the test rotor spacings. A consequence of this assumption is that the significant reductions previously noted in the sound pressure levels of the interaction tones are due to increased decay of the forward blades wakes with increased rotor spacing. This reduction in interaction tone levels due to spacing was not fully evident in the earlier unclipped configurations of this study, because their levels were masked by the interaction noise as a result of the tip vortex interacting with the aft rotor blades.

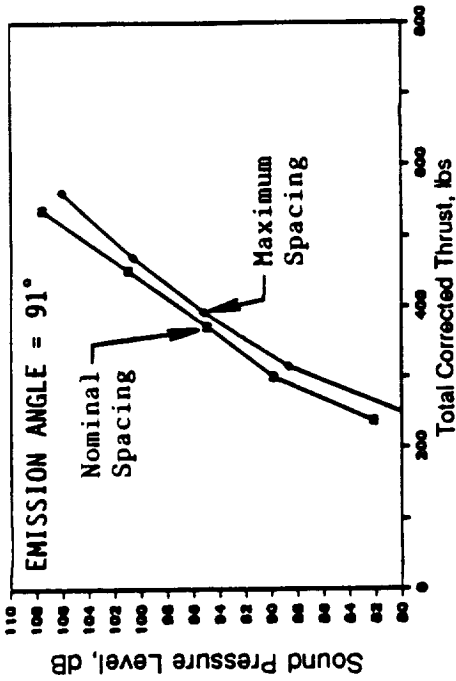
Maximum PNL and dBA reductions in a range of 3 dB to 8 dB were noted over most of the thrust conditions; also for a given thrust, significantly greater reduction is noticed, relative to unclipped configuration, over aft quadrant angles greater than 100°.

7.1.1.4.4 F-11/A-11 (11+9) at Open Pitch: Series 4

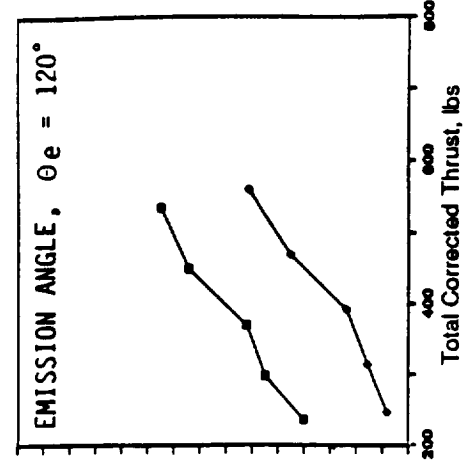
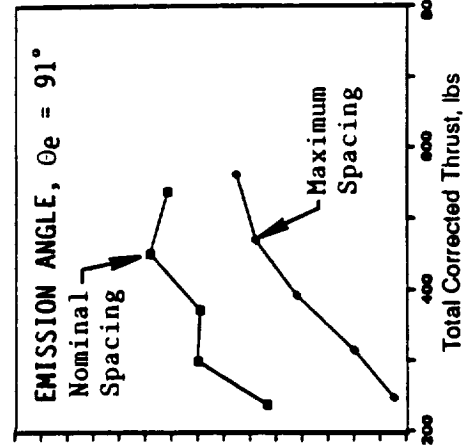
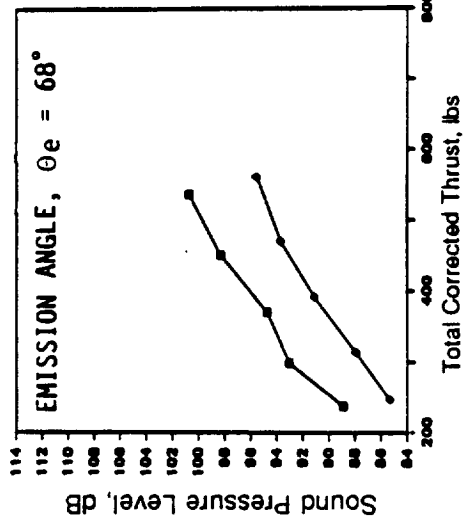
The F-11/A-11 blade configuration 11+9 (with 11 forward and 9 aft blades) was tested at two open pitch angles of 44.8°/43.3° at both maximum and supermaximum rotor-to-rotor spacings. Figure 274 shows, for these test conditions, the impact of the increased rotor-to-rotor spacing in terms of the normalized axial distance between the trailing edge of the forward blade and the quarter-chord point of the aft blade. Since data obtained during one of the test runs with pitch angles of 44.8°/43.3° are questionable, due to a telemetry problem, selected acoustic data measured for the pitch-angle setting of 48.7°/45.3° are provided as follows:

- Figure 275 shows model-scale narrow-band data at the microphone location of 97° and for tip speeds of 220 mps (720 fps) and 192 mps (630 fps)

- MODEL SCALE
- $M_0 = 0.25$
- 8.2 M (27 FT) SIDELINE
- $36.3^\circ/42.7^\circ$



a) FWD AND AFT ROTOR BPF AND HARMONICS



b) ROTOR TO ROTOR INTERACTION TONES SUM

Figure 270. Model-Scale Tone Sum Levels of F-7/A-7c (9+8) as a Function of Total Thrust.

- F7A7 (CLIPPED); 9x8; 36.3°/42.7°
- 3.05 M (10. FT) DIA; 0.25 M₀; 549 M (1800 FT) SIDELINE

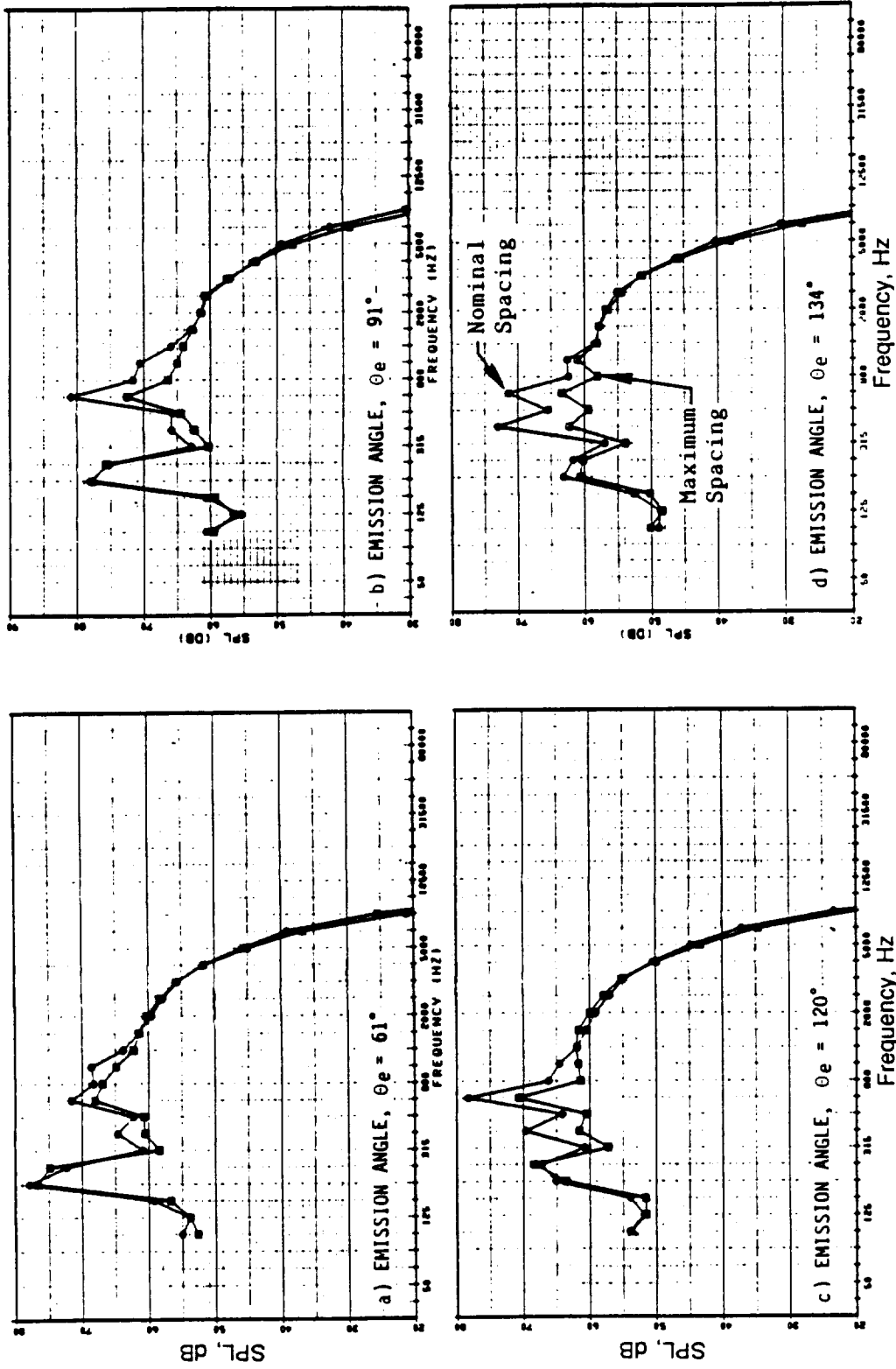


Figure 271. A Comparison of Spectra of the F-7/A-7c at Tip Speed of 247 mps (810 fps).

• F7A7; 9x8; 36.3°/42.7°
 • 3.05 M (10.0 FT) DIA; 0.25 M₀; 549 M (1800 FT) SIDELINE

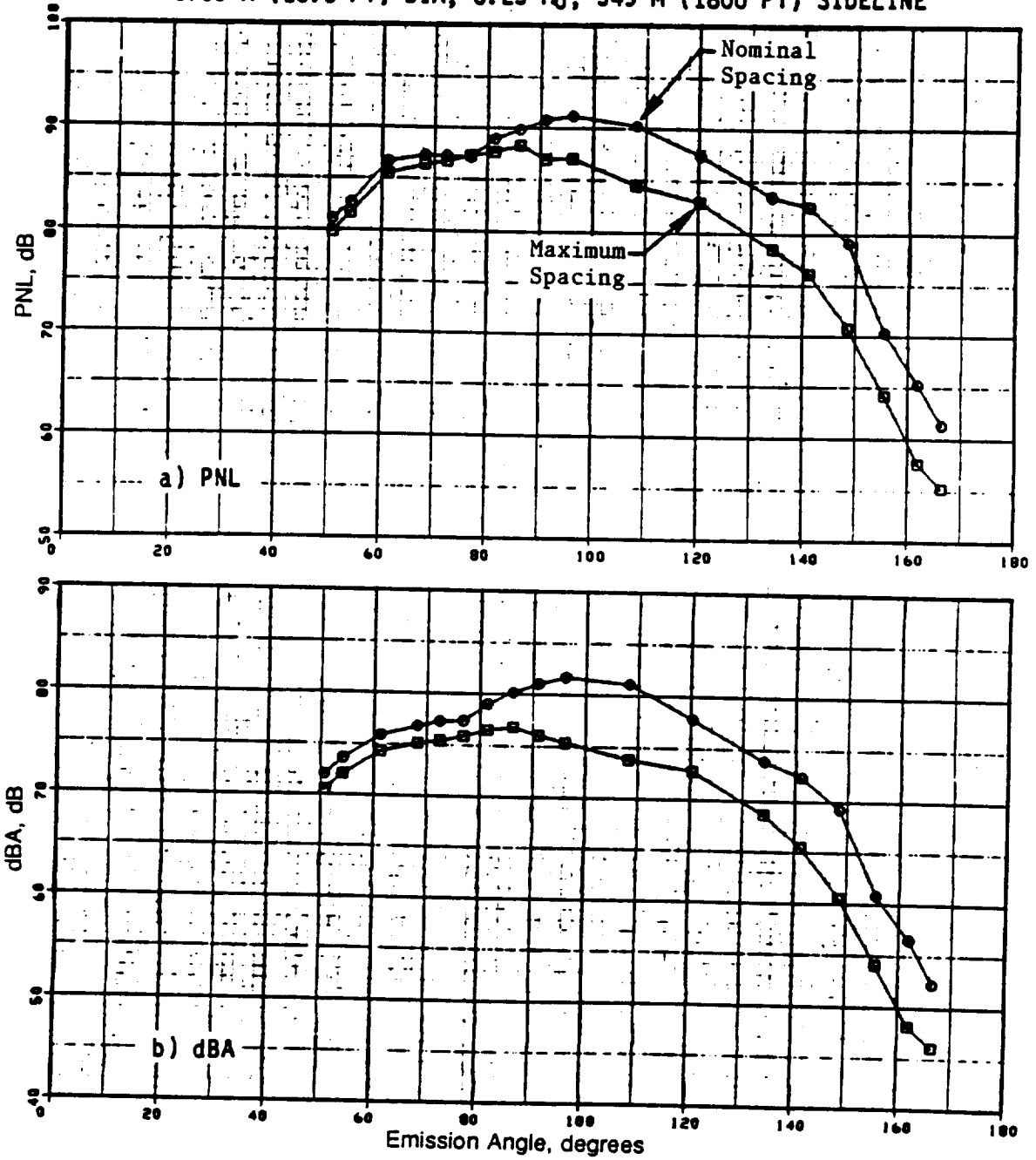


Figure 272. PNL and dBA Directivity Comparison of F-7/A-7 Clipped at a Tip Speed of 247 mps (810 fps).

ORIGINAL PAGE IS
 OF POOR QUALITY

•F7A7; 9x8; 36.3°/42.7°
 •3.05 M (10.0 FT) DIA; 0.25 M₀; 549 M (1800 FT) SIDELINE

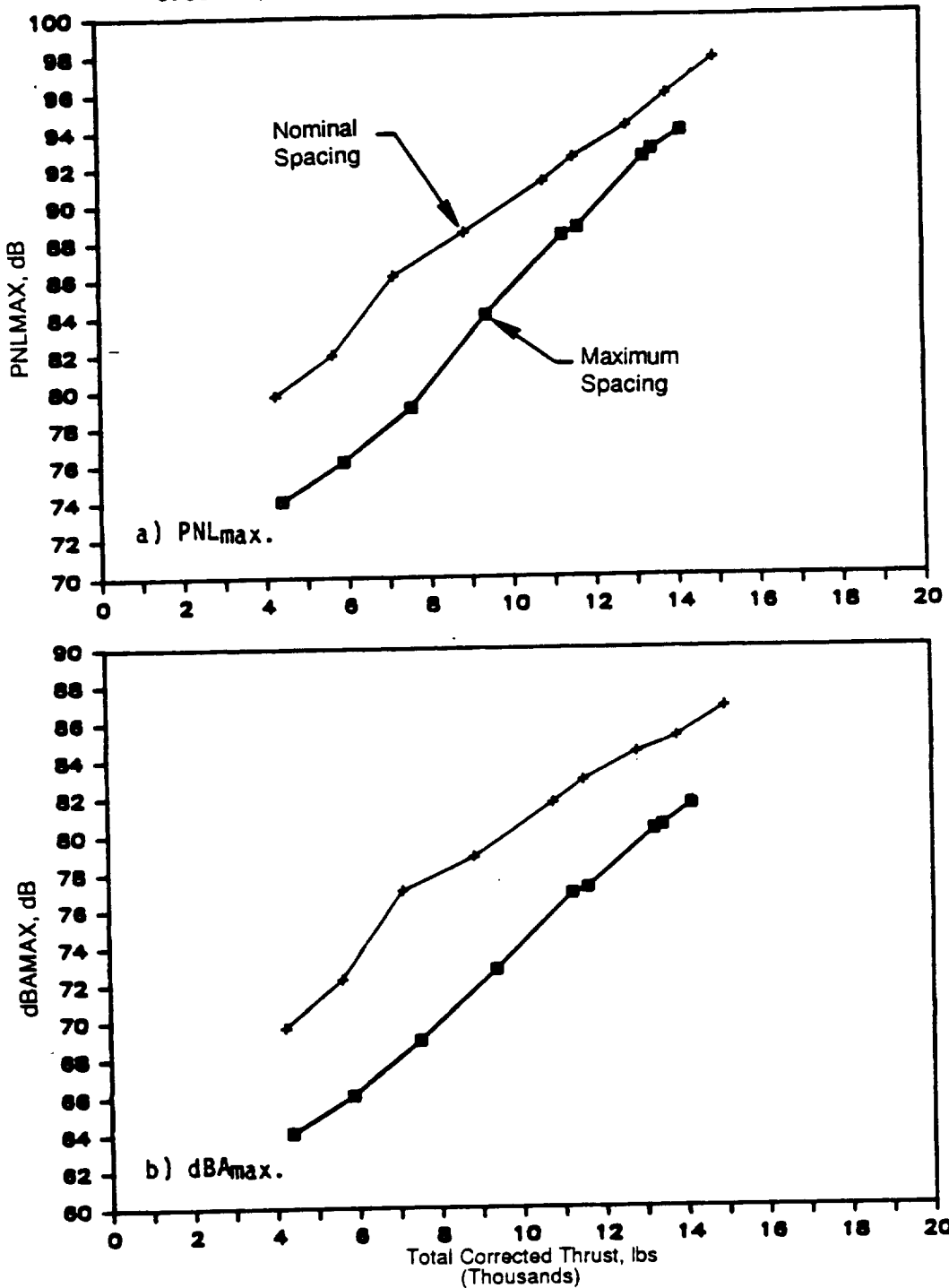


Figure 273. Effect of Rotor-to-Rotor Spacing on the Maximum PNL and dBA of the F-7/A-7 Clipped.

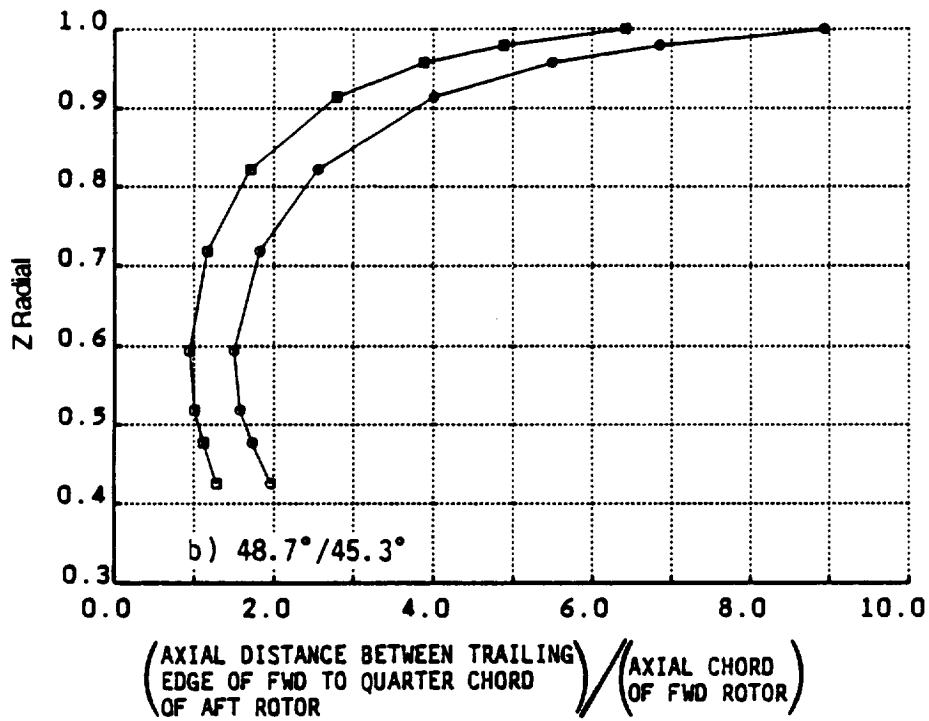
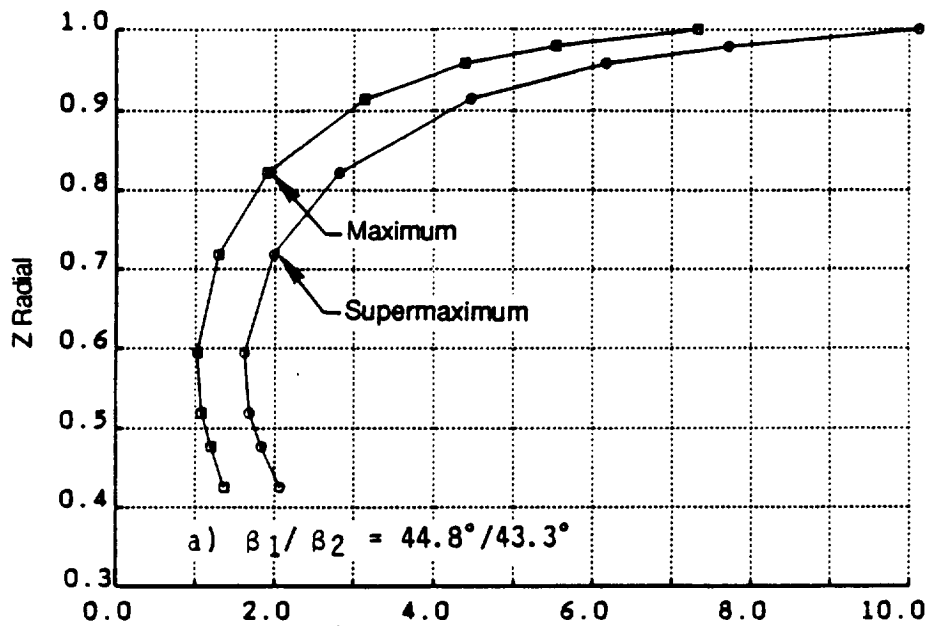


Figure 274. Rotor-to-Rotor Spacing Comparison for F-11/A-11 Blades.

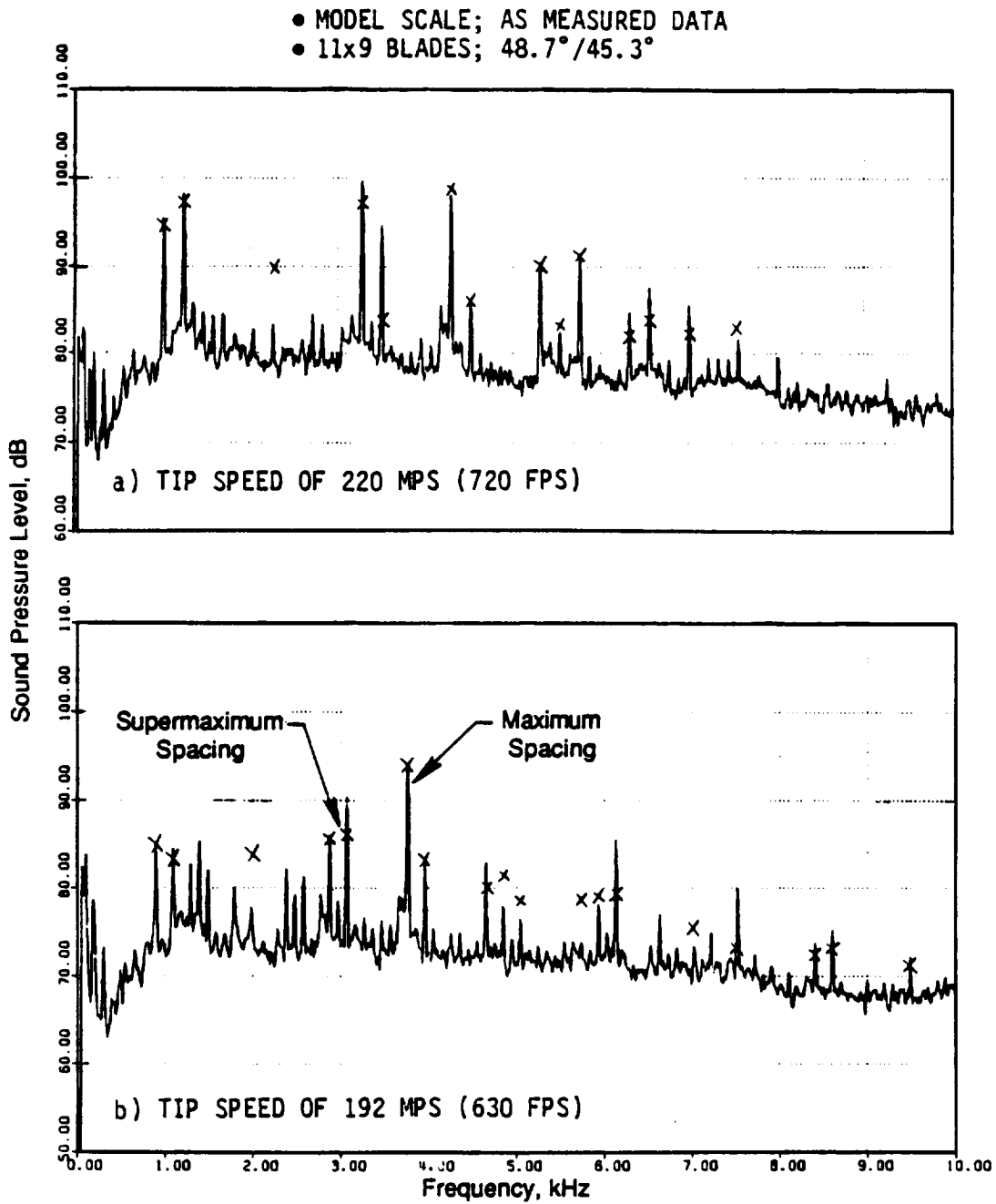


Figure 275. Typical Narrow-Band Comparison of F-11/A-11 for Maximum and Supermaximum Spacing at a Microphone Angle of 97°.

- Figure 276 presents a scaled spectral data comparison at flight emission angles of 61°, 96°, 120°, and 134° for a tip speed of 220 mps (720 fps)
- Figure 277 demonstrate scaled PNL and dBA directivities at tip speed of 220 mps (720 fps)
- Figure 278 provides data that is similar to that of Figure 277, but at a tip speed of 192 mps (630 fps)
- Figure 279 plots the maximum PNL and dBA as a function of total thrust.

As with the results of the F-7/A-7 blades, no significant effect of the change in spacing is noted at BPF; therefore, no impact of spacing is observed on the steady-loading noise. Again, like the F-7/A-7 (9+8) unclipped blades, the significant impact of spacing is the reduction in the A+2F interaction tone level. PNL and dBA reductions in peak noise region are in the range of 1 dB to 3 dB over most of the thrust range. This reduction is similar to that noticed with open pitch data for F-7/A-7 blades of Series 1.

This study on the effect of increased spacing with the F-7/A-7 and F-11/A-11 blade designs is concluded by providing two general observations that are made based on steady- and interaction-noise results of the four test series presented in this section. Increasing rotor spacing from nominal to maximum, in the case of model-scale F-7/A-7 blades, and from maximum to supermaximum, in the case of model-scale F-11/A-11 blades, had no effect on steady-loading noise, but did result in a reduction in the aerodynamic rotor-to-rotor interaction noise.

The amount of the interaction noise reduction due to the increased rotor spacing depended on the presence or absence of tip-vortex interaction. With no tip-vortex-to-rotor interaction, as assumed with the F-7/A-7c (9+8) clipped blades of Series 3, the benefit of the increased rotor spacing on interaction noise was found to be substantial. Considering the sum of SPL's of all interaction tones as a measure of the rotor-to-rotor interaction, an 8 dB to 10 dB reduction was observed in the peak noise region for the clipped configuration. This reduction is attributable to the benefit of increased wake decay resulting from the increased rotor spacing. The corresponding reduction obtained with unclipped F-7/A-7 9+8 blades of Series 2 that contain tip-vortex interaction was approximately 4 dB.

Accordingly, this seems to indicate that the interaction noise levels due to tip-vortex interaction are more or less of the same order of magnitude as those due to wake/rotor interaction with nominally spaced rotors; therefore, only a partial benefit (approximately 3 dB) would be obtained by substantially reducing either one of these effects. It was concluded from this study that significant reductions in interaction noise could be obtained by first reducing the tip-vortex interaction by clipping the aft blades, and then increasing the wake decay by increasing the rotor spacing. If clipping is not done, the benefit obtainable with the increase in spacing would be masked by interaction noise levels due to tip-vortex interaction.

The impact of interaction noise reduction, measured with increased rotor spacing on the total noise (PNL, OASPL, and dBA), depends on associated levels of the steady-loading noise. Significant benefit in the steady-loading noise levels for a given thrust were noted with configurations at open pitch angles, due to decreased tip speed, and with configurations having an increased number of blades. As a result of this reduction in steady-loading noise, sound pressure level reductions at higher harmonics due to increased spacing were found to have a greater impact on the total noise of such a configuration.

• 3.05 M (10.0 FT) DIA; 0.25 M₀; 549 M (1800 FT) SIDELINE

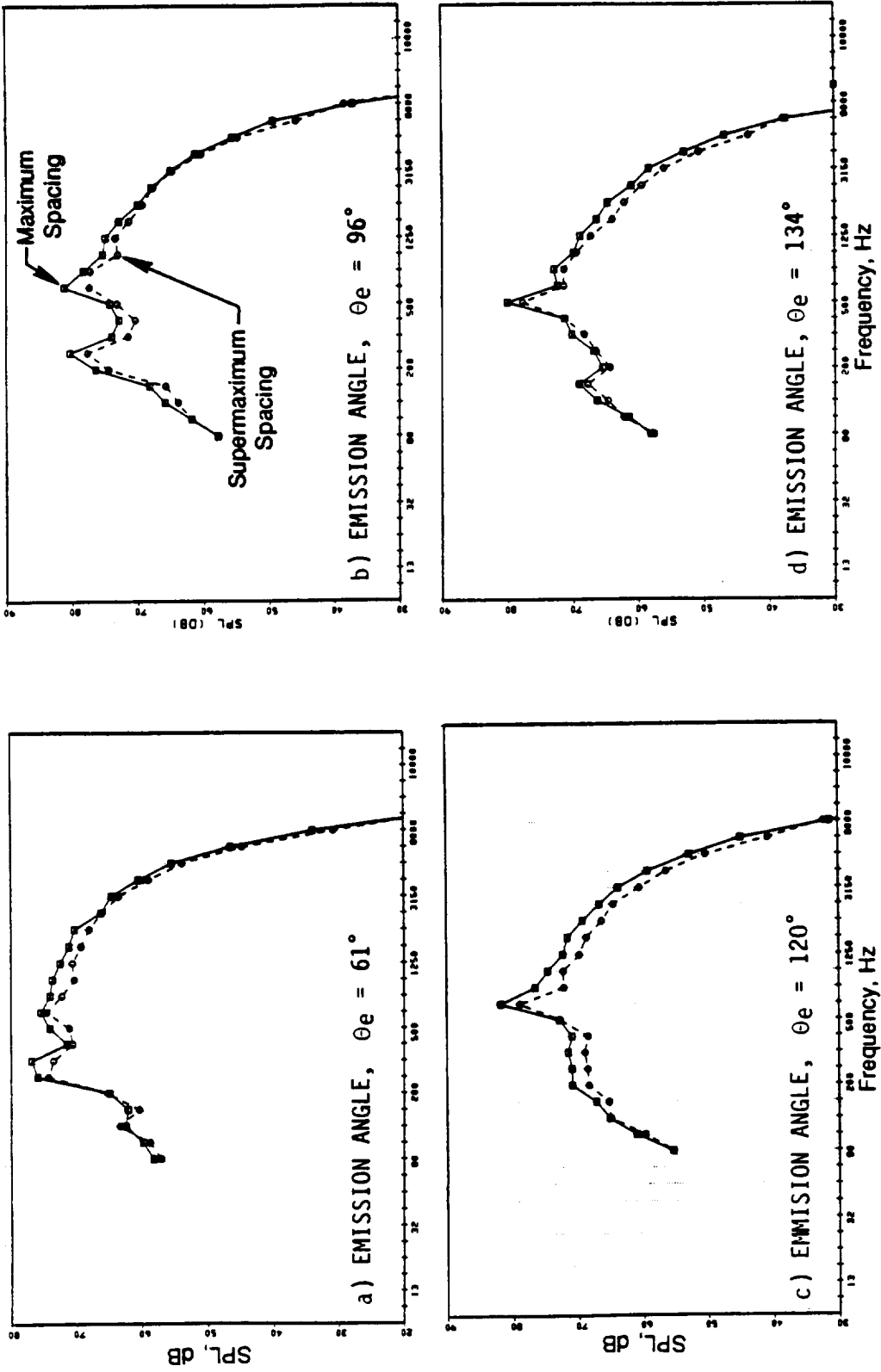


Figure 276. Comparison of Spectra of F-11/A-11 (11+9; 48.7°/45.3°) with Maximum and Supermaximum Rotor Spacings at Tip Speed of 220 mps (720 fps).

• 3.05 M (10.0 FT) DIA; 0.25 M₀; 549 M (1800 FT) SIDELINE

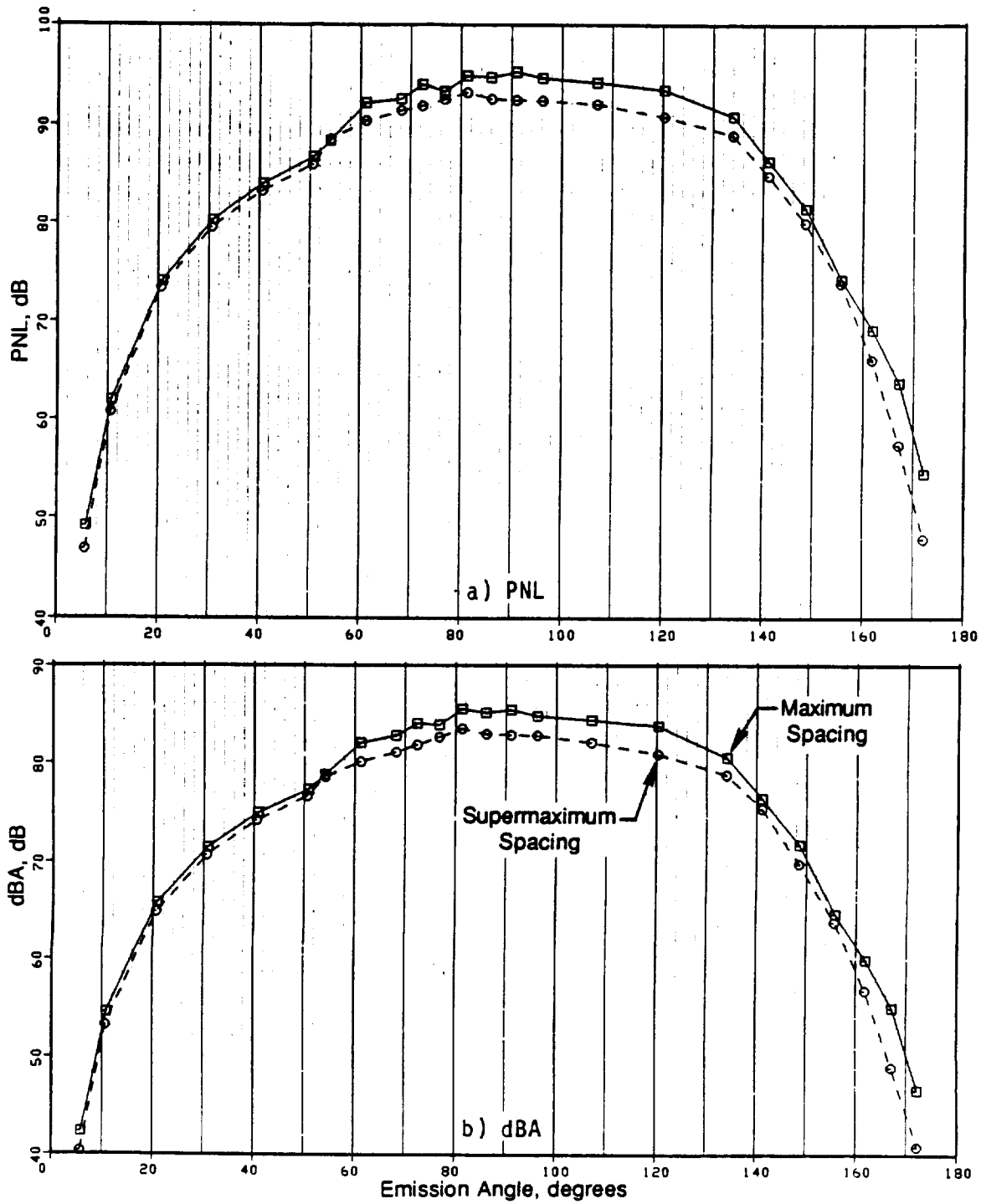


Figure 277. PNL and dBA Directivity Comparison of F-11/A-11 (11+9; 48.7°/45.3°) at Tip Speed of 220 mps (720 fps).

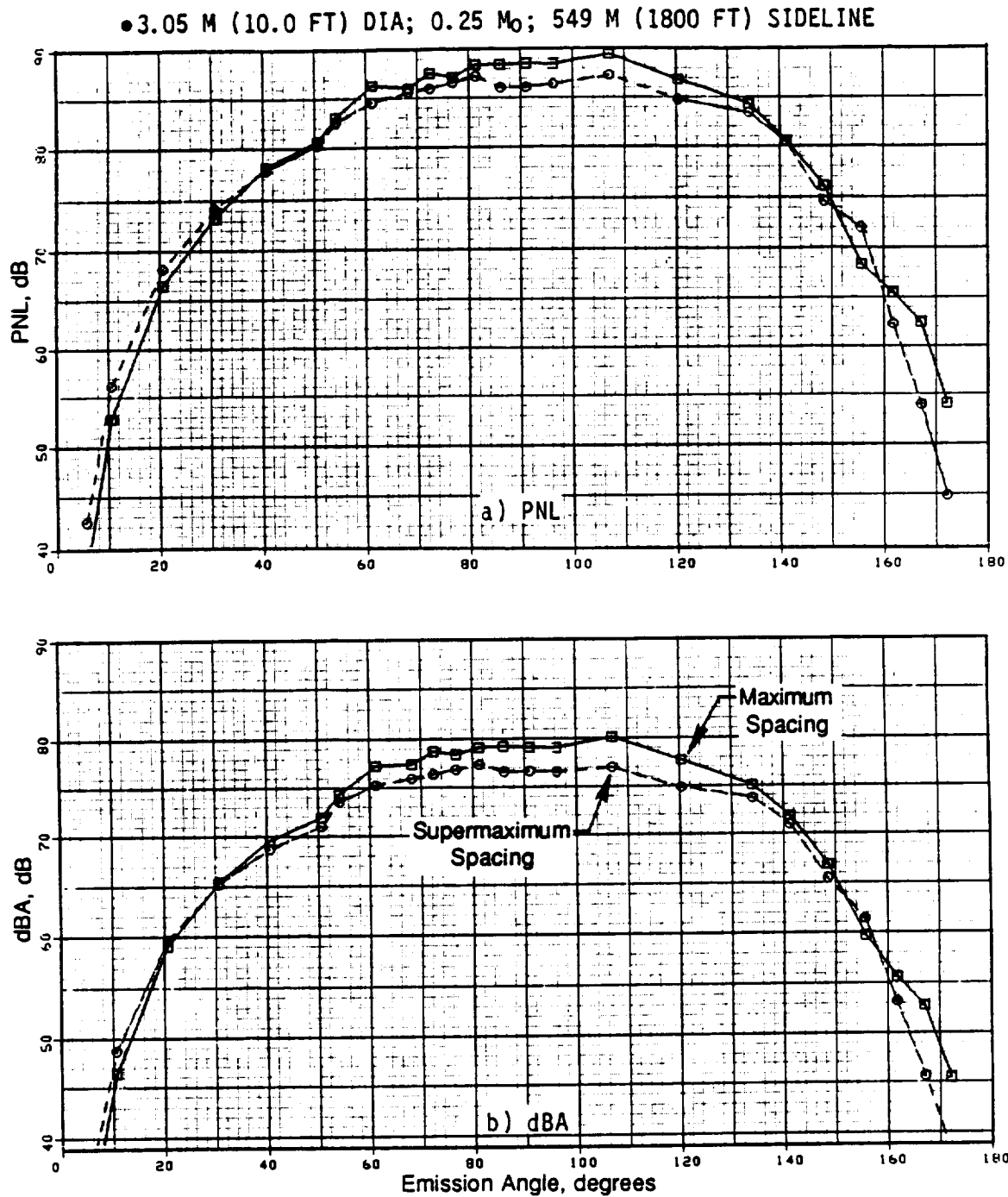


Figure 278. PNL and dBA Directivity Comparisons of F-11/A-11 (11+9; 48.7°/45.3°) with Maximum and Supermaximum Spacings at Tip Speed of 192 mps (630 fps).

● 3.05 M (10.0 FT) DIA; 0.25 M₀; 549 M (1800 FT) SIDELINE

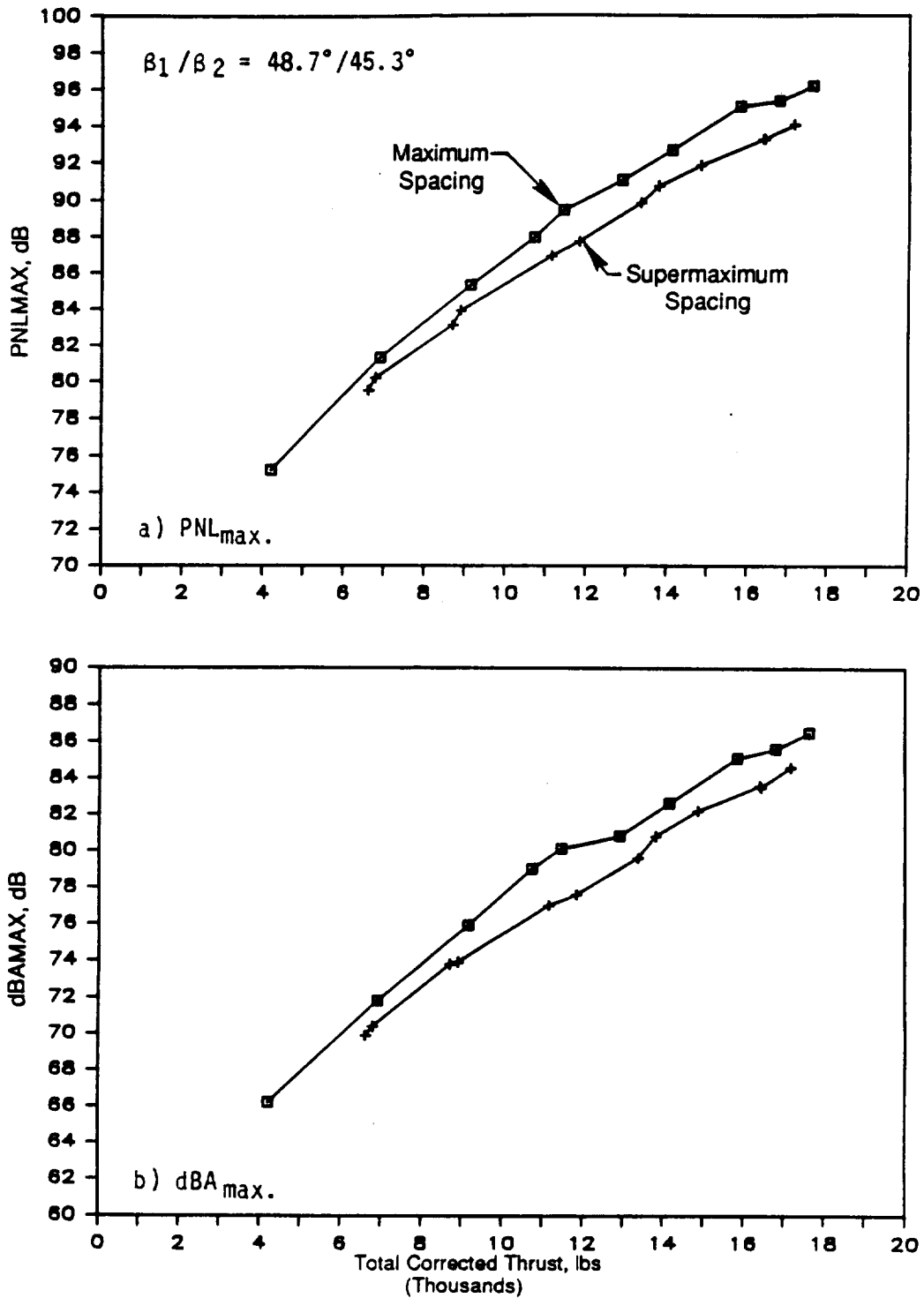


Figure 279. Effect of Rotor-to-Rotor Spacing on the Maximum PNL and dBA of F-11/A-11 (11+9).

Finally, the impact of the increased spacing on EPNL for configurations of this test series is provided in Figure 280 for typical takeoff and cutback thrust conditions. For all of the unclipped configurations, the benefit from increased spacing was approximately 1 dB at takeoff, and with a range of 1 dB to 5 dB at cutback; for the clipped configuration, this benefit was increased to 2.5 dB at takeoff and 5.5 dB at cutback.

7.1.1.5 Effect of Tip Speed

To determine the benefit of decreasing tip speeds of counterrotating fan blades on their acoustic characteristics at fixed takeoff and cutback thrust conditions, tests were conducted with different blade-pitch angles for various configurations. Table 61 summarizes the various configurations utilized in these study tests of the F-7/A-7 and F-11/A-11 blades; all of these tests were performed without a mounting pylon.

The acoustic data measured during the six series of tests (Table 61) are presented and discussed in this section. The presented results are data at a simulated flight Mach number of 0.25.

7.1.1.5.1 F-7/A-7 (8+8) at Nominal Rotor Spacing: Series 1

The F-7/A-7 (8+8) blade configuration was tested during Series 1 using a nominal pitch-change-axes spacing ($X/D_t = 0.169$) at blade-pitch angles of 36.0/35.2, 37.9/37.4, 40.0/38.0, 43.3/40.4, and 53.9/40.4. The effect of the increased blade-pitch setting conditions on rotor-to-rotor spacings, in terms of the normalized axial distance between the trailing edge of a

Table 61. Summary of Cell 41 Tip Speed Variation Tests.

Test Series	Configuration	Blade Number	Rotor Spacing	Pitch Angles	Run No.
1	F-7/A-7	8+8	Nominal	36.0/35.2	14
				37.9/37.4	12
				40.0/38.0	15
				43.3/40.4	13
				53.9/40.4	16
2	F-7/A-7	8+8	Maximum	37.9/37.4	27
				40.3/40.3	28
3	F-7/A-7	9+8	Maximum	36.3/37.4	35
				38.4/37.4	32
				41.8/41.4	37
4	F-7/A-7c	9+8	Maximum	36.3/42.7	43
				41.8/48.3	41
5	F-11/A-11	11+9	Maximum	38.7/38.9	109
				44.8/43.3	94
				48.7/45.3	110
				54.2/47.5	112
6	F-11/A-11	11+9	Supermaximum	44.8/43.3	140
				48.7/45.3	139

F-11/A-11

F-7/A-7

BLADE DESIGN		F-7/A-7		F-11/A-11	
BLADE NUMBERS	8+8	8+8	9+8 (Clipped)	11+9	
PITCH ANGLE	37.9°/37.4°	43.3°/40.4°	38.4°/37.4°	48.7°/45.3°	
SPACING	SMALLER X/Dt = 0.169	0.169	0.169	0.24	
	LARGER X/Dt = 0.240	0.24	0.24	0.32	

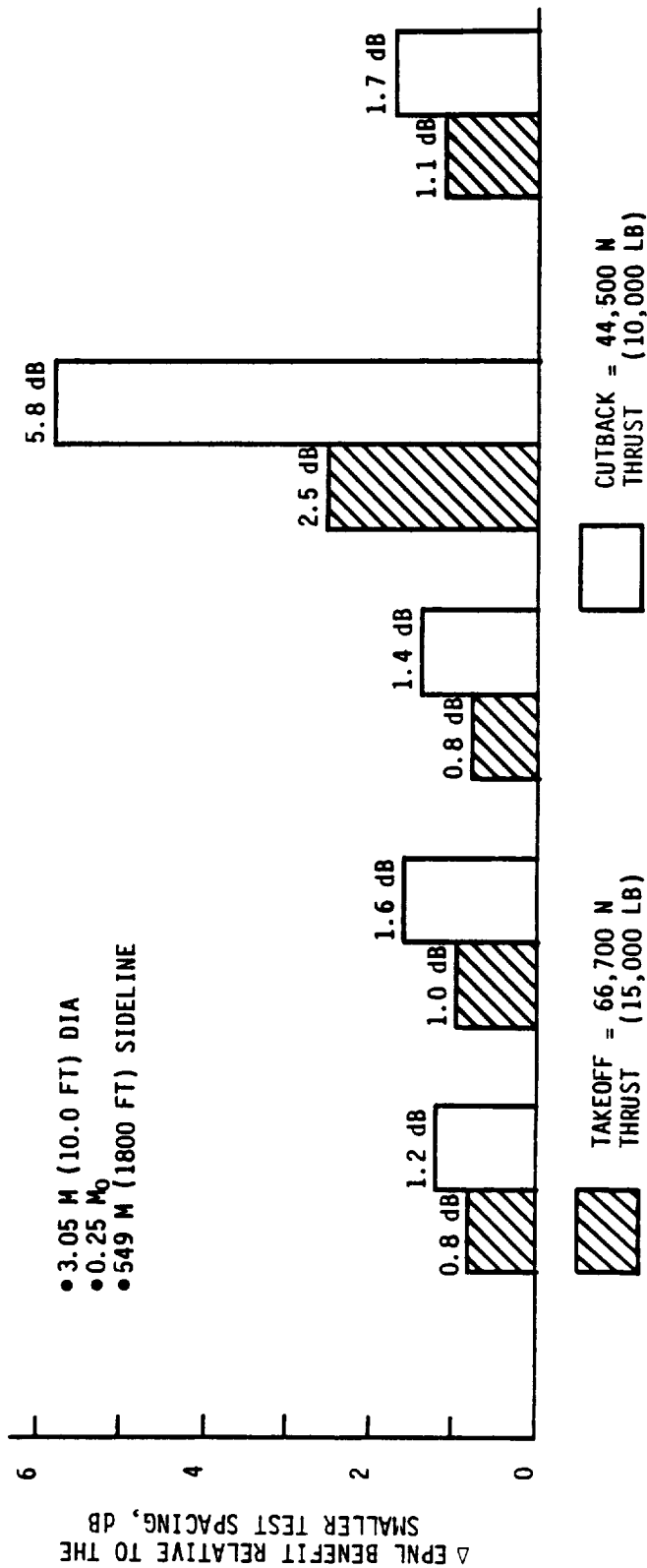


Figure 280. Effect of Rotor-to-Rotor Pitch-Change-Axes Spacing on EPNL Data for F-7/A-7 and F-11/A-11 Configurations.

forward blade and the quarter-chord point of an aft blade, is depicted in Figure 281. This figure reveals that this effective distance between the forward and aft blades decreases by increasing blade-pitch angles (that is, more open pitch setting).

Figure 282 provides data for total thrust and power. The data for thrust versus tip speed indicate the pitch angles of 36.0/35.2, 37.9/37.4, 40.0/38.0, and 43.3/40.5 resulted in typical takeoff thrust of 66,700 N (15,000 lb) at sequentially reduced tip speeds of 274 mps (900 fps), 264 mps (865 fps), 250 mps (820 fps), and 238 mps (780 fps), respectively. However, the power for a given thrust indicates an increase in the power absorbed with decrease of tip speed, indicating a decrease in aerodynamic efficiency. For example, required power at takeoff is observed to increase from 9620 kW (12,900 shp) to 9920 kW (13,300 shp) for a decrease in tip speed from 274 mps (900 fps) to 238 mps (780 fps). Upon opening the blades to a significantly more open pitch setting (53.9/40.4), power absorption increases accordingly to 11,200 kW (15,000 shp) for the same thrust. The above-listed pitch settings also resulted in typical cutback thrusts of 44,500 N (10,000 lb) at tip speeds of 242 mps (795 fps), 216 mps (710 fps), 221 mps (725 fps), and 207 mps (680 fps), respectively.

Figure 283 presents the acoustic data in terms of the scaled and maximum OASPL, PNL, and dBA as a function of total thrust, and indicates reductions of 3 dB and 2.5 dB in the measured maximum levels OASPL and PNL of takeoff tip speed from 274 mps (900 fps) to 238 mps (780 fps). Further reduced tip speed, achieved by increasing the pitch angle from 43.3/40.4 to 53.0/40.4, resulted in an increase in noise level comparable to that measured at 43.0/40.4. The effect of variation in tip speed at cutback is less significant than at takeoff due to the fact that the total noise at cutback is dominated by rotor-to-rotor interaction noise; whereas at takeoff, steady-loading noise dominates.

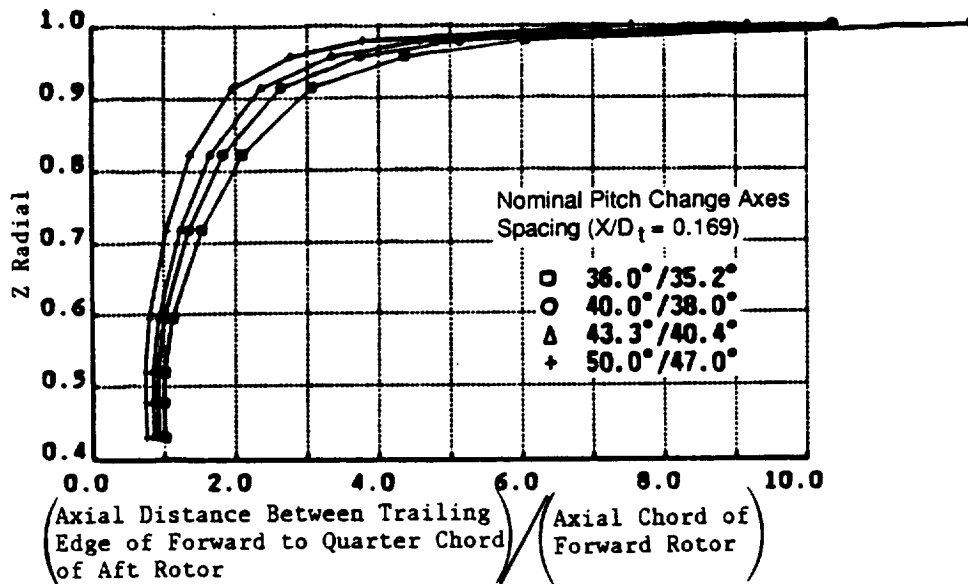


Figure 281. Variation in Blade Spacing as a Function of Radii for the F-7/A-7 at Different Test Pitch Angles.

● 3.05 M (10.0 FT) DIA; 0.25 M_0 ; 549 M (1800 FT) SIDELINE

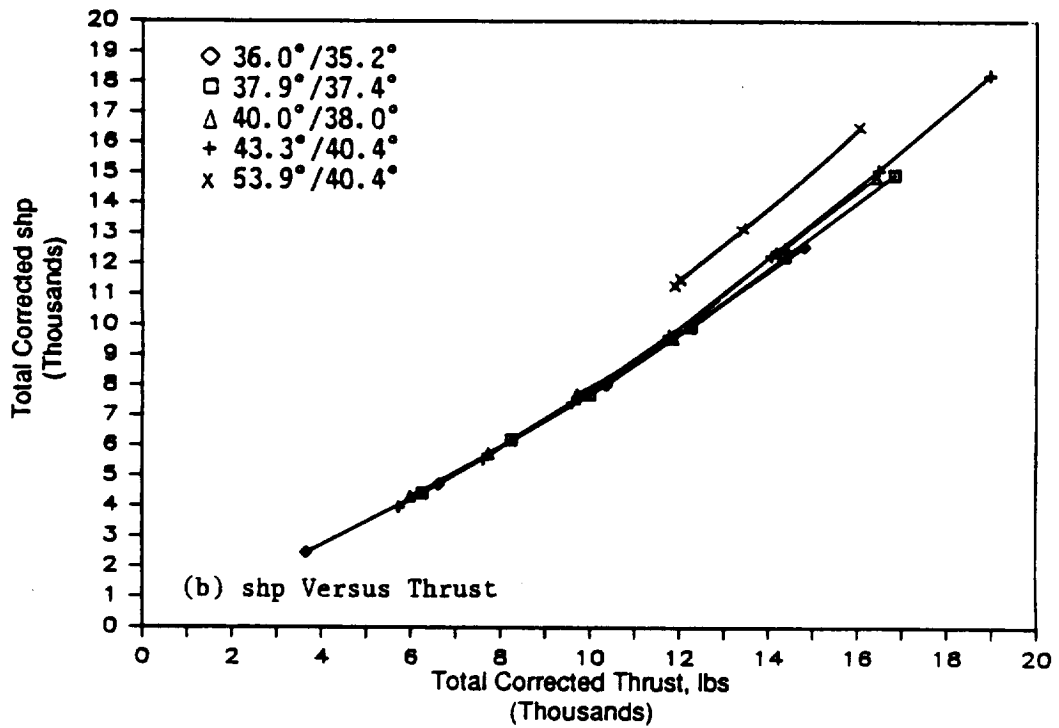
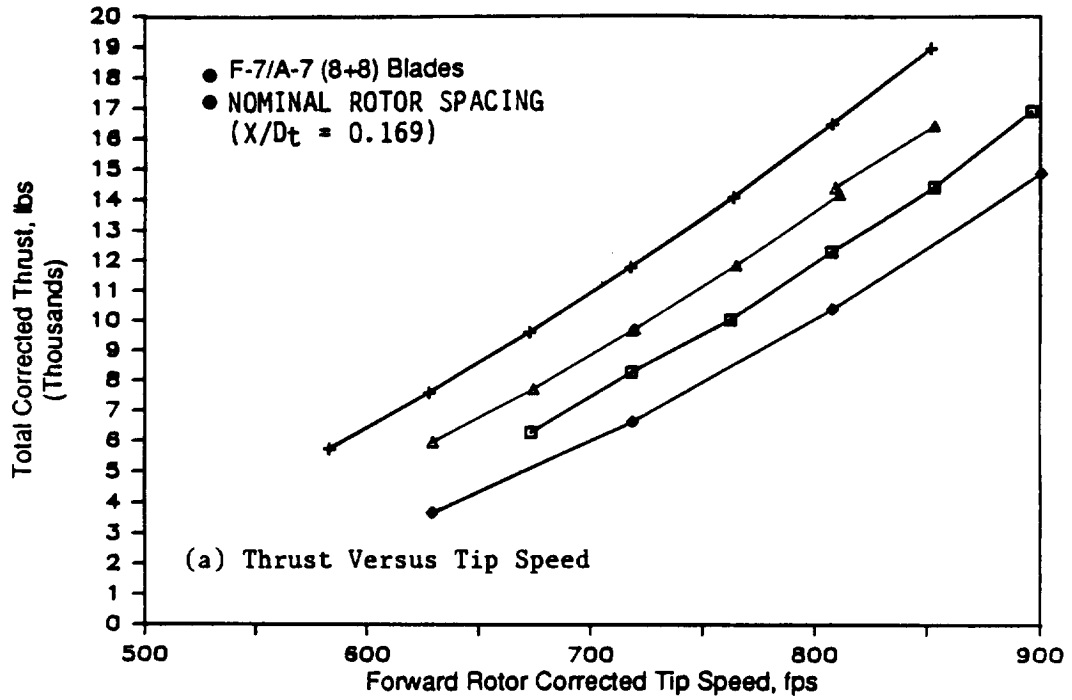


Figure 282. Aero Performance of the F-7/A-7 at Different Blade-Pitch Angles.

● 3.05 M (10.0 FT) DIA; 0.25 M₀; 549 M (1800 FT) SIDELINE

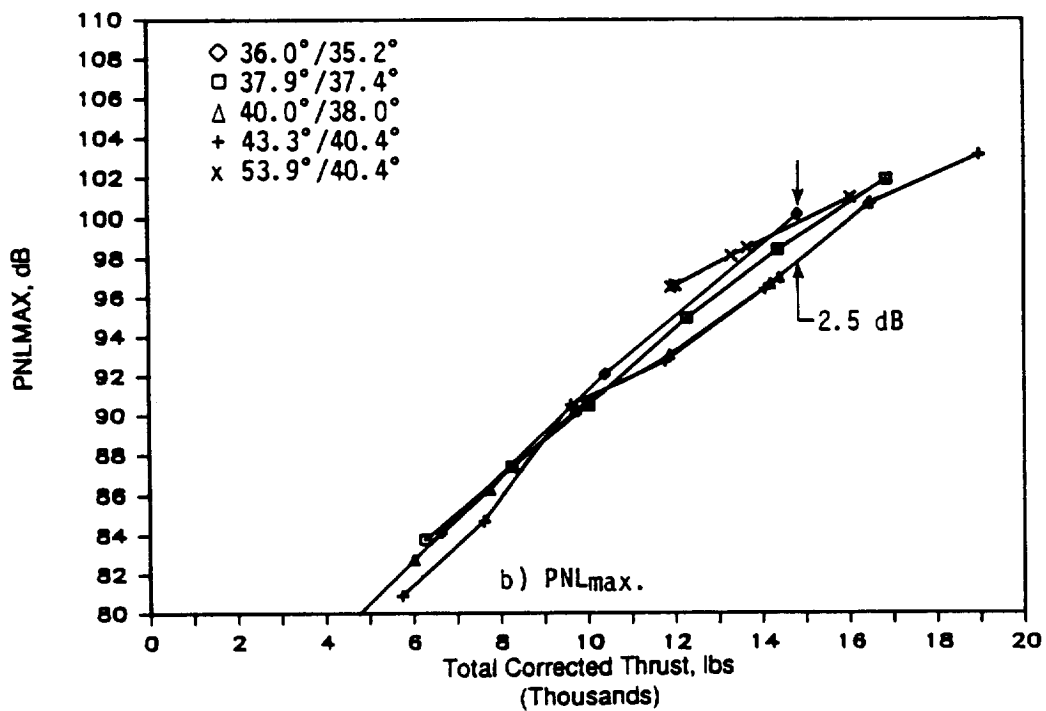
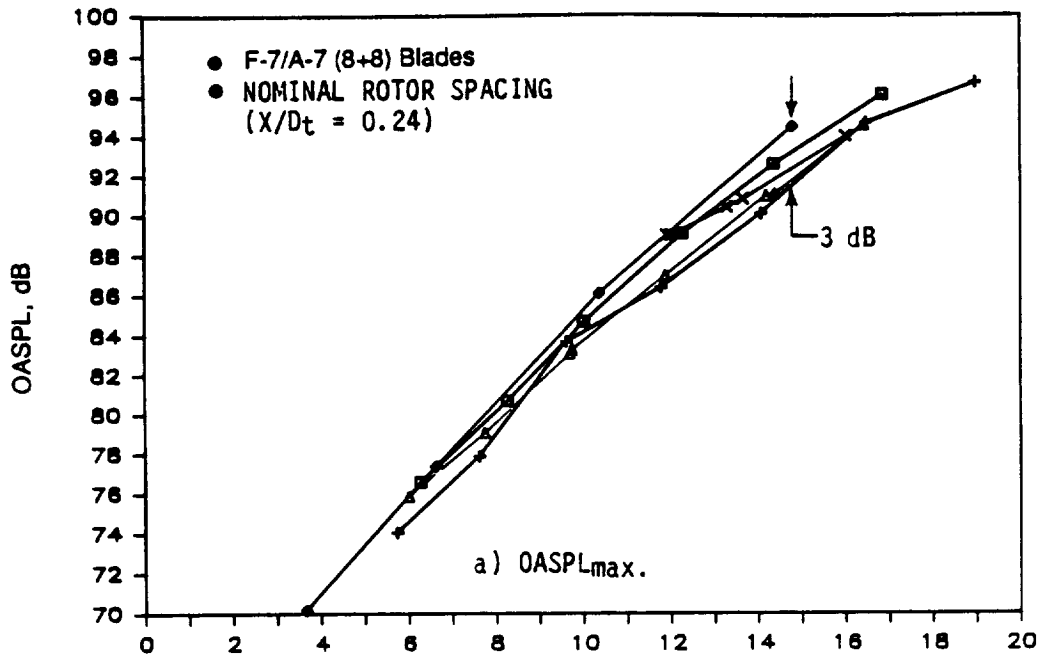


Figure 283. Acoustic Data of the F-7/A-7 at Different Blade-Pitch Angles.

● 3.05 M (10.0 FT) DIA; 0.25 M₀; 549 M (1800 FT) SIDELINE

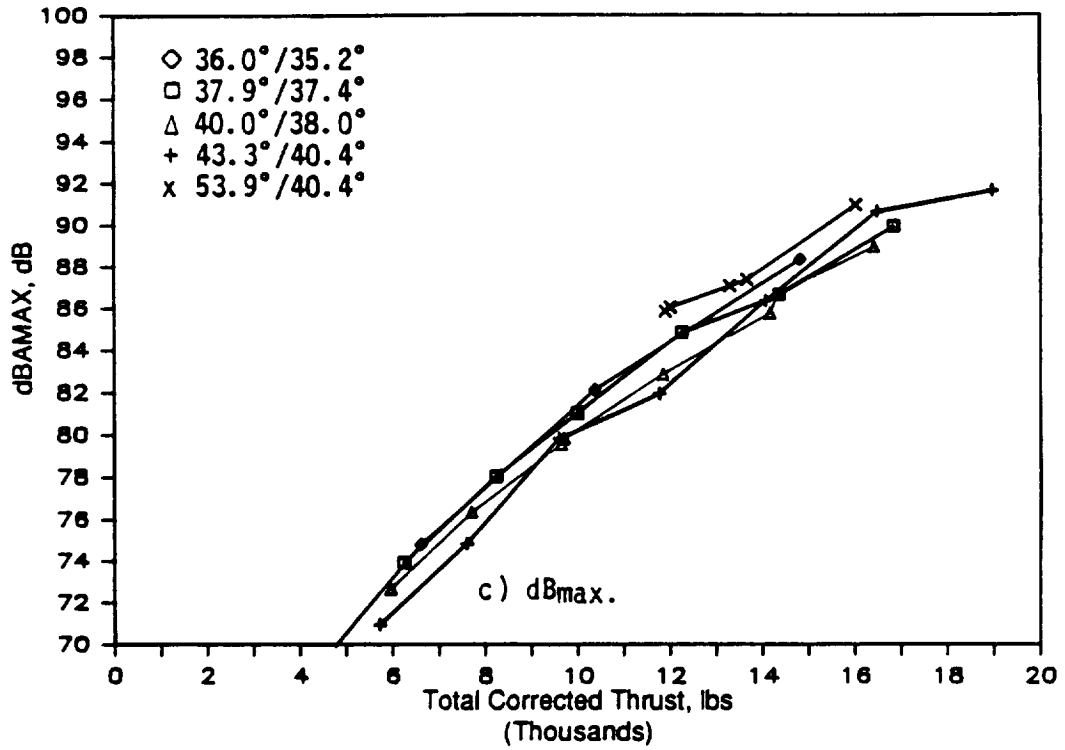


Figure 283. Acoustic Data of the F-7/A-7 at Different Blade-Pitch Angles (Concluded).

Figures 284 through 286 plot the OASPL and PNL directivities and selected spectra for typical cutback and takeoff thrust conditions. Acoustic benefit of decreased tip speed in directivity data is noted more at emission angles in the region of the plane-of-rotation. The spectral data of Figure 286 shows a systematic decrease in the SPL's at BPF's, indicating a corresponding decrease in steady-loading noise with the decrease of tip speed.

Figures 287 and 288 provide model-scale narrow-band spectral comparisons for cutback and takeoff conditions, respectively, at the microphone angle of 92° . In addition, model-scale tone level directivities of the blade passing frequency and harmonics for these two cases are presented in Figures 289 and 290 from available narrow-band spectra; these figures demonstrate significant reductions in the SPL's of the BPF, indicating steady-loading noise decreases with a decrease in tip speed. Reductions also are noted in the sound pressure levels of the 2x BPF, 4x BPF, 5x BPF, and in the levels of the sums of the harmonics; however, no significant effect is noted in the level of the 3xBPF tone with the variation in tip speed.

The model-scale BPF level (at an emission angle of 91°) is summarized for the four test pitch angles (Figure 291, View A), indicating lines of constant tip speed; as described in Subsection 6.1.1.2, these levels are a measure of the steady-loading noise in the region of the plane-of-rotation. These data are replotted in View B (Figure 291), to indicate that steady-loading noise continuously decreases with a decrease in tip speed.

The net benefit in EPNL for a change from nominal pitch angle of $36.0^\circ/35.2^\circ$ to an open pitch angle (lower tip speeds) of $43.3^\circ/40.4^\circ$ was determined to be 1.5 dB and 1 dB, respectively, for typical takeoff and cutback thrust conditions, with the F-7/A-7 (8+8) configuration at a nominal pitch-change-axes spacing.

7.1.1.5.2 F-7/A-7 (8+8) at Maximum Rotor Spacing: Series 2

The F-7/A-7 blade configuration (8+8) also was tested with maximum pitch-change-axes spacing ($X/D_t = 0.24$) at the blade-pitch angles of $37.9^\circ/37.4^\circ$ and $43.3^\circ/40.4^\circ$; Figures 292 through 296 present selected data from these tests.

Figure 292 plots data for total thrust and power, indicating that the test pitch angles ($37.9^\circ/37.4^\circ$ and $43.3^\circ/40.4^\circ$) yielded a typical takeoff thrust of 66,700 N (15,000 lb) at tip speeds of 264 mps (865 fps) and 240 mps (790 fps), respectively. Tip speeds corresponding to the typical cutback thrust of 44,500 N (10,000 lb) were noted to be 233 mps (765 fps) and 210 mps (690 fps). As with the nominally spaced F-7/A-7 (8+8) data, an increase in absorbed power for a given thrust indicates a decrease in aerodynamic efficiency with the tip speed decrease.

The acoustic data contained in Figures 293 through 296 reveals reductions in the range of 2 dB to 3 dB in the peak noise values for thrusts greater than typical cutback; these reductions also are noted over an emission angle range of $70^\circ < \sigma_e < 110^\circ$. One-third-octave band spectral comparisons of Figure 296 show systematic decreases in the SPL at the BPF, indicating a steady-loading noise reduction that corresponds with tip speed reduction. Benefit at some of the higher interaction frequencies is also noted at typical takeoff.

7.1.1.5.3 F-7/A-7 (9+8) at Maximum Rotor Spacing: Series 3

Testing the F-7/A-7 (9+8) at the maximum rotor pitch-change-axes spacing ($X/D_t = 0.24$) with blade-pitch settings of $36.3^\circ/37.4^\circ$, $38.4^\circ/37.4^\circ$, and $41.8^\circ/41.4^\circ$ resulted in the performance data presented in Figure 297. Plotting the thrust versus tip speed indicates that a takeoff thrust of 66,700

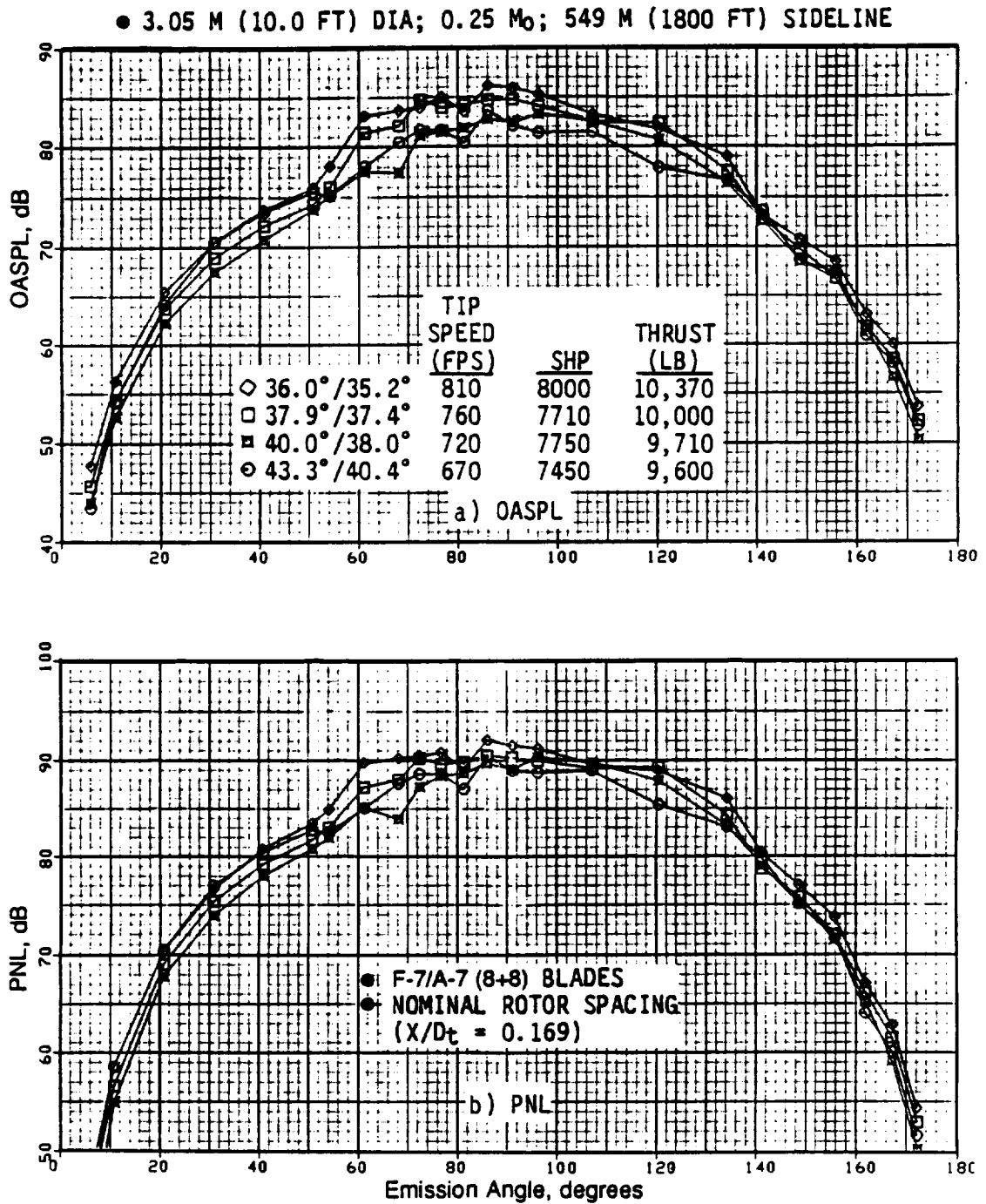


Figure 284. The OASPL and PNL Directivities of F-7/A-7 for Different Tip Speeds at a Typical Cutback.

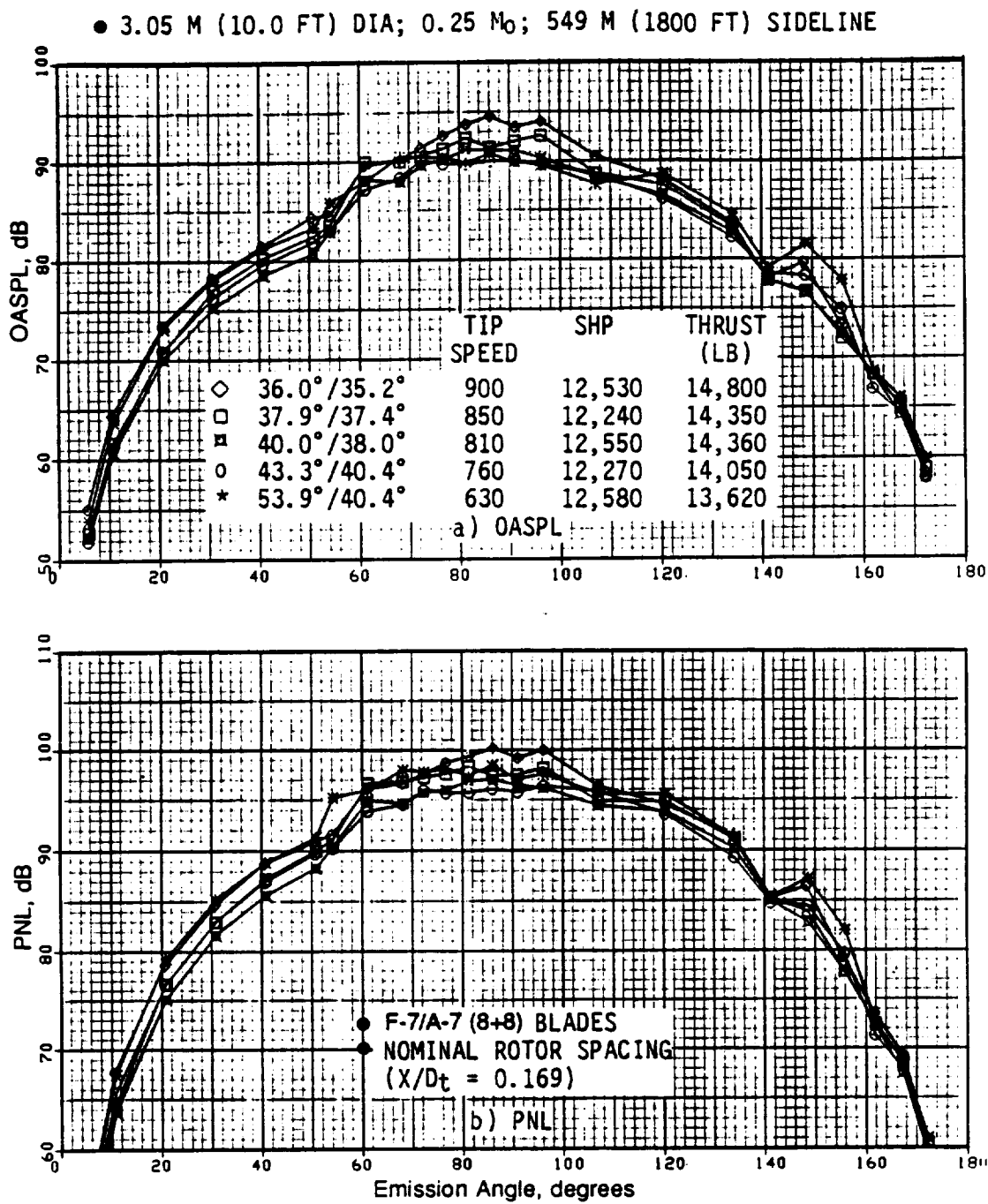


Figure 285. The OASPL and PNL Directivities of F-7/A-7 for Different Tip Speeds at Typical Takeoff.

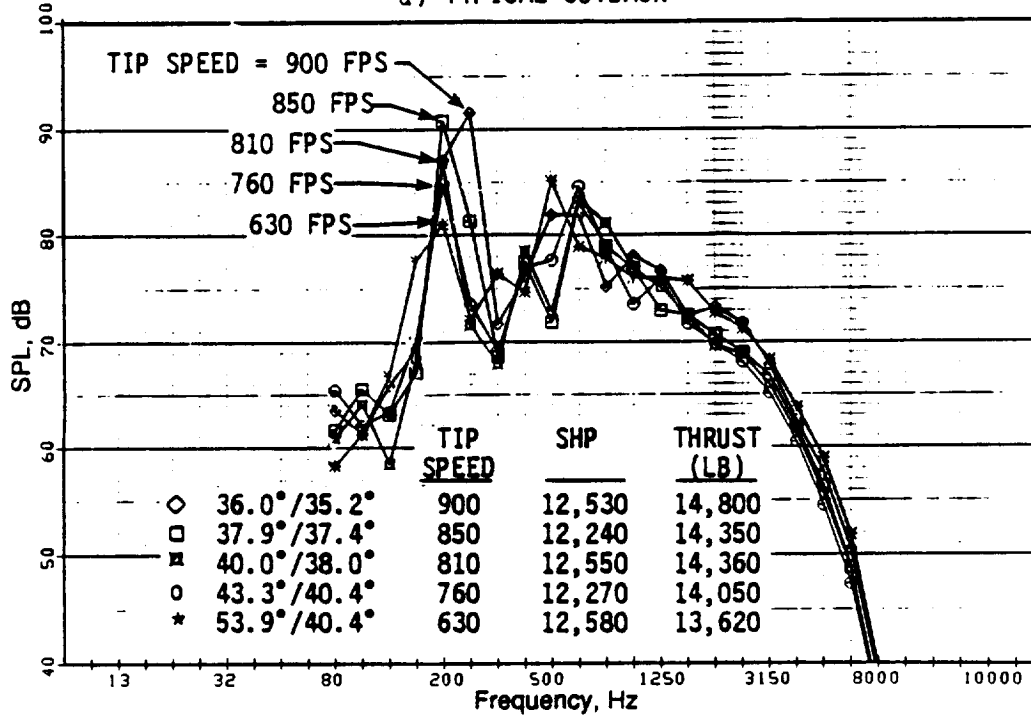
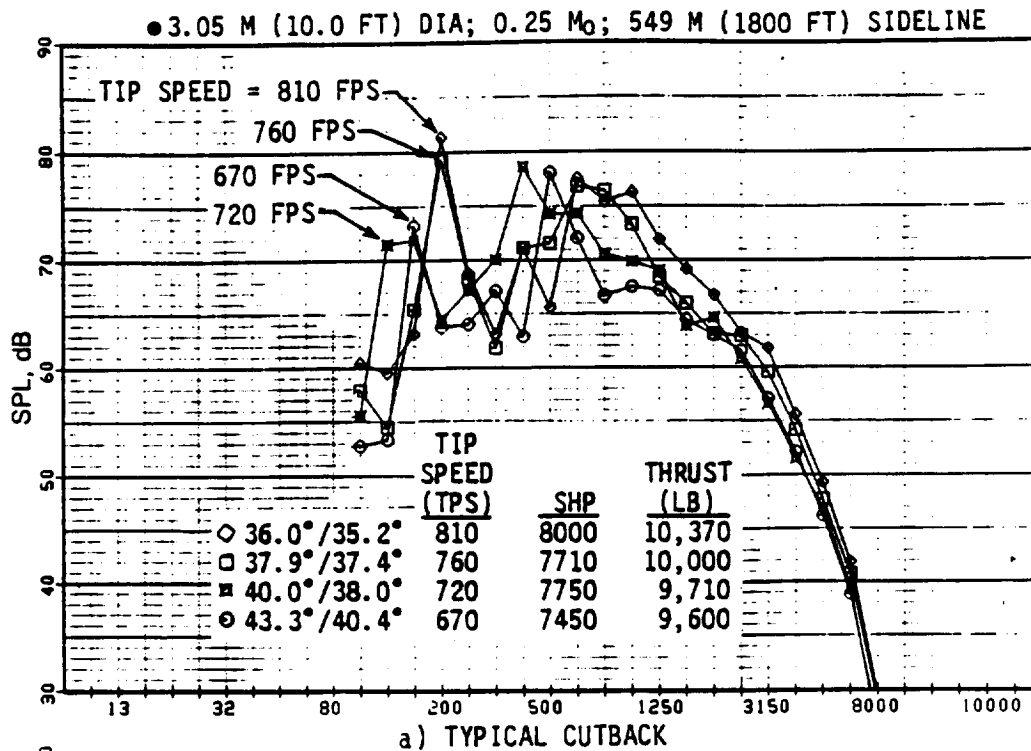
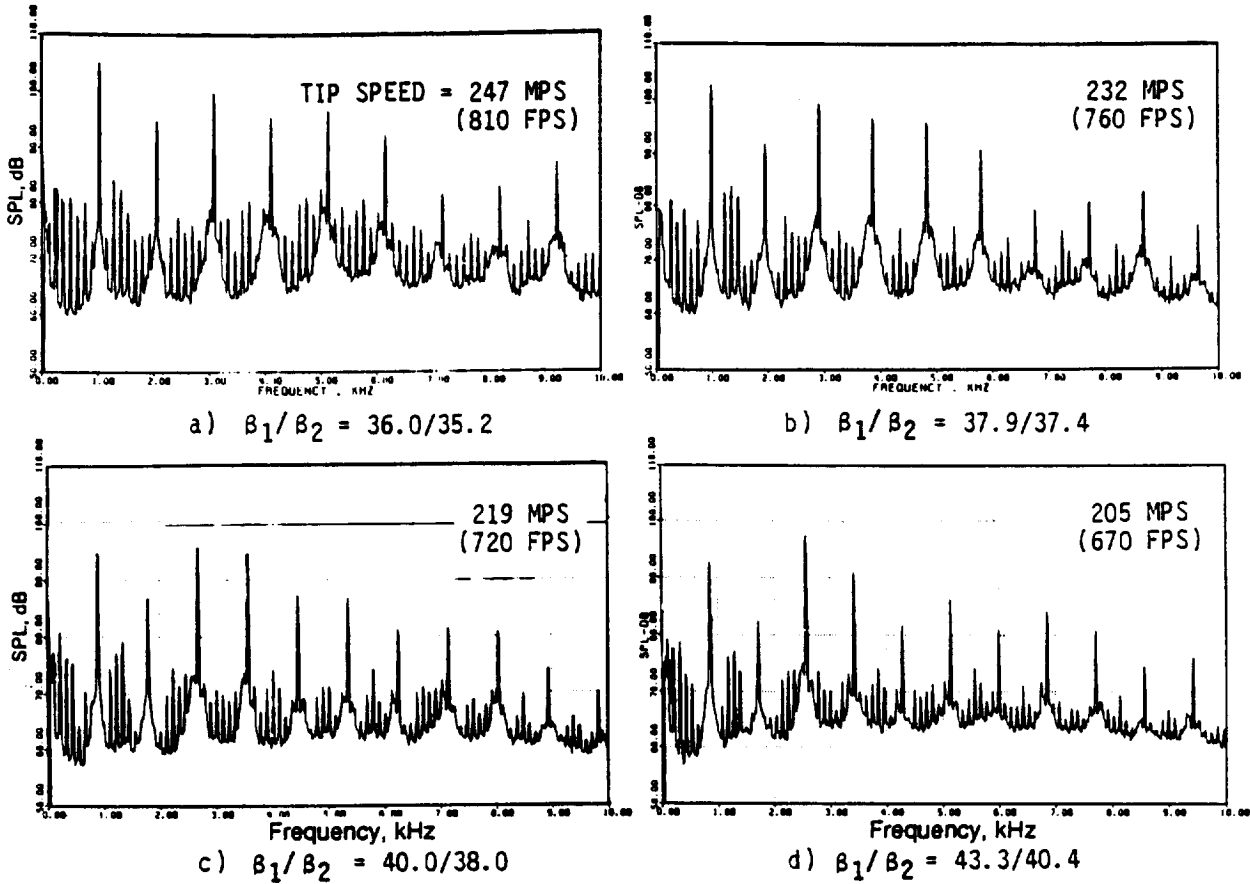


Figure 286. Spectra at a 96° Emission Angle for Different Tip Speeds of the F-7/A-7 (8+8) with Nominal Rotor Spacing.

MODEL SCALE; AS MEASURED DATA F7A7; 8x8 BLADES; NOMINAL ROTOR SPACING
 ($X/D_t = 0.169$); MICROPHONE ANGLE, $\theta_m = 92^\circ$.



	THRUST		POWER	
	N	LB	KW	SHP
a)	1920	(432)	248	(333)
b)	1855	(417)	240	(322)
c)	1793	(403)	236	(316)
d)	1780	(400)	232	(311)

Figure 287. Selected Model-Scale Narrow-Band Spectra for Different Tip Speeds at Typical Cutback.

MODEL SCALE; AS MEASURED DATA F7A7; 8x8 BLADES; NOMINAL ROTOR SPACING
 ($X/D_t = 0.169$); MICROPHONE ANGLE, $\theta_m = 92^\circ$

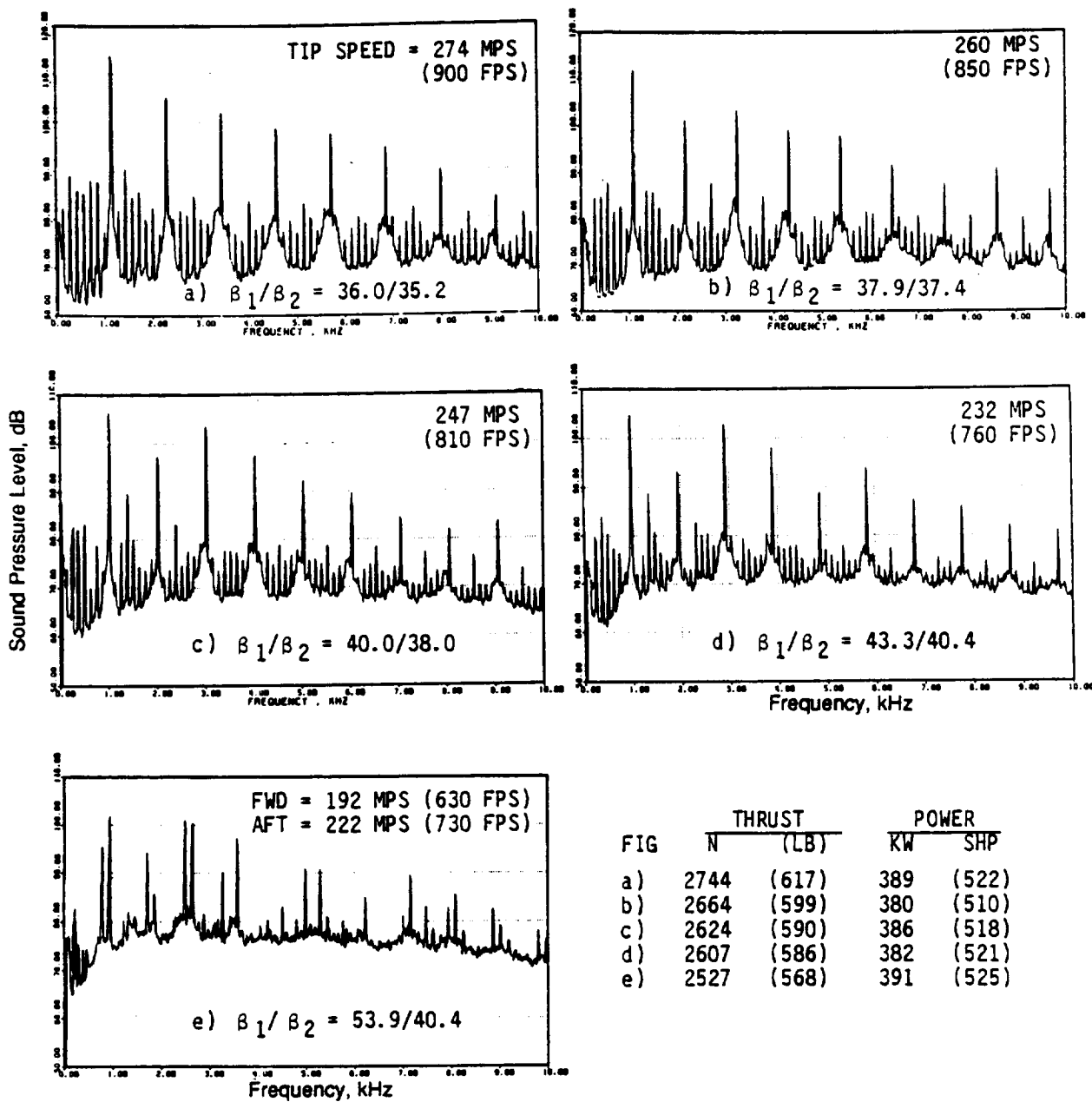


Figure 288. Selected Model-Scale Narrowband Spectra for Different Tip Speeds at Typical Takeoff.

● MODEL SCALE; 8.2 M (27 FT) SIDELINE; 0.25 M₀
 ● 12.5 Hz NARROWBAND DATA

THRUST		POWER	
N	LB	KW	SHP
△ 1920	(432)	248	(333)
□ 1855	(417)	240	(322)
○ 1780	(400)	232	(311)

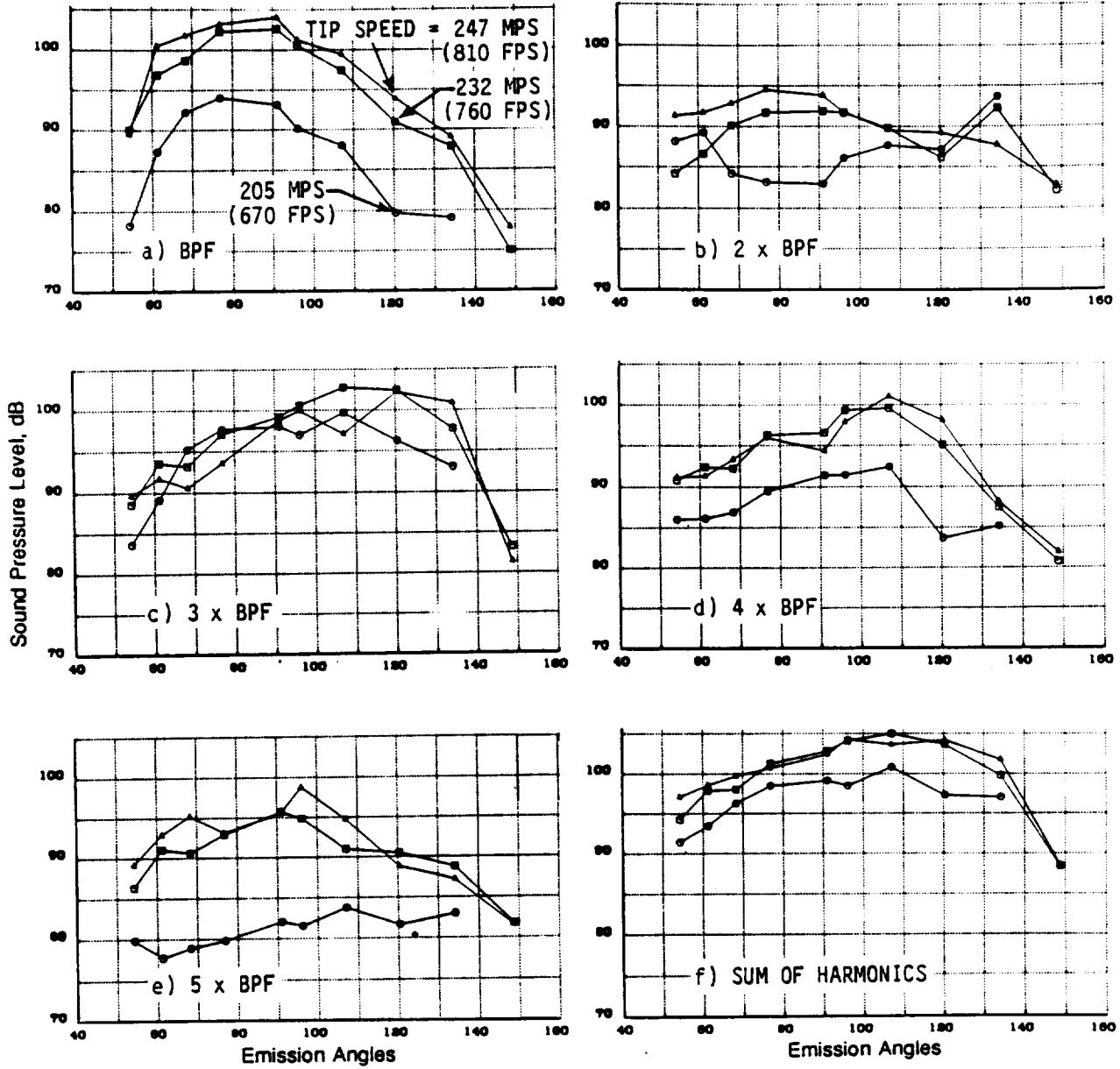


Figure 289. Model-Scale Tone Level Directivities of F-7/A-7 (8+8, Nominal Rotor Spacing) for Different Tip Speeds at Typical Cutback.

● MODEL SCALE; 8.2 M (27 FT) SIDELINE; 0.25 M₀
 ● 12.5 Hz NARROWBAND DATA

FIG	THRUST		POWER	
	N	(LB)	KW	SHP
□	2664	(599)	380	(510)
○	2607	(586)	382	(521)

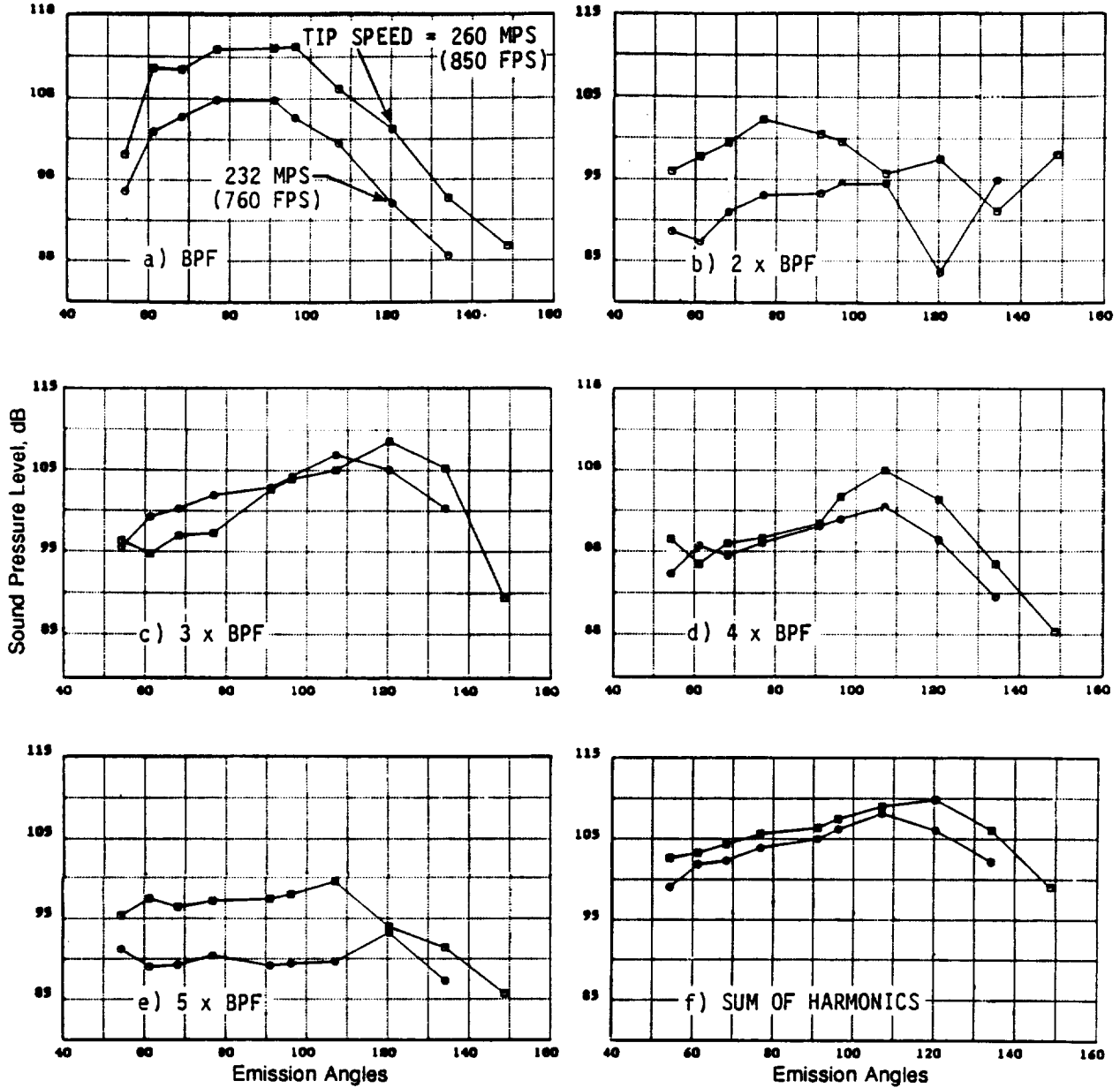
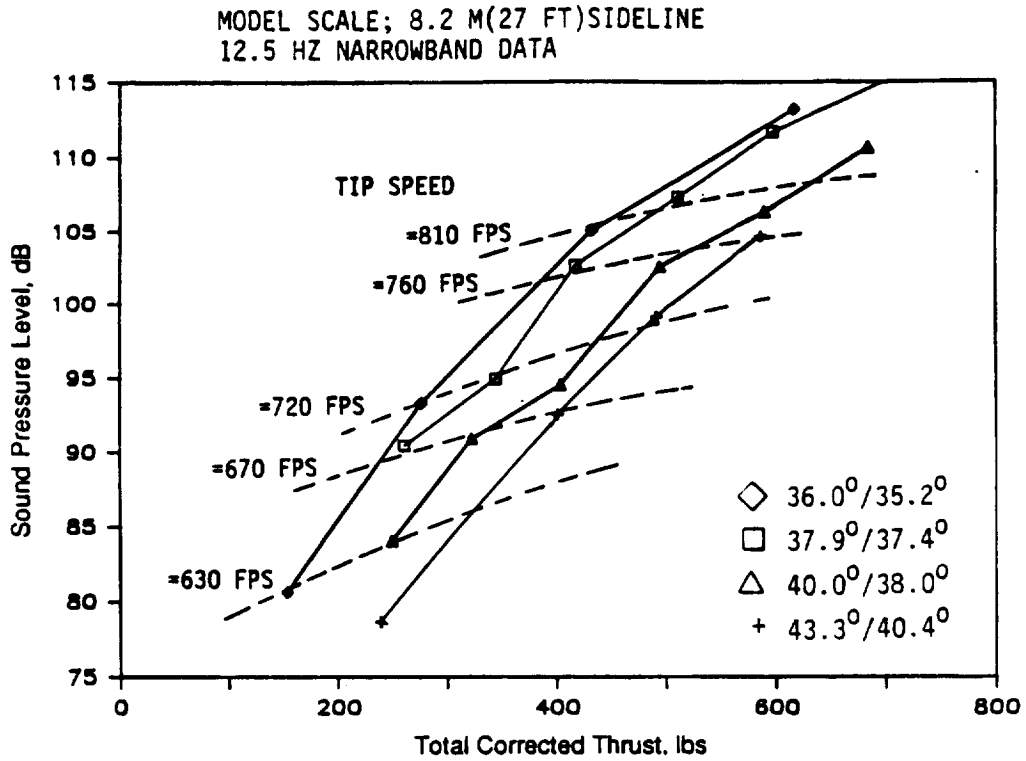
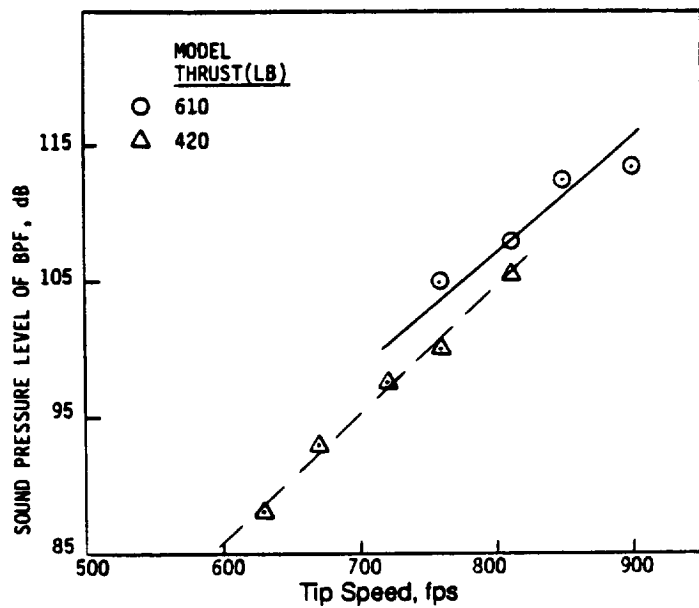


Figure 290. Model-Scale Tone Level Directivities of F-7/A-7 (8+8, Nominal Rotor Spacing) for Different Tip Speeds at Typical Takeoff.



a) BPF Sound Pressure Level @ Emission Angle, $\theta_e=91^\circ$ vs Model Thrust



b) BPF Sound Pressure Level @ Emission Angle, $\theta_e=91^\circ$ vs Tip Speed

Figure 291. Effect of Tip Speed on the Steady-Loading Noise of the F-7/A-7 (8+8).

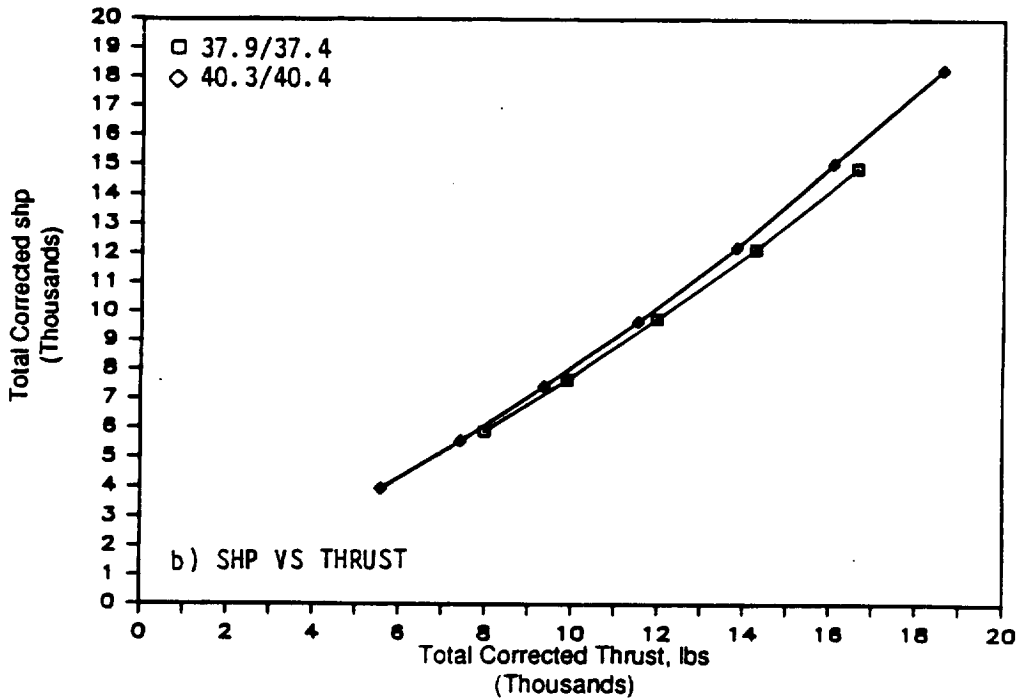
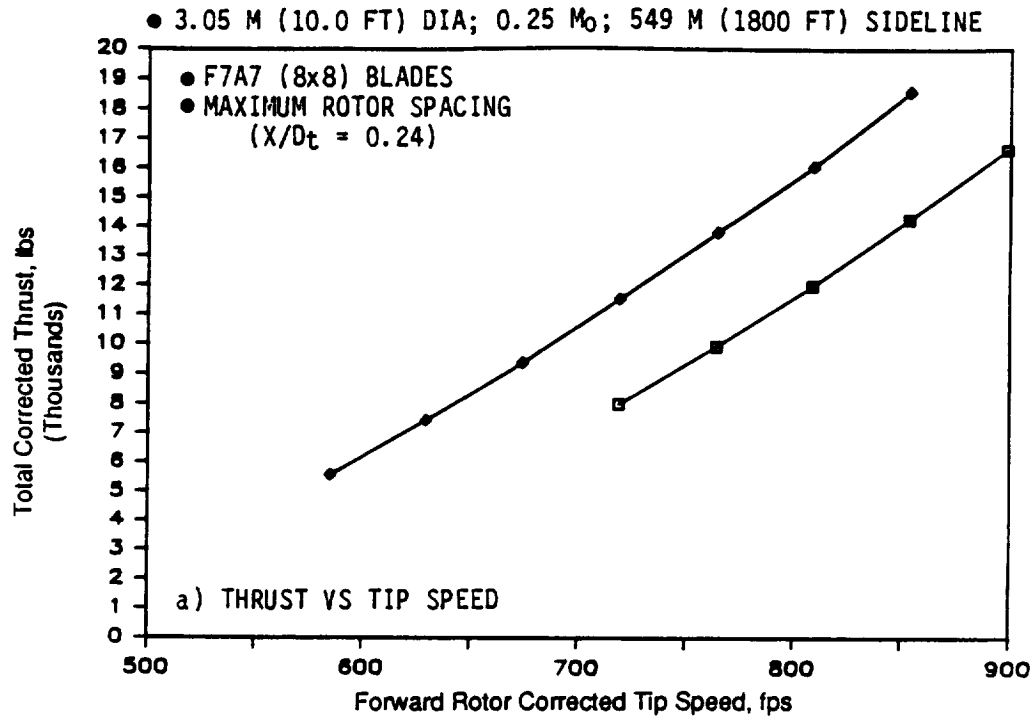


Figure 292. Aero Performance of F-7/A-7 at Different Blade-Pitch Angles.

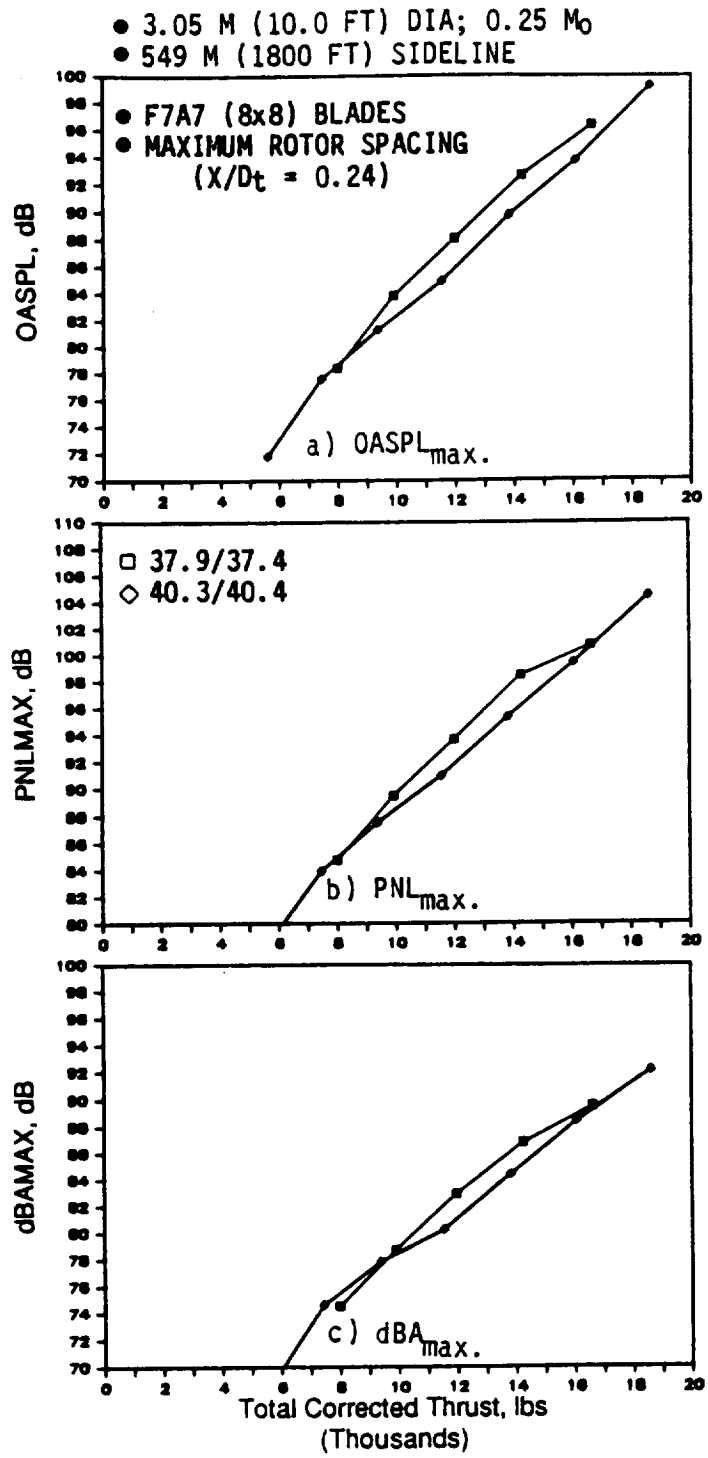


Figure 293. Acoustic Data of F-7/A-7 at Different Blade-Pitch Angles.

● 3.05 M (10.0 FT) DIA; 0.25 M₀; 549 M (1800 FT) SIDELINE

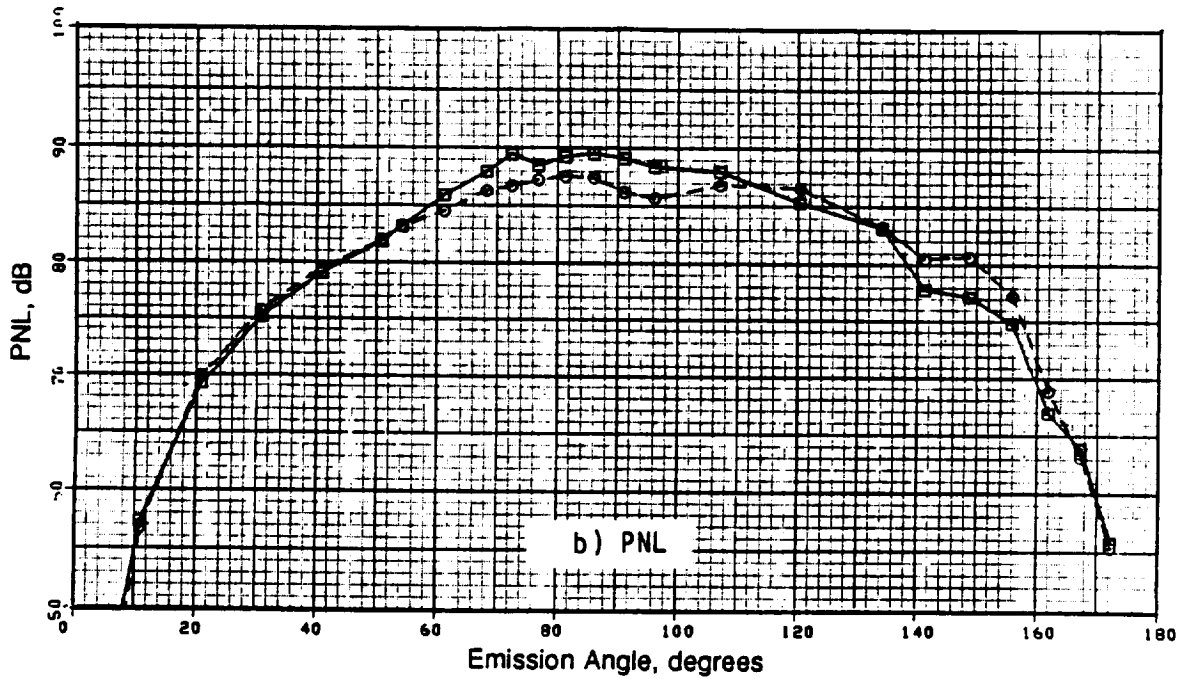
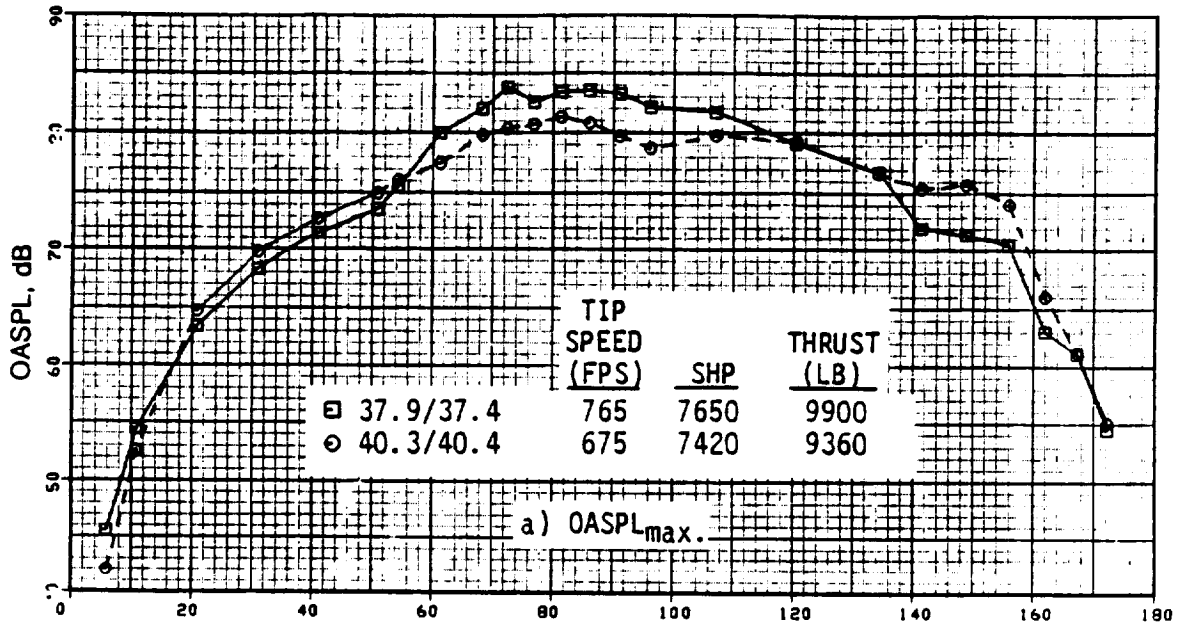


Figure 294. OASPL and PNL Directivities of F-7/A-7 (8+8, Maximum Rotor Spacing) for Different Tip Speeds at a Typical Cutback.

● 3.05 M (10.0 FT) DIA; 0.25 M₀; 549 M (1800 FT) SIDELINE

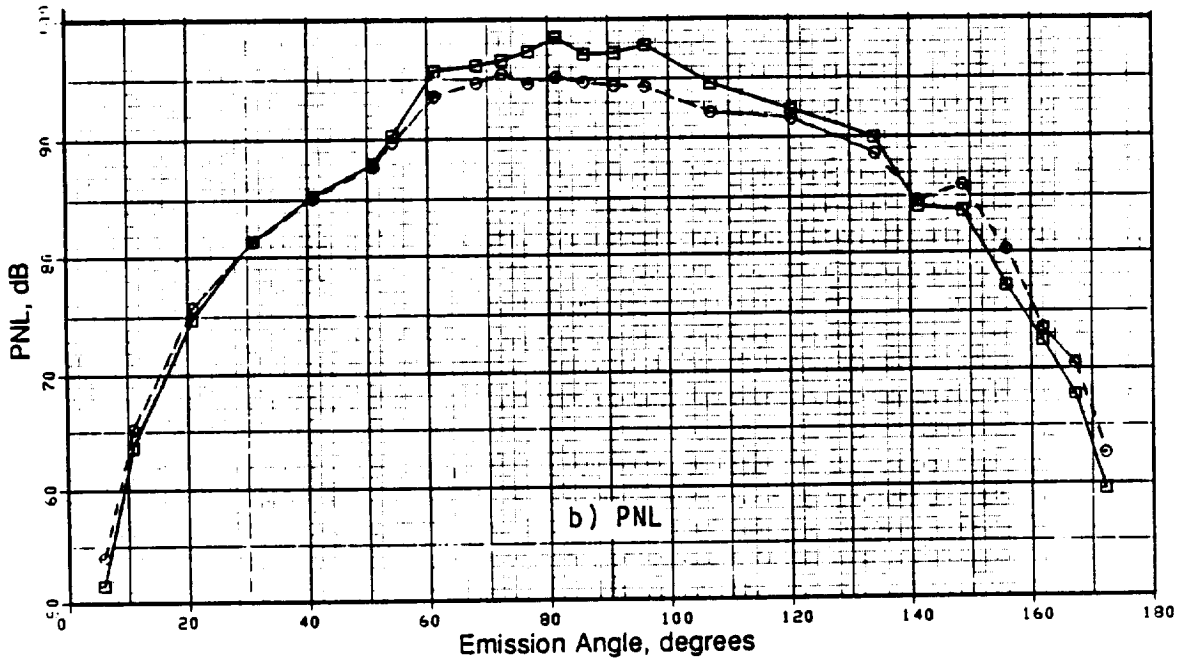
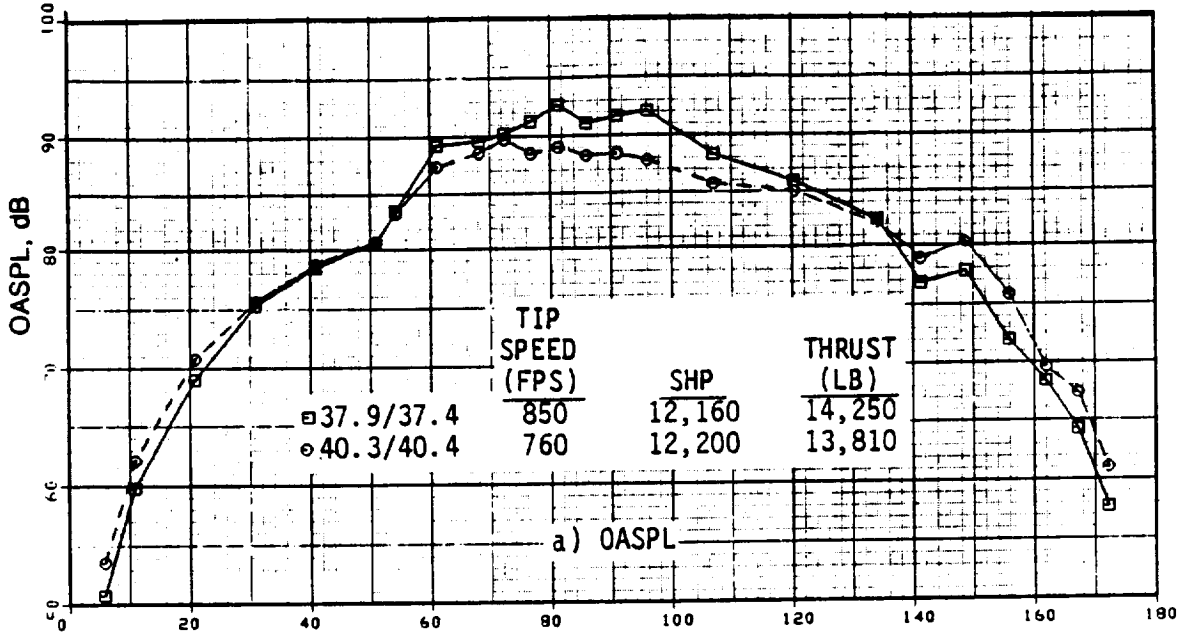


Figure 295. OASPL and PNL Directivities of F-7/A-7 (8+8, Maximum Rotor Spacing) for Different Tip Speeds at Typical Takeoff.

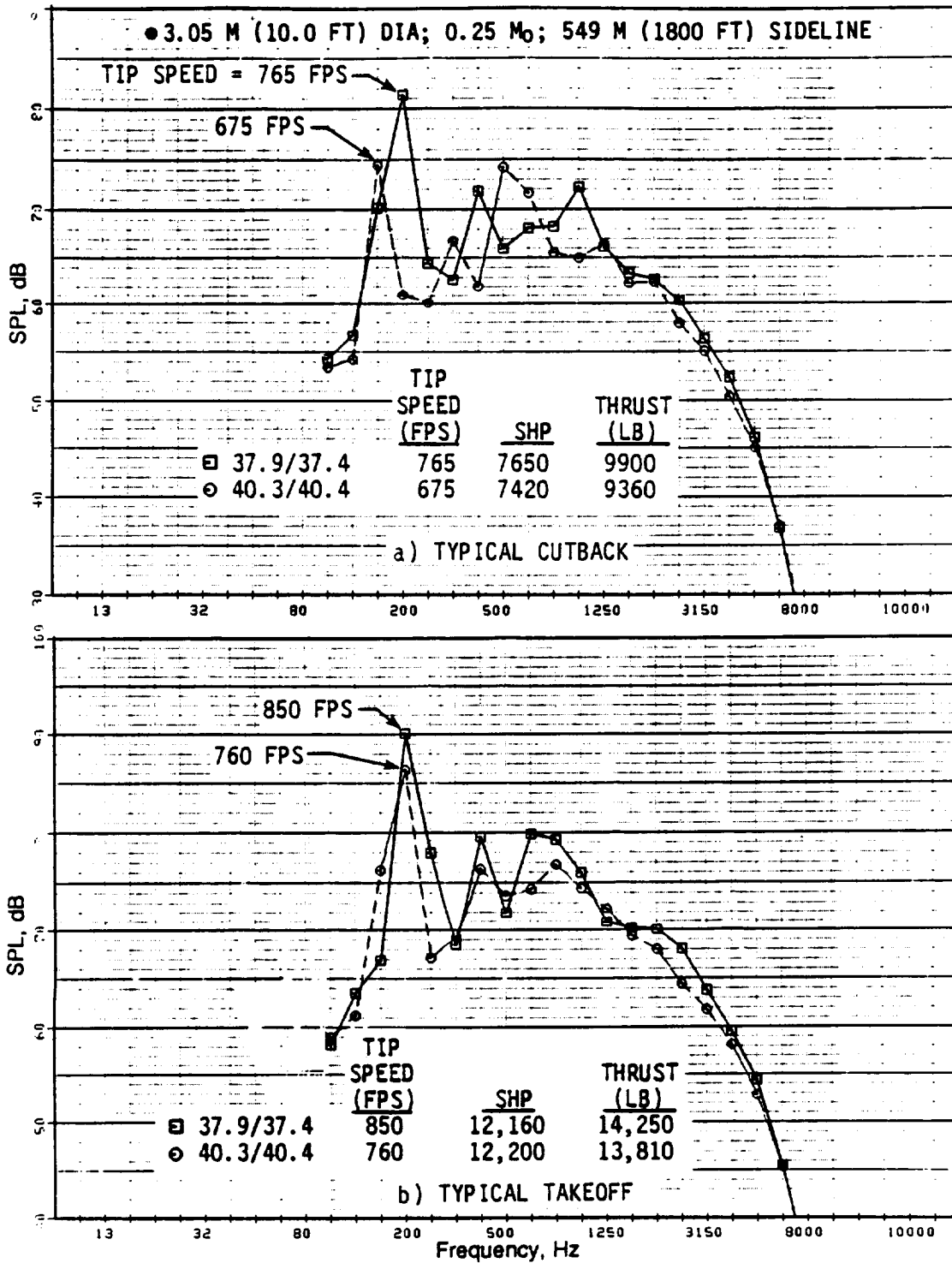


Figure 296. Spectra at an Emission Angle of 91° for the F-7/A-7 (8+8, Maximum Rotor Spacing) at Different Tip Speeds.

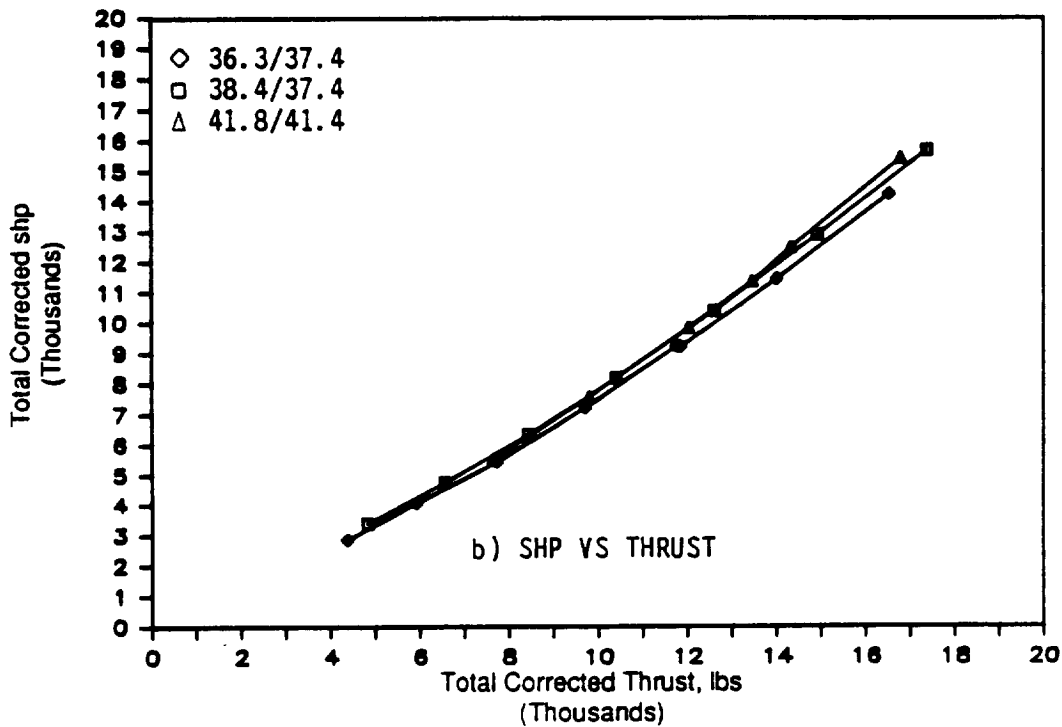
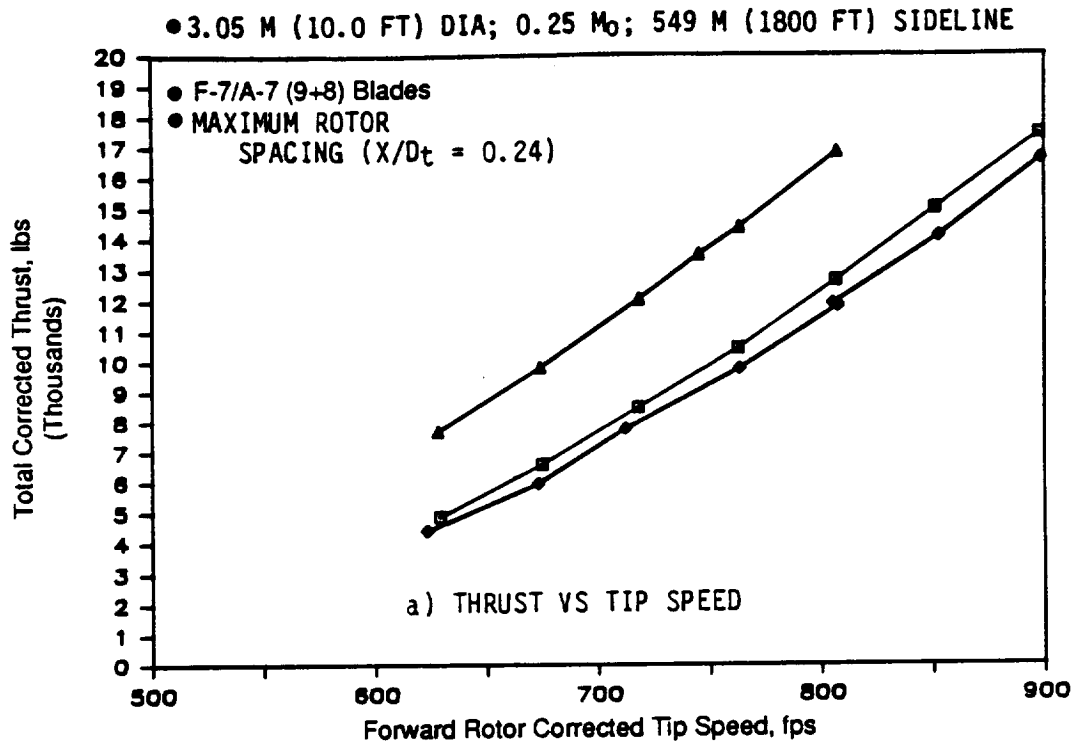


Figure 297. F-7/A-7 Aero Performance at Different Blade-Pitch Angles.

N (15,000 lb) was achieved at tip speeds of 268 mps (880 fps), 262 mps (860 fps), and 239 mps (785 fps), respectively. These pitch settings resulted in a cutback thrust of 44,500 N (10,000 lb) at sequentially reduced tip speeds of 236 mps (775 fps), 232 mps (760 fps), and 207 mps (680 fps), respectively. As with the F-7/A-7 (8+8) tests, decreased aerodynamic efficiency is noted with a decrease in tip speed for a given total thrust.

An acoustic data set similar to that of Series 1 is depicted in Figures 298 through 303. The scaled maximum noise level data of Figure 298 and the directivity data (Figures 299 and 300) reveal reductions of 3 dB at takeoff and 2 dB at cutback for the previously cited decrease in tip speeds. The 1/3-octave-band spectral data (Figure 301) also demonstrate a progressive decrease in SPL's at the BPF's with tip speed decrease; this indicating a decrease in steady-loading noise with reduced tip speed.

Figure 302 shows model-scale narrow-band spectra for typical takeoff and cutback at a microphone angle of 92°. Figure 303 compares model-scale tone sum level directivities of the loading noise for the aft and forward rotors, as well as the total steady-loading and rotor-to-rotor interaction noises for these test conditions. The expected decrease both in steady-loading tone and total steady-loading noise levels are noted at takeoff and cutback. Although a reduction is noted in the total interaction noise levels at takeoff (due to tip speed reduction), an increase is noted at cutback. Perhaps an increased wake strength with increased pitch angle is required to obtain an equivalent thrust at a lower tip speed.

Narrow-band spectra (Figure 302) also indicates an increase in the broadband noise at cutback with tip speed reduction. The combined effect of these observations at cutback is to indicate decreased total noise benefits with tip speed reduction at lower tip speeds than at takeoff tip speeds. Some of these observations with steady and interaction noise levels are demonstrated in the model-scale tone sum data provided (Figure 304) as a function of total thrust.

This discussion of the F-7/A-7 (9+8) data is concluded with Figure 305 depicting the impact of tip speed decrease on EPNL, indicating a decrease of 2 EPNdB for corresponding reductions in tip speeds from 268 mps (880 fps) to 239 mps (880 fps) at takeoff, and from 236 mps (775 fps) to 207 mps (680 fps) at cutback.

7.1.1.5.4 F-7/A-7c (9+8) at Maximum Rotor Spacing: Series 4

This test series is similar to those conducted in Series 3 except the aft blades are clipped at 75% of their span. A schematic comparing planforms of the clipped and unclipped (F-7/A-7c and F-7/A-7) configurations was presented previously (Figure 266). Aeroperformance data for the clipped series at the pitch angles of 36.3°/42.7° and 41.8°/48.3° are presented in Figure 306. Further, thrust versus tip speed data demonstrate that, with the pitch settings used in these tests, the typical takeoff thrust 66,700 N (15,000 lb) was achieved at tip speeds of 270 mps (885 fps) and 247 mps (810 fps), and the typical cutback thrust of 44,500 N (10,000 lb) was obtained at tip speeds of 239 mps (785 fps) and 213 mps (700 fps). As with the unclipped blades, decreased aerodynamic efficiency required more power to be absorbed at a lower tip speed for a given thrust.

Figure 307 compares acoustic data (in terms of scaled and maximum OASPL, PNL, and dBA) as a function of total thrust. Despite a 2 dB reduction noted in the maximum OASPL data, no benefit is observed in the maximum PNL or dBA for decreased tip speeds for a given thrust. This is confirmed by directivity data of Figure 308. Again, typical spectral comparison (Figure 309) indicates a reduction in the level associated with the BPF and, therefore, the steady-loading noise.

● 3.05 M (10.0 FT) DIA; 0.25 M₀; 549 M (1800 FT) SIDELINE

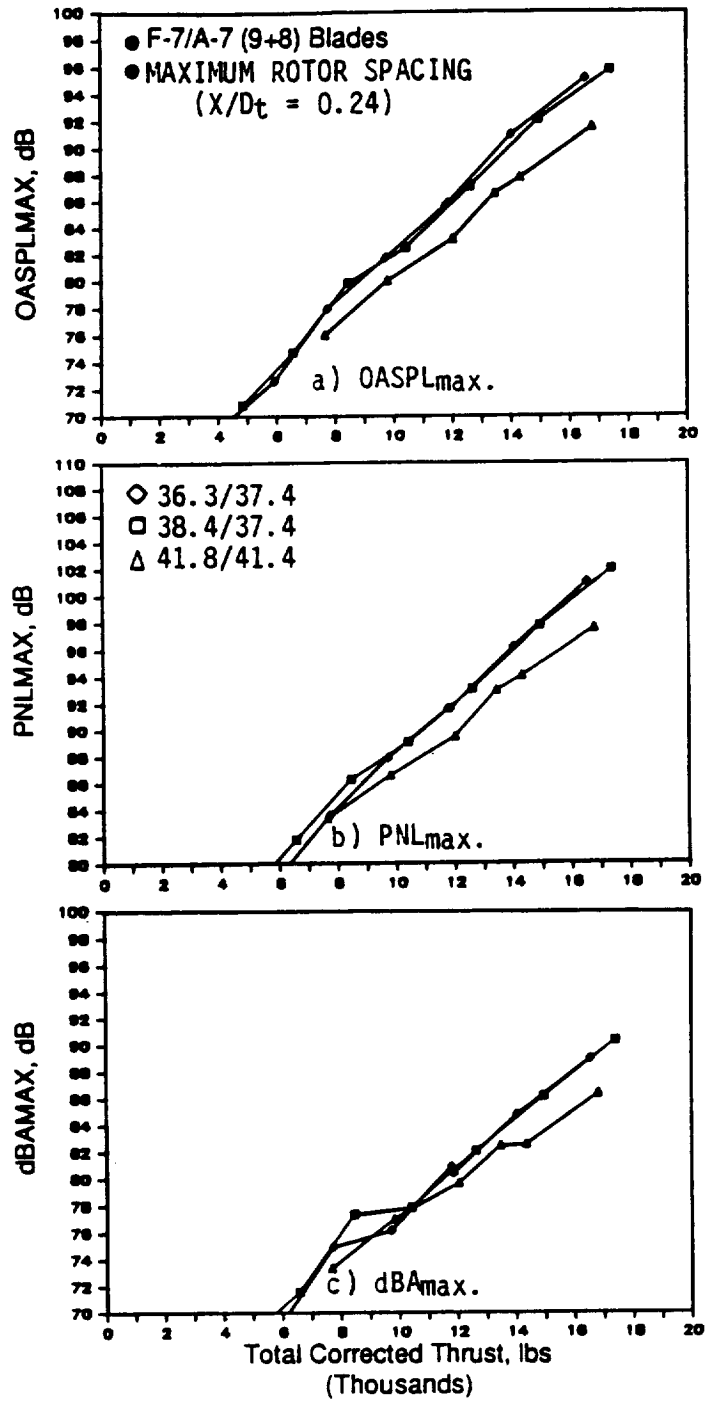


Figure 298. F-7/A-7 Acoustic Data at Different Blade-Pitch Angles.

● 3.05 M (10.0 FT) DIA; 0.25 M₀; 549 M (1800 FT) SIDELINE

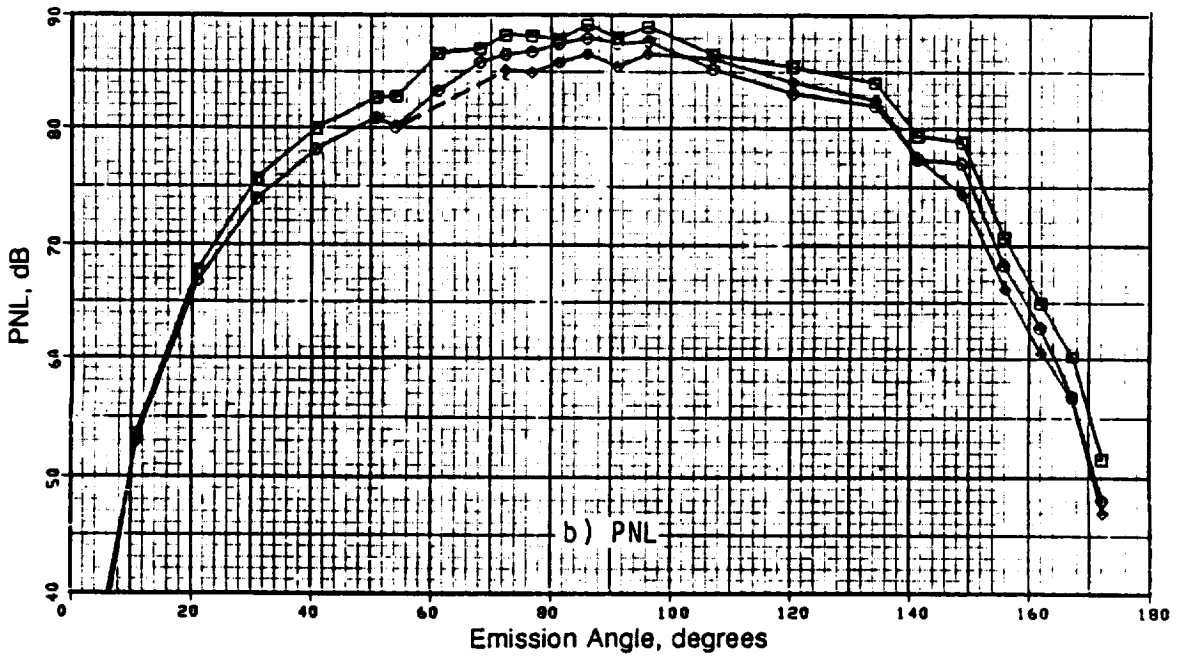
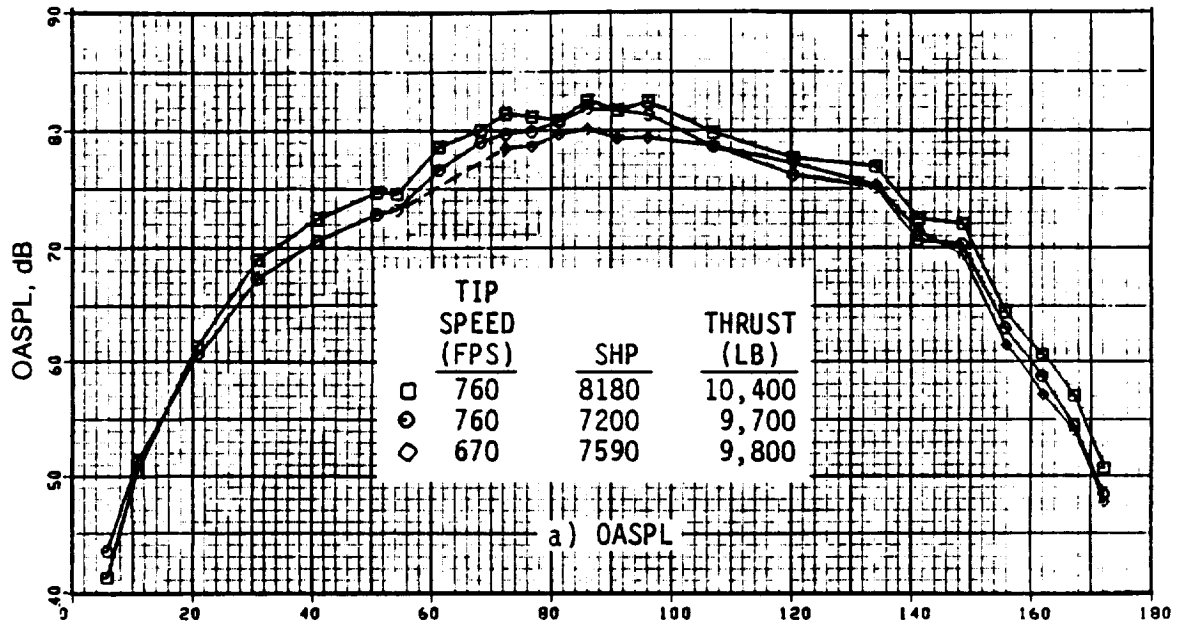


Figure 299. OASPL and PNL Directivities of F-7/A-7 (9+8, Maximum Rotor Spacing) at Different Tip Speeds for a Typical Cutback.

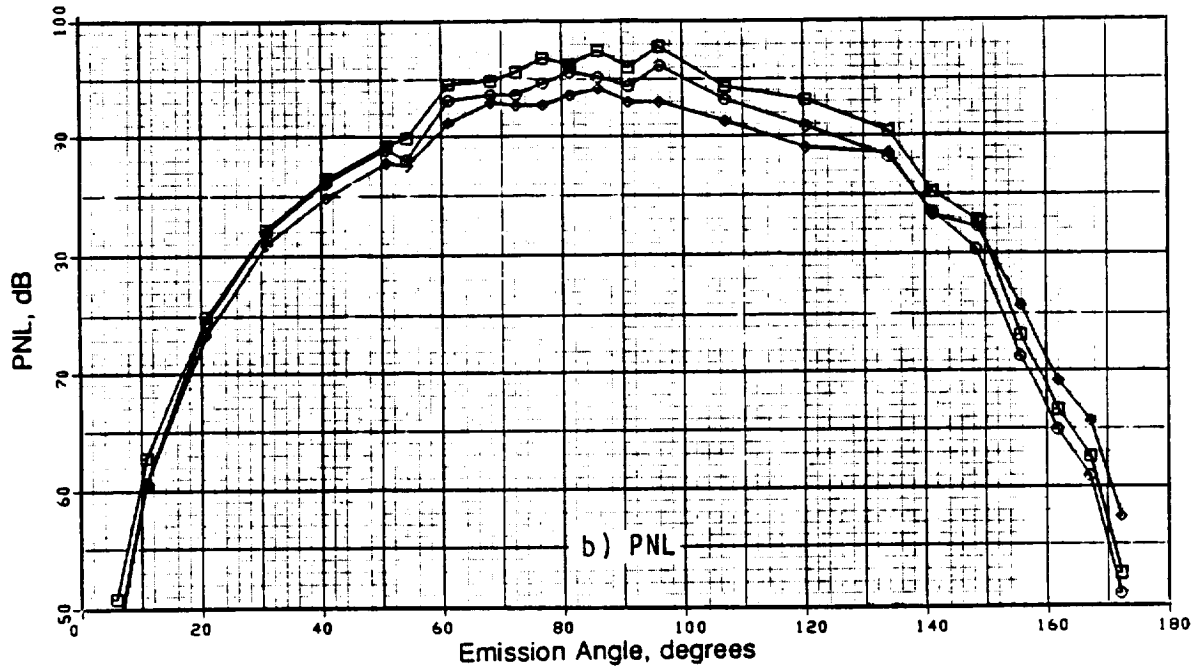
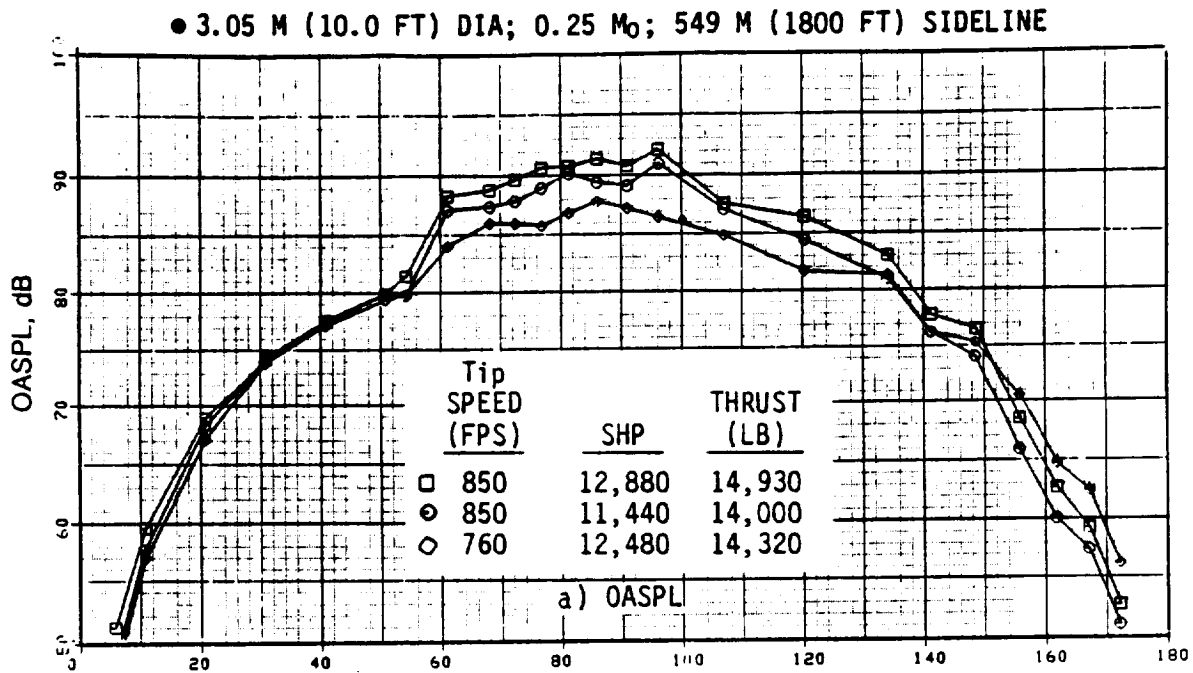


Figure 300. OASPL and PNL Directivities of F-7/A-7 (9+8, Maximum Rotor Spacing) at Different Tip Speeds at Takeoff.

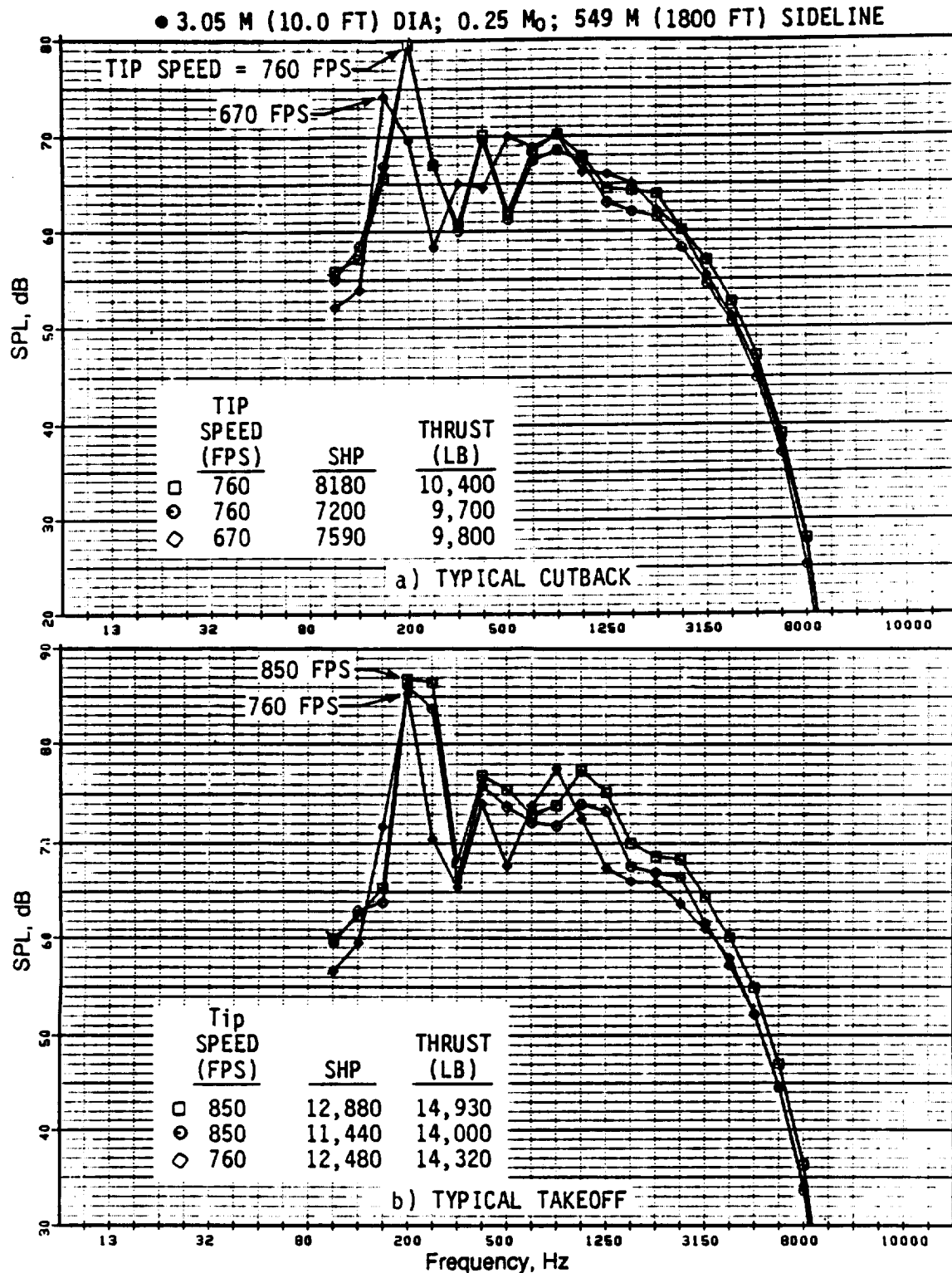
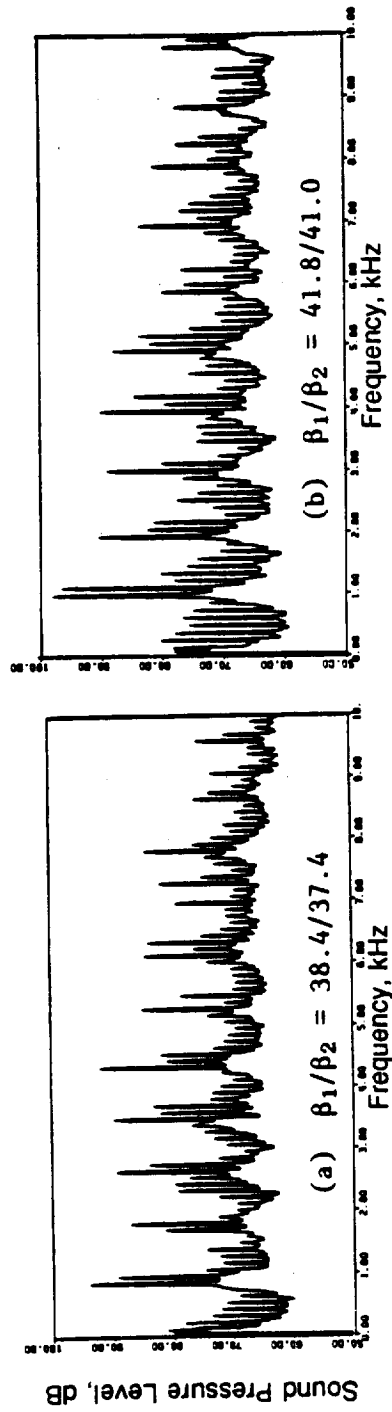


Figure 301. Spectra at an Emission Angle of 91° for the F-7/A-7 (9+8, Maximum Rotor Spacing) at Different Tip Speeds.

MODEL SCALE; AS MEASURED DATA
 F7A7; 9x8 BLADES; MAXIMUM ROTOR SPACING ($X/D_t = 0.24$)
 MICROPHONE ANGLE, $\theta_m = 92^\circ$



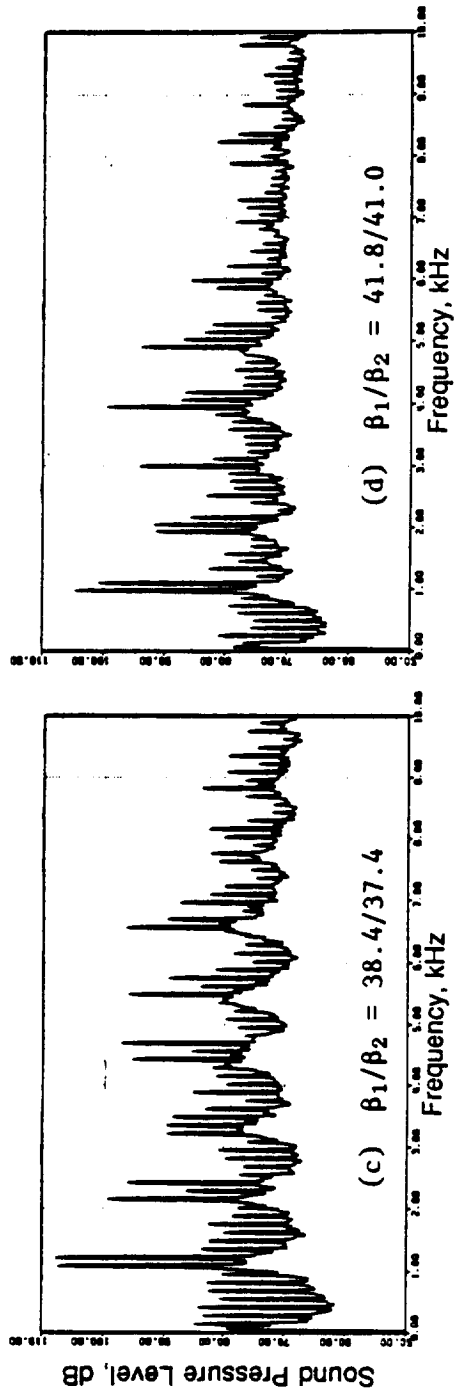
TIP SPEED = 233 MPS (760 FPS)
 THRUST = (434 LB)
 POWER = (340 SHP)

205 MPS (670 FPS)
 (410 LB)
 (320 SHP)

● Cutback

Figure 302. Selected Typical Model-Scale Narrow-Band Spectra of F-7/A-7 for Different Tip Speeds.

MODEL SCALE; AS MEASURED DATA
 F7A7; 9x8 BLADES; MAXIMUM ROTOR SPACING (X/Dt = 0.24)
 MICROPHONE ANGLE, $\theta_m = 92^\circ$



TIP SPEED = 260 MPS (850 FPS)
 THRUST = 2760 (620 LB)
 POWER = 399 KW (535 SHP)

232 MPS (760 FPS)
 2670 N (600 LB)
 388 KW (520 SHP)

● Takeoff

Figure 302. Selected Typical Model-Scale Narrow-Band Spectra of F-7/A-7 for Different Tip Speeds (Concluded).

- MODEL SCALE; 8.2 M (27 FT) SIDELINE; 0.25 M₀
- 12.5 HZ NARROWBAND DATA

- TIP SPEED = 233 MPS (760 FPS) ○ 205 MPS (670 FPS)
- THRUST = (434 LB) (410 LB)
- POWER = (340 SHP) (320 SHP)

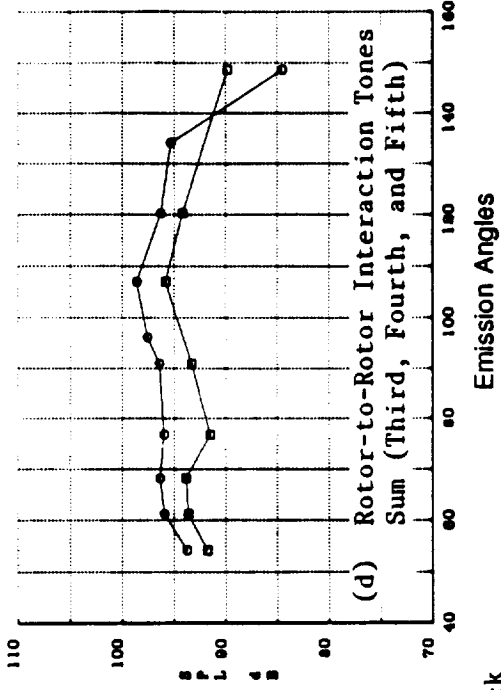
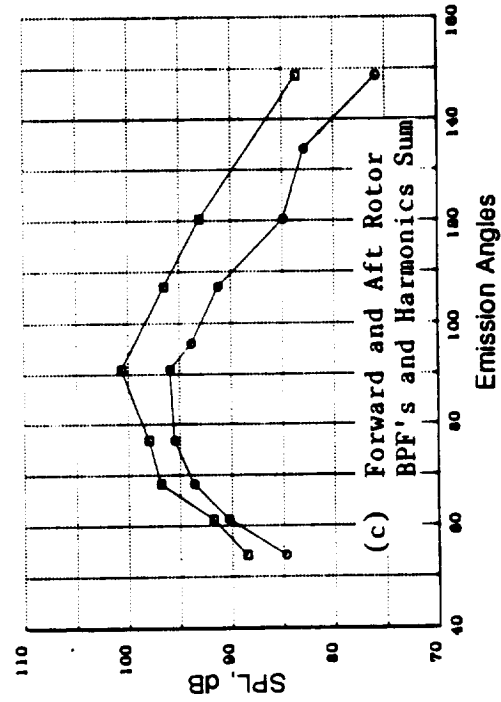
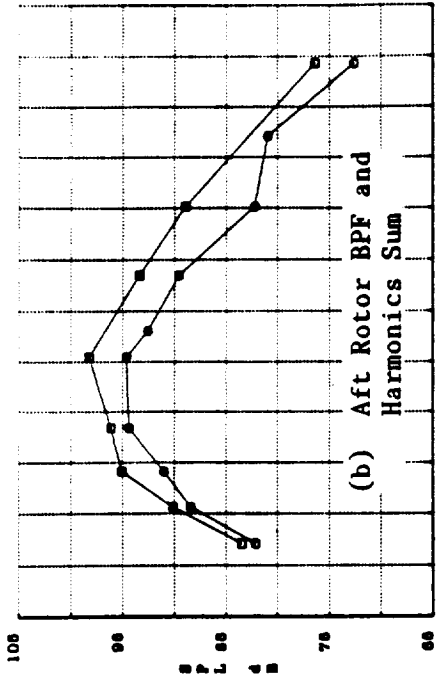
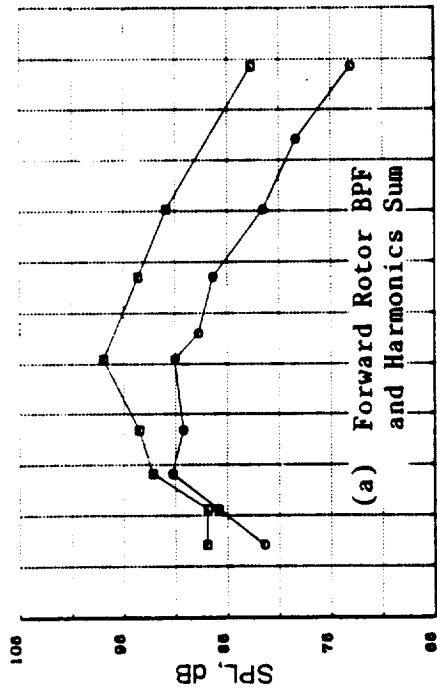
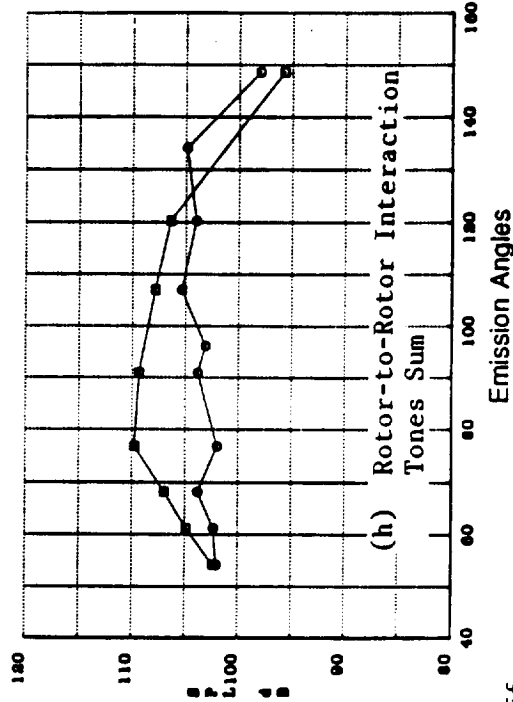
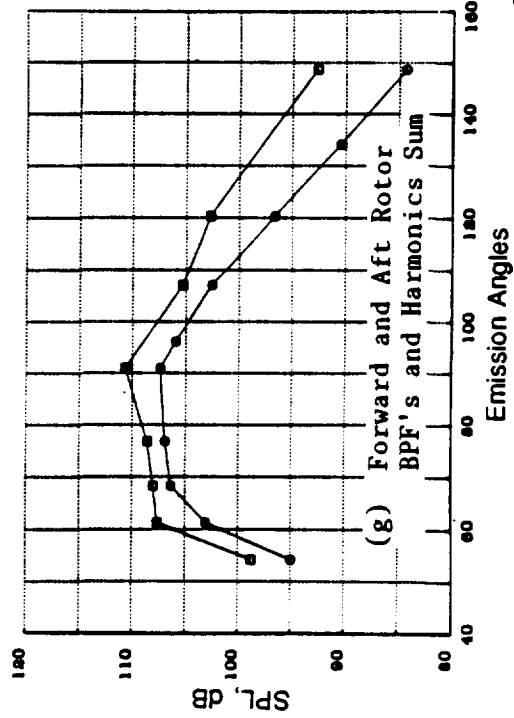
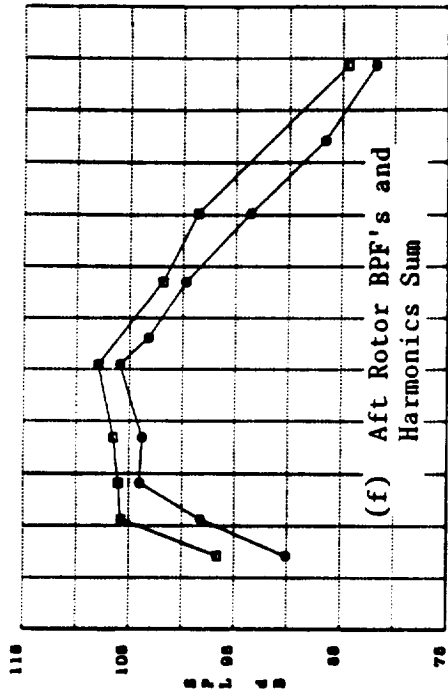
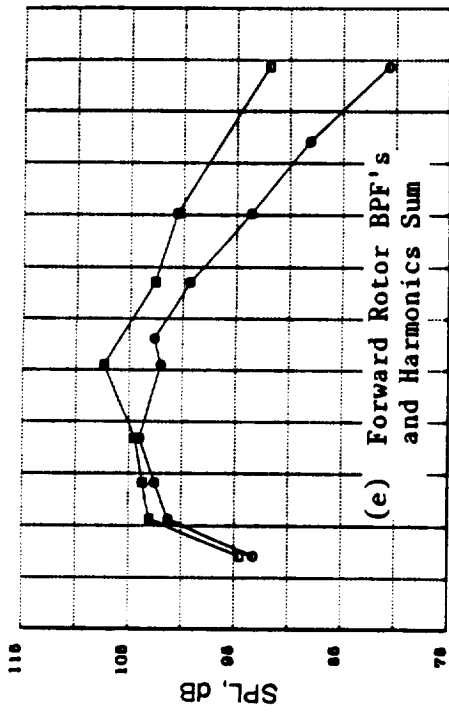


Figure 303. Model-Scale Typical Tone Sum Level Directivities of F-7/A-7 (9+8, Maximum Rotor Spacing) for Different Tip Speeds.

● MODEL SCALE; 8.2 M (27 FT) SIDELINE; 0.25 M₀
 ● 12.5 Hz NARROWBAND DATA

TIP SPEED = □ 260 MPS (850 FPS) ○ 232 MPS (760 FPS)
 THRUST = 2760 (620 LB) 2670 N (600 LB)
 POWER = 399 KW (535 SHP) 388 KW (520 SHP)



● Takeoff

Figure 303. Model-Scale Typical Tone Sum Level Directivities of F-7/A-7 (9+8, Maximum Rotor Spacing) for Different Tip Speeds (Concluded).

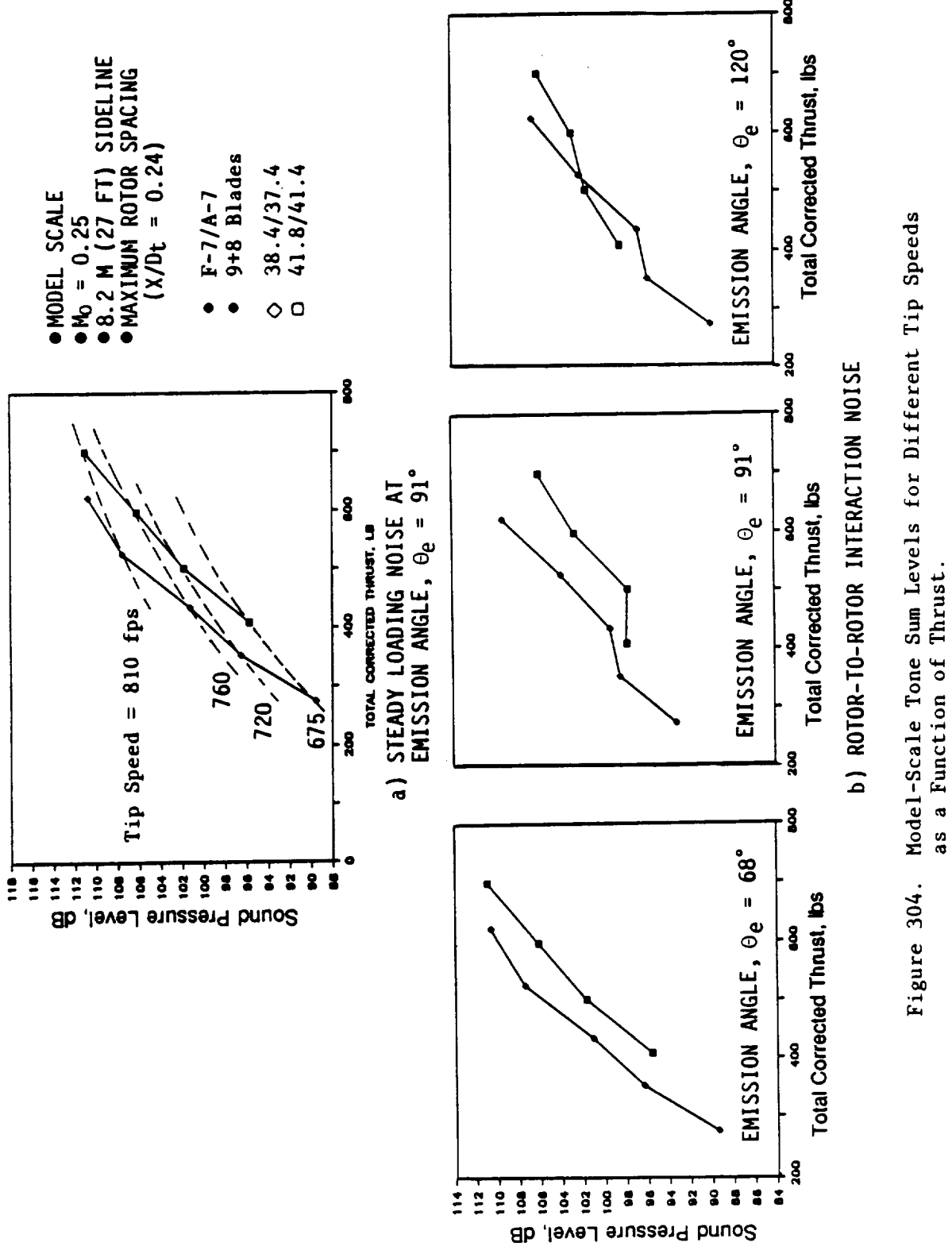


Figure 304. Model-Scale Tone Sum Levels for Different Tip Speeds as a Function of Thrust.

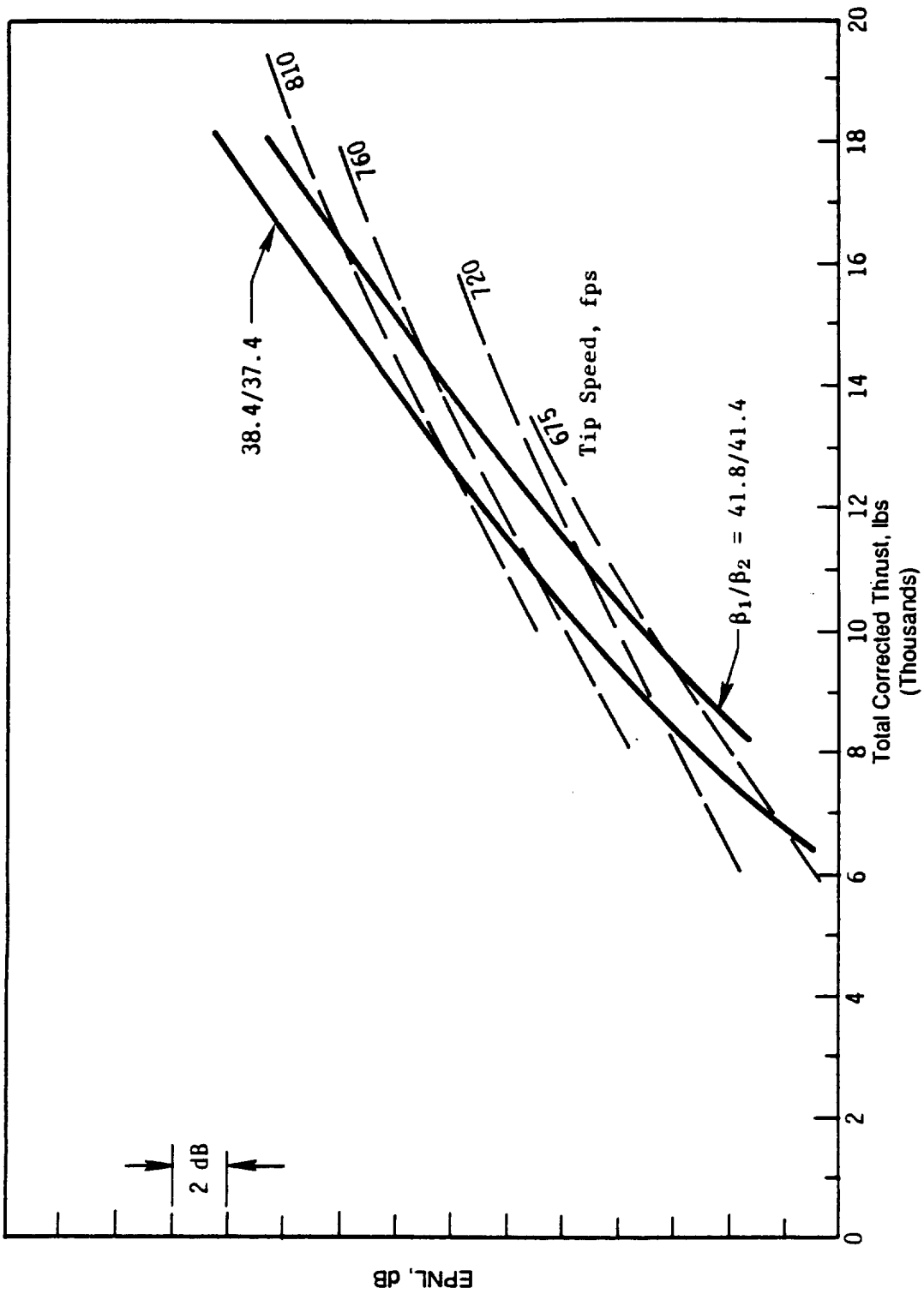


Figure 305. Benefit of Reduced Tip Speed on EPNL of F-7/A-7 (9+8, Maximum Rotor Spacing).

● 3.05 M (10.0 FT) DIA; 0.25 M_0 ; 549 M (1800 FT) SIDELINE

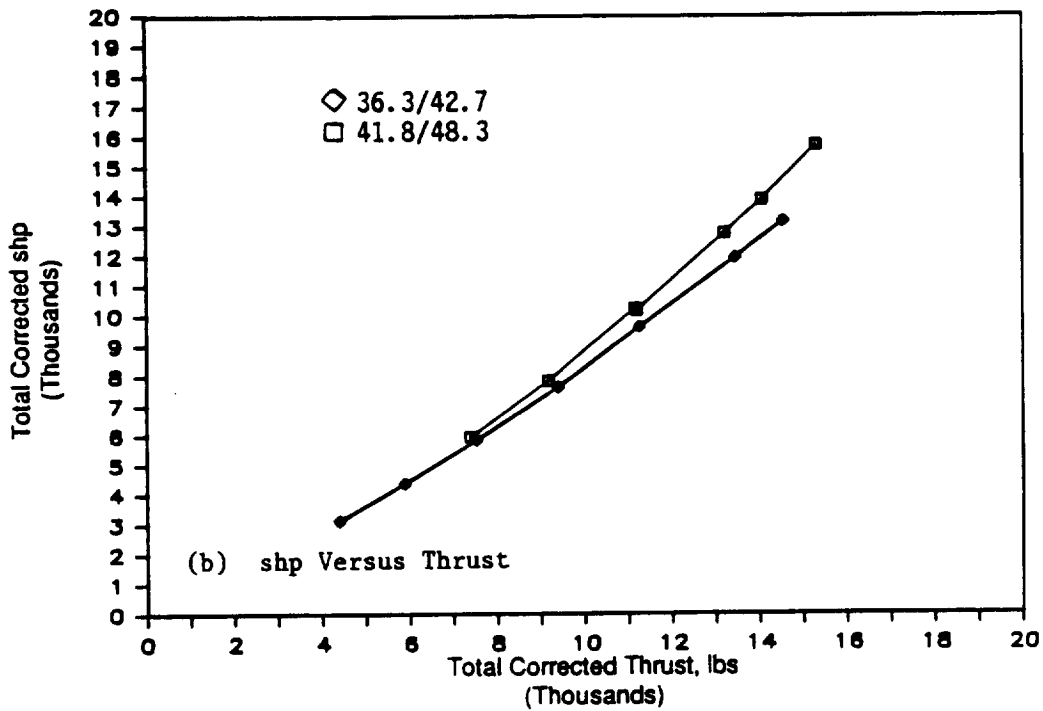
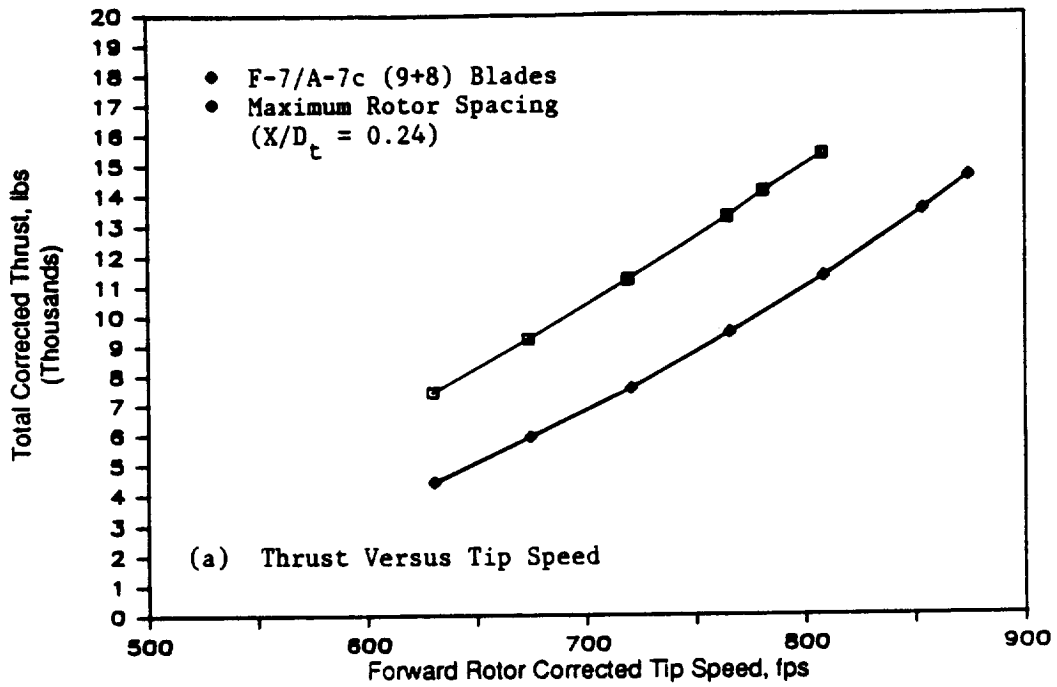


Figure 306. Aero Performance of the F-7/A-7c (Clipped) at Different Blade-Pitch Angles.

● 3.05 M (10.0 FT) DIA; 0.25 M_0 ; 549 M (1800 FT) SIDELINE

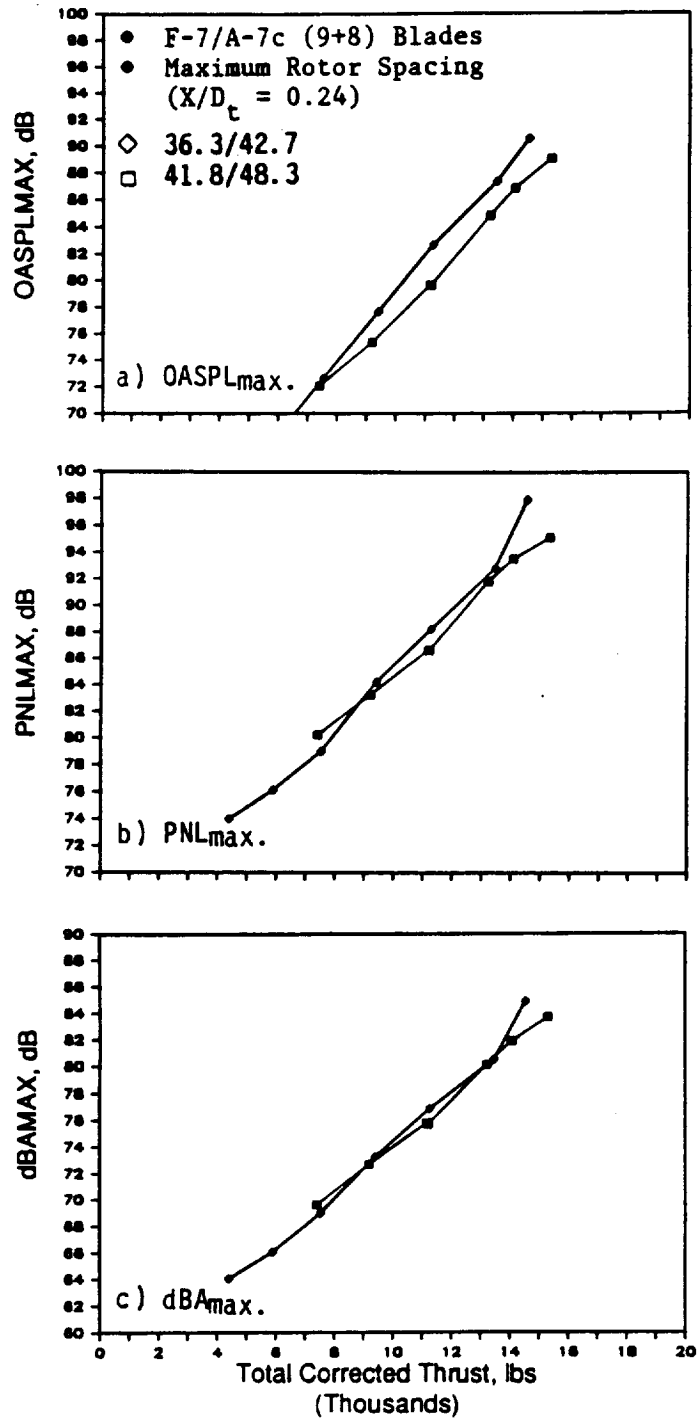


Figure 307. Acoustic Data at Different Blade-Pitch Angles.

C.6

● 3.05 M (10.0 FT) DIA; 0.25 M₀; 549 M (1800 FT) SIDELINE

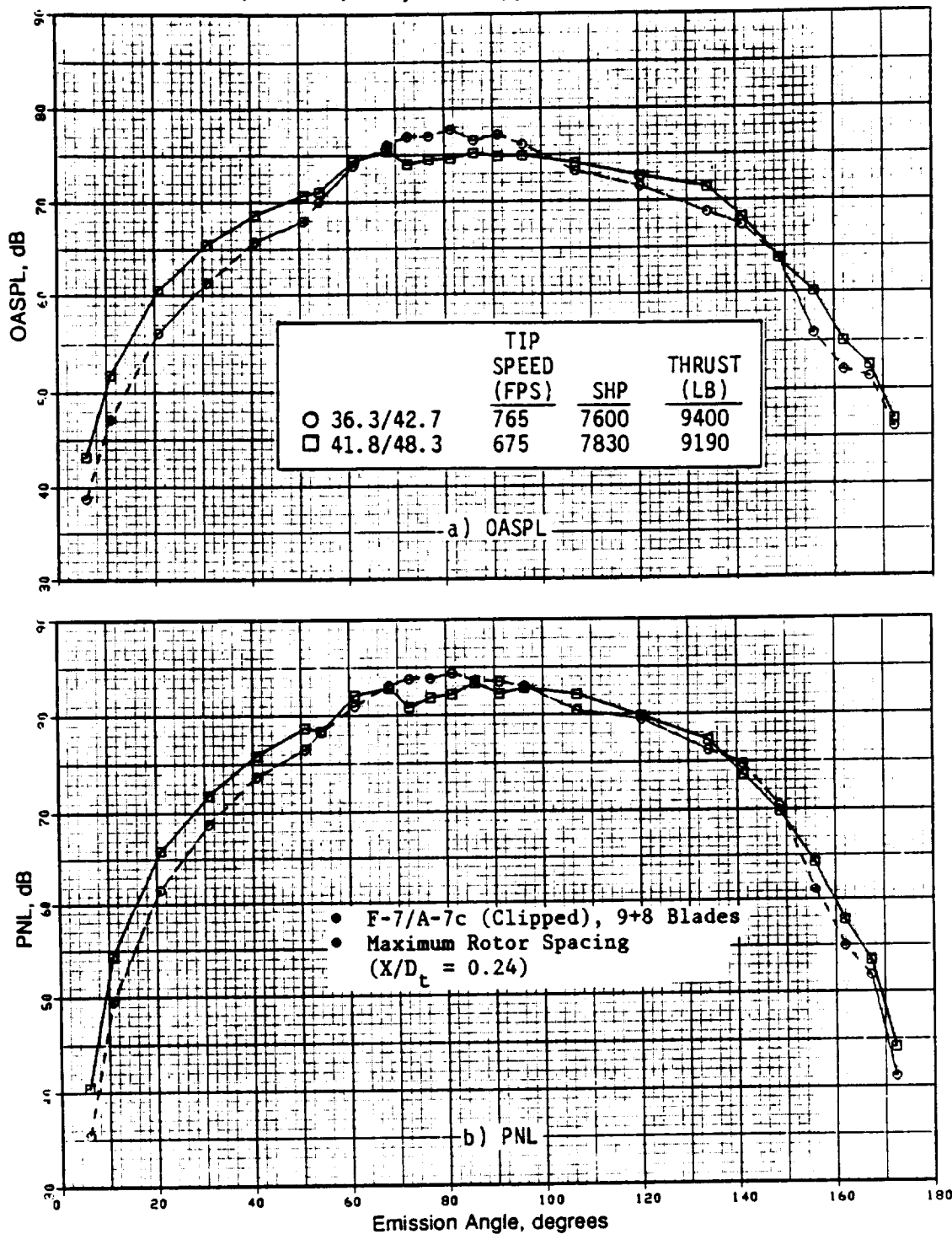


Figure 308. OASPL and PNL Directivities for Different Tip Speeds at a Typical Cutback.

• 3.05 M (10.0 FT) DIA; 0.25 M₀; 549 M (1800 FT) SIDELINE

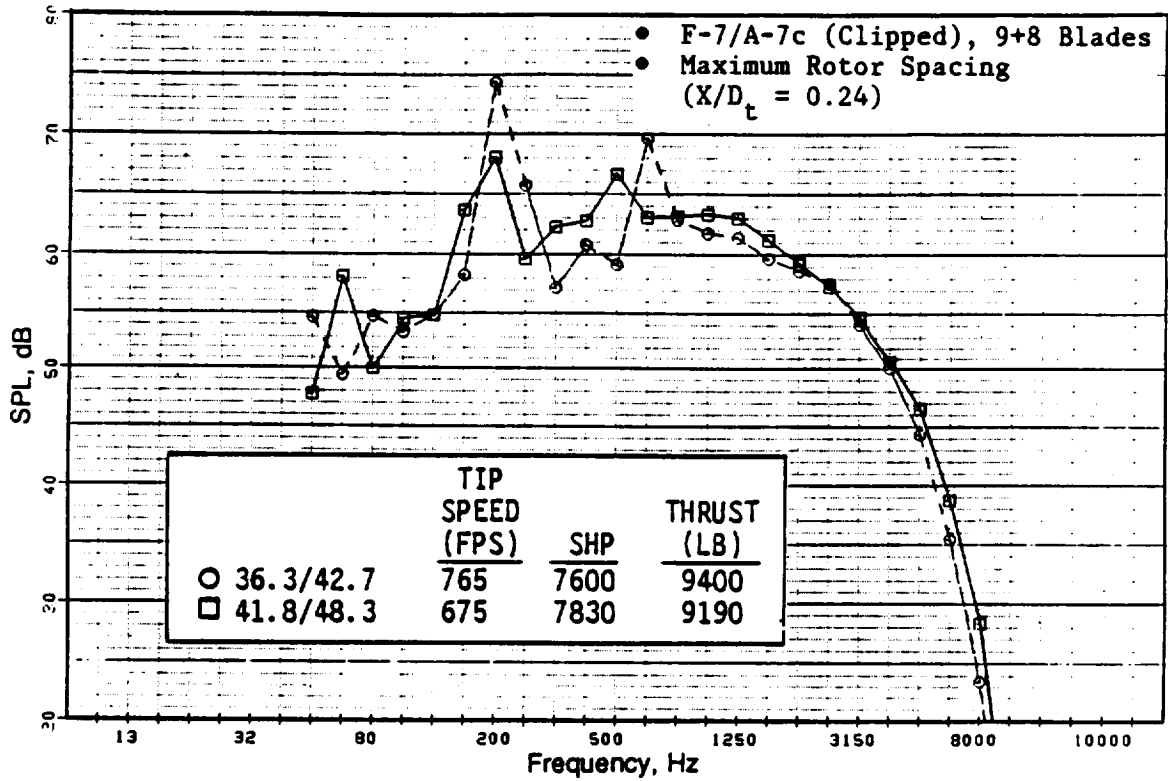


Figure 309. Spectra (Emission Angle, 91°) for Different Tip Speeds at Typical Cutback.

A set of narrow-band data is illustrated in Figures 310 through 312. The narrow-band spectra (Figure 310) depicts the increase in broadband levels with a corresponding decrease of tip speed for a given thrust. Although the sum tone data (Figures 311 and 312) indicate a reduction in the steady-loading noise of both rotors, no significant impact is noted with the total rotor-to-rotor interaction tone sums with decreasing tip speeds. Unlike the unclipped F-7/A-7, the combined effects of these changes have no significant impact on the EPNL values due to reduced tip speeds. This suggests a different impact of tip-speed changes on the wake interaction and tip-vortex interaction noise components.

7.1.1.5.5 F-11/A-11 (11+9) Blades at Maximum Rotor Spacing: Series 5

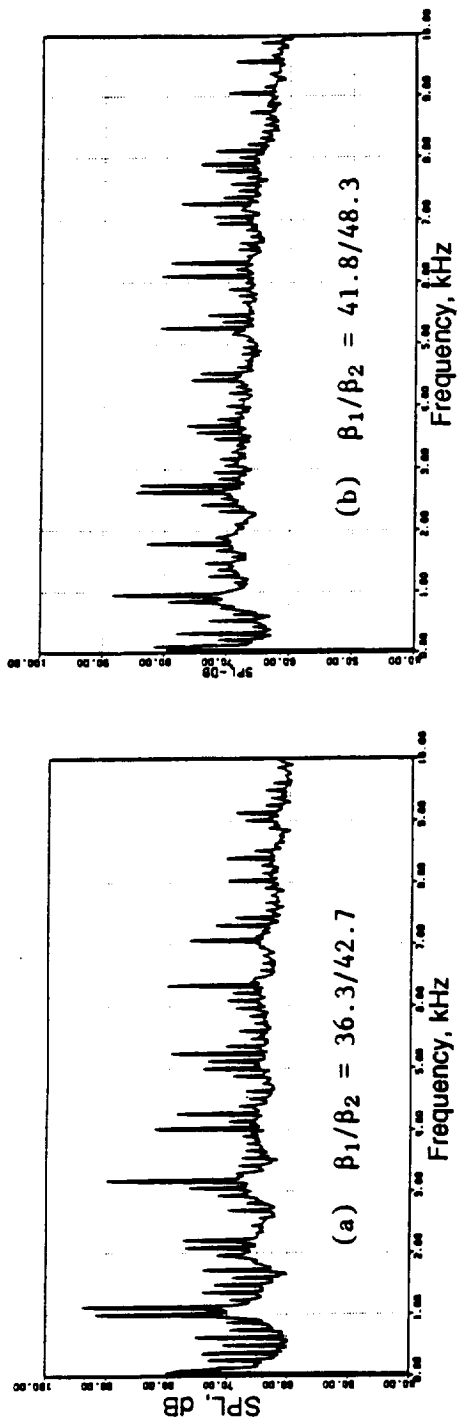
The F-11/A-11 (11+9) blade configuration at the maximum rotor spacing ($X/D_t = 0.24$) was tested at pitch angles of: $38.7^\circ/38.9^\circ$, $44.8^\circ/43.3^\circ$, $48.7^\circ/45.3^\circ$, and $54.2^\circ/47.5^\circ$. Increased blade-pitch-angle effects on the normalized spacing between the trailing edge of a forward blade and the quarter-chord point of an aft blade are illustrated in Figure 313, indicating a progressive decrease in this effective spacing with an increase in blade-pitch setting that is needed for reduced tip speeds for a given thrust.

The total thrust and power data are presented in Figure 314, except data from the pitch setting $44.8^\circ/43.3^\circ$, as those test data were questionable due to a problem with the telemetry system. Thrust versus tip speed data indicate that the test pitch settings of $38.7^\circ/38.9^\circ$, $48.7^\circ/45.3^\circ$, and $54.2^\circ/47.5^\circ$ resulted in typical takeoff thrust of 66,700 N (15,000 lb) at correspondingly reduced tip speeds of 256 mps (840 fps), 210 mps (690 fps), and 198 mps (650 fps). The thrust versus power data prove that to attain this thrust, successively increased absorption powers of 9,700 kW (13,000 shp), 10,440 kW (14,000 shp), and 11,190 kW (15,000 shp) are required due to the decreased aerodynamic efficiency with reduced tip speeds. Tip speeds for a cutback thrust of 44,500 N (10,000 lb) are observed to be 225 mps (740 fps), 186 mps (610 fps), and 172 mps (565 fps) for the test pitch angles used in this series of tests.

Figure 315 identifies acoustic data (in terms of the scaled and maximum OASPL, PNL, and dBA), as a function of total thrust, indicating reductions in peak noise levels to be in the range of 2 dB to 3 dB for an open pitch setting of $48.7^\circ/45.3^\circ$, compared to the nominal pitch setting of $38.7^\circ/38.9^\circ$. However, a more open condition ($54.2^\circ/47.5^\circ$) reverses this trend and increases the noise level, relative to the open pitch condition of $48.7^\circ/45.3^\circ$, by about 1 dB. The typical directivity at takeoff thrust (Figure 316) confirms this trend between the three data sets over an emission angle range of 60° to 120° .

Figure 316 also compares typical spectra for these test conditions, and although indicating progressive reduction in the sound pressure levels at the BPF's, increases in the levels of the third harmonic are noted for successive increases of tip speeds. The increased pitch angle needed to produce a given thrust at a lower tip speed results in a stronger wake which, combined with the accompanying reduction in the spacing between blades (Figure 313), causes the rotor-to-rotor interaction noise to increase for large reductions of tip speeds. Furthermore, successively lowering the tip speeds for a given thrust results in increased broadband noise levels, as seen from the typical narrow-band spectra in Figure 317 for typical takeoff and cutback conditions.

- MODEL SCALE: AS MEASURED DATA
- F-7/A-7 Clipped; 9+8 Blades, Maximum Rotor Spacing ($X/D_1 = 0.24$)
- MICROPHONE ANGLE, $\Theta_m = 92^\circ$



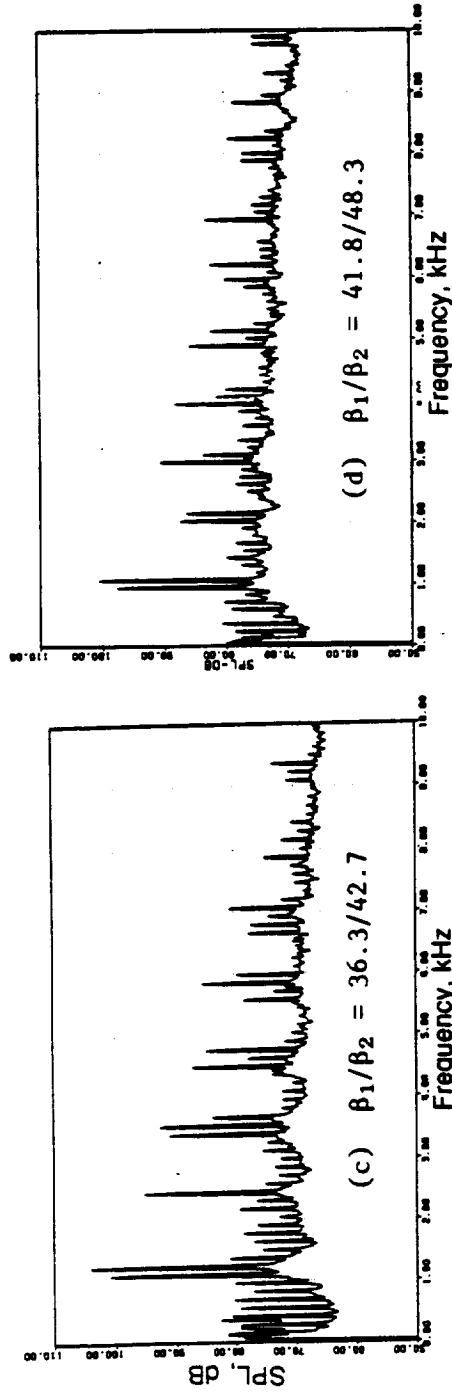
TIP SPEED = 233 MPS (765 FPS)
 THRUST = 1735 N (390 LB)
 POWER = 239 KW (320 SHP)

204 MPS (670 FPS)
 1690 N (380 LB)
 264 KW (330 SHP)

● Cutback

Figure 310. Selected Typical Model-Scale Narrow-Band Spectra of F-7/A-7c (Clipped) for Different Tip Speeds.

- MODEL SCALE; AS MEASURED DATA
- F-7/A-7 Clipped; 9+8 Blades, Maximum Rotor Spacing ($X/D_t = 0.24$)
- MICROPHONE ANGLE, $\theta_m = 92^\circ$



TIP SPEED = 260 MPS (850 FPS)
 THRUST = 2490 N (560 LB)
 SHP = 369 KW (495 SHP)

233 MPS (765 FPS)
 2450 N (551 LB)
 395 KW (531 SHP)

● Takeoff

Figure 310. Selected Typical Model-Scale Narrow-Band Spectra of F-7/A-7c (Clipped) for Different Tip Speeds (Concluded).

● MODEL SCALE; 8.2 M(27 FT.) SIDELINE
 ● 12.5 HZ NARROWBAND DATA ; MODEL THRUST=1800 N(400 LB)

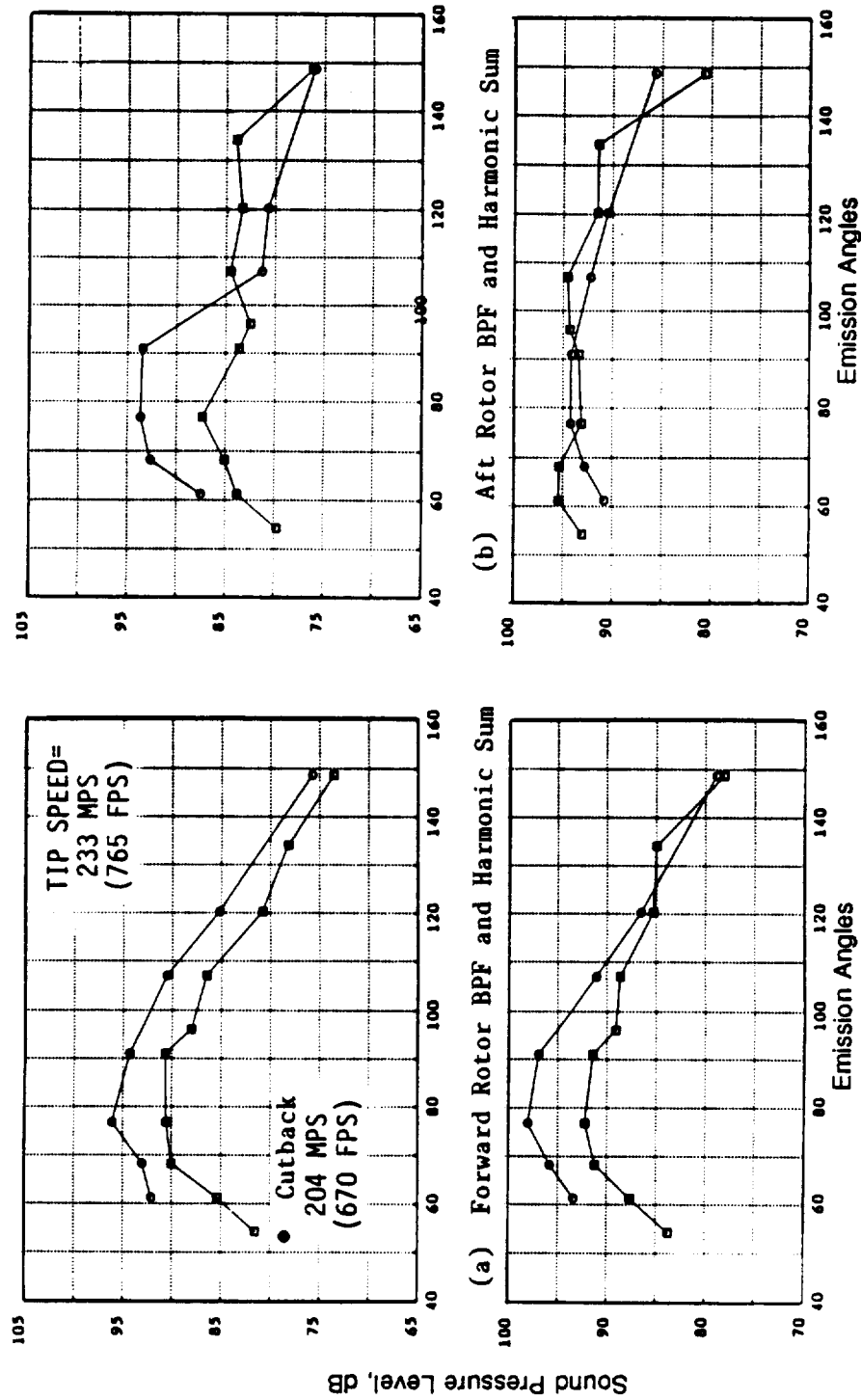


Figure 311. Model-Scale Tone Sum Level Directivities of Clipped F-7/A-7 for Different Tip Speeds.

● MODEL SCALE; 8.2 M(27 FT.) SIDELINE
 ● 12.5 HZ NARROWBAND DATA; THRUST=2450 N(550 LB)

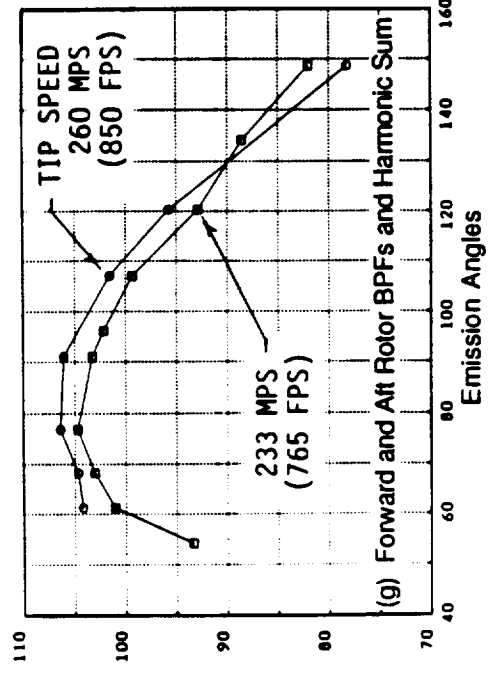
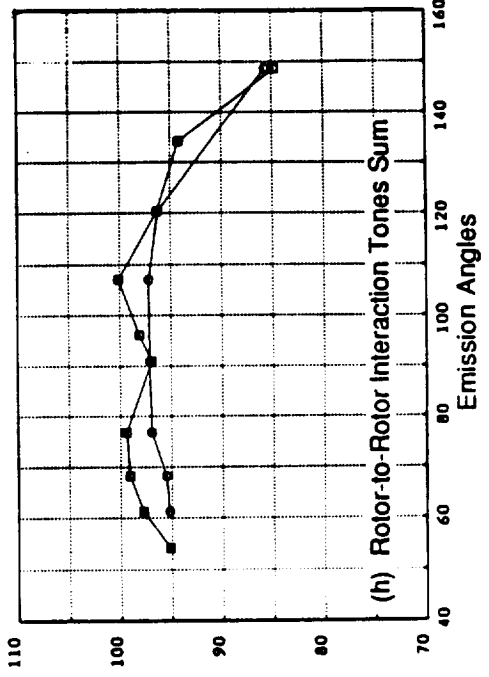
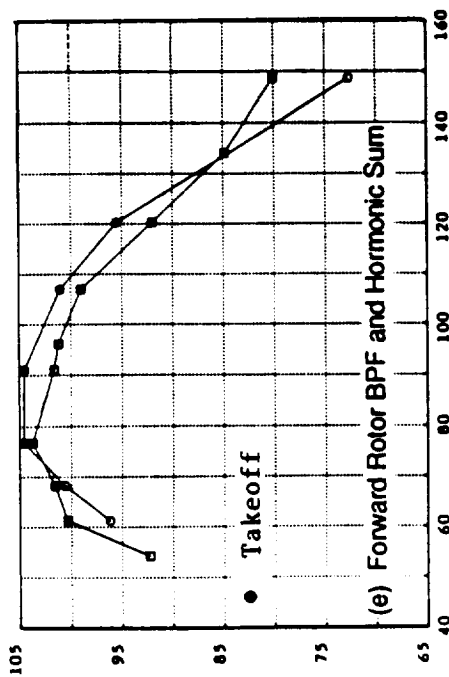
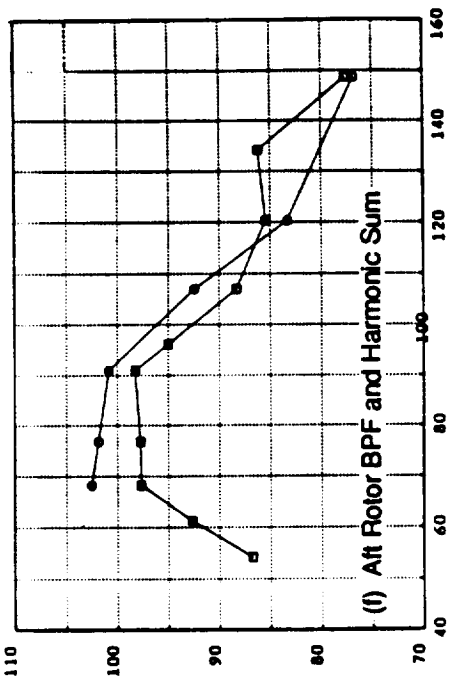


Figure 311. Model-Scale Tone Sum Level Directivities of Clipped F-7/A-7 for Different Tip Speeds (Concluded).

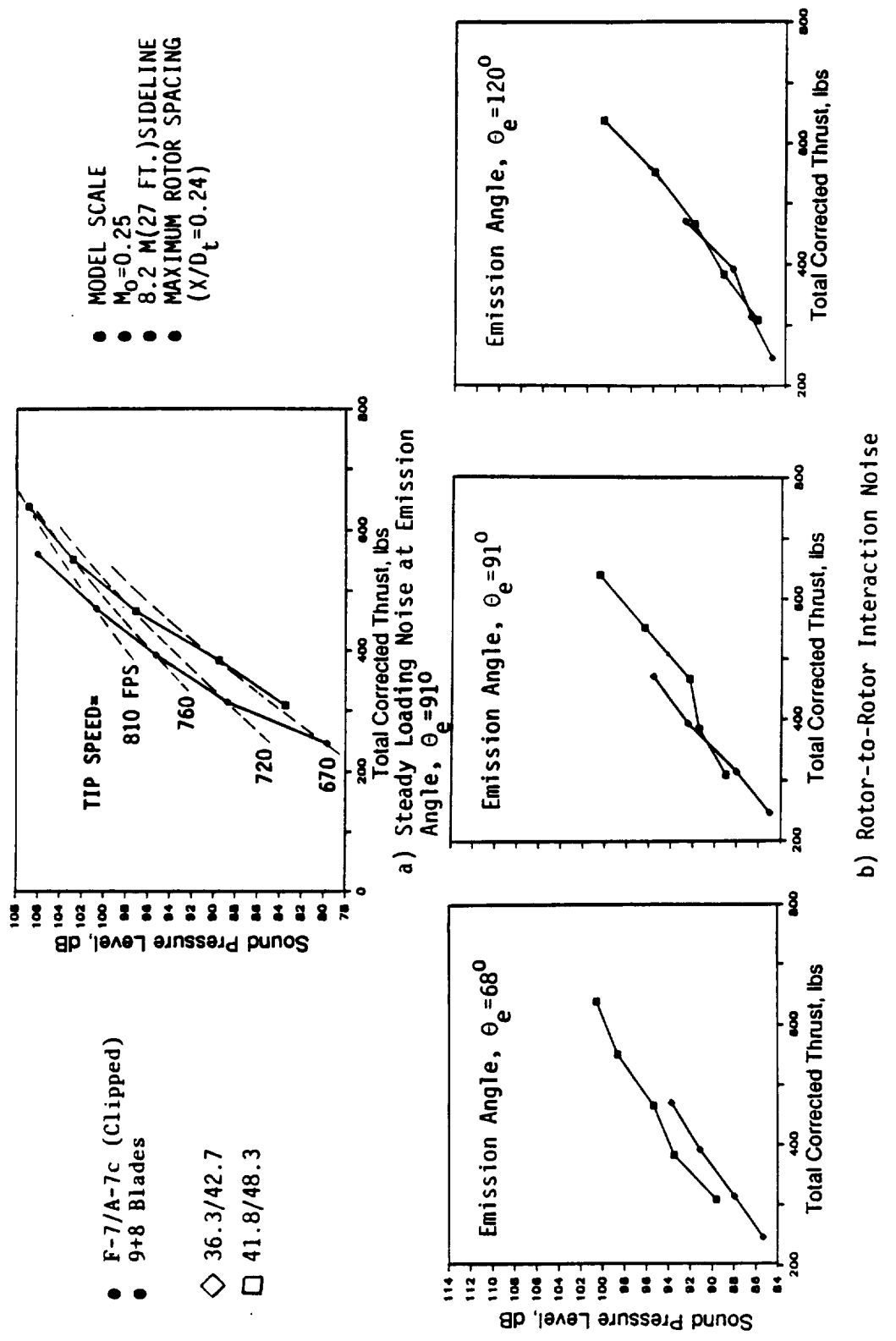


Figure 312. Model-Scale Tone Sum Levels for Different Tip Speeds as a Function of Thrust.

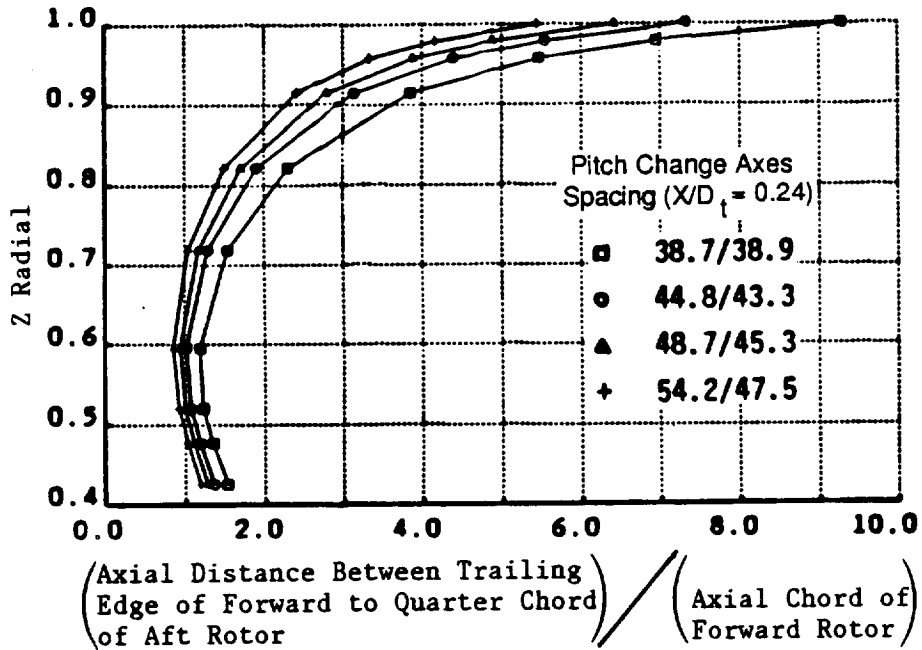


Figure 313. Variation in Blade Spacing as a Function of Radii for F-11/A-11 for Different Test Pitch Angles.

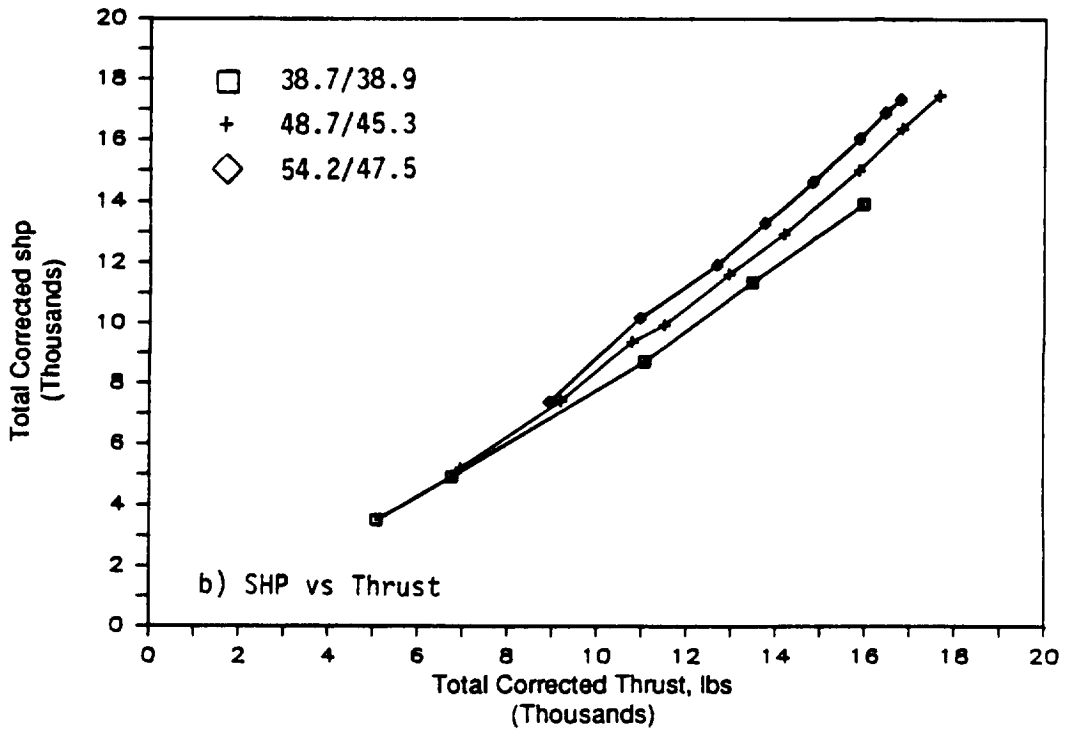
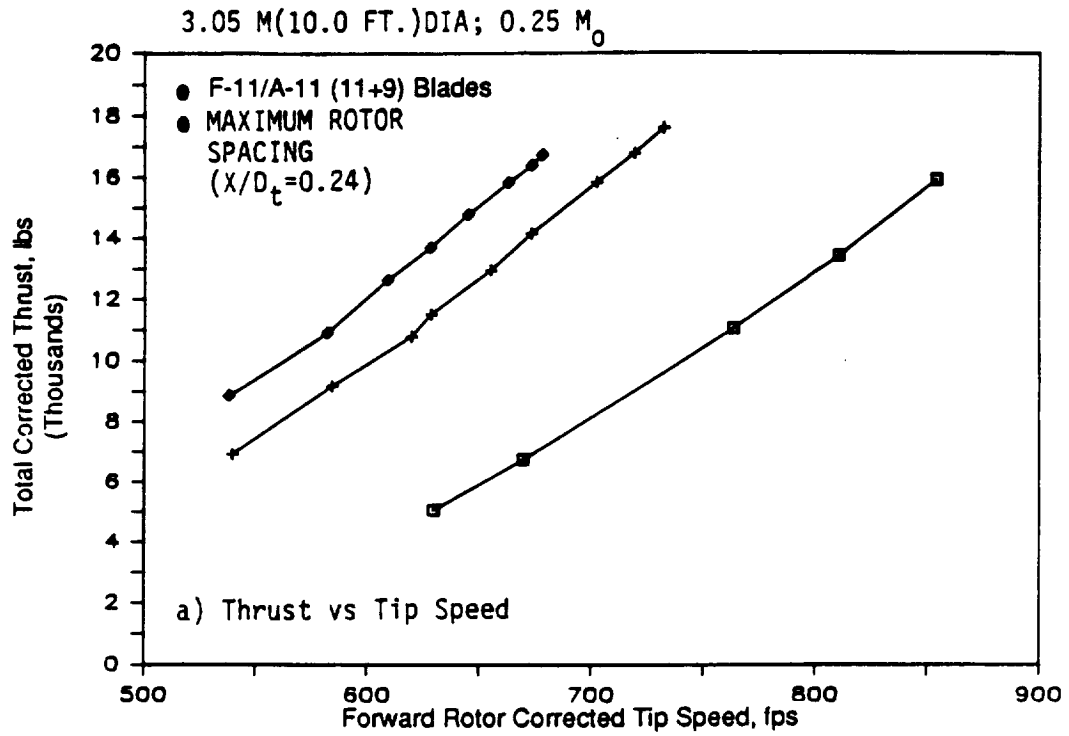


Figure 314. F-11/A-11 Aero Performance at Different Blade-Pitch Angles.

3.05 M(10.0 FT.)DIA; 0.25 M₀; 549 M(1800 FT.)SIDELINE

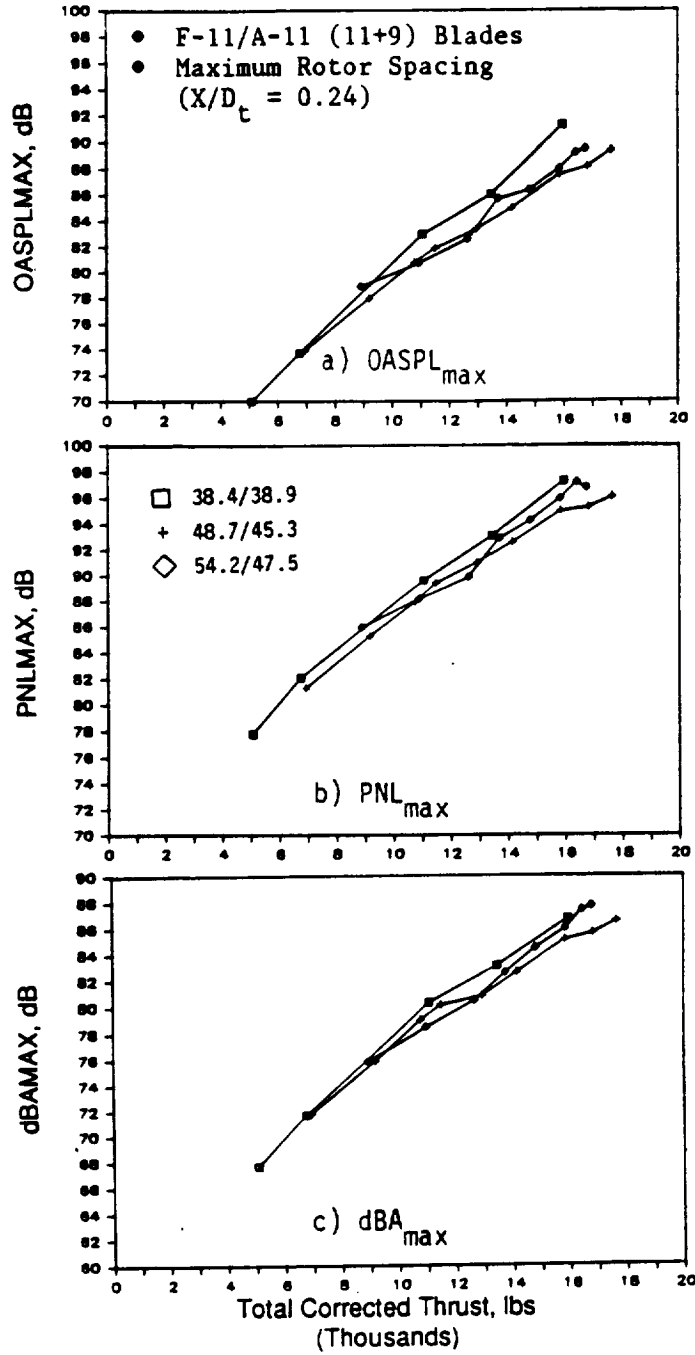


Figure 315. F-11/A-11 Acoustic Data at Different Blade-Pitch Angles.

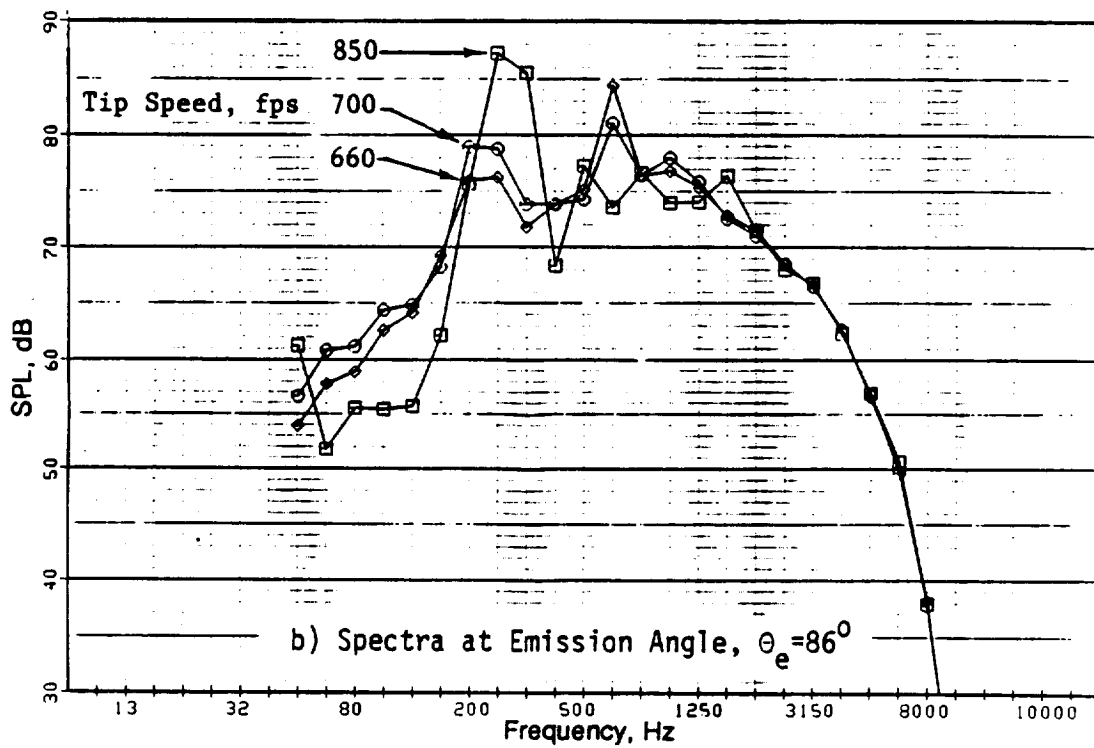
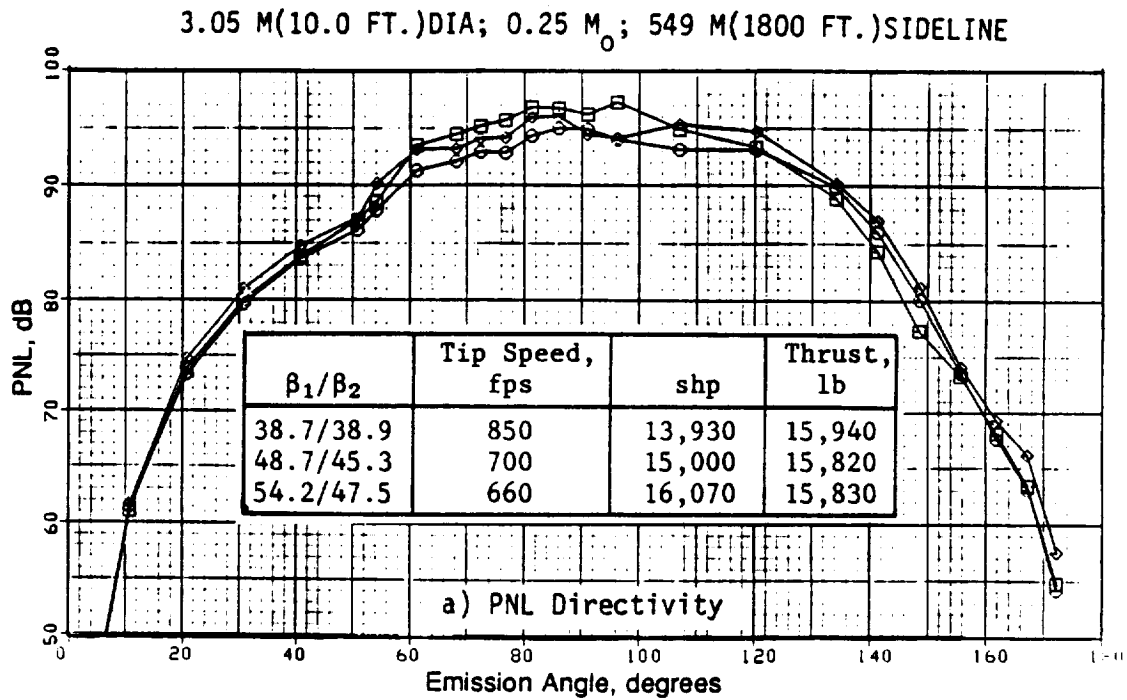


Figure 316. PNL Directivity and a Spectra of F-11/A-11 (11+9, Maximum Rotor Spacing) for Different Tip Speeds at a Typical Takeoff.

MODEL SCALE; AS MEASURED DATA
 F11A11; 11x9 BLADES; MAXIMUM ROTOR SPACING
 MICROPHONE ANGLE, $\Theta_m=92^\circ$

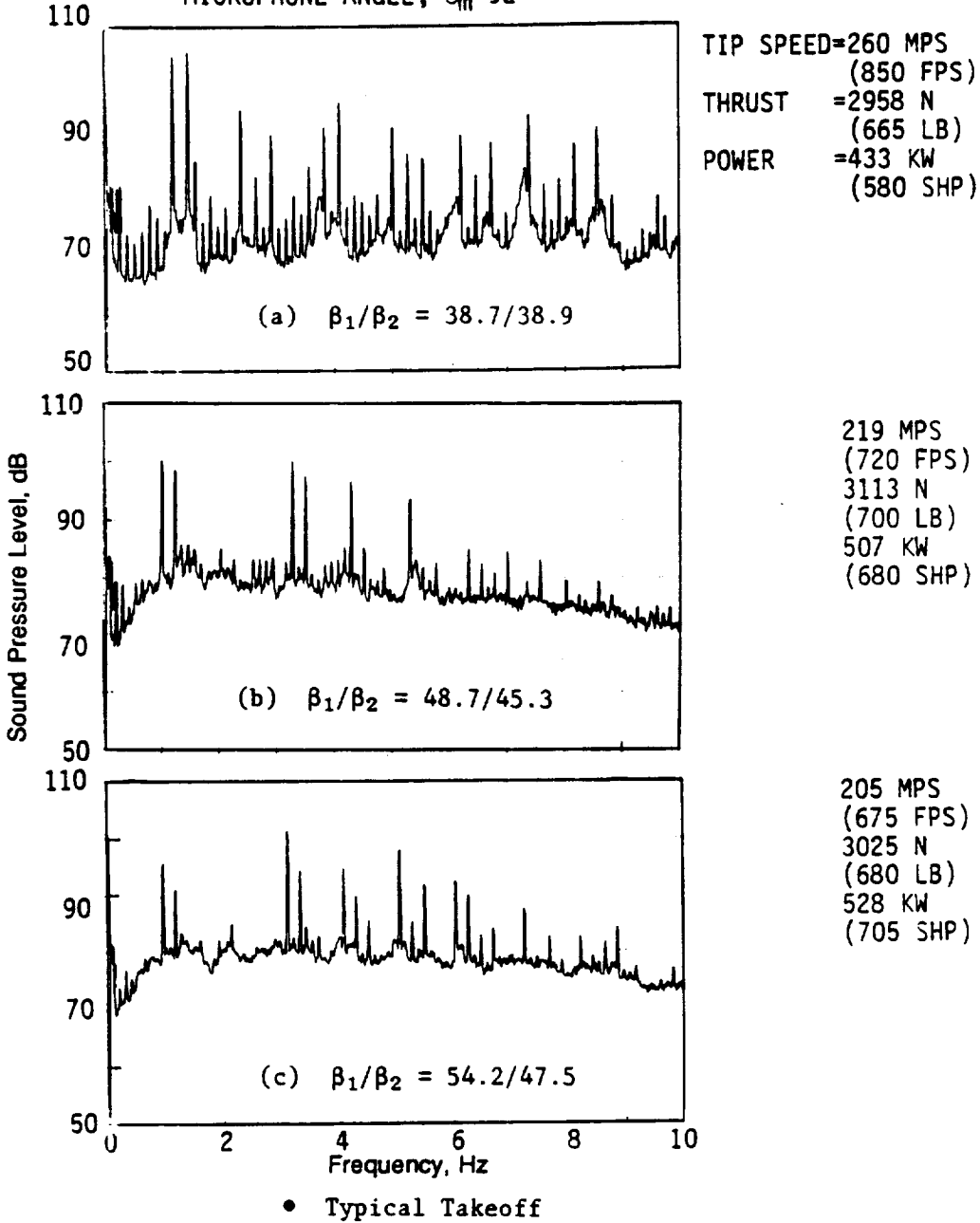


Figure 317. Selected Model-Scale Narrow-Band Spectra of F-11/A-11 for Different Tip Speeds.

MODEL SCALE; AS MEASURED DATA
 F11A11; 11x9 BLADES, MAXIMUM ROTOR SPACING
 MICROPHONE ANGLE, $\theta_m = 92^\circ$

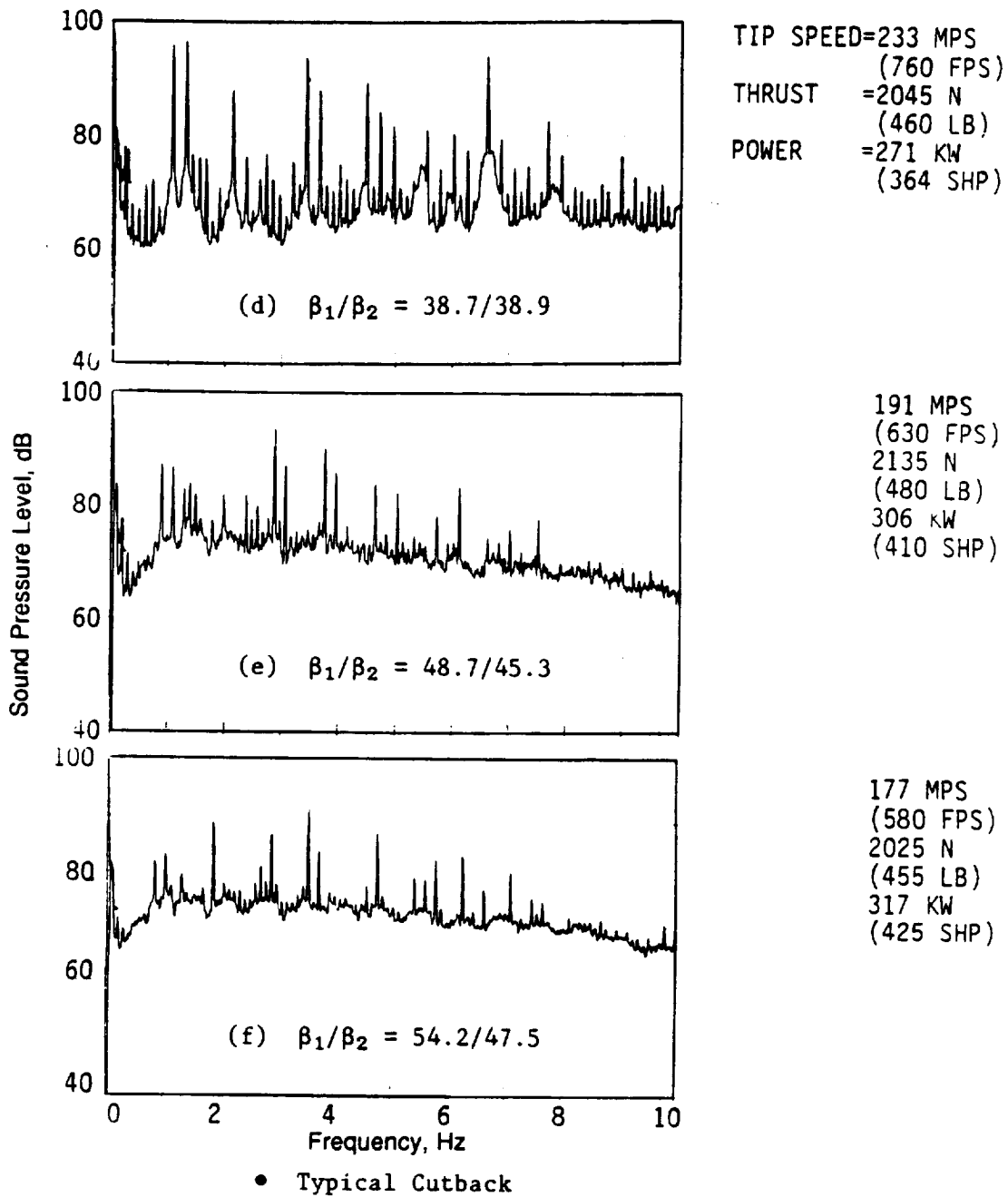


Figure 317. Selected Model-Scale Narrow-Band Spectra of F-11/A-11 for Different Tip Speeds (Concluded).

Decreasing takeoff tip speed from 256 mps (840 fps) to 210 mps (690 fps) resulted in an EPNL reduction of 1 dB; however, additionally decreasing the tip speed to 198 mps (650 fps), increased the EPNL by 1 db.

7.1.1.5.6 F-11/A-11 (11+9) at Supermaximum Rotor Spacing: Series 6

The F-11/A-11 (11+9) blade configuration was also tested at the designed supermaximum spacing ($X/D_t = 0.32$) at two blade-pitch settings, $44.8^\circ/43.3^\circ$ and $48.7^\circ/45.3^\circ$. Figure 318 illustrates the total thrust and power data from these tests. The thrust versus tip speed data indicate typical takeoff thrust of 66,700 N (15,000 lb) at 225 mps (740 fps) and 210 mps (690 fps) tip speeds. In agreement with all other performance data of this study, Figure 318 shows decrement in aerodynamic efficiency with decrease of tip speed.

Figure 319 demonstrates the acoustic data (in terms of scaled and maximum OASPL, PNL, and dBA), as a function of total thrust and indicates 1 dB to 2 dB increases in maximum PNL and dBA noise levels with the open pitch setting, as compares to the $44.8^\circ/43.3^\circ$, at typical takeoff. Similar to that observed with Series 5 data, this increase with reduced tip speed is due to sound pressure levels at the rotor-to-rotor interaction harmonics (Figure 320). In addition, the model-scale 10-kHz narrow-band comparison (Figure 321) shows an increase in the broadband levels with increase of tip speed.

The model-scale tone sum directivity data at typical takeoff presented in Figure 322 confirms this increase in rotor-to-rotor interaction noise (over an emission angle range of 70° to 110°), along with a decrease in steady-loading noise for the test tip speed reduction. The model-scale tone sum levels for Series 6 are illustrated as a function of total thrust in Figure 323. These increased rotor-to-rotor interaction noise levels resulting from the reduction in tip speed are noted over a range of high thrust conditions. As with all of the other tests of this study, the steady-loading noise reduces in conjunction with decreasing tip speed.

7.1.1.6 Effect of Reduced Diameter Aft Blades

The aft blades of the model-scale F-7/A-7 design measure 17.8 cm (7 in.) from hub to tip; these blades were clipped at 75% span to yield the reduced diameter aft blades utilized in this study. The objective was to determine what acoustic benefit, if any, could be achieved with a configuration in which tip vortices from the forward blades are not interacting with the aft blades and, thus, to reduce a component of the rotor-to-rotor interaction noise of a two-rotor counterrotating fan configuration. An illustration of a planform of a clipped aft blade was previously provided as Figure 266.

The individual test configurations of this clipped aft blade study and the reference unclipped test comparisons are summarized as:

Series	Configuration	Pitch Angles, deg	Run No.
1	F-7/A-7	36.3/37.4	35
	F-7/A-7c	36.3/42.7	43
2	F-7/A-7	41.8/41.4	37
	F-7/A-7c	41.8/48.3	41

All of these tests used the 9+8 configuration blades, spaced at a maximum spacing ($X/D_t = 0.24$) between the rotor pitch-change axes. As detailed above, to make up for the loss in thrust at a given

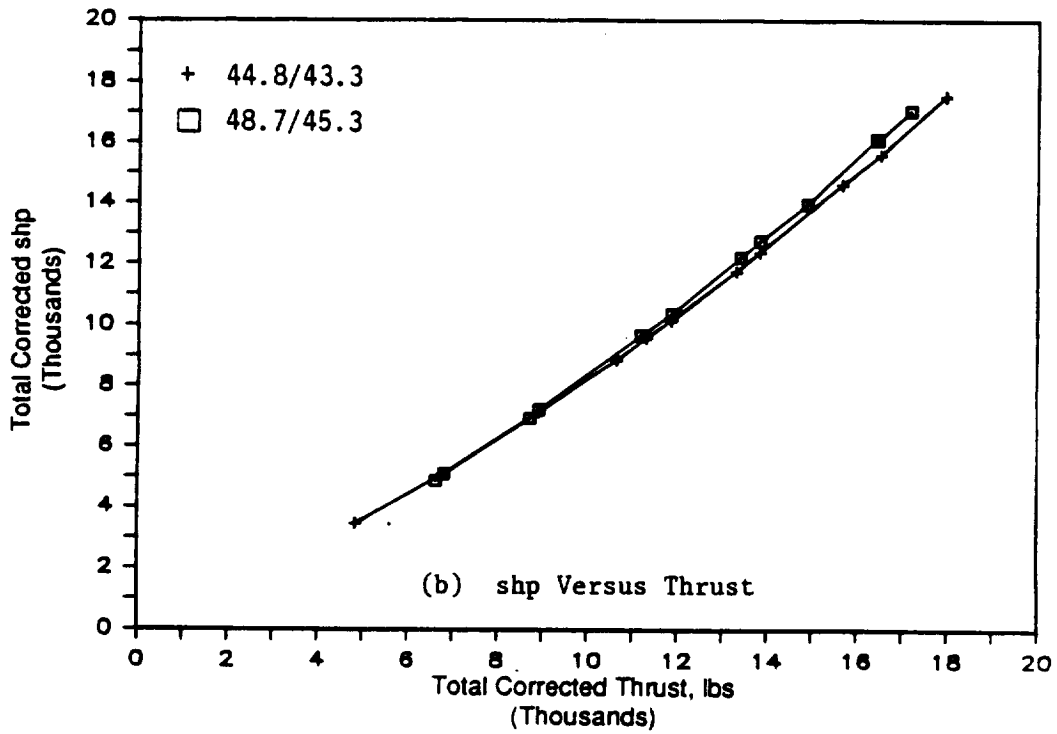
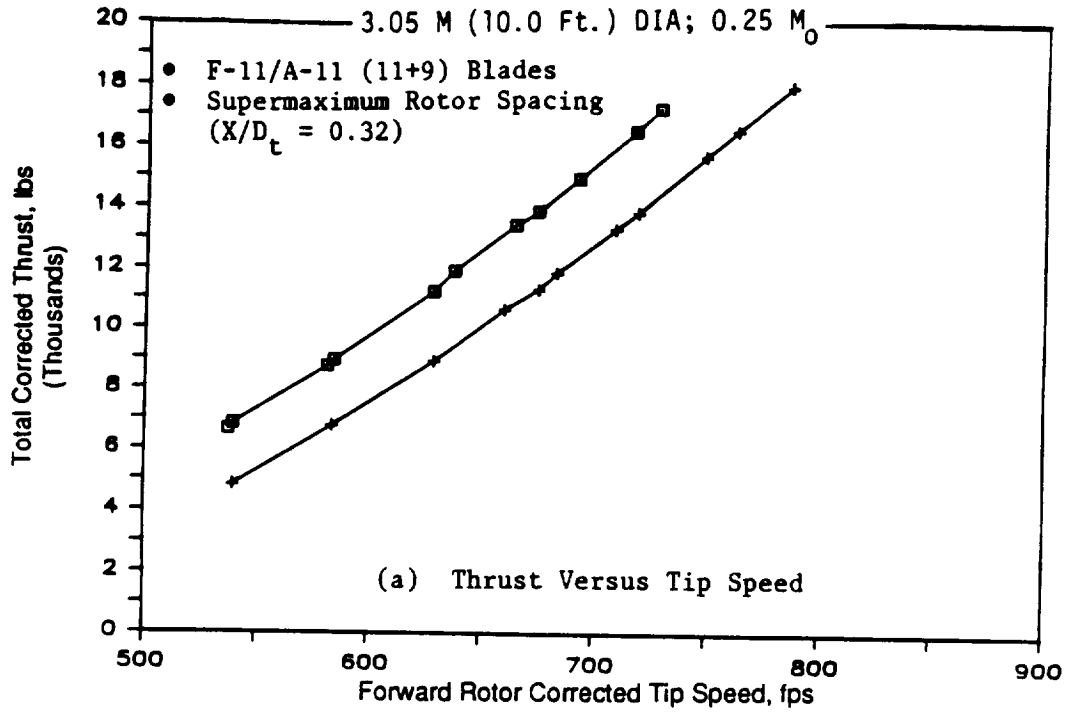


Figure 318. F-11/A-11 Aero Performance at Different Blade-Pitch Angles.

3.05 M(10.0 FT.)DIA; 0.25 M₀; 549 M(1800 FT.)SIDELINE

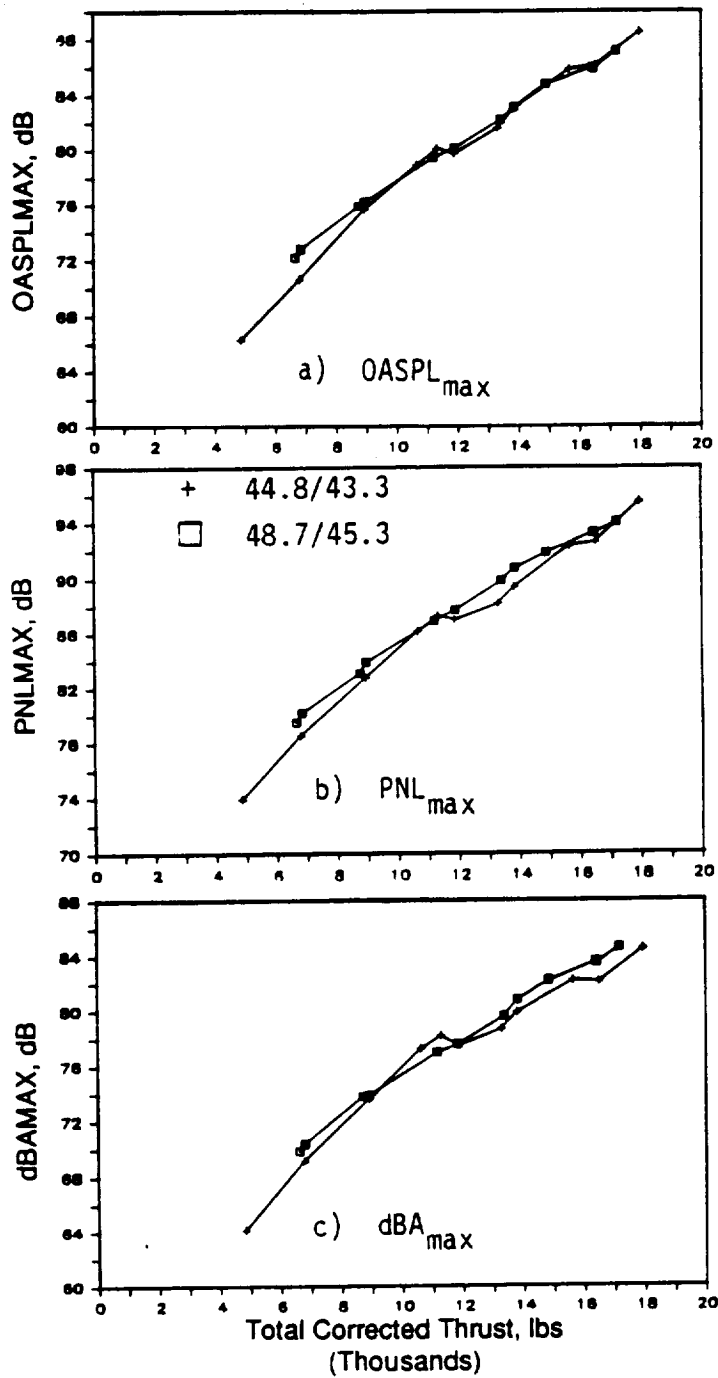


Figure 319. Acoustic Data for F-11/A-11 (11+9 Supermaximum Spacing) at Different Pitch Angles.

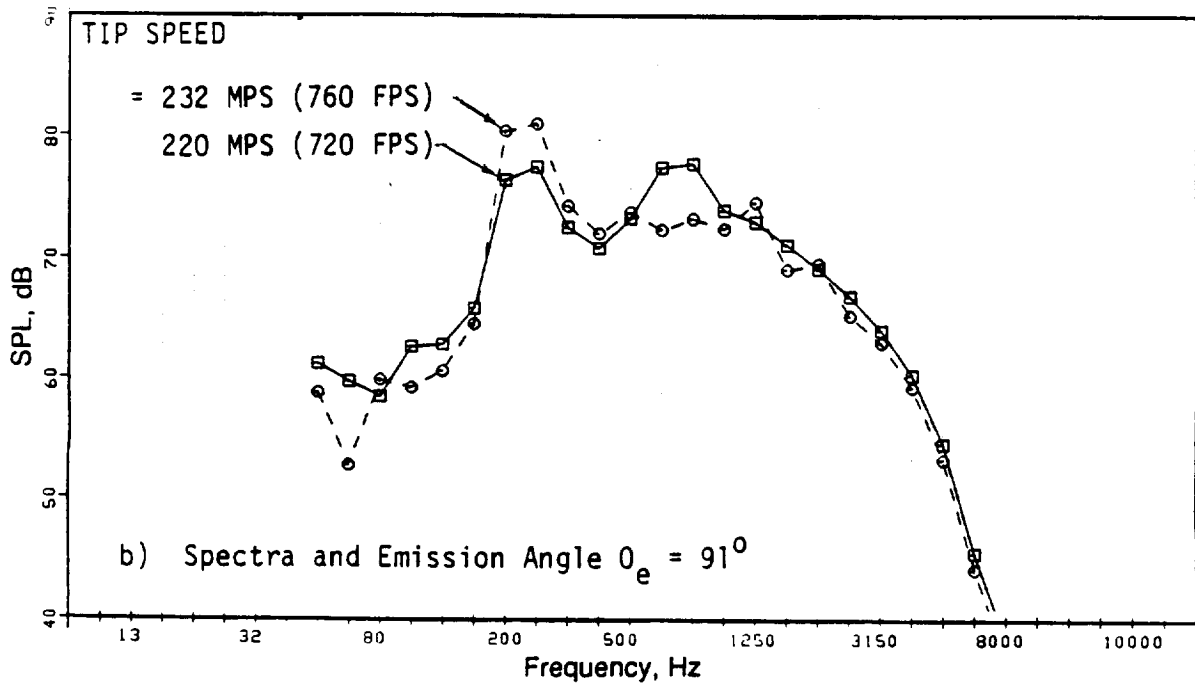
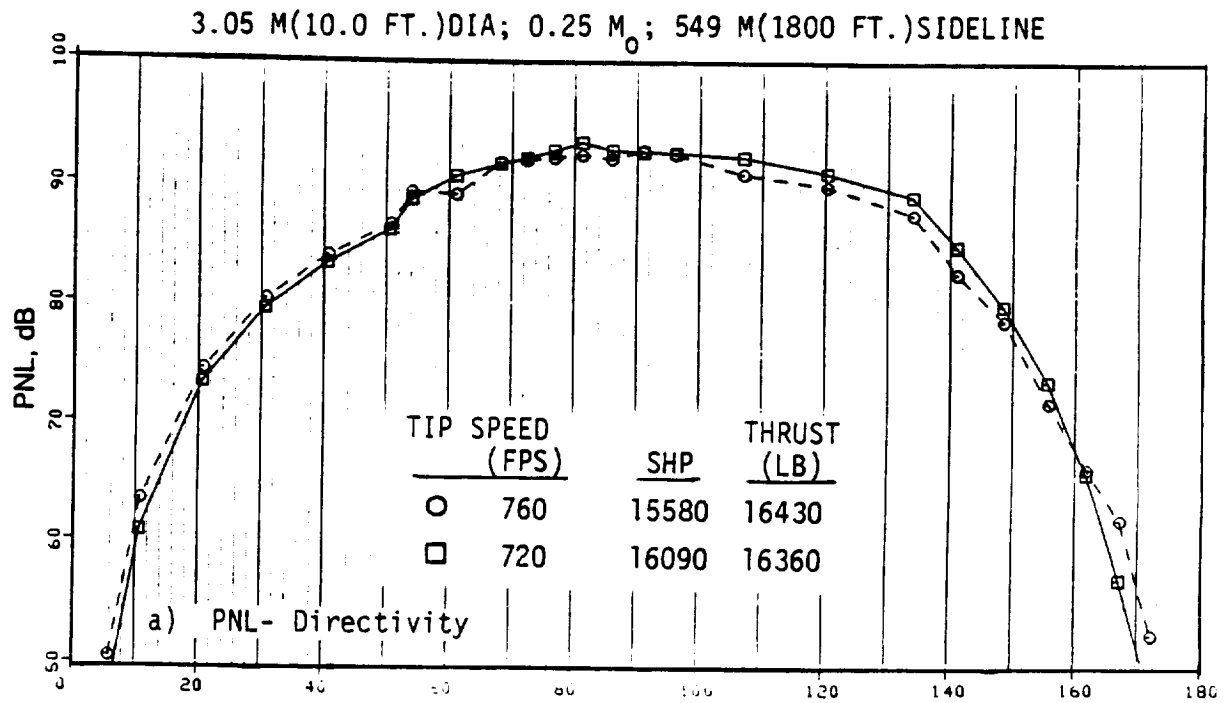


Figure 320. PNL Directivity and a Spectra of F-11/A-11 (11+9, Supermaximum Spacing) for Different Tip Speeds at Typical Takeoff.

- Model-Scale: As-Measured Data
- F-11/A-11, 11+9 Blades
- Supermaximum Rotor Spacing
- Microphone Angle, $\theta_m = 92^\circ$

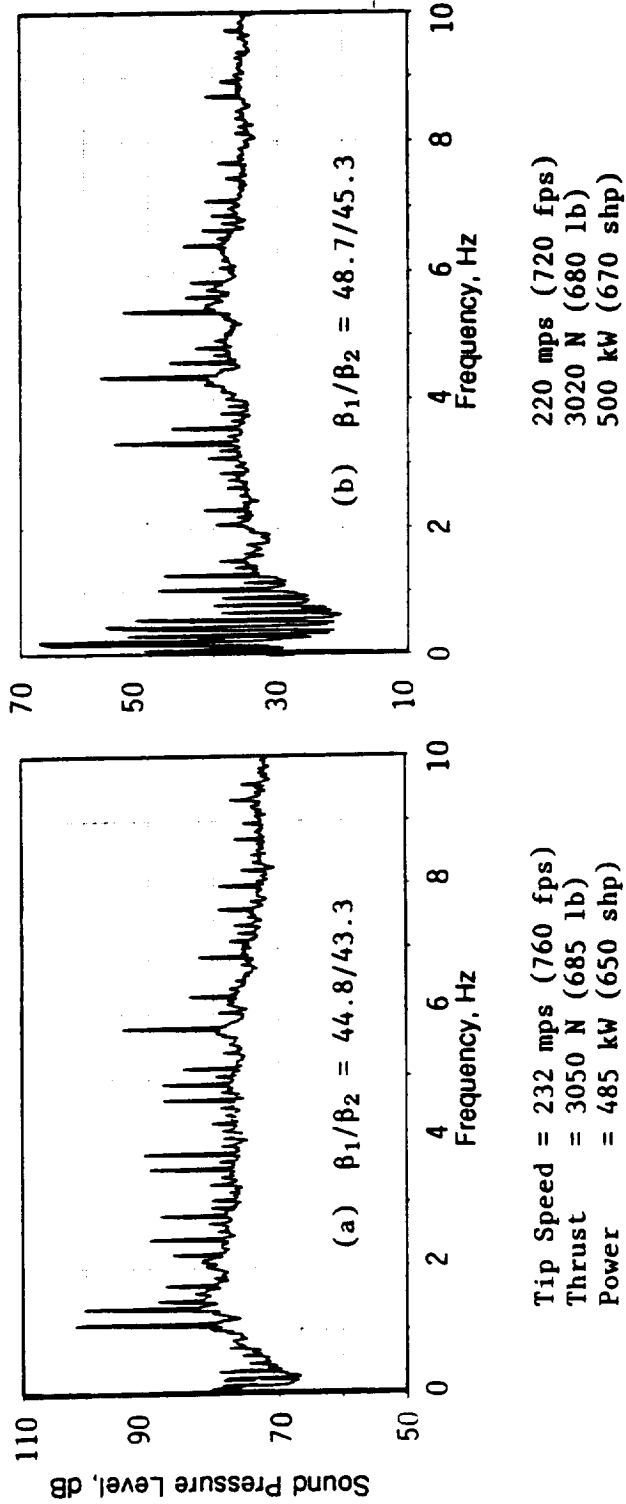


Figure 321. Selected Model-Scale Narrow-Band Spectra of F-11/A-11 for Different Tip Speeds at Typical Takeoff.

MODEL SCALE; 8.2 M(27 FT.) SIDELINE
12.5 HZ NARROWBAND DATA

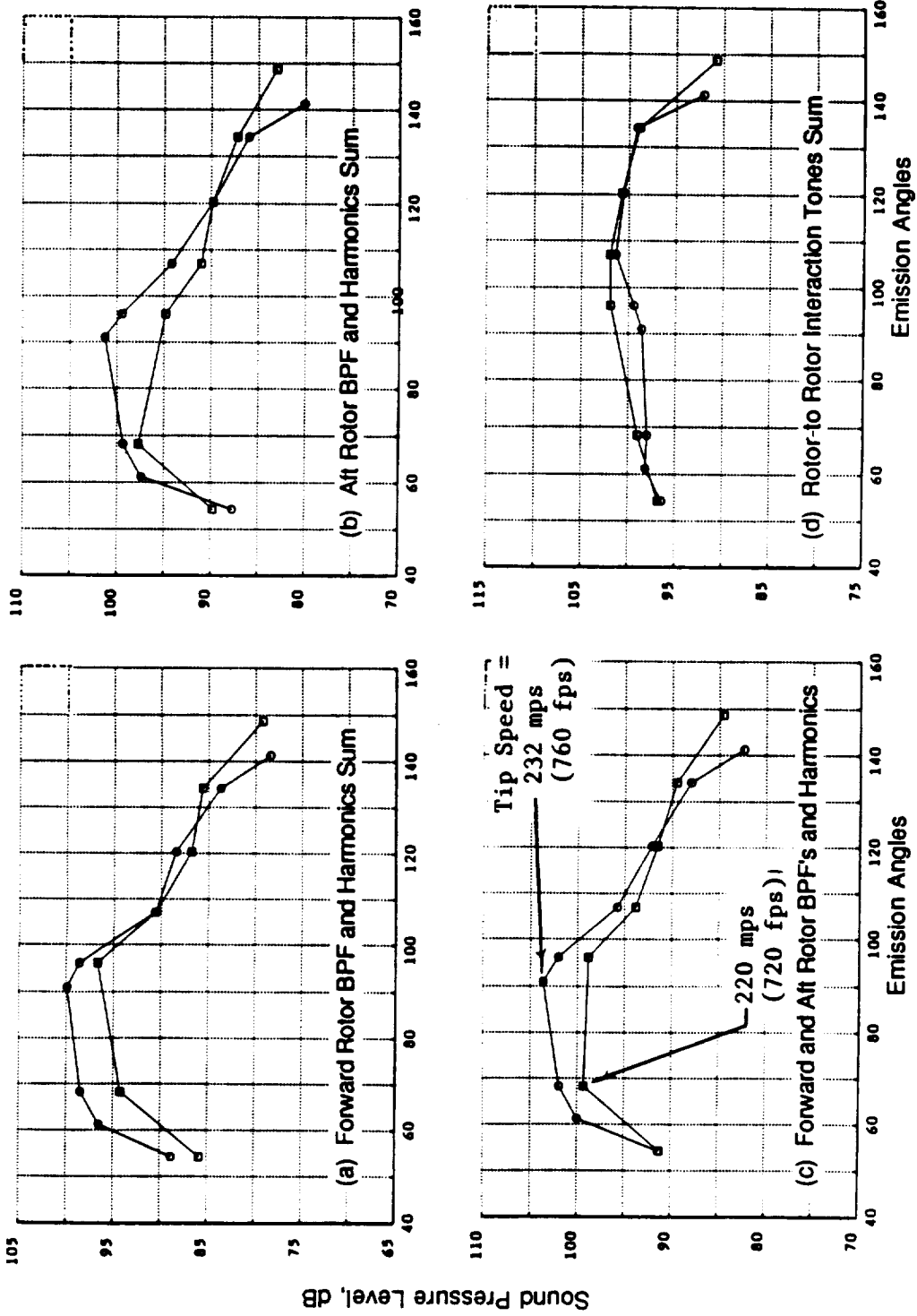
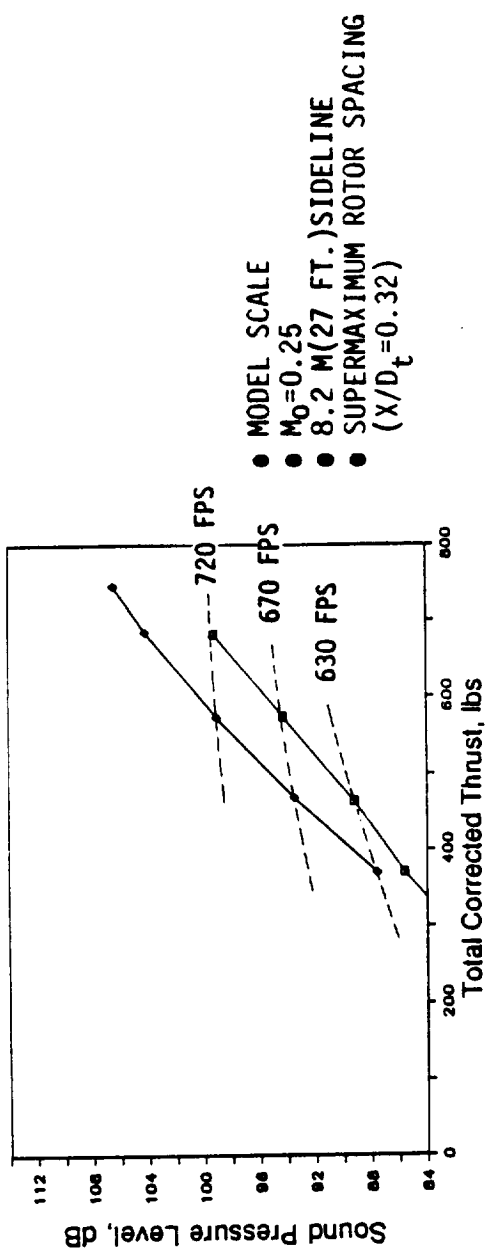


Figure 322. Model-Scale Tone Sum Level Directivities of F-11/A-11 (11+9 Supermaximum Spacing) for Different Tip Speeds at Typical Takeoff.

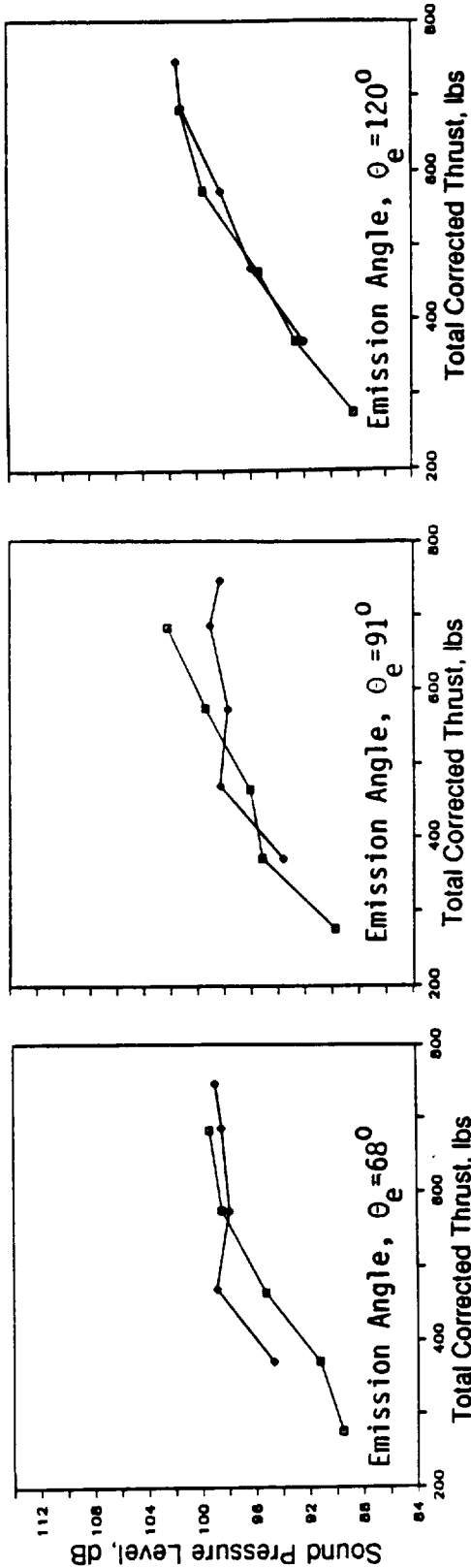


a) Steady Loading Noise at Emission, $\theta_e = 91^\circ$

F11A11
11x9 BLADES

- ◇ 44.8/43.3
- 48.7/45.3

- MODEL SCALE
- $M_0 = 0.25$
- 8.2 M(27 FT.) SIDELINE
- SUPERMAXIMUM ROTOR SPACING
($X/D_t = 0.32$)



b) Rotor-to-Rotor Interaction Noise

Figure 323. Model-Scale Tone Sum Levels for Different Tip Speeds as a Function of Thrust.

rpm due to clipping, the clipped aft blades were set at a more open pitch angle, compared to the unclipped aft blades. The acoustic data results presented in this section were acquired at a simulated flight Mach number of 0.25.

7.1.1.6.1 Nominal Pitch Angle: Series 1

Both the unclipped (F-7/A-7) and aft clipped (F-7/A-7c) blade configurations were tested at nominal blade-pitch angles of 36.3°/37.4° and 36.3°/42.7°, respectively. Typical takeoff and cutback thrusts of 66,700 N (15,000 lb) and 44,500 N (10,000 lb) were attained at tip speeds in the proximity of 265 mps (870 fps) and 236 mps (775 fps). As previously described (Subsection 6.1.2), there was a decrease in the efficiency with the F-7/A-7c for a given thrust, compared to the corresponding unclipped test.

Figure 324 depicts the acoustic data in terms of the scaled and maximum OASPL, PNL, and dBA as a function of total thrust and indicates reduced peak noise levels (in the range of 3 dB) for all thrusts less than 57,800 N (13,000 lb); this reduction decreases with increases in thrust.

OASPL and PNL directivities and selected spectra at a thrust in the range of a typical cutback are illustrated in Figures 325 and 326, demonstrating the benefit of clipping on total noise levels over all of the measured angles ($50 < \sigma_e < 160$). While the reduction is 3 dB at the peak noise angles, the benefit with clipping increases through a range of 5 dB to 7 dB in the aft angles between 90° and 140°. Figure 326 shows that the presence of the aft clipped blade resulted in dramatic reductions in higher frequency SPL's at all angles.

Assuming that the length of clipping on the aft blade was sufficient to avoid interaction of the aft blades with tip vortices from the forward rotor blades, reduction in this higher frequency sound pressure level is attributed mainly to the absence of vortex/rotor interaction tones. The reduction noted in these spectra at the blade passing frequency is mainly due to the reduced tip speed of the aft rotor.

Figure 327 provides a narrow-band spectral comparison between unclipped and clipped configurations. Since no narrow-bands for unclipped configuration with pitch angles of 36.3°/37.4° were available for analysis, narrow-band spectral data of unclipped tests with pitch angle of 38.4°/37.4° were substituted. These data demonstrate a significant reduction in interaction tones occurring beyond 3xBP F, particularly in the aft quadrant. This is further demonstrated in the model-scale rotor-to-rotor interaction tone sum level directivities of Figure 328 for a typical cutback thrust. Finally, a comparison of tone sum data of configurations at the nominal pitch (Figure 329) indicates significant interaction tone sum benefit with a clipped aft blade over a range of thrust.

7.1.1.6.2 Open Pitch Angles: Series 2

The unclipped and clipped F-7/A-7 blades were also tested at open pitch angles of 41.8°/41.4° and 41.8°/48.3°, respectively. Typical takeoff and cutback thrusts of 66,700 N (15,000 lb) and 44,500 N (10,000 lb) were attained at tip speeds of approximately 239 mps (785 fps) and 209 mps (685 fps). As with the nominal pitch, there was a degradation in performance with the clipped blades.

Figure 330 shows the acoustic data in terms of scaled and maximum OASPL, PNL, and dBA as a function of total thrust. Like that measured at the nominal pitch, these data indicate a reduction of about 3 dB in peak noise levels for cutback thrust; no significant benefit is observed at takeoff conditions.

3.05 M(10.0' FT.)DIA; 0.25 M₀; 549 M(1800 FT)SIDELINE

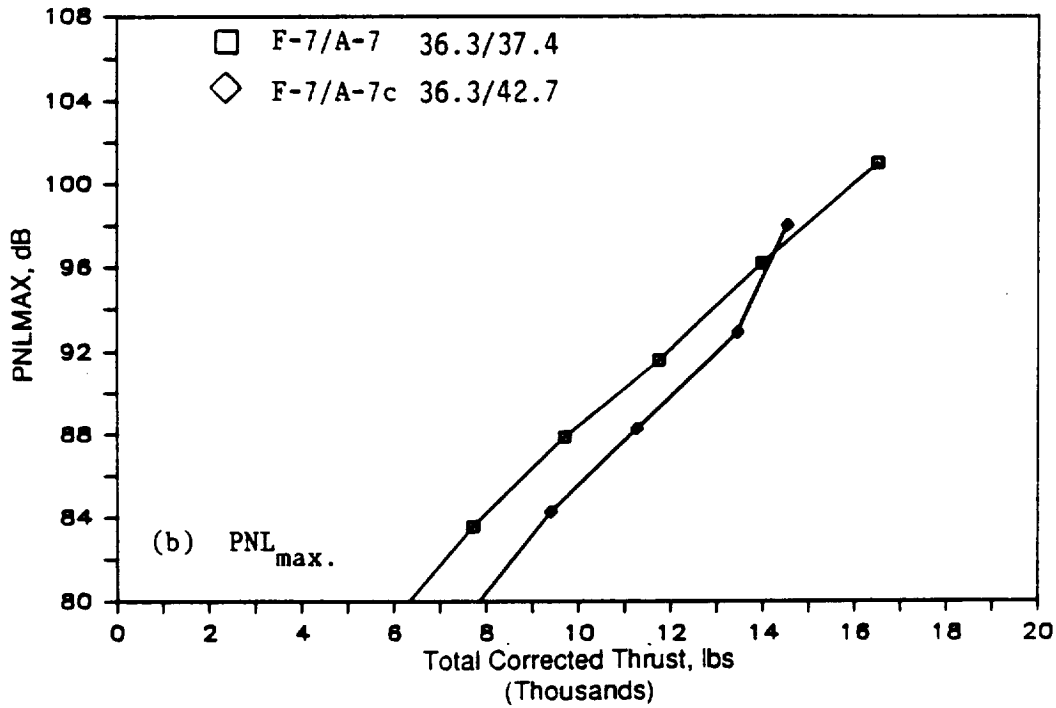
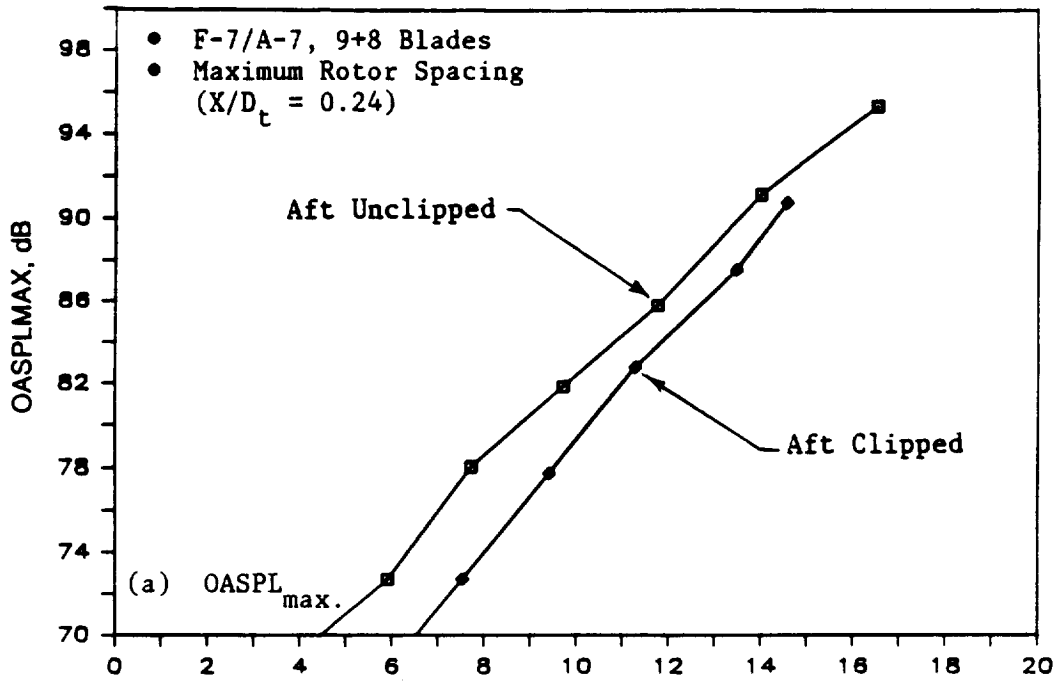


Figure 324. Effect of Clipped Aft Blade on the Maximum OASPL, PNL, and dBA of F-7/A-7 (9-8), Nominal Pitch.

3.05 M(10.0 FT.)DIA; 549 M(1800 FT.)SIDELINE

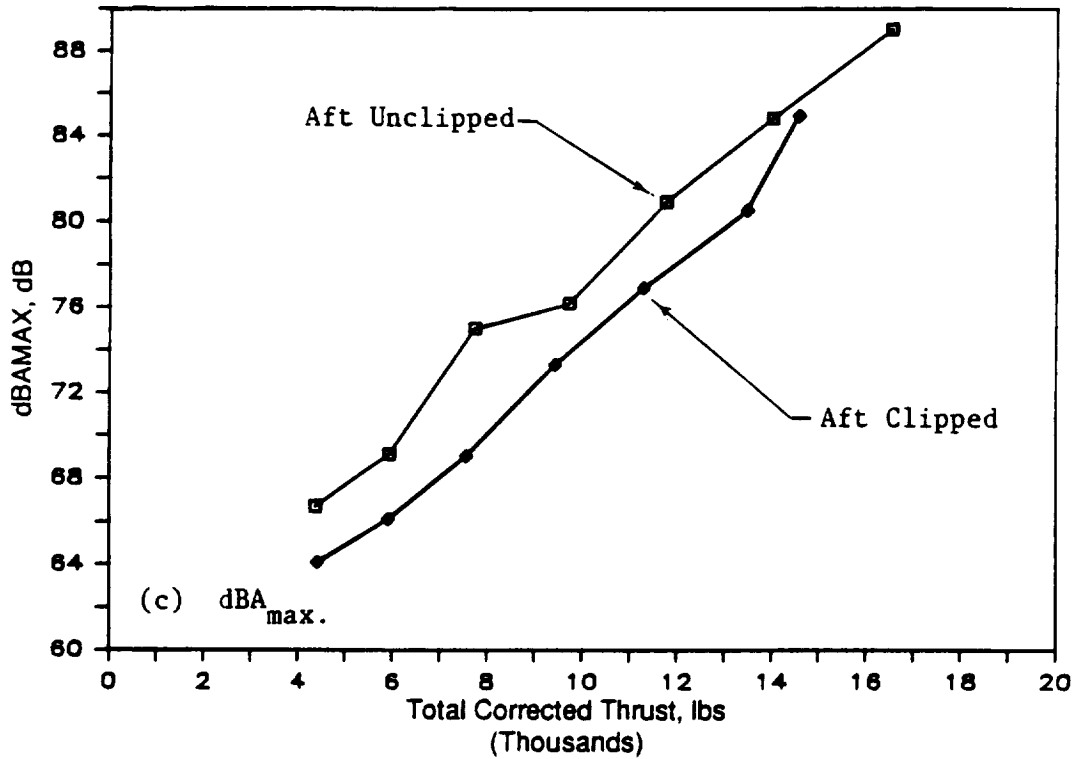


Figure 324. Effect of Clipped Aft Blade on the Maximum OASPL, PNL, and dBA of F-7/A-7 (9+8), Nominal Pitch (Concluded).

3.05 M(10.0 FT.)DIA; 0.25 M₀; 549 M(1800 FT)SIDELINE

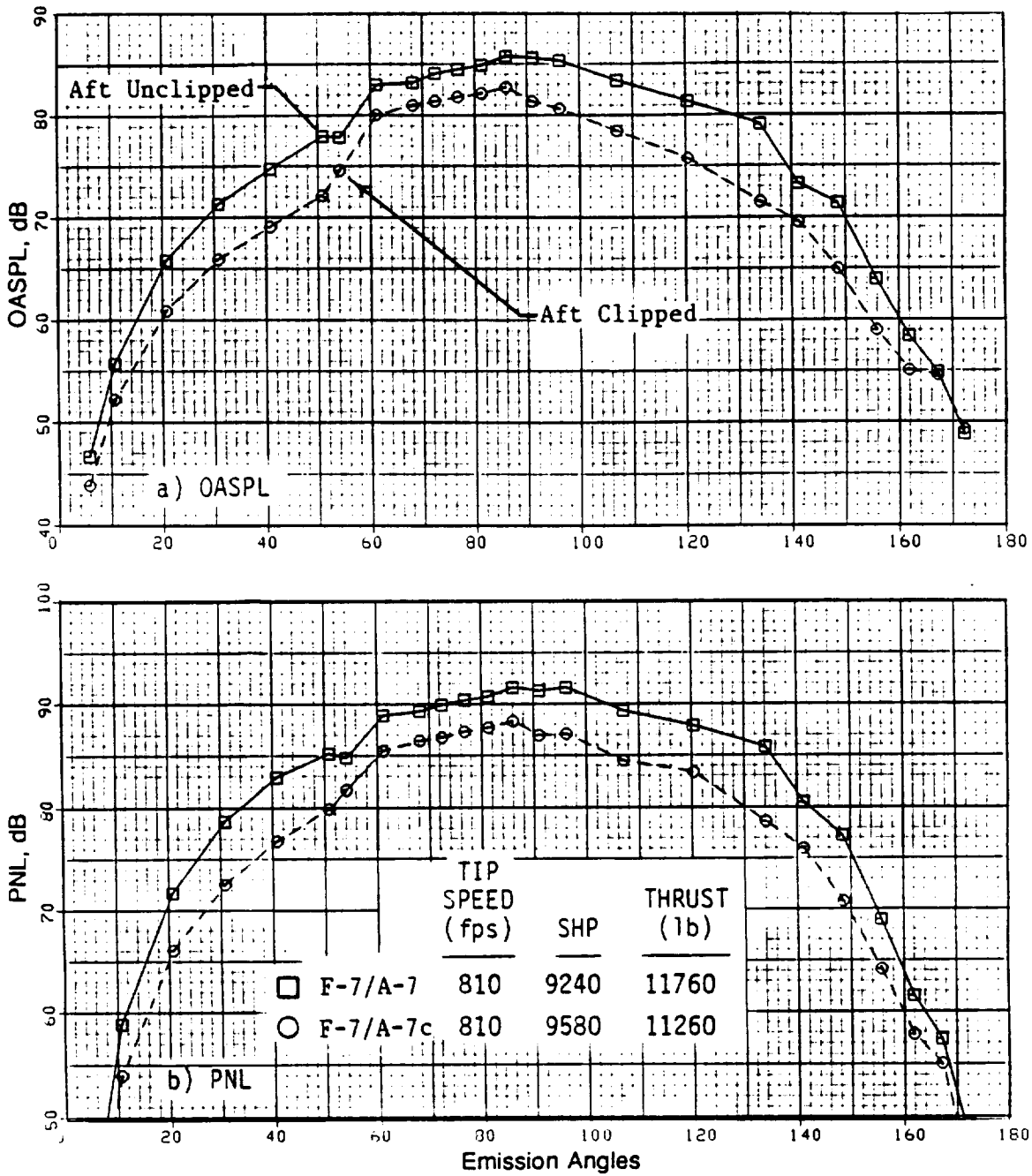


Figure 325. OASPL and PNL Directivity Comparison of F-7/A-7 (9+8; Nominal Pitch) at Cutback.

3.05 M(10.0 FT.)DIA; 0.25 M₀; 549 M(1800 FT.)SIDELINE

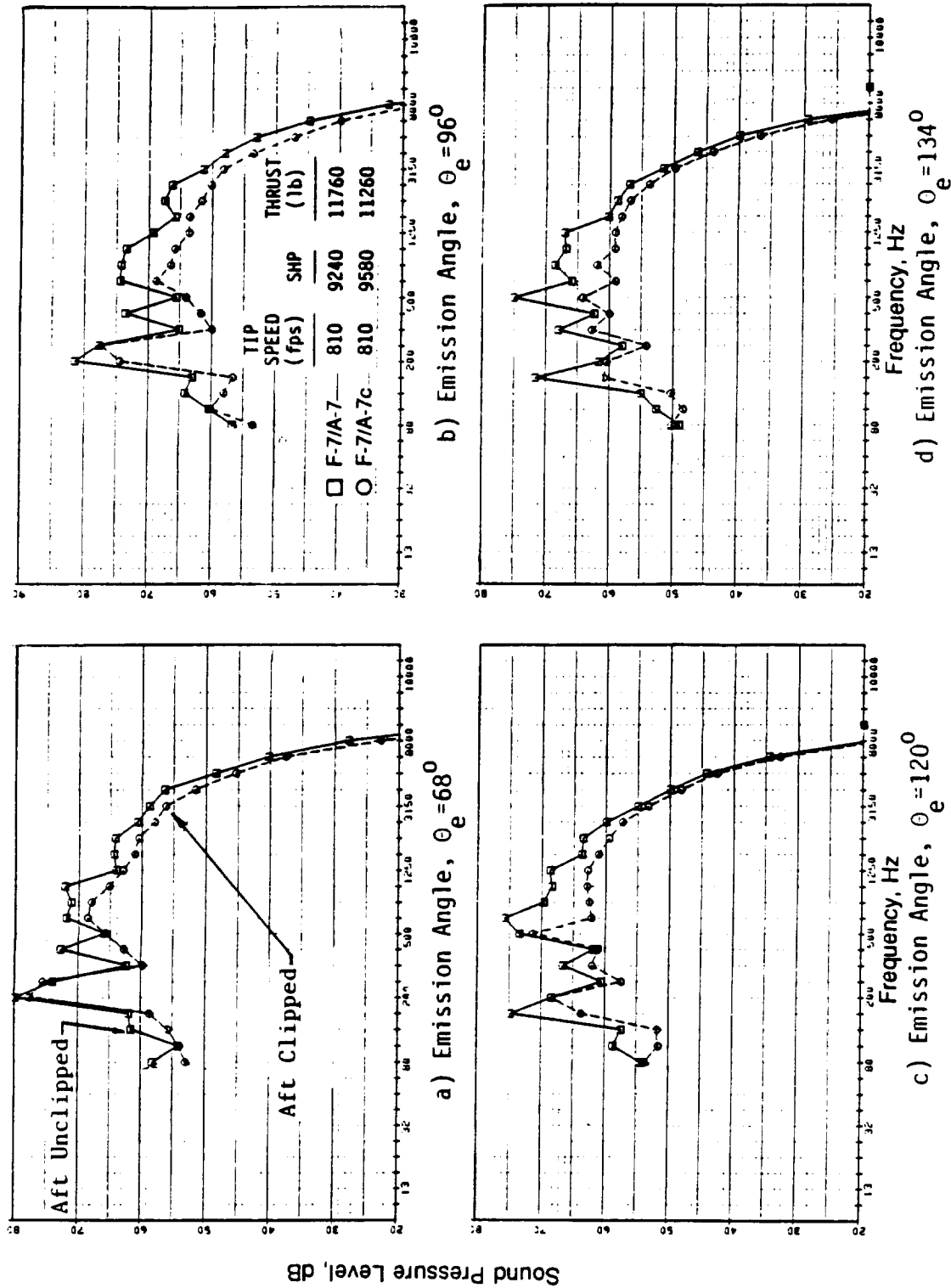
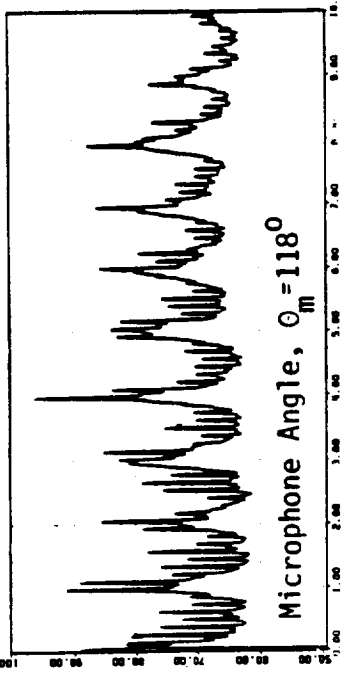
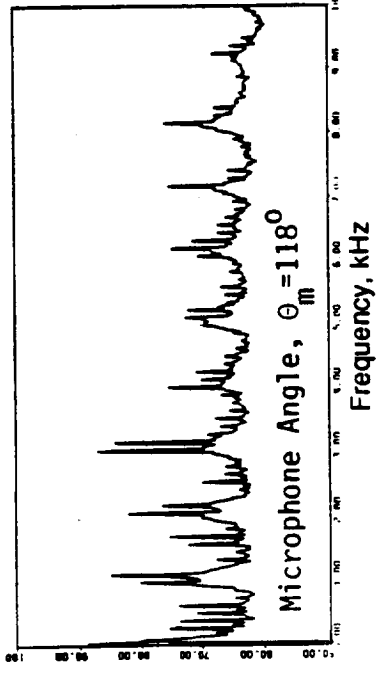


Figure 326. Selected Spectra of Aft Unclipped and Clipped F-7/A-7 (9+8) at Cutback.

- MODEL SCALE; AS MEASURED DATA
- 9x8 BLADES



(a) F-7/A-7; 38.4/37.4 (Tip Speed = 760 fps; shp = 340; Thrust = 430 lb)



(b) F-7/A-7c; 36.3/42.7 (Tip Speed = 765 fps; shp = 320; Thrust = 390 lb)

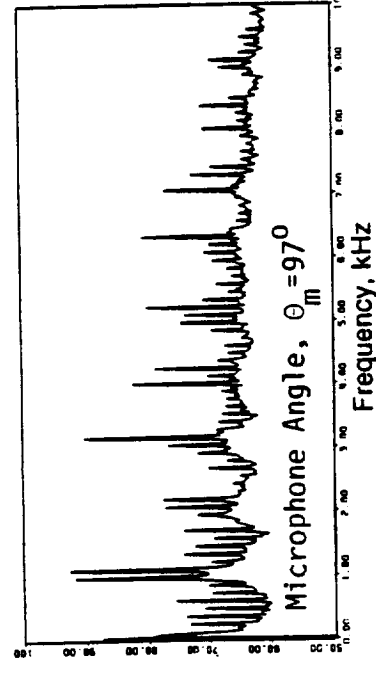
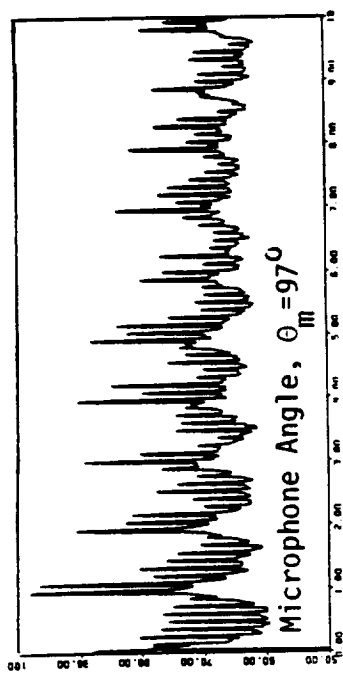


Figure 327. Narrow-Band Spectra of the Unclipped and Clipped F-7/A-A-7 (Nominal Pitch) at Cutback.

- MODEL SCALE; 0.25 M_0 ; 8.2 M(27 FT)SIDELINE
- MODEL THRUST=1850 N(415 LB)
- 12.5 HZ NARROWBAND DATA

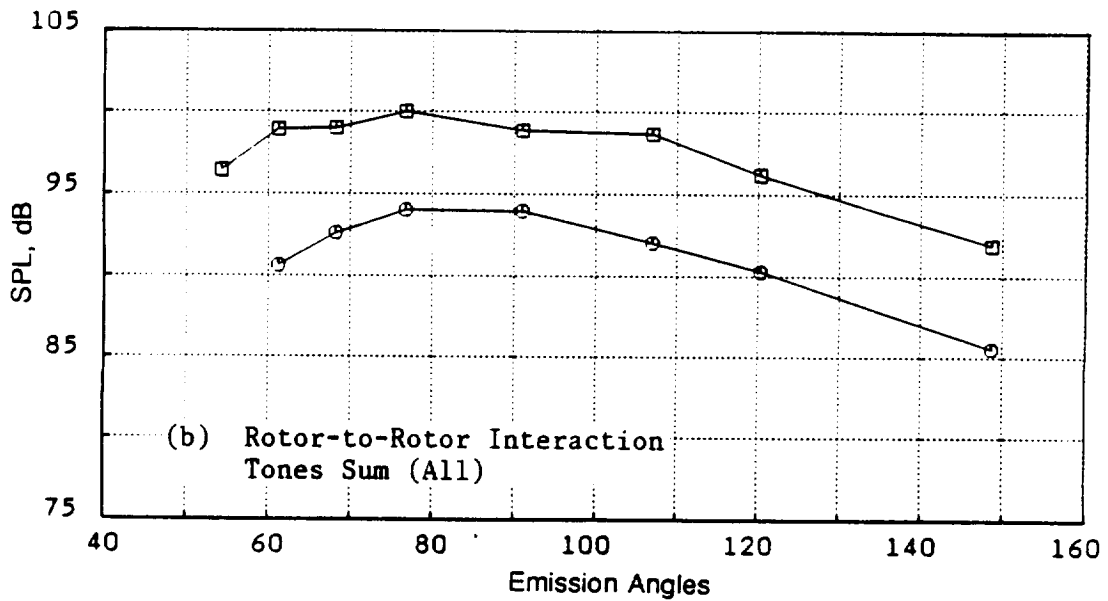
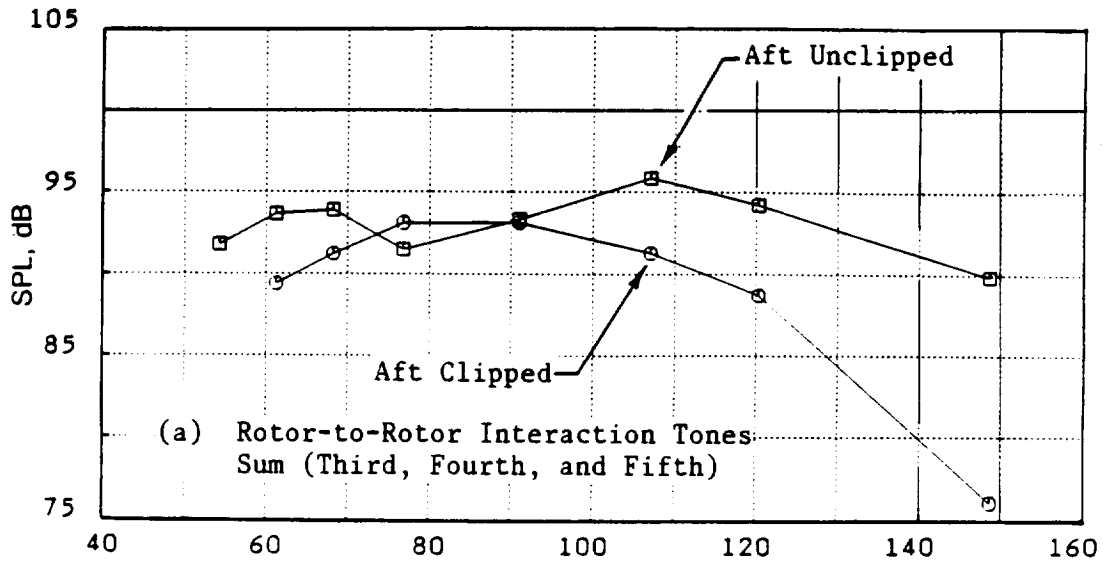
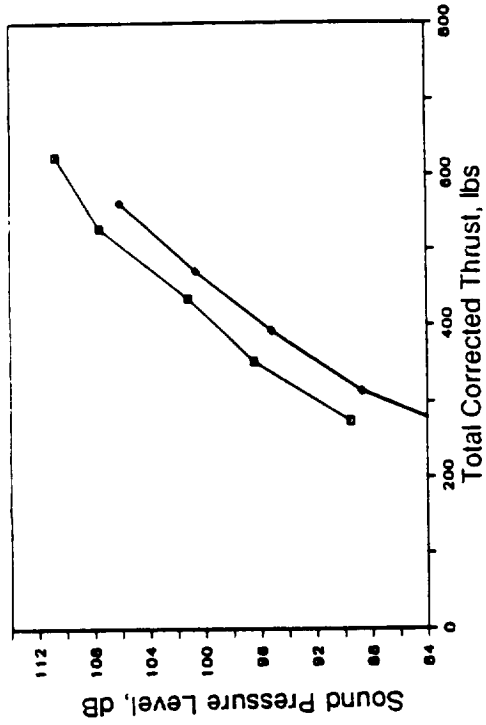


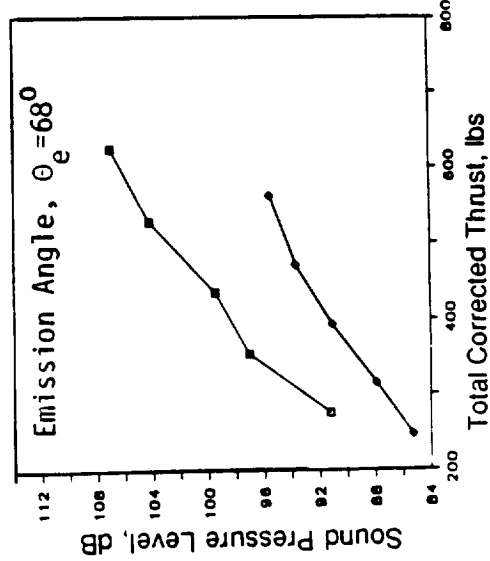
Figure 328. Directivity of Rotor-to-Rotor Interaction Noise of the Unclipped and Clipped F-7/A-7 (9+8; Nominal Pitch) at Cutback.

□ F-7/A-7 38.4/37.4
 ◇ F-7/A-7c 36.3/42.7

● MODEL SCALE
 ● $M_0=0.25$
 ● 8.2 M(27 FT)SIDELINE



a) Fwd and Aft Rotor BPF and Harmonics Sum at Emission Angle, $\theta_e = 91^\circ$



b) Rotor-to-Rotor Interaction Tones Sum

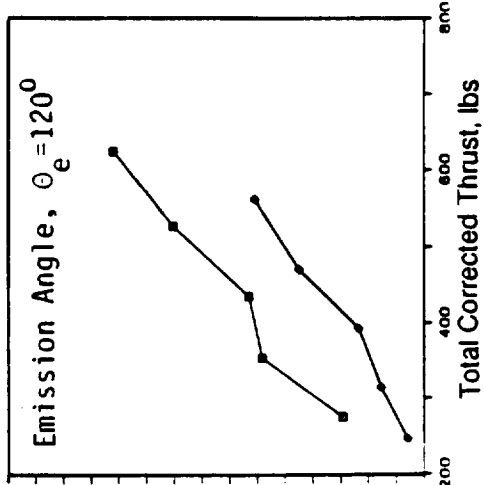


Figure 329. Model-Scale Tone Sum Levels of F-7/A-7 and F-7/A-7c (9+8; Nominal Pitch) as a Function of Total Thrust.

3.05 M(10.0 FT.)DIA; 0.25 M₀; 549 M(1800 FT.)SIDELINE

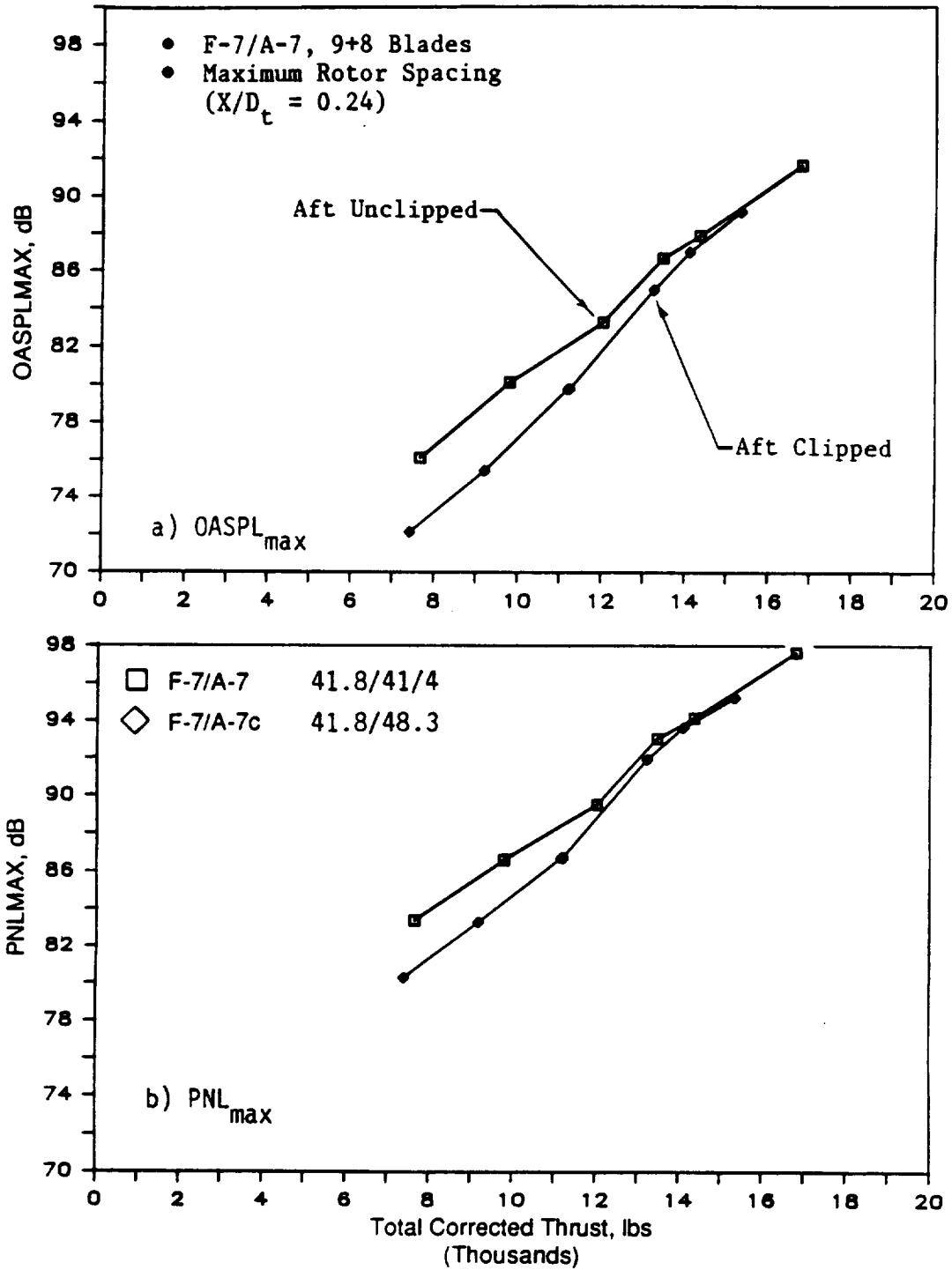


Figure 330. Effect of Clipped Aft Blade on Maximum OASPL, PNL, and dBA of F-7/A-7 (9+8), Open Pitch.

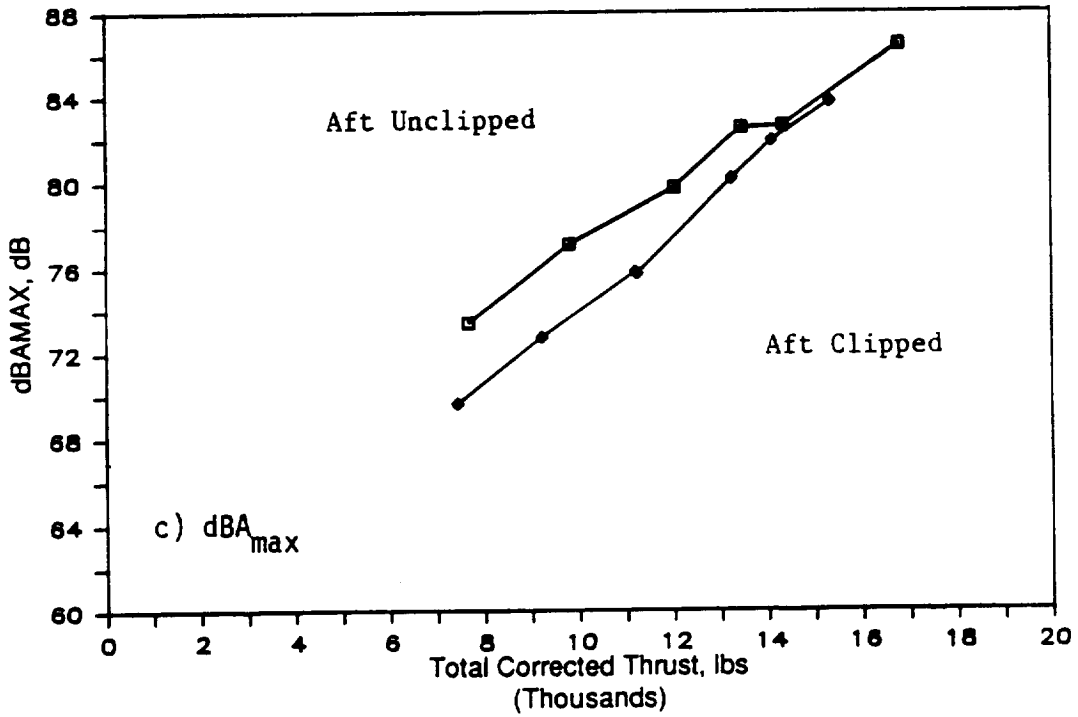


Figure 330. Effect of Clipped Aft Blade on Maximum OASPL, PNL, and dBA of F-7/A-7 (9+8), Open Pitch (Concluded).

The OASPL and PNL directivities and selected spectra for typical cutback thrust conditions are plotted in Figures 331 and 332. The benefit of clipping for total noise levels is shown over most of the measured angles ($70 < \theta_e < 140$). In agreement with the data presented for nominal pitch, this spectral comparison indicates significantly decreased levels of higher harmonics. As shown in Figure 333, these directivities also were measured for thrust in the range of a typical takeoff and indicate no significant benefit of clipping, except in aft angles; however, the corresponding spectra (Figure 334) indicates benefit of clipping in the plane-of-rotation as well.

The reason for not observing any benefit of clipping at high thrust (such as takeoff) is that overall noise levels at such conditions are dominated by steady-loading noise; however, if higher blade numbers had been used, instead of the 9+8 configuration, it is believed that the benefit of clipping would have been observed, even at takeoff thrust.

Figure 335 compares narrow-band spectra for unclipped and clipped configurations at cutback and takeoff conditions; these data sets reveal significant reductions in the interaction tones of the 3xBPF and beyond, and as with the nominal pitch, this reduction is most significant in the aft quadrant. This benefit occurs again over most of the thrust range. Figure 336 summarizes the rotor-to-rotor interaction tone sum levels as a function of thrust.

This section concludes by comparing, in Figure 337, the F-7/A-7c (9+8) blade data with data from the F7A7 (8+8) baseline test at a typical cutback condition. This data demonstrates reductions, attained with the clipped aft blade configuration (F-7/A-7c), of 7 dB to 8 dB in the plane-of-rotation and of 9 dB in most of the aft quadrants.

7.1.1.7 Effect of Test Mach Number Variation for Fixed Pitch Angle

All of the Cell 41 acoustic data presented thus far in this report were measured at a freejet Mach number of 0.25. During the various configuration tests, acoustic data were measured over a Mach number range of 0.2 to 0.3, in order to assess the effect of Mach number variation on the measured community noise data. The test configurations employed for this discussion are:

Series	Blade Configuration	Pitch Angle, deg	Test Mach No.
1	F-7/A-7 (9+8)	38.4/37.4	0.20
			0.23
			0.25
			0.30
2	F-7/A-7 (11+9)	38.3/38.6	0.20
			0.25

Forward and aft rotors for all of these tests were spaced at maximum spacing ($X/D_t = 0.24$) between the rotor pitch-change axes. Performance and acoustic data from these two series of tests are briefly discussed in this section.

3.05 M(10.0 FT.)DIA; 0.25 M₀; 549 M(1800 FT.)SIDELINE

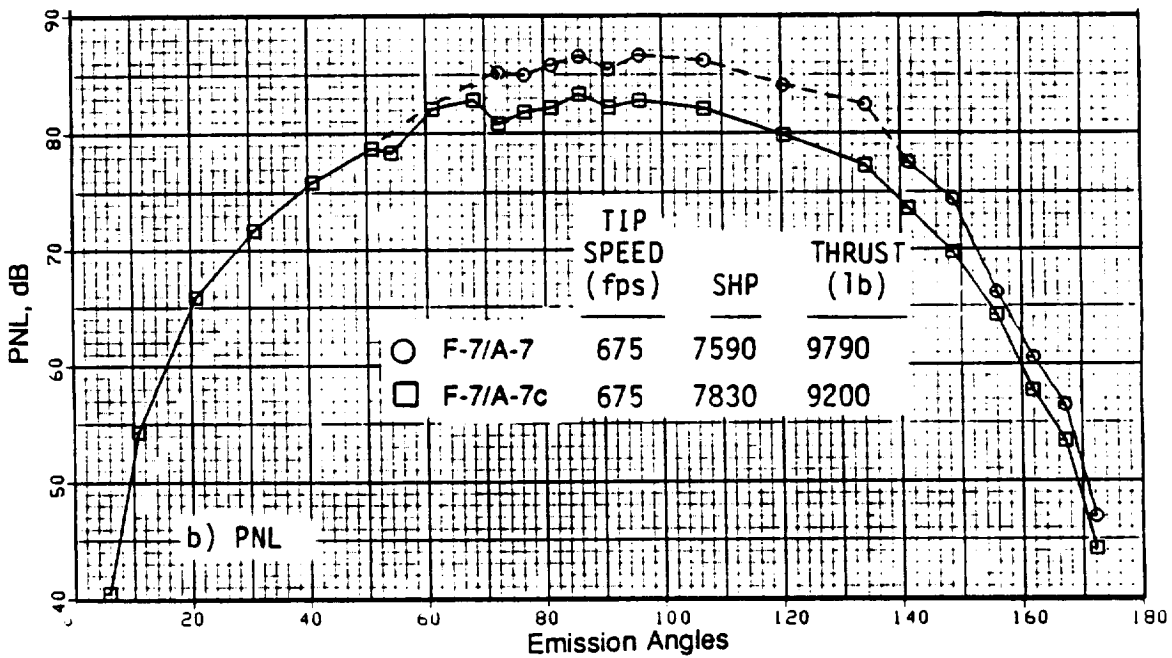
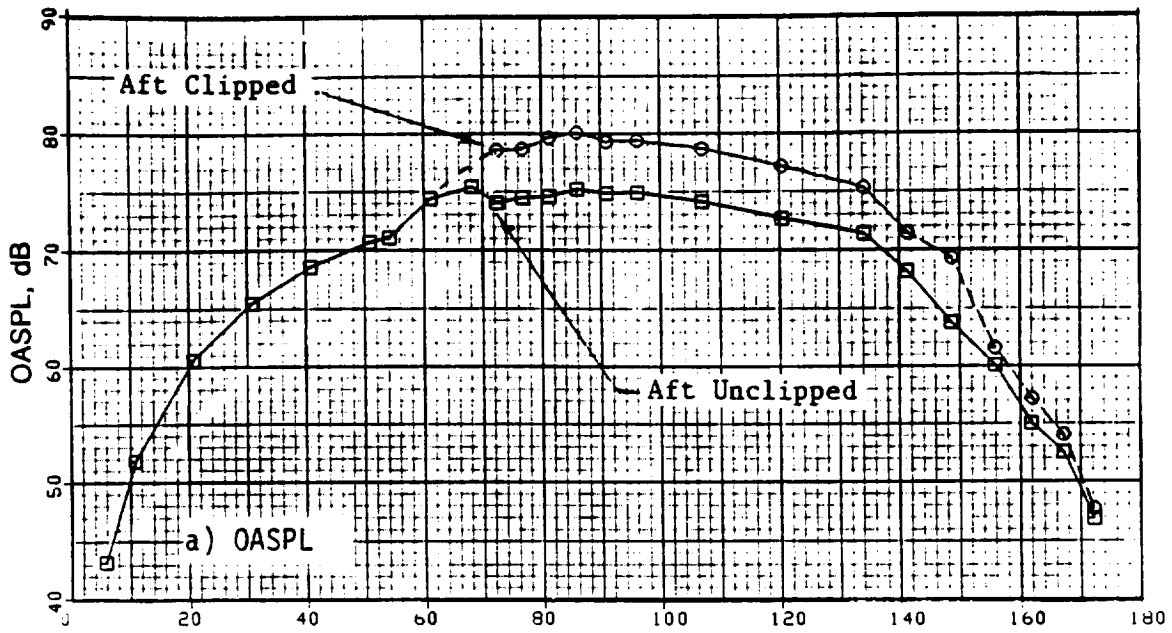


Figure 331. OASPL and PNL Directivity of the F-7/A-7 (9+8; Open Pitch) Configurations at Cutback.

3.05 M(10.0 FT.)DIA; 0.25 M₀; 549 M(1800 FT.)SIDELINE

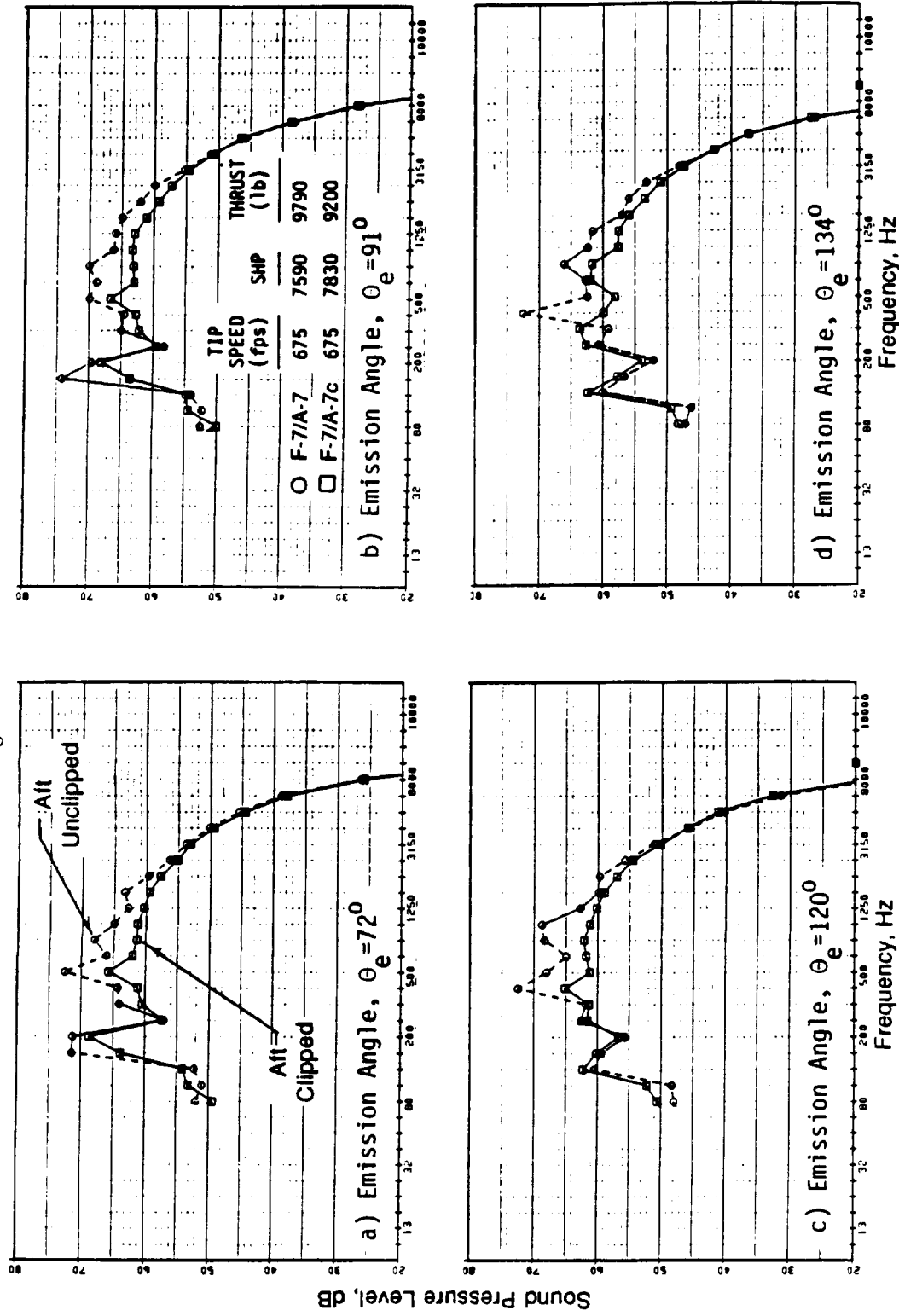


Figure 332. Selected Spectra of the F-7/A-7 (9+8, Open Pitch) Configurations at Cutback.

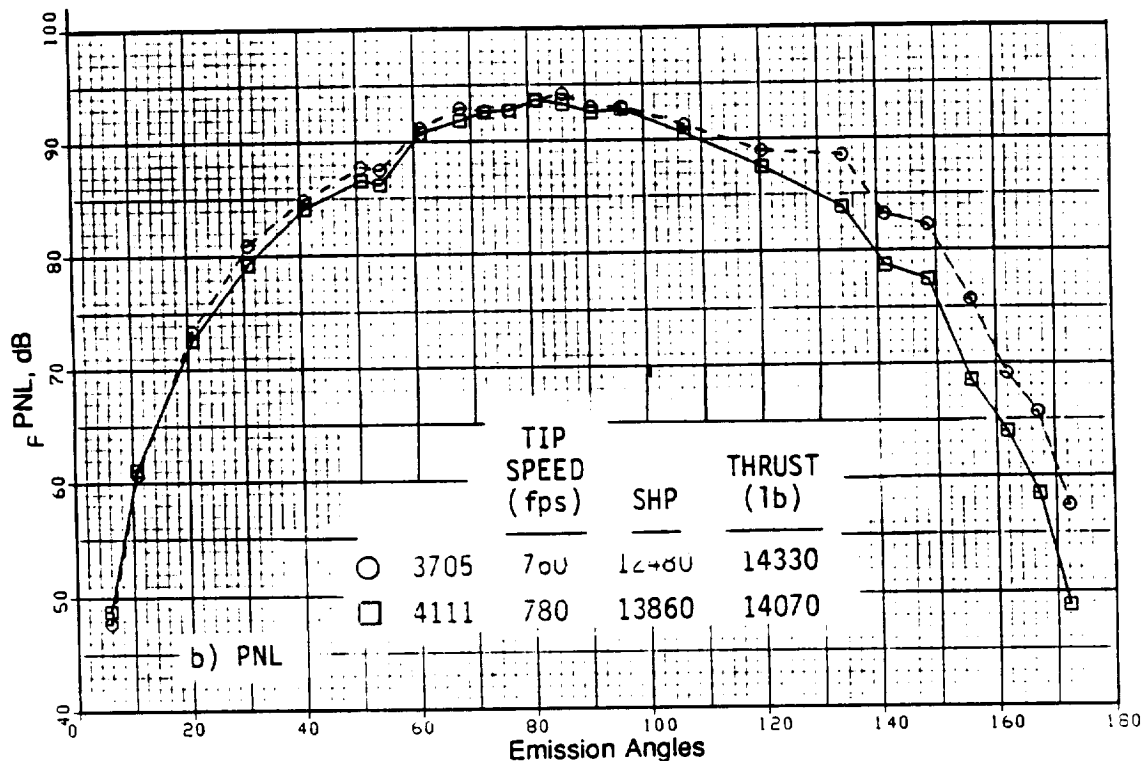
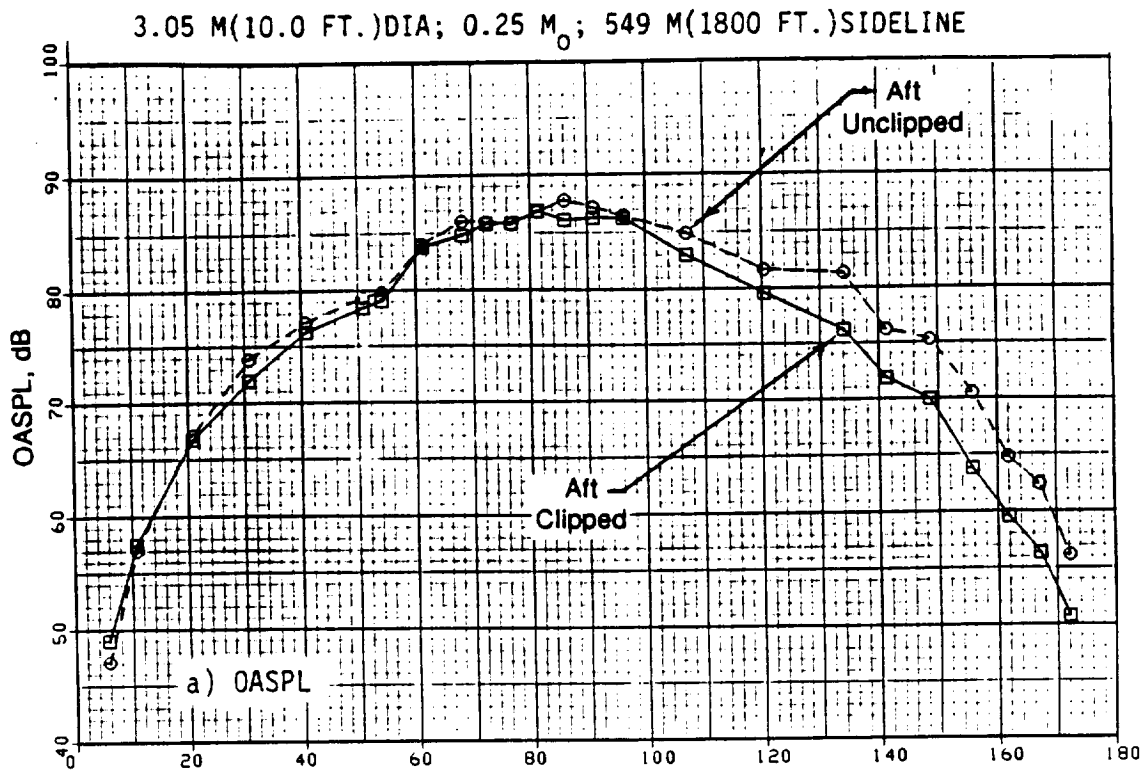


Figure 333. OASPL and PNL Directivity of the F-7/A-7 (9+8; Open Pitch) Configurations at Typical Takeoff.

3.05 M(10.0 FT.)DIA; 0.25 M₀; 549 M(1800 FT.)SIDELINE

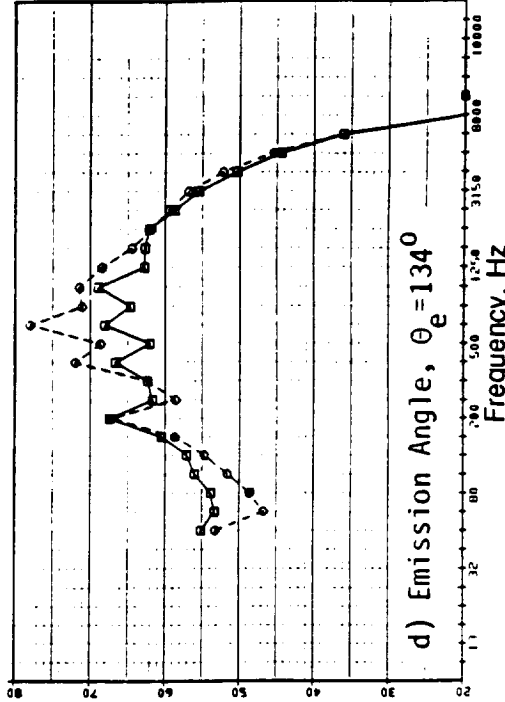
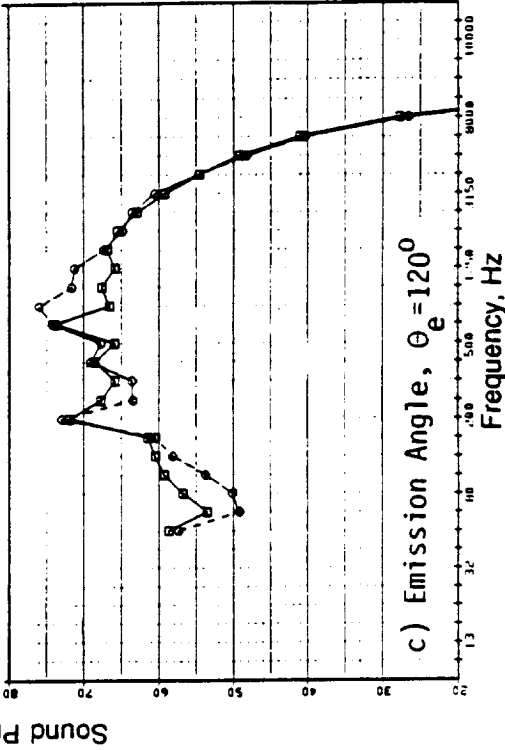
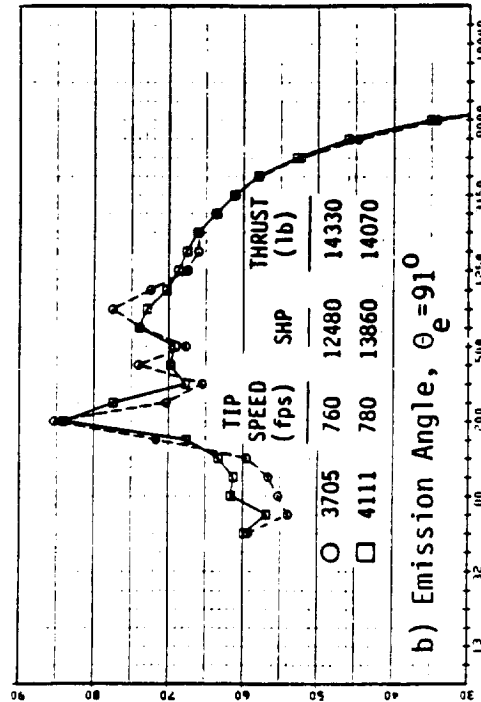
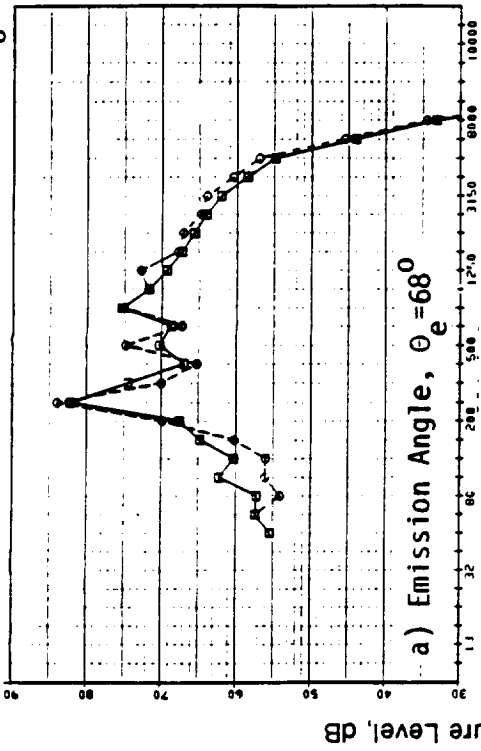
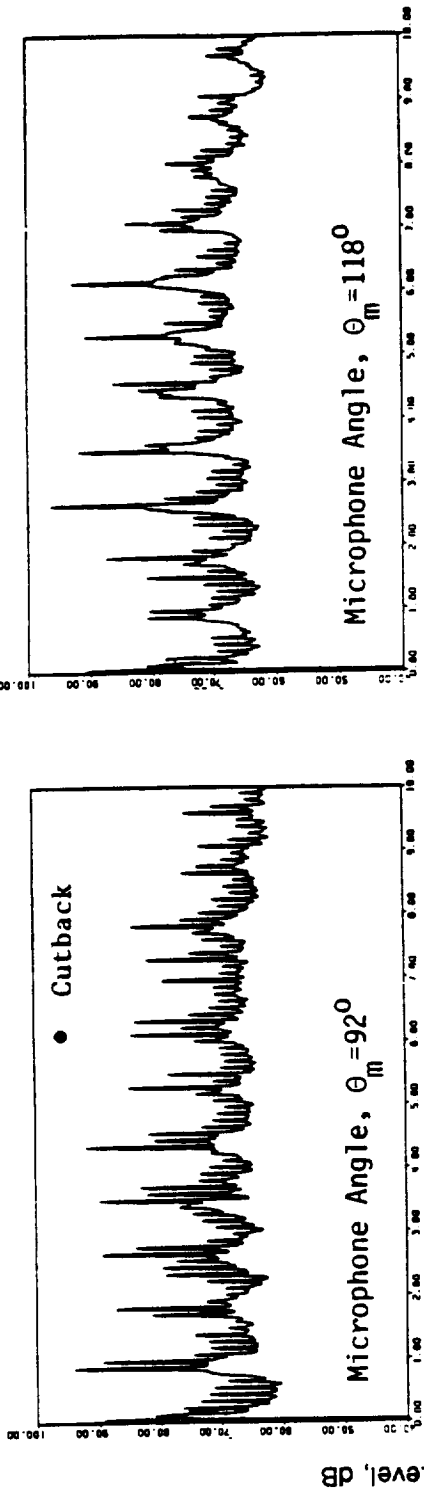
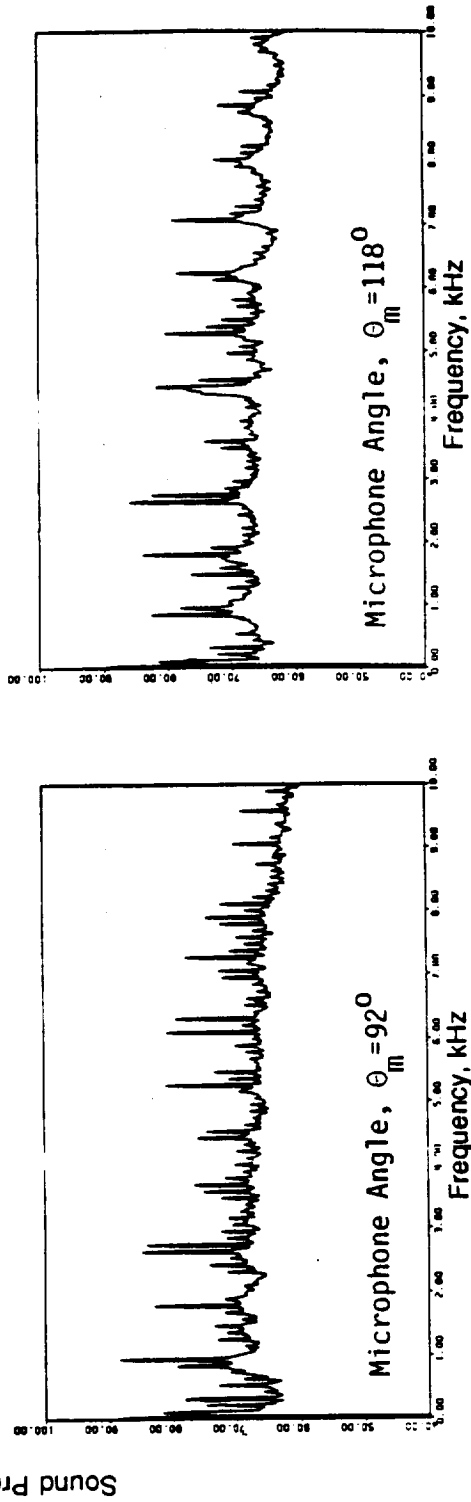


Figure 334. Selected Spectra of the F-7/A-7 (9+8 Open Pitch) Configurations at a Typical Takeoff.

- MODEL SCALE; AS MEASURED DATA
- 9x8 BLADES



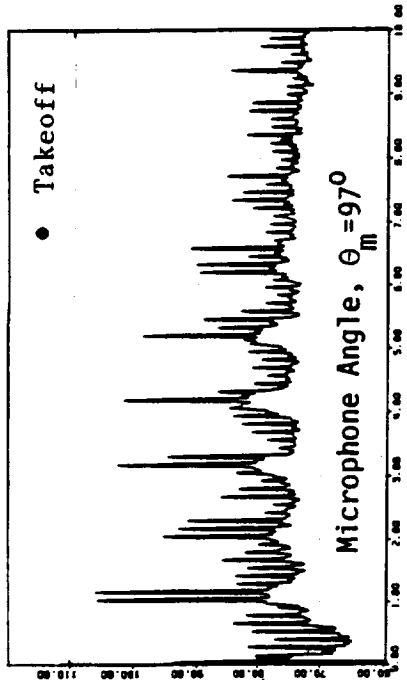
(a) F-7/A-7; 41.8/41.4 (Tip Speed = 675 fps; shp = 7590; Thrust = 9790 lb)



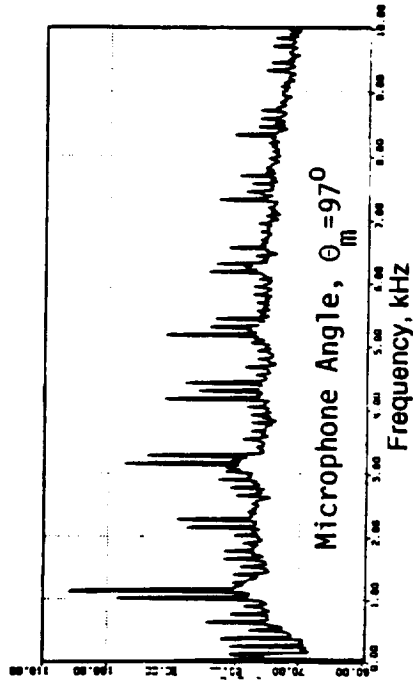
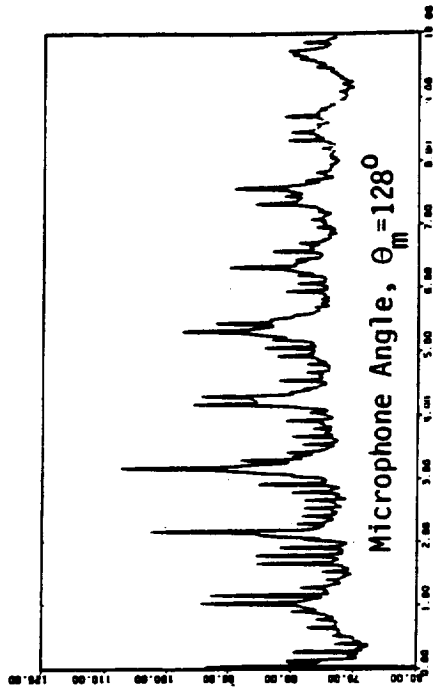
(b) F-7/A-7c; 41.8/48.3 (Tip Speed = 675 fps; shp = 7830; Thrust = 9190 lb)

Figure 335. Narrow-Band Spectra of Aft Unclipped and Clipped F-7/A-7, Open Pitch.

- MODEL SCALE; AS MEASURED DATA
- 9x8 BLADE



(c) F-7/A-7; 41.8/41.4 (Tip Speed = 810 fps; shp = 15,440; Thrust = 16,780 lb)



(d) F-7/A-7c; 41.8/48.3 (Tip Speed = 810 fps; shp = 15,700; Thrust = 15,300 lb)

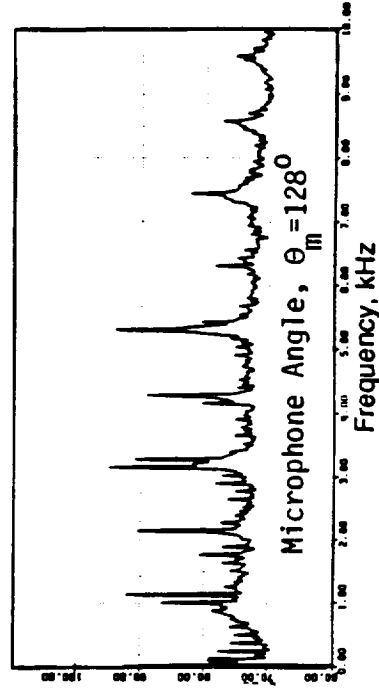
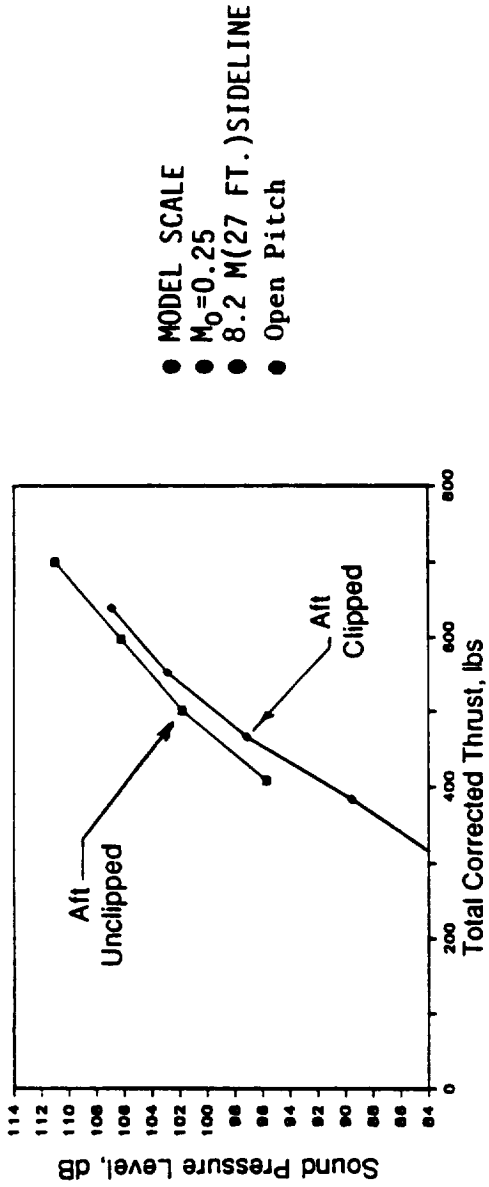


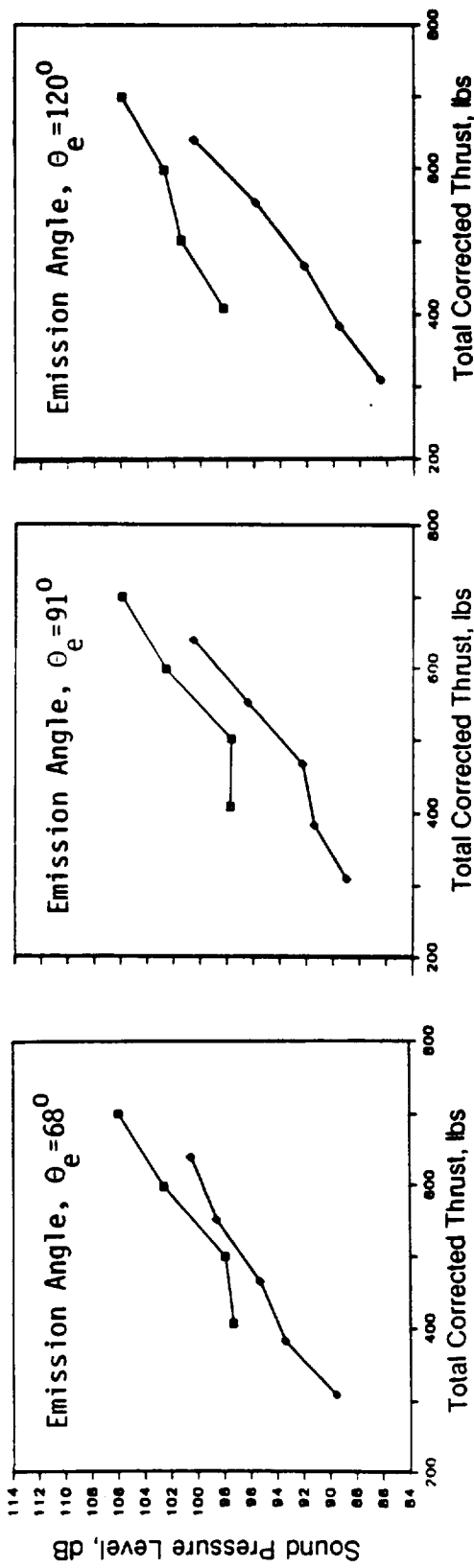
Figure 335. Narrow-Band Spectra of Aft Unclipped and Clipped F-7/A-7, Open Pitch (Concluded).



a) Fwd and Aft Rotor BPF and Harmonics at Emission Angle, $\theta_e = 91^\circ$

- F-7/A-7 41.8/41.4
- ◇ F-7/A-7c 41.8/48.3

- MODEL SCALE
- $M_0 = 0.25$
- 8.2 M(27 FT.) SIDELINE
- Open Pitch



b) Rotor-to-Rotor Interaction Tone Sum

Figure 336. Model-Scale Tone Sum Levels as a Function of Total Thrust.

3.05 M (10.0 FT.) DIA; 0.25 M₀; 549 M (1800 FT.) SIDELINE

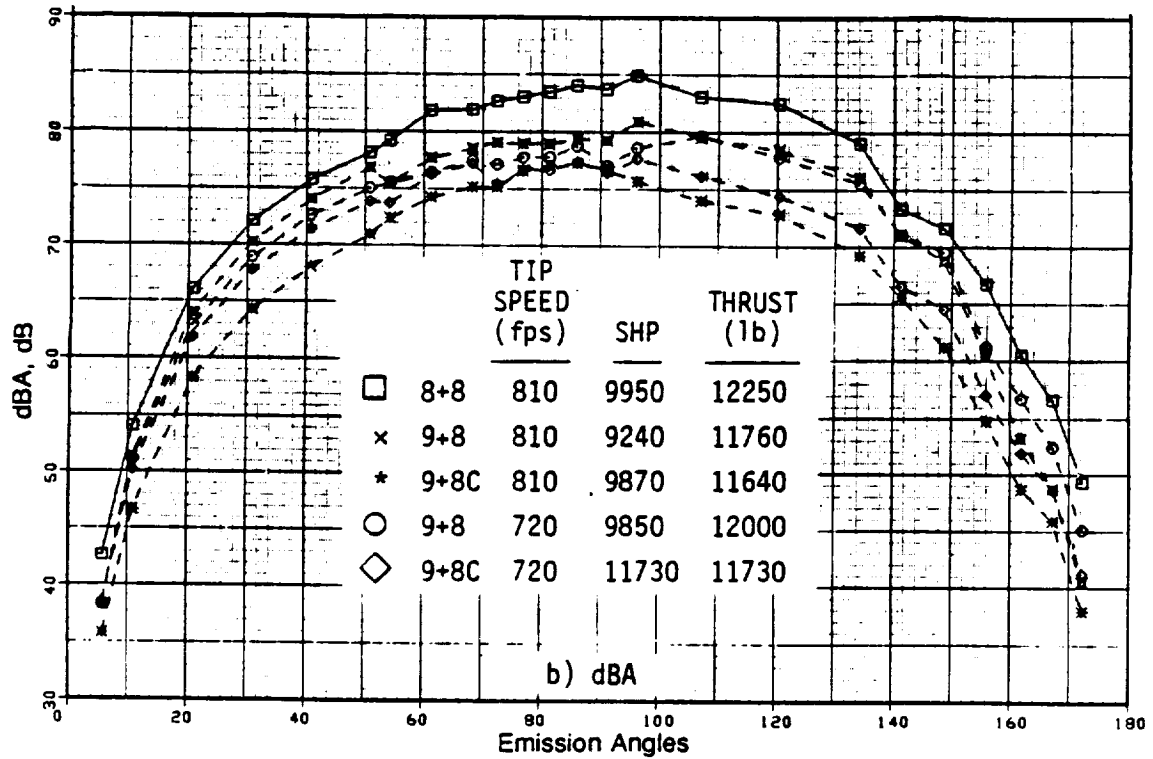
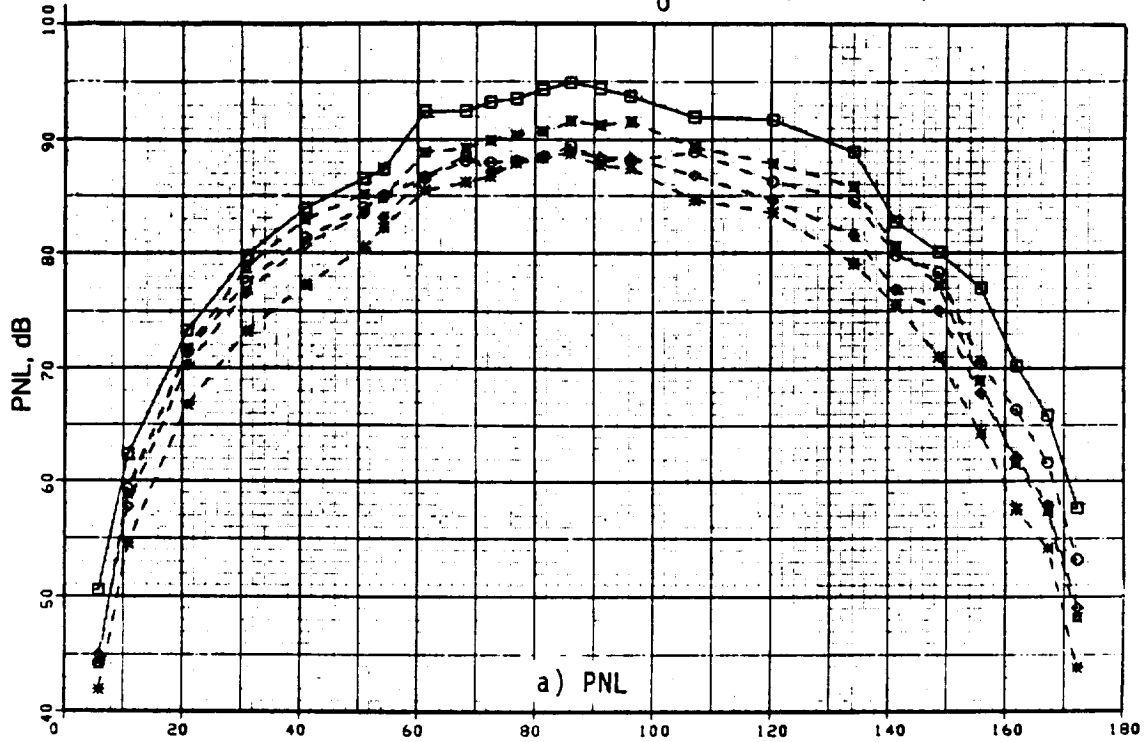


Figure 337. OASPL and PNL Directivity of F-7/A-7c (9+8) Compared to Baseline F-7/A-7 (8+8).

7.1.1.7.1 F-7/A-7 (9+8) at Maximum Spacing: Series 1

The F-7/A-7 (9+8) configuration was tested at Mach 0.20, 0.23, 0.25, and 0.30 with a fixed nominal-pitch angle. A comparison of the measured thrust and power data for these four test Mach numbers (Figure 338) substantiates that for a given angle, the loading increases with a decrease of Mach number; consequently, required thrust is obtained at a lower tip speed. In addition, the efficiency over the test range improves with a decrease in Mach number.

The acoustic data comparison (Figure 339) is presented in terms of scaled maximum OASPL, PNL, and the calculated EPNL, as functions of thrust and shp at Mach numbers of 0.20, 0.23, 0.25, and 0.30. Plotted as a function of thrust, these maximum OASPL and PNL data demonstrate that the peak noise values reduce with a decrease of Mach number for a given thrust due to decreased tip speed. For a given shp, acoustic data at the various Mach numbers correlate within a noise spread of 2 dB; EPNL values for a given shaft power indicate the data for flight Mach 0.2 to be greater due to the larger duration correction, even though the corresponding maximum PNL is lower. Combined effects of variation in efficiency, duration correction, and tip speed, result in the EPNL data as a function of thrust to correlate within 2 dB for Mach numbers increasing from 0.2 to 0.3.

7.1.1.7.2 F-7/A-7 (11+9) at Maximum Spacing: Series 2

The F-7/A-7 (11+9) configuration was also tested at Mach numbers of 0.2 and 0.25 with a fixed nominal pitch. The thrust and power measured at the two test Mach numbers are presented in Figure 340; similar to the Series 1 data, a decrease of tip speed with decrease of Mach number for a given thrust and a corresponding improvement in efficiency is noted. The acoustic data (in terms of the scaled and maximum OASPL, PNL, and the calculated EPNL) as functions of total thrust and shaft horsepower are depicted in Figure 341. In harmony with the results of Series 1, peak OASPL and PNL show reduced levels at flight Mach 0.2 (relative to those at flight Mach 0.25), due to reduced tip speed for a given thrust. When plotted against shp, these acoustic data correlate within a noise band of less than 2 dB; the EPNL data at the Mach numbers 0.2 and 0.25 also correlate within 1 dB for a given thrust.

PNL directivity and selected spectra at emission angles of 91° and 120° are depicted in Figure 342 for cutback and high thrust conditions. These data clearly reflect the decrease in the sound pressure levels at the blade passing frequencies and, hence, the steady-loading noise levels with decrease of Mach number due to a reduction in tip speed. As previously discussed (Section 7.1.1.5), some increase in interaction noise components occurs with decreased tip speed and Mach number. This is particularly evident in aft quadrants and where higher overall noise levels correspond with lower Mach numbers; these observations are also demonstrated (Figure 343) in the narrow-band tone sum directivities for cutback and high thrust conditions and in Figure 344 for the model-scale tone sum levels, as a function of total thrust.

7.1.1.8 Assessment of a Mounting Pylon

To determine the effect of a mounting pylon on acoustic characteristics of counterrotating blades, selected MPS tests were conducted at Cell 41 both with and without a pylon. Whereas, Section 5.1 described the scale model test pylon, this section briefly describes the test configurations and summarizes the acoustic analyses results. A total of five test series were conducted, utilizing model-scale F-7/A-7 and F-11/A-11 blade configurations. Table 62 identifies these configurations and summarizes test conditions.

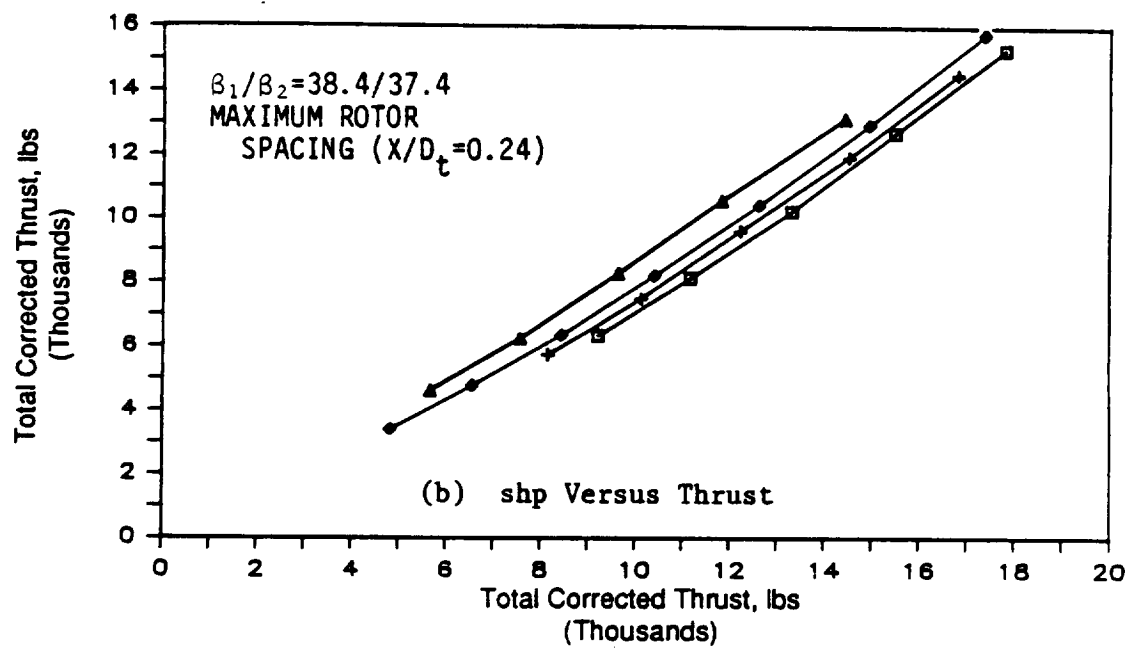
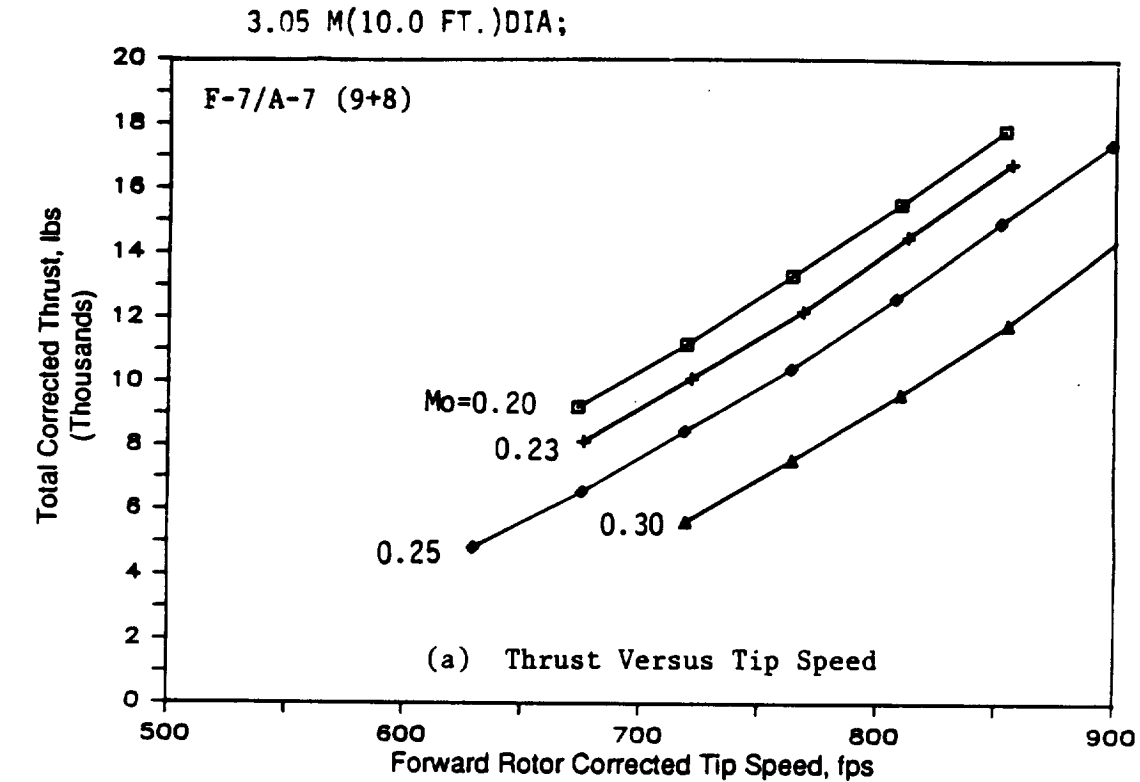


Figure 338. Aero Performance of F-7/A-7 (9+8) for Various Community Mach Numbers.

3.05 M(10.0 FT.)DIA; 549 M(1800 FT.)SIDELINE

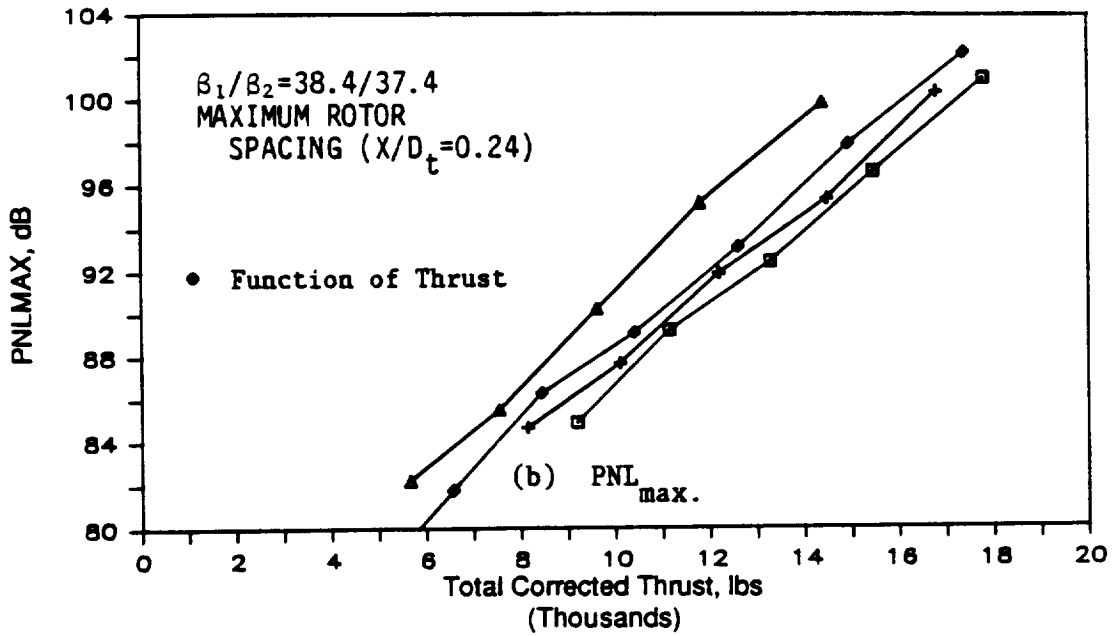
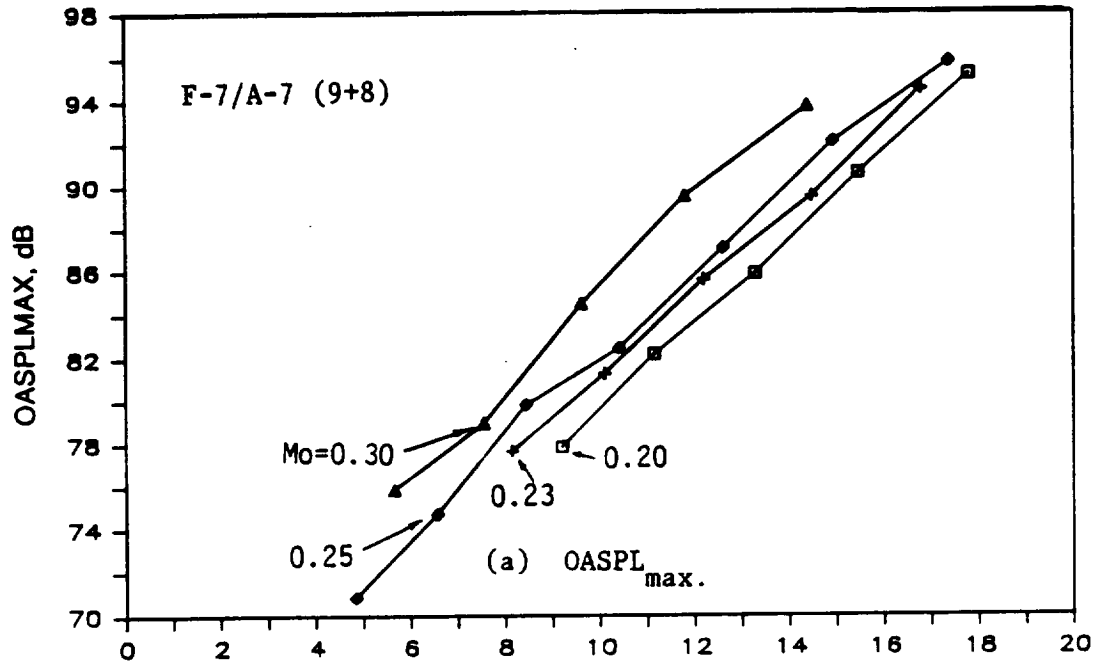


Figure 339. The Acoustic Data of F-7/A-7 (9+8) at a Pitch Angle of 38.4/37.4 at Various Community Mach Numbers.

3.05 M(10.0 FT.)DIA; 549 M(1800 FT.)SIDELINE

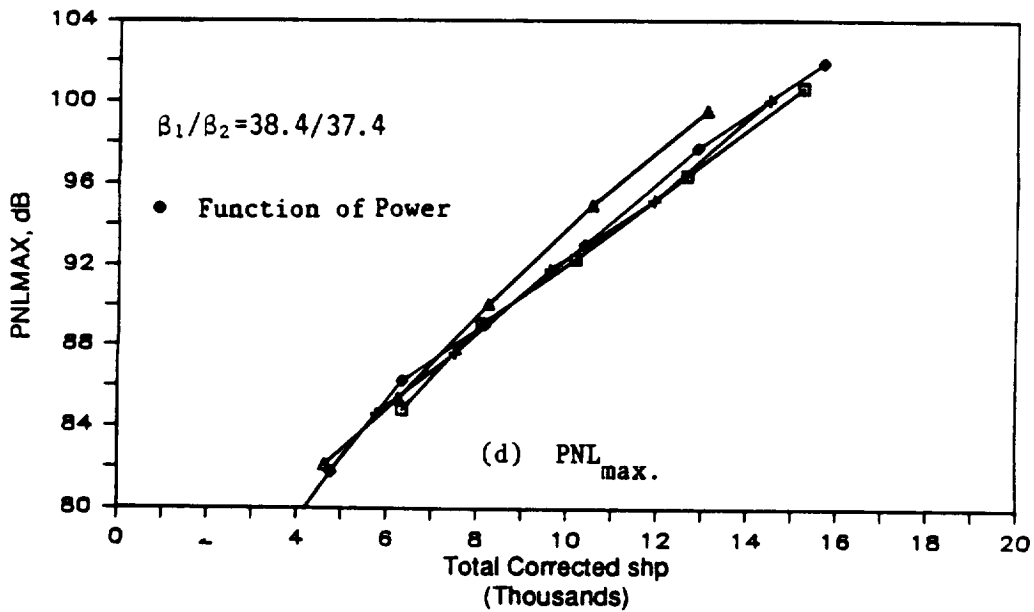
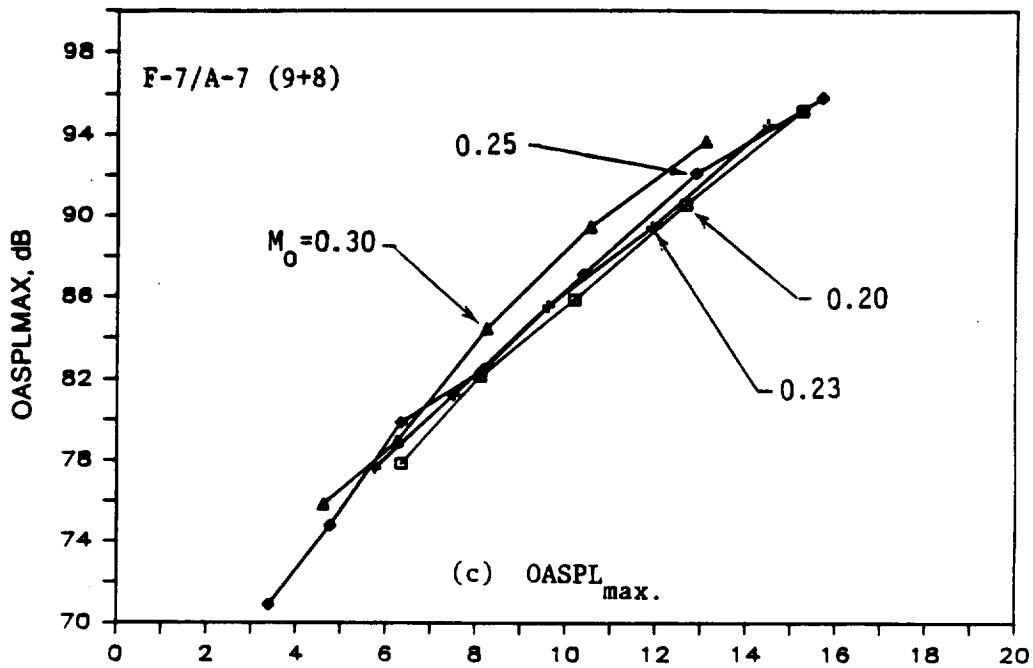


Figure 339. The Acoustic Data of F-7/A-7 (9+8) at a Pitch Angle of 38.4/37.4 at Various Community Mach Numbers (Continued).

3.05 M(10.0 FT.)DIA; 549 M(1800 FT.)SIDELINE

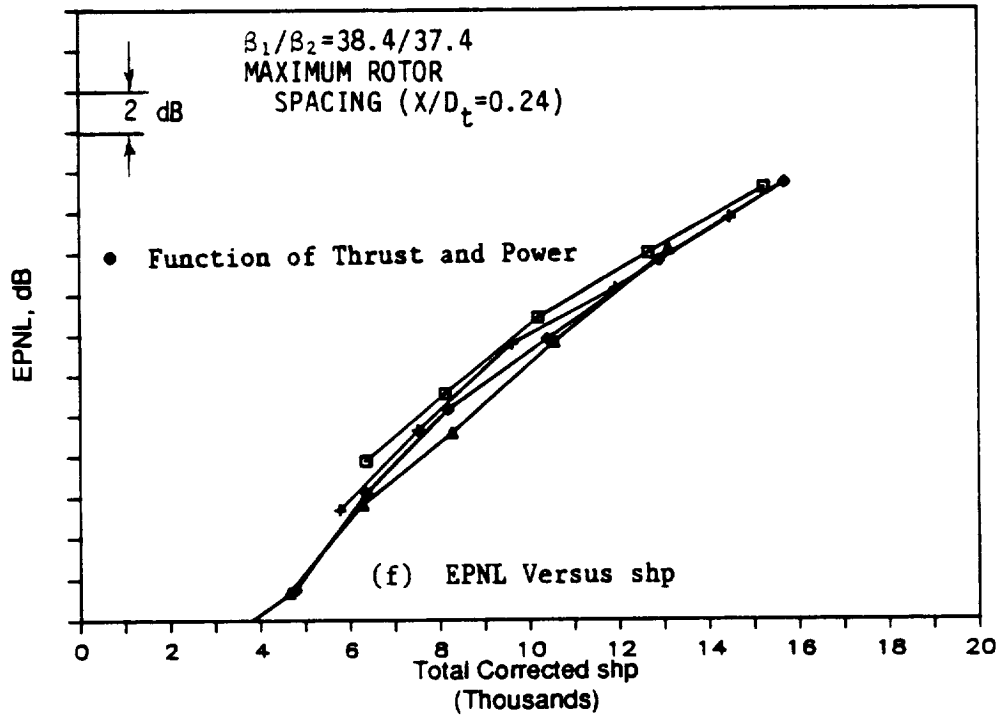
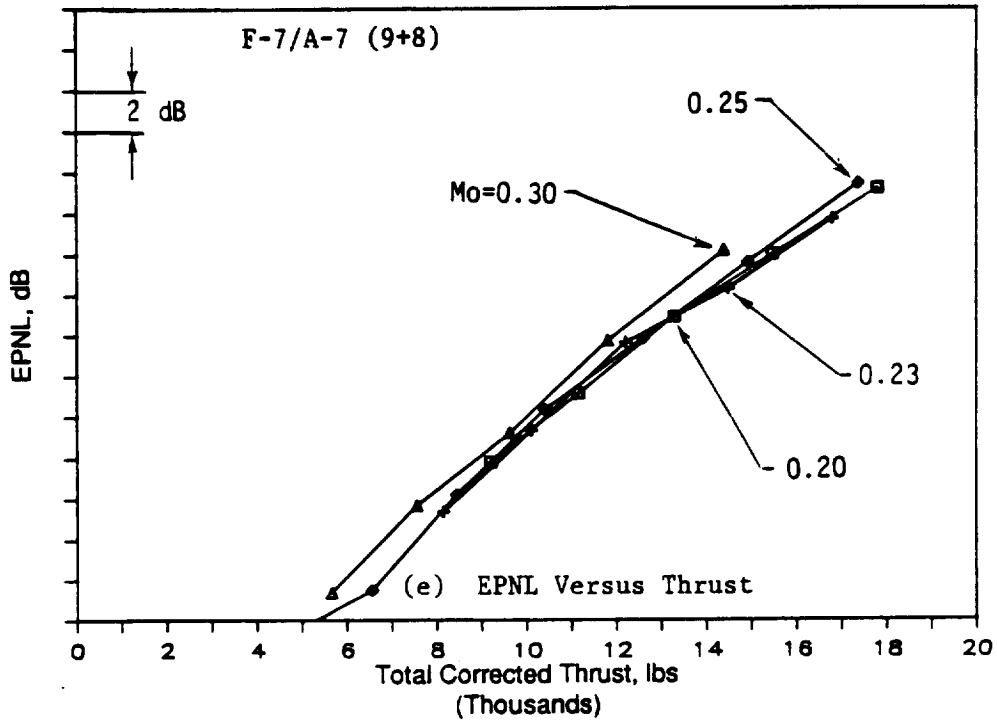


Figure 339. The Acoustic Data of F-7/A-7 (9+8) at a Pitch Angle of 38.4/37.4 at Various Community Mach Numbers (Concluded).

3.05 M(10.0 FT. MPA; 549 M(1800 FT.)SIDELINE

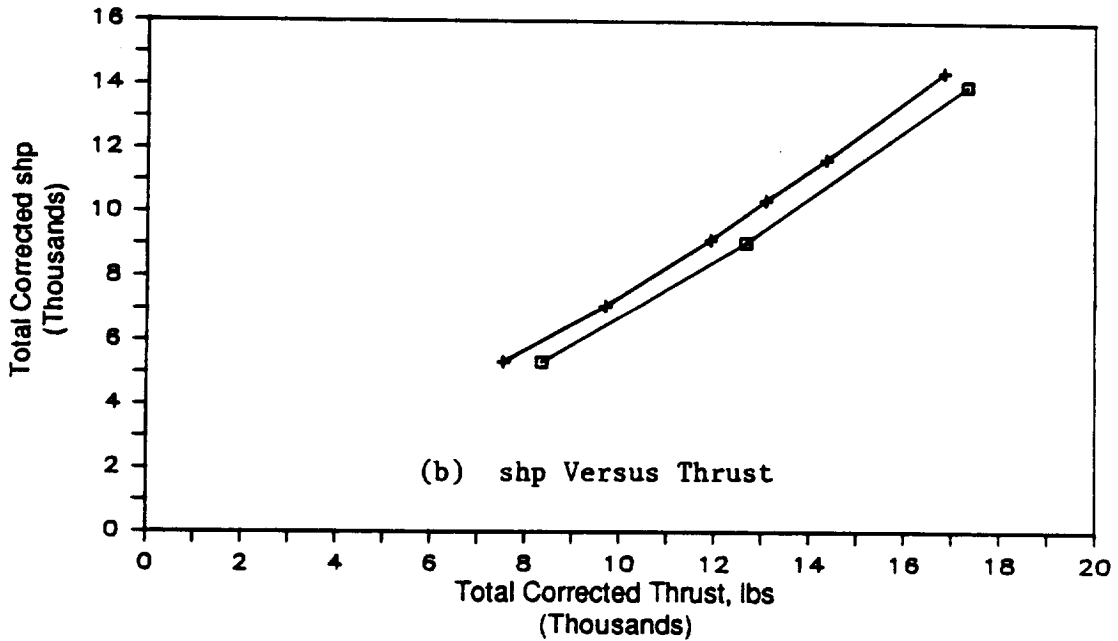
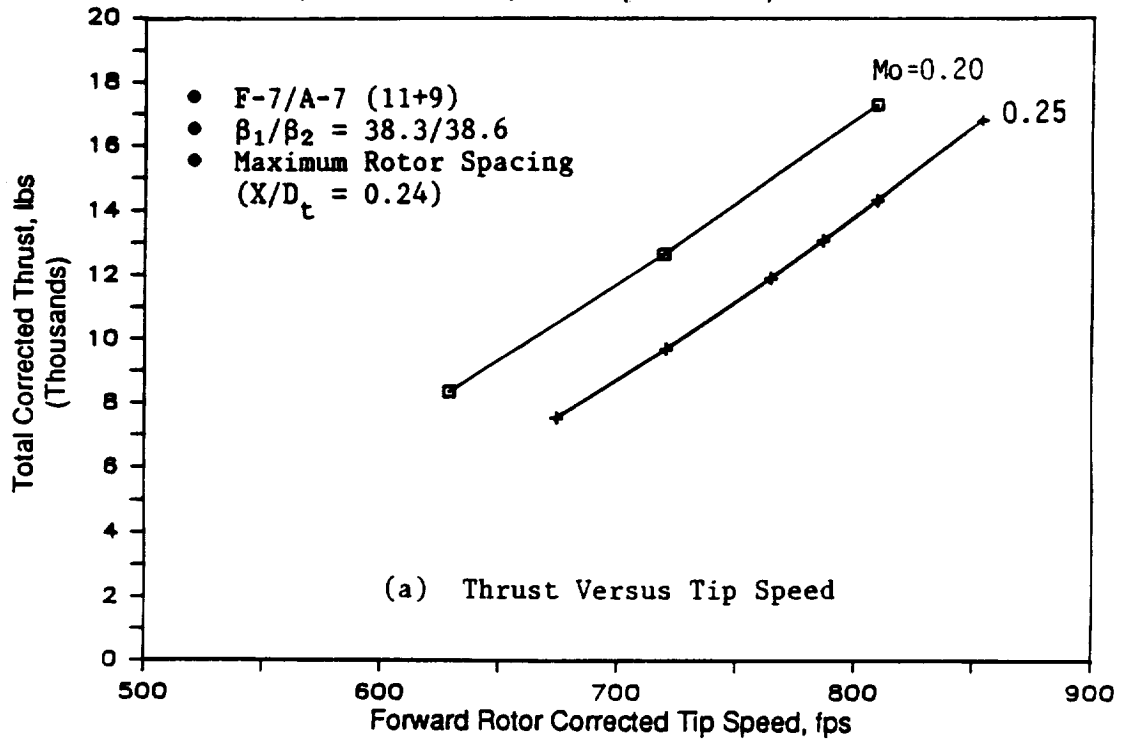


Figure 340. Aero Performance of F-7/A-7 (11+9) for Various Community Mach Numbers.

3.05 M(10.0 FT.)DIA; 549 M(1800 FT.)SIDELINE

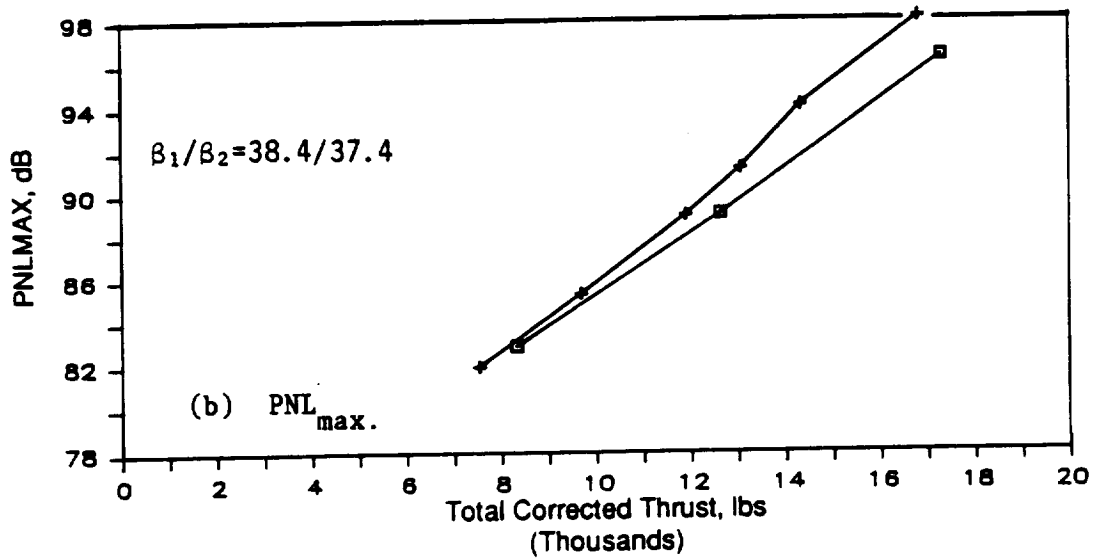
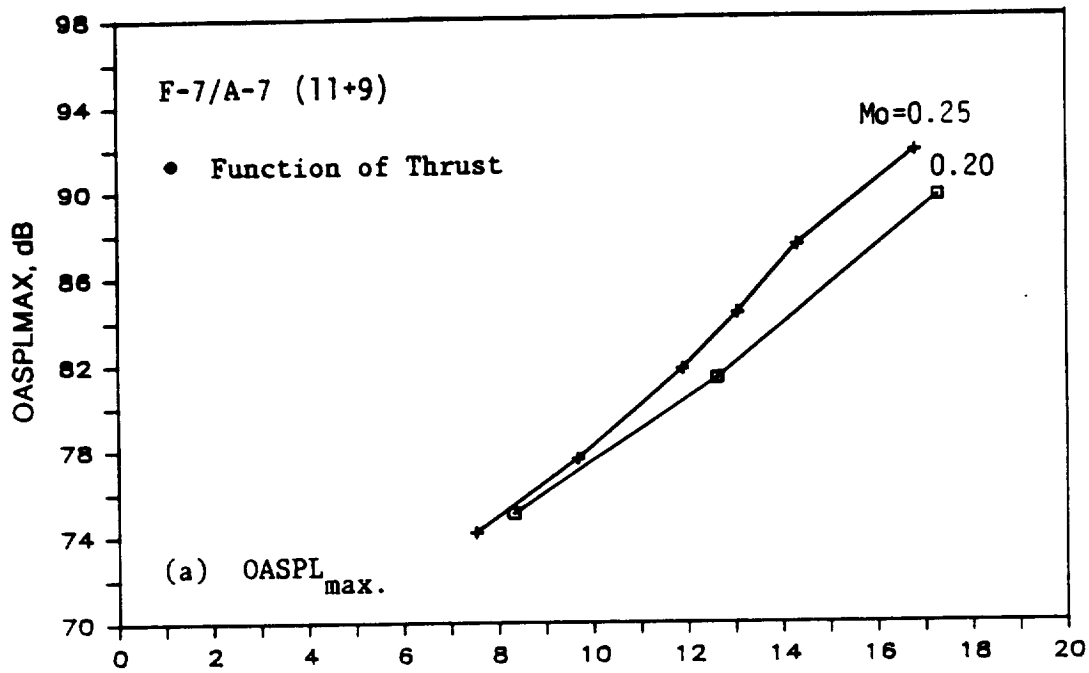


Figure 341. Acoustic Data of F-7/A-7 (11+9) at a Pitch Angle of 38.4/37.4 for Various Community Mach Numbers.

3.05 M(10.0 FT.)DIA; 549 M(1800 FT.)SIDELINE

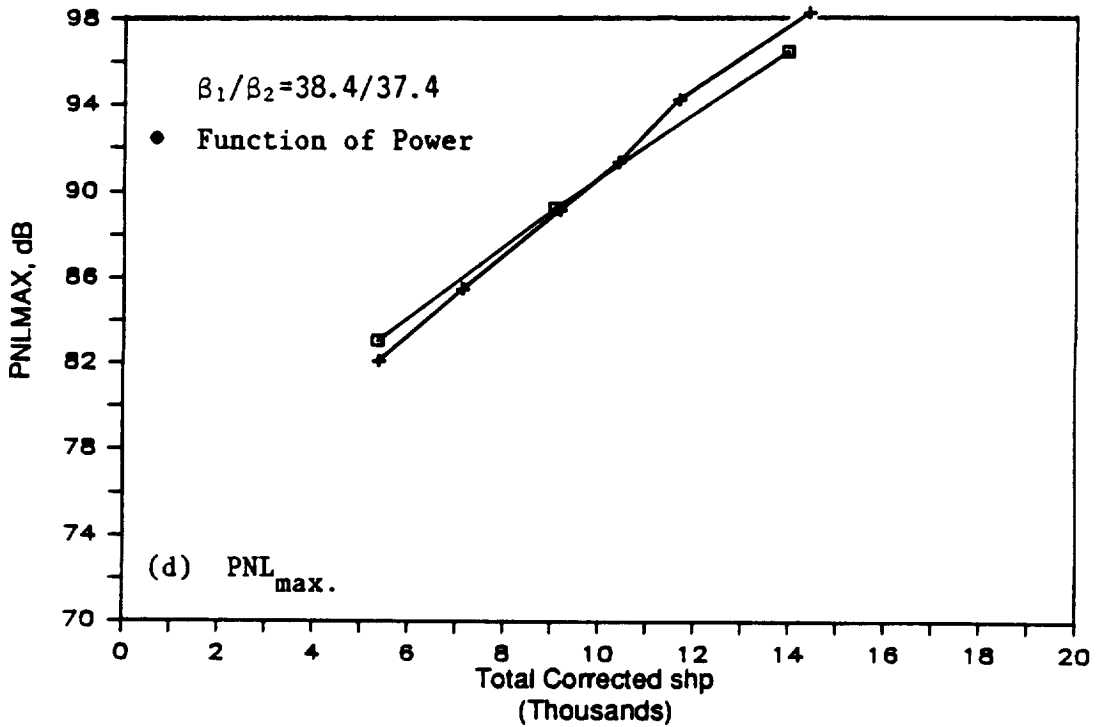
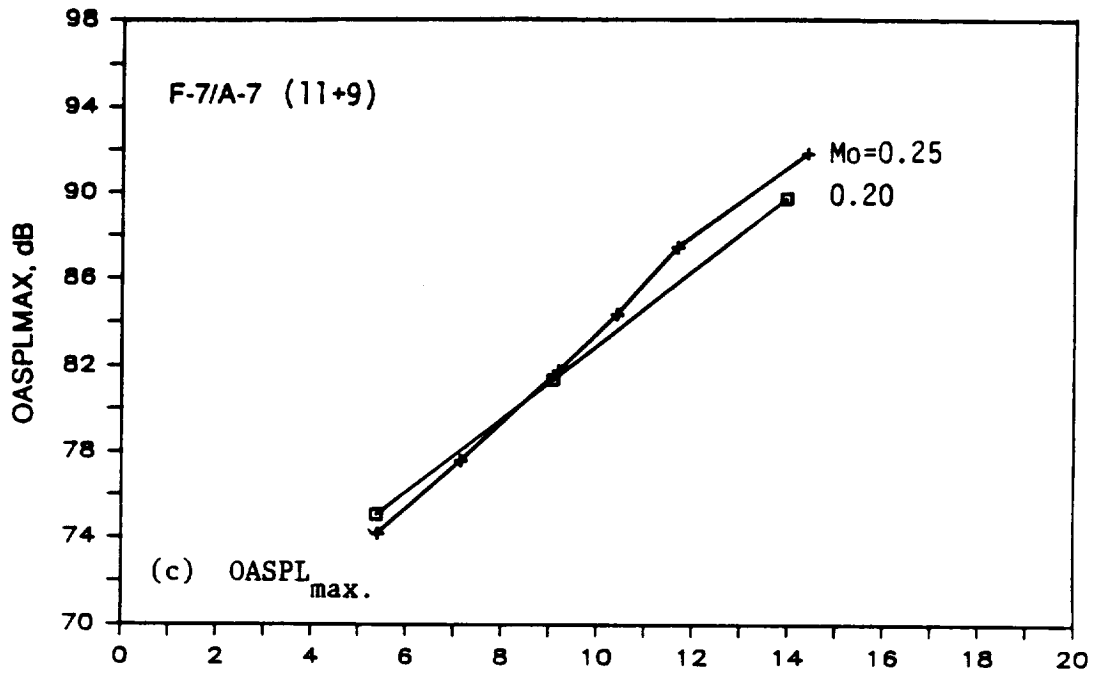


Figure 341. Acoustic Data of F-7/A-7 (11+9) at a Pitch Angle of 38.4/37.4 for Various Community Mach Numbers (Continued).

3.05 M(10.0 FT.)DIA; 549 M(1800 FT.)SIDELINE

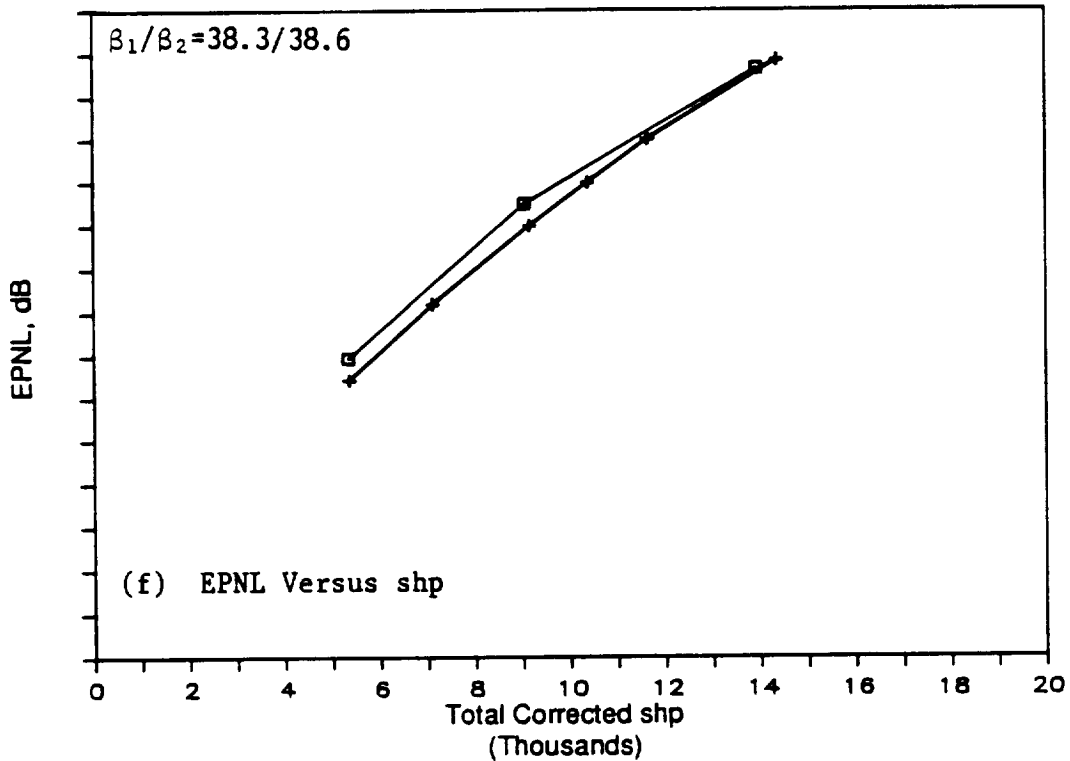
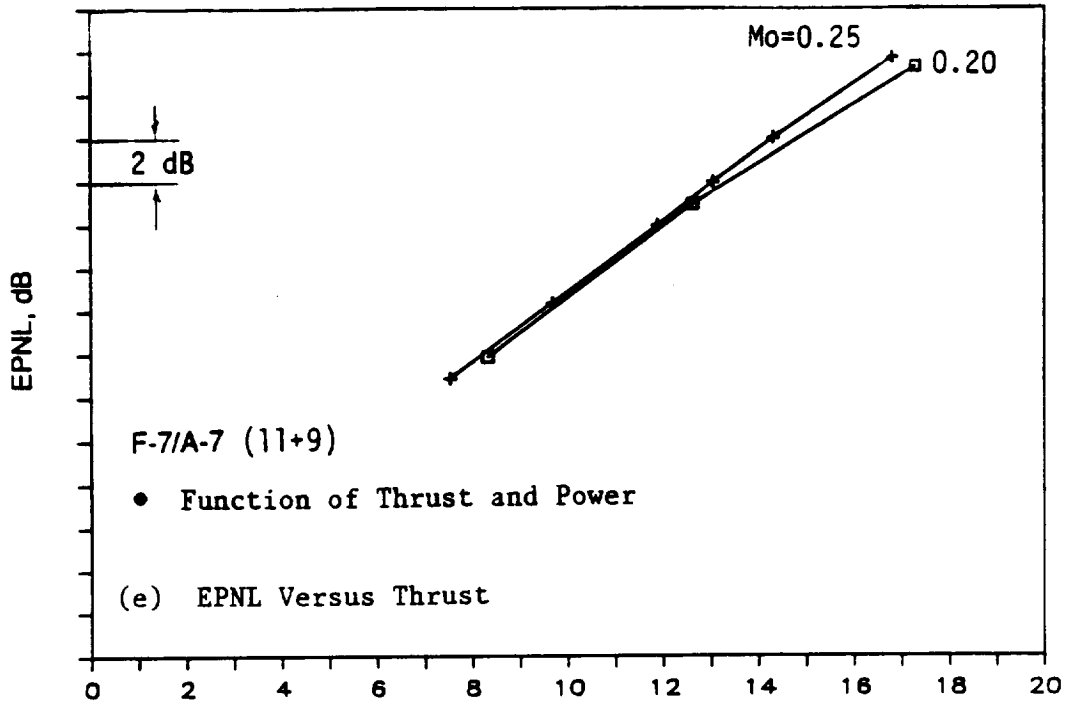


Figure 341. Acoustic Data of F-7/A-7 (11+9) at a Pitch Angle of 38.3/38.6 for Various Community Mach Numbers (Concluded).

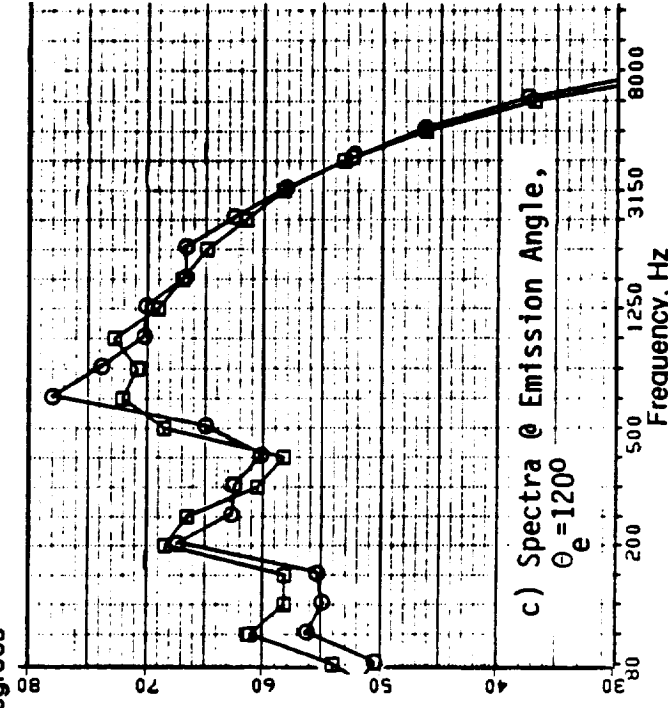
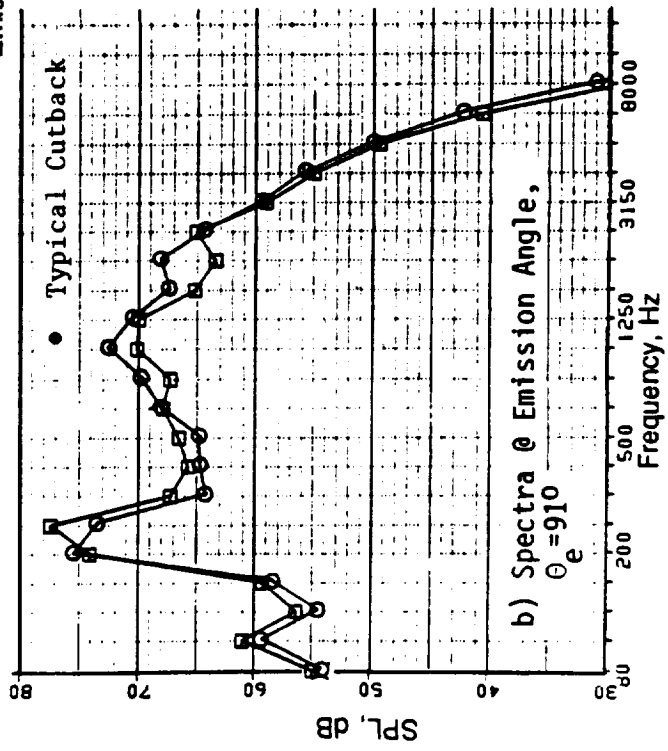
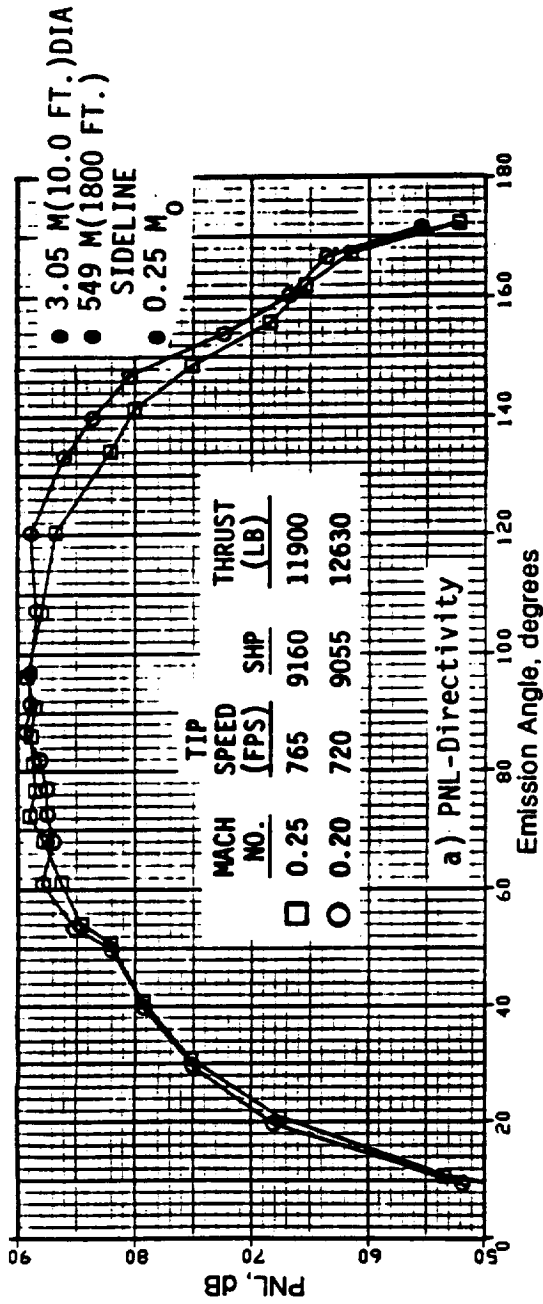


Figure 342. PNL Directivity and Selected Spectra for F-7/A-7 (11+9), with Pitch Angle of 38.3/38.6.

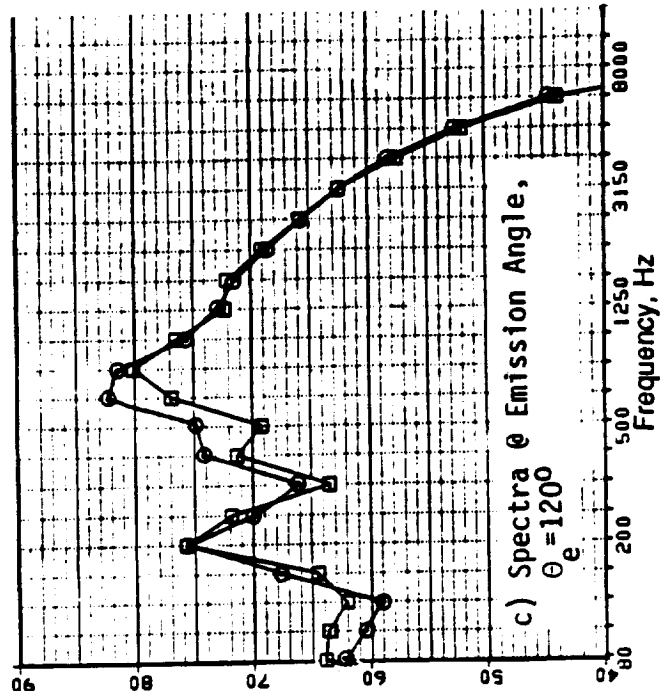
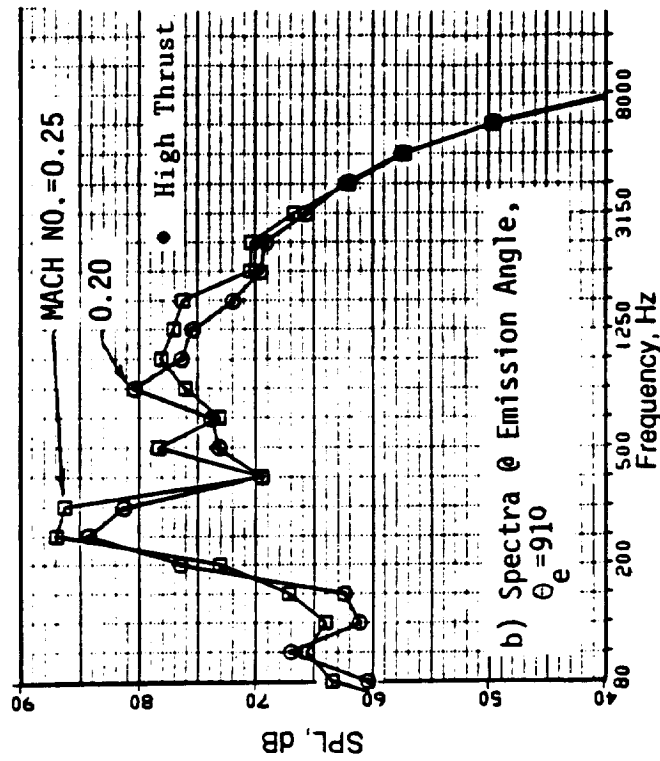
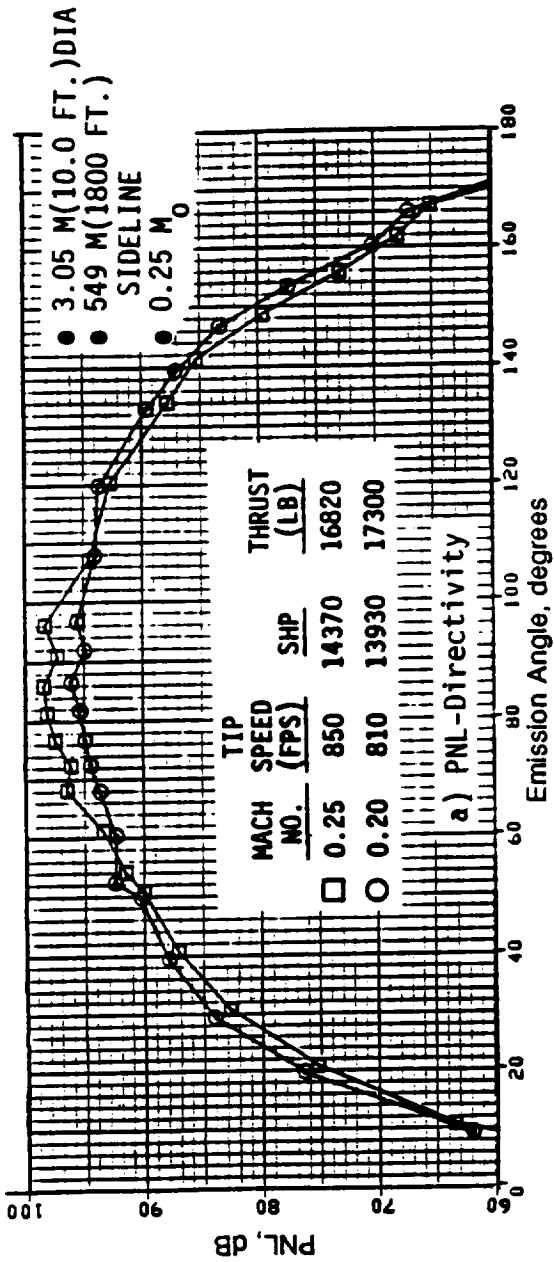


Figure 342. PNL Directivity and Selected Spectra for F-7/A-7 (11+9), with Pitch Angle of 38.3/38.6 (Concluded).

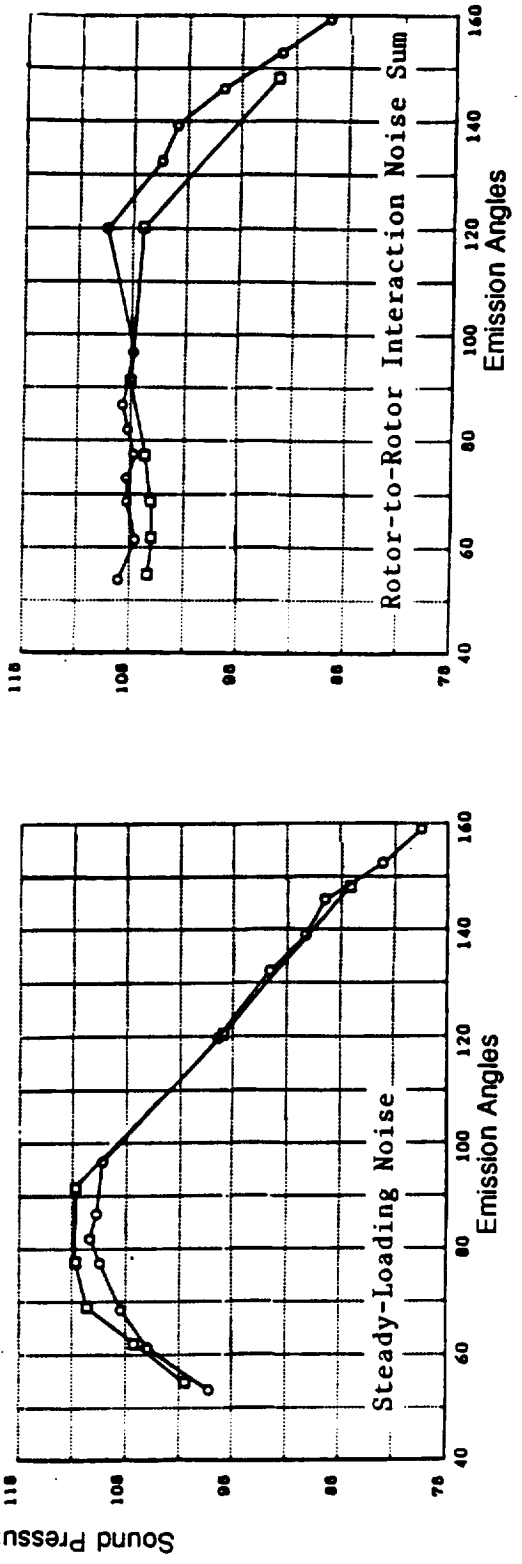
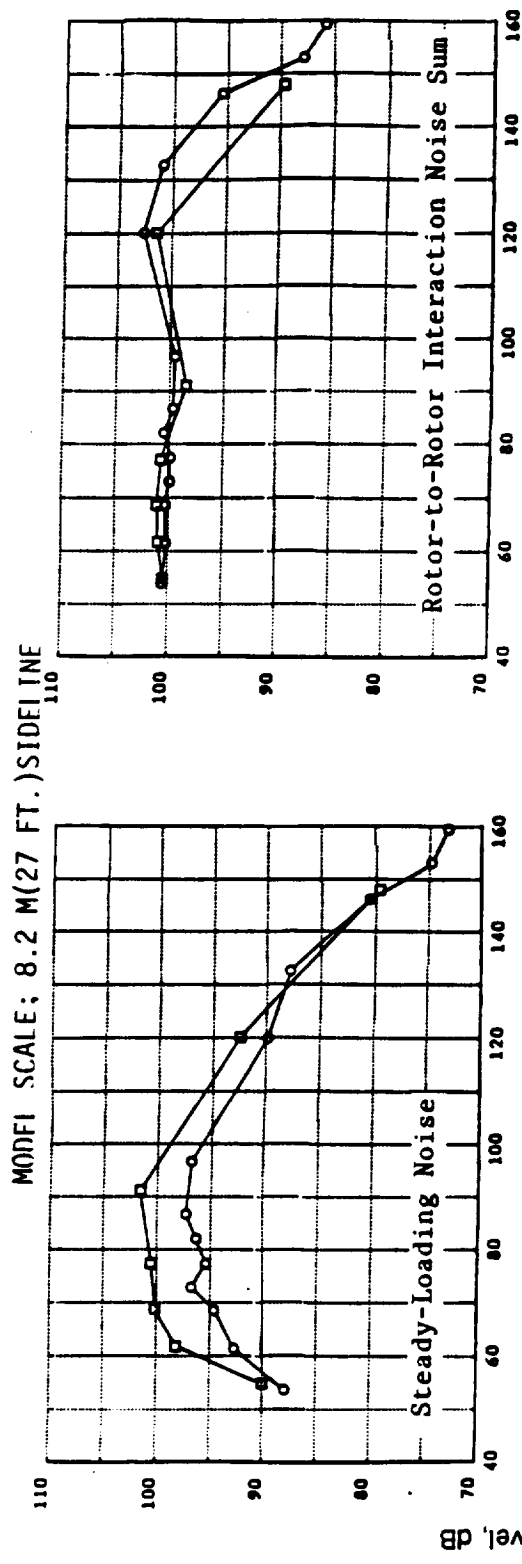
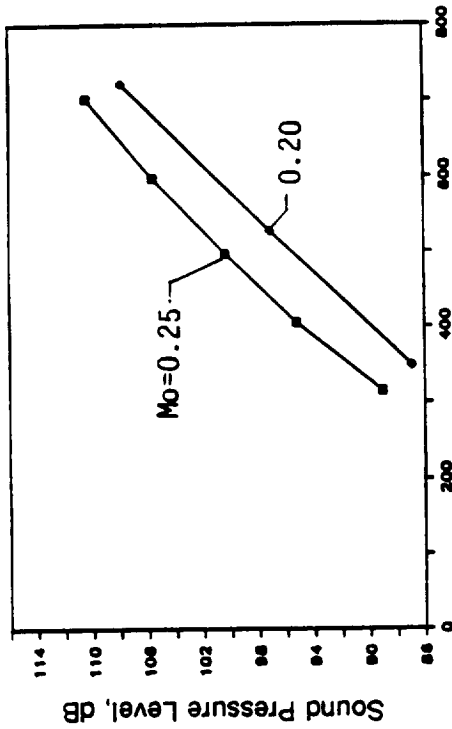
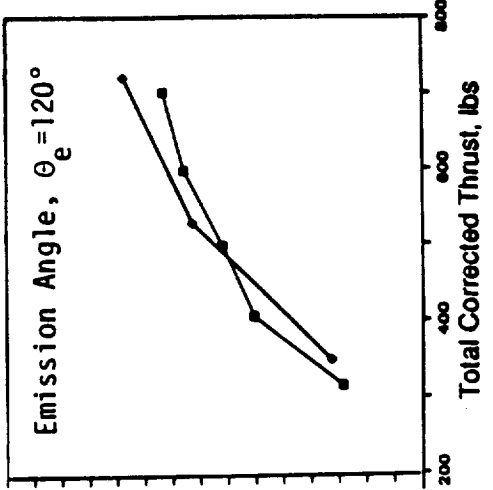
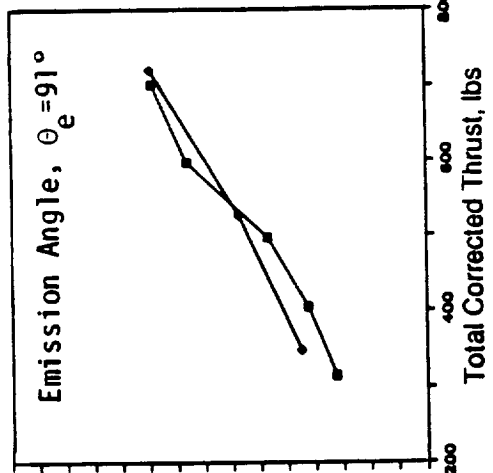
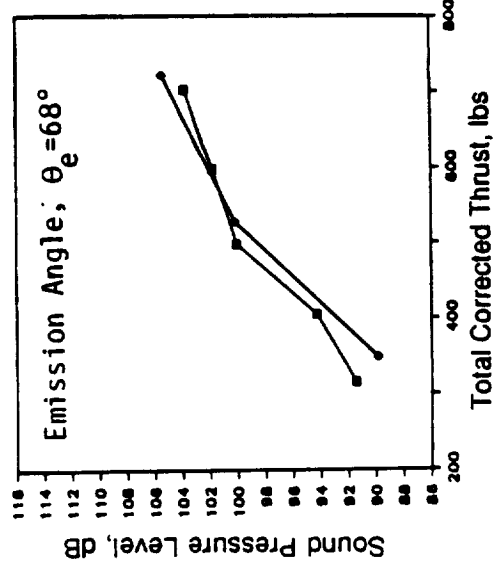


Figure 343. Model-Scale Tone Sum Directivities of F-7/A-7 (11+9, 38.3/38.6) at Flight Mach Numbers 0.25 and 0.20 for Cutback and High Thrust.

- Model Scale
- 8.2M (27 FT) Sideline
- Maximum Rotor Spacing ($X/D_t = 0.24$)
- $\beta_1/\beta_2 = 38.3/38.6$



a) Steady Loading Noise @ Emission Angle, $\theta_e = 91^\circ$



b) Rotor to Rotor Interaction Noise

Figure 344. Model-Scale Tone Sum Levels at Mach Numbers 0.25 and 0.20 for F-7/A-7 as a Function of Thrust.

Table 62. Cell 41 Pylon Test Summary.

Series	Blade Configuration	Blade Spacing	Pitch Angle	Pylon/ Spacing	Run Nos.
1	F-7/A-7 (8+8)	Nominal	37.9/37.4 (Nominal)	None/	95
				Nominal	96
2	F-7/A-7 (9+8)	Maximum	41.8/41.4 (Open)	None/	37
				Close	38
				Nominal	39
3	F-7/A-7c (9+8)	Maximum	36.3/42.7 (Nominal)	None/	43
				Nominal	46
4	F-7/A-7c (9+8)	Nominal	36.3/42.7 (Nominal)	None/	45
				Nominal	46
5	F-11/A-11 (11+9)	Maximum	54.2/47.5 (Open)	None/	112
				Nominal	113

For the MPS tests, nominal and maximum rotor spacings refer to the axial spacing between pitch-change axes of the forward and aft rotors, and are equal to 10.6 cm (4.16 in.) and 15 cm (5.90 in.), respectively; yielding spacing-to-diameter ratios of 0.169 and 0.24. However, test pylon spacings (Figure 345) termed "nominal" and "close," are defined by the axial distance between the trailing edge of the pylon at the hub and the forward rotor pitch-change axis, and are equal to 7.46 cm (2.94 in.) and 4.75 cm (1.87 in.), respectively.

This section discusses the acoustic data measured (at a simulated flight Mach number of 0.25) during the above-described five series of tests. Results presented are measured data with no angle-of-attack.

7.1.1.8.1 F-7/A-7 (8+8) and F-7/A-7 (9+8): Series 1 and 2

The F-7/A-7 with 8 forward and 8 aft blades (nominal pitch, nominal rotor spacing) was tested with the pylon mounted at nominal spacing. The F-7/A-7 with 9 forward and 8 aft blades (open pitch, maximum rotor spacing) was tested with the pylon mounted at both close and nominal pylon spacings. The acoustic data in terms of the scaled maximum levels of OASPL, PNL, and dBA (with and without the pylons) are compared in Figure 346 as a function of total thrust. Figure 346 indicates the effect of the nominal spaced pylon on PNL and OASPL to be 0.5 dB to 1.0 dB for the 8+8 and 1 dB to 2 dB for the 9+8. Moving the pylon position from nominal to close doubled this effect, to 2 dB to 3 dB for the 9+8 configuration. These effects of pylon on noise levels are observed for thrusts that are greater than 35,500 N (8,000 lb), including typical takeoff and cutback conditions; the impact of pylon on maximum dBA; however, for all of these conditions appears to be less significant.

The typical OASPL and PNL directivities (Figure 347) and selected spectra (Figure 348) of the F-7/A-7 (8+8) configuration, both with and without nominal spaced pylon and for a typical cutback thrust, are presented. The impact of pylon on the directivity is seen only in the region of the plane-of-rotation. The impact on spectra is noted mostly at the BPF at all microphone locations; however, no significant effect on total noise levels in the forward and aft quadrants is noted; since

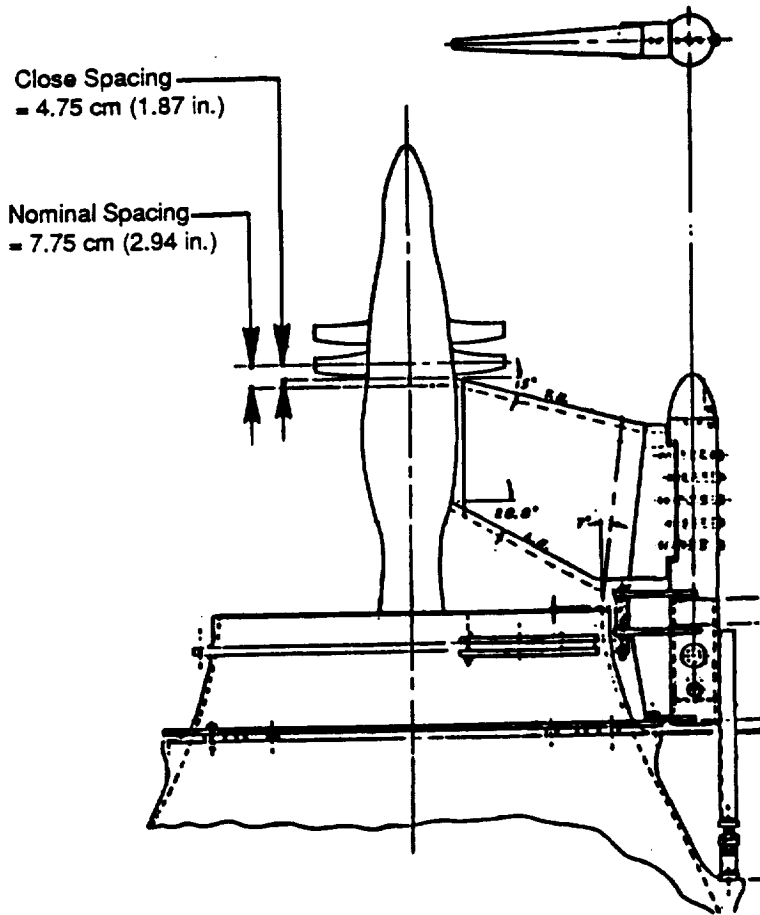


Figure 345. Schematic of MPS Cell 41 Setup, Detailing the Nominal and Close Pylon Positions.

ORIGINAL PAGE IS
OF POOR QUALITY

F-7/A-7; 0.25 M₀ 3.05m (10.0 ft) Diameter 549m (1800 ft) Sideline

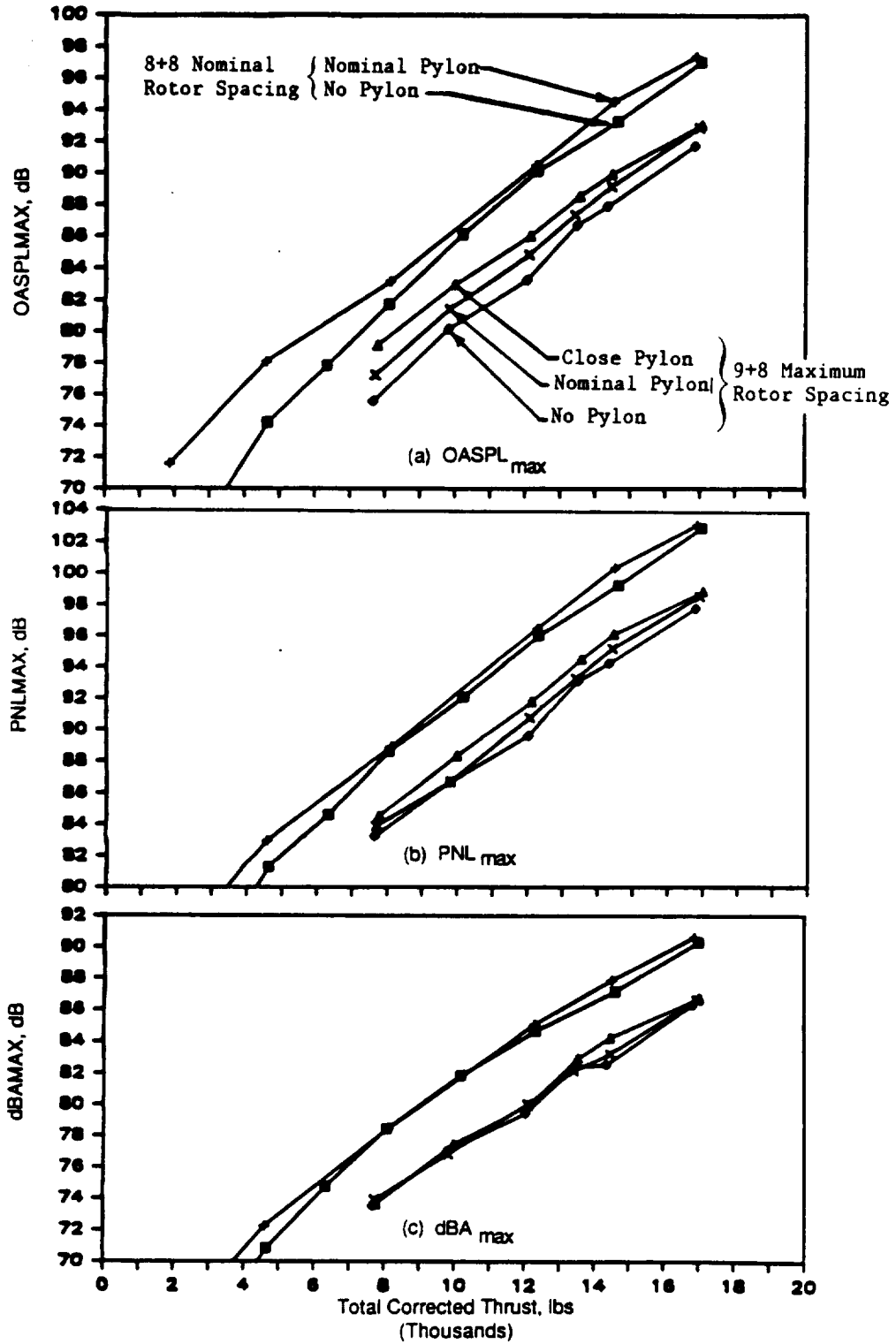


Figure 346. Effects of Pylon on Maximum Noise Data of F-7/A-7 with 8+8 and 9+8 Blades.

F-7/A-7 8+8, NOMINAL ROTOR SPACING, 37.9/34.4; 90% RPM
 3.05m (10.0 FT.) DIA.; 0.25 M_n ; 549m (1800 FT.) SIDELINE

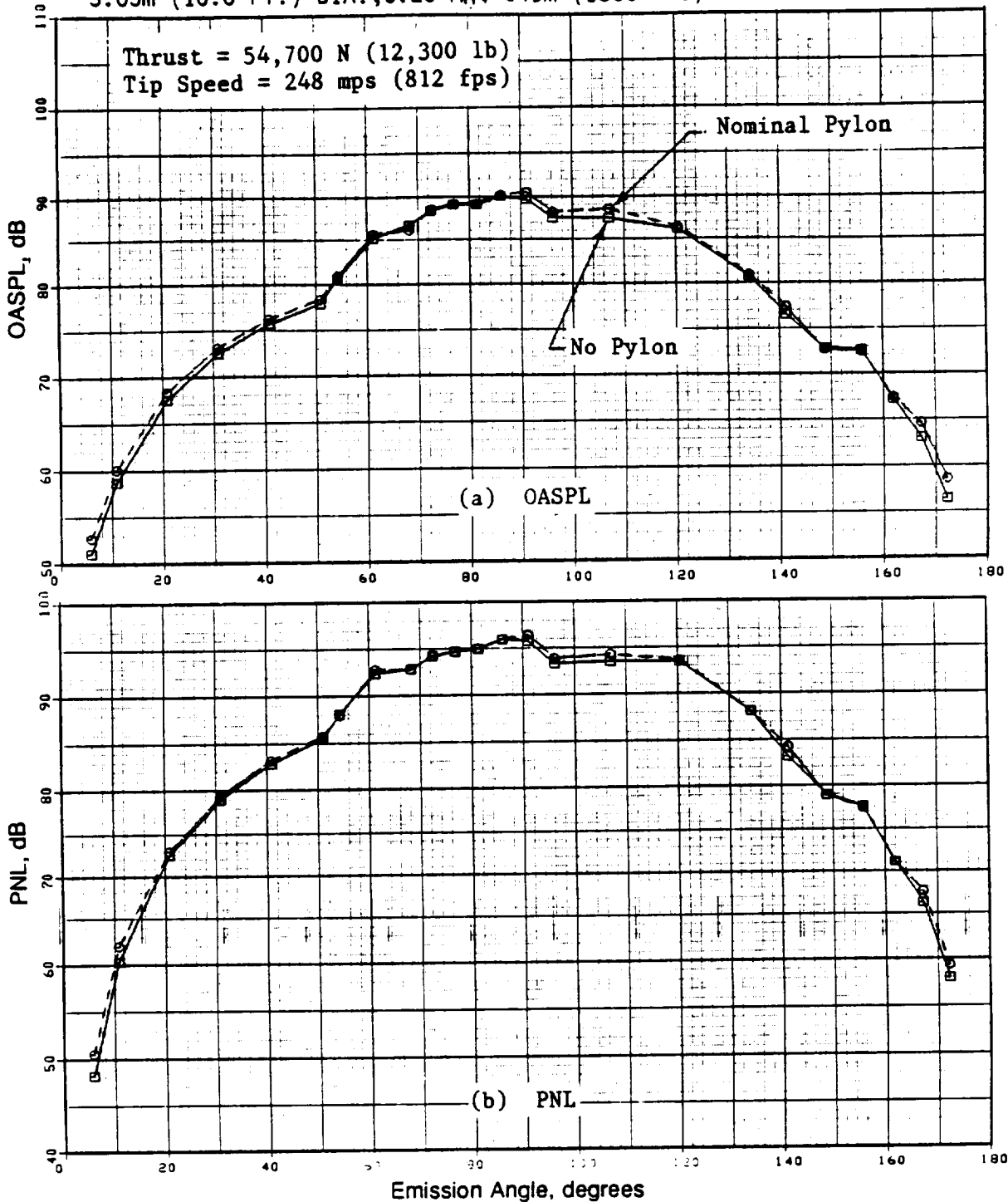


Figure 347. A Comparison of OASPL and PNL Directivities of F-7/A-7 (8+8) With and Without Nominal Pylon.

F-7/A-7; 8+8; Nominal Rotor Spacing; 37.9/37.4; 90% rpm
 3.05 m (10 ft) Diameter; Flight Mach No. 0.25; 549 m (1800 ft) Sideline

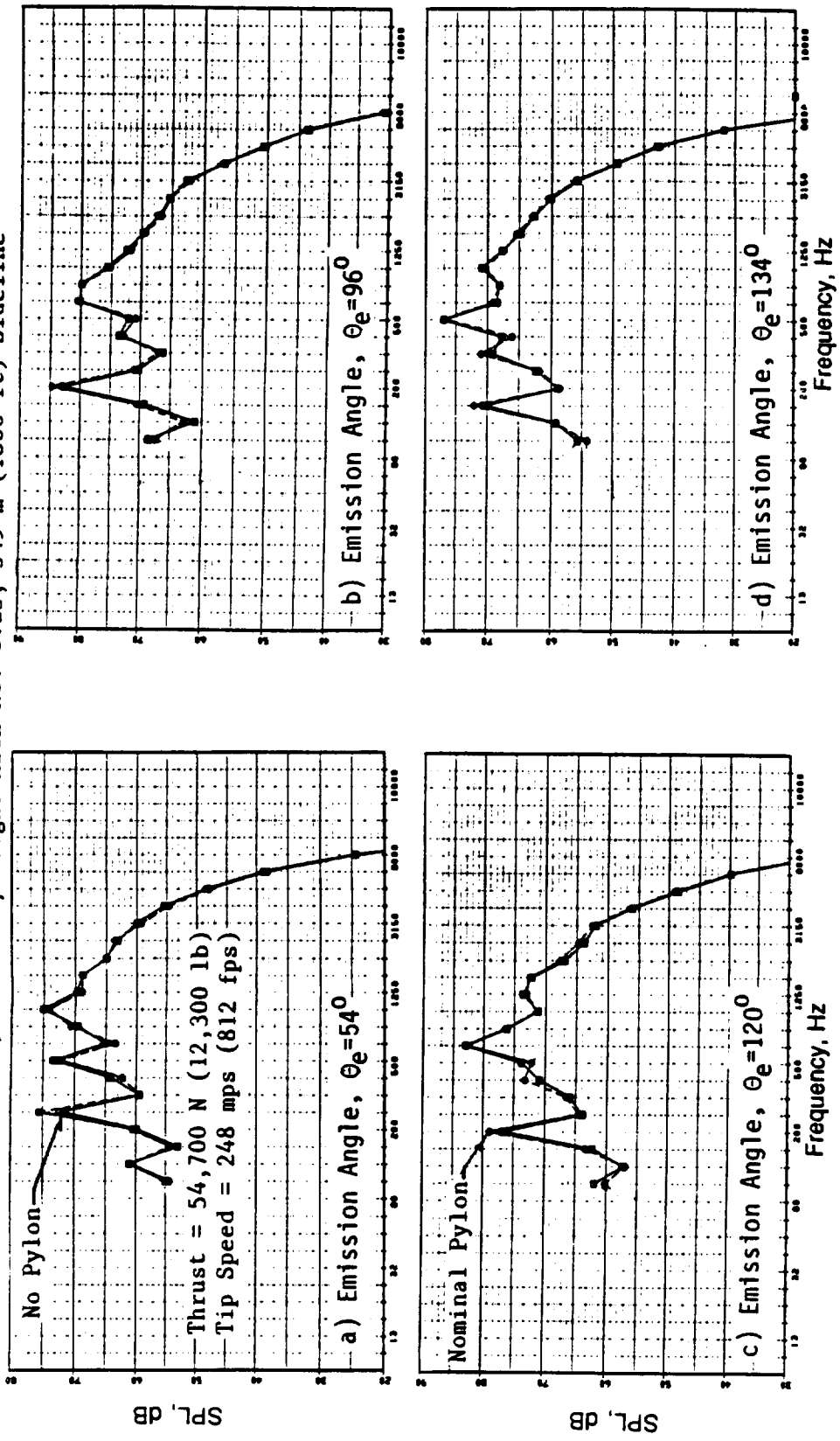


Figure 348. Spectral Comparison of F-7/A-7 (8+8) With and Without Nominal Pylon.

at these angles, the total noise levels are governed by the sound pressure level of the third harmonic, which is greater than the SPL at BPF. Since this configuration (8+8) has an equal number of blades and these data are from a condition with both rotors rotating at equal tip speed, the impact of the pylon on noise levels due to forward and aft rotors could not be separately ascertained.

Figures 349 through 352 compares the acoustic data of the F-7/A-7 (9+8) configuration with the corresponding data from nominal and close pylon-mounted configurations for typical takeoff and cutback thrust conditions. The amount of noise increase noted in peak OASPL and PNL (Figure 346) due to nominal and close pylons, relative to no pylon data, is observed also over a wide range of emission angles extending from 60° to 120° (Figures 349 and 351). As shown in Figures 350 and 352, the significant effect of the pylon on the spectra is the observed increase in the sound pressure levels at BPF and, to a lesser extent, at $2 \times \text{BPF}$.

For example, at cutback thrust and with the pylon in close position, the sound pressure level at BPF of the forward rotor increases by as much as 8 dB to 10 dB over emission angles of $60^\circ < \sigma_{\bar{e}} < 120^\circ$. The sound pressure level at the aft rotor BPF also increases, over a range of 3 dB to 10 dB, with significant impact in the aft quadrant. However, moving the pylon from the close position to nominal reduces this pylon effect by approximately one-half; no significant increase in sound pressure levels is noted at higher harmonics.

Since the F-7/A-7 (9+8) had an unequal number of blades, it was easy to separate individual tones and identify those due to the steady-loading noise of the forward and aft rotors and those resulting from the rotor-to-rotor interaction noise. These narrow-band model-scale tone data corresponding to previously defined test conditions (Figures 328 through 331) were processed as was described in Section 6.1.1.2; these results are presented in Figure 353 illustrating the directivities of sums of SPL's at the forward rotor BPF and harmonics, the aft rotor BPF and harmonics, and all of the rotor-to-rotor interaction tones. Observations made earlier from the scaled spectral data of Figures 350 and 352 on effects of nominal and close-spaced pylons are evident from these model-scale tone results.

The noise components, due to interaction of the pylon/wake with the rotor were identified by subtracting the sound pressure level sums at rotor blade passing frequencies and harmonics of a no-nylon F-7/A-7 (9+8) configuration from the corresponding tone sum data of the two pylon-mounted tests. Figure 354 summarizes the pylon/rotor interaction noise data directivity for typical takeoff and cutback conditions presented in Figure 353. Utilizing these data, Figure 355 is issued to describe the variation of steady-loading noise, rotor-to-rotor interaction noise, and pylon-to-rotor interaction noise as a function of thrust. The sound pressure levels from those sources (Figure 355), for the test configuration, are more or less equal in the region of cutback thrust, and due to the steady-loading noise and pylon/rotor interaction noise being approximately equal at cutback, the effect of pylon on total noise is in the range of 3 dB.

Discussion of the F-7/A-7 Series 1 and 2 acoustic test results is hereby concluded by demonstrating the impact of a mounting pylon on the EPNL values, compared to a no-nylon configuration. This comparison is made in Figure 356 for typical takeoff and cutback thrusts with no angle-of-attack, indicating the nominal pylon effect is 0.7 dB and 1.2 dB at typical takeoff and cutback conditions for the F-7/A-7 test configurations. This increases to 1.5 dB and 2.2 dB, respectively, when moving the pylon to a close position.

F-7/A-7; 9+8; Maximum Rotor Spacing; 41.8/41.4; 85% rpm
 3.05 m (10 ft) Diameter; 549 m (1800 ft) Sideline

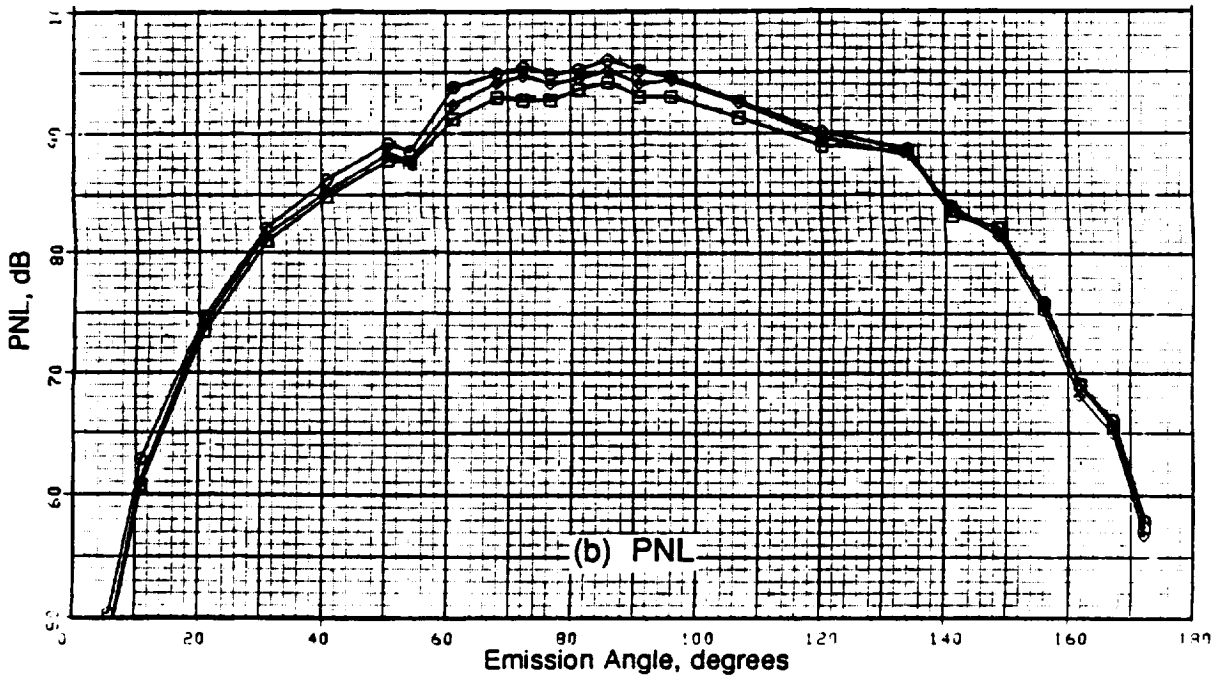
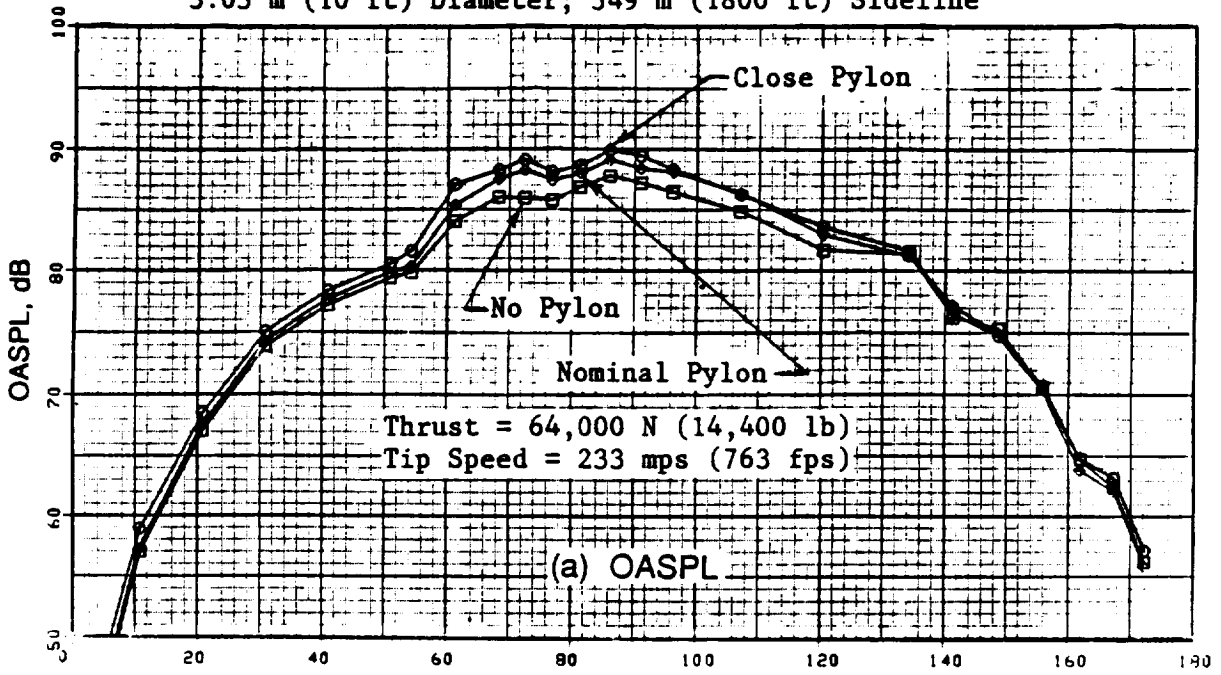


Figure 349. OASPL and PNL Directivities of F-7/A-7 (9+8) Without any Pylon and With Nominal and Close Pylons at Typical Takeoff.

F-7/A-7; 9+8; Maximum Rotor Spacing; 41.8/41.4; 85% rpm
 3.05 m (10 ft) Diameter; 549 m (1800 ft) Sideline

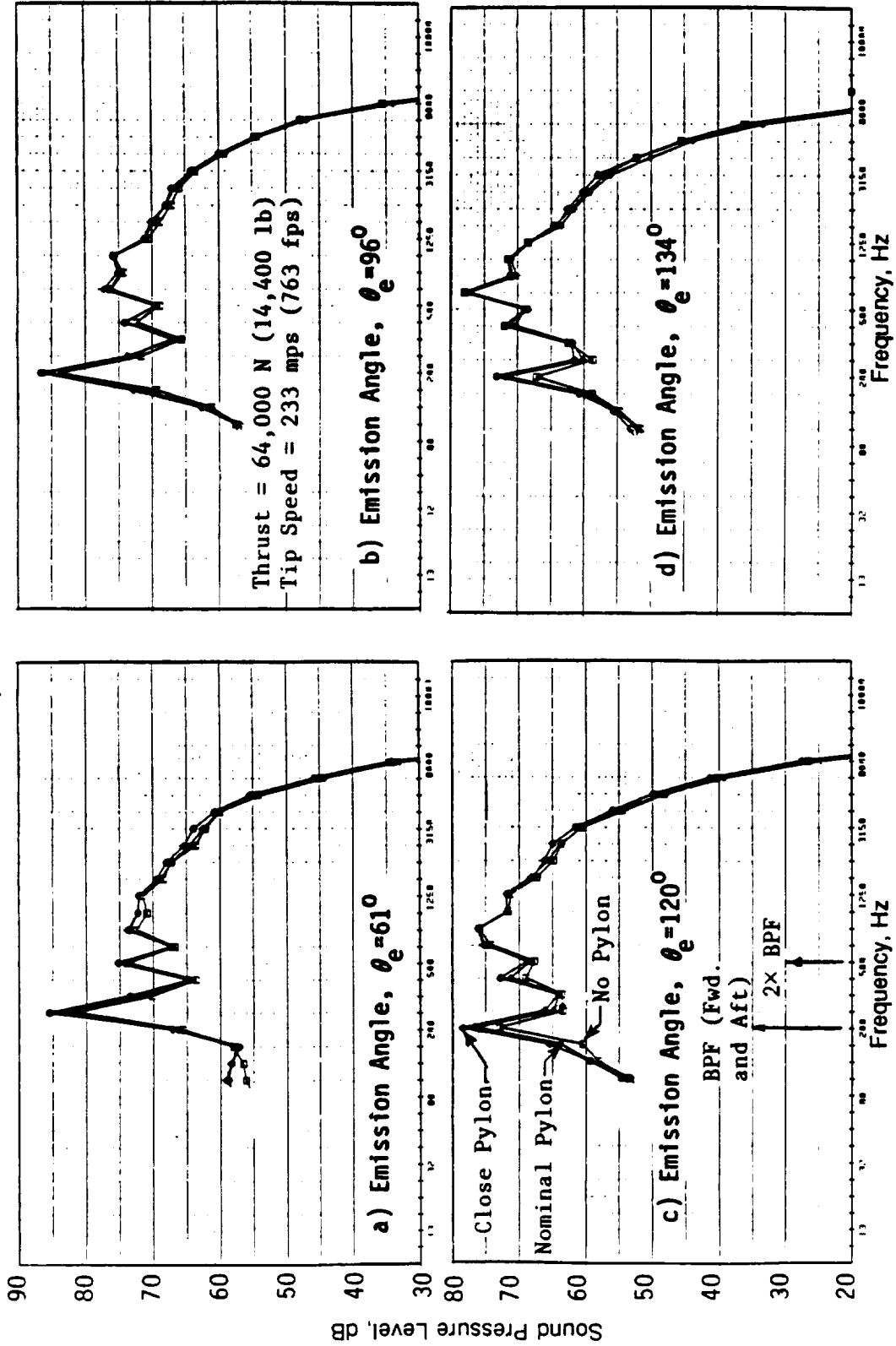


Figure 350. Spectral Comparison of F-7/A-7 (9+8) With No Pylon and With Nominal and Close Pylons at Typical Takeoff.

F-7/A-7; 9+8; Maximum Rotor Spacing; 41.8/41.4; 75% rpm
 3.05 m (10 ft) Diameter; 549 m (1800 ft) Sideline

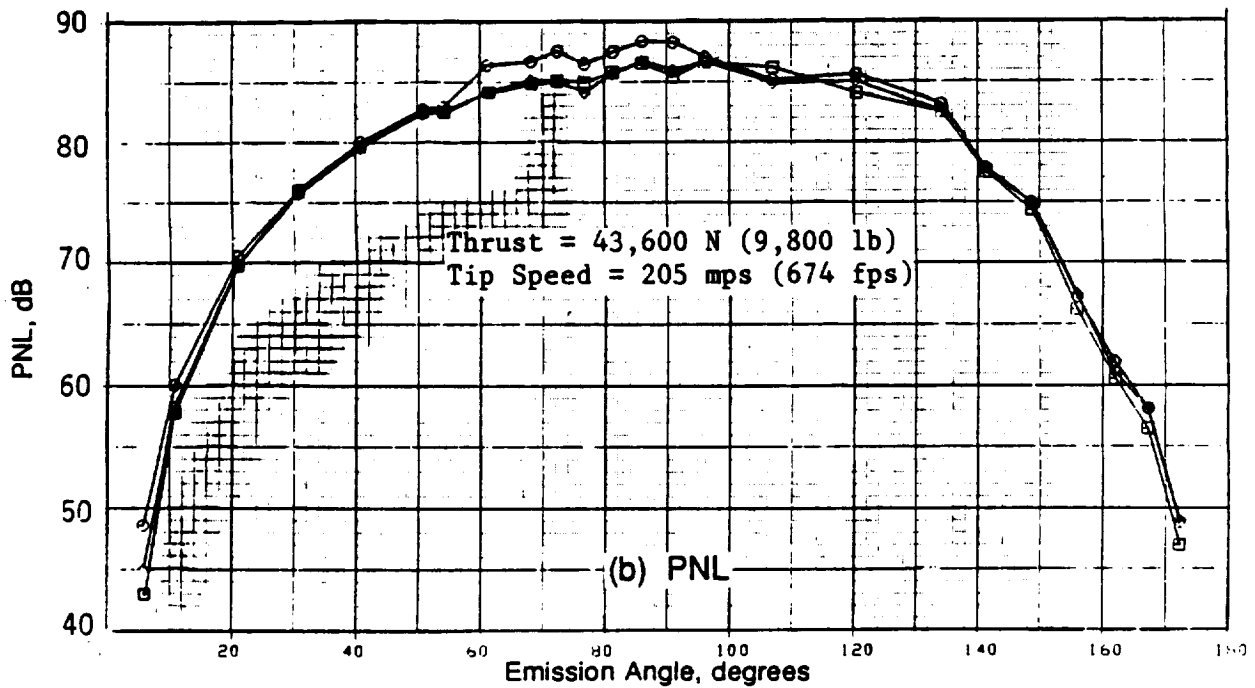
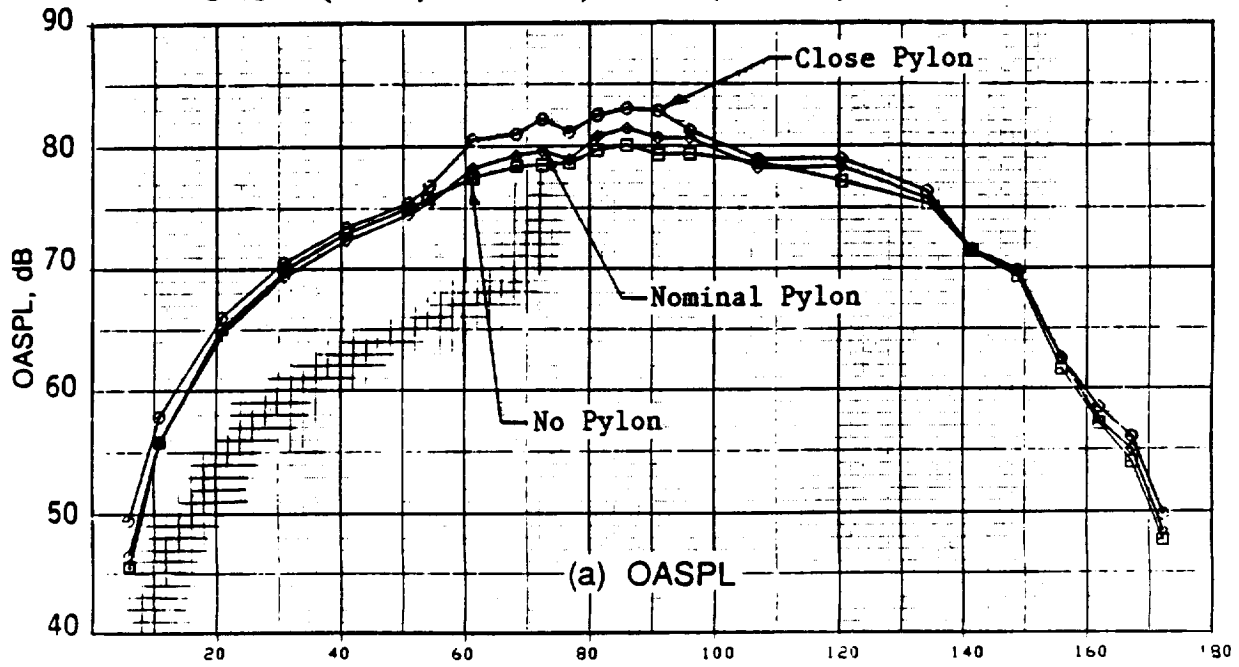
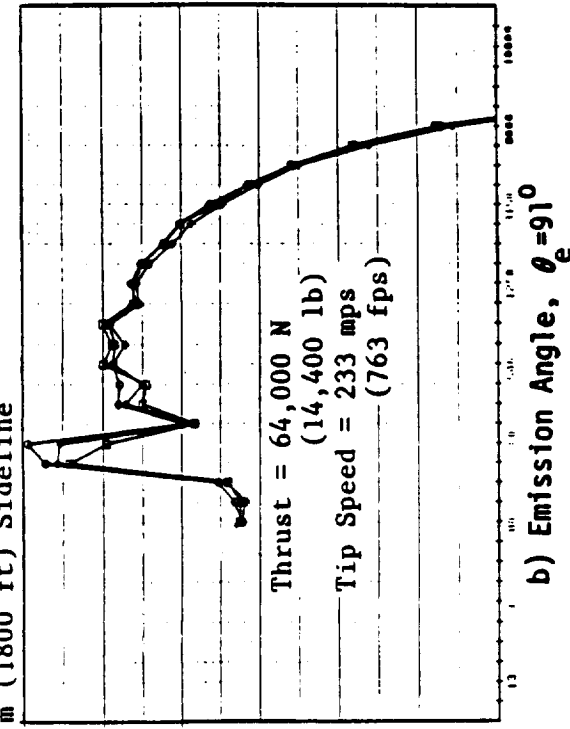
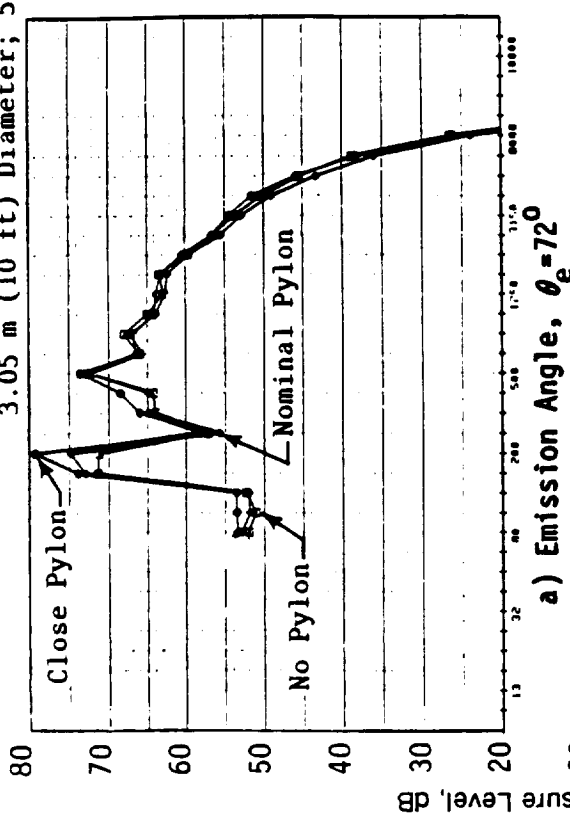


Figure 351. OASPL and PNL Directivities Without Pylon and With Nominal and Close Pylons at Typical Cutback.

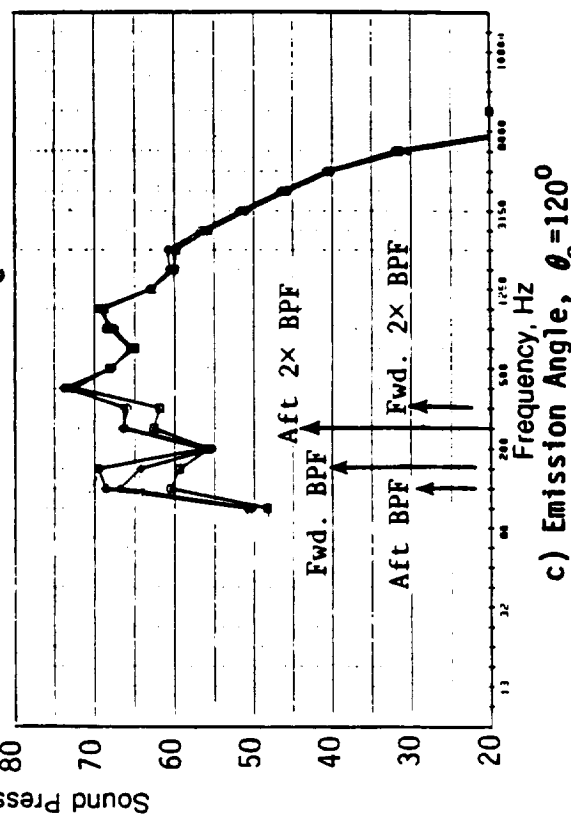
E-7/A-7; 9+8; Maximum Rotor Spacing; 41.8/41.4; 75% rpm
 3.05 m (10 ft) Diameter; 549 m (1800 ft) Sideline



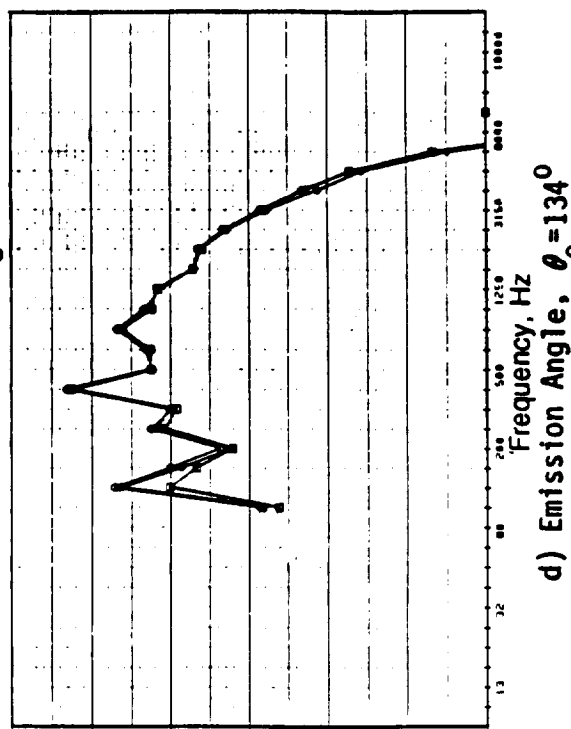
a) Emission Angle, $\theta_e = 72^\circ$



b) Emission Angle, $\theta_e = 91^\circ$



c) Emission Angle, $\theta_e = 120^\circ$



d) Emission Angle, $\theta_e = 134^\circ$

Figure 352. Spectral Comparison Without Pylon and With Nominal and Close Pylons at Typical Cutback.

F-7/A-7; 9x8; MAX. ROTOR SPACING: 41.8/41.4; 85% RPM
 MODEL SCALE; 8.23m (27 FT.)SIDELINE

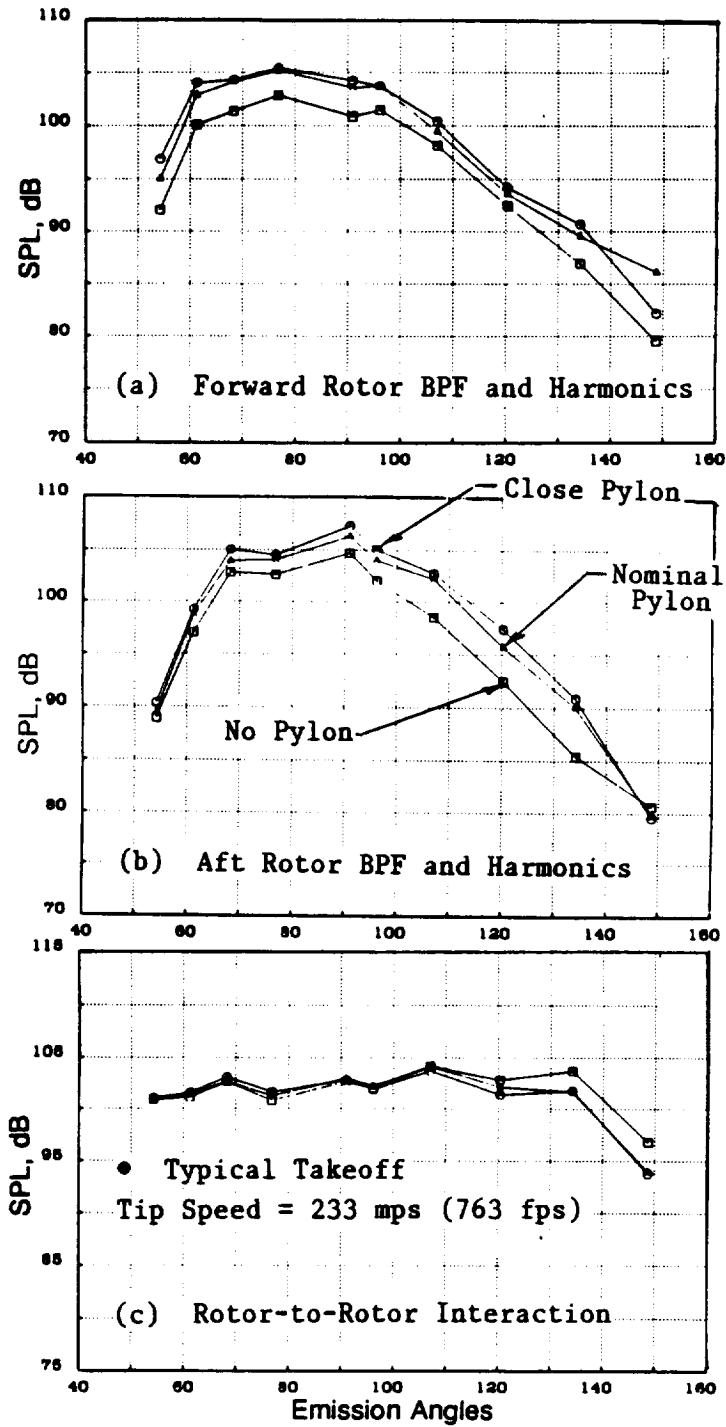


Figure 353. Comparison of Forward Rotor, Aft Rotor, and Rotor-to-Rotor Interaction Tone Sum Results of F-7/A-7 (9+8) With No Pylon, and With Nominal and Close Pylons.

F-7/A-7; 9x8; MAX. ROTOR SPACING; 41.8/41.4; 75%
 MODEL SCALE; 8.23m (27 FT.) SIDELINE

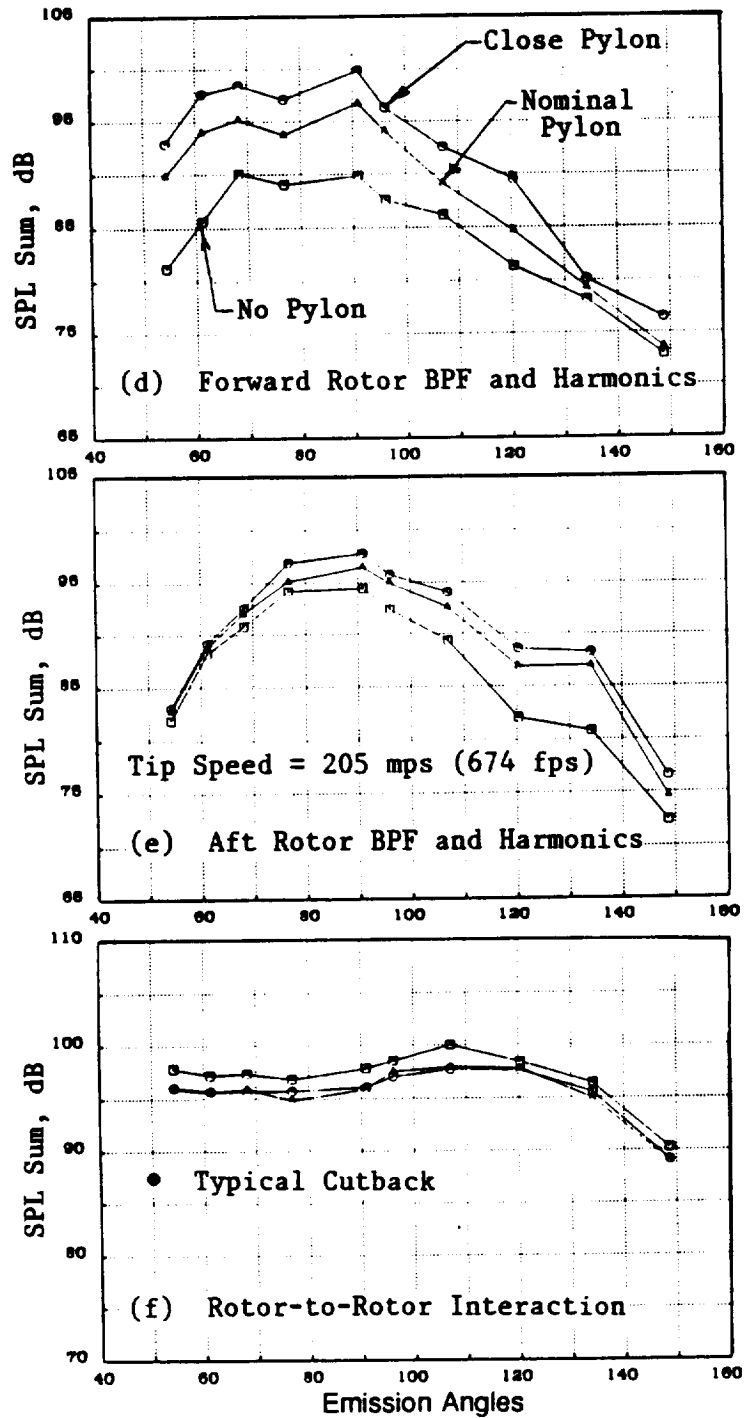
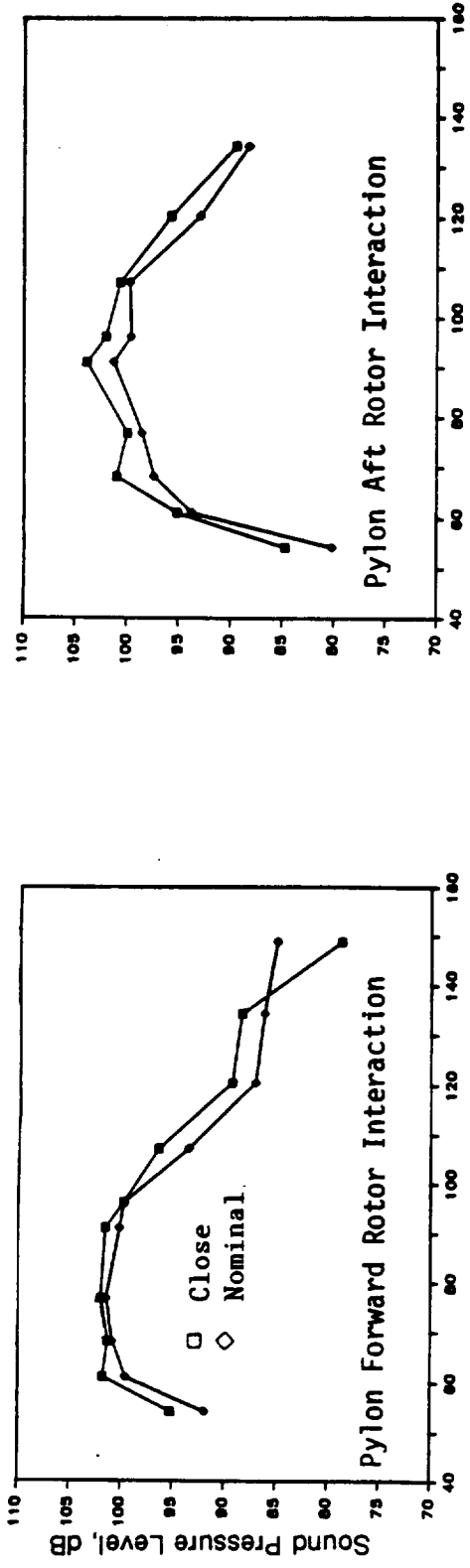
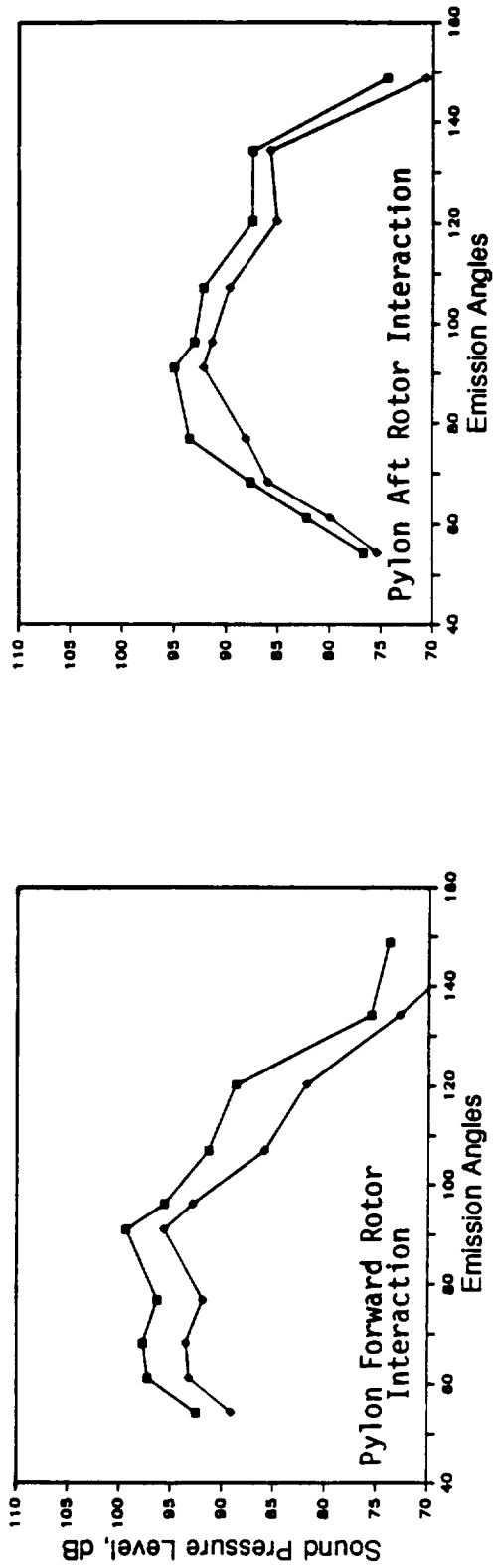


Figure 353. Comparison of Forward Rotor, Aft Rotor, and Rotor-to-Rotor Interaction Tone Sum Results of F-7/A-7 (9+8) With No Pylon, and With Nominal and Close Pylons (Concluded).

F-7/A-7; 9x8; MAX. ROTOR SPACING MODEL SCALE; 8.23 M(27 FT.) SIDELINE



(a) Tip Speed = 233 mps (763 fps); 85% rpm



(b) Tip Speed = 205 mps (674 fps); 75% rpm

Figure 354. Directivity of Pylon/Rotor Interaction Noise with Nominal and Close Pylons at Typical Takeoff and Cutback.

- MODEL SCALE; 0.25 M_0 ; 8.23 M(27 FT.)SIDELINE
- F7A7; 9x8; MAXIMUM ROTOR SPACING ($X/D_t=0.24$)
- 41.8/41.4 (12.5 HZ NARROWBAND DATA)
- EMISSION ANGLE, $\theta_e=91^\circ$

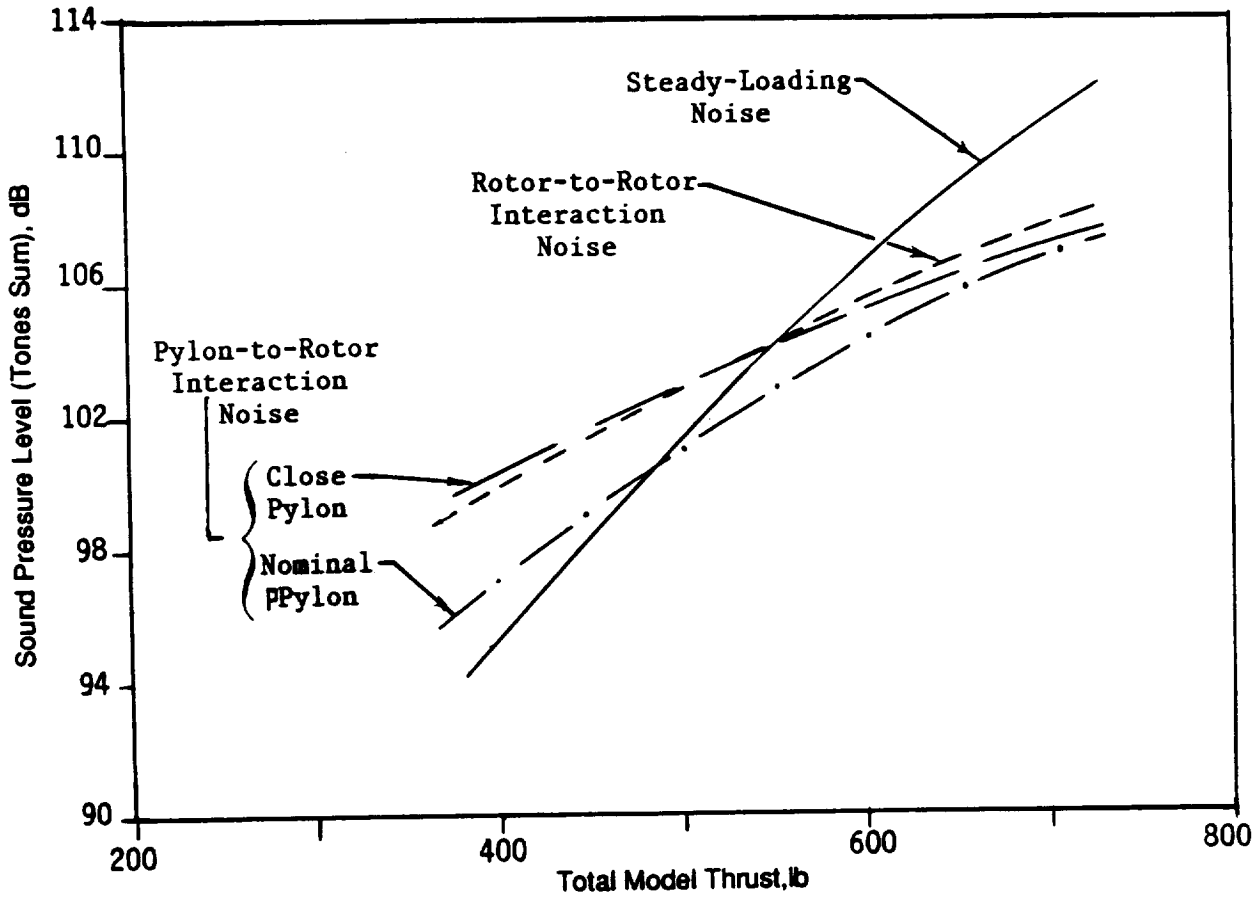


Figure 355. Steady-Loading, Rotor-to-Rotor, and Pylon-to-Rotor Interaction Noise Components as a Function of Total Thrust.

3.05 M(10.0 FT)DIA; 0.25 M₀; 549 M(1800 FT.)SIDELINE
 THRUST: TAKEOFF=66700 N(15000 LB); CUTBACK=44500 N(10000 LB)

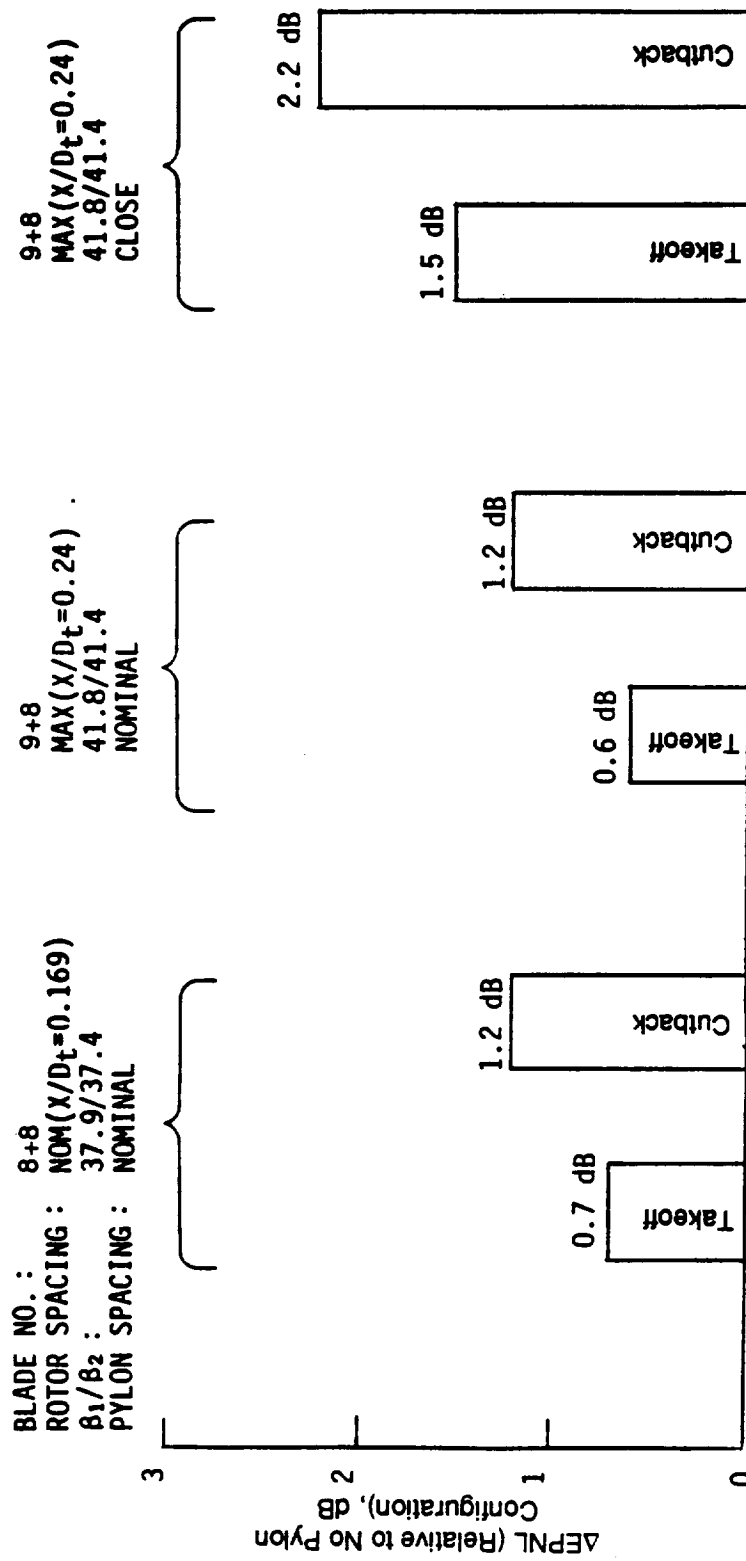


Figure 356. Effect of a Mounting Pylon on the EPNL of F-7/A-7 Configuration with 8+8 and 9+8 Blades.

7.1.1.8.2 F-7/A-7c (9+8) at Maximum and Nominal Rotor Spacings: Series 3 and 4

The F-7/A-7c (9+8), having the 8 aft blades clipped at 75% of the blade height, was tested at nominal pitch with maximum rotor spacing ($X/D_t = 0.24$), and with the pylon spaced at nominal position. This configuration also was tested with nominal rotor spacing ($X/D_t = 0.169$). Figures 357 through 359 are provided to compare selected acoustic data from these tests and corresponding data obtained with no pylon.

Figure 357 compares the acoustic data for the F-7/A-7c (9+8) with maximum and nominal rotor spacings, as a function of total thrust. Like the unclipped F-7/A-7 (9+8) maximum rotor spacing data previously presented, the effect of nominal spaced pylon on the PNL is about 1.0 dB to 2.0 dB for thrust values greater than 35,500 N (8,000 lb) for the maximum spaced clipped configuration. However, with the F-7/A-7c (9+8) and using nominal rotor spacing, the pylon effect is limited to 0.5 dB over most of the test range. These differences in the pylon effect on total noise of the F-7/A-7c (9+8) at nominal and maximum spacing are also noted in the directivities presented in Figure 358.

An explanation for differences in pylon effect observed with the maximum spacing, relative to nominal, is to be found in typical spectral comparisons (Figure 359) for the F-7/A-7c (9+8) at the two test rotor spacings, indicating that the impact of pylon at the blade passing frequencies are more or less the same for the two different spaced configurations. However, because the levels associated with higher harmonics are lower with maximum spacing than are those with nominal spacing (that is, increased spacing benefit), the sound pressure level changes at blade passing frequencies due to pylon, contribute more to the total noise of the maximum spacing configuration. Similar to other pylon configurations of this study, these spectral comparisons indicate no effect of pylon on rotor-to-rotor interaction harmonics levels.

7.1.1.8.3 F-11/A-11 (11+9): Series 5

The F-11/A-11 with 11 forward and 9 aft blades (very open pitch, maximum rotor spacing) was tested with the pylon mounted at nominal spacing. Selected acoustic data are shown in Figures 360 and 361. As seen from the directivity data, the pylon impact is limited to 1 dB mostly in the region of the plane-of-rotation and only at the BPF and 2xBPF.

This section on the assessment of use of a mounting pylon is concluded by summarizing some observations noted during the discussion of the results from the five test series of this study. For a given blade, interaction between the blade and the pylon wake occurs once in a revolution (1/rev); therefore, the effect of pylon-wake/rotor interaction should be noted at blade passing frequency and its harmonics.

From the tests conducted, it was observed that, for a given pylon/rotor system, the pylon/rotor interaction noise generally was significant at BPF and, to a lesser extent, at 2xBPF. These are the frequencies at which the steady-loading noise dominates over the peak noise region. The effect of the pylon/rotor interaction was not significant at higher harmonics, the levels of which are determined by the aerodynamic rotor-to-rotor interaction noise components.

For a given blade-pitch setting and a given thrust, the pylon effect at frequencies corresponding to BPF is more significant in the aft and forward quadrants than in the regions of the planes-of-rotation of the rotors. This is due to the fact that steady-loading noise levels, which are

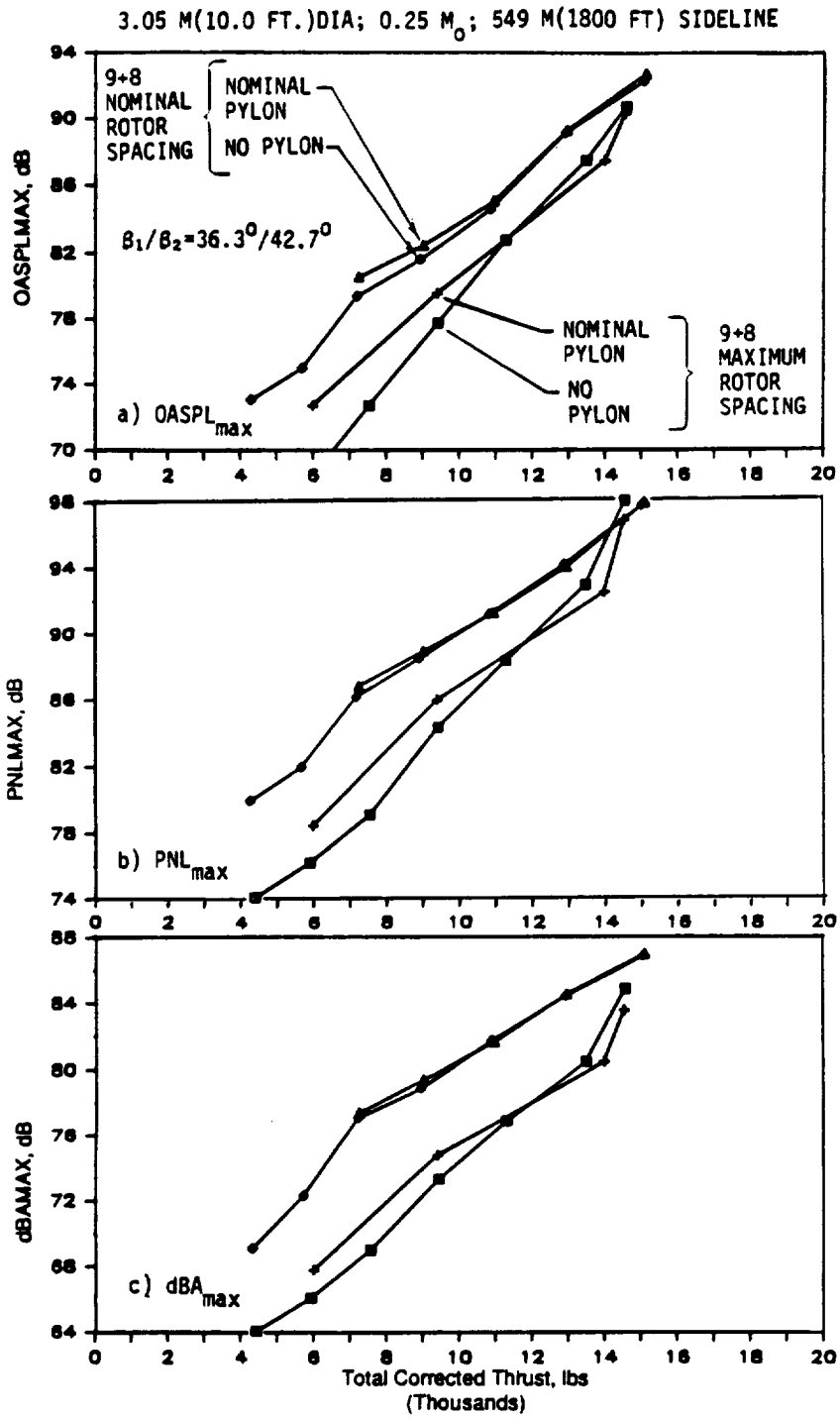


Figure 357. Effects of Pylon on Maximum Noise Data of F-7/A-7c at Maximum Rotor Spacing.

3.05 M(10.0 FT)DIA; 0.25 M_0 ; 549 M(1800 FT)SIDELINE

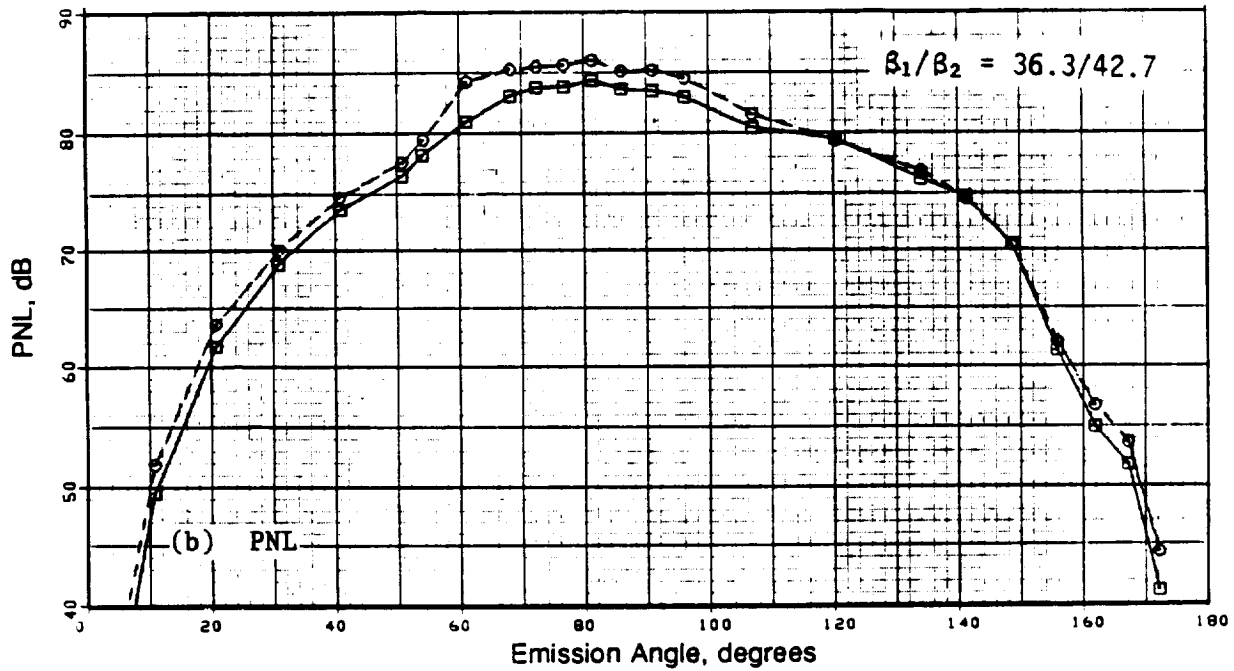
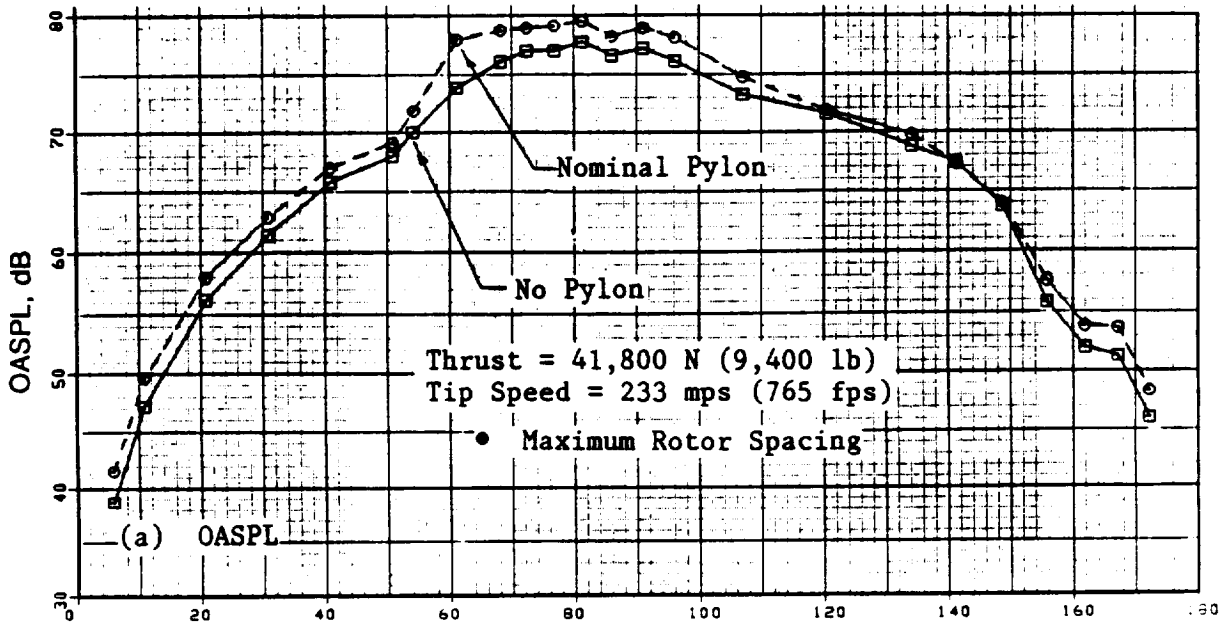


Figure 358. A Comparison of OASPL and PNL Directivities of F-7/A-7c (9+8) With and Without Nominal Pylon at Typical Cutback.

3.05 M(10.0 FT.)DIA; 0.25 M_0 ; 549 M(1800 FT)SIDELINE

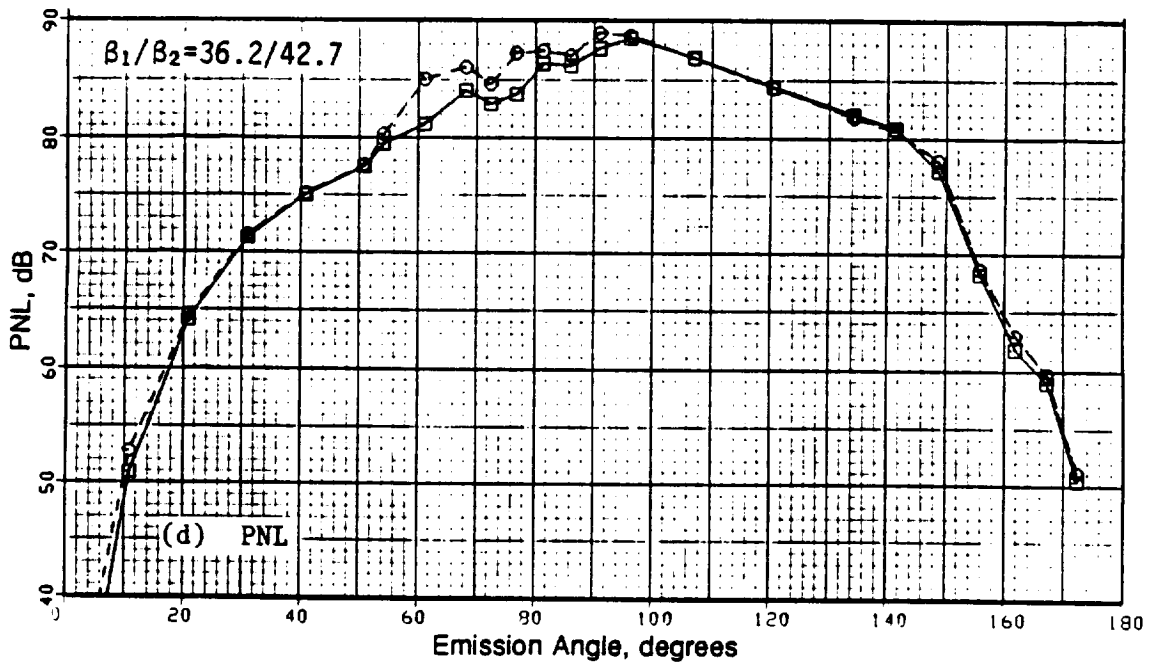
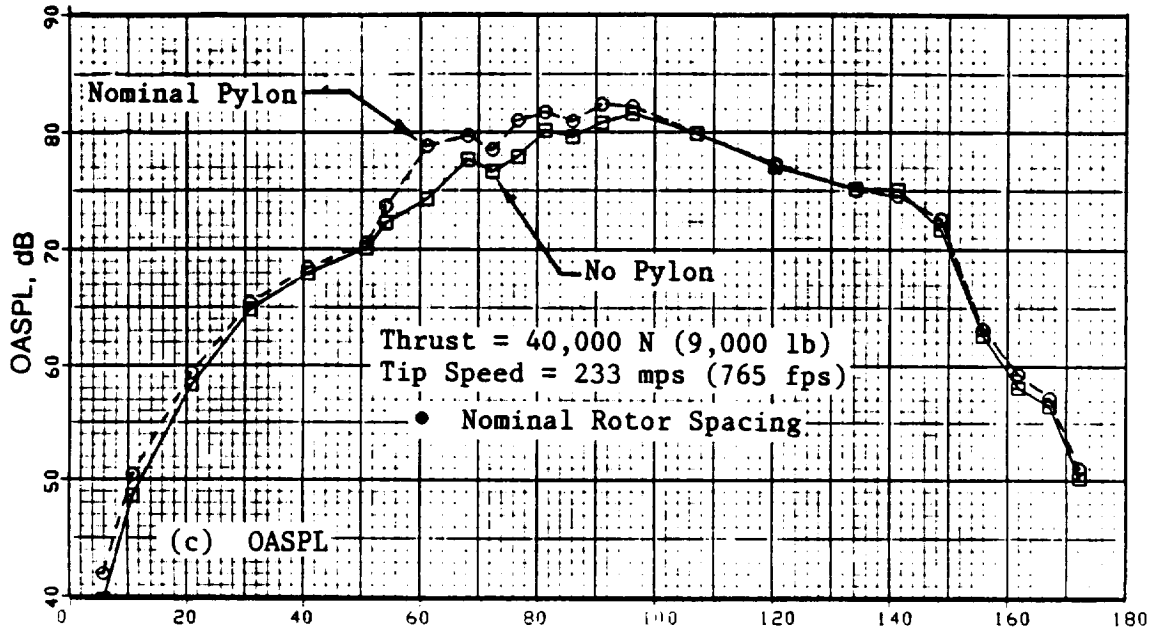


Figure 358. A Comparison of OASPL and PNL Directivities of F-7/A-7c (9+8) With and Without Nominal Pylon at Typical Cutback (Concluded).

3.05 M(10.0 FT.)DIA; 0.25 M₀; 549 M(1800 FT)SIDELINE

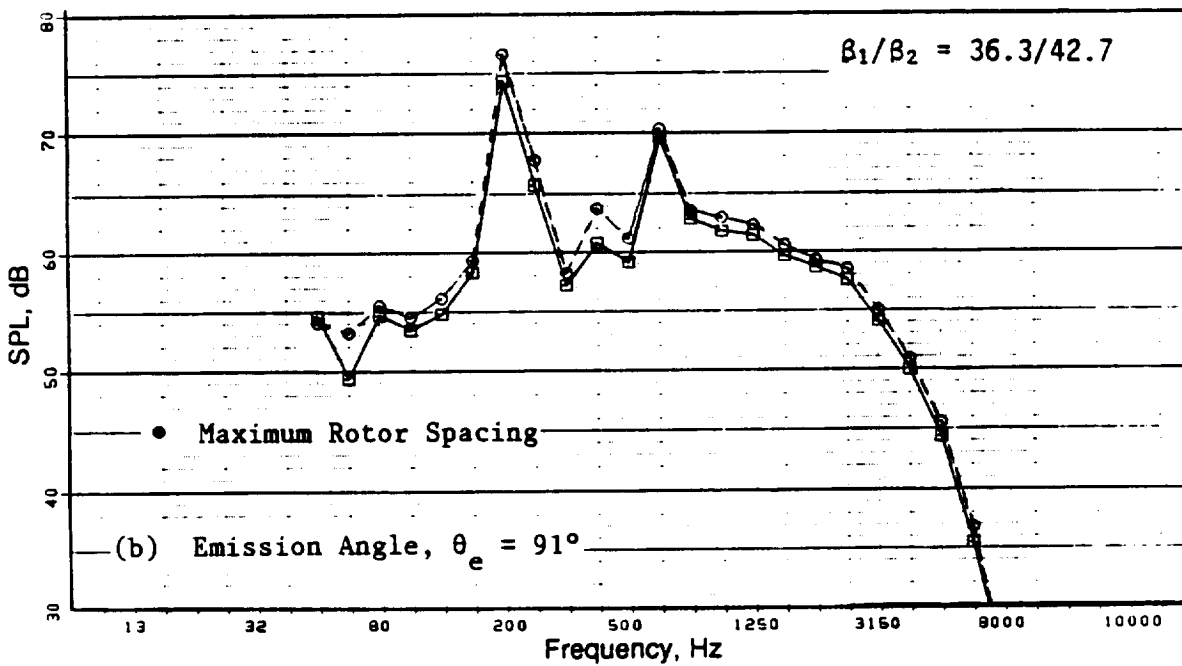
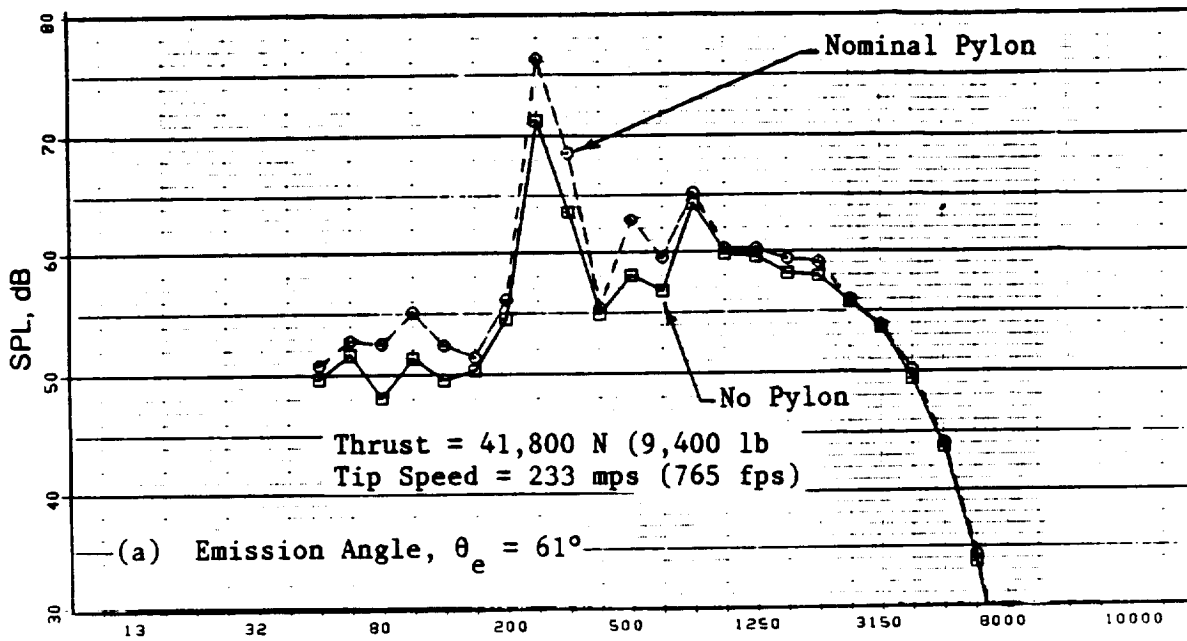


Figure 359. A Spectral Comparison of the F-7/A-7c (9+8) With and Without Nominal Pylon at Typical Cutback.

3.05 M(10.0 FT.)DIA; 0.25 M₀; 549 M(1800 FT.)SIDELINE

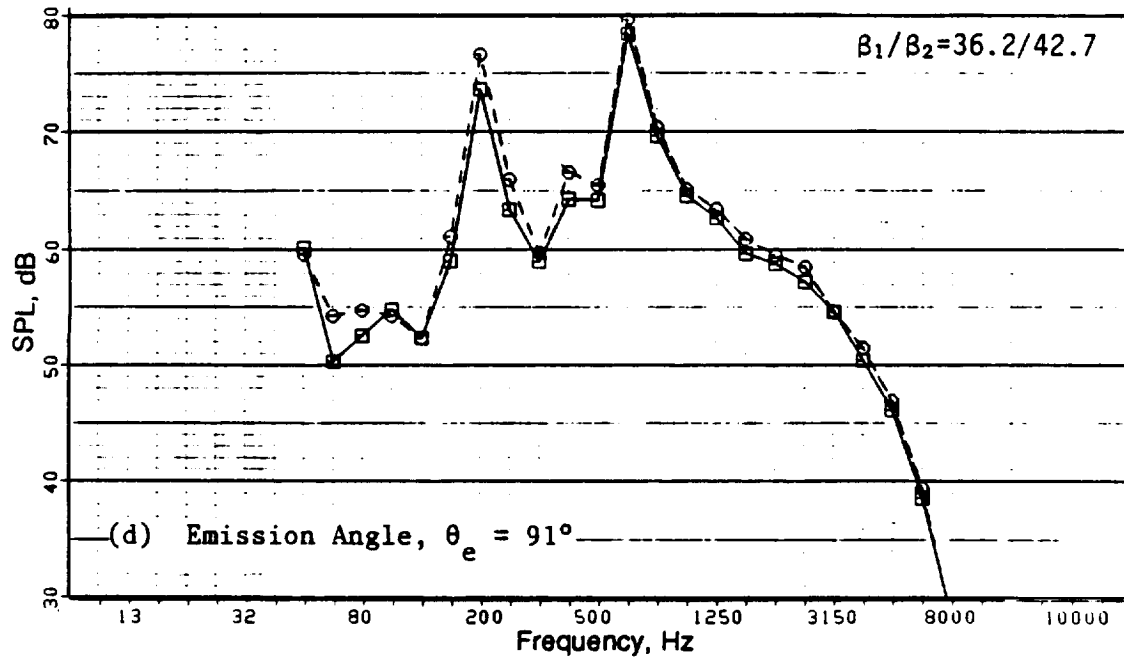
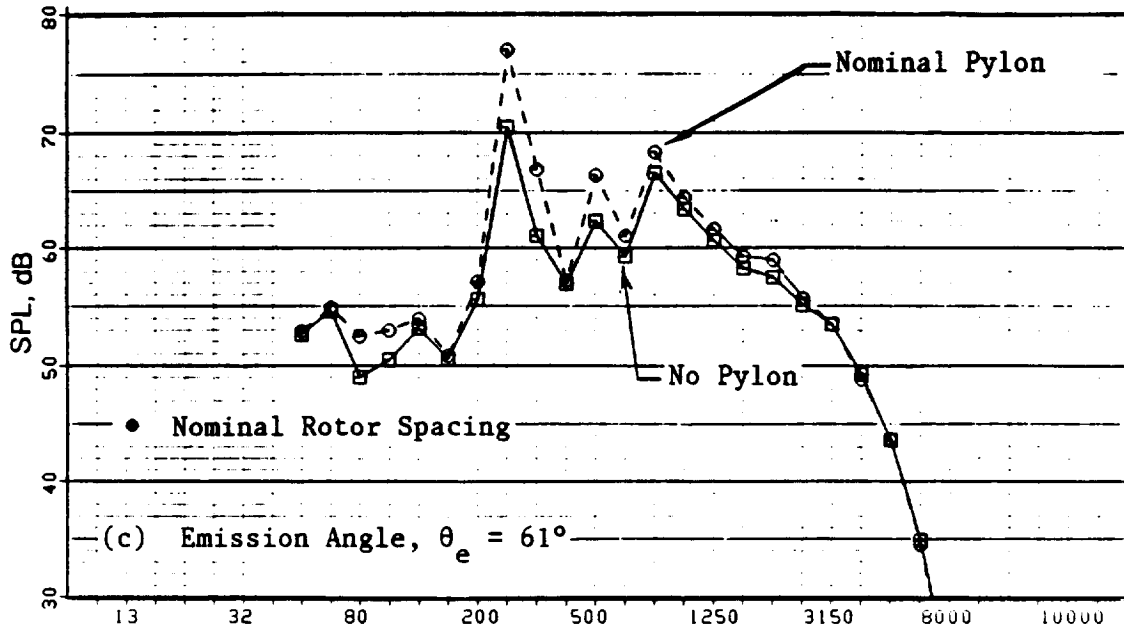


Figure 359. A Spectral Comparison of the F-7/A-7 (9+8) With and Without Nominal Pylon at Typical Cutback (Concluded).

3.05 M(10.0 FT.)DIA; 0.25 M₀; 549 M(1800 FT.)SIDELINE

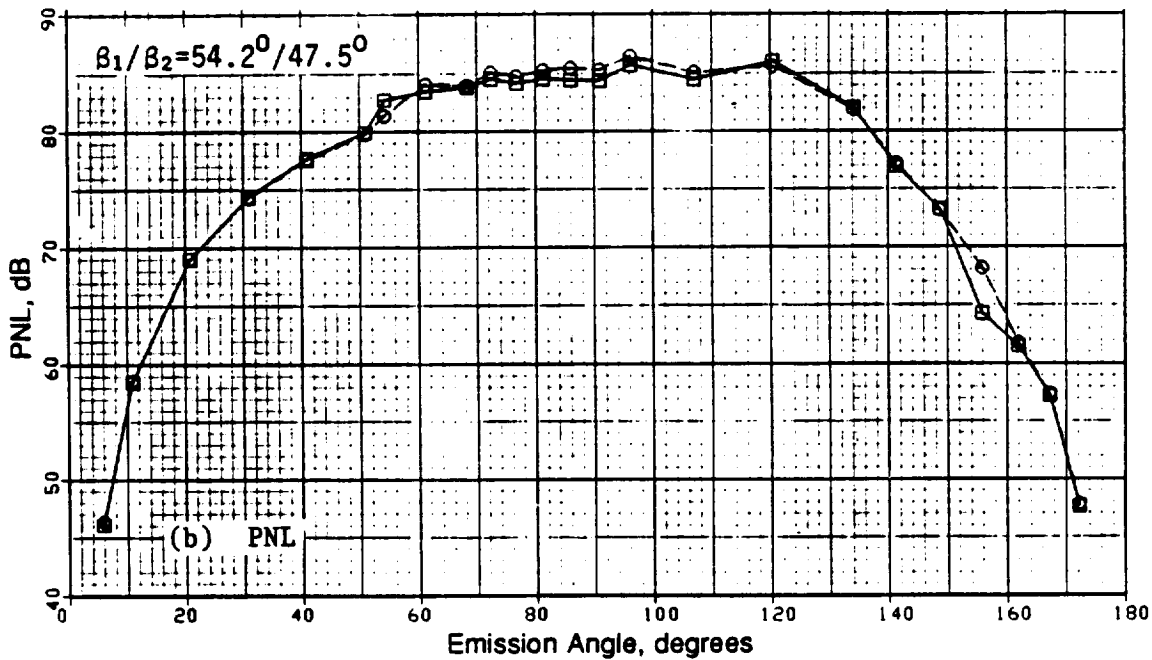
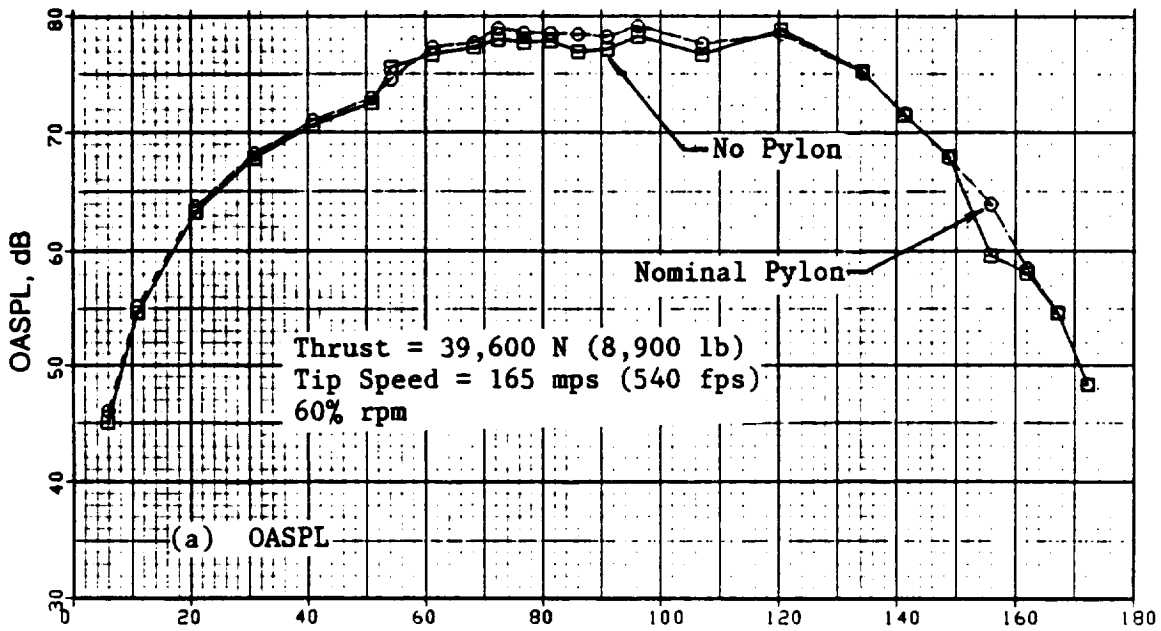


Figure 360. Comparison of OASPL and PNL Directivities With and Without Nominal Pylon.

3.05 M(10.0 FT.)DIA; 0.25 M₀; 549 M(1800 FT.)SIDELINE

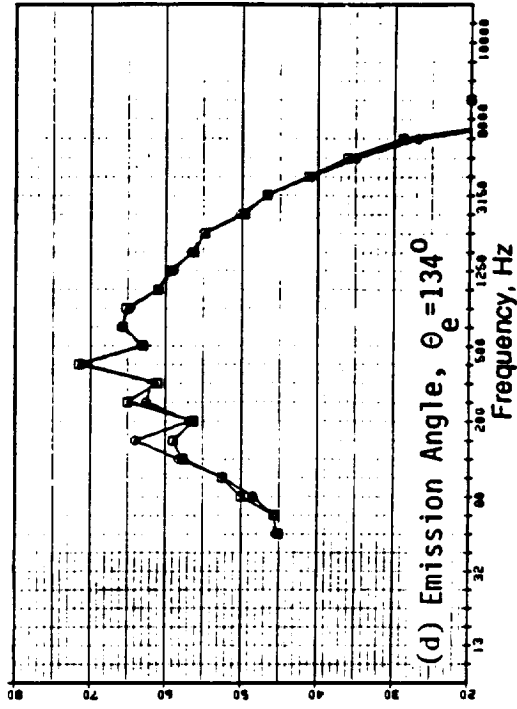
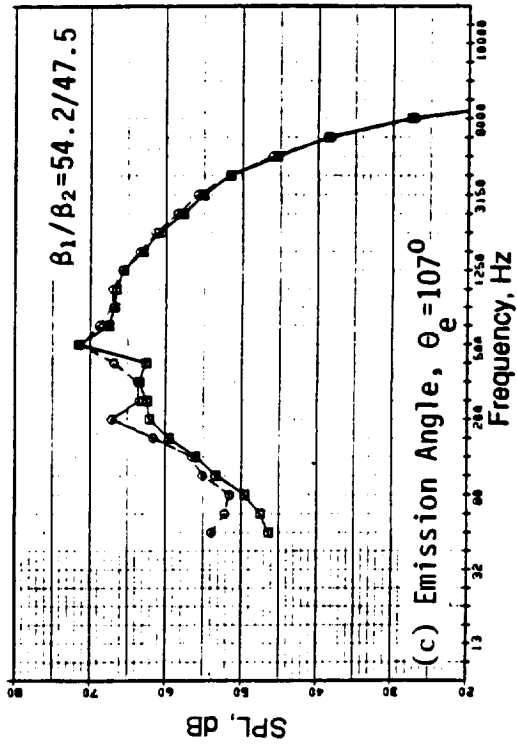
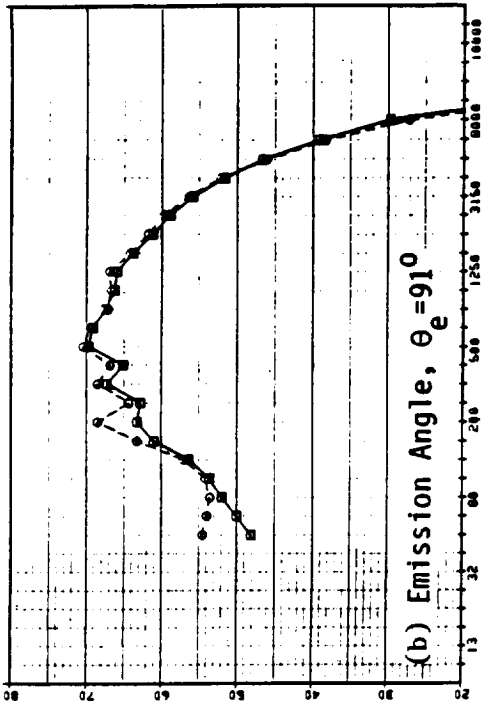
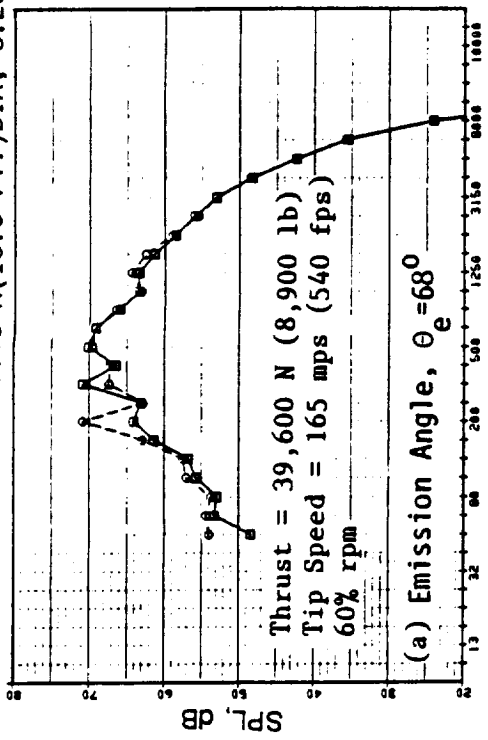


Figure 361. Spectral Comparison of F-11/A-11 (11+9) With and Without Nominal Pylon.

at their peak levels in the plane-of-rotation, decrease significantly in the front and aft quadrants. Also, for a given configuration and an operating freejet Mach number, the pylon effect decreases with increased thrust. Since, for a given freejet Mach number, steady-loading noise increases faster with thrust than does interaction noise due to pylon wake and rotor, the pylon effect is masked by the higher steady-loading noise levels at the higher thrust settings. As a consequence, the pylon effect at the blade passing frequency generally is more significant at lower thrust settings.

The level of steady-loading noise depends upon, among other parameters, the number of blades and the pitch setting (or tip speed) for a given thrust; the pylon-wake/rotor interaction effect also depends on these parameters. For example, for a given thrust, either an increase in blade numbers (decreasing the loading per blade) or a change in pitch setting from nominal to open pitch (decreasing the tip speed), results in a decrease in the steady-noise levels. Under such situations, the effect of pylon is more significant. For example, in comparing the F-7/A-7 with 8+8 blades at nominal pitch, the pylon effect is more significant for the F-7/A-7 with 9+8 blades at open pitch.

An increased spacing between the pylon and the forward rotor (from close to nominal) results in an increased decay of the pylon-wake defect before its interaction with the forward blades. Therefore, this increase in pylon spacing results in the observed decrease in the pylon effect on the forward rotor sound pressure levels. As expected, a decrease in rotor-to-rotor spacing from maximum to nominal also results in the same effect of pylon on sound pressure levels at the blade passing frequency of the forward rotor.

7.1.1.9 Community Noise Status from Measured Model-Scale Data

A two-engine airplane has been defined for a typical mission, in order to assess the aircraft community noise status. The altitude, speed, and thrust requirements relative to FAR (Federal Aviation Requirements), Part 36, Stage 3 noise measurements are listed in Table 63.

Data measured at Cell 41 have been scaled to a 10-foot diameter engine-size fan. Noise levels are expressed in terms of NPD (noise/power/distance) curves. Figure 362 (Views A through C) plots the freefield and single-engine effective perceived noise levels as functions of fan corrected thrusts for the three distances of sideline, cutback, and approach. View A presents the NPD curves for the F-7/A-7 (8+8) blade with nominal pitch-change-axes spacing, and in View B the NPD curves are shown with blade numbers increased to 11+9 and at maximum spacing between the pitch-change axes. Finally, View C demonstrates the NPD curves for the F-7/A-3 (11+8) configuration having

Table 63. Aircraft/Engine Information for FAR, Part 36, Stage 3 Noise Assessment.

Condition	Altitude/ Range, ft	Correct Fan Thrust ¹ , klb	Flight Mach No.
Sideline	1800	14.0	0.25
Cutback	2200	9.0	0.25
Approach	400	5.0	0.25
¹ Fan thrust is approximately equal to 95% engine thrust			

3.05 M(10.0 FT.)DIA; 0.25 M₀; 549 M(1800 FT.)SIDELINE

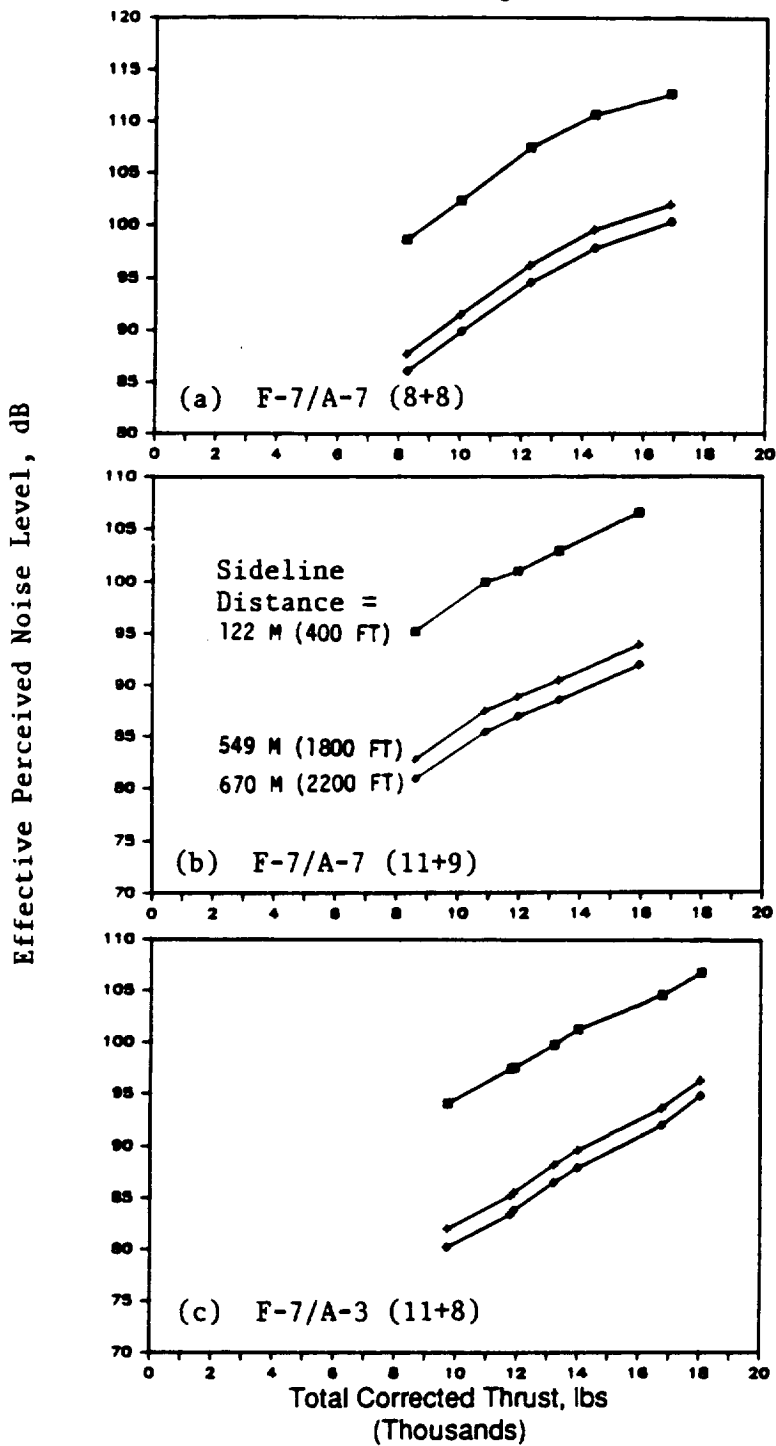


Figure 362. Noise Power Distance Curves as a Function of Corrected Thrust.

short aft blades. From each set of these charts, noise levels are determined for the altitude and thrust specified in Table 63; adjustments are then made as follows:

- +3.0 dB to account for a two-engine airplane
- +2.5 dB for the ground reflection to a 4-foot microphone
- +1.0 dB at cutback power to represent the influence of the core engine noise
- +2.0 dB at approach condition to include core engine as well as airframe noise contributions.

Table 64 compares resultant noise levels with FAR, Part 36, Stage 3 noise limits for a two-engine airplane with a maximum TOGW (takeoff gross weight) of 130,000 lb. Although the results indicate that the aircraft does not meet the FAR, Part 36, Stage 3 limits for the 10-foot diameter F-7/A-7 (8+8) blade configuration; the F-7/A-7 (11+9), with increased blade number and rotor spacing, will lower the noise levels enough to meet the certification rule with trade. With a blade configuration such as that of the F-7/A-3 (11+3), the aircraft meets the rule with margin at greater than 80% confidence limit for a standard deviation of 2.5 dB.

Furthermore, it should be noted that an alternate way to reduce noise, at the same required engine thrust, is to use a larger fan diameter; for example, in order to conduct the mission of Table 63, an 11-foot diameter fan could be utilized instead of the 10-foot diameter fan. The projected noise levels of Table 64 would be reduced by approximately 2.5 dB EPN. Consequently, using the F-7/A-7 (11+9) blade configuration would meet the FAR, Part 36, Stage 3 requirements without trade and with reasonable margin, and the same airplane would be about 3 dB to 7 dB EPN below the rule by utilizing the F-7/A-3 (11+8) configuration, depending upon its measurement condition and location.

Table 64. Noise Status Projection, EPNdB.

<ul style="list-style-type: none"> • Aircraft TOGW = 130,000 lb • Fan Diameter = 10 feet • Two-Engine Aircraft • Microphone Height, 4-feet 				
Condition	FAR Part 36 Stage 3 Limit	Blade Configuration		
		F-7/A-7 ¹ (8+8)	F-7/A-7 ² (11+9)	F-7/A-3 ³ (11+8)
Sideline	95.9	104.5	96.8	95.2
Cutback	90.2	94.2	88.2	85.7
Approach	99.8	102.0	97.9	95.0
Certification Status Code: ¹ Fail ² Pass with Trade ³ Pass with Margin				

7.1.1.10 Summary of Acoustic Results

A comprehensive acoustic test series which was conducted at the GEAE (GE Aircraft Engines) anechoic facility, Cell 41, with the MPS Rig No. 2 tested a total of 49 different configurations, and model-scale data were obtained at more than 800 various test conditions simulating freefield community noise measurements of a counterrotating fan.

During the course of this program, the test facility's anechoic quality was verified, and the repeatability of measured acoustic and aeroperformance results was established. The measured acoustic data were processed to obtain 1/3-octave band and narrow-band spectra. The 1/3-octave band were scaled to the desired engine-size using the scaling criteria that were evaluated during this program, and as described in Section 3.2.1. The scaled data were then extrapolated to the required sideline distance and fly-over analyses conducted to obtain EPNL values. The narrow-band spectra for selected test conditions were processed to obtain model-scale directivities of sound pressure levels of various individual tones and tone summations that describe the steady-loading, rotor-to-rotor interaction, and pylon-wake/rotor interaction noise components. These two sets of acoustic results were analyzed to evaluate different blade designs, blade numbers, blade spacings, tip speeds, and test Mach numbers. In addition, these data were analyzed to determine benefit with reduced diameter aft blades and to evaluate the impact of a mounting pylon at two spacings; the following observations and conclusions were derived from these analyses:

1. The lower sweep and activity factor design of F-5/A-5 ($15^\circ/18^\circ$; 120/126) is noisier than the higher sweep and activity factor of the baseline F-7/A-7 ($34^\circ/31^\circ$; 147/152) or the F-1/A-1 ($33^\circ/30^\circ$; 150/158) designs. The F-1/A-1 is quieter than F-7/A-7 due to a slightly improved performance. The F-11/A-11 blades also with a high sweep and higher activity factor ($37^\circ/34^\circ$; 180/200) and, hence, a wider chord yielded a slightly smaller rotor-to-rotor interaction noise than the F-7/A-7; however, this design did not yield any significant EPNL benefit compared to F-7/A-7.
2. An increased blade count produces acoustic benefit that is particularly significant, as it is twofold. Steady-loading noise decreases due to reduced blade loading and tip speed. A consequence of this is the second benefit; namely, decreases in the rotor-to-rotor interaction noise caused by the aft rotor blades rotating at a lower tip speed interacting with weakened wakes and tip vortices from the forward rotor blades. The combined effect results in an acoustic benefit of, perhaps, 9.6 EPNdB at a thrust of 44,500 N (10,000 lb) for a blade number increase from a 4+4 to an 8+8 at nominal spacing ($X/D_t = 0.17$). Likewise, increasing blade count from an 8+8 configuration to an 11+9 with both at maximum rotor spacing ($X/D_t = 0.24$) results in an additional 3.4 EPNdB benefit, which increases to 5 EPNdB for a typical takeoff thrust of 62,300 N (14,000 lb).
3. For all unclipped F-7/A-7 configurations tested in this study, the benefit of increased spacing between the rotor pitch-change axes from nominal ($X/D_t = 0.17$) to maximum ($X/D_t = 0.24$) was limited to 1 EPNdB at takeoff and 1.5 EPNdB at cutback; however for an aft-reduced-diameter configuration, the spacing benefit increased to 2.5 EPNdB at takeoff and 5.5 dB at cutback. This increased benefit of spacing with aft-clipped configuration was due to significant reductions noted in the interaction tones of the second, third, fourth, and fifth harmonics, and in

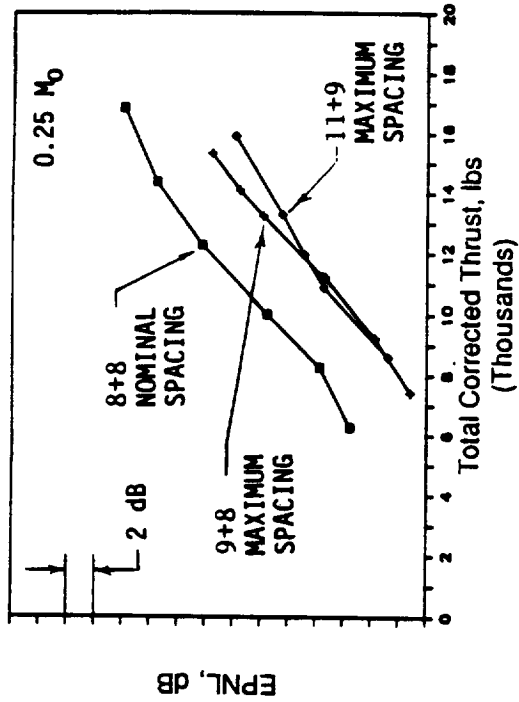
particular, in the levels of A+F, A+2F, A+3F and A+4F tones. Assuming that the length of clipping on the aft blade was sufficient to prevent any interaction of the tip vortex of the forward blade with the aft blade, the reductions are attributed to increased decay of the forward blade wakes with increased rotor spacing. Similar reductions in the interaction tone levels, as a result of spacing, were not fully evident with equal-diameter configurations, as their levels were masked by the interaction noise due to the forward blade tip vortex interacting with the aft rotor blades.

4. The steady-loading noise for a given thrust and blade number decreases with tip speed. A reduction in total noise is also attained by decreasing the tip speed; however, a decrease of tip speed beyond an optimum increases the overall noise levels. The increased pitch angle required to produce a given thrust at a lower tip speed may result in stronger wakes; this, combined with the accompanying reduction in spacing between the blades, causes rotor-to-rotor interaction noise to increase for decrease of tip speed beyond the optimum.
5. A reduced-diameter, aft blade configuration produced dramatic reductions in sound pressure levels beyond the 3xBPF compared to an equal-diameter configuration. The significant reductions observed in interaction tone sum levels are attributed mainly to the absence of vortex/rotor interaction tones. Net benefit in EPNL between F-7/A-7 (9+8) unclipped and clipped configurations was in the range of 2 dB.
6. The combined effects of improved efficiency, increased duration correction, and reduced tip speed resulted in EPNL data for a Mach number decrease from 0.3 to 0.2 to correlate within a band of 2 dB.
7. The pylon effect is noted mostly at the BPF and 2x BPF of the forward rotor; the impact of the pylon/rotor interaction noise depends on the levels of steady-loading noise of the configurations. Higher steady-loading noise levels such as are expected with higher thrust settings or with configurations having a low blade count mask the influence of the pylon. Generally, effect of pylon is more significant at conditions with low steady-loading noise, such as cutback and approach. Increased spacing between the pylon and the forward rotor results in an increased decay of the pylon-wake defect, also, and reduces the impact of pylon on the forward rotor. Presence of a pylon had no effect on the rotor-to-rotor interaction noise levels.

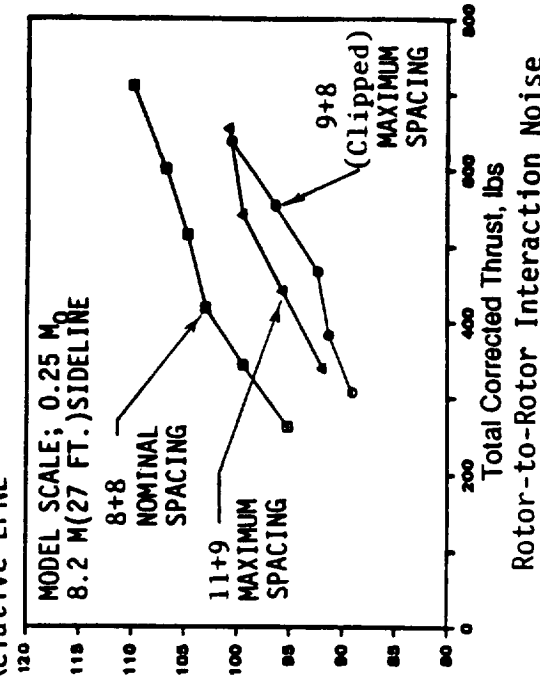
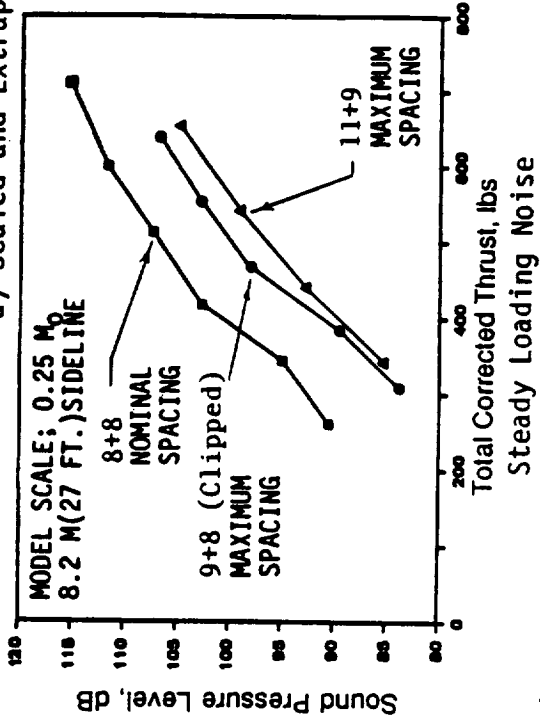
This section is concluded by presenting data from two runs that highlight the reduction in steady-loading noise by increasing blade numbers and decrease in rotor-to-rotor interaction noise by using a reduced-diameter aft blade. The selected configurations are the F-7/A-7 with 11+9 blades and the F-7/A-7c (9+8) with clipped aft blade. Figure 363 compares these data with the baseline F-7/A-7 (8+8) data, suggesting that even lower overall noise levels could be achieved by the combined effect of increased blade numbers and reduced aft diameter.

7.1.2 Aerodynamic

Because the emphasis of Cell 41 testing was on acoustics, limited aerodynamic performance results will be reported for this testing. These results will concentrate on F-7/A-7 and F-11/A-11 rotor-to-rotor spacing effects and F-11/A-11 blade number variation effects on efficiency.



a) Scaled and Extrapolated Relative EPNL



b) Model Scale Tone Sum Levels

Figure 363. Cell 41 Acoustic Highlights.

Figure 364 illustrates the F-7/A-7 (8+8) performance data from Cell 41 at Mach 0.25 for nominal and maximum rotor-to-rotor spacing configurations at typical takeoff pitch-angle combinations, demonstrating that the efficiency of the nominal spacing configuration is better than that of the maximum spacing configuration and that the improvement increases loading parameters.

The F-11/A-11 (11+9) maximum and supermaximum spacing performance data at Mach 0.25 are shown for two different pitch-angle combinations in Figure 365. With a pitch-angle setting of 44.8°/43.3°, the efficiency demonstrated by the supermaximum spacing configuration is approximately 1.0 point better than that achieved with maximum spacing. However, at the blade-pitch-angle setting of 48.7°/45.3°, there is no noticeable effect of rotor-to-rotor spacing variation on efficiency.

Figure 366 shows the effect of blade number variation on the performance of F-11/A-11 supermaximum spacing configuration for two different pitch-angle combinations. In both cases, the 13+11 blade arrangement is more efficient than the 11+9 blade arrangement by between 0.5 and 3.0 points, depending on loading parameters. Figure 366 demonstrates that for both the 13+11 and 11+9 blade number arrangements, the more highly loaded configurations (more open pitches) are less efficient at a given loading parameter level.

7.1.3 Aeromechanics

7.1.3.1 Blades

Although the typical data presented in Section 6.1.3 and in the CDR indicate a sudden increase in stress for the F-5 blade at 8700 rpm, which resembles an instability signal, the data analysis efforts failed to establish adequate evidence to assert that it was a flutter phenomenon. High stress for the F-5 blade was attributed to separated flow vibration.

The F-11 blade, which in its original shape experienced instability, was clipped at the tip along the trailing edge and then tested in Cell 41. Figure 170 (presented in Subsection 6.1.3) is a typical result from one of several runs and shows no flutter response at the low Mach number (Mach 0.34) testing. However, when tested at the NASA 8x6 wind tunnel, the F-11 blade fluttered at the Mach numbers 0.8 and 0.9; therefore, it can be concluded that the clipping did not stabilize the F-11 blade. Data used to formulate this conclusion is available in Appendix P of the Comprehensive Data Report for the NAS3-24080 contract.

Series 7 blades tested in Cell 41 were mainly for the purpose of testing the aeromechanical hub.

7.1.3.2 Aeromechanical Hub

To simulate the structural operating condition of the UDF® Demonstrator engine, which has an actuator system and other mechanisms in the blade root that make the blade root boundary condition more flexible, the aeromechanical hub was designed, fabricated, and tested with Series 7 (Demo) blades. These tests were performed both in Cell 41 and then, later, in the NASA 8x6 tunnel.

The original A-7 blade had a 13°-ply reference angle and experienced flutter; the instability occurred at the second mode frequency around 375 Hz. A redesigned A-7 blade with a 35°-ply reference angle was tested which experienced the same instability. A series of flutter-control devices were tested then.

Figures 171 through 173 (Section 6.1.3) demonstrate how the flutter could be controlled by installing either platform adaptor seals or a friction damper on the aeromechanical hub. Other

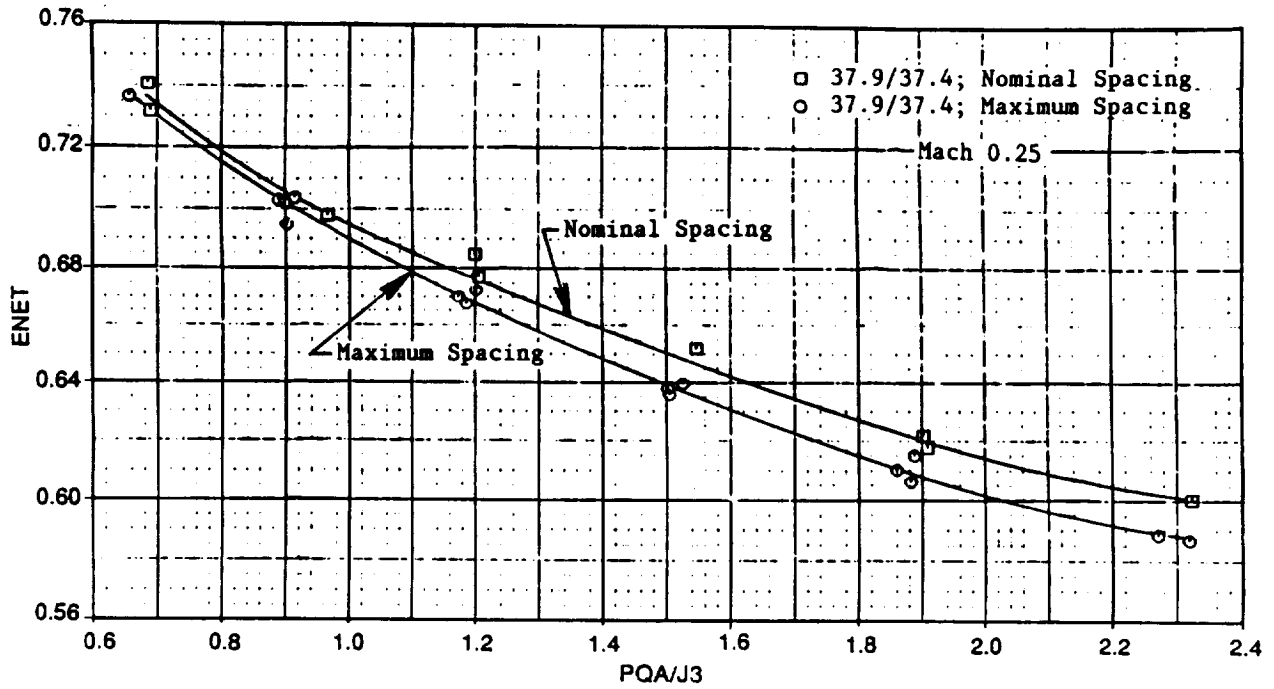


Figure 364. Effect of Rotor-to-Rotor Spacing Variation on F-7/A-7 (8+8) Low Speed Performance (Cell 41).

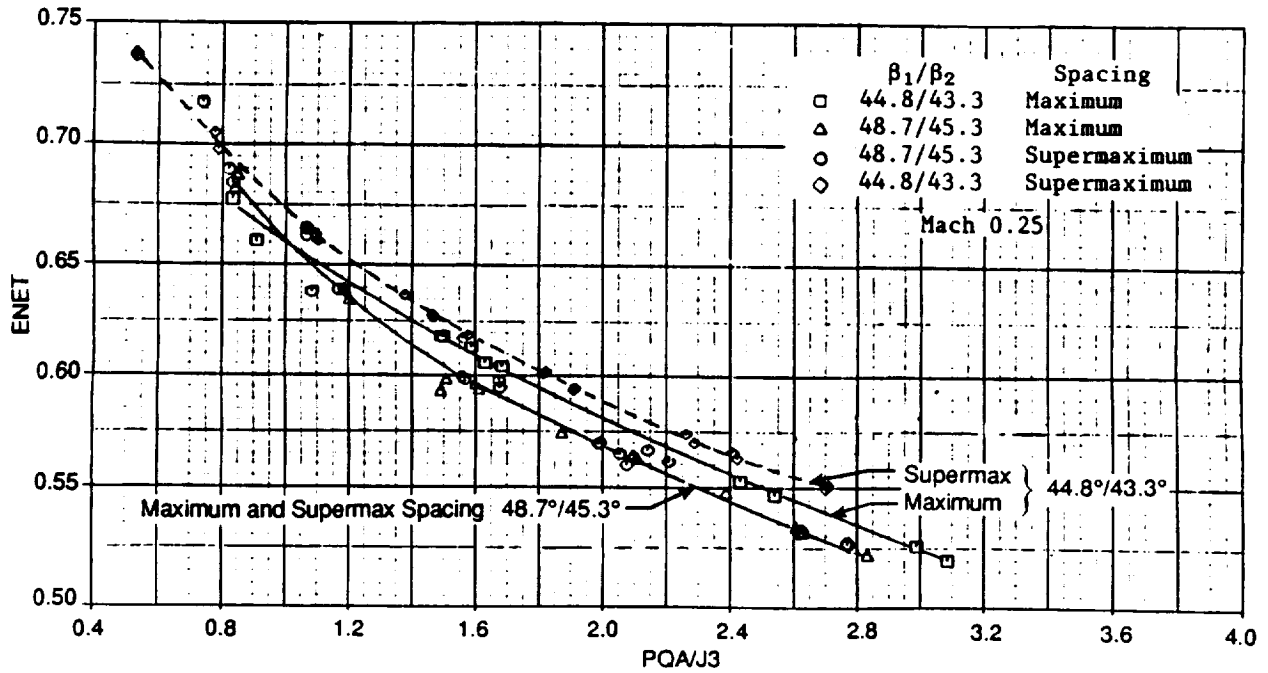


Figure 365. Effect of Rotor-to-Rotor Spacing Variations on the F-11/A-11 (11+9) Cell 41 Low Speed Performance at Mach 0.25.

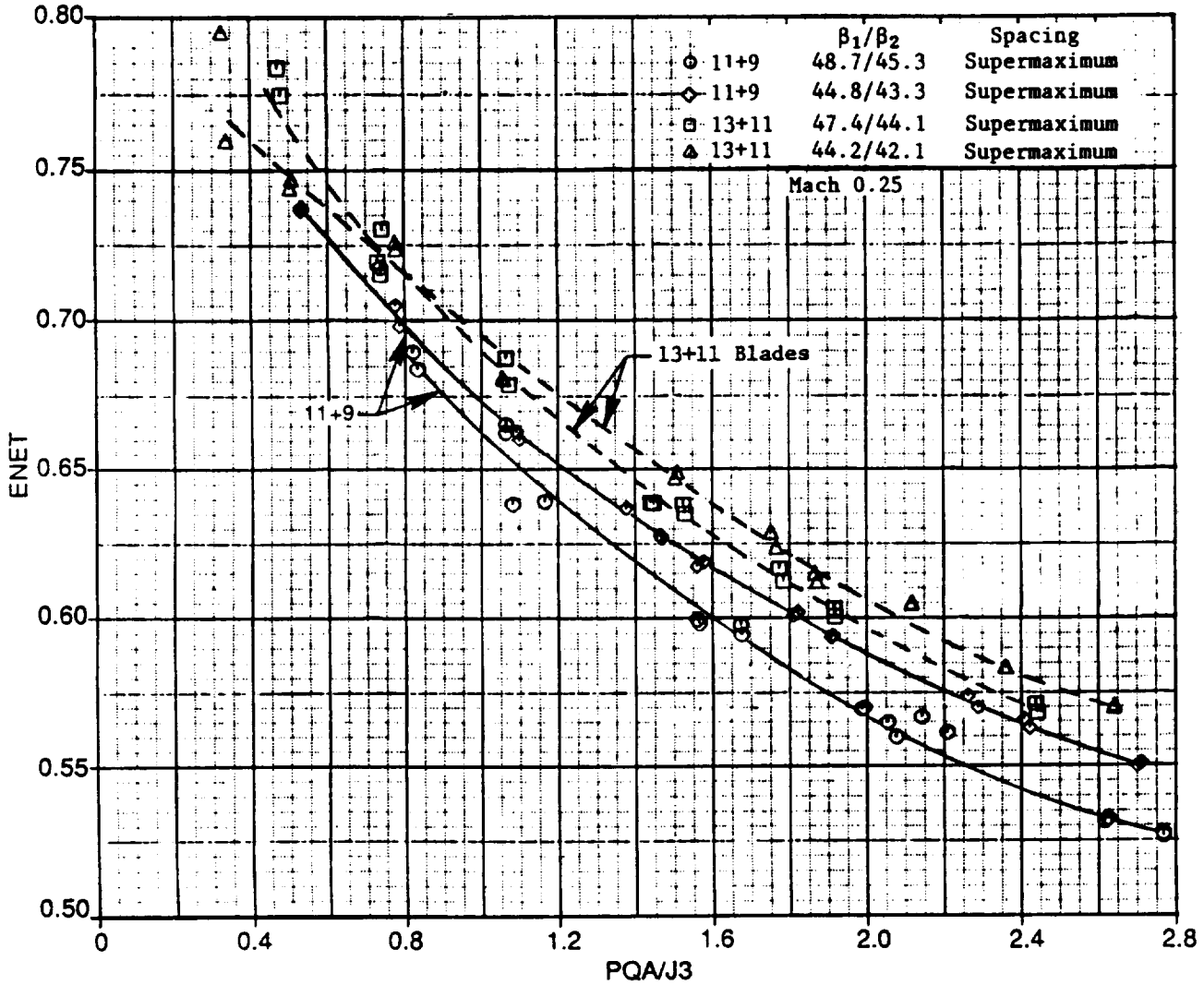


Figure 366. Effect of Blade Number Variation on F-11/A-11 (Supermaximum Spacing) Low Speed Performance in Cell 41 at Mach 0.25.

measures, such as cropping the blade tip (to a certain amount) also demonstrated the capability to control flutter.

7.2 Rig 3/NASA 8x6 Supersonic Wind Tunnel

7.2.1 Aerodynamic Performance

Because testing in the NASA 8x6 wind tunnel was basically performance oriented, performance results from all test facilities will be addressed in this section. Aerodynamic performance testing was conducted in the NASA 8x6 supersonic and 9x15 low speed wind tunnels, as well as in the GE low speed, anechoic test chamber, Cell 41. Early model testing of the F-4/A-4, F-5/A-5, and F-7/A-7 configurations was also performed at the BTWT (Boeing Transonic Wind Tunnel). The MPS SN003 horizontal-drive unit was used to drive the UDF® counterrotating blades tested in NASA's 8x6 and 9x15 tunnels; whereas, the vertical-drive unit (SN002) was used in the Cell 41 tests. The BTWT was used to test the SN001 horizontal-drive unit.

The F-7/A-7, F-11/A-11, and F-21/A-21 configurations were tested at high speed in NASA's 8x6 wind tunnel, and at low speed in Cell 41. Low Mach number testing of F-7/A-7 and F-11/A-11 was also done in the NASA 9x15 tunnel. Using the F-7/A-7, the rotor-to-rotor spacing and flight Mach number effects were investigated at both high- and low-speed. Mismatched speed effects also were studied. Due to high blade stresses, the original F-11/A-11 configuration was limited to a short performance mapping test near the design point. In order to reduce stresses and blade tip deflection, the tip TE (trailing edge) corner of the F-11 blades was clipped and data was again collected. The F-21/A-21 configuration investigated effects of two different shapes of the forebody and aftbody; the F-21 blade also had to be clipped at the tip TE to reduce the tip deflections and blade instability. Strain gauges were removed from F-21/A-21 blades near the end of the test, and the performance effect was determined.

The UDF® blades were tested in the wind tunnels over a wide range of Mach numbers, pitch angles, and rotor speeds. The blades were first set to pitch angles that would produce equal rotor torques at the design speed, and tunnel air speed was increased to the test Mach number with the blades windmilling. The rotors were then powered to the minimum speed above windmill, and data taken with equal rotor speeds at several increments up to 110% design speed. The tunnel Mach number was then adjusted slightly up and down from the nominal setting, and the test was repeated with the same pitch angles and at the same equal rotor-speed conditions.

The initial pitch angles tested were chosen so as to produce the power required along the maximum climb flight path at 100% speed on both rotors and with equal rotor torques; additional pitch angles were set and tested to yield both higher- and lower-than normal levels at constant Mach numbers.

It should also be noted that all NASA data presented was corrected for centrifugal effects and blade strain gage factor (except for the data discussed in Section 7.2.1.3.1).

7.2.1.1 F-7/A-7 Performance Results

The overall performance of the F-7/A-7 was mapped in the NASA 8x6 tunnel at Mach numbers of 0.67, 0.72, 0.76, 0.80, and 0.85; data were taken with five different pitch-angle settings at tunnel Mach numbers where the blade stress levels allowed. These data are presented in Figures 367 through 371 (Views A and B, each) as net efficiency versus the disk loading parameter, and as the power coefficient versus advance ratio. At the design Mach number, the pitch angles of 58.5°

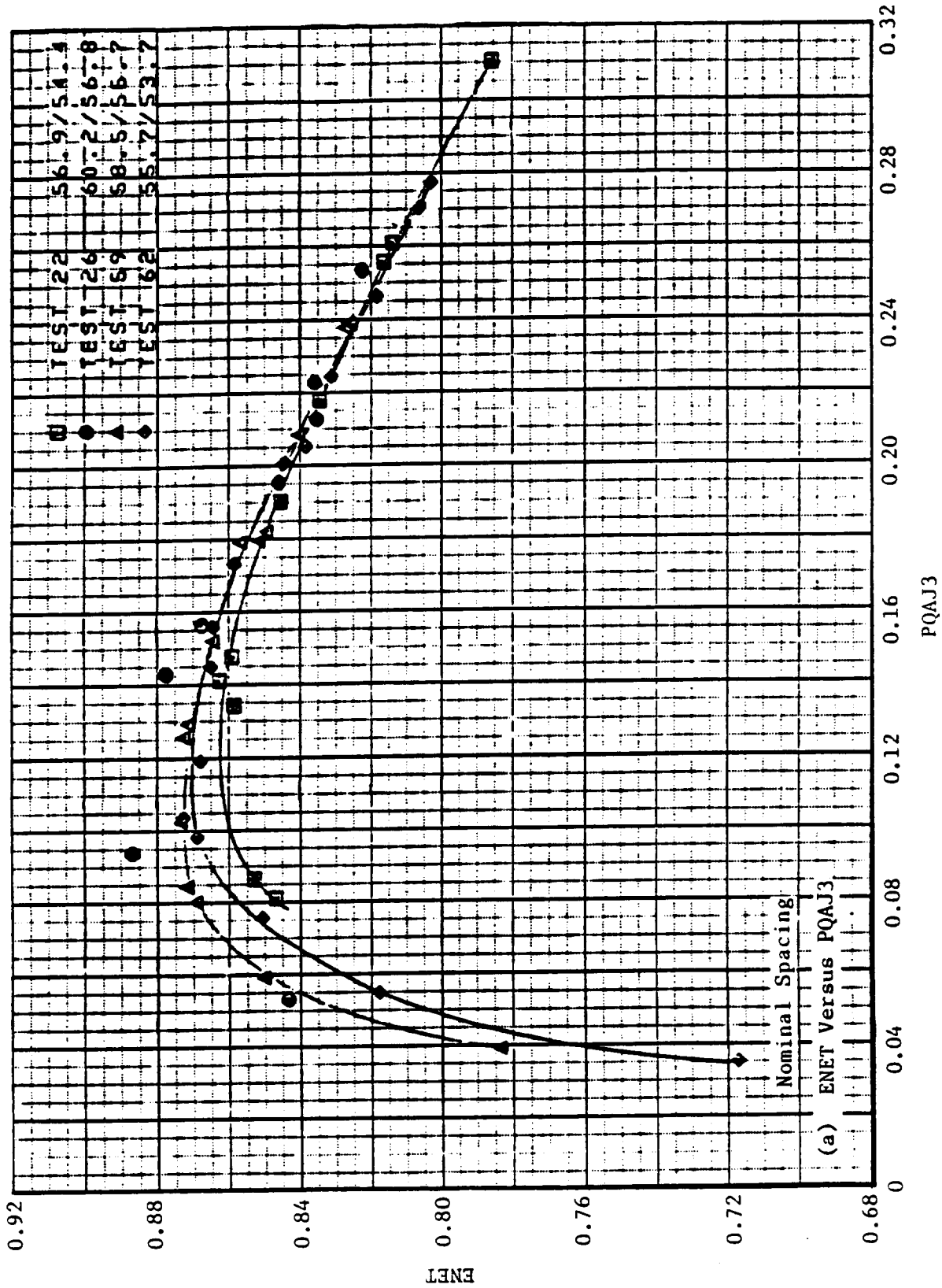


Figure 367. F-7/A-7 (8+8) Overall Performance in 8x6 Tunnel at Mach 0.67.

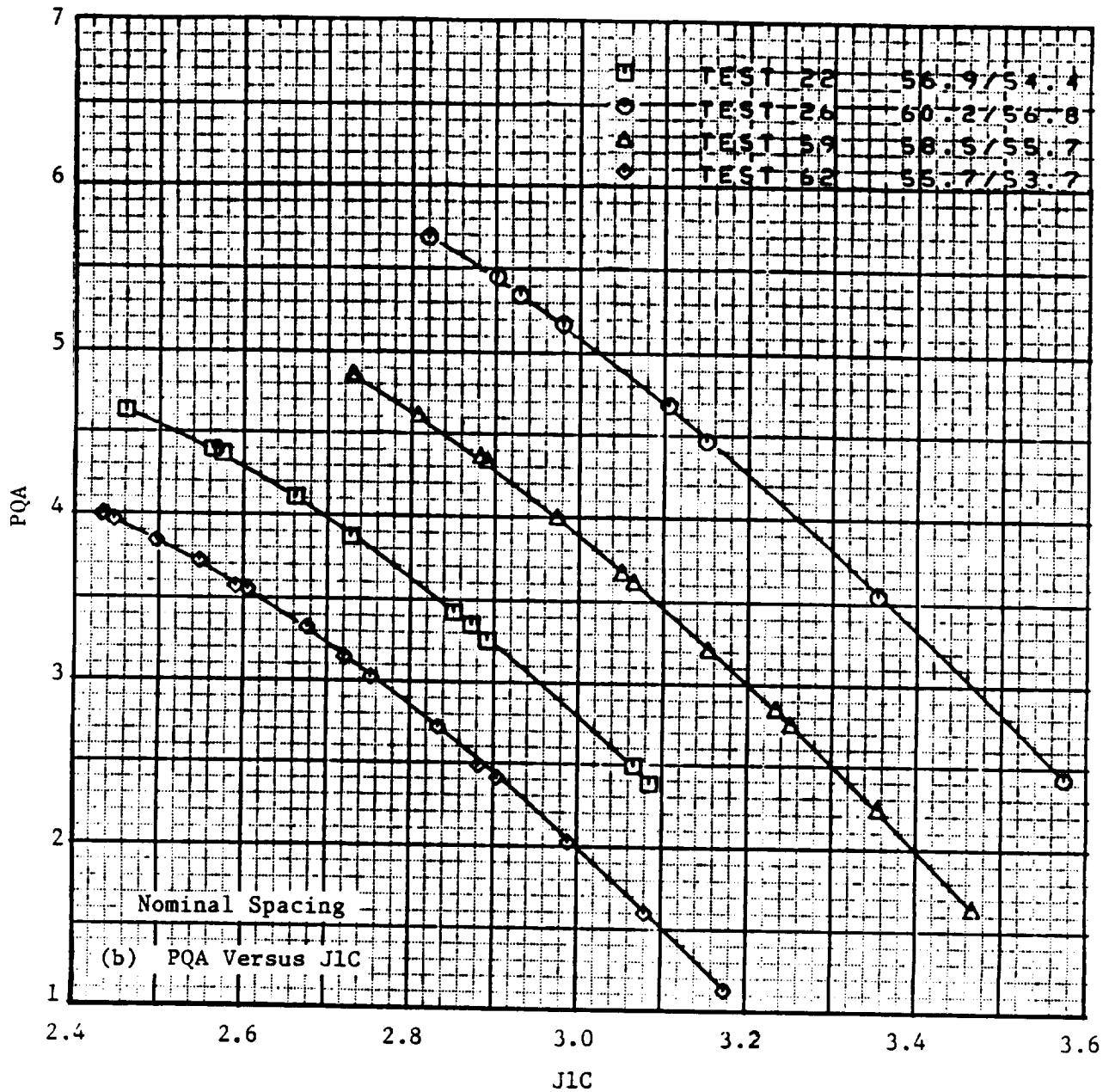


Figure 367. F-7/A-7 (8+8) Overall Performance in 8x6 Tunnel at Mach 0.67 (Concluded).

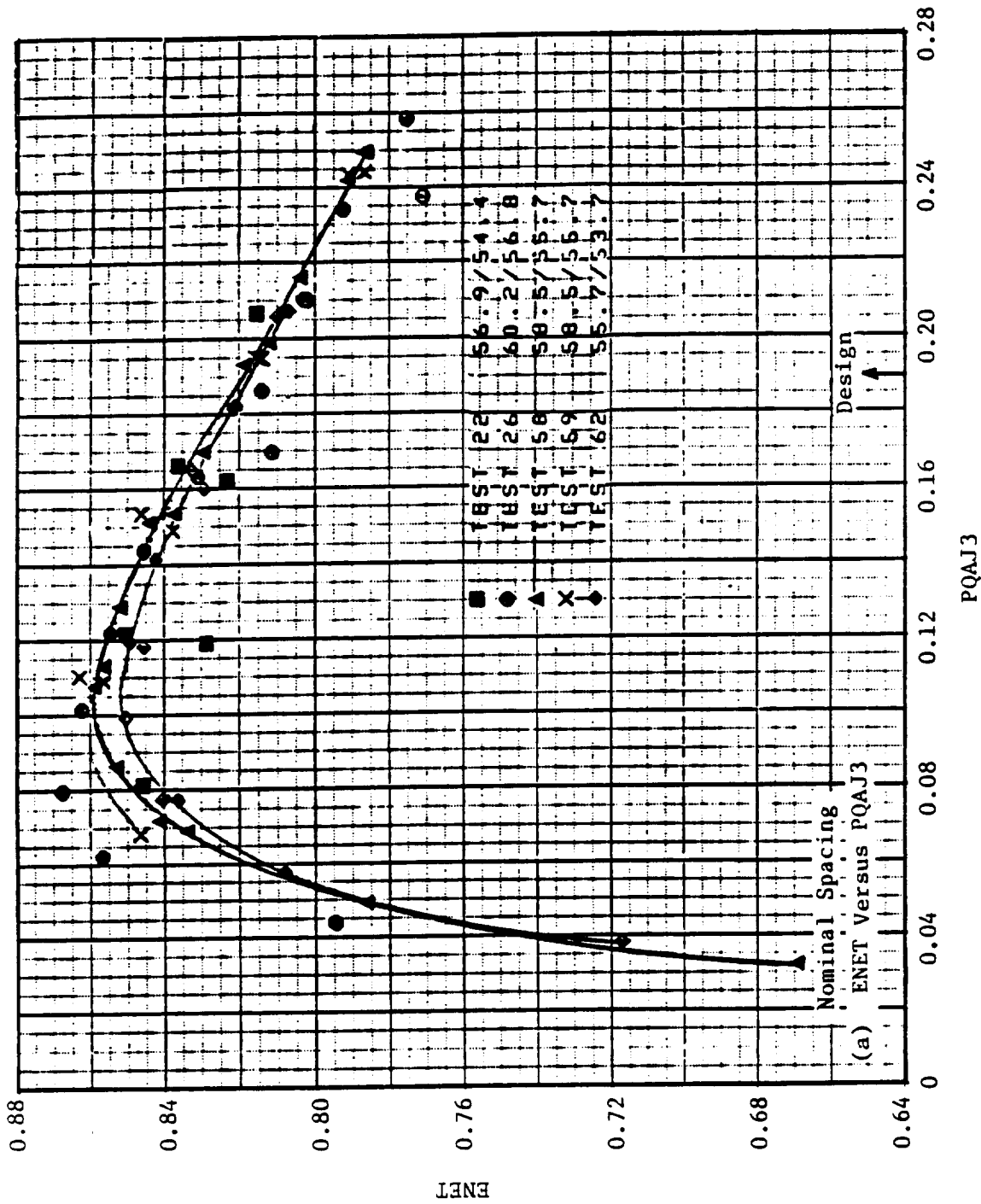


Figure 368. F-7/A-7 (8+8) Overall Performance in the NASA 8x6 Wind Tunnel at Mach 0.72.

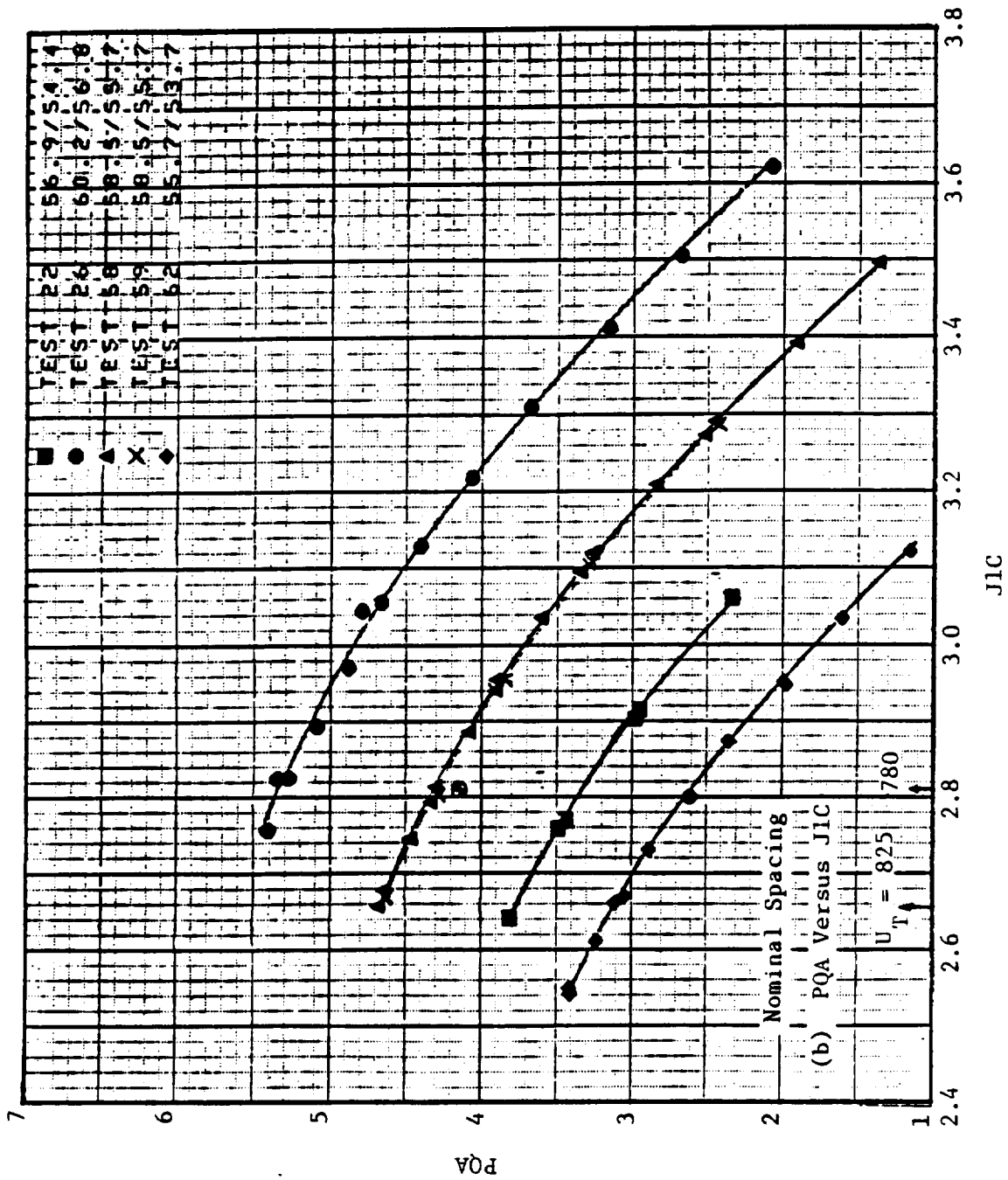


Figure 368. F-7/A-7 (8+8) Overall Performance in the NASA 8x6 Wind Tunnel at Mach 0.72 (Concluded).

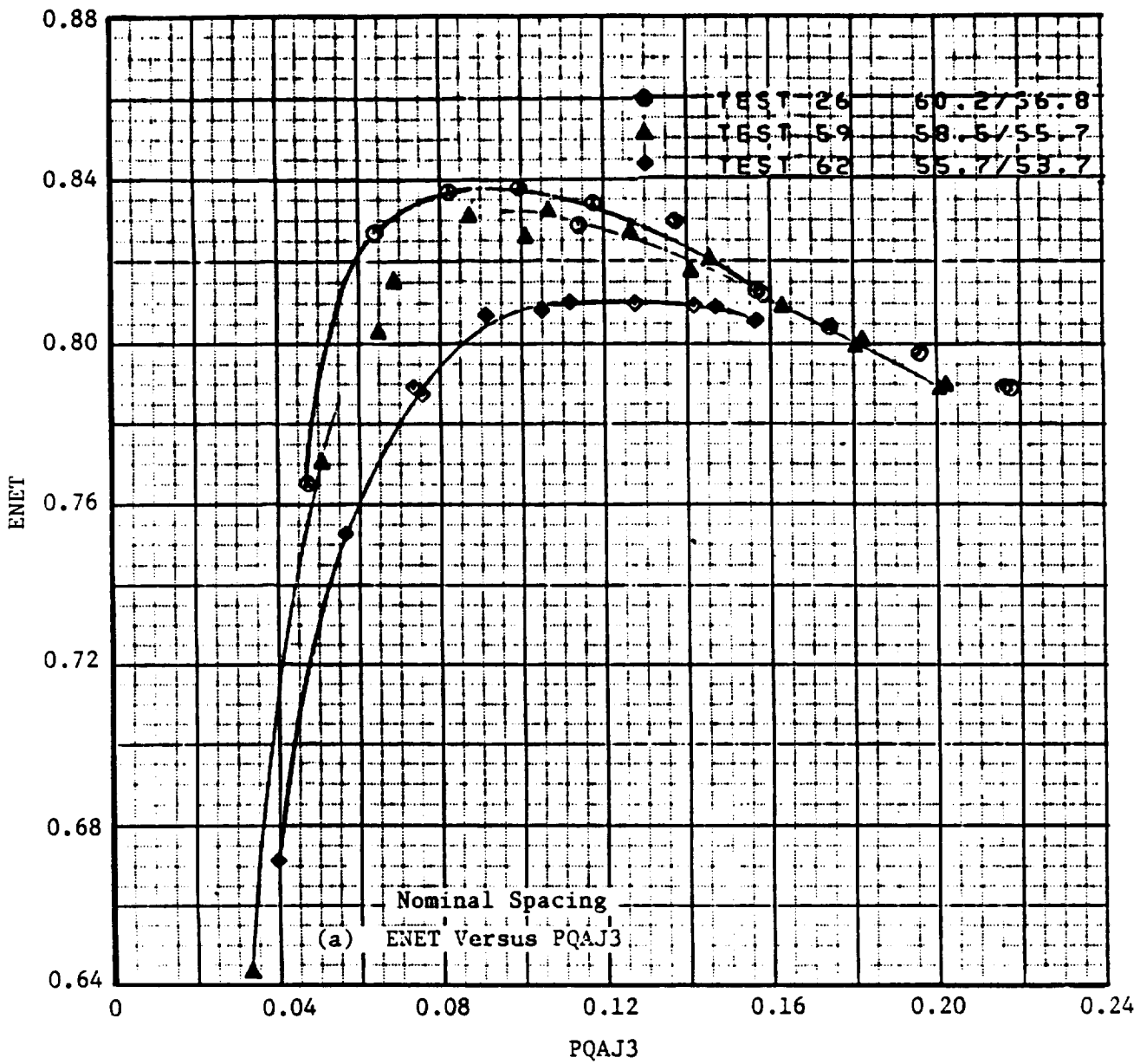


Figure 369. F-7/A-7 (8+8) Overall Performance in NASA 8x6 Wind Tunnel at Mach 0.76.

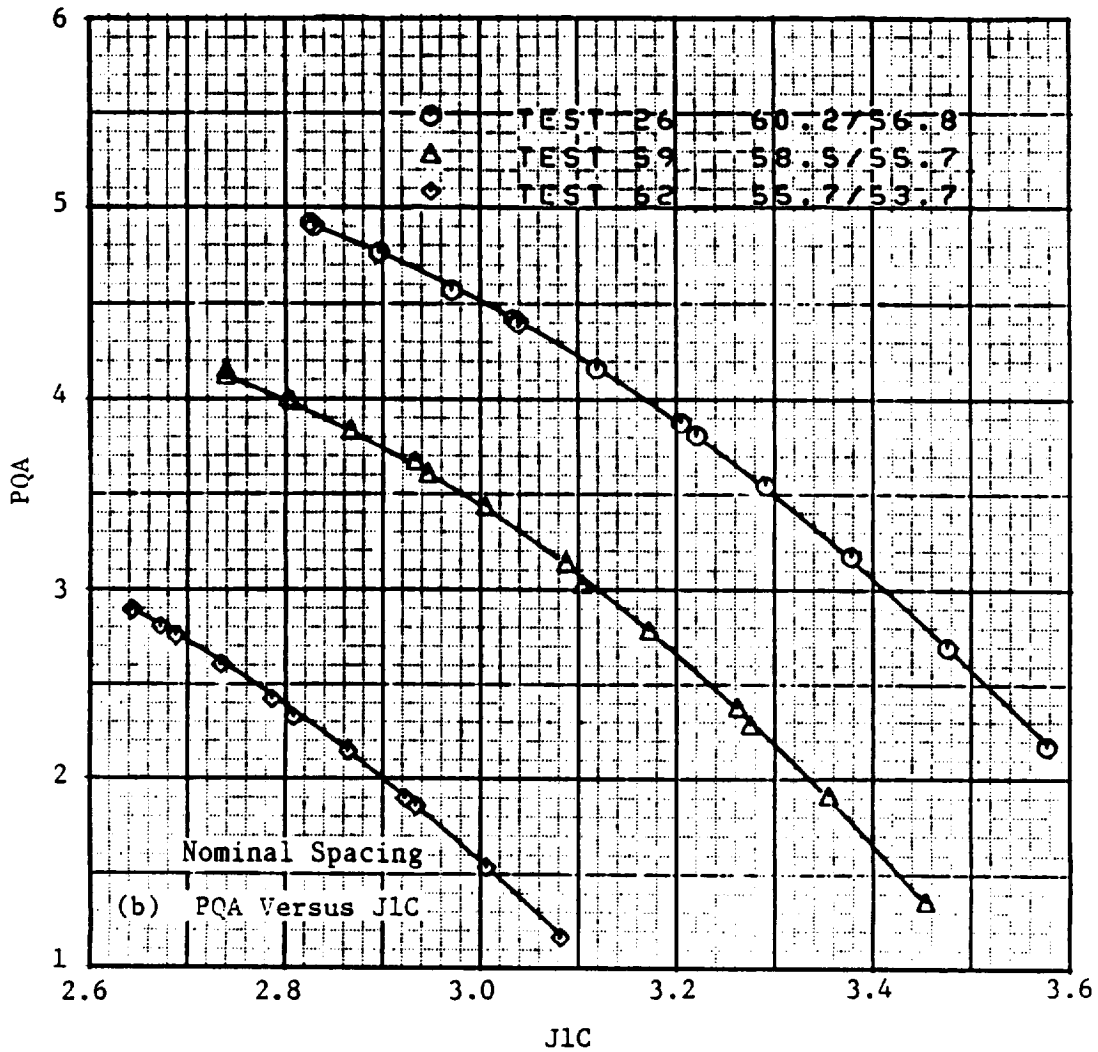


Figure 369. F-7/A-7 (8+8) Overall Performance in NASA 8x6 Wind Tunnel at Mach 0.76 (Concluded).

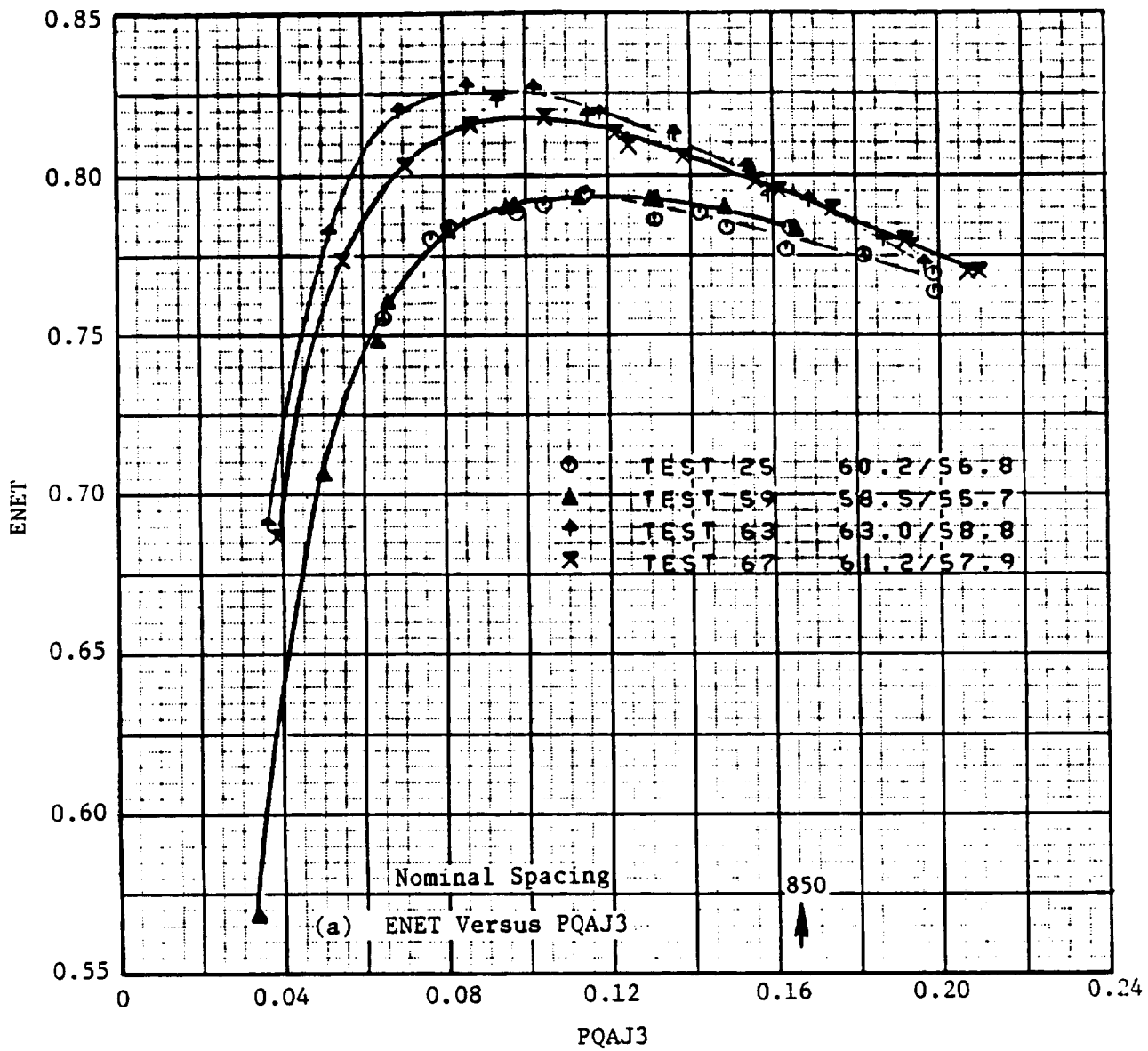


Figure 370. F-7/A-7 (8+8) Overall Performance in NASA's 8x6 Tunnel at Mach 0.8.

ORIGINAL PAGE IS
OF POOR QUALITY

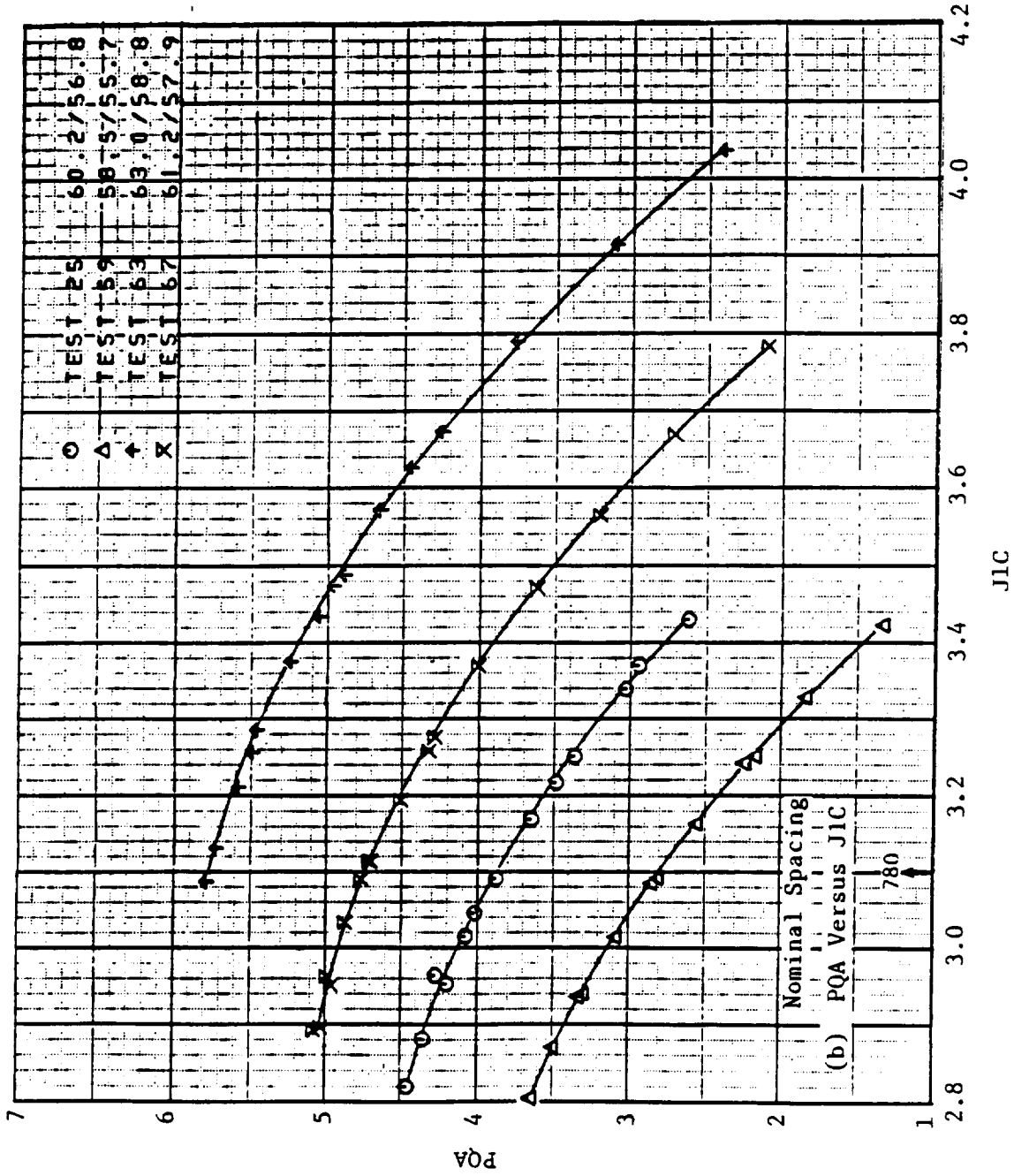


Figure 370. F-7/A-7 (8+8) Overall Performance in NASA's 8x6 Tunnel at Mach 0.8 (Concluded).

ORIGINAL PAGE IS OF POOR QUALITY

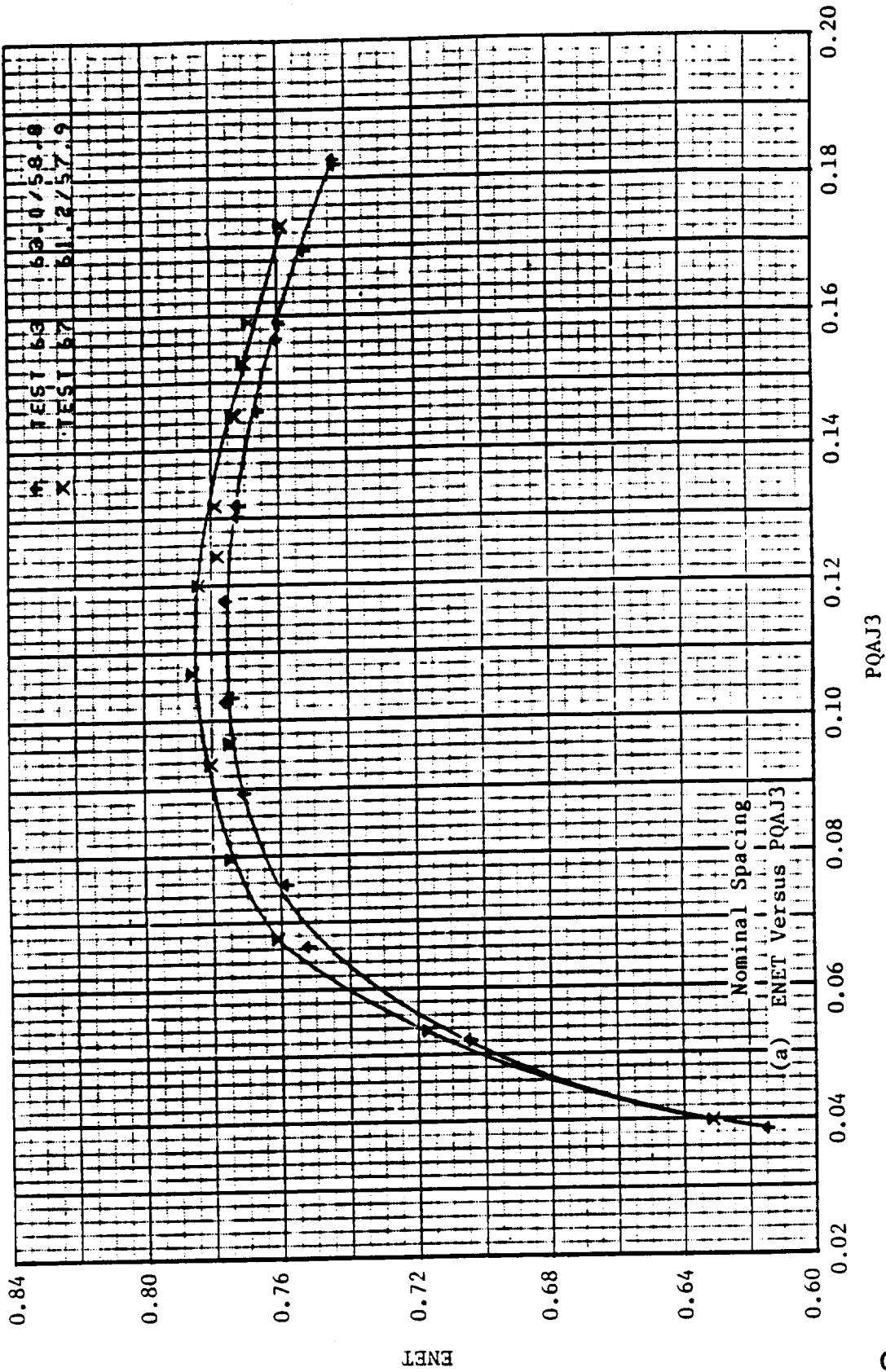


Figure 371. Overall Performance for F-7/A-7 (8+8) at Mach 0.85.

ORIGINAL PAGE IS
OF POOR QUALITY

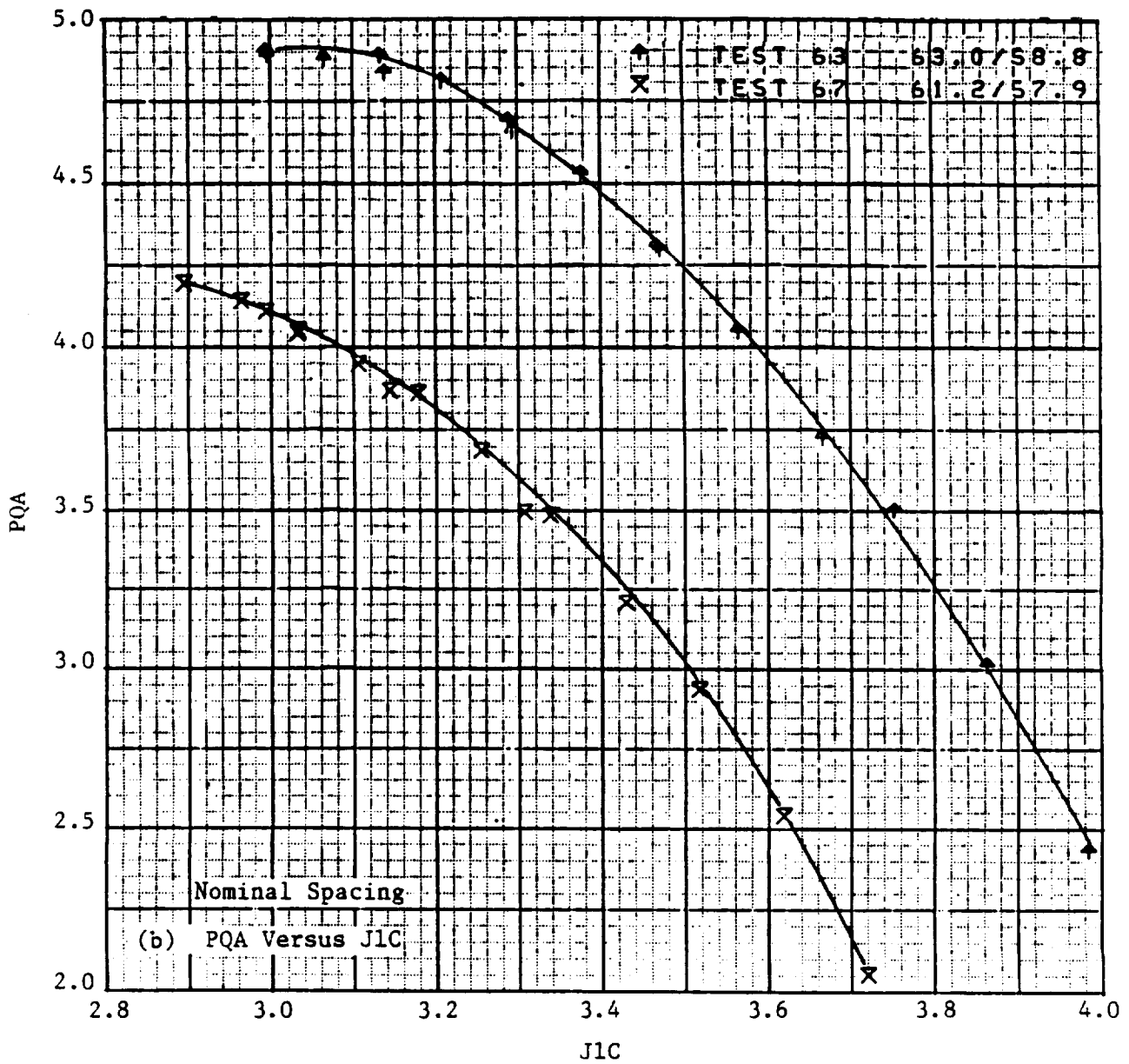


Figure 371. Overall Performance for F-7/A-7 (8+8) at Mach 0.85 (Concluded).

ORIGINAL PAGE IS
OF POOR QUALITY

forward and 55.7° aft produce approximately the design power coefficient at the design advance rotor. The net efficiency values include a dynamic calibration factor for the force balances and an adder for strain gauge removal. The measured design point efficiency with these corrections applied is 0.82.

These data were crossplotted to obtain the effects of flight Mach number at constant loading and pitch angles. Figure 372 demonstrates that the efficiency falls off rapidly as the Mach numbers and tip speeds are increased. At constant design tip speed (237.7 m/s), the efficiency rises slightly from Mach 0.67; peaks near Mach 0.75, and then falls off at higher Mach numbers. Figure 373 shows the efficiency trend with disk loading at constant design tip speed and Mach number; this trend indicates that a 10% increase in disk loading will cost approximately 0.6 point in net efficiency.

7.2.1.1.1 Rotor Spacing Effects

Rotor spacing effects were investigated from Mach 0.67 to 0.80, for three different spacings of the rotor pitch-change axes. The spacings varied with the minimum axial distance to blade-diameter ratio (Z/D) of 0.14, a nominal distance ratio of 0.17, and a maximum ratio of 0.24. The nominal spacing, at which most of the wind tunnel testing was conducted, was 10.57 cm (4.16 in.). Figure 374 depicts that for the various spacings, power absorbed at Mach 0.72 by the rotors is the same over a wide range of rotor speeds.

Figure 375 illustrates the spacing effect on net efficiency at Mach 0.72 as a function of the disk loading parameter. The minimum spacing provides the highest efficiency at all Mach 0.72 loading levels; approximately 0.3 point better at design and higher loadings, to 1.0 point better at the lower levels. Maximum spacing data show 2 points worse in efficiency than nominal spacing at low loadings, and 1.4 points worse at the higher loading levels. Other F-7/A-7 wind tunnel data (Figure 376) reveals that at slightly lower Mach numbers (0.67), nominal to maximum spacing effect is 1 to 2 points in net efficiency, and the minimum to nominal effect is less. Data taken at Mach 0.80 indicates a difference in efficiency of approximately 2 points between nominal and maximum spacings, and of 1.0 to 1.5 points between nominal and minimum spacings. The Cell 41 test data taken at Mach 0.25 (Figure 364) indicates these rotor spacing effects are similar, depending on the loading levels.

Proximity of the downstream rotor to the upstream rotor has a pronounced effect on the torque split between rotors; this is demonstrated in Figure 377 for the three different axial spacings. At equal power and rpm, total torque remains the same, but the split between rotors is different. The torque ratio decreases as spacing increases, since the induced effect of the downstream rotor is diminished. If the spacing were further increased, the effect would continue to lessen to the extreme condition where the downstream rotor is so far removed from the upstream rotor that it acts as an isolated blade row, having no effect at all.

7.2.1.1.2 Angle-of-Attack/Pylon Effects

Since limited angle-of-attack testing was conducted in the 8x6 tunnel, and no pylon was employed there, the BTWT data will be used for discussion in this section. Aerodynamic performance data were taken in the BTWT to assess the effect of angle-of-attack, both with and without pylon. All BTWT data were corrected for centrifugal effects and incorporate the freestream Mach number calibration derived by Krynytzky (see Reference 38). These data however do not include a correction for blade strain gauges. The three plots in Figure 378 demonstrate the net efficiency, power coefficient, and torque ratio parameters as a function of advance ratio for the

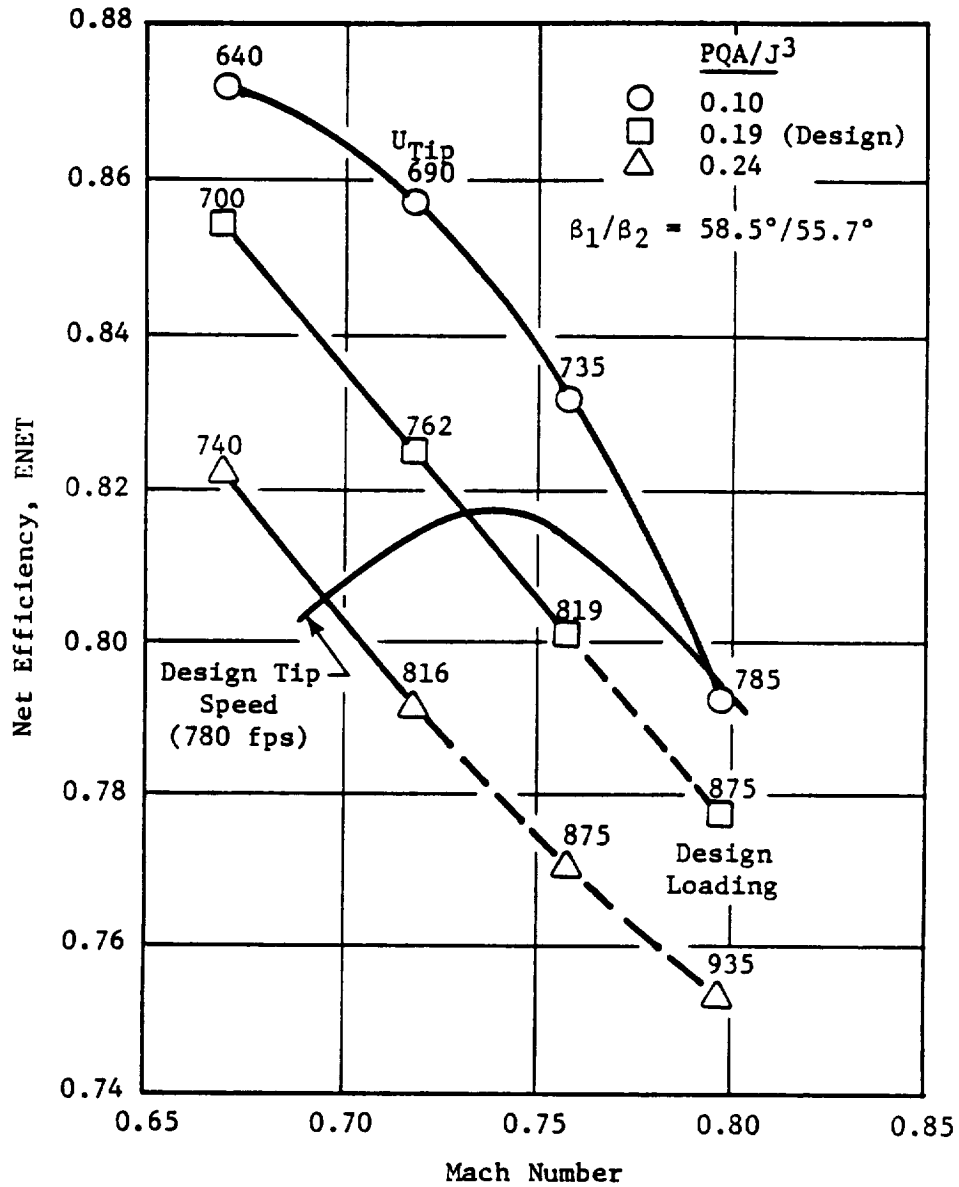


Figure 372. Mach Number Effect on F-7/A-7 (8+8) Nominal Spacing Overall Performance.

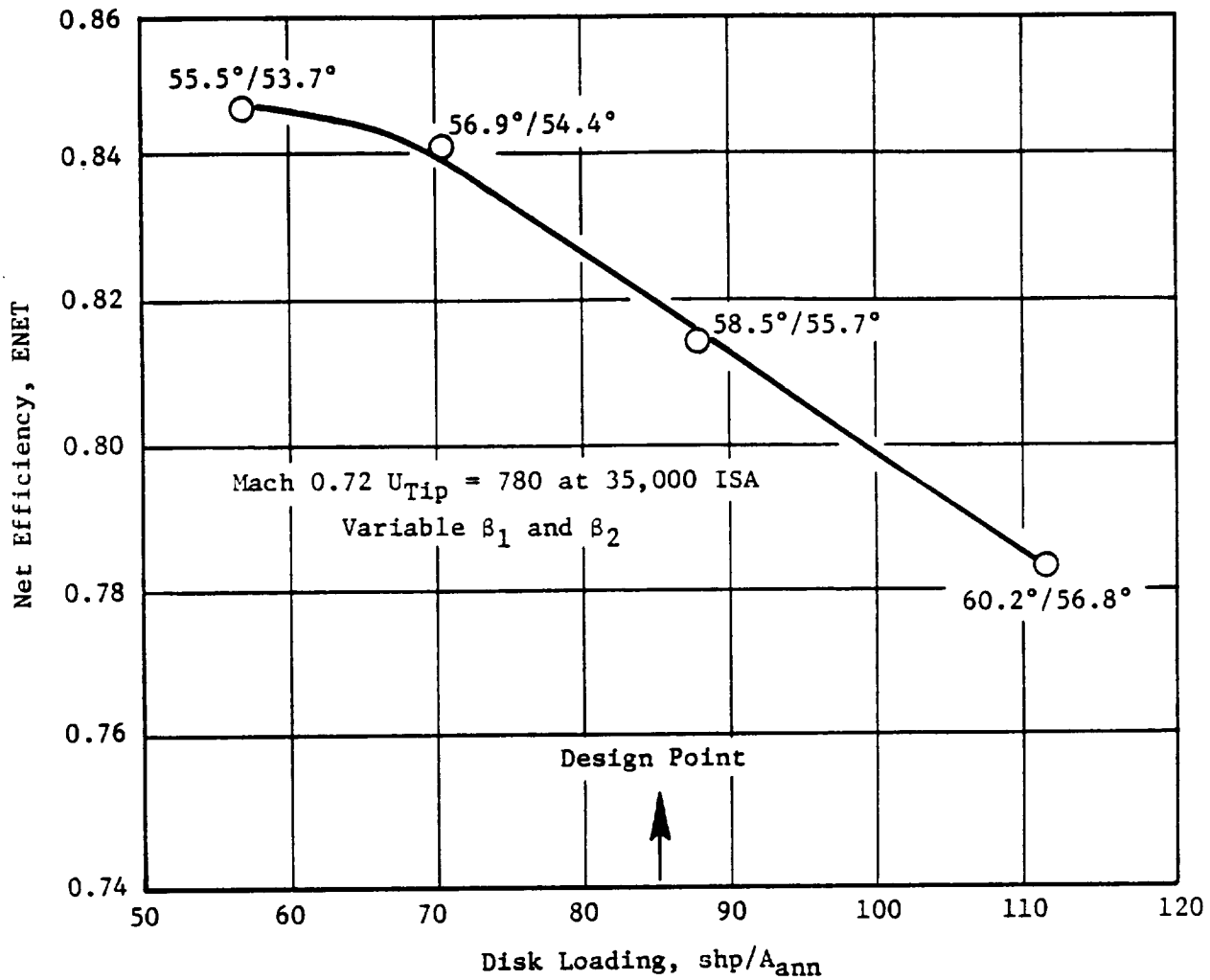


Figure 373. Disk Loading Effect on F-7/A-7 (8+8) Nominal Spacing Overall Performance.

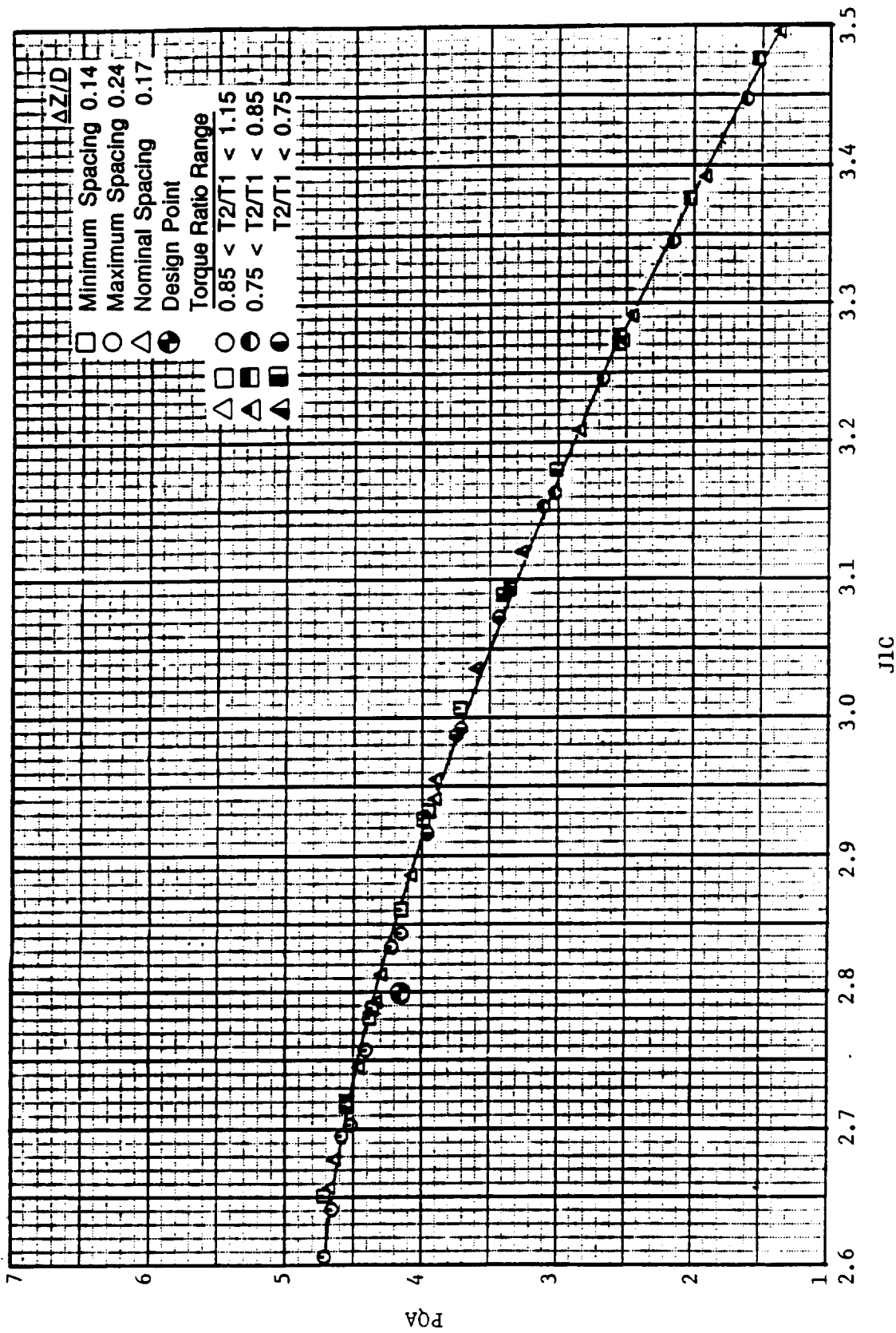
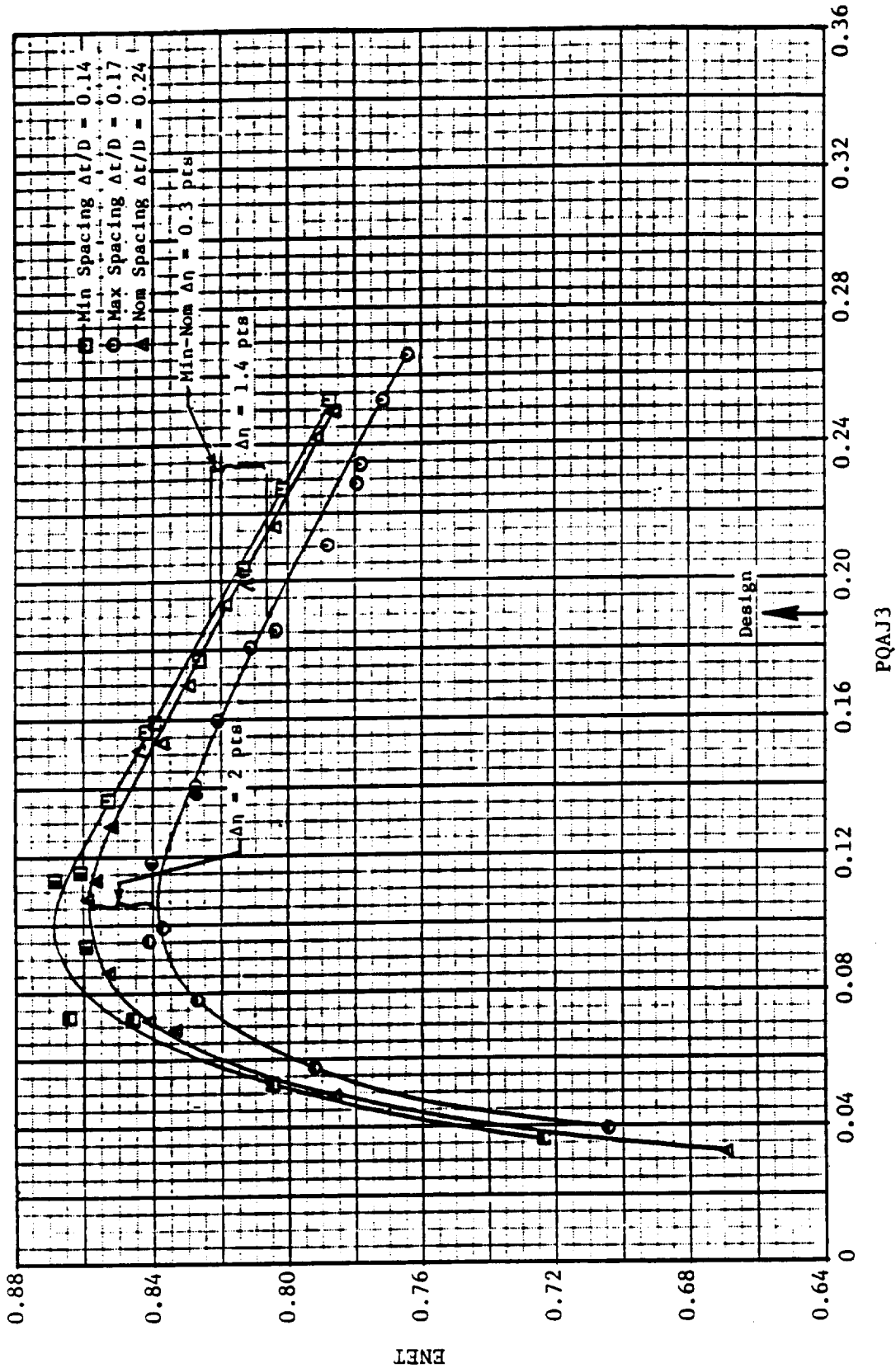


Figure 374. Spacing Effect on F-7/A-7 Power Absorption at Mach 0.72.



PQAJ3

Figure 375. Rotor Spacing Effect on F-7/A-7 Net Efficiency at Mach 0.72.

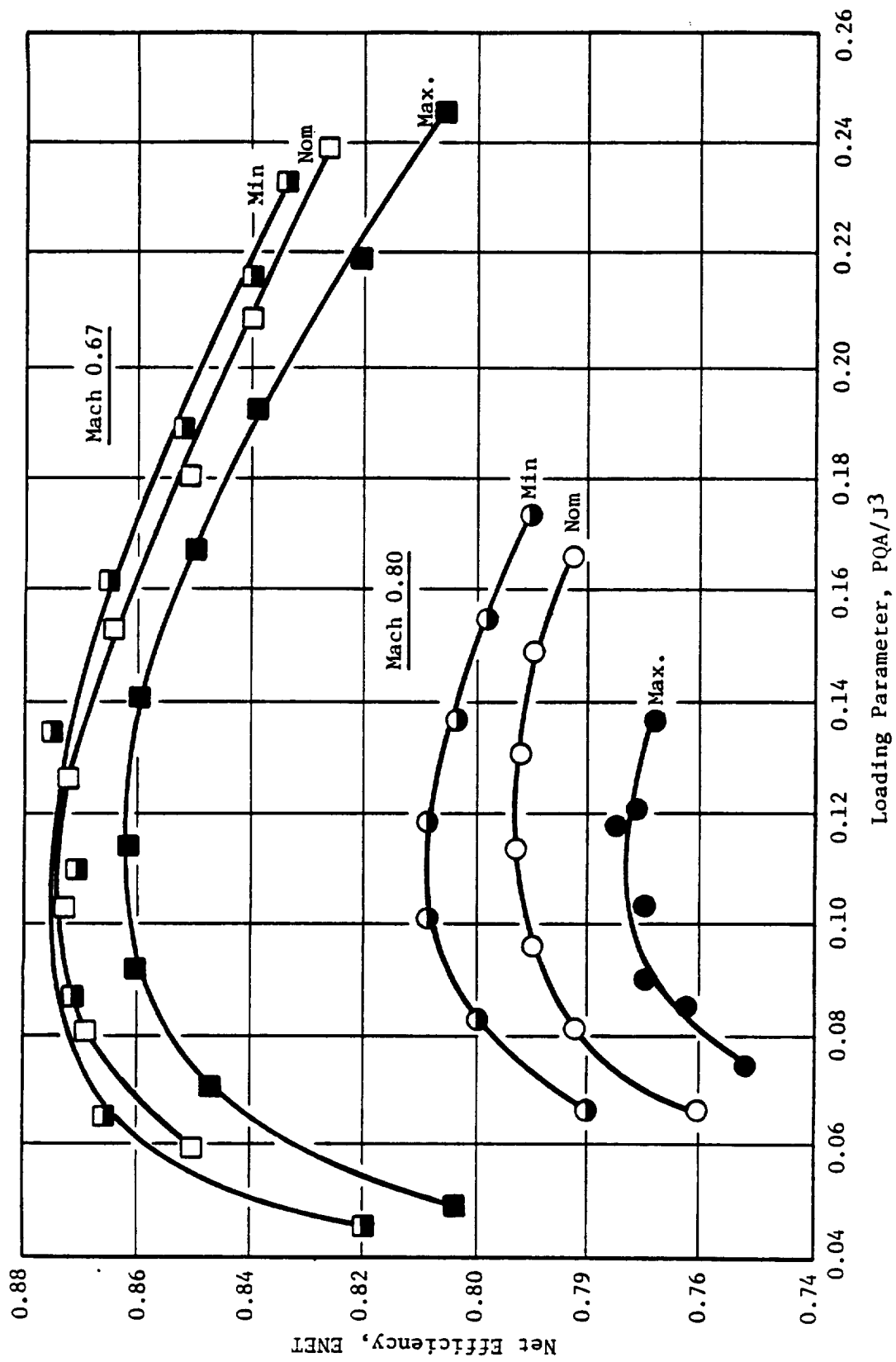


Figure 376. Rotor Spacing Effect on F-7/A-7 Net Efficiency at Mach Numbers 0.67 and 0.80.

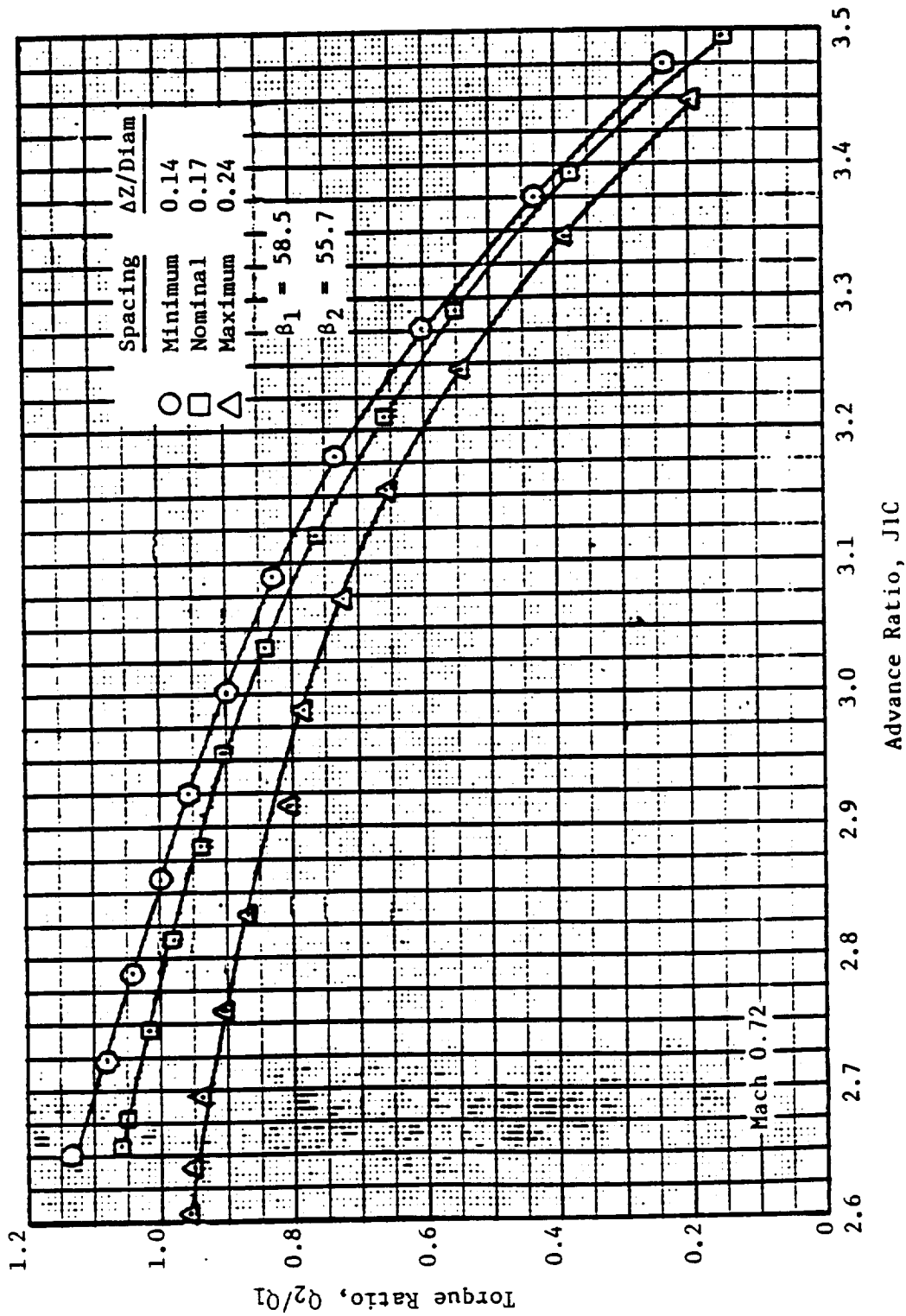
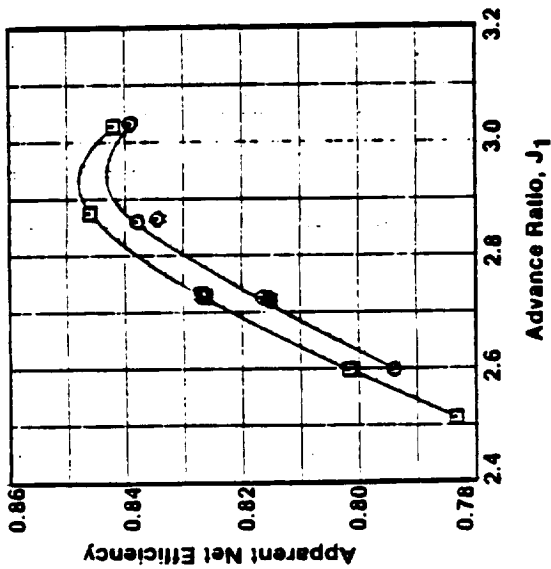
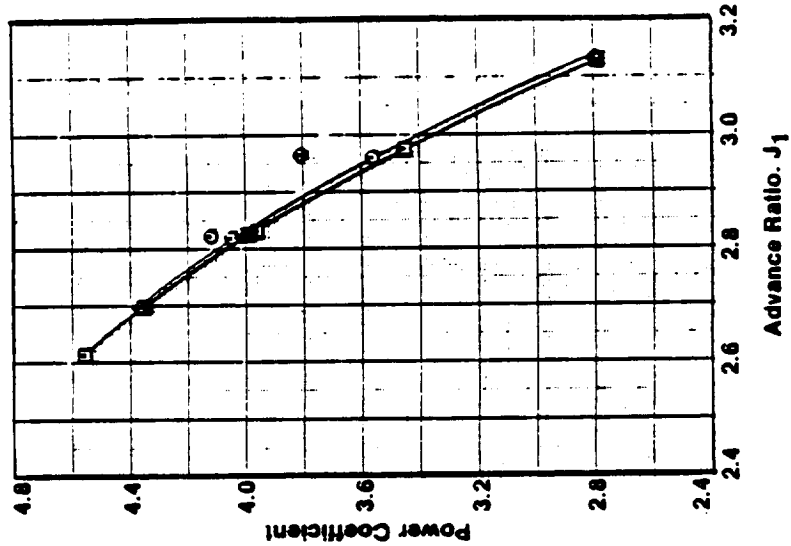
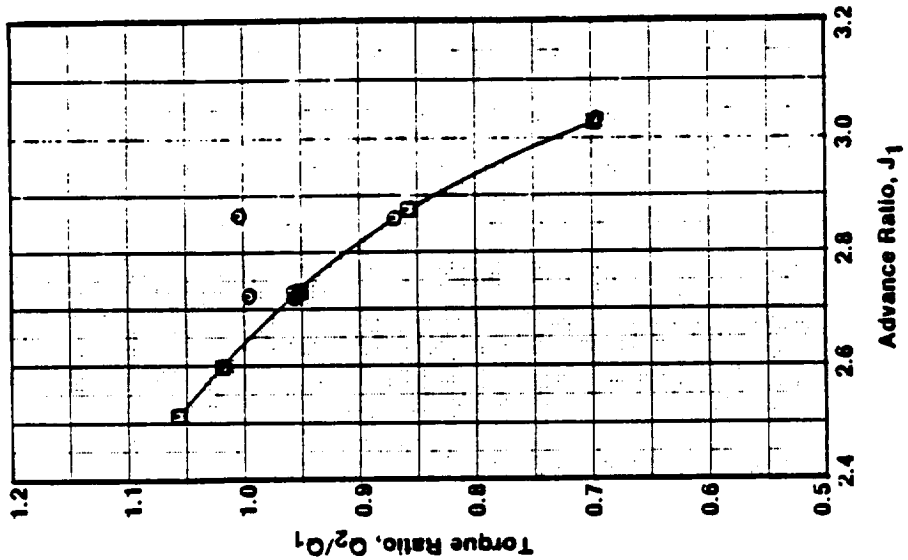


Figure 377. Spacing Effects on Baseline F-7/A-7 Torque Ratio at Mach 0.72.



	α	β_1	β_2
○	0	56.9	54.4
□	2	56.9	54.4

Figure 378. Effect of Angle-of-Attack on F-7/A-7 (8+8), at Mach 0.70 with No Pylon (in BTWT).

F-7/A-7 configuration without pylon at Mach 0.70. Data are shown for two angles-of-attack (0° and 2°), with constant-pitch angles. Since the model is rotated in the tunnel on a platform by the angle-of-attack (α), freestream velocity (V_o) in the direction of thrust is equivalent to $V_o \cos \alpha$. Correcting the advance ratio by the cosine causes the data to collapse to one curve for all angles-of-attack on the power coefficient plot. The effect on the torque ratio lines is to spread them further apart with increasing angle-of-attack.

Measured thrust is in the direction of the model centerline axis skewed from the freestream tunnel direction by the angle-of-attack. The normal force on the blades as a result of the model direction relative to the airflow was not measured; therefore, its streamwise component is not accounted for in the efficiency calculation. The word "apparent" has been added to the efficiency label to indicate that it is not a true efficiency.

With the pylon installed, the test points were repeated at the same Mach number and blade-pitch angles. Power coefficient, apparent net efficiency, and torque ratio data are presented in Figure 379. Since the pylon drag is not measured by the rotor force balances and not otherwise accounted for in the overall thrust, the apparent efficiency values with pylon are about the same as the pylon-off data, but slightly higher. Now, the freestream velocity correction is no longer appropriate to collapse the power coefficient lines because of the angular momentum change caused by the pylon.

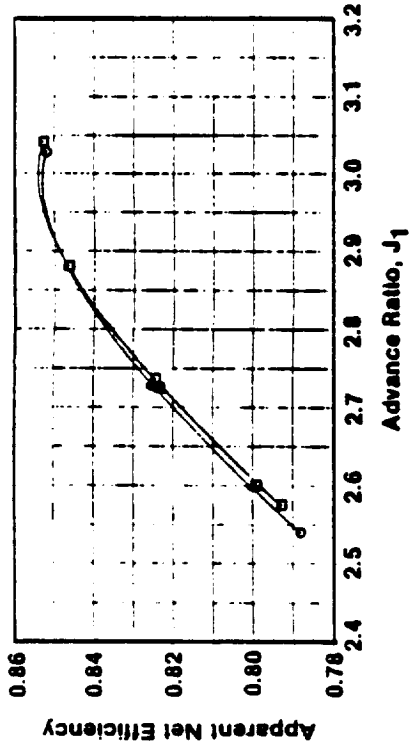
The pylon effect is most noticeable in how it affects the level of torque ratio. With increasing angle-of-attack, the pylon acts like an inlet guide vane, producing counter swirl into the forward rotor and loading it relative to the aft rotor.

At Mach 0.24, the torque ratio varies from 1.0 at 0° angle-of-attack to 0.85 at 5° , and to 0.60 at 16° (Figure 380). The large split in torque per stage, observed from testing with constant-pitch angles and constant speeds, will be corrected in the installed engine by varying the blade-pitch angles and maintaining equal speeds as the airplane climbs out from takeoff at some angle-of-attack. The direction of pitch-angle change will also vary from a right-hand engine to a left-hand engine; since the direction of forward rotation is down-inboard on the airplane right side, and up-inboard on the left side.

7.2.1.1.3 Mismatched Rotor Speed Effects

The NASA 8x6 wind tunnel data were taken at Mach 0.72 with unequal rotor speeds over a wide range of rpm's. Figure 381 depicts net efficiency plotted against the power loading parameter for two different speed ratios, as well as equal rotor speed reference data. Testing was conducted with the aft rotor speed 10% higher and then 10% lower, than that of the forward rotor. Holding pitch angles constant, as was necessary in this type of model test, means the rotor torque splits are not equal as the rpm's are increased. When the aft rotor is running 10% faster than the forward rotor, the ratio of the aft-to-forward rotor torque varies from 1.04 to 1.32. When the aft rotor is running 10% slower, its torque varies between 23% and 74% of the forward rotor torque.

Test data reveal that the net efficiency is higher at low loadings when the torques are within 25% of being equal. The lower efficiency line ($N2/N1 = 0.91$) at low loadings indicates torque ratios that are much less matched and, thus, lower efficiencies; however data taken at high loading levels show that when torque ratios are within 25% of being matched, the speed ratio has little effect on net efficiency. A comparison of the data (Figure 381) reveals those test points with torque ratios closest to 1.0 have the highest efficiencies.



	α	β_1	β_2
○	0	56.9	54.4
□	2	56.9	54.4

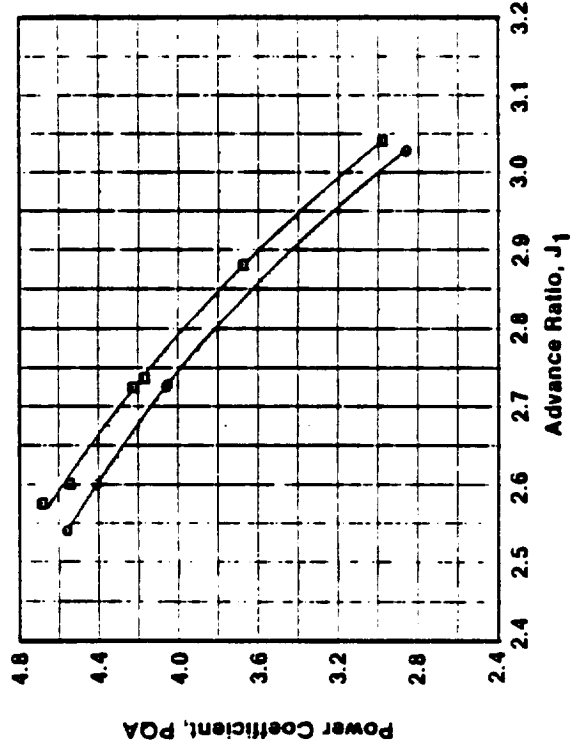
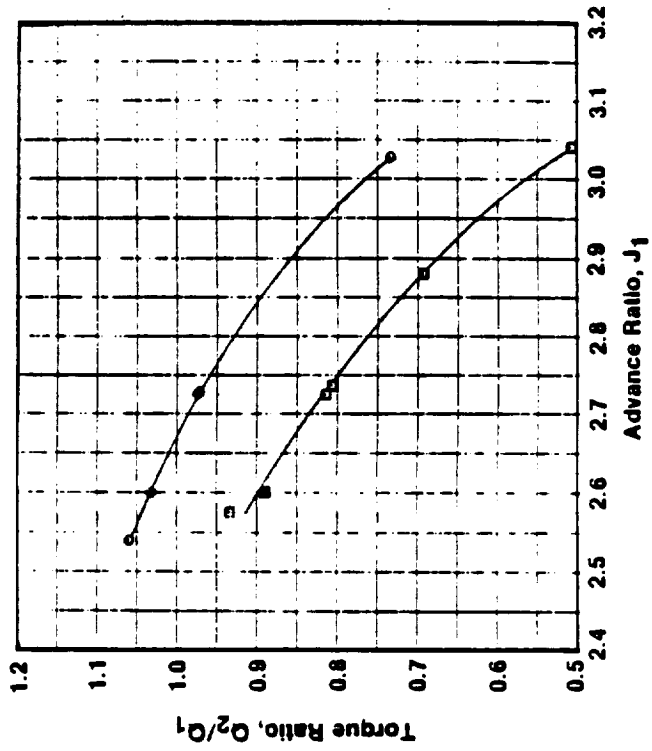


Figure 379. Effect of Angle-of-Attack on F-7/A-7 (8+8), at Mach 0.70 with Pylon On (in BTWT).

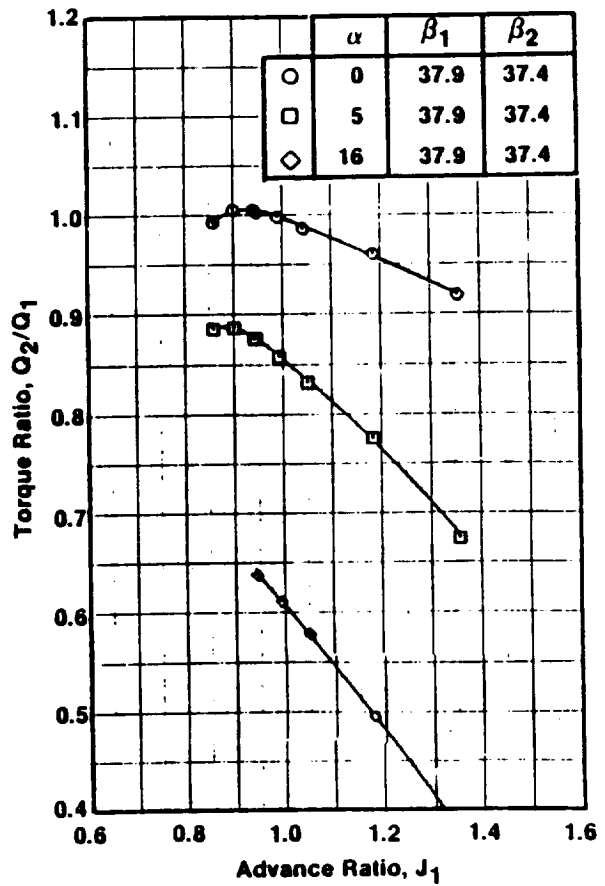
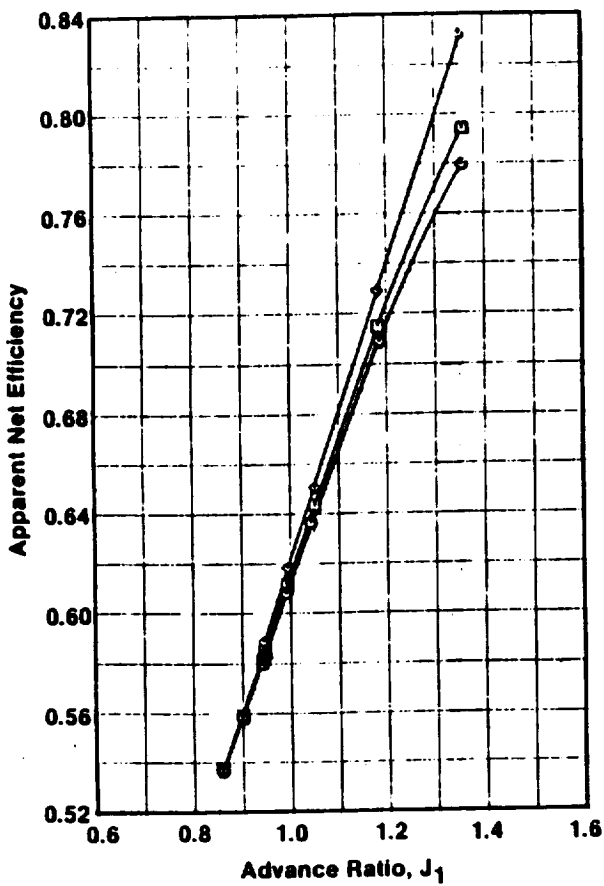
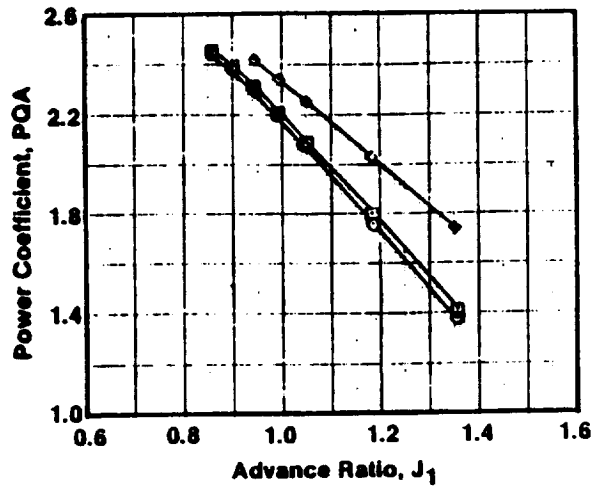


Figure 380. Effect of Angle-of-Attack on Baseline F-7/A-7 at Mach 0.24 with Pylon On (in BTWT).

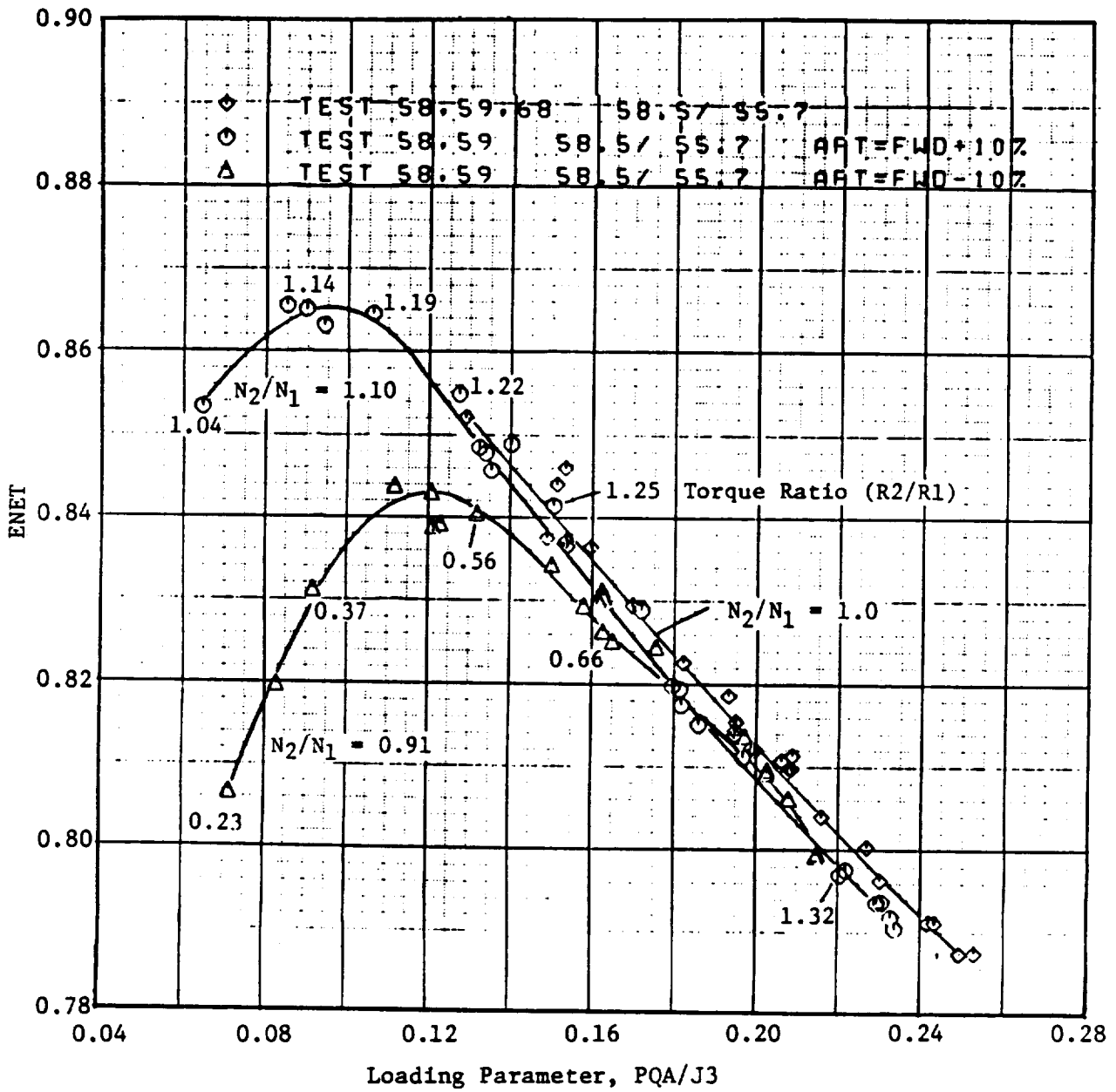


Figure 381. Effect of Mismatched rpm's on F-7/A-7 (8+8) Nominal Spacing Performance at Mach 0.72 (ENET Versus PQA/J3).

Figure 382 plots the power coefficient as a function of the advance ratio of the forward rotor for three different speed ratios. If plotted, versus an average advance ratio, these data would appear at the same advance ratios for the same average speeds. However, when the aft rotor is running 10% faster than the forward rotor, the power absorbed is approximately 8% higher than if the speeds were equal. Conversely, when the forward rotor is running 10% faster than the aft, the power absorbed is approximately 10% lower.

7.2.1.2 F-11/A-11 Performance Results

The F-11/A-11 (11+9) design was tested in the NASA high- and low-speed wind tunnels, as well as in Cell 41. Due to high blade stresses, a limited amount of high speed performance data were acquired at Mach 0.72 and 0.80, but further testing was performed after clipping the trailing edge corners at the tip of the F-11 blades. The data presented in Figures 383 and 384 were taken at Mach 0.72 for the unclipped and clipped blades, and at Mach 0.80 for the clipped blade only. The clipping had the effect of reducing the efficiency by about 2 points at Mach 0.72. Unclipped F-11 data were not available at Mach 0.80 at high enough power for a good comparison; however, Mach 0.80 performance with the clipped blade demonstrates an efficiency of 0.809 at design loading. At more open pitch angles, and with the blades running slower, the efficiency was almost 1.0 point better.

Data taken in Cell 41 at Mach 0.25 were previously presented as Figures 365 and 366; data taken with the same pitch angle, but with different rotor spacings shows little effect (Figure 365) on Mach 0.25 efficiency when varying the spacing from 15.0 cm (5.9 in.) to 19.9 cm (7.84 in.). Reference is made to Figure 366, which illustrates the Mach 0.25 data taken (at Cell 41) with different numbers of blades in each rotor. The number of blades were varied from design configuration (11+9) to 13+11; the addition of two blades in each row showed a gain of about 2 to 3 points in the takeoff efficiency. Although high speed data were not taken, it is expected that additional blade blockage would lead to higher shock losses, and thus, would have an adverse effect on the cruise fan efficiency.

7.2.1.3 F-21/A-21 Performance Results

The F-21/A-21 blade configuration was tested both in NASA's high speed wind tunnel and in GE's low speed anechoic facility (Cell 41). At high flight speeds in the NASA wind tunnel, data was obtained with both a standard and a modified forebody and aftbody. The flowpath of the modified forebody, shown in Figure 385, has a slimmer nacelle shape with less flow diffusion ahead of the blades. The maximum curvature occurs at the forward rotor LE (leading edge). The modified aftbody, also illustrated in Figure 385, incorporates a larger hub diameter just downstream of the aft rotor, allowing for more favorable hub streamline curvature and, thus, more effective area-ruling through the aft blade row.

The test results for the two forebody shapes are presented for the power coefficient versus advance ratio, and net efficiency versus disk loading as plotted in Figure 386. The blades absorb approximately 15% less power with the same pitch angles when tested with the slim nacelle forebody; at the Mach 0.80 loading levels tested, the net efficiency is about 2 points worse. At slightly lower flight Mach conditions, the slim nacelle is about 1.0 to 1.5 points worse.

The modified aftbody exhibited a significant performance improvement at high flight Mach numbers. Data taken at Mach 0.80 (Figure 387) demonstrate a 3.0-point increase in net efficiency at the design loading. Larger increases in efficiency occur at lower than design loadings. Data in Figure 388 show an increase in power absorbed by the rotors with the new aftbody shape. The net efficiency at Mach 0.72 is compared (Figure 389) for the different forebody and aftbody

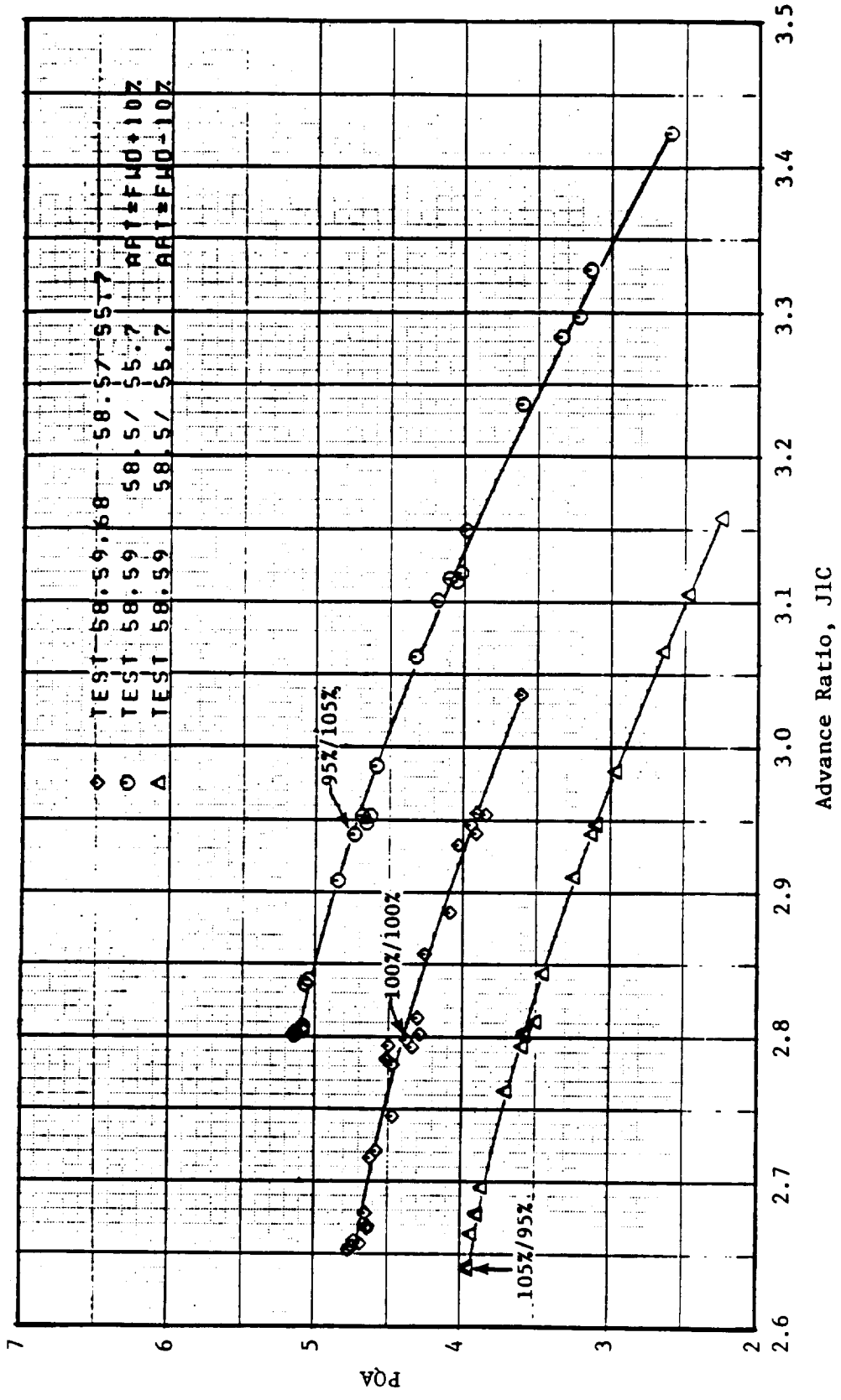


Figure 382. Effect of Mismatched Speed on the F-7/A-7 (8+8) Nominal Spacing Performance at Mach 0.72.

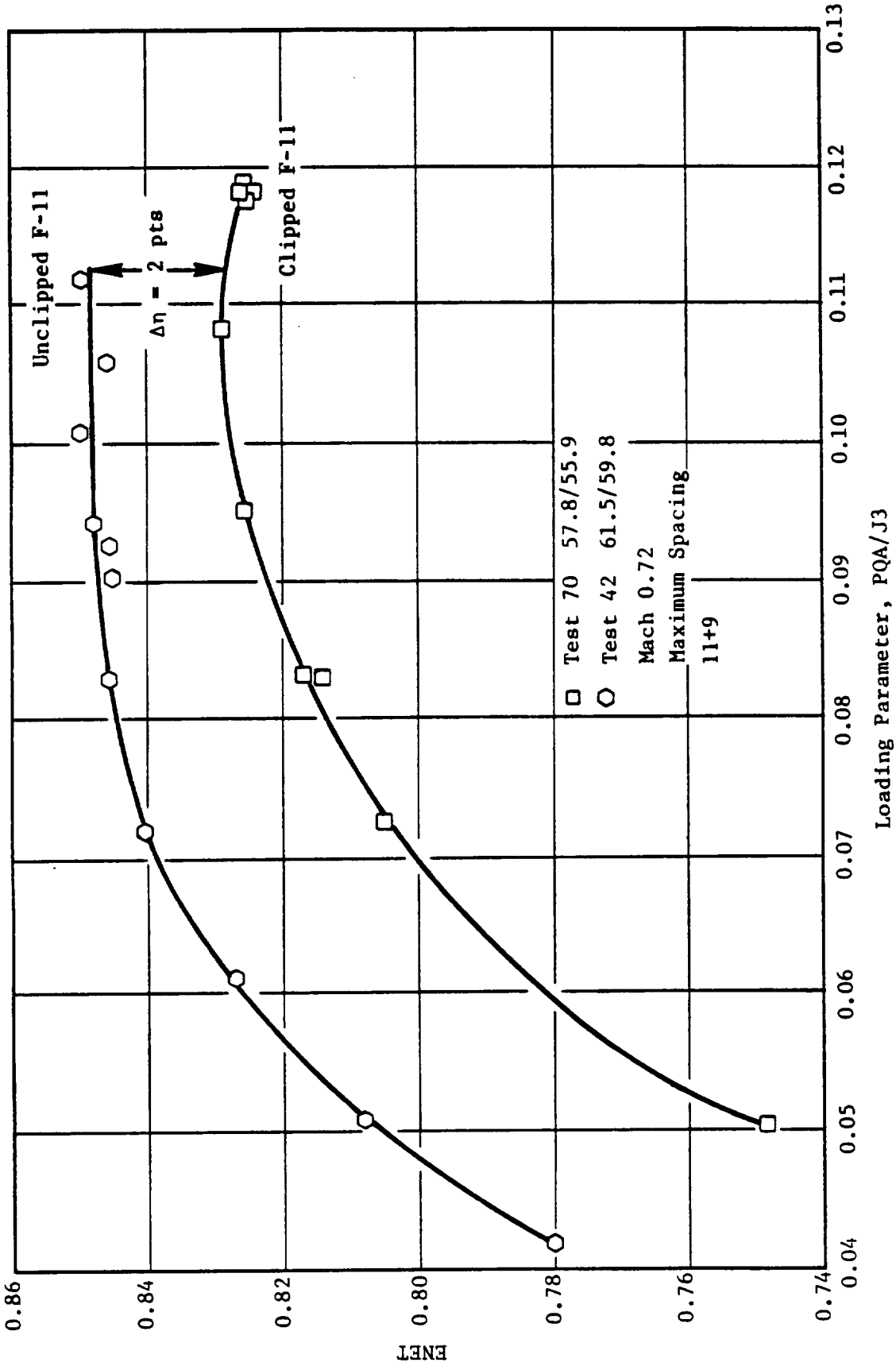


Figure 383. Effect of F-11 Clipping (for Stability) on F-11/A-11 Performance Measured in 8x6 Tunnel.

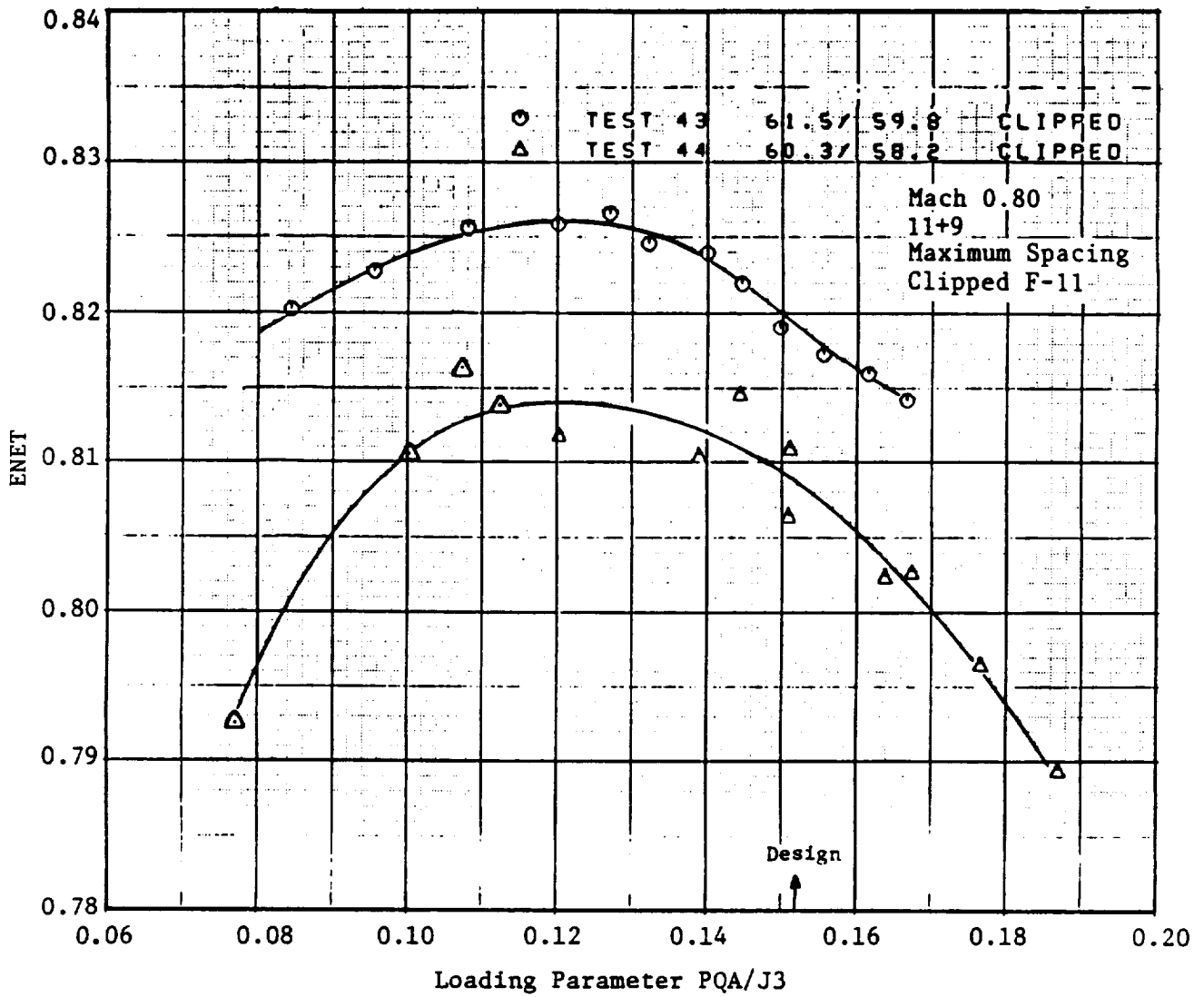


Figure 384. Disk Loading Effect on F-11c/A-11 Performance at Mach 0.80.

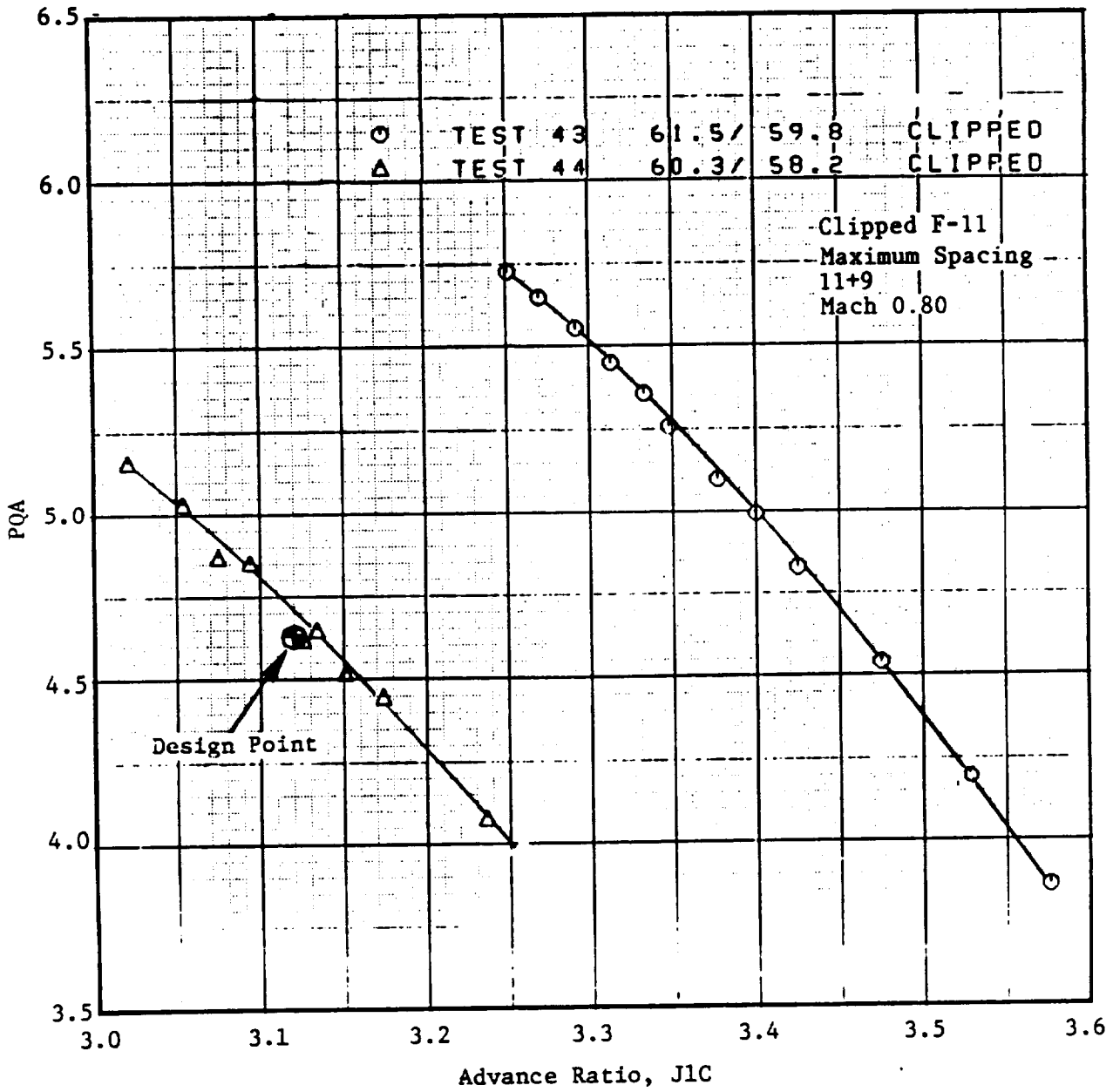


Figure 384. Disk Loading Effect on F-11c/A-11 Performance at Mach 0.80 (Concluded).

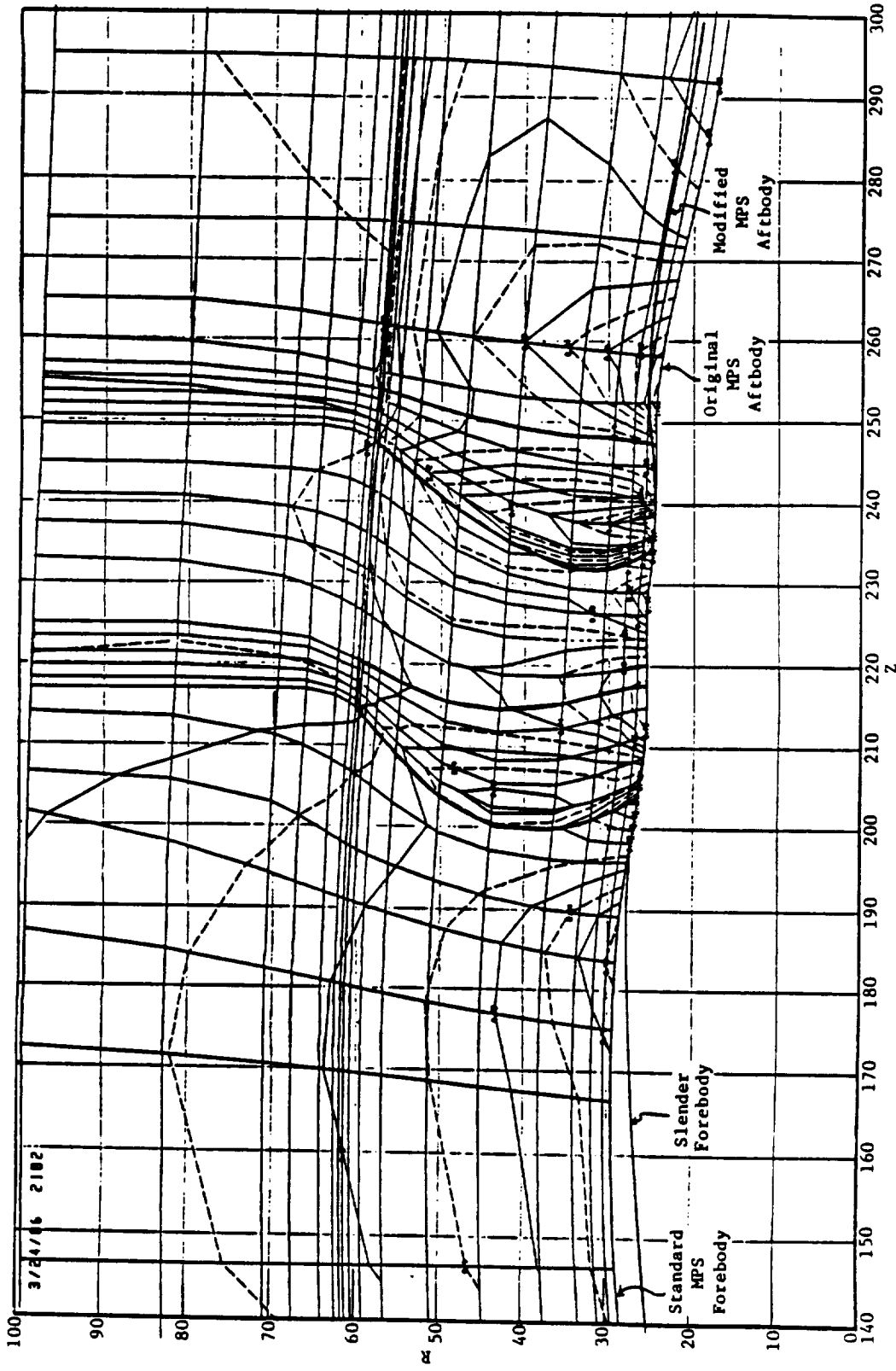


Figure 385. Comparison of Standard and Modified Forebodies and Aftbodies for F-21/A-21.

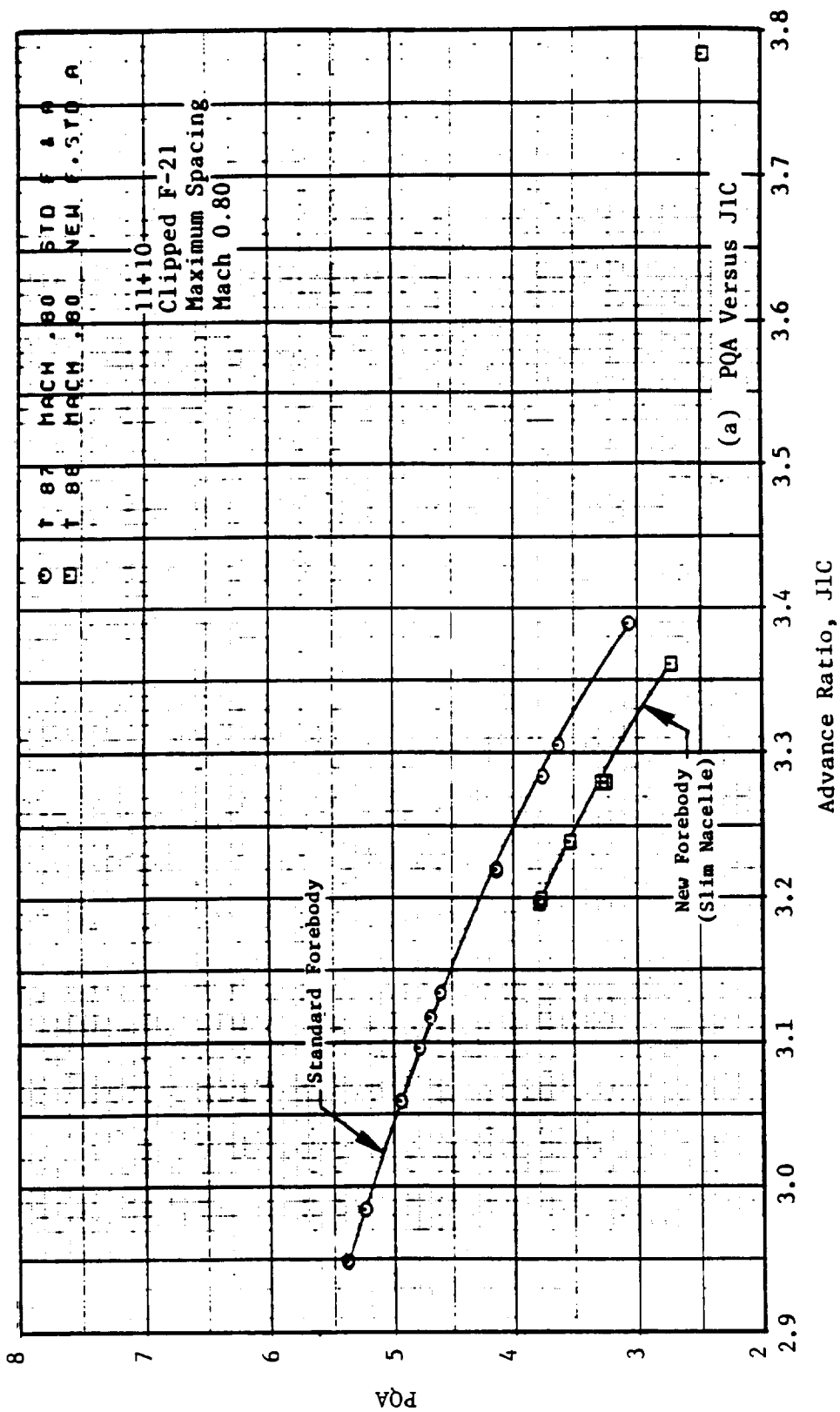


Figure 386. F-21c/A-21 Performance Comparison Between Standard and New Forebody Configurations in 8x6 Tunnel.

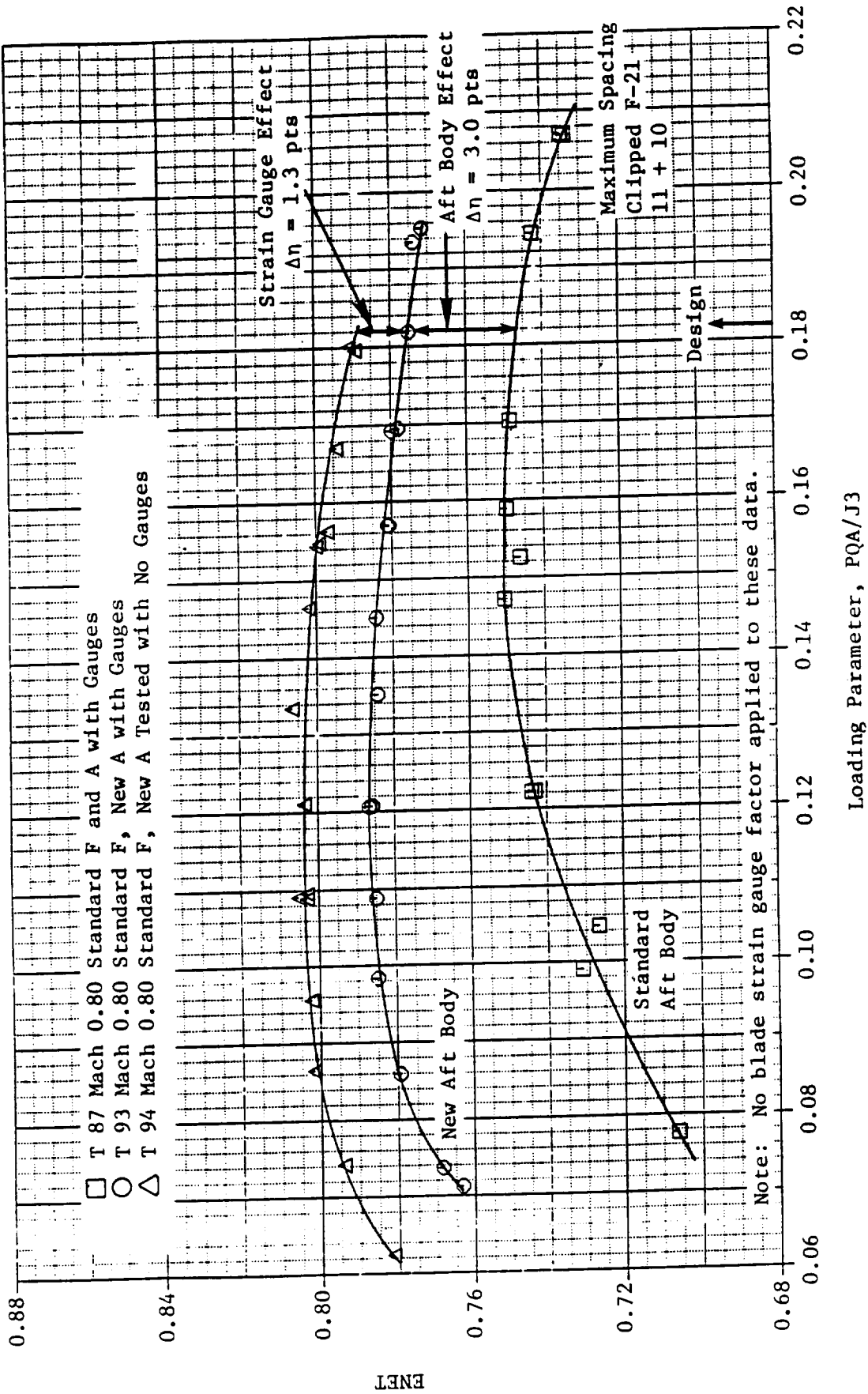


Figure 387. Effects of Aftbody Configuration and Blade Strain Gauges on F-21c/A-21 Performance in 8x6 Tunnel (ENET Versus PQA/J3).

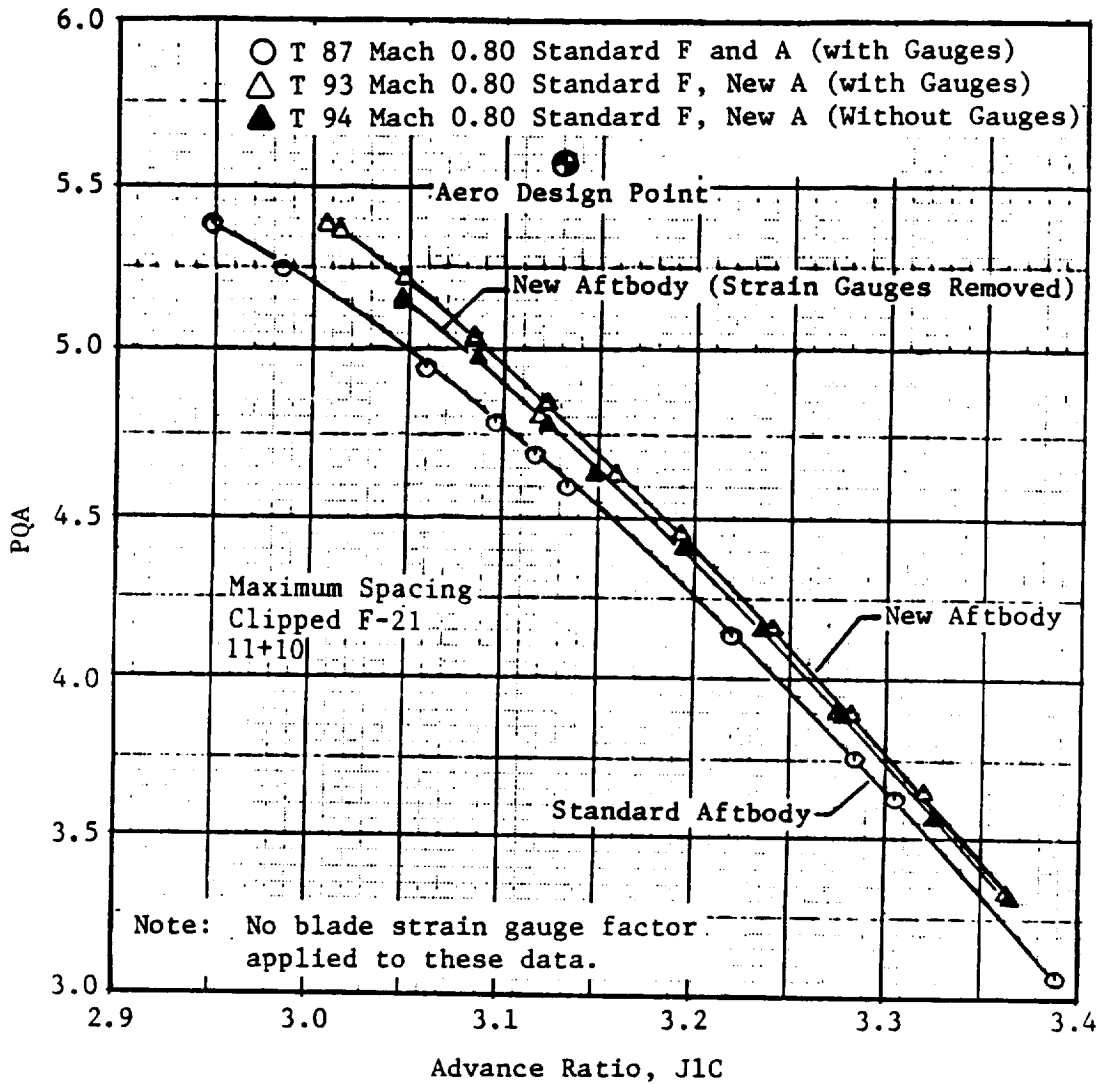


Figure 388. Effects of Aftbody Configuration and Blade Strain Gauges on F-21c/A-21 Performance in the 8x6 Tunnel (PQA Versus J1C).

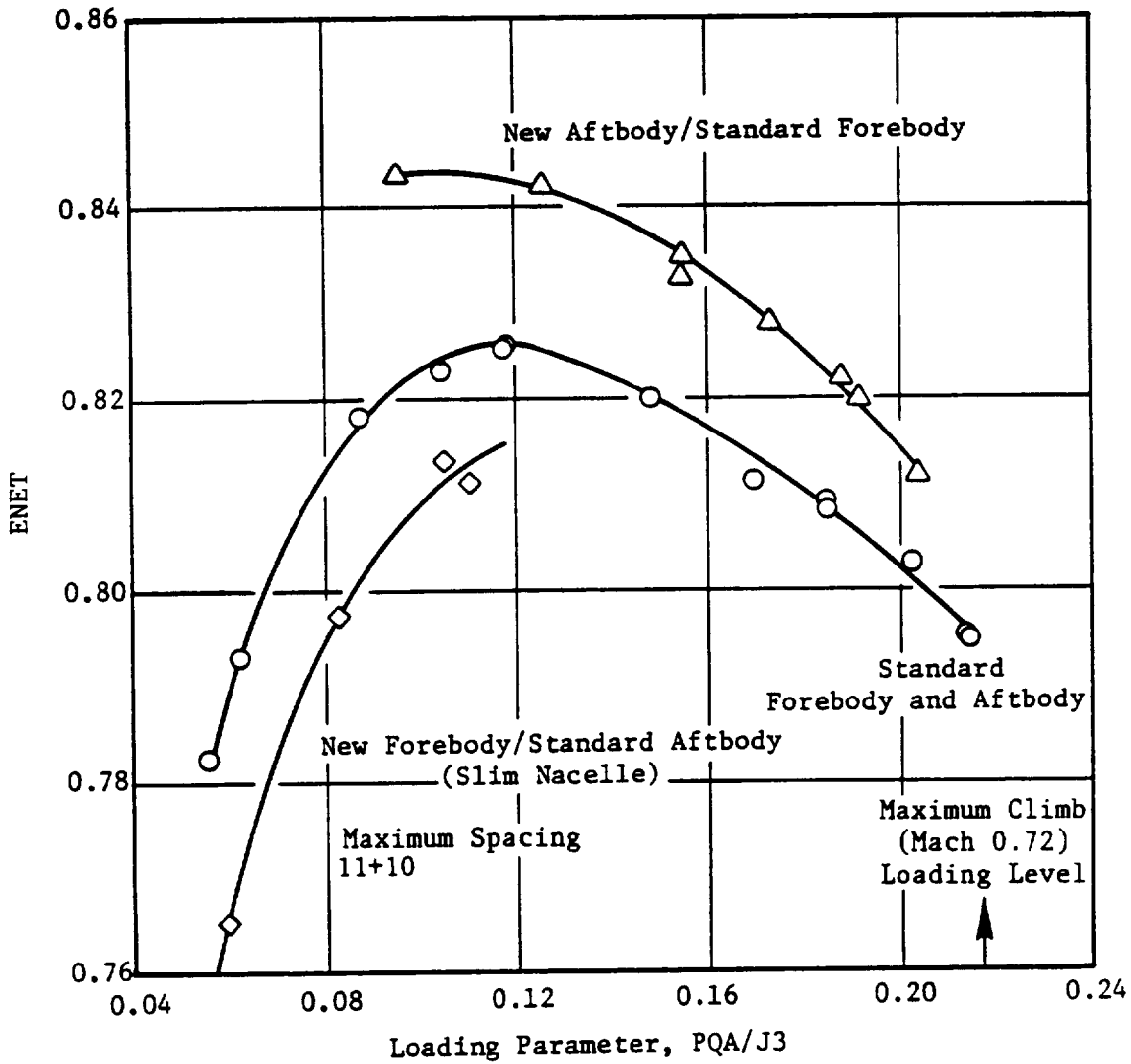


Figure 389. Performance Summary for F-21c/A-21 in 8x6 Tunnel.

configurations. At this lower flight speed, the net efficiency gain with the new aftbody is between 1 and 2 points.

7.2.1.3.1 Blade Strain–Gauge Effect

The effect of performance loss resulting from the application of strain gauges to the blades was investigated at the conclusion of the F–21/A–21 test. After baseline data was obtained with the new aftbody and the blades strain–gauged as normal, the gauges were removed and the test repeated at the same pitch angles. These data (with no blade strain gauge factor applied) are depicted in Figures 387 and 388. Removing the strain gauges improved the efficiency at all loading levels, by as much as 2 points, and indicated a gain of 1.3 points at the Mach 0.80 design loading level. At Mach 0.76, the effect on efficiency was 1.1 points.

7.2.1.4 F–4/A–4 Performance Results

The F–4/A–4 UDF® scale model configuration was tested in the BTWT (Boeing Transonic Wind Tunnel) over a wide–range of flight Mach numbers from takeoff to maximum climb. Data were taken with one pitch setting per Mach number and are shown in Figure 390. The power coefficient and net efficiency are plotted versus the forward rotor advance ratio. Design point efficiency is approximately 2 points lower than that of the F–7/A–7.

7.2.1.5 F–5/A–5 Performance Results

The F–5/A–5 scale model blades also were tested in the BTWT with similar Mach number and pitch–angle settings. Figure 391 presents the performance map data of power coefficient and efficiency as a function of advance ratio. When compared to the longer chord F–4/A–4 blades, the F–5/A–5 configuration has a 1 point lower net efficiency.

7.2.2 Aeromechanics

7.2.2.1 Blades

As summarized in Table 65, the 8x6 wind tunnel tests using the F–7/A–7 (with a 13°–ply reference angle) mounted on the rigid hub had several instability encounters at different Mach numbers and pitch–angle settings. Flutter occurred at about 350 Hz, which is around the 1F mode frequency. The typical results were depicted in two representative frequency amplitude time history diagrams (Figures 174 and 175) which were presented in Section 6.2.2; however, for a complete listing of the various flutter conditions and flutter responses at those conditions, the reader is referred to the CDR and Task V reports.

Both the 11– and 21–blade series experienced instability in their original design shape. The F–11 fluttered at about 540 Hz (around the second mode frequency), while the F–21 exhibited instability at about 500 Hz (also around the second mode frequency). Both blades were clipped in an attempt to rectify this situation, but the instability persisted. The CDR and Task V reports contain more detailed discussions pertaining to testing, aeromechanical performance, and results of these blades.

7.2.2.2 Aeromechanical Hub

The aeromechanical hub tests with the F–7/A–7 were performed with such flutter–control devices as blade platform adaptor seals and friction dampers installed. After the data reduction and analysis, it was concluded that this set of tests was free from flutter. A typical Campbell diagram from one of the tests was presented in Figure 180; the CDR provides a more complete description of test conditions and resulting Campbell diagrams.

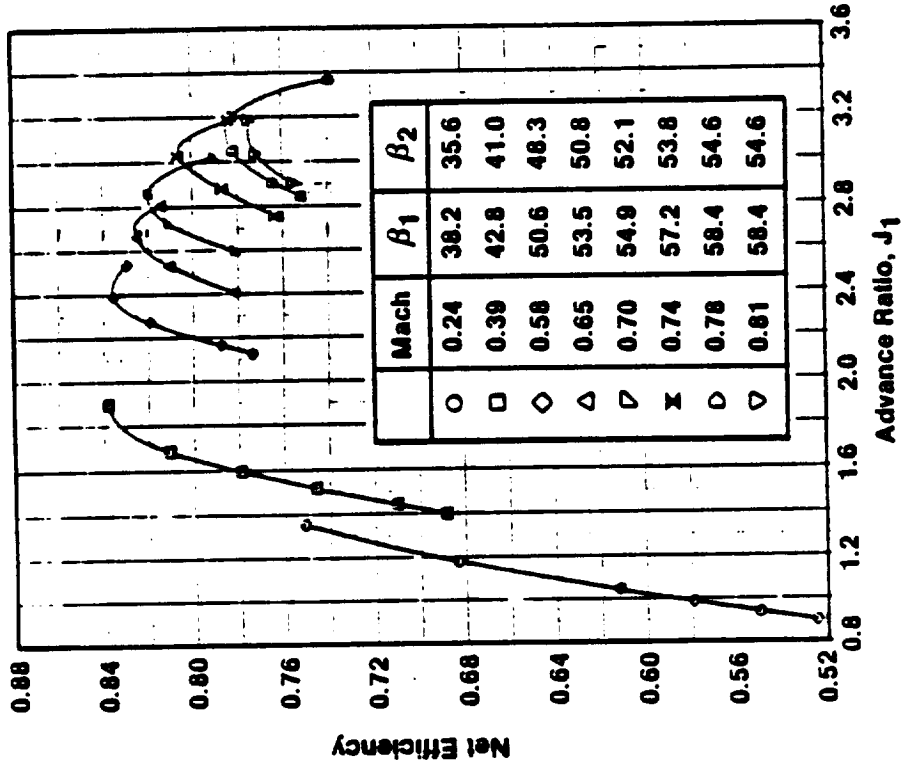
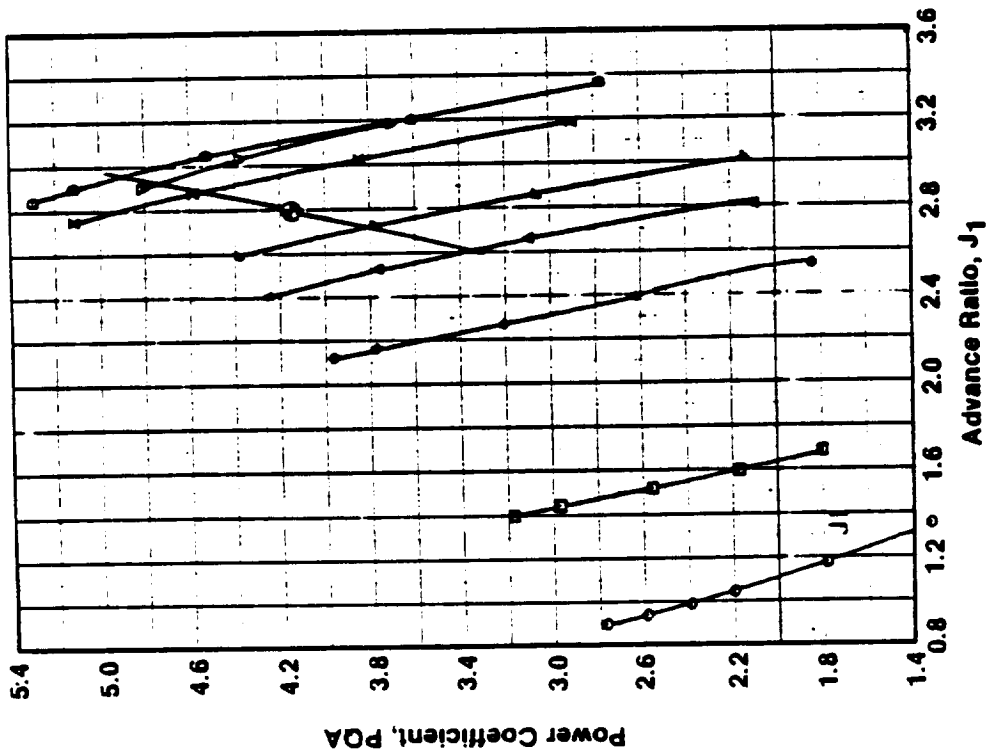


Figure 390. F-4/A-4 Performance Map.

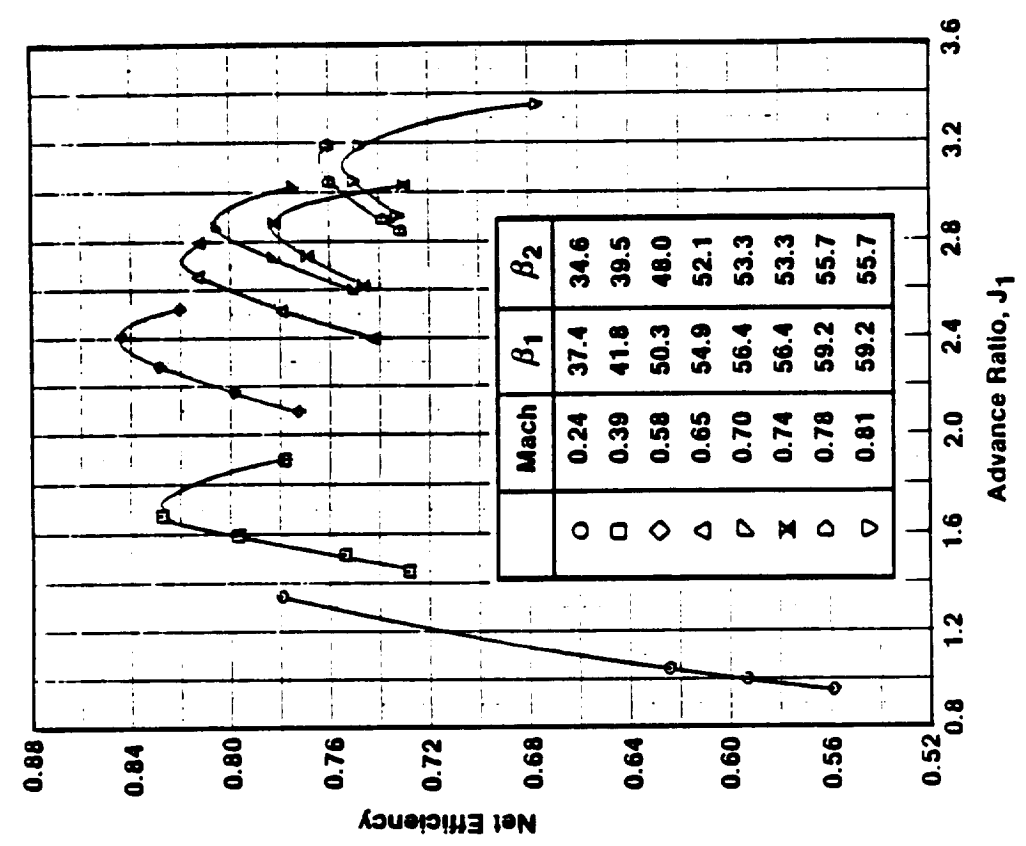
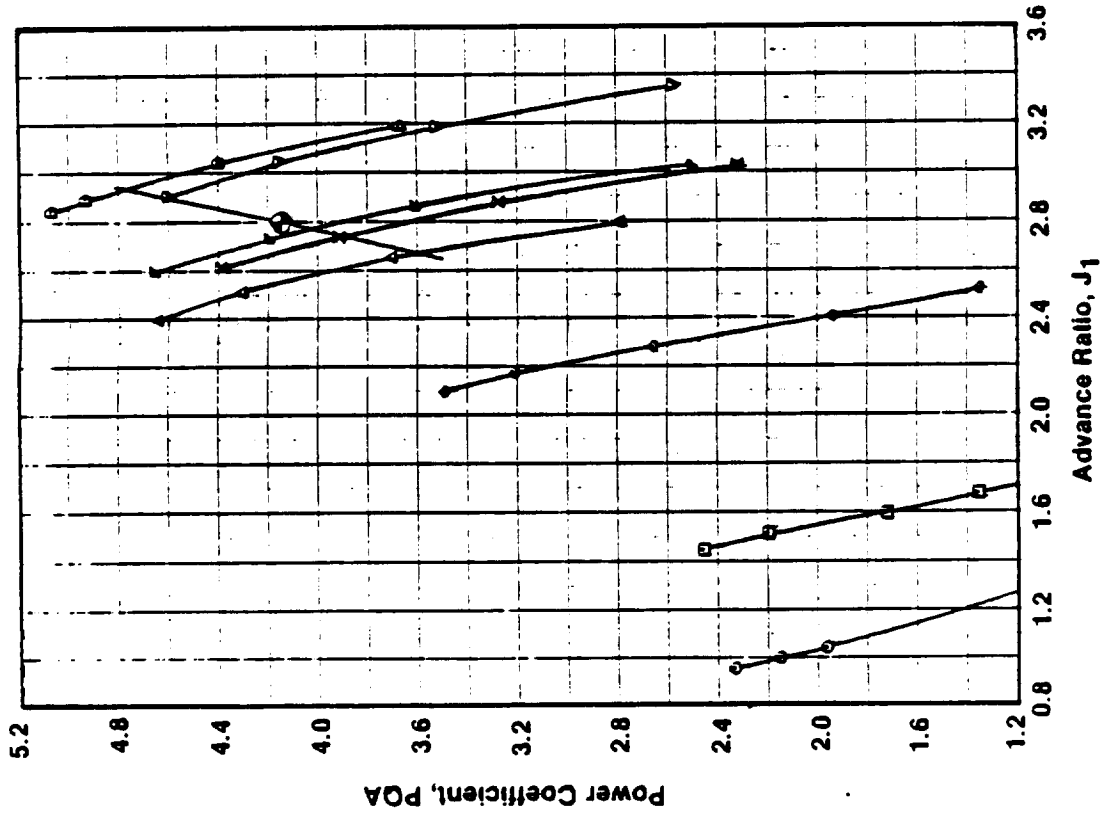


Figure 391. The F-5/A-5 Performance Map.

Table 65. Summary of F-7/A-7 Flutter Events at the NASA 8x6 Wind Tunnel, with a Hub Configuration¹ of 8+8.

Test Date	Pitch Angles	Mach	Speed	Stress (Ksida)	Flutter Frequency (Hz)	Comments
2/14/86	58.5/55.7	0.60	6270	24	360	A7 Flutter Near 1F Mode
2/20/86	58.5/58.7	0.67	6470	17.5	330	A7 Flutter Near 1F Mode
2/21/86	61.7/55.7	0.67	6170	4	310	F7 Flutter
2/22/86	55.7/53.7	0.60	6750	15	360	A7 Flutter
2/24/86	49.1/51.0	0.50	6950	12	345	A7 Flutter
2/26/86	49.6/48.0	0.50	7520	16	365	A7 Flutter

¹ All of the above configurations are with no pylon installed and both F-7 and A-7 blades with a 13°-ply reference angle

It is concluded that the aeromechanical hub flutter problem experienced in Cell 41 was resolved with the effective installation of the above-mentioned flutter-control devices on the original design blade geometry.

7.2.3 Discussion of Acoustic Results

7.2.3.1 Assessment of Data Quality

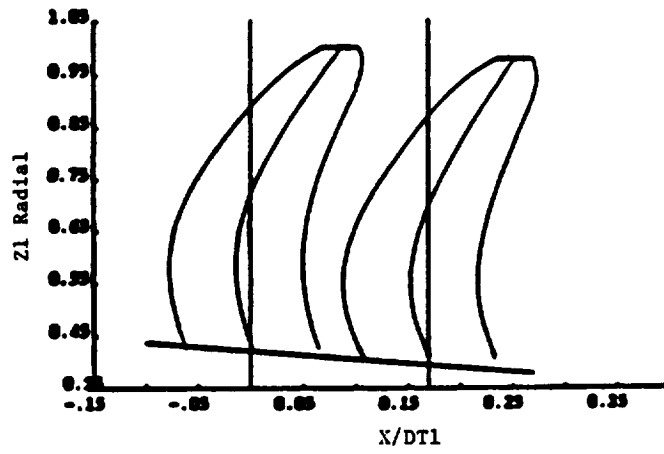
The validity of acoustic data taken in an untreated wind tunnel operating at high subsonic Mach numbers has been discussed previously in the context of single-rotation high speed propfan testing (for example, References 39 through 42). The tests described herein provided an opportunity for the comparison of experimental data taken in this manner with data from an acoustically treated wind tunnel and, also, with theoretical predictions.

Three model blade designs were tested in this series of NASA 8x6 tunnel tests. They are shown in planform at their design spacings in Figure 392, and Table 66 identifies relevant design parameters. Of these, blades designated as F-7/A-7 were tested in more configurations than were either the F-11/A-11 or F-21/A-21. The F-7/A-7 blades were also tested in the acoustically treated BTWT and, thus, were selected for this comparison.

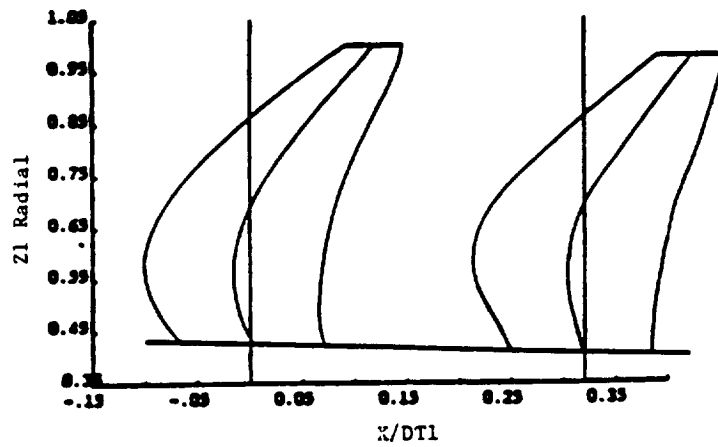
Results for the F-7/A-7 operating at its design point of 0.72 Mach, 100% corrected rpm, are shown in Figures 393 through 397. Performance information for the data points considered is given in Table 67.

The translating acoustic plate used for data acquisition and the analysis system employed are described in Subsection 6.2.3 of this report. Figures 393 through 395 indicate the directivity of the first three harmonics of the BPF (blade passing frequency) at each of the four plate positions.

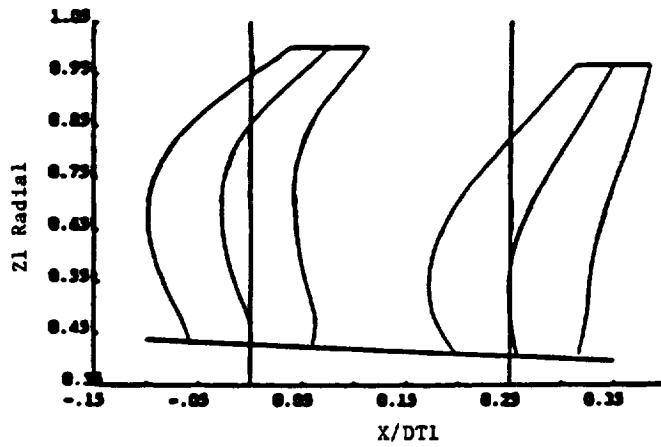
As the blades were configured with an equal number of blades (eight) on each row, the tones seen are composed of isolated rotor noise of the forward and aft rows operating independently, together



(a) F-7/A-7

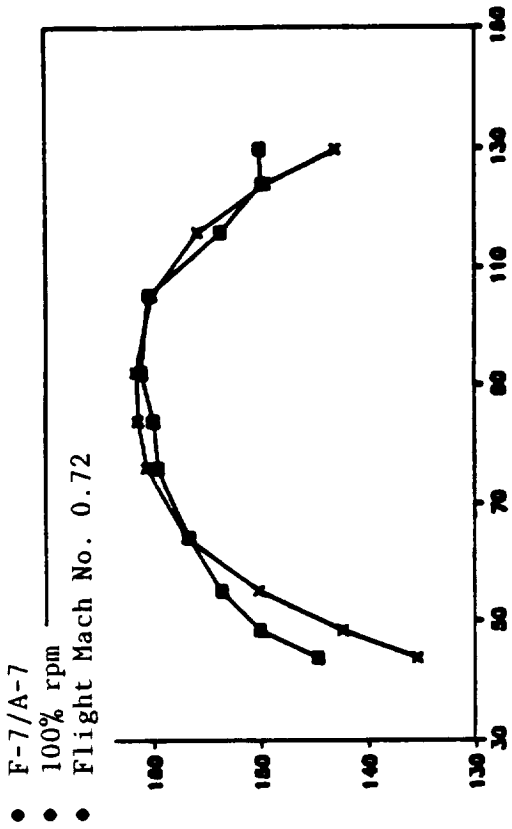


(b) F-11/A-11

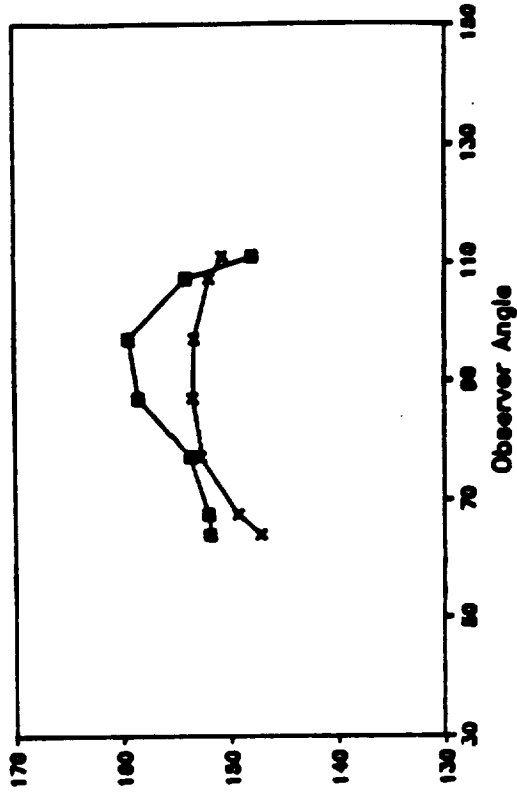


(c) F-21/A-21

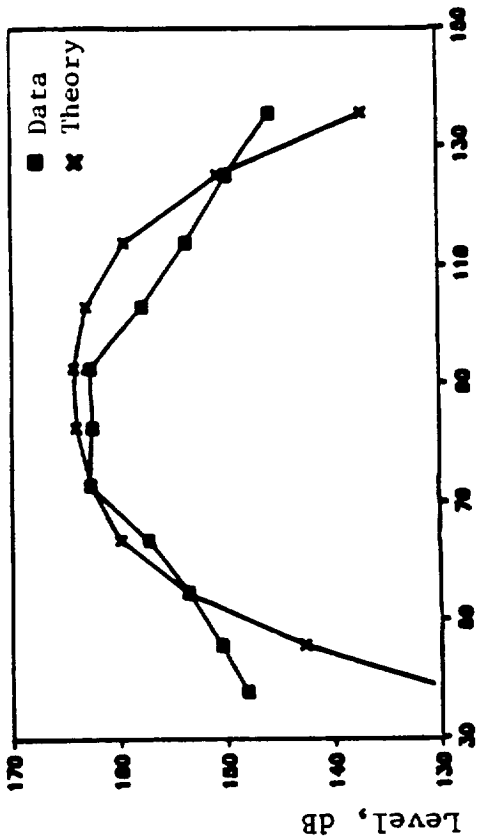
Figure 392. MPS Blade Planforms Tested in the 8x6 Wind Tunnel.



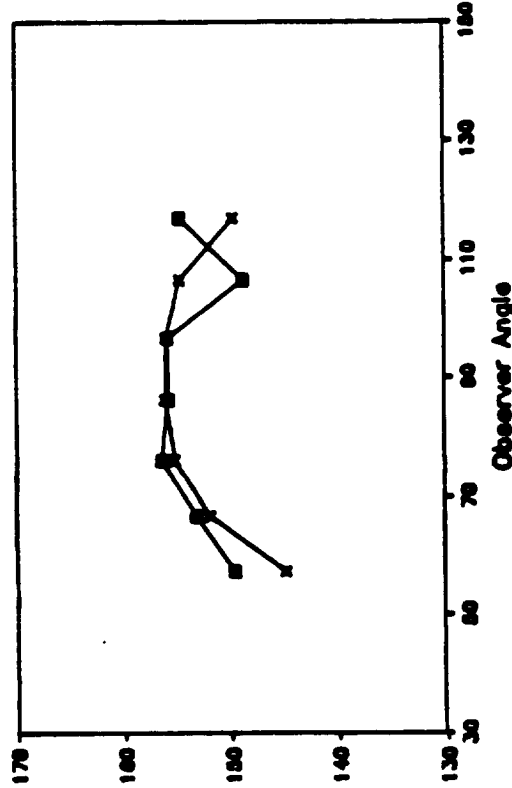
(b) Plate Position 2 (Reading 2049)



(d) Plate Position 4 (Reading 2047)

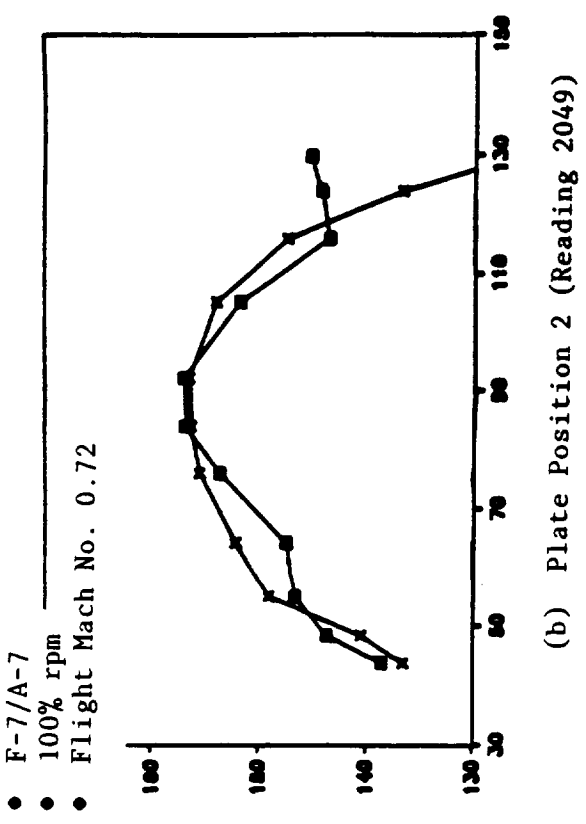


(a) Plate Position 1 (Reading 2050)

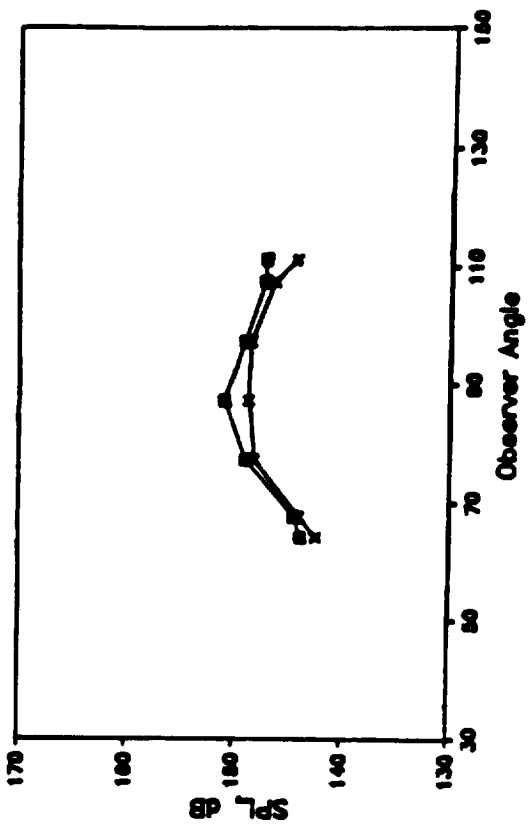


(c) Plate Position 3 (Reading 2048)

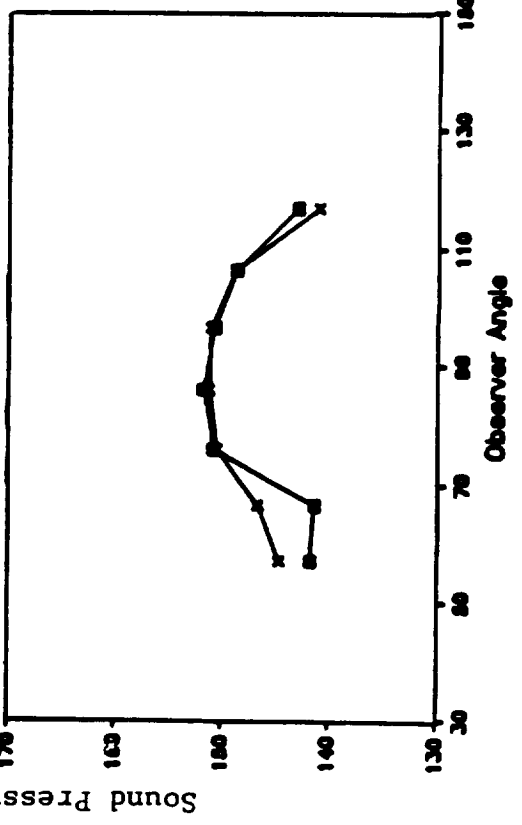
Figure 393. Comparison of Data and Theory for the BPF Tone at Different Plate Positions.



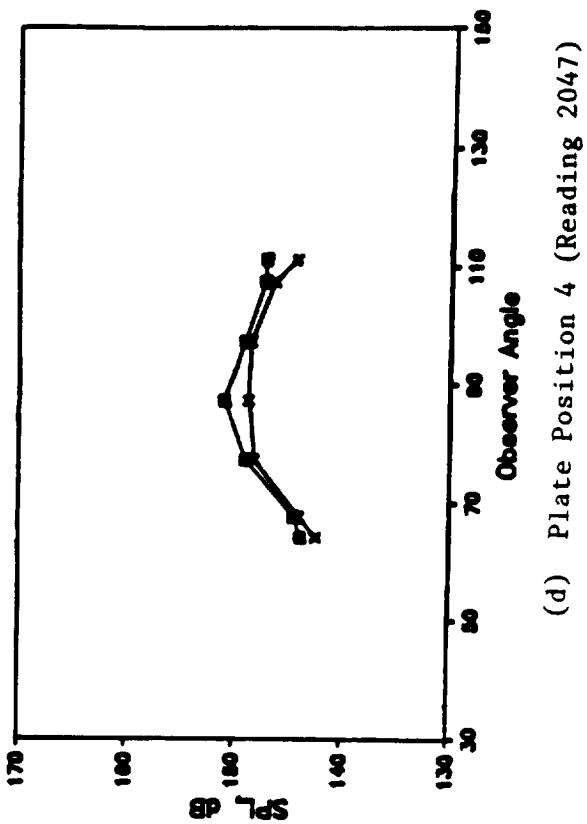
(a) Plate Position 1 (Reading 2050)



(b) Plate Position 2 (Reading 2049)



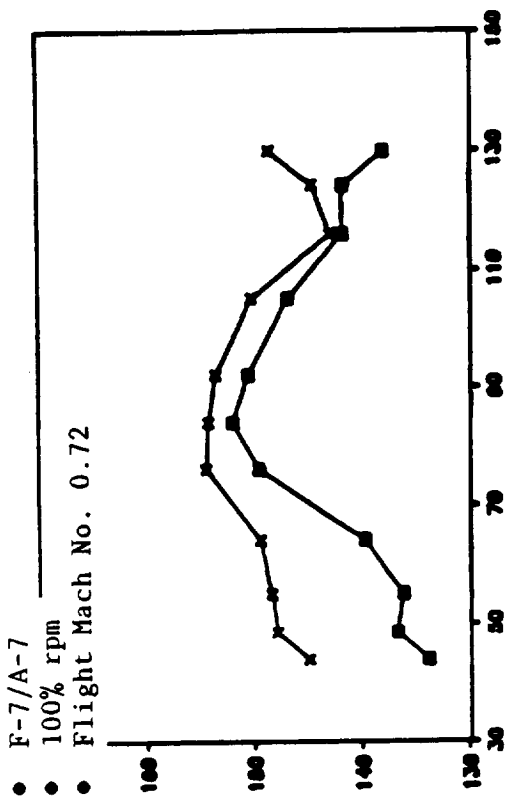
(c) Plate Position 3 (Reading 2048)



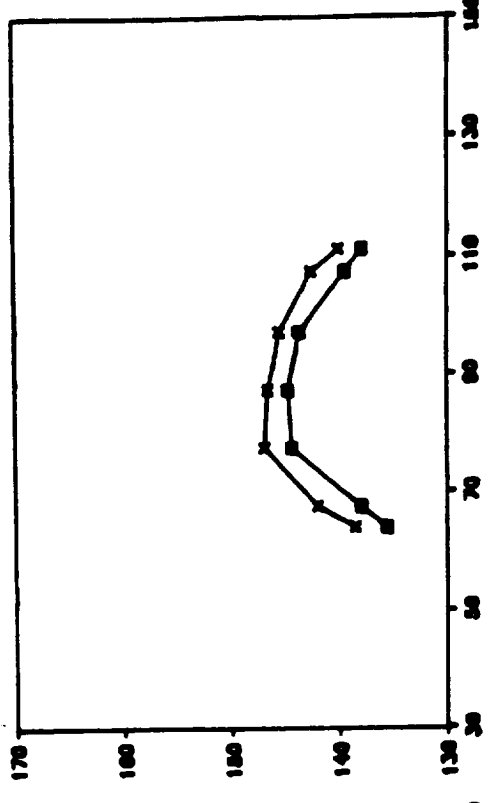
(d) Plate Position 4 (Reading 2047)

Figure 394. Comparison of Data and Theory for the 2x BPF Tone at Different Plate Positions.

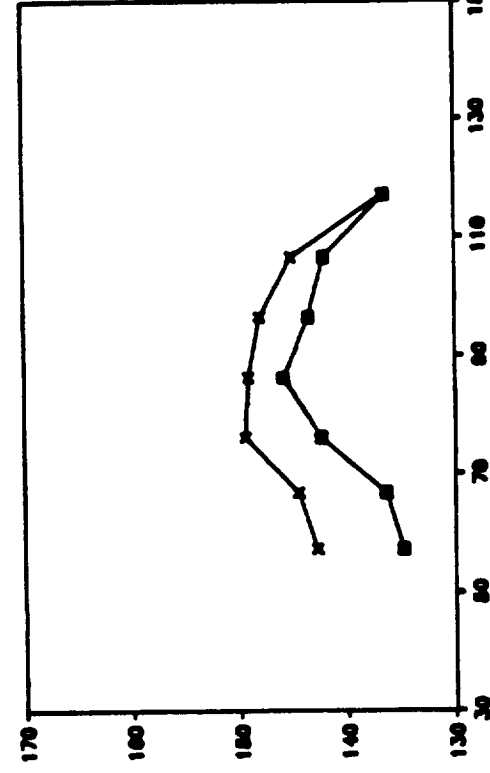
ORIGINAL PAGE IS OF POOR QUALITY



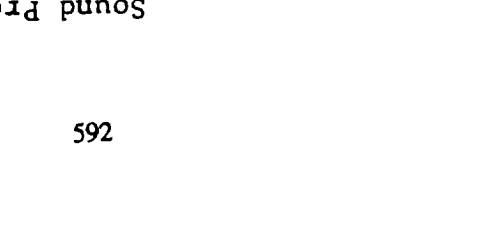
(a) Plate Position 1 (Reading 2050)



(b) Plate Position 2 (Reading 2049)



(c) Plate Position 3 (Reading 2048)



(d) Plate Position 4 (Reading 2047)

Figure 395. Comparison of Data and Theory for the 3x BPF Tone at Different Plate Positions.

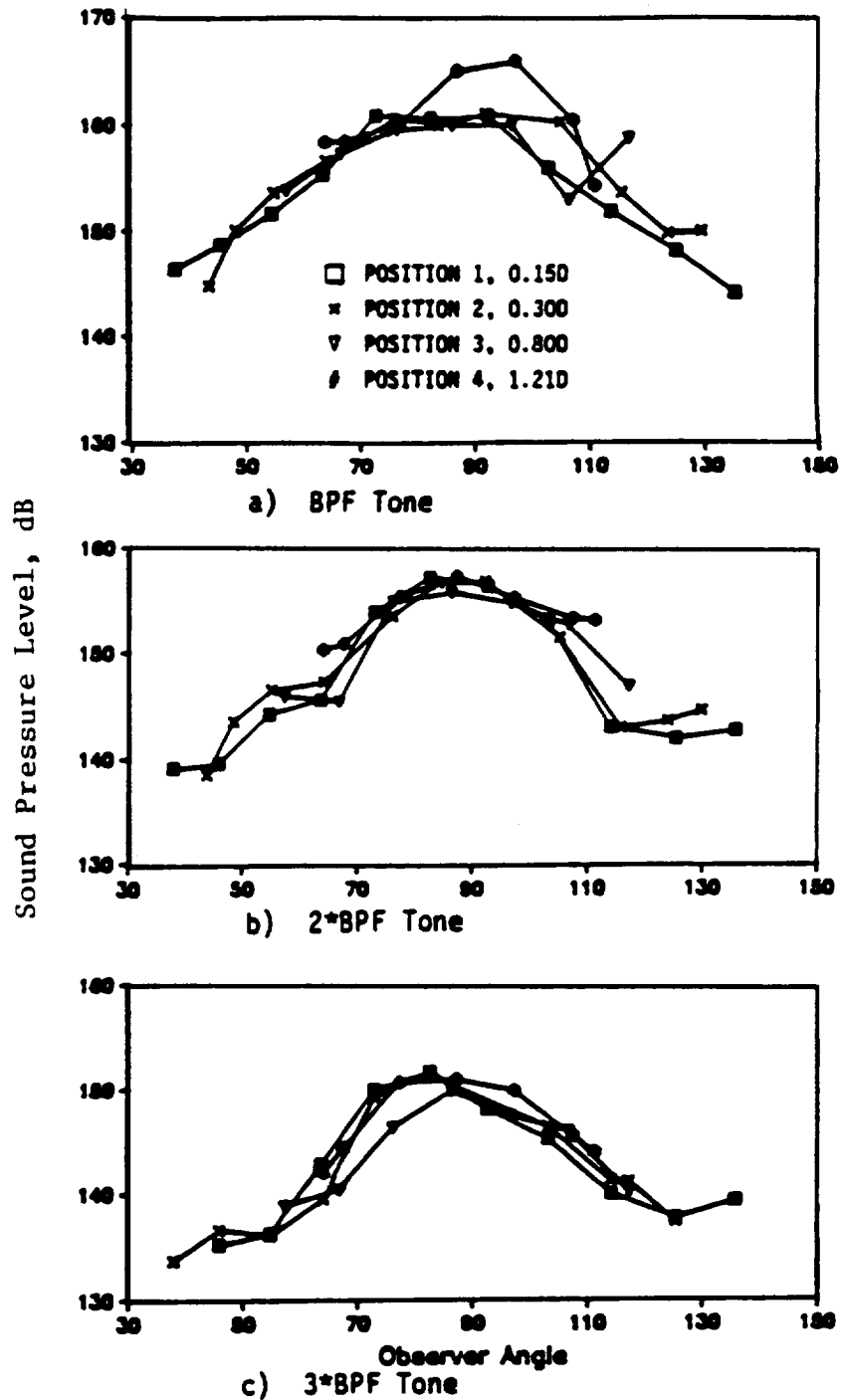


Figure 396. Collapse of Data (from Different Plate Positions) at Plate Position 2, Using the Inverse-Square Law (Readings 2047 through 2050).

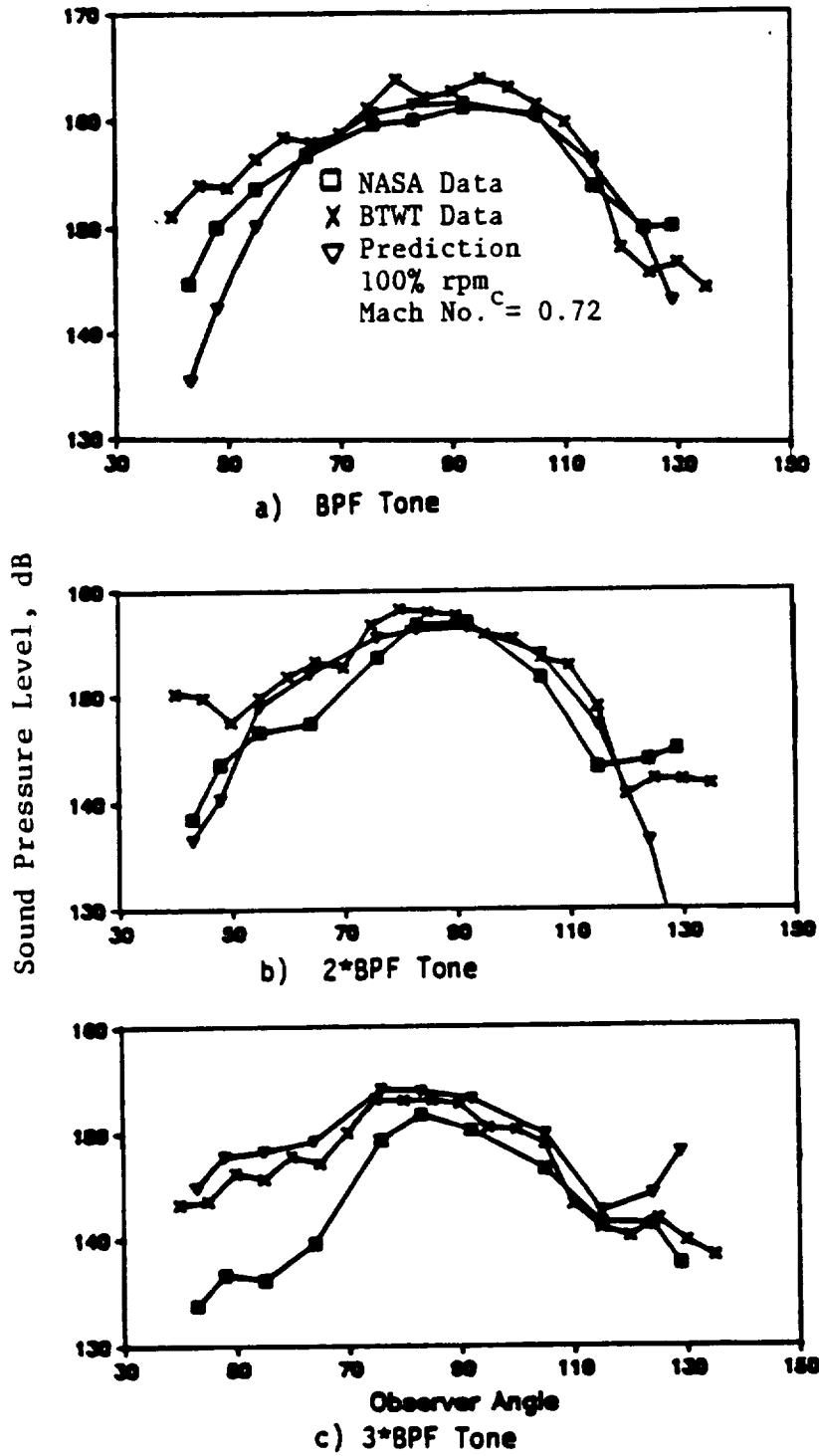


Figure 397. Comparison of 8x6 Data with Theory and Data from BTWT for the F-7/A-7, at Plate Position 2.

ORIGINAL PAGE IS
 OF POOR QUALITY

Table 66. MPS Blade Design Parameters.

Configuration	F-7/A-7	F-11/A-11	F-21/A-21
Design M_o	0.72	0.8	0.8
NB	8+8	11+9	11+10
Tip Sweep (1)	34	37	45
Tip Sweep (2)	31	34	25
Activity Factor (1)	147	180	173
Activity Factor (2)	152	200	121
PCA $\Delta z/D_{t1}$	0.17	0.32	0.25
D_{t1} (m)	0.625	0.625	0.625

with rotor-to-rotor interaction tones at BPF harmonics greater than unity; all of which occur at the same frequency for each harmonic. These figures also demonstrate the results of a theoretical prediction calculation; examination of these figures reveals that, for plate Positions 1 through 3, for the first two harmonics of BPF, the data and prediction are in very good agreement as to peak level, with moderately good agreement on the directivity.

However, for three times BPF, it appears that the prediction is higher in level everywhere, particularly in the forward region. At a tip clearance-to-diameter ratio of only 0.15, plate Position 1 is, undoubtedly, in the acoustic near-field of the model. The directivity shown in the data for the BPF tone at this position (Figure 393) is of a different character than that seen at Positions 2 or 3. It was observed during the test that, whereas generally, the effect of the plate on the performance of the model was minimal, with the plate in this position, performance deteriorated.

Data from plate Position 4 also appears anomalous, with a BPF tone that peaks at a higher level than that observed at Position 3, which is closer to the rotors. Consequently, it was decided to concentrate on data acquired at plate Position 2 (where the angular range covered was greater than at Position 3) for the remainder of this discussion. Final justification for this choice is shown in Figure 396, where data from all four plate positions are presented collapsed at Position 2 by means of the simple inverse-square law.

Figure 397 compares the same data taken at Position 2 with data from a nominally identical run in the acoustically treated BTWT. The BTWT data were taken with a free-field traversing microphone and have been adjusted to NASA conditions by adding 6 dB to account for the presence of the solid plate and have also been adjusted for differences in static pressure between these two tunnels and for differences in distance of the microphone location relative to the MPS. The theoretical prediction is also shown.

As seen, these three curves are in very good agreement in the aft portion of the directivity pattern, with the NASA data tending to drop in level, going forward from the peak more rapidly than either the prediction or BTWT data. Dittmar, et al. (Reference 42) attributes this dropping off in the forward arc to the effects of refraction in the plate boundary layer, which would explain why the free-field prediction and BTWT measurement are unaffected.

Table 67. Performance Parameters of Acoustic Test Points (8x6 Wind Tunnel).

Reading No.	Mach No.	Ts, ° R	Ps, psi	rpm1	rpm2	Nominal %, rpm	MHT1	MHT2	shp1	shp2	β 1	β 2
F-7/A-7 (8+8)	0.72	517.39	12.318	8283	8316	100	1.076	1.0639	399.62	370.13	56.9	54.4
2047												
2048												
2049												
2050												
3684 (Nominal)		510.96	12.153	8258	8306		1.0765	1.0631	471.99	465.24	58.5	55.7
3452 (Minimum)		485.98	12.616	8148	8209		1.084	1.0714	489.31	516.66		
3597 (Maximum)		482.84	12.755	8153	8205		1.0863	1.0729	535.42	482.03		
4377 (Preliminary)	0.80	471.91	11.518	8005	8065		1.1373	1.1253	527.53	394.77	61.2	57.9
(Final)	0.80	472.26	11.518	8005	8065		1.1352	1.1232	528.2	394.8	61.2	57.9
F-21/A-21 (11+10)												
5300	0.80	467.48	12.028	7994	8044	100	1.1287	1.1126	450.87	488.10	60.2	61.6
5186	0.80	483.59	11.532	7847	7892	96	1.1095	1.094	494.19	417.11	61.8	61.2
F-11/A-11 (11+9)												
2839	0.80	481.87	11.657	7698	7808	95	1.1059	1.0973	486.2	558.7	61.5	59.8

To summarize, these results indicate that, in and aft of the peak noise region, measurements obtained in this fashion in an untreated tunnel operating at high subsonic Mach numbers can provide useful information with regard to the noise generated by counterrotating fan models.

7.2.3.2 Effects of Rotor-to-Rotor Spacing

Three rotor pitch-change-axis spacings designated nominal, minimum, and maximum are available on the MPS model. When normalized by the F-7/A-7 blade diameter, these correspond to the spacing/diameter ratios of 0.169, 0.136, and 0.241, respectively. The F-7/A-7 blades were tested at these three spacings, and of the data available, those instances where blades were running closest to their design point ($M_0 = 0.72$, 100% rpmc) were selected for analysis. The readings used for this comparison are listed in Table 67 as: 3684 (nominal), 3452 (minimum), and 3597 (maximum); relevant performance parameters, in terms of physical quantities, also are given.

Figure 398 depicts the spanwise variation of the axial distance from the TE of Rotor 1 to the 1/4-chord point of Rotor 2, normalized by the axial chord of Rotor 1, when the blades are set at pitch angles ($\beta_{0.75}$) of $58.5^\circ/55.7^\circ$. At low flight speeds, such as would be encountered in the community noise regime, it would be anticipated that the increases in spacing/chord ratio from minimum spacing to maximum spacing would result in a corresponding decrease in the rotor-to-rotor interaction tones.

Therefore, for these cases of equal blade number and nearly equal rpm for each rotor, where the filter bandwidth is too large (at 32 Hz) to separate out the individual tones, it would be anticipated that for BPF harmonics equal to and greater than the third (the point at which the interaction tones would be expected to dominate the spectrum), there would be a decrease in tone noise with increased spacing. Figure 399 illustrates that for this example of high speed, where the helical tip Mach number of each rotor is greater than unity, there is virtually no difference between the noise measured at each harmonic, up to and including the fifth, for all three spacings.

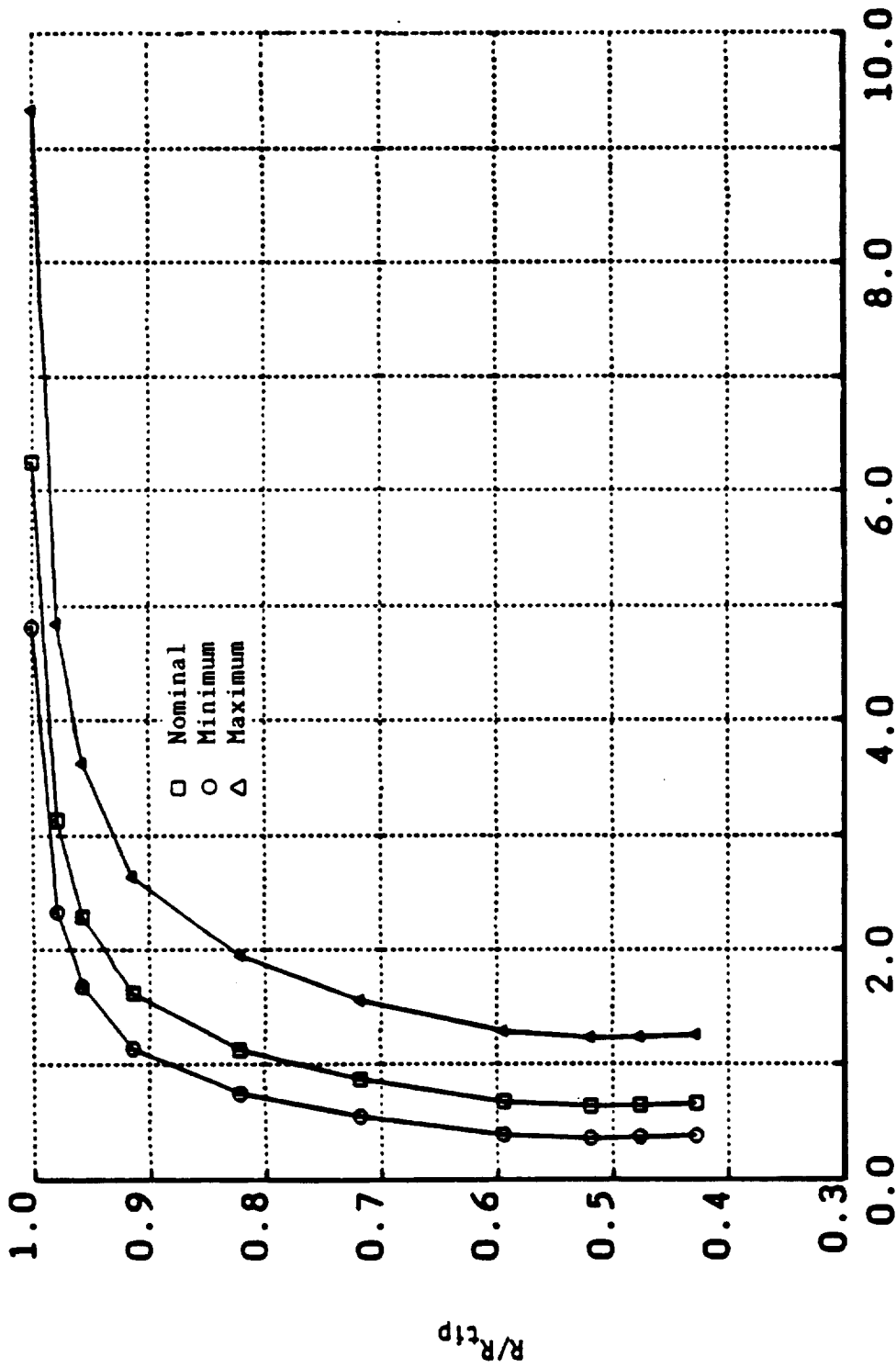
Note, that levels plotted here have been adjusted to take into account the differences in tunnel static pressure. In fact, if the power absorbed by the rotors under each condition is adjusted to that which would be required under nominal spacing conditions (Reading 3684) of temperature and pressure, it is possible to account for at least some of the differences observed. The major difference between the levels measured at the different spacings occurs in the forward arc, at about 70° observer angle; here, the level at maximum spacing is observed to be considerably higher (of the order of 7 dB) than the levels observed at the other two spacings. The reason for this is unclear.

Dittmar (Reference 34) re-reduced recorded data from spacing tests at three Mach numbers with a very narrow filter bandwidth, in order to investigate the interaction tones in detail. Such an analysis was not possible here, given the form in which the data were received.

7.2.3.3 Effects of Blade Design

The three blade designs that were tested under the NAS3-24080 contract have different design requirements with regard to flight Mach number and disk loading. In addition, neither the F-11/A-11 nor F-21/A-21 was tested as per design intent, due to instabilities in the forward rotor which required some geometric modifications be made during the test. Further, upon manufacture of the blades, it became apparent that F-7/A-7 blades have higher camber than the design intent, and that F-21/A-21 blades are thicker than was intended.

The decision was made to compare the acoustic results for these blades at a tunnel Mach number of 0.8; this being the design condition for F-11/A-11 and F-21/A-21 blades. Suitable data points



Axial Spacing:Chord Ratio (Rotor 1 TE to $\frac{1}{4}$ -Chord of Rotor 2)

Figure 398. Spanwise Variation of Axial Blade-to-Blade Spacing, Normalized by Rotor 1 Axial Chord, Under Cruise Conditions.

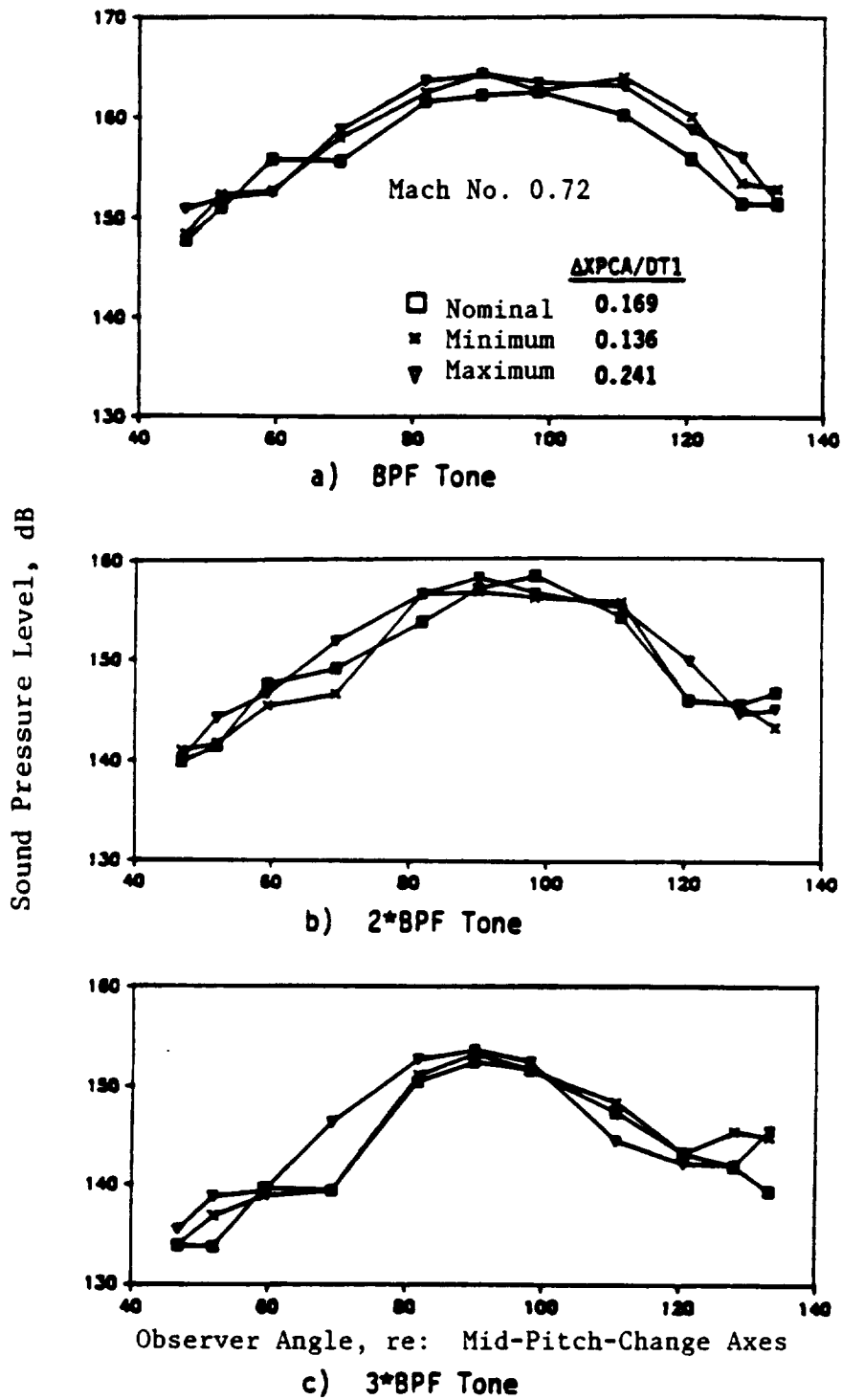
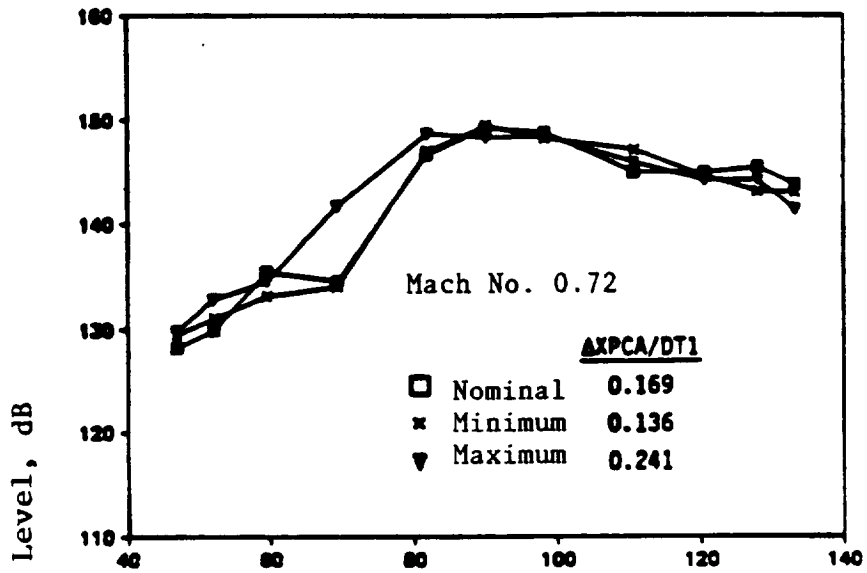
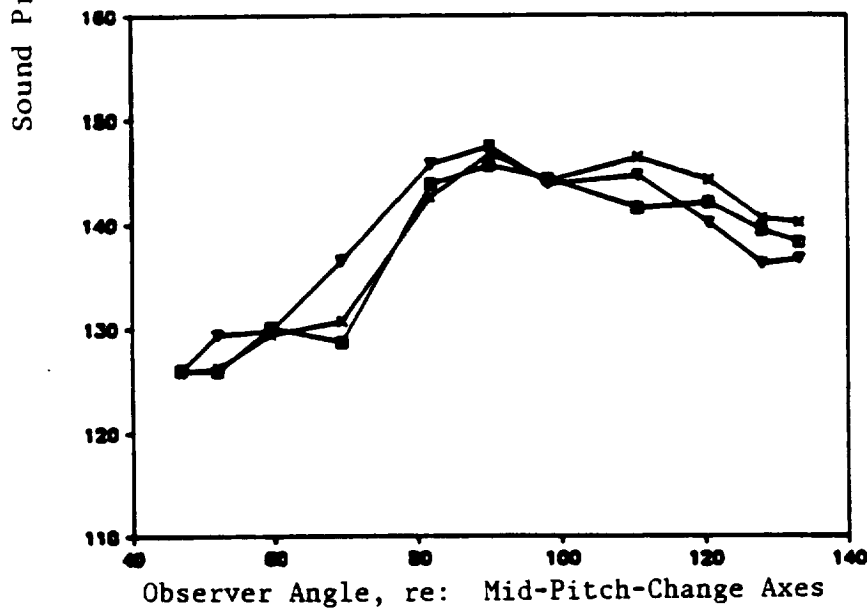


Figure 399. The Effect of Rotor Spacing on Tone Noise at Cruise for the F-7/A-7, at 100% rpm_c.



d) 4*BPF Tone



e) 5*BPF Tone

Figure 399. The Effect of Rotor Spacing on Tone Noise at Cruise for the F-7/A-7, 100% rpm_c (Concluded).

for comparison in terms of performance parameters were hard to find; therefore, it was decided to compare the F-7/A-7 with the F-21/A-21, both designs at 100% corrected rpm and similar PQA; and to then compare the F-21/A-21 with the F-11/A-11, both designs at approximately 95% corrected rpm. All comparisons use data from maximum spacing test points.

The test readings chosen for comparison are listed in Table 67 and are: F-7/A-7, Reading 4377; F-21/A-21, Readings 5300 and 5186; and F-11/A-11, Reading 2839. Table 67 also indicates that although overall performance figures are similar, the split between rotors varies from reading to reading. This tends to complicate interpretation of the results.

Figure 400 illustrate the initial comparison between the F-7/A-7 and the F-21/A-21. Because the F-7/A-7 is configured with 8+8 (forward+aft) blades; while the F-21/A-21 has 11+10 blades, and the rotors were running at approximately equal speeds, comparison has been made on the basis of tone sum. The F-7/A-7 spectrum automatically gives the sum of tones from both rotors; the F-21/A-21 tones were added antilogarithmically to give:

$$BPF = 10 \log_{10} \left[10 \left(\frac{SPL(BPF1)}{10} \right) + 10 \left(\frac{SPL(BPF2)}{10} \right) \right] \text{etc.} \quad (50)$$

As evidenced by this comparison, there is very little difference between the two blade designs. There is a possibility that the F-7/A-7 tones are slightly higher than those from F-21/A-21, but there is no dramatic difference between the two blade designs.

Figure 401 illustrates the individual BPF tone components for F-21/A-21, Reading 5300, clearly portraying the important role of the rotor-alone tones at these high helical tip Mach numbers, as well as the relatively unimportant contribution of the rotor-to-rotor interaction tones. This can be contrasted with the results shown in Sections 7.1.1 and 7.3.1 of this report, wherein low speed data are discussed.

To gain greater insight into these results, the analytical model employed in the blade evaluation study of Section 3.4 of this report was utilized to predict the noise for F-7/A-7, Reading 4377, and F-21/A-21, Reading 5300. The results of these predictions are compared with data in Figure 402 for the F-7/A-7 case and in Figures 403 through 406 for F-21/A-21. Figure 402 depicts two predictions; one with the rotor-alone steady-loading and thickness noise only, and the second with the inclusion of rotor-to-rotor interaction tones. The drop-off of the data in the forward arc (ascribed in Section 7.2.3.1 to the boundary layer on the plate) is seen to be more severe here, at the increased Mach number ($M_0 = 0.8$) than was observed at $M_0 = 0.72$. The increase in steepness of the drop with increasing frequency can also be seen. Both of these phenomena support the idea of refraction of sound in the plate boundary layer. The effect of including interaction tones in the prediction is most noticeable in the forward arc of the third harmonic.

Figure 403 compares the predicted and measured tone sum directivities for F-21/A-21, Reading 5300. It should be noted at this point that the 21-series blades, when manufactured, were found to be thicker than was designed. The prediction was made using the design coordinates. Figure 404 is a comparison of prediction and data for the individual BPF tones; and it can be seen that although the forward rotor peak level is predicted well, there are differences in the directivity patts that could result from differences in the thickness noise component and possible shortcomings in the theoretical model.

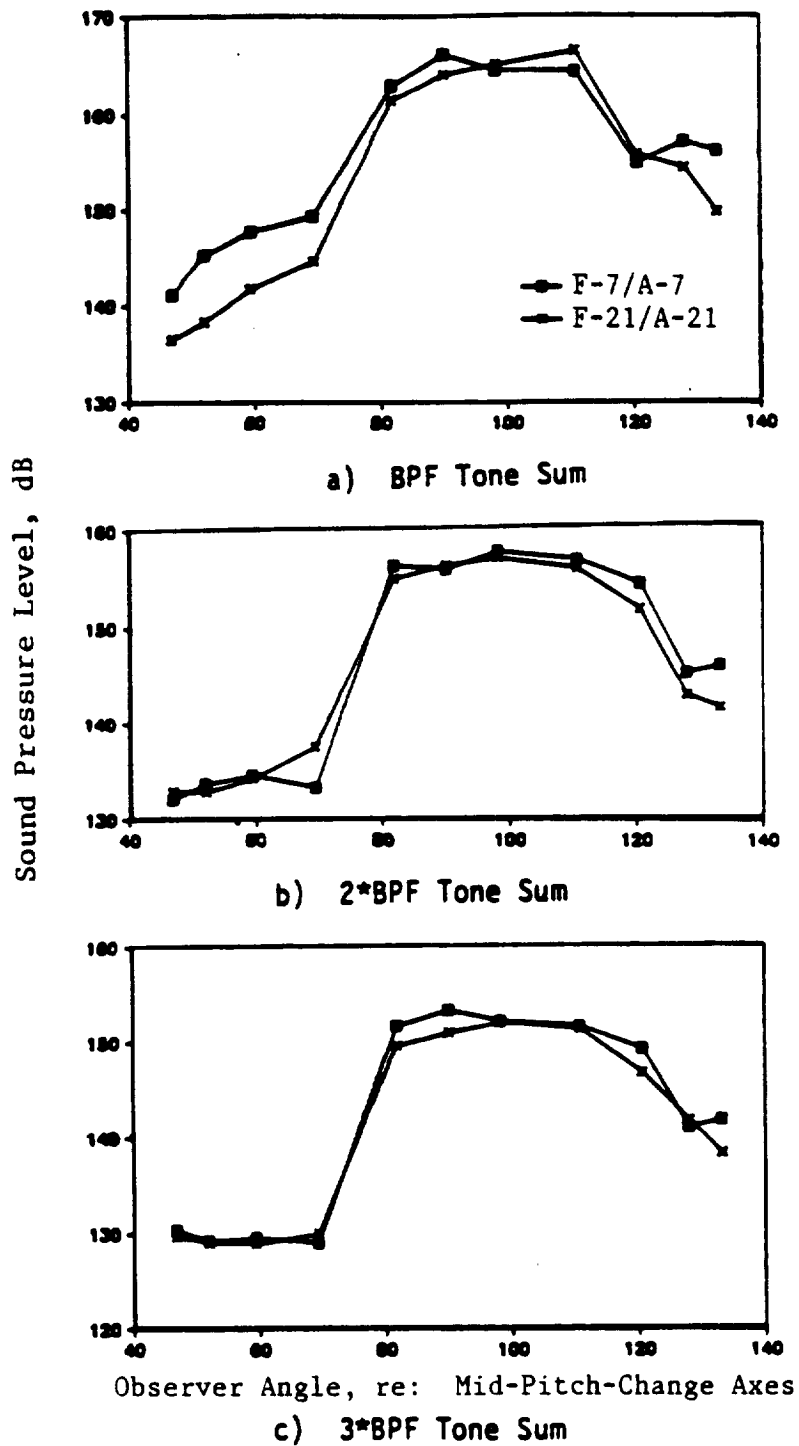
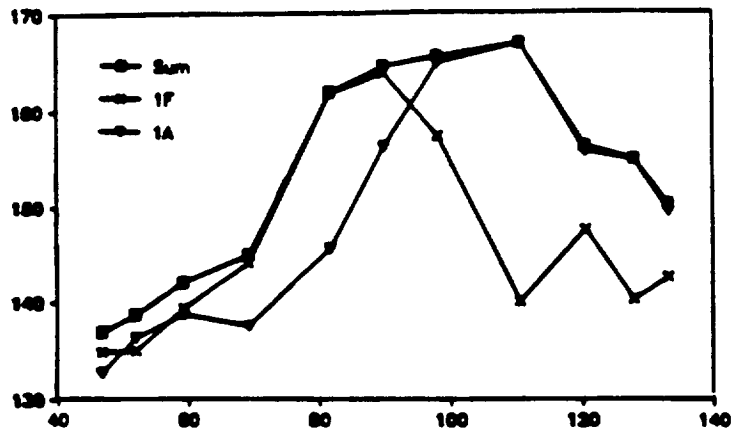
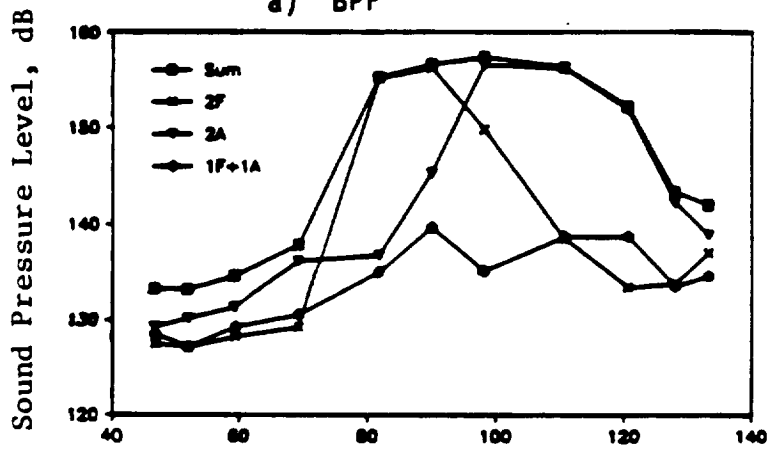


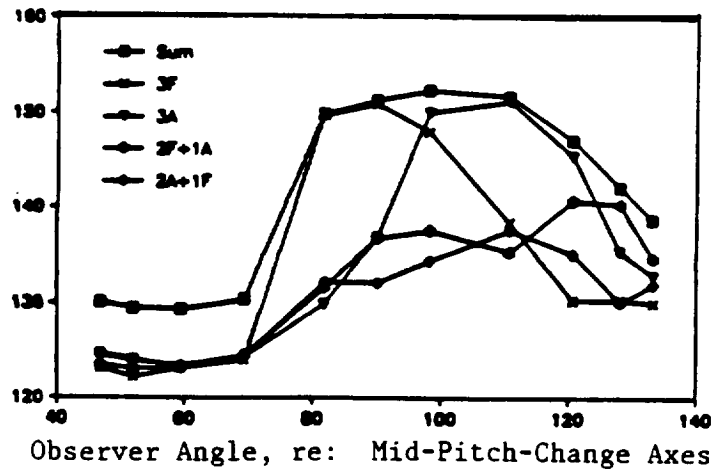
Figure 400. Tone Sum Comparison of F-7/A-7 and F-21/A-21 (Mach 0.8, 100% rpm_c, at Maximum Spacing).



a) BPF



b) 2*BPF



Observer Angle, re: Mid-Pitch-Change Axes

c) 3*BPF

Figure 401. Components of BPF Tones for F-21/A-21, Reading 5300, 100% rpm_c, Mach 0.80.

ORIGINAL PAGE IS OF POOR QUALITY

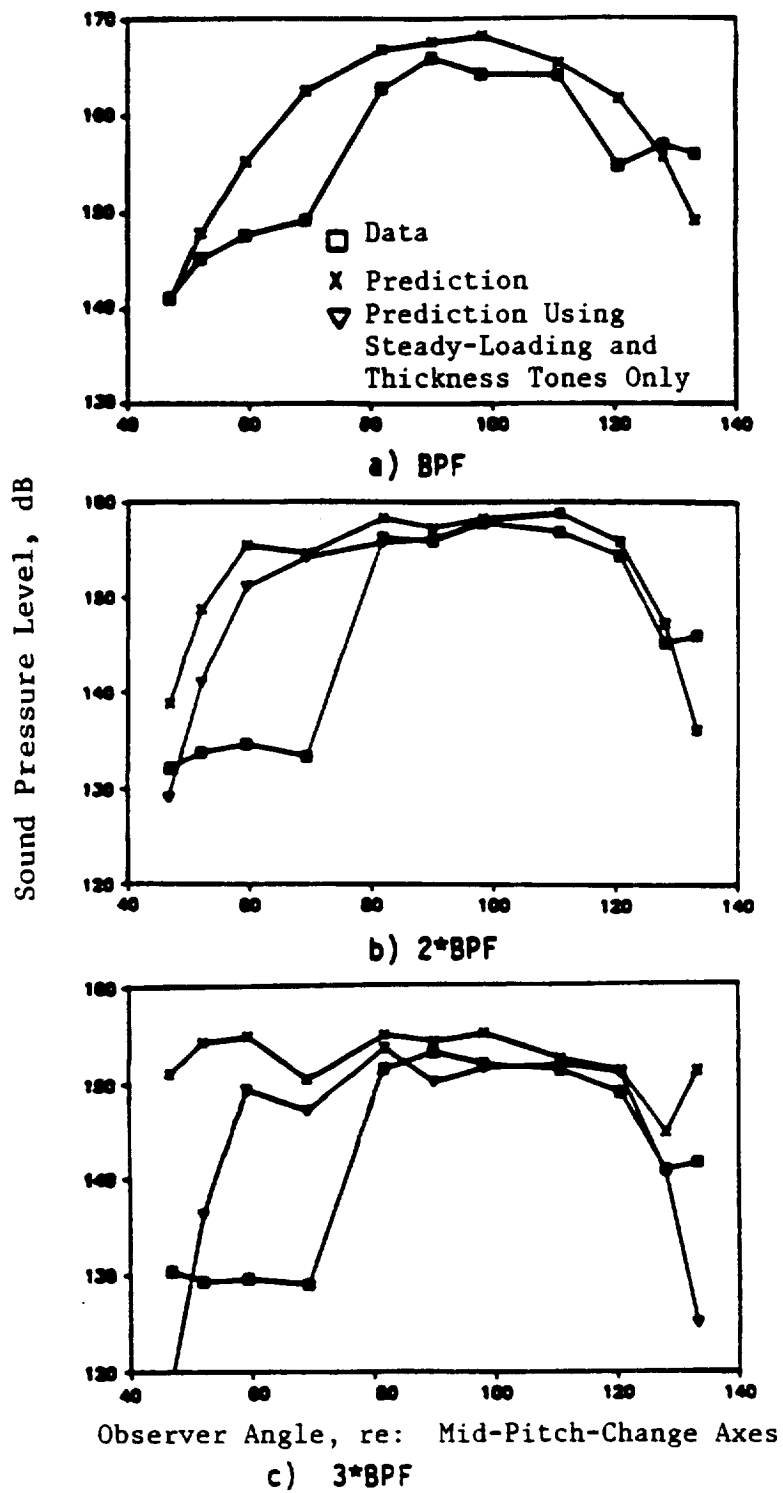
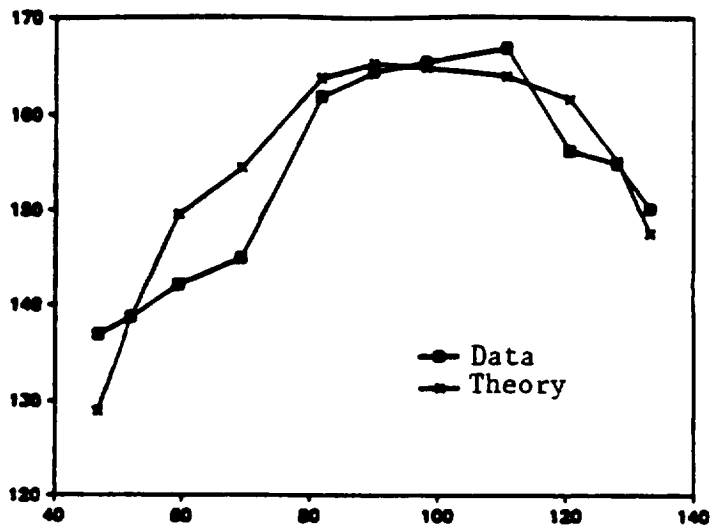
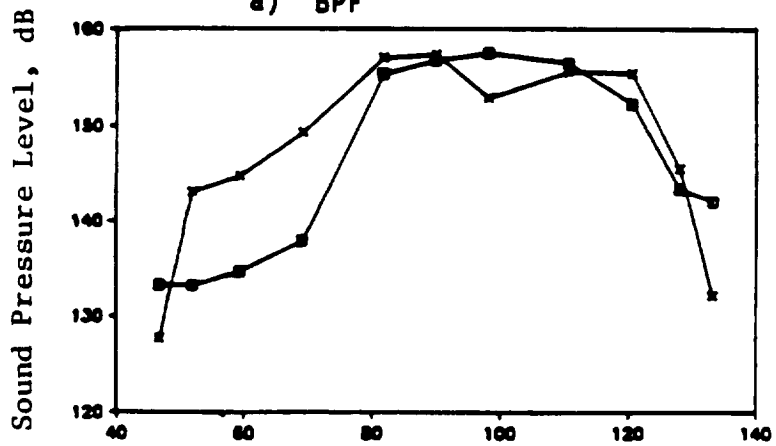


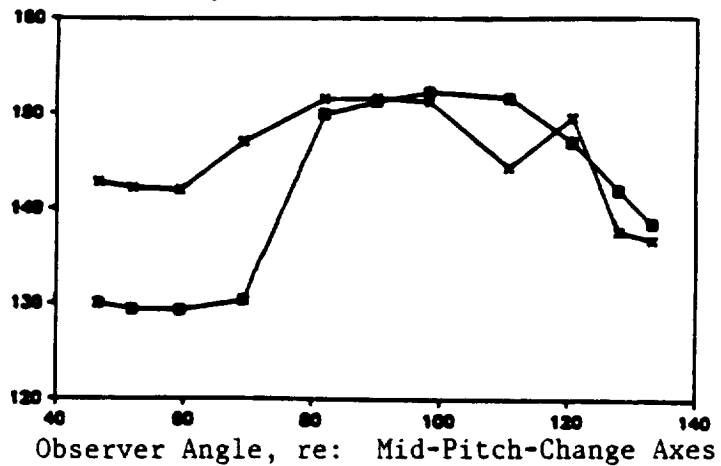
Figure 402. F-7/A-7 Data/Theory Comparison for Reading 4377, at 100% rpm_c, Mach 0.80.



a) BPF



b) 2*BPF



c) 3*BPF

Figure 403. F-21/A-21 Tone Sum Data/Theory Comparison for Reading 5300, at 100% rpm_c, Mach 0.80.

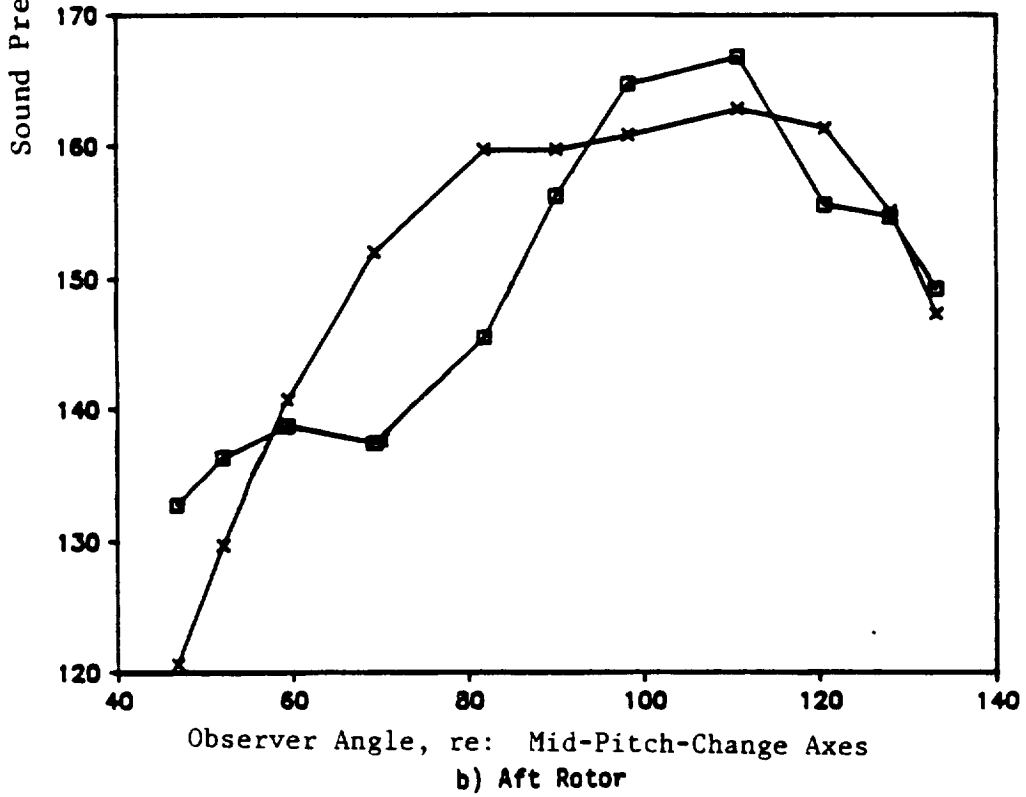
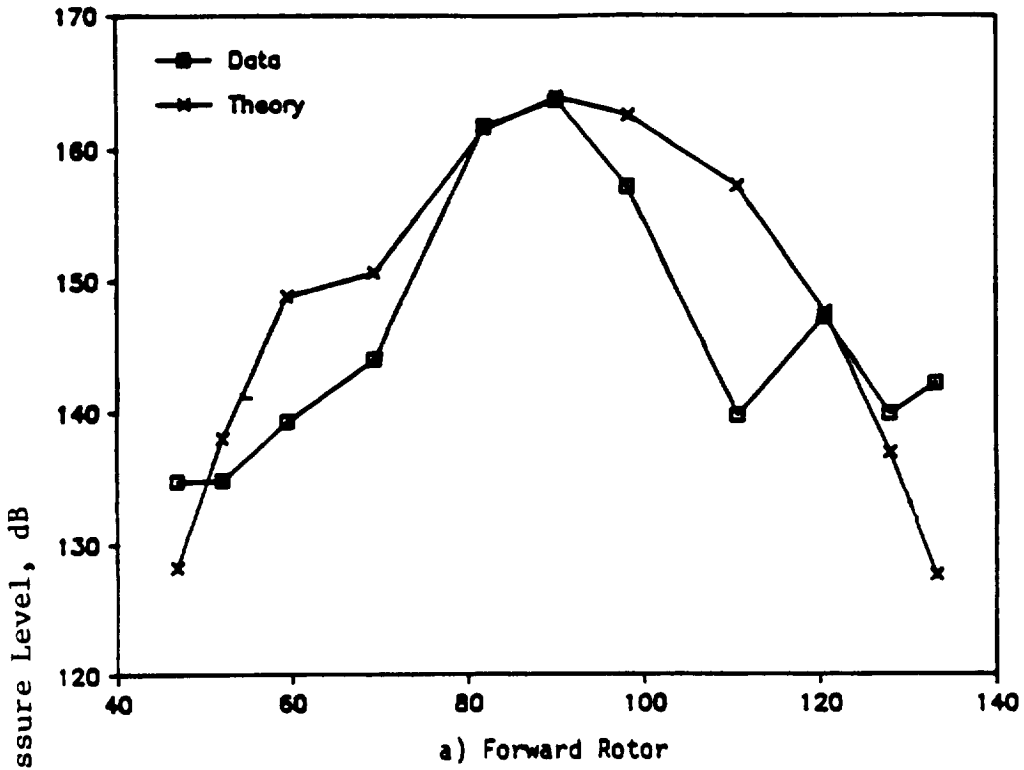
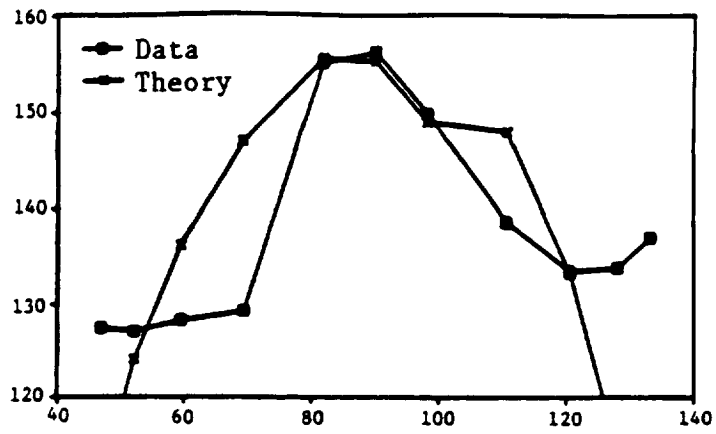
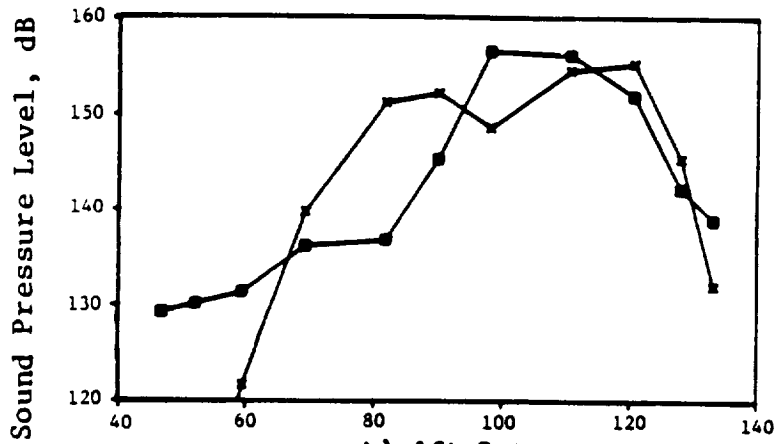


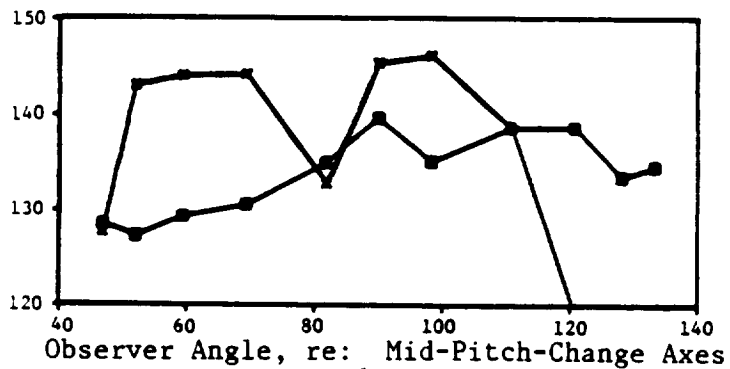
Figure 404. F-21/A-21 BPF Tone Data/Theory Comparison for Reading 5300.



a) Forward Rotor



b) Aft Rotor



Observer Angle, re: Mid-Pitch-Change Axes

c) 1F+1A Interaction Tone

Figure 405. F-21/A-21 2x BPF Tone Data/Theory Comparison (Reading 5300).

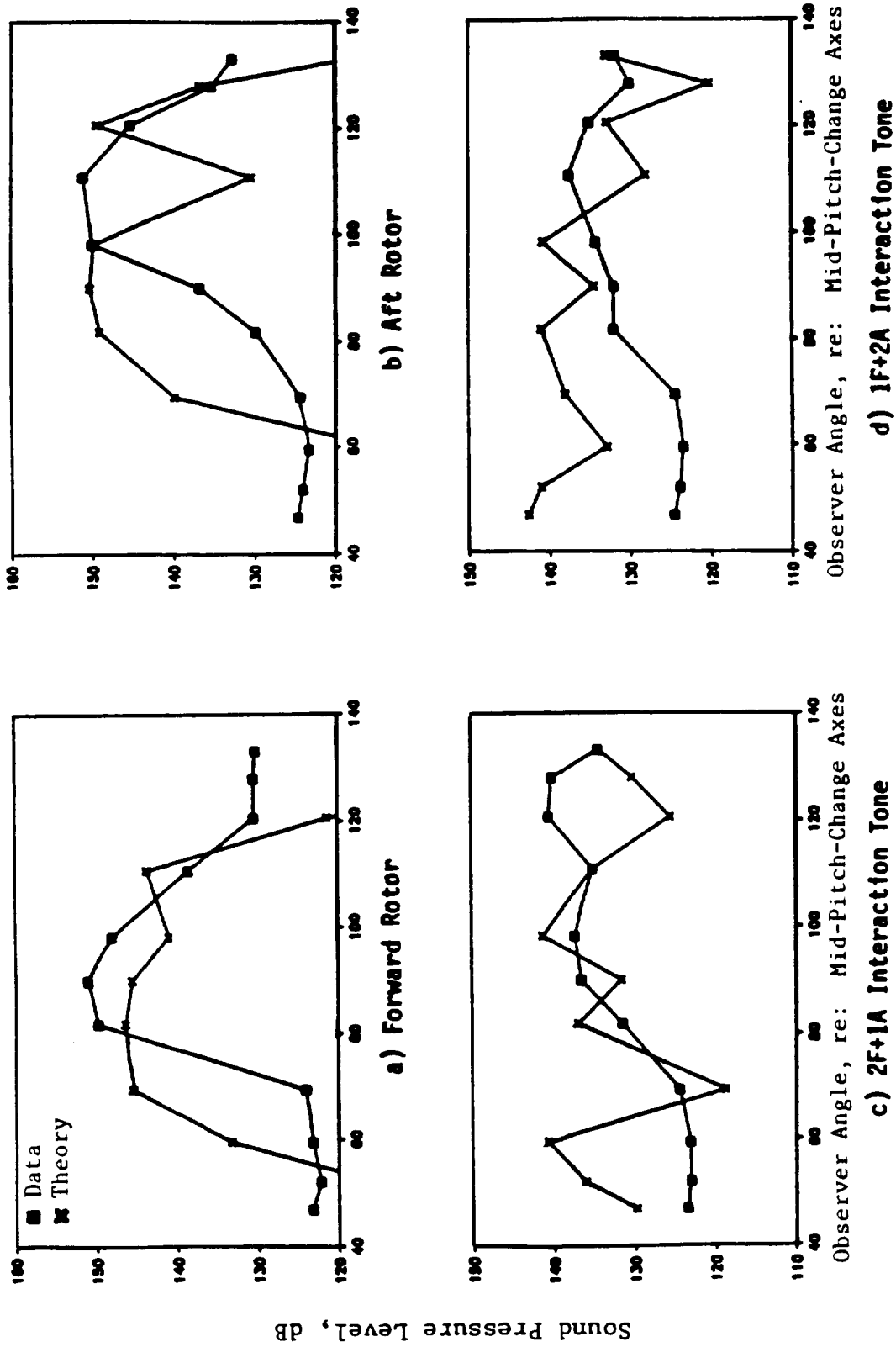


Figure 406. A Comparison of F-21/A-21 3x BPF Tone Data/Theory for Reading 5300.

Figures 401 through 406 demonstrate that both the prediction and the data show approximately equal levels for the tone sum BPF harmonics, although there are some discrepancies in the details comprising these totals. It was decided to examine the predicted steady-loading and thickness components of both rotor (forward and aft) BPF tones in order to gain some understandings that could result from differences in the thickness noise component and possible shortcomings in the theoretical model.

Figures 401 through 406 demonstrate that both the prediction and the data show approximately equal levels for the tone sum BPF harmonics, although there are some discrepancies in the details comprising these totals. It was decided to examine the predicted steady-loading and thickness components of both rotor (forward and aft) BPF tones in order to gain some understanding of the noise generation mechanisms at work.

Figure 407 compares separate predictions for both the steady-loading and thickness noise for the BPF tones of the forward and aft rotors of F-7/A-7, Reading 4377, and F-21/A-21, Reading 5300. At first glance, the difference in predicted steady-loading noise peak levels for forward rotors appears strange, when compared with the lack of difference predicted for the aft rotors, but after the power absorbed is reviewed on a per-blade basis, the differences are reasonable. Thickness noise of both designs is predicted to be of the same peak level, but the A-21 directivity shape suggests a cancellation effect is predicted in the peak region. Figure 408 demonstrates the predicted steady-loading and thickness contributions to the total BPF tones for the F-21/A-21, Reading 5300. It can be seen that for both rotors, the steady-loading term is predicted to dominate in the aft arc, with the thickness contribution providing both the peak and the forward arc levels. Contrast this with Figure 409, where the same information is plotted for F-7/A-7, Reading 4377; wherein, the loading and thickness terms are depicted as having an almost equal role in the BPF tone noise generated.

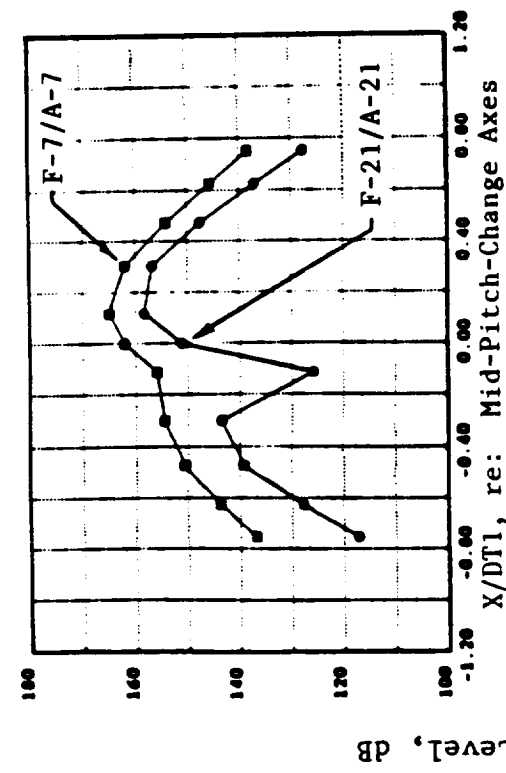
This implies that errors in manufacturing, with regard to the thickness distribution, would be expected to have a greater effect on F-21/A-21 blades under these conditions than on F-7/A-7. A further point to emerge from this study is the demonstration that reducing disk loading under cruise conditions is not solely sufficient to guarantee a reduction in noise.

Figures 410 and 411 compare the BPF tones of F-21/A-21, Reading 5186, and those of F-11/A-11, Reading 2839. The rotors were running at approximately 95% corrected speed, as no comparable data were taken at 100% speed. Once again, it appears that thickness noise is dominating the tone, as differences in loading for the aft rotor are significant enough to anticipate an impact on the noise if loading were the only source-mechanism present.

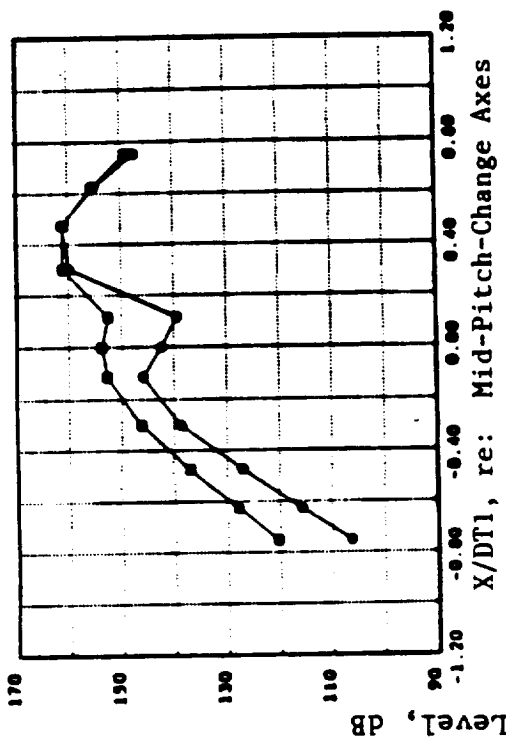
7.3 Rig 3/NASA 9x15 and Cell 41 Data Comparisons

7.3.1 Discussion of Acoustic Results Measured at the NASA Lewis 9x15 Wind Tunnel

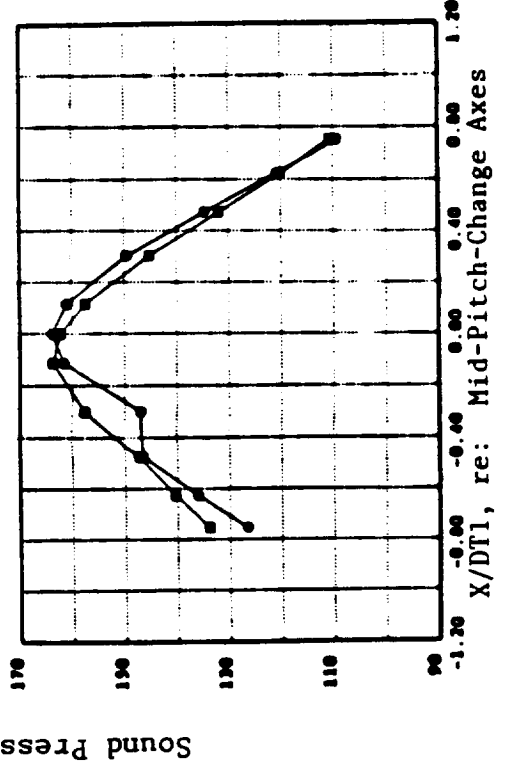
The scope of tests conducted at the NASA Lewis 9x15 wind tunnel was previously discussed in Section 5.3. Section 6.3.1 described the acoustic data acquisition and reduction procedures which were implemented; processed results are presented and discussed in this section. The analyses includes comparison of select data measured in the wind tunnel with the corresponding Cell 41 data for a matching configuration and for test conditions. This is followed by an analyses of data measured at the 9x15 wind tunnel utilizing the F-7/A-7 (11+9) configuration at three rotor-to-rotor pitch-change-axes spacings designated as: minimum ($X/D_t = 0.136$), nominal ($X/D_t = 0.169$), and



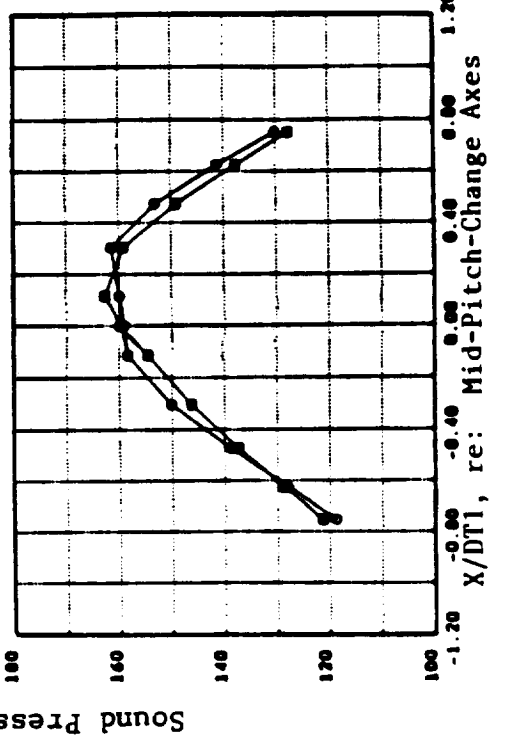
(a) Forward Rotor Steady Loading Noise



(b) Alt Rotor Steady Loading Noise

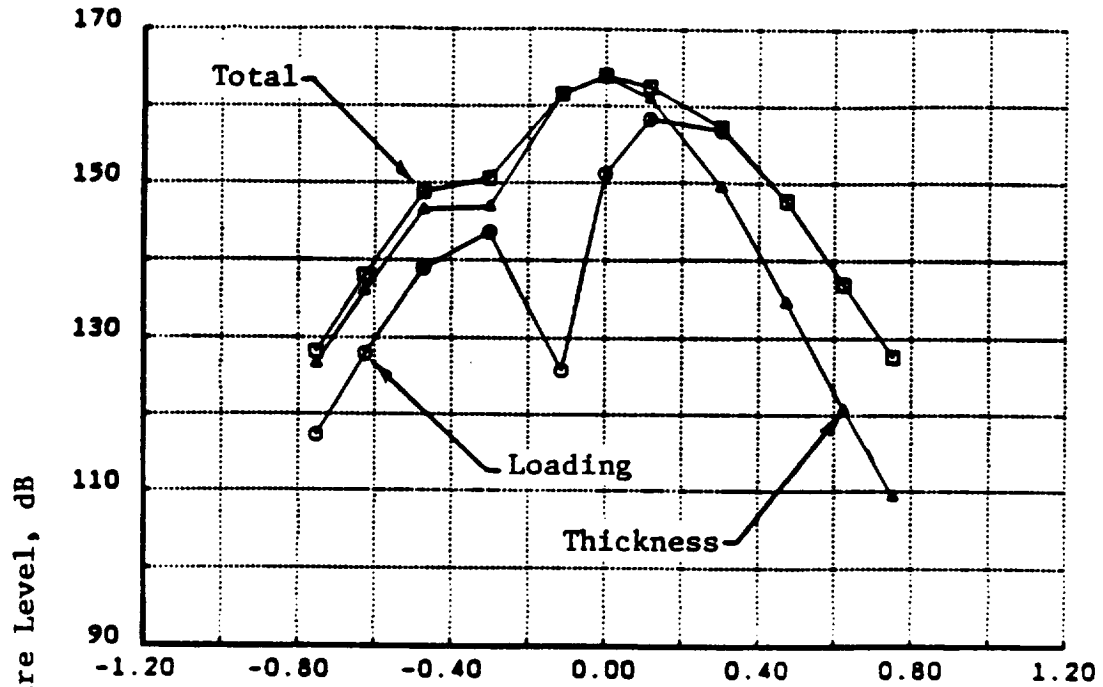


(c) Forward Rotor Thickness Noise

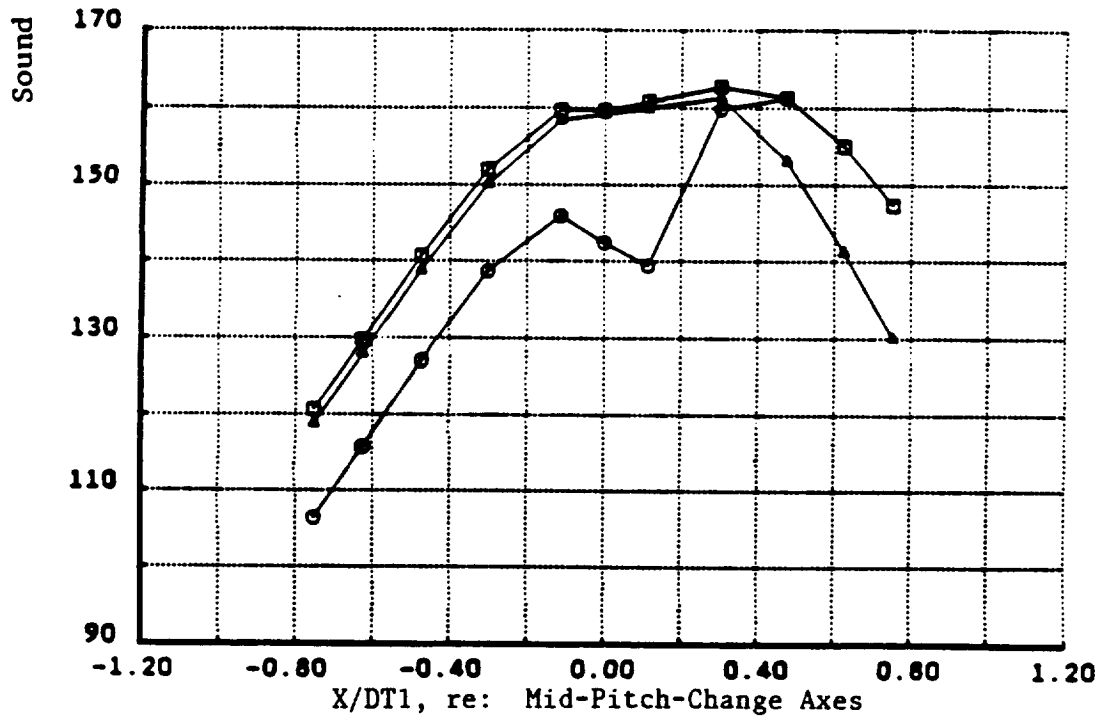


(d) Alt Rotor Thickness Noise

Figure 407. Comparison of Predicted Steady-Loading and Thickness Components of BPF for the F-7/A-7 (Reading 4377) and the F-21/A-21 (Reading 5300).

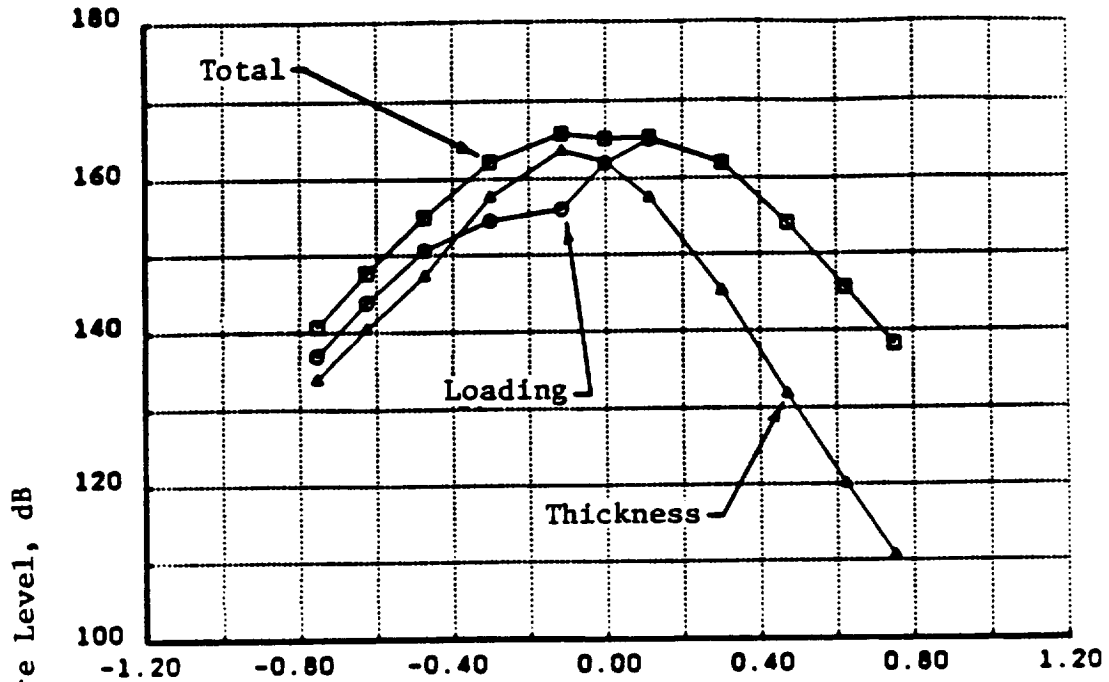


a) Forward Rotor

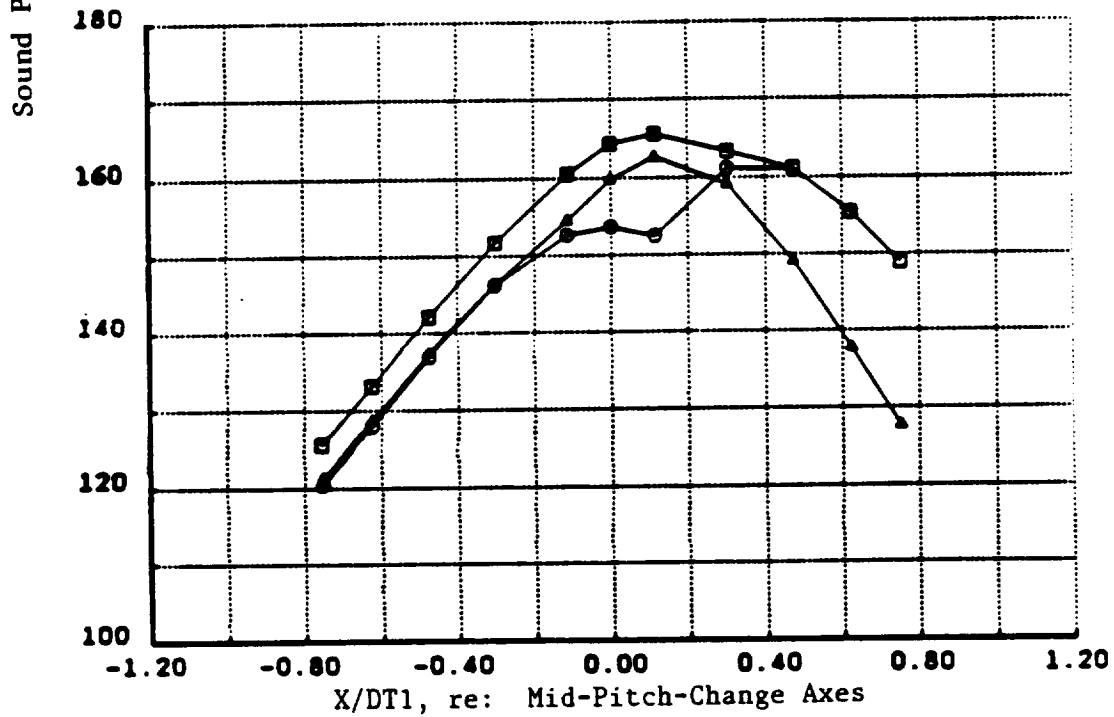


b) Aft Rotor

Figure 408. Predicted Steady-Loading and Thickness Contributions to BPF Tones for F-21/A-21 (Reading 5300).



a) Forward Rotor



b) Aft Rotor

Figure 409. Predicted Steady-Loading and Thickness Contributions to BPF Tones for the F-7/A-7 (Reading 4377).

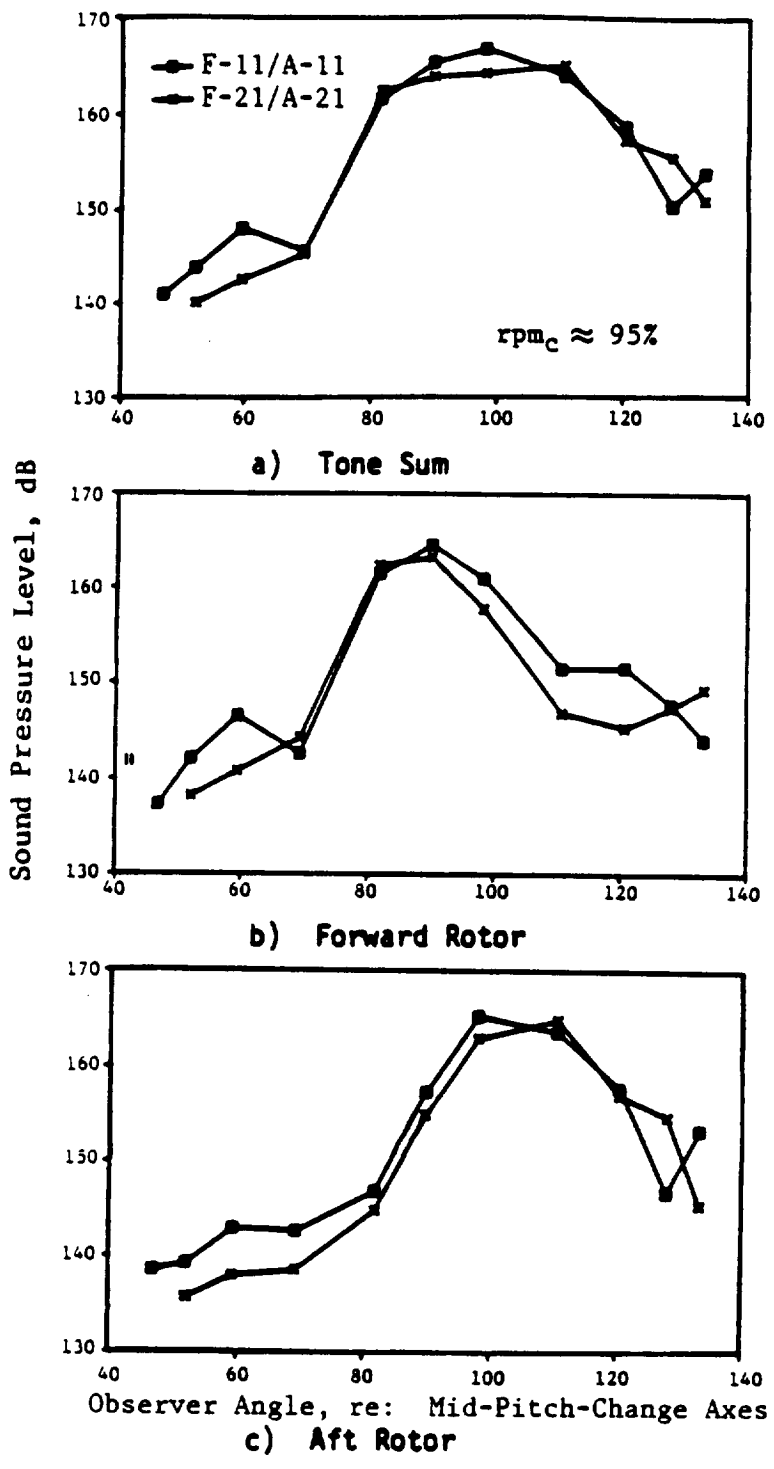
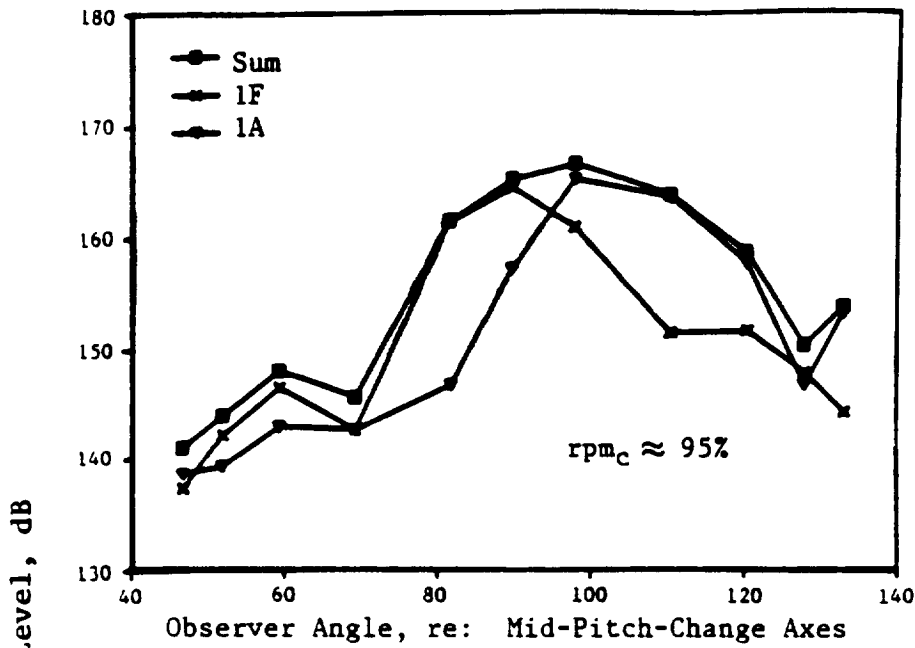
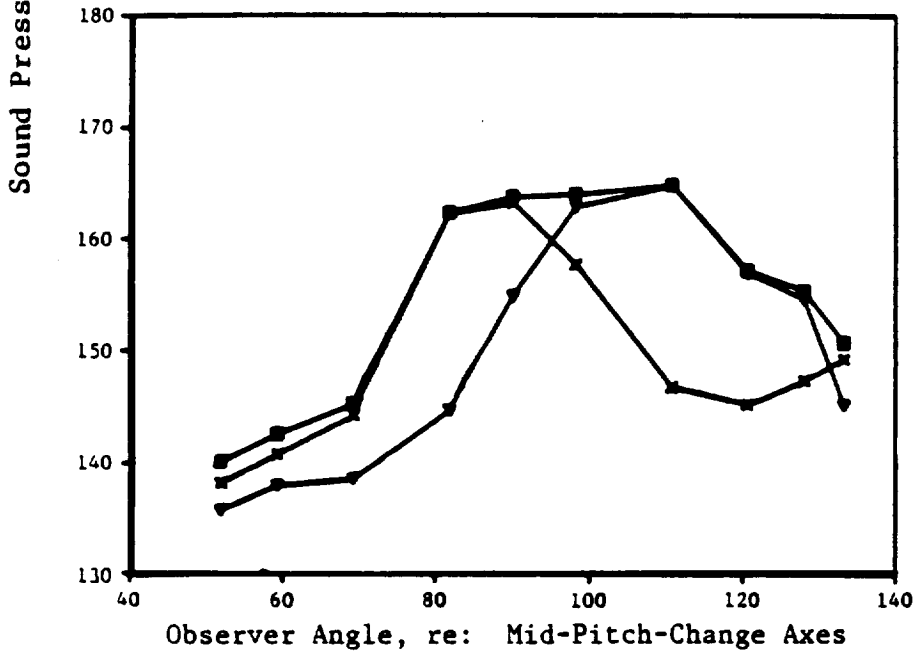


Figure 410. Comparison of F-11/A-11 and F-21/A-21 (Readings 2839 and 5186, respectively) BPF Tones at Mach Number 0.80.



(a) F-11/A-11



(b) F-21/A-21

Figure 411. Components of BPF Tones for F-11/A-11 (Reading 2839) and F-21/A-21 (Reading 5186) at Mach Number 0.80.

maximum ($X/D_t = 0.24$). The presented data are results at a simulated flight Mach number of 0.2 and were measured without a pylon.

7.3.1.1 NASA Lewis 9x15 and Cell 41 Data Comparisons

As described in Subsection 6.3.1, acoustic data were obtained from two translating microphones traversing parallel to the MPS axis at a 0° angle-of-attack. These microphones were located on a sideline of 1.37 m (4.5 ft) and 1.68 m (5.5 ft) from the MPS axis. For a given F-7/A-7 (11+9) test condition, data from both microphones were processed to obtain the narrow-band spectra, that were then extrapolated to a reference sideline distance of 8.2 m (27 ft). This reference sideline distance was chosen because it corresponds to the reference sideline distance used in Cell 41. The resultant sum tone data (Figure 412) indicate that both microphones yield reasonably equivalent data which is representative of the steady-loading and rotor-to-rotor interaction noise. Based on this comparison, and the fact that the 1.68 m (5.5 ft) microphone was closer to the tunnel wall than the 1.37 m (4.5 ft) microphone was, it was decided to only process acoustic data from the 1.37 m (4.5 ft) microphone.

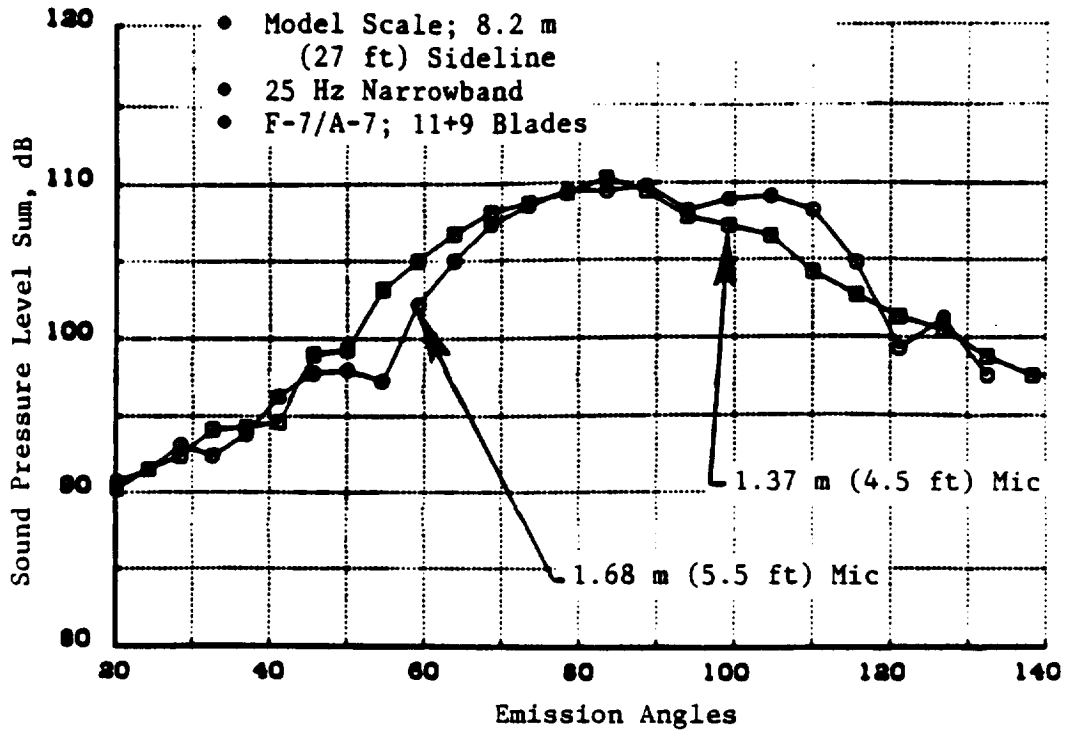
Among the series of tests conducted at the 9x15 wind tunnel, one test with the F-7/A-7 (11+9) configuration at maximum rotor spacing was at a pitch-setting condition that reasonably matched a test conducted earlier in Cell 41 for a given Mach number of 0.20. These matching test conditions at the 9x15 wind tunnel are identified by the acoustic Test Points 296 through 315. The aerodynamic performance measured in the wind tunnel, in terms of total thrust versus tip speed, and total absorbed shaft power versus total thrust (Figure 413), are compared with the corresponding Cell 41 data. While these two sets of data are comparable, a higher thrust was measured at the 9x15 wind tunnel, relative to Cell 41, for a given tip speed. This difference could have been caused by small differences in pitch-angle settings; as the two test sites did not use the same calibrated pitch-setting block.

Figures 414 through 418 compare the acoustic data measured at Cell 41 and at the 9x15 wind tunnel for a selected tip speed of 247 mps (810 fps). For this comparison, the NASA 9x15 acoustic data was processed up to 20 kHz. An examination of the model-scale tone results presented in Figure 414 indicates:

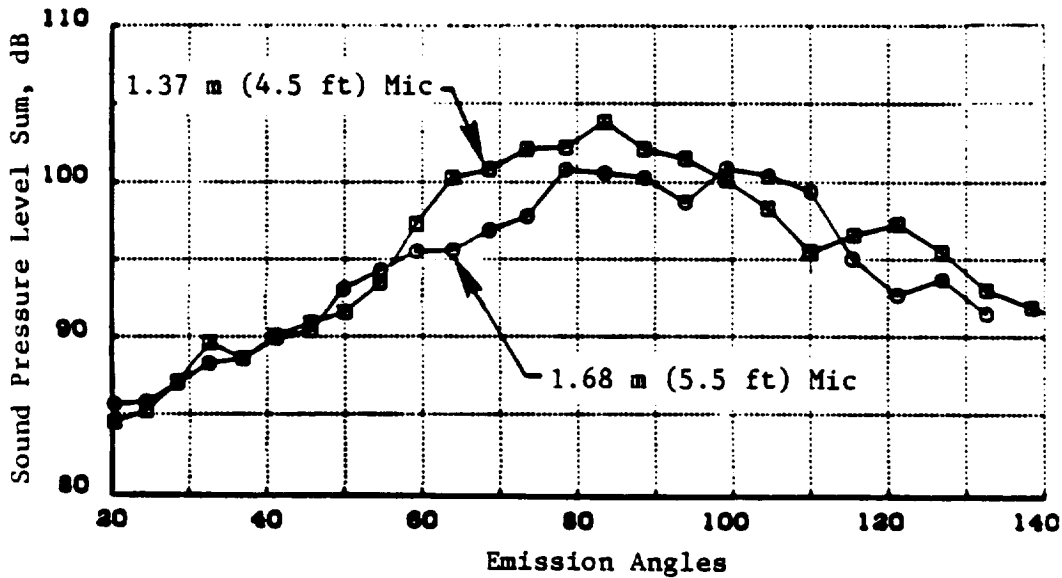
- Equal sound pressure sum tone levels for forward rotor BPF's and harmonics, and for the 3rd, 4th, and 5th interaction tone sum noise
- Higher sound pressure tone sum levels for the aft rotor BPF's and harmonics and the first rotor-to-rotor interaction noise.

Part of this difference could be due to the anechoic characteristics of the two facilities; also, the test rig in the 9x15 wind tunnel was operating at a slightly loaded aft-rotor condition, compared to that of the Cell 41 test condition. This suggests that some of the suspected pitch-setting error that could have caused the increased performance is on the aft rotor. The effect of this increased aft-rotor noise is also noticed in the total steady-loading noise (Figure 415). The rotor-to-rotor interaction tones sum at the NASA 9x15 tunnel is also higher, than the equivalent data of Cell 41. The first interaction tone is partially responsible for this increase in total level. The remainder of the increase must be due to sound pressure levels of the higher harmonics.

Figure 416 provides a model-scale 1/3-octave-band spectral comparison of Cell 41 data and 9x15 wind tunnel translating microphone data at selected emission angles, and an OASPL (overall sound pressure level) directivity comparison. Even though the general trend in data between these



(a) Forward and Aft Rotor BPF's and Harmonics Sum



(b) Rotor-to-Rotor Interaction Tones Sum

Figure 412. Comparison of Acoustic Data from the Traversing Microphones.

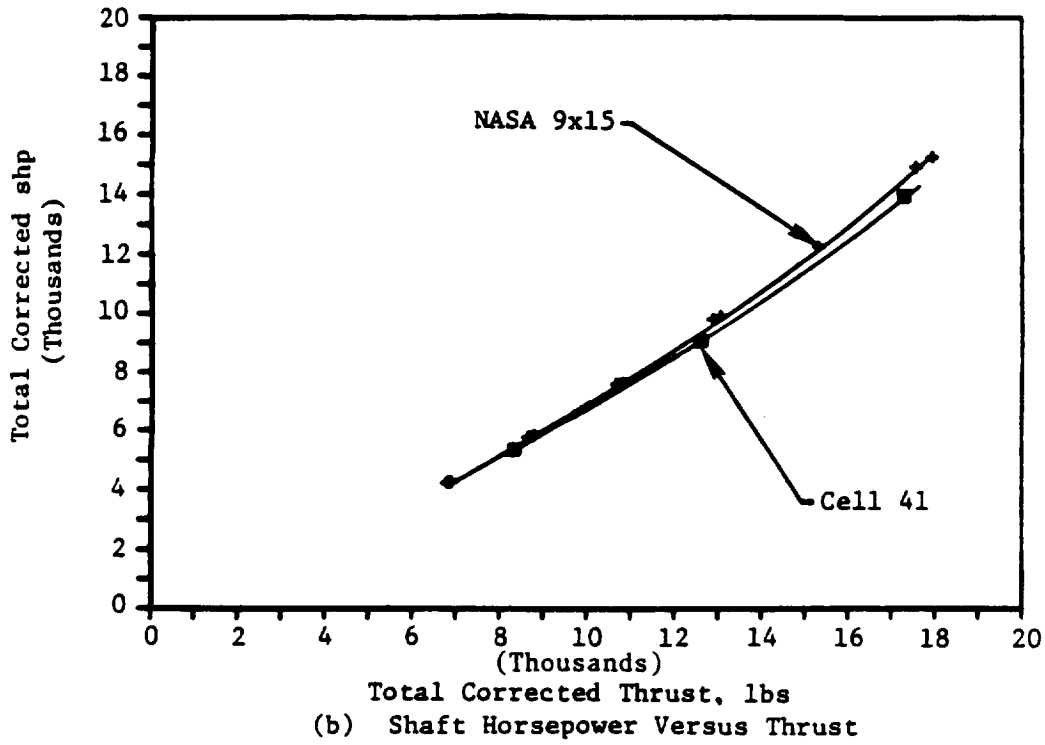
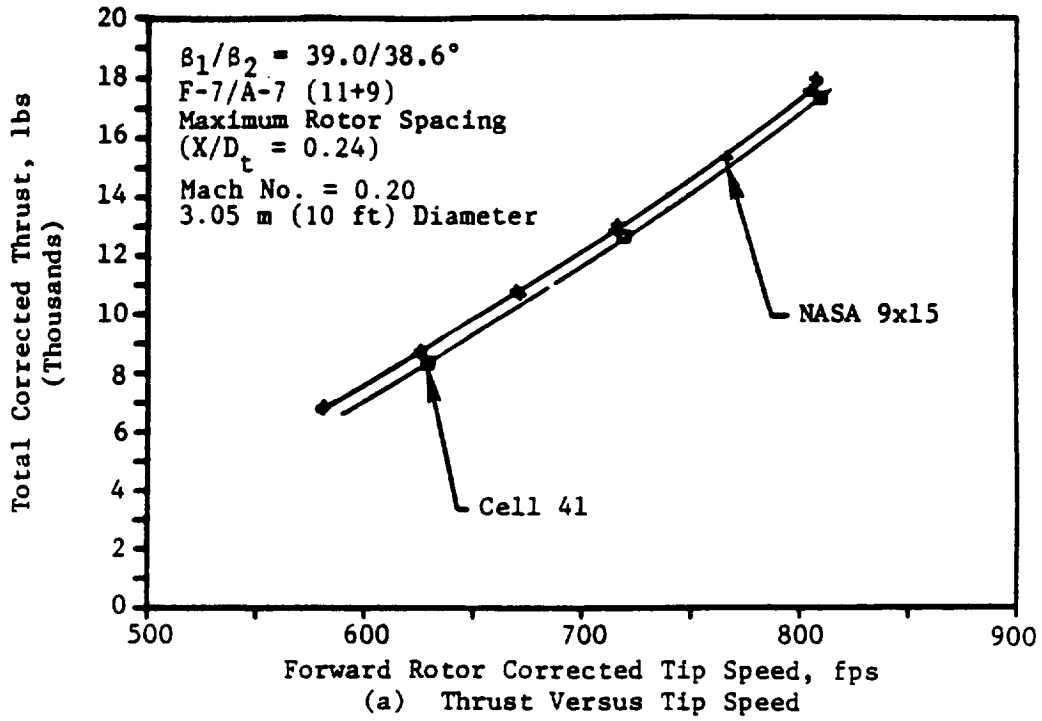
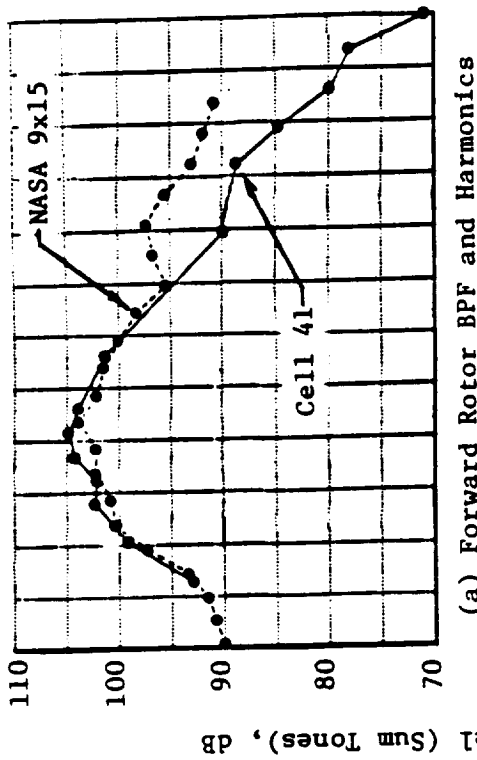
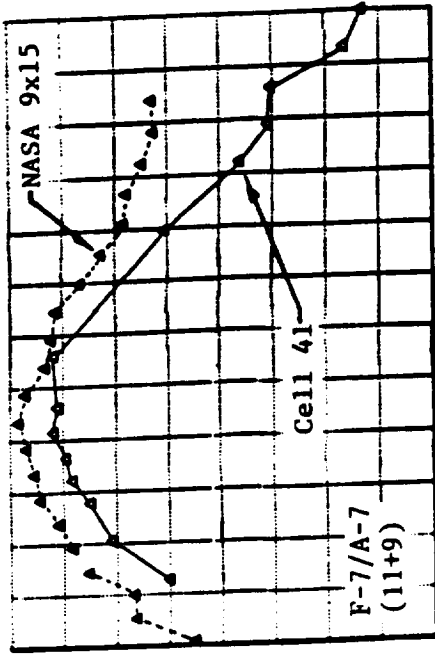


Figure 413. Comparison of Measured Aerodynamic Performance.

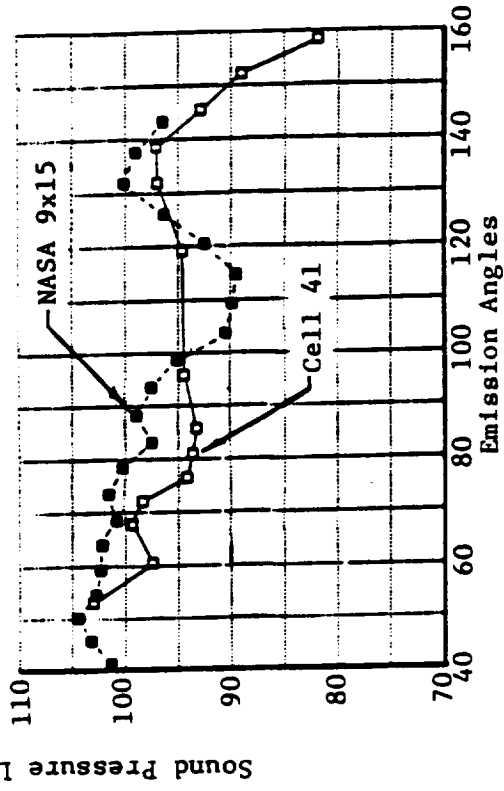
Model Scale: 8.2 m (27 ft) Sideline, Mach No. 0.20



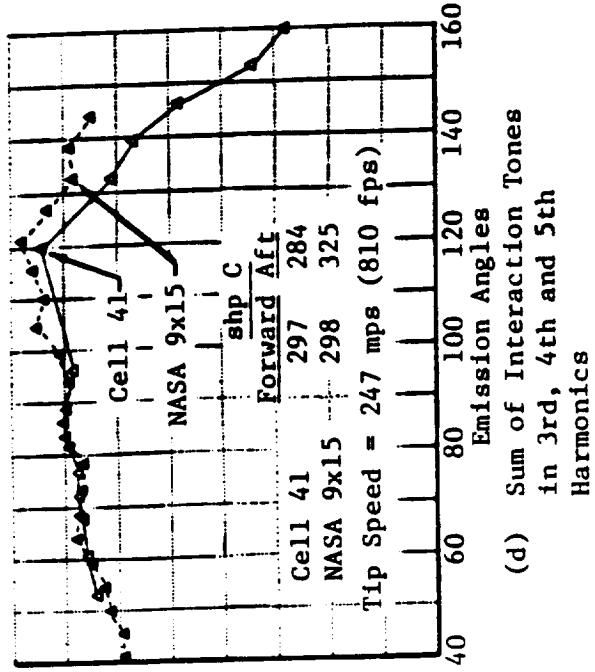
(a) Forward Rotor BPF and Harmonics



(b) Aft Rotor BPF and Harmonics

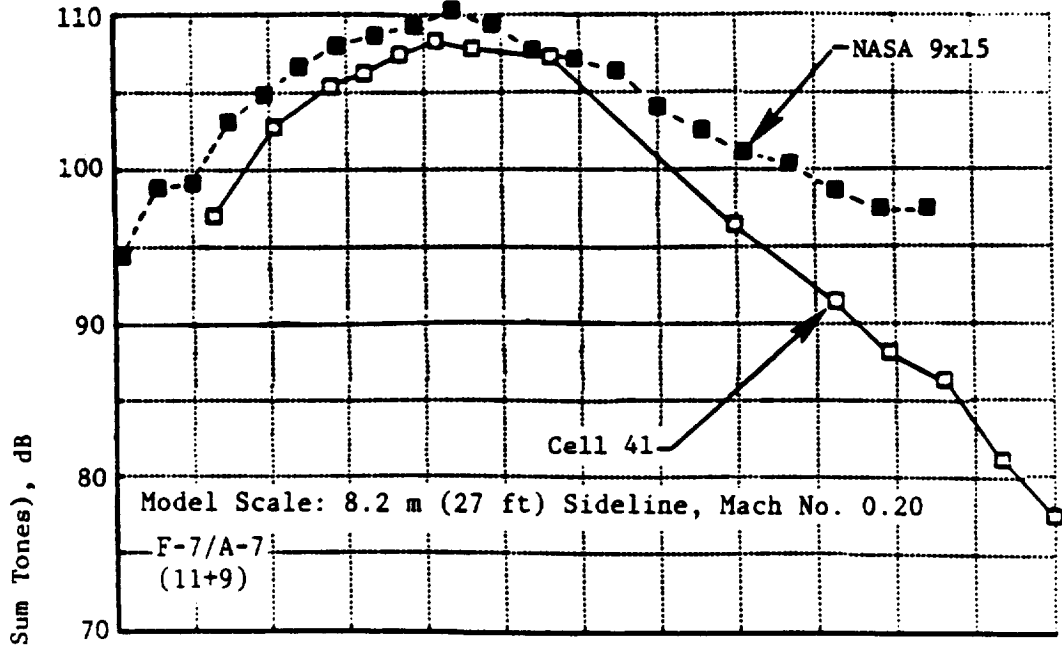


(c) First Rotor-to-Rotor Interaction Tone (A+F)

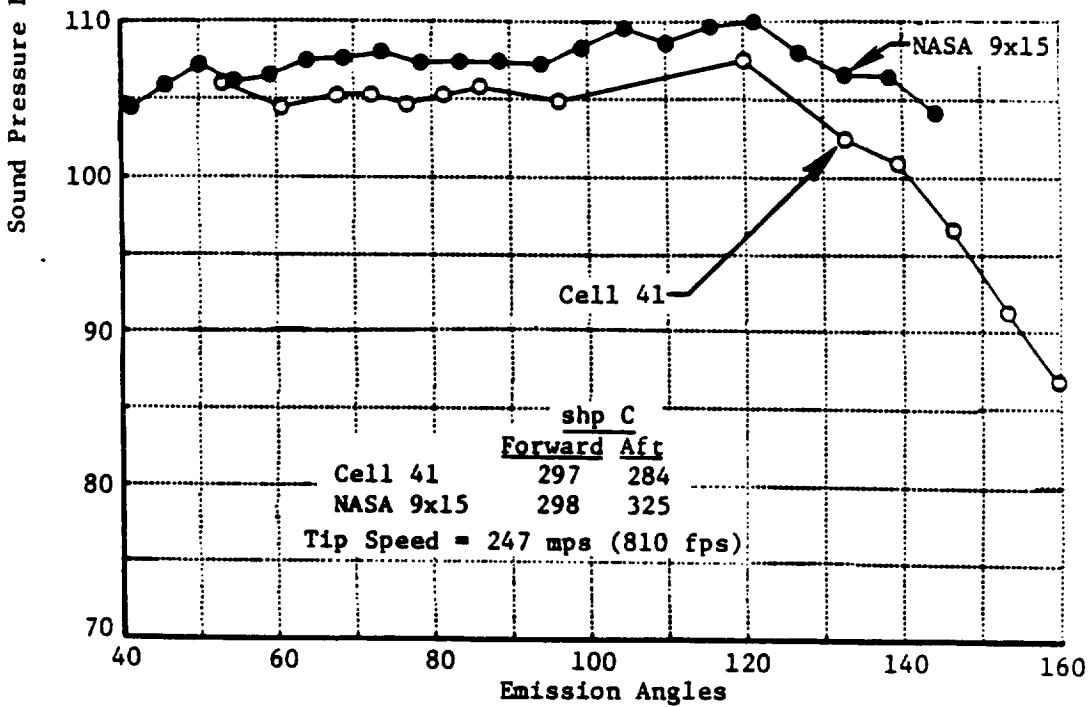


(d) Sum of Interaction Tones in 3rd, 4th and 5th Harmonics

Figure 414. A Comparison of Acoustic Narrow-Band Data Measurements.

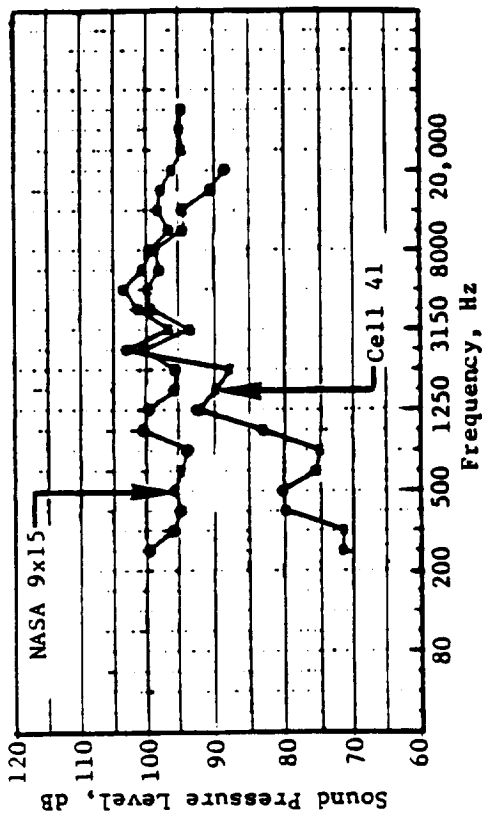


(a) Steady Loading Noise

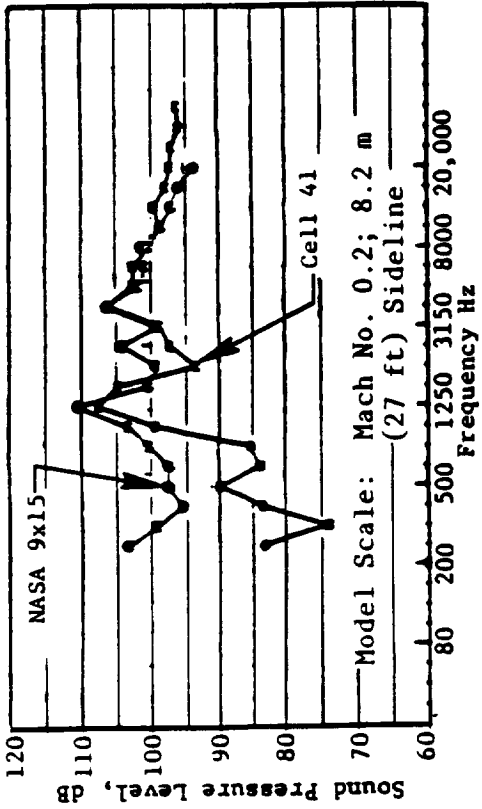


(b) Rotor-to-Rotor Interaction Noise

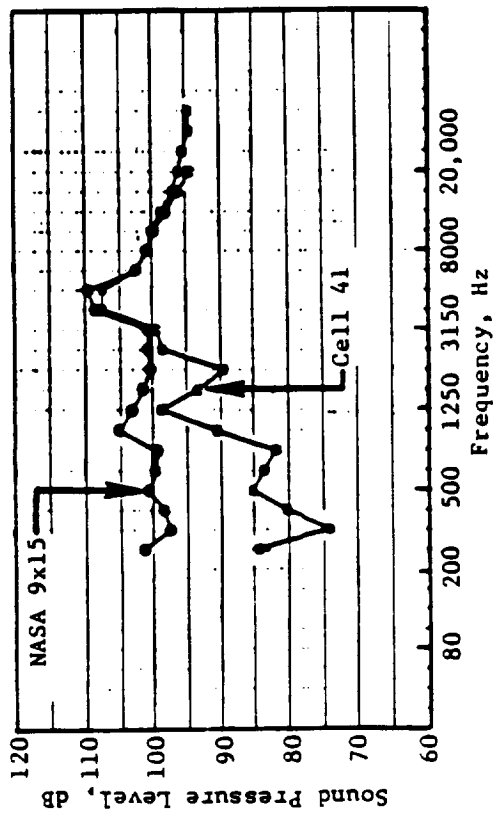
Figure 415. Comparison of Measured Steady-Loading and Rotor-to-Rotor Interaction Noise Data.



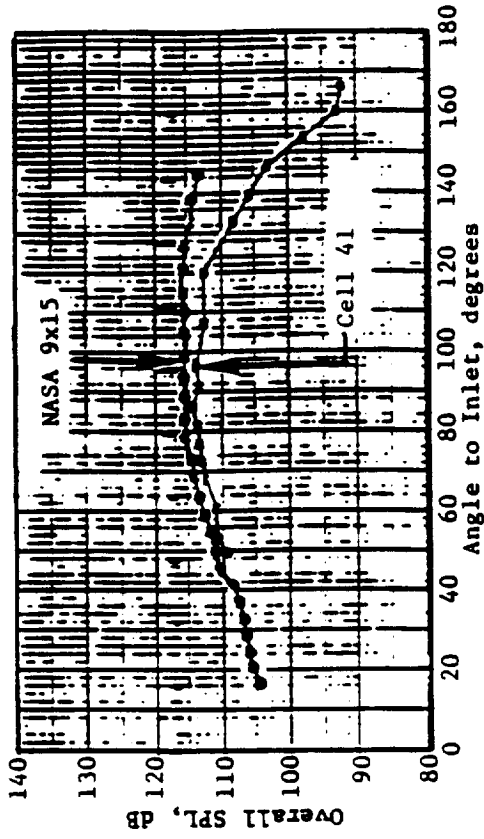
(a) Spectra; Emission Angle, $\theta_e = 50^\circ$



(b) Spectra; Emission Angle, $\theta_e = 91^\circ$



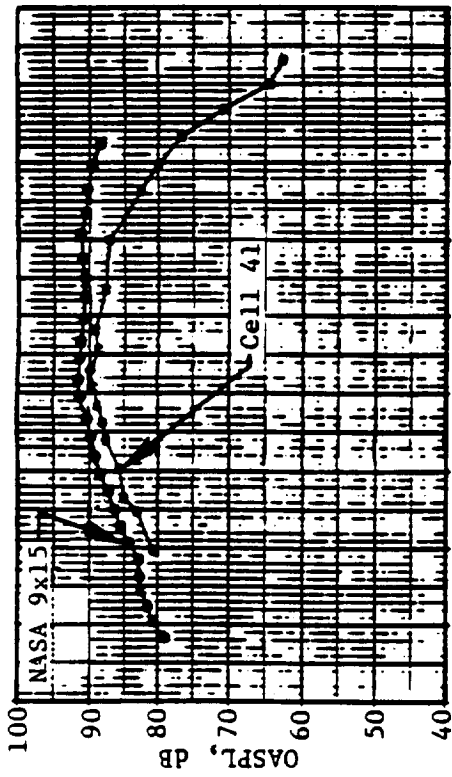
(c) Spectra; Emission Angle, $\theta_e = 120^\circ$



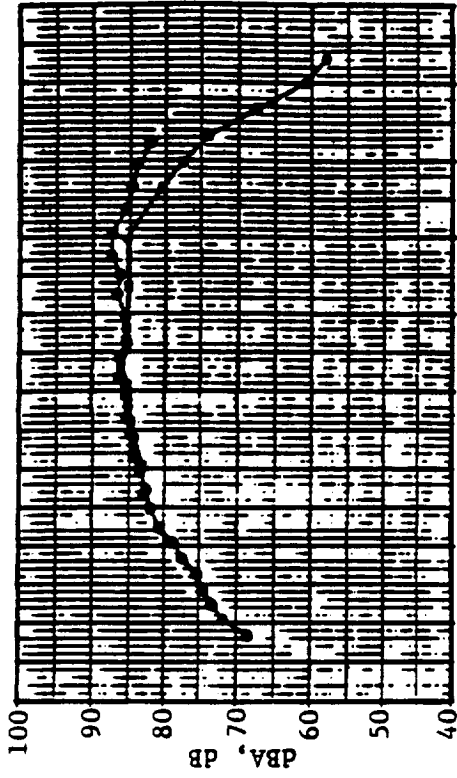
(d) Overall Sound Pressure Level

Figure 416. Selected Model-Scale Spectral and Overall Sound Pressure Level Directivity Comparison of Data Measured at Tip Speed of 247 mps (810 fps).

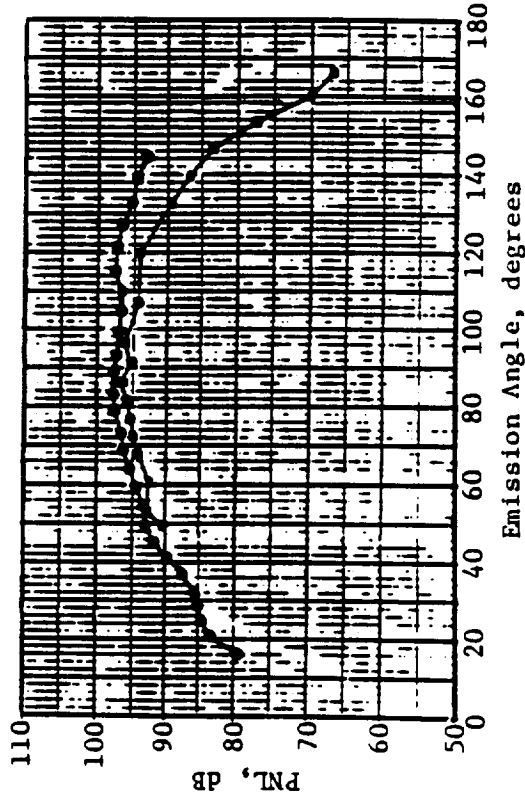
Model Scale: 5.05 m (10 ft) Diameter; Mach No. 0.20; 549 m (1800 ft) Sideline



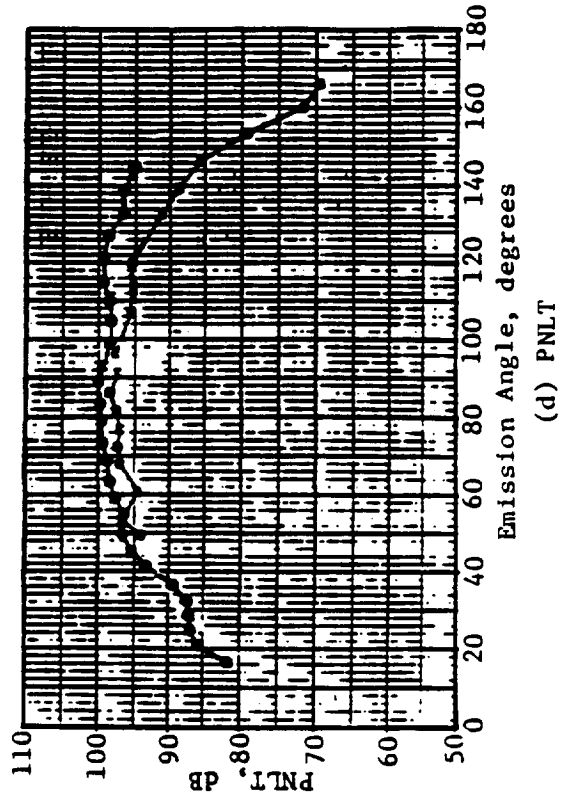
(a) OASPL



(b) dBA



(c) PNL



(d) PNL

Figure 417. Comparison of Cell 41 and NASA 9x15 Measured Model-Scale Acoustic Data.

3.05 m (10 ft) Dia.; Mach No. 0.20; 549 m (1800 ft) Sideline

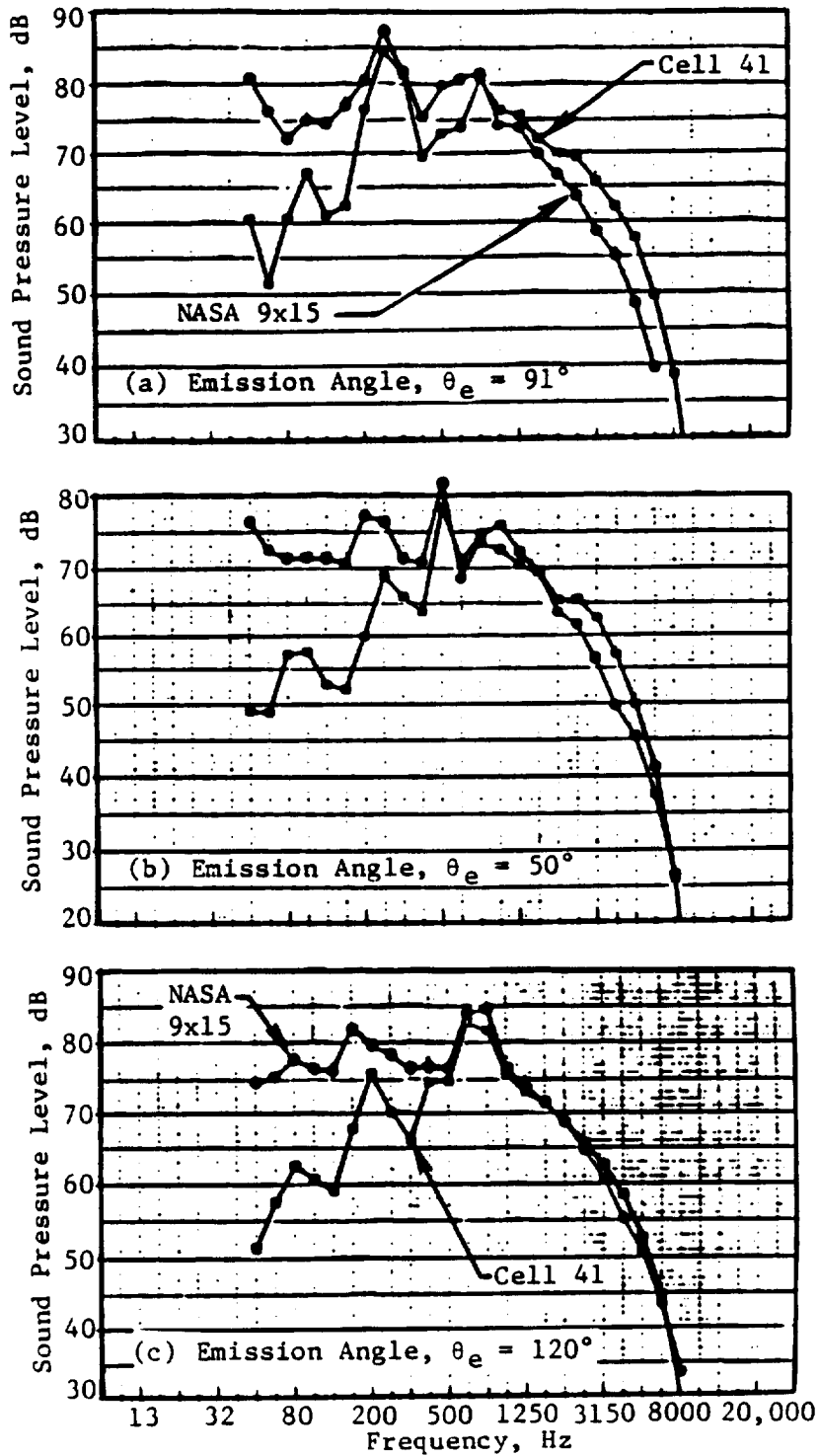


Figure 418. A Comparison of SPL Results Using Cell 41 and NASA 9x15 Measured Model-Scale Data.

ORIGINAL PAGE IS
OF POOR QUALITY

two facilities compares well, differences are noted in broadband noise levels. The low frequency broadband noise levels in the 9x15 wind tunnel are higher; whereas, the higher frequency broadband noise levels are higher at Cell 41.

The OASPL directivity comparison reveals significant differences between the two facilities beyond 120° in the aft quadrant. The reason for this high noise level in the 9x15 tunnel is due to the difference in construction of the test rigs. The Cell 41 test rig collects exhaust gas from the driving turbine and exhausts it outside of the cell; however, the 9x15 wind tunnel test rig exhausts directly out at the back and into the wind tunnel. This causes additional jet noise at aft angles and contaminates the data.

Figures 417 and 418 present a comparison of scaled and extrapolated data. In the plane-of-rotation of the rotors, OASPL, PNL, and PNLT levels measured in the 9x15 wind tunnel are observed to be higher by 1.5 to 2.0 dB, but the dBA levels are almost the same because of the differences in facility spectral content and noise level parameter weighting factors. The shapes of these directivities are very similar up to aft angle of 120°, but diverge later due to the exhaust of the rig into the 9x15 tunnel. The scaled spectral comparison of Figure 418 shows broadband noise level differences noted earlier with the model-scale spectra.

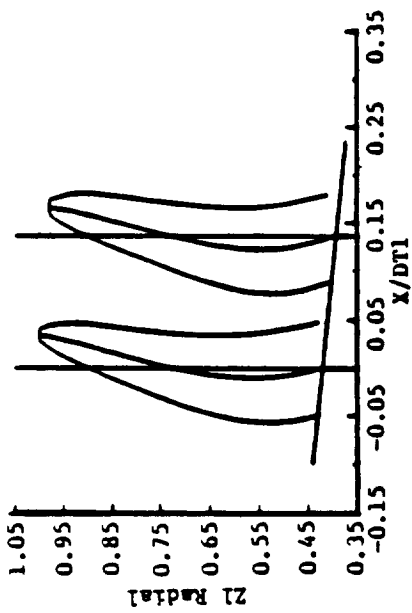
From the acoustic data presented in this section, it is concluded that the shear-layer correction method (Reference 32) which is used to correct the freejet measured data of the anechoic facility is applicable to the Cell 41 setup. In addition, the overall acoustic data from these two facilities are within 2.0 dB, at all angles where meaningful comparisons can be made, with data from the NASA 9x15 wind tunnel being higher, compared to that of Cell 41.

7.3.1.2 Effect of Rotor-to-Rotor Axial Spacing

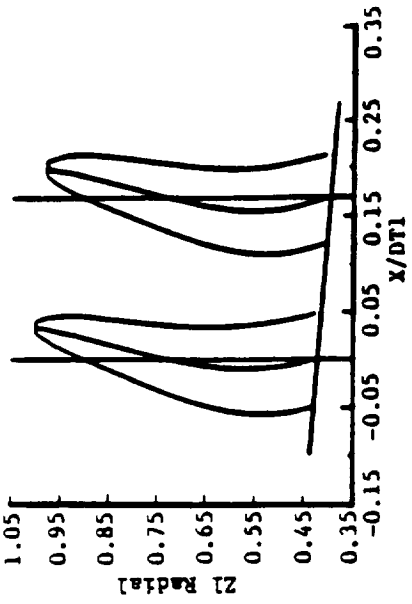
In order to determine the effect, if any, of variation in spacing between pitch-change axes of the forward and aft rotors, MPS tests were conducted at the 9x15 wind tunnel with an F-7/A-7 configuration having 11 forward and 9 aft blades. The pitch angles were set at 36.4°/36.5°, and tests were conducted at three rotor-to-rotor pitch-change-axes spacings. These are identified herein as: minimum ($X/D_t = 0.136$), nominal ($X/D_t = 0.169$), and maximum ($X/D_t = 0.24$) spacings. Figure 419 illustrates the axial projections of the blades for the three test configurations and the impact of increased spacing on the normalized radial distribution of the axial distance between the trailing edge of a forward blade and a 1/4-chord point of an aft blade.

The aerodynamic performance data measured at the three spacings are shown in Figure 420. Accordingly, it is concluded that for acoustic data comparison purposes, there is no significant change in performance for a given tip speed at the test spacings. A typical tone sum noise directivity comparison for the three spacings at a tip speed of 260 mps (850 fps) is provided (Figure 421); thrust and power for the data of Figure 421 are summarized in Table 68.

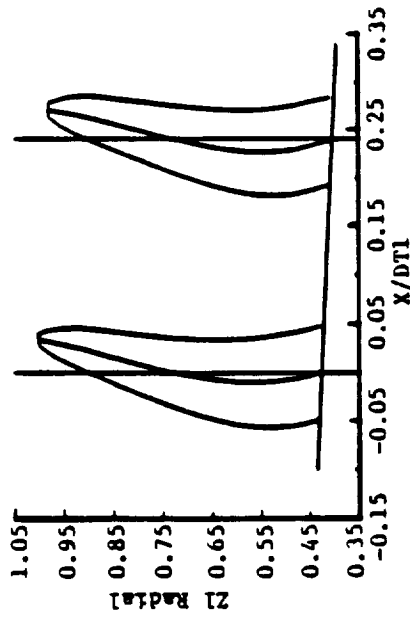
Acoustic data represented in Figure 421 contain directivities of the sum levels of forward and aft rotor BPF's and harmonics; first interaction tone level; sum levels of all interaction tones in the 3rd, 4th, and 5th harmonics; that is, the sum levels of (2A+F), (A+2F), (3A+F), (2A+2F), (A+3F), (4A+F), (3A+2F), (2A+3F), and (A+4F) tones; and sum levels of all interaction tones. Figure 421 also indicates some smaller differences in the directivities of the steady-loading noise with variation in the pitch-change-axes spacings. This is due, perhaps, to observed differences in the thrust split between the two rotors, although total thrust is approximately equal for the three spacings at the test tip speed. An examination of the directivity of the sound pressure level of the first interaction tone



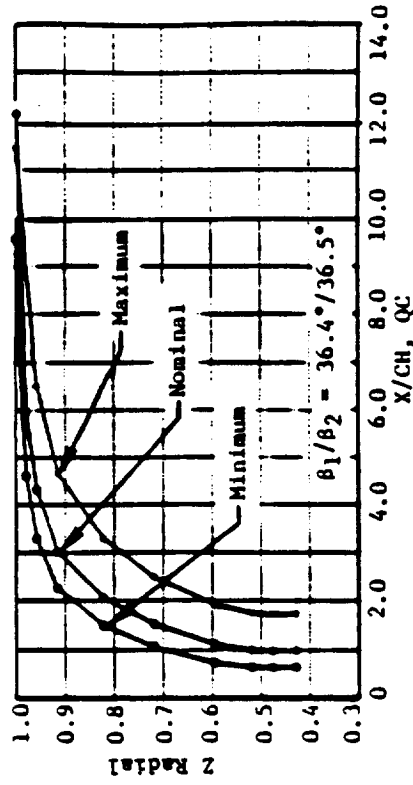
(a) Minimum; $X/D_t = 0.136$



(b) Nominal; $X/D_t = 0.169$

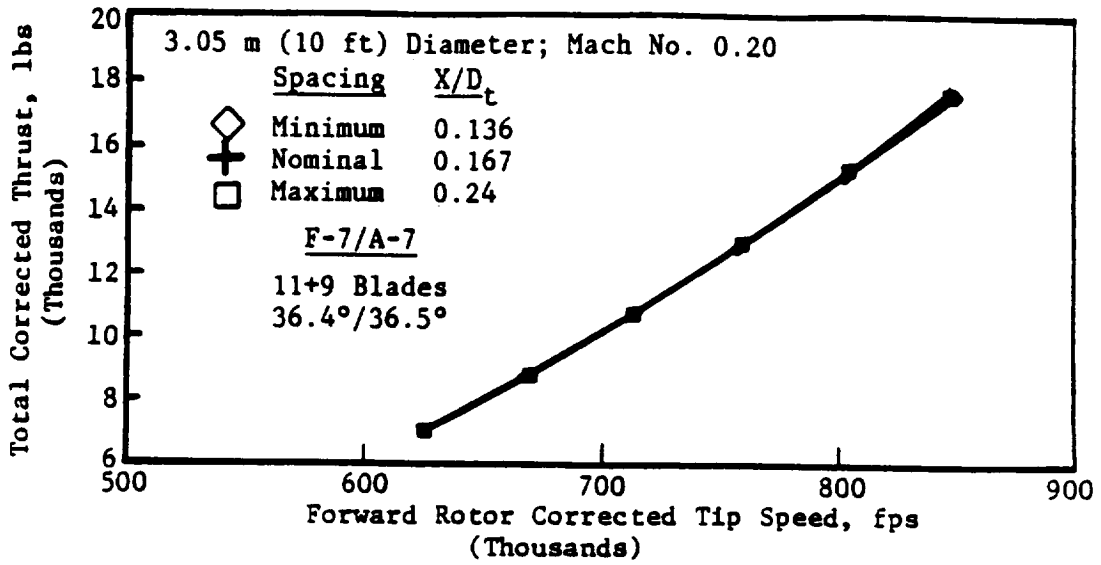


(c) Maximum; $X/D_t = 0.24$

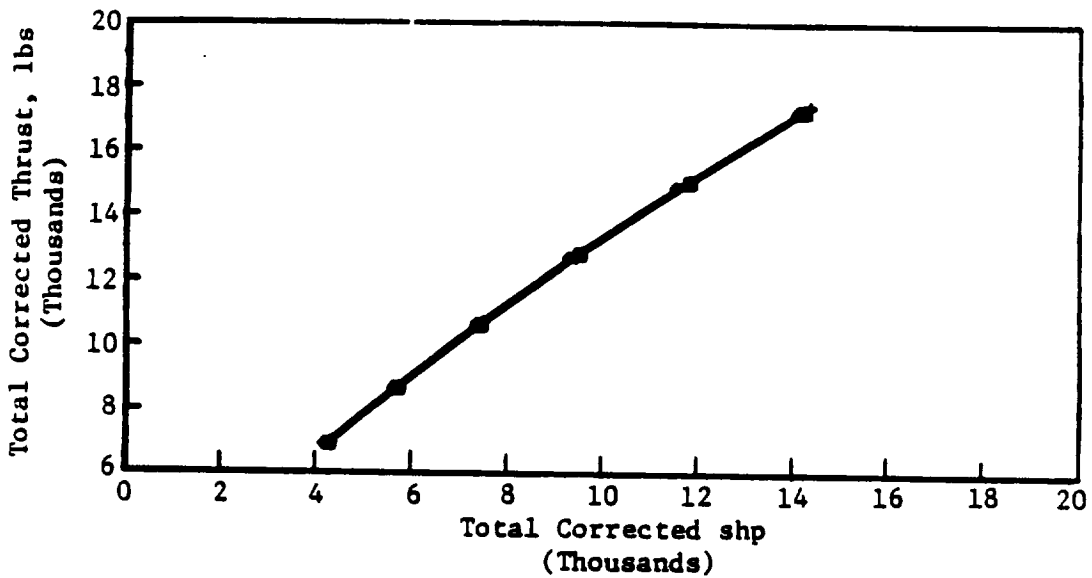


(d) Blade Spacing

Figure 419. Comparison of Axial Projections and Spacing for Pitch-Change-Axes Spacing Tests with F-7/A-7 Blades at the NASA Lewis 9x15 Wind Tunnel.



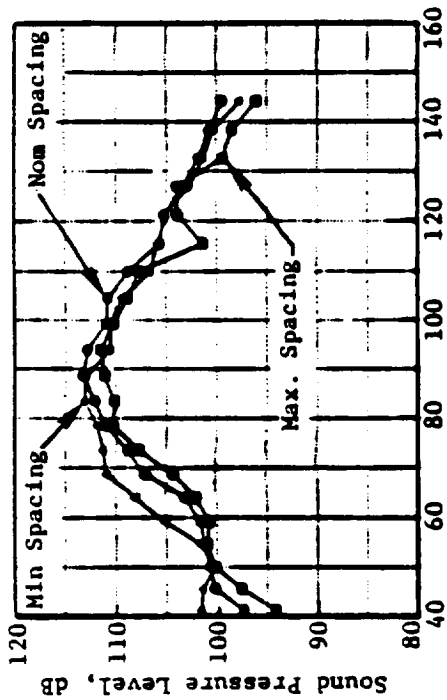
(a) Thrust Versus Tip Speed



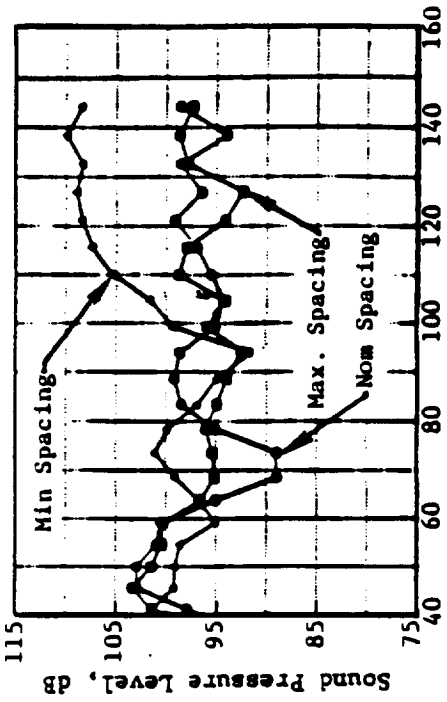
(b) Thrust Versus Shaft Horsepower

Figure 420. Performance Comparison at Three Spacings Between Pitch-Change Axes of Forward and Aft Blades.

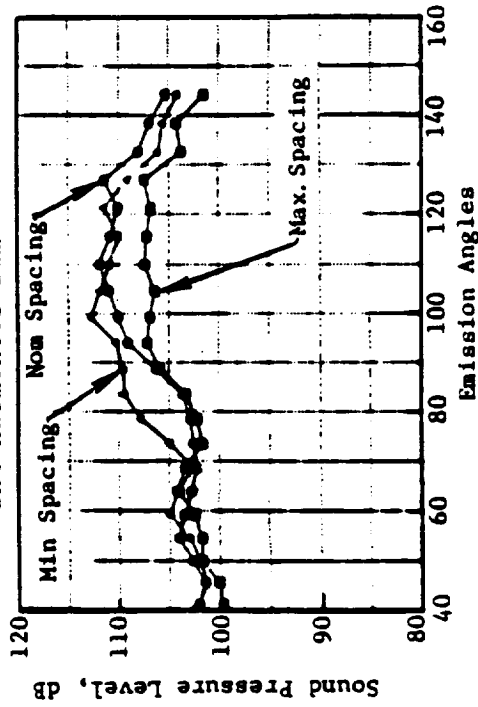
Model Scale: Mach No. 0.2; 8.2 m (27 ft) Sideline



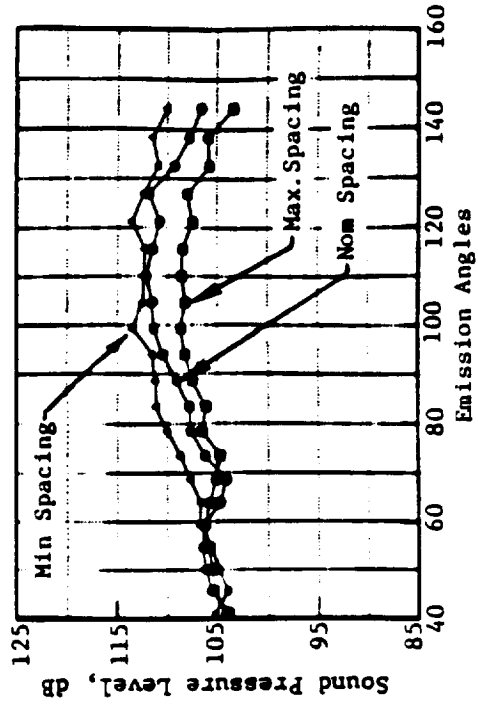
(a) Forward and Aft Rotor BPF's and Harmonics Sum



(b) First Interaction Tone



(c) The 3rd, 4th, and 5th Interaction Tones Sum



(d) All Rotor-to-Rotor Interaction Tones Sum

Figure 421. Model-Scale Tone Sum Directivities of F-7/A-7 for Different Axial Spacings at 260 mps (850 fps).

Table 68. Axial Spacing Comparison for the F-7/A-7 (11+11) MPS Tests in NASA's 9x15 Tunnel.

Spacing	Nominal Thrust				Power			
	Forward		Aft		Forward		Aft	
	N	lb	N	lb	kw	shp	kw	shp
Maximum	1641	(369)	1388	(312)	207	(278)	215	(288)
Nominal	1597	(359)	1486	(334)	204	(273)	225	(302)
Minimum	1757	(354)	1512	(340)	202	(271)	226	(303)

(Figure 421, View B) indicates significant systematic decrease in this interaction tone level, for spacing increase from minimum to nominal, and then from nominal to maximum.

The peak steady-loading noise and peak rotor-to-rotor interaction tone sum levels for these spacings at test tip speeds of 259 mps (850 fps), 232 mps (760 fps), and 190 mps (625 fps) are shown in Figure 422 as a function of the nondimensional-distance between pitch-change axes that is normalized with the maximum chord of the forward blade. These data indicate significant benefit is achieved with spacing increase in the rotor-to-rotor interaction noise sum levels. A decrease in tip speed or thrust for a given pitch setting decreases this benefit; however, the impact on steady-loading noise is minimal and is mainly due to differences in the loading splits between the two rotors.

Similar rotor-to-rotor spacing effects testing was conducted by NASA-Lewis in the 9x15 wind tunnel on a counterrotating propeller configuration with a reduced aft rotor diameter (F7/A3). Results of this testing are presented in Reference 43.

7.3.2 Aerodynamic

Because the 9x15 wind tunnel test emphasis was directed toward acoustics, rather than performance, only limited aerodynamic data was analyzed for this test.

However, Reference 44 presents the effects on aeroperformance parameters of rotor-to-rotor spacing variations and unmatched power split and rotational speed between the rotors for the F-7/A-7 8+8 and 11+9, and the F-7/A-3 11+9 configurations at several different pitch-angle settings, and the F-7/A-7 11+9 configuration. In addition, pylon and fuselage proximity effects on aeroperformance parameters can be determined by evaluating pertinent data from Reference 45 for the F-7/A-7 11+9 and F-7/A-3 11+9 maximum spacing configurations. All data from References 44 and 45 are for a Mach number of 0.20.

7.3.3 Aeromechanical

During all testing conducted in the 9x15 wind tunnel, all of the blade configurations were well-behaved, aeromechanically speaking; no flutter events were observed. Several test conditions and model configurations were investigated; including different Mach numbers (up to Mach 0.22, maximum), different rotor-to-rotor spacings, various pitch-angle settings, the 8+8 and 11+9 blade arrangement configurations, and different angles-of-attack.

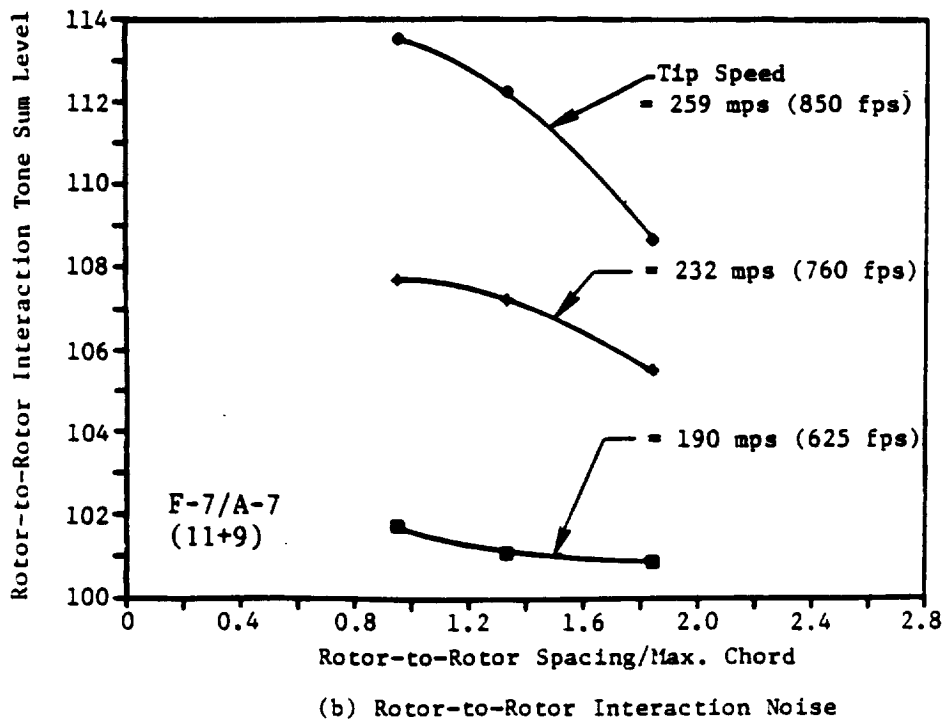
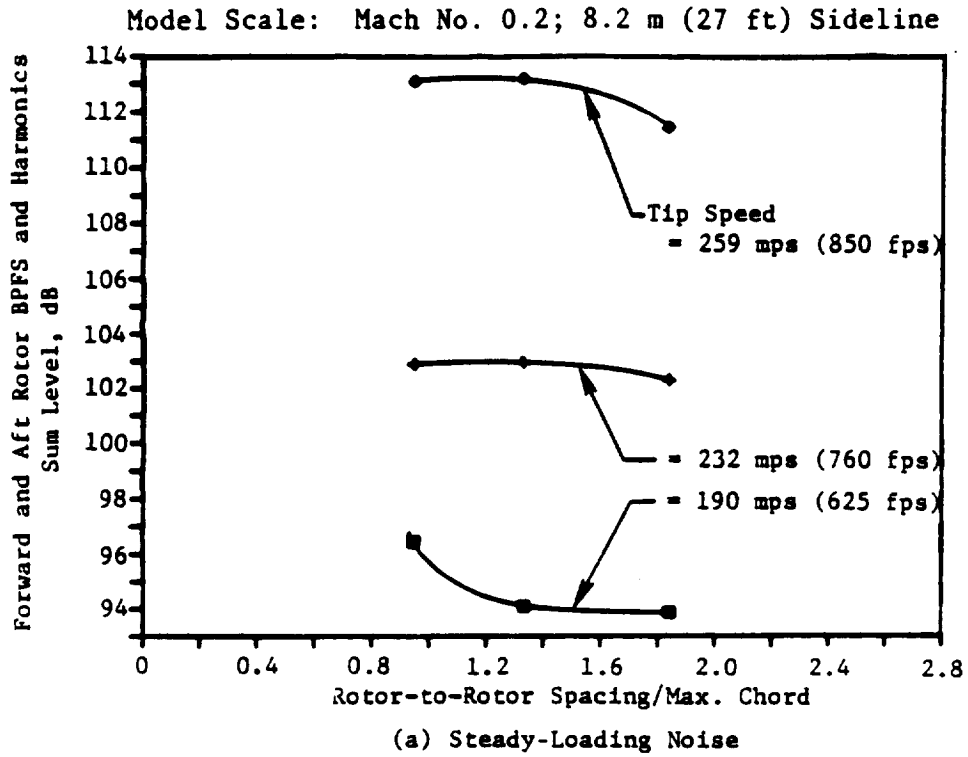


Figure 422. Model-Scale Peak Steady-Loading and Interaction Tone Sum Levels from Three Spacing Tests.

Except for high angles-of-attack (up to 16°) where the 1/rev stress was high, with a maximum value of approximately 7 ksida, or 45% of the 1F scope limits; the stress levels were very much contained (the maximum overall stress level was about 7 ksida).

The high stress level due to the high angle-of-attack was very similar to that observed for the F-4/A-4 blades, previously tested at the BTWT facility. This situation and applicable test results were reported in the Comprehensive Data Report (CDR).

8.0 LOW-RADIUS-RATIO MODULE AND DYNAMIC CALIBRATION LOADING FIXTURE SYSTEM

8.1 Low Module

GE is responsible for the overall design and fabrication of a low-radius-ratio, counterrotating, hub shaft module which will be adaptable to the MPS Rig 3 for use in the 8x6 wind tunnel at NASA Lewis.

This low-radius-ratio hub shaft module design will feature approximate radius ratios of 0.23 and 0.26 for the first- and second-stage rotors, respectively, and a hub balance system having an accuracy goal within the range of 0.5% to 1.5% for both thrust and torque measurements.

As subcontractor to GEAE, the BCAC (Boeing Commercial Airplane Company), has developed the preliminary design, and results from the design study have been approved by the NASA Project Manager. The detailed module design work, including development of manufacturing drawings, has been performed by Boeing with the objective of maximum commonality with the Rig 3 radius-ratio of 0.4. GE supported the design effort with detailed structural dynamic analysis and with design analysis of bearings, seals, and drives as required.

The hardware was fabricated, instrumented, assembled, and provided to NASA at no cost to the contract. GE will be responsible both for delivering the completed hardware to NASA Lewis and for providing the necessary on-site hardware support for the module at NASA Lewis. A chronological history of the work associated with the low-radius-ratio module from the beginning of the contract is presented in the Comprehensive Data Report.

8.2 Dynamic Calibration Rig Loading Fixture Subsystem

GE is responsible for the overall design, including the establishment of design requirements of a dynamic calibration rig capable of being utilized with both the high- and low-radius-ratio MPS modules in the 8x6 wind tunnel area at NASA Lewis. A subcontractor, the Belcan Corporation, has developed the preliminary design, and the results from the preliminary design study have been approved by the NASA Project Manager. The detailed system design work is being performed as follows:

- Dynamometer System and Support Structure – Belcan (Subcontractor)
- Precision Secondary Standard – Boeing
- Calibration Fixture Assembly – GE
- Fixture Interface with Simulator – GE.

The dynamometer system and support structure are being fabricated by Belcan. The dynamic calibration fixture and precision secondary standard will be fabricated, assembled, and provided to NASA at no direct cost to this contract. GE will acceptance-test the dynamic calibration fixture and secondary standard, deliver hardware with drawings and operation manuals to NASA, and provide on-site hardware support at NASA Lewis through the acceptance test.

A chronological history of the activity associated with the dynamic calibration rig is presented in the Comprehensive Data Report.

9.0 CONCLUSIONS

9.1 Acoustic

Because such an extensive amount of acoustic testing, data analyses, and reduction was conducted in the three facilities associated with the execution of NASA Contract NAS3-24080, conclusions resulting from these efforts will be divided into separate sections devoted solely to the findings uncovered from each of these test facilities.

9.1.1 GE Anechoic Freejet Facility (Cell 41)

A comprehensive acoustic test series which was conducted at the GEAE (GE Aircraft Engines) anechoic facility, Cell 41, with the MPS Rig No. 2 tested a total of 49 different configurations, and model-scale data were obtained at more than 800 various test conditions simulating free-field community noise measurements of a counterrotating fan.

During the course of this program, the test facility's anechoic quality was verified, and the repeatability of measured acoustic and aeroperformance results was established. The measured acoustic data were processed to obtain 1/3-octave band and narrow-band spectra. Using the scaling criteria that were evaluated during this program, and as described in Section 3.2.1, the one-third-octave band data were scaled to the desired engine-size. These scaled data were then extrapolated to the required sideline distance, and fly-over analyses were performed to obtain EPNL values. Narrow-band spectra for select test conditions were processed to obtain model-scale directivities of sound pressure levels of various individual tones and tone summations that describe the steady-loading, rotor-to-rotor interaction, and pylon-wake/rotor interaction noise components.

These two sets of acoustic results were analyzed to evaluate different blade designs, blade numbers, rotor-to-rotor spacings, tip speeds, and test Mach numbers. Further, these data were analyzed to determine the benefit with reduced-diameter aft blades and to evaluate the impact of a mounting pylon at two spacings. Analyses of these data led to the following observations and conclusions:

1. The lower sweep and activity factor design of F-5/A-5 ($15^\circ/18^\circ$; 120/126) is noisier than the higher sweep and activity factor of the baseline F-7/A-7 ($34^\circ/31^\circ$; 147/152) or the F-1/A-1 ($33^\circ/30^\circ$; 150/158) designs. Due to a slightly improved performance, the F-1/A-1 is quieter than the F-7/A-7; however, the F-11/A-11 blades, also possessing a high sweep and higher activity factor ($37^\circ/34^\circ$; 180/200) and, hence a wider chord, yielded a slightly smaller rotor-to-rotor interaction noise than did the F-7/A-7. However, this design did not yield any significant EPNL benefit relative to a comparable F-7/A-7 configuration.
2. An increased blade count produces acoustic benefit that is particularly significant, as it is twofold. Steady-loading noise decreases due to a reduction in blade loading and tip speed. A consequence of this is the second benefit; namely, a decrease in rotor-to-rotor interaction noise caused by aft rotor blades rotating at a lower tip speed interacting with weakened wakes and tip vortices from the forward rotor blades. The combined effect results in an acoustic benefit of, perhaps, 9.6 EPNdB at a thrust of 44,500 N (10,000 lb) for a blade number increase from a 4+4 to an 8+8 configuration, at nominal spacing ($X/D_t = 0.17$). Likewise, an increased blade count, from an 8+8

configuration to an 11+9, both set at maximum rotor-to-rotor spacing ($X/D_t = 0.24$), results in an additional benefit of 3.4 EPNdB. This added benefit increases to 5 EPNdB for a typical takeoff thrust of 62,300 N (14,000 lb).

3. For all unclipped F-7/A-7 configurations tested in this study, the benefit of increased spacing between the rotor pitch-change axes from nominal ($X/D_t = 0.17$) to maximum ($X/D_t = 0.24$) was limited to 1 EPNdB at takeoff and 1.5 EPNdB at cutback. For an aft-reduced-diameter blade configuration; however, this spacing benefit increased to 2.5 EPNdB at takeoff and 5.5 dB at cutback. This increased benefit of spacing with the aft-clipped blade configurations was due to significant reductions noted in the interaction tones of the second, third, fourth, and fifth harmonics, and in particular, in the levels of A+F, A+2F, A+3F and A+4F tones. Assuming that the length of clipping on the aft blade was sufficient to prevent any interaction of the tip vortex of the forward blade with the aft blade, the reductions are attributed to increased decay of the forward blade wakes with increased rotor-to-rotor spacing. Similar reductions in the interaction tone levels, as a result of spacing, were not fully evident with the equal-diameter blade configurations, as their levels were masked by the interaction noise due to the forward blade tip vortex interacting with the aft rotor blades.
4. For a given thrust and blade number, the steady-loading noise decreases with tip speed. A reduction in total noise is also attained with a decrease in tip speed; however, decreasing the tip speed beyond an optimum increases the overall noise levels. The increased pitch angle required to produce a given thrust at a lower tip speed may result in stronger wakes; this, together with the accompanying reduction in spacing between blades as a result of the blade-pitch angle change, causes the rotor-to-rotor interaction noise to increase for a decrease of tip speed beyond the optimum.
5. A reduced-diameter, aft blade configuration produced dramatic reductions in sound pressure levels beyond the 3xBPF compared to an equal-diameter blade configuration. Significant reductions observed in interaction tone sum levels are attributed mainly to the absence of vortex/rotor interaction tones. The net benefit in EPNL between F-7/A-7 (9+8) unclipped and clipped configurations was in the range of 2 dB.
6. The combined effects of improved efficiency, increased duration correction, and reduced tip speed resulted in EPNL data for a Mach number decrease from 0.3 to 0.2 to correlate within a band of 2 dB.
7. The pylon effect is noted mostly at the BPF and 2xBPF of the forward rotor; the impact of the pylon/rotor interaction noise depends on the levels of steady-loading noise of the configurations. Higher steady-loading noise levels such as are expected with higher thrust settings or with configurations having a low blade count mask the influence of the pylon. The pylon effect, generally, is more significant at conditions with low steady-loading noise, such as cutback and approach. In addition, an increase in spacing between the pylon and forward rotor results in an increased decay of the pylon-wake defect and reduces the impact of pylon on the forward rotor. Presence of a pylon had no effect on the rotor-to-rotor interaction noise levels.

9.1.2 NASA Lewis 8x6 Wind Tunnel

The analysis of the acoustic data acquired from testing of the F-7/A-7, F-11/A-11, and F-21/F-21 blade configurations on MPS SN003 in the NASA Lewis 8x6 wind tunnel led to the following observations and conclusions:

1. Analyses of data obtained with the translating acoustic plate in the untreated, working section of the NASA 8x6 wind tunnel included a comparison of these data both with free-field data from an equivalent test in a treated wind tunnel, and with the results of analytical prediction. This comparison reveals that these measurements, in and aft of the peak noise region, can provide useful information with regard to the noise generated by counterrotating fan models at high subsonic flight speeds; however, those data forward of the peak region are contaminated by the presence of the boundary layer on the plate.
2. Effects of changes in pitch-change-axis spacing are reflected in the rotor-to-rotor interaction tones. At the high helical tip Mach numbers studied, steady-loading and thickness sources dominate, leading to negligible changes in the tone noise of the equal blade number and equal rpm cases examined.
3. Reducing the steady-loading noise by increasing the number of blades does not, as in the low speed case, necessarily reduce the BPF tone levels. Thickness (volume displacement) noise is a prime contributor, whose importance becomes more apparent as the loading per blade is reduced. The noise from blade designs which have a high tip helical Mach number is a function of the phase relationship between these sources.

9.1.3 NASA Lewis 9x15 Wind Tunnel

The analysis of the acoustic data acquired during testing of the F-7/A-7 and F-11/A-11 blade configurations on MPS SN003 in the NASA Lewis 9x15 wind tunnel yielded the following observations and conclusions:

1. The comparison of acoustic data measured at the NASA Lewis 9x15 wind tunnel with the corresponding Cell 41 test data indicates these acoustic data are comparable. However, the data from the NASA 9x15 tunnel is found to have measured overall levels that are higher by approximately 2 dB than that of Cell 41. While the 9x15 wind tunnel has a higher low frequency broadband level compared to Cell 41, it was also noted to have a lower level of high frequency broadband noise relative to that of the Cell 41.
2. The rotor-to-rotor interaction noise level benefit noted during the Cell 41 spacing tests was confirmed by the tests at NASA's 9X15 wind tunnel.
3. The comparison of the data from Cell 41 and the NASA 9x15 wind tunnel facilities demonstrates the applicability of the method (described in Reference 32) that has been used to correct the freejet simulated acoustic data of Cell 41.

9.2 Aerodynamics

Scale model, counterrotating unducted fan configurations were tested in NASA's 8x6 and 9x15 wind tunnels, the BTWT (Boeing transonic wind tunnel), and in GE's anechoic chamber, freejet

facility, Cell 41. Aerodynamic performance data were measured for each configuration over a wide range of Mach numbers and pitch angles. Also, effects of loading, rotor-to-rotor spacing, number of blades, pylon/angle-of-attack, mismatched rotor speeds, and blade clipping were demonstrated. The most significant performance results are as follows:

1. Data were obtained with several blade-angle combinations, up to a maximum Mach number of 0.90. The corrected net efficiency at the maximum climb Mach 0.72 design point is 82%; the efficiency at takeoff is 62%.
2. Large rotor-to-rotor spacings have a significant effect on the net efficiency at high Mach numbers.
3. When the advance ratio is corrected by $\text{Cos } \alpha$ to account for the skewed thrust direction, power coefficient lines at different angles-of-attack and constant-pitch angles collapse to a single line.
4. The symmetrical pylon, installed at an angle-of-attack, acts like an inlet guide vane, producing swirl to the forward rotor; this swirl unloads or loads the forward rotor, depending on the direction of its rotation with respect to the pylon. If pitch angles are not changed to compensate for this, unequal torque splits between rotors result.
5. Data taken with unequal rotor speeds show very little effect on efficiency at loadings and torque ratios near the cruise design point. When the torque ratios are substantially different from 1.0, the overall efficiency can be 2 to 5 points lower than nominal.
6. Clipping the blades at the tip (for stability) has a significantly adverse effect on blade performance.
7. The shape of the forebody and aftbody can have a significant effect on performance, demonstrating the need for hub flowpath area-ruling.
8. The F-4/A-4 and F-5/A-5 blade designs with lower aero tip sweep demonstrated lower aero performance.
9. The higher aspect ratio F-5/A-5 configuration was approximately 1 point worse in efficiency at high speed than was the F-4/A-4 configuration.

9.3 Aeromechanics

An evaluation of the test programs conducted in the GE anechoic chamber (Cell 41), and in the NASA Lewis 8x6 and 9x15 wind tunnel facilities revealed that except for blade design, where blade sweep, thrust, camber, etc. are considered, the effects of the major variable engine design parameters of interest (such as, rotor-to-rotor spacing, blade number, reduced-diameter-aft blades, and pylon presence) had no significant impact on the aeromechanical performance of the F-4/A-4, F-5/A-5, F-7/A-7, F-11/A-11, and F-21/A-21 MPS blade configurations.

10.0 REFERENCES

1. Alsip, M.N., Sullivan, J.P., and Keith, J., "Numerical Methods Applied to the Design and Analysis of a Cascade of Wings," NASA CR-182208, October 1988.
2. Smith, L.H., Jr., "Unducted Fan Aerodynamic Design," ASME Paper No. 87-GT-233, June 1987.
3. Rohrbach, C., Metzger, F.B., Black, D.M., and Ladden, R.M., "Evaluation of Wind Tunnel Performance Testing of an Advanced 455 Swept Eight-Bladed Propeller at Mach Numbers from 0.45 to 0.85," Hamilton-Standard, Windsor Locks, Connecticut, NASA Contractor Report 3505, NAS3-20769, March 1982.
4. Glauert, H., "Airplane Propeller," *Aerodynamic Theory*, Vol. IV, W.F. Durand, Ed., Dover, 1963.
5. Gutin, L., "On the Sound Field of a Rotating Propeller," Translated as NACA Technical Memorandum No. 1195, 1983.
6. Morse, P.M. and Ingard, K.U., *Theoretical Acoustics*, McGraw-Hill Book Company, New York, 1968.
7. Knowles, K., "Importance of Broadband Noise for Advanced Turboprops," *Journal of Aircraft*, Vol. 24, No. 6, 1987, pp. 386-391.
8. Farassat, F., "Quadrupole Source in Prediction of the Noise of Rotating Blades - A New Source Description," AIAA-87-2675, AIAA 11th Aeroacoustics Conference, October 1987.
9. Hanson, D.B. and Fink, M.R., "The Importance of Quadrupole Sources in Prediction of Transonic Tip Speed Propeller Noise," *Journal of Sound and Vibration*, Vol. 62, No. 1, 1979, pp. 19-38.
10. Holmes, D.G. and Tong, S.S., "A Three-Dimensional Euler Solver for Turbomachinery Blade Rows," *Journal of Engineering for Gas Turbine and Power*, Vol. 107, April 1985, pp. 258-264.
11. Whitfield, C.E., Glibe, P.R., Mani, R., and Mungur, P., "High Speed Turboprop, Aeroacoustic Study (Single Rotation)," NASA CR-182257, May 1989.
12. Majjigi, R.K. and Glibe, P.R., "Development of a Rotor Wake/Vortex Model," NASA-CR-174849, June 1984.
13. Majjigi, R.K., Venishi, K., and Glibe, P.R., "An Investigation of Counterrotating Tip Vortex Interaction," NASA CR-185135, October 1989.
14. Hanson, D.B., "Helicoidal Surface Theory for Harmonic Noise of Propellers in the Far Field," *AIAA Journal*, Vol. 18, No. 10, October 1980, pp. 1213-1220.
15. Richards, E.J. and Mead, D.J., Eds., *Noise and Fatigue in Aeronautics*, John Wiley and Sons, London, England, 1968.
16. Mixson, J.S., Farassat, F., et al., "Interior Noise Considerations for Advanced High Speed Turboprop Aircraft," *AIAA Journal of Aircraft*, Vol. 20, No. 9, September 1983.

17. Rauscher, M., *Introduction to Aeronautical Dynamics*, John Wiley and Sons, Inc., 1953, p. 373.
18. Sears, W.R., "Some Aspects of Nonstationary Aerofoil Theory," *Journal of Aeronautical Sciences*, Vol. 8, 1941, pp. 104-118.
19. Amiet, R.K., "Effects of Compressibility in Unsteady Lift Theories," Article in *Unsteady Aerodynamics*, R.B. Kinney, Ed., Proceedings of a Symposium on Unsteady Aerodynamics, University of Arizona, March 18-20, 1975, pp. 631-653.
20. Johnsen, I.A., et al., Eds., "Aerodynamic Design of Axial Flow Compressors," NASA SP-36, 1965.
21. Lakshminarayana, B., "Methods of Predicting the Tip Clearance Effects in Axial Flow Turbomachinery," *ASME Journal of Basic Engineering*, Vol. 92, Series D., September 1970, pp. 467-482.
22. Lamb, H., *Hydrodynamics*, 6th Edition, Dover Publications, New York, 1945, p. 224.
23. Mason, W.H. and Marchman, J.F., III, "The Farfield Structure of Aircraft Wake Turbulence," AIAA Paper No. 72-40, 1972
24. Grow, T.L., "Effect of a Wing on its Tip Vortex," *Aircraft*, Vol. 6, Number 1, January-February 1969, pp. 37-41.
25. McCormick, B.W., Tangler, J.L., and Sherrieb, H.E., "Structure of Trailing Vortices," *Journal of Aircraft*, Vol. 5, No. 1, May-June 1968, pp. 260-267.
26. Tangler J.L., Wohlfeld, R.M., and Miley, S.J., "An Experimental Investigation of Vortex Stability, Tip Shapes, Compressibility, and Noise for Hovering Model Rotors," NASA CR-230d5, September 1973.
27. Kemp, H.H. and Sears, W.R., "The Unsteady Forces Due to Viscous Wakes in Turbomachinery," *Journal of Aeronautic Sciences*, Vol. 22, No. 7, July 1955, pp. 478-483.
28. Bisplinghoff, R.L., et al., *Aeroelasticity*, Addison-Wesley Publishing Co., Inc., 1955.
29. Swallow, R.J. and Aiello, R.A., "NASA Lewis 8x6 Foot Supersonic Wind Tunnel," NASA TMX-71542, May 1974.
30. Hughes, Christophere E., "Flowfield Measurements in the NASA Lewis Research Center 9-by 15-foot Low-Speed Wind Tunnel," NASA TM 100883, March 1987.
31. Yuska, J.A., Diedrich, J.H., and Clough, N., "Lewis 9x15 Foot V/STOL Wind Tunnel." NASA TMX-2305, July 1971.
32. Ahuja, K.K., Tester, B.J., and Tanna, H.K., "The Freejet as a Simulator of Forward Velocity Effects on Jet Noise," NASA CR-3056, October 1978.
33. Shields, F.D. and Bass, H.E., "Atmospheric Absorption of High Frequency Noise and Amplification to Fractional Octave Bands." University of Mississippi, NASA CR-2760, June 1977.
34. Dittmar, J.H., "The Effect of Front-to-Rear Propeller Spacing on the Interaction of Noise of a Model Counterrotation Propeller at Cruise Conditions," NASA TM 100121, August 1987.

35. Dittmar, J.H., "The Cruise Noise of Counterrotation Propeller of Angle of Attack in Wind Tunnel," NASA TM 88869, October 1986.
36. Dittmar, J.H. and Stang, D.B., "Noise Reduction for Model Counterrotation Propeller at Cruise by Reducing Aft-Propeller Diameter," NASA TM 88936, May 1987.
37. Woodward, R.P., "Noise of a Model High Speed Counterrotation Propeller and Simulated Takeoff/Approach Conditions (F-7/A-7)," NASA TM 100206, October 1987.
38. Krynytzky, A.J., "Mach Number Corrections for a Two-Foot Propeller Rig in Solid and Slotted Test Sections," AIAA 88-2056, AIAA 15th Aerodynamic Testing Conference, May 1988.
39. Dittmar, J.H., Blaha, B.J., and Jeracki, R.J., "Tone Noise of Three Supersonic Tip Speed Propellers in a Wind Tunnel at 0.8 Mach Number," NASA TM 79046, December 1978.
40. Dittmar, J.H. and Lasagna, P.L., "A Preliminary Comparison Between the SR-3 Propeller Noise in Flight and in a Wind Tunnel," NASA TM 82805, April 1982.
41. Dittmar, J.H., Lasagna, P.L., and Mackall, K.G., "A Preliminary Comparison Between the SR-6 Propeller Noise in Flight and in a Wind Tunnel," NASA TM 83341, May 1983.
42. Dittmar, J.H., Burns, R.J., and Leciejewski, D.J., "An Experimental Investigation of the Effect of Boundary Layer Refraction on the Noise from a High Speed Propeller," NASA TM 83764, September 1984.
43. Woodward, R.P. and Gordan, E.P., "Noise of a Model Counterrotation Propeller with Reduced Aft Rotor Diameter at Simulated Takeoff/Approach Conditions (F-7/A-3)," NASA TM 100254d/AIAA-88-0263, December 1987.
44. Hughes, Christopher E. and Gayyaniga, John A., "Summary of Low-Speed Wind Tunnel Results of Several High-Speed Counterrotation Propeller Configurations," NASA TM 100945/AIAA-88-3149, July 1988.
45. Hughes, Christopher E. and Gayyaniga, John A., "Low-Speed Wind Tunnel Performance of High-Speed Counterrotation Propellers Angle-of-Attack," NASA TM 102292/AIAA-89-2583, July 1989.



1. Report No. NASA CR-185158	2. Government Accession No.	3. Recipient's Catalog No.	
4. Title and Subtitle Experimental Performance and Acoustic Investigation of Modern, Counterrotating Blade Concepts - Final Report		5. Report Date January 1990	
		6. Performing Organization Code	
7. Author(s) G.E. Hoff, et al.		8. Performing Organization Report No.	
		10. Work Unit No. 535-03-01	
9. Performing Organization Name and Address GE Aircraft Engines One Neumann Way P.O. Box 156301 Cincinnati, Ohio 45215-6301		11. Contract or Grant No. NAS3-24080	
		13. Type of Report and Period Covered Contractor Report 11/83-12/87	
12. Sponsoring Agency Name and Address NASA-Lewis Research Center 21000 Brookpark Road Cleveland, Ohio 44135		14. Sponsoring Agency Code	
		15. Supplementary Notes Project Manager, F.M. Humenik, Propulsion Systems Division NASA-Lewis Research Center	
16. Abstract <p>This report describes the work performed by GEAE (GE Aircraft Engines) on NASA Contract NAS3-24080 to evaluate, both theoretically and experimentally, the aerodynamic, acoustic, and aeromechanical performance of GE-defined counterrotating blade concepts. Analytical methods development and design are addressed in this document. Utilizing the analytical methods which evolved during the conduct of this work, aerodynamic and aeroacoustic predictions were developed, which were, in turn, compared to NASA and GE wind tunnel test results.</p> <p>The detailed mechanical design and fabrication of five different composite shell/titanium spar counterrotating blade set configurations are presented. Design philosophy, analyses methods, and material geometry are addressed, as well as the influence of aerodynamics, aeromechanics, and aeroacoustics on the design procedures. Blade fabrication and quality control procedures are detailed; bench testing procedures and results of blade integrity verification are presented; and instrumentation associated with the bench testing also is identified. Additional hardware to support specialized testing is also described, as are operating blade instrumentation and the associated stress limits.</p> <p>The five GE-designed counterrotating blade concepts were scaled to a tip diameter of 2 feet, so they could be incorporated into MPS (model propulsion simulators). Aerodynamic and aeroacoustic performance testing was conducted in the NASA Lewis 8x6 supersonic and 9x15 V/STOL (vertical or short takeoff and landing) wind tunnels and in the GE freejet anechoic test chamber (Cell 41) to generate an experimental data base for these counterrotating blade designs. Test facility and MPS vehicle matrices are provided, and test procedures are presented. Effects on performance of rotor-to-rotor spacing, angle-of-attack, pylon proximity, blade number, reduced-diameter aft blades, and mismatched rotor speeds are addressed. Counterrotating blade and specialized aeromechanical hub stability test results are also furnished herein.</p>			
17. Key Words (Suggested by Author(s)) MPS (Model Propulsion Simulator, Propfan, Counterrotating Blades, Unducted Fan, Acoustic and Performance Experiments		18. Distribution Statement Unlimited Distribution	
19. Security Classif. (of this report) Unclassified	20. Security Classif. (of this page) Unclassified	21. No. of Pages	22. Price

